107 Springer Proceedings in Physics

A. G. Cullis
J. L. Hutchison
(Eds.)

Microscopy of Semiconducting Materials

Proceedings of the
14th Conference,
April 11–14, 2005, Oxford, UK

Springer

SPRINGER PROCEEDINGS IN PHYSICS 107

SPRINGER PROCEEDINGS IN PHYSICS

87 **Proceedings of the 25th International Conference on the Physics of Semiconductors**
Editors: N. Miura and T. Ando

88 **Starburst Galaxies**
Near and Far
Editors: L. Tacconi and D. Lutz

89 **Computer Simulation Studies in Condensed-Matter Physics XIV**
Editors: D.P. Landau, S.P. Lewis, and H.-B. Schüttler

90 **Computer Simulation Studies in Condensed-Matter Physics XV**
Editors: D.P. Landau, S.P. Lewis, and H.-B. Schüttler

91 **The Dense Interstellar Medium in Galaxies**
Editors: S. Pfalzner, C. Kramer, C. Straubmeier, and A. Heithausen

92 **Beyond the Standard Model 2003**
Editor: H.V. Klapdor-Kleingrothaus

93 **ISSMGE**
Experimental Studies
Editor: T. Schanz

94 **ISSMGE**
Numerical and Theoretical Approaches
Editor: T. Schanz

95 **Computer Simulation Studies in Condensed-Matter Physics XVI**
Editors: D.P. Landau, S.P. Lewis, and H.-B. Schüttler

96 **Electromagnetics in a Complex World**
Editors: I.M. Pinto, V. Galdi, and L.B. Felsen

97 **Fields, Networks, Computational Methods and Systems in Modern Electrodynamics**
A Tribute to Leopold B. Felsen
Editors: P. Russer and M. Mongiardo

98 **Particle Physics and the Universe**
Proceedings of the 9th Adriatic Meeting, Sept. 2003, Dubrovnik
Editors: J. Trampetić and J. Wess

99 **Cosmic Explosions**
On the 10th Anniversary of SN1993J (IAU Colloquium 192)
Editors: J. M. Marcaide and K. W. Weiler

100 **Lasers in the Conservation of Artworks**
LACONA V Proceedings, Osnabrück, Germany, Sept. 15–18, 2003
Editors: K. Dickmann, C. Fotakis, and J.F. Asmus

101 **Progress in Turbulence**
Editors: J. Peinke, A. Kittel, S. Barth, and M. Oberlack

102 **Adaptive Optics for Industry and Medicine**
Proceedings of the 4th International Workshop
Editor: U. Wittrock

103 **Computer Simulation Studies in Condensed-Matter Physics XVII**
Editors: D.P. Landau, S.P. Lewis, and H.-B. Schüttler

104 **Complex Computing-Networks**
Brain-like and Wave-oriented Electrodynamic Algorithms
Editors: I.C. Göknar and L. Sevgi

105 **Computer Simulation Studies in Condensed-Matter Physics XVIII**
Editors: D.P. Landau, S.P. Lewis, and H.-B. Schüttler

106 **Modern Trends in Geomechanics**
Editors: W. Wu and H.S. Yu

107 **Microscopy of Semiconducting Materials**
Proceedings of the 14th Conference, April 11–14, 2005, Oxford, UK
Editors: A.G. Cullis and J.L. Hutchison

Volumes 60–86 are listed at the end of the book.

A.G. Cullis J.L. Hutchison
(Eds.)

Microscopy of Semiconducting Materials

Proceedings of the 14th Conference,
April 11–14, 2005, Oxford, UK

With 489 Figures

Springer

Professor A.G. Cullis
Department of Electronic
and Electrical Engineering
University of Sheffield
Mappin Street
Sheffield, S1 3JD, UK

Dr J.L. Hutchison
Department of Materials
University of Oxford
Parks Road
Oxford, OX1 3PH, UK

Published in association with Canopus Publishing Limited, Bristol, UK

ISSN 0930-8989

ISBN-10 3-540-31914-X Springer Berlin Heidelberg New York

ISBN-13 978-3-540-31914-6 Springer Berlin Heidelberg New York

Library of Congress Control Number: 2005939046

This work is subject to copyright. All rights are reserved, whether the whole or part of the material is concerned, specifically the rights of translation, reprinting, reuse of illustrations, recitation, broadcasting, reproduction on microfilm or in any other way, and storage in data banks. Duplication of this publication or parts thereof is permitted only under the provisions of the German Copyright Law of September 9, 1965, in its current version, and permission for use must always be obtained from Springer-Verlag. Violations are liable to prosecution under the German Copyright Law.

Springer is a part of Springer Science+Business Media.
springer.com
© Springer-Verlag Berlin Heidelberg 2005
Printed in the UK

The use of general descriptive names, registered names, trademarks, etc. in this publication does not imply, even in the absence of a specific statement, that such names are exempt from the relevant protective laws and regulations and therefore free for general use.

Cover concept: eStudio Calamar Steinen
Cover production: *design & production* GmbH, Heidelberg
Printing: Short Run Express, Exeter, UK

Printed on acid-free paper SPIN: 11610021 54/3141/mh 5 4 3 2 1 0

Preface

This volume contains the invited and contributed papers presented at the fourteenth conference on 'Microscopy of Semiconducting Materials' held at the University of Oxford on 11–14 April 2005. The event was organised with sponsorship by the Royal Microscopical Society, the Electron Microscopy and Analysis Group of the Institute of Physics and the Materials Research Society. This conference series focuses upon the most recent international advances in semiconductor studies carried out by all forms of microscopy: its truly international flavour was evident in that it was attended by delegates from approaching 20 countries.

Semiconducting materials allow the fabrication of advanced (opto)electronic devices ranging from ultrahigh speed FET and bipolar transistors to light emitters and detectors covering a very wide range of photon frequencies. However, to achieve the ultimate performance it is essential to optimise the structures of transistors with feature sizes often of less than 0.1 microns and also to understand the nature of, for example, advanced alloys of III-V and especially III-nitride materials. Efficient control of semiconductor processing on the nanometre scale is a vital concern and in order to achieve all of these goals, it is essential to exploit the techniques of advanced microscopy to characterise the materials at close to the atomic scale. For the highest spatial resolution, electron microscopy in its various forms provides the most wide-ranging information. Recent advances in instrumentation, from lens aberration correction in both TEM and STEM instruments and atomic level electron energy loss spectroscopy, to various scanned probe microscopy techniques, were all covered with both overviews and new results being presented. The work described at the present conference thus demonstrates the high level of on-going world-wide activity in all these areas.

Each camera-ready manuscript submitted for publication in this volume has been reviewed by at least two referees and modified accordingly; the editors are very grateful to the following colleagues for their rapid and careful refereeing work of the papers:

P E Batson, H Bender, P D Brown, N Browning, C B Carter, H Cerva, D Cherns, B Daudin, D Donnet, R Dunin-Borlowski, K Durose, M W Fay, K Furuya, F Glas, P J Goodhew, A Gustafsson, C Hetherington, C J Humphreys, P Koenraad, A Lauwers, S Mahajan, C Norenberg, Y Ohno, F M Ross, M Schowalter, E Spiecker, P Sutter, R Timm, T Walther, Y-L Wu.

The planning and organisation of an individual conference takes place over a two year cycle and work on the present meeting has been underpinned by Lucy Haworth, who deserves our very special thanks. We are also grateful for the assistance ably provided by Keith Fraser (University of Oxford) in meticulously correcting the proof copies of many manuscripts.

A G Cullis
October 2005 *J L Hutchison*

Contents

Preface ..... **v**

Part I Epitaxy: Wide Band-Gap Nitrides

Structural properties of GaN quantum dots **(Invited paper)**
B Daudin, *J-L Rouvière*, *D Jalabert*, *J Coraux*, *V Favre-Nicolin*, *H Renevier*, *M H Cho*, *K B Chung*, *D W Moon*, *M G Proietti*, *J M Llorens*, *N Garro*, *A Cros and A García-Cristóbal* 3

Stranski-Krastanov growth for InGaN/GaN: wetting layer thickness changes
N K van der Laak, *R A Oliver*, *M J Kappers*, *C McAleese and C J Humphreys* 13

Investigation of $In_xGa_{1-x}N$ islands with electron microscopy
A Pretorius, *T Yamaguchi*, *M Schowalter*, *R Kröger*, *C Kübel*, *D Hommel and A Rosenauer* 17

First stage of nucleation of GaN on (0001) sapphire
Y B Kwon, *J H Je*, *P Ruterana and G Nouet* 21

InGaN-GaN quantum wells: their luminescent and nano-structural properties
J S Barnard, *D M Graham*, *T M Smeeton*, *M J Kappers*, *P Dawson*, *M Godfrey and C J Humphreys* 25

Evolution of InGaN/GaN nanostructures and wetting layers during annealing
R A Oliver, *N K van der Laak*, *M J Kappers and C J Humphreys* 29

Origins and reduction of threading dislocations in GaN epitaxial layers **(Invited paper)**
S Mahajan 33

Oxygen segregation to nanopipes in gallium nitride
M Hawkridge and D Cherns 45

Strain relaxation in (Al,Ga)N/GaN heterostructures
P Vennégues, *J M Bethoux*, *Z Bougrioua*, *M Azize*, *P De Mierry and O Tottereau* 51

A TEM Study of AlN Interlayer Defects in AlGaN/GaN Heterostructures
P D Cherns, *C McAleese*, *M J Kappers and C J Humphreys* 55

Reduction of threading dislocation density using *in-situ* SiN_x interlayers
R Datta, *M J Kappers*, *J S Barnard and C J Humphreys* 59

The nucleation structure for cracks in AlGaN epitaxial layers
R T Murray, *P J Parbrook*, *G Hill and I M Ross* 63

Microstructural and optical characterisation of InN layers grown by MOCVD
P Singh, *P Ruterana*, *G Nouet*, *A Jain*, *J M Redwing and M Wojdak* 67

Structural properties of InN thin films grown with variable growth conditions on GaN/Al_2O_3 by plasma-assisted MBE
A Delimitis, *Ph Komninou*, *Th Kehagias*, *Th Karakostas*, *E Dimakis*, *A Georgakilas and G Nouet* 71

Growth and surface characterization of piezoelectric AlN thin films on silicon (100) and (110) substrates
S Saravanan, *E G Keim*, *G J M Krijnen and M Elwenspoek* 75

Characterization and structuring of nitride-based heterostructures for vertical-cavity surface-emitting lasers
R Kröger, *C Kruse*, *J Dennemarck*, *D Hommel and A Rosenauer* 79

Characterization of defects in ZnS and GaN
J Deneen, *S Kumar*, *C R Perrey and C B Carter* 83

Part II Epitaxy: Silicon-Germanium Alloys

Use of moire fringe patterns to map relaxation in SiGe on insulator structures fabricated on SIMOX substrates
A Domenicucci, *S Bedell*, *R Roy*, *D K Sadana and A Mocuta* 89

TEM measurement of the epitaxial stress of Si/SiGe lamellae prepared by FIB
M Cabié, *G Benassayag*, *A Rocher*, *A Ponchet*, *J M Hartmann and F Fournel* 93

Strain relaxation of SiGe/Si heterostructures by helium ion implantation and subsequent annealing: Helium precipitates acting as dislocation sources
Norbert Hueging, *Martina Luysberg*, *Knut Urban*, *Dan Buca*, *Bernd Hollaender*, *Siegfried Mantl*, *Matcio J Morschbacher*, *Paulo F P Fichtner, Roger Loo and Matty Caymax* 97

TEM investigation of Si/Ge multilayer structure incorporated into MBE grown Si whiskers
N Zakharov, *P Werner*, *G Gerth*, *L Schubert*, *L Sokolov and U Gösele* 103

Local compositional analysis of GeSi/Si nanoclusters by scanning Auger microscopy
G A Maximov, *D E Nikolitchev and D O Filatov* 107

A study of processed and unprocessed dual channel Si/SiGe MOSFET device structures using FIB and TEM
A C K Chang, *D J Norris*, *I M Ross*, *A G Cullis*, *S H Olsen and A G O'Neill* 111

Part III Epitaxy: Growth and Defect Phenomena

Novel TEM method for large-area analysis of misfit dislocation networks in semiconductor heterostructures **(Invited paper)**
E Spiecker, *J Schöne*, *S Rajagopalan and W Jäger* 117

Beta to alpha transition and defects on SiC on Si grown by CVD
F M Morales, *Ch Förster*, *O Ambacher and J Pezoldt* 131

Strain relaxation and void reduction in SiC on Si by Ge predeposition
F M Morales, *P Weih*, *Ch Wang*, *Th Stauden*, *O Ambacher and J Pezoldt* 135

Defect generation in high In and N content GaInNAs quantum wells: unfaulting of Frank dislocation loops
M Herrera, *D González*, *J G Lozano*, *M Hopkinson*, *M Gutierrez*, *P Navaretti*, *H Y Liu and R García* 139

Structural characterisation of spintronic GaMnAs and GaMnN heterostructures grown by molecular beam epitaxy
M W Fay, *Y Han*, *S V Novikov*, *K W Edmonds*, *K Wang*, *B L Gallagher*, *R P Campion*, *C T Foxon and P D Brown* 143

TEM determination of the local concentrations of substitutional and interstitial Mn and antisite defects in ferromagnetic GaMnAs
F Glas, *G Patriarche*, *L Thevenard and A Lemaître* 147

First-principles calculations of 002 structure factors for electron scattering in strained $In_xGa_{1-x}As$
A Rosenauer, *M Schowalter*, *F Glas and D Lamoen* 151

Structural characterisation of MBE grown zinc-blende $Ga_{1-x}Mn_xN$/GaAs(001) as a function of Ga flux
Y Han, *M W Fay*, *P D Brown*, *S V Novikov*, *K W Edmonds*, *B L Gallagher*, *R P Campion and C T Foxon* 155

Magic matching in semiconductor heterojunctions
B Pécz, *Á Barna*, *V Heera and W Skorupa* 159

Changes in plasmon peak position in a GaAs/$In_{0.2}Ga_{0.8}As$ structure
R Beanland, *A M Sánchez*, *A J Papworth*, *M H Gass and P J Goodhew* 163

Investigation of the electrical activity of dislocations in ZnO epilayers by transmission electron holography
E Müller, *P Kruse*, *D Gerthsen*, *R Kling and A Waag* 167

A TEM study of Mn-doped ZnO layers deposited by RF magnetron sputtering on (0001) sapphire
M Abouzaid, *P Ruterana*, *G Nouet*, *C Liu*, *F Yun*, *B Xiao*, *S-J Cho*, *Y-T Moon and H Morkoç* 171

Part IV High Resolution Microscopy and Nanoanalysis

Aberration-corrected HREM/STEM for semiconductor research **(Invited paper)**
C J D Hetherington, *D J H Cockayne*, *R C Doole*, *J L Hutchison*, *A I Kirkland and J M Titchmarsh* 177

Spherical aberration correction and exit-plane wave function reconstruction: Synergetic tools for the atomic-scale imaging of structural imperfections in semiconductor materials
K Tillmann, *A Thust*, *L Houben*, *M Luysberg*, *M Lentzen and K Urban* 183

Strain mapping from HRTEM images
P L Galindo, *A Yáñez*, *J Pizarro*, *E Guerrero*, *T Ben and S I Molina* 191

Quantification of the influence of TEM operation parameters on the error of HREM image matching
J Pizarro, *E Guerrero*, *P Galindo*, *A Yañez*, *T Ben and S I Molina* 195

ConceptEM: a new method to quantify solute segregation to interfaces or planar defect structures by analytical TEM and applications to inversion domain boundaries in doped zinc oxide
T Walther, *A Rečnik and N Daneu* 199

Electron holography of doped semiconductors: when does it work and is it quantitative? **(Invited paper)**
R E Dunin-Borkowski, *A C Twitchett*, *P A Midgley*, *M R McCartney*, *T Kasama*, *D Cooper and P K Somodi* 203

Why does a p-doped area show a higher contrast in electron holography than a n-doped area of the same dopant concentration?
A Lenk, *U Muehle and H Lichte* 213

Interference electron microscopy of reverse-biased p-n junctions
P F Fazzini, *P G Merli*, *G Pozzi and F Ubaldi* 217

Off-axis electron holography of focused ion beam milled GaAs and Si p-n junctions
D Cooper, *A C Twitchett*, *I Farrer*, *D A Ritchie*, *R E Dunin-Borkowski and P A Midgley* 221

Towards quantitative electron holography of electrostatic potentials in doped semiconductors
P K Somodi, *R E Dunin-Borkowski*, *A C Twitchett*, *C H W Barnes and P A Midgley* 225

Three-dimensional analysis of the dopant potential of a silicon *p-n* junction by holographic tomography
A C Twitchett, *T J V Yates*, *P K Somodi*, *S B Newcomb*, *R E Dunin-Borkowski and P A Midgley* 229

Ab initio computation of the mean inner Coulomb potential for technologically important semiconductors
M Schowalter, *A Rosenauer*, *D Lamoen*, *P Kruse and D Gerthsen* 233

Part V Self-Organised and Quantum Domain Structures

Electron beam induced deposition of position and size controlled structures on the nanometre scale **(Invited paper)**
K Furuya, *K Mitsuishi*, *M Shimojo*, *M Song*, *M Tanaka and M Takeguchi* 239

The structure of coherent and incoherent InAs/GaAs quantum dots
D Zhi, *M J Hÿtch*, *R E Dunin-Borkowski*, *P A Midgley*, *D W Pashley*, *B A Joyce and T S Jones* 243

Electron microscopy and optical spectroscopy of single InAs/InP quantum dots
D Chithrani, *D D Perovic*, *R L Williams*, *J Lefebvre*, *P J Poole and G C Aers* 247

Vertical correlation-anticorrelation transition in InAs/GaAs quantum dot structures grown by molecular beam epitaxy
M Gutiérrez, *M Hopkinson*, *M Herrera*, *D González and R García* 251

Effect of annealing on anticorrelated InGaAs/GaAs quantum dots
M Gutiérrez, *M Hopkinson*, *A I Tartakovskii*, *M S Skolnick*, *M Herrera*, *D González and R García* 255

Nanoanalysis of InAs/GaAs quantum dots using low-loss EELS spectra
A M Sánchez, *M H Gass*, *A J Papworth*, *R Beanland*, *V Drouot and P J Goodhew* 259

Structural analysis of the effects of a combined InAlAs-InGaAs capping layer in 1.3-μm InAs quantum dots
C M Tey, *A G Cullis*, *H Y Liu*, *I M Ross and M Hopkinson* 263

Microstructural studies of InAs/GaAs self-assembled quantum dots grown by selective area molecular beam epitaxy
J C C Lin, *I M Ross*, *P W Fry*, *A I Tartakoskii*, *R S Kolodka*, *R Hogg*, *M Hopkinson*, *A G Cullis and M S Skolnick* 267

Chemical composition and strain distribution of InAs/GaAs(001) stacked quantum rings
T Ben, *A M Sánchez*, *S I Molina*, *D Granados*, *J M García and S Kret* 271

In distribution in InGaAs quantum wells and quantum islands
D Litvinov, *D Gerthsen*, *A Rosenauer*, *T Passow*, *M Grün*, *C Klingshirn and M Hetterich* 275

Activation energy for surface diffusion in GaInNAs quantum wells
M Herrera, *D González*, *J G Lozano*, *M Hopkinson*, *M Gutierrez*, *P Navaretti*, *H Y Liu and R García* 279

Growth and surface structure of silicon nanowires observed in real time in the electron microscope
F M Ross, *J Tersoff*, *S Kodambaka and M C Reuter* 283

Self-catalytic growth of gallium nitride nanoneedles under Ga-rich conditions
Andrew S W Wong, *Ghim W Ho*, *Pedro M F J Costa*, *Rachel A Oliver and Colin J Humphreys* 287

Nanocontacts fabricated by focused ion beam: characterisation and application to nanometre-sized materials
F Hernández, *O Casals*, *A Vilà*, *J R Morante*, *A Romano-Rodríguez*, *M Abid*, *J-P Abid*, *S Valizadeh*, *K Hjort*, *J-P Collin and A Jouati* 291

Cross-sectional studies of epitaxial growth of InP and GaP nanowires on Si and Ge
M A Verheijen, *E P A M Bakkers*, *A R Balkenende*, *A L Roest*, *M M H Wagemans*, *M Kaiser*, *H J Wondergem and P C J Graat* 295

Quantitative measurements of the inhomogeneous strain field of stacked self-assembled InAs/InP(001) quantum wires by the Peak Finding Method
T Ben, *S I Molina*, *R García*, *D Fuster*, *M U González*, *L González*, *Y González and S Kret* 299

Measurement of the mean inner potential of ZnO nanorods by transmission electron holography
E Müller, *P Kruse*, *D Gerthsen*, *A Rosenauer*, *M Schowalter*, *D Lamoen*, *R Kling and A Waag* 303

Quantum effects in band gap-modulated amorphous carbon superlattices
V Stolojan, *P Moreau*, *M J Goringe and S Ravi P Silva* 307

Structure of rolled-up semiconductor nanotubes
N Y Jin-Phillipp, *Ch Deneke*, *J Thomas*, *M Kelsch*, *R Songmuang*, *M Stoffel and O G Schmidt* 311

Defects and interfaces in nanoparticles
C R Perrey, *J Deneen and C B Carter* 315

TEM characterization of magnetic Sm- and Co-nanocrystals in SiC
J Biskupek, U Kaiser, H Lichte, A Lenk, G Pasold and W Witthuhn 319

Microscopy of nanoparticles for semiconductor devices
J Deneen, C R Perrey, Y Ding, A Bapat, S A Campbell, U Kortshagen and C B Carter 323

Structural and electrophysical properties of a nanocomposite based upon the Si-SiO_2 system
L M Sorokin, V I Sokolov, A E Kalmykov and L V Grigoryev 327

HRTEM and XRD analysis of P6mm and Ia3d double gyroidal WO_3 structures
E Rossinyol, J Arbiol, F Peiró, A Cornet, J R Morante, L A Solovyov, B Tian and D Zhao 333

Part VI Processed Silicon and Other Device Materials

Research highlights and impacts upon industry for nanoelectronics in the university system of Taiwan **(Invited paper)**
You-Lin Wu, Huey-Liang Hwang and Chuen-Horng Tsai 339

TEM investigations of epitaxial high-κ dielectrics on silicon
E Bugiel, H J Osten, A Fissel, O Kirfel and M Czernohorsky 343

Damage layer in silica-based low-k material induced by the patterning plasma process studied by energy-filtered TEM
O Richard, F Iacopi, Zs Tőkei and H Bender 347

Measurement of field-emission properties of a single crystal silicon emitter using scanning electron microscopy
T C Cheng, H T Hsueh, W J Huang, M N Chang, J S Wu and S C Kung 351

Efficient, room-temperature, near-band gap luminescence by gettering in ion implanted silicon
D J Stowe, K J Fraser, S A Galloway, S Senkader, R J Falster and P R Wilshaw 355

On the mechanism of {113}-defect formation in Si
L I Fedina, S A Song, A L Chuvilin, A K Gutakovskii and A V Latyshev 359

The evolution of low defect density structures in silicon-on-sapphire thin films during post-ion implantation heat treatments
W R McKenzie, H Domyo, T Ho and P R Munroe 363

HREM study of an epitaxial growth defect
A Renard and B Domengès 367

Resonant Raman microscopy of stress in silicon-based microelectronics
E Bonera and M Fanciulli 371

TEM study of silicon implanted with fluorine and boron applied to piezoresistor manufacturing
M Wzorek, *J Kątcki*, *J Ratajczak*, *B Jaroszewicz*, *K Domański and P Grabiec* 375

Silicides for advanced CMOS devices **(Invited paper)**
A Lauwers, *J A Kittl*, *M J H van Dal*, *O Chamirian*, *M A Pawlak*, *C Torregiani*, *J Liu*, *A Benedetti*, *O Richard*, *H Bender*, *J G M van Berkum*, *M Kaiser*, *A Veloso*, *K G Anil*, *M de Potter and K Maex* 379

Transmission electron microscopy characterisation of Ti and Al/Ti contacts on GaN and AlGaN/GaN
B Van Daele, *G Van Tendeloo*, *W Ruythooren*, *J Derluyn*, *M R Leys and M Germain* 389

Dynamics of Au Adatoms on Electron-Irradiated Rough Si Surfaces
K Torigoe, *Y Ohno*, *T Ichihashi and S Takeda* 393

Corrosion of FIB-milled Cu during air exposure
H Bender, *O Richard*, *P Van Marcke and C Drijbooms* 397

Part VII Device Studies

FIB applications for semiconductor device failure analysis **(Invited paper)**
D M Donnet and H Roberts 403

A method for 3D failure analysis using a dedicated FIB-STEM system
T Kamino, *T Yaguchi*, *M Konno*, *T Hashimoto*, *T Ohnishi and K Umemura* 409

Failure analysis studies in pseudomorphic SiGe channel *p*-MOSFET devices
A C K Chang, *I M Ross*, *D J Norris*, *A G Cullis*, *Y T Tang*, *C Cerrina and A G R Evans* 413

TEM specimen preparation technique for III-V semiconductor devices by using a novel FIB-Ar ion milling method
K Tanabe, *T Matsuda*, *H Sasaki and F Iwase* 417

Focused ion beam micromilling of GaN photonic devices with gas enhanced etching techniques
W C Hung, *T Wang*, *Hung-Cheng Lin*, *Guan-Ting Chen*, *Jen-Inn Chyi and A G Cullis* 423

An organic two dimensional photonic crystal microcavity processed by focused ion beam milling
W C Hung, *A M Adawi*, *R Dean*, *A Cadby*, *L G Connolly*, *A Tahraoui*, *D G Lidzey and A G Cullis* 427

Failure analysis of degraded (In,Ga)P/GaAs heterojunction bipolar transistors by TEM
H Kirmse, *W Neumann*, *U Zeimer*, *R Pazirandeh and W Oesterle* 433

Strain measurements of ULSI devices using LACBED with TSUPREM modeled displacements
A Kenda, *H Cerva*, *P Pongratz*, *M Hierlemann and R Liebmann* 437

Electron holography for visualisation of different doped areas in silicon-germanium heterojunction bipolar transistors
U Muehle, *A Lenk*, *A T Tilke*, *C Wagner*, *C Dahl and H Lichte* 441

Ar sputter shadow method (ASSM) - a novel way to overcome the charging effect during AES bond pad analysis
H-M Lo, *J-S Luo and J D Russell* 445

Part VIII Scanning Electron and Scanning Probe Advances

Challenges and opportunities of Ångstrom-level analysis **(Invited paper)**
P E Batson 451

Sub-Ångstrom and 3-dimensional STEM for semiconductor research
A R Lupini, *M F Chisholm*, *M Varela*, *K Van Benthem*, *A Y Borisevich*, *Y Peng*, *W H Sides*, *J T Luck and S J Pennycook* 459

Cathodoluminescence studies of AlGaAs/GaAs core-shell nanowires
A Gustafsson, *N Sköld*, *W Seifert and L Samuelson* 463

Carrier diffusion lengths of (In,Ga)As, GaAs and (In,Ga)(As,N) quantum wells studied by spatially resolved cathodoluminescence
U Jahn, *T Flissikowski*, *H T Grahn*, *R Hey*, *E Wiebicke*, *A K Bluhm*, *J Miguel-Sánchez and A Guzmán* 467

An analysis of the alpha parameter used for extracting surface recombination velocity in EBIC measurements
V K S Ong and O Kurniawan 471

The effects of boundary conditions on dopant region imaging in scanning electron microscopy
M Ferroni, *P G Merli and V Morandi* 475

A cross-sectional scanning tunneling microscopy study of GaSb/GaAs nanostructures
R Timm, *A Lenz*, *J Grabowski*, *H Eisele and M Dähne* 479

Atomistic structure of spontaneously-ordered GaInP alloy revealed by cross-sectional scanning tunneling microscopy and polarized cathodoluminescence spectroscopy
Y Ohno 483

Carrier distribution in quantum nanostructures studied by scanning capacitance microscopy
F Giannazzo, V Raineri, S Mirabella, G Impellizzeri, F Priolo, M Fedele and R Mucciato 487

Mapping of the effective electron mass in III-V semiconductors
M H Gass, A M Sánchez, A J Papworth, T J Bullough, R Beanland and P R Chalker 491

Reconstruction of images of surface height in scanning electron microscopy
C G H Walker, M M El Gomati and V Romanovsky 495

Low energy scanning analytical microscopy (LeSAM) for Auger and low voltage SEM imaging of semiconductors
V Romanovsky, M El-Gomati, T Wells and J Day 499

The electric field and dopant distribution in p-i-n structures observed by ionisation potential (dopant contrast) microscopy in the HRSEM
E Grunbaum, Z Barkay, Y Shapira, K Barnham, D B Bushnell, N J Ekins-Daukes, M Mazzer and P R Wilshaw 503

Localized energy levels associated with dislocations in ZnSe revealed by polarized CL spectroscopy under light illumination
Y Ohno 507

Electron microscopy characterisation of ZnS:Cu:Cl phosphors
A Łaszcz, J Kątcki, J Ratajczak, M Płuska and M Cież 511

Resistive contrast in R-EBIC from thin films
K Durose and H Tatsuoka 515

A diode model for SEM-REBIC contrast in ZnO varistors
A G Wojcik and L E Wojcik 519

The effect of barrier height variations in alloyed Al-Si Schottky barrier diodes on secondary electron contrast of doped semiconductors
F Zaggout and M El-Gomati 523

Author index **527**

Subject index **533**

Part I

Epitaxy: Wide Band-Gap Nitrides

Structural properties of GaN quantum dots

B Daudin, J-L Rouvière, D Jalabert, J Coraux, V Favre-Nicolin, H Renevier, M H Cho[1], K B Chung[1], D W Moon[1], M G Proietti[2], J M Llorens[3], N Garro[3], A Cros[3] and A García-Cristóbal[3]

CEA/Grenoble, Department of Fundamental Research on Condensed Matter/ SP2M, 17 rue des Martyrs, 38054-Grenoble cedex 9, France
[1] Korea Research Institute of Standards and Science, Nano-Surface Group, 1 Doryong-Dong, Yuseong-Gu, Daejeon, 305-600, Korea (ROK)
[2] University of Zaragosa, Zaragosa, Spain
[3] Materials Science Institute, University of Valencia, P O Box 22085, E46071 Valencia, Spain

ABSTRACT: The strain state and the deformation profile of GaN quantum dots embedded in AlN have been measured by high resolution electron microscopy, medium energy ion scattering and grazing incidence X-ray diffraction. The results are compared with theoretical calculations, allowing one to conclude that GaN quantum dots experience a non biaxial strain which drastically decreases when going from the basal plane up to the apex of the dots. We also demonstrate that AlN is distorted in the surroundings of the dots, which provides the driving force for vertical correlation of GaN dots when the AlN spacer between successive planes is thin enough.

1. INTRODUCTION

The sustained interest for many years in quantum dots (QDs) of semiconductors relies on their three-dimensional carrier confinement properties which make them potentially very attractive for applications such as low threshold lasers as proposed by Arakawa and Sakaki (1982), single photon emission (Michler et al 2000, Santori et al 2000, Moreau et al 2001), quantum cryptography, single electron transistor (Fulton and Dolan 1987) or quantum computing. However, the practical realisation of devices simultaneously requires a good control of the size distribution of quantum dots and of their nucleation sites as well as of their structural, electrical and optical properties. Among the various parameters of interest, the strain state of QDs embedded in a matrix is an important one, which is closely related to their optical properties. This is of particular importance in the case of the III-nitride semiconductor family. As a matter of fact, due to the lack of a center of symmetry, the most usual wurtzite crystallographic phase of these materials exhibits both piezoelectric and spontaneous polarization. Because of the elevated value of the piezoelectric constants (see the calculations of Fiorentini et al (1999)), a huge internal electric field is currently observed in nitride heterostructures. It may be as high as several MV/cm in the case of GaN/AlN quantum wells, as shown by Adelmann et al (2003), or for GaN QDs embedded in AlN as studied by Simon et al (2003), Andreev and O'Reilly (2000 and 2001). Then, a strong red shift of the luminescence is induced as a consequence of the resulting quantum confined Stark effect, leading to luminescent emission at energies smaller than the GaN gap value for GaN/AlN quantum wells thicker than about 4 nm and for GaN/AlN QDs higher than 2.5 nm.

It is the objective of this article to report on the different experimental techniques allowing one to measure the strain in GaN quantum dots and to relate it with the optical properties. More precisely, high resolution transmission electron microscopy (HRTEM), X-ray diffraction under grazing incidence and medium energy ion scattering (MEIS) have been used. The satisfactory agreement between the experiments and theoretical calculations performed in the framework of the elastic

continuum model has allowed us to conclude that GaN quantum dots embedded in AlN experience a combination of hydrostatic and biaxial strain leading to a gradient of elastic relaxation along the growth axis.

2. SAMPLES

The samples have been grown by plasma-assisted molecular beam epitaxy (PAMBE) in a commercial chamber equipped with standard effusion cells for Ga and Al. The N flux was produced by dissociation of N_2 in a radio-frequency plasma cell. The substrate was a 2-μm thick AlN layer deposited on sapphire as detailed by Shibata et al (2002). After a standard degreasing procedure and acid etching, the substrate was fixed with In on a molybdenum sample holder and introduced into the growth chamber. Prior to the growth of GaN QDs, an AlN buffer layer, about 100 nm thick, was grown in order to improve the surface quality. Then, GaN QDs were grown by depositing the equivalent of 6 monolayers (MLs) of GaN. The growth of the GaN QDs was performed according to the modified Stranski-Krastanow (SK) growth mode studied by Adelmann et al (2002) and Gogneau et al (2003): GaN was grown on AlN in Ga-rich conditions which results in the formation of a Ga bilayer on the surface as described by Northrup et al (2000). This metal layer stabilizes the 2D GaN layer and inhibits the 2D/3D transition, characteristic of the usual SK growth mode, which was observed by Daudin et al (1997) when growing GaN in N-rich conditions. After depositing GaN, both Ga and N fluxes were suppressed. Then, the thermal evaporation of the stabilizing Ga bilayer was followed by a reorganization of the 2D GaN layer and the formation of 3D islands as described in detail by Gogneau et al (2003). The samples used in the present study were a superlattice of vertically correlated GaN QDs (for HRTEM) and single planes of GaN dots uncapped or capped with an increasing quantity of AlN (for MEIS and X Rays diffraction). Details on the samples are given in the relevant sections.

3. RESULTS

3.1 High Resolution Electron Microscopy

Once deposited, GaN quantum dots can be covered by AlN in order to recover a smooth surface. Next, the operation can be repeated, allowing one to grow superlattices of planes of GaN QDs in an AlN matrix. Depending on the thickness of the AlN spacer, GaN QDs can be correlated or not, according to the model proposed by Tersoff et al (1996). In this work, it was established that the deformation of the surrounding matrix by dots actually leads to a modulation of the elastic potential and to the preferential nucleation of the upper dots just above the lower ones.

Figure 1 (which is part of a 2Kx2K image taken with a CCD camera) zooms on a GaN QD which is part of a superlattice of planes of GaN QDs embedded in AlN, with an AlN spacer thin enough (about 10 nm) to result in vertical correlation of dots.

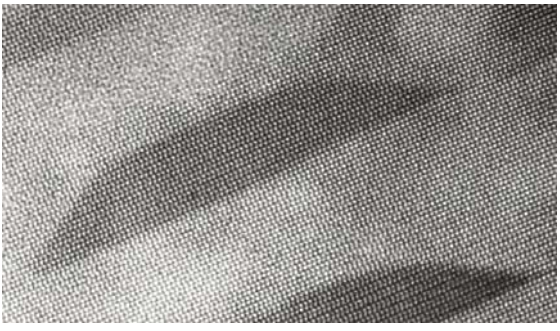


Fig. 1: HRTEM image of GaN quantum dots embedded in AlN taken along a <2,-1,-1,0> direction

A quantitative analysis of the whole image has been performed using the geometrical phase analysis technique (Hytch et al 1998, Rouvière and Sarigiannidou, unpublished). The result is displayed in Fig.2a and 2b which are maps of the local *c* and *a* lattice parameters, respectively. It demonstrates that compressed GaN QDs induce strain in the surrounding AlN matrix. In particular, it is found that AlN above the dots exhibits an expanded *a* lattice parameter, that is to say that AlN is in tension and constitutes a privileged nucleation centre for the upper GaN dots, which leads to the building-up of vertical correlation of GaN QDs.

Combining the results in Fig.2a and 2b, it is possible to extract a map of *c/a* ratio value which is shown in Fig. 2c. An average value of 1.64 is found in the GaN QDs, allowing one to conclude that GaN QDs are relaxed to a large extent, as *c/a* would be 1.69 in the hypothesis of a biaxial strain and equal to 1.625 in a bulk GaN crystal (see Fig. 6).

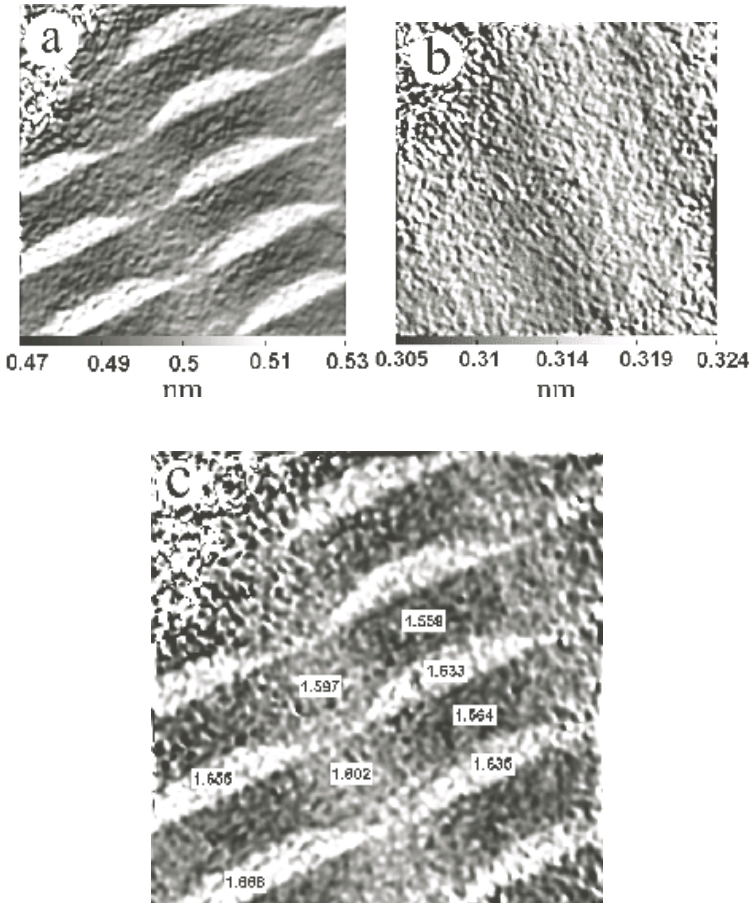


Fig. 2: Maps of the whole 2Kx2K CCD image shown in Fig. 1. (a) map of the *c* lattice parameter; (b) map of the *a* lattice parameter; (c) *c/a* mapping extracted from results displayed in Fig. 2a and 2b. Note that the relaxed values of *c* and *a* are 0.5185 nm and 0.3189 nm, respectively, leading to a *c/a* ratio of 1.625

3.2 Medium Energy Ion Scattering (MEIS)

A more detailed knowledge of deformation profile in GaN QDs can be obtained by medium energy ion scattering (MEIS) experiments which were performed using a 101 keV incident H^+ ion beam, $\theta_{in} \sim 7°$ off the [0001] direction (see Fig. 3). The energy and angular distribution of scattered protons were measured with a two-dimensional detector described by Tromp et al (1991), whose energy resolution, $\Delta E/E$, is about 3×10^{-3} and angular resolution is 0.1°. The scattering geometry was chosen in order to observe a range of ± 10° around the [1-101] direction in the (11-20) plane.

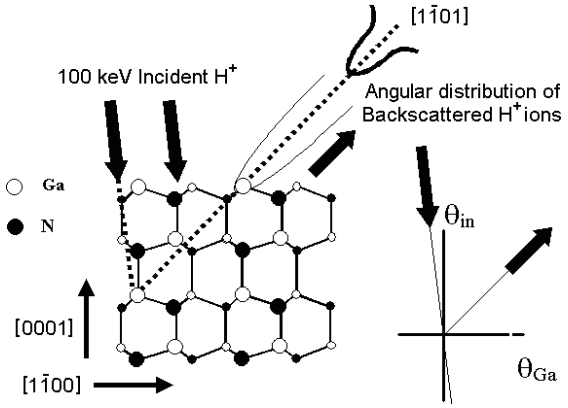


Fig. 3: Scheme of the scattering geometry in the (11-20) plane for medium ion energy scattering experiments.

Then, by measuring the backscattered proton energy as a function of scattering angle, it is possible to determine the change in shadowing direction as a function of depth which is related, in the case of GaN QDs, to their deformation profile along the growth axis. Figure 4 shows the result in the case of uncovered QDs. A similar experiment has been performed in the case of one plane of GaN QDs covered with 20 monolayers of AlN. The deformation profile extracted from the data is shown in Fig. 5. It is worth noting that, at the top of dots, the *c/a* ratio is equal to the value corresponding to relaxed GaN. However, it must be recalled at this stage that MEIS does not allow one to independently determine *c* and *a*, preventing the conclusion that GaN QDs are completely relaxed at their tops.

In order to better understand the MEIS results, simulations of the strain distribution in a single lattice-mismatched wurtzite GaN/AlN quantum dot have been performed. The calculations have been done in the framework of the elastic continuum theory by using the inclusion method developed by Eshelby (1957), which considers the dot as a misfitting inclusion (GaN) in an infinite matrix (AlN). In order to describe the dot geometry, we have adopted a truncated cone shape with height 3 nm, and base and top diameters equal to 13.3 and 3 nm, respectively, leading to an aspect ratio of 0.22. Furthermore, the dot is assumed to lie on a 0.5-nm-thick two-dimensional wetting layer. The output of the calculations is the full inhomogeneous strain tensor $\varepsilon_{ij}(\mathbf{r})$, from which the local strained values of *a* and *c* are obtained as $a(\mathbf{r}) = (1+\varepsilon_{pp}(\mathbf{r}))a_0$ and $c(\mathbf{r}) = (1+ \varepsilon_{zz}(\mathbf{r}))c_0$, respectively. This procedure does not take into account the distortion caused by the shear strains, which are found to be very small throughout most of the dot volume.

The detailed results of the calculation are reported elsewhere by Jalabert et al (2005). In order to facilitate the comparison with MEIS data, the theoretical depth profile of *c/a* extending from $z = -0.5$ nm (wetting layer underneath the QD) to $z = 3$ nm (top of the QD) is shown in Fig. 6. The values represented have been obtained by averaging the calculated *c/a* over the dot cross section perpendicular to the *z* axis.

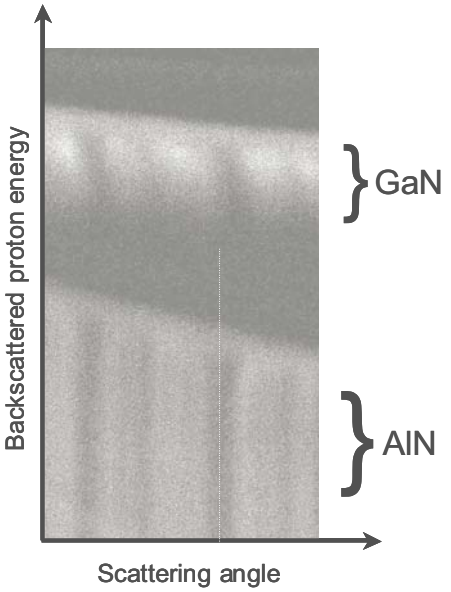


Fig. 4: Backscattering proton energy as a function of scattering angle for one plane of uncovered GaN QDs on AlN. The dotted line is an eye guide to visualise the channelling dip in AlN substrate. Note the deviation from this line in the GaN region, which puts in evidence the gradient of deformation in GaN QDs as a function of depth

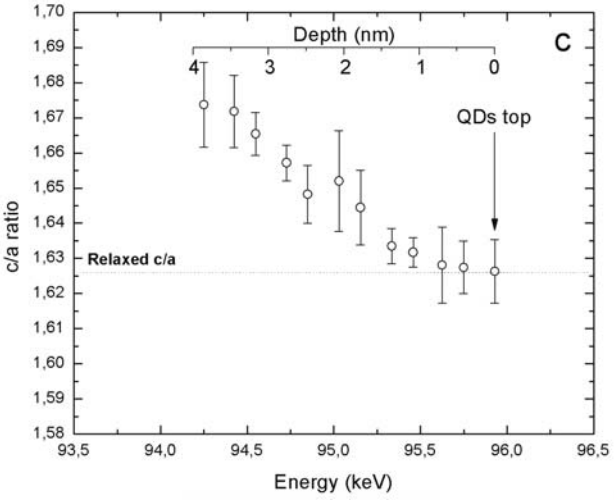


Fig. 5: *c/a* ratio as a function of depth in GaN QDs covered with 20 MLs of AlN (about 5 nm)

From the satisfactory agreement between calculations and experimental results shown in Fig. 5, we conclude that the general trends of the measured gradient of *c/a* through the QD are well reproduced in the theoretical analysis. As a matter of fact, the calculations establish that, inside the dot, the in-plane lattice parameter *a* is always compressed, although to a different values depending on the position, whereas the parameter *c* is expanded in the base and compressed at the top of the dot as commented in details by Jalabert et al (2005). This behaviour is very sensitive to the dot morphology and aspect ratio and results in a strain state quite inhomogeneous. As a whole, this strain state

drastically differs from the biaxial strain characteristic of two-dimensional films, which is frequently invoked to describe the deformation of self-assembled QDs. It is worth noting that in the region of the AlN/GaN interface, the calculated *c/a* value of 1.675 agrees very well with the experimental value and still lies relatively away from the biaxial value.

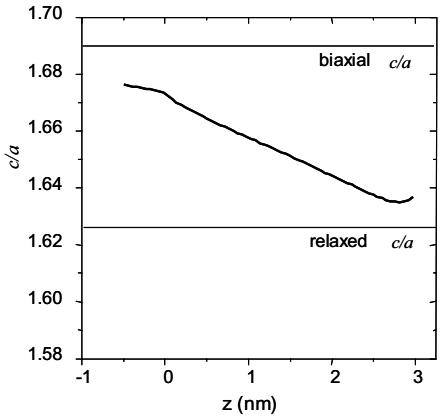


Fig. 6: calculated depth profile of the in-plane averaged *c/a*. The two full lines indicates the value of *c/a* corresponding to relaxed, unstrained GaN and to two-dimensional GaN layer biaxially strained to AlN, respectively.

3.3 Grazing Incidence X-ray Scattering

An alternative approach to determine the strain state of QDs consists of performing anomalous diffraction at grazing incidence (GIDAFS). As schematised in Fig. 7, taking advantage of the reduced penetration depth for α_i smaller than the critical angle value allows one to measure one single plane of capped/uncapped dots. Furthermore, the X-ray energy can be tuned across the absorption Ga K-edge where the Ga atoms scattering power is strongly modified and diffraction becomes chemically selective, giving direct information on composition. This technique has been applied to the case of a single plane of uncapped/capped GaN QDs which were studied as a function of the thickness of capping layer, namely 0 (S1967), 2 (S1956), 5 (S158), 10 (S1959) and 20 (S1961) MLs, to elucidate also the role of the AlN capping layer on the QDs strain field.

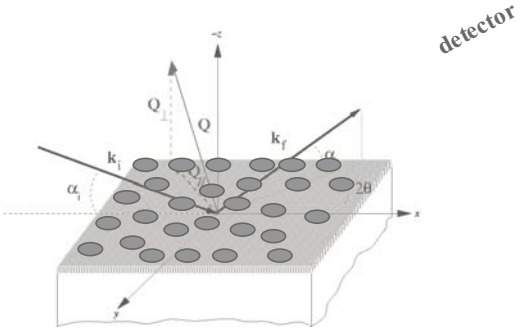


Fig. 7: Schematics of a grazing incidence diffraction experiment. α_i is of the order of the critical angle so that penetration of XRays is reduced to some tens of nm allowing one to measure only one plane of capped/uncapped dot

The experiment was performed at the Ga K-edge (10.367 keV) at the French Collaborative Research Group beamline BM2 at ESRF, by using a 8-circles diffractometer equipment. We measured

the diffuse scattering intensity, close to the in-plane (30-30) Bragg reflection of the AlN substrate as a function of energy and close to the Ga K-edge. The incidence angle was α_i=0.15º, lower than the critical angle α_c=0.20º, for which the total reflection regime takes place. We recorded two different kinds of scan a) h-scans in the range of 2.9-3 with k=l=0 for 12 different energy values varying from 10.268 to 10.418 keV, i.e. close to the Ga K-edge (see Fig.8) b) energy scans at fixed Q-vector, corresponding to the QDs maximum contribution to the diffuse scattering (i.e. at the maximum of the partial structure factor of the Ga atoms profile, F_A, recovered from the multiwavelength h-scans, as discussed by Letoublon et al (2004). The energy scans (shown in Fig. 9) were recorded in quite a large energy interval, about 1000eV, to allow quantitative analysis of both the edge and extended oscillations region.

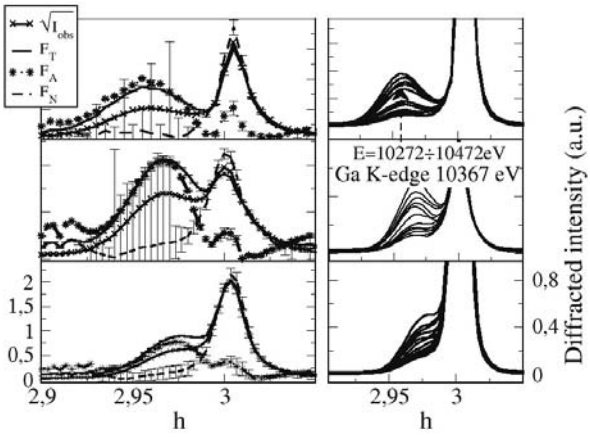


Fig. 8: hkl-scans for samples s1967 (no AlN capping: upper), s1956 (2ML AlN capping: middle), s1959(10ML AlN capping: lower). Right panels: diffracted intensity for different energies of the incident photons. Left panels: Multiwavelength anomalous diffraction (MAD) extraction of the partial structure factors F_A and F_T

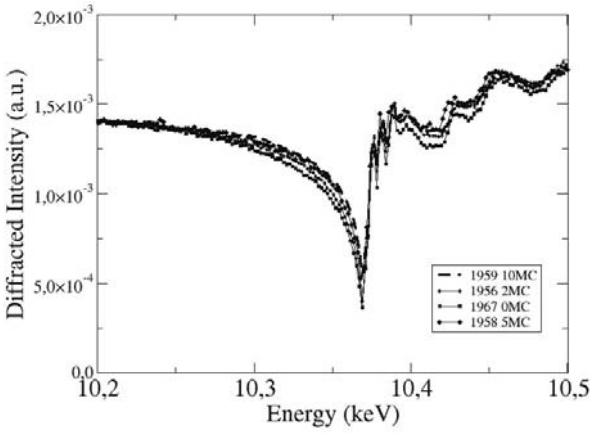


Fig. 9: GIDAFS spectra for 0, 2, 5 and 10 ML AlN capping, measured at top of F_A.

From the hkl scans we can recover, without any starting model, the structure factor F_A , i.e. the contribution of the Ga atoms to diffraction, and determine the in-plane lattice parameter *a* from the F_A

maximum position. One can see in Fig. 8 that the F_A maximum shifts towards higher h values corresponding to lower *a* values as the capping layer thickness increases, that is, we monitor the effect of the capping layer on the in-plane QDs' strain. The lattice parameter *a* is reported in table 1 where we see that it drops from 3.157 Å to 3.147Å. These values stay in between of the GaN and AlN bulk *a* values, 3.189 Å and 3.112 Å, respectively, i.e., the QDs exhibit an average partial in-plane relaxation.

Analysis of the EDAFS oscillations provides the microscopic local environment of the Ga resonant atom: interatomic distances, *c* lattice parameter, in the QDs.

The results are shown in Table 1 and in Fig.10 where the background subtracted EDAFS oscillations are compared with best fit curve for sample s1967 (uncovered QDS).

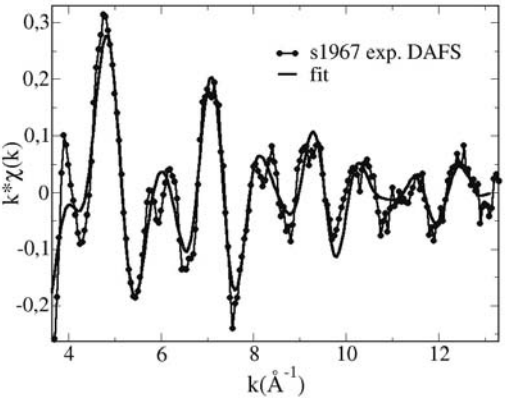


Fig. 10: Experimental EDAFS for the free standing QDs sample (s1967), compared with the best fit result.

We find a tendency to an over-strained regime (with respect to the purely biaxial strain case) that suggests a complex mechanism of strain accommodation and deserves further investigations.

	Bulk	***GaN/AlN***	***S1967 (1pl. no cap)***	***S1956 (1pl. + 2MLcap)***	***S1958 (1pl. + 5MLcap)***	***S1959 (1pl. + 10MLcap)***
R_1(Ga-N) (Å)	-	-	1.93	1.94	1.94	1.94
σ_1^2 (Å)^2	-	-	$2x10^{-3}$	$4x10^{-3}$	$4x10^{-3}$	$1x10^{-3}$
R_2 (Ga-Ga) // (Å)	3.188	3.11	3.156(diff.)	3.147 (diff.)	3.149(diff)	3.14 (diff.)
σ_2^2 (Å)^2	-	-	$6x10^{-3}$	$8x10^{-3}$	$4x10^{-3}$	$7x10^{-3}$
R_2(Ga-Ga)⊥ (Å)	3.18	-	3.190	3.18	3.180	3.186
c	5.186	5.26	5.25±0.02	5.23±0;03	5.22±0.02	5.25±0.04
c/a	1.626	1.69	1.66	1.66	1.66	1.67

Table 1 : EDAFS best fit values for interatomic distances and Debye-Waller factors obtained by IFEFFIT minimisation (Newille et al. 1995) using theoretical fitting standards provided by FEFF8 code developed by Ankudinov et al (1998). The amplitude and phase correction factors have been obtained by cristallographic analysis of the DAFS lineshape (Proietti et al 1999). R_1 and R_2 refer to interatomic distances, (diff.) refers to diffraction results

From results in Table 1, it appears that the *c/a* ratio as determined by EDAFS is about 1.66, clearly between the 1.626 value of relaxed bulk GaN and the 1.69 value of GaN biaxially strained on

AlN. As viewed by MEIS, 1.66 corresponds to the *c/a* value in the lower part of uncapped and AlN-capped GaN QDs (see Jalabert et al (2005) and Fig. 5). By comparison, EDAFS experiments provide an average value of *c/a*. Actually, due to the facetted shape of GaN QDs (see Daudin et al 1997), most of the diffracting volume corresponds to the base of the truncated hexagonal pyramid, giving more weight to the contribution of this part of the dots, consistent with experimental results. By contrast, HRTEM experiments potentially provide a detailed mapping of *c/a* parallel and perpendicular to the growth axis. However, the analysis may be intrinsically perturbed by thin foil effects resulting from sample preparation. As a whole, it appears that the combined use of the three techniques described here is complementary and eventually leads to a realistic knowledge of the deformation of GaN QDs embedded in AlN.

4. CONCLUSION

In conclusion, it has been shown that the complementary use of HREM, MEIS and GIDAFS allows one to measure the strain state and the deformation profile of semiconductor quantum dots with a spatial resolution in the monolayer range. It has been found that GaN QDs experience a non biaxial strain and significantly distort the surrounding AlN matrix, which provides the driving force for dot vertical correlation. The experimental results are in reasonable agreement with those of calculations performed in the framework of elastic continuum theory. We conclude that the dots are partly relaxed, and that capping them with AlN leads to a progressive increase of their relaxation/deformation stage.

ACKNOWLEDGEMENTS

We acknowledge Y Genuist, Y Curé and M Lafossas for their technical help.

REFERENCES

Adelmann C, Gogneau N, Sarigiannidou E, Rouvière J L and Daudin B 2002 Appl. Phys. Lett. **81**, 3064

Adelmann C, Sarigiannidou E, Jalabert D, Hori Y, Rouvière J L and Daudin B 2003 Appl. Phys. Lett. **82**, 4154

Andreev A D and O'Reilly E P 2000 Phys. Rev. B **62** 15851

Andreev A D and O' Reilly E P 2001, Appl. Phys. Lett. **79**, 521

Ankudinov A L, Ravel B and Rehr J J 1998 Phys. Rev. B **58** 7565

Arakawa Y and Sakaki H 1982 Appl. Phys. Lett. **40**, 939

Daudin B, Widmann F, Feuillet G, Samson Y, Arlery M and Rouvière J L 1997 Phys. Rev. B **56**, 7069

Eshelby J D 1957 Proc. R. Soc. London, Ser. A **241**, 376

Fiorentini V, Bernardini F, Della Sala F, Di Carlo A and Lugli P 1999, Phys. Rev. B **60** 8849

Fulton T A and Dolan G J 1987 Phys. Rev. Lett. **59**, 109

Gogneau N, Jalabert D, Monroy E, Shibata T, Tanaka M and Daudin B 2003 J. Appl. Phys **94**, 2254

Hÿtch M J, Snoeck E and Kilaas R 1998 Ultramicroscopy **74** 131

Jalabert D, Coraux J, Renevier H, Daudin B, Mann-Ho C, Kwun-Bum C, Moon D W, Llorens J M, Garro N, Cros A and García-Cristóbal A 2005 Physical Review B, in press

Letoublon A, Favre-Nicolin V, Renevier H, Proietti M G, Monat C, Gendry M, Marty O and Priester C 2004 Phys. Rev. Lett. **92** 186101

Michler P, Kiraz A, Becher C, Schoenfeld W V, Petroff P M, Lidong Zhang, Hu E, and Imamoglu A 2000 Science **290**, 2282

Moreau E, Robert I, Manin L, Thierry-Mieg V, Gérard J M, and Abram I 2001 Phys. Rev. Lett. **87**, 183601

Newville M, Ravel b, Haskel D, Rehr J J and Stern E A 1995 Physica B **208-209**, 154

Northrup J E, Neugebauer J, Feenstra R M and Smith A R 2000 Phys. Rev. B **61**, 9932

Rouvière J L and Sarigiannidou 2005, unpublished

Santori C, Pelton M, Solomon G, Dale Y, and Yamamoto Y 2000 Phys. Rev. Lett. **86**, 1502

Simon J, Pelekanos N T, Adelmann C, Martinez-Guerrero E, Andre R, Daudin B, Le Si Dang, and Mariette H 2003 Phys. Rev. B **68** 35312

Proietti M G, Renevier H, Hodeau J L, Garcia J, Bérar J F and Wolfers P 1999 Phys. Rev. B **59**, 5479
Shibata T, Asai K, Nagai T, Sumiya S, Tanaka M, Oda O, Miyake H and K. Hiramatsu K 2002 Mat. Res. Soc. Symp. Proc. 693, 541
Tersoff J, Teichert C and Lagally M G 1996 Phys. Rev. Lett. **76**, 1675 Tromp R M, Copel M, Reute M C, von Hoegen M H , Speidell J and Koudis R 1991 Rev. Sci. Instrum. **62**, 2679
Wang Y P and Meltzer R S 1992 Phys. Rev. B **45**, 10119

Stranski-Krastanov growth for InGaN/GaN: wetting layer thickness changes

N K van der Laak, R A Oliver, M J Kappers, C McAleese and C J Humphreys

Department of Materials Science and Metallurgy, University of Cambridge, Pembroke Street, Cambridge CB2 3QZ, United Kingdom

ABSTRACT: We have investigated InGaN nanostructures grown by atmospheric pressure metal-organic vapour phase epitaxy. The variation of the 3D nanostructure density and the wetting layer thickness with growth time have been studied. The nanostructure density was found to saturate with increasing growth time, but unexpectedly, the nanostructure size was also seen to stabilise. We have used high-resolution transmission electron microscopy (HRTEM) to further investigate the wetting layer growth and quantify changes with InGaN growth time.

1. INTRODUCTION

The self-assembled growth of nanostructures following the Stranski-Krastanov (SK) growth mode has been achieved for a number of material systems including Si_xGe_{1-x}/Si (Eaglesham and Cerullo 1990), $In_xGa_{1-x}As/GaAs$ (Ruvimov et al 1995), and GaN/AlN (Chamard et al 2004). Growth of InGaN nanostructures has also been achieved by both molecular beam epitaxy (MBE) and metal-organic vapour phase epitaxy (MOVPE). Typical SK growth in InGaAs/GaAs materials systems follows a regime in which the nanostructure density increases with growth time. At a certain wetting layer thickness misfit dislocations are introduced and the nanostructures coalesce resulting in a transition back to 2D growth (Tachibana et al 1999). The latter authors have reported growth of InGaN/GaN quantum dots at atmospheric pressure by MOVPE. 3D islands were reported to form on top of a 2D wetting layer (WL) akin to SK growth, and the density of the 3D islands was seen to increase with growth time. However, unlike the InGaAs/GaAs system, coherent nanostructures were observed with continued growth time. Here we report our observations of atmospheric MOVPE growth of InGaN/GaN nanostructures.

2. EXPERIMENTAL

Two sample sets were grown for this work in a 6 x 2" CCS-Thomas Swan MOVPE reactor. The first series comprised uncapped InGaN epilayers of increasing thickness and were characterised using a Veeco Dimension 3100 atomic force microscope (AFM) in tapping mode. The second series comprised similar InGaN layers which were capped immediately after growth with 7.5 nm of GaN deposited at the InGaN growth temperature and were used for cross-sectional HRTEM analysis. The HRTEM analysis was performed using a JEOL 4000-EX II HRTEM. A fuller description of the growth can be in found in Oliver et al (2005).

3. RESULTS

Figure 1 shows a series of AFM images of InGaN epilayers with different growth times. After 15 s of InGaN growth (Fig. 1a), flat terraces with decorated step edges and a low nanostructure density of about 8.9 x 10^7 cm^{-2} is observed. After 31 s of growth time (Fig. 1b) the nanostructure density increases quickly to approximately 2 x 10^9 cm^{-2} and then appears to stabilise with longer

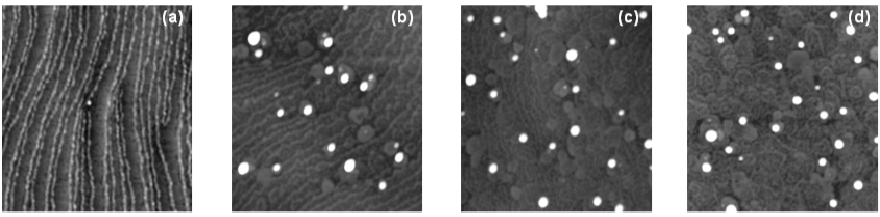


Fig. 1: 1 μm × 1 μm AFM scans of InGaN epilayers grown on GaN (a) Growth time, t = 15 s, image height, h = 1.56 nm, (b) t = 31 s, h = 15.97 nm, (c) t = 62 s, h = 22.35 nm (d) t = 93 s, h = 13.89 nm. In all the images, some nanostructures are seen as bright white features as the displayed contrast has been adjusted in order to allow the detailed structure of the wetting layer to be easily seen.

growth times (Fig. 2). The modal nanostructure height is also observed to increase sharply, then plateau (Fig. 3) which suggests that the 3D island growth stabilises after 31 s of InGaN growth time.

This in itself is surprising as the amount of InGaN material in the system is increasing, yet neither continued island growth nor coalescence of the nanostructures as seen in the InGaAs/GaAs system occurs. A closer examination of the AFM images shows that at 31 s of InGaN growth time 2D islands are now present. The density of these islands increases up to 125 s of InGaN growth where the wetting layer is dominated by irregular 2D islands, completely covering the terrace structure seen in Fig. 1a.

This change in the wetting layer was further investigated by HRTEM. A series of capped InGaN layers for 31, 46, 62, and 93 s were studied in cross-section to deduce if any changes in the WL could be seen and quantified. Lattice fringe images were obtained by tilting the sample 7 ° off the [11-20] zone axis, so that the systematic (0002) row of reflections was excited. The crystal was oriented at the symmetry position and the objective aperture selected the three beams, 0, (0002) and (000-2) to form the lattice image. Under certain conditions such as on-zone axis, lattice fringes can be observed in the high-resolution images. The nominal thickness can be determined by measuring across successive (0002) interplanar distances along the growth direction of the material. The (0002) interplanar spacing, *d*, for GaN was taken to be 2.593 Å and this was used to determine the distance over 10 lattice fringe spacings in the underlying GaN layer, so that an internal reference scale was established for each sample. The distance across the InGaN WL was measured and the absolute distance was determined using the GaN internal reference scale. Once an absolute scale for each sample is determined, the number of pixels spanning the area of interest, i.e. the InGaN epilayer, can be correlated to the scale and the thickness determined. This procedure was performed consistently for each sample and the average WL thickness (and hence the total amount of material in the WL) was determined. Figs. 4a-d show typical HRTEM images for the different InGaN growth times. As the WL has some roughness, the mean thickness was determined using measurements from several

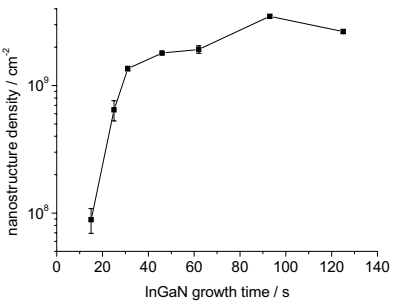


Fig. 2: Variation of InGaN nanostructure density with growth time.

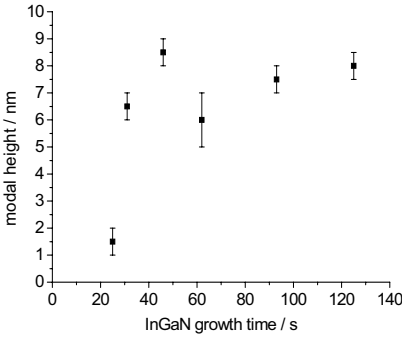


Fig. 3: Variation of the modal InGaN nanostructure height with growth time.

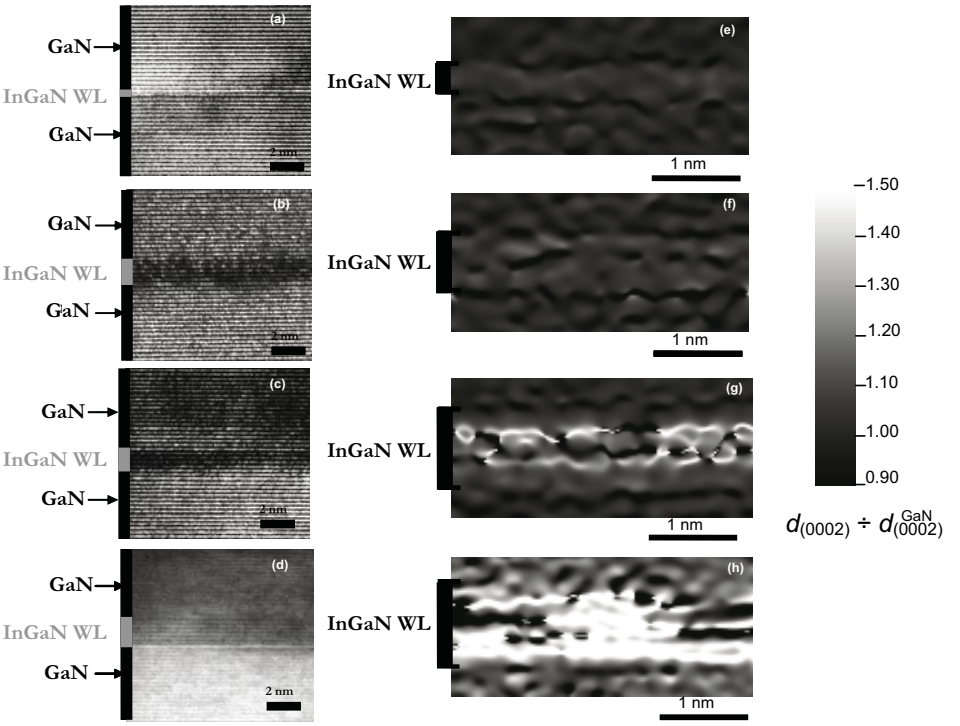


Fig. 4: (a-d) HRTEM lattice fringe images showing a typical wetting layer region for 31, 46, 62, and 93 s of InGaN growth time, respectively and, (e-h) lattice parameter maps extracted from the images demonstrating changes in the wetting layer thickness for 31, 46, 62, and 93 s of InGaN growth time, respectively.

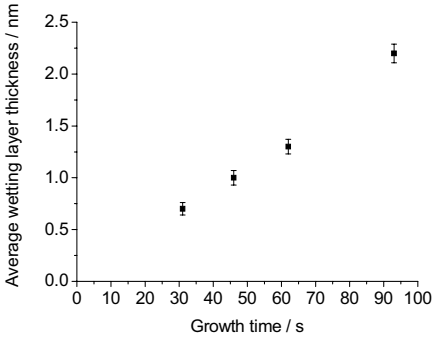


Fig. 5: Variation of the InGaN wetting layer thickness as measured by HRTEM on capped InGaN layers.

images and this mean, which can be seen to increase with growth time across the range of samples, is shown in Fig. 5.

Lattice parameter maps were also used to characterise the WL thicknesses. Figs. 4e-h show the lattice parameter maps extracted from the same regions displayed in the HRTEM images. The maps show the ratio of the measured $d_{(0002)}$ lattice spacing as a function of the GaN $d_{(0002)}$ lattice spacing. As the d spacing for InGaN is larger than that for GaN, the InGaN WL will appear as brighter regions in the lattice parameter maps. The maps indicate that, as the growth time increases, the InGaN WL thickness increases. What is also apparent, is that as the InGaN growth time is increased the intensity of the bright regions increases. This may be attributed to the increasing strain contribution within the InGaN WL and suggests that more indium is being incorporated with increasing InGaN growth time. This is not surprising as our SIMS analysis of InGaN quantum wells shows that the amount of indium incorporated in the well increases with well thickness.

4. DISCUSSION

The data shows that after approximately 31 s the nanostructure density saturates and plateaus, while the modal height remains stable. This indicates that the nanostructure distribution stabilises. The TEM investigation has shown that the WL increases in thickness as the InGaN growth time is increased. This is consistent with the AFM observations which show an increase of 2D islands under the same growth conditions. However, if the WL were to increase and no material were added to the nanostructures, the 2D layer would eventually cover the nanostructures and both the size and density would decrease. Hence, it is suggested that material may be added simultaneously to the WL layer and the 3D nanostructures in order to maintain the density and height distribution.

This deviation from the normal SK paradigm could be explained by the relatively low temperatures and high pressures at which the growth was carried out. The WL appears to grow by partial formation and merging of flat 2D islands. At low temperatures and high pressures the adatom mobility is reduced, hence the adatoms diffusing across the WL surface may form clusters that grow by accretion. As the 3D island density is relatively low (ca. 2 x 10^9 cm^{-2}) distances between the islands are relatively large, so the 3D nanostructures may grow in a similar fashion to the WL by adatoms impinging close to or on the islands. This would suggest that the growth mode is kinetically controlled. However, recent results have suggested that the crystal structure of the 3D islands is zincblende, not wurtzite, which may alter our understanding of the growth process.

5. CONCLUSIONS

In summary, we have shown that, in atmospheric pressure MOVPE growth of InGaN on GaN, the wetting layer thickness increases via the formation and merging of 2D islands while the 3D nanostructure density and height increase sharply and then stabilise for longer InGaN growth times. It has been suggested that slow kinetically controlled growth may account for these observations; however we have noted that a phase change from wurtzite to zincblende may also play a role.

REFERENCES

Chamard V, Schülli T, Metzger T H, Sarigiannidou E, Rovuière J-L, Tolan M, Adelmann C Eaglesham D J and Cerullo M 1990 Phys. Rev. Lett. **64**, 1943

Oliver R A, Kappers M J, Humphreys C J Humphreys and Briggs G A D 2005 J. Appl. Phys. 97, 013707

Ruvimov S, Werner P, Scheerschmidt K, Gösele U, Heydenreich J, Richter U, Ledentsov N N, Grundmann M, Bimberg D, Ustinov V M, Egorov A Yu, Kop'ev P S and Alferov Zh I 1995 Phys. Rev. B. **51**, (20), 14776

Tachibana K, Someya T and Arakawa Y 1999 Appl. Phys. Lett. **74**, 383

Investigation of $In_xGa_{1-x}N$ islands with electron microscopy

A Pretorius, T Yamaguchi, M Schowalter, R Kröger, C Kübel[1], D Hommel and A Rosenauer

Institute of Solid State Physics, University of Bremen, Bremen, Germany
[1] Fraunhofer Institute for Manufacturing and Advanced Materials (IFAM), Bremen, Germany

ABSTRACT: $In_xGa_{1-x}N$ islands grown by molecular beam epitaxy are analysed by transmission electron microscopy. Samples are compared which were of different nominal In concentrations and with or without GaN capping. The optimum imaging conditions for evaluation are described with special focus on polarity determination during analysis.

1. INTRODUCTION

Research on the $In_xGa_{1-x}N$ material system has increased dramatically since the first development of light emitting diodes and laser diodes in the blue to violet spectral range (Nakamura et al 1993, 1996). In principle, the band gap can be tuned by x to achieve emission over the whole spectral range. However, the high defect density and the miscibility gap (Ho and Stringfellow 1996) of the $In_xGa_{1-x}N$ system makes the growth of high quality structures difficult. In recent years, many problems were overcome and much progress was achieved in the growth of quantum well lasers, but the quality of quantum dot (QD) structures is still poor. The fabrication of QD lasers is of increasing interest because it is expected that the threshold current density for the laser emission can be reduced in comparison to quantum well lasers. The realisation of QD lasers with tailored band gap requires a high uniformity of size and composition distribution of the QDs. In this work we study composition and microstructure of uncapped and capped $In_xGa_{1-x}N$ islands by high resolution transmission electron microscopy (HRTEM).

2. EXPERIMENTAL

The structure of the samples consists of a 2 µm thick metal-organic vapour phase epitaxy (MOVPE) GaN film deposited on (0001) sapphire. On top, a thin GaN buffer layer was grown by molecular beam epitaxy (MBE) and finally the $In_xGa_{1-x}N$ was deposited. Growth and sample parameters are listed in Table 1.

sample	A	B	C
$T_g(In_xGa_{1-x}N)$ [°C]	450	510	510
T_g(GaN, cap) [°C]	---	---	510
In flux/(In + Ga flux)	0.54	0.69	0.69
island density [cm^{-2}]	$3.6x10^{10}$	$1.5x10^{11}$	---
x within islands	~1.0	~1.0	~0.5-0.6
x of wetting layer	~0.6	0.12-0.25	

Table 1: Sample parameters (T_g growth temperature).

Transmission electron microscopy (TEM) was performed using a CM20 UT (Philips). Z-contrast measurements were performed with a Tecnai F20 ST. Cross-sectional TEM samples were prepared in the <11-20> zone axis (ZA) employing a tripod method. After mechanical polishing of the samples, they were ion milled in a PIPS (Gatan) with Ar^+ ions at 5.4 kV and an angle of ±5°.

3. POLARITY MEASUREMENT AND CONCENTRATION CALCULATION

For evaluation of x of $In_xGa_{1-x}N$ islands, layer strain state analysis was used. Optimum imaging conditions for two-beam imaging were employed (Rosenauer and Gerthsen 2004). For that the specimen was tilted by 6° around the [0001] axis in order to apply a centre of Laue circle (COLC) of (12 -12 0 2.2). As $In_xGa_{1-x}N$ is a noncentrosymmetric material, Friedel's law is violated and the intensity I_{0002} of the 000+2 beam differs from $I_{000\text{-}2}$. For optimum imaging conditions, the primary and the 000+2 beams were selected using the objective aperture. The resulting interference fringe pattern was recorded using imaging plates. In order to select the 000+2 beam the polarity of the crystal as defined in Fig. 1 was measured at very thin specimen regions in GaN using the method described by Mader and Rečnik (1998). The accuracy of the method with respect to mistilt was checked by Bloch wave calculations using EMS (electron microscopy image simulation, Stadelmann 1987). Comparison of I_{0002} and $I_{000\text{-}2}$ for small tilts around the ZA was performed for a specimen thickness up to 20 nm. For the <11-20> ZA I_{0002} is more intense than $I_{000\text{-}2}$ for the whole analysed tilt region up to a specimen thickness of 10 nm. For a 14 nm thick specimen an example image is given in Fig. 2.

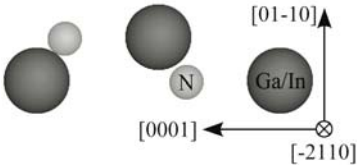


Fig. 1: Polarity of $In_xGa_{1-x}N$.

The In concentration was finally derived from the measured distance of the 0002 fringes using elasticity theory. Elastic constants used for calculations were taken from Wright (1997) and Kanoun et al (2004). For each evaluation of x the elastic constants were linearly interpolated. Depending on different relaxation states of the TEM specimen or the relaxation due to misfit dislocations, different values for x were calculated (Fig. 3). In case of unknown relaxation of the evaluated $In_xGa_{1-x}N$, large errors of x were obtained with increasing 0002 fringe distance.

Images for quantitative evaluation of x were taken after no longer than 60 s in the electron beam to minimise electron induced damage of the TEM specimen (Smeeton et al 2003). No change of phase (wurtzite ↔ sphalerite) or of the form of the islands was observed which could be attributed to electron irradiation during TEM analysis.

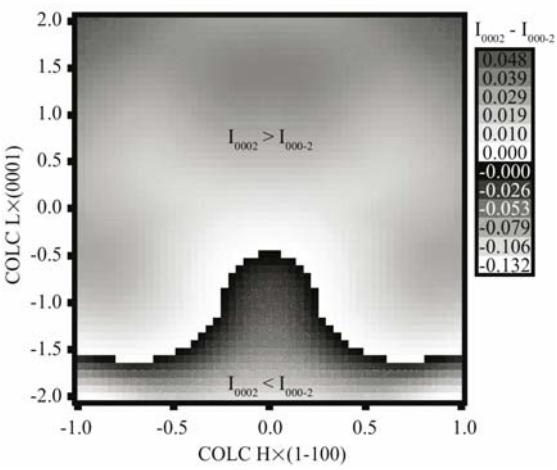


Fig. 2: Difference of intensity between 0002 and 000-2 beams calculated for GaN close to the <11-20> ZA for a specimen thickness of 14 nm.

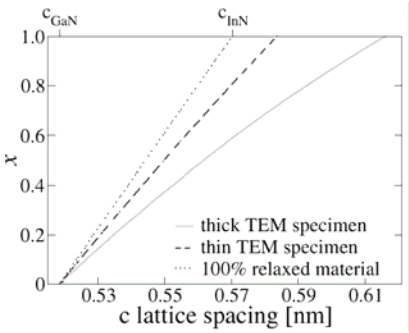


Fig. 3: Calculation of x from measured 0002 fringe distance, i. e. c/2, for different relaxation of a <11-20> ZA TEM specimen.

4. RESULTS AND DISCUSSION

Atomic force microscopy (AFM) of sample A showed islands of diameter 20-50 nm and average height 4 nm with a density of 3.6×10^{10} cm^{-2}. HRTEM analysis using the <11-20> ZA showed

that most islands consist of a mixture of sphalerite and wurtzite material. Only very few pure wurtzite or pure sphalerite islands were observed. The growth correlation between the phases was <0001>||<111>, <11-20>||<-101> and <1-100>||<11-2>. The pure wurtzite islands contain about equidistant dislocations with Burgers vector component parallel <1-100> (Fig. 4), which originate at the interface of the buffer GaN to $In_xGa_{1-x}N$. Pure wurtzite islands did not show pronounced faceting. From HRTEM ZA images x was derived from the measured projected in-plane lattice constant and the projection of the lattice constant in growth direction. By this, the relaxation of the islands due to misfit dislocations could be taken into account and a distinction between sphalerite and wurtzite phase could be made. Nevertheless, this analysis is more inaccurate due to the inevitable delocalisation when employing more than two beams for image formation. The lattice constants of the islands were compared to the buffer GaN lattice constants and a concentration of nearly 1.0 in both pure wurtzite and sphalerite islands was found whereas x of the wetting layer amounts to approximately 0.6. Although stacking faults are found in the wetting layer, no misfit dislocations were observed.

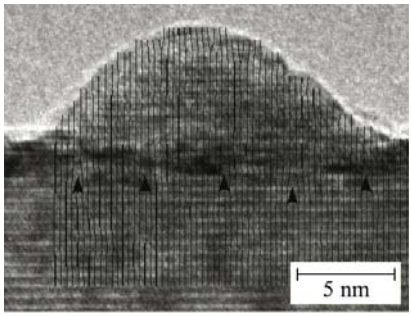


Fig. 4: Pure wurtzite $In_xGa_{1-x}N$ island of sample A viewed in <11-20> ZA. Arrows mark cores of misfit dislocaions.

To grow pure wurtzite $In_xGa_{1-x}N$ islands, growth conditions were changed to reduce the In concentration. In the uncapped sample B islands of average diameter of 20-40 nm, average height of 4 nm, and density of $1.5x10^{11}$ cm^{-2} were observed. From HRTEM along the <11-20> ZA all islands are wurtzite. The islands contain many, almost equidistant misfit dislocations with Burgers vector component in <1-100> direction similar to sample A (Fig. 4). No pronounced faceting of the islands is observed (Fig. 5). x was derived from images recorded using optimum imaging conditions for strain state analysis as described above. Values of 0.6 to 1.0 are calculated for a strained to fully relaxed island (Fig. 3). Using the average distance of lattice planes terminating at dislocation cores, the degree of relaxation of the islands was estimated. In this way, a value for x of the islands close to 1.0 is obtained. The wetting layer has a thickness of approximately 3 nm and does not show stacking faults or misfit dislocations. Hence, the In concentration was derived under the assumption of a totally strained $In_xGa_{1-x}N$ layer, i. e. thick TEM specimen, and amounts between 0.12 – 0.25.

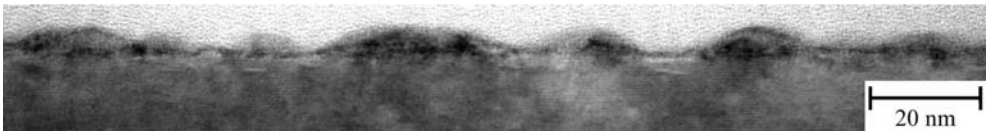


Fig. 5: Overview of islands in sample B. The image was made using optimum imaging conditions for strain state analysis in <11-20> ZA.

In order to analyse the overgrowth of $In_xGa_{1-x}N$ islands with GaN and for photoluminescence measurements, a 8 nm thick capping layer was grown (sample C). The cap layer was deposited at the same temperature as the $In_xGa_{1-x}N$ in order to prevent In redistribution due to diffusion. Furthermore, the capping was done at Ga-rich conditions to obtain a smooth surface of the GaN layer. The In concentration in this sample was measured using strain state analysis from 0002 fringe images and amounts to 0.5-0.6 for a totally strained $In_xGa_{1-x}N$ layer. The layer thickness is ~3.3 nm. Many defects with Burgers vector component in <0001> and <1-100> direction originate in the $In_xGa_{1-x}N$ region so that analysis of fluctuations is difficult, as no larger regions could be found to be suitable for analysis. The observed fluctuations (Fig. 6a) are supposedly due to the distorted lattice. Z-contrast analysis could not detect islands but showed a rather homogeneous In distribution. Photoluminescence showed strong yellow luminescence which can be attributed to the numerous dislocations originating in the $In_xGa_{1-x}N$ region.

For the uncapped samples a change of growth conditions changed only x of the wetting layers. The islands consist in both samples A and B of almost pure InN. Still a change to pure wurtzite phase islands is observed for the samples with lower In concentration in the wetting layer. Possibly, the

higher $In_xGa_{1-x}N$ growth temperature of sample B is responsible for the phase change.

In HRTEM images of sample C no cubic inclusions in the $In_xGa_{1-x}N$ region were observed. Nevertheless, the GaN cap layer exhibits cubic inclusions 1-2 nm above the $In_xGa_{1-x}N$ (Fig. 6b). Samples containing $In_xGa_{1-x}N$ grown under the same conditions as sample A, but with a GaN cap layer showed cubic inclusions starting in the $In_xGa_{1-x}N$ region. After ~10 nm cap layer growth all further deposited GaN had sphalerite structure. Hence it is believed that, although the cubic inclusions in $In_xGa_{1-x}N$ islands of sample A may facilitate the growth of cubic GaN, the main reason for occurrence of cubic inclusions in the cap layer are the growth conditions of the cap. It may be possible to obtain very thin wurtzite GaN cap layers using the applied growth conditions.

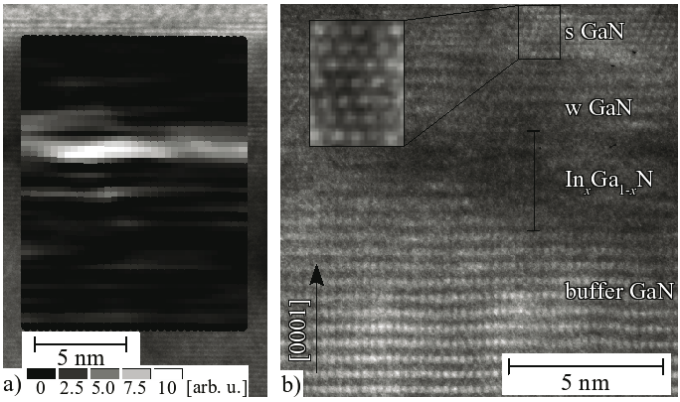


Fig. 6: a) Map of strain in sample C. b) HRTEM in <11-20> ZA of sphalerite inclusions in the GaN cap layer (w wurtzite, s sphalerite). The inset shows the ABC stacking of the sphalerite {111} planes.

5. CONCLUSION

$In_xGa_{1-x}N$ islands could be realised by MBE growth. For growth at lower temperature the islands exhibit an In concentration of ~1.0 and consist of a mixture of sphalerite and wurtzite phase. Growth at higher temperature results in pure wurtzite islands of comparable In concentrations, only the In concentration of the wetting layer is reduced from ~0.6 to ~0.2.

A GaN cap layer on pure wurtzite islands contains cubic inclusions starting 1-2 nm above the $In_xGa_{1-x}N$ region. These are attributed to the growth conditions of the cap layer. Observed fluctuations of strain in the wurtzite $In_xGa_{1-x}N$ region supposedly have their origin in the numerous dislocations generated at the interface of buffer GaN and $In_xGa_{1-x}N$.

ACKNOWLEDGEMENT

Funding by the Deutsche Forschungsgemeinschaft under contract number KR 2195/3-1 is gratefully acknowledged.

REFERENCES

Ho I-H and Stringfellow G B 1996 Appl. Phys. Lett. **69**, 2701
Kanoun M B, Merad A E, Merad G, Cibert J and Aourag H 2004 Sol.-Stat. Electronics **48**, 1601
Mader W and Rečnik A 1998 phys. stat. sol. (a) **166**, 381
Nakamura S, Senoh M, and Mukai T 1993 Jpn. J. Appl. Phys. **32**, L8
Nakamura S, Senoh M, Nagahama S-I, Iwasa N, Yamada T, Matsushita T, Sugimoto Y, and Kiyoku H 1996 Appl. Phys. Lett. **69**, 4056
Rosenauer A and Gerthsen D 2004 Proc. 13th EMC **1**, 103
Smeeton T M, Kappers M J, Barnard J S, Vickers M E and Humphreys C J 2003 Appl. Phys. Lett. **83**, 5419
Stadelmann P A 1987 Ultramicroscopy **21**, 131
Wright A F 1997 J. Appl. Phys. **82**, 2833

First stage of nucleation of GaN on (0001) sapphire

Y B Kwon[1], J H Je[1], P Ruterana[2] and G Nouet[2]

[1]Synchrotron X-ray Laboratory, Department of Materials Science and Engineering, Pohang University of Science and Technology, Pohang 790-784, Korea
[2]SIFCOM UMR 6176 CNRS, ENSICAEN, 6 Bld Marechal Juin 14050 Caen cedex, France

ABSTRACT: The origin of threading dislocations (TDs) in GaN epitaxial layers grown on sapphire (0001) substrate is investigated using moiré fringes from plan-view transmission electron microscopy. The studied samples are nucleation layers deposited at 540°C for times ranging from 20s to 180s. This initial stage growth gives rise to islands which are randomly rotated and relaxed with misfit dislocations. The islands that start to coalesce from 60s growth time keep this random orientation and this leads to the bending of 60° misfit dislocations in the interface plane to form *a*-type TDs inside low angle boundaries.

1. INTRODUCTION

Gallium nitride (GaN) has attracted considerable interest for optoelectronic devices operating in the blue–green to ultraviolet regime (Nakamura et al 1994, Morkoç et al 1995). The TDs behave as non-radiative recombination centers and affect carrier mobility by acting as charged scattering centers (Look et al 1999). It was shown that TDs originated inside the buffer layer (Narayanan et al 2001). This is in contrast with the previous report based on the observations that the TDs form sub-grain boundaries subsequent to the mosaic growth of GaN on sapphire (Ning et al 1996). However, the final microstructure after the heat treatment and growth of the thick active layer is dependent on the particular growth conditions and may hide the mechanisms that govern the formation of the TDs.

In this work, we investigate early stage deposited GaN layers and follow the evolution of the moiré patterns. It is shown that, although the islands relax early by the formation of misfit dislocations, this relaxation is not completed. The residual strain leads to a random rotation of the islands on the substrate surface, which constitutes a possible origin of TDs at coalescence of these islands.

2. EXPERIMENT

GaN nucleation layers were grown on *c*-plane sapphire substrates by MOCVD. The substrates were cleaned with solvents and subjected to *in situ* pretreatment under a H_2 flow at 1100°C. The nucleation layers were grown at 560°C using trimethylgallium (TMGa) and ammonia (NH_3). The investigated sample growth times were 20, 40, 60, 120 and 180s. HREM was used to determine the epitaxy and microstructure of the GaN layers. Observations were carried out using a 002B Topcon electron microscope operating at 200 kV with a point-to-point resolution of 0.18 nm and JEOL 2011 FEG microscope.

3. RESULTS AND DISCUSSION

An isolated island growing on the substrate shows a partial relaxation due to the presence of misfit dislocations at the interface (Fig. 1a,b). GaN islands transform from hexagonal to cubic structure. The strain of GaN layer was greatly reduced by introducing misfit dislocations in the islands even for these short growth times (Degave et al 2002).

Figures 2a and 2b show non-rotation and rotation of moiré fringes from GaN islands in plan-

view samples, respectively. It is seen that three sets of moiré fringes appear in both cases. However the details and symmetry of the pattern are different. The pattern of moiré fringes in Fig. 2a is for a thick GaN film and is symmetric. It shows three sets of moiré fringes, as represented by black dashed lines, which are aligned in the same manner along the background atomic image (white dashed lines), while for the GaN island, the moiré pattern (white dashed lines) is not aligned along the background atomic image (white dotted lines) (Fig. 2b). A rotation of the island gives rise to a rotation of the moiré fringes image. Therefore, inside these islands of 40s growth, a rotation already exists. By comparing the simulation of different rotation angles, it is deduced that the rotation for 40s growth of GaN islands is in the range of about 4°.

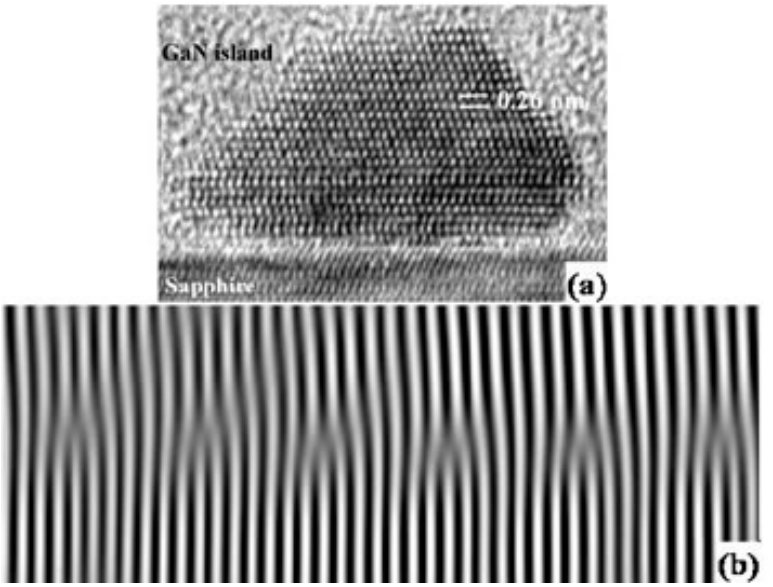


Fig. 1: (a) Cross-sectional TEM image obtained from 40s growth and (b) Fourier filtered image using the $\{1\bar{1}00\}$ spots in GaN and $\{11\bar{2}0\}$ spots in sapphire

Moiré fringes for a 60s growth of the GaN nucleation layer showing only one set of moiré fringes are also present (Fig. 3). GaN islands start to coalesce from 60s growth and moiré fringes are not continuous from one grain to the next. In this case, we also tried to extract rotation angles of GaN islands. Of course, it is not possible to apply the schematic simulation to such images because the three sets of moiré fringes are not present. So we apply the conventional equations of moiré fringe distance as follows:

$$D=d_1d_2/(d_1^2+d_2^2-2d_1d_2\cos\varphi)^{1/2} \quad (1)$$

$$D=d_1d_2/(d_1-d_2) \quad \text{if two planes are parallel i.e. } \varphi=0 \quad (2)$$

$$D=d/\varphi \quad \text{if two plane distances are same i.e. } d_1=d_2 \quad (3)$$

where d_1 and d_2 are interplanar distances of GaN and sapphire, respectively; while φ is the rotation angle between the GaN island and sapphire substrate. D is the moiré fringe distance as measured from the plan-view image. Equation (1) can be used to calculate a rotation angle. However, there are three variables in only one equation. Actually, in our cases, this equation may be applied to GaN nucleation layer systems: First, the interplanar distance of the sapphire substrate is known. Second, the interplanar distance of GaN is near the equilibrium value because the strain is mainly relaxed by introducing misfit dislocations from 40s growth GaN nucleation layer (Fig. 1). Therefore, only one variable remains in Eq.(1). In order to extract the rotation angle, we have used two possibilities which

lead to the formation of high intensity moiré fringes, i.e. GaN($1\bar{1}\bar{2}0$)//Sapphire($1\bar{1}00$) and GaN($1\bar{1}00$)//Sapphire($1\bar{1}\bar{2}0$). The interplanar distances of GaN($1\bar{1}\bar{2}0$) and Sapphire($1\bar{1}00$) are 1.5945Å and 1.3735 Å while those of GaN($1\bar{1}00$) and Sapphire($1\bar{1}\bar{2}0$) are 2.762Å and 2.379Å, respectively. By using these spacings, we determined the rotation angles of several islands for the various growth time samples of GaN nucleation layers. The rotation angles are randomly distributed and can be as large as 12 degrees in some cases. When these randomly rotated islands meet at

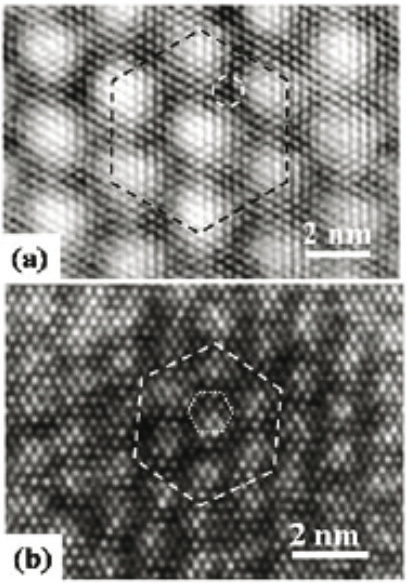


Fig. 2: Plan-view moiré images of (a) non-rotation of relaxed layer and (b) about 4 degrees rotation of GaN nucleation island.

coalescence, the misfit dislocations which cannot continue from one grain to the next will easily bend to form the low angle grain boundary dislocations. This is clearly visible in plan view images of a thick GaN layer and the TDs are arranged in low angle grain boundaries. Ning *et al.*(1996) were the first to propose that mosaic growth of GaN would lead to the formation of TDs at the low angle grain

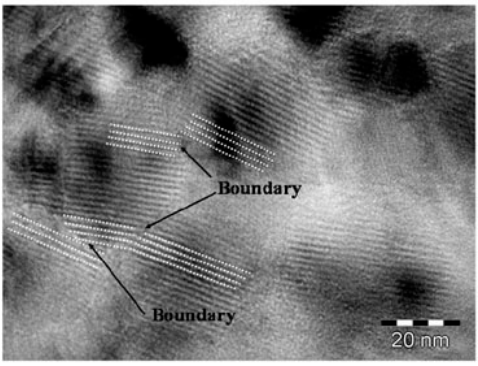


Fig. 3: Plan-view image of moiré fringe of 60s grown GaN nucleation layer

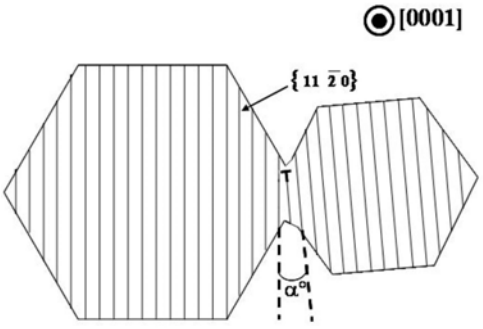


Fig. 4: A schematic of the formation of a grain boundary dislocation at the contact plane of two GaN islands. The two islands are rotated ($\alpha°$) around the axis[0001], normal to the film/substrate interface

boundaries. However in their investigation, no reason was provided for the mosaic growth and no connection was proposed between the misfit dislocations and the threading ones. Of course the dislocations cannot terminate just in the grain boundary as vertical defects. So we need their continuity when they reach the substrate surface and the only way is to connect to the misfit dislocations (Kehagias et al 2001). The threading dislocation is formed from the interface during coalescence (Fig. 4). Our results clearly suggest that the origin of the threading dislocation is the coalescence between differently rotated islands. This coalescence takes effect in the GaN nucleation layer after 60s growth. Due to lateral growth, some grains can reach a critical size and overcome the smallest grains. This process leads to an evolution of the grain size resulting in a mosaic microstructure different to that of the nucleation layers.

4. CONCLUSIONS

The rotation of islands in GaN nucleation layer is analyzed using moiré fringe patterns. The random distribution of the rotation angle strongly suggests that coalescence of adjacent GaN islands leads to the bending of the misfit dislocations, which directly transform into threading edge dislocations with Burgers vector $\mathbf{b}=1/3<11\bar{2}0>$.

ACKNOWLEDGEMENTS

This work was supported by STAR project (KISTEP and French Embassy in Seoul) and CNRS-KOSEF international collaboration. This work was also supported by the BK21 project and by the Korea Institute of Science and Technology Evaluation and Planning (KISTEP) through the NRL project. For the French part, it was supported by the EU under contract MRTN-CT-2004-005583.

REFERENCES

Degave F, Ruterana P, Nouet G, Je J H and Kim C C 2002 J. Phys.: Condens. Matter **14,** 13019
Kehagias Th, Komninou Ph, Nouet G, Ruterana P and Karakostas Th 2001 Phys. Rev. B. **64**, 195329
Look D C and Sizelove J R 1999 Phys. Rev. Lett. **82**, 1237
Morkoc H and Mohammad S N 1995 Science **267,** 51
Nakamura S, Mukai T and Senoh M 1994 Appl. Phys. Lett. **64,** 1687
Narayanan V, Lorenz K, Wook Kim and Mahajan S 2001 Appl. Phys. Lett. **78**, 1544
Ning X J, Chien F R, Pirouz P, Yang J W and Asif Khan M 1996 J. Mater. Res.**11**

InGaN-GaN quantum wells: their luminescent and nano-structural properties

J S Barnard, D M Graham[1], T M Smeeton[2], M J Kappers, P Dawson[1], M Godfrey[1] and C J Humphreys

Department of Materials Science, University of Cambridge, Pembroke Street, Cambridge CB2 3QZ, UK
[1] School of Physics and Astronomy, University of Manchester, Manchester, M13 9PL, UK
[2] Now at: Sharp Laboratories of Europe, Edmund Halley Road, Oxford OX4 4GB, UK

ABSTRACT: The luminescent and nano-structural properties of InGaN-GaN quantum wells have been investigated as a function of indium content. Photoluminescence spectra of single quantum wells show an excitonic emission mechanism that is localised on a length scale of 12-30Å. Using high-resolution STEM high-angle annular dark field imaging we have looked for nano-structural features in high-indium content multiple and single quantum wells. We find the existence of apparent well width fluctuations in the MQW sample with suggestions of indium fluctuations as well. In the single quantum well, we find a reasonably homogeneous well with no obvious signs of clustering or well width fluctuations.

1. INTRODUCTION

Dislocations in GaN are now established as non-radiative centres for carriers generated in InGaN quantum wells (Cherns et al 2001). However, quantum well devices based on this system operate with modest efficiency (tens of percent) and the mechanism responsible is widely debated (Chichibu et al 1998). The temperature dependence of the radiative efficiency suggests that the mechanism confines or localises free charges with potential barriers similar to room temperature energies. At present, two models are posed: in the indium-clustering model, band-gap minima caused by indium-rich regions form localised states that trap electrons and holes by quasi-electric forces (Kroemer, 2001). In the well-width fluctuation model, quantum well thickness variation coupled with strong electric fields, confine the electrons and holes to opposite edges of the well. Monolayer steps in the well result in offsetting the electron/hole confinement energies either side. Free carrier hopping between wells of different thickness becomes 'frozen out'.

The prevailing view is that strong indium clustering is responsible for localisation and is based on the observation of strong diffraction contrast within the quantum well in bright-field and high-resolution images. However, such localised strain contrast increases rapidly under the electron beam, even in commercially available devices, suggesting that beam damage may be largely responsible for the contrast seen (Smeeton et al 2003). Thus we have been pursuing low-current electron beam techniques that can discriminate between indium and gallium atoms, so that we may reliably ascertain the existence of indium clustering and quantum well width fluctuations.

2. EXPERIMENTAL DETAILS

InGaN-GaN quantum wells were grown between 710^{o}C and 800^{o}C in a Thomas Swan 6×2 inch metal-organic chemical vapour deposition (MOCVD) reactor and the growth details have been reported elsewhere (Barnard et al 2003). Single and multiple quantum well samples were both grown.

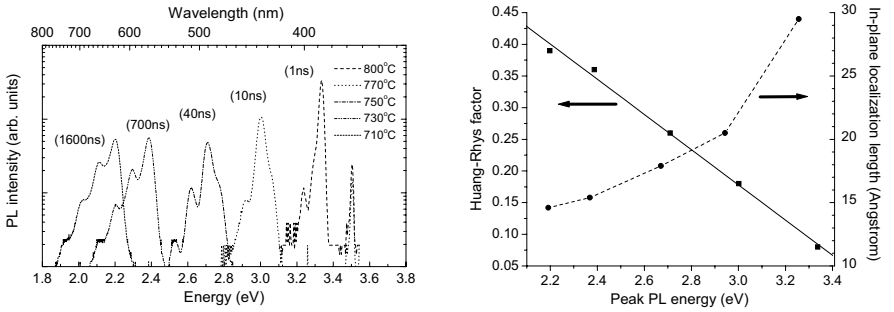


Fig. 1: Low-temperature PL spectra of the SQW series (a). As the indium content increases (right-to-left) the phonon-replication increases. From the relative intensities, the exciton-phonon coupling strength can be extracted and converted to an in-plane localisation length scale, inferred in (b).

Low-temperature (6K) photoluminescence (LT-PL) experiments were performed on the SQW samples only. PL spectra were acquired using an argon ion laser (λ=363.8 nm) and detected using a cooled GaAs photomultiplier. Time-resolved PL (TR-PL) spectra were taken using a cavity dye laser, frequency doubled to λ=290 nm and detected using a time-correlated single-photon counting system.

TEM samples were tripod polished, dimpled and low-energy ion-milled to electron transparency. Hot saturated solutions of potassium hydroxide (60^{o}C) etched away the outer ion-damaged layers of the sample. These were washed in water and inserted into the microscope immediately; this gave thin, clean areas of GaN and InGaN. Scanning TEM high-angle annular dark-field imaging (STEM-HAADF) was done on an FEI tecnai F20 FEGTEM operating at 200 keV. It forms a <2.5 Å electron probe, allowing high-resolution imaging of the quantum well interfaces. All images were taken along the [11-20] direction owing to the large thermal diffuse scattering.

3. RESULTS

Optical spectra taken of the single quantum wells showed three distinct behaviours as the indium content increased (Fig. 1a). First, as expected, the peak PL energy drops owing to both a reduced band-gap and the Stark effect. Second, the decay time of the spectra systematically increased by over three orders of magnitude, again owing to the Stark effect. Reduced power densities had to be used for the highest indium content wells to conform to low-injection conditions. Third, we saw a steady increase in the degree of phonon replication on the low energy side of the PL peak. The strength parameter of phonon replication (the Huang-Rhys factor, *S*) was measured by fitting Poisson-distributed Gaussians to each spectrum (Fig. 1b). *S* is directly related to the in-plane extension of the electron-hole wave-function that describes the couple electron-hole pair i.e. the exciton, and is a measure of its degree of localisation. Inversion of the Huang-Rhys factors, gave localisation length scales of between 12Å for the 26% indium quantum well and 30Å for the 5% indium well.

Originally, we used STEM-HAADF to look at quantum wells grown in a MQW configuration (Fig. 2a). Here we saw direct evidence that, for sufficiently thin specimens of the highest indium content well (710^{o}C growth temperature), the upper interface of the quantum well is littered with monolayer fluctuations. For example between points **A** and **B** there is a monolayer change in height. Step **B** extends for about 1nm before stepping down again. At **C** however, the upper interface is poorly defined suggesting either genuine grading or inclined quantum well steps. This quantum well was the third in a series of ten and it was seen to strain-relax by V-pit formation at the sixth well, suggesting that strain accumulation in these wells was a factor to consider in the interpretation.

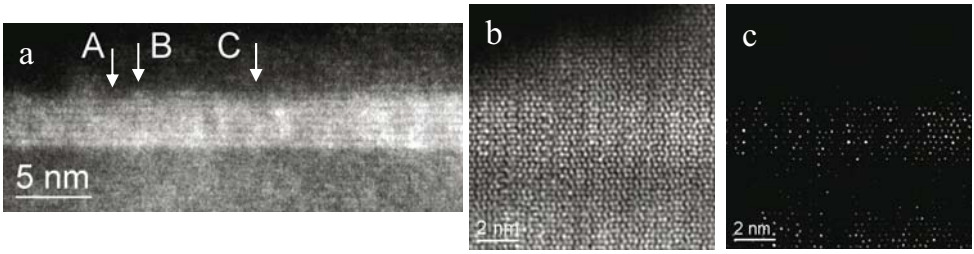


Fig. 2: STEM-HAADF images of quantum well number three in a ten-well MQW stack (a) and a SQW (b & c). The indium occupies the slightly brigher band in the centre. Thicker parts of the GaN show up at the bottom of the image.

Figure 2b shows a higher resolution HAADF image of the corresponding SQW specimen. Here the specimen thickness is much lower, around 2 to 3 nanometres, and the atomic columns show up quite clearly. Thickness was estimated from convergent beam electron diffraction patterns by calculating the intensity ratios of the (0002)/(000-2) beams and comparing to Bloch-wave simulations. Error in the thickness was ±5Å. By adjusting the intensity thresholds of Fig. 2b, the InGaN well shows up more clearly and indium-occupied columns stand out (Fig. 2c). Notice that a few columns have very bright contrast, suggesting more-than-average numbers of indium atoms. For a number of areas on the SQW sample, we calculated the mean and variance of the *intensities* of each of the atomic columns in the InGaN and GaN, with a view to comparing these to the same calculation performed on modelled and simulated STEM-HAADF images of random and clustered alloys.

4. INDIUM CLUSTERING: VARIANCE-BASED SIGNATURES

We compared the mean and variance with two models. First, we used a model in which the HAADF intensity is proportional to the length of the atomic string (m) and the number of indium atoms (n) it contains. Each atom was assumed to scatter independently and that the scattered intensity denuded the incident beam by a very small fraction. Each Ga atom contributed *1* unit of intensity and each In atom *1+F*, where *F* was calculated from a single atom scattering to $50<\beta<200$ mrad using Kirkland's STEMSLIC program (Kirkland 1997). Its value was $F=1.06$ i.e. In scatters twice as effectively as Ga. It is easy to show that, for an alloy $In_xGa_{1-x}N$, the mean intensity is $m(1+xF)$ and the variance goes as $\sigma^2 \approx m$ (Fig. 3).

Second, we used the STEMSLIC program to simulate dynamical propagation of the electron probe through an alloy in both randomised and clustered indium configurations. We used 26Å×22Å super-cells with five mono-layers of $In_{0.2}Ga_{0.8}N$ surrounded by five mono-layers of GaN. We calculated the mean and variance over a range of thickness from a single bi-layer (1.6Å) to sixteen bi-layers (50.1Å). Owing to dynamical diffraction, the depth of the In atom in the atomic column affects the amplitude of the electron wave scattered to high angles, so becomes another source of variance. Thus the variance of the dynamically scattering random In atoms is higher than the simple scattering model, but still decreases monotonically with thickness.

For ordered InGaN, we made up super-cells of GaN with pure InN dots of about $1nm^3$. Again, the effect of dynamical diffraction meant that the height of the dot affected the variance measured, so we averaged over several dot-height configurations to get the mean (Fig. 3). What is evident from the variance-thickness plots is that, for perfectly clustered material, the variance goes through a peak at that thickness corresponding to the dot size, whereas un-clustered indium shows no such peak.

Extraction of the variance of experimental images required removal of the thickness variance term and this was estimated by analysing the indium-free GaN either side of the InGaN. Scatter plots of HAADF variance versus thickness showed both negative and positive values over the whole thickness range (not shown), suggesting that no indium clustering was present. Variance measurement was applied to the SQW sample only.

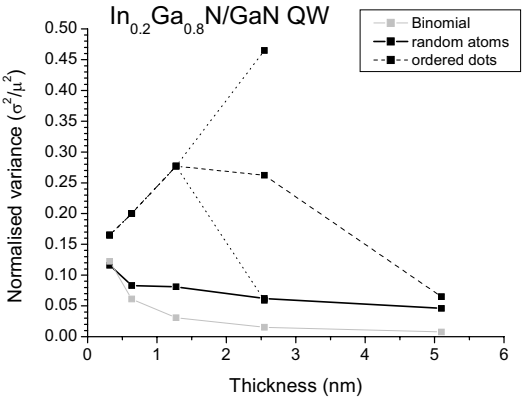


Fig. 3: Plots of variance (σ^2) normalised against the mean (μ) for all the models considered. The lowest variance occurs for the random independent model (Binomial), followed by the dynamical simulations (random atoms). The clustered indium shows a peak and we have indicated how the cluster depth affects the variance (ordered dots).

5. DISCUSSION

The occurrence of monolayer well width fluctuations for an InGaN MQW on such a fine scale is the first we know of. Gross well width fluctuations were observed by Narayan et al (2002), but the amplitude and the wavelength of the fluctuations they saw was large. However, the existence of a strained well underneath the well shown may have induced the fluctuation through the underlying stress-fields. We have yet to investigate the well-to-well evolution of the MQW stack as a whole.

The SQW has no underlying stress and our variance-based measurements showed no signs of indium clustering. However, our procedure is flawed. To get a reliable estimation of the variance requires large data sets and, with the thickness variations across the samples, it is hard to get reliable variance values from small areas of the sample. Better approaches would reconstruct the intensity distributions of atomic columns, using Bayesian methods, for given sample thickness and test for bimodality there. However, when we compared the images of simulated random InGaN (not shown) to the experimental images (Fig. 2c), no major differences were seen. If indium clustering is present, then it is small. This is perhaps not surprising, given the variation in band-gap (0.7-3.6 eV) for InGaN, back-of-the-envelope calculations show an indium concentration fluctuation of a few atomic percent is sufficient to create potential minima of a few tens of meV.

We acknowledge FEI and the Isaac Newton Trust for financial support.

REFERENCES

Barnard J S, Kappers M J, Thrush E J and Humphreys C J 2003 Inst. Phys. Conf. Ser. **180**, 281

Cherns D, Henley S J and Ponce F A 2001 Appl. Phys. Lett. **78,** 2691

Chichibu S, Sota T, Wada K and Nakamura S 1998 J. Vac. Sci. Technol. **B16**, 2204

Graham D M, Soltani-Vala A, Dawson P, Godfrey M J, Smeeton T M, Barnard J S, Humphreys C J and Thrush E J 2005 J. Appl. Phys. *accepted*

Kirkland E J 1998 Advanced Computing in Electron Microscopy (Plenum)

Narayan J, Wanf H, Ye J, Hon S, Fox K, Chen J C, Choi H K and Fan J C C 2002 Appl. Phys. Lett. **81**, 841

Smeeton T M, Kappers M J, Barnard J S, Vickers M E and Humphreys C J 2003 Appl. Phys. Lett. **83**, 5419

Evolution of InGaN/GaN nanostructures and wetting layers during annealing

Rachel A Oliver, Nicole K van der Laak, Menno J Kappers and Colin J Humphreys

Department of Materials Science and Metallurgy, University of Cambridge, Pembroke Street, Cambridge, CB2 3QZ, United Kingdom

ABSTRACT: InGaN nanostructures grown by metal-organic vapour phase epitaxy were annealed in NH_3 for varying lengths of time. In the early stages of the anneal, the nanostructure number density is stable, but an unusual phenomenon is observed whereby previously randomly distributed nanostructures form small clusters. At longer anneal times, the epilayer starts to decompose and the nanostructure density decreases simultaneously, but the clustering persists even for rather low nanostructure densities. Cluster formation may be due to the thermodynamics of nanostructure growth on an undulating substrate surface.

1. INTRODUCTION

The growth of self-assembled InGaN nanostructures is exciting increasing interest, since the localisation of carriers is believed to be essential in the successful operation of InGaN/GaN light-emitting diodes (LEDs) (Smeeton et al 2003). Self-assembled InGaN nanostructures (or quantum dots) could, if appropriately optimised, provide improved localisation and hence better device performance. However, little is understood about the competing roles of kinetics and thermodynamics in Stranski-Krastanov growth of InGaN nanostructures. Kamins et al (1999) suggest that to distinguish between the effects of equilibrium thermodynamics and of Ostwald ripening, one should anneal the nanostructure array at constant material coverage. However, InGaN may start to decompose when annealed, complicating data interpretation. Here, we describe the annealing of InGaN nanostructure arrays grown by metal-organic vapour phase epitaxy (MOVPE) under an NH_3 atmosphere, and some surprising effects which are observed.

2. EXPERIMENTAL

The InGaN nanostructures were grown by MOVPE on GaN pseudo-substrates as has been previously described (Oliver et al 2005). The amount of InGaN deposited for each sample was approximately 5 monolayers (ML). The samples were annealed at growth temperature (710 °C) for varying lengths of time, under an NH_3 flow, with N_2 as carrier gas. They were then examined *ex situ* using a Dimension 3100 atomic force microscope (AFM) to assess the changes in morphology caused by the anneal process. Photoluminescence (PL) measurements were also performed at room temperature on the epilayers.

3. RESULTS

AFM images of samples annealed for a range of times are shown in Fig. 1. The variation in nanostructure number density with time is illustrated in Fig. 2. For anneal times of up to 60 s (Fig. 1a-d) the nanostructure density is fairly stable, but drops rapidly for anneal times of 90 – 120 s (Fig 1e–g). For the longest anneal times, the nanostructure density continues to decrease, but falls less steeply (Fig. 1h and i). A more surprising result is that the nanostructures, which are initially fairly randomly distributed over the substrate surface, start to form small clusters. This is evident for anneal times of 60 s and above, but is most marked for in the sample annealed for 240 s (Fig 1h), where almost all the nanostructures appear to be in extended clusters, leaving the majority of the surface

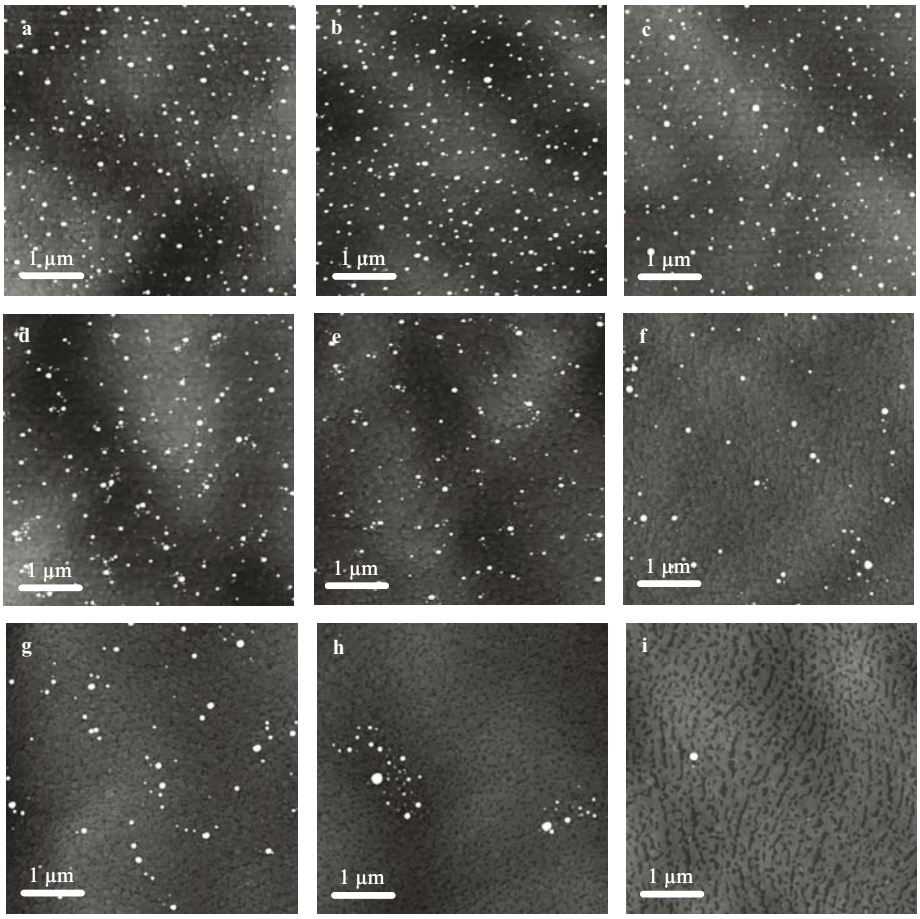


Fig. 1: AFM images of InGaN nanostructure arrays annealed for (a) 0.5 s, (b) 15 s, (c) 30 s, (d) 60 s, (e) 75 s, (f) 90 s, (g) 120 s, (h) 240 s and (i) 480 s. The greyscale in these images has been adjusted to allow both the 3D nanostructures and the WL to be clearly seen.

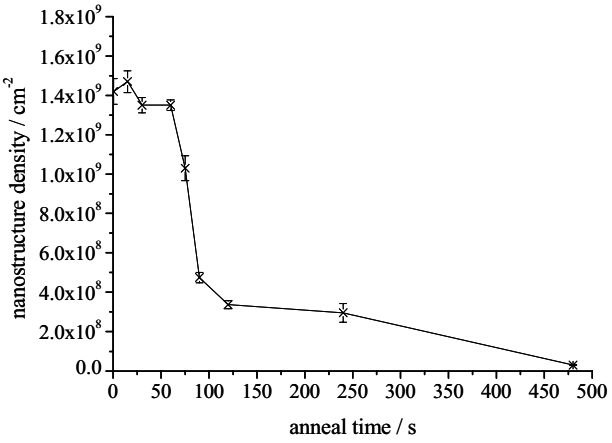


Fig. 2: Variation of nanostructure density with anneal time.

bare. An additional change occurs in the morphology of the two-dimensional (2D) wetting layer (WL) underlying the three dimensional (3D) nanostructures. The WL is initially composed of a mixture of terraces and irregular 2D islands 2 – 3 ML high and ca. 70 nm in width. For anneal times of 30 s and above, pits form in the flat WL, and increase in both size and number at longer anneal times. After 480 s of annealing (Fig. 1i), the epilayer morphology is almost entirely dominated by elongated pits in the WL, whose long axes appear to follow the prevailing

direction of the step edges in the underlying GaN pseudo-substrate.

PL measurements will not be discussed in detail here. However, it may be noted that as the anneal time increased, a blue shift in the peak PL wavelength was observed, suggesting that the indium content of the film was decreasing. This implies that the formation of pits may be due to the decomposition of indium rich regions, which are unstable at the anneal temperature.

4. ANALYSIS

Although the formation of nanostructure clusters is evident to the eye, to assess changes in the extent of clustering with time, we must develop a mathematical metric. For a number of AFM images of each sample, the pixel coordinates of the centre of each nanostructure were found and tabulated allowing centre maps to be drawn. A spreadsheet based macro was then written which allowed the automated finding of the 1st and 2nd nearest neighbouring nanostructure for each nanostructure in the array and the calculation of 1st and 2nd nearest neighbour (NN) distances. Then, for each sample, centre maps for control nanostructure arrays with no clustering were generated based on lists of random numbers from www.random.org, with a nanostructure density equal to the average density for the sample in question. The mean 1st and 2nd NN distances were calculated for these random arrays, with the number of arrays being large enough to reduce the standard error on this mean to less than 1%. The same mean NN distances were calculated for the real samples, allowing the following clustering metrics to be used: C_1 = (mean NN distance for real sample)/(mean NN distance for appropriate control arrays); C_2 = (mean 2nd NN distance for real sample)/(mean 2nd NN distance for appropriate control arrays). The variation in C_1 and C_2 with anneal time is illustrated in Fig. 3. Note that C_1 or $C_2 = 1$, indicates no clustering, whilst decreasing values of C_1 or C_2 indicate an increase in the degree of clustering. Hence, the graph shows that in the first 60 s, the clustering

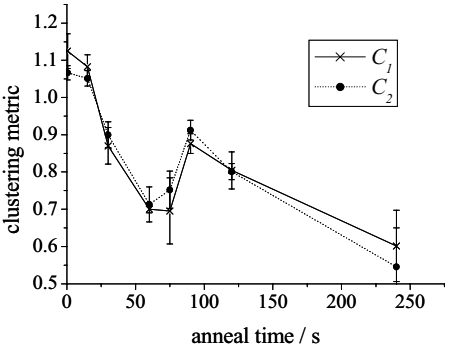


Fig. 3: Variation of the clustering metrics C_1 and C_2 with anneal time.

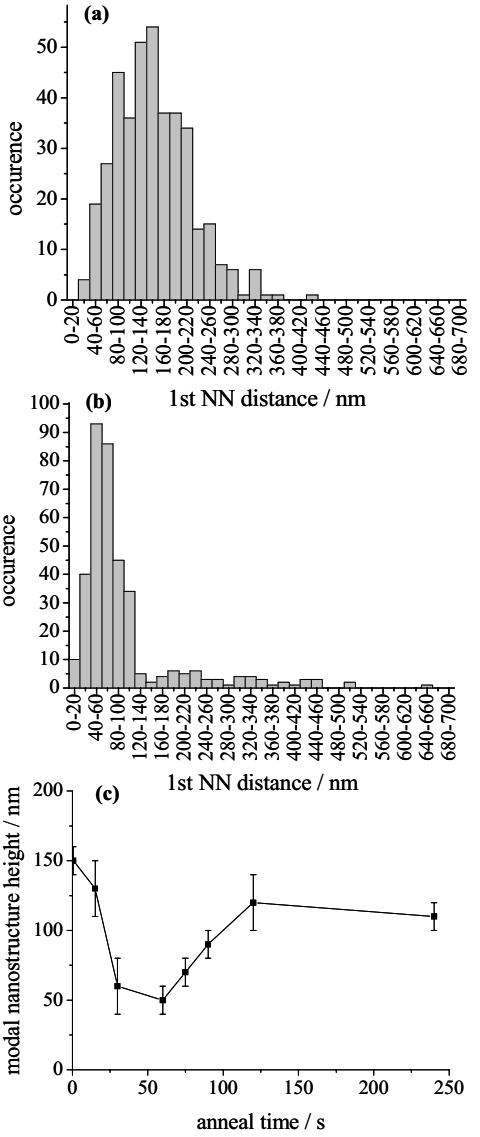


Fig. 4: Histograms of NN distances for samples annealed for (a) 0.5 s and (b) 60 s; (c) shows the variation in the modal dot height with anneal time.

increases monotonically. Between 60 s and 90 s, in the period when the dot density increases most steeply, the level of clustering decreases. Thereafter, the extent of the clustering increases again.

Using the data generated by the analysis macro, it is also possible to draw histograms showing the frequency of occurrence of the NN distances. Fig. 4a and b illustrate the change in the distribution of nearest neighbour distances which occurs when the anneal time is increased from 0.5 s to 60 s. The distribution becomes much more negatively skewed, with a smaller full width at half maximum. Fig. 4c shows the variation in the mode of the distribution with anneal time. In the first 60 s the mode decreases. However, mirroring the changes in C_x, it then increases again up to an anneal time of 240s.

5. DISCUSSION

The above analysis may give us some insight into why the observed clustering occurs. One suggestion might be that the overall energy of the epilayer is reduced when the nanostructures are close together. However, although the modal distance between nanostructures initially decreases with anneal time, once the nanostructure density starts to decrease, it rises again. The nanostructures do not get closer and closer together, as they might if they were stabilised by proximity. This is unsurprising, given the theoretical work of Müller and Kern (1998), which suggests that a pair of nanostructures coming into close proximity will effectively repel one another due to their elastic interaction via the substrate.

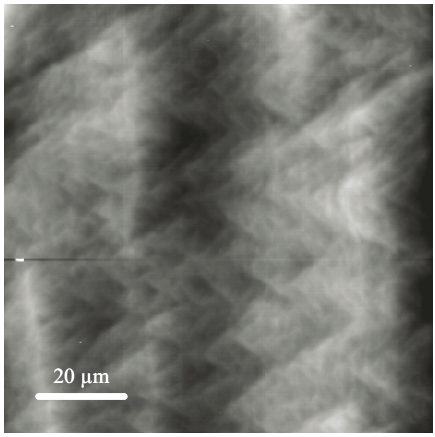


Fig. 5: Broad scale AFM image of a GaN pseudo-substrate , showing surface undulations on a variety of length scales.

However, Kukta and Kouris (2005) suggest that on a sinusoidally undulating substrate, the epilayer surface energy may be decreased by clustering nanostructures in the valleys but the epilayer strain energy may be reduced by clustering the nanostructures on the peaks. Since the GaN substrate shows significant broad-scale undulations (Fig 5) on a variety of length scales, this energetic consideration may drive the clustering process.

Another question which we may consider is the cause of the loss of nanostructure density at anneal times above 60 s. The nanostructure density only starts to decrease after significant clustering has occurred. The increase in C_1 and C_2 as the density decreases suggests that nanostructures are lost from the clusters. It is possible that, once the nanostructures are in closer proximity, material can diffuse easily between them allowing Ostwald ripening to occur. However, the clusters may be evaporating. Further analysis of nanostructure sizes is thus required.

6. CONCLUSIONS

Annealing InGaN nanostructure leads to a decrease in nanostructure density, the formation of pits in the wetting layer and the appearance of nanostructure clusters. The driving force for clustering formation may be the undulating substrate morphology. Further investigation is needed to determine whether the loss of nanostructure density is due to nanostructure evaporation or to Ostwald ripening.

REFERENCES

Kamins T I, Medeiros-Ribeiro G I, Ohlberg D A A, and Williams R S 1999 J. Appl. Phys. **85,** 2
Kukta R V and Kouris D 2005 J. Appl. Phys. **97,** 033527
Müller P and Kern R 1998 J. Cryst. Growth **193,** 257
Oliver R A, Kappers M J, Humphreys C J, and Briggs G A D 2005 J. Appl. Phys. **97,** 013707
Smeeton T M, Kappers M J, Barnard J S, Vickers M E, and Humphreys C J 2003 Appl. Phys Lett. **83,** 5419

Origins and reduction of threading dislocations in GaN epitaxial layers

S Mahajan

Department of Chemical & Materials Engineering, Arizona State University, Tempe, AZ

ABSTRACT: We examined, using AFM and TEM, GaN nucleation layers (NLs) and early stages of high temperature (HT) GaN overgrowth on annealed NLs and HT GaN layers grown for different durations. We demonstrate that threading dislocations (TDs) do not form at the coalescence of HT GaN growths. We identify two sources of TDs: highly defective regions in NLs and point defects present in HT GaN. We developed a novel approach for reducing TDs. We refer to it as *in situ* epitaxial layer overgrowth. This process entails depositing *in situ* a very thin silicon nitride layer on as-deposited NLs, followed by HT growth. The density of TDs is reduced to $2x10^8$ cm^{-2}. We ascertain the origin of the observed reduction.

1. INTRODUCTION

The group III nitrides are scientifically interesting and technologically relevant materials. The bandgaps of InN, GaN, and AlN are, respectively, 0.8, 3.42 and 6.20 eV. The intermediate values of bandgaps can be accessed by mixing binaries to develop ternary and quaternary compositions. These materials have applications in light emitting, high power, high frequency and high temperature devices, a versatile family of semiconductors. If we can dope AlN in a controlled manner and can design stable contacts, devices operating up to 1000ºC would be feasible.

Epitaxial structures required for various device types are generally grown on sapphire and silicon carbide substrates using metalorganic chemical vapor deposition (MOCVD) and molecular beam epitaxy (MBE). A common feature of these structures is the presence of a high density of threading dislocations (TDs). The majority of TDs are **a** type, but **c** and **c+a** dislocations are also observed (Ning et al 1996, Wu et al 1998, Lorenz et al 2000 and Narayanan et al 2002).

An interesting question is how do TDs evolve? Ning et al (1996) suggested that they form by the replication of tilt and twist boundaries defining misoriented and tilted islands present in NLs during the growth of high temperature (HT) GaN. Wu et al (1998) proposed that misoriented islands develop during the HT growth and their subsequent coalescence leads to TDs.

Lorenz et al (2000) and Narayanan et al (2002) showed experimentally the absence of the TDs at coalescence fronts of islands. They demonstrated that the HT growth occurs in certain regions of NLs that have been ramped to a high temperature. As a result, randomly distributed and separated growth patches develop on the surface of an NL. They also showed that even when the patches are separated from each other, they are aligned with each other. So these patches can coalesce without the introduction of sub-boundaries in the overgrowth. They identified two sources of TDs: highly defective regions in NLs and incorporation of point defects during the HT growth.

TDs have deleterious effects on long term reliability of light emitters. So a number of growth protocols have been developed to reduce the density of TDs. These techniques are referred to as epitaxial layer overgrowth (ELOG) (Nam et al 1997 and Sakai et al 1997), pendeo-

epitaxy (PE) (Davis et al 2001), cantilever epitaxy (CE) (Folstaedt et al 2002) and facet-controlled layer overgrowth (FACELO) (Hiramatsu et al 2000). Recently, Fang (2004) developed *in situ* epitaxial layer overgrowth. The layers grown by these techniques have characteristic distributions and varying efficacy in reducing TDs.

The objectives of this paper are two fold. First, to present experimental results on origins of TDs and develop a comprehensive understanding of their formation. Second, to show our results on *in situ* ELOG and compare its efficacy in reducing TDs with those of the techniques listed above.

2. ORIGINS OF TDs

2.1 Two-Step Epitaxy

The lattice mismatch between GaN and sapphire or silicon carbide substrate is substantial. We can show using nucleation theory that if we were to deposit GaN directly on these substrates at high temperature, the growth would nucleate as isolated islands. These islands would subsequently grow into pillars during additional growth, leading to discontinuous layers. Amano et al (1986) proposed an elegant solution to obviate the pillar problem using a growth protocol shown schematically in Fig. 1. This approach is referred to as two-step epitaxy. The first step consists of depositing a GaN or AlN NL on sapphire at low temperature (LT). Subsequently, the NL is heated to HT where device quality GaN layers are grown.

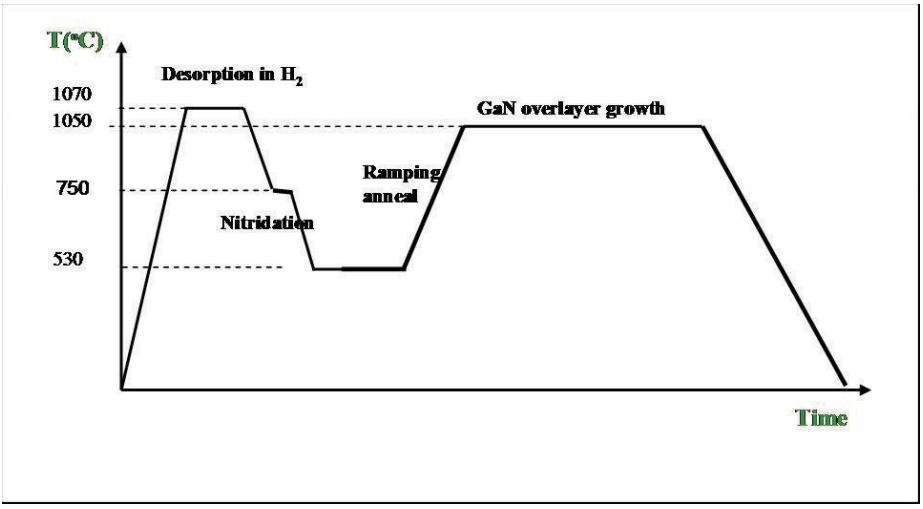


Fig. 1. Schematic of growth sequence

2.2. Microstructural Characteristics of NLs

To distinguish between proposed explanations for origins of TDs, we need to know what NLs consist of. Are they amorphous? Are they continuous? What changes do occur on ramping to HT? We addressed these issues for the first time, and these results are reproduced as Figs. 2 and 3.

Figures 2a and b show, respectively, plan-view images of as-grown and annealed GaN NLs. The observed diffraction patterns are presented as insets. It is clear that an as-deposited NL has a sub-grain structure whose average size is ~20nm. There is no change in grain size on ramping to HT, Fig. 2b. It appears that NL may have evaporated from certain regions on annealing. Furthermore, the observed diffraction patterns show that the sub-grains are rotated by ±5º around the [0001] axis and that the rotation angle does not change on annealing. Also, the presence of slightly dark sub-grains in Fig. 2 implies a tilt away from the [0001] direction.

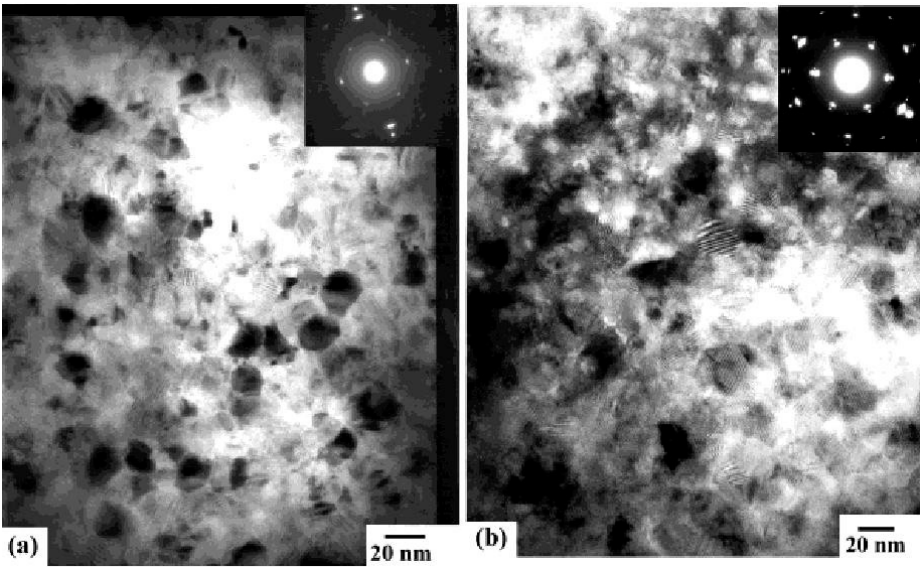


Fig. 2. Plan-view (0001) BF images of (a) as-grown and (b) annealed GaN NLs.

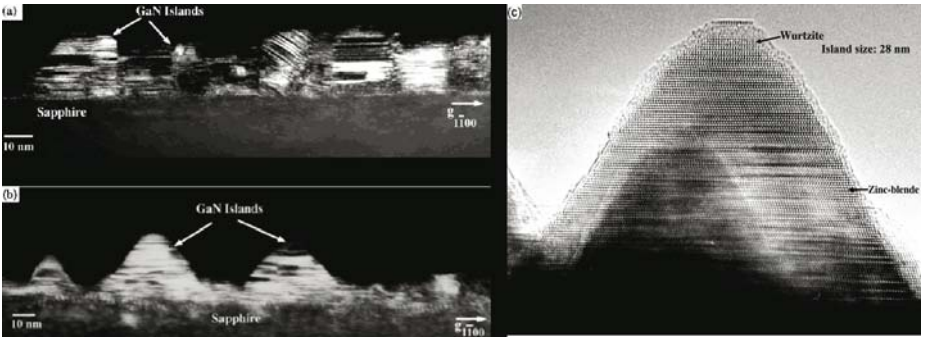


Fig. 3. WB images of (a) as-grown and (b) annealed GaN NLs. The NLs were deposited for 3 min at 530ºC and 300 mbar and annealed to 1030ºC. (c) HRTEM image of an island in the annealed GaN NL.

When examined in cross-section, microstructures of an NL change substantially on heating to HT. This is shown in Fig. 3. Figure 3a is cross-sectional image of an as-deposited NL. The layer consists of highly faulted sub-grains. A sub-grain tilted away from the [0001] direction is also seen in the middle of the micrograph. The microstructure is simplified on ramping to HT, Fig. 3b. The sub-grains have evolved into faceted and stepped islands that are still highly faulted and tilted sub-grains seem to have been eliminated. A HREM image of one of the islands shown in Fig. 3b reveals that the major portion of an as-deposited island has the zinc-blende structure, whereas its top portion has the wurtzitic structure. We propose that during ramping, hydrogen etches GaN and reacts with layer to form GaH_2 that evaporates. Subsequently, GaH_2 reacts with NH_3 to form GaN on top of the island. Since this growth is at HT, it has the wurtzitic structure.

2.3. Early Stages of HT GaN Growth

To understand how HT GaN grows on annealed NLs, we examined growth surfaces after 5, 20, 50 and 75 sec deposition of HT GaN using AFM. These results are shown in Fig. 4. It is evident from these figures that the growth occurs only in certain regions. With the additional growth, patches of HT GaN develop as shown in Figs. 4c and d. The patches are very flat at the top and have inclined side facets that are stepped.

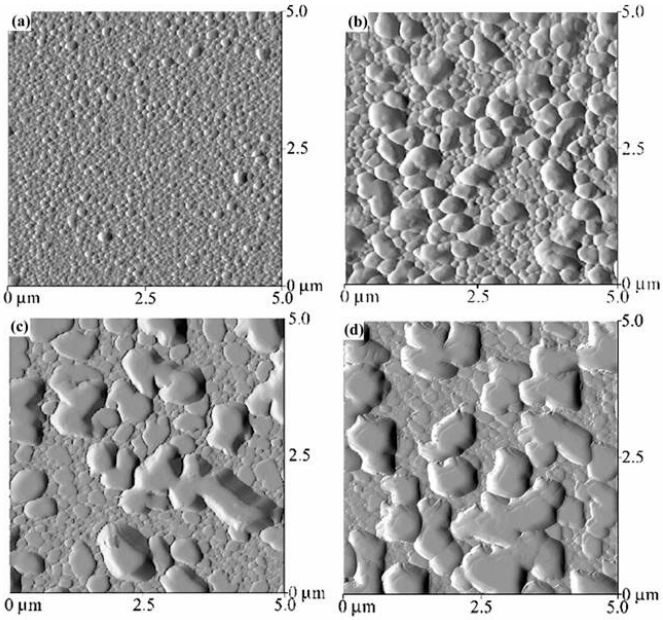


Fig. 4. 5µm x 5µm AFM scans of the surfaces of samples after HT GaN growth for (a) 5s, (b) 20s (c) 50s and (d) 75s on annealed GaN NLs.

We also examined short term growths in plan-view. An image from a 20 sec sample is shown in Fig. 5. The growth regions are distorted hexagons, i.e., parallel sides are unequal in length. Narayanan et al (2002) attributed this inequality to the energy difference between the Ga and N terminated facets, the former having a lower energy due to the absence of dangling bonds.

A higher magnification image of growth patches in Fig. 5a is shown in Fig. 5b. The two patches that are separated form each other show parallel Moire' fringes, implying that they are well aligned with each other. Narayanan et al (2002) suggested that based on the energy considerations, the HT growth occurs preferentially in those regions of NL that have the following orientation relationship with sapphire:

$$[0001]_{GaN} // [0001]_{sapphire} \text{ and } \langle 11\bar{2}0 \rangle_{GaN} // \langle 1\bar{1}00 \rangle_{sapphire}$$

Any deviation from this relationship due to rotation of sub-grains around the [0001] direction may preclude HT growth in those regions.

We also examined growth patches in cross-section by TEM. Figures 6a and b show two contiguous patches in a 20 sec growth sample for two different operating reflections. Two significant observations are: patches are free of TDs and NL is highly defective and faulted. Figures 6c and d show two coalescing patches. It is clear that TDs do not form where the patches coalesce.

Furthermore, the larger patch on the right contains **a** and **c** type dislocations that appear to originate from a highly faulted NL.

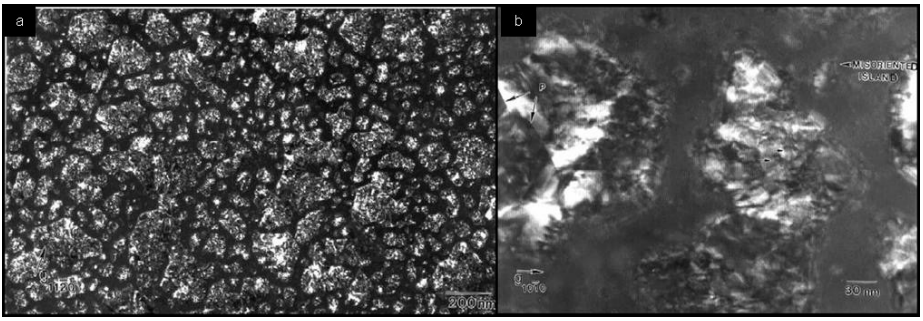


Fig. 5. WB plan-view images of GaN islands after HT GaN growth for 20 s imaged using (a) the $(11\bar{2}0)$ and (b) the $(10\bar{1}0)$ reflections.

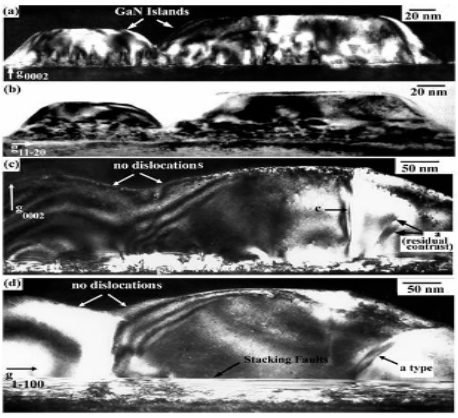


Fig. 6. (a), (b) WB and BF cross-sectional images of GaN islands after HT GaN growth for 20s obtained using (a) the (0002) and (b) the $(11\bar{2}0)$ reflections. (c), (d) WB cross-sectional images after HT GaN growth for 75s obtained using (c) the (0002) and (d) the $(1\bar{1}00)$ reflections.

The observations in Fig. 6 are not consistent with the suggestions of Ning et al (1996) and Wu et al (1998) regarding the origins of TDs. A ramification of Fig. 5b is that TDs should not form when well-aligned growth patches coalesce, an assessment consistent with the results of Figs. 6c and d.

2.4. Time Evolution of HT GaN Growth

The AFM scans of surfaces after 2, 4, 6 and 9 min of HT GaN growth are shown in Fig. 7. The salient features of these micrographs are the following. First, growth patches have flat tops and stepped facets. Second, NL is covered by the lateral migration of stepped facets. Third, for our growth conditions, a continuous layer evolves in 9 min.

An interesting question is how oriented and misoriented sub-grains in an NL are covered by lateral growth of patches without the formation of TDs, see Figs. 6a and b? We suggest that geometrically necessary dislocation networks develop at interfaces between misoriented islands and growth patches. Thus, we could avoid TDs in a growth patch.

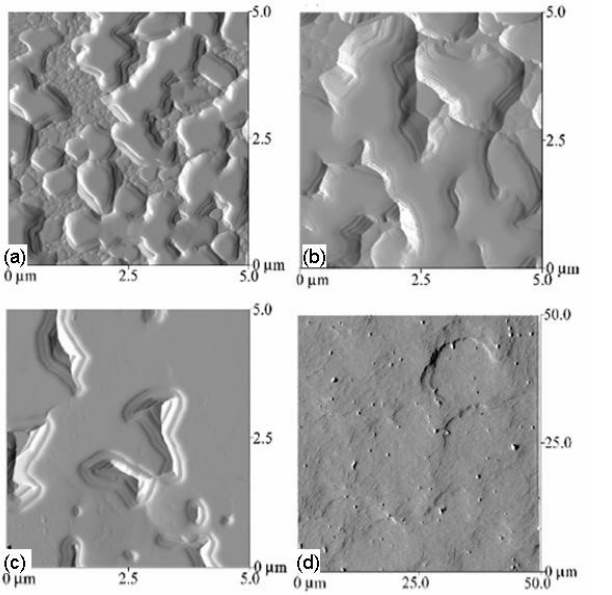


Fig. 7. (a), (b), (c) 5µm x 5µm AFM scans of the surfaces of samples after HT GaN growth for (a) 2 min, (b) 4 min and (c) 6 min, (d) 50µm x 50µm AFM scan after HT GaN growth for 9 min.

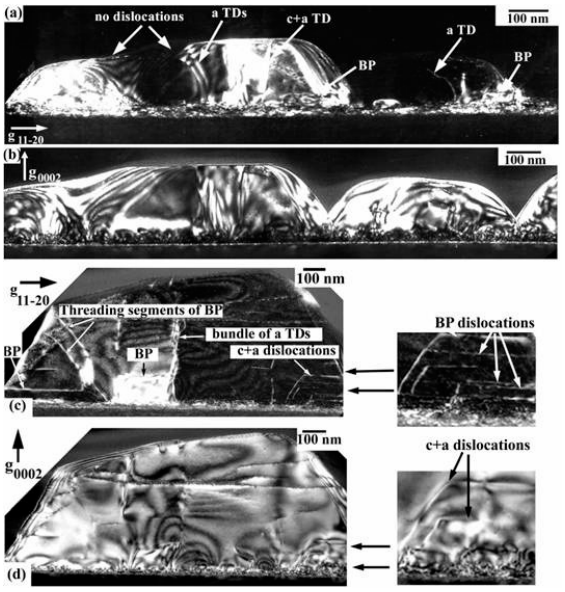


Fig. 8. (a), (b) WB cross-sectional images of GaN islands after HT GaN growth for 2 min obtained using (a) the $(11\bar{2}0)$ and (b) the (0002) reflections. (c), (d) WB cross-sectional images after HT GaN growth for 4 min obtained using (c) the $(11\bar{2}0)$ and (d) the (0002) reflections.

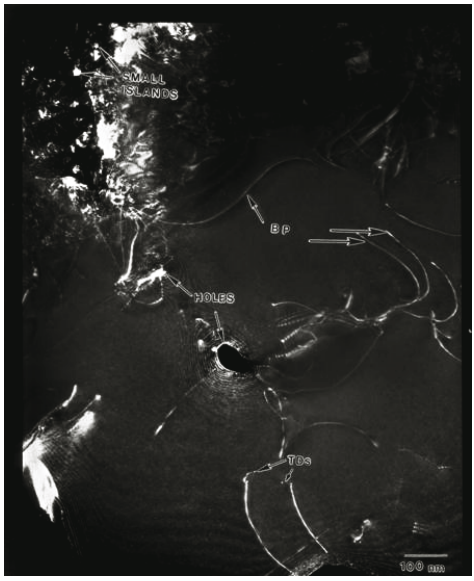


Fig. 9. Plan-view WB image of a large growth patch after HT GaN growth for 6 min obtained using the $(1\bar{2}10)$ reflection.

Figures 8a, b and 8c, d show, respectively, growth patches in cross-section after 2 and 4 min of HT growth. Again, TDs are not observed at the coalescence of patches in Figs. 8a and b. Basal plane (BP) **a** dislocations and **a** and **c+a** type TDs are seen. With the exception of BPs, TDs appear to form from NLs. Furthermore, **a** type BPs dislocations become TDs and terminate on a facet, see Fig. 8c.

Figure 9 shows a plan-view image of an HT layer after 6 min of growth. Its salient features are the presence of BP dislocations, holes and a small sub-grain of NL that is not yet covered by an HT layer.

An interesting question concerns the formation of BPs. We envisage that they form by the condensation of point defects. It is well known that GaN layers grown by MOCVD contain Ga vacancies (Saarinen et al 1998). If these vacancies and N vacancies plate out on two contiguous (0001) planes and followed by a $\langle 1\bar{1}00\rangle$ shear, an intrinsic stacking fault could form. If this fault unfaults by the nucleation of a Shockley partial along the bounding partial, a loop of BP dislocation could form.

The formation of **c** type dislocations may involve the coalescence of two contiguous intrinsic or extrinsic faults separated by c/2. As argued by Narayanan et al (2002), **a** type TDs evolve form from defective regions in an NL. We suggest that **c+a** dislocations result form according the following reaction between **a** and **c** type dislocations: $\frac{1}{3}\langle 11\bar{2}0\rangle + [0001] \rightarrow \frac{1}{3}\langle 11\bar{2}3\rangle$

The above reaction is energetically favorable.

2.5. Formation of Mosaic Structure in HT GaN

Speck and co-workers (Wu et al 1998) suggested that mosaic structure observed in fully grown HT GaN is related to the sub-grain structure present in an NL. In order to test their hypothesis, we examined the distribution of TDs in fully coalesced and fully grown layers in plan-view. These results are shown in Fig. 10. It is clear that TDs are distributed at random after a 9 min of growth. However, layers grown for, 3 hr show a mosaic structure whose size is very much larger than the sub-grain size of 20nm in an NL.

We suggest that the mosaic structure observed in a fully grown layer has no direct correlation with the sub-grain structure in an NL. However, the size of mosaic structure could depend on the quality of an NL. The poorer quality, the smaller the size of mosaic structure. Furthermore, the mosaic structure evolves due to elastic interactions between **a** type TDs and its development must involve glide and climb.

3. Reduction of TDs

3.1. Possible Approaches and Concept of in situ ELOG

Schematics of patterned structures used in (a) ELOG, (b) PE, (c) CE, and (d) FACELO are shown in Fig. 11. They essentially employ the same idea of selected area growth. First, a GaN seed layer, a few micron thick, is grown by two-step epitaxy that is schematically shown in Fig. 1. A mask layer of SiO_2 or Si_3N_4 is then deposited in a separate chamber. Windows are subsequently opened in the mask layer using photolithography, creating unmasked and masked regions. The patterned wafer is returned to a growth chamber to deposit additional HT GaN.

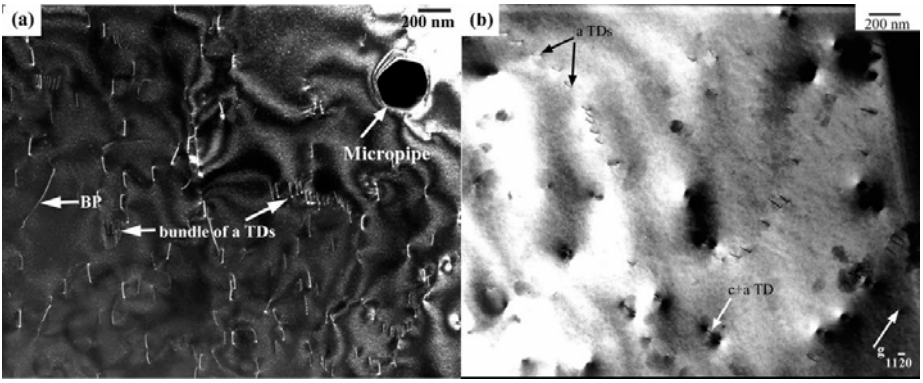


Fig. 10. (a) plan-view WB image after HT GaN growth for 9 min obtained using the $(10\bar{1}0)$ reflection. (b) plan-view BF image of a fully grown GaN epitaxial layer obtained using the $(11\bar{2}0)$ reflection.

Since the above protocols require three steps, i.e., growth of an HT layer, *ex situ* deposition of a mask layer and patterning, we tried to develop a simpler approach. Let us imagine a situation where we *in situ* deposit an extremely thin layer of silicon nitride on an as-deposited NL shown in Fig. 3a. Two distinct situations could arise: silicon nitride either planarizes the NL exposing closely spaced GaN seed crystals or deposits in a conformal fashion. If the latter happens, we will not be able to grow HT GaN on this silicon nitride/NL composite because MOCVD GaN does not want to grow on silicon nitride. We refer to this approach as *in situ* ELOG (Fang 2004), and is shown schematically in Fig. 12.

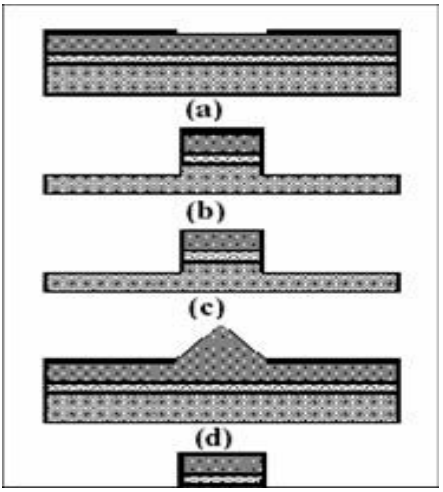


Fig. 11. Schematics of patterned structures used in (a) ELOG, (b) PE, (c) CE, and (d) FACELO techniques. Differently shaded regions represent mask layer, seed layer, nucleation layer, and substrate, respectively.

3.2. Microstructures of as-Deposited and Annealed Silicon Nitride/GaN NL/Sapphire Composites

We performed design of experiments to determine an optimal thickness of silicon nitride. We thus ascertained this thickness to be 2nm. Figures 13a and b show, respectively, as-deposited and annealed composites. Comparing Figs 13b and 3b, it is clear that the presence of silicon nitride has a considerable influence on the metamorphosis of as-deposited sub-grains in an NL on annealing. Silicon nitride appears to prevent the evaporation of GaN during ramping to HT. A plausible reason could be that silicon nitride and GaN react to form a protective ceramic layer.

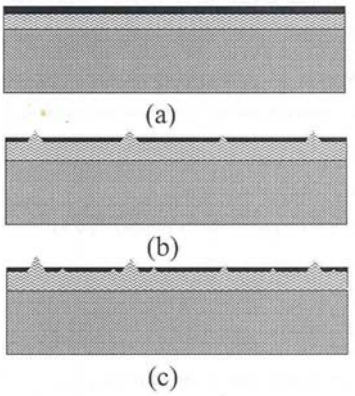


Fig. 12. Schematics of patterned structures used in (a) ELOG, (b) PE, (c) CE, (d) FACELO and ABLEOG. Different Shaded regions represent substrate, NL, seed layer and mask layer, respectively.

3.3. Microstructures of HT GaN Grown on Annealed Silicon Nitride/GaN NL/Sapphire Composites

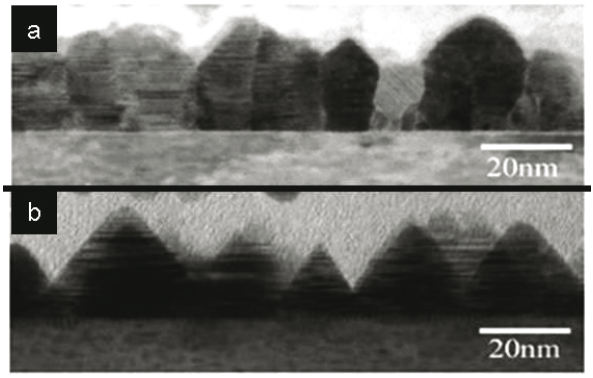


Fig. 13. TEM cross-sectional BF images of (a) as-grown silicon nitride/GaN NL/sapphire composite, (b) annealed silicon nitride/GaN NL/sapphire composite; all images were obtained using the (1-100) reflection. The silicon nitride layer is about 3nm thick.

Cross-sectional and plan-view images obtained from a HT layer deposited on the above composite consisting of 2nm thick silicon nitride layer are shown in Fig. 14a and b, respectively. The solid arrows in Fig 14a delineate **a** type dislocations, whereas the open arrows mark **c+a** type dislocations. Furthermore, a micro-void at the overgrowth/composite interface is observed. TDs appear to bend and terminate on surfaces of the void. It is also clear form Fig. 14b that TDs are randomly distributed in a fully grown HT layer, an advantage over other reduction techniques, where low and high TD density regions develop. The density of TDs is estimated to be ~2 X 10^8 cm^{-2}, two orders of magnitude lower than that observed in the absence of a silicon interlayer (Narayanan et al 2002).

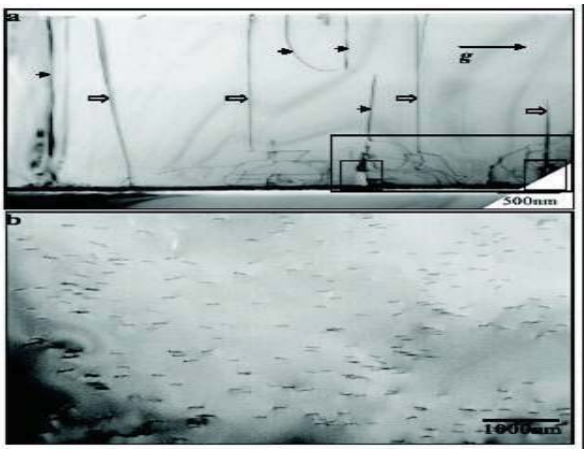


Fig. 14. TEM (a) cross-sectional image formed using $(10\bar{1}0)$ reflection and (b) plan-view image of GaN overlayer grown on Si_3N_4(~2nm)/GaN NL composite.

We envisage that micro-voids are largely responsible for reducing the density of TDs. Imagine a situation where HT growth is initiated from protruding GaN seed crystals present in an annealed silicon nitride/GaN NL/sapphire composite, see Fig. 12. Fang (2004) showed that initially the vertical growth rate is much higher than the lateral growth rate. These vertical islands grow laterally and then coalesce just as in CE. This could explain the formation of micro-voids at the overgrowth/silicon nitride/GaN NL/sapphire interface. Furthermore, the separation between GaN NL seeds is considerably smaller than that can be achieved between stripes in ELOG using conventional photolithography. This feature should reduce the probability of introducing TDs as growth occurs laterally over masks.

4. CONCLUSIONS

GaN NLs consist of sub-grain structure and are highly defective. When HT growth is carried out on annealed NLs, growth patches develop selectively in certain regions. We demonstrate that these patches are well-aligned with each other. TDs do not form when patches coalesce, a result that is inconsistent with the suggestion of Wu et al (1998). We identified two sources of TDs: highly defective NLs and point defects in HT overgrowth. Furthermore, we showed a lack of correlation between the sizes of sub-grains of NLs and mosaic structures in HT layers.

We showed two orders of magnitude reduction in the density of TDs using *in situ* ELOG, a simple and elegant approach. TDs tend to terminate on micro-voids that develop at the overgrowth/silicon nitride/Ga NL/sapphire interface, resulting in a lower TD density.

ACKNOWLEDGEMENTS

It is indeed my pleasure to acknowledge the contributions of X. Fang, M. Gonsalves, W. Kim, K. Lorenz, V. Narayanan and X. Zhang to this work. I am also grateful to NSF and AFOSR for financial support.

REFERENCES

Amano H, Sawaki N, Akasaki I and Toyoda Y 1986 Appl. Phys. Lett. **48**, 353

Davis R F, Gehrke T, Linthincum K J, Zhelve T S, Preble E A, Rajagopal P, Zorman C A and Mehregany M 2001 J. Cryst. Growth **225**, 134

Fang X PhD dissertation 2004 Arizona State University

Folstaedt D M, Provencio P P, Missert N A, Mitchell C C, Koleske D D, Allerman A A and Ashby C I H 2002 Appl. Phys. Lett. **81**, 2758

Hiramatsu K, Nishiyama K, Onishi M, Mizutani H, Narukawa M, Motogaito A, Miyake H, Iyechika Y and Maeda T 2002 J. Cryst. Growth **221**, 316

Lorenz K, Gonsalves M, Kim W, Narayanan V and Mahajan S 2000 Appl. Phys. Lett. **77**, 3391

Nam O H, Bremser N D, Zhelva T and Davis R F 1997 Appl. Phys. Lett. **71**, 2638

Narayanan V, Lorenz K, Kim W and Mahajan S 2002 Phil. Mag. A **82**, 885

Ning X J, Chien F R, Pirouz P, Yang J W and Khan M A 1996 J. Mater. Res. **11**, 580

Saarinen K, Seppala P, Oila I, Hautojarvi P, Corbel C, Briot O and Aulombard R L 1998 Appl. Phys. Lett. **73**, 3253

Sakai A, Sunakawa H and Usui A 1997 Appl. Phys. Lett. **71**, 2259

Wu X, Fini P, Tarsa E J, Heying B, Keller S, Mishra U K, Denbaars S P and Speck J S 1998 J. Crystal Growth **189-190**, 231

Oxygen segregation to nanopipes in gallium nitride

M Hawkridge and D Cherns

H H Wills Physics Laboratory, Royal Fort, Tyndall Avenue, Bristol BS8 1TL

ABSTRACT: The formation of nanopipes in GaN has been linked to impurity segregation. In this paper, a combination of high angle annular dark field imaging and electron energy loss spectroscopy in the Daresbury SuperSTEM is used to investigate the core structure and composition of open core dislocations (nanopipes) in GaN films grown by hydride vapour phase epitaxy. The results show evidence for segregation of oxygen to the nanopipe surfaces. Quantitative analysis suggests that up to several monolayers of nitrogen can be replaced by oxygen. The implications of these results for understanding the electrical properties and core structure of dislocations in GaN are discussed.

1. INTRODUCTION

Threading dislocations in GaN are known to affect the optical and electronic properties of devices. In order to understand these properties, understanding of the core structure and composition of dislocations is required. In fact, recent work has suggested, albeit indirectly, that segregation of impurities to dislocations is a major factor affecting the core structure of dislocations.

Threading dislocations in GaN are of 3 types, with Burgers vectors 1/3<11-20> (edge dislocations), 1/3<11-23> (mixed dislocations) and <0001> (screw dislocations). Our previous work has shown that in undoped GaN grown by metal-organic chemical vapour decomposition (MOCVD) screw dislocations are of open core type (nanopipes) whereas edge and mixed dislocations appear to have closed cores (Cherns et al 1997). In MOCVD grown GaN heavily n-doped with Si (Cherns et al 2000), nanopipes were non-uniform containing constricted (closed core) segments as well as more open structures. In contrast, MOCVD $Al_{0.03}Ga_{0.97}N$ heavily doped with Mg showed strong evidence for Mg-segregation to dislocations with both edge and mixed dislocations being open core on a fine scale (Cherns et al 2002). In GaN grown by molecular beam epitaxy (MBE) under Ga-rich conditions, we have reported open core dislocations of mixed type (Baines et al 2003). These open core dislocations were decorated with amorphous material believed to contain excess Ga, although no conclusive proof of this was obtained.

In this paper, we examine the core structure of dislocations in GaN grown by hydride vapour phase epitaxy (HVPE). A combination of high angle annular dark field (HAADF) imaging and electron energy loss spectroscopy (EELS) in the Daresbury SuperSTEM is used to show the presence of substantial quantities of oxygen on the surfaces of open core screw dislocations. The results are compared with transmission electron microscope (TEM) observations on plan-view and cross-sectional specimens. The significance of the results for understanding the core structure and the electronic properties of dislocations in GaN are discussed.

2. EXPERIMENTAL

A series of samples with varying thickness of epitaxial layer (0.6, 5 and 55μm) were grown by HVPE on (0001) oriented sapphire substrates. No buffer layer was employed to reduce dislocation density and no deliberate removal of impurity was made. Electron transparent samples were prepared in both plan view and cross-sectional orientation by a standard mechanical polishing technique and dimpling, followed by low-energy ion milling in a Gatan PIPS™ thinner to electron transparency.

Samples were examined in a Philips EM430 TEM operating at 250kV and in the 'SuperSTEM' at Daresbury Labs, UK.

The SuperSTEM is equipped with an HAADF detector and an electron energy loss (EEL) spectrometer that allows for high resolution lattice imaging in parallel with chemical analysis. The nature of HAADF and EELS also means that results are virtually directly interpretable, after some refinement.

After recording an atomic image, line scans were made across the cores of several nanopipes in each sample of varying GaN layer thickness. Each scan was selected to include the oxygen and nitrogen K-edges and the gallium $M_{2,3}$-edge. For each point along the scan, a quantitative measure of each element's concentration was extracted from the EELS data by fitting a power law to a 20-100eV window preceding the edge of interest to strip away the phonon background. An appropriate integration window (>20eV) was then selected after the edge from the background stripped data to give a number proportional to the areal density of the corresponding element. In order to compare the amount of each element to the others present, the integrated data was scaled to the N bulk signal. The O was scaled to the N by using scattering cross-sections and the Ga signal was scaled to the N by assuming that the average Ga signal was equal to the average N signal away from the dislocation core.

3. RESULTS AND DISCUSSION

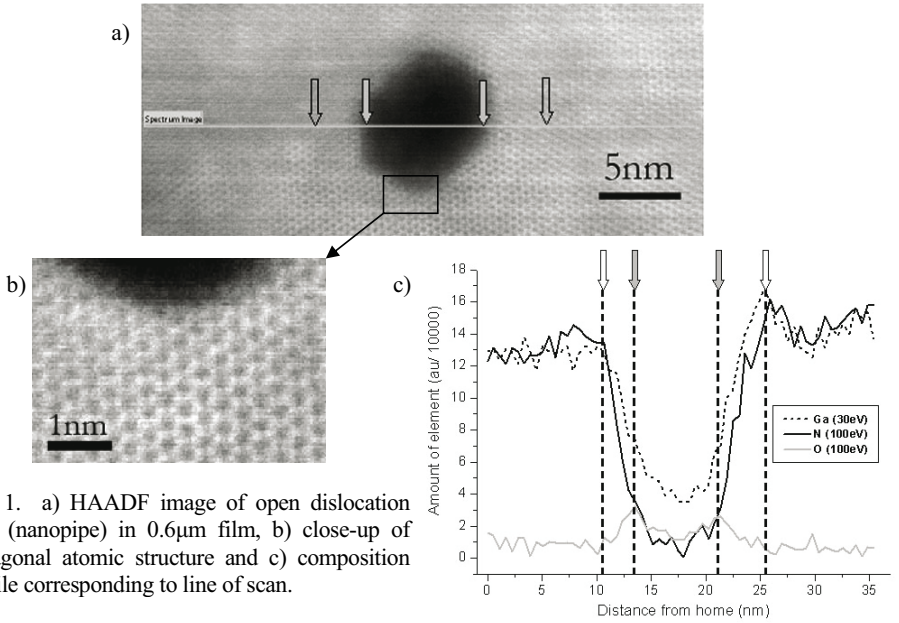


Fig. 1. a) HAADF image of open dislocation core (nanopipe) in 0.6μm film, b) close-up of hexagonal atomic structure and c) composition profile corresponding to line of scan.

Figure 1 shows a HAADF image of a nanopipe set in the hexagonal GaN bulk looking down the [0001] zone axis. The lattice image is proportional to Z^2 so that generally the brighter the image, the more material there is. The close-up of the HAADF image clearly shows the lattice structure of atoms as bright points on a dark background. HAADF is also advantaged with minimal coherent scattering effects to consider such as contrast oscillations related to thickness variations. The faces of the pipe lie on the {10-10} planes and the spatial resolution is about 1.3Å. Below the HAADF image, the refined EELS data is shown yielding the compositional variation across the scan. A Burgers circuit drawn on the HAADF images and cross-sectional TEM $\mathbf{g}\cdot\mathbf{b}$ analysis showed that the nanopipes are screw type.

As the edge of the pipe is approached, the N signal is observed to drop away from the bulk concentration (marked on the lattice image by an unfilled arrow). This coincides with a rise in the O

signal to a maximum at the walls of the nanopipe (indicated by a filled arrow). This transition occurs over an average of 15 atomic spacings.

During this rise in O content, the lattice structure remains clearly discernible. This implies that the O is substituting for N in an otherwise unaltered crystal structure. If this is the case, the replacement of N with O requires Ga vacancies to maintain charge neutrality. This is indeed consistent with a drop in the Ga signal coinciding with the O and N signal changes.

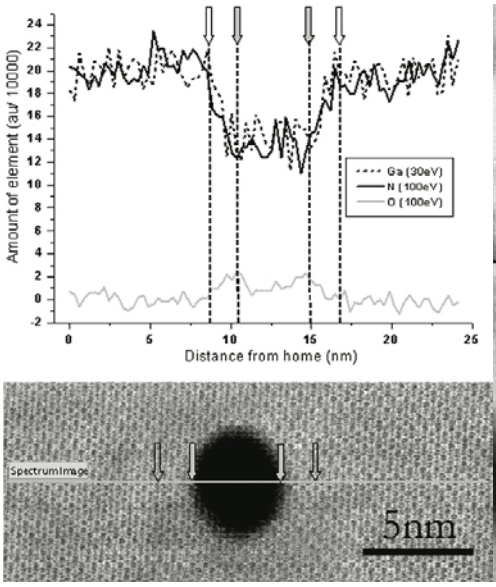


Fig. 2. Composition profile across nanopipe core in 5μm film and HAADF image of pipe.

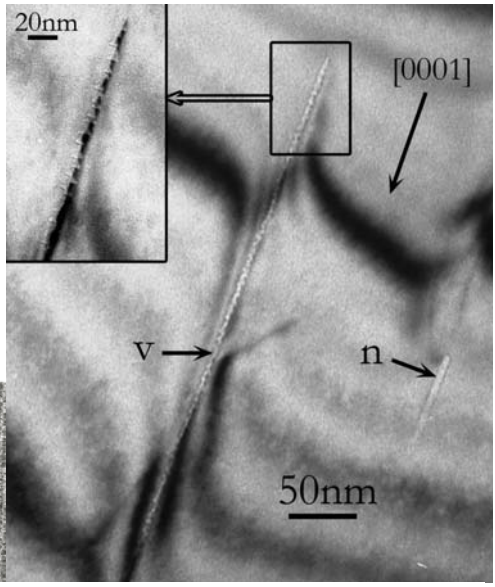


Fig. 3. Cross-sectional TEM images of a nanopipe (n) and a screw type dislocation (v) lined with triangular voids (see inset).

Data from the 5μm GaN layer sample also shows evidence of O at the walls of the pipes, as shown in Fig. 2. A similar compositional structure to the 0.6μm thick sample is also seen in the replacement of N with O coinciding with a drop in the Ga signal. Such a similar structure being found comparatively far from the GaN/ Sapphire interface demonstrates that the O is both from the GaN (bulk or surface) and/ or the Sapphire substrate and not from sample preparation, which would result in a random O distribution in each sample.

The cross-sectional image in Fig. 3 shows an example of a regular diameter nanopipe and the image of a dislocation v, whose Burgers vector was confirmed as screw-type using a conventional $\mathbf{g} \cdot \mathbf{b}$ analysis. This dislocation is seen to be open core in places with triangular voids. These structures are not believed to be the result of electron irradiation as reported by Pailloux et al (2005) as the irradiation times here are short in comparison to those reported. Such changes in structure could account for the apparently large spread of the O EELS signal. If the diameter of the pipe is varying with depth into the foil, this would produce a blurring of a thinner structure lining the walls of the pipe, creating a wider Gaussian O profile as observed. If the O peaks either side of the core in Figs. 1 and 2 are integrated, the total amount would be equal to up to 2-3 monolayers on the walls of a constant diameter core.

There is further evidence for faceting of end-on nanopipes in the HAADF image. In Figs. 1 and 2, the edges of the pipe are not crisp and there appears to be a continuation of the crystal structure into the core, which accounts for the N and Ga EELS signals present there. This is emphasised by the BF image in Fig. 4a where the darker spots now indicate the atomic sites. As can be seen, the crystal structure extends into the overall brighter core, gradually being masked out by the speckled contrast of an amorphous filling.

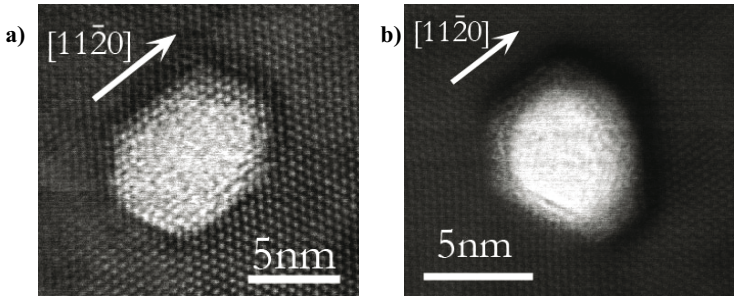


Fig. 4. Bright field STEM images of pipe cores a) corresponds to Fig. 1 and 5a b) corresponds to Fig. 5b.

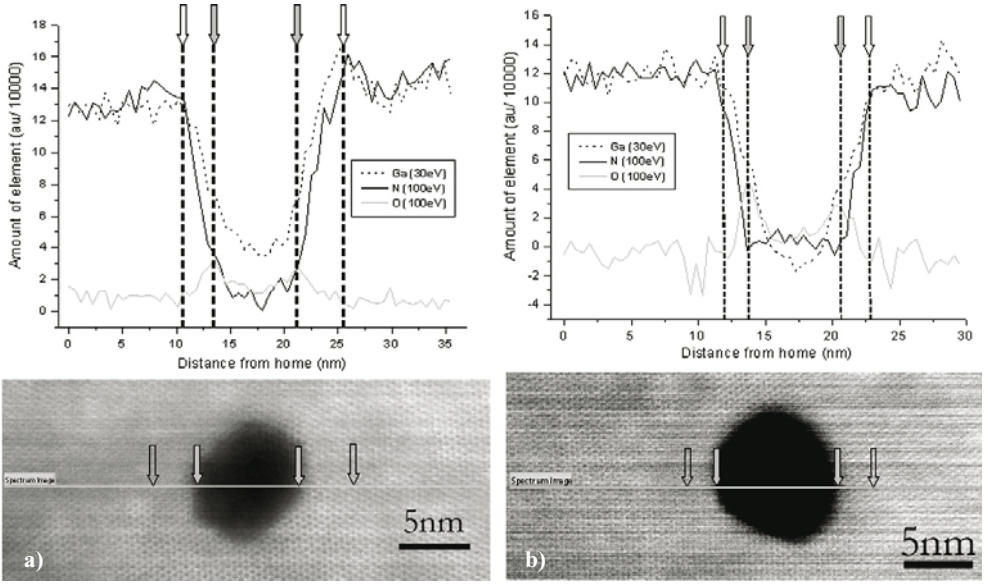


Fig. 5. Composition profile across a) faceted core (data from Fig. 1) and b) regular diameter core nanopipe core.

In comparison to a constricted core, the data in Fig. 5b (presented next to a copy of the data from Fig. 1 for comparison) comes from a pipe with less diameter variation. Here, the edges of the pipe are sharp in HAADF and there appears to be no crystalline material in the core, which is again emphasised in Fig. 4b where only the speckled contrast is visible in the core. This structure is mirrored by the EELS signal where the Ga and N signals drop to zero in the core. Also, the O peak is much sharper, spreading over only an average of 6 monolayers.

A similar result for O segregation was found in MOCVD grown GaN by Arslan et al (2003) who found O content over 20 atomic spacings. They interpreted this as a gradual change however, whereas our data suggests a narrower, possibly more discreet O distribution.

Introduction of impurity segregants such as O, H, Si and Mg to dislocations in GaN have been modelled to produce extrinsic defect complexes that are electrically active (Elsner et al 1998), creating deep levels in the band gap. Here, we have presented good evidence of O segregation to the walls of nanopipes in HVPE GaN material both near and at a comparative distance from the substrate interface.

This O segregation has been shown to coincide with Ga vacancies, which would form the defect complexes modelled in theory, except for their distribution leading up to the pipe surface.

Observations from cross-sectional samples show diameter constrictions in the cores that are backed up by plan view STEM images. Consideration of these diameter variations suggests that the distribution of O leading up to the pipe surface could be as narrow as 2-3 monolayers and observations from more regular diameter cores appear to support this trend. Such a distribution would fit more closely with a V_{Ga}-$(O_N)_3$ complex as modelled by Jones et al (1999).

One possible reason for the changes in core diameter is the presence of the O. If the O were to segregate to the dislocation, it could prevent overgrowth causing the core to open up in the shape of a V in cross section, as observed. Then, when the local supply of oxygen is depleted, segregation stops, the pipe is overgrown and the process starts again. This is one possible model for the formation of voids similar to our model suggested for Mg precipitate formation along dislocations in heavily Mg doped MOCVD $Al_{0.03}Ga_{0.97}N$ (Cherns et al 2002). A constant diameter core would have a balance of segregation and supply during growth to maintain a more regular diameter.

The amorphous material filling the core in the plan-view images is mostly carbon. This was detected as a large peak in the EELS signal from the carbon K-edge. Cross-sectional sample analysis at the SuperSTEM showed that the cores of the structures are in fact empty after growth. In Fig. 6, the core appears darker overall in HAADF because there is less material and brighter in BF because there is less scattering. This indicates that the amorphous carbon is a result of sample preparation. If there were a Ga filled core as predicted by Northrup et al (1997), the core would appear brighter in ADF due to higher average Z and darker in BF, due to stronger scattering. The Ga is also predicted to form a hexagonal crystalline structure rotated 6° relative to the GaN and there is no evidence of this in plan view or cross section.

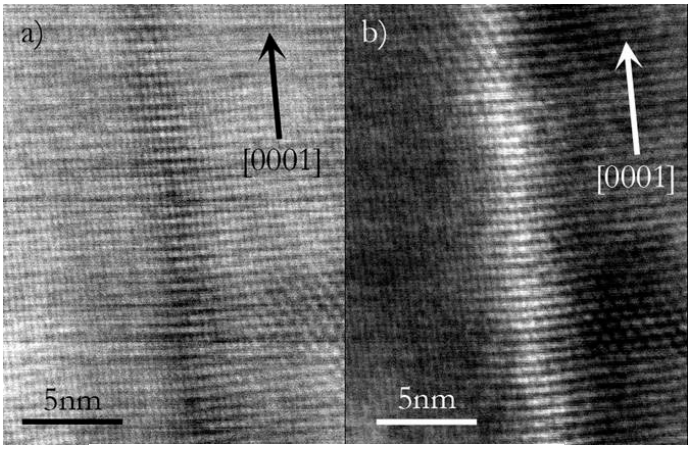


Fig. 6. – X-S STEM images of nanopipe core
a) HAADF image b) bright field image.

Combining this cross-section STEM data with the consideration of diameter variations of the cores leads to the conclusion that Ga segregation is not responsible for nanopipe formation or optoelectronic properties. This is consistent with the fact that the pipe diameters are so large (5-50nm) (Jones et al 1998).

4. CONCLUSION

Open core dislocations (nanopipes) were examined in samples of 0.6, 5 and 55μm thick layer GaN using the Daresbury SuperSTEM. HAADF and EELS taken together in parallel across the open cores suggest a replacement of nitrogen with oxygen segregated from either the GaN or the sapphire leading up to the walls of the nanopipe. Coinciding with this change, the gallium EELS signal is observed to drop away from the bulk signal which is consistent with gallium vacancies forming to

maintain charge neutrality. This compositional change is believed to be no more than a few monolayers thick when considering the structural changes seen to occur throughout the foil in cross-sectional TEM images. The data is consistent with a picture of O segregation to the walls of the nanopipe possibly forming at most a few (2-3) monolayers of V_{Ga}-$(O_N)_3$ defect structures consistent with theoretical modelling by Jones et al (1998).

There was no evidence found for a Ga filled core being responsible for the nanopipe structures as modelled by Northrup (2001). Indeed, the cores were shown by cross-sectional STEM to be empty after growth of the GaN.

ACKNOWLEDGEMENTS:

Thanks go to D. Look of Semiconductor Research Centre Wright State University and R. Molnar of Lincoln Laboratory, Massachusetts Institute of Technology for providing the samples and the SuperSTEM team for use of their facilities. We are grateful to the US Office of Naval Research (Dr Colin Wood) for financial support under grant #N00014-03-1-0579

REFERENCES

Arslan I and Browning N D 2003 Phys. Rev. Lett. **91**, 165501
Baines M Q, Cherns D, Hsu J W P and Manfra M J 2003 Mat. Res. Soc. Symp. Proc. **743**, L2.5.1
Cherns D 2000 J. Phys.: Condensed Matter **12**, 10205
Cherns D, Wang Y Q, Liu R and Ponce F A 2002 Appl. Phys. Lett. **81**, 4541
Cherns D, Young W T, Steeds J W, Ponce F A and Nakamura S 1997, J of Crystal Growth **178**, 201
Elsner J, Jones R, Haugk M, Gutierrez R, Frauenheim Th, Heggie M I, Öberg S and Briddon P R 1998 Appl. Phys. Lett. **73**, 3530
Jones R, Elsner J, Haugk M, Gutierrez R, Frauenheim Th, Heggie M I, Öberg S and Briddon P R 1999 Phys. Stat. Sol. (a) **171**, 167
Northrup J E 2001 Appl. Phys. Lett. **78**, 2288
Pailloux F, Colin J, Barbot J F and Grilhé J 2005 Appl. Phys. Lett. **86**, 131908

Strain relaxation in (Al,Ga)N/GaN heterostructures

P Vennéguès, J M Bethoux, Z Bougrioua, M Azize, P De Mierry and O Tottereau

Centre de Recherche sur l'Hétéro-Epitaxie et ses Applications, Centre National de la Recherche Scientifique, Rue Bernard Grégory, Sophia Antipolis,06560 Valbonne, France

ABSTRACT: Strain relaxation mechanisms in metal-organic vapour phase epitaxy grown (Al,Ga)N/GaN heterostructures are presented. Relaxation first occurs through a 2D-3D transition. For pure AlN, misfit **a**-type dislocations are introduced at the coalescence front of growth islands. For (Al,Ga)N (Al concentration≤70%), the second relaxation step is cracking. When cracked, relaxation of the films occurs by the introduction of long and straight **a+c-**type dislocations and small bowed **a-**type dislocation half-loops bordering the cracks. These two relaxing features lead for $Al_{0.2}Ga_{0.8}N$ films above 2µm thick to full relaxation.

1. INTRODUCTION

AlGaN/GaN heterostructures are the basis of both optoelectronic and electronic devices. Because of the large lattice mismatches (2.4% for AlN/GaN), strain relaxation studies in this system are of great importance. It has been already noted that the classical Matthews-Blakeslee relaxation process, which occurs by the bending of pre-existing dislocations, is not operative in wurtzite [0001] oriented films (Jahnen et al 1998). Other relaxation mechanisms have been observed in tensile strained (Al,Ga)N/GaN heterostructures depending on the Al concentration, the growth technique and the growth parameters. Relaxation by cracking of the film has been frequently reported (Einfeldt et al 2000, Bethoux et al 2003). It has been recently observed that the cracking is accompanied by the introduction of **a+c**-type misfit dislocations resulting from the glide of dislocation half loops from the surface of the film on inclined $\{11\bar{2}2\}$ planes (Floro et al. 2004). Morphological relaxation has also been reported with a possible introduction of **a-**type misfit dislocations at the coalescence front of growth islands in both plasma-assisted molecular beam epitaxy (Bourret et al 2001) and metal-organic vapour phase epitaxy grown films (Vennéguès et al 2005).

In this paper, we study the relaxation mechanisms in metal-organic vapour phase epitaxy (MOVPE) grown (Al,Ga)N/GaN heterostructures for a large Al concentration range (20-100%). Atomic force microscopy (AFM), panchromatic cathodoluminescence (CL) imaging and transmission electron microscopy (TEM) in both plan-view and cross-section are used to investigate the resulting film microstructure. X-ray diffraction (XRD) is used to measure the strains. The samples may be separated depending upon whether they are cracked or not. The studied uncracked samples are thin single layers (7nm≤thickness≤115nm, 43%≤Al concentration≤100%) and one AlN/GaN multilayer sample with varying AlN thicknesses. The relaxation of cracked films is studied on a series of $(Al_{0.2},Ga_{0.8})N$/GaN hetero-structures with varying thicknesses (0.2µm≤thickness≤6µm). The heterostructures are grown on GaN templates deposited on (0001) sapphire and realised using the so-called "Si/N" treatment which resulted in layers with a dislocation density in the mid 10^8 cm^{-2}. Details of the growth conditions are reported elsewhere (Vennéguès et al 2005, Bethoux et al 2003).

2. RESULTS

2.1 AlN/GaN

All single layer AlN samples exhibit the same surface morphology as that shown in Fig. 1a which corresponds to a 40nm thick layer: a mesa-like surface with well-defined mesa-edges aligned along the $\langle 11\bar{2}0 \rangle$ directions. The mesa-like islands are separated by V-trenches which are seen in Fig. 1b. For the thinnest AlN samples (thickness<40nm), the apexes of the V-trenches reach the interface AlN/GaN and no additional dislocations are observed. For the thickest samples (thickness≥40nm), V-trench apexes do not reach the interface and misfit dislocations are observed (indicated by arrows in Fig. 1b) below the apexes of the V-trenches and also below the flat part of the islands. Misfit dislocations are, therefore, formed at the coalescence front of 3D islands as already reported by other authors (Bourret et al 2001). The material in the vicinity of the facets is at least partially elastically relaxed and, therefore, V-trench formation is an effective way to relax the strain. The V-trench formation is a stress-induced phenomenon related to the elastic strain energy (Bourret et al 2001): in the multilayered sample, the thinnest layers are flat whereas undulations of the surface may be observed from the 3.5nm thick layer (Fig. 2a). The critical thickness for the 2D-3D transition is between 2 and 3.5nm, under our growth conditions. This 2D-3D transition is accompanied by the appearance of new **a**-type threading dislocations (Fig. 2b). These dislocations are the threading arms of misfit dislocations observed in the AlN/GaN (not shown) interfaces and which are similar to the ones observed in 3D AlN single layers (Fig. 1b). The relaxation process of AlN/GaN heterostructures may be therefore be described as follow: first a 2D-3D transition occurs with an elastic relaxation at the island facets. Then, **a**-type dislocations are generated at the coalescence front of these islands. It should be noted that **a** type dislocations in the basal plane do not experience any resolved shear stress in the case of biaxial strain. The reason for the presence of **a**-type dislocations below the flat part of the islands should, therefore, be investigated further. The measured density of misfit dislocations corresponds to full relaxation when AlN layers are capped by GaN (multilayer). It is not the case for AlN single layers *i.e.* when the coalescence is induced by AlN overgrowth.

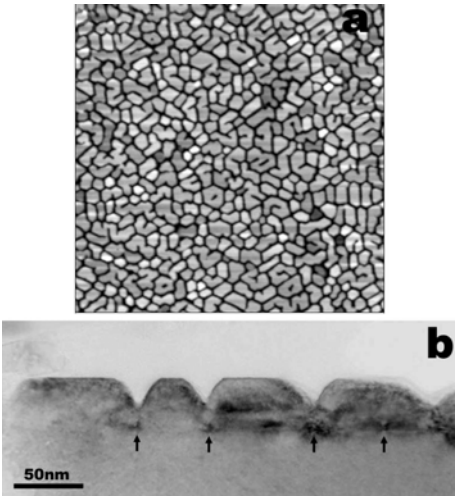


Fig. 1: 40nm thick AlN layer; (a) 2µm × 2µm AFM image; (b) cross-section TEM image; arrows indicate misfit dislocations.

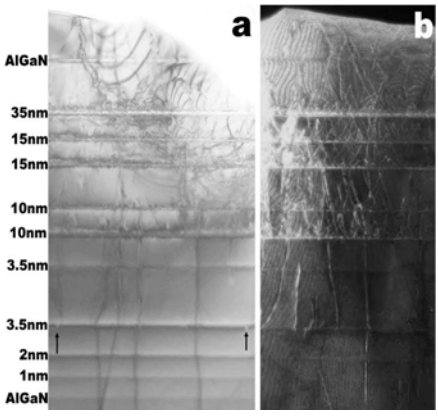


Fig. 2: cross-section TEM images of the AlN/GaN multilayer; (a) multi-beam image. The AlN thicknesses are indicated. Arrows indicate surface undulations in the 3.5-4nm thick AlN layer. (b) $(11\bar{2}0)$ dark field cs-TEM image. New **a**-type threading dislocations (white lines) are observed from the 3.5nm thick AlN layer.

The critical thickness for the 2D-3D transition (which is between 2nm and 3.5nm in our case) is reached when the energy gain by elastic relaxation of islands edges is equal to the energy necessary to create the two V-trench surfaces. Therefore, it drastically depends on the growth conditions and the 2D-3D transition may be avoided by using very low NH_3 fluxes (Gherasimova et al 2004).

2.2 (Al,Ga)N/GaN

A surface morphology similar to the one shown in Fig. 1a is also observed for samples with Al concentrations down to 43%. But the critical thickness for the 2D-3D transition increases when the Al concentration decreases and is around 20nm for an Al concentration of 43%. As a consequence, for the observed (Al,Ga)N/GaN single layers (Al concentration≤70%), the apexes of the V-trenches never reach the heterointerface. Islands are formed above a continuous (Al,Ga)N layer. In this case, no misfit dislocations are formed when islands coalesce. The strain is only partially relaxed by the free island facets and further growth leads to cracking.

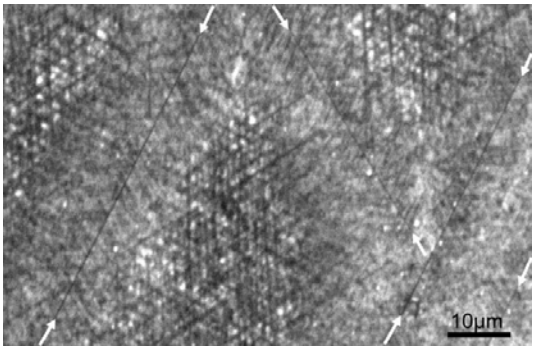


Fig. 3: plan-view panchromatic CL image of a 350nm-thick $Al_{0.2}Ga_{0.8}N$ film Arrows outline cracks.

But, the amount of strain that can be relieved thanks to the crack formation is also very small (Bethoux et al 2003). As a consequence, further relaxation mechanisms are expected for thicker films. We have studied these following mechanisms of relaxation on a series of $(Al_{0.2},Ga_{08})N$/GaN cracked hetero-structures with varying thicknesses from 0.2 to 6µm. XRD shows that the relaxation is gradual and depends mainly on the film thickness. A complete relaxation is obtained for thicknesses above 2µm.

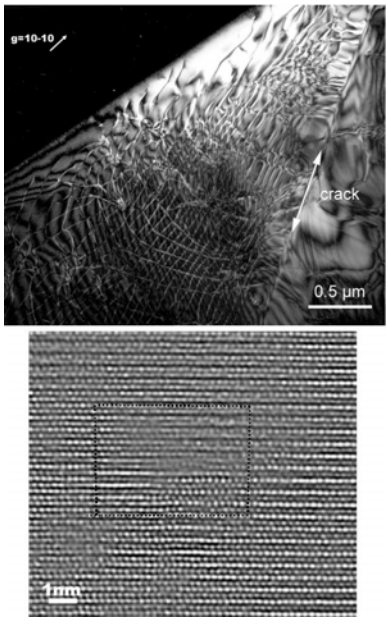


Fig. 4: (a) $(10\bar{1}0)$ dark field plan view TEM image of a 200nm-thick $Al_{0.2}Ga_{0.8}N$ film. A crack is outlined; (b) Fourier-filtered HRTEM image along $[11\bar{2}0]$ zone axis of a dislocation. A Burgers circuit shows that it is an **a**-type dislocation.

The microscopic features responsible for this gradual relaxation are studied in the following. The panchromatic CL image of a 350nm thick sample (Fig. 3) shows the areas with the characteristic contrasts observed in such cracked samples.

The arrows indicate the cracks which are aligned along $<11\bar{2}0>$. Two different contrast zones are observed. Far from the cracks, long lines parallel to $<10\bar{1}0>$ directions are observed. By a combination of plan-view dark field and cross-section high resolution TEM images (Bethoux et al 2005), these lines have been identified as **a+c**-type pure edge misfit dislocations resulting from the glide of half-loops on inclined $\{11\bar{2}2\}$ planes from the surface of the film, as already observed by other authors (Floro et al 2004). Closer to the cracks, a zone about 15 µm in extent is observed with faint contrast. Plan-view TEM observations (Fig. 4a) reveal that this zone corresponds to an area with a high density of in-plane misfit dislocations. These dislocations have an **a** in-plane component which makes an angle of 60° with the

direction of the cracks they are bordering. High-resolution cross-section images (Fig. 4b) show that they are **a**-type misfit dislocations. These dislocations are bowed and form half-loops anchored on the cracks. This strongly suggests that they are emitted from the cracks. Their mean line direction is the direction of the crack *i.e.* they are 60° dislocations. They, therefore, have a lower efficiency than the **a+c-**type edge dislocation to release the strain.

Full relaxation may be obtained when the minimum distance between **a+c-**type edge dislocations is 300nm or 60nm between 60° **a**-type dislocations. This is what is observed for samples with thicknesses above 2µm in agreement with XRD results. The relaxation is therefore obtained by two relaxing features, the long and straight **a+c-**type edge dislocations and the cracks bordered by bowed 60° **a**-type dislocations.

3. CONCLUSION

The relaxation of strain in MOVPE grown (Al,Ga)N/GaN heterostructures involves different mechanisms. The first one corresponds to a 2D-3D transition with the formation of mesa-like islands. The critical thickness for this transition is very dependent on the growth conditions. In the case of AlN/GaN, dislocations form when islands coalesce. For (Al,Ga)N, such a dislocation nucleation mechanism is not possible because the coalescence front of the islands is not in the interface. In this case, the second stage of the relaxation is the cracking of the films for thick enough layers.

After the initial cracking, the relaxation proceeds either by the introduction of **a+c-**type edge dislocations or by further cracking and the introduction of 60° **a**-type dislocations bordering the cracks. **a+c-**type edge dislocations result from the glide of half-loops on inclined $\{11\bar{2}2\}$ planes from the surface of the film. The observed microstructure suggested that 60° **a**-type dislocations are emitted from the cracks. **a** type dislocations in the basal plane do not experience any resolved shear stress in the case of a biaxial strain. Nevertheless, we have observed **a**-type dislocations in the basal plane either in the form of half-loops bordering the cracks or also below the flat part of the mesa-like islands of AlN films. This implies the existence of a resolved shear stress which can be induced by the elastic relaxation of the free surfaces (either cracks or island facets) as already proposed (Jain et al 1996, Johnson et al 1997).

ACKNOWLEDGMENT

This work is supported by the ECC contract MRTN-CT-2004-005583 (PARSEM).

REFERENCES

Bethoux J-M, Vennégues P, Natali F, Feltin E, Tottereau O, Nataf G, De Mierry P and Semond F 2003 J. Appl. Phys. **94**, 6499

Bethoux J M and Vennégues P 2005 J. Appl. Phys. *accepted*

Bourret A, Adelmann C, Daudin B, Rouvière J L, Feuillet G and Mula G 2001 Phys. Rev. B **63**, 245307

Einfeldt S, Kirchner V, Heinke H, DieBelberg M, Figge S, Vogeler K and Hommel D 2000 J. Appl. Phys. **88**, 7029

Floro JA, Follstaedt D M, Provencio P, Hearne S J and Lee S R 2004 J. Appl. Phys. **96**, 7087

Gherasimova M, Cui G, Ren Z, Su J, Wang X L, Han J, Higashimine K and Otsuka N 2004 J. App. Phys. **95**, 2921

Jahnen B et al. 1998, MRS Internet J. Nitride Semicond. Res. **3**, 39

Jain S C, Maes H., Pinardi K and DeWolf I 1996 J. Appl. Phys. **79**, 8145

Johnson H T and Freund L B 1997 J. Appl. Phys. **81**, 6081

Vennégues P, Bougrioua Z, Bethoux J-M, Azize M and Tottereau O 2005 J. Appl. Phys. **97**, 4912

A TEM Study of AlN Interlayer Defects in AlGaN/GaN Heterostructures

P D Cherns, C McAleese, M J Kappers and C J Humphreys

Department of Materials Science and Metallurgy, University of Cambridge, Pembroke Street, Cambridge, CB2 3QZ, UK

ABSTRACT: A series of $Al_{0.47}Ga_{0.53}N$/GaN heterostructures with a range of different AlN interlayer thicknesses has been examined. We find that when the interlayer thickness is greater than ~5nm, it becomes possible to grow 250nm of AlGaN without cracking. The interlayers are then believed to be sufficiently relaxed to place the AlGaN under compressive strain. The mechanisms for this relaxation have been studied using high angle annular dark field (HAADF) imaging, conventional transmission electron microscopy (TEM) and electron energy loss spectroscopy (EELS). It is found that relaxation takes place through both the small-scale cracking of the interlayer and the generation of misfit dislocations at the GaN/AlN interface. EELS has also been used to probe the Al content of the material filling the interlayer cracks, showing it to be depleted of Al compared to the rest of the AlGaN.

1. INTRODUCTION

There is great interest in the growth of optoelectronic devices based on AlGaN/GaN heterostructures that emit at UV wavelengths. Due to the lattice parameter mismatch between GaN (a=3.1893 Å) and AlN (a=3.1130 Å), AlGaN alloys grown on a GaN template layer will be under tensile strain. Above a critical thickness, which decreases with increasing Al content but is typically ~5nm for pure AlN, this leads to the formation of networks of cracks for strain relief (McAleese et al 2004). Han et al (1999) found crack formation in AlGaN to be extremely detrimental to device performance. Amano et al (1999) report that the use of an AlN interlayer allows an AlGaN layer to be grown on GaN, crack-free beyond the critical thickness. The interlayer is sufficiently relaxed to place the subsequent AlGaN layer under compressive strain and hence prevent crack formation. Han et al (2001) suggest that interlayer relaxation occurs by initial cracking and subsequent generation of misfit dislocations. In the present study we use scanning transmission electron microscopy (STEM), conventional TEM and electron energy loss spectroscopy (EELS) to investigate the mechanisms by which relaxation of the AlN interlayer takes place. A series of 5 AlGaN/AlN/GaN samples have been examined, with AlN interlayer thicknesses of 1, 5, 10, 30 and 50nm.

2. EXPERIMENTAL

The samples studied consist of ~250nm of nominally $Al_{0.47}Ga_{0.53}N$ on ~5μm thick GaN template layers, with a thin AlN interlayer deposited prior to AlGaN growth. All samples were grown on a Thomas Swan 6 x 2'' reactor by metalorganic vapour phase epitaxy (MOVPE) using *c*-plane sapphire substrates. The organometallic precursors were trimethylgallium and trimethylaluminium, and ammonia was the nitrogen source. Both the AlGaN layer and AlN interlayer were grown at 1020 °C and 50 Torr reactor pressure. The only change made between the samples was the growth time for the AlN interlayer, hence varying the interlayer thickness since the growth rate was kept the same. From X-ray diffraction (reciprocal space mapping of the symmetric (002) and asymmetric (105) reflections to determine the *a* and *c* lattice parameters), the composition of the $Al_xGa_{1-x}N$ layer was determined to be x=0.47.

Cross-sectional TEM samples were prepared by mechanical polishing, dimpling and ion milling

in a Gatan Precision Ion Polishing System. Conventional TEM images were taken on a JEOL 2000FX microscope operating at 200kV. The STEM HAADF images and EELS spectra were obtained on an FEI Tecnai F20, operating at 200kV, with a Gatan Imaging Filter (GIF) attached.

For high resolution HAADF images, the sample was in the <11-20> orientation, and the fringes observed correspond to the unit cell height. For the EELS analysis and the associated HAADF images, the sample was edge-on, close to <11-20> orientation. Changes in Al content have been inferred from the intensity of the Al L_3 edge at 73eV energy loss. The background to the edge has been removed by fitting to a power law of the form AE^{-r} (Egerton 1996), and the edge intensity has been integrated over a 30eV window. The probe used was ~1nm and was moved over 30 points at 4.5nm spacing, with an acquisition time of 6 seconds per point. The HAADF intensity was also recorded at each point. Immediately after acquisition, the sample thickness was recorded by repeating the linescan over the low loss part of the spectrum (<100eV). The thickness was obtained from these measurements using the log–ratio method described in Egerton (1996) The HAADF profiles were used to check for sample drift between the scans and the measured thicknesses were used to scale the integrated edge intensities in order to give values proportional to the Al concentration. The dispersion was set to 0.2eV per channel for each acquisition.

3. RESULTS AND DISCUSSION

3.1 AlN Interlayer Cracking

Small-scale interlayer cracking has been observed in the 5, 10, 30 and 50nm interlayer samples. It is seen from the images in Fig. 1a and b that the cracks are filled during growth of the AlGaN capping layer. The images show an increase in HAADF intensity in the material that fills in the crack, implying higher atomic number, and therefore in this case suggesting a depletion in the Al content of the AlGaN. Figure 1b shows the presence of a void below the crack in the 10nm interlayer, similar to those seen by Bethoux et al (2003) in MBE-grown AlN on GaN and MOCVD-grown AlGaN on GaN.

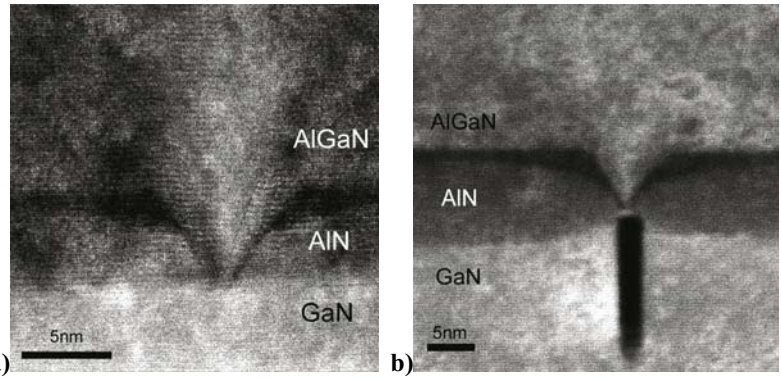


Fig. 1. a)HR - HAADF image of the area of the filled “V-shaped” crack in the 5nm interlayer sample. b) HR - HAADF image of the area of the filled “V-shaped” crack and associated void in the 10nm interlayer sample.

An explanation for the increase in intensity above the crack, given by Bethoux et al (2003) is mass transport of Ga occurring during growth of the AlGaN layer, leaving Al–poor AlGaN inside the crack and a void in the GaN template. However, it can be seen from Fig. 1a that there is not always a void in the GaN corresponding to these cracks and, therefore, other mechanisms must also be considered for the depletion of Al in this region.

3.2 Effect of Interlayer Thickness

It has been found that the AlN interlayers in our samples were only effective in preventing cracking in the AlGaN layer if they are thicker than 5nm – i.e. approximately the critical thickness for

crack-free AlN growth on GaN. For example, Fig. 2a shows cracking in the AlGaN layer of the 1nm interlayer sample. Although Fig. 1a) demonstrates cracking in the interlayer of the 5nm interlayer sample, there is also evidence (as in Fig. 2b) of cracking in the subsequent AlGaN layer of the same sample, indicating insufficient relaxation of the interlayer. The samples with 10, 30 and 50 nm interlayers all exhibited a crack-free AlGaN capping layer, an example of which is shown in Fig. 2c.

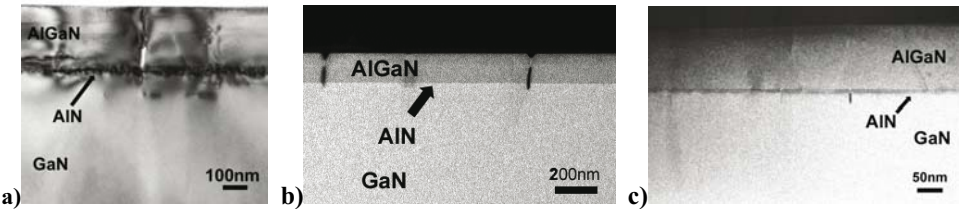


Fig. 2. **a)** Bright Field TEM image with g=(0002) of a crack in the AlGaN layer of the 1nm interlayer sample. **b)** HAADF image of cracks in the AlGaN layer of the 5nm interlayer sample. **c)** HAADF image of a crack-free AlGaN capping layer grown on a 10nm interlayer.

3.3 AlGaN Compositional Changes Above Interlayer Cracks

Figure 3 shows EELS data obtained from 2 linescans taken using the 50nm interlayer sample. The STEM probe was first moved across an unperturbed region of the interlayer from GaN to AlGaN, then the same experiment was repeated across the apex of the overgrown V-defect in the AlN interlayer.

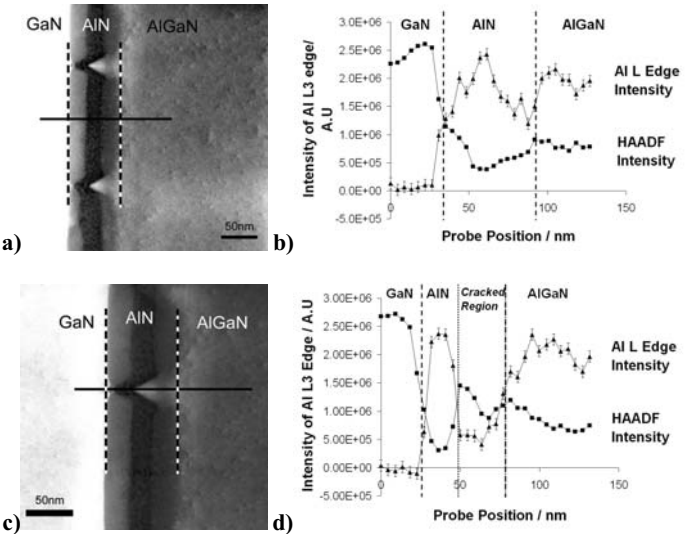
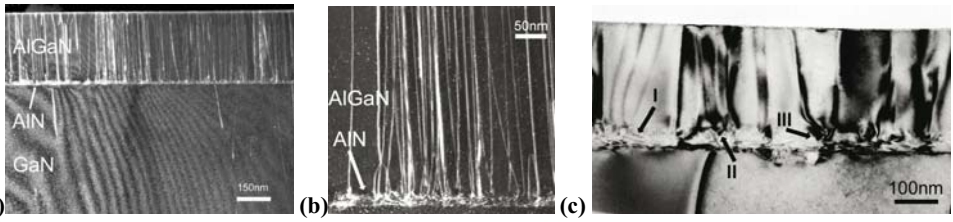


Fig. 3. **a)** HAADF image, showing a linescan over an uncracked area. **b)** Plots of Al L edge intensity and HAADF intensity over the linescan of a). **c)** HAADF image, showing a linescan over an cracked area. **d)** Plots of Al L edge intensity and HAADF intensity over the linescan of c).

The results from an unperturbed AlN region show a previously unexpected inhomogeneity in Al content over the AlN interlayer. There appear to be 3 distinct alloy compositions rather than a single uniform intensity. This is seen clearly in both the HAADF intensity plot and from the Al edge intensity. From the cracked region, it can be seen that the increase in HAADF intensity inside the interlayer crack corresponds to a sharp dip in Al edge intensity, supporting the existence of a region of Al-depleted AlGaN.

3.4 Generation of Dislocations at the Interlayer

Weak beam dark field (WBDF) images of the 30nm interlayer sample can be seen in Fig. 4a and b. Edge and mixed type dislocations are visible under these imaging conditions. It can be observed initially that there is an increase in edge type threading dislocations at the interlayer. It can also be seen from Fig. 4b, that there are a significant number of misfit dislocations running along the AlN/GaN interface. These can be seen bending up through the interlayer and threading through the AlGaN. From WBDF images, it is not clear where the cracks in the interlayer are located due to a lack of Z contrast; therefore it is necessary to use bright field imaging, as in Fig. 4c. Again, at point (I), misfit dislocations can be observed bending up into the AlGaN layer. Also, (II) and (III) indicate cracks in the interlayer, from which dislocations can be seen to originate, bowing outwards, before threading to the surface. So, it seems that the cracks in the interlayer are directly related to the increase in threading edge dislocation density that has previously been reported (Lafford et al 2003). From our work with these samples, it is not clear whether all the misfit dislocations in the AlN are directly related to cracks, in contrast to Vennegues et al (2005).



(a) **(b)** **(c)**

Fig. 4. (a) WBDF image, g = (11-20), of the 30nm interlayer sample. (b) WBDF image, g = (11-20), of the 30nm interlayer sample. (c) BF image, g = (11-20), of the 50nm interlayer sample.

TEM images taken with g = (0002) indicate that there is no equivalent increase in screw or mixed threading dislocation density.

4. CONCLUSIONS

It has been shown that AlN interlayers above 5nm thickness are an effective way of growing crack-free $Al_{0.47}Ga_{0.53}N$ on GaN. The interlayers relax sufficiently to exert compressive strain on the AlGaN layer. This relaxation occurs by small scale cracking of the interlayer and by generation of misfit dislocations, which are found to bend up through the interlayer and result in an increase in the edge-type threading dislocation density of the subsequent AlGaN layer. EELS results indicate that the AlGaN filling the cracks has a lower Al content than the rest of the AlGaN layer.

REFERENCES

Amano H, Iwaya M, Hayashi N, Kashima T, Katsuragawa M, Takeuchi T, Wetzel C and Akasaki I 1999 MRS Internet J. Nitride Semicond. Res. 4s1, G10.1

Egerton RF 1996 Electron Energy Loss Spectroscopy in the Electron Microscope, 2nd edition (Plenum Press, New York and London)

Han J, Crawford MH, Shul RJ, Hearne SJ, Chason E, Figiel JJ and Banas M 1999 MRS Internet J. Nitride Semicond. Res. 4S1 G7.7

Han J, Waldrip KE, Lee SR, Figiel JJ, Hearne SJ, Peterson GA and Myers SM 2001 Appl Phys Lett **78**, 67

Lafford TA, Parbrook PJ and Tanner BK 2003 Appl Phys Lett **83**, 5434

McAleese C, Kappers MJ, Rayment FDG, Cherns P and Humphreys CJ 2004 J. Crystal Growth **272**, 475

Vennegues P, Bougrioua Z, Bethoux JM, Azize M and Tottereau O 2005 J Appl Phys **97**, 024912

Reduction of threading dislocation density using *in-situ* SiN_x interlayers

R Datta, M J Kappers, J S Barnard and C J Humphreys

Department of Materials Science and Metallurgy, University of Cambridge, Cambridge CB2 3QZ, United Kingdom

ABSTRACT: *In-situ* SiN_x interlayers (ILs) have been used in order to reduce the density of threading dislocations (TDs) in MOVPE grown GaN and the mechanisms of TD reduction have been investigated by transmission electron microscopy (TEM). It was found that, such ILs are very efficient for reducing the density of all types of TDs via a mechanism of TD bending through 90º and subsequently forming loops, depending on the availability of the right partner. A new mechanism for bending of TDs through 90º is briefly discussed.

1. INTRODUCTION

The reduction of threading dislocations (TDs) in GaN is important, as TDs act as non-radiative recombination centres and generally reduce the efficiency of light emitting diodes (LEDs), in particular of UV-emitting structures. Several different methods have been employed (such as ELOG, *in-situ* SiN_x masking, etc.) (Vénneguès et al 2000, Lahreche et al 1999, Frayssinet et al 2002) for reducing the density of TDs and improvements in the final device performance have also been reported (Nakamura et al 1998, Kozodoy et al 1998). The reduction mechanisms for different type of TDs are strongly dependent on the kind of technique employed during the growth. Here, we report significant reduction of edge type TDs followed by screw and mixed type TDs by SiN_x IL deposition at reduced temperature. The reduction and the possible mechanisms for bending of TDs through 90º are discussed based on the TEM observations.

2. EXPERIMENTAL

The samples were grown in a 6×2 in. close-coupled showerhead MOVPE reactor manufactured by Thomas Swan Scientific Equipment Ltd. Trimethylgallium (TMGa) and ammonia gas were used as precursors for Ga and N, respectively. The 2 μm-thick GaN epilayers were grown on c-plane sapphire under conditions such that the threading dislocation density was deliberately high at around mid-10^9 cm^{-2}. Next, the reactor temperature was reduced from 1010 ºC to 850 ºC for deposition of the SiN_x ILs (5×120 sec., the first and the second digits represents the number of SiN_x IL and the duration of the SiN_x treatment respectively) using silane and ammonia. In between the ILs, a very thin layer of GaN was deposited at 860 ºC. After that, the GaN growth was continued under the standard epilayer growth conditions of 1010 ºC, 100 Torr and V/III of 1800. Cross-sectional and plan-view TEM samples were prepared by conventional mechanical thinning and Argon-ion milling. The samples were examined using a CM30 (300 kV) transmission electron microscope.

3. RESULTS

The in-situ SiN_x treatment at reduced temperature is quite effective in reducing the number of any type of dislocations threading to the surface, as indicated by the cross-sectional weak-beam dark-field (WBDF) TEM micrographs shown in Fig. 1. The screw and mixed type TDs are visible in Fig. 1a with g=<0002>, g-5g condition, zone axis near <11-20>, whereas edge and mixed type TDs are visible

in Fig.1b with g=<11-20>, g-3g condition, zone axis near <01-10>. TD density values are calculated from the cross-sectional sample and the area parallel to the (0001) plane is considered. The area of the analysis below and above (near the surface) the SiN_x ILs is calculated first, by determining the thickness at different points using the CBED technique and then by interpolation and numerical integration using thickness and length data. A length of 14 μm parallel to (0001) plane is considered in order to calculate the area as shown schematically in Fig. 2. Table 1 summarizes the density of different types of TDs below and above the SiN_x ILs. The density of edge type TDs is reduced by two orders of magnitude, as can be seen from table 1. To verify the above method for calculating TDs density on the cross-sectional TEM images, the TD density at the surface has been determined from a plan-view sample (Datta et al 2004a) and an average value of ~2-3×10^8 cm^{-2} is obtained, which is in excellent agreement with the result from Table 1.

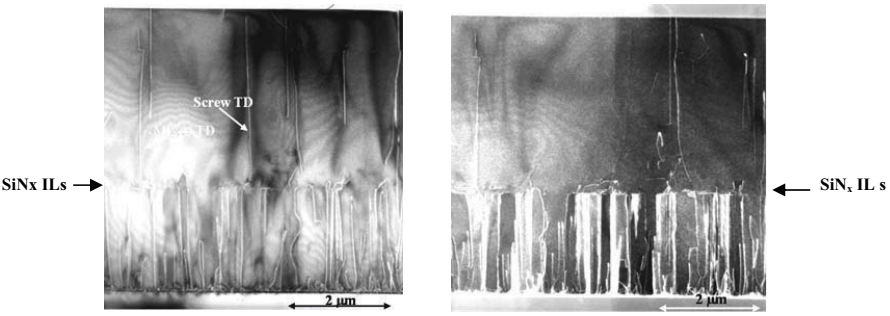


Fig. 1: (a) Screw and mixed type TDs (g=<0002>) and (b) edge and mixed type TDs (g=<11-20>) can be seen to be stopped from propagating upwards by the SiN_x ILs. Both are weak beam dark field (WBDF) TEM images.

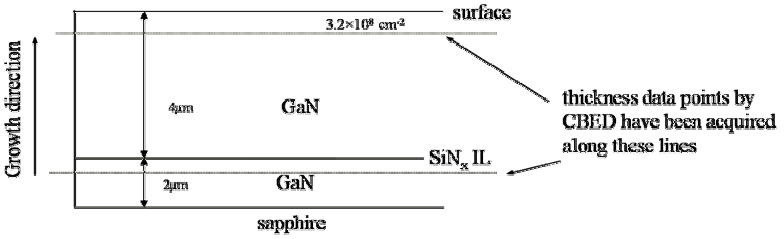


Fig. 2: Schematic representation of the GaN film and the SiN_x ILs deposition. CBED thickness data points have been collected along the dashed lines.

Table 1: Effects of SiN_x ILs deposition on the density of the different types of TDs.

Interlayer Region	Edge (cm^{-2})	Screw (cm^{-2})	Mixed (cm^{-2})	Total Density (cm^{-2})
1 (0-2 μm)	4.3×10^9	8×10^8	7.5×10^8	6×10^9
2 (2-6 μm)	2.8×10^7	8.5×10^7	2.0×10^8	3.2×10^8 (density near surface)

The mechanism of TD reduction by the insertion of the SiN_x ILs has been studied. We have found no evidence of a masking effect by the ILs (each IL may be a non-uniform monolayer coverage and not detectable in conventional TEM), and it appears that 90º bending and the step movement of TDs, are the main mechanisms leading to TD reduction through loop formation. Fig. 3a shows the example of step movements for mixed type TDs. In Fig. 3b, two screw TDs can be seen stepping towards each other and forming a loop. Edge type TDs are seen to bend through 90º in Fig. 3c and subsequently forming loops.

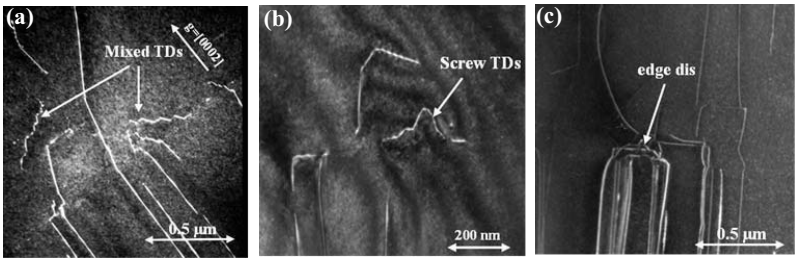


Fig. 3: WBDF-TEM images showing examples of step movement (a) for mixed TDs. (b) step movement and loop formation for screw TDs, and (c) step movement and loop formation for edge TDs.

4. DISCUSSIONS

Now, it is very important to look at the in situ reflectometry plot (not presented in the paper) during the SiN_x ILs depositions. After silane dosing drop in reflectivity has been observed. The drop in reflectivity trace suggests the change in growth mode predominantly from 2D to 3D. After the deposition of SiN_x ILs, the temperature is again increased to the original growth temperature and the gain in reflectivity can be observed which changes the growth mode again to 2D. It was shown that the change in the growth mode from 3D to 2D caused bending of threading dislocations by 90^0 while growing of GaN over silane treated (in the presence of ammonia) layer (Frayssinet et al 2002). However, in our case no masking effect was observed due to SiN_x ILs deposition. Hence, the reduction mechanisms of TDs in this case is purely due to a change in growth mode, which helps TDs bending through 90º and subsequent loop formation if a right partner is found. The bending segment of edge type TDs and other TDs have been formed due to the similar change in growth mode non-uniformly in a very small length scale (~ nm) which has helped in encountering with TDs with opposite sense and loops are formed. The effect of bending at large length scale can be found in ref. (Datta et al 2004b). Contreras et al (2002) used silicon delta-doping in GaN grown on n-type Si (111) substrate. They observed the reduction only for screw type TDs by the formation of square loops and also the formation of kink when right type of dislocations was missing from forming loops. Edge type TDs were unaffected by Si delta-doping. But in our case we have observed significant reduction in terms of edge type TDs using SiN_x ILs. Reduction has also been observed for screw and mixed type of TDs. Here in this case, the change in growth mode is brought in by both SiN_x ILs depositions (with thin GaN in between) and use of intermediate temperature (~850 ºC). Very tiny GaN islands are formed due to such treatment (Fig. 4) and the TDs are bent over through the side facets of those islands.

The mechanism of bending of TDs through 90º has already been explained using elastic energy reduction and image force analysis (Liliental-Weber et al 1999). But elastic energy reduction can not explain the bending of all types of TDs (for example for screw and mixed type TDs, the energy is increased after bending) and the pinning effect was not considered during image force analysis. Hence, we propose a new mechanism which can explain the bending of all types of TDs. This new mechanism is based on the formation of steps, equal to the magnitude of the Burgers vector of the TDs, at the inclined side facets of the GaN islands, and subsequently change in the GaN growth mode from 3D to



Fig. 4: SiN_x ILs lead to the formation of very tiny islands. TDs bend over by these small islands.

2D and depending on the direction of atomic ledge movement, TDs will bend over. The step formation is due to the non-parallel Burgers vector of dislocations and strain relaxation with respect to the island

side facet. As an example, step formation due to an edge type TD at the side facet is shown schematically in Fig. 5. Depending on the direction of the atomic ledge movement, i.e. if the ledges move from top to bottom, it can not see the projected dislocation line along the 'c' direction before hand and hence, it will become a screw TD after bending. Bending of other types of TDs (mixed and screw) can be explained in a similar fashion but due to the limitation of space here the detailed mechanism of TD bending and the step movement will be published elsewhere.

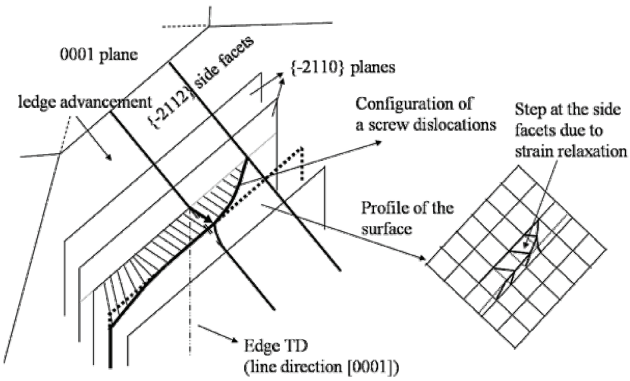


Fig. 5: Schematic representation of bending of an edge type TD through 90º.

5. CONCLUSIONS

The deposition of SiN_x ILs at reduced temperature results in the reduction of all types of TDs in MOVPE-grown GaN. The interlayer changes the growth mode from 2D to 3D and the formation of facetted islands is crucial to the reduction mechanism. The bending process of TDs is explained in terms of TD step formation and atomic ledge movement.

ACKNOWLEDGEMENT

One of the authors (R. D.) is grateful to Cambridge Commonwealth Trust, Marconi Cambridge Scholarship and Overseas Research Student Award for providing funding.

REFERENCES

Contreras O, Ponce F A, Christen J, Dadgar A and Krost K 2002 Appl. Phys. Lett. **81**, 4712
Datta R, Kappers M J, Barnard J S and Humphreys C J 2004a Appl. Phys. Lett., **85**, 3411
Datta R, Kappers M J, Barnard J S and Humphreys C J 2004b Mater. Res. Soc. Symp. Proc. Vol. 831, MRS Fall Meeting
Frayssinet E, Beaumont B, Faurie J P, Gibart P, Makkai Z, Pécz B, Lefebvre P and Valvin P 2002 MRS Internet J. Nitride Semicond. Res. **7**, 8
Kozodoy P, Ibbetson J P, Marchand H, Fini P T, Keller S, Speck J S, DenBaars S P and Mishra U K 1998 Appl. Phys. Lett. **73**, 975
Lahreche H, Vennegues P, Beaumont B and Gibart P 1999 J. Crystal Growth **205**, 245
Liliental-Weber Z, Benamara M, Swider W, Washburn J, Park J, Grudowski P A, Eiting C J, and Dupuis R D 1999 MRS Internet J. Nitride Semicond. Res. **4**, Suppl. 1, G4.6
Nakamura S, Senoh M, Nagahama S, Iwasa N, Yamada T, Matsushita T, Kiyoku H, Sugimoto Y, Kozaki T, Umemoto H, Sano M and Chocho K 1998 Appl. Phys. Lett. **72**, 211
Vénneguès P, Beaumont B, Bousquet V, Vaille M and Gibart P 2000 J. Appl. Phys. **87**, 4175

The nucleation structure for cracks in AlGaN epitaxial layers

R T Murray, P J Parbrook[1], G Hill[1] and I M Ross[1]

Materials Science and Engineering, University of Liverpool, Liverpool, L69 3GH, UK
[1] Electronic and Electrical Engineering, University of Sheffield, Sheffield, S1 3JD, UK

ABSTRACT: When an epitaxial layer is under tensile strain due to lattice mismatch, cracks are expected to form above a critical thickness. In the case of Group III nitrides grown on the sapphire (0001) plane, the epitaxial layer displays hexagonal symmetry and cracks form on all three $\{1\bar{1}00\}$ planes. Where two or, with even greater emphasis, three cracks coincide at a point forming a Y junction, it is highly probable that this location contains a nucleating feature. Such triple points feature a trumpet shaped opening with a strong resemblance to those found at the mouth of hollow-core dislocations in these materials. Scanning, transmission and focused ion beam microscopy have revealed that a nanopipe exists below the trumpet which in turn lies above a dislocation.

1. INTRODUCTION

All epitaxial layers whose lattice parameters are below those of their substrates experience tensile stress and are likely to crack when they exceed a critical thickness t_c given by $t_c = \Gamma/Mf^2$ where Γ is the surface energy of the weakest plane, f is the misfit and M is the two-dimensional equivalent of Youngs modulus (Murray et al 2003a). However cracks can only form if locally the stress exceeds the breaking strength of the epitaxial crystal. It is commonly observed that cracks form as the epilayer approaches t_c for values of f well below the theoretical breaking strain; hence a stress enhancing nucleus is required. We will discuss the morphology of features found to initiate cracks.

2. EXPERIMENTAL

As demonstrated by Murray et al (2003b), nuclei give rise to triple, double and single start events and they clearly label the points of crack initiation in AlGaN on sapphire structures. Scanning electron microscopy (SEM) and transmission electron microscopy (TEM) has been applied to study these locations in plan-view and in cross section, using both direct and replica specimen preparation. Replicas were prepared using standard cellulose acetate/carbon/AuPd recipes followed by SEM or TEM. Site-specific cross sections were also prepared using a JEOL *Fabrika* dual column focussed ion beam (FIB) miller operating at 30kV. The thinned FIB cross sections were transferred ex-situ onto a holey carbon support film using glass probe micromanipulator.

Layers of $Al_xGa_{1-x}N$ ($0 \leq x \leq 0.5$) between 60 and 500nm thick were grown on GaN layers of approximately 1.2μm thickness (Table 1). At this thickness the large misfit with the Al_2O_3 substrate was almost totally relaxed and the effective misfit is between the AlGaN and GaN layers.

3. CRACK INITIATION IN AlGaN

The crack conjunctions which, on a probability argument, have been shown to be initiators (Murray 2003b) are frequently decorated by a six faceted trumpet; such trumpets can also be found

free from cracks. They may, therefore, precede crack formation and have been shown to be associated with hollow core screw dislocations (Cherns et al 1997, 2001).

Wafer	Al Content x	Misfit F x 10^{-3}	Thickness of AlGaN layer (nm)	Pits in Crack
A	0.2	4.8	400	Yes
B	.3	7.3	60	No
C	.4	9.6	500	Yes
D	.5	12.0	60	Yes
E	.5	12.0	400	Yes
F	.3	7.3	400	Yes

Table 1: Nominal composition, layer thickness and crack details for the various wafers studied

4. MORPOLOGY OF THE CRACK INITIATOR

Plan-view SEM with variable tilts of the specimen reveal the faceted trumpet to be bounded by $\{1\bar{1}02\}$ planes which can have their tips beneath the AlGaN and within the GaN buffer layers. Radiating from the apexes of the trumpet may be zero, one, two or three cracks. When there are two cracks, they may emerge at either 120° or 180° to each other and in some cases the 180° geometry can appear to be a single crack (Fig. 1) for typical SEM resolutions.

The cracks themselves display a V shaped opening of lesser depth and width than the pit. Where the cracks radiate at an angle other than 180° from the pit, SEM micrographs indicate the presence of a nanopipe going down towards the buffer layer (Fig. 2). This phenomenon was also observed in negative replicas examined in both the SEM and TEM with a typical nanopipe diameter of ~50nm.

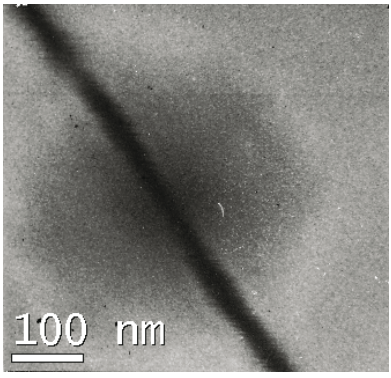


Fig. 1: A trumpet from which 2 cracks have been emitted at 180° and which appear to be continuous. Wafer A.

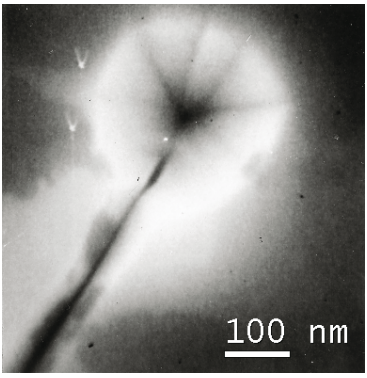


Fig. 2: A faceted trumpet with apparent nanopipe core shown dark. Note also the narrow crack and its open V top. Wafer A.

Further details of crack and pit morphology have been uncovered using cross-section techniques. Firstly, SEM of fractures crossing the cracks nearly orthogonally show that for thicker layers a narrow crack proceeds downwards from the open V for several tens of nanometres. Before it reaches the buffer, the crack opens into a cavity which is widest at this interface. The same features are revealed more clearly in Fig. 3, which is a $\langle 11\bar{2}0 \rangle$ cross section prepared for TEM by ion milling at 5° and 5 keV. The presence of the cavity under both preparative techniques gives confidence that it is a real feature that forms during the period when the wafer is at high temperature in the MOCVD chamber and that it probably forms after the crack has propagated.

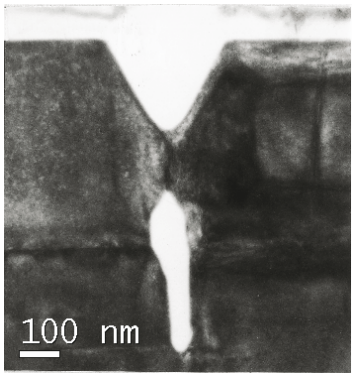


Fig. 3: TEM $[11\bar{2}0]$ cross section showing 'V' groove, crack, and the void formed at the AlGaN/buffer interface. Wafer E.

Pursuing a similar philosophy, cross-sections of pits have been attempted using tripod polishing and FIB; only FIB has been able to isolate the exact location of a pit. However, specimens prepared by FIB milling can be hazardous to interpret because of the damage caused by the energetic ion beam and by possible redeposition of sputtered material on nearby surfaces. Thus a significant proportion of each section is amorphous and some voids may fill with detritus. Therefore, FIB results should be confirmed using other approaches. All the cross sections prepared by FIB milling have been extracted from wafer D which delineates nuclei very clearly and consists of an epilayer of $Al_{0.5}Ga_{0.5}N$ of 60 nm thickness. Where the cross-section misses a trumpet, a pair of V shaped grooves from the diverging cracks, equal in width and depth at 100 nm, was found with their tips in the buffer layer (Fig. 4). Surprisingly, no actual crack such as in Fig. 3 was seen in this case, as shown in Fig. 5, which illustrates location e described in Table 2.

Location	V Width	Pit Width	Pit Depth	Pipe Length	Pipe Diameter	Epilayer Thickness
Pit a	100	800	600	900	-	60
Pit c	-	500	500	250	100	70
Near Pit e	100	-	-	-	-	70

Table 2: Measurements derived from FIB cross-sectional analysis on Wafer D (nm)



Fig. 4: Two 'V' capped cracks which would meet a third at triple point e. Some 2000Å above the plane imaged. Note the nanopipe which is running off centre in a $000\bar{1}$ direction. Wafer D.

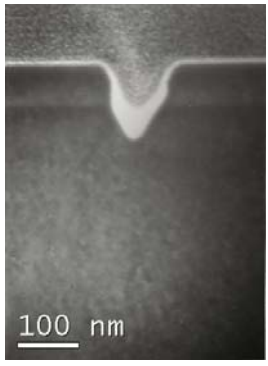


Fig. 5**:** Same area as Fig.4 in $[2\bar{1}\bar{1}0]$ orientation looking along one of the 'V' grooves which penetrates into the buffer layer. No crack is visible.

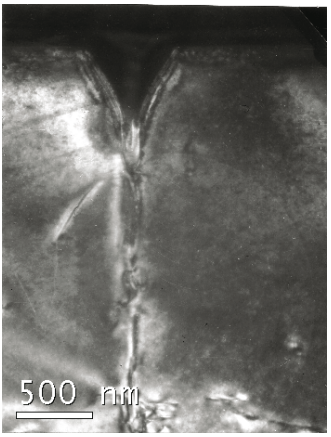


Fig. 6: Pit C tilted slightly from $[11\bar{2}0]$ to give approximate two beam conditions. Dark field, $g = (1\bar{1}00)$. A nanopipe extends from the trumpet further into the buffer layer and is coated by the epilayer. (On top is a protective deposit of Pt and an epoxy layer). A threading dislocation extends downward from the nanopipe to the sapphire and remains in contrast despite g.b = 0 being satisfied for **b** = [0001.]

Figure 6, however, shows a section through a trumpet from which a single crack has propagated. A trumpet (Table 2) is much deeper than the epilayer and obviously pre-existed it as the $\{1\bar{1}02\}$walls of the pit are sheathed by it. Running down from the trumpet is a pipe of diameter 100nm from which dislocations extend to the sapphire substrate. A further contrasting "pipe" extends at least a micron into the sapphire and may be a hollow core dislocation.

To establish the Burgers vector of the dislocations beneath the pipe, dark field images using $g = \pm(10\bar{1}0)$ were recorded under approximately two beam conditions. Neither gave the extinction expected for a screw dislocation with u = [0001]. However, it is still probable that the dislocations are screw in nature with **b** = [0001] but with the expected contrast disturbed by both the thickness and redeposition caused by the ion beam. In these three cross-sections the V grooves proceed from the apexes of the trumpet.

5. DISCUSSION

The role of a crack initiator is to increase the local stress to the level where bond breakage occurs. Neither the apex of a trumpet nor a nanopipe as described in this paper cause sufficient stress amplification by their geometry alone. It must, therefore, be postulated that somewhere within their atomic structures a further more intense stress enhancer lurks.

REFERENCES

Cherns D, Young W T, Steeds J W, Ponce F A and Nakamura S 1997 J. Cryst. Growth. **178**, 201
Cherns D, Henley S J and Ponce F A 2001 App. Phys. Lett. **78**, 2691
Murray R T, Hill G, Hopkinson M and Parbrook P J 2003a Phil. Mag. **83**, 3077
Murray R T, Parbrook P J and Hill G 2003b Inst. Phys. Conf. Ser. **180**, 351

Microstructural and optical characterisation of InN layers grown by MOCVD

P Singh, P Ruterana, G Nouet, A Jain[1], J M Redwing[1] and M Wojdak[2]

SIFCOM, UMR 6176 CNRS ENSICAEN,6 Bd du Maréchal Juin, 14050 Caen CEDEX, France
[1] Department of material science and engineering, Materials Research Institute, The Pennsylvania State University, University Park, PA 16802, USA
[2] CIRIL, UMR 6637 CNRS CEA ENSICAEN, 6 Bd du Maréchal Juin, 1450 Caen CEDEX, France

ABSTRACT : We have investigated indium nitride layers grown by MOCVD. These layers were grown on different types of buffer layers such as Ga polar GaN, N polar GaN, low temperature AlN and nitrided sapphire. The microstructure was determined by transmission electron microscopy. X-ray diffraction for the 0002 rocking curves gave us a full width at half maximum as low as 0.18° for the indium nitride layers. Photoluminescence measurements were carried out at room temperature and at 10K. From these measurements the InN layer on the Ga polar GaN buffer layer seemed to have the best optical properties and crystalline quality; however, the morphology still needs improvement.

1. INTRODUCTION

Recently, Davydov et al (2002) succeeded in growing monocrystalline films of indium nitride that emitted at 0.7eV. The use of a buffer layer made it possible to grow InN films of good crystalline quality by reducing the lattice mismatch between InN and the sapphire substrate. Yamaguchi et al (1999) were among the first to use a GaN buffer layer. Since then other groups have reported on the growth of InN on different buffer layers. Lu et al (2001) used AlN as a buffer layer. Very recently, Mitate et al (2005) have used convergent beam electron diffraction to determine the polarity of InN films. The polarity of the GaN buffer layer plays an important role as the growth mode is not the same for the 2 polarities (Bhuiyan et al 2003). In this paper, growth morphology of InN on different substrates at different V/III ratios is studied. The growth morphology, microstructure, optical and crystalline quality of the samples are discussed.

2. EXPERIMENTAL

The investigated layers were grown on 4 types of substrates Ga-polar GaN, N-polar GaN, low temperature AlN and nitrided sapphire. The samples along with the substrates and growth conditions are listed in table 1. The V/III ratio was varied from 5000 to 15000. As can be seen in table 1, there was a change in the growth rate of the samples from 0.32 μ/hr to 0.54 μ/hr. The growth temperature was around 540°C. The PL measurements were carried out on all the samples using a Kr^+ laser at low temperature (7°K) and at room temperature, the pump power used was 200mW and the excitation wavelength was 647 nm. The photoluminescence spectra were corrected for set-up response. TEM samples were prepared by dimpling down to 10 μm and electron transparency was obtained by cold ion milling with samples cooled at liquid nitrogen temperatures. We carried out TEM analysis on a JEOL 2010 analytical microscope operated at 200KV. X-Ray diffraction was performed by recording the (0002) rocking curves.

Table 1

Substrate	Substrate thickness nm	Growth temperature °C	V/III ratio	Growth rate μ/hr
Ga polar GaN (4B)	6000	520	15000	0.36
Ga polar GaN (4D)	6000	540	5000	0.54
N polar GaN (4C)	300	560	10000	0.32
Low temperature AlN (3A)	3	540	15000	0.39
Nitrided sapphire (4A)	-	540	10000	---

3. RESULTS AND DISCUSSION

Figure 1 shows the TEM images of the samples grown on the 4 different buffer layers. Figures 1a and b show samples 4B and 4D which are InN layers grown on Ga polar GaN substrates. Sample 4B has triangular islands and shows a beginning of coalescence (Fig. 1a). The individual islands have very good crystalline quality as seen from its bright field image. Misfit dislocations can be seen at the InN/GaN interface. On the other hand sample 4D has curvy topped islands which show a better coalescence than the islands of sample 4B. However its crystalline quality is lower as can be seen from the numerous defects in the dark field image (Fig. 1b). This difference is a good indication that the V/III ratio is playing a critical role on the layer quality.



Fig. 1a

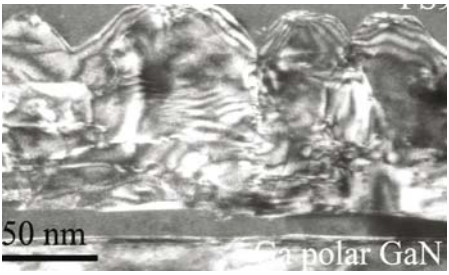


Fig. 1b

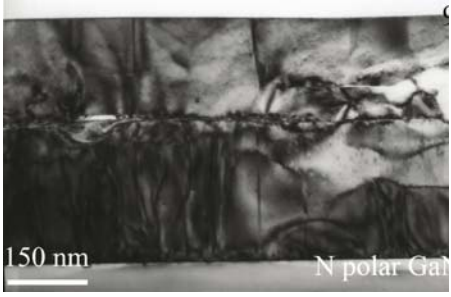


Fig. 1c



Fig. 1d

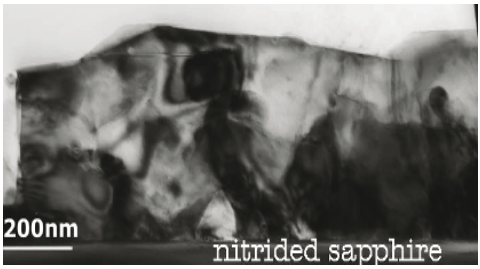


Fig. 1e

Fig. 1. TEM images for InN samples: a) 4B, b) 4D, c) 4C, d) 3A, e) 4A.

A micrograph of sample 4C which has an InN layer grown on an N polar GaN buffer layer is presented in Fig. 1c. The InN layer shows fewer dislocations than the GaN underlying layer and has a flat surface. At the GaN/InN interface there are rather flat voids which lie in the basal plane. These voids may be responsible for relaxing the strain at the interface, thus leading to a 2D growth mode for the InN layer and a reduction of the number of dislocations. For the sample 3A in Fig. 1d, the InN layer is grown on top of a low temperature AlN layer. The surface is undulating and rough and a semicircular void can be seen at the AlN/ InN interface. The last sample 4A shown in Fig. 1e consists of an InN layer which has a very irregular surface directly grown on a nitrided sapphire substrate.

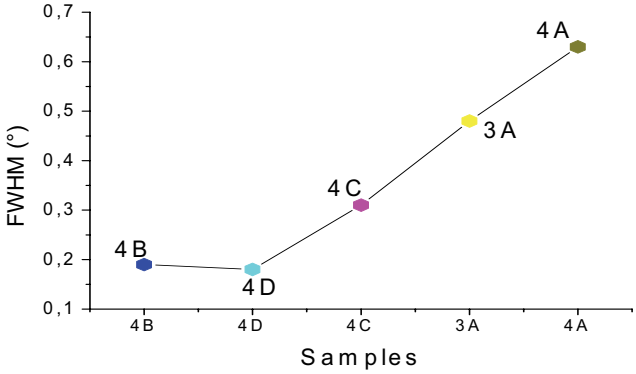
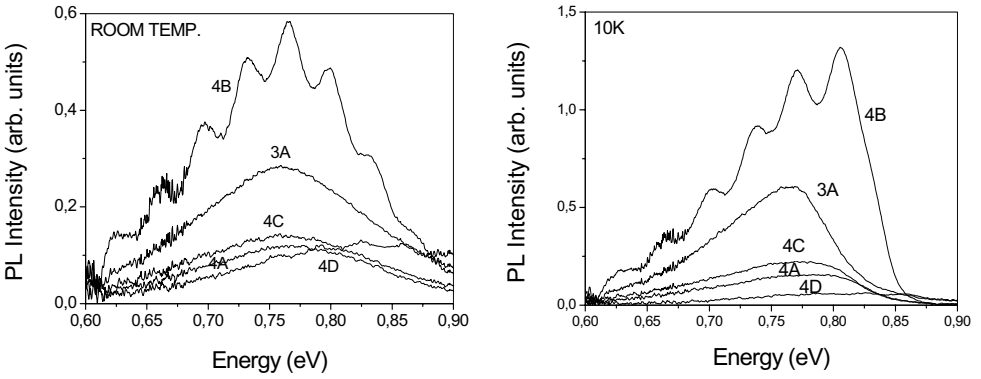


Fig. 2. FWHM for the 5 InN samples.

Even though the dark field image of sample 4D (Fig. 1b) shows defects and stacking faults its FWHM is smaller than that of sample 4B. Sample 4C has a FWHM of 0.31° and a maximum FWHM of 0.68° was recorded for sample 4A. Sample 3A had a FWHM of 0.48°. Normally, the crystalline quality of an InN layer grown on an AlN buffer layer should be higher due to a lattice mismatch of only 13% between InN/AlN compared to 25% between InN/sapphire. This high value of the FWHM could be due to the small thickness of the low temperature AlN layer used here (3 nm).

Photoluminescence spectra for the 5 samples at room temperature and at 7K are shown in Fig. 3. All the samples measured at room temperature have a broad peak width of 0.3eV and more. This band decreases by 0.05 eV at 10K. At both temperatures 4B produces, the most intense signal among the 5 samples. The intensity is increased by almost 3 times at 10K but the band gap experiences a blue shift from 0.76 eV to 0.8 eV at 10K. Sample 4D on the other hand has the highest PL band gap at both temperatures. Its intensity was the lowest among all the 5 samples. The emission of the highest photon energy was observed for the sample 4D, which had a PL peak at about 0.85 eV at low temperature.



a. b.

Fig. 3. Photoluminescence spectra for the 5 InN samples at: a) room temperature and b) 7K.

Sample 3A (low temperature AlN buffer layer) had a constant PL band gap of 0.76 eV at both temperatures. 4C showed a variation of 0.2 eV when measured at RT (0.76eV) and 10K (0.78 eV). Sample 4A emitted at 0.76 eV at room temperature and 0.77 eV at 10K. However the signals at both temperatures for samples 4D, 4C and 4A were not intense due to their lower crystalline quality as can be seen from the FWHM and the TEM images.

4. SUMMARY

We have studied InN samples grown on different types of buffer layers at a temperature of 540°C. Voids at the interface seem to relax the InN layers and hence reduce the number of dislocations. Considering that the polarity of InN is the same as that of the buffer layer, it is noticed that N polar InN favours 2D growth. On top of GaN buffer layers, the FWHM of InN layers were smaller compared to those of AlN and nitrided sapphire buffer layers and even more so for the InN on Ga polar GaN. The PL emission at 0.76 eV is shown to correspond to the layers exhibiting the best crystalline quality

ACKNOWLEDGEMENT

This work was supported by EU Marie Curie RTN contract MRTN-CT-2004-005583.

REFERENCES

Yamaguchi S, Kariya M, Nitta S, Takeguchi T, Wetzel C., Amano H and Akasaki I 1999 J. Appl. Phys. **85**, 7682

Lu H, Schaff W J, Hwang J, Wu H, Koley G and Eastman L F 2001 Appl. Phys. Lett. **79,** 1489

Daydov V Y, Klochikhin A A, Seisyan P, Emstev V V, Ivanov S V, Bechstedt F, Furthmuller J, Harima H, Mudryi A V, Adherhold J, Semchinova O and Graul J 2002 Phys. Status Solidi B **229**, R1

Bhuiyan A G, Hashimoto A, Yamamoto A 2003 J. Appl. Phys. **94,** 2779

Mitate T, Mizuno S, Takahata H, Kakegawa R, Matsuoka T, Kuwano N 2005 Appl. Phys. Lett. **86**, 134103

Structural properties of InN thin films grown with variable growth conditions on GaN/Al_2O_3 by plasma-assisted MBE

A Delimitis, Ph Komninou, Th Kehagias, Th Karakostas, E Dimakis[1], A Georgakilas[1] and G Nouet[2]

Department of Physics, Aristotle University of Thessaloniki, GR-54124 Thessaloniki, Greece
[1] Microelectronics Research Group, Department of Physics, University of Crete, P.O. Box 2208, 71003 Heraklion-Crete, Greece; and IESL, FORTH, P.O. Box 1527, 71110 Heraklion-Crete, Greece
[2] ENSICAEN/SIFCOM UMR CNRS 6176, 6 Bld du Marechal Juin, 14050 Caen Cedex, France

ABSTRACT: The structural characteristics of compact and columnar InN films grown by molecular beam epitaxy on GaN templates are investigated by transmission electron microscopy. Compact mode of growth is favoured at low substrate temperatures, below 500 ^oC, and by the introduction of an InN nucleation layer prior to the InN epilayer growth. Improved quality compact InN films, having threading dislocations with densities on the order of 10^9-10^{10} cm^{-2}, are achieved by using high In/N flux ratios. Compact films generally exhibit higher in-plane lattice constant values than columnar ones and, consequently, higher densities of InN/GaN interfacial misfit dislocations.

1. INTRODUCTION

Research developments in the fabrication of thin films and devices based on indium nitride have shown a rapidly increasing trend in recent years. The material has attracted a high interest due to its optimum optical and electrical properties, such as small band gap value (Davydov et al 2002) and high electron drift velocity (Foutz et al 1999), which makes it ideal for optoelectronic and microelectronic applications. Consequently, the study of growth conditions and their correlation with the structural properties of InN is of primary importance (Lu et al 2003), especially since the film quality obtained up to now is not satisfactory. Transmission electron microscopy (TEM) is a powerful tool for the analysis of the microstructure of materials; however, only few electron microscopy studies of InN epilayers have been reported up to now (Lu et al 2003, Araki et al 2003, Komninou et al 2004).

This study aims to correlate the microstructure of InN films grown on GaN templates with the different growth conditions employed, such as the substrate temperature, epilayer thickness, In/N flux ratio and pre-growth of an InN nucleation layer. The structural defects in the InN/GaN interface and in the epilayers have been studied by means of TEM and high-resolution electron microscopy (HRTEM). In order to evaluate the quality of the epilayers, detailed calculations of the density of threading dislocations (TDs) have been performed. The variations in the lattice parameters of the films were investigated by electron diffraction analysis and directly related to the density of misfit dislocations (MDs) present at the InN/GaN interface.

2. EXPERIMENTAL DETAILS

The InN films were grown on Ga-face 2.5 μm thick GaN/Al_2O_3 (0001) templates by radio frequency (rf) plasma-assisted molecular beam epitaxy (MBE). Prior to the film deposition, a GaN buffer layer, up to 50 nm thick, was grown under Ga-rich conditions to improve surface purity and favour the step-flow growth mode. The details of the growth conditions of the various InN films are summarised in Table 1. In the case of sample S3, a polycrystalline AlN cap layer was grown on top of InN for protection purposes.

Table 1: Conditions of growth for the InN epilayers on top of GaN/Al_2O_3 templates.

Sample	Thickness (nm)	Growth temperature (^oC)	In/N flux ratio	InN nucleation layer (nm)	Mode of growth
S3	300-500	500	0.14	-	columnar
S4	900	300	0.76	-	compact
T1	900	475	0.25	50	compact
T4	250	500	0.17	30	compact
T7	1050	400	0.76	180	compact

Cross-section TEM (XTEM) specimens were prepared by standard mechanical thinning, followed by ion milling in liquid nitrogen ambient. TEM and HRTEM observations were performed in a JEOL 2010 electron microscope with a point to point resolution of 0.19 nm and C_s=0.5 mm.

3. RESULTS AND DISCUSSION

The morphological differences between compact and columnar growth mode are best outlined in the XTEM images of Fig. 1. In Fig. 1a, a part of the compact InN film of sample T7 is presented, taken with the 0002 reflection. The InN epilayer, grown at 400 ^oC, has a total thickness of about 1.05 μm. The epitaxial relationship of InN and GaN is illustrated in the electron diffraction pattern of Fig. 1(a) that corresponds to the [11 $\bar{2}$ 0] zone axis and was determined to be [0001] GaN // [0001] InN, (0 $\bar{1}$10) GaN // (0 $\bar{1}$10) InN. Fig. 1b clearly reveals the columnar morphology of sample S3. The InN columns are grown in a detached column configuration; their width was up to 1.5 μm and their thickness ranged from 300 to 500 nm. The same epitaxial relationship between InN and GaN was also deduced from electron diffraction patterns. These results show that compact growth modes can be achieved at relatively low substrate temperatures and by the introduction of a nucleation layer prior to the film growth. Higher substrate temperatures do not favour the nucleation of the initial InN islands and result in low mobility of nitrogen adatoms, leading to discrete island growth (Dimakis et al 2004).

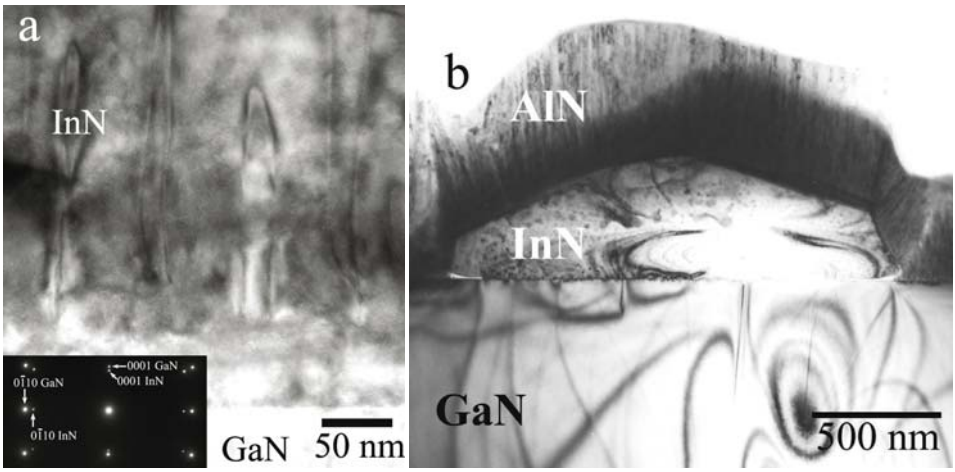


Fig. 1: (a) XTEM image from the compact InN film T7, taken with the 0002 reflection. The film has a total thickness of 1050 nm. The electron diffraction pattern, shown in Fig. 1a reveals the [11 $\bar{2}$ 0] GaN and InN zone axes, illustrating the exact epitaxial growth of InN on GaN templates. (b) XTEM image of a separated InN column in the film S3, obtained with the 0002 reflection.

The crystal quality of InN films was qualitatively evaluated by measurements of the density of the crystal defects present in the epilayer. The predominant structural defect in all compact samples studied was TDs of edge, screw and mixed type character [Fig. 1a], whereas the columnar film S3

revealed a quite large number of dislocation loops, as also shown in Fig. 1b. The density of all types of TDs was estimated and the results are presented in Table 2.

Table 2: Threading dislocations density measurements in the InN thin films.

Sample	Dislocation Character		
	Pure Edge (cm^{-2})	Pure Screw (cm^{-2})	Mixed (cm^{-2})
S4	$2.2\ 10^{10}$	$1.9\ 10^{9}$	$6.2\ 10^{9}$
T1	$2.3\ 10^{10}$	$1.1\ 10^{9}$	$2.7\ 10^{9}$
T4	$1.5\ 10^{10}$	$1.6\ 10^{9}$	$3.9\ 10^{9}$
T7	$1.4\ 10^{10}$	$1.2\ 10^{9}$	$1.8\ 10^{9}$

In accordance to the $\mathbf{g}\cdot\mathbf{b}=0$ visibility criterion for dislocations, TEM experiments revealed that TDs of pure edge character have a Burgers vector that lies in the (0001) basal plane, i.e. equal to $\mathbf{b}=1/3\langle 11\bar{2}0\rangle$, whereas for pure screw dislocations $\mathbf{b}=[0001]$. Edge type TDs have a density in the order of 10^{10} cm^{-2}, which is higher by an order of magnitude compared to screw or mixed type dislocations. The density of TDs is lower for compact films with an InN nucleation layer and becomes even smaller with increasing thickness of the nucleation layer. The lower dislocation density of sample T7 in comparison to the other compact films illustrates that a high (0.76) In/N flux ratio is also required for growing high quality InN thin films.

Electron diffraction experiments were employed to reveal the variations in the lattice constants of wurtzite InN in all samples. Detailed measurements of the *a* and *c* values could be readily obtained by taking the lattice constants of Al_2O_3 as a reference and the results are summarized in Table 3. In general, among a large number of samples grown under various conditions, there is a tendency of compact InN films to exhibit higher values for *a* axis and smaller values for *c* axis compared to columnar InN. This inevitably results in a larger spacing of MDs that are introduced at the InN/GaN interfacial area in order to accommodate the lattice mismatch between the InN and GaN crystals. In lack of accurately measured bulk InN constants, a qualitative comparison between the samples cannot be directly performed. However, all the measured values lie within the range reported in the literature (Bhuiyan et al 2003), with compact InN exhibiting slightly higher values for the in-plane lattice constant compared to the ones most often encountered (Davydov et al 2002).

Table 3: Measurements of the lattice constants and misfit dislocation spacing in the InN films.

Sample	a (nm)	c (nm)	Misfit dislocation spacing (nm)
S3	0.3534	0.5702	2.83
S4	0.3548	0.5702	2.73
T1	0.3544	0.5692	2.76
T4	0.3542	0.5696	2.77
T7	0.3529	0.5697	2.87

The improved properties of compact InN films with InN nucleation layers were also outlined by HRTEM observations of the InN/GaN interfacial area, as that is depicted in Figs. 2a and 2b for compact InN T7 and columnar InN S3 films, respectively. The electron beam direction was along $[2\bar{1}\bar{1}0]$ in both cases. The insets are Fourier filtered images of a part of the interface using only the in-plane spatial frequencies, in order to illustrate the exact position of the interface and to reveal the position of MDs. An atomically flat interface is outlined for sample T7, in contrary to the roughness exhibited for the interface of sample S3. The GaN $\{10\bar{1}0\}$ half planes clearly reveal the position of the projected edge component of the MDs in the interface. The dislocations appear in an average of 10.40 GaN planes in T7 and 10.25 planes in S3, i.e the fringes are shown to terminate in an average plane sequence of 10-10-10-11-11 in T7 and 10-10-10-11 GaN planes in S3. Similar values for the MD spacing were also deduced from measurements of the Moiré fringe spacing in conventional TEM micrographs (Komninou et al 2004).

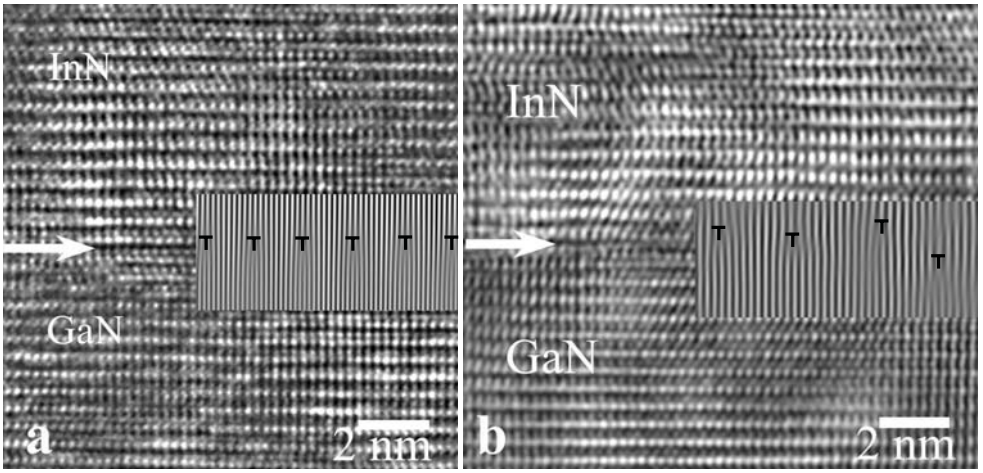


Fig. 2: HRTEM images from the interfacial area of (a) the compact T7 and (b) the columnar InN S3 epilayers. The electron beam direction was along $[2\bar{1}\bar{1}0]$. The insets in both images are Fourier filtered images of a part of the InN/GaN interface using the $10\bar{1}0$ spatial frequencies, revealing the exact position of the MDs.

4. CONCLUSIONS

The structural properties of compact and columnar InN films grown by rf plasma-assisted MBE on GaN/Al_2O_3 templates have been investigated by TEM and HRTEM. A clearly defined epitaxial orientation relationship of [0001] GaN // [0001] InN, $(0\bar{1}10)$ GaN // $(0\bar{1}10)$ InN between InN and GaN was found in all samples. Low substrate temperatures, high In/N flux ratios and the introduction of an InN nucleation layer were requirements for obtaining compact epilayers of improved quality. Compact InN films had TDs as their predominant defect, with a density in the order of 10^9-10^{10} cm^{-2}. Any variations in the lattice parameters were readily illustrated by means of electron diffraction and related with the MD spacing. Higher *a* axis values were generally deduced for compact films compared to columnar ones, which also corresponded to a higher density of misfit dislocations in the InN/GaN interface for compact InN.

ACKNOWLEDGEMENT

This work was supported by EU Marie Curie RTN contract MRTN-CT-2004-005583 (PARSEM).

REFERENCES

Araki T, Ueta S., Mizuo K, Yamaguchi T, Saito Y and Nanishi Y 2003 Phys. Stat. Sol. (c) **0**, 429

Bhuiyan A G, Hashimoto A and Yamamoto A 2003 J. Appl. Phys. **94**(5), 2779

Davydov V Yu, Klochikhin A A, Seisyan R P, Emtsev V V, Ivanov S V, Bechstedt F, Furthmüller J, Harima H, Mudryi A V, Aderhold J, Semchinova O and Graul J 2002 Phys. Stat. Sol. (b) **229**(3), R1

Dimakis E, Konstantinidis G, Tsagaraki K, Adikimenakis A, Iliopoulos E and Georgakilas A 2004 Superlatt. Microstruct. **36**, 497

Foutz B E, O'Leary S K, Shur M S and Eastman L F 1999 J. Appl. Phys. **85** 7727

Komninou P, Kehagias Th, Delimitis A, Dimitrakopulos G P, Kioseoglou J, Dimakis E, Georgakilas A and Karakostas Th 2004 Super. and Microstr. **36**, 509

Lu C J, Bendersky L A, Lu H and Schaff W J 2003 Appl. Phys. Lett. **83**, 2817

Growth and surface characterization of piezoelectric AlN thin films on silicon (100) and (110) substrates

S Saravanan, E G Keim[1], G J M Krijnen and M Elwenspoek

Transducers Science and Technology Laboratory and
[1] Central Materials Analysis Laboratory
Mesa+ Institute for Nanotechnology, University of Twente, Hogekamp, P.O. Box 217, 7500 AE Enschede, The Netherlands

ABSTRACT: This work investigates the fundamental growth of c-axis oriented piezoelectric AlN thin films by RF reactive sputtering on p-type (100) and (110) silicon substrates. Substrates are treated with a 1% HF solution before deposition to remove the native oxide followed by back-sputtering using argon ions. X-ray diffraction shows a (0001) oriented columnar texture of AlN grains which is the preferred orientation for piezoelectric applications. TEM shows the presence of a 4 nm thick semi-crystalline interface between silicon and the AlN layer. A basic growth mechanism is proposed from microstructural observations.

1. INTRODUCTION

RF reactive sputtering offers advantages over other processes for depositing AlN thin films on various substrates, and facilitates micromachined device fabrication processes. Okano et al. (1992) suggested that using this technique highly (0001) oriented piezoelectric AlN thin films can be grown at relatively low temperature. Piezoelectric AlN MEMS devices find applications such as microactuators, resonators, acoustic modulators, etc. The surface morphology of AlN thin films with many orientations exhibited a granular, worm-like, columnar surface of grains, as detailed by Cheng et al (1996). In this paper, we have studied the microstructure of AlN thin films with (0001) orientation deposited on Si (100) and Si (110) substrates by RF reactive sputtering using X-ray diffractometry (XRD), scanning electron microscopy (SEM) and transmission electron microscopy (TEM). Growth observations are presented showing the existence of a semi-crystalline interlayer. From a detailed analysis near the AlN/Si interface region of the sample along its thickness direction from the interlayer the texture, morphology and microstructure of AlN thin films is elucidated.

2. EXPERIMENTAL PROCEDURE

The deposition of AlN thin films was performed at a substrate temperature of 355^{O}C in a Nordiko-2000 RF reactive sputtering system. Prior to that, the p-type silicon substrates were treated using a 1% hydrogen fluoride (HF) solution to remove the native oxide and subsequently kept in vacuum. Back sputtering using pure argon plasma was done to remove any monolayer formed by the residual gases inside the vacuum chamber. The deposition was carried out using optimised sputter parameters as shown in Table 1. For a better piezoelectric performance, AlN with a (0001) orientation grown perpendicular to the substrate is required as indicated by Naik et al (1996). The substrate temperature was kept at 355^{O}C before the deposition started.

Crystalline orientation and texture were determined by XRD (Philips Expert II) with Cu kα radiation generated from a 40 kV, 30 mA X-ray source. A rocking curve scan was also performed at 2θ where the (0001) reflection occurs. The surface morphology and cross-section of the samples were observed by SEM (LEO 1550 FEG). Samples were prepared for cross-sectional TEM (XTEM) studies in a Philips CM30T following the recipe by Keim et al (2001/2) to study the growth mechanism.

Table 1. AlN deposition parameters

Parameters	Values
Sputter pressure (mbar)	7.2×10^{-3}
RF power (W)	350
Ar:N_2 flow rate (sccm)	7:6
Substrate temperature (deg. C)	355
Back Sputtering	
RF power (W)	150
Ar pressure (mbar)	1.2×10^{-2}
Duration (min)	8

3. RESULTS AND DISCUSSION

3.1 Preferential (0001) Texture

The thickness of the layers was found to be 580 nm as measured by ellipsometry. The deposited films contain mainly the wurtzitic phase of AlN and no other reflections are observed from XRD as shown in Fig. 1a. The 2θ - reflection occurs at 35.87^{O} and 35.91^{O} for AlN thin films on Si (100) and Si (110), respectively. The rocking curves measured at 2θ - reflections are shown in Fig. 1b with Gaussian fitted curves, of 3.3^{O} and 2.9^{O} FWHM for films on Si (100) and Si (110), respectively. It shows the predominant (0001) texture of AlN with the c-axis normal to the silicon substrates.

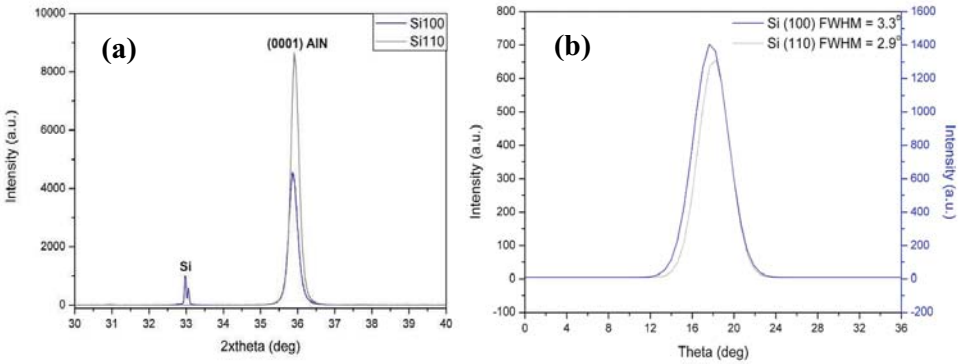


Fig. 1: XRD intensity peaks for (a) 2θ scan and (b) rocking curves (Gaussian fitted) of AlN thin films with (0001) texture deposited on the Si (100) and Si (110) substrate, respectively.

3.2 Surface Morphology

Samples were cleaved into many pieces. The images of Fig. 2a and b show the surface morphology of AlN thin films on Si (100) and Si (110) substrates, respectively, with a substrate tilt angle of 5^{O}. The top

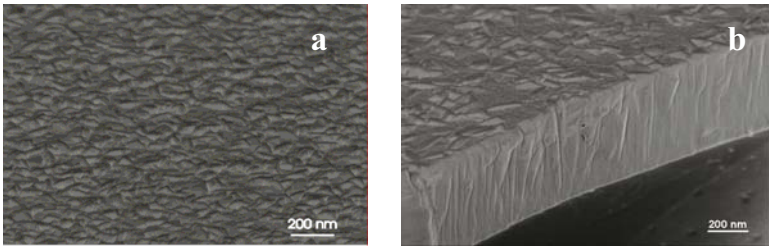


Fig. 2: Surface morphology of AlN thin films on (a) Si (100) and (b) Si (110) substrates using SEM. surface shows an average crystallite size of AlN thin films that varies from 20-50 nm. The crystallites

surface shows an average crystallite size of AlN thin films that varies from 20-50 nm. The crystallites are closely packed together without any trapped pin-holes on the surface.

3.3 Interface Properties

TEM images were obtained at the interface between the AlN thin film and silicon substrate to understand the initial stages of growth and subsequent evolution of microstructures. The XTEM lattice images are shown in Fig. 3a and b for the Si (100) and Si (110) substrates, respectively. A clear thin interface with a thickness of approx. 4 nm was observed on both substrates. It can also be observed that (0001) columnar AlN crystallites originate from the interface layer. The interface layers are highly defective and disordered because of a larger mismatch in lattice parameters between the silicon substrate and AlN.

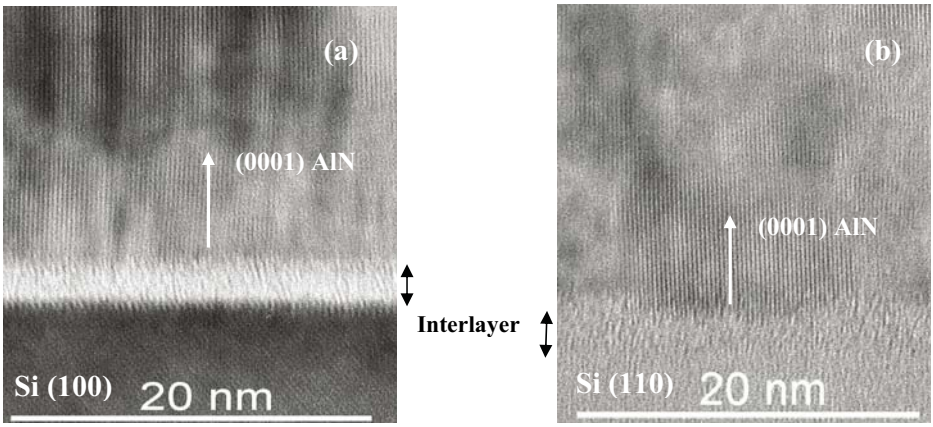


Fig. 3: TEM lattice images at the AlN/Si interface region. The thickness of the interface layer is 4 nm.

To understand the microstructure properties of the interface layers, dark field (DF) images were recorded. These are shown in Fig. 4a and b, they confirm the presence of various sizes of bright spots within the interface layer indicating that the interface layer is not completely amorphous but semi-crystalline in nature.

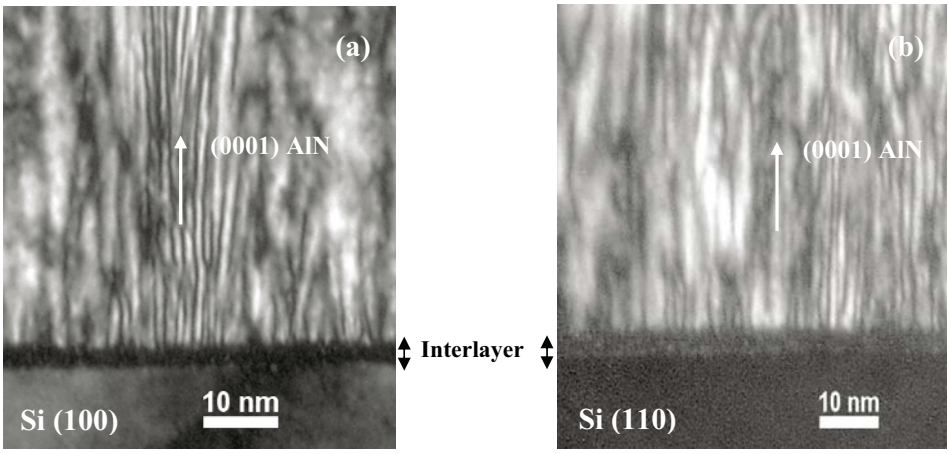


Fig. 4: Dark field TEM images at the AlN/Si interface region.

3.4 Discussion

Investigations from bright and dark field images reveal that a few atomic layers of AlN grains at the interface layer are semi-crystalline on both silicon substrates. This semi-crystalline nature can be explained from the following facts: First, the mismatch in lattice parameters causes AlN grains to nucleate in an amorphous phase initially, and they are highly defective. Second, the mobility of ad-atoms at the inter-layer is not enough to find the minimum surface energy plane due to a relatively low substrate temperature, therefore no epitaxial growth of AlN thin films occurs. Based on a microstructure analysis of the AlN thin films, a growth model is proposed as shown in Fig. 5. It consists of a transition layer which is a semi-crystalline AlN thin film of thickness less than 4 nm, followed by a direct columnar AlN layer which is running through the entire thickness of the film. They are strained and have dislocation defects. The semi-crystalline inter-layer thus forms nucleation sites for the preferential columnar orientation of AlN which has a minimum surface energy related to other faces as mentioned by Stevens et al (1994). These inter-layers are not hydrogenated AlN (AlN:H) because the substrates were back sputtered with argon before deposition. Also, we do not expect silicon nitride formation at the interface since the deposition was done at relatively low temperatures, as mentioned earlier by Bing-Hwai et al (2002).

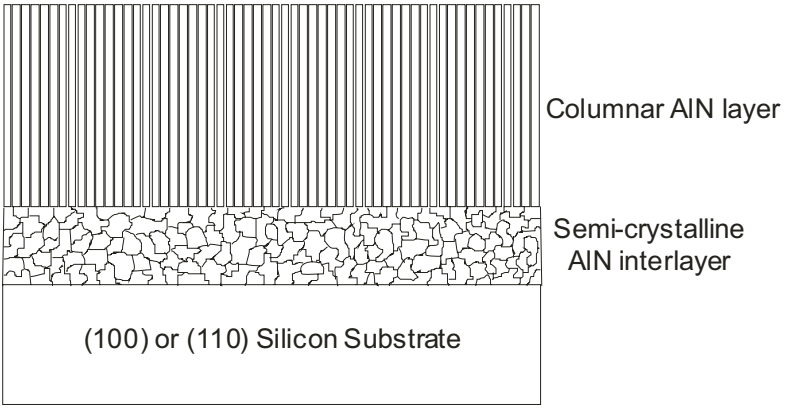


Fig. 5: Schematic representation of the growth mechanism of AlN thin film on Si substrates

4. CONCLUSIONS

Preferential (0001) oriented piezoelectric AlN thin films deposited on silicon (100) and (110) substrates have been studied for their orientation, surface morphology and interface properties. SEM and XTEM observations show dense, columnar crystallites of AlN. Microstructural investigations show two distinct layers: (1) a transition and (2) a columnar AlN layer. The inter-layer (1) between the AlN film and silicon substrate is semi-crystalline in nature and it is believed to be the origin of nucleation sites for columnar growth of AlN grains. The lowest surface energy is along the (0001) direction and it is consistent with all deposited films regardless of the nature of (100) or (110) silicon substrate, which is an essential prerequisite for piezoelectric thin film applications.

REFERENCES

Cheng C C, Chen Y C, Wang H J and Chen W R 1996 J. Vac. Sci. Technol. A **14**, 2238
Hwang B H, Chen C S, Lu H Y and Hsu T C 2002 Mat. Sci. Eng. A **325**, 380
Keim E G, Bijker M D and Lodder J C 2001 J. Vac. Sci. Technol. A **19**, 1191
Keim E G, Nguyen L T, Lodder J C 2002 Proc. Microscopy & Microanalysis Meeting, (Quebec, Canada) p 1346CD
Naik R S, Reif R, Lutsky J J and Sodini C G 1996 J. Electrochem. Soc. **143**, 691
Okano H, Takahashi T, Tanaka T, Shibata K and Nakano S 1992 Jap. J. Appl. Phys. **31**, 3446
Stevens K S, Ohtani A, Kinniburgh M and Beresford R 1994 Appl. Phys. Lett. **65**, 321

Characterization and structuring of nitride-based heterostructures for vertical-cavity surface-emitting lasers

R Kröger, C Kruse, J Dennemarck, D Hommel and A Rosenauer

Institute of Solid State Physics, University of Bremen, Bremen, Germany

ABSTRACT: A new approach for nitride-based distributed Bragg reflectors as mirrors for vertical-cavity surface-emitting lasers was investigated by means of transmission electron microscopy. These layers consisted of multiple stacks of GaN layers in conjunction with a superlattice of alternate layers of AlN and GaN or – in order to reduce tensile strain – a superlattice of AlN and $In_xGa_{1-x}N$ with x = 0.25. The AlN/GaN-based superlattice showed cracks and a high interface roughness whereas smooth layers without cracks could be found for the structure containing the AlN/$In_xGa_{1-x}N$ superlattice. The $In_xGa_{1-x}N$ layers were homogeneous, although indications for In-segregation could be observed. Mesas of these structures were prepared by the focused ion-beam technique.

1. INTRODUCTION

Nitride based semiconductors have been found to be suitable for the realization of light emitters in the whole spectral region. Due to this fact, new devices based on these materials are a major current research topic. Since GaN based laser diodes have been successfully demonstrated as edge-emitters, new more efficient and better scaleable approaches are being developed. Vertical-cavity surface-emitting lasers (VCSELs) with a small optical active region offer these advantages not only for technological applications but also for devices, which enable fundamental research, i.e. with polariton lasers (see Malpuech 2002). However, using nitride compounds for this purpose creates various problems, such as the complex layer structure that requires a large number of distributed Bragg-reflectors (DBRs). This is necessary to realize sufficiently high reflectivities to achieve stimulated emission from the optically active region since the difference in refractive index of the nitride alloys is comparably small. The combination of materials with different lattice parameters gives rise to strain, which can limit the thickness of the deposited structure before cracking occurs. In the literature either AlGaN/GaN, which leads to significant strain (Fernandez 2001) or a lattice matched structure using $Al_{0.82}In_{0.18}N$ instead of AlGaN (Carlin 2005) as low index material is reported. This work presents results obtained with a different approach using a DBR mirror containing a combination of a superlattice (SL) of AlN and either GaN or $In_xGa_{1-x}N$ with x = 0.25 for the low index material. This structure has a reduced tensile strain with respect to the GaN substrate. However, the interface structure, the strain state and possible material transport by diffusion and segregation have to be investigated thoroughly. Using high resolution transmission electron microscopy (HRTEM) these issues were addressed. Furthermore, the surface structuring by means of the focused ion-beam (FIB) technique was explored as a method to realize mesas suitable for VCSEL creation.

2. EXPERIMENTAL DETAILS

DBR multilayers with mirror pairs containing a 42 nm thick GaN layer and multiple stacks of GaN and either a superlattice of nominally 0.5 nm GaN and 2 nm AlN or a superlattice containing nominally 1.1 nm $In_xGa_{1-x}N$ (x = 0.25) and 1.4 nm AlN were deposited by molecular beam epitaxy (MBE) on top of a GaN template layer, which had been provided by metal organic vapor phase epitaxy (MOVPE) on a (0001) sapphire substrate. This layer stack was optimized for a maximum room temperature reflectivity at a wavelength of 420 nm, which is the targeted emission wavelength of

the VCSEL. Both DBR structures were used for the realization of a full VCSEL structure containing three InGaN quantum wells in the cavity. The transmission electron microscopy (TEM) investigations were carried out using a CM20 UT TEM. The cross sectional TEM sample preparation and the surface structuring was performed by a dual-beam focused ion beam system (Nova, FEI).

3. RESULTS AND DISCUSSION

The multilayer with AlN/GaN SL DBR showed already severe cracking when investigated by light microscopy. A high density of crystallographically oriented cracks occurred throughout the complete film leaving areas of 10 to 20 µm apparently intact (not shown here). However, it can be seen from the bright field TEM image given in Fig. 1 that the structure contained cracks which were subsequently overgrown leading to a deterioration of the DBR layers in the vicinity of the former crack. A more detailed look at the SL showed that the AlN/GaN layer structure was maintained further away from the cracks (see insert in Fig. 1).

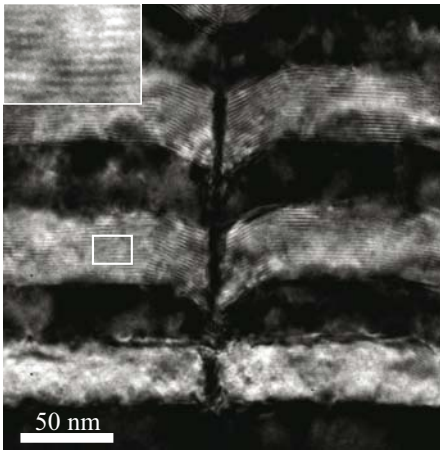


Fig. 1.: Bright-field TEM image of a DBR structure containing an AlN/GaN superlattice. Overgrown cracks and an increased interface roughness deteriorate the film structure. The insert shows a magnification of the white rectangle in the image.

For the DBR structure containing the $In_xGa_{1-x}N$/AlN superlattice, no cracks were observed and the TEM analysis showed a smooth interface structure of the DBR over a range of several tens of microns. The bright field TEM image in Fig. 2(a) shows smooth and undistorted interfaces.

A strain state evaluation from an HRTEM image from the SL region was carried out using the optimized imaging conditions described by Rosenauer (2004). The HRTEM image was taken in [01$\underline{1}$0] zone axis using two beam conditions, namely the (0002) and the (0000) reflections with a strongly excited (0004) reflection. The resulting lattice fringe image was processed as is described by Rosenauer (1997) performing Fourier filtering of the (0002) reflection, and defining a grid and a reference lattice (in the GaN region of the DBR). Figure 2(b) displays a grey scale coded map of the local distance of the grid nodes relative to the reference region (at the bottom of the image). The maximum distance values vary between 1.02 and 1.04 which is equivalent to a 2 to 4 % increase of the lattice parameter or a maximum In mole fraction of x = 0.2 to 0.4, which is - in the error limits - fairly in agreement with the intended In mole fraction of x = 0.25. A more exact In concentration evaluation is hampered by the fact that it is difficult to estimate the correct Al concentration in the vicinity of the $In_xGa_{1-x}N$ layer. Local distance values of less than one correspond to AlN (with a lower lattice parameter compared to GaN) whereas values larger than one correspond to InGaN. From the local distance map the layer structure is found to start from the GaN with a layer showing a larger lattice parameter than that of GaN, namely a $In_xGa_{1-x}N$ layer. Clearly distinguishable are layers with lattice

parameters smaller than that of GaN, namely AlN or AlGaN. The $In_xGa_{1-x}N$ layers are comparatively homogeneous and smooth at the bottom but they are somehow smeared out in growth direction. This is confirmed by Fig. 2(c), which shows the average local distance for each lattice fringe. The $In_xGa_{1-x}N$ related peaks show a tail in the growth direction reaching up to 2 nm into the AlN layer whereas the onsets of the $In_xGa_{1-x}N$ layers are significantly sharper. This could be an indication for In-segregation during growth. However, a quantitative evaluation of the lattice fringe images requires a more detailed knowledge of the chemical shift involved and its influence on lattice positions.

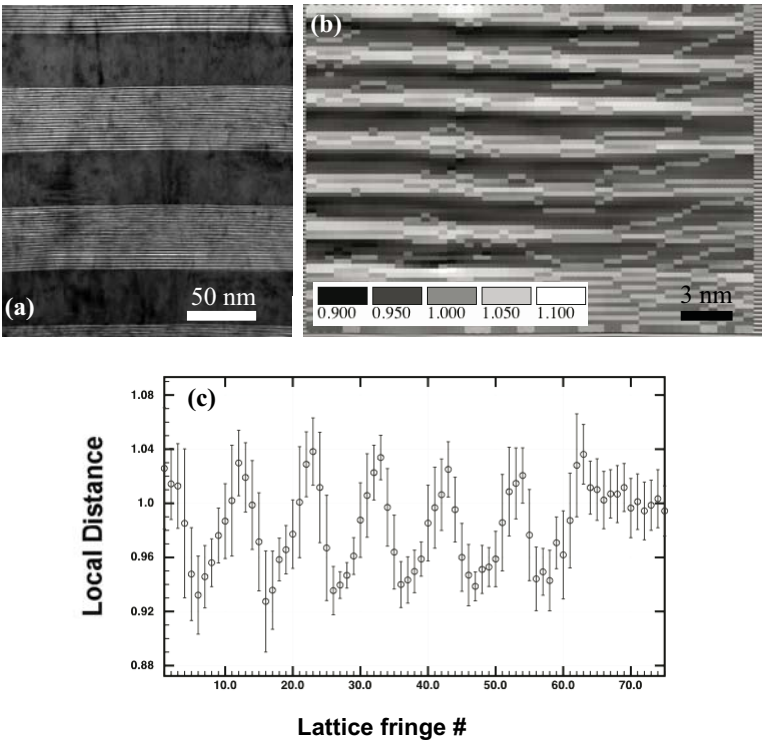


Fig. 2: (a) Bright-field TEM image of the DBR with a AlN/$In_xGa_{1-x}N$ SL. (b) Local distance map of the SL. The grey scale indicates the range of strain. (c) Average distance as a function of the number of lattice fringes.

These findings emphasize the importance of In segregation into the AlN layers, which is likely to affect the index contrast (i.e. the difference of the refractive indices) and the strain state of the layers, which determines the interface roughness. However, as is also confirmed by reflectance measurements (not shown here) the $In_xGa_{1-x}N$/AlN superlattice approach fulfills the requirements for a suitable DBR structure compatible with a VCSEL.

To investigate whether the FIB technique is suitable for the creation of VCSEL mesas, DBR and complete VCSEL structures were etched by this method. Especially the surface damage and the damage on the sidewalls of such mesas by the 30 kV Ga beam is of great importance. In order to reduce the damage caused by the Ga ion-beam a pre-structuring technique was developed such that the maximum Ga ion dose during FIB structuring could be minimized. To achieve this a 100 nm SiO_2 layer was deposited by sputtering to act as a hard mask for the subsequently employed chemically assisted ion beam etching, which uses an Ar-Plasma and Chlorine to etch photo-lithographically predefined structures into the sample surface. By this technique rough mesas of about 5 µm diameter could be created, which could then be fine etched by the FIB. Beside the better sample protection this gives also the advantage of a reduced FIB etching time. A result of the mesa etching is shown in

Fig. 3(a). It shows a bright field TEM image of a circular DBR structure that was created using the FIB. The base diameter of the mesa was about 100 nm whereas at the top the diameter amounted to about 60 nm. The HRTEM image shown in Fig. 3 (b) and taken along the [01$\underline{1}$0] crystallographic direction shows an amorphous layer of 1 to 2 nm thickness. The microstructure of the mesa does not show a significant damage by the FIB. Hence, the FIB is a suitable tool for the creation of nitride based VCSEL mesas.

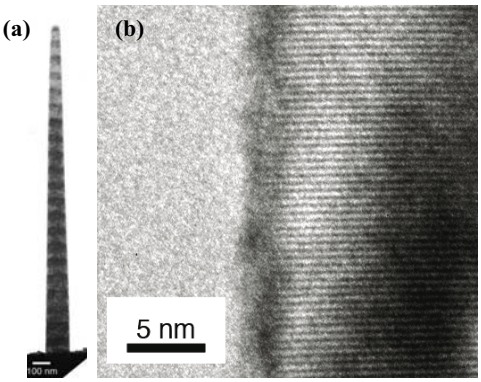


Fig. 3: (a) DBR mesa created by the FIB technique. (b) Side-wall of the mesa at the top: an amorphous layer and lattice fringes are visible.

4. SUMMARY

A microstructural investigation of nitride-based multilayers for use as distributed Bragg-reflectors revealed that using alternating layers of an AlN/$In_xGa_{1-x}N$ superlattice results in largely crack free layers suitable for use as mirrors for vertical-cavity surface emitting lasers, compared to a strongly tensile strained AlN/GaN superlattice structure. The AlN/$In_xGa_{1-x}N$ superlattice was smooth and the $In_xGa_{1-x}N$ layer indicated In segregation into the AlN layer during growth. Moreover, the focused ion beam technique was found to be a suitable way for the structuring of VCSEL mesas of good crystal quality to diameters as small as 100 nm.

ACKNOWLEDGMENTS

We gratefully acknowledge funding by the *Deutsche Forschungsgemeinschaft* (contract number: KR 2195/3).

REFERENCES

Carlin J F, Dorsaz J, Feltin E, Butté E, Grandjean N, Laügt M and Ilegems M 2005 Appl. Phys. Lett. **86**, 31107

Fernandez S, Naranjo F B, Calle F, Sanchez-Garcia M A, Calleja E, Vennegues P, Trampert A and Ploog K H 2001 Appl. Phys. Lett. **79**, 2136

Malpuech G, Carlo A D, Kavokin A V, Baumberg J J, Zamfirescu A and Lugli P 2002 Appl. Phys. Lett. **81**, 412

Rosenauer A and Gerthsen D 2004 Proc. 13th EMC, 103

Rosenauer A, Remmele T and Gerthsen D 1997 Optik **105**, 99

Characterization of defects in ZnS and GaN

J Deneen, S Kumar, C R Perrey and C B Carter

Department of Chemical Engineering and Materials Science; University of Minnesota, Minneapolis, MN 55455, USA

ABSTRACT: The compound semiconductors ZnS and GaN both exhibit a wide direct bandgap and chemical and thermal stability. ZnS can be grown as long belt-like structures, making it potentially useful as a nanoscale component in electronic devices. Since the properties of nanoscale materials typically differ from those of their bulk counterparts, a fundamental understanding of the structure of the ZnS nanostructures is essential, particularly since they contain significant numbers of planar defects. Commercial samples of GaN also contain large numbers of planar defects which are not well understood. The present study will discuss similar defects in the two materials.

1. INTRODUCTION

The unique properties of compound semiconductors make them an attractive area of research and desirable for many diverse applications. ZnS, a II-IV semiconductor, is used in flat-panel displays, solar cells and other optoelectronic devices. Recently nanostructures of ZnS have gained particular interest as potential components in electronic devices as discussed by Gupta (1999) and Park (2002) because they can be easily grown into long belt-like structures. The III-V semiconductor GaN can enable the coherent fabrication of heterostructures with (Ga,Al)N for blue-light emitting devices, as described by Nakamura (1997), but lattice defects in this material are still not well understood. This study investigates the different types of defects that are found in both ZnS and GaN.

2. EXPERIMENTAL

The ZnS nanostructures were produced by a vapour-liquid-solid (VLS) growth technique and deposited onto carbon support films for investigation. The polycrystalline GaN films were deposited on sapphire substrates by hydride vapour-phase epitaxy (HVPE). Plan-view TEM samples were prepared using traditional dimpling and ion-milling techniques. The planar defects have been analyzed by a combination of bright field (BF), dark field (DF) and high-resolution (HR) imaging techniques with selected-area diffraction (SAD). Diffraction contrast imaging was carried out on a FEI Tecnai T12 operating at 120kV; the lower voltage optimizes the accuracy of diffraction-contrast studies. The HR imaging was performed on an FEI Tecnai G2 F30 operating at 300kV. The HR imaging of the planar defects in the ZnS samples was accomplished using the C_S-corrected Philips CM200 FEG ST in Jülich, Germany.

3. RESULTS

3.1 ZnS Nanostructures

The particles are long, broad bands which are frequently quite bent and which typically exhibit one of two geometries. As illustrated in Fig. 1, they are usually flat along one edge with the other edge either flat (like a ribbon) or faceted (like a saw). In both cases the nanoparticles are wurtzite structure,

in contrast to the bulk form which is normally zinc blende. The (0001) plane in the nanosaws is parallel to the long, flat edge, and in the ribbons is perpendicular to it. The SAD pattern in Fig. 1 shows the relative orientation of the two particles.

The orientation of the particle growth gives interesting insight into the growth mechanism. The shape of the saw particle can be explained by a two-step growth process described previously by Wang (2003). First there is fast growth along the $[10\bar{1}0]$ to form the wurtzite body. This forms polar surfaces; the S-terminated edge is inert while the Zn-terminated edge is active, initiating self-catalyzed growth perpendicular to the body. Small islands nucleate along the (0001) Zn-terminated edge and grow to form teeth. This is illustrated in two ways. First, the particles without facets tend to have the (0001) perpendicular to that of the saw, as shown in Fig. 1, so there is no active surface to nucleate teeth. Second, a boundary typically forms between adjacent teeth that originate at the edge of the body as shown in Fig. 2. The body of the particle, at the bottom of the image, is a perfect crystal until the base of the teeth. The tooth on the right grew as a continuation of the perfect crystal from the body. The tooth on the left grew with a stacking fault at this interface. When the two teeth formed the vertical interface, the stacking fault faceted from the (0001) to the $(11\bar{2}0)$, leading to a c/2 translation.

Both the saws and ribbons contain numerous planar defects. In the saws the defects run along both the entire length of the saw in the body of the particle and across the teeth. High resolution imaging confirms that the body of the saw is wurtzite structure and the teeth, after a series of planar defects, are zinc blende as shown in Fig. 3.

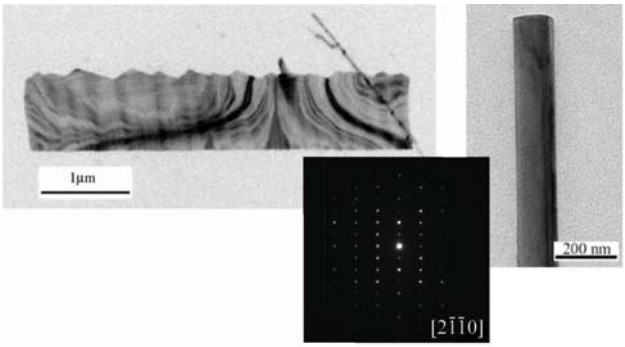


Fig. 1: BF images of two ZnS nanoparticles with the SAD pattern showing the relative orientation of the two particles.

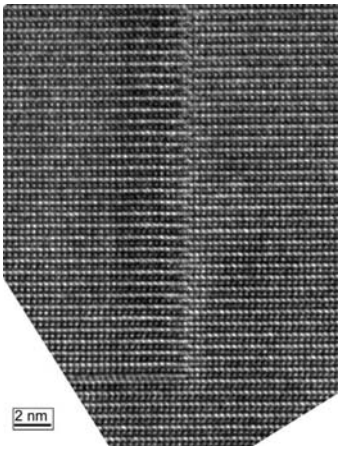


Fig. 2: HR image showing the interface between two teeth. The perfect wurtzite crystal is visible at the bottom of the image.

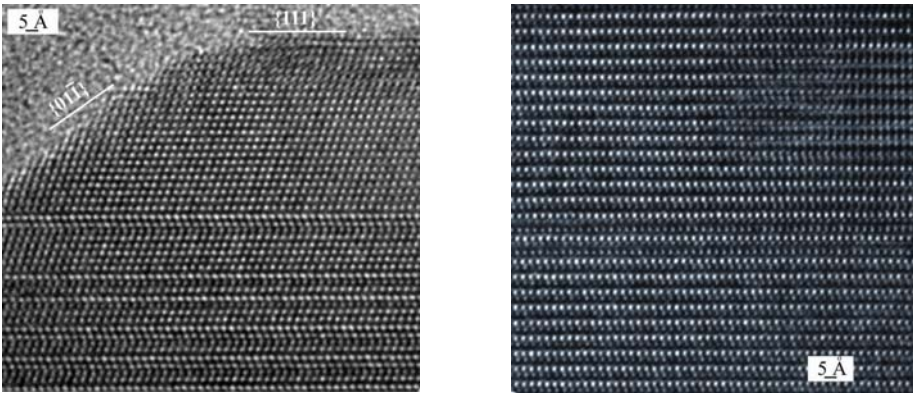


Fig. 3: HR images showing planar defects in the teeth (left) and across the length of the saw (right). The body of the saw is clearly wurtzite while the tooth is zinc blende.

3.2 Defects in GaN

One of the difficulties in studying planar defects in GaN is that the density of defects is often so high that features in diffraction-contrast images of different defects overlap. There is also considerable interest in the synthesis of bulk poly- and mono-crystalline GaN where planar defects are again present but are often more suitable for detailed analysis. The present study of such defects in polycrystalline GaN seeks to quantify the structure of stacking faults, anti-phase domain boundaries (APBs; also known as inversion-domain boundaries, IBDs, Kuwano (1994), Potin et al (1999), Kioseoglou (2002)), grain boundaries, phase boundaries and the relation of these defects to dislocations.

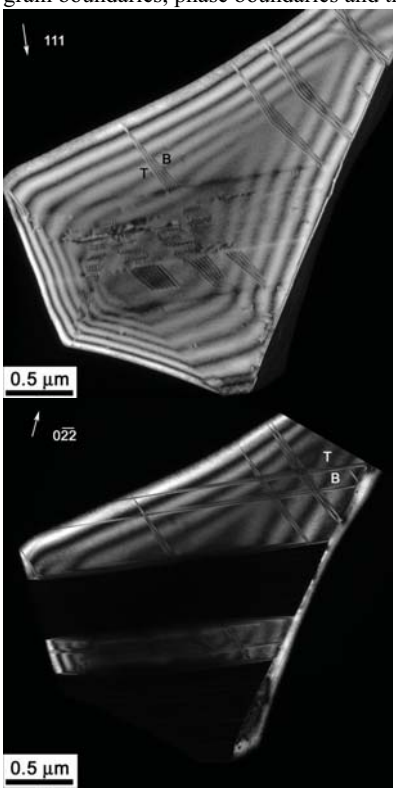


Fig. 4(top): DF image using the common 111/0001 reflection

Fig. 5(bottom): DF using the 0$\bar{2}\bar{2}$ reflection for the cubic grain

Phase boundaries in this report are illustrated by the boundary between the two polymorphs of the GaN structure, namely the cubic fcc (zinc blende) structure and the hexagonal (wurzite) structure. Figure 4 actually shows three different grain orientations. The area has been imaged using CDF conditions (CDF: centered DF images). The large cubic grain which are in contrast in both images contains the well defined stacking faults. Top/bottom (TB) contrast has been used to characterize the planar defects. This analysis showed that both intrinsic and extrinsic stacking faults are present. Comparison of the two images in this Figure shows that the center wurzite structure layer (appearing as a dark band in Figure 5) has actually cut through the stacking fault labeled TB in Figure 4. This observation shows that the cubic grain formed during growth but that before the sample was imaged in the TEM, parts of it had already begun to transform to the hexagonal phase. There are interesting segments of the original stacking faults remaining as dislocations in the new wurzite-structured material. These features will be discussed elsewhere (Carter et al 2005).

The structure of APBs in wurzite-structure materials is also unusual and has been the subject of some debate. In particular, this study has considered implications of the faceting of these interfaces and their relationship to APBs in AlN (McKernan et al 1990) and in materials such as GaAs and GaP, which have the related zinc blende structure (McKernan et al 1991, Cho et al 1985, 2001, Cohen et al 2002, Carter et al 2005). The image shown in Fig. 6 illustrates the faceting of an APB. One facet is parallel to (0001) while the other, which is also inclined to the beam in this figure, is consistent with being parallel to a $\{10\bar{1}1\}$ plane. Faceting parallel to $\{10\bar{1}1\}$ has been reported recently by Iwamoto et al (2003). It is noted that this is plane is the same as that which is seen when GaN pyramids grow on masked substrates (Yang et al 1999). The more common facet plane, which was also reported by Iwamoto et al, is the $\{10\bar{1}1\}$ prismatic plane. The two diagrams shown in Fig. 7 illustrate two interesting features that become clearer when the three-dimensional nature of inversion domains is considered. (The full details of these structures will be reported elsewhere (Carter et al 2005).) The first case shows how a pair of inclined $\{10\bar{1}1\}$ APB facets can terminate an inversion domain with only one type of anti-site bond being involved; it is suggested that this might be likely as a method for avoiding N-N antisite bonding. The second case illustrates a complexity which is introduced when an APB which lies on the $\{10\bar{1}1\}$ and has a c/2 rigid-body translation, facets onto another plane, such as the (0001) plane. The translation parallel to the boundary causes a closure failure at the junction (emphasized here by not closing

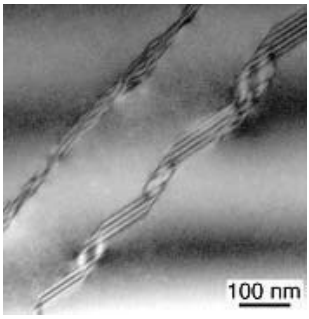


Fig. 6: Faceted ABP

the Volterra cuts); these closure failures can be accommodated by a pair of partial (interfacial) dislocations. Incidentally, this figure also shows that, if an inversion domain is enclosed by two parallel (0001) facets, then these parallel APB facets must include opposite anti-site bonds if both facets lie on the glide (as opposed to shuffle) plane. Similar dislocations occur at junctions in other APBs and on faceting twin boundaries that have associated rigid-body translations.

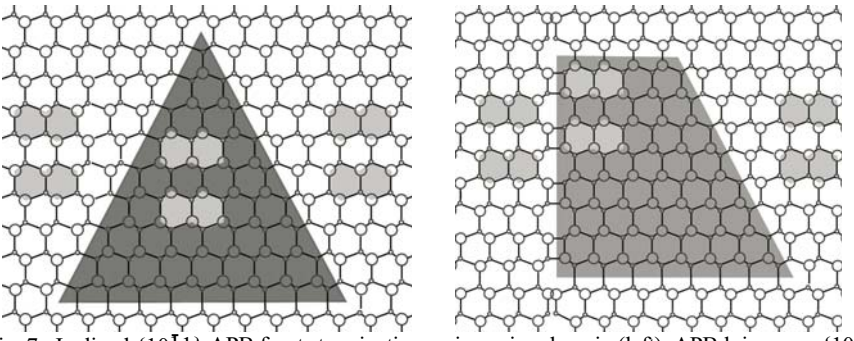


Fig. 7: Inclined {10$\bar{1}$1} APB facets terminating an inversion domain (left). APB lying on a {10$\bar{1}$1} with a c/2 translation (right). Small and large circles represent the Ga and N, respectively.

4. CONCLUSIONS

The compound semiconductors ZnS and GaN both have unique defect structures. This study demonstrates the use of a combination of techniques, including bright field, dark field and high-resolution imaging along with selected-area diffraction, which can be used to fully characterize the defects.

ACKNOWLEDGEMENTS

The GaN research was funded by the NSF through grant number NSF-DMR-0102327. JD, SK, CRP and CBC also acknowledge support from the 3M Heltzer Endowed Chair. We gratefully acknowledge Dr. Subhadra Chaudhuri of the Indian Association for the Cultivation of Science for the provision of the nanostructures used. The authors also thank Dr. Markus Lentzen and Prof. Knut Urban, Research Center Jülich, for access to the aberration-corrected HRTEM. We would also like to thank Nicole Munoz and Dr. Biswapriya Deb for many helpful discussions.

REFERENCES

Carter C B, Kumar S. and Basu J 2005 in preparation.
Cho N-H and Carter C B 2001 J. Mater. Sci. **36**, 4209
Cho N-H, De Cooman B C, Carter C B, Fletcher R and Wagner D K 1985 Appl. Phys. Lett. **47** (8), 879
Cohen D and Carter C B 2002 J. Microsc. **208**, 84
Gupta S, McClure J C and Singh V P 1999 Thin Solid Films **299**, 22
Iwamoto C, Shen X Q, Okumura H, Matsuhata H and Ikuhara Y 2003 J. Appl. Phys. **93**(6), 3264
Kioseoglou J, Dimitrakopulos G P, Polatoglou H M, Lymperakis L, Nouet G and Komninou Ph 2002 Diamond & Rel. Mater. **11**, 905
Kuwano N, et al 1994 Jpn J. Appl. Phys. **33**(Part 1, No 1A), 18
McKernan S and Carter C B 1990 Mater. Res. Soc. Proc. **167**, 259
McKernan S, Rasmussen D R and Carter C B 1991 Inst. Phys. Conf. Ser. **117** (3), 139
Nakamura S and Fasol G 1997 The Blue Laser Diode: GaN Based Light Emitters and Lasers
Park W, King J S, Neff C W, Liddell C and Summers C J 2002 Phys. Stat. Sol. **2**, 949
Potin V, Nouet G and Ruterana P 1999 Phil. Mag. A **12**, 2899
Wang Z L, Kong X Y and Zuo J M 2003 Phys. Rev. Lett. **91**, 185502
Yang W, McPherson S, Mao Z, McKernan S and Carter C B 1999 J. Crystal Growth **204**, 270

Part II

Epitaxy: Silicon-Germanium Alloys

Use of moire fringe patterns to map relaxation in SiGe on insulator structures fabricated on SIMOX substrates

A Domenicucci, S Bedell[1], R Roy[2], D K Sadana[1] and A Mocuta

IBM STG 2070 Route 52 Hopewell Jct, NY 12533, USA
[1] IBM STG 1101 Kitchawan Road Route 134 Yorktown Heights NY 10598, USA
[2] Pillsbury, Winthrop, Shaw and Pittman LLP, 1650 Tysons Boulevard, McClean VA 22102-4859, USA

ABSTRACT: Strain engineering has become extremely important in the semiconductor industry as a means of achieving device performance enhancement as device scaling runs out of steam. It is important to detect strain as a function of position in device sized areas in order to assess the viability of different process schemes. In the present work, Moire fringe patterns were used to measure and map the relaxation effects in SiGe and Si/SiGe structures fabricated on SIMOX substrates. Initially, measurements of the strain state using the Moire technique were correlated with those obtained by x-ray diffraction for blanket SiGe on insulator films over the range 0.2-0.8%. Using this correlation as a basis, several interesting relaxation characteristics were found on patterned structures. Evidence of a rhombohedral relaxation was seen for rectangular SiGe mesas fabricated by patterning and then homogenizing SiGe/Si bilayers on SIMOX substrates. The magnitude of the relaxation was found to depend of the size of the structure and the distance to the nearest edge. Elastic relaxation of Si lines was also seen. Lastly, evidence of non uniform relaxation was seen in the SiGe template in wide channel areas of silicide-contacted device structures.

1. INTRODUCTION

In recent years, strained Si on insulator MOSFETs have been proposed as a means to meet the requirements of higher drive currents and lower operating voltage. Several approaches involving SGOI substrates have been used to fabricate the strained Si/relaxed SiGe mesas needed for device fabrication. One approach involves the use of relaxed SiGe on insulator (SGOI) substrates fabricated by applying the separation by implanted oxygen (SIMOX) technology to SiGe layers grown on Si substrates (Takagi 2001). In a second approach, the SGOI substrate is formed by oxidizing a SiGe/Si on insulator structure, the so-called Thermally Mixed-SGOI or TM-SGOI process (Mizuno 2002). A third approach uses a wafer bonding technique to fabricate Si/SiGe mesas (Yin 2002). Building CMOS devices using any of the aforementioned substrates involves patterning the substrate and subsequent processes which involve heat treatments. Such processes are likely to cause additional relaxation effects which will change the stress state of the device structures and hence change the designed device enhancement. It is important to determine the magnitude and spatial extent of these relaxation effects so that various process integration schemes can be evaluated. Previously, Raman spectrometry, micro–x-ray diffraction, and nanobeam electron diffraction have been used for such characterization (Yin 2002). In this paper, Moire fringe patterns formed in a TEM are used to map relaxation effects in SGOI structures fabricated from SIMOX SOI substrates using the TM-SGOI process.

2. MEASUREMENT OF RELAXATION IN TM-SGOI SUBSTRATES : MOIRE VS X-RAY DIFFRACTION

2.1 The TM-SGOI Process Using SIMOX Starting Substrates

The TM-SGOI process is shown pictorially in Fig. 1. A Si-Ge layer (Ge between 15-20%) is epitaxially grown on a previously fabricated SIMOX substrate whose Si thickness is between 30 and 145 nm. The SiGe layer is pseudomorphic with respect to the superficial Si of the SIMOX substrate and is therefore compressively strained. This structure is subjected to a high temperature oxidation/anneal either as a blanket layer or after photolithographic patterning, during which the Ge is rejected from the growing oxide and diffuses (is mixed) into the Si layer below. The resulting structure has a SiGe layer which is relaxed or partially relaxed. In addition the SiGe layer has the same crystal orientation as the Si below the buried oxide. This orientation relationship is important for the interpretation of the Moire fringe patterns discussed below.

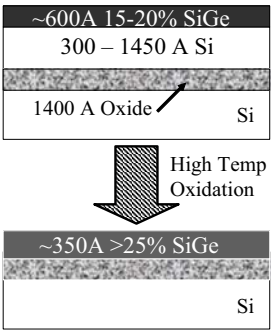


Fig. 1. TM-SGOI process.

2.2 Measurement of Relaxation in SGOI Substrates Fabricated From SIMOX SOI Using Moire Fringes

TM-SGOI substrates were fabricated with varying Ge concentrations and hence varying relaxations. The resultant relaxation in each substrate was characterized using standard x-ray diffraction (XRD) techniques (Segmuller 1989). Plan view TEM samples were then prepared using a previously described "dimple and etch technique" (Domenicucci 1998). Moire fringe patterns (Hirsch 1965) were recorded in an FEI Tecnai T20 TEM both in areas where Si remained below the buried oxide (BOX) and where Si was removed. In areas where Si remained below the BOX, a Moire pattern was formed by double diffraction (Fig. 2). In areas where the Si was removed, the resulting contrast would be governed by the number and relationship of the overlayers. When Moire patterns were observed, they were of a translational nature, since the SiGe lattice (001) direction was aligned with that of the underlying Si .substrate. In this case, the Moire fringe spacing, Λ, is given by

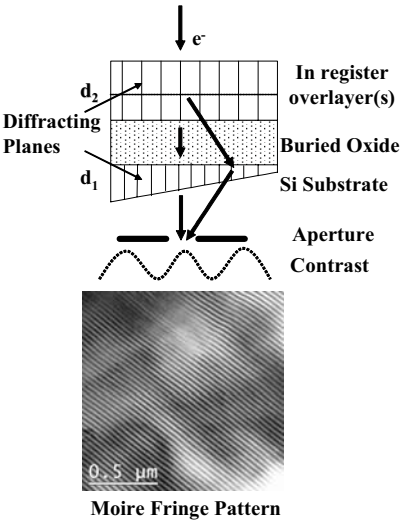


Fig. 2. Moire fringe formation.

$$\Lambda = \frac{dSiGe \times dSi}{dSi + dSiGe}$$

, where dSiGe and dSi are the d-spacings for SiGe and Si which correspond to the reflection chosen for imaging (Hirsch 1965). Fig. 3 shows the percent d-spacing difference as derived from Moire pattern fringe spacing plotted against that determined from XRD. Excellent agreement is seen. The graph indicates that Moire fringes can be used as a ruler to examine d-spacing, and hence relaxation, in TMSGOI layers, using the Si substrate as a reference crystal.

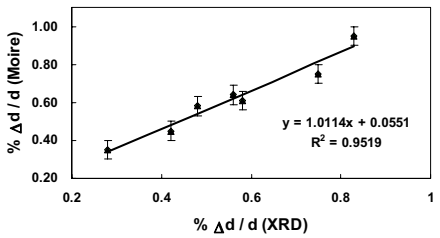


Fig. 3. Percent d-spacing difference – from Moire vs from X-ray diffraction.

3. RELAXATION IN RECTANGULAR vs SQUARE SiGe MESAS FORMED BY PATTERNING AND MIXING

Rectangular and square SiGe mesas (18 atomic % Ge) were formed by patterning and mixing SiGe bilayers. Moire analysis was performed on 11μm x 50μm, 4μm x 15μm, 6μm x 6μm, and 4μm x 4μm structures. Figure 4 shows Moire fringes formed using <220> reflections from the center of the 4μm x 15μm rectangle. The fringes for planes parallel to the long dimension of the rectangle have a wider spacing than for those from planes perpendicular to the long dimension indicating that the film relaxed asymmetrically. An examination of the relationship of the (220) and (-220) planes with respect to the Si diamond cubic lattice indicates that the relaxation is rhombohedral in nature (Fig. 5). Table 1 gives the results typical for the structures examined. The relaxation in the centre of a particular structure depends on the size and shape of the feature – asymmetric (rhombohedral) for the rectangles and symmetric for the squares. No evidence of misfit dislocations was seen in any of the structures. These relaxation phenomena are consistent with the elastic relaxation reported for SiGe islands bonded onto compliant substrates (Yin 2002).

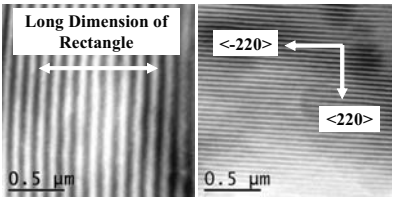


Fig. 4. <220> Moire fringes in the center of a 4③m x 15③m rectangle.

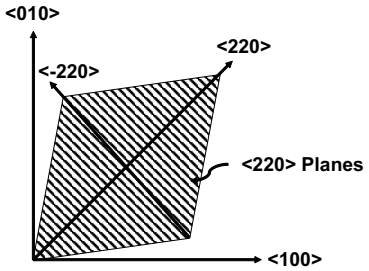


Fig. 5. D spacing difference in (220) planes giving rhombohedral distortion.

4. ELASTIC RELAXATION OF Si LINES ON TM-SGOI SUBSTRATES

200nm wide Si lines aligned along the <110> direction were patterned from pseudomorphic Si – TM-SGOI bilayers (Fig. 6). Moire fringe images were taken of the line structures with Si remaining below the buried oxide layer and with the Si removed. Both <220> and <-220> reflections were used so that fringes were recorded for planes parallel and perpendicular to the long dimension of the lines. Fig. 7 shows typical Moire patterns obtained. With Si below the buried oxide (Fig 7(a)&(b)), fringes were well formed in both lines (L) and spaces (S) for planes perpendicular to the long dimension of the lines. For planes parallel to the long dimension of the lines, the Moire patterns were disrupted in the lines, but well formed in the spaces. With the Si removed below the BOX (Fig. 7(c)&(d)), fringes were seen only for planes parallel to the long dimension of the lines and only in the areas of the lines and not in the areas of the spaces. The experimental observations indicate that the Si lines were relaxing for planes parallel to the long dimension of the lines with respect to the SiGe template layer.

Structure	% Δd/d,<220> Fringes	% Δd/d,<220> Fringes
4μm x 15μm	0.38	0.25
4μm x 4μm	0.37	0.36

Table 1. Relaxation in rectangular vs. square mesas.

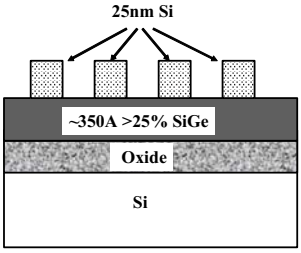


Fig. 6. Strained Si lines on an SGOI template.

5. RELAXATION IN DEVICE CHANNEL AREAS

Device structures fabricated on TM-SGOI substrates were also analyzed by the Moire fringe technique. The structures consisted of polysilicon gate MOSFETs with self aligned cobalt silicide contacts. Plan view TEM samples were prepared and samples examined in several states: 1) with Si

below the BOX and gate polysilicon partially removed, 2) with Si below the BOX and gate polysilicon removed, and 3) without Si below the BOX and gate polysilicon removed. Results showed that the Moire fringe patterns were insensitive to presence of the polysilicon gate material and that the Moire patterns were completely destroyed by the removal of the Si substrate below the BOX. This indicates that the strain state of the channel region was not greatly affected by the gate material and that the TM-SGOI / strained Si overlayer were in register. Fig. 8 gives typical results for case 2) above, the gate polysilicon removed and Si below the BOX in place. The spacing for fringes parallel to the long dimension of the channel is less than the spacing for fringes perpendicular to the channel long dimensional, indicating that the channel is in a state of rhombohedral strain.

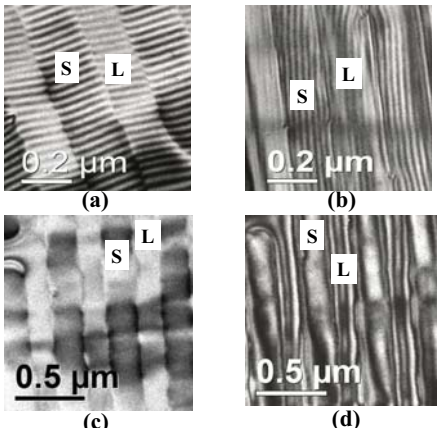


Fig. 7. Moire patterns from Si lines on TM-SGOI with (a&b) and without (c&d) Si.

6. SUMMARY

Moire patterns were shown to be a useful tool to measure and map relaxation in TM-SGOI structures. First, the amount of relaxation as determined by Moire fringe spacing was found to be in excellent agreement with that determined by XRD for blanket SGOI substrates. The two dimensional nature of the patterns was then used to measure and map several interesting relaxation phenomena. Evidence of rhombohedral relaxation was seen for both SiGe mesas formed by patterning and then mixing SiGe/SOI bilayers and in channel regions for silicided MOSFET structures fabricated on TM-SGOI substrates. Moire fringe analysis also showed that Si lines on TM-SGOI substrates relaxed elastically for planes parallel to their long dimension, but that no relaxation occurred for planes perpendicular to this dimension.

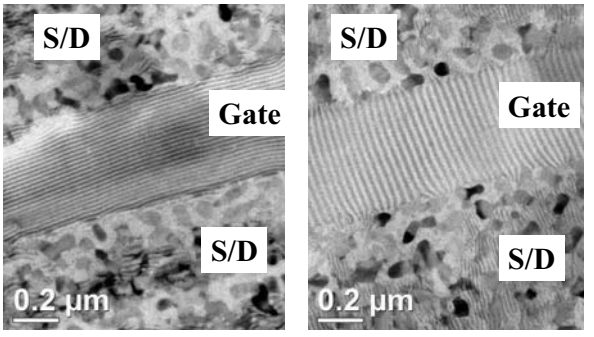


Fig. 8. Moire fringes in device channel region indicating rhombohedral strain.

REFERENCES

Domenicucci A, Cunningham B and Tsang P 1998 Mat. Res. Soc. Symp. Proc. **523,** 103

Hirsch P B, Howie A, Nicholson R B, Pashley D W and Whelan M J 1965 Electron Microscopy of Thin Crystals, 357

Mizuno T, Sugiyama N.; Tezuka T and Takagi S 2002 Appl. Phys. Lett. **80**, 601

Segmuller A, Noyan I C and Speriosu V S 1989 Prog. Crystal Growth and Char. **18** pgs 21

Takagi S, Mizuno T, Sugiyama N, Tezuka T and Kurobe A 2001 IEICE Trans. Electron. **E84 C**, 1043

Usuda K, Minuno T, Tezuka T, Sugiyama N, Moriyama Y, Nakaharai S and Takagi S 2004 Appl. Surf. Sci. **224** 113

Yin H, Huang R, Hobart K D, Suo Z, Kuan T S, Inoki C K, Shieh S R, Duffy T S, Kub F J and Sturm J C, 2002 J. Appl. Phys. **91**,9716

TEM measurement of the epitaxial stress of Si/SiGe lamellae prepared by FIB

M Cabié, G Benassayag, A Rocher, A Ponchet, J M Hartmann[1] and F Fournel[1]

CEMES-CNRS, BP 94347, 31055 Toulouse Cedex 4, France
[1] CEA-DRT – LETI/DTS – CEA/GRE, 38054 Grenoble Cedex 9, France

ABSTRACT: The misfit stress between an epilayer and its substrate can be determined, via the Stoney formula, from the sample curvature generated by the relaxation of this stress. This curvature method has been transposed to transmission electron microscopy. The Stoney model assumes the observed zones present particular dimensions and geometry. Finite element calculations have shown that narrow rectangular lamellae cut by focused ion beam comply well with the criteria of the model. This technique has been applied to analyse a Si/SiGe(001) structure.

1. INTRODUCTION

A useful method of stress measurement in semiconductor layers is the curvature method based on the curvature generated to relax the stress in the layer. A relationship between the radius of curvature R and the stress has been established by Stoney (1909) in the particular case of uniaxial stress. This model has been extended to biaxial stress by Townsend and Barnett (1987); the resulting analytical formula is given below:

$$\sigma_0 = \frac{E_s}{6\left(1-\nu_s\right)} \frac{h_s^2}{h_l R} \qquad (1)$$

where h_s and h_l are respectively the thickness of the substrate and the layer, E_s and ν_s the Young modulus and the Poisson ratio of the substrate, and σ_0 the in-plane component of the epitaxial stress. Generally this curvature is measured by laser beam reflection or by X ray diffraction. We have adapted this method to transmission electron microscopy (TEM). We show in this article that in spite of the peculiarities of the samples thinned for TEM observation, the Stoney model is still valid. This is illustrated by the experimental results obtained on a Si/SiGe strained structure. Attention is focused on the influence of large and small deformations on the curvature of the thinned areas observed by TEM. In this context, finite element calculations have been carried out to check in which mechanical conditions the model can be used. This analysis has led to the determination of a criterion regarding the size of the observed zones.

2. PECULIARITIES OF THE TEM SAMPLES

To be observed by TEM, the specimens are prepared as plan view by thinning the substrate. Fig. 1 shows a typical scanning electron microscopy image of the centre of a thinned sample. It appears clearly that the sample is highly bent as the edges of the hole (i.e. the thinnest parts) have rolled. This amplification of the curvature with a low ratio h_s/h_l is in accordance with the Stoney model where R varies linearly with (h_s^2/h_l). Due to the thinning, the thickness increases when we move away from the edges of the hole. The sample has also cleaved spontaneously, during the thinning, along two main perpendicular directions corresponding to the <110> crystallographic directions.

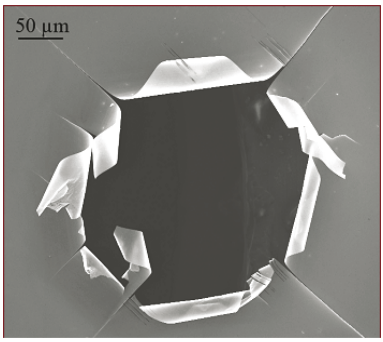


Fig. 1: Typical SEM image of the center of the TEM thinned sample showing the bending of the thin areas.

3. PRINCIPLE OF THE TEM METHOD

As mentioned above the stress can be determined from the Stoney relationship between the curvature and the substrate thickness. In the particular case of thinned samples, the thickness of the sample varies with the distance from the edges of the hole. The measurements of both the curvature and the sample thickness use bend contours under conventional imaging in plan view geometry. We have shown that the radius of curvature R is linearly related to the distance between the –g and +g bend contours in bright field image. The thickness of the sample is determined in the same area from the variations of the diffracted intensity with the Bragg deviation in dark field image. The substrate thickness is then deduced by removing the layer thickness measured on a cross-sectional specimen. More details of the method are described elsewhere by Ponchet et al (2004).

4. PRESENTATION OF THE STUDIED STRUCTURE

The investigated structure is a 16 nm tensile-strained Si layer grown by reduced pressure chemical vapour deposition on a pseudo substrate. This pseudo substrate consists of a 1.6 µm $Si_{0.8}Ge_{0.2}$ layer grown on top of a graded SiGe buffer layer itself deposited on a (001) Si substrate (Hartmann et al 2004). It is expected to be nearly completely relaxed. The nominal misfit between the silicon layer and the $Si_{0.8}Ge_{0.2}$ pseudo substrate calculated using the relationship given by Dismukes et al (1964) is –0.76%.

The observation of a TEM plan view specimen has revealed the presence of some misfit dislocations at the t-Si/SiGe interface. The nucleation of these dislocations is due to the presence in the SiGe pseudo substrate of threading dislocations emerging from the graded buffer layer. The density of these misfit dislocations is about 10^4 cm^{-1}. This value is too low to induce a significant relaxation of the stress inside the tensile-strained Si layer, as a full relaxation would correspond to a density of about 10^6 cm^1.

5. EXPERIMENTAL RESULTS OF TEM CURVATURE MEASUREMENTS

The curvature is measured along rectangular lamellae (Fig. 2) obtained spontaneously by cleavage during the thinning process or cut by focused ion beam (FIB) milling after the thinning. The (440) (respectively $(4\bar{4}0)$) bend contours allow us to measure the curvature R_y (respectively R_x) along the direction x (respectively y) of the lamella. R_x can also be measured along the x direction by displacing the [001] zone axis. R_x and R_y are the radii of curvature of a line initially parallel to the direction x, respectively y. The couples of experimental data (R,h_s) (reported in Fig. 3) measured at different positions on several lamellae are fitted by a curve verifying the Stoney relation (1), the only adjustable parameter being the epitaxial stress σ_0. It is worth noting that when the ratio h_s/h_l is small (as happens for our thinned samples), the Stoney relation (1) has to be corrected by a factor depending on the thickness and the elastic constants of both the substrate and the layer (Freund et al 1999). The experimental value of the stress determined for this sample is equal to 1.03±0.12GPa.

Some results (corresponding to the open circles in Fig. 3) have not been considered for the fit. We explain why in the following section.

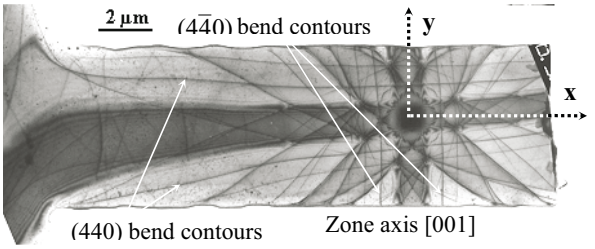


Fig. 2: TEM bright field image of a lamella cut by FIB, obtained for an orientation of the electron beam parallel to the [001] zone axis. The bend contours appear as dark lines. The axes x and y correspond respectively to the [1 $\bar{1}$ 0] and [110] crystallographic directions. The lamella is fixed to the rest of the sample by one side (at the left of the image).

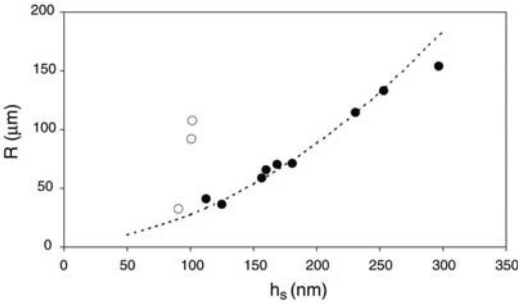


Fig. 3: Radius of curvature as a function of the substrate thickness. Dashed line: best fit of the experimental values (full circles). Open circles: experimental values that not comply with the condition of small deformations.

6. MECHANICAL CRITERIA OF VALIDITY OF THE MODEL

The Stoney formula (1) is valid for small deformations only, which means that the bow must be significantly smaller than the sample thickness. When this condition is not satisfied, the relationship between the curvature and the stress is no longer linear. This behaviour is generally encountered with large wafers where the dimensions are very large with regard to the thickness. Freund et al (1999), for example, have done finite element calculations to simulate the curvature of circular plates of radius ρ. They compare the variations of a normalised curvature K as a function of a normalised stress S, such as the equality between K and S is equivalent to the Stoney formula (1), where:

$$K = \frac{\rho^2}{4\,R\,h_s} \quad \text{and} \quad S = \frac{3}{2}\,\frac{(1-\nu_s)}{E_s}\,\frac{\sigma_0 \rho^2 h_f}{h_s^3} \tag{2}$$

They show that for small S the relationship between K and S is linear. It is the linear regime of small deformations where the curvature is isotropic and uniform, and where the Stoney model is valid. For large S, the calculated curvature is smaller than the curvature predicted by the Stoney model. This curvature becomes non uniform over the whole plate, the center of the plate being less bent than the edges. This is the regime of large deformations where the relationship between K and S is no longer linear.

To simulate the curvature of the lamellae observed by TEM, we have calculated the curvature of a rectangular plate presenting a ratio between the length and the width equal to 2 (Cabié et al 2005). The results are reported in Fig. 4 by using the same normalisation as Freund where the dimension parameter ρ has been replaced by the half width of the rectangular plate. We have observed the same non uniformity of the curvature for large S. In addition, an asymmetry appears between the curvature of the two main axes of the lamella: the curvature K_x calculated at the centre of the rectangular plate is similar to the curvature calculated at the centre of a circular plate, while the curvature K_y is smaller. According to this analysis, we have considered that the hypothesis of small deformations is verified for S smaller than 0.15. Indeed, the difference between K_x or K_y and S is then less than 4%, i.e. negligible with regard to the experimental error. This condition on S imposes a condition on the width of the plate.

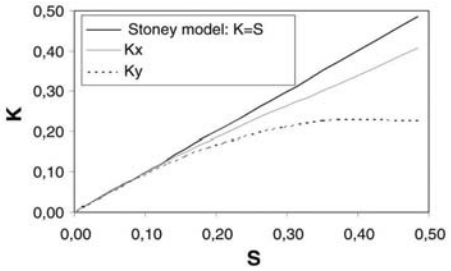


Fig. 4: Normalised curvature K versus normalised stress S. Stoney model (in bold); curvature K_x (K_y) of the large (small) axis of the plate calculated at the centre of a rectangular plate.

The experimental results of Fig. 3 have been reported in the normalised units S and K (Fig. 5). The full circles are in the linear regime as they verify S<0.15, while the open circles are in the non linear regime of large deformations. These data, which would have led to an underestimation of the stress, have not been selected for the fit. For example, the curvature of the points labelled 1 and 2 in Fig. 5, has been measured for a similar thickness of 110 nm, for two lamellae of different widths equal to 2.8 µm and 4.1 µm respectively. The curvature of the points labelled 3 and 4 has been measured for two different lamellae of the same width of 2.8 µm but at different substrate thicknesses of 125 nm and 100 nm respectively. These comparisons illustrate the fact that the condition of small deformations depends on both the lamella width and the local substrate thickness for a given sample (i.e. for a given stress and a layer thickness).

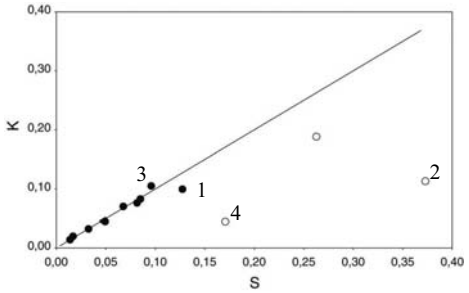


Fig. 5: Normalised curvature K versus normalised stress S. Line in bold: Stoney model. Full circles: experimental values verifying the condition of small deformations. Open circles: experimental values in the regime of large deformations.

7. CONCLUSION

The TEM curvature method is well adapted to epitaxial stress measurements. The in-plane component of the stress measured on a 16 nm tensile-strained Si layer grown on top of a $Si_{0.8}Ge_{0.2}$ virtual substrate is equal to 1.03±0.12 GPa, i.e. quite close to the expected value of 1.37 GPa. The conditions of validity of the model have been verified for the particular characteristics of the TEM lamellae when the size of these lamellae does not exceed critical values insuring the linearity between the curvature and the stress. In order to well control the geometry and the dimensions of such lamellae, particularly for materials which do not cleave easily like Si, we have developed a process to cut these lamellae by FIB. A similar analysis was performed on a GaInAs/GaAs structure (Cabié et al 2005).

REFERENCES

Cabié M, Ponchet A, Rocher A, Durand L and Altibelli A 2005 Appl. Phys. Lett. *in press*
Dismukes J P, Ekstrom L and Paff R J 1964 J. Phys. Chem. **68**, 3021
Freund L B, Floro J A and Chason E 1999 Appl. Phys. Lett. **74**, 1987
Hartmann J M, Bogumilowicz Y, Holliger P, Laugier F, Truche R, Rolland, Séméria M N, Renard V, Olshanetsky E B, Estibals O, Kvon Z D and Portal J C 2004 Semicond. Sci. Technol. **19**, 311
Ponchet A, Cabié M and Rocher A 2004 Eur. Phys. J. Appl. Phys. **26**, 87
Stoney G G 1909 Proc. R. Soc. London Ser. A **82**, 172
Townsend P H and Barnett D M 1987 J. Appl. Phys. **62**, 4438

Strain relaxation of SiGe/Si heterostructures by helium ion implantation and subsequent annealing: Helium precipitates acting as dislocation sources

Norbert Hueging, Martina Luysberg, Knut Urban, Dan Buca[1], Bernd Hollaender[1], Siegfried Mantl[1], Matcio J Morschbacher[2], Paulo F P Fichtner[2]; Roger Loo[3] and Matty Caymax[3]

Institute of Solid State Research, Research Center Juelich and Center of Nanoelectronic Systems for Information Technology, Juelich, Germany
[1] Institute of Thin Films and Interfaces, Research Center Juelich Center of Nanoelectronic Systems for Information Technology, Juelich, Germany
[2] University Federal do Rio Grande do Sul, Porto Alegre, Brazil
[3] IMEC, Leuven, Belgium

ABSTRACT: The strain relaxation process of pseudomorphic SiGe/Si(100) heterostructures has been investigated by ex-situ and in-situ transmission electron microscopy, Rutherford backscattering spectroscopy and ion channelling. SiGe layers with Ge contents between 19 and 27 at% were implanted with doses of 0.7 - 1.5x10^{15} He/cm^{-2} and annealed at temperatures from 200°C up to 950°C. Helium precipitates in overpressurised, platelet shaped volume defects underneath the heterostructure interface during low annealing temperatures of 400°C. The precipitates decay into arrangements of a larger central precipitate surrounded by a ring system of smaller bubbles. At higher temperatures a transformation from platelet-like to a spherical bubble is observed and for temperatures above 800°C coalescence of entire bubbles is found in in-situ TEM heating experiments. Particular emphasis is placed on the onset of the strain relaxation process which occurs after thermal treatment around 600°C. The processes involved are verified by in-situ experiments. The nucleation of dislocation loops at the helium filled precipitates, their enlargement and the formation of misfit dislocation segments elongating via the movement of threading dislocation segments are observed. Thus, helium precipitates are unambiguously identified as dislocation sources and, therefore, promote the strain relaxation of epitaxial SiGe layers.

1. INTRODUCTION

Strain engineering promises a fundamental advancement of the electronic properties of silicon to improve the performance of nanoelectronic devices without further scaling. Indeed, large enhancements of charge carrier mobilities due to strain in silicon is reported (Armstrong and Maiti 1998) and can be realised by using strain relaxed $Si_{1-x}Ge_x$/Si heterostructures which serves as virtual substrates.

H or He implantation and subsequent annealing has proven to be an effective strain relaxation process. Using this method good quality and highly relaxed SiGe films with thicknesses of 100-200 nm and Ge contents of up to 30 % can be produced (Mantl et al 1999, Holländer et al 2001, Luysberg et al 2002, Cai et al 2004). The detailed relaxation mechanism, however, is still under debate. One mechanism proposes the relaxation of the layer solely by dislocation glide and was verified by simulations (Schwarz 2003). The source of the dislocations is not further assessed. As a starting point dislocation loops are assumed to appear within the epilayer. A second model suggests dislocation loops nucleating at the overpressurised precipitates underneath the SiGe/Si interface (Trinkaus et al 2000). These loops glide to the interface, where one part of the loop is pinned forming a misfit segment. The other laces up to the free surface and vanishes. The two remaining threading dislocation segments (TDs) move apart and elongate the misfit segment releasing elastic strain in the epilayer. While in the former concept a very small number of TDs move over large distances, the latter model predicts a high number

of TDs, moving shorter distances and annihilating by interaction with other TDs of opposite Burgers vector. The annihilation radius enlarges with the ability of the dislocations to climb.

Quantitative pressure measurements at helium filled precipitates in silicon revealed that the shear stress reaches the critical value for dislocation formation (Hueging et al 2003, Tillmann et al 2004). This suggests that dislocation loops may nucleate at helium precipitates. Alternatively, strain relaxation using Si ion implantation (Hollaender et al 2004) suggests that point defects created by the implantation may act as a source of dislocations to promote strain relaxation.

In order to get more detailed information about the relaxation mechanism, He implanted SiGe/Si structures are studied by Rutherford backscattering spectroscopy/ion channeling (RBS/C) and transmission electron microscopy (TEM). In-situ heating experiments in the TEM allow a direct observation of the origin of morphological changes like the nucleation and propagation of dislocations.

2. EXPERIMENT

SiGe layers with thicknesses between 100 and 200 nm, and Ge contents of 19 - 27 at%, were grown by chemical vapour deposition technique on 200 mm Si(001) substrates. The pseudomorphic structure was confirmed by strain measurements using RBS/C experiments. The wafers were implanted with He^+ ions at room temperature, 7° off the crystallographic [001] direction in order to minimize ion channelling. The He^+ ion energy was adapted to the layer thickness to achieve an implantation depth profile with its maximum at a depth corresponding to the doubled SiGe layer thickness.

For the in-situ annealing experiments pieces of 2 x 2 cm^2 were preannealed in a furnace for one minute at 420°C in order to pre-form He filled and overpressurised defects and to avoid artefacts due to thin foil effects after TEM sample preparation. Electron transparent plan view samples were prepared by standard mechanical grinding followed by Ar^+ ion milling until perforation.

The in-situ annealing experiments were done in a JEOL 4000FX TEM operated at 400 kV equipped with a GATAN-heating holder. For imaging purposes an in-column GATAN TV camera Type 673 in combination with a digital video recording system enables observations at 25 frames per second at a resolution of 720 x 576 pixels.

Additional ex-situ experiments using 150 nm $Si_{74}Ge_{26}$ heterostructures were performed to prove that the processes are not driven by thin foil effects or electron radiation. After He ion implantation the samples were annealed at temperatures up to 950°C for 10 minutes in an Ar atmosphere. The relaxation degree was measured by RBS/C and the microstructure was investigated by plan view and cross section TEM.

3. RESULTS AND DISCUSSION

In order to give an overview of the structural changes occurring during annealing we first describe the results of the ex-situ annealing series and then focus on the in-situ observations.

In the as implanted samples neither helium precipitates nor dislocations are formed and even after thermal treatment up to 350°C no changes are visible. As shown in Fig. 1a and b under dynamical (400) two beam conditions the morphology changes after annealing temperatures of 400°C. Platelet like precipitates form underneath the heterostructure interface and show similar characteristics as observed for implantation studies in pure silicon (Hueging et al 2003, Tillmann et al 2004).The platelets with typical diameters ranging from 40 nm to 120 nm are uniformly distributed below the SiGe/Si interface and dominantly show {100} habit planes with preferential orientation parallel to the wafer surface plane (001). At the start of the decay process these large platelet like precipitates are surrounded by a ring system of smaller spherical bubbles. Due to the large He pressure of up to 13 GPa (Tillmann et al 2004), the surrounding Si matrix is heavily strained and so can be easily visualised as large contrast areas under dynamical imaging conditions.

Some precipitates are decorated with dislocation loops. No misfit dislocations are observed at this point indicating no relaxation, in agreement with RBS/C measurements. This morphological stage represents the starting point of the relaxation process and is consistent with that of the in-situ samples preannealed at 420°C.

After 10 minutes annealing at 950°C as a final state, spherical bubbles remain under the heterostructure interface and show no strain induced contrast under dynamical imaging conditions. Small dislocation loops are observed underneath the interface, while a very dense misfit dislocation network appears in the interface (Fig 1c and d).

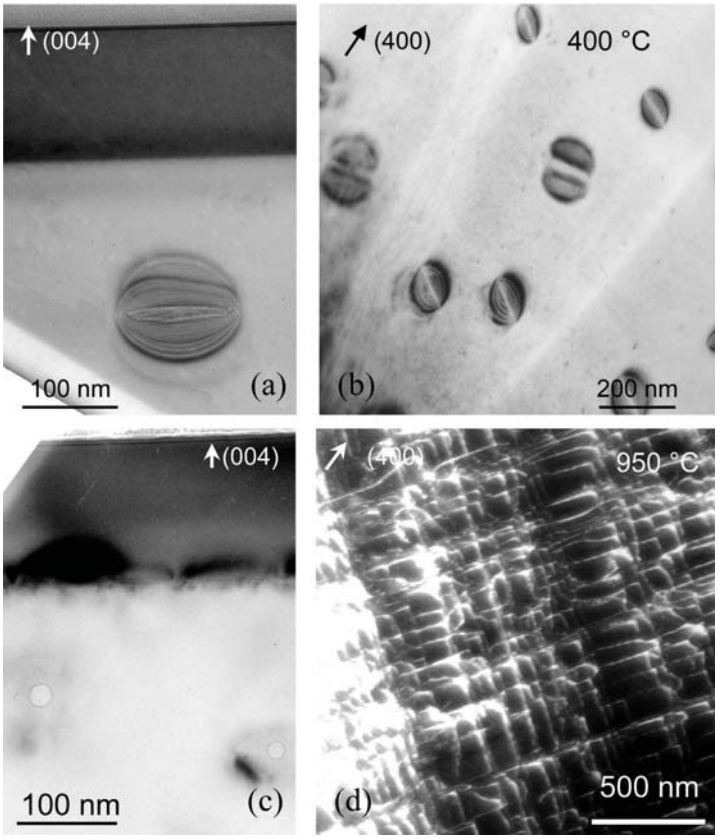


Fig. 1: Ex-situ annealed samples after 400°C treatment for 10 minutes in cross sectional (a) and plan view (b) orientation show platelet like shaped helium precipitates under high pressure, causing strain induced contrast fringes under the dynamical (400) imaging conditions chosen. This contrast disappears for the corresponding samples after 950°C treatment (c), empty spherical bubbles remain underneath the surface. A dense misfit dislocation network in the interface appears under weak beam imaging conditions at plan view samples (d).

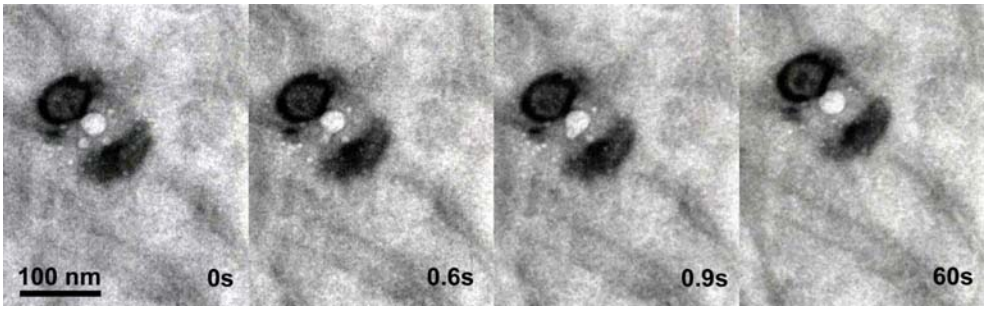


Fig. 2: Time evolution of the bubble arrangements observed in the in-situ TEM under kinematical underfocused imaging conditions at 800°C in a plan-view specimen. Coarsening of the planar bubble arrangements by coalescence takes place until mostly single bubbles remain after longer annealing times. The dark regions induced by residual dynamical diffraction effects due to the high pressure inside the precipitates decrease in size for longer annealing times.

Before the formation and movement of dislocations responsible for the strain relaxation are studied more in detail, we turn the attention to the transformation of the precipitates from platelets to single spherical voids.

During annealing the He platelets decay into planar arrangements of bubbles as reported in literature (Fichtner et al 1997, Beaufort 2000, Hueging et al 2003). Having undergone a shape transformation and outdiffusion of helium, the bubbles show a coarsening behavior upon annealing at higher temperatures, which is demonstrated by video frames obtained at 800°C (Figure 2). The bubbles show bright contrast due to the kinematical, under focused imaging conditions adjusted. A large central bubble is surrounded by smaller ones. All bubbles move in a stochastic manner during the experiment. The coalescence of two bubbles can be clearly observed. The dark contrast lobes indicate that the bubble arrangement causes strain in the surrounding Si matrix. These contrasts diminish during several minutes of annealing.

In previous investigations it could not be clarified whether the coarsening mechanism in silicon is driven by coalescence or is dominated by Ostwald ripening (Beaufort et al 2000, Raineri et al 2000, Luysberg et al 2002), where the latter would require diffusion through the bulk from small precipitates to larger ones. This investigation shows that entire bubbles can move stochastically within the bubble arrangement and finally coalesce. Therefore, surface diffusion, i.e. Si diffusion on the surface of the bubble, is the fundamental process of the movement.

In-situ annealing experiments within the electron microscope at temperatures around 600°C allow us to study the formation and movement of dislocations, since strain measurements by RBS/C indicate a relaxation process starting at this temperature regime.

The onset of strain relaxation has been visualised in Fig. 3. which shows a plan view sample in the TEM under dynamical (400) imaging conditions at a nominal temperature of 620°C, which coincides approximately with those of the ex-situ series. Four video frames taken within 2.2 seconds of observation show the overpressurised helium precipitates underneath the epilayer interface as dark contrast areas. TDs between the sample surface and the heterostructure interface are passing the observation area, leaving behind straight misfit dislocations. The decoration of a misfit dislocation by curved threading segments can clearly be seen and is marked by arrows in the second and third frames of Fig. 3.

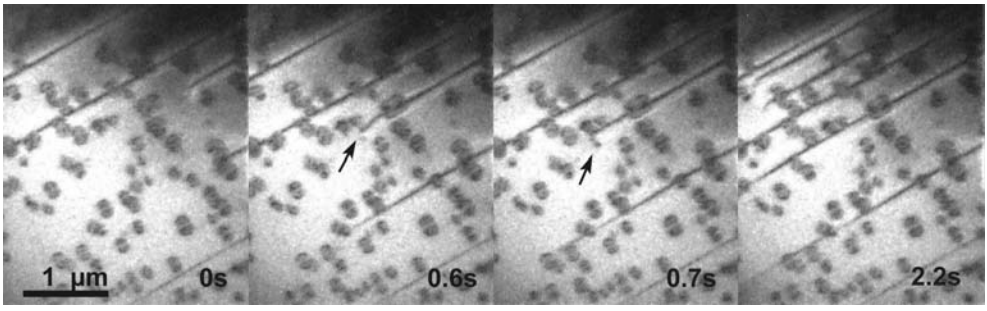


Fig. 3: Time evolution of the defect structure recorded in the TEM under dynamical [400] bright field imaging conditions at 620°C in a plan view specimen. Curved threading dislocations are moving through the SiGe layer (marked by black arrows) and leave behind straight misfit dislocations reducing the epitaxial strain.

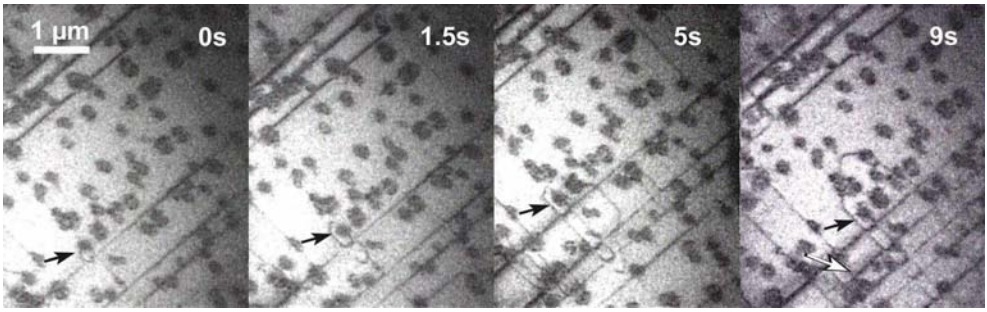


Fig. 4: Time evolution of the defect structure recorded in the TEM under dynamical [400] bright field imaging conditions at 650°C in a plan view specimen. Dislocation loops nucleate at helium filled platelets underneath the heterostructure interface (marked with black arrows) and enlarge parallel the epilayer interface for distances of several microns. Threading dislocations move more than 30 times faster through the area of observation (white arrow in last frame).

Dislocation loops nucleate at helium precipitates as presented in Fig. 4. The platelet marked with the black arrow denotes the ejection of a dislocation loop, which further enlarges as time proceeds. The enlargement of the dislocation loop in both <110> directions over several microns seems to be influenced by the strain field of the He platelets located underneath the SiGe/Si interface. The last picture of the series clearly shows that the dislocation loop bows around the underlying platelets obviously hindering its movement. This pinning due to the strain fields around the platelets is frequently observed in our experiments. During the enlargement of the loop, further TDs are passing the observed area. Their propagation speed is more than thirty times faster than the propagation of the loop segments. As discussed in more detail in Hueging et al (2005) the comparison of dislocation speeds and loop size to sample thickness leads to the interpretation of climb involved in the dislocation loop enlargement. The climb process at these low temperatures may be promoted by a supersaturation of point defects created during the helium ion implantation. As a consequence at the end of the relaxation process TDs seem to have an increased ability to climb, resulting in an enhanced annihilation radius corresponding to the description of Trinkaus et al 2000.

Dislocation loops in the crystal do not contribute to the strain relaxation since one dislocation segment relieves strain, while the opposite segment builds up strain. If the latter segment laces up to the wafer free surface, strain relaxation is achieved by TDs moving through the epilayer, as observed in Fig. 3.

During the experiments more and more threading dislocations are passing through the area of observation. As a consequence the increasing density of the resulting misfit dislocation network hinders a prolonged imaging of the same area. This problem can be avoided by using patterned samples. Standard lithography and reactive ion etching techniques are used to pattern the uniform epilayer. As a result, separated square SiGe fields on a Si substrate with dimensions between 2x2 and 10x10 µm are used for in-situ experiments. In this case the path lengths of the TDs is limited by the structure size. As a result, even the dislocation loop nucleation can be observed beyond the onset of the relaxation process and the probability of observing a dislocation loop lacing up increases. Such an event is shown in Fig. 5 showing 4 frames of a patterned plan view sample at 720°C. At the precipitate marked by an arrow in the first two frames a dislocation loop nucleates and immediately laces up to the surface resulting in a straight misfit dislocation segment with two open ends. The open ends are marked by arrows in the two last frames. Due to the higher temperature this process occurred very fast and could be visualised within very few video frames. From the moment of the nucleation to the point the threading segments leave the area of observation less than one quarter of a second elapsed.

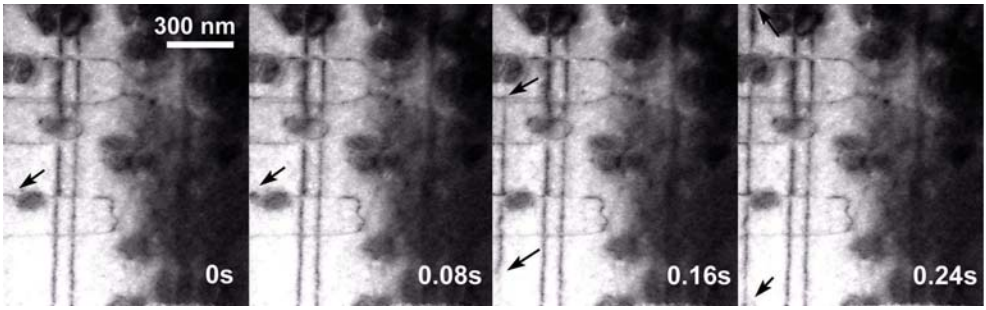


Fig. 5: Structured plan view sample at 720°C within a few video frames. A dislocation loop nucleates at a helium precipitate and laces up to the heterostructure surface (marked by black arrows). Both threading segments move apart in opposite direction until they leave the area of observation.

4. CONCLUSION

The morphological evolution of helium implanted SiGe/Si heterostructures under thermal treatment revealed unambiguously helium filled, platelet-like precipitates acting as dislocation sources. The nucleation, the enlargement and the unlacing of dislocation loops resulting in misfit dislocation networks have been observed in in-situ TEM experiments and coincide with the onset of relaxation measured around 600°C for accompanying ex-situ samples. Dislocation glide as well as climb mechanisms have been observed in this study and reveal that both processes have to be taken into account in the strain-relaxation model. After decay of the plate-shaped precipitates in spherical bubble arrangements, coarsening of the defect structure has been shown to be driven by coalescence at temperatures of 800°C.

REFERENCES

Armstrong G and Maiti C 1998 Sol.-State Electron. **42**, 498

Beaufort M, Oliviero E, Garem H, Godey S, Ntsenzok E, Blanchard C and Barbot J 2000 Phil. Mag. B **80**, 1975

Cai J, Mooney P, Christiansen S, Chen H, Chu J and Ott J 2004 J. Appl. Phys. **95**, 5347

Fichtner P, Kaschny R, Yankov R, Muecklich A and Kreißig U 1997 Appl. Phys. Lett. **61**, 2656

Holländer B, Lenk S, Mantl S, Trinkaus H, Kirch D, Luysberg M, Hackbarth T, Herzog H and Fichtner P 2001 Nucl. Instrum. Methods Phys. Res. B **175–177**, 357

Holländer B, Buca D, Mörschbächer M, Lenk S, Mantl S, Herzog H , Hackbarth T, Loo R, Caymax M and Fichtner P 2004 J. Appl. Phys. **96**, 1745

Hueging N, Tillmann K, Luysberg M, Trinkaus H and Urban K 2003 Microsc. of Semicond. Mat. **180**, 373

Hueging N, Luysberg M, Urban K, Buca D and Mantl S 2005 Appl. Phys Lett. **86**, 042112

Luysberg M, Kirch D, Trinkaus H, Holländer B, Lenk S, Mantl S, Hackbarth T, Herzog H and Fichtner P 2002 J. Appl. Phys. **69**, 4290

Mantl S, Holländer B, Liedtke R, Mesters S, Herzog H, Kibbel H and Hackbarth T 1999 Nucl. Instrum. Methods Phys. Res. B **147**, 29

Raineri V, Saggio M and Rimini E 2000 J. Mater. Res. **15**, 1449

Schwarz K 2003 Phys. Rev. Lett. **91**, 145503-1

Tillmann K, Hueging N, Trinkaus H and Luysberg M 2004 Microsc. and Microanal. **10**

Trinkaus H, Holländer B, Rongen S, Mantl S, Herzog H, Kuchenbecker J and Hackbarth T 2000 Appl. Phys. Lett. **76**, 3552

TEM investigation of Si/Ge multilayer structure incorporated into MBE grown Si whiskers

N Zakharov, P Werner, G Gerth, L Schubert, L Sokolov and U Gösele

Max-Planck-Institute of Microstructure Physics, Weinberg 2, D-06120 Halle(Saale), Germany

ABSTRACT: The TEM was used to monitor the composition of thin Ge layers incorporated into Si nanowhiskers grown by molecular beam epitaxy (MBE) on a <111> Si substrate. The method of chemical analysis was developed for this particular case. It has been found that doping of Si whiskers by Ge slows down the whisker growth and can even result in their dissolution. This phenomenon is interpreted in terms of additional elastic energy introduced by the Ge atoms into Si nanowhisker.

1. INTRODUCTION

There is a big interest nowadays in different kinds of nanostructures driven by the possibility to explore the quantum size effects. For this purpose the size of structural elements should be comparable with the de Broglie wavelength λ of the charge carriers, which is about 10 nm. Usually such bandgap engineering is implemented by local variation in the composition of the crystal. At the same time the modern growth techniques such as MBE, MOCVD and others open the way to create artificial structures where the local composition varies on the atomic scale (formation of QDs, QWs and so on). In this situation to monitor the compositional variations in such structures an adequate method for chemical analysis characterised by atomic spatial resolution has to be used. One of these can be transmission electron microscopy (TEM), because the electrons are scattered differently by different atomic species $\sigma \sim Z$, where σ- cross-section of electron scattering, Z-atomic number (Lenz 1954).

Extensive investigations of silicon whisker growth by the so-called "vapour-liquid-solid" (VLS) technique started already in the sixties (Wagner 1964, 1965, Givargizov 1975). In this technique small liquid metal droplets are used as seeds. Further growth occurs due to the high accommodation coefficient of vapour-phase species on liquid surfaces, where the reduction reaction between $SiCl_4$ and H_2 occurs at the gold-silicon eutectic. The necessary supersaturation of ad-atoms is determined entirely by vapour pressure, which can be easily varied. Recently MBE was successfully used for Si whisker growth (Schubert 2004). In this technique a uniform flux of Si atoms impinges on a <111> Si surface with previously deposited tiny Au droplets. At a first glance no whiskers should grow, however this is not the case. Whiskers grow under Au droplets consuming Si ad-atoms from substrate. The driving force for this process is the difference between the chemical potential of Si ad-atoms in distorted surface layer of Si substrate due to Si/Au solid solution formation and on the top of the whisker where the elastic energy can relax (Zakharov et al 2005). The goal of this paper is to investigate the Ge/Si heterostructure formation in MBE grown Si whiskers using the analytical ability of TEM.

2. EXPERIMENTAL DETAILS

The whiskers were grown by MBE on <111> oriented 5" Si wafers with small Au droplets varying between 10 nm and 300 nm in diameter. Growth occurred at T_S = 545°C and constant Si and Ge fluxes of 0.05 nm/sec and 0.01 nm/sec, respectively, were used.

The grown structures were investigated using a JEM 4010 transmission electron microscope with an acceleration voltage of 400 kV. Images were taken with a slow scan CCD camera to retain the linearity between electron flux and output signal.

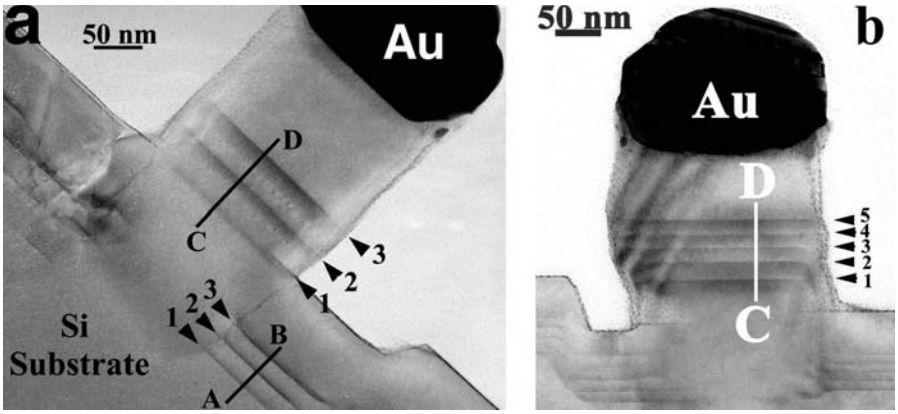


Fig.1. (a) 3 Ge layers with nominal thickness 0.5, 1.0 and 1.5 nm were deposited over equal time intervals. The variation of Ge concentration x in whisker and substrate was analysed along directions CD and AB respectively. (b) 5 Ge layers with nominal thickness 1 nm were deposited with the same time interval as markers.

To monitor the Ge distribution in the Si/Ge multilayer structures the images were taken with a large objective aperture β_{obj} = 0.01 rad. to minimise the influence of diffraction contrast from structural defects and elastic strains. Under these conditions, contrast in the image was determined by scattering of electron outside the objective aperture β_{obj}. Ge atoms were randomly distributed over Si crystal lattice positions (no ordering). In this case (Heidenreich 1964):

$$Q=N\sigma_{at}, \quad (1)$$

where Q is the total cross-section of electron scattering for an object containing N atoms/cm^3 and σ_{at} is the total cross section per atom for scattering outside objective aperture β_{obj}. N can be written in the following way $N = N_0 x$, where N_0 is the number of atoms per cm^3 in Si and x is the concentration of Ge atoms in $Si_{(1-x)}$ Ge_x. Hence

$$Q = N_0 \, \sigma_{at} \, x \quad (2)$$

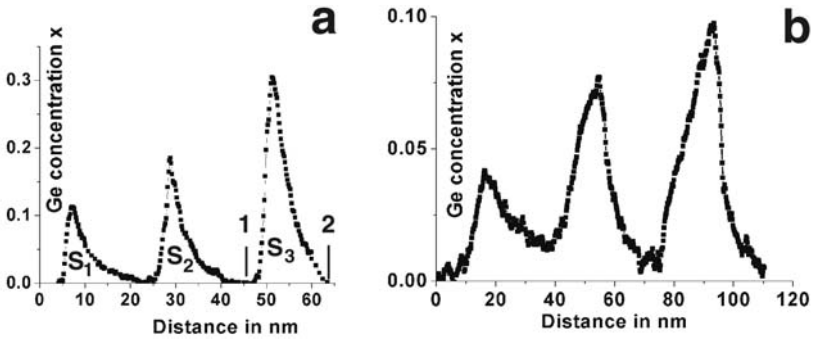


Fig. 2. Variation of Ge concentration along AB (a) and CD (b) (see Fig. 1a) in substrate and whisker, respectively. (a) 1-2 integration limits in eq.(4).

This expression shows that the total cross section Q is proportional to the concentration x in solid solution $Si_{(1-x)}Ge_x$. Figure 2a supports this statement where the area under each peak S_n changes proportionally to the thickness δ_n of deposited Ge layer. In this case we will obtain:

$$\Delta I(y) = N_0\, \sigma_{at}\, t\, x(y) = K\, x(y), \qquad (3)$$

where $\Delta I(y)$ is the intensity profile measured along AB or CD in Fig. 1, t is the specimen thickness which can be considered with a good accuracy as a constant in the region of interest, $K = N_0\, \sigma_{at} t$-const. The parameter K can be determined from the normalisation condition:

$$K = \frac{1}{\delta_n} \int_1^2 \Delta I(y)\, dy\,, \qquad (4)$$

where δ_n is the thickness of the deposited Ge layer known from the MBE growth experiment, the integration is performed e.g. over the interval 1-2 (see Fig. 2a). Thus, expressions (3), (4) give us the possibility to determine the variation of Ge concentration $x(y)$ using the intensity profile.

3. RESULTS AND DISCUSSION

Using this technique, we investigate the formation of Si/Ge vertical heterostructures in whiskers by the MBE growth technique. Three thin layers of Ge 0.5 nm, 1 nm and 1.5 nm thick were deposited during whisker growth over equal time intervals. The Si flux was interrupted during Ge deposition. The concentration profiles measured along A-B in the substrate and C-D in the whisker (see Fig. 1a) are shown in Figs. 2a and b, respectively. First of all one should point out that Ge deposition occurred during a very short time interval. However the peak half-widths in Figs. 2a and b are approximately 2 and 10 times larger than the deposited layer thickness, respectively. There is an obvious difference between the Ge concentration profiles measured in the substrate and whisker. In the first case, the Ge concentration almost instantly reaches its maximum value after Ge flashing and then drops slowly due to Ge atom segregation. In the case of the whisker, the situation is practically reversed. Growth of Ge concentration x occurs relatively slowly after flashing and then drops sharply. The slow growth of the Ge concentration in the first stage is due to the time needed for Ge atoms to be transported from the gold droplet surface to the Si/Au interface, where the growth occurs.

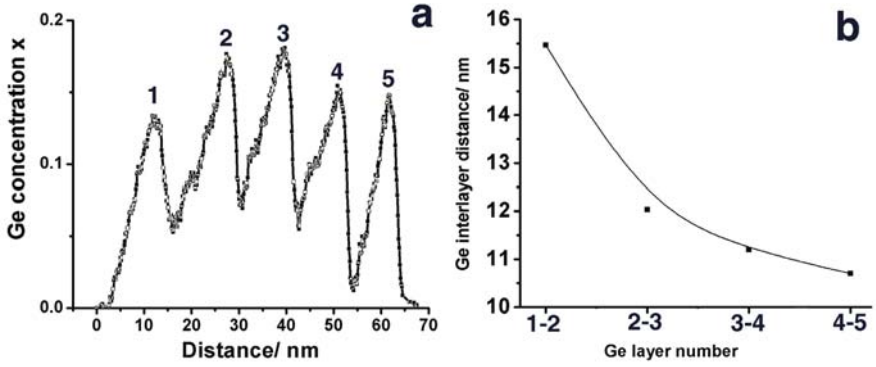


Fig. 3. (a) Compositional profile measured along CD in Fig. 1b. (b)Variation of the distances between Ge layers in (a). N-(N+1)-distance between N and N+1 Ge layers. The Si growth rate decreases due to incorporation of Ge layers.

It has been found that Ge doping decreases the growth rate of whiskers. To investigate the dynamics of this phenomenon we deposited 5 Ge layers 1 nm thick each as time markers with the same time interval (Fig. 1b). Fig. 3a depicts the Ge concentration profile in one such whisker. The graph in Fig. 3b demonstrates decreasing of the interlayer distance from 15.5 to 11 nm with the layer number. This finding is in contradiction with the results received from the conventional CVD-VLS technique, where the $Si_{1-x}Ge_x$ whiskers with composition $x \leq 0.45$ can be grown (Sandulova 1963). This

phenomenon can be explained by the reduction of supersaturation $\Delta\mu/\kappa T$ due to additional elastic energy introduced by Ge atoms into the Si matrix $\Delta\mu_e = 9x\omega G\varepsilon^2$ (Nabarro 1940), where G is the shear modulus, $\varepsilon = (r_m - r_i)/r_m$ is the atomic misfit parameter, r_m and r_i are the atomic radii of Si and Ge, respectively. Thus, the real supersaturation can be written as:

$$\Delta\mu/\kappa T = (\Delta\mu_0 - \Delta\mu_e)/kT \quad (5)$$

Hence, there is a critical impurity concentration x_c at what the supersaturation drops to zero and whiskers stop growing. We observed such a growth interruption for $x_c = 0.05$, which would correspond to $\Delta\mu_e = 0.01$ eV. These results demonstrate that without Ge doping the whisker growth occurs at a supersaturation of about $\Delta\mu_e/kT \sim 0.15$. Thus, the Ge doping can be used as a tool to measure adatom supersaturation.

4. CONCLUSIONS

TEM was successfully used to monitor the Ge distribution in Si nanowhiskers. The driving force for MBE whisker growth is the relaxation of elastic energy. Thin Ge layers can be incorporated into the whisker, however the interfaces are not sharp. Widening of Ge layers in the whisker is explained by the time needed for Ge atoms to be transported from the gold droplet surface to the Si/Au interface, where the growth occurs. Ge doping reduces the supersaturation and slows down whisker growth. Doping with 5% Ge stops completely the whisker growth.

ACKNOWLEGEMENTS

This work has been supported by the SANDiE project. We thank A Frommfeld, S Hopfe and C Münx for technical assistance.

REFERENCES

Givargizov E I 1975 J. Cryst. Growth **31**, 20
Heidenreich R D 1964 Fundamentals of Transmission Electron Microscopy Ed. R E Marshak, New York, p. 29
Lenz F 1954 Zeit. Naturforschung **9a**, 185
Nabarro F R N 1940 Proc. Roy. Soc. **A175**, 519
Sandulova AV 1963 Dokl. Akad. Nauk SSSR **153**, 330
Schubert L, Werner P, Zakharov N D, Gerth G, Kolb F, Long L, Gösele U and Tan TY 2004 Appl. Phys. Lett. **84**, 24
Wagner R S, Ellis W C, Jackson K and Arnold S M 1964 J. Appl. Phys. **35**, 2993
Wagner R S and Ellis W C 1965 Trans. Met. Soc. AIME **233**, 1053
Zakharov N D, Werner P, Gerth G, Schubert L, Sokolov L and Gösele U 2005 Appl. Phys. Lett. *submitted*

Local compositional analysis of GeSi/Si nanoclusters by scanning Auger microscopy

G A Maximov, D E Nikolitchev and D O Filatov

Research and Educational Center for Physics of Solid State Nanostructures, University of Nizhny Novgorod, 23 Gagarin Ave 603950 Nizhny Novgorod, Russia

ABSTRACT: The analytic potential of scanning Auger microscopy for study of the composition of semiconducting nanostructures was demonstrated. The objects of investigation were self-assembled GeSi nanoclusters grown on silicon substrates by molecular beam epitaxy. The practicability of local compositional analysis of single GeSi nanoclusters was shown. The measurement technique was developed and local depth composition profiling of nanoclusters was fulfilled with 50 nm lateral resolution. The concentration obtained by scanning Auger microscopy is in a good agreement with results calculated using photoelectric measurements.

1. INTRODUCTION

Nanoelectronics is developing vigorously today. Systems with element sizes of a few nanometers have already been created. It is well known that the properties of solid state nanostructures (carrier energy spectrum, electronic and optical properties) are defined to a considerable extent by the size, shape and composition of nanoobjects. For geometric characterization of nanostructures the scanning probe microscopy (SPM) methods can be successfully applied. For estimation of nanostructure composition the non-local methods unable to obtain reliable chemical composition of single nanoobjects have been applied (Krasil'nik et al 2001). One of the methods which could solve the problem of nanometer scale analysis is scanning Auger microscopy.

The objective of this work is to estimate the analytic potential of scanning electron/Auger microscopy (SEM/SAM) with nanometer probe diameter in the field of nanoobject morphology and local composition study using the example of GeSi nanoclusters formed on silicon substrates.

2. EXPERIMENTAL

2.1 Apparatus

SEM/SAM investigations were carried out using an ultrahigh-vacuum instrument MultiProbe S™ manufactured by Omicron Nanotechnology GmbH (Germany). Auger electrons were excited using the FEI SEG-20 electron gun (accelerating voltage – up to 25 keV, beam current – up to 100 nA, electron probe diameter – 20 nm). Auger spectra were recorded with the use of hemispherical energy analyzer EA-125. The system also included an ion gun for sample cleaning and depth profiling by Ar^+ ion sputtering.

To determine SEM/SAM lateral resolution and real electron probe size, a test sample was based on the Cr/Ni structure. The element sizes on the sample surface were from 1000 nm to 10 nm according to atomic force microscopy (AFM) measurements. The resolution in SEM and SAM mode was 20 nm and 25 nm, respectively.

2.2 GeSi Nanostructures

GeSi nanostructures being investigated were made by Stranski-Krastanov self-assembling with the use of 1) molecular beam epitaxy (MBE) and 2) sublimation molecular beam epitaxy with a

gaseous germanium source. Surface morphology was investigated by AFM. In the first case, the uniform cluster arrays with 300 nm lateral size, 40 nm height and 5×10^8 cm^{-2} surface density were observed. Nanostructures made by the second method had arrays of nanoclusters with 100 – 900 nm lateral size, 20 – 100 nm height and 2×10^7 - 7×10^8 cm^{-2}surface density (Fig. 1).

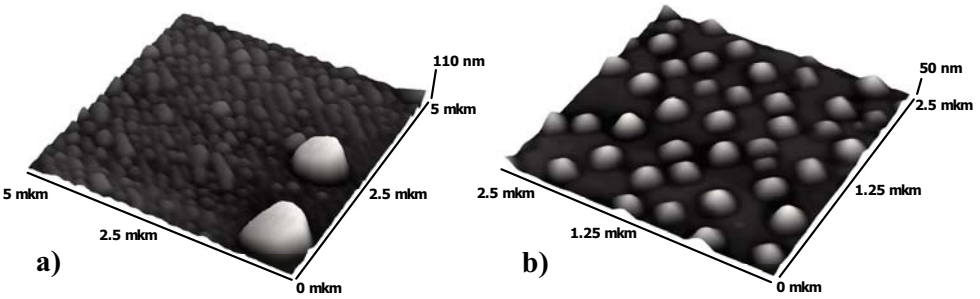


Fig. 1. AFM-images of GeSi heterostructures a) sublimation MBE and b) MBE.

2.3 Problem of Auger Nanoanalysis

During SEM/SAM investigation of semiconducting objects, the effect of sample surface charging became apparent and led to electron probe shift and defocusing (Seah and Spenser 2000). Owing to the existence of surface charge, the spatial resolution is 2-3 times less than for well conducting samples. During GeSi nanocluster investigation the resolution was 50 nm in SEM and 70 nm in SAM mode (Fig. 2).

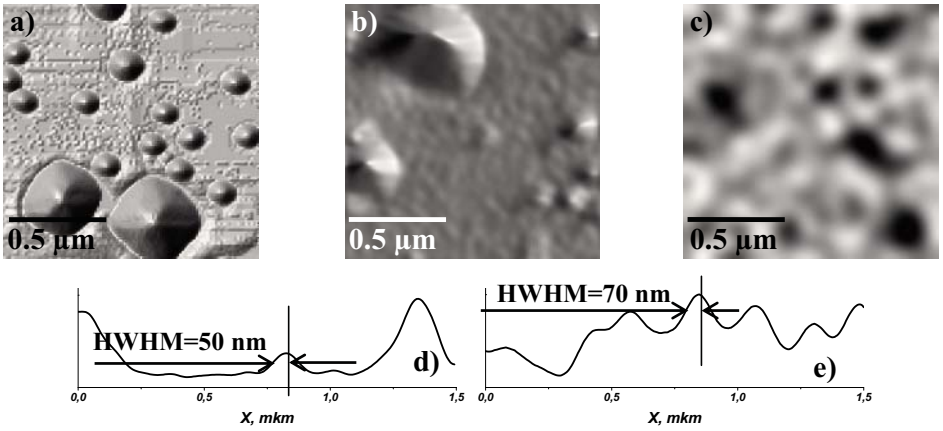


Fig. 2. a) AFM, b) SEM, c) SAM images of GeSi nanoclusters, d) intensity of secondary electron profile in SEM mode, and e) Ge line intensity in SAM mode.

Shift and defocusing of the electron beam were the main problems during recording of Auger spectra at a defined point chosen on the SEM image and during acquisition of the Ge surface distribution. By applying a positive potential to the sample this effect could be decreased but not completely eliminated. To solve this problem a special method was used: the electron probe was positioned at a chosen point and Auger spectra were recorded within a short time interval during which the probe shift was negligible and it remained on the island. Then the instrument was switched to SEM mode again, beam correction was made and the procedure was repeated. Auger spectra obtained after several (10-20) cycles were averaged to increase the signal-to-noise ratio.

2.4 Concentration of Ge and Si in Oxide

A calibration curve was built to determine the Ge and Si concentration in nanoislands (Fig. 3). For that the compositional analysis of specially made samples of GeSi solid solutions with different Ge content was carried out layer-by-layer. The test-samples were made by growth of polycrystalline GeSi films of 50 – 100 nm thickness on high-alloyed silicon substrate using MBE. Averaged concentrations of germanium and silicon in films were determined independently by X-ray diffraction.

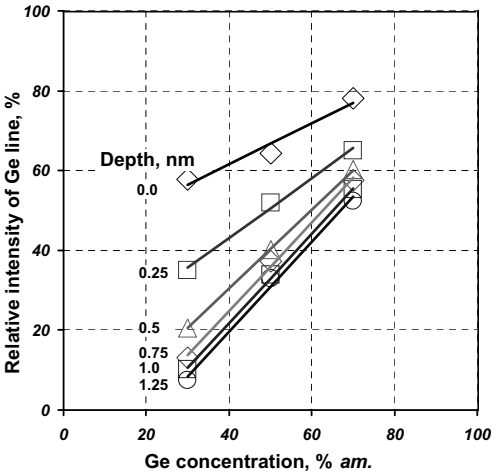


Fig.3. Graduated characteristics for different oxide layer depth.

After preparation, the test samples were located in air (as the investigated samples) before being put into the vacuum chamber of the Auger spectrometer. During this process the surface layer was oxidized. The calibration curve was built for several depth values to determine the concentration of Ge in oxide. It was discovered that concentration ratio of germanium and silicon had differences in oxide and in the depth of the sample (LeGoues et al 1989). The ion sputtering of GeSi nanoclusters was carried out layer-by-layer and Ge concentration was determined from the graduated characteristic for the proper depth of ion sputtering. There was the hypothesis that nanoclusters and GeSi solid solutions oxidised equality.

3. RESULTS AND DISCUSSION

The germanium and silicon depth distribution in the nanoclusters and between them is shown in Fig. 4. Calculation of Ge concentration was done considering that the rest of the basic composition was silicon. The average germanium concentration obtained during local SAM measurements was 10 – 20% lower than value obtained from X-ray diffraction and Raman spectroscopy measurements (Valakh et al 2004). This could be explained by the different modes in which samples were measured. The probe diameter in the case of the calibration curve was 30 μm but during nanostructure investigation it was 50 nm. The fact that Ge Auger line intensity decrease after switching to nanoprobe mode will need to be taken further into account for accurate Ge profiling of nanoclusters.

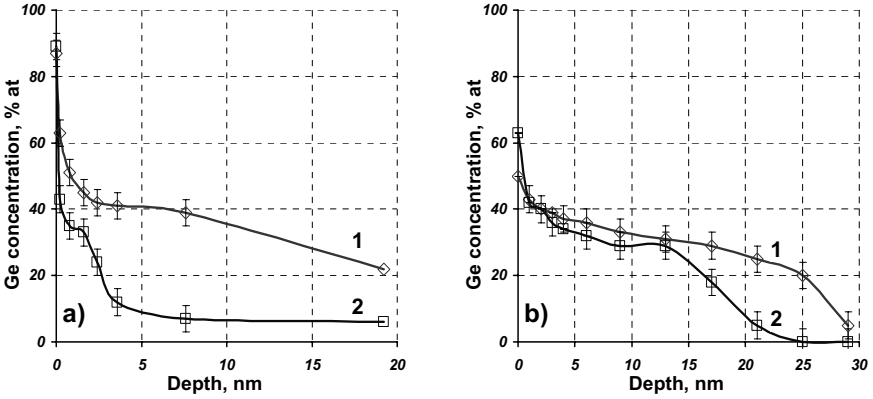


Fig. 4. Depth distribution of Ge in nanoisland (1) and between them (2) for different growth methods: a) sublimation MBE and b) MBE.

To estimate the accuracy (avoiding systematic error) of concentration measurements independent experiments were done. The Ge concentration in Ge_xSi_{1-x} islands was measured using photovoltage spectroscopy at a semiconductor/electrolyte junction. The experiment was carried out in an electrolytic cell using the satellite samples grown under the same conditions as the samples for SAM investigation (in the case of sublimation MBE) but nanoclusters were covered with a 40 nm thick Si layer. The method of measurements and spectral analysis of photovoltage spectroscopy has been described by Maksimov et al (2005). The x value was 0.52±0.10. This value is near to the average Ge concentration (x=0.53) acquired for the depth distribution of Ge in nanoclusters (Fig. 4a).

4. CONCLUSIONS

As a result of this work, the practicability of local compositional analysis with nanometer resolution of self-assembled GeSi/Si nanostructures using scanning Auger microscopy has been shown. The SEM/SAM lateral resolution was determined and amounted to 50 nm in SEM and 70 nm in SAM mode for GeSi/Si structures. The measurement technique was developed and profiling of Ge and Si concentrations in nanoclusters was carried out for GeSi heterorostructures. The concentration obtained using SAM measurements is in good agreement with results of photoelectric measurements.

ACKNOWLEDGEMENTS

The work has been supported by the Joint Russian American Program "Basic Research and Higher Education" (BRHE) sponsored jointly by US Civilian Research and Development Foundation (CRDF) with Russian Ministry of Education (Award #REC-NN-001). Samples for investigation were provided by V.G.Shengurov (Physical-Technical Research Institute, University of Nizhny Novgorod) and A.V.Novikov (Institute for Physics of Microstructures, Russian Academy of Sciences).

REFERENCES

Krasil'nik Z F, Dolgov I V, Drozdov Yu N, Filatov D O, Gusev S A , Lobanov D N, Moldavskaya L D, Novikov A V, Postnikov V and Vostokov N V 2001 Thin Solid Films **367**, 171

LeGoues F K, Rosenberg R, Nguyen T, Himpsel F and Meyerson B S 1989 J. Appl. Phys. **64**, 1724

Maksimov G A, Krasil'nik Z F, Filatov D O, Kruglova M V, Morozov S V, Remizov D Yu, Nikolichev D E and Shengurov V G 2005 Phys. Solid State, **47**, 22

Seah M P and Spenser S J 2000 J. Electron Spec. **109**, 291

Valakh M Ya, Dzhagan V N, Lytvyn P M, Yuhimchuk V A, Krasil'nik Z F, Novikov A V and Lobanov D N 2004 Phys Solid State **46**, 88

A study of processed and unprocessed dual channel Si/SiGe MOSFET device structures using FIB and TEM

A C K Chang, D J Norris, I M Ross, A G Cullis, S H Olsen[1] and A G O'Neill[1]

Department of Electronics and Electrical Engineering, University of Sheffield, Sheffield, S1 3JD, UK
[1] School of Electrical, Electronic and Computer Engineering, University of Newcastle, Newcastle, NE1 7RU, UK

ABSTRACT: We present the analysis of a series of Si/SiGe dual channel MOSFET device structures and their corresponding unprocessed blanket layers using transmission electron microscopy. These layers comprise a linear graded $Si_{0.85}Ge_{0.15}$ virtual substrate, followed by a compressively strained $Si_{0.70}Ge_{0.30}$ layer and capped with a tensile strained Si layer. It is found that high temperature metal oxide semiconductor processing induces Ge out-diffusion from the strained SiGe layer while the strained Si layer thickness was reduced by 50 % at the wafer edge due to cross wafer growth variations of the channel layers at low temperatures.

1. INTRODUCTION

The 4.2% lattice mismatch between Si and Ge atoms can be utilised to create high mobility strain-engineered devices (Fischetti and Laux 1996). While *p*-MOS devices are able to adopt a 'sandwich' Si/SiGe/Si layer structure where a pseudomorphic SiGe layer functions as the *p*-channel, some *n*-channel and dual channel device structures require a compositionally graded SiGe virtual substrate (VS) (Fitzgerald et al 1991) to act as a buffer layer between the Si substrate and channel layers. This enables complete relaxation of lattice mismatch strain via purpose made misfit dislocation generation, which is contained within the VS. In this study, we look at state-of-the-art Si/SiGe dual channel metal oxide semiconductor field effect transistor MOSFET devices as well as their corresponding unprocessed blanket layers grown on linear graded VS accompanied with a constant composition SiGe buffer layer. Dual channel architecture increases the robustness of the material to strain relaxation by the sequential growth of tensile and compressively strained layers, while band offsets between the oppositely strained materials can be used to create high mobility surface *n*- and buried *p*-channel MOSFETs (Olsen et al 2003a). Wafer centre and edge layers were also compared to reveal any growth discrepancies relating to the Ge concentration and channel layer thicknesses. Focused ion beam (FIB) cross-sectioning (Chang et al 2005) has been adopted to prepare site specific TEM samples of sub-micron gate length devices to compare with the conventional mechanically polished and Ar^+ ion milled unprocessed blanket layers.

2. EXPERIMENTAL

Surface strained Si dual channel MOSFETs were fabricated on relaxed $Si_{0.85}Ge_{0.15}$ VS on bulk Czochralski Si(100) wafers (Olsen et al 2003a). The VS was grown by ultra low-pressure chemical vapour deposition (ULPCVD) in a modified molecular beam epitaxy system using a linear grading rate of 10 % Ge/μm at 650ºC. Stress-relief layers were incorporated into this section of the VS to encourage misfit dislocation generation and strain relaxation of the VS. The channel layers comprised a 8 nm compressively strained $Si_{0.70}Ge_{0.30}$ buried *p*-channel layer, enabling high mobility hole confinement, followed by a 16 nm strained Si layer grown at a reduced temperature of 550ºC with the intension of minimising the Ge diffusion into the channel. Site-specific thin sections for TEM analysis were prepared using a dedicated dual column JEOL 'Fabrika' FIB miller from devices at the

centre and edge of the wafer. The VS of the corresponding unprocessed blanket layers was grown at a higher temperature of 830ºC without stress-relief layers and cross-sectioned for TEM using conventional mechanical polishing and subsequent Ar^+ ion milling. All the cross-sections were analysed using a JEOL 2010F field emission gun transmission electron microscope, equipped with an Oxford LINK/ISIS X-ray energy-dispersive spectrometer (EDS) and a means of performing scanning transmission electron microscopy (STEM) facilitating STEM bright-field (BF) and high angle annular dark field (HAADF) imaging.

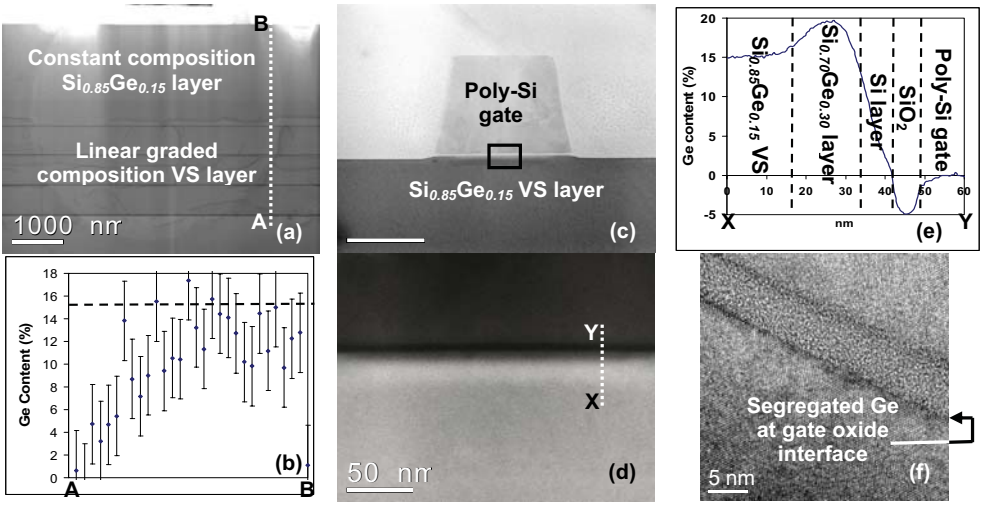


Fig. 1: (a) STEM BF micrograph of the wafer centre device structure. (b) Ge content profile measured across the VS detailing an average Ge concentration of 12.5±3.5 at.% in the constant composition region. (c) STEM BF image of gate stack. (d) HAADF image of the channel layers, showing diffused strained Si (dark) layer between strained $Si_{0.70}Ge_{0.30}$ (light) layer and SiO_2 layer. (e) Ge content profile across the channel layers, detailing significant diffusion present. (f) HREM micrograph of layers under gate electrode, showing Ge segregated at Si/SiO_2 interface.

3. RESULTS AND DISCUSSION

Cross-sectional TEM micrographs and their corresponding analytical data of the wafer centre and edge device structures are shown in Figs. 1 and 2, respectively. STEM BF images of the layer structures in both regions (Figs. 1a and 2a) of the wafer reveal minimal threading dislocations confined within the graded region of the VS buffer layer as expected. However, EDS probed point analysis across the VS (plotted as graphs in Figs. 1b and 2b) have revealed a reduction in average Ge concentration within the constant composition region from 12.5±3.5 at.% at the wafer centre to 7.0±2.5 at.% at the wafer edge. While STEM BF images of the gate stack (Figs. 1c and 2c) show general structural uniformity in gate fabrication, the HAADF micrographs from the region under the gate electrode observed in Figs. 1d and 2d reveal considerable diffusion between the channel layers. This was verified by the Ge concentration profiles derived from the Z contrast images (Figs. 1e and 2e) taken over the compressively strained SiGe layer in each case. The profile clearly demonstrates a significant Ge out-diffusion has occurred as detailed by its Gaussian-like profile. Peak Ge compositions of 19.7±3.5 at.% and 8.9±2.5 at.% were also recorded in what was supposed to be a strained $Si_{0.70}Ge_{0.30}$ layer while the strained Si layer thicknesses were found to be 7 nm and 4 nm for the wafer centre and edge respectively. High resolution electron microscope (HREM) images of the gate oxide layer shown in Figs. 1f and 2f revealed intended thicknesses of 6 nm at both regions of the wafer, highlighting that a successful high temperature oxidation process was achieved. On the other hand, the dark bands present at the Si/SiO_2 interfaces suggest Ge segregation (Norris et al 2001) has occurred due to the expulsion of Ge atoms from the

growing oxide, which also leads to the noted interface roughening. This therefore strengthens the earlier argument that Ge out-diffusion has occurred in these high thermal budget processed devices.

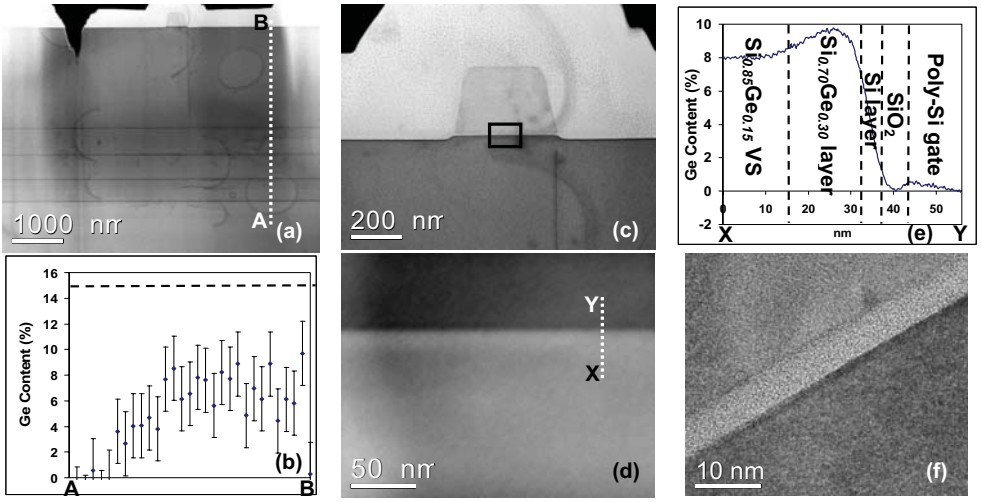


Fig. 2: (a) STEM BF micrograph of the wafer edge device structure. (b) Ge content profile measured across the VS detailing an unanticipated low average Ge concentration of 7.0±2.5 at.% in the VS constant composition region. (c) STEM BF image of the gate stack. (d) HAADF image of the channel layers, showing diffused strained Si layer (dark) between the strained $Si_{0.70}Ge_{0.30}$ layer (light) and SiO_2 layer. (e) Ge content profile across the channel layers, detailing significant diffusion present and reduced Ge concentrations in the SiGe layers. (f) HREM micrograph of layers under gate.

STEM BF micrographs of the VS buffer layer within the corresponding unprocessed blanket layers are given in Figs. 3a and 4a. These images reveal an increase in the threading dislocation density confined within the graded region compared to the layers used in the processed device structures. This could be attributed to the higher growth temperature (830°C) employed, which encourages strain relaxation, resulting in misfit dislocation generation. Graphical data (Figs. 3b and 4b) from EDS measurements taken across the VS also show that higher average Ge concentrations were recorded in the constant composition region. However, the same trend of a reduced average Ge composition was also noted in the blanket layers at the wafer edge (14.0±2.0 at.%) when compared to that of the wafer centre (16.5±2.5 at.%). Most interesting of these results are the interfaces of the channel layers observed (Figs. 3c and 4c) in the blanket layers. They appear well defined with abrupt interfaces, showing little sign of Ge-out diffusion. This is verified by the higher Ge content (~27 at.%) recorded in the compressively strained SiGe layer, providing further evidence that Ge out-diffusion observed in the device structures was indeed a consequence of high temperature MOS processing. In addition, an almost 50% reduction in the thickness of the strained Si layer was found at the wafer edge (8.0 nm) when compared to the wafer centre (15.7 nm). Low temperature (550ºC) growth of the channel layers accounts for this anomaly, which is the result of radial variation in growth rates by the LPCVD technique, as suggested by Olsen et al (2003b). This would subsequently lead to a performance degradation of devices at such regions. Growth variations were also noted in the VS with reductions in average Ge concentrations within the constant composition region observed at the wafer edge of both processed and unprocessed structures, despite different VS growth temperatures employed. Lower than anticipated Ge concentrations were also recorded in the constant composition region of the processed device structures. Incidentally, this may be related to the lower temperatures (650ºC) used in their VS growth combined with the high thermal budget employed for device fabrication. Therefore, considerable effort and engineering of the growth conditions is required to ensure high performance yields are maintained across the wafer of such dual channel Si/SiGe device structures.

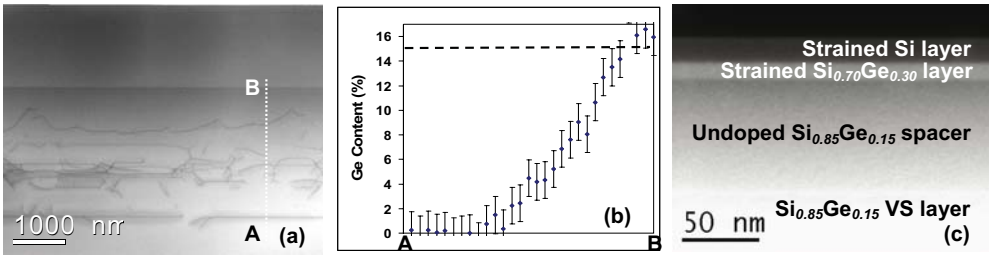


Fig. 3: (a) STEM BF micrograph of the wafer centre blanket layer, showing confined dislocations in the graded VS region. (b) Ge content profile across the VS, detailing an average Ge content of 16.5±2.5 at.% within the constant composition region. (c) HAADF image of the abrupt channel layers.

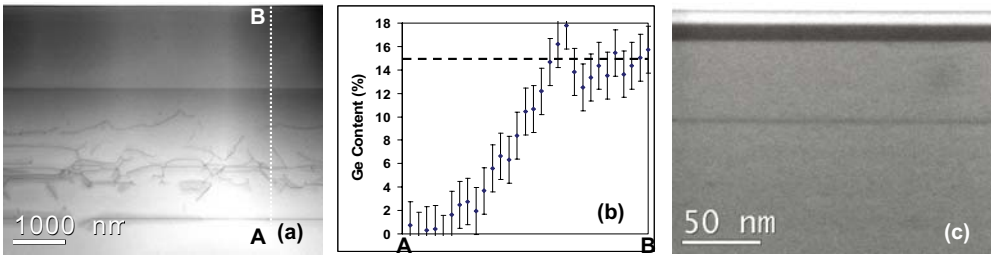


Fig. 4: (a) STEM BF image of the wafer edge blanket layer, showing confined dislocations in the graded VS region. (b) Ge content profile across the VS: its constant composition buffer records an average Ge content of 14.0±2.0 at.%. (c) STEM BF image of the abrupt channel layers.

4. CONCLUSIONS

TEM analysis has shown that whilst unprocessed blanket layers have abrupt channel layer interfaces which display general accordance with desired growth specifications, the channel layers under the gate stack in the processed dual channel MOSFET devices all exhibit diffused interfaces, which is a clear consequence of high temperature (1050ºC) MOS processing. A 50 % reduction in the thickness of the strained Si layer and decrease in Ge concentrations at the wafer edge was observed from both the processed devices and blanket layers, most certainly related to low temperature radial variations in growth rates.

ACKNOWLEDGEMENTS

The authors kindly acknowledge the Engineering and Physical Sciences Research Council (EPSRC) for supporting this work (GR/R65626/01 and GR/S02150/01)

REFERENCES

Chang A C K, Ross I M, Norris D J, Cullis A G, Tang Y T, Cerrina C and Evans A G R 2005 Thin Solid Films *in press*

Fischetti M V and Laux S E 1996 J. Appl. Phys. **80**, 2234

Fitzgerald E A, Xie Y-H, Green M L, Brasen D, Kortan A R, Michel J, Mii Y–J and Weir B E 1991 Appl. Phys. Lett. **59**, 811

Norris D J, Cullis A G, Braithwaite G, Grasby T J, Whall T E and Parker E H C 2001 Inst. Phys. Conf. Ser. **169,** 185

Olsen S H, O'Neill A G, Driscoll L S, Kwa K S K, Chattopadhyay S, Waite A M, Tang Y T, Evans A G R. Norris D J, Cullis A G, Paul D J and Robbins D J 2003a IEEE Trans. Electron. Devices **50**, 1961

Olsen S H, O'Neill A G, Chattopadhyay S, Kwa K S K, Driscoll L S, Zhang J, Robbins D J and Higgs V 2003b J. Appl. Phys. **94**, 6855

Part III

Epitaxy: Growth and Defect Phenomena

Novel TEM method for large-area analysis of misfit dislocation networks in semiconductor heterostructures

E Spiecker[1], J Schöne[1,2], S Rajagopalan[1] and W Jäger[1]

[1] Mikrostrukturanalytik, Technische Fakultät, Universität Kiel, Kaiserstr. 2, 24143 Kiel, Germany
[2] Fraunhofer Institut für Solare Energie Systeme ISE, Heidenhofstr. 2, 79110 Freiburg, Germany

ABSTRACT: We describe an efficient method for characterising quantitatively distributions of misfit dislocations over macroscopic distances along interfaces of complex multilayer heterosystems in semiconductor epitaxy and present first applications to complicated buffer layer structures in high-efficiency solar cells. In a first step, a wedge-shaped sample whose edge runs across the heterostructure at an extremely shallow angle is produced by combining ion-beam bevel polishing with crystal cleavage. By tilting the sample in the TEM, misfit dislocations intersecting the cleavage plane close to the sample edge can be imaged over large distances. Moreover, their Burgers vectors can be determined by evaluating the termination of thickness fringes in weak-beam dark-field images. The applicability of the method is demonstrated for the analysis of 60° misfit dislocations in an interface of a step-graded $In_xGa_{1-x}As$ buffer layer embedded in an InGaP/InGaAs/Ge triple solar cell structure. The analyses of the Burgers vectors clearly reveal an asymmetry in the population of the different glide systems in agreement with crystallographic layer tilt measured by high-resolution XRD. The example shows the great potential of the TEM method for obtaining statistically relevant data on misfit dislocation networks in complicated heterostructures. Potential applications of the method are discussed.

1. INTRODUCTION

Since the development of semiconductor heteroepitaxy some decades ago, misfit dislocations have become an integral part of various types of semiconductor devices. Application examples range from strained Si electronic devices grown on top of relaxed $Si_{1-x}Ge_x$ buffer layers (Harame et al 2004) to high-efficiency InGaP/InGaAs/Ge triple solar cells which contain relaxed $In_{1-x}Ga_xAs$ buffer layers (Bett et al 2004). In such devices, the function of the misfit dislocations is to relax in-plane strain resulting from lattice-mismatched heteroepitaxy. The in-plane lattice constant of the growth surface can be tailored such that it leads to subsequent defect-free growth of the device-active layers. However, the formation of misfit dislocation networks is a complicated self-assembled process. While some general concepts have been established, for instance the occurrence of a critical layer thickness, the actual relaxation process sensitively depends on the growth parameters. Therefore, each application of a new buffer concept generally requires adequate characterisation tools.

High-resolution X-ray diffraction (HRXRD) is by far the most powerful technique for measuring strain relaxation in multilayer structures (Holý et al 1999, Fewster 2000). With HRXRD the evolution of the in-plane and out-of-plane lattice constants across buffer layers can be determined. Moreover, HRXRD allows us to readily reveal and quantify phenomena like layer mosaicity and crystallographic layer tilt (Mooney et al 1994, Holý et al 1995). During the last decade, considerable progress has been made in the attempt to extract quantitative information about the dislocation network itself by analysing HRXRD spectra and reciprocal space maps (RSM) in more detail. Quantitative models are now available which allow one to deduce from RSM statistical data about the density and spatial correlation of misfit dislocations and about the dislocation population of different glide systems (Holý et al 1995, Kaganer et al 1997).

On the other hand, transmission electron microscopy (TEM) is the most important microscopic technique for characterisation of misfit dislocation networks (Fitzgerald 1991, Beanland et al 1996). TEM allows us to characterise individual dislocations and dislocation reactions even in cases of high dislocation densities typically encountered in semiconductor buffer layers. However, a challenge has been the quantitative analysis of the contributions of misfit dislocations to layer strain relaxation, crystallographic tilting and mosaicity by statistically relevant large-area dislocation characterisation. So far, there exists no TEM method which allows us to gather such data for buffer layers which contain misfit dislocation networks in several interfaces. One reason for this is that the TEM investigations of semiconductor buffer layers still use the same sample preparation methods that Abrahams and co-workers (Abrahams et al 1969, Abrahams and Buiocchi 1974) developed more than 30 years ago in their pioneering work on graded buffer layers. Another reason is that the Burgers vector analysis of 60° misfit dislocations, which are the dominating dislocations in the low-misfit regime, is difficult in plan-view geometry because of the presence of out-of-plane components of the Burgers vectors. Pronounced sample bending due to residual layer strain makes a large area Burgers vector analysis via the `invisibility criterion´ already unpractical for the simplest case of a two-dimensional dislocation network located in the interface of a single layer heterostructure. To overcome these problems several other TEM-methods have been applied, like the evaluation of dislocation reactions at nodes of the dislocation network (Dixon and Goodhew 1990), the analysis of diffraction line splittings in large-angle convergent beam electron diffraction patterns (Wang et al 1993), and the evaluation of bend contour splittings in conventional bright-field or dark-field images (Spiecker and Jäger 2002). However, none of these techniques is capable of dealing with the technologically much more relevant case of graded buffer layers containing dislocation networks in several interfaces.

In this paper we describe a novel bevel-polish and cleavage (BPC) TEM sample preparation method which allows us to study large numbers of misfit dislocations in the different interfaces of buffer layers (section 2). We show that the Burgers vectors of the misfit dislocations can be directly deduced from the termination of thickness fringes in weak-beam dark-field (WBDF) images (section 3). We apply the method to 60° misfit dislocations in a $In_xGa_{1-x}As$ buffer layer and make a first comparison between the asymmetric dislocation population of glide systems (from TEM) and the crystallographic layer tilt revealed by HRXRD (section 4). Finally, we discuss the applicability of the method and suggest several applications (section 5).

2. BEVEL-POLISH AND CLEAVAGE PREPARATION METHOD

The individual steps of the BPC method are illustrated in Fig. 1. First, a relatively large piece (>5 mm x 5 mm) of the wafer material containing the heterostructure on top is mechanically thinned from the backside to a final thickness of ~ 100 μm (Fig. 1a). In the next step, ion beam milling is performed from the wafer front side until a shallow crater is produced in the heterostructure (Fig. 1b). During ion-beam milling the individual layers of the heterostructure appear as concentric rings on the surface. If the rings are optically visible their evolution can be nicely monitored during ion-beam milling, allowing one to stop the milling at an appropriate time. If the rings are not directly visible, other methods of detecting the crater depth and shape have to be applied, e.g. Tolansky interference microscopy. Under usual ion beam milling conditions (e.g. 8° incidence angle) craters with bevel angles as small as 0.1° are readily obtained. While this may be surprising at first glance, a closer inspection immediately shows that the spreading of the ion-beam on the surface rather than the angle of incidence mainly determines the bevel angle for shallow craters. After remounting the sample from the holder of the ion-beam milling machine it is cleaved along a {110} crystallographic plane so that the cleavage plane crosses the bevel-polished sample area (Fig. 1c). If a good cleavage plane is obtained the sample is cut into smaller pieces by further cleavage and the individual pieces are glued on TEM slot grids (Fig. 1d). The samples are inserted in the TEM column with the wafer backside pointing towards the incident electron beam (Fig. 1e, left). By tilting the sample the individual layers of the heterostructure can be analysed in the narrow electron-transparent region along the sample edge formed by the cleavage plane and the bevel-polished surface.

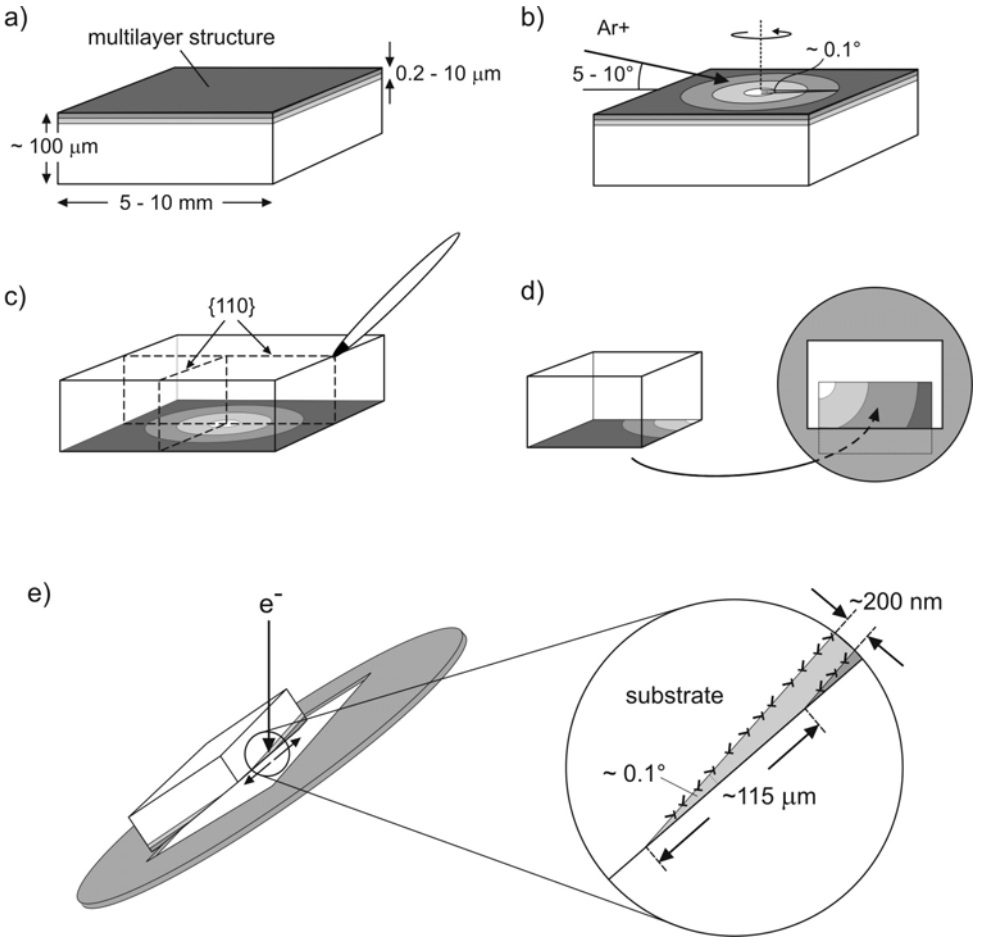


Fig. 1. Steps of the BPC preparation method: a) Mechanical backside thinning of a relatively large sample piece down to a thickness of ~ 100μm, b) Small-angle bevel polishing across the layers by front-side Ar+ ion-beam milling. c) Crystal cleavage on {110} planes. d) Mounting of the individual sample pieces on TEM slot grids. e) TEM investigation of dislocations at the edge of the tilted sample. The enlarged section shows typical dimensions involved: For a bevel angle of ~ 0.1° and a step-graded buffer layer composed of individual layers of ~ 200 nm thickness each layer occurs over a distance of ~ 115 μm along the sample edge. Assuming that the interfaces contain misfit dislocations with mean spacing of ~ 200 nm, almost 600 dislocations in each interface can be studied from a single TEM sample.

Figure 1e (right) shows typical dimensions of a TEM sample prepared by the BPC method, using a step-graded buffer layer as example. Assuming that the bevel angle produced by ion-beam milling is ~ 0.1° and that the thickness of the individual layers in the buffer is ~ 200 nm, the distance over which an individual layer appears at the sample edge amounts to L = 200 nm/tan 0.1° ~ 115 μm. If we further assume that the individual interfaces of the buffer layer contain misfit dislocations with a mean spacing of ~ 200 nm more than 500 dislocations can be studied in each interface by TEM analysis along the edge of a single TEM sample. Another important advantage of BPC-prepared samples is their usage for Burgers vector analysis via weak-beam dark-field (WBDF) imaging (see section 3).

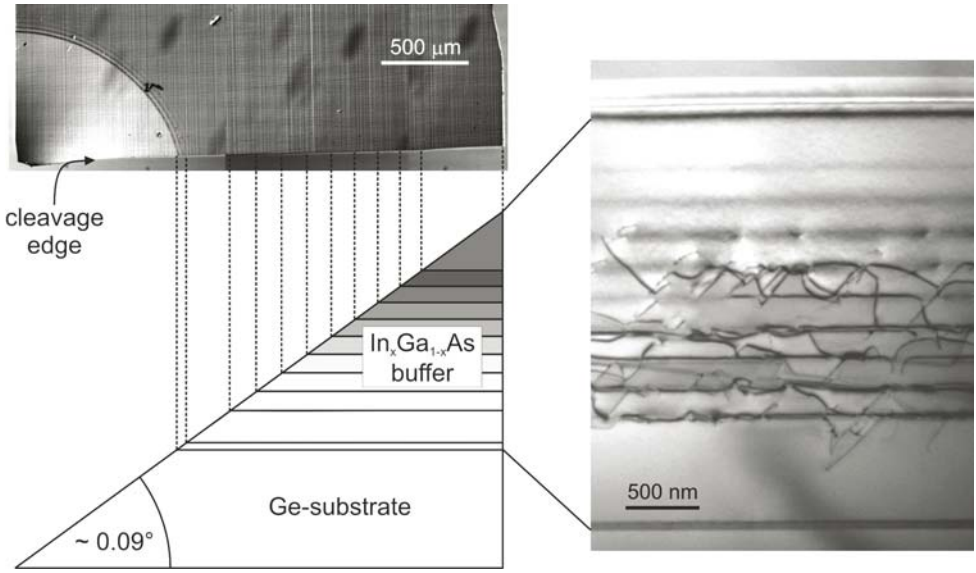


Fig. 2. Top left: Plan-view optical micrograph of the InGaAs-buffer layer after applying the BPC preparation method (cf. Fig. 1, preparation step d). The Ge-substrate and the InGaAs-buffer appear bright golden and dark grey, respectively. Although not revealed in the optical micrograph the individual layers of the step-graded buffer appear one after the other on the surface along the cleavage edge as indicated by the schematic drawing below. Notice the small bevel angle of ~ 0.09°. Right: Conventional cross-section TEM BF-image of the step-graded buffer layer. Misfit dislocations have mainly been formed in the first six interfaces. Threading arms link the dislocation networks in adjacent interfaces. For details see text.

As an example, we have applied the BPC-method to a $In_{0.65}Ga_{0.35}P/In_{0.17}Ga_{0.83}As$/Ge triple solar cell structure which contained a step-graded InGaAs buffer layer between the Ge and the $In_{0.17}Ga_{0.83}As$ for the purpose of accommodating the lattice mismatch of ~ 1.2%. For an overview Fig. 2 (right) shows first a conventional cross-section TEM image of the buffer layer. The buffer contains ten layers with different nominal In-concentrations ranging from 0.2% (lattice-matched to Ge) to 17.1%. The lower six interfaces show dense dislocation networks which are linked by threading arms penetrating through the layers. In contrast, the upper interfaces are essentially free of misfit dislocations indicating the presence of residual compressive strain at the final In-concentration of 17.1% in agreement with HRXRD measurements (Bett et al 2004). Before applying the BPC method we removed the InGaP top cell (~ 1.5 µm thick) and the InGaAs middle cell (~ 1.8 µm thick) by wet-chemical etching, so that only the $In_xGa_{1-x}As$ buffer layer remained on the surface obtained. Removal of thick top-layers which are not relevant for the TEM-study has generally the advantage that the time for ion-beam milling is reduced leading to craters of smaller depth with considerably smaller bevel angles. After back-side thinning of the sample to ~ 100 µm (cf. Fig. 1a) we placed the sample on a conventional plan-view graphite holder (Ø ~ 9 mm) of a PIPS machine (Gatan) and fixed it at one corner with a tiny piece of wax, so that it could be removed mechanically after the bevel-polishing without using chemical solvents. Fig. 2 (top left) shows an optical micrograph of the sample surface after front-side ion-beam milling and subsequent crystal cleavage (cf. Fig. 1b,c). The surface reveals the characteristic cross-hatch pattern which has obviously survived the wet-chemical etching and the front side ion-beam milling. The Ge-substrate appears bright (golden color) and can be clearly discriminated from the $In_xGa_{1-x}As$ buffer layer which appears dark grey. Because of the small variations of the In-concentration in the buffer layer, the individual concentration steps are indistinguishable in the optical micrograph. In Fig. 2 segments along the cleaved sample edge have been assigned to the individual concentration steps assuming a fixed slope angle of the crater, which

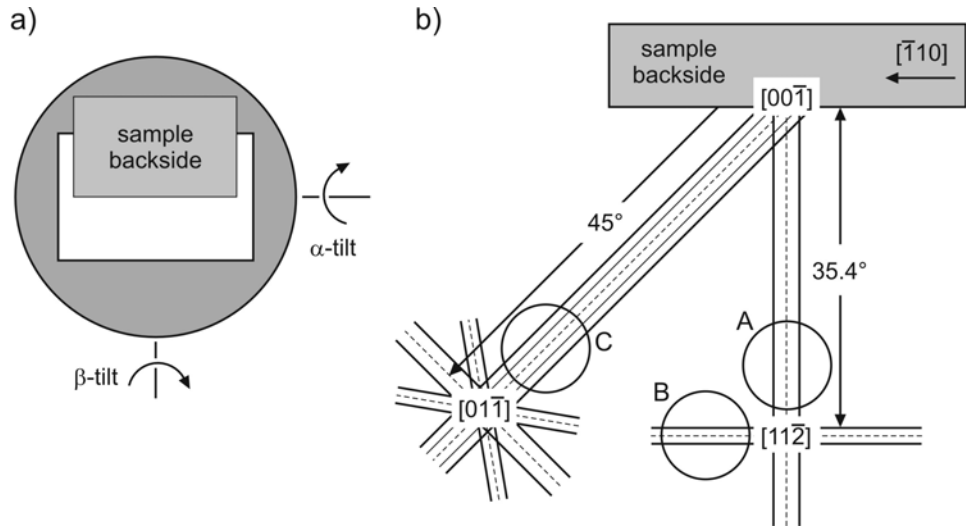


Fig. 3. a) Mounting of the BPC-prepared sample in the TEM holder with the backside pointing towards the incoming electron beam and the sample edge oriented parallel to the holder (α-tilt) axis. b) Schematic Kikuchi-pattern for sample tilting showing convenient excitation conditions for TEM characterisation of misfit dislocations. The misfit component and the twist/tilt components of the Burgers vectors of 60° misfit dislocations can be characterised in region A (excitation of **g** = (-220), see Fig. 4) and in region B (excitation of g=(111), see Fig. 5), respectively. Determination of the crystal polarity which allows to discriminate between α- and β-dislocations can be carried out in region C (see Fig. 7).

actually turned out to be a fairly good approximation for shallow craters. From the total buffer layer thickness and the lateral extension of the crater in the buffer-layer region the bevel-angle can be seen to be as small as ~ 0.09°. The cleaved sample shown in Fig. 2 is still too large for fitting onto a single TEM grid. Therefore, the sample was cleaved once more in the vertical direction approximately in the middle of the buffer layer and the two pieces were glued on two separate slot grids for the TEM investigation.

3. TEM INVESTIGATION

Figure 3a illustrates the way the BPC-prepared samples are mounted in the TEM holder. The backside of the sample points towards the incident electron beam. The cleavage plane is aligned parallel to the holder axis in order to allow convenient sample rotation about the cleavage edge using the α-tilt. Fig. 3b shows a sketch of the sample together with a schematic Kikuchi-map which is used to specify some sample orientations which are particularly useful for imaging and analysing misfit dislocations. After inserting the sample in the TEM column the crystal is close to the [00-1] zone axis orientation with the incident beam parallel to the (110) cleavage plane. By tilting the crystal about the [-110] direction one follows the vertical Kikuchi band towards the [11-2] zone axis. The lower sample edge with the buffer layer becomes electron transparent, as shown in the perspective view Fig. 1e (see also Figs. 4-6). Close to the [11-2] zone axis, at the regions A and B, respectively, appropriate imaging conditions for the reflections (-220) and (111) can be adjusted. It will be shown later (Figs. 4, 5) that WBDF imaging with these reflections is particularly useful for the Burgers vector analysis of 60° misfit dislocations. Furthermore by tilting the sample towards the [01-1] zone axis, which requires a combination of α-tilt and β-tilt, crystal orientations can be adjusted, for which the reflection (200) and two high odd-index reflections, like (11,1,1) and (-9,1,1), are simultaneously excited (region C). These excitation conditions can be exploited for determining the sign of the crystal polarity in polar layers by convergent beam electron diffraction (CBED). In the case of the InGaP/InGaAs/Ge solar cell structure

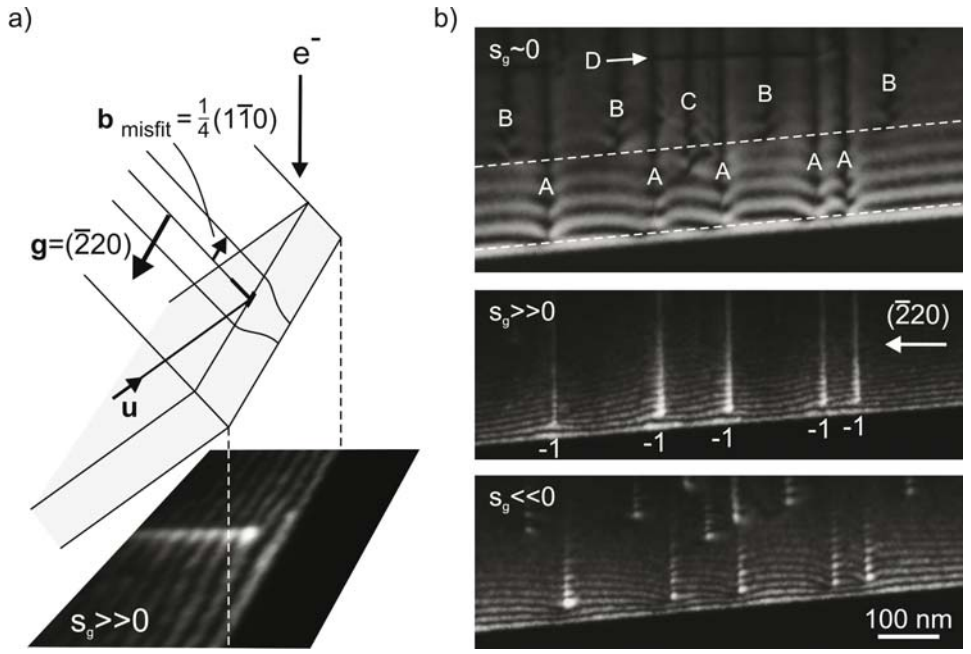


Fig. 4. Determination of the misfit component of the Burgers vectors of 60° misfit dislocations from (-220) weak-beam dark-field (WBDF) images. a) Schematic of the wedge-shaped sample containing a 60° misfit dislocation relaxing compressive layer strain (only the misfit component of the Burgers vector is shown) and corresponding thickness-fringe termination in a (-220) WBDF image. b) DF images formed with **g** = (-220) near Bragg-condition (top) and under weak-beam condition with large positive (middle) and large negative excitation error (bottom). The images show five misfit dislocations (marked A) contained in the second interface of the step graded buffer layer (cf. Fig. 2) and further dislocations (marked B, C) in or close to the next interface below. The projected intersection lines of the two interfaces and the cleavage plane are marked by dashed lines in the topmost DF-image. The value of **g**·**b** (=-1 for the five dislocations A) can be directly deduced from the termination of the thickness fringes in the WBDF-images at the intersection points of the dislocations with the cleavage plane. As expected all five dislocations contribute to relaxation of compressive layer strain. The dislocation marked D belongs to the array of perpendicular dislocation along [-110].

the sign of the crystal polarity tells us how the polar InGaAs material grows on the non-polar Ge substrate. Moreover, knowing the sign of the crystal polarity allows us to discriminate between α-dislocations and β-dislocations in the buffer layer.

3.1 Misfit Component of the Burgers Vector

Figure 4 illustrates the imaging of misfit dislocations with the (-220) reflection (area A in Fig. 3) and the determination of the misfit component of the Burgers vectors from WBDF images. A typical DF-image taken close to Bragg-condition ($s_g \sim 0$) is shown in the top part of Fig. 4b. Because of the wedge-shape of the BPC-prepared sample thickness fringes ran parallel to the sample edge. Misfit dislocations are clearly revealed as broad dark lines interrupting the thickness fringes. The five misfit dislocations marked A all end at the same small distance from the sample edge whereas the four misfit dislocations marked B end at a larger distance from the edge. The reason for this is that the dislocations A and B belong to different interfaces of the step graded buffer with the dislocations B belonging to an interface closer to the substrate (cf. Fig. 1e). The dislocation marked C ends between

the dislocations A and B. Hence, it can be concluded that this dislocation is located inside the layer between the two interfaces. In the centre and bottom part of Fig. 4b WBDF images taken with large positive respective negative excitation error are shown. As expected for WBDF images the spacing of the thickness fringes is reduced and the dislocations appear as narrow bright lines. At the end point of each dislocation line, corresponding to the intersection of the dislocation with the cleavage plane, a single thickness fringe terminates from either the right or left side, depending on the sign of the excitation error.

According to Ishida et al (1980) the termination of thickness fringes in WBDF images of dislocation/surface intersections can be exploited for the determination of the Burgers vector of the dislocation. The number of terminating thickness fringes is equal to $\mathbf{g}\cdot\mathbf{b}$ with $\mathbf{g}$ and $\mathbf{b}$ denoting the diffraction vector and Burgers vector, respectively. The side from which the terminating fringe enters depends on the sign of $\mathbf{g}\cdot\mathbf{b}$ and the sign of the excitation error s_g. Fig. 4a schematically shows the geometry of the sample in a perspective view together with a WBDF-image of a single 60° misfit dislocation. Since the dislocation contrast in the image is largely determined by the misfit component of the 60° dislocation ($\mathbf{g}\cdot\mathbf{b} = \mathbf{g}\cdot\mathbf{b}_{misfit}$) the drawing illustrates only this component. It can be seen either from simple geometrical considerations or from an analysis similar to that given by Ishida et al. that for the chosen excitation condition ($\mathbf{g}$ = (-220), $s_g >> 0$) the observed termination of the thickness fringe corresponds to the illustrated case of a half plane inserted from the substrate side. This dislocation has the "correct" sign of the Burgers vector for relaxing compressive in-plane strain in the $In_xGa_{1-x}As$ buffer layer. The same conclusion applies for the dislocations in Fig. 4b. We have studied many dislocations in this way by simply shifting the sample under the electron beam. Due to the complete absence of sample bending in the wedge-shaped BPC-prepared samples the excitation condition remains fixed during sample shift allowing fast collection and convenient analysis of WBDF-images. So far we did not find any dislocation with a "wrong" sign of the Burgers vector, as reported by some other authors (Dixon and Goodhew 1990, Matragano et al 1996)

3.2 Twist and Tilt Component of the Burgers Vector

Figure 5 illustrates the imaging of misfit dislocations with the (111) reflection (area B in Fig. 3) and the determination of the twist and tilt component of the Burgers vectors. Fig. 5b shows DF-images of the same group of dislocations shown by Fig. 4b. The top image in Fig. 5b was obtained near Bragg condition ($s_g \sim 0$) whereas the two images below were taken under weak-beam conditions with $s_g >> 0$ and $s_g << 0$, respectively. Terminations of thickness fringes at the dislocations are nicely revealed in both WBDF-images. Changing the sign of s_g changes the side from which the terminating fringe enters. Four of the five dislocations show termination of one fringe, indicating $\mathbf{g}\cdot\mathbf{b} = 1$ (for the sign see below), whereas the dislocation on the left shows weak contrast and no fringe termination, pointing to $\mathbf{g}\cdot\mathbf{b} = 0$. Fig. 5a shows again a WBDF image of two dislocations together with a schematic of the sample in perspective view. Since the images are insensitive to the misfit component of the Burgers vector ($\mathbf{g}\cdot\mathbf{b}_{misfit} = 0$) only the twist and tilt components of the Burgers vectors are shown. The twist (or screw) component of the 60° misfit dislocation can either be +¼[110] or -¼[110]. On the other hand, the tilt component may correspond to either +½[001] or -½[001]. Thus there are four possible combinations of twist and tilt components. It can be seen either from geometrical considerations or from an analysis similar to that given by Ishida et al (1980) that for the chosen excitation condition ($\mathbf{g}$ = (111), $s_g >> 0$), the observed termination of thickness fringes from the right side corresponds to the case $\mathbf{g}\cdot\mathbf{b} = 1$, which uniquely determines both, the twist and tilt component (bold arrows). Similarly, thickness fringe termination from the left would correspond to case $\mathbf{g}\cdot\mathbf{b} = -1$, in which case the tilt and twist component of the Burgers vector would be uniquely identified as indicated by the dashed vectors. However, for dislocations which show no thickness fringe termination, $\mathbf{g}\cdot\mathbf{b} = 0$, like for the dislocation on the left in Fig. 5b, i.e. there remain two possible combinations of twist and tilt component, namely ¼[110] - ½[001] or -¼[110] + ½[001]. In order to completely determine the Burgers vector for such dislocations a WBDF image formed with a different reflection has to be evaluated, e.g. a reflection of type {113}. However, for a more efficient statistical evaluation of several hundreds of misfit dislocations it may be sufficient to use only (111) WBDF images and live with the fact that the Burgers vector is only completely determined for about half of the dislocations. The analytical results for the remaining dislocations can also be included in a statistical analysis (cf. section 4 and Tab. 1).

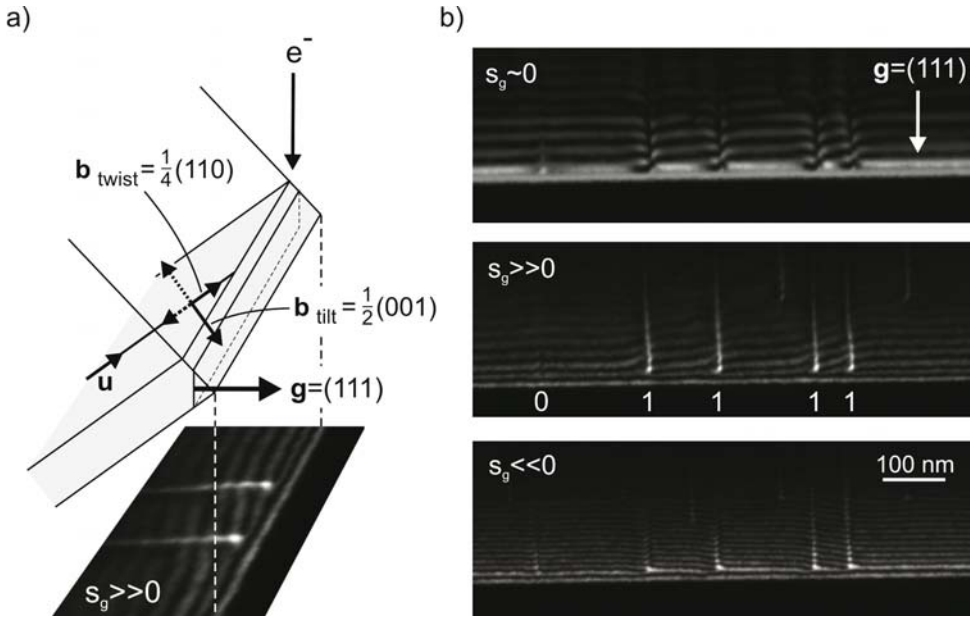


Fig. 5. Determination of the screw and tilt components of the Burgers vectors of 60° misfit dislocations from (111) weak-beam dark-field (WBDF) images. a) Experimental (111) WBDF image of two 60° misfit dislocations and perspective view of the sample showing the possible twist (= screw) and tilt components of the Burgers vector. b) Dark-field images formed with **g**=(111) near Bragg-condition (top) and under weak-beam condition with large positive (middle) and large negative (bottom) excitation error. The images show five misfit dislocations in an interface of the step graded buffer layer (cf. Fig. 4). The values of **g**·**b** indicated in the middle image can be deduced from the termination of the thickness fringes at the intersection points of the dislocations with the cleavage plane (for details see text).

3.3 Direction and Magnitude of Substrate Miscut

Substrate miscut can lead to pronounced asymmetries in the population of the glide systems of 60° misfit dislocations, giving rise to phenomena like crystallographic layer tilt (see section 4). In this situation, Burgers vector analysis as described above is only meaningful if the absolute orientation of the miscut in the TEM sample is known. Figure 6 illustrates how this information can be obtained in a straightforward manner during TEM work by exploiting projection effects in TEM images of the sample edge. For the InGaP/InGaAs/Ge-sample studied here the [001] substrate miscut pointed towards the [-110] in-plane direction and amounted to nominally 6°. The cleavage plane of the TEM sample was chosen to be (110) (Fig. 6a) since the main interest was to study dislocations running parallel to the step edges (see section 4). As result of the sample miscut the angle between the projected sample edge and the projected dislocation lines in (-220) images deviates from 90° by a small angle β (Fig. 6b,c). The orientation of the miscut (or the step direction) can be directly deduced from the direction of this deviation. Moreover, the miscut angle γ can be estimated with the relationship $\tan\gamma = \tan\beta/\cos\alpha$ (α: sample tilt angle with respect to [001]) which is obtained from simple geometrical considerations. For the image shown in Fig. 6c $\alpha \sim 40°$ and $\beta \sim 4.5°$, giving a miscut angle of $\gamma = 5.9°$ which is very close to the nominal value of 6°. The analysis is generally not expected to give such precise values of the miscut angle, however. Possible errors can result from changes in the projected edge direction due to the bevel angle (~ 0.1°) introduced by the BPC preparation, due to crystallographic layer tilt resulting from an asymmetric population of the glide systems (< 0.5°, cf. section 4) and due to a bad cleavage. Thus, the aim of the analysis is more to determine the direction of the miscut rather than its absolute value.

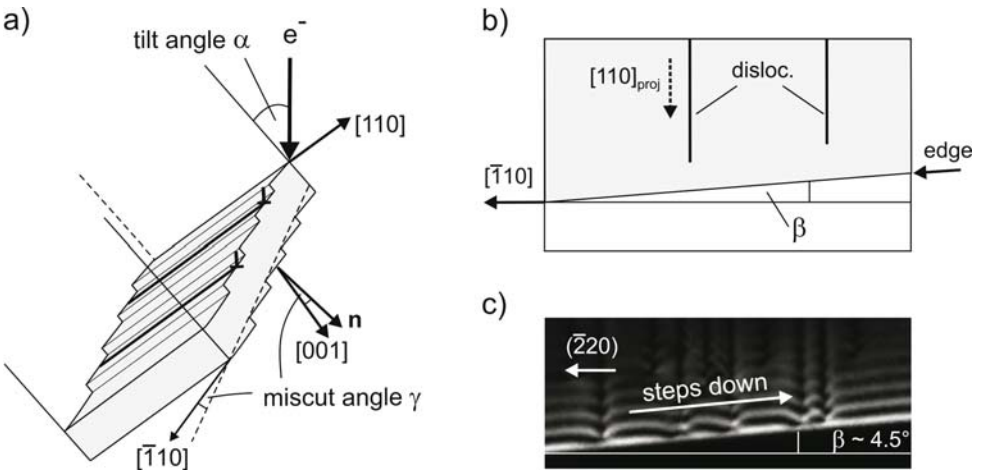


Fig. 6. Determination of the direction of miscut from projection effects in (-220) dark images of the wedge-shaped crystal sample: a) perspective view, b) projection from the direction of the incident electron beam, and c) experimental (-220) dark field image (cf. Fig. 4). The angle between the (projected) dislocation direction and the (projected) sample edge deviates from 90° by a small angle β. The sign of β directly shows the direction of the miscut. The miscut angle can be estimated from the angle β and the tilt angle α using the relationship $\tan \gamma = \tan \beta / \cos \alpha$.

3.4 Crystal Polarity: α- and β-Dislocations

If the heterostructure contains polar materials, like the III-V or II-VI compound semiconductors, a complete characterisation of the dislocations has to include also the determination of the sign of the crystal polarity. Knowing the crystal polarity allows to discriminate between α- and β-dislocations. In the case of the InGaP/InGaAs/Ge-sample studied here the question of crystal polarity is particularly interesting because polar materials (InGaAs, InGaP) were grown on top of a non-polar substrate (Ge), which may result in the growth of domains with opposite polarities separated by inversion domain boundaries. For the case investigated here, however, one of the two polarities has been successfully suppressed by the growth of a special nucleation layer on the vicinal Ge substrate, as we could show by our TEM analysis. The sign of the remaining polarity can be determined from the wedge-shaped TEM sample by tilting the crystal towards a <101> zone axis, as indicated in the schematic Kikuchi pattern in Fig. 3b (region C). Close to this zone axes the convergent beam electron diffraction (CBED) method by Taftø and Spence (1982) for determining the sign of the crystal polarity can be applied. We have carried out the polarity analysis in the bottom-most layer of the InGaAs-buffer since this layer has a negligible In-concentration (0.2%) and therefore can be treated in the polarity analysis like GaAs (see Fig. 7). The result of the analysis is shown also by the projected Ga-As dumbbell structure in the schematic cross-section Fig. 8a. It follows that the dislocations with line direction **u** = [110] running parallel to the step edges of the vicinal substrate are β-dislocations whereas the dislocations running perpendicular to the step edges are α-dislocations (following the convention after Ulhaq-Bouillet et al (1994)). We finally mention that while the CBED method by Taftoe and Spence (1982) allows to reliably determine the polarity of compounds with a small mass difference of the constituting atoms, like GaAs, a different but related method (Spiecker et al. 2003a, 2003b) has to be used if compounds with a large mass difference are to be studied, like InP.

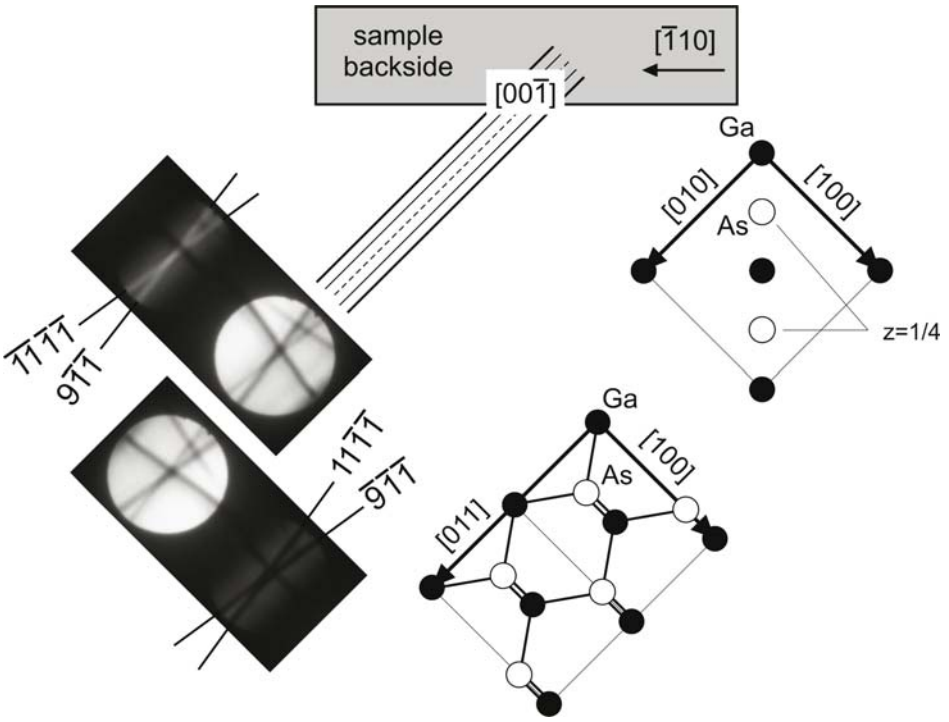


Fig. 7. Determination of the sign of the crystal polarity in the BPC-prepared sample by applying the CBED-method by Taftoe and Spence (1982) to the bottom-most layer (0.2 % In) of the InGaAs-buffer. The analysis is carried out near the [01-1] zone axis (cf. Fig. 3b, region C). The [01-1] projected unit cell is deduced from the dynamic contrast asymmetries between the (200) and (-200) CBED-disks. From the corresponding projection of the unit cell in the [00-1] zone axis the Ga-As dumbbell structure in cross-section geometry can be easily deduced (cf. Fig. 8a).

4. APPLICATION EXAMPLE: DETERMINATION OF CRYSTALLOGRAPHIC LAYER TILT

The growth of buffer layers on vicinal substrates generally results in an asymmetric dislocation population of the different glide systems of 60° misfit dislocations. As a consequence the [001] direction of layers above the dislocation network is tilted relative to the [001] direction of the substrate. This phenomenon is known as “crystallographic layer tilt”. According to Nagai (1974) there is also a coherent contribution to the crystallographic layer tilt, i.e. a contribution not related to dislocations. However, in the presence of an asymmetric dislocation population the tilt due to dislocations generally dominates. For the InGaP/InGaAs/Ge triple solar cell structure studied in this work Fig. 8b shows a high-resolution XRD reciprocal space map (RSM) of the (004) reflection which clearly reveals the presence of crystallographic layer tilt. The 6° substrate miscut towards [1-10] is reflected in a corresponding rotation of the scan box with respect to the coordinate system comprised of coordinates parallel and perpendicular to the surface. The InGaP and InGaAs layers above the step-graded $In_xGa_{1-x}As$ buffer layer show a layer tilt of 0.32° relative to the Ge-substrate. The tilt has the effect of reducing the miscut or the density of surface/interface steps in the upper layers. From the direction and size of the layer tilt it is expected that the tilt is caused by an asymmetry in the dislocation population of the (-111) and (1-11) glide planes, containing more dislocations on (-111) planes, as indicated in the schematic drawing Fig. 8a. Referred to the Burgers vectors of the dislocations this means that there should exist a net tilt component due to different numbers of 60° misfit dislocations with $\mathbf{b}_{tilt}$ = +a/2[001] and -a/2[001].

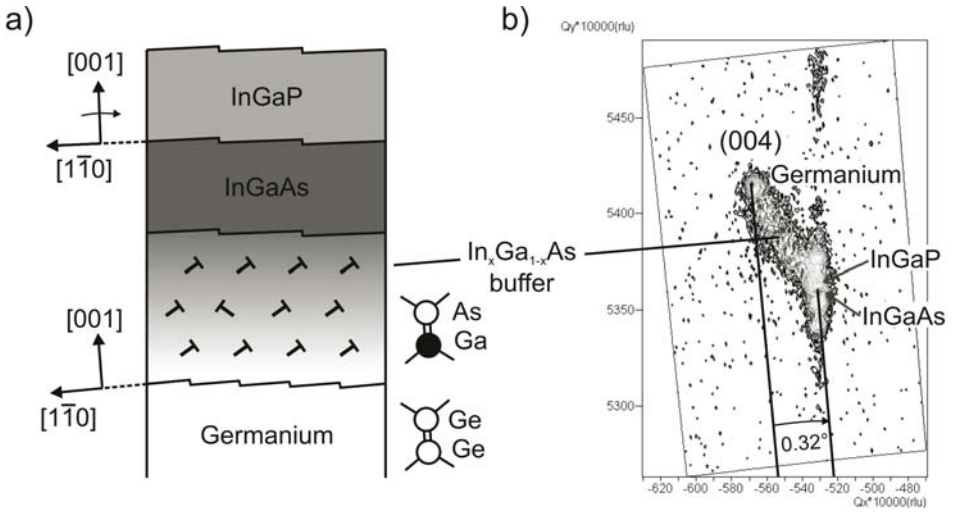


Fig. 8. Preferential population of 60° misfit dislocations on the glide plane (-111) relative to (1-11) and corresponding crystallographic layer tilt measured by HRXRD. a) Simplified drawing of the InGaP/InGaAs/Ge triple solar cell structure. An asymmetric dislocation population of the two glide planes and its effect on the [001] direction and the step density in the upper layers and interfaces are illustrated. Also the result of the polarity analysis (section 3.4) is indicated by the projected Ga-As dumbbell structure. b) XRD Reciprocal Space Map (RSM) of the (004) reflection showing that the 6° miscut of the Ge-substrate is reduced in the top-layers by about 0.32°.

Our novel TEM method can be used to investigate such asymmetries in the Burgers vector distribution. In order to obtain statistically relevant data the Burgers vector analysis, illustrated in Figs. 3 and 4 for a small group of five dislocations, has to be extended to as many as possible dislocations. In practice series of WBDF images taken along the sample edge have to be evaluated with respect to the termination of thickness fringes at dislocation/cleavage-plane intersections. As a first application and in order to show the applicability of the method we have analysed ~ 300 misfit dislocations with line direction [110] in the first interface of the graded buffer layer (between 0.2% and 5.5% Indium) by taking series of (111) WBDF images covering a total length of 65 µm along the sample edge. We emphasise that the series have been taken in one run by simply shifting the sample relative to the incident electron beam and sometimes adjusting the focus, without changing only once the sample orientation. For each dislocation the value of $(111)\cdot\mathbf{b}$ has been deduced from the termination of the thickness fringes (cf. Fig. 4). The results are given in the last column of Tab. 1. Since we did not find any dislocation with a "wrong" sign of the Burgers vector from (-220) WBDF images (cf. Fig. 3) Tab. 1 only lists those glide systems which contribute to relaxation of compressive layer strain. In addition to the four glide systems of 60° misfit dislocations with line direction $\mathbf{u}$ = [110] the table contains the 90° or Lomer dislocation which can be formed by reaction of two 60° dislocations. However, from analyses of (-220) WBDF images we did not find any Lomer dislocation among the ~ 300 dislocations investigated (see last column of Tab. 1).

The result show a pronounced asymmetry (135:20 or 87%:13%) in the populations of the glide systems ½[101](-111) and ½[0-1-1](1-11) for which $(111)\cdot\mathbf{b}$ = +1 and $(111)\cdot\mathbf{b}$ = -1, respectively. Since the (110) plane is a symmetry plane in the sample the observed asymmetry directly reflects an asymmetry in the population of the tilt component $\mathbf{b}_{tilt}$ of the Burgers vectors (and not of the twist component $\mathbf{b}_{twist}$). From symmetry arguments a similar asymmetry is expected for the group of 142 dislocations belonging to either of the glide systems ½[0-11](-111) and ½[10-1](1-11), which both fulfill $(111)\cdot\mathbf{b}$ = 0 and can therefore not be discriminated from the (111) WBDF images alone. In accordance with this statistical interpretation is the observation that the number of dislocations with either $(111)\cdot\mathbf{b}$ = +1 or -1 is of the same order as the number of dislocations with $(111)\cdot\mathbf{b}$ = 0.

Dislocation type	Glide system (**b**, **n**)	$\mathbf{b}_{misfit}$	$\mathbf{b}_{twist}$	$\mathbf{b}_{tilt}$	(111)·**b**	# dislocations (1st interface)
60°	½[101](-111)	¼[1-10]	¼[110]	½[001]	1	135
	½[0-11](-111)	¼[1-10]	¼[-1-10]	½[001]	0	142
	½[10-1](1-11)	¼[1-10]	¼[110]	½[00-1]	0	
	½[0-1-1](1-11)	¼[1-10]	¼[-1-10]	½[00-1]	-1	20
edge	½[1-10](001)	½[1-10]	-	-	0	0*

Tab. 1. Glide systems and corresponding Burgers vector components (misfit, twist, tilt) of misfit dislocations along **u** = [110] that relax compressive layer strain, and results of the Burgers vector analysis of ~ 300 dislocations in the 1st interface of the step-graded InGaAs-buffer. The numbers in the last column have been obtained from evaluation of a long series of (111) WBDF images covering a total distance of 65 μm along the sample edge (* from (-220) WBDF images). The mean dislocation spacing in the interface is 173 nm. Only for 10 dislocations, not included in the list, the value of (111)·**b** could not be reliably determined from the thickness fringe termination because of contrast interference with the contrast of dislocations along **u** = [1-10].

The preferred occurrence of dislocations on (-111) glide plane relative to those on (1-11) is in agreement with a crystallographic layer tilt that reduces the miscut, as observed also by the HRXRD measurements (Fig. 8b). The angle of the crystallographic layer tilt to which the dislocations in the first interface contribute can be estimated as follows using the data of Tab. 1: According to a 87%:13% asymmetry in the population of the two possible tilt components 74 out of 100 dislocations effectively contribute to crystallographic layer tilt, since the tilt components of the remaining 26 dislocations cancel out. The crystallographic layer tilt can therefore be described by an array of interface edge dislocations with Burgers vectors $\mathbf{b}_{tilt}$ = ½[001] (in units of the lattice constant) and mean spacing of 173 nm/0.74 = 233 nm. Using the formula for a small-angle grain boundary the tilt can be estimated to $\alpha \sim |\mathbf{b}_{tilt}|/233$ nm =0.07°. Assuming similar contributions from the other interfaces containing dislocations the 0.32° crystallographic layer tilt measured by HRXRD can be realistically assigned to the asymmetric population of the glide systems with 60° misfit dislocations.

5. DISCUSSION, SUMMARY AND CONCLUSION

The results demonstrate that the novel TEM method is capable of characterising quantitatively distributions of large numbers of misfit dislocations over macroscopic distances along interfaces which are deeply buried in a complex semiconductor heterostructure. Quantitative characterisation means not only the evaluation of dislocation densities in the individual interfaces but also the determination of the Burgers vectors of the individual dislocations. The method allows us for the first time to obtain statistically relevant data on the dislocation population of glide systems also in more complex semiconductor heterostructures. In a first application we have applied the method to a graded buffer layer in a high-efficiency triple solar cell. The analysis demonstrates that the method is capable of dealing with "real" structures consisting of, for instance, polar and non-polar materials, layers with residual strain and thick top-layers.

The main advantages of the BPC preparation method compared to conventional preparation methods are:

- the extremely small bevel angle produced by the front-side ion-beam milling allows the study of large numbers of dislocations at different depths below the surface,
- the wedge-shape of the sample makes it possible to use thickness fringes in WBDF-images for reliable Burgers vector determination, and
- the complete absence of sample bending enables a fast investigation of many dislocations along the sample edge because the excitation conditions stay constant while shifting the sample relative to the imaging electron beam.

The most crucial step of the BPC method is the crystal cleavage (Fig. 1c). One important

question is whether the cleavage process itself introduces dislocations. Only after very bad cleavage resulting in strongly faceted cleavage surfaces one occasionally observes some clues of additional dislocations which, however, can be easily distinguished from the misfit dislocations. No such additional dislocations were observed for the case shown in Fig. 3a, however. We have carefully checked also the opposite sample piece produced by the cleavage process and have found a one-to-one correspondence of the misfit dislocations on either sides of the cleavage plane. Other interesting points of concern are which types of heterostructures show sufficiently good cleavage behaviour to allow application of our method, and whether good cleavage can be achieved across the dislocated heterostructure. So far we have tested the method for InGaAs-buffer layers grown on Ge and GaAs substrates. GaAs, like other zincblende compounds, shows a much better cleavage behaviour than Ge, so that the wide field of mismatched heterostructures based on III-V or II-VI zincblende materials should be accessible. We are currently testing the method for GeSi/Si heterostructures. Si is known to show good cleavage behaviour on (110) planes if the sample is made thin enough.

The new method to characterise by TEM distributions of misfit dislocations over macroscopic distances quantitatively with respect to their Burgers vectors allows us to address a range of current research topics in the field of mismatched heteroepitaxy, as well as revisiting some long-standing problems which could not be solved so far because of the lack of an appropriate TEM method. Several applications of the new method are:

- correlation between the asymmetric population of glide systems and crystallographic layer tilt (cf. section 4),
- correlation between Burgers vector bunching and layer mosaicity,
- relationship between Burgers vector bunching and surface cross-hatching,
- role of Lomer dislocations for strain relaxation in graded buffer layers,
- determination of spatial correlation functions of dislocation arrangements for quantitative comparison with experimental and simulated reciprocal space maps (RSM),
- presence (or absence) of misfit dislocations with a “wrong” sign of the Burgers vector and
- determination of dislocation densities in buried interfaces with good statistics.

Furthermore the method can also be used for a quick inspection of the quality of complex heterostructures. With some experience the BPC preparation can be carried out in less than 1h.

In conclusion, we have developed a TEM method which allows us to characterise quantitatively distributions of misfit dislocations over large macroscopic distances along interfaces in semiconductor heterostructures. The method combines a novel BPC sample preparation with the imaging and Burgers vector analysis of dislocations by the weak-beam dark-field (WBDF) imaging technique. The applicability of the method has been convincingly demonstrated by analysing misfit dislocations in an interface of a complex semiconductor multilayer system consisting of step-graded $In_xGa_{1-x}As$-buffer layers embedded in an InGaP/InGaAs/Ge triple solar cell structure. By evaluating the glide systems of several hundreds of 60° misfit dislocations in a deeply buried interface, estimating their contribution to crystallographic layer tilt, and showing a first correlation with high-resolution XRD measurements of this phenomenon, we demonstrated the great potential of the method for obtaining statistically relevant data on misfit dislocation networks. This opportunity opens a wide field of applications important for a better understanding of the formation of misfit dislocation networks in semiconductor heterostructures.

ACKNOWLEDGEMENTS

We are indebted to F Dimroth and A Bett from the Fraunhofer Institute for Solar Energy Systems (ISE) in Freiburg (Germany) for providing the InGaP/InGaAs/Ge triple solar cell heterostructures used in this study and for many valuable discussions.

REFERENCES

Abrahams M S, Weisberg L R, Buiocchi C J and Blanc J 1969 J. Mater. Sci. **4**, 223
Abrahams M S and Buiocchi C J 1974 J. Appl. Phys. **45**, 3315
Beanland R, Dunstan D J and Goodhew P J 1996 Adv. Phys. **45** 87
Bett A. W, Baur C, Dimroth F and Schöne J 2004 MRS, Fall Meeting, Boston USA

Dixon R H and Goodhew P J 1990 J Appl Phys **68** 3163
Fewster P F 2000 X-ray Scattering from Semiconductors (London, Imperial College Press)
Fitzgerald E A 1991 Mater. Sci. Rep. **7**, 87
Harame D L, Koester S J, Freeman G, Cottrel P, Rim K, Dehlinger G, Ahlgren D, Dunn J S, Greenberg D, Joseph A, Anderson F, Rieh J-S, Onge S, Coolbaugh D, Ramachandran V, Cressler J D and Subbanna S 2004 Appl. Surf. Sci. **224** 9
Holý V, Li JH, Bauer G, Schäffler F and Herzog H-J 1995 J. Appl. Phys. **78**, 5013
Holý V, Pietsch U and Baumbach T 1999 High-Resolution X-Ray Scattering from Thin Films and Multilayers (Berlin, Springer)
Ishida Y, Ishida H, Kohra K and Ichinose H 1980 Phil. Mag. **42**, 453
Kaganer V M, Köhler R, Schmidbauer M, Opitz R and Jenichen B 1997 Phys. Rev. B **55**, 1793
LeGoues F K, Mooney P M and Chu J O 1993 Appl. Phys. Lett. **62**, 140
Matragano M J, Ast D G, Shealy J R and Krishnamoorthy V J. 1996 Appl. Phys. **79**, 8371
Mooney P M, LeGoues F K, Tersoff J and Chu J O 1994 J. Appl. Phys. **75**, 3968
Nagai H 1974 J. Appl. Phys. **45**, 3789
Spiecker E and Jäger W 2002 J. Phys.: Condens. Matter **14**, 12767
Spiecker E, Jäger, Ch, Lu, H and Jäger W 2003 Microsc. Microanal. **9** (Suppl. 3), 94
Spiecker E, Jäger, Ch, Lu, H and Jäger W 2003 Inst. Phys. Conf. Ser. No. **180**, 233
Taftø, J and Spence, J C H 1982 J. Appl. Cryst. **15**, 60
Ulhaq-Bouillet C, Lefebvre A and Di Persio J 1994 Philos. Mag. A **69**, 995
Wang J, Steeds J W and Woolf D A 1992 Phil. Mag. A **65**, 829

Beta to alpha transition and defects on SiC on Si grown by CVD

F M Morales, Ch Förster, O Ambacher and J Pezoldt

Department of Nanotechnology, Centre for Micro- and Nanotechnology (ZMN), TU-Ilmenau, Gustav-Kirchhoff-Strasse 7, D-98693 Ilmenau, Germany, paco.morales@tu-ilmenau.de

ABSTRACT: The features of α-SiC (0001) epitaxially grown on top of β-SiC(111)/Si(111) is reported by means of transmission electron microscopy (TEM). Hexagonal and rhombohedral polytype nuclei, mainly 4H-SiC, appear after the growth of a fixed cubic SiC thickness which is related to the selected growth conditions: Si/C ratio and growth temperature. The defect structure of these multilayer systems (voids, planar defects, facets and polycrystalline top clusters) and the hexagonality of the SiC surface are determined and described.

1. INTRODUCTION

SiC belongs to a group of materials able to form different structures. They only differ in the higher order coordination spheres and exhibit different stacking sequences along the direction of the close-packed basal plane. This structural behavior is called polytypism. From the point of view of solid-state devices, the most interesting property is the band gap. In the case of SiC, this parameter varies from 2.4 eV for β-SiC (3C) to 3.4 eV for α-SiC (2H). These large variations in band gap energies make SiC work as a family of different semiconductor materials with identical chemical composition. Therefore, chemical degradation is not possible in heterostructures or low-dimensional structures based on different polytypes of SiC. The precondition for the formation of such exciting structures is the intentional control of polytype transition during epitaxial growth or device processing. In this context, it is important to work out rules for a desired polytype change as a consequence of changing technologically relevant parameters.

α to β polytype transitions can be induced under equilibrium conditions, i.e. epitaxial growth at supersaturations exceeding a critical limit, ion implantation, mechanical deformation or thermal and/or pressure shocking. The reverse transition from β to α is possible during heteroepitaxial growth of β-SiC on α-SiC (0001) substrates in cold wall chemical vapor deposition (CVD) reactors while pulsed laser deposition allow the formation of β (3C) or α (2H or 4H-SiC) polytypes on sapphire. It is definitely of greater difficulty to induce the transition from cubic (β) to hexagonal and/or rhombohedral (α) SiC, and even more difficult when the conditions do not vary during the growth process as it is in the current experiments. Control of heteropolytypic transitions from the cubic phase to the hexagonal one was achieved only with solid source molecular beam epitaxy (MBE) (Fissel 2003) or by a combination of sublimation growth and ion implantation (Pezoldt 1992). If Si is used as substrate, β-SiC is normally grown by CVD or MBE. Nevertheless, at this time there is no reliable technique to grow α- SiC polytypes on the cubic phase. A few attempts by CVD have shown the presence of hexagonal domains included in cubic SiC layers on Si (Pfennighaus 1997) or via nano-sized silicon nitride precursors, not fully orientated α-SiC could be grown on Si (Liu 1999). Here, it has been possible to delimitate the region of temperatures and Si to C fluxes where the β to α SiC transformation occurs in ultra high vacuum CVD on Si (UHV-CVD). The aim of this work is to study the microstructure of these original α-SiC/β-SiC/Si heterostructures using TEM.

2. EXPERIMENTAL

The deposition was carried out in a UHV chamber with a base pressure of $1x10^{-8}$ mbar. For the growth, a mixture of SiH_4, C_2H_4 and H_2 is used. The RCA cleaned Si (111) wafers were loaded and

transferred into the deposition chamber, out-gassed at 350°C for 30 min and heated to 450°C. In order to carbonize the Si surface, C_2H_4 was introduced with a flow rate of 7 sccm. After 10 min, the temperature was increased up to 940°C with a heating rate of 0.3 K/s. Thereafter the flow rates of H_2 and C_2H_4 were set up to 10 and 1 sccm respectively while SiH_4 was varied between 1 and 2 sccm. The substrate temperature was selected to be between 950 and 1050°C with a deposition time from 60 and 720 min. Finally, the substrate was cooled down at 2 K/s. Specimens for plan-view (PVTEM) and cross-section (XTEM) observations were prepared using mechanical thinning and Ar^+ milling in a Gatan Precision Ion Polishing System (PIPS) system. Conventional TEM (CTEM) was carried out in a TECNAI 20S-TWIN (FEI) and a JEOL 2010F electron microscope was used for high-resolution TEM (HRTEM), while selected area electron diffraction (SAED) was performed in both microscopes.

3. RESULTS AND DISCUSSION

TEM inspection has demonstrated that samples consist of SiC layer(s) heteroepitaxially placed on the Si (111) substrate. There appeared two groups of specimens, the first developed only cubic SiC layers, and the second showed the appearance of α-SiC 3D nuclei after the cubic SiC layer had reached a definite thickness depending on the growth conditions. The α and β SiC layers exhibit some characteristic defects as voids at the interface beneath the SiC layer, stacking faults (SF) and twins oblique and parallel to the interface in the β-SiC structure, faceting of α-SiC nuclei often continuing {111} walls dividing cubic SiC domains and sometimes top polycrystalline SiC hillocks. In a previous report (Morales 2005) it has been stated by RHEED experiments that 4H-SiC and, to a minor extent, 6H-SiC are the main phases formed among the α-SiC nuclei, even though other rhombohedral or hexagonal polytypes, α-SiC varieties mixed in syntactic coalescence and one dimensionally disordered SFs were found. Depending upon the growth conditions, α and/or β-SiC form on top of an initial β-SiC layer. α-SiC develops under relatively C-rich conditions (Si/C ratio=1.3-1.9) compared to the growth conditions where only β-SiC is stabilized (Si/C>2). Si rich conditions allowed faster growth rates. It could be concluded that α–SiC develops after the formation of an effective cubic capping thickness when the Si out-diffusion from the substrate stops and new thermodynamic conditions (C rich) make the ordered cubic structure develop disordered SFs, giving rise to SF long range ordering and new polytype formation. Figure 1a shows the typical structure of one of the samples where the β to α transition occurs. 3D nuclei of α-SiC appear after 85 nm of β-SiC for the sample grown at 1000°C at a Si/C ratio of 1.65. Every α-SiC nucleus reaches a thickness of up to 30 nm and its size and shape is associated with the width of the terraces developed in different domains at the top of the stepped cubic SiC subsurface. These domains, often twinned against each other, are the result of the coalescence of SiC crystals. They are arranged in two symmetric and inverted orientations related to the possible equivalent atomic sites on the Si substrate in the nucleation stage and promoted by initial roughness or the creation of SFs on the first grown layers. As a result, double positioning boundaries (DPBs) appear as oblique SFs through the cubic SiC layers inclined ±70.5° with respect to the interface plane (angles that correspond to those between {111} planes in a fcc structure). SAED patterns in PVTEM preparations showed 022 reflections for β-SiC oriented in the [111] zone axis (brighter spots in Fig. 1b, see also simulation in Fig. 1d) and a set of weaker spots aligned with the cubic 224 reflections and placed at 1/3 and 2/3 of their distances (encircled). These diffraction patterns are characteristic for short period hexagonal or rhombohedral SiC polytypes taken along the [0001] direction, being the inner reflections associated to $01\bar{1}0$ planes of the hcp primitive cell that characterize both structures (see simulation for 4H-SiC in Fig. 1c). Moreover, diffraction patterns taken in this orientation, besides giving useful data about the isotropy of the structure in the perpendicular *a* and *b* axes, do not give any information on the ordering of close-packed SiC layers along the *c* axis of growth. In this way, a high density of one dimensionally disordered (ODD) SFs parallel to the surface plane would also promote the formation of such diffraction patterns. More detailed structural information can be extracted from XTEM SAED patterns taken along the <110> direction of the Si substrate. Aligned Si and SiC diffraction spots in the patterns taken from near-interface regions are indicative of domains in the β-SiC epilayer grown heteroepitaxially (Fig. 1e) or sometimes twinned with respect to the latter by {111} or {112} planes (extra spots (T) in Fig. 1f). On the other hand, when the SiC surface nuclei contribute to the diffraction (Fig. 1g with Si and Fig. 1h), streaking and new extra spots (S) aligned and vertically joining the β-SiC reflections appear and indicate disordered and ordered SFs along the [111] direction, respectively.

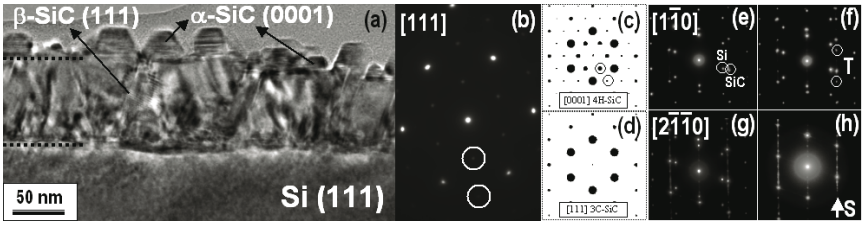


Fig. 1. (a) BF-XTEM micrograph from a sample with α-SiC surface nuclei. (b) PVTEM-SAED pattern and simulated diffraction for α-SiC (4H) (c) and β-SiC (d). (e-f) SAED patterns along the <110> zone axis from the Si/SiC near-interface region and (g-h) taking into account the SiC surface nuclei.

Figure 2 shows an HRTEM micrograph in XTEM, 90° rotated with respect to Fig. 1, for a sample grown at 1000°C using a Si/C relation of 1.45 (β-SiC layer ~50 nm). Local regions where respective fast Fourier transform (FFT) spectra were taken are labeled; showing single crystalline Si (1); ODD SFs in parallel (2), oblique (4) and their cross directions (3); defect free β-SiC crystal (5) and α-SiC single-crystal (6). Since FFTs are equivalent to SAED patterns, some reciprocal reflections are labeled in the fcc and hcp systems. Moreover, the overlapping of two twinned areas showed unusual features that in the past were often misinterpreted as 9R-SiC inclusions in the cubic matrix. These regions are often located near the Si substrate. The respective SAED pattern and FFT spectra are shown along with its HREM micrographs in Fig. 3a. Aligned extra dots in the FFT at one and two thirds of the distance between related contributions of the β-SiC resemble the α-SiC structure. Furthermore, investigations by Kaiser (1999a) have clarified by means of image simulations that these structures with three fold periodicity showing fringes spaced three times the {111} interplanar spacing of SiC (~0.75 nm) should be unambiguously associated to an overlapping of 3C-SiC domains which {112}/{112} or {115}/{111} Σ3 twin boundaries are parallel or inclined about 30° to the <110> direction.

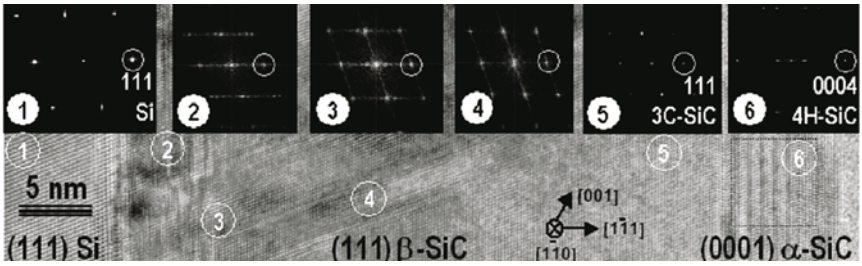


Fig. 2. HREM micrograph from a Si/β-SiC/α-SiC heterostructure and FFTs associated to labelled local regions.

Figure 3b shows the HREM picture of the squared region in Fig. 2. The structure of the 4H-SiC island reasonably matches with the simulation (conditions: 14 nm thick; 65 nm defocus), and the corresponding ABCBA… stacking sequence. A micro-twin is also noticed (between dotted lines). Note that smearing out of contrast related to atomic columns can be occasioned by deviations of milliradians with respect to the [2$\bar{1}\bar{1}$0] direction (Kaiser 1999b). Since the micrograph was registered when the Si substrate was orientated in the <110> zone axis, there must exist a small misorientation (tilt or twin) between both crystals. Pure α-SiC polytypes were not always observed and the coexistence of different polytypes in syntactic coalescence can be worked out. Furthermore, the occurrence of ODD has to be taken into account. As it is displayed in Fig. 3c, at the boundary of the β to α-SiC transition, the ABCA… stacking sequence of layers is firstly disrupted and subsequently long range ordered. Note that in certain cases, the zig-zag stacking sequence is not perfect in the α-SiC region and does not exhibit a parallel advance. These intrinsic SFs are bordered by a Shockley partial dislocation and were often observed. The smearing out of contrast in certain planes is likely to be promoted by the commented possible small tilting and/or overlapping of domains where the stacking sequence is not fully coincident. Fine investigations of α-SiC related extra reflections in SAED patterns taken from small areas are not straightforward and must be cautiously carried out. Even though 4H-SiC assignable reflections have predominantly appeared among the studied RHEED and SAED patterns, assuming syntactic coalescence of

only pure hexagonal and rhombohedral polytypes, it is possible to index spots as those shown in Fig. 4 as possibly caused by 6H, 2H, 15R; 21R, 27R, 33R and 51 R-SiC polytypes. This SAED pattern was registered from an α-SiC pyramidal island around 30 nm width and 15 nm height. Since available smaller SAED apertures were bigger than these small nuclei, some asymmetries were observed in the diffraction patterns. Furthermore, the 01-1N row of reflections is used in the analysis since it is readily understood that diffraction effects due to SFs in hcp crystals appear only in the [0001] direction. Figure 4b shows this expanded region in both inverted contrasts to allow a better visualization of diffraction spots. In these lines, the minimum measured distance between two extra spots is inversely proportional to the period of the hexagonal or to 1/3 of the period of rhombohedral polytype(s) inside the α-SiC nuclei. Arrows in grey stand for 4H-SiC reflections for which structure some reflections have also been indexed in the overview SAED pattern. It is known that disordered SFs could originate additional diffraction effects, namely; change in the diffraction peak intensities, broadening of the diffraction peaks, displacement of the peaks and asymmetry of the peak shapes (Sato and Nasu 1990). For these reasons, we would not strongly claim the undoubted contingency of the presented polytypes but would hypothesize that traces of their characteristic zig-zag sequences are commonly repeated inside the structure of α-SiC nuclei. In conclusion, in UHV-CVD growth, the formation of nanoscale α-SiC on β-SiC/Si(111) templates is possible at low temperatures (950-1050°C) by adjusting Si/C ratios. The α- to β-SiC transition is favoured under carbon-rich conditions. The defect microstructure has been assessed by TEM studies.

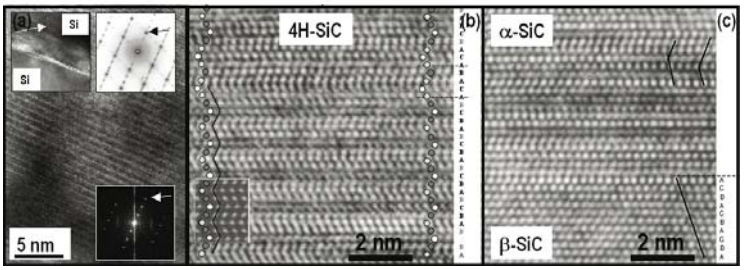


Fig. 3. HREM micrographs from a β-SiC 3-fold twinned area (a); a 4H-SiC island (b) and β to α transition (c).

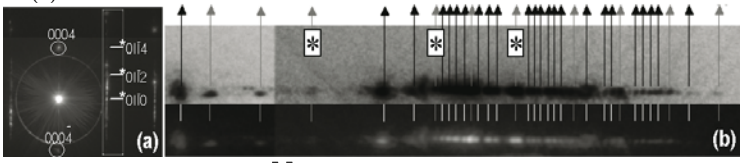


Fig. 4. SAED pattern along the $[2\bar{1}\bar{1}0]$ zone axis of an isolated α-SiC nucleus, exhibiting syntactic coalescence.

ACKNOWLEDGEMENT

F M Morales would like to thank the Alexander von Humboldt Foundation for economic support under a Humboldt Research Fellowship (SPA/1114640 STP).

REFERENCES

Fissel A 2003 Phys. Rep. **379**, 149
Kaiser U, Chuvilin A, Brown P D and Richter W 1999a Microsc. Microanal. **5**, 420
Kaiser U, Chuvilin A and Richter W 1999b Ultramicroscopy **76**, 2
Liu R, Yang B, Fu Z, Chen Q, Hong L, Li M, Liu Z and Ruan Y 1999 Thin Solid Films **345**, 188
Morales F M, Förster Ch, Ambacher O and Pezoldt J 2005 Proc. Electrochem. Soc. *in press*
Pezoldt J, Kalnin A A and Savelyev W D 1992 Nucl. Instr. Meth. **B65**, 361
Pfennighaus K, Fissel A, Kaiser U, Wendt M, Kraüßlich J, Peiter G, Scröter B and Richter W 1997 Mat. Sci. Eng. **B46**, 164
Sato R and Nasu M 1990 J. Phys. Soc. Japan, **59**, 166

Strain relaxation and void reduction in SiC on Si by Ge predeposition

F M Morales, P Weih, Ch Wang, Th Stauden, O Ambacher and J Pezoldt

Department of Nanotechnology, Centre for Micro- and Nanotechnology (ZMN), TU-Ilmenau Gustav-Kirchhoff-Strasse 7, D-98693 Ilmenau, Germany, paco.morales@tu-ilmenau.de

ABSTRACT: In this work, 120 nm cubic SiC layers have been grown on Si (111) by SSMBE, depositing 1ML of Ge at different temperatures before carbonization. In every case, SiC was epitaxially grown on Si (111) showing characteristic defects and more relaxation than a reference sample where Ge was not employed. Depending on the temperature of Ge predeposition, a reduction of voids or stacking faults was achieved. The residual strain depended on this temperature, as was confirmed by electron diffraction and infrared ellipsometry measurements.

1. INTRODUCTION

SiC layers supported on Si substrates show a highly strained and faulted structure due to the large lattice and thermal mismatch between these two materials. Residual stress leads to dislocation generation in high temperature processing and to wafer bowing that is detrimental to photolithography. Carbonization of the Si surface before SiC overgrowth partially releases these problems and is a common step in the fabrication of these heterostructures after Nishino et al (1983). In order to reduce the residual stress and to improve the electronic and optical properties of SiC on Si, many methods demonstrating an impact on the interface quality have been developed (Zhou et al 1993, Di Ciocci et al 1997, Hatayama et al 1997, Camassel 1998, Okhysen et al 2000, Zhang et al 2003). Device applications can benefit if the residual stress is reduced and the most feasible technique to preserve the properties of these heterojunctions consists on the modification of the Si substrate surface with other group IV elements (Mitchel et al 1998, Zekentes and Tsagaraki 1999, Masri et al 1999, Chassagne et al 2004). Improvements of the electrical (Pezoldt et al 2001) and crystallographic (Morales et al 2004) properties and a reduction of residual stress (Zgheib et al 2004) in 3C-SiC layers grown over Si (111) were recently reported when Ge is incorporated in molecular beam epitaxy (MBE) experiments. Voids often form in the interface region behind the SiC layer due to Si out-diffusion but the presence of Ge seems to restrain this mechanism. The aim of this work is to extend this series of studies, focusing on the effect of the Ge predeposition temperature on the microstructure of SiC/Si layers mainly using transmission electron microscopy (TEM) techniques.

2. EXPERIMENTAL

120 nm-thick SiC layers were grown by solid source MBE (SSMBE) on B-doped Si(111) wafers in an UMS 500 Balzers system. The detailed growth procedure is described elsewhere (Morales et al 2004) and in summary consists of the deposition of 1 ML of Ge at temperatures ranging from 25°C to 852°C plus 6 ML of C at 325^{o}C, a subsequent increase of temperature and the growth of SiC at 1000^{o}C. An additional reference sample was grown without using Ge. The SiC/Si heterostructures were studied by conventional and high-resolution TEM (CTEM-HREM) and selected-area electron diffraction (SAED) in Tecnai 20S-Twin (FEI) and JEOL JEM-2000EX/THR electron microscopes. Specimens were prepared for cross-sectional and plan-view TEM (XTEM-PVTEM) using mechanical thinning and Ar^{+} milling in a Gatan precision ion polishing system (PIPS). Stress was calculated from SAED and Fourier transform infrared (FTIR) ellipsometry (Sentech SE 900) measurements.

3. RESULTS AND DISCUSSION

3.1 Microstructural Characterization

The first inspection for every sample was by PVTEM. The SiC layers showed a SAED pattern with characteristics shown in Fig. 1a taken from the sample with Ge predeposited at 325°C. Reflections related to SiC appear as low angle arcs instead of being dots. This is indicative of the so-called mosaic structure, where domains forming the SiC epilayer are slightly misoriented with respect to each other. Due to stress and surface roughness, some of the forming 3D nuclei grow with tilted and/or twisted components. This mosaic structure accommodates the high lattice mismatch, though the higher intensity in the centre of the arced reflections indicates that the major part of these subgrains is placed in perfect heteroepitaxy. Figs. 1b-d show triangular voids formed at the SiC/Si interface beneath the Si layer on samples without Ge (b), and with Ge predeposited at 325°C (c) and 825°C (d). These voids are faceted by {111} planes of Si with their sides along <110> directions and result from Si outdiffusion. Only the sample without Ge showed hexagonal voids, not common in these structures and reported to be energetically less favourable by Jinschek et al (2001). The inset in Fig. 1b is representative of both Si and SiC aligned 022 reflections and other double diffraction spots.

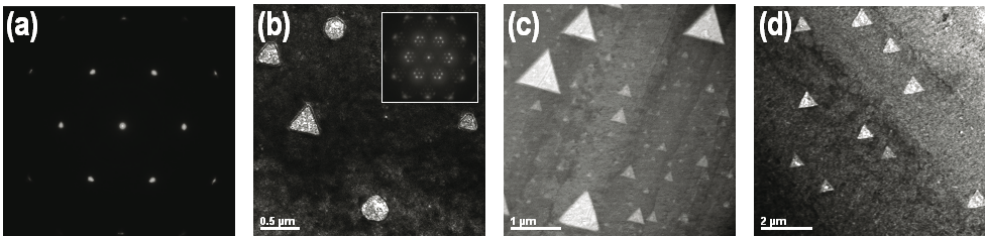


Fig. 1. SAED patterns (a-b inset) and BF-TEM micrographs (b-d) taken in <111> direction for different samples. Arcing in 022 reflections of SiC is associated to the mosaic structure of the epilayer (a). Typical voids with triangular shape were found for every sample. Only in the sample without Ge, hexagonal voids were evident (b).

A complete study of void sizes and their surface occupation was carried out from high magnification optical micrographs. Table 1 presents the collected data where the surface area studied for every sample was around 26000 μm^2. In these photographs, only voids bigger than 0.2 μm^2 were visible but it has been possible to get confident results neglecting not visible small voids by assuming the exponential distributions of void sizes, reported for similar structures (Morales et al 2003, Morales et al 2004). In this way, the contribution of "invisible" voids would not affect significantly the studied parameters. As a general rule, samples with Ge predeposition at temperatures lower than 500°C showed less surface occupation by voids than the reference one, without Ge. This is in agreement with previous investigations where a reduction and in some cases, a complete suppression of void formation was achieved (Morales et al 2004). On the other hand, samples precovered with Ge at higher temperatures displayed a stronger development of voids. This indicates that not only the quantity of Ge, but also the temperature of predeposition plays an important role in the limitation of Si outdiffusion. Note that the presence of voids decreases the actual mismatch in the SiC/Si heteroepitaxy because the Si substrate exerts a lower influence on the SiC overlayer. The fact that specimens having more voids present higher stress than others showing less void surface occupation (those predeposited at lower temperature) demonstrates that Ge is definitely implicated in the stress reduction mechanism.

SAMPLE	A	B	C	D	E	F	G	H
Temp. Ge predep. (°C)	reference	325	410	500	579	660	743	852
Void´s surface occup. (%)	7.22	5.79	3.77	15.78	7.12	17.82	14.65	13.6
Maximum void size (μm^2)	5.5	3.25	1.53	5.09	3.93	3.61	5.89	6.62
Average void size (μm^2)	0.82	0.84	0.46	1.01	0.58	0.56	0.74	0.72
Number of voids	2287	1774	2113	4699	3154	8222	5139	4929

Table 1. Data referring to void formation extracted from the analysis of areas of 26000 μm^2 in every sample.

SiC layers exhibited a series of typical defects in their structures. Fig. 2a shows an HREM image of the heterointerface in sample B (predeposited with Ge at 325°C). The contrast originating just at the interface is characteristic of both Si and SiC lattice overlap and it was found in many regions. Roughness promoted by

the reactivity of Ge and C with Si in the first stages of the growth is associated to this event (Pezoldt et al 2004), although the good orientation relationship between both structures is evident. The SiC layers are not free from planar defects and both twins and stacking faults (SFs) had developed. Moreover, the overlap of two twinned areas showed unusual features that in the past were often confused with 9R-SiC inclusions inside the cubic SiC matrix. Examples of these regions and the respective fast Fourier transform (FFT) spectra are squared in HREM micrographs of Figs. 2b and c. Aligned extra dots in the FFT at one and two thirds the distance between {111} and {002} related contributions of the β-SiC (encircled) resembles the α-SiC structure where ordered SFs disrupt the ABCA… characteristic sequence of layers in β-SiC. Furthermore, investigations by Kaiser et al (1999) have clarified by means of HREM image simulations that these contrasts showing fringes spaced three times the (111) interplanar distance of SiC (~0.75 nm) should be unambiguously associated to an overlap of 3C-SiC domains where {112}/{112} or {115}/{111} twin boundaries are parallel or inclined about 30° to the <110> direction. Furthermore, FFTs labelled as "B" and "C" in Fig. 2c are typical for nondefective and randomly stacked regions of the 3C-SiC layer.

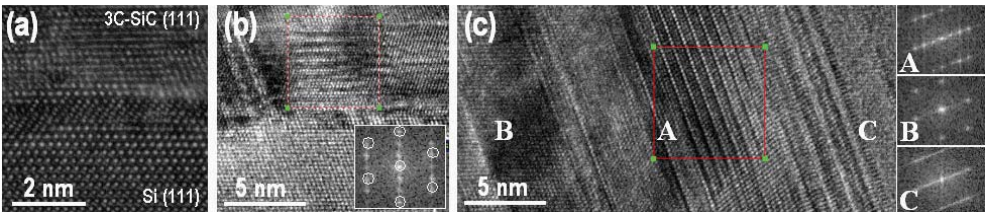


Fig. 2. (a) HREM micrograph of the SiC/Si interface; (b,c) three fold periodicity promoted by twin overlap.

Considering the HREM and SAED patterns, it was concluded that one dimensionally disordered oblique SFs inclined ±70.5° with respect to the interface plane are the most common defects in these structures. Such angles correspond to those between {111} planes in a cubic FCC structure. In many cases, these stacks are sectioning well-defined domains that originate SiC surface steps. This is clear in Fig. 3a which is magnified detail of the bright field TEM micrograph of the SiC/Si structure of sample B (Fig. 3b). Figures 3c, d and e present SAED patterns taken in the <110> zone axis of samples A, B and H, respectively. Special care was taken in using similar apertures and times of exposure in order to make comparative statements. Streaking associated to the commented oblique SFs (smooth continuous lines connecting the SiC reflections) and extra twin-related diffraction spots placed along these streaks are mostly visible for sample B, can be inferred for H and are less clear for A. Thus, samples with Ge predeposition at lower temperatures develop more of these peculiar defects.

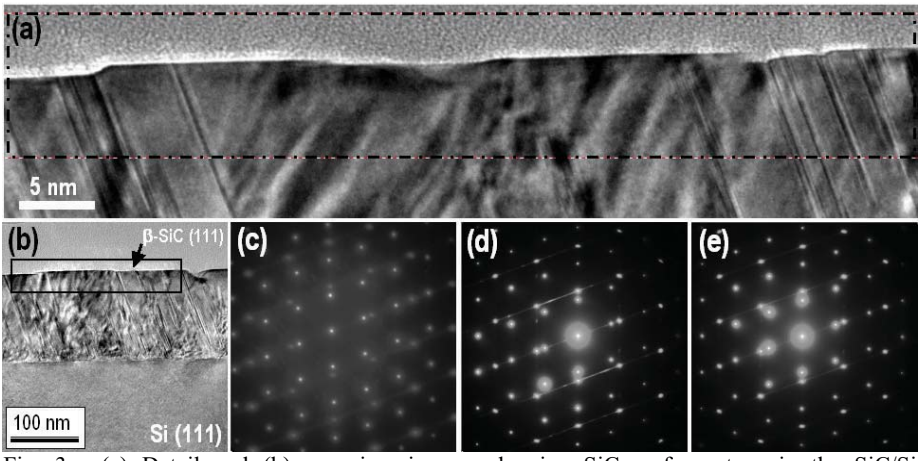


Fig. 3. (a) Detail and (b) overview images showing SiC surface steps in the SiC/Si heterostructures of sample B. (c-e) SAED patterns taken along the <110> zone axis of samples A (c), B (d) and H (e) showing that streaking due to oblique SFs is more common for samples predeposited with Ge at lower temperature.

3.2 Stress Measurement

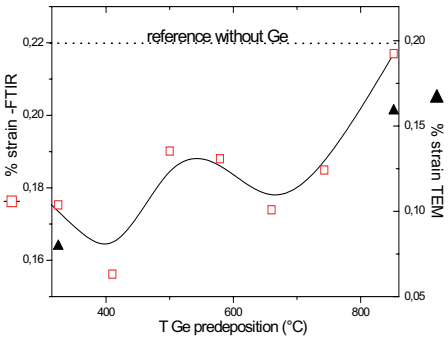


Fig. 4. Values of residual tensile strain for selected samples by FTIR and TEM.

Residual strain in the SiC layers was calculated from FTIR ellipsometry measurements. TO phonon modes were extracted and stress was calculated by the equation presented by Rohmfeld et al (2002) taking TO for relaxed 3C-SiC as 795.9 cm^{-1}. In a second step, residual strain is calculated by Hooke´s law, being E=748 GPa the β-SiC Young´s modulus (Gmelins 1959). On the other hand, strain was calculated from distances measured in high resolution digitized PVTEM SAED patterns from three selected samples (A, B and H), taking into account the Si substrate to SiC layer 022 reflection distance ratios and assuming the Si structure as relaxed. In this way, a good agreement in tendency was obtained as is shown in Fig. 4. The dashed line indicates the value for the reference sample measured by both methods. Note that those samples containing Ge always show lower values nearer the relaxed state. Lower stress values by TEM could be due to sample preparation, since SAED patterns for Si and SiC layers are taken in regions where the Si is very thin and its tensile effect on the overgrown layer is lower than in the case of samples tested by ellipsometry.

4. CONCLUSIONS

The presence of Ge predeposited before the carbonization stage in SiC/Si heterostructures leads to a reduction of stress. Additionally, more relaxed layers are associated with lower temperatures of Ge predeposition, fewer voids and greater development of oblique SFs.

ACKNOWLEDGEMENTS

F M M would like to thank the Alexander von Humboldt Foundation for financial support on Research Fellowship SPA/1114640 STP: all authors acknowledge the support by EU grant G5RD-CT-2002-00704.

REFERENCES

Camassel J 1998 J. Vac. Sci. Technol. **B16**, 1648
Chassagne T, Ferro G, Haas H, Leycuras A, Mank H and Monteil Y 2004 Mater. Sci. Forum **457**, 265
Di Ciocci L, Letertre F, Le Tiec Y, Papon A M, Jassaud C and Bruel M 1997 Mater. Sci. Eng. **B46**, 349
Gmelins Handbuch der Anorganischen Chemie 1959, Silicium, Part B, Weinheim, Verlag Chemie
Hatayama T, Fuyuki T and Matsunami H 1997 Appl. Phys. Let. **70**, 1411
Jinschek J, Kaiser U and Richter W 2001 J. Electron Microsc. **50**, 3
Kaiser U, Chuvilin A, Brown P D and Richter W 1999 Microsc. Microanal. **5**, 420
Masri P, Moreaud N, Averous M, Stauden Th, Wöhner T and Pezoldt J 1999 MRS Symp. Proc. **572**, 213
Mitchel S, Spencer M G and Wongtchotigul K 1998 Mater. Sci. Forum **264,** 231
Morales F M, Molina S I, Araújo D, Cimalla V and Pezoldt J 2003 Mater. Sci. Forum **433**, 285
Morales F M, Zgheib Ch, Molina S I, Araújo D, García R, Fernández C, Sanz-Hervás A, Masri P, Weih P, Stauden Th, Cimalla V, Ambacher O and Pezoldt J 2004 phys. stat. sol. **c1**, 341
Nishino S, Powell J A and Will H A 1983 Appl. Phys. Lett. **42**, 460
Okhysen M E, Mazzola M S and Lo Y H 2000 Mater. Sci. Forum **338**, 305
Pezoldt J, Förster Ch, Weih P, and Masri P 2001 Appl. Surf. Sci. **184**, 79
Pezoldt J, Zgheib Ch, Masri P, Averous M. Morales F M, Kosiba R, Ecke G, Weih P and Ambacher O 2004 Surf. Interface Anal. **36**, 969
Rohmfeld S, Hundhausen M, Ley L, Zorman CA and Mehregany M 2002 J. Appl. Phys. **91**, 1113
Zekentes K and Tsagaraki T 1999 Mater. Sci. Eng., **B61-62**, 559
Zgheib Ch, Masri P, Weih P, Ambacher O and Pezoldt J 2004 Mater. Sci. Forum **457**, 301
Zhang Z C, Chen Y H, Li D B, Zhang F Q, Yang S Y, Ma B S, Sun G S, Wang Z G and Zhang X P 2003 J. Cryst. Growth **257**, 321
Zhou G L, Ma Z, Lin M E, Shen T C, Allen L H and Morkoç H 1993 J. Cryst. Growth **134**, 167

Defect generation in high In and N content GaInNAs quantum wells: unfaulting of Frank dislocation loops

M Herrera, D González, J G Lozano, M Hopkinson[1], M Gutierrez[1], P Navaretti[1], H Y Liu[1] and R García

Departamento de Ciencia de los Materiales e I. M. y Q. I., Universidad de Cádiz, Apartado 40, 11510 Puerto Real, Cádiz, Spain
[1] Department of Electronic and Electrical Engineering, University of Sheffield, Mappin Street, Sheffield S1 3JD, UK

ABSTRACT: We have studied by transmission electron microscopy the defect generation in GaInNAs quantum wells when increasing the In and N contents in the range 20-35% and 1.3-2.3%, respectively. This analysis has shown the appearance of extrinsic Frank dislocation loops for In ≥ 25%, and of threading dislocations for In=35% and N ≥ 1.4%. It is proposed that the threading dislocations are formed from the unfaulting of the Frank loops. A new theoretical model for the process of unfaulting of extrinsic loops is proposed, which has allowed us to calculate the stacking fault energy in the GaInNAs alloy.

1. INTRODUCTION

The quaternary compounds of GaInNAs with N content lower than 5% have attracted recent interest due to the possibility of obtaining laser diodes in the emission range 1.3-1.5 μm. The considerable redshift in the emission peak of this new system with regard to GaInAs alloys is due to the high electronegativity and small size of the nitrogen atom, which leads to a large value of the bowing parameter (Kondow 1996). This fact, together with the reduction of the reticular misfit with GaAs substrates, is expected to reduce the problems of defect formation and 3D growth present in the ternary GaInAs alloys.

However, the increase in the In and N composition has been shown to degrade the optical properties of the alloy (Spruytte 2001). Despite the efforts addressed to the understanding of the effect of the introduction of N on the plastic relaxation mechanisms of the GaInNAs alloy, little is known in this respect. Moreover, basic properties of this system such as its stacking fault energy also remain unknown. This work is focused on the defect generation in GaInNAs quantum wells when increasing the In and N contents. Our experimental results have allowed us to calculate the stacking fault energy of this alloy.

2. EXPERIMENTAL

Samples were grown by molecular beam epitaxy (MBE) on (001) GaAs substrates in a VG V80H MBE system equipped with an Oxford Applied Research HD25 radio-frequency plasma source for N. The N flux was controlled by monitoring the intensity of the atomic N plasma emission with a photodiode. The nitrogen content in the epilayers was calibrated from the X-ray diffraction analysis of bulk samples and GaNAs quantum wells grown using similar plasma emission intensities. The samples consisted of five GaInNAs quantum wells between $GaAsN_{0.007}$ barriers with In-N compositions of 20%-1.3%, 25%-1.6%, 35%-1.1%, 35%-1.4% and 35%-2.3%, respectively. The growth temperature was 460ºC throughout the quantum well region.

Specimens were prepared by mechanical thinning followed by Ar+ ion milling for cross-sectional and planar view transmission electron microscopy (TEM) analysis. TEM studies were performed with JEOL 1200EX and JEOL 2011 microscopes.

3. RESULTS

The study by TEM of the sample with the lower In content (20%) has shown planar quantum wells without structural defects. However, on increasing the In composition to 25%, 3D features and extrinsic Frank dislocation loops have been observed. For 35% In and N content ≥1.4, beside the loops and the non-planar morphology, threading dislocations (TDs) are formed, as is shown in Fig. 1a for the structure with 2.3% N. It should be highlighted that misfit dislocations have not been found in any of the samples studied. The characterization of the threading dislocations by means of the invisibility criterion has shown that approximately one third of the dislocations have Burgers vector ½*a*<101], one third ½*a*<011] and the remaining ones ½*a*<110]. This means that despite two thirds of the dislocations having the typical 60º Burger vector out of growth plane, one third of them have 60º Burgers vectors lying in the growth plane. In order to understand the mechanisms of formation of these dislocations, we have calculated the curve of critical layer thickness for plastic relaxation according to the classical model of Matthews-Blakeslee (1974). This calculation showed that the thickness of the GaInNAs wells is lower than the critical value; therefore, the formation of dislocations by the Matthews-Blakeslee mechanism is not thermodynamically favourable in these samples. In addition, misfit dislocations have not been observed in these structures, therefore the TDs could not have been formed from misfit relief mechanisms. As detailed in a previous paper (Herrera, in press), a plausible explanation for the appearance of the threading dislocations is that they are the result of the unfaulting of the Frank dislocation loops by the reaction with two Shockley partials (Garner 1988). In fcc structures, the habit plane of Frank dislocation loops are {111} type because of the lower stacking fault energy. In these {111} planes, there are three possible Shockley partial dislocations that could take part in the coalescence reaction with the loop. The result of the reaction of a Frank extrinsic dislocation loop with two of these Shockley partial dislocations is the formation of a perfect dislocation, with one of the 1/2a<110> type Burgers vectors. Because the probability of occurrence of these three reactions in the material is the same, the unfaulting of the Frank loops gives place to perfect dislocations, one third with each of the Burgers vector observed in our study. This points out the fact that the mechanism of formation of the threading dislocations is the unfaulting of the dislocation loops to form perfect dislocations that glide to the surface of the structure (Herrera, in press). In the following, we discuss the thermodynamics of the unfaulting process of a Frank dislocation loop, with the objective to calculate the stacking fault energy of the GaInNAs system.

4. DISCUSSION

The classical treatment of the unfaulting of Frank dislocation loops considers that a Frank loop unfaults into a perfect one when reaching a critical radius in which the energy of the second one is lower than the first one. The energetic balance for this process is expressed as (Hirth 1982)

$$E_{SF} + E_{l,Frank} = E_{l,perfect} \tag{1}$$

where

$$E_{SF} = \pi r^2 \gamma \tag{2}$$

$$E_{l,Frank} = 2\pi r \frac{\mu b_{Frank}^2}{4\pi(1-\nu)}\left(\ln\left(\frac{8\alpha r}{b_{Frank}}\right)-1\right) \tag{3}$$

$$E_{l,perfect} = 2\pi r \frac{\mu b_{out}^2}{4\pi(1-\nu)}\left(\ln\left(\frac{8\alpha r}{b_{out}}\right)-1\right) + 2\pi r \frac{2-\nu}{2(1-\nu)}\frac{\mu b_{in}^2}{4\pi}\left(\ln\left(\frac{8\alpha r}{b_{in}}\right)-2\right) \tag{4}$$

r is the radius of the dislocation loop, μ is the shear modulus, ν is the Poisson ratio, α is the dislocation core factor, γ is the stacking fault energy per unit surface, b_{in} and b_{out} are the components of the Burgers vector of a perfect loop inside and outside the habit plane of the loop, respectively, and b_{Frank} is the Burgers vector modulus of the Frank dislocation loop. In our case, $b_{Frank} = b_{out} = a/\sqrt{3}$ and $b_{in} = a/\sqrt{6}$, where a is the lattice parameter. Therefore, we can obtain a relationship between the critical radius for the unfaulting process, r_{cri}, and γ as:

$$\gamma = \frac{\mu a^2}{24\pi r_{cri}} \frac{2+\nu}{(1-\nu)} \left(\ln\left(\sqrt{6} \frac{\alpha r_{cri}}{a} \right) \right) \quad (5)$$

As can be seen, to calculate the stacking fault energy of the GaInNAs alloy it is necessary to know the critical radius for the unfaulting of the dislocation loops. In order to obtain an estimation of this critical radius, we have studied by TEM in planar view the distribution of density and size of the dislocation loops in samples with 35% of In. Fig. 1b shows the histogram of the distribution of loops in the sample with 35% In and 1.4% N. As it can be observed, there is one interval with a density of loops which is rather high, centred at 12 nm. On increasing the radii of the loops, the amount of defects in each interval is progressively diminished. However, in this progression there is one step larger than the other ones located at 19.5±1.5 nm, the difference in density of loops between those intervals of the histogram being more than two times higher than the observed in the values of radius of 13.5 nm, 22.5 nm, 25.5 nm, 28.5 nm, etc. In sample A35-2.3, the abnormally high step is placed at 22.5±1.5 nm. According to the reasoning about the formation of the threading dislocations, the drastic diminishing in the density of loops could be due to their unfaulting into perfect loops that glide to the surface of the structure to form threading fragments. Therefore, the radius where the density of loops abruptly decreases could constitute an estimation of the critical radius for the unfaulting of the loops.

With the experimentally measured critical radius and the classical expression in (5), we have calculated the stacking fault energy for the $Ga_{0.65}In_{0.35}N_{0.023}As$ alloy (using for a, μ and ν the values obtained from the extrapolation of those of the binaries), obtaining 83±2 mJ/m^2. This value is notably high compared to the stacking fault energy of $Ga_{0.65}In_{0.35}As$ calculated by extrapolation from the values of the binaries (Takeuchi 1999), which is about 38.5 mJ/m^2. The addition of small amounts of nitrogen can modify the stacking fault energy of the GaInAs system, but we would expect a reduction instead of an increase given that it favours the trend of a wurtzite stacking inside the zinc-blende structure and this fact signifies a fall in the γ (Montero-Ocampo 2002). Moreover, it should be mentioned that the classical model does not differentiate between intrinsic and extrinsic loops, although the first ones just need one Shockley partial to suffer the unfaulting and the second ones two. Because of these reasons, we do not find appropriate the classical model to calculate the stacking fault energy in our GaInNAs samples, and we are proposing a new model for this purpose. We think that the thermodynamic treatment of the unfaulting process of extrinsic loops would be more accurate if we also consider the formation energy of the two Shockley partial dislocations that participate in the process. Hence, we can write the energetic balance of the global process as

$$E_{SF} + E_{l,Frank} + 2E_{Shockley} = E_{l,perfect} \quad (6)$$

where

$$E_{Shockley} = 2\pi r \frac{\mu b_{Shockley}^2}{4\pi} \left(\cos(\beta)^2 - \frac{\sin(\beta)^2}{1-\nu} \right) \ln\left(\frac{\alpha r}{b_{Shockley}} \right) \quad (7)$$

where β is the angle between the Burgers vector and the dislocation line for the Shockley segments, being in our case $\beta=\pi/6$ and $b_{Shockley} = a/\sqrt{6}$. Thus, the stacking fault energy can be expressed as

$$\gamma = \frac{\mu a^2}{4800\pi r_{cri}(1-\nu)} \left(400\nu \ln\left(\frac{\alpha r_{cri}}{a} \right) + 32 + 343\nu \right). \quad (8)$$

From this equation, a critical radius of a loop of 19.5±1.5 nm (In and N compositions of 35% and 1.4%, respectively) corresponds to a γ of the material of 37±2 mJ/m^2. Similarly, for In content of 35% and N of 2.3%, a value of the γ of 33±2 mJ/m^2 is calculated. As can be observed, the consequence of the introduction of N in the GaIn(N)As alloy is a reduction in the γ of the material. To our knowledge, this is the first estimation of γ and its influence of the N introduction in GaInNAs alloys found in the literature. The significance of the decrease of the stacking fault energy with N is that it provides a serious handicap for N-rich GaInNAs growth. The lower the fault energy, the higher is the density of stacking faults and twins in the material. Therefore, defect formation for N-rich GaInNAs is not controlled by the plastic relaxation of the lattice mismatch, but by stacking fault generation such as Frank dislocation loops.

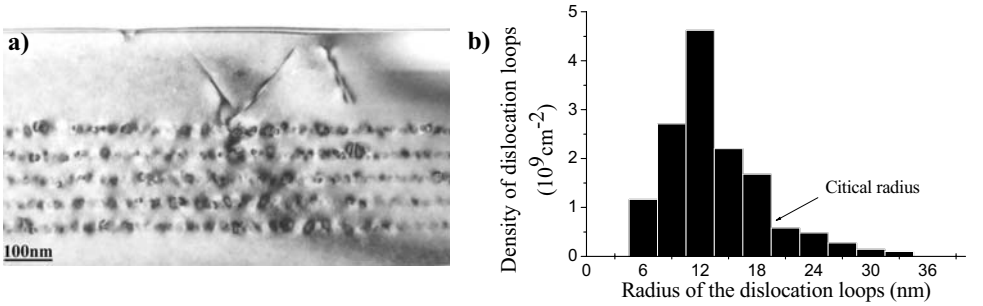


Fig. 1: a) 220BF micrograph of the sample with In=35% and N=2.3%, showing dislocation loops and threading dislocations. b) Distribution of size of the dislocation loops in the sample with In=35% and N=1.4%.

5. CONCLUSIONS

In this work, the effect of the increase in the In and N contents on the structural quality of GaInNAs quantum wells is analyzed. Our results have shown extrinsic Frank dislocation loops in the samples with In ≥ 25% and the appearance of threading dislocations for In=35% and N ≥ 1.4%. The threading dislocations are proposed to form from the unfaulting of the Frank dislocation loops by reaction with two Shockley partial dislocations. We propose a new theoretical model for the energetic balance of the unfaulting of the Frank loops into perfect ones. With this model and the experimentally measured critical radius of the loops, an estimation of the stacking fault energy of GaInNAs has been made, obtaining 37 mJ/m^2 and 33 mJ/m^2 for $Ga_{0.65}In_{0.35}N_{0.014}As$ and $Ga_{0.65}In_{0.35}N_{0.023}As$, respectively. The introduction of N in GaInNAs results in a reduction of the stacking fault energy of the alloy, therefore defect generation in this system is mainly governed by the formation of stacking faults such as Frank dislocation loops instead of by plastic relaxation due to the lattice mismatch.

ACKNOWLEDGMENTS

Financial support from the Spanish ministry of Education, EPSRC (UK) and CICYT project MAT2001-3362 (Spain) is gratefully acknowledged.

REFERENCES

Garner F A and Gelles D S 1988 J. Nucl. Mater. **159,** 286

Herrera M, González D, García R, Hopkinson M, Navaretti P, Gutiérrez M and Liu H Y Thin Solid Films, in press

Hirth J P and Lothe J 1982 Theory of dislocations, Wiley-Interscience Publications, New York.

Kondow M, Uomi K, Niwa A, Kitatani T, Watahiki S and Yazawa Y 1996 Jpn. J. Appl. Phys. **35**, 1273

Matthews J W and Blakeslee A E 1974 J. Cryst. Growth **27,** 118

Montero-Ocampo C, Juarez R and Salinas Rodriguez A 2002 Metall. & Mat. Trans. **33A,** 2229

Spruytte S G, Coldren C W, Harris J S, Wamplet W, Krispin P, Ploog K and Larson M C 2001 J. Appl. Phys. **89**, 4401

Takeuchi S and Suzuki K 1999 Phys. Stat. Sol. *(a)* **171,** 99

Structural characterisation of spintronic GaMnAs and GaMnN heterostructures grown by molecular beam epitaxy

M W Fay, Y Han, S V Novikov, K W Edmonds, K Wang, B L Gallagher, R P Campion, C T Foxon and P D Brown

School of Mechanical, Materials and Manufacturing Engineering and School of Physics and Astronomy, University of Nottingham, University Park, Nottingham NG7 2RD

ABSTRACT: Observations of orthogonal orientations demonstrate the development of banded contrast features on inclined $\{\bar{1}\,\bar{1}\,\bar{1}\}_B$ planes for the [110] projection within micron thick samples, attributed to a compositional fluctuation in the Mn content. The relationship of Mn content and layer critical thickness for the onset of precipitate and stacking fault formation is investigated. The formation of a Mn-O layer at the surface of the samples is also observed. The growth of GaMnN/(001)GaAs heterostructures with and without AlN/GaN buffer layers is also compared. Layers without buffer layers show MnAs inclusions into the GaAs, with a reduced Mn content of the GaMnN layer significantly below the nominal composition. The use of AlN/GaN buffer layers is found to greatly reduce the density of these MnAs inclusions, retaining a higher proportion of the Mn within the epilayer.

1. INTRODUCTION

Ferromagnetic semiconductors raise the possibility of spintronic devices that combine both electronic and magnetic properties (Ohno 1998). Theoretically, ferromagnetism at room temperatures is achievable within GaMnAs and GaMnN for very high Mn concentrations (Dietl et al 2000), and this in principle can be achieved under non-stoichiometric growth conditions using molecular beam epitaxy (MBE). However, the development of these systems is limited by the low solubility of Mn in GaAs and GaN and the defect microstructure formed, comprising both point and extended structural defects.

2. EXPERIMENTAL DETAILS

Thin (50nm) and thick (1µm) $Ga_{1-x}Mn_xAs$ epitaxial layers with a SIMS determined Mn composition of 2.2, 5.6 or 9at% were grown at temperatures of 255, 210 or 185°C, respectively, on (001) oriented semi-insulating GaAs substrates, using As_2 to reduce the concentration of As antisite defects (Campion et al 2003). Buffer layers of 100nm thickness, high temperature (580°C) GaAs followed by 50nm thick, growth temperature GaAs provided template material for $Ga_{1-x}Mn_xAs$ growth. Magnetic measurements of these samples confirmed strong anisotropic ferromagnetism of these $Ga_{1-x}Mn_xAs$ layers with the easy and hard directions of magnetisation corresponding to the $[1\,\bar{1}\,0]$ and [110] directions, respectively (Sawicki et al 2005). $Ga_{1-x}Mn_xN$ layers with a target thickness of 0.3µm and Mn content ranging from 0.04% to 6.6at% were grown at 680°C using plasma assisted-MBE on semi-insulating (001) GaAs (Novikov et al 2005). Samples grown on 0.15µm thick GaAs buffer layers were compared with samples grown on AlN/GaN/GaAs (each 0.15µm in thickness) buffer layers.

Electron transparent specimens prepared in plan view and cross sectional geometry using sequential mechanical polishing, dimpling and argon ion beam milling were assessed using conventional diffraction contrast techniques. Information on the chemical distributions in the layers was obtained using energy dispersive x-ray (EDX) analysis, electron energy loss spectroscopy (EELS)



Fig.1. <110> many beam bright field TEM image of a defect free 50nm thick $Ga_{0.944}Mn_{0.056}As$/(001)GaAs epilayer.

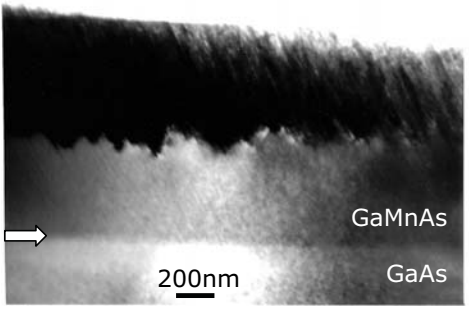


Fig. 3. <110> many beam bright field TEM image of a 1µm thick $Ga_{0.91}Mn_{0.09}As$ layer.

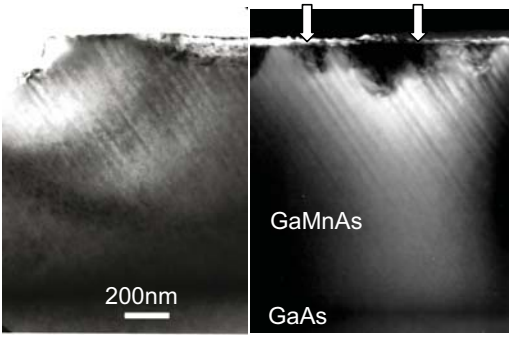


Fig. 2. (a) Bright field TEM image of a 1µm thick $Ga_{0.944}Mn_{0.056}As$ layer tilted slightly off the [110] projection. A domain structure and contrast reminiscent of ordering is apparent on $\{\bar{1}\,\bar{1}\,\bar{1}\}_B$ planes.
(b) Dark field TEM image of a 1µm thick $Ga_{0.95}Mn_{0.05}As$ layer tilted slightly off the [110] projection.

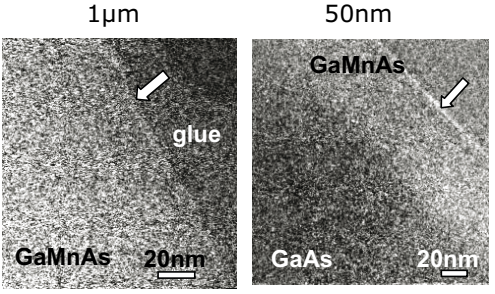


Fig. 4. Mn sensitive EFTEM images from the surface of a 1µm thick $Ga_{0.944}Mn_{0.056}As$ layer and a 50nm thick annealed $Ga_{0.91}Mn_{0.09}As$ layer.

and energy filtered TEM (EFTEM) techniques using JEOL 2000fx and 4000fx instruments. The absolute crystal polarity of TEM sample foils was established using convergent beam electron diffraction (Ishizuka and Taftø 1984).

3. RESULTS AND DISCUSSION

50nm and 1µm thick $Ga_{0.978}Mn_{0.022}As$ epilayers showed no extended structural defects. Thin 50nm layers of $Ga_{0.944}Mn_{0.056}As$ similarly showed no extended defects, as shown in Fig. 1. In contrast, 1µm thick $Ga_{0.944}Mn_{0.056}As$ epilayers exhibited domains of highly faulted twin structures at the layer surface (Fig. 2, black regions arrowed) and an irregular growth surface on the scale of 10 to 20 nm. Of particular interest, a faint banded structure on one set of inclined advancing $\{\bar{1}\,\bar{1}\,\bar{1}\}$B planes, reminiscent of ordering, was visible in the [110] projection, corresponding to the direction of hard magnetisation, accentuated close to the ½(115) diffraction condition. However, it is noted that additional spots due to ordering were not discernible in selected area diffraction patterns due to the large spacing and diffuse nature of these banded features. This banded contrast became stronger further away from the $Ga_{1-x}Mn_xAs$/GaAs interface, although there was a perception of faint contrast at the original $Ga_{1-x}Mn_xAs$ /GaAs interface as a point of origin. This banded contrast was not observed within any thin 50nm layers, and hence is tentatively attributed to a modulated composition fluctuation becoming accentuated during growth due to accumulating epilayer strain.

A marked effect on the development of the defect microstructure was observed by increasing the Mn concentration further. 5-10nm sized precipitates and surface stacking faults were observed within thin

50nm $Ga_{0.91}Mn_{0.09}As$ layers, while the corresponding 1µm thick $Ga_{0.91}Mn_{0.09}As$ samples showed an abrupt transition from defect free growth to a band comprising a high density of stacking faults preferentially aligned on one set of inclined {111} planes, commencing ~500nm from the $Ga_{1-x}Mn_xAs$/GaAs interface (Fig 3). Precipitates, tentatively attributed to MnAs, were observed at the onset of the stacking faults.

Elementally sensitive maps obtained from both the 50nm and 1µm thick layers indicated a relatively uniform distribution of Mn throughout all $Ga_{1-x}Mn_xAs$ samples, with a peak in the Mn content at the layer surface of both samples (arrowed in Fig. 4). This Mn layer was associated with a strong O signal. The perception of a Mn-O layer at the surface suggests the oxidation of a surface Mn layer, consistent with recent X-ray absorption studies (Edmonds et al 2004). This indicates that Mn is acting as a surfactant, with segregation of Mn at the growth surface in response to the build up of misfit strain.

Hall-effect measurements unambiguously showed that the $Ga_{1-x}Mn_xN$ samples had strong p-type conductivity. Figure 5 presents a <110> cross sectional TEM image of a $Ga_{0.97}Mn_{0.03}N$/GaAs(001) sample. This image is typical of all the $Ga_{1-x}Mn_xN$/GaAs(001) samples investigated with a line of voids at the nitride/GaAs interface, and intriguingly a high density of inclusions extending into the GaAs buffer layer. It is suggested that the line of voids are due to preferential milling of localised strain centres at the interface, although some cooperative voiding mechanism associated with the formation of inclusions remains a possibility (Tricker et al 1998). The line of the original GaAs/GaAs interface is also perceived, presumably delineated by a remnant oxide layer (Fig.5 arrowed). EELS analysis revealed the inclusions to be rich in Mn, with no significant edges corresponding to N or O being detectable (Fig 6a). Complementary EDX spectra from both cross sectional and plan view samples confirmed the presence of high levels of As as well as Mn within such inclusions, also showing a deficiency of Ga as compared with the surrounding GaAs matrix (Fig. 6b). Associated diffraction patterns confirmed that such inclusions adopted a hexagonal structure, with a and c lattice parameter spacings of 3.72 and 5.69 Å, respectively, consistent with the formation of α-MnAs (ASM 1992). It is considered that such MnAs inclusions develop during growth, due to the limited solid solubility of Mn in $Ga_{1-x}Mn_xN$ for the growth conditions used, with the displacement of Ga from the GaAs substrate through a process of differential cross diffusion. Although MnAs is a ferromagnetic metal with a T_c of around 313K, similar properties are observed for the layers grown with and without AlN buffer layers, suggesting that the inclusions do not make a significant contribution to the electrical properties in the layers investigated here. Transport properties will not be affected as the inclusions are not continuous.

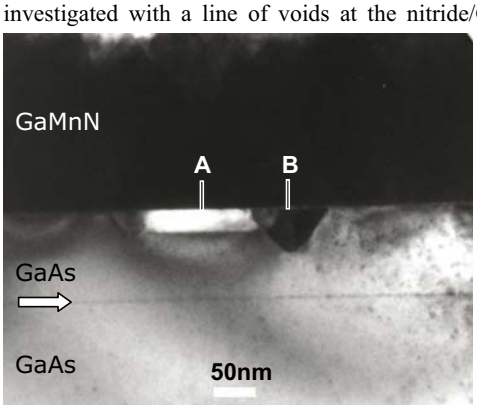


Fig 5. <110> many beam bright field TEM image of $Ga_{0.97}Mn_{0.03}N$/GaAs(001) showing (A) a void and (B) an inclusion at the interface.

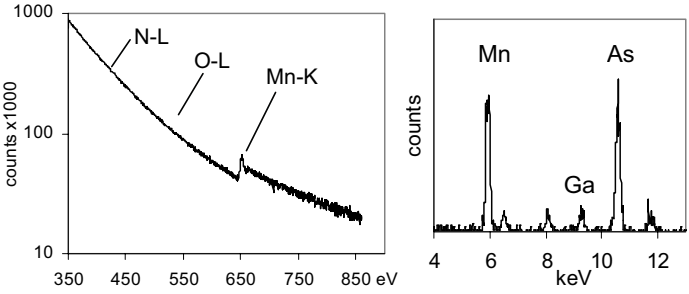


Fig. 6. a) EELS and b) EDX spectra obtained from an inclusion viewed in cross section, confirming the material to be MnAs.

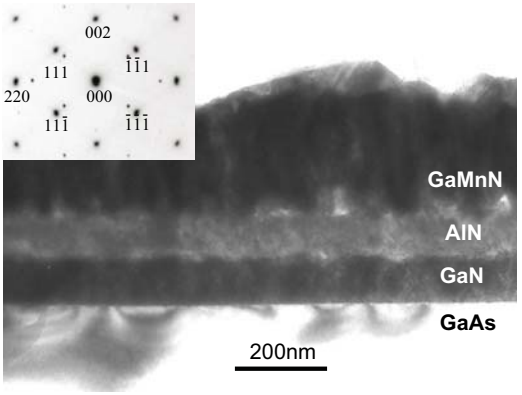


Fig. 7. <110> many beam bright field TEM image of a $Ga_{0.982}Mn_{0.018}N$/AlN/GaN/ GaAs/GaAs(001) epilayer with associated diffraction pattern inset.

Figure 7 shows a <110> many beam cross sectional TEM image of a $Ga_{0.982}Mn_{0.018}N$/AlN/GaN/GaAs (001) epilayer. A continuous zincblende AlN layer can be seen with a relatively abrupt interface. Although the AlN layer exhibited rotated columnar grains, the $Ga_{1-x}Mn_xN$ layer was again found to be single crystal cubic, albeit highly faulted with a fine subgrained structure on the scale of ~100nm. Notably, such AlN/GaN buffer layers were found to be largely effective in suppressing the formation of MnAs inclusions into the GaAs. Accordingly, the use of AlN/GaN buffer layers has implications for the control of Mn content, alloy uniformity and the p-type behaviour of $Ga_{1-x}Mn_xN$ epilayers grown by PA-MBE.

4. SUMMARY

The microstructure of $Ga_{1-x}Mn_xAs$ layers is strongly dependent on the layer thickness. Since thin and thick layers of nominally the same composition exhibit such different microstructures, caution is required when applying the results for thick layers from other characterisation techniques to explain the functional properties of thinner layers. The high levels of faulting associated with the 1μm thick $Ga_{0.944}Mn_{0.056}As$ and $Ga_{0.91}Mn_{0.09}As$ samples is considered to be a response to the development of misfit strain.

Strongly p-type zincblende $Ga_{1-x}Mn_xN$ epilayers grown by PAMBE show α-MnAs inclusions at the $Ga_{1-x}Mn_xN$/GaAs(001) interface extending into the GaAs buffer layer. The use of AlN/GaN buffer layers was found to be effective in suppressing the formation of such inclusions.

ACKNOWLEDGEMENTS

The authors would like to acknowledge the contributions of B Ja Ber and A P Kovarsky for the SIMS studies. This work was supported under EPSRC contracts GR/S25630/01 and GR.S81407/01

REFERENCES

Alloy phase diagrams, ASM handbook, Volume 3, Metals Park, Ohio: American Society for Metals International, 1992.

Campion R P, Edmonds K W, Zhao L X, Wang K Y, Foxon C T, Gallagher B L and Staddon C R 2003 J Cryst Growth **247**, 42

Dietl T, Ohno H, Matsukara F, Cibert J and Ferrand D 2000 Science **287,** 1019

Edmonds K W, Farley N R S, Campion R P, Foxon C T, Gallagher B L, Johal T K, Van der Laan G, MacKenzie M, Chapman J N and Arenholz E 2004 Appl. Phys. Lett. **84** 4065

Ishizuka K and Taftø J 1984 Acta Cryst. **B40**, 332

Kaminska E, Piotrowska A, Dietl T , Gallagher B L, cond-mat/0410544, Phys. Rev. B *in press*

Novikov S V, Edmonds K W, Zhao L X, Giddings A D, Wang K Y, Campion R P, Staddon C R, Fay M W, Han Y, Brown P D and Sawicki M J Vac Sci and Tech B *in press*

Ohno H 1998 Science **281**, 95

Sawicki M, Wang K Y, Edmonds K W, Campion R P, Staddon C R, Farley N R S, Foxon C T, Papis E, Tricker D M, Brown P D, Cheng T S, Foxon C T and Humphreys C J 1998 Appl. Surf. Sci. **123/124**, 22

TEM determination of the local concentrations of substitutional and interstitial Mn and antisite defects in ferromagnetic GaMnAs

F Glas, G Patriarche, L Thevenard and A Lemaître

CNRS , Laboratoire de Photonique et de Nanostructures, route de Nozay, 91460 Marcoussis, France

ABSTRACT: We present a TEM method for the analysis of the minority constituents in the ferromagnetic semiconductor GaMnAs. The method relies chiefly on the high sensitivity of the structure factor of weak 002-type reflections to the concentrations and locations of the interstitial Mn atoms. High spatial resolution is obtained by combining local structure factor measurement from dark field images and X-ray analysis. We find that Mn interstitials with As neighbours dominate and that their concentration decreases upon annealing.

1. INTRODUCTION

Combining electronic and magnetic properties in a single spintronics device has become a major aim of information technology. To this end, a particularly interesting material is GaMnAs, a ferromagnetic semiconductor compatible with the well-mastered GaAs system (Matsukura et al 2002), where Curie temperatures T_C higher than 160 K have already been measured. Boosted by predictions of possible room temperature ferromagnetism, a large effort is currently devoted to the controlled fabrication of this material and to the determination and understanding of its physical properties.

Crystalline GaMnAs is essentially a GaAs matrix where a small fraction of the Ga atoms is replaced by substitutional Mn atoms behaving as acceptors. Ferromagnetism stems from the exchange interaction between the localized magnetic moments and the delocalized holes, both originating from these Mn atoms. In order to incorporate even a few percent of Mn, GaMnAs has to be grown at low temperature, which induces the formation of other point defects. Two of these, isolated Mn interstitials and As_{Ga} antisites (As atoms at Ga sites), are highly detrimental to ferromagnetism, being donors compensating the holes. It is thus important to quantify these atomic species, locally if possible.

We describe the GaMnAs crystal with respect to a GaAs reference matrix where As atoms occupy a face centred cubic (fcc) sublattice with one atom at $(0,0,0)$ and Ga atoms a second fcc sublattice translated from the former by $\mathbf{R} = a\,(¼,¼,¼)$, with a the lattice parameter of the alloy. In GaMnAs, the Mn atoms occupy either Ga sites or interstitial sites. Among the many possible interstitial sites of the sphalerite structure, those most often considered are two types of tetrahedral sites and hexagonal sites (Fig. 1). The tetrahedral sites constitute two fcc lattices translated from the As sublattice by $2\mathbf{R}$ and $3\mathbf{R}$. A Mn atom has four Ga nearest neighbours (NNs) in the former (hereafter 'type-1') and four As NNs in the latter ('type-2'). Similarly, the hexagonal sites constitute four translated fcc sublattices.

We lack detailed estimations of the abundances of these various defects. Indeed, few structural studies so far have gone beyond the mere determination of the total Mn concentration. However, Yu et al (2002) used particle induced X-ray emission and Rutherford backscattering to determine the macroscopic concentration of Mn interstitials, assumed to lie in undifferentiated tetrahedral sites, and showed that the increase of T_C occurring during annealing is, as expected, accompanied by a reduction of the interstitial concentration. Tuomisto et al (2004) quantified macroscopically Ga vacancies and As_{Ga}. Conversely, some theoretical studies (e.g. Mašek et al 2003) assume that only type-2 interstitials exist. Calculations indeed confirm that this is the most stable of the abovementioned interstitial positions for an isolated Mn atom, although associations of a type-1 interstitial with one or two substitutional Mn might be even more stable (Mahadevan and Zunger 2003, Edmonds et al 2004).

Here, we show that it is possible to measure precisely the concentrations of minority species by combining several transmission electron microscopy (TEM) techniques. To this end, we first fabricated thin ferromagnetic GaMnAs layers by molecular beam epitaxy on GaAs (001) substrates at

temperatures between 250 and 310°C after depositing a GaAs buffer at 600°C. As-grown and annealed samples were studied by TEM at 200 kV. In Sections 2 and 3, we describe our method (see also Glas et al 2004) and illustrate it by analysing a particular as-grown sample (Table 1, Figs. 2 and 3).

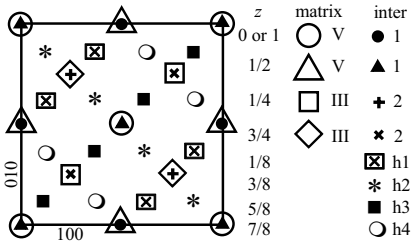


Fig. 1. Sites in the fcc unit cell. z is the reduced coordinate along the 001 direction. V, III, 1, 2 indicate respectively As and Ga matrix sites and type-1 and type-2 tetrahedral interstitial sites. hp: the four types of hexagonal interstitials.

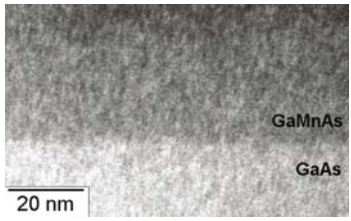


Fig. 2. TEM 002 DF image of a ferromagnetic GaMnAs layer (with $T_C = 66\,\mathrm{K}$) grown on a GaAs substrate, before annealing.

2. TEM WEAK REFLECTION IMAGING AND FIRST QUANTITATIVE ANALYSIS

Figure 2 is a typical TEM 002 dark field (DF) image. The 002 intensity is obviously much lower for the GaMnAs layer than for the GaAs buffer layer or substrate. As a first approximation, the images corresponding to such 'weak' reflections $\mathbf{g}_{hkl}$ (with h, k, l even, $h+k+l = 4n+2$), which have low structure factors (SF) $F_\mathbf{g}$ and correspondingly high extinction distances ($\xi_{002} \approx 865\,\mathrm{nm}$ in GaAs) may be analysed by using the two-beam kinematical approximation, whereby the intensity at exact Bragg incidence is proportional to $t^2\, V_c^{-2} \left| F_\mathbf{g} \right|^2$, with t the specimen thickness and V_c the unit cell volume. Hence, if t is uniform, the image maps the SF variations, with a small correction due to possible variations of V_c. In practice, we measure the ratio $\rho_\mathbf{g}$ of the DF intensities recorded locally in GaMnAs and in neighbouring GaAs (Table 1). The kinematic approximation is justified by $t << \xi_\mathbf{g}$ and by calculations showing that, for $\mathbf{g} = 002$, dynamical effects remain weak in the closely related InGaAs alloys (Cagnon et al 2001), although the latter are more mismatched than the present layers.

For quantitative analysis, we initially consider the following atomic species: Ga and As at their proper sites, As_{Ga} antisites, substitutional Mn and tetrahedral and hexagonal interstitial Mn. We ignore As vacancies (not yet detected in bulk layers) and Ga vacancies, present only at very low concentrations (Tuomisto et al 2004). Hence, assuming random occupation of the relevant sites, neglecting static atomic displacements (Glas 2004) and leaving aside the Debye-Waller factors (which will almost cancel each other when we compute ratios of DF intensities), the SF for reflection 002 is:

$$F_{002} = 4\left[c^V_{As} f_{As} - \left(c^{III}_{Ga} f_{Ga} + c^{III}_{As} f_{As} + c^s_{Mn} f_{Mn}\right) + c^1_{Mn} f_{Mn} - c^2_{Mn} f_{Mn}\right] + 4i \sum_{p=1}^{4} (-1)^p c^{hp}_{Mn} f_{Mn} \qquad (1)$$

where f_A is the appropriate atomic scattering amplitude (ASA) for atom A, c^σ_A is the concentration of matrix atom A on matrix sublattice σ (III or V) and c^s_{Mn}, c^1_{Mn} c^2_{Mn} and c^{hp}_{Mn} are the concentrations of Mn atoms occupying respectively substitutional sites, the two types of tetrahedral and hexagonal ($p = 1$ to 4) interstitial sites. The phase of the contribution of each site is calculated from Fig. 1. A unit concentration corresponds to the occupation of all the sites of one fcc matrix sublattice. Hence, $c^V_{As} = 1$ and $c^{III}_{Ga} + c^{III}_{As} + c^s_{Mn} = 1$. Except c^V_{As} and $c^{III}_{Ga} \sim 1$, all concentrations are at most a few percents. Eq. (1) holds for all weak reflections except for sign changes for the hexagonal interstitials.

In GaAs, $F_\mathbf{g} = 4(f_{As} - f_{Ga})$ is low because the contributions of Ga and As (which have close atomic numbers) nearly cancel each other. This remains true in GaMnAs for the contributions of the atoms belonging to the two matrix sublattices, since Mn is also close to Ga and As in atomic number. However, there are further contributions from the interstitials. Numerically, assuming equal scattering angles for GaMnAs and bulk GaAs and using ASAs from Doyle and Turner (1968), the SF (in nm) is:

$$F_{002}(\mathrm{GaMnAs}) \approx F_{002}(\mathrm{GaAs}) + 0.012\, c^s_{Mn} - 0.264\, c^{III}_{As} + 2.204\left(c^1_{Mn} - c^2_{Mn}\right) + 2.204\, i \sum_{p=1}^{4} (-1)^p\, c^{hp}_{Mn} \quad (2)$$

with $F_{002}(\mathrm{GaAs}) \approx 0.2633\,\mathrm{nm}$. For all reasonable point defect concentrations, the hexagonal

interstitials only contribute a small term in quadrature which increases the SF modulus negligibly. We shall thus ignore them, which leaves us with four unknowns, namely $c^s_{Mn}, c^1_{Mn}, c^2_{Mn}, c^{III}_{As}$.

More importantly, F_{002} is virtually independent of the substitutional Mn concentration and eight times more sensitive to the concentrations of tetrahedral interstitial Mn than to that of As_{Ga} antisites. If, as a first approximation, we retain only these interstitials, Eq. (2) rewrites $F_{002}(\text{GaMnAs})/F_{002}(\text{GaAs}) \approx 1 + 8.38\left(c^1_{Mn} - c^2_{Mn}\right)$. Hence, SF and DF intensity are highly sensitive to tetrahedral interstitials. Moreover, the two types have opposite effects: type-1 interstitials increase F_{002} whereas type-2 interstitials reduce it. Since $F_{002} > 0$ for all conceivable concentrations, the same holds for the DF signal. Experimentally, the latter is always lower in our as-grown GaMnAs than in GaAs. This proves that type-2 interstitials dominate. Using our simple formula, the measured ratio ρ_{002} also yields a first estimate $\tilde{c}^1_{Mn} - \tilde{c}^2_{Mn}$ of the difference of interstitial concentrations (Table 1).

The present technique is related to, but different from, the use of weak reflections to measure the concentrations of matrix atoms in stoichiometric ternary III-V alloys, such as AlGaAs or GaInAs (Cagnon et al 2001, Patriarche et al 2004). Both techniques are based on the low values of the GaAs SF and on its correlative high sensitivity to even small compositional changes. However, in standard ternary alloys, it is the substitution on a given sublattice of atoms having different ASAs (Ga and Al or Ga and In) which produces the contrast. Here, the substitution-induced contrast is very low because Mn and As scatter similarly to Ga; instead, the high contrast is due to additional scatterers, the interstitial atoms. Of course, both techniques have the same contrast detection limit, which we estimate to be about 1% in terms of ρ_{002}. This translates into a detection limit of only $6\text{x}10^{-4}$ for $\left|c^1_{Mn} - c^2_{Mn}\right|$.

ρ_{002}	r_G	r_M	$a_\perp$ (nm)	$\left(\tilde{c}^2_{Mn} - \tilde{c}^1_{Mn}\right)$ (%)	c^2_{Mn} (%)	c^s_{Mn} (%)	c^{III}_{As} (%)
0.79	0.917	0.070	0.56900	1.26	1.20	5.89	1.26

Table 1. ρ_{002}: ratio of the 002 DF intensities for GaMnAs and GaAs. r_G, r_M: ratios of the Ga and Mn concentrations to that of As. $a_\perp$: lattice parameter along [001]. $\left(\tilde{c}^2_{Mn} - \tilde{c}^1_{Mn}\right)$: difference of the concentrations of the two types of Mn interstitials estimated by neglecting all other minority species. c^2_{Mn}, c^s_{Mn} and c^{III}_{As}: concentrations calculated by assuming no type 1 interstitial. Except $a_\perp$, all values pertain to a given analysed area. For typical values of uncertainties, see Glas et al (2004).

3. DETAILED QUANTITATIVE ANALYSIS

It is possible to refine our first analysis by using additional data gathered from the same specimen area. Namely, we measure by energy dispersive X-ray analysis the ratios r_G and r_M of the atomic concentrations of Ga and Mn to that of As (Table 1). This yields two more relations between our four unknowns, $\left(1 - c^{III}_{As} - c^s_{Mn}\right) = r_G\left(1 + c^{III}_{As}\right)$ and $\left(c^s_{Mn} + c^1_{Mn} + c^2_{Mn}\right) = r_M\left(1 + c^{III}_{As}\right)$. From these and Eq. (2), we deduce a single relation linking two given variables, *e.g.* c^2_{Mn} and $c_{Mn} = c^s_{Mn} + c^1_{Mn} + c^2_{Mn}$:

$$F_{002} = 4\left\{2\left(f_{As} - 2f_{Mn}\right) - \left[r_M^{-1}\left(f_{As} - 2f_{Mn}\right) + r_G\, r_M^{-1}\left(f_{Ga} - 2f_{Mn}\right) - f_{Mn}\right]c_{Mn} + 2f_{Mn}\, c^2_{Mn}\right\} \quad (3)$$

All other concentrations are easily calculated from these two variables: $c^s_{Mn} = 2 - (r_G + 1)c_{Mn}/r_M$, $c^1_{Mn} = c_{Mn} - c^s_{Mn} - c^2_{Mn}$, $c^{III}_{As} = c_{Mn}/r_M - 1$ and $c^{III}_{Ga} = r_G\, c_{Mn}/r_M$. Hence, for any set of experimental data (F_{002}, r_G and r_M), each concentration c_{Mn} corresponds to a unique set of minority species concentrations (Fig. 3). In practice, F_{002} is obtained from the measured ρ_{002} as follows. X-ray diffraction yields the lattice parameter $a_\perp$ along [001], from which the 002 scattering angle and the ASAs can be accurately evaluated. TEM reveals a coherent GaAs/GaMnAs interface, so that $V_c = a_0^2\, a_\perp$, with a_0 the lattice parameter of GaAs. Thus, $F_{002} = (a_\perp/a_0)(\rho_{002})^{1/2}\, F_{002}(\text{GaAs})$.

The values of Fig. 3 are the only ones compatible with our experiments on the particular area analysed. The admissible range of total Mn concentration is remarkably narrow. In any case, the interstitials are mainly of type-2 and $\left(c^2_{Mn} - c^1_{Mn}\right)$ remains close to our first estimate $\left(\tilde{c}^2_{Mn} - \tilde{c}^1_{Mn}\right)$ (Table 1). Moreover, all theoretical and experimental studies show that the high ratios of interstitial to substitutional Mn found in most of Fig. 3, apart from its left section, are incompatible with ferromagnetism. To proceed further, we thus assume, following Mašek (2003), that only type-2 interstitials exist. Then, $c^1_{Mn} = 0$, $c_{Mn} = r_M\left(c^2_{Mn} + 2\right)/\left(1 + r_G + r_M\right)$ and:

$$c^2_{Mn} = \left(f_{As} + r_G f_{Ga} + r_M f_{Mn}\right)^{-1}\left[2r_G\left(f_{As} - f_{Ga}\right) + 2r_M\left(f_{As} - f_{Mn}\right) - ¼\left(1 + r_G + r_M\right)F_g\right] \quad (4)$$

All relevant concentrations are thus uniquely determined (Table 1). Note that in the area analysed the fraction of type-2 interstitial Mn is equal to the global fraction of interstitials (types 1 and 2) measured macroscopically by Yu et al (2002) in as-grown samples, namely 17 % of the total Mn concentration.

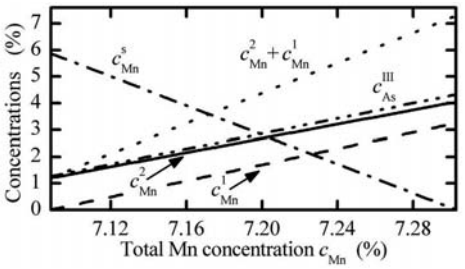


Fig. 3. Variations with the total Mn concentration of the concentrations of Mn interstitial and substitutional atoms and of antisite defects, compatible with the TEM results of Table 1, calculated from Eq. (3). The c_{Mn} range is determined by the constraints $c^1_{Mn} \geq 0$ and $c^s_{Mn} \geq 0$. This figure pertains only to a given zone of a given specimen, but is typical of our analyses.

4. DISCUSSION AND CONCLUSIONS

We devised a TEM method for measuring the concentrations of all minority constituents currently considered as relevant to the magnetic properties of GaMnAs. This is an unexpected achievement since TEM is usually unable to identify, let alone to quantify, minor non-matrix constituents, and site-sensitivity requires specific techniques involving the careful control of channelling conditions. Here, we show that, in a favourable case, standard TEM techniques provide such information and sensitivity.

The main reason of this success is the high sensitivity of the 002 DF intensity to the tetrahedral Mn interstitials. Moreover, the sign of the contrast between GaMnAs and GaAs reveals which of the two types dominates. All our analyses of as-grown and annealed samples show GaMnAs darker than GaAs, from which we deduce the prevalence of type-2 interstitials. However, annealed samples show a reduced contrast, consistent with the expected out-diffusion of Mn interstitials (for the sample analysed in Sections 2 and 3, annealing raises T_C up to 138 K and reduces c^2_{Mn} from 1.2 % to about 0.7 %). Moreover, whereas the 002 intensity is usually uniform in as-grown layers, annealing often induces spatial variations, which we are currently analysing in terms of minor constituent distributions.

More generally, under the assumption $c^1_{Mn} = 0$, all concentrations are uniquely determined; without this hypothesis, narrow concentration ranges are obtained. To determine c^1_{Mn}, we need a fourth experimental measurement adding a new relation to the three already available between our four unknowns. Using another weak reflection is difficult: either the diffracted intensity is extremely low or double diffraction hampers the analysis (case of 222). Strong reflections are of course also sensitive to the minority constituents, but only very weakly: for typical concentrations, their SFs only change by a fraction of % with respect to GaAs. Their possible use for quantitation is thus limited by factors which could be neglected for weak reflections, in particular dynamic and static displacements and disorder. Alternatively, we currently study the use of a modified channelling-enhanced analysis.

REFERENCES

Cagnon J, Buffat P A, Stadelmann P A and Leifer K 2001 Microsc. Semicond. Mater. 2001, eds A G Cullis and J L Hutchison (Bristol , IoP) Inst. Phys. Conf. Ser. **169**, p 37

Doyle P A and Turner P S 1968 Acta Cryst. A **24**, 390

Edmonds K W, Bogusławski P, Wang K Y, Campion R P, Novikov S N, Farley N R S, Gallagher B L, Foxon C T, Sawicki M, Dietl T, Buongiorno Nardelli M and Bernholc J 2004 Phys. Rev. Lett. **92**, 037201

Glas F 2004 Phil. Mag. **84**, 2055

Glas F, Patriarche G, Largeau L and Lemaître A 2004 Phys. Rev. Lett. **93**, 086107

Mahadevan P and Zunger A 2003 Phys. Rev. B **68**, 075202

Mašek J, Kudrnovský J and Máca F 2003 Phys. Rev. B **67**, 153203

Matsukura F, Ohno H and Dietl T 2002 Handb. Magn. Mater. (Amsterdam, Elsevier) vol **14**, p 1

Patriarche G, Largeau L, Harmand J C and Gollub D 2004 Appl. Phys. Lett. **84**, 203

Tuomisto F, Pennanen K, Saarinen K and Sadowski J 2004 Phys. Rev. Lett. **93**, 055505

Yu K M, Walukiewicz W, Wojtowicz T, Kuryliszyn I, Liu X, Sasaki Y and Furdyna J K 2002 Phys. Rev. B **65**, 201303

First-principles calculations of 002 structure factors for electron scattering in strained $In_xGa_{1-x}As$

A Rosenauer, M Schowalter, F Glas[1] and D Lamoen[2]

Institut für Festkörperphysik, Universität Bremen, Otto-Hahn-Allee 1, 28359 Bremen, Germany
[1] CNRS - Laboratoire de Photonique et de Nanostructures, Route de Nozay, 91460 Marcoussis, France
[2] Departement Fysica, Universiteit Antwerpen, Groenenborgerlaan 171, B-2020 Antwerpen, Belgium

ABSTRACT: We report on computation of 002 structure factors for electron scattering in strained and unstrained $In_xGa_{1-x}As$ alloys (x=0 to 1) by the linearised augmented plane-wave+local orbitals (LAPW+lo) method. The calculations of strained $In_xGa_{1-x}As$ were performed according to the strain state in specimens with large, small, and intermediate thickness in the electron beam direction. Additionally, the effect of static atomic displacements is taken into account. The calculated 002 structure factor vanishes at an In concentration of 16.4 %. This value is in good agreement with previously reported experimental measurements. Our results are a significant improvement with respect to the isolated atom approximation which predicts a value of 22.5 %.

1. INTRODUCTION

Research on semiconductor nanostructures has increased because of many possible applications in optoelectronic devices. In semiconductor laser structures, the composition distribution of the active region strongly influences the performance of the device. Investigation of interrelations between growth parameters and composition distribution requires accurate measurement of the composition distribution on an atomic scale. Several methods have been developed to determine the composition distribution in semiconductor nanostructures by transmission electron microscopy (TEM). High resolution TEM methods include techniques exploiting the chemical sensitivity of the (002) beam in sphalerite type materials. For these techniques, (002) dark field images (Petroff 1974, Cagnon et al 2003, Patriarche et al 2004) or fringe images stemming from 2-beam interference of the transmitted beam and the (002) beam (Rosenauer 2003) are used. Extraction of quantitative chemical information requires a comparison with measured calibration curves (Cagnon et al 2003, Patriarche et al 2004) or with theoretical simulations (Rosenauer 2003). These simulations are conventionally based on structure factors calculated from atomic scattering amplitudes, which e.g. were published by Doyle and Turner (1968), Weickenmeier and Kohl (1991) and Su and Coppens (1997). In these papers, atomic scattering amplitudes are computed for isolated atoms so that the redistribution of electrons due to bonding of atoms cannot be taken into account. Moreover, Glas (2003, 2004) showed that the structure factors are also affected by local static displacements which occur in most sphalerite type alloys because the atoms which share at least one of the two sublattices have different covalent radii.

In this work, we show that these effects significantly change the 002 structure factor of an $In_xGa_{1-x}As$ alloy. We demonstrate that redistribution of electrons can be taken into account by introduction of modified atomic scattering amplitudes (MASAs) that are derived from *ab initio* computations within the density functional theory formalism. The advantage of using MASAs is the possibility to take into account static atomic displacements and Debye-Waller factors by appropriate correction factors.

2. CALCULATION OF STRUCTURE FACTORS

2.1 Isolated Atom Approximation

In the isolated atom approximation, the structure factor $F_\kappa^{hkl}(\mathbf{a})$ with Miller indices *hkl* for electron scattering in a binary (strained) sphalerite type crystal κ (here GaAs or InAs) is given by:

$$F_{\kappa}^{hkl}(\mathbf{a}) = \sum_{\nu=1}^{2}\sum_{j=1}^{4} D_{\nu,\kappa}^{hkl}(\mathbf{a}) f_{\nu,\kappa}^{hkl}(\mathbf{a}) \exp\left[2\pi i \mathbf{g}^{hkl}(\mathbf{a}) \cdot \mathbf{r}_{j,\nu}(\mathbf{a})\right], \tag{1}$$

where **a** is a vector describing the lattice parameters of the unit cell along the [100], [010] and [001] directions (which may differ in a strained unit cell), ν indicates the sublattice (metal or non-metal), $f_{\nu,\kappa}^{hkl}(\mathbf{a})$ is the atomic scattering amplitude of an atom in the sublattice ν of a crystal κ, $D_{\nu,\kappa}^{hkl}(\mathbf{a})$ describes the damping of $f_{\nu,\kappa}^{hkl}(\mathbf{a})$ by thermal vibration, j counts the 4 atoms in sublattice ν with positions $\mathbf{r}_{j,\nu}(\mathbf{a})$ within the non-primitive crystal unit cell, and $\mathbf{g}^{hkl}(\mathbf{a}) = \left(h/a_{[100]}, k/a_{[010]}, l/a_{[001]}\right)$ is the reciprocal lattice vector. In our definition, $f_{\nu,\kappa}^{hkl}(\mathbf{a})$ contains the relativistic correction necessary for high-energy electron diffraction. $D_{\nu,\kappa}^{hkl}(\mathbf{a})$ is connected with the temperature dependent Debye-Waller factors $B_{\nu,\kappa}(T)$ according to:

$$D_{\nu,\kappa}^{hkl}(\mathbf{a}) = \exp\left\{-1/4\, B_{\nu,\kappa}(T)\left[g^{hkl}(\mathbf{a})\right]^2\right\}. \tag{2}$$

In a very good approximation, the structure factors of the ternary crystal $In_xGa_{1-x}As$ are given by:

$$F_{In_xGa_{1-x}As}^{hkl}(\mathbf{a}) = xF_{InAs}^{hkl}(\mathbf{a}) + (1-x)F_{GaAs}^{hkl}(\mathbf{a}). \tag{3}$$

To take into account the strain state of a thin $In_xGa_{1-x}As$ layer buried in GaAs within a thin cross section TEM specimen, we define the [001] direction as the growth direction, the specimen is thinned along [010] direction, and the specimen is assumed infinitely large along the [100] direction. Applying elasticity theory, the lattice parameter vector **a** of a strained $In_xGa_{1-x}As$ layer is given by:

$$\mathbf{a}(x,s) = a_{bulk}(x)(\mathbf{1} - \boldsymbol{\varepsilon}(x,s)), \tag{4}$$

where $a_{bulk}(x)$ is the bulk lattice parameter of $In_xGa_{1-x}As$. The strain $\boldsymbol{\varepsilon}(x,s)$ is given by:

$$\boldsymbol{\varepsilon}_{[100]} = f(x); \quad \boldsymbol{\varepsilon}_{[010]} = f(x)\frac{s[c_{11}(x)+c_{12}(x)]-c_{12}(x)}{c_{11}(x)+c_{12}(x)(1-s)}; \quad \boldsymbol{\varepsilon}_{[001]} = -f(x)\frac{(1+s)c_{12}(x)}{c_{11}(x)+c_{12}(x)(1-s)}, \tag{5}$$

Where the $c_{ij}(x) = xc_{ij,InAs} + (1-x)c_{ij,GaAs}$ are the elastic constants of $In_xGa_{1-x}As$. The misfit $f(x)$ is:

$$f(x) = (a_{bulk}(0) - a_{bulk}(x))/a_{bulk}(x) \quad \text{with} \quad a_{bulk}(x) = xa_{InAs} + (1-x)a_{GaAs}. \tag{6}$$

The parameter s in Eq. (5) describes the specimen thickness. The value s=1 corresponds to the limit of an infinitely thick specimen, and s=0 describes an infinitely thin specimen. A strain factor of s=0.5 corresponds to an "intermediate" thickness.

2.2 Density Functional Theory

To take the effect of electron redistribution in chemical bonds into account, we applied density functional theory (DFT) methods using the "WIEN2k" program package. We calculated X-ray scattering structure factors provided by the "lapw3" program that separately lists contributions to the scattering amplitude stemming from spheres around the metal atoms, spheres around the non-metal atoms, and the interstitial region outside the spheres. The radii of the spheres were chosen 10 % smaller than the nearest-neighbour distance. These contributions will in the following be denoted $X_{\nu,\kappa}^{hkl}(\mathbf{a})$, where κ corresponds to the binary crystal (GaAs or InAs), ν=1 corresponds to the metal sublattice, ν=2 denotes the non-metal sublattice, and ν=3 corresponds to the interstitial region. The total X-ray scattering structure factor is thus given e.g. for GaAs by:

$$X_{GaAs}^{hkl}(\mathbf{a}) = X_{Ga,GaAs}^{hkl}(\mathbf{a}) + X_{As,GaAs}^{hkl}(\mathbf{a}) + X_{\text{interstitial},GaAs}^{hkl}(\mathbf{a}) = \sum_{\nu=1}^{3} X_{\nu,GaAs}^{hkl}(\mathbf{a}). \tag{7}$$

Using these values, modified atomic scattering amplitudes (MASAs) $f'^{hkl}_{\nu,\kappa}(\mathbf{a})$ can be defined which replace the atomic scattering factors $f_{\nu,\kappa}^{hkl}(\mathbf{a})$ in Eq. (1):

$$f'^{hkl}_{\nu,\kappa}(\mathbf{a}) = \frac{e^2 m_0\left(1+\frac{eU}{m_0c^2}\right)}{2\pi h_P{}^2 \varepsilon_0 (g^{hkl}(\mathbf{a}))^2}\left(Z_{\nu,\kappa} - \frac{X^{hkl}_{\nu,\kappa}(\mathbf{a})}{\tau_\nu} - \frac{X^{hkl}_{3,\kappa}(\mathbf{a})}{2\tau_\nu}\right) \quad \text{with } \tau_\nu = \sum_{j=1}^{4}\exp\left[2\pi i g^{hkl}(\mathbf{a})\cdot r_{j,\nu}(\mathbf{a})\right], \quad (8)$$

where ν=1,2 (metal or non-metal), e is the unsigned electron charge, m_0 is the rest mass of an electron, U is the acceleration voltage, c is the speed of light in vacuum, h_P is Planck's constant, ε_0 is the dielectric constant in vacuum and $Z_{\nu,\kappa}$ is the nuclear charge of atom ν in binary crystal κ.

For the computation of the 002 structure factors in ternary $In_xGa_{1-x}As$ we applied the following procedure: For a certain In-concentration x and strain factor s we obtained the lattice parameter vector $\mathbf{a}(x,s)$ of the strained $In_xGa_{1-x}As$ layer from Eq. (4). Then we computed the MASAs $f'^{002}_{Ga,GaAs}(\mathbf{a}(x,s))$, $f'^{002}_{As,GaAs}(\mathbf{a}(x,s))$ of a strained GaAs unit cell, and the MASAs $f'^{002}_{In,InAs}(\mathbf{a}(x,s))$ and $f'^{002}_{As,InAs}(\mathbf{a}(x,s))$ of a strained InAs cell. Note that the lattice parameter is the same for both cells. For the DFT calculation with the "Wien2K" program we used the generalized gradient approximation of Perdew et al. (1996). The number of sampling points in the full Brillouin zone and the interstitial plane-wave vector cut-off were chosen by converging the (002) structure factors to a precision better than $5\cdot10^{-2}$ %. A TEM acceleration U=200 kV was assumed. The MASAs were calculated for In-concentrations x between 0 and 1 in steps of 0.01. Strain parameters s equal to 0, 0.5 and 1 were used. In addition, the calculations were performed for bulk unstrained $In_xGa_{1-x}As$. The computed MASAs have been fitted by third-order polynomials:

crystal	element		$s=0$	$s=0.5$	$s=1$	bulk
GaAs	Ga	p_1	-7.725E-4	1.304E-3	2.933E-3	2.619E-4
		p_2	1.789E-3	6.326E-4	2.738E-3	-1.009E-3
		p_3	4.295E-2	5.282E-2	6.602E-2	3.205E-2
		p_4	5.384E-1	5.383E-1	5.383E-1	5.383E-1
	As	p_1	-9.497E-4	7.797E-4	1.760E-3	3.178E-4
		p_2	4.945E-4	-7.600E-4	8.080E-4	-1.547E-3
		p_3	4.446E-2	5.300E-2	6.426E-2	3.471E-2
		p_4	5.907E-1	5.906E-1	5.907E-1	5.907E-1
InAs	In	p_1	-7.940E-4	1.446E-3	3.050E-3	2.278E-4
		p_2	1.271E-3	1.904E-4	3.182E-3	-1.372E-3
		p_3	5.889E-2	7.218E-2	9.013E-2	4.348E-2
		p_4	8.311E-1	8.311E-1	8.311E-1	8.311E-1
	As	p_1	-1.403E-3	9.827E-4	2.536E-3	1.902E-4
		p_2	1.442E-3	-8.390E-4	-2.023E-4	-1.411E-3
		p_3	4.306E-2	5.147E-2	6.235E-2	3.443E-2
		p_4	5.831E-1	5.831E-1	5.831E-1	5.830E-1

Table 1: Table of polynomial coefficients for the modified atomic scattering amplitudes of strained $In_xGa_{1-x}As$. The parameter s describes the strain state according to Eq. (5). The bulk material lattice parameter was used for the column "bulk". All values are given in units of nm.

$$f'^{002}_{\nu,\kappa}(\mathbf{a}(x,s)) = p_1(s)x^3 + p_2(s)x^2 + p_3(s)x + p_4(s). \quad (9)$$

A list of all polynomial coefficients is given in Table 1. The corresponding structure factors of the 002 reflection in $In_xGa_{1-x}As$ for different strain states is obtained from Eq. (3) using the structure factors of the binary crystals from Eq. (1), where the atomic scattering factors $f^{hkl}_{\nu,\kappa}(\mathbf{a})$ are replaced by the MASAs $f'^{002}_{\nu,\kappa}(\mathbf{a}(x,s))$ as given in Eq. (9).

B	A		$s=0$	$s=0.5$	$s=1$	bulk
As	Ga	p_1	0.0123	0.0144	0.0188	0.0095
		p_2	0.0019	-0.0004	-0.0057	0.0051
		p_3	-0.0142	-0.0139	-0.0131	-0.0145
		p_4	1.0000	1.0000	1.0000	1.0000
Ga	As	p_1	0.0104	0.0126	0.0169	0.0078
		p_2	0.0185	0.0151	0.0087	0.0223
		p_3	-0.0433	-0.0430	-0.0423	-0.0435
		p_4	1.0000	1.0000	1.0000	1.0000
As	In	p_1	0.0120	0.0139	0.0185	0.0093
		p_2	0.0021	-0.0001	-0.0057	0.0053
		p_3	-0.0141	-0.0138	-0.0128	-0.0145
		p_4	1.0000	1.0000	1.0000	1.0000
In	As	p_1	0.0123	0.0157	0.0224	0.0086
		p_2	0.0221	0.0191	0.0124	0.0254
		p_3	-0.0227	-0.0230	-0.0230	-0.0222
		p_4	0.9883	0.9883	0.9882	0.9883

Table 2: Table of polynomial coefficients for the SD correction factors of strained $In_xGa_{1-x}As$, with A the atom considered and B its nearest neighbour.

2.3 Static Atomic Displacements

Besides charge redistribution, the structure factors of $In_xGa_{1-x}As$ are also affected by local structural distortions. Indeed, in any III-V alloy where atoms having different covalent radii share at least one sublattice, there exists an average perfect periodic structure, but the equilibrium positions of the atoms are displaced from their sites (although these static atomic displacements (SDs) are small enough for any atom to be unambiguously assigned to a given site). To take both charge redistribution and

static displacements (SDs) into account, we adopt the following approach. We simulate large $In_xGa_{1-x}As$ super-cells consisting of N unit cells with various In compositions x and in various strain states s. Atoms are first placed at the sites of a perfect average crystal with parameters $\mathbf{a}(x,s)$ (Eq. (4)). The overall dimensions of the super-cell are taken (and subsequently kept) equal to large multiples (typically 50) of the components of $\mathbf{a}$. The SDs $\mathbf{u}_{j,\nu,n}$ (atom j in sublattice ν of unit cell n) are then calculated numerically by using the extended valence force field (VFF) model (Keating 1966, Martin 1970) as detailed previously (Glas et al 1990, 2004). From the SDs, we derive $F_\kappa^{002}(\mathbf{a}(x,s))$ by:

$$F_\kappa^{hkl}(\mathbf{a}) = \frac{1}{N}\sum_{n=1}^{N}\sum_{\nu=1}^{2}\sum_{j=1}^{4} f'^{hkl}_{\nu,\kappa}(\mathbf{a}) \exp\left[2\pi i \mathbf{g}^{hkl}(\mathbf{a}) \cdot \left\{\mathbf{r}_{j,\nu}(\mathbf{a}) + \mathbf{u}_{j,\nu,n}(\mathbf{a})\right\}\right]. \qquad (10)$$

The results yield SD correction factors $d^{002}_{A,B}(\mathbf{a}(x,s))$, where A is the atom under consideration and B is its nearest neighbour, so that the structure factor of the (002) reflection can be written as:

$$\begin{aligned} F^{002} = {} & 4(1-x)\left(D^{002}_{Ga,GaAs} d^{002}_{Ga,As} f'^{002}_{Ga,GaAs} - D^{002}_{As,GaAs} d^{002}_{As,Ga} f'^{002}_{As,GaAs}\right) \\ & + 4x\left(D^{002}_{In,InAs} d^{002}_{In,As} f'^{002}_{In,InAs} - D^{002}_{As,InAs} d^{002}_{As,In} f'^{002}_{As,InAs}\right) \end{aligned} . \qquad (11)$$

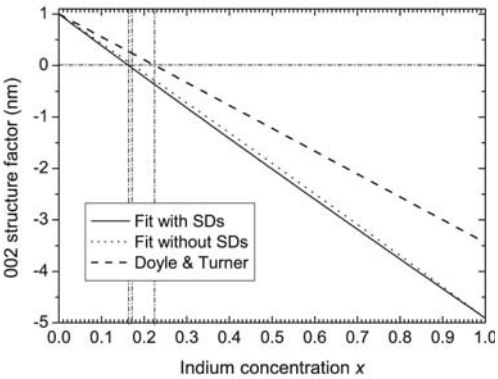


Fig. 1: 002 structure factors computed by DFT with and without SD correction for bulk unstrained $In_xGa_{1-x}As$ in comparison with the isolated atom approximation (Doyle and Turner atomic scattering factors). The values are normalized with respect to GaAs. Vertical bars mark the zero in the three cases.

The resulting values for $d^{hkl}_{\nu,\kappa}(\mathbf{a}(x,s))$ for different x and s have again been fitted by polynomials in analogy to Eq. (9), whose coefficients are listed in Table 2. Fig. 1 compares the resulting structure factors for the 002 reflection in bulk unstrained $In_xGa_{1-x}As$ calculated for $D^{002}_{\nu,\kappa}=1$. We find that the structure factor vanishes at an In-concentration of x=0.164. Cagnon et al (2003) and Patriarche et al (2004) measured values of x=0.17 and 0.18, respectively. Thus, taking into account redistribution of electrons and SDs is a significant improvement with respect to the isolated atom approximation which predicts x=0.225.

ACKNOWLEDGEMENT

A R and D L acknowledge financial support from the FWO-Vlaanderen under contract G.0425.05.

REFERENCES

Cagnon J, Buffat P A, Stadelmann P A and Leifer K 2003 Inst. Phys. Conf. Ser. **180**, 203
Doyle P A and Turner P S 1968 Acta Cryst. A **24**, 390
Glas F, Gors C and Hénoc P 1990 Phil. Mag. B **62**, 373
Glas F 2003 Inst. Phys. Conf. Ser. **180**, 191
Glas F 2004 Phil. Mag. **84**, 2055
Keating P N 1966 Phys. Rev. **145**, 637
Martin R M 1970 Phys. Rev. B **1**, 4005
Patriarche G, Largeau L, Harmand J C and Gollub D 2004 Appl. Phys. Lett. **84**, 203
Perdew J P, Burke K and Ernzerhof M 1996 Phys. Rev. Lett. **77**, 3865
Petroff P M 1974 J. Vac. Sci. Technol. **14**, 973
Rosenauer A 2003 Transmission electron microscopy of semiconductor nanostructures-an analysis of composition and strain, (Heidelberg, Berlin, Springer Tracts in Modern Physics 182)
Su Z and Coppens P 1997 Acta Cryst. A **53**, 749
Weickenmeier A and Kohl H 1991 Acta Cryst. A **47**, 590

Structural characterisation of MBE grown zinc-blende $Ga_{1-x}Mn_xN$/GaAs(001) as a function of Ga flux

Y Han, M W Fay, P D Brown, S V Novikov[1], K W Edmonds[1], B L Gallagher[1], R P Campion[1] and C T Foxon[1]

School of Mechanical, Materials and Manufacturing Engineering, University of Nottingham, University Park, Nottingham NG7 2RD, UK
[1] School of Physics and Astronomy, University of Nottingham, University Park, Nottingham NG7 2RD, UK

ABSTRACT: $Ga_{1-x}Mn_xN$ films grown on semi-insulating GaAs(001) substrates at 680°C with fixed Mn flux and varied Ga flux demonstrated a transition from zinc-blende/wurtzite mixed phase growth for low Ga flux (N-rich conditions) to zinc-blende single phase growth with surface Ga droplets for high Ga flux (Ga-rich conditions). N-rich conditions were found favourable for Mn incorporation in the GaN lattice. α-MnAs inclusions were identified extending into the GaAs buffer layer.

1. INTRODUCTION

III-V ferromagnetic semiconductors are of interest because of their potential application within spintronic device structures (Wolf et al 2001). Theoretical prediction of the Curie temperature for various semiconductors (Dietl et al 2000) suggests that a T_C value above room temperature is possible for zinc-blende GaN containing 5 at% Mn and a hole concentration of $3.5\times10^{20}cm^{-3}$. In view of the limited solid solubility of Mn in GaN, it becomes necessary to use non equilibrium growth techniques such as plasma-assisted molecular beam epitaxy (PAMBE) to establish appropriate conditions for the growth of uniform $Ga_{1-x}Mn_xN$ alloys. To date, high p-type $Ga_{1-x}Mn_xN$ layers with carrier concentrations exceeding $10^{18}cm^{-3}$ have been obtained by PAMBE (Novikov et al 2004).

Earlier work on the growth of zinc-blende GaN suggests that exact control of the III:V ratio close to the stoichiometric condition allows the production of single phase zinc-blende epitaxial layers, whilst deviation to Ga or N-rich conditions reportedly produces mixed zinc-blende and wurtzite material (Brandt et al 1995; Giehler et al 1995; Ruvimov et al 1997). More recently, various Mn-N or Ga-Mn-N precipitations have been reported for wurtzite GaN epilayers grown on sapphire substrates (e.g. Kuroda et al 2003 and Nakayama et al 2003).

In this paper, the influence of the Ga:N ratio on the microstructural development of $Ga_{1-x}Mn_xN$/GaAs(001) grown by PAMBE is assessed using a variety of complementary analytical techniques.

2. EXPERIMENTAL

Zinc-blende $Ga_{1-x}Mn_xN$ epilayers were grown on semi-insulating (001) oriented GaAs substrates at 680°C by PAMBE. Briefly, a GaAs buffer layer of thickness ~0.15μm was deposited to provide a clean surface for epitaxy. Following initiation of the N plasma, the Mn and N shutters were opened whilst the As shutter was closed. The Mn flux was fixed at a level of 1.0×10^{-8} mbar while the Ga:N ratio was varied by changing the Ga flux from 7.5×10^{-8} mbar to $1.2\text{x}10^{-6}$ mbar. This corresponded to a transition from N-rich to Ga-rich conditions, with the latter being identified

by the development of Ga droplets on the growth surface. An overall chamber pressure of 2-3×10^{-5} mbar was maintained by a flow of N_2. The growth conditions for the sample set are summarised in Table 1.

The bulk and fine scale defect microstructure of each sample was assessed. A Philips X-pert diffractometer was initially used to assess the bulk crystal structure of the deposited epilayers. The complementary technique of reflection high energy electron diffraction (RHEED) using a modified JEOL 2000FX transmission electron microscope, with as-grown or HCl etched specimens mounted vertically, immediately beneath the projector lens, was then applied to appraise the sample near surface microstructure. Sample morphology was assessed using an FEI XL30 scanning electron microscope operated at 15-20kV. Samples for TEM investigation across the stoichiometric range were prepared in plan-view and cross-sectional geometries using sequential mechanical polishing and argon ion beam thinning. Samples were assessed using conventional diffraction contrast techniques using JEOL 2000FX and 4000FX instruments and energy dispersive X-ray (EDX) analysis using an Oxford Instruments ISIS system.

Table 1. Growth details of $Ga_{1-x}Mn_xN$ /GaAs(001) sample set

Sample	Tg / °C	N_2 / ×10^{-5} mbar	Ga flux / ×10^{-7} mbar	Mn flux / ×10^{-8} mbar	XRD FWHM/°	Ga:N ratio
A	680	2-3	0.75	1	1.15	N-rich
B	680	2-3	1.5	1	0.97	N-rich
C	680	2-3	2.5	1	1.07	N-rich
D	680	2-3	4.6	1	1.17	~1:1 (slightly N-rich)
E	680	2-3	8.0	1	0.95	Ga-rich
F	680	2-3	10	1	0.75	Ga-rich
G	680	2-3	12	1	0.86	Ga-rich

3. RESULTS AND DISCUSSION

The formation of zinc-blende $Ga_{1-x}Mn_xN$ was confirmed by XRD spectra obtained across the sample set. Variation in the full width at half maxima (FWHM) values for the 002 reflection across the stoichiometric range (Table 1) suggests that the layer structural quality becomes optimised for conditions of slightly Ga rich growth. However, no evidence for the presence of second phase wurtzite material was discerned for any of the spectra. As observed using SEM, the sample grown closest to ~1:1 stoichiometric conditions appears specular, indicative of a smooth surface. Samples grown under N-rich conditions appear to exhibit a slightly rougher surface, whilst samples grown under Ga-rich conditions showed increasing amounts of Ga droplets on the sample surface with increasing Ga flux.

RHEED patterns recorded along <110> projections for samples A, D and G are presented in Fig. 1(a-c). It is noted that clear, sharp spots was only obtained for the Ga-rich samples after removal of surface Ga droplets using boiling HCl. All the samples demonstrated the cubic structure with extra spots and/or streaks indicating varying degrees of mixed phase growth and stacking disorder on inclined {111} planes. In particular, a transition from mixed hexagonal/cubic (α/β) phase growth for N-rich conditions to single phase cubic material for Ga-rich conditions was observed (as distinct from the previous indications of XRD).

By way of example, for sample A grown under N-rich conditions, dominant diffraction spots from both cubic and hexagonal material were identified (Fig. 1a). The indexing of Fig. 1a is clarified with reference to the schematic diagram of Fig. 1d which illustrates the orientation relationship between the two phases, with $<110>_\beta$ // $<11\bar{2}0>_\alpha$ and $\{111\}_\beta$ // $\{0001\}_\alpha$. It is noted that the extra spots due to the hexagonal phase became faint with increasing Ga flux, disappearing when the Ga:N ratio approached 1:1 stoichiometry (Fig. 1b).

For samples grown under N-rich conditions and ~1:1 stoichiometry, streaks preferentially aligned along one <111> direction were also observed, indicating the preferential alignment of planar defects (i.e. thin microtwins and stacking faults) inclined to the growth surface on just one set of {111} planes (Figs 1 a and b). Similar streaks were observed along both <111> directions for samples

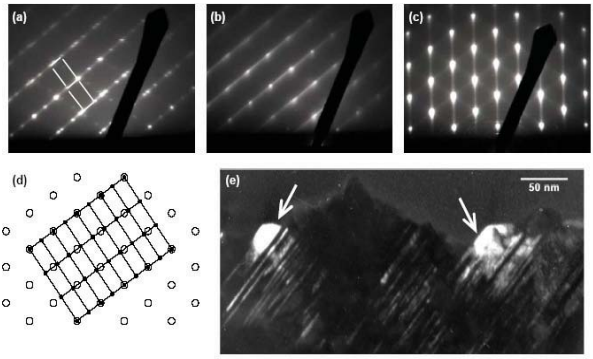


Fig. 1. <110> RHEED patterns for as-grown $Ga_{1-x}Mn_xN$/GaAs(001): (a) sample A, (b) sample D and (c) sample G (HCl etched). (d) Schematic illustration for (a) denoting diffraction spots corresponding to the zinc-blende (open circles) and wurtzite (solid dots) phase; (e) Dark-field, cross-sectional TEM image of the near surface microstructure of sample A suggesting that the wurtzite GaMnN phase arises due to localised small grains at the growth surface (arrowed).

grown under Ga-rich conditions, again attributable to a high density of inclined planar defects (Fig. 1c). It is noted that samples grown under N-rich and nearly 1:1 stoichiometric conditions exhibited strong anisotropy in the distribution of planar defects, being present for just one <110> sample projection, whilst samples grown under Ga-rich conditions exhibited planar defects for both orthogonal <110> and $<1\bar{1}0>$ sample projections. This variation in the anisotropic distribution of planar defects suggests that this effect is associated with the transition from N-rich to Ga-rich growth, i.e. due to differences in III:V stoichiometry at the growth surface during the process of epilayer nucleation, rather than being due to slight vicinality of the substrate surface. In addition, the presence of streaks perpendicular to the shadow edge of samples grown under Ga-rich conditions (Fig. 1c), following HCl etching, are attributed to patches of relatively smooth surface. More precisely, however, the diffraction effect of streaks perpendicular to the growth surface is attributed to the material that is not perfectly flat, but with slight local misorientations combined with some degree of surface disorder (Cowley 1992).

Overall, the indication from these RHEED patterns together with XRD spectra and SEM observation is that nearly 1:1 stoichiometry (or slightly Ga-rich conditions) correspond to an optimised microstructure.

Figure 1e shows a centred dark field image formed from a diffraction spot attributed to only wurtzite $Ga_{1-x}Mn_xN$, as distinct from an overlap of spots due to wurtzite $Ga_{1-x}Mn_xN$ and microtwin spots from the zinc-blende $Ga_{1-x}Mn_xN$ located at 1/3<111> positions. This indicates the localisation of small grains of wurtzite $Ga_{1-x}Mn_xN$ at the growth surface. However, the overlap from stacking fault streaks through the objective aperture, due to slight imaging beam convergence, also contributes to this dark field image, partially highlighting the stacking disorder on one set of {111} planes. Since selected area diffraction experiments provided no evidence for the presence of wurtzite domains through the bulk of the epilayer and no evidence was found for hexagonal phase material at the epilayer/substrate interfaces, the formation of wurtzite $Ga_{1-x}Mn_xN$ are attributed to a cool down effect at the end of growth whereby a slight change in surface stoichiometry might have occurred under N-rich conditions, allowing small grains of the more stable hexagonal phase to be established. The small volume fraction of these surface hexagonal grains explains why they were not detectable by XRD.

EDX measurements from the epilayers during TEM observation indicated a variation in the Mn content across the sample set, with a relatively uniform Mn content of ~3.3at% for sample A, peaking at a value of 4±0.3% for sample D, while the Mn content was below the detectability limit of EDX for samples grown under Ga rich conditions. This is consistent with reports of MBE grown wurtzite $Ga_{1-x}Mn_xN$/sapphire which demonstrate that N-rich (and Mn-rich) conditions are required for the successful incorporation of Mn into the crystal lattice (Haider et al 2003; Kuroda et al 2003), as assessed using EDX and SIMS respectively.

By way of illustration, Fig. 2a presents a dark field image of Sample A, demonstrating the highly faulted nature of the epilayer, and pyramidal precipitates (arrowed) extending into the GaAs buffer layer. EDX measurements confirmed the presence of Mn and As within such inclusions (Fig. 2c), whilst associated selected area electron diffraction patterns (Fig. 2b) confirmed that the inclusions comprised α-MnAs. The indexing of Fig. 2b is clarified with reference to the schematic diagram of Fig. 2d. The orientation relationship here between α-MnAs and GaAs is given by $<11\bar{2}0>_{MnAs}$ // $<110>_{GaAs}$ and $\{0001\}_{MnAs}$ // $\{111\}_{GaAs}$. It is emphasised that such MnAs inclusions extending into the buffer layer were

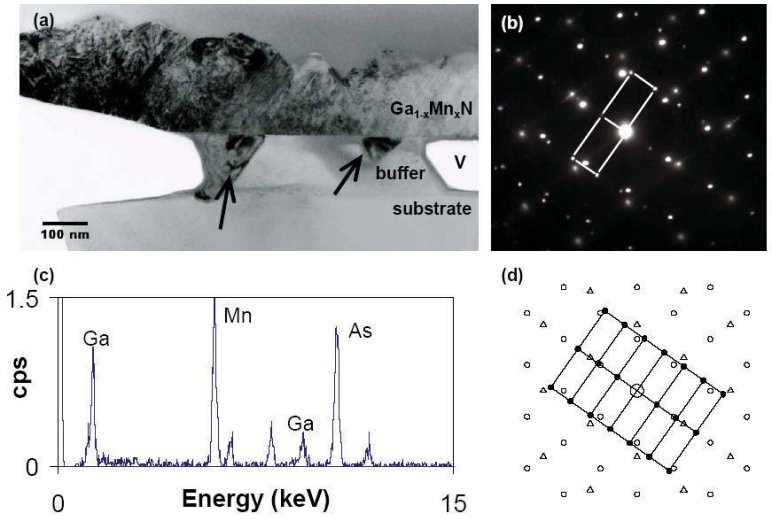


Fig. 2. (a) 002 dark field image of sample A showing α-MnAs inclusions extending into the GaAs buffer layer. (b) Selected area diffraction pattern recorded from the region of an inclusion. (c) EDX spectra demonstrating the inclusions predominantly comprise Mn and As. (d) Schematic illustration denoting diffraction spots due to zinc-blende $Ga_{1-x}Mn_xN$ (open triangles); GaAs (open circles) and α-MnAs (solid dots).

identified within all the samples with decreasing size upon transition to Ga-rich growth conditions. No evidence for Ga-Mn-N or Mn-N inclusions was found in these samples.

In view of the very different levels of hardness of the epilayer and substrate, it is considered that voids present within the GaAs buffer layer as marked in Fig. 2a arise due to preferential ion beam milling of localised strain centres. However, some co-operative mechanism associated with MnAs precipitate formation during the process of growth might also be implicated in their initial formation.

In summary, N-rich conditions are required for the incorporation of Mn within $Ga_{1-x}Mn_xN$, whilst slightly Ga-rich conditions are associated with optimised structural properties. All samples exhibited MnAs inclusions extending into the GaAs buffer layer, arising from the limited solid solubility of Mn in GaN.

ACKNOWLEDGEMENTS

This work was supported by the EPSRC grants GR/S25630/01 and GR/S81407/01. Y Han would like to thank Keith Dinsdale, Martin Roe, Nicola Weston and Julie Thornhill for their kind technical support.

REFERENCES

Brandt O, Yang H, Jenichen B, et al. 1995 Phys. Rev. B **52**, R2253
Cowley J M (1992) Electron Diffraction Techniques. Electron Diffraction: An Introduction. J M Cowley. Oxford, Oxford University Press. **1**
Dietl T, Ohno H, Matsukura F, et al. 2000 Science **287**(5455), 1019
Giehler M, Ramsteiner M, Brandt O, et al. 1995 Appl. Phys. Lett. **67**(6), 733
Haider M B, Constantin C, Al-Brithen H, et al. 2003 J. Appl. Phys. **93**(9), 5274
Kuroda S, Bellet-Amalric E, Giraud R, et al. 2003 Appl. Phys. Lett. **83**(22), 4580
Nakayama H, Mashita H, Kulatov E, et al. 2003 J. Magn. Magn. Mater. **258-259**, 323
Novikov S V, Edmonds K W, Giddings A D, et al. 2004 Semicond. Sci. Technol. **19**, L13
Ruvimov S, Liliental-Weber Z, Washburn J, et al. 1997 Appl. Phys. Lett. **71**(20), 2931
Wolf S A, Awschalom D D, Buhrman R A, et al. 2001 Science **294**(5546), 1488

Magic matching in semiconductor heterojunctions

B Pécz, Á Barna, V Heera[1] and W Skorupa[1]

Research Institute for Technical Physics and Materials Science, Hungarian Academy of Sciences, P.O.Box 49, H-1525 Budapest, Hungary
[1] Forschungszentrum Rossendorf, Institute of Ion Beam Physics and Materials Research, D-01314 Dresden, Germany

ABSTRACT: Matching of m crystal planes of a grown layer to n planes of the substrate is observed in many cases, when the difference in the lattice parameters is large. This kind of magic matching is explained by coincidence planes. Two examples are shown in this paper. SiC grains perfectly oriented to the substrate were prepared by high temperature ion implantation of Si into natural diamond. Considering the (111) lattice planes and the cases when 5 planes of SiC match to 6 planes in diamond, or 4 planes of SiC match to 5 planes in diamond, the misfit is reduced to about 2% in both cases having opposite signs. High resolution images taken at the SiC/diamond interface were investigated and both of the above mentioned domains were found. When we consider the regular distribution of the above two domains, i.e. matching of 9 SiC lattice planes to 11 diamond planes a misfit value below 0.1% is obtained. This explains how the ion beam synthesised SiC can grow epitaxially despite the huge difference in lattice parameters. GaN synthesised in GaAs by ion implantation is presented as another example where magic matching of 5:4 reduces the misfit to 0.8%. That value is low enough to be compensated by elastic deformation of the lattice, therefore the insertion of another domain is not needed.

1. INTRODUCTION

Heteroepitaxial semiconducting layers are grown usually when the lattice misfit is low, typically 1-2%. However, there are cases when the misfit is high, but still the grown layer is single crystalline and epitaxial to the substrate. Such a configuration can be explained by the coincidence lattice planes (Matthews 1975 and Vook 1982), what we also can call magic matching in heterojunctions. Matching of m crystal planes of the substrate to n planes in the growing layer can be observed. For example 4 lattice planes of the first crystal matches to 3 lattices of the second one, or 5 to 4, or 11 to 10, etc. When the difference in the lattice parameters of the two crystals is large m and n are small numbers, while those numbers are larger, when the misfit is small. Such a configuration can be considered as a half crystallographic plane inserted into one of the crystals periodically, what is called a geometrical dislocation (Trampert and Ploog 2000). For the realistic cases m=n+1, otherwise the misfit would be very large, for example 40% for the case of 5 to 3 matching.

The classical misfit is defined as: $f_0=(a_0-a_l)/a_0$,

where a_0 is the lattice spacing of the substrate and a_l is the lattice spacing of the layer. Calculating the misfit between cubic SiC and diamond, the above equation results in -0.223, which means 22.3% misfit. In our experiments natural diamond was implanted with silicon at high temperature and we could prepare such heterojunctions by ion beam synthesis (Heera et al 2000). Other examples for ion beam synthesis can be found for example in the papers of Weishart et al (2003) and in Lindner (2003). Selected area diffraction patterns proved that all of the SiC formed is epitaxial to the diamond lattice. In this paper we try to answer the question how that was possible despite the huge misfit.

2. EXPERIMENTAL

SiC/diamond and GaN/GaAs interfaces are investigated and analyzed in this study. Both of the samples studied were prepared by ion beam synthesis, which means ion implantation at high temperature.

Cubic SiC grains were formed in natural IIa diamond implanted at 150 keV to $3x10^{17}$ Si^{+}/cm^{2} at a temperature of 900°C. The implanted zone is a buried layer with crystalline 3C-SiC domains (stripes) in perfect epitaxial relation to the diamond substrate. Cubic GaN grains were formed in GaAs(100) implanted with nitrogen at 200 keV to $6x10^{17}$ $ions/cm^{-2}$ at 600°C.

The implanted layers were investigated by cross-sectional transmission electron microscopy (TEM). Transparent samples for TEM were prepared by low angle, Ar ion beam milling. The images presented here were taken in a JEOL 3010 UHR microscope operating at 300 kV.

3. RESULTS AND DISCUSSION

Figure 1 shows the implanted diamond with a cubic SiC stripe in the middle in high resolution. The diffraction pattern in Fig. 1 shows that the formed SiC is completely epitaxial to the diamond matrix. Figure 2 is an enlarged image of the former one and also tilted in order to show the matching (111) type lattice planes in vertical position. In the middle part of Fig. 2 one can see a matching of 4 to 5, i.e 4 planes of SiC matches to 5 planes of diamond. The coincidence misfit (this is the deviation from the perfect coincidence) is defined by the following equation:

$$F_0=(m\ a_0-n\ a_l)/m\ a_0$$

Obviously a matching configuration is advantageous energetically when F_0 is far smaller than f_0. The fact that the value of F_0 is not exactly zero predicts that hat the m/n matching is interrupted by a domain in which m/n is smaller, or higher depending on the sign of F_0. Calculating the value of F_0 for the above crystal for m/n=4/5 we receive F_0=-0.022, which belongs to 2.2% of misfit.

Investigating Fig. 2 carefully we can trace two other domains on the left and right sides of the image, in which m/n=5/6. Calculating F_0 for this case we receive 0.019, which means 1.9% of misfit. All together that means that we have a matching of the two crystals with a configuration shown by the drawing above Fig.1. SiC and diamond matches with coincidence lattices forming two different domains. It is worth calculating the value of F_0 for the case of m/n is 9/11, (this means that in this coincidence we have two geometrical dislocations) and this results in F_0=0.00088, which means a misfit, which is smaller 0.1%. Such a matching can explain the epitaxial growth of the two crystals.

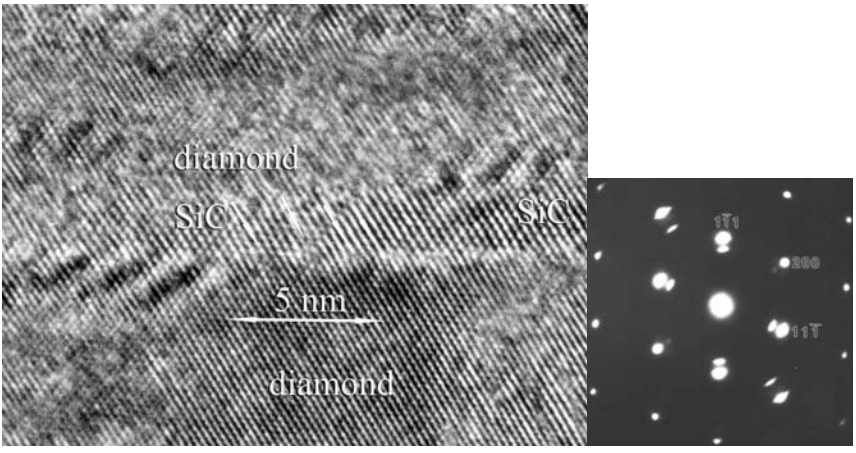


Fig. 1 Cubic SiC formed in natural diamond due to silicon implantation at 900°C. The selective area diffraction pattern shows a perfect orientational matching of the two crystals.

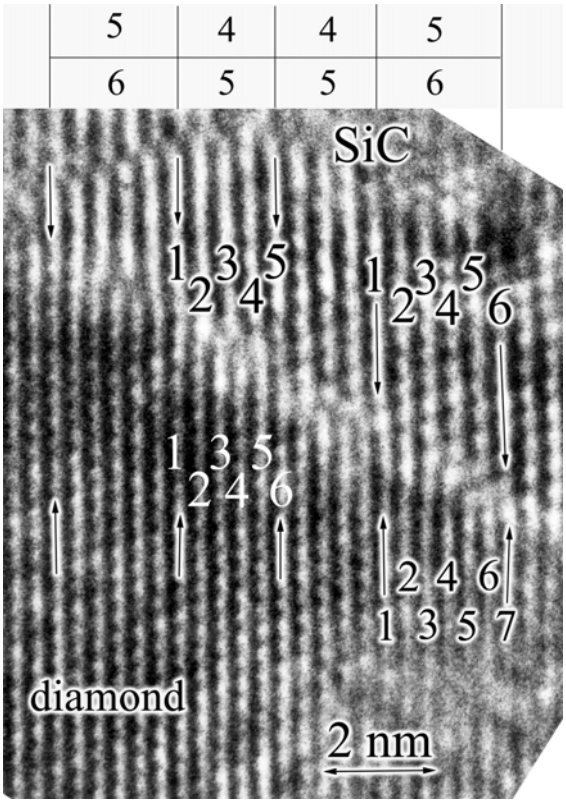


Fig. 2. Enlarged part of the former image. Arrows indicate the coincidence lattice planes. The drawing above the image explains the m/n matching of domains.

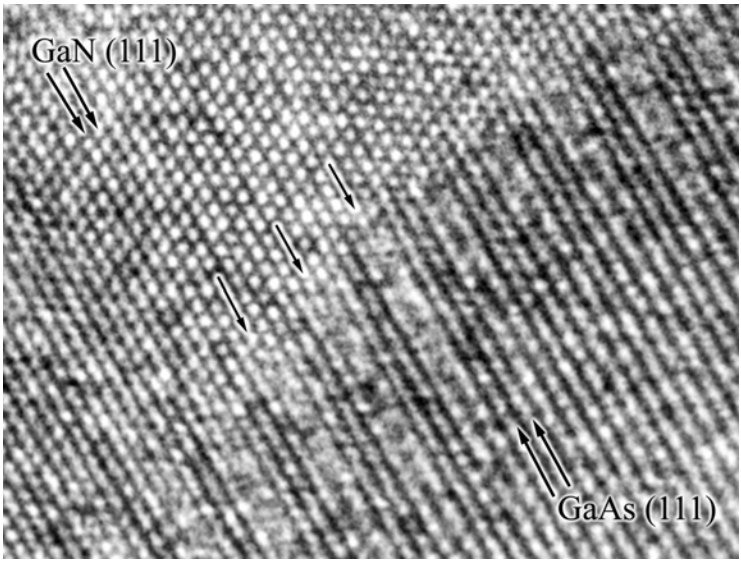


Fig. 3. High resolution image showing the interface between GaN and GaAs. Three of the misfit dislocations are marked by arrows in the middle of the image.

Our next example for coincidence lattice is shown in Fig. 3, which shows the interface of cubic GaN/GaAs. The image is taken on a relatively large (10 nm wide and 50 nm long) cubic GaN grain which was formed by the implantation of nitrogen into GaAs at high temperature (Pécz et al 2004). The (111) lattice spacing of GaAs is 0.3263 nm, while in cubic GaN that is 0.259 nm. Calculating the misfit with the above values yields f_0=-0.2598, which means a very high misfit of about 26%. However, GaN was formed epitaxially in GaAs despite the very high misfit. Three arrows mark geometric dislocations in the middle of the image. One can recognise that 5 planes of GaN match to 4 planes in GaAs by coincidence lattice planes. The corresponding coincidence misfit is F_0=-0.0079. This means that in this system the remaining misfit is less than 0.8%, which can be compensated by the elastic deformation of the lattice. In this system there is no need for the insertion of domains with another coincidence.

4. SUMMARY

Two examples were shown in which interfaces of semiconducting materials were grown in epitaxial orientation despite the huge misfit. This magic matching in heterostructures is explained by coincidence lattice planes. In the case of GaN/GaAs the matching could be predicted without the high resolution images by the comparison of lattice parameters. However, in the case of SiC/diamond the close investigation of the high resolution images gave us further information on the two different domains of coincidence lattices. Therefore the high resolution investigation of interfaces in heterostructures is recomended in the cases when epitaxy is observed despite the large misfit.

SiC/diamond epitaxy is observed by two coincidence lattice domains with m/n=4/5 and m/n=5/6 matching. The regular, alternating combination of those two domains decreases the misfit below 0.1%.

ACKNOWLEDGEMENTS

This work was supported by OTKA T 047141 and B. Pecz acknowledges the support of Bolyai Janos Scholarship (Hungary).

REFERENCES

Heera V, Fontaine F, Skorupa W, Pécz B and Barna Á 2000 Appl. Phys. Lett., **77**, 226
Matthews J W 1975 Epitaxial Growth Part B, ed. Matthews JW (Academic Press, New York) 559
Lindner J K N 2003 Appl. Physics A **77**, 27
Pécz B, Tóth L, Dobos L, Szuts T, Heera V, Skorupa W and Dekorsy T 2003 IOP Conf. Ser. Proc., **180**, 441
Trampert A and Ploog K H 2000 Cryst. Res. Tech. **35,** 793
Vook R W 1982 International Metals Reviews, **27**, 209
Weishart H, Heera V, Eichhorn F, Pecz B, Barna A and Skorupa W 2003 J. Appl. Phys. **94**, 1195

Changes in plasmon peak position in a GaAs/$In_{0.2}Ga_{0.8}As$ structure

R Beanland, A M Sánchez[1], A J Papworth[2], M H Gass[3] and P J Goodhew[2]

Bookham Inc, Caswell, Towcester, Northants NN12 8EQ, UK
[1] Departamento de Ciencia de los Materiales e IM y QI, Universidad de Cádiz, Apdo 40 E-11510 Puerto Real (Cadiz), Spain
[2] Department of Engineering, Materials Science, University of Liverpool, L69 3GH, UK
[3] Department of Materials Science and Metallurgy, Pembroke St. University of Cambridge, CB2 3QZ, UK

ABSTRACT: We have investigated changes in the plasmon loss peak seen in electron energy loss spectra from a 15 nm $In_{0.2}Ga_{0.8}As$ layer in GaAs using a VG HB601 UX FEG-STEM. We observe a relative shift in plasmon peak position which is independent of sample thickness but varies slightly with diffraction condition. We interpret this behaviour as being primarily due to changes in lattice parameter, thus giving a new technique for the quantitative measurement of strain at the nm scale. The resolution of the technique is comparable to that of annular dark field images.

1. INTRODUCTION

Electron energy loss spectrum (EELS) maps have become an invaluable tool for analysis of composition at the nm scale. The main application is in the use of core-loss edges, which can give a direct measure of relative atomic concentration. Another possible application is in the use of the plasmon energy loss peak, which has the advantage of a much greater signal to noise ratio. A typical plasmon loss peak from GaAs is shown in Fig. 1. The peak has a Lorentzian profile, corresponding to a damped oscillation of the valence electrons induced by the incident beam. The *3d* Ga core-loss edge is visible to the right of the peak. A fit to the central part of the peak is shown as a dashed line, using the equation (Kundmann 1988)

$$I(E) \propto \frac{E}{\left(E'^2_p - E^2\right)^2 + E^2\Gamma^2} \qquad (1)$$

where Γ is the damping coefficient ($1/\tau$, where τ is the lifetime of the plasmon) and E'_p is given by $E'^2_p = E_g^2 + E_p/\varepsilon_c$, where E_g is the Penn band gap, (the energy of maximum optical absorption); ε_c is the core dielectric constant and E_p is the energy corresponding to the natural oscillation of the free electron plasma,

$$E_p = \hbar\omega_p = \hbar\left(\frac{ne^2}{\varepsilon_0 m_0}\right)^{0.5} \qquad (2)$$

where n is the density of valence electrons, e is the electron charge, $\varepsilon_0$is the permittivity of free space, and m_0 is the electron rest mass. The full width at half maximum (FWHM) is equal to Γ. The fit was made using $n = 1.77 \times 10^{29}$ cm^{-3} (an average of 4 valence electrons for each of the 8 atoms per unit cell), E_g = 5.0 eV and allowing Γ and ε_c as free parameters. The best fit was obtained with Γ = 4.4 eV and ε_c = 1.0063. If it is possible to extract some of the parameters in equations (1) and (2) from plasmon peak maps, they may allow a completely new approach to the characterisation of compound semiconductor materials. We have analysed a simple test structure – a thin $In_{0.2}Ga_{0.8}As$/GaAs layer in GaAs – using plasmon peak mapping to determine the influence of material and experimental parameters on the most easily extracted plasmon peak parameters, i.e. the position of maximum energy loss E_{max} obtained by fitting a curve to the central part of the peak, and the fitted peak FWHM.

2. EXPERIMENTAL

The specimen was a 15 nm $In_xGa_{1-x}As$ layer in GaAs with $x = 0.20$. The study was performed using a VG HB601 UX FEG-STEM operating at 100kV, equipped with the Gatan ENFINA™ parallel electron energy loss spectrometer (PEELS) system. A collection aperture semi-angle of 1.34 mrad was used. This is a relatively small collection aperture (Ferrari et al. 2000) and was used since it gives significantly increased energy resolution, determined to be 0.35 eV as measured from the FWHM of the zero-loss peak. Typical dwell times were 300 ms, giving a plasmon peak intensity from GaAs of ~2000 counts, depending on specimen thickness. The electron probe size was 0.8 nm FWHM; maps were collected with roughly 1 nm spacing between data points. Single scattering distributions (SSDs) were derived from the raw spectra using a Fourier-log deconvolution method.

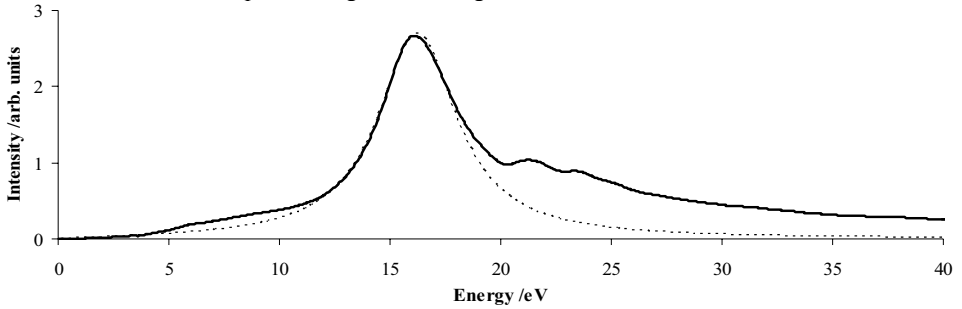


Fig. 1. Plasmon energy loss peak from GaAs and fitted curve (dashed) using equation (1).

3. RESULTS

Figure 2 shows three images of the $In_{0.2}Ga_{0.8}As$ layer; an annular dark field image, the position of the plasmon peak E_{max}, and FWHM = Γ. The well is clearly visible in all three images. The peak energy shifts from 16.2 eV in GaAs to 15.7 eV in the $In_{0.2}Ga_{0.8}As$ layer, and Γ increases from about 4.4 eV to 5.1 eV, indicating greater damping of the plasma oscillation in the $In_xGa_{1-x}As$ layer. These images were taken with the beam parallel to the interfaces, i.e. centred in the 002 Kikuchi lines, with the sample tilted a few degrees away from the [110] zone axis.

A graphical analysis is shown in Fig. 3. Figure 3a shows the shift in E_{max}; also shown are two lines corresponding to a perfectly abrupt structure, in which all parameters are unchanged from the fit in Fig. 1 apart from n, via the lattice parameter. It is simplest to consider the two extremes which may occur: a pseudomorphically strained layer, in which the in-plane lattice parameters are constrained to be equal to that of GaAs and that perpendicular to the interfaces is enlarged due to the Poisson effect; or a completely relaxed layer which has the natural lattice parameter of $In_{0.2}Ga_{0.8}As$ in all directions. The experimental curve lies between the two, as would be expected for a thin specimen (estimated to be 24 nm thick in this case). The effect of the change in band gap is relatively small: when E_g is changed to the appropriate value for $In_{0.2}Ga_{0.8}As$ of 4.6 eV, the peak shifts to slightly higher energies (dashed line for the strained curve in Fig. 3). Since the uncertainty in strain state is much larger than this shift, Fig. 2b can be considered to be an image of the strain in the material.

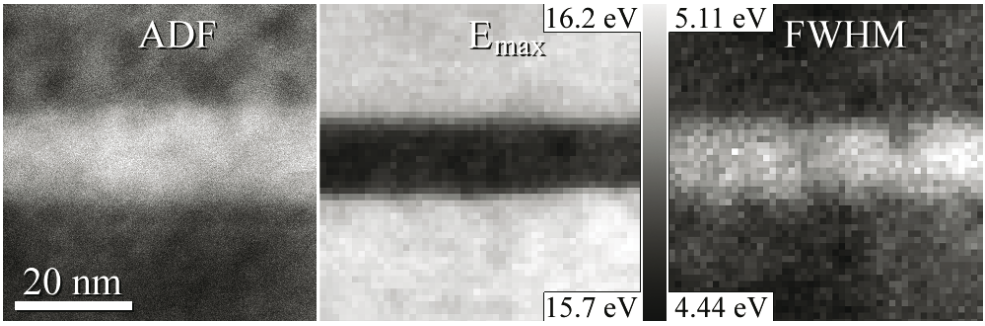


Fig. 2. Annular dark field, plasmon peak energy E_{max} and FWHM images of an $In_{0.2}Ga_{0.8}As$ layer.

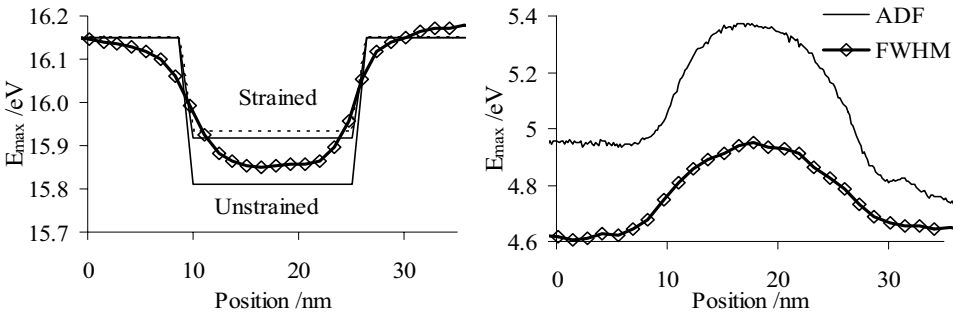


Fig. 3. Graphical representation of the images in Fig. 2.

Although the plasmon peak shift may be simply interpreted as being (mainly) due to changes in lattice parameter, the information in maps of Γ is more complex. The correlation between increased Γ and the $In_{0.2}Ga_{0.8}As$ layer indicates that the plasmons are more heavily damped, i.e. have a shorter lifetime. Plasmon decay occurs via intraband transitions and thus is sensitive to the band structure of the material. It may be possible to use this effect to probe band structure at a similar resolution.

It is also apparent from Fig. 3 that the resolution of the plasmon image is comparable to that of the ADF image; a line from the ADF image, scaled to fit within the range of the graph, is shown in Fig. 3b. This is significantly better than expected from classical delocalisation calculations, a finding we have in common with other studies of plasmon peak mapping (e.g. Daniels et al. 2003).

If plasmon peak mapping of semiconductors is to be a reliable technique, the experimental conditions which affect E_{max} and Γ must be understood. One important factor is the lateral momentum transferred from the high energy electron to the plasmon. As the valence electrons behave in a similar way to a free-electron gas for plasmon transitions, the dispersion curves generally follow a parabolic dependence up to some critical value. The momentum transferred can be changed by shifting the detector aperture off the optical axis, or equivalently by tilting the incident beam. Simple vector addition shows that the lateral momentum transferred to the plasmon is proportional to the angle between incident and detected beams. Thus, the shift in E_{max} should be proportional to the square of this angle, although it is known that dispersion is anisotropic – so the magnitude will also vary depending on the direction of displacement relative to the crystal axes (Raether 1980).

This experiment was performed with the incident beam and detector aperture on the optical axis, thus lateral momentum transfer will be zero - as long as no elastic event occurs which deflects the electron prior to the plasmon loss. However, if the specimen is oriented such that there is strong diffraction occurring, it is quite likely that an electron will be diffracted before producing a plasmon. So we may expect shifts in E_{max} due to dispersion when strong diffraction occurs. In this case we will detect a mixture of undiffracted and diffracted electrons, and the shift will depend upon the fraction of electrons diffracted prior to losing energy to a plasmon and the diffraction vector **g**. Figure 4 shows graphical data derived in a similar manner to Fig. 3, with the electron beam incident along the [110] zone axis, as well as the centre of the 002, 220 and 111 Kikuchi lines a few degrees away from [110]. There are significant shifts in the peak position – ~0.1 eV – between the different diffraction conditions; it is also clear that the magnitude of the shift is slightly different for $In_{0.2}Ga_{0.8}As$ and GaAs. This indicates that care is needed

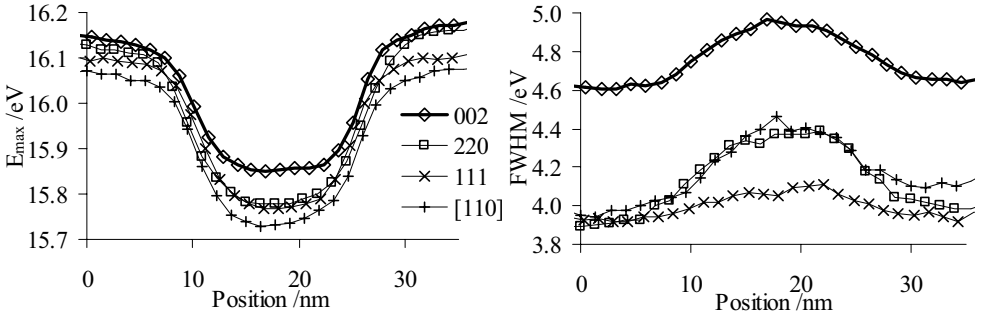


Fig. 4. Variation of E_{max} and FWHM with diffraction conditions.

to choose appropriate diffraction conditions if the technique is to be used as a quantitative technique to measure strain; further work is needed. Figure 4 also shows a dependence of Γ on diffraction conditions. All apart from 002 have lower Γ – approximately 4.0 eV rather than 4.6 eV in GaAs, implying that intraband transitions are stronger along [001].

Another experimental parameter which affects plasmon peak parameters is specimen thickness. Figure 5 shows 3 data sets measuring peak position in GaAs as a function of thickness with the beam aligned along the centre of the 002 and 220 Kikuchi bands. In general there are only small changes in peak position with thickness (<0.1 eV) over a large range. However, where the specimen is very thin E_{max} shifts to much higher energies. The lack of continuity in the data may be a result of differences in sample orientation between each measurement: even small differences close to the Bragg condition may give large changes in the fraction of diffracted electrons contributing to the spectra.

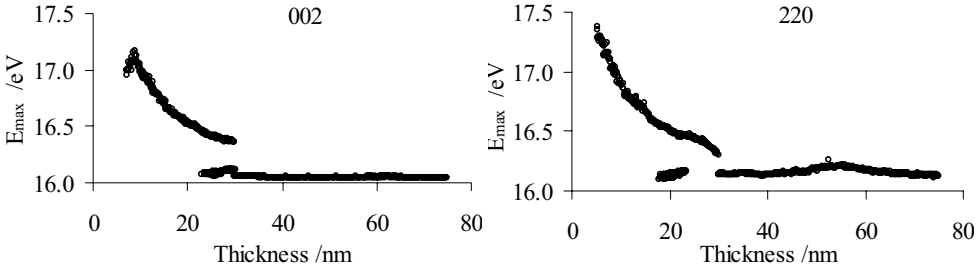


Fig. 5. Variation in E_{max} in GaAs as a function of thickness.

4. DISCUSSION

In principle, quantitative measurement of local strains at the nm scale using the shift of the plasmon peak should be quite straightforward. Although band gap, core dielectric constant and damping are needed to reproduce the true peak position, all of these effects are smaller than the shift due to change in lattice parameter and in any case tend to shift the whole curve on the energy scale, leaving the relative shift unchanged. The insensitivity to specimen thickness – above some lower limit – gives it a distinct advantage over techniques using lattice imaging, and while it cannot compete with such techniques in terms of absolute resolution, there are many structures of practical interest where a resolution of a few nm is sufficient. The main difficulty seems to lie in the sensitivity to diffraction conditions. When electrons that have suffered both diffraction and energy loss contribute to the data, the technique becomes sensitive to the band structure of the material due to dispersive effects. While this is of great interest in itself, it should be avoided if a simple strain measurement is required.

Measurement of Penn band gap using plasmon peak shift in lattice-matched structures may also be possible, although as the shift is about ten times smaller than that due to strain it may prove difficult experimentally. A more approach, using the dielectric function derived from the SSD, may be needed.

5. SUMMARY AND CONCLUSION

We have used a $In_{0.2}Ga_{0.8}A$/GaAs structure to investigate the influence of material parameters on plasmon peak position and FWHM. The primary factor influencing plasmon peak position is the electron density, which offers a simple and direct technique for measurement of strain with nm scale resolution. Other influences are clearly present – the change in peak position and FWHM with diffraction conditions indicate that momentum transfer to the plasmon needs to be carefully controlled.

REFERENCES

Daniels H R, Brydson R, Brown A and Rand B 2003 Ultramicroscopy **96**, 547

Ferrari A C, Libassi A, Tanner B K, Stolojan V, Yuan J Brown, L M Rodil, S E Kleinsorg B and Robertson J 2000 Phys Rev B**62**, 11089

Kundmann M K 1988 Ph.D. Thesis, University of California at Berkeley

Raether H 1980 Excitation of Plasmons and Interband Transitions by Electrons (Springer-Verlag, Berlin)

Investigation of the electrical activity of dislocations in ZnO epilayers by transmission electron holography

E Müller, P Kruse, D Gerthsen, R Kling[1] and A Waag[2]

Laboratorium für Elektronenmikroskopie, Universität Karlsruhe, D-76128 Karlsruhe, Germany
[1] Abteilung Halbleiterphysik, Universität Ulm, D-89069 Ulm, Germany
[2] Institut für Halbleitertechnologie, Universität Braunschweig, D-38106 Braunschweig, Germany

ABSTRACT: The electrical activity of threading dislocations in epitaxial n-ZnO layers was investigated by electron holography in a transmission electron microscope. By reconstructing the phase of the image wave in the vicinity of dislocations, the electrostatic potential associated with charged dislocations can be detected. Comparing the measured and theoretically expected potential, a line charge of 2 e/nm was found.

1. INTRODUCTION

Epitaxial ZnO layers frequently contain high densities of threading dislocations, which exceed values of 10^9 cm^{-2}. If the dislocations are electrically active, the overall charge balance of the material can be influenced significantly and the charge-carrier mobility is strongly reduced. In particular, with respect to the difficulty of achieving p-doped ZnO, it appears to be advisable to study charged states at dislocations. Previous studies have already shown that 60° (Zn)-glide dislocations which are generated during plastic deformation are electrically active in n-ZnO (Ossip'yan et al 1986). In the present work, we focus on threading dislocations in epitaxial n-ZnO layers whose structure differs from deformation-induced dislocations because they do not lie on the (0001) glide plane. Threading dislocations often exhibit edge or screw character with lines oriented parallel to the [0001] direction.

Due to the strong disturbance of the translational symmetry of the crystal, dislocations with an edge component are expected to generate deep electronic states in the energy gap of a semiconductor. If the Fermi level does not coincide with the occupation limit of the band of electronic states the dislocation will be charged (Alexander and Teichler 1991). To maintain overall charge neutrality, a charged dislocation will be screened by a space charge region of opposite sign. The resulting potential V at a distance r from the dislocation line was already calculated by Read (1954)

$$V(r) = \frac{Q}{4\pi\varepsilon\varepsilon_0}\left[\ln\left(\frac{R^2}{r^2}\right) - \left(\frac{r^2}{R^2}\right) + 1\right] \qquad (1)$$

where Q=qe is the charge per dislocation length and ε = 8.9 the dielectric constant of the material (Landolt Börnstein 1987). The Read radius $R = \sqrt{q/(\pi N_{sc})}$ corresponds to the radius of the space charge region where N_{sc} is the density of compensating charges available for screening.

Electron holography in a transmission electron microscope allows the retrieval of the phase of the electron wave. This provides the possibility to study the interaction of the incident electrons with the electrostatic potential of a charged dislocation with high spatial resolution as already shown by Cherns and Jiao (2001) for dislocations in GaN. After passing a sample with thickness t, the phase of the transmitted beam Δφ is shifted with respect to the reference wave (Reimer 1984). If a charged

dislocation is present, the mean inner potential V_0 of the material is locally modified by the potential $V(r)$ ($r = \sqrt{x^2 + z^2}$) which induces a phase shift given by Eq.(2).

$$\Delta\varphi = C_E \int_0^t (V_0 + V(r))\, dz \qquad (2)$$

The constant C_E = 7.29x10^6 rad V $^{-1}$m $^{-1}$ is determined by the electron energy which was measured precisely for the transmission electron microscope used in this study applying convergent beam electron diffraction (Kruse et. al 2003).

The goal of the present work was to determine quantitatively the line charge of dislocations in n-ZnO by comparing the measured and calculated phase shifts at dislocations using Eqs.(1) and (2).

2. EXPERIMENTAL TECHNIQUES

A Philips CM 200 FEG/ST transmission electron microscope, equipped with a Möllenstedt biprism installed in the selected-area aperture holder was used. The electrostatic potential of the biprism was set at approximately 150 V leading to an interference fringe distance of 0.2 nm. Holograms were obtained by orienting a straight dislocation line parallel to the biprism whereas the reference wave is transmitted through the undisturbed crystal on the other side of the biprism. The holograms are recorded with a slow-scan CCD camera with 2048x2048 pixels. The principle of the technique and the numerical reconstruction procedure are outlined in detail by Lehmann and Lichte (2002) and Kruse et al (2003). The microscope magnification was calibrated by taking high-resolution images in a zone-axis orientation and comparing the lattice-fringe distances with the known lattice parameters of ZnO.

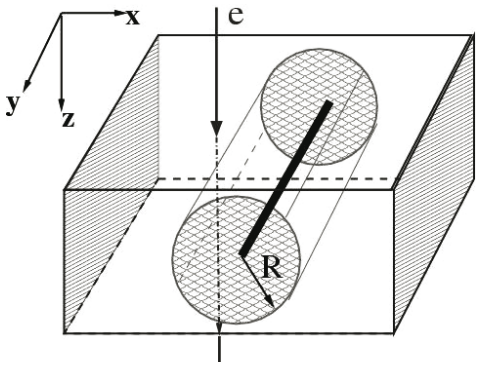


Fig. 1. Schematics of the experimental geometry with the dislocation oriented perpendicular to the electron beam

Cross-section samples along the <11$\bar{2}$0> and <1$\bar{1}$00> -zone axes were prepared by the procedure described in Strecker et al (1999) and analysed in such a manner that the threading dislocations were oriented perpendicular to the electron beam (Fig. 1). All investigated ZnO layers were grown by metal organic vapour phase epitaxy on Al_2O_3(0001) substrates. Details of the growth procedure can be found in Gruber et al (2002).

3. RESULTS

Equation (2) is only valid in the absence of dynamical interactions between transmitted and scattered electron waves. Dynamical contributions to phase shifts can be avoided if the intensity of the Bragg reflections is minimized by an appropriate sample orientation. However, dislocations are difficult to localize under kinematical

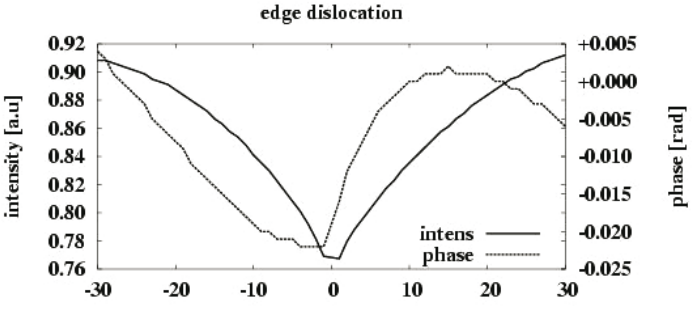


Fig. 2. Computed intensity and phase for an edge dislocation in the middle of a TEM sample with t=150nm

diffraction conditions because they do not generate any contrast.

To assess dynamical contributions under two-beam conditions we have carried out simulations by solving recursively the Howie-Whelan equations for a crystal with an edge or screw dislocation (Hirsch et al 1977). The calculations were carried out numerically and the results for an edge dislocation imaged under (g,4g) weak-beam conditions with $\vec{g} = (11\bar{2}0)$ are depicted in Fig. 2. Under (g,4g) conditions, the amplitude of the image wave is modified in the vicinity of the dislocation but the phase shift remains negligibly small with respect to the phase detection limit in electron holography. Thus the position of the dislocation can be identified.

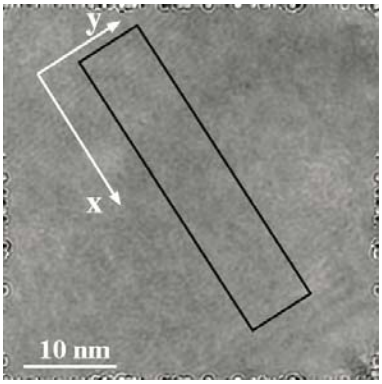


Fig. 3. Phase of the electron wave in an area containing a dislocation

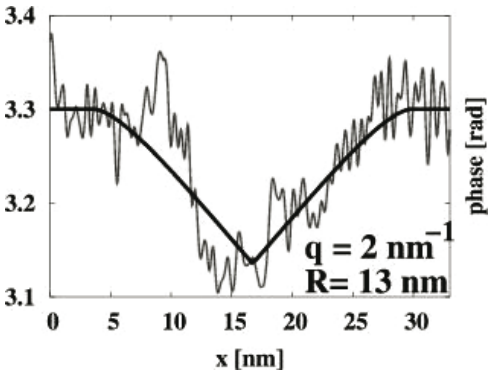


Fig. 4. Measured phase change perpendicular to the dislocation line and fit according to Eq. (1)

Figure 3 shows the evaluated phase of an electron hologram for the transmitted beam where a dislocation is oriented parallel to the y-direction. To reduce the noise and to eliminate the contribution of local thickness variations, the phase profile perpendicular to the dislocation line along the x direction was obtained by averaging the phase along the y direction inside the dark frame indicated in Fig. 3. The resulting phase profile is plotted in Fig. 4. The line represents the best fit of the expected phase shift from Eq. (1) and (2) using the line-charge density as a fit parameter. The best fit was obtained for Q = 2 e/nm^{-1}. The Read radius R depends on the line charge and on the density of compensating charges and can be also calculated by the recursive fit. Taking into account that the line charge of the dislocation outside the Read-cylinder is completely compensated, the radius R can be determined alternatively from the measured value of R, which was 13 nm in the case of Fig. 4.

4. DISCUSSION

A key point of our work is the analysis of dislocations in cross-section samples where the dislocations lines are oriented perpendicular to the electron beam. This geometry provides several advantages compared to a dislocation orientation parallel to the electron beam used by Cherns and Jiao (2001), although the phase shift is not maximized. First, the formation of pits at the intersection of the dislocation with the surface due to ion etching of the sample can be avoided. By analyzing embedded dislocations, phase shifts by local thickness changes due to pits can be eliminated definitely. Second, dynamical contributions to the phase shift are easier to control. If the electron-beam is oriented parallel to the dislocation line, the dislocation strain field can locally tilt the lattice such that dynamical diffraction conditions apply in the vicinity the dislocation, i.e. Bragg reflections are strongly excited, even if kinematical conditions are chosen for the undisturbed crystal.

Regarding the accuracy of the determined line charge, the largest error results from the dielectric constant of ZnO with significantly differing values published in the literature (Landolt Börnstein 1987). Another source of error is the sample thickness. If the sample thickness is smaller than the diameter of the Read cylinder (2 R) the electrical field of the line charge leaks into the vacuum region. Thus the effective dielectric constant decreases, leading to a smaller value of q. For an

accurate treatment of this situation the field distribution outside the sample has to be calculated requiring an additional parameter for the fit of the measured phase curve.

The determined value for q is large, but it agrees with the trend towards high line charges in ZnO according to Ossip'yan et al (1986). It has to be noted that the electrical activity of dislocations is not necessarily induced by intrinsic electronic dislocation states but can be also due to a high concentration of point defects accumulated in the vicinity of the dislocation core.

The high negative dislocation line charge in n-ZnO indicates that dislocations can provide acceptor states with a high concentration if the dislocation density is high. This will lower the free electron concentration. Due to the amphoteric nature of the dislocation states in a partially filled band they act as donors, if the Fermi energy is located below the occupation limit of the dislocation states. Pinning of the Fermi energy at the occupation limit of the band is expected if the concentration of shallow donors is reduced and the shallow acceptor density is increased. Therefore, dislocation states could contribute to the difficulty of obtaining p-type ZnO with low resistivity.

5. SUMMARY

By reconstructing the phase of the transmitted beam by transmission electron holography, indications for a high negative line charge at threading dislocations in n-ZnO can be found. Analyzing dislocations in cross-section samples with dislocation lines oriented perpendicular to the electron beam means that knowledge of the sample thickness is unnecessary. Furthermore dynamical contributions to the phase shift can be controlled more easily. Comparing the measured phase shift with the theoretically expected distribution, a line charge of approximately 2 e/nm was found. The observation of charged dislocations shows that they can have a strong influence on the mobility and concentration of charge carriers in ZnO if they are present at a high density.

ACKNOWLEDGEMENTS

The authors are very much indebted to M Lehmann and H Lichte (Technical University Dresden) for their valuable help in solving experimental problems and fruitful discussions. The work was financially supported by the network of competence "Functional Nanostructures" of the State of Baden-Württemberg (Germany) and the Deutsche Forschungsgemeinschaft (DFG).

REFERENCES

Alexander H and Teichler H 1991 in: Materials Science and Technology, Vol. **4**, chap.6, W. Schröter, ed., North-Holland Pub. Company, 249-319

Cherns D and Jiao C G 2001 Phys. Rev. Lett. **87**, 205504

Hirsch P, Howie A, Nicholson R, Pashley D W and Whelan M J 1977 Electron Microscopy of Thin Crystals (Malabar, Florida, Krieger) p. 250

Kruse P, Rosenauer A and Gerthsen D 2003 Ultramicroscopy **96**, 11

Gruber T, Kirchner C, Thonke K, Sauer R.and Waag A 2002 Physica Status Solidi A **192**,166

Landolt Börnstein 1987 Numerical Data and Functional Relationships in Science and Technology, Semiconductors: Intrinsic Properties of Group IV Elements and III-V, II-VI and I-VII Compounds (Heidelberg,Springer) p. 165

Lehmann M and Lichte H 2002 Microsc. Microanal. **8**, 447

Ossip'yan Yu A, Petrenko V F, Zaretski A V and Whitworth R W 1986 Adv. Phys. **35** 115

Read W T 1954 Theory of Dislocations in Germanium, Phil. Mag. **45**, 775

Reimer L 1984 Transmission Electron Microscopy (Berlin-Heidelberg, Springer) p. 56

Strecker A, Mayer J, Baretzky B, Eigenthaler U, Gemming T H, Schweinfest R and Rühle M 1999 J. Electron Microsc. **48**, 235

A TEM study of Mn-doped ZnO layers deposited by RF magnetron sputtering on (0001) sapphire

M Abouzaid, P Ruterana, G Nouet, C Liu[1], F Yun[1], B Xiao[1], S-J Cho[1], Y-T Moon[1] and H Morkoç[1]

SIFCOM UMR 6176 CNRS-ENSICAEN, 6, Boulevard du Marechal Juin, 14050 Caen Cedex, France
[1] Department of Electrical Engineering, Virginia Commonwealth University, Richmond, VA 23284

ABSTRACT: In order to understand the origin of the observed magnetic behaviour, microstructural analysis of Mn-doped ZnO thin films is carried out. In the investigated samples, the doping was started after deposition of about a 150 nm pure ZnO layer on the sapphire substrate. The high Mn content layer exhibits substantial magnetization. TEM analysis reveals Mn-related precipitates in the high Mn-doped ZnO film. The low Mn doped ZnO layer exhibits a columnar structure and it is shown that this is disrupted by high Mn doping.

1. INTODUCTION

Transition-metal-doped ZnO has attracted the attention of researchers as a promising diluted magnetic semiconductor (DMS) material for use in spintronics. Based on the prediction of Dietl et al. (2000), considerable effort has been focused on achieving a reliable ZnO-based DMS with a Curie temperature above room temperature by doping with transition metals (Pearton et al 2004), especially Mn and Co. Transition metal-doped ZnO thin films have been prepared mainly by pulsed-laser deposition (PLD), molecular-beam epitaxy (MBE), and sputter deposition (Lim et al 2004). Among these techniques, the radio frequency (rf) sputtering deposition is a simple method for preparing reasonably high quality ZnO thin film (Özgür et al 2004). In this paper, we report on the structural analysis of ferromagnetic Mn-doped ZnO thin films deposited on sapphire by rf magnetron sputtering using transmission electron microscopy (TEM).

2. EXPERIMENTAL

The ZnO buffer layer was deposited at 650 °C and the Mn-doped ZnO film was deposited at 550 ºC. An RF power of 150 W was used to sputter the ZnO target. The DC power applied to the Mn target was 5 W for the Mn-doped ZnO film. The targets were pre-sputtered for 5 minutes before the actual deposition to remove contamination from the target surface. The as-deposited film was annealed at 850 ºC for 1 hour in an air ambient in order to improve the crystalline quality. We report on the analysis of two layers (L1:Mn 5%, and L2 :Mn 10%) grown on (0001) sapphire.

Cross sectional TEM samples were prepared by gluing two pieces of the film face to face, cutting into slices followed by mechanical polishing down to100 μm and then dimpling to 10 μm. The electron transparency was finally obtained by ion-milling with the sample holder kept at LN2 in order to minimize the irradiation damage. The observations were carried in an 002B Topcon high resolution electron microscope operated at 200 kV.

3. RESULTS AND DISCUSSION

After annealing, the magnetization was measured and a substantial effect is shown in Fig. 1 for the layer L2. For layer L1 (5 % Mn) the effect was very small, therefore, it may be assumed that the increase of the Mn content plays an important role in the formation of this hysteresis.

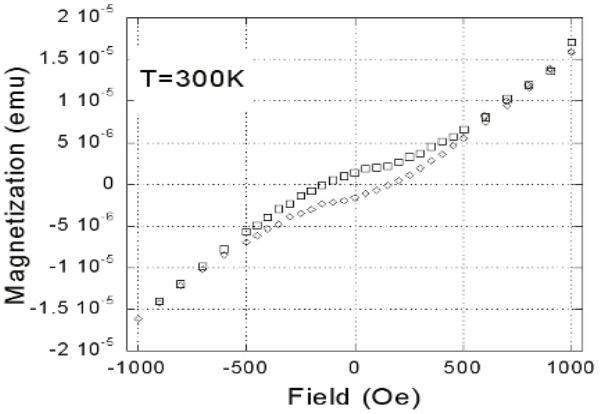
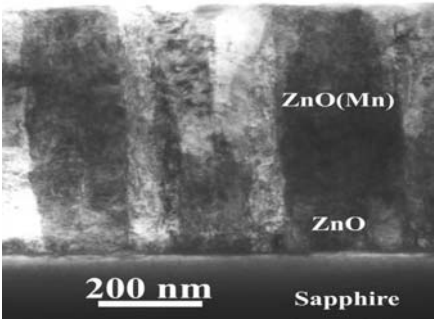
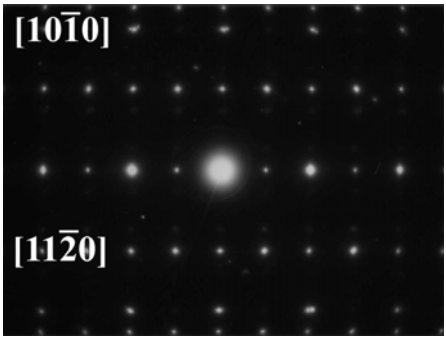


Fig. 1: Magnetization field for the ZnO (Mn) L2 layer with 10% Mn content.

A bright field image of L1 is shown in Fig. 2. As can be noticed, the deposition has given rise to a columnar structure in the film. This image was recorded along the $[10\bar{1}0]$ zone axis of sapphire and the corresponding diffraction pattern of the ZnO film (Fig. 2b) shows that the columns are imaged along the usual two conventional zone axes ($[1\bar{1}20]$ and $[10\bar{1}0]$) that are often encountered when a Wurtzite structure material is grown on the [0001] sapphire surface.



(a)



(b)

Fig. 2: (a) Cross sectional TEM showing the columnar growth in the ZnO film L1, (b) Diffraction taken from the ZnO (Mn) phase.

A micrograph of the film doped with 10 % Mn is shown in Fig. 3, the Mn doping was started after the deposition of about 150 nm. This figure points to a clear structural difference between the doped and undoped areas. The undoped region still exhibits a columnar growth.

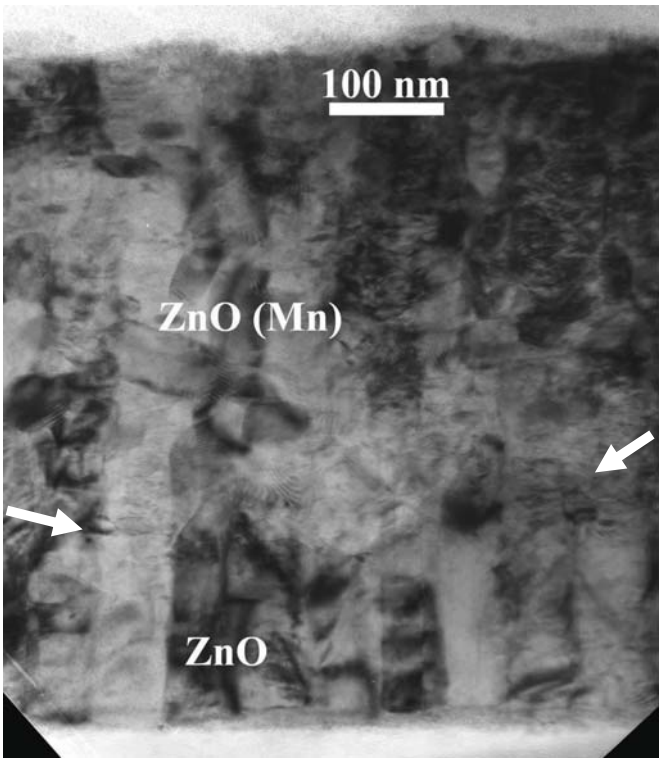


Fig. 3: (a) BF cross sectional TEM of the Mn doped ZnO film L2 with Mn content of 10%.

The interface between the doped and undoped areas is rough as shown by the white arrows. As the Mn was introduced, the columnar growth appears to be disrupted as seen in the image. In corresponding diffraction images, the two zone axes patterns are no longer clearly visible, they are blurred by polycrystalline spots. As shown by the image contrast, a large number of precipitates form with various morphologies. Some are elongated parallel to the ZnO basal plane and others have a rather round shape. As can be seen in Fig. 4, the precipitate size is between 40-50 nm. If now we focus on the rather rounded shape precipitates, analysis of the lattice spacings and angles shows that these crystallites are cubic. A number of them are often imaged along a <110> zone axis and their EDS analysis gave systemetically $MnZnO_3$ stoichiometry.

The EDS analysis shows enrichment of the precipitates in Mn, independent of their shape. Around the precipitates, the Mn content is depleted down to 2-3%. The detailed crystallographic relationship of these precipitates with the ZnO (Mn) matrix is still under analysis.

4. SUMMARY

The microstructure of Mn doped ZnO layers obtained by rf sputtering on (0001) sapphire is presented. It is shown that substantial magnetization is exhibited in the layer which contains Mn-rich precipitates that are crystalline and have various shapes. However, it is not yet clear whether these precipitates have a predominant effect on the magnetization effect and this needs further investigation.

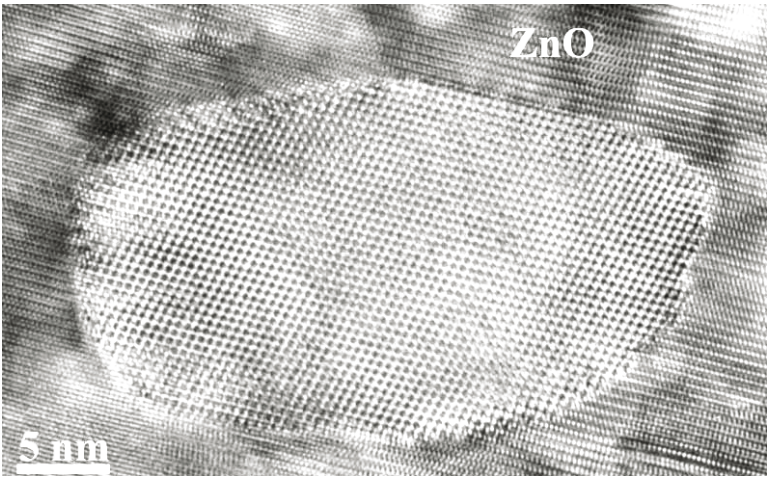


Fig. 4: A round shaped precipitate in sample L2, image is recorded along a <110> zone axis of the cubic system.

REFERENCES

Dietl T, Ohno H, Matsukura F, Cibert J, and Ferrant D 2000 Science **287**, 1019
Lim S W, Jeong M C, Ham M H, and Myoung J M 2004 Jpn. J. Appl. Phys., Part 2 **43**, L280
Özgür Ü, Teke A, Liu C, Cho S J, Morkoç H, and Everitt H O 2004 Appl. Phys. Lett. **84**, 3223
Pearton S J, Norton D P, Ip K , Heo Y W, and Steiner T 2004 J. Vac. Sci. Technol. B **22**, 932

Part IV

High Resolution Microscopy and Nanoanalysis

Aberration-corrected HREM/STEM for semiconductor research

C J D Hetherington, D J H Cockayne, R C Doole, J L Hutchison, A I Kirkland and J M Titchmarsh

University of Oxford, Dept Materials, Parks Rd, Oxford OX1 3PH

ABSTRACT: Aberration correction leads to a substantial improvement in the resolution of transmission electron microscopes. The JEM-2200FS in Oxford (Begbroke site) is equipped with correctors for both TEM and STEM. Alignment of the TEM and STEM correctors is achieved through variations of the Zemlin tableaux. The microscope can be used to study the same or similar regions of a sample in both TEM and STEM modes.

1. INTRODUCTION

Semiconductors, having relatively open structures compared to close-packed metals, were an early candidate for high resolution TEM studies. In particular, the <1-10> zone in silicon presented two sets of {111} lattice planes of spacing 0.31nm, a distance that could be resolved by early 200kV microscopes. There was naturally a drive to improve the resolution of the microscopes in order to extend the range of HREM characterisation. For example, the <100> zone which offered improved contrast between III/V semiconductor layers such as GaSb and AlSb layers (Murgatroyd et al 1986) required 0.19nm spaced {022} planes to be resolved. "Microscopy of semiconducting materials" in the broader sense of the phrase would include imaging of the metallization layers to be found in devices; for example, aluminium with 0.23nm spaced {111} planes. More importantly, the projected structures of surfaces, interfaces and defects require high resolutions to image important features. Indeed, the scale of semiconductor devices is shrinking and the properties of a device depend more and more on atomic configurations of interfaces and layers only a few atoms thick (e.g. Mardinly 1999).

Higher resolution in the TEM can be achieved through several schemes (Hetherington 2003). Exit-wavefunction restoration from a through-focal series corrects the aberrations in software (Kirkland and Meyer 2004) thereby extracting the full benefits of the improved information limit offered by field emission guns. Holography offers another route (Lichte 1991). Aberration correction in the electron microscope hardware itself required a radical departure from the traditional lens design. Scherzer (1936) proved that any electron optical system always has positive spherical aberration, if the system is rotationally symmetric (alongside 3 other conditions) but went on to propose the use of a multipole lens having negative spherical aberration as a means to aberration correction (Scherzer 1947). The eventual construction of the corrector relied on suitable magnetic materials and power supply stability, and its successful implementation relied on online image acquisition and fast computation to measure the aberrations and then to adjust the power supplies to the multipole lenses and other components in the corrector. Thus it was not until the 1990s that aberration correctors were introduced. CEOS adopted a hexapole design for TEM and STEM (Haider et al 1998) and NION adopted an octapole/quadrapole assembly for STEM (Krivanek et al 1999).

Two recent examples of the application of aberration corrected EM to semiconductors are the characterisation of a) the coordination of atoms at the interface of $NiSi_2$ on Si(100) investigated in an aberration corrected STEM by Falke et al (2004) and b) the structure of a multiple stacking fault and bounding dislocation in GaAs by Tillmann et al (2004).



Fig. 1 JEM-2200FS with two C_s correctors (metallic appearance) above and below objective lens. Operation of the microscope is via computers in the foreground.

2. ABERRATION CORRECTORS ON THE OXFORD JEM-2200FS

The JEM-2200FS installed in the Department of Materials at Oxford University has two CEOS correctors, one to correct the prefield of the objective lens that forms the probe for STEM, and another to correct the postfield that forms the TEM images. Figure 1 shows the microscope installation and it has been described in more detail by Hutchison et al (2005) and Sawada et al (2005). The correctors are based on a pair of strong hexapoles and two transfer round-lens doublets (Haider et al 1998). The primary aberrations of the first hexapole are compensated for by the second hexapole. Meanwhile, a secondary aberration is also induced by the two hexapoles, namely the spherical aberration C_s. The hexapoles can then be excited to the degree required for the negative C_s of the corrector to match exactly the positive C_s of the microscope objective lens. Figure 2 shows a schematic ray diagram of the effect. Other series of weak multipoles are included for the adjustment of the beam axis and correction of the parasitic aberrations out to third order.

When used in TEM mode, the illumination should be parallel or close to parallel. To achieve this with the hexapoles of the upper STEM corrector still excited, an adjustment may be made to the transfer lenses in the corrector. It is then straightforward to switch from TEM to STEM mode and time is not spent waiting for the STEM corrector hexapoles to stabilise. Alternatively the upper corrector hexapoles and lenses may be switched off for TEM work, with only a small excitation of one hexapole to compensate for a remnant 3-fold astigmatism in the illuminating beam. The TEM corrector is left on almost continuously, with only occasional experiments requiring the hexapoles to

be switched off to investigate the effects of C_s. In general a zero C_s is used for focal series collection; for other observations, C_s might be adjusted to have a small (~50μm) positive or negative value to suit the imaging conditions required (Lentzen et al 2002).

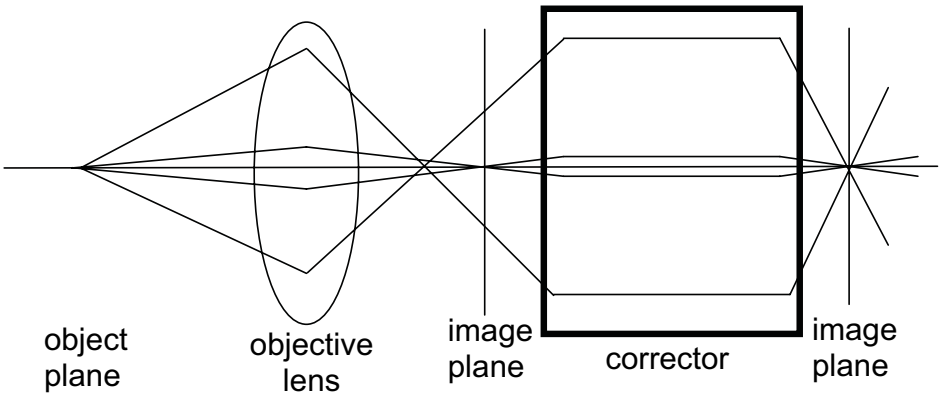


Fig. 2 Ray diagram illustrating correction of C_s. Rays leaving object at high angles are overfocussed at first image plane, but are correctly focussed at second image plane.

3. TEM ALIGNMENT AND PERFORMANCE

Spherical aberration has the greatest effect on beams that are scattered out to high angles, as can be seen in the ray diagram in Fig. 2. The thin amorphous films that are typically used in microscope alignments scatter only weakly at higher angles. Hence the image formed with beam incident along the optic axis, or its Fourier transform (the diffractogram), would be expected to be insensitive to the aberrations beyond the first order (first order aberrations are focus and 2-fold astigmatism). Furthermore antisymmetric aberrations such as 3-fold astigmatism do not affect the diffractogram of the untilted image. If the incident beam is tilted out to a high angle with respect to the optic axis, as in a Zemlin tableau, then the lens aberrations induce a defocus and a two-fold astigmatism in each image (Zemlin et al 1978, Zemlin 1979). An analysis of these defects in the diffractograms allows the aberration coefficients to be calculated.

To align our corrector, we first correct the 2-fold astigmatism on the untilted image and adjust the focus to an underfocus (weaker objective lens) that produces 5 or so rings in the diffractogram of thin amorphous films images taken at 300,000x. We then record images with a range of beam tilts and azimuths. With aberrations out to the third order corrected, or at least set to sufficiently low values, linear transfer extends out to the information limit, measured at 0.12nm for 10% transfer (Hutchison et al 2005).

4. STEM ALIGNMENT AND PERFORMANCE

The alignment for high resolution STEM proceeds via several stages.

(I) With the post-specimen lenses set to imaging mode (not diffraction mode), the condenser aperture may be centred on the voltage centre and initial adjustments made to 2-fold astigmatism and coma in the pre-specimen lens forming the probe. The TEM is returned to diffraction mode and a high-angle annular dark field detector inserted.

(II) For correction of higher orders, a particular specimen is required, namely 5-10nm diameter gold particles on an amorphous C or Ge film. This standard specimen is first imaged with an untilted probe and the focus and 2-fold astigmatism adjusted. Just as a Zemlin tableau is used in TEM, the STEM alignment proceeds with the acquisition of scanned images taken at around 300,000x for several beam tilts and azimuths. In fact a pair of images is acquired at each tilt, one underfocussed and another overfocussed. Any aberrations in the lens combined with the beam tilt lead to a distortion in the probe shape and size. The consequent distortion of the scanned images relative to the initial image taken with an untilted beam can be displayed as discs. Analysis of the discs allows the aberration coefficients to be calculated and corrections may then be applied by the CEOS software.

(III) The standard specimen is replaced by the sample to be examined. As might be expected, the new specimen usually affects the lens field and further small adjustments are required to the focus, 2-fold astigmatism and coma. These are achieved manually through observation of a ronchigram of thin amorphous material taken with the largest condenser aperture inserted. A final fine tuning is possible directly on lattice images of perfect crystal.

For HR-STEM, we typically use a condenser aperture that gives a semiangle of beam convergence of 16mrad. 16mrad at 200kV roughly equates to 24mrad at 100kV, the convergence angle commonly used on the C_s-corrected SuperSTEM (Bleloch 2004). The probe size on a TEM/STEM microscope may be assessed by recording a TEM image. For the present gun and "standard" conditions, a FWHM value of around 0.15nm for the probe image has been recorded with an energy spread of 1.0eV and a current of 16pA. An adjustment of condenser lenses and gun voltages has allowed a FWHM of 0.105nm to be recorded. How closely the size of the probe at the image plane corresponds to size of the actual probe at the object plane, given that the image is formed by a system whose resolution limit is of the same scale as the object itself (~0.1nm), is not clear and is the subject of further investigation. A more conventional means of assessing the probe size is the resolution of fine detail in a scanned image, and we have observed atomic columns in silicon <110> (0.136nm) and gold <111> (0.144nm).

The use of the larger condenser aperture, semiangle of convergence of 32mrad, appears not to compromise the probe size too severely. Ronchigrams from the microscope contain a flat region out to this angle and even beyond. The use of a larger aperture leads to enhanced signals for microanalysis and imaging. Alternatively the same signal may be collected a) during a shorter exposure time thereby reducing specimen movement during the image or spectrum acquisition or b) using a lower gun emission with reduced energy spread.

5. APPLICATIONS

Two examples are shown here to illustrate the versatility of the microscope to accomplish a variety of imaging methods.

GaAs cleaves along {110} planes and 90 degree wedge-shaped TEM specimens may be made. The known geometry makes the GaAs wedge a suitable candidate for studying the scattering process of fast electrons in a material and the mismatch of contrast between experimental and simulated HREM images. Figure 3a shows an image from a through-focal, energy-filtered, aberration-corrected series, with detail in Fig. 3b. The Fourier transform in Fig. 3c includes 440 spots which correspond to a spacing in the image of 0.1nm.

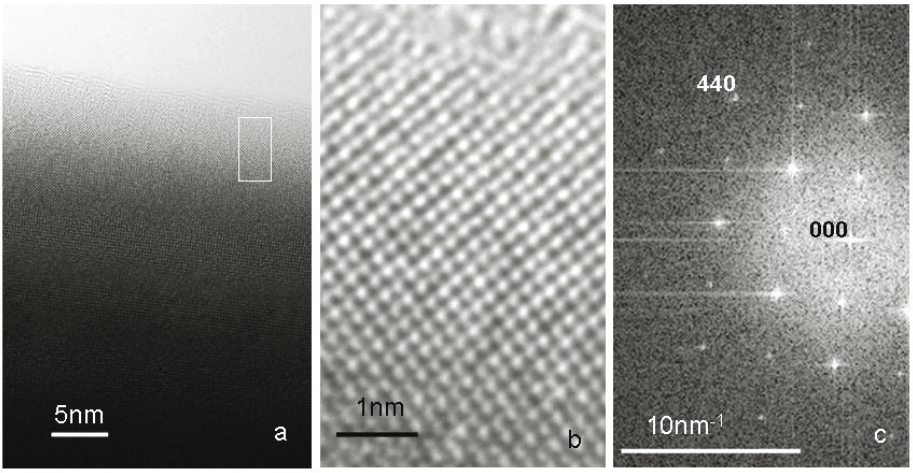


Fig. 3a) Energy-filtered, aberration-corrected image of GaAs wedge, b) detail c) FFT

Films deposited onto suitable substrates may form bicrystals with twin boundaries lying perpendicular to the plane of the foil (Westmacott et al 2001). Figure 4 shows TEM and STEM images of a gold {111} foil that has been removed from the germanium substrate. The 220 reflections at 0.144nm must be resolved to image the gold lattice in this orientation. Twin boundary facets on {11-2} planes separate the crystals with foil normals of [111] and [-1-1-1]. The STEM image shows a facet junction. The TEM image shows a single facet approaching the edge of a hole (arrowed); the very thin foil has allowed the boundary to relax so that it appears inclined to the beam at the thicker region, and to have disappeared in the thinner region.

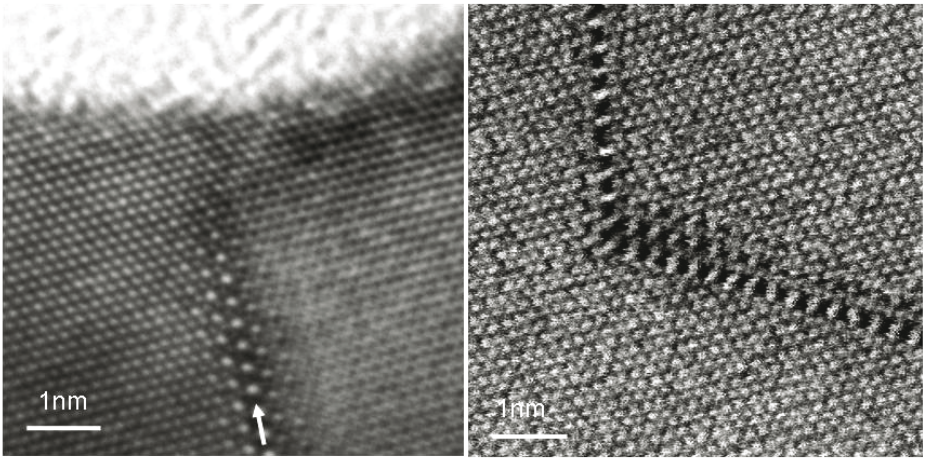


Fig. 4 TEM image (left) and HAADF-STEM image (right) of gold foil viewed down <111>

6. CONCLUSIONS AND FUTURE DEVELOPMENTS

Aberration correction applied to TEM and STEM has brought the point resolution and probe size close to the 0.1nm level, greatly benefiting the high resolution study of semiconductors and other materials.

A further improvement to the performance is expected on the addition to the gun of a monochromator: a reduced energy spread of the illumination will lead to an extension of the damping envelope functions for imaging, not to mention enhanced EELS capabilities. The addition of a piezo drive to the height control mechanism will facilitate the collection of through focal series of images without the need to alter the objective lens excitation.

Aberration correction results in higher intensities in smaller probes and the acquisition of probe images on the CCD is hindered by saturation of pixels. Faster shutter speeds and an increased magnification of the projector system below the omega filter will allow satisfactory imaging of the probe and also help with the acquisition of the central spot in diffraction patterns and the zero loss peaks in electron energy loss spectra.

7. ACKNOWLEDGEMENTS

The JEM-2200FS was funded by the UK Engineering and Physical Sciences Research Council. We are grateful to JEOL Ltd. for its support, P Hartel of CEOS for advice about the correctors, C Boothroyd and R Dunin-Borkowski for help with the GaAs observation, T Radetic and U Dahmen for supplying the gold foil and J Mercer-Lynch for help with the microscope.

REFERENCES

Bleloch A 2004 SuperSTEM School, Daresbury UK, July 2004
Falke U, Bleloch A, Falke M and Teichert S 2004 Phys. Rev. Lett. **92**, 116103
Haider M, Rose H, Uhlemann S, Schwan E, Kabius B and Urban K 1998 Ultramicroscopy **75**, 53
Hetherington CJD 2003 Inst. Phys. Conf. Ser. **179**, 219
Hutchison J L, Titchmarsh J M, Cockayne D J H, Doole R C, Hetherington C J D, Kirkland A I and Sawada H 2005 Ultramicroscopy **103**, 7
Kirkland A I and Meyer R R 2004 Microscopy and Microanalysis **10**, 401
Krivanek O L, Dellby N, Lupini A R 1999 Ultramicroscopy **78**, 1
Lentzen M, Jahnen B, Jia C L, Thust A, Tillmann K, Urban K 2002 Ultramicroscopy **92**, 233
Lichte H 1991 Advances in Optical and Electron Microscopy **12**, 25
Mardinly A J 1999 Inst. Phys. Conf. Ser. **164**, 575
Murgatroyd I J, Hutchison J L and Kerr T M 1986 Proc. **XI**th Int. Congress on EM, 1477
Sawada H, Tomita T, Naruse M, Honda T, Hambridge P, Hartel P, Haider M, Hetherington C, Doole R, Kirkland A, Hutchison J, Titchmarsh J and Cockayne D 2005 J. Electron Microscopy **54**, 119
Scherzer O 1936 Z. Phys. **101**, 593
Scherzer O 1947 Optik **2**, 114
Tillmann K, Thust A and Urban K, 2004 Microscopy and Microanalysis **10**, 185
Westmacott K H, Hinderberger S and Dahmen U 2001 Phil. Mag. A **81**, 1547
Zemlin F, Weiss K, Schiske P, Kunath W and Herrmann K-H 1978 Ultramicroscopy **3**, 49
Zemlin F 1979 Ultramicroscopy **4**, 241

Spherical aberration correction and exit-plane wave function reconstruction: Synergetic tools for the atomic-scale imaging of structural imperfections in semiconductor materials

K Tillmann, A Thust, L Houben, M Luysberg, M Lentzen and K Urban

Ernst Ruska-Centrum für Mikroskopie und Spektroskopie mit Elektronen, Institut für Festkörperforschung, Forschungszentrum Jülich GmbH, D-52425 Jülich, Germany

ABSTRACT: With the availability of resolution boosting and delocalisation minimising techniques, high-resolution transmission electron microscopy (HRTEM) forges ahead with respect to the atomic-scale imaging of semiconductor materials. In the present study the benefits accruing from a combination of two state-of-the-art techniques, i.e. spherical aberration correction (SAC) and exit-plane wave function (EPWF) reconstruction, are illustrated by highlighting their combined use for the atomic-scale characterisation of common lattice defects in lattice mismatched as well as ion implanted semiconductor layer systems. Moreover, practical advantages of the retrieval of the EPWF not only for the elimination of residual imaging artefacts but also for the proper orientation of specimens during operation of the electron microscope are demonstrated.

1. INTRODUCTION

In spite of recent advances in instrumentation, disadvantageous limitations of point resolution, the lack straightforward interpretability of experimental images, as well as image delocalisation in the vicinity of interfaces and lattice defects remain three major challenges in high-resolution transmission electron microscopy. Consequently, two strategies to overcome these deficiencies, inevitable during operation of "classical" medium voltage instruments equipped with field emission gun emitters and operated under high-resolution conditions, have attracted much interest in recent years.

On the one hand, spherical aberration corrector elements are practically usable these days. By this means the point resolution for phase contrast imaging conditions was shown to be extendable to the information limit of the instrument in-line with a rather low image delocalisation (Lentzen et al 2002). On the other hand, numerical retrieval techniques enable the extraction of the exit-plane wave function from a through-focus series of micrographs (Coene et al 1996, Thust et al 1996a). By means of the latter, all spatial information up to the information limit can be retrieved, also allowing for a subsequent elimination of residual lens aberrations (Thust et al 1996b, Thust 2002). Furthermore, the on-line retrieval of the EPWF during operation of the microscope was shown to be a suitable tool for precise sample alignment when analysing the symmetry properties of "local" diffraction patterns evaluated from the complex-valued exit-plane wave function (Tillmann et al 2004). In the present study we focus on the benefits accruing from a combination of these state-of-the-art techniques for the atomic scale imaging of structural imperfections in semiconductor materials.

2. BASIC RELATIONS OF NEGATIVE SPHERICAL ABERRATION IMAGING

When the electron microscope is operated as a variable spherical aberration instrument, the set-up of the aberration coefficient C_S emerges as an additional parameter for the simultaneous optimisation of the phase contrast and the image delocalisation. In particular, when employing an

optimised negative value of $C_S < 0$ combined with an overfocus setting $Z_{opt} > 0$ of the objective lens, i.e. when adjusting positive phase contrast, a substantial contrast improvement can be achieved since the phase contrast and the nonlinear dark field signals add rather than subtract as is usual when applying "classical" HRTEM imaging modes (Lentzen 2004).

Calculations balancing a high amount of positive phase contrast versus a widely minimised image delocalisation lead to an optimised negative spherical aberration (Lentzen et al 2002, Jia et al 2004)

$$C_S = -64/27 \ \lambda^{-3} g_{max}^{-4} \qquad (1)$$

with λ and $1/g_{max}$ denoting the electron wavelength and information limit of the instrument, respectively. With this setting an overfocus

$$Z_{opt} = 16/9 \ \lambda^{-1} g_{max}^{-2} \qquad (2)$$

yields widely direct interpretable high-resolution micrographs accompanied by a residual image delocalisation of

$$R = 16/27 \ g_{max}^{-1}. \qquad (3)$$

With this tuning, Z_{opt} replaces the Scherzer condition of "classical" HRTEM and the partially coherent phase contrast transfer function of the instrument, displayed in Fig. 1, is positive up to the information limit and characterised by a broad pass-band. Simplifying the imaging process to linear theory, a weak phase object is then imaged under bright atom contrast conditions. Choosing an aberration corrected CM-200 FEG ST instrument, the aforementioned parameter settings yield $Z_{opt} = 11.6$ nm, $C_S = -40.6$ µm and $R = 0.08$ nm when putting to use an electron wavelength of $\lambda = 2.51$ pm and an information limit of $1/g_{max} = 0.125$ nm with the latter value measured from a Young's fringe analysis (Lentzen et al 2002).

3. BENEFITS FROM THE RETRIEVAL OF THE EXIT-PLANE WAVEFUNCTION

The additional numerical retrieval of the exit-plane wave function $\Psi(\mathbf{r})$ from a through focus series of micrographs offers further improvements: $\Psi(\mathbf{r})$ is free from nonlinear imaging artifacts and by the combination of many images taken at different defoci, the low frequency gap in the phase contrast transfer function, i.e. the insufficient contrast transfer of low spatial frequencies caused by employing a rather small C_S value during imaging, will be reduced considerably. Furthermore, by extracting information from about 10 to 15 images, the signal-to-noise ratio at high spatial frequencies can be substantially improved. Even the application of small C_S values, which is a prerequisite to obtain phase contrast, induces a parasitic delocalisation R whereas the numerically retrieved $\Psi(\mathbf{r})$ is ideally free from any delocalisation effects.

Moreover, the availability of the complex-valued quantity $\Psi(\mathbf{r})$ allows for the numerical *a posterior* measurement of residual lens aberrations. This aspect is of special practical importance, as

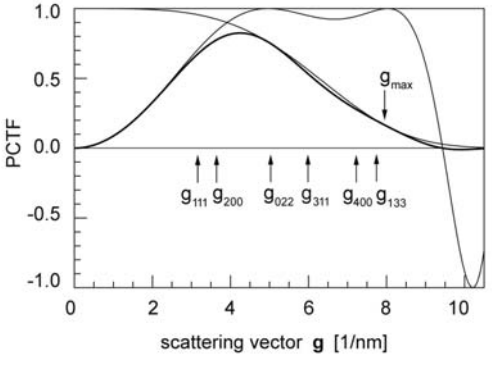


Fig. 1: Partially coherent contrast transfer function (thicker black line) based on parameters $\lambda = 2.51$ pm, $C_S = -40.6$ µm, $Z = 11.6$ nm together with 0.2 mrad for the semi-angle of beam convergence and 6.4 nm for the half-width of the Gaussian spread of defocus. Arrows indicate crystalline reflections in GaAs.

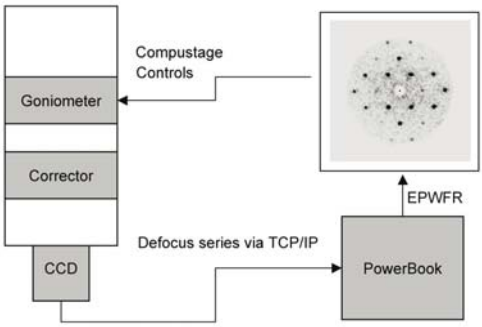


Fig. 2: Basic composition of microscope controls yielding a proper tuning of the specimen alignment. Through-focus series of images are transferred to a PowerBook used for the retrieval of the EPWF and for the evaluation of "local" diffraction patterns of the specimen area under investigation. Potential pattern asymmetries are used for the fine-tuning of the microscope goniometer.

experience shows that not all aberrations of the microscope are sufficiently constant over the period of operation or cannot be determined before the experiment with sufficient accuracy. In detail, the measurement of even aberrations, i.e. the defocus Z and the twofold astigmatism A_2, are based on the processing of the weak signals originating from amorphous overlayers (Thust et al 1996b) while the procedure to determine odd aberrations, i.e. the axial coma B_2 and the threefold astigmatism A_3, results from the analysis of the degree of symmetry with respect to crystalline features visible in the phase $\Phi(\mathbf{r})$ and amplitude $A(\mathbf{r})$ images of the exit-plane wave function (Thust et al 2002).

Finally, since $\Psi(\mathbf{r})$ is complex-valued, we may calculate "local" diffraction patterns from specimen areas as small as desired, which must not be confused with the centrosymmetric power spectrum obtained from the Fourier transformation of a real image intensity distribution or with selected area diffraction patterns from the specimen area under illumination. When evaluated during operation of the microscope, the judgement of the symmetry properties of these "local" diffraction patterns is a most convenient tool for the proper orientation of specimen areas under investigation, cf. the arrangement drawing displayed in Fig. 2. At specimen thicknesses 2 nm < t < 8 nm corresponding tuning procedures ensure a proper zone axis sample alignment of semiconductor samples with an accuracy well below 3 mrad (Tillmann et al 2004).

4. EXPERIMENTAL RESULTS

Both of the techniques described in the preceeding sections can be applied to a wide range of interface and defect structure problems in semiconducting materials and devices. In the following we highlight their combined use by discussing applications to specific cases.

4.1 Multiple Stacking Faults in GaAs (110)

The images displayed in Fig. 3 show the terminating zone of a multiple stacking fault in GaAs viewed along the crystallographic [$\bar{1}$10] direction. Both, the experimental micrograph $I(\mathbf{r})$ taken under Z_{opt} conditions as well as the phase image $\Phi(\mathbf{r})$ numerically retrieved from a through focus series of 15 images, reveal separated contrast dots at spacings of a = 0.14 nm with the latter showing a comparably improved signal-to-noise ratio. In the Z_{opt} image, the kidney-shaped distortions of the dumbbells are due to the residual aberrations as determined from the retrieved EPWF and amounting to A_1 = 2.2 nm (83°), B_2 = 110 nm (83°), and A_3 = 150 nm (43°) with the values in parentheses indicating azimuth angles inclined with the [001] direction. The minor smear out of the contrast dots to elongated tenons on the upper right image area, however, indicates that these regions are slightly out of optimum defocus, which is most probably due to the wedge-shaped geometry of the sample. The dumbbells inside the stacking fault plane are not resolved in the Z_{opt} micrograph, which may be due to the residual image delocalisation, mechanical instabilities, or a genuine structural effect.

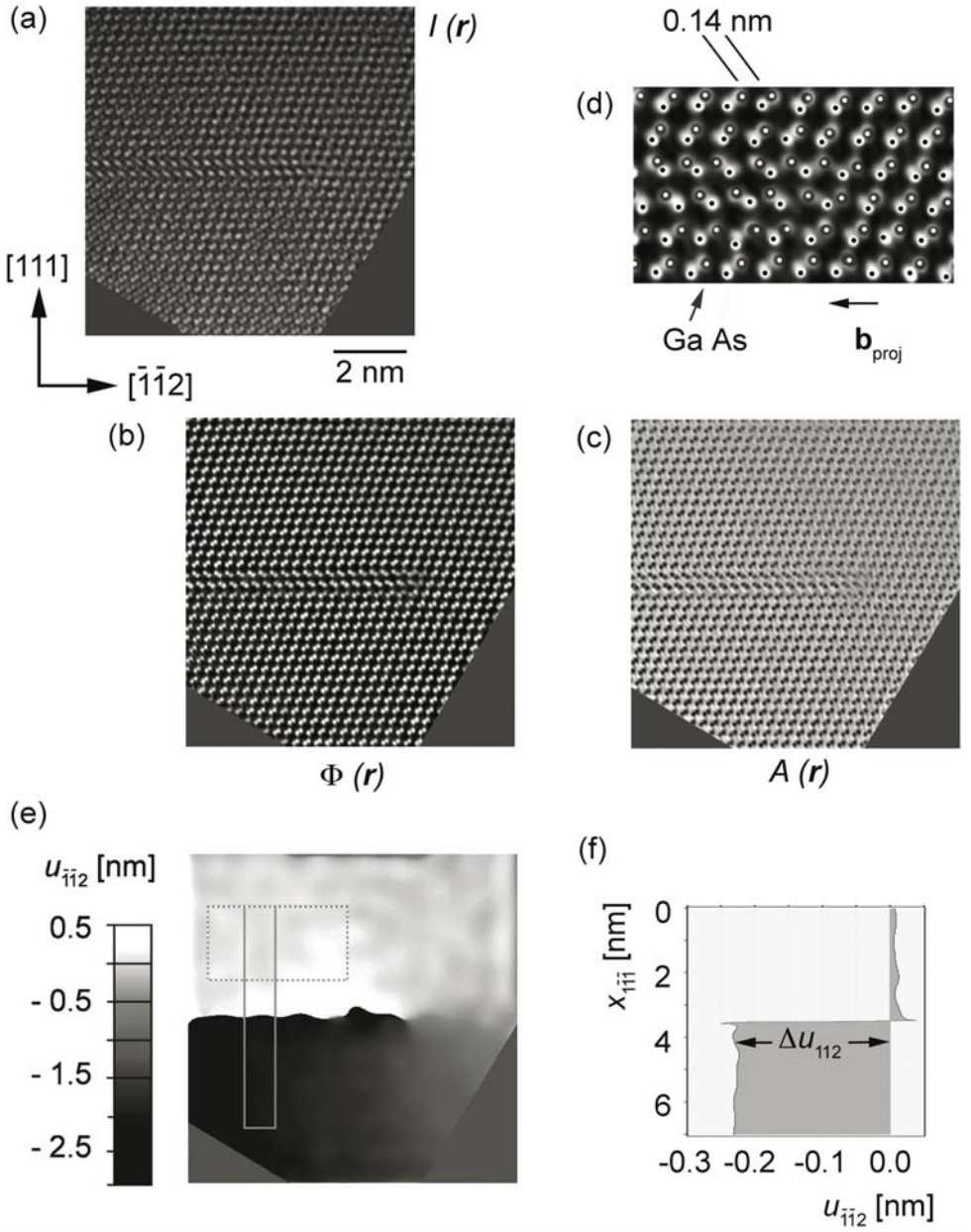


Fig. 3: Double stacking fault bound by two 30° partial dislocations with $\mathbf{b}_{proj} = a/6$ [$\bar{1}\bar{1}$2]. (a) Z_{opt} image, (b) retrieved phase Φ(**r**) and (c) amplitude A(**r**) images calculated from the associated through-focus series of images. (d) Magnified clipping Φ(**r**) with the positions of the atomic columns superimposed. (e) Contour representation of the lattice displacements along the [$\bar{1}\bar{1}$2] direction with respect to the dashed darker grey framed area as gained from the analysis of the phase image. (f) Displacement profile measured perpendicular to the stacking fault at the area indicated by the lighter grey frame.

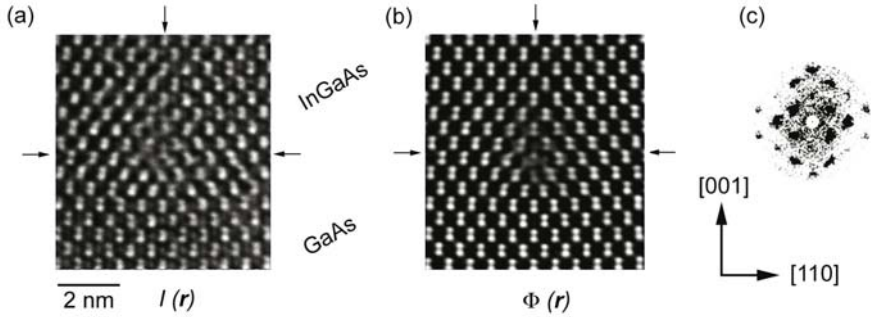


Fig. 4: (a) Z_{opt} image I(**r**) of a Lomer type edge dislocation, (b) phase image Φ(**r**) and (c) diffraction pattern calculated from the EPWF and demonstrating proper sample alignment. Arrows indicate the position of the dislocation core.

Both, the retrieved phase Φ(**r**) and amplitude A(**r**) images allow for an accurate identification of the atomic arrangement of the stacking fault and, especially, the core structure of the dislocation terminating the defect. As can be seen from the direct comparison of the Z_{opt} micrograph I(**r**) and the phase image Φ(**r**), the latter is characterised by a perceptibly increased signal-to-noise ratio, by less sensitivity with respect to sample thickness variations, and by clearly resolved dumbbells down to the dislocation core.

When measuring the polarity of the sample, e.g. by the evaluation of a set of relevant reciprocal-space amplitudes from the complex function Ψ(**r**) and the subsequent trimming of simulated data, individual bright contrast dots in the Φ(**r**) image may be directly associated with gallium and arsenic column positions (Tillmann et al 2004). This course of action allows for the direct identification of single atom columns, which are superimposed to the magnified clipping of the phase image.

Finally, a Burgers circuit around the dislocation core yields a projected closing vector $\mathbf{b}_{proj} = a/6\ [\bar{1}\bar{1}2]$ for the entire defect, which would be compatible with two adjacent 30° partial dislocations bounding a double stacking fault. To check this model hypothesis, the elastic displacement component $\Delta u_{\bar{1}\bar{1}2}$ along the $[\bar{1}\bar{1}2]$ direction of the Burgers vector, i.e. along the longitudinal direction of the stacking fault, has been evaluated from the Φ(**r**) image using geometrical phase analysis algorithms (Hÿtch et al. 1998). The correspondingly measured $\Delta u_{\bar{1}\bar{1}2}(\mathbf{r})$ distribution reveals strong displacement gradients ambient to the dislocation core as well as two mainly undistorted lattices that are homogeneously shifted against each other at the left-sided image regions. When measuring the mutual displacement $\Delta u_{\bar{1}\bar{1}2} = 0.234$ nm ± 0.06 nm between the upper and the lower crystal areas, owing to the widely minimised image delocalisation this quantity is in excellent agreement with $2\,|\mathbf{b}_{proj}| = 0.231$ nm associated with two parallel 30° partial dislocations.

4.2 Interfacial Edge Dislocations in InGaAs/GaAs (110)

As another example to investigate the lattice defects at atomic resolution, Fig. 4 displays images of an edge dislocation close to an InGaAs/GaAs heterointerface. In the experimental Z_{opt} micrograph I(**r**) the dumbbell structure of the matrix materials is clearly visible, although the atomic arrangement in the proximity of the dislocation core is not well resolved. Contrastingly, the retrieved phase image Φ(**r**) additionally reveals a detached atomic column at the dislocation core as is indicated by the horizontal and vertical arrows added to the image. This detached column, thus directly provides the existence of a Lomer edge dislocation of glide set type (Hornstra 1958).

As can be shown from the comparison of the experimental Z_{opt} micrograph with a variety of simulated images the fundamental non-resolvability of the dislocation core will neither be due to

(i) the residual image delocalisation, (ii) a locally decreased sample thickness, (iii) an immutably reduced occupancy of the atomic columns during image recording or (iv) thin foil relaxation in the vicinity of the highly strained dislocation core (Tillmann et al 2004). Instead, the practically improved resolution of the phase image $\Phi(\mathbf{r})$ results from the intrinsic averaging of structurally redundant information coming along with the electron beam induced time-dependent structural transformation of the sample, which will be particularly pronounced close to the highly strained regions nearby the dislocation core. While numerical retrieval techniques purge these information by averaging, a single Z_{opt} micrograph simply represents a snap-shot of a sample under illumination.

4.3 Chromium Implantation Induced Lattice Defects in GaN

Implantation of transition metals into semiconductors is considered as a candidate process for the fabrication of diluted magnetic semiconductors. Figure 5a displays lattice defects, produced after Cr implantation into GaN in the subsurface region after rapid thermal annealing, in an experimental Z_{opt} micrograph. Besides Cr-rich precipitates (P) a high density of stacking faults is observed, whose formation is related to the segregation of interstitials or vacancies: Extrinsic (E) stacking faults bounded by Frank partial dislocations with Burgers vector $\mathbf{b} = 1/2\ [0001]$ and intrinsic (I_1) stacking faults bounded by Frank-Shockley partials with $\mathbf{b} = 1/6\ [20\bar{2}3]$.

A magnified view of the core of a Frank partial dislocation is shown in the Z_{opt} image displayed in Fig. 5b and the phase image retrieved from the focal series shown in Fig. 5c. Although not fully resolved, Ga and N columns with a dumbbell distance of 0.129 nm, close to the information limit of the instrument, are discernible. The phase image of the dislocation core reveals an additional atomic column (arrow in Fig. 5c), presumably nitrogen which is not clearly detected in the Z_{opt} image. Hence the improved signal-to-noise ratio in the phase image discloses that a core structure with Ga-Ga bonds compliant with the Z_{opt} micrograph does not reflect the full core structure of the dislocation.

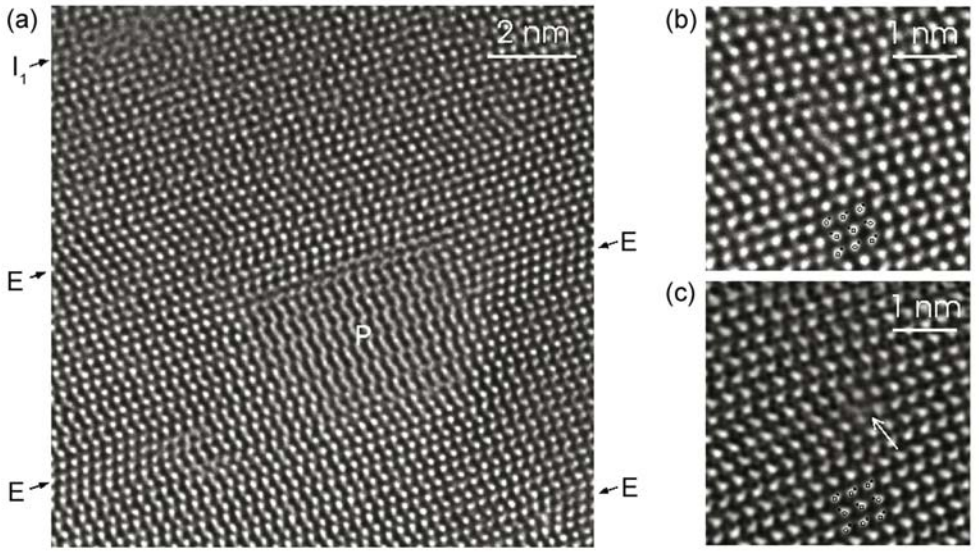


Fig. 5: Lattice defects in Cr implanted GaN viewed along the $[11\bar{2}0]$ direction. (a) Z_{opt} micrograph. P: Cr-rich precipitate; E: extrinsic stacking fault; and I_1: intrinsic stacking fault. (b) Magnified Z_{opt} image of a Frank partial dislocation with $\mathbf{b} = 1/2\ [0001]$. (c) Corresponding phase image retrieved from the focal series. The arrow indicates an additional atomic column not resolved in the Z_{opt} image.

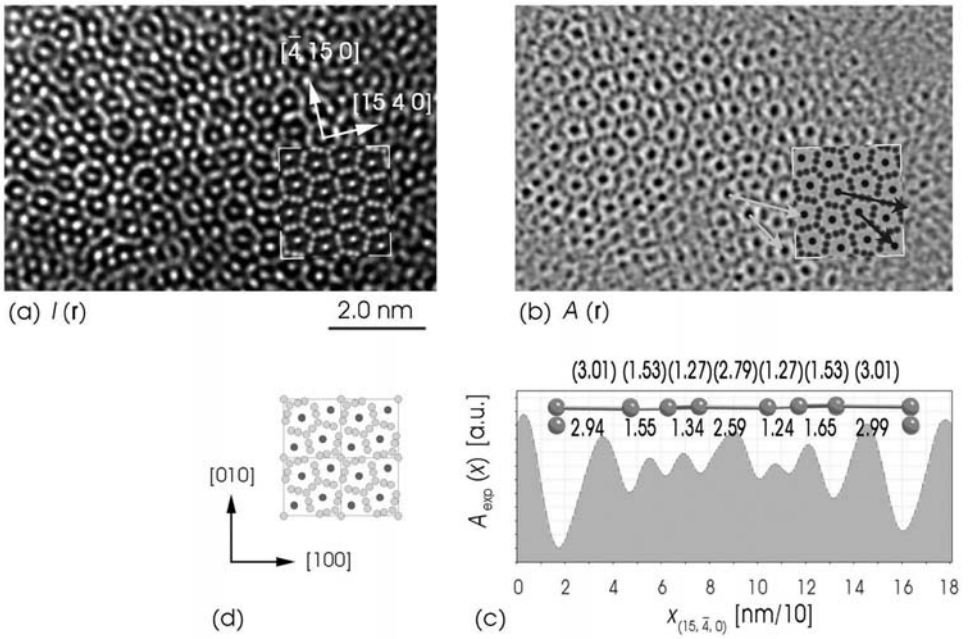


Fig. 6: (a) High-resolution Z_{opt} micrograph showing a β-phase tantalum crystallite viewed along the [001] zone axis. The 2 x 2 unit cell insertion shows a calculated image assuming $t = 1.5$ nm, $Z = 11.6$ nm, $A_1 = 4.2$ nm (110°), $B_2 = 70$ nm (340°), and $A_3 = 120$ nm (0°) as simulation parameters with the values in parentheses indicating azimuth angles inclined with the horizontal image axis. (b) Amplitude image A(**r**) together with a simulated insertion. (c) Line profiles $A_{exp}(x)$ extracted from the amplitude image along the [15$\bar{4}$0] direction taken at the position of the lighter grey dashed arrow in the A(**r**) image. The occupancy of the columns is indicated by the number of atoms drawn in at the extrema positions. Spacings Δx_{exp} between adjacent amplitude minima have been extracted from the displayed $A_{exp}(x)$ profile and are compared with theoretical data specified in parentheses. (d) 2 x 2 unit cell structure model with the lighter and darker grey dots indicating singly and doubly occupied tantalum columns, respectively.

4.4 Tantalum Metallisation Layers

Room temperature magnetron sputter deposition of tantalum thin films on semiconductor substrates usually results in the formation of polycrystalline coatings. Grains mainly nucleate in the metastable β-phase (space group $P4_2/mnm$) of tantalum, which shows atomic column spacings as small as 0.127 nm when viewed along the [001] direction. Since grain boundary diffusion becomes admittedly relevant at elevated temperatures, the atomic-scale investigation of the defect structure associated with β-phase crystallites is, hence, the key to understand the diffusion barrier properties of tantalum metallisation layers, which are also used for promoting the adhesion of subsequently deposited copper contacts to silicon substrates.

Figure 6 displays a Z_{opt} micrograph taken from an extended β-phase tantalum crystallite and the amplitude image A(**r**) of the exit-plane wavefunction together with simulated image insertions. As before, the image contrast of the Z_{opt} micrograph is somewhat bleary and characterised by a less advantageous signal-to-noise ratio when compared to the A(**r**) image. Line profiles extracted from the amplitude image along the crystallographic [15$\bar{4}$0] direction reveal that projected column spacings of

0.127 nm are clearly resolved. The comparison of simulated and experimental $A_{exp}(x)$ profiles, however, demonstrates a slightly reduced effective resolution of the A(**r**) image, which will be due to either specimen vibrations, image contributions from amorphous overlayers of the sample or a minor misalignment of the specimen (Tillmann et al 2005).

Moreover, close inspection of the A(**r**) image reveals that the entire crystallite is composed of four grains, which are separated by asymmetric 30° tilt boundaries with segments running mainly along the ‹100› and ‹110› directions inside a common (001) plane. The formation of these boundaries may be well explained by the adsorption of tantalum atoms of laterally expanding grains at misaligned unit cell positions (Tillmann et al 2005).

5. CONCLUSIONS

In summary, a combination of negative spherical aberration imaging and the numerical retrieval of the exit-plane wave function has been applied to the investigation of common lattice defects in semiconductor materials at atomic resolution. It has been demonstrated that recent improvements in the resolution power of transmission electron microscopes enable the imaging of the finest structure details with column spacings well below 0.13 nm at directly interpretable contrast features also coming along with an extensively minimised image delocalisation when micrographs are taken under directly interpretable bright-atom contrast conditions applying a $C_S < 0$ set-up of the instrument and an optimum defocus $Z_{opt} > 0$. This imaging mode, thus, allows for a largely direct interpretation of experimental images down to the information limit of the instrument.

Additionally, the numerical retrieval of the exit-plane wave function allows for the successful elimination of artificial contrast features still visible in micrographs taken under optimised defocusing conditions, which is especially beneficial when investigating the structure of lattice defects and heterointerfaces at atomic resolution. Beyond this genuine purpose, the retrieval of the exit-plane wave function was demonstrated to be a most suitable tool for the recognition and the on-line correction of minor sample misalignments, as well as for the determination and numerical correction of residual lens aberrations.

ACKNOWLEDGEMENTS

The authors are grateful to A Förster, M P Weides, V Guzenko and D Meertens for making available the samples investigated and for indefatigable specimen preparation work.

REFERENCES

Coene WMJ, Thust A, Op de Beeck M and van Dyck D 1996 Ultramicroscopy **64**, 109
Hornstra J 1958 J. Phys. Chem. Solids **5**, 129
Hÿtch MJ, Snoeck E and Kilaas R 1998 Ultramicroscopy **74**, 131
Jia CL, Lentzen M and Urban K 2004 Microsc. Microanal. **10**, 174
Lentzen M, Jahnen B, Jia CL, Thust A, Tillmann K and Urban K 2002 Ultramicroscopy **92**, 233
Lentzen M 2004 Ultramicroscopy **99**, 211
Thust A, Coene WMJ, Op de Beeck M and van Dyck D 1996a Ultramicroscopy **64**, 211
Thust A, Overwijk MHF, Coene WMJ and Lentzen M 1996b Ultramicroscopy **64**, 249
Thust A, Jia CL and Urban K 2002 Proc. ICEM-15, Vol. **3**, ed R Cross (Durban: Microscopy Society of Southern Africa) pp 167-168
Tillmann K, Thust A, and Urban K 2004 Microsc. Microanal. **10**, 185
Tillmann K, Thust A, Gerber A, Weides MP and Urban K 2005 Microsc. Microanal. *accepted*

Strain mapping from HRTEM images

P L Galindo[1], A Yáñez[1], J Pizarro[1], E Guerrero[1], T Ben[2] and S I Molina[2]

Universidad de Cádiz, Polígono Río San Pedro s/n 11510 , Puerto Real (Spain)
[1] Departamento de Lenguajes y Sistemas Informáticos. CASEM
[2] Departamento de Ciencia de los Materiales e Ing. Metalúrgica y Q. Inorgánica. F. Ciencias

ABSTRACT: Strain mapping is defined as a numerical image processing technique that measures the local shifts of image details around a crystal defect with respect to the ideal, defect-free, positions in the bulk. The most common algorithms for strain mapping are based on peak finding (real space) and geometric phase (Fourier space) methods. In this paper, we discuss both algorithms and propose an alternative algorithm (*Peak Pairs*) based on the detection of pairs of intensity maxima in the affine transformed space which exhibits good behavior at dislocations. Quantitative results are reported from experiments to determine local stresses in different types of quantum heterostructures.

1. INTRODUCTION

The field of stress and strain in heteroepitaxy has known large developments during the last decade. New techniques have been used to set up new devices in which functionalities are obtained through structure at the nanometre scale. The elastic stress stored in the device can induce various phenomena which have to be evaluated, understood and predicted. Recent advances in digital imaging and image-processing techniques offer the possibility of locally determining the elastic strain of materials at the atomic scale using high-resolution transmission electron microscopy (HRTEM) images. However, the reliability of strain profiles relies on the assumption of a constant spatial relationship between the intensity maxima in the image and the relative positions of the atomic columns in the specimen. This is not true in all cases, due to some known effects, such as thin foil relaxation, local crystal tilts, surface relaxation and the appearance of shifts in lattice fringes due to thickness and/or composition variation across the material. Nevertheless, the average strain of thicker layers can be determined with sufficient accuracy (Tillmann et al 1999).

In order to calculate strain profiles, several approaches have been described in the literature. The most common algorithms used for strain mapping are based on peak finding (real space) and geometric phase (Fourier space). *Peak finding* methods (see review in Kret et al 2001) work in real space, building a two-dimensional reference lattice associated to a non-distorted region of the material, and identifying the local displacements of a grid that is built up from the set of intensity maxima in the HRTEM image. The lattice displacements are then used to determine the strain distribution of the specimen. The *Geometric phase* method (Hÿtch et al 1998) works in Fourier space, and consists of filtering the image with an asymmetric filter at a Bragg spot of the Fourier transform of a HRTEM lattice image and performing an inverse Fourier transform. The phase component of the resulting complex image gives information about local displacement in a given direction. Local strain is derived by analyzing the derivative of the displacement obtained from two non-collinear components. Peak finding approaches have some advantages when the image has different materials across the image, because of the global character of the Fourier transform. On the other hand, geometric phase exhibits superior performance when determining strain factors around dislocations.

In this paper we introduce a real space approach, which is based in the detection of pairs of intensity maxima in the affine transformed space, where it is possible to use the Euclidean distance, thus reducing the errors in the determination of pairs, especially when dislocations appear in the image.

2. THE *PEAK PAIRS* APPROACH

The first stages of the procedure are similar to other real space algorithms as detailed in Kret et al (2001). First, a Wiener filter is used to reduce the noise of the experimental image (Rosenauer et al 1996). The Wiener filter is a type of linear filter that is applied to an image adaptively, tailoring itself to the local image variance, and preserving edges and other high frequency parts of the image, assuming Gaussian white additive noise. It lowpass filters an intensity image using neighbourhoods of size m-by-n to estimate the local image mean and standard deviation, creating a pixel-wise Wiener filter with these estimates. In order to obtain a fringe image instead of the dot patterns, a Bragg-filter is applied to the Fourier-transformed image, but researchers should extremely careful, given that non-existent periodicities may be introduced, and/or fine details may be removed at this stage.

Local maxima are defined as those pixels of a given intensity (t) whose external boundary pixels all have a value less than t (8-connected neighbourhood). Local maxima are identified on a pixel basis on the Bragg-filtered image, so its maximum resolution is 1x1 pixels. In order to obtain sub-pixel resolution, we considered initially two approaches: 2D interpolation (linear, spline, polynomial) and function maximization. However, interpolation requires sampling the image at fractional locations, generating matrices of values at sub-pixel resolution, at which to interpolate the data. The higher the desired precision is, the higher the dimension of the matrices should be, thus increasing the computational requirements to process a given image. Once the image has been interpolated, it is easy to determine the position of the peak at subpixel resolution. The second approach requires less computational effort, but assumes that the local shape of grey values around a peak is quadratic. We propose to fit a 2-D quadratic function using a 8-connected neighbourhood of 2 pixels around each local maxima: $z(x,y) = a \cdot x^2 + b \cdot y^2 + c \cdot x \cdot y + d \cdot x + e \cdot y + f$

Once the quadratic function has been fitted to the neighbourhood of a peak, it is easy to determine the maximum of this function by setting derivatives to 0 as follows:

$$\frac{\partial z}{\partial x} = 0 \quad , \quad \frac{\partial z}{\partial y} = 0 \quad \Longrightarrow \quad \begin{vmatrix} 2a & c \\ c & -2b \end{vmatrix} . \begin{vmatrix} x_{\max} \\ y_{\max} \end{vmatrix} = \begin{vmatrix} -d \\ -e \end{vmatrix}$$

This allows us to determine precisely the peak (x_{max},y_{max}) at sub-pixel resolution. This approach is more sensitive to noise, but it has shown to be much faster than interpolation, achieving enough precision in the experiments.

Two non-collinear vectors should be selected to determine the basis vectors that will be used as the references to which determine the strain of the specimen. The reference area should be taken on the same image, but outside of deformed regions. If this is not possible, the least deformed zone near the area of interest should be selected.

Once the reference vectors a=(a_x,a_y) and b=(b_x,b_y) have been chosen, these may be used to define an affine transformation. An *affine transformation* maps variables (*e.g.* pixel intensity values located at position (x,y) in an input image) into new variables (x',y') by applying a linear combination of translation, rotation, scaling and/or shearing (*i.e.* non-uniform scaling in some directions) operations. The main advantage of affine transformations is that they preserve lines and parallelism, and therefore are well suited to the transformation of crystalline images. In the case of a non-stressed material, this transformation would generate a perfectly square grid.

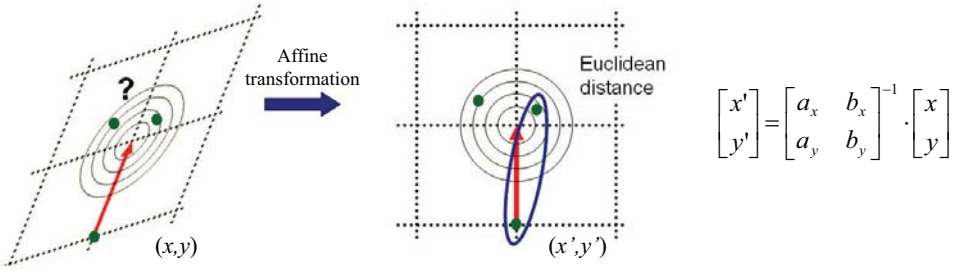


Fig. 1. Affine transformation defined by reference vectors a(a_x,a_y) and b(b_x,b_y). This transformation allows the use of Euclidean distance when searching the optimal "partner" of a given peak.

It also allows the use of Euclidean distance in order to determine the most probable "partner" of a given maximum of intensity in the peak pair's identification stage. In fact, we associate the partner of a given peak as the nearest peak in the transformed space using Euclidean distance, as shown in Fig. 1. The selection of pairs of peaks along two non-collinear directions, gives us the possibility to determine precisely the strains around dislocations, as shown in Fig. 2.

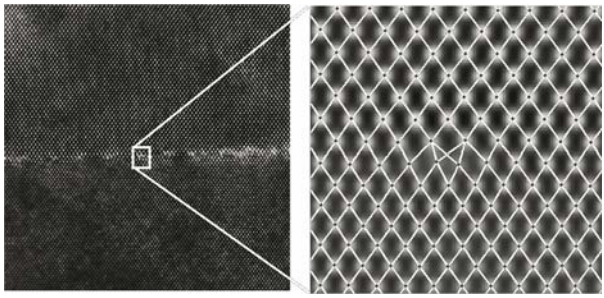


Fig. 2. Example of the pair identification process along two non-collinear directions, showing the Peak Pairs behaviour around a dislocation. (Original HREM image, courtesy of Kret et al (2003).)

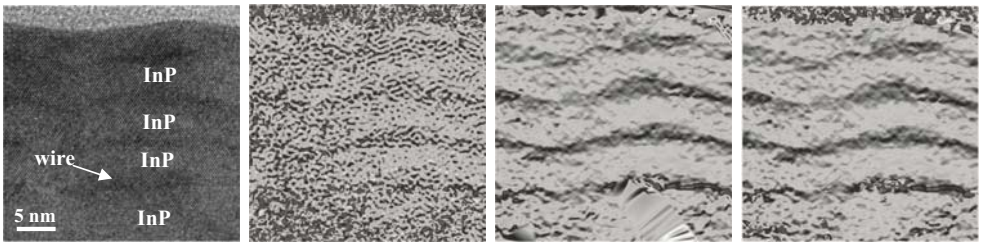
In order to determine the strain factors, we use the distortion at a given point in two non-collinear directions using each detected pair, by solving the following set of linear equations:

$$\left.\begin{aligned} u_x &= a_x \cdot e_{xx} + a_y \cdot e_{xy} \\ u_y &= a_y \cdot e_{yy} + a_x \cdot e_{yx} \\ v_x &= b_x \cdot e_{xx} + b_y \cdot e_{xy} \\ v_y &= b_y \cdot e_{yy} + b_x \cdot e_{yx} \end{aligned}\right\} \qquad \begin{bmatrix} e_{xx} \\ e_{xy} \end{bmatrix} = \begin{bmatrix} a_x & a_y \\ b_x & b_y \end{bmatrix}^{-1} \cdot \begin{bmatrix} u_x \\ v_x \end{bmatrix} \qquad \begin{bmatrix} e_{yx} \\ e_{yy} \end{bmatrix} = \begin{bmatrix} a_x & a_y \\ b_x & b_y \end{bmatrix}^{-1} \cdot \begin{bmatrix} u_y \\ v_y \end{bmatrix}$$

where u_x, u_y are the coordinates of the displacement with respect to reference vector $a=(a_x,a_y)$, and v_x,v_y are the coordinates of the displacement with respect to reference vector $b=(b_x,b_y)$. Once the lattice distortion tensor is determined for each maximum in the image, and by simple interpolation, we determine the continuous distortion field.

3. EXPERIMENTAL RESULTS

In order to test the algorithm under different situations, Geometric Phase, Peak Finding and Peak Pairs algorithms were applied to an HREM image of stacked quantum wires of InAs(P) on an InP substrate to show its behaviour under abrupt changes of contrast. Fig. 3 shows that in this case, Peak finding and Peak Pairs algorithms neatly find the strain associated to quantum wires. Peak Finding has errors in the lower part of the image due to great changes in contrast at the lower wire. This error is propagated along the map, while in the Peak Pairs approach, this effect only produces local errors in the wire.

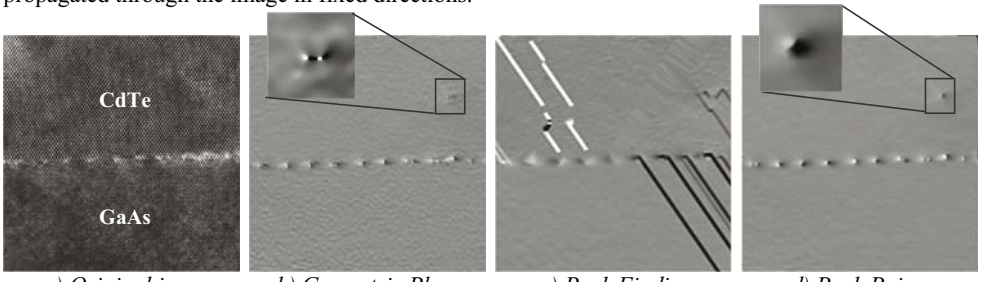


a) Original image *b) Geometric Phase* *c) Peak Finding* *d) Peak Pairs*

Fig. 3. Strain maps (e_{yy}) of quantum wires of InAs(P) on an InP substrate showing performance of different algorithms on inhomogeneous surfaces and abrupt changes of contrast.

Geometric Phase gets low resolution due to the existence of two different, non-uniformly distributed, materials across the image. The global character of the Fourier transform produces difficulties in the proper identification of these materials, inducing errors in the strain images. Experiments have been made applying a low-pass filter to geometric phase maps, but results do not improve very much, and resolution in dislocations is reduced.

The procedure was also applied to an HREM image of the GaAs/CdTe interface along the [110] zone axis (courtesy of Kret et al 2003), in order to compare the limitations of each method on dislocation core measurements. Figure 4 shows that Peak Finding exhibits numerous artefacts in the strain due to errors when fitting a square matrix to a non-square grid of intensity peaks in the presence of numerous dislocations along the interface. These errors originate at dislocations and, even worse, propagated through the image in fixed directions.



a) Original image *b) Geometric Phase* *c) Peak Finding* *d) Peak Pairs*

Fig. 4. Strain maps (e_{xy}) of GaAs/CdTe interface showing performance of different algorithms on dislocations. Dislocation details are shown for Geometric phase and Peak Pairs algorithms.

On the other hand, Geometric Phase and Peak Pairs results are promising. However, a higher level of noise and strange artefacts in dislocations appear in Geometric Phase strain maps.

4. CONCLUSION

In this paper we introduce the *Peak Pairs* algorithm, a new real space procedure for strain mapping. Basically, it works on a Bragg-filtered image, locating pairs of peaks along a predefined direction and distance in the affine transformed space defined by a pair of basis vectors. This transformation greatly reduces potential errors in the determination of *partners* of a given peak. It offers the advantages of a real space approach and its behaviour is unaltered in the presence on dislocations as well as in the strain mapping of inhomogeneous surfaces.

ACKNOWLEDGEMENTS

We thank S. Kret for helpful discussions and for providing us beautiful high-quality experimental images. We also thank M. Hytch for kindly providing us the basic Geometric Phase scripts and L. Gonzalez for providing us the quantum wires sample imaged by HRTEM in Fig. 2a. This research was supported by Spanish MCyT under projects NANOSELF(TIC-2002-04096-C03-02) and SUSIN(MAT2004-01234), Junta de Andalucía (PAI research groups TIC-145 and TEP-0120) and network of excellence SANDiE (Contract NMP4-CT-2004-500101 of the VI European Framework Programme).

REFERENCES

Hÿtch M J, Snoeck E and Kilaas R 1998 Ultramicroscopy **74**, 131
Kret S, Dłużewski P, Dłużewski and Laval J Y 2003 Philosophical magazine **83**, 231
Kret S, Ruterana P, Rosenauer A and Gerthsen D 2001 Phys. Stat. Sol. (b) **227**, 247
Rosenauer A, Kaiser S, Reisinger T, Zweck J, Gebhardt W and Gerthsen D 1996 Optik **101**, 1
Tillmann K, Lentzen M and Rosenfeld R 1999 Inst. Phys. Conf. Ser. **164**, 15

Quantification of the influence of TEM operation parameters on the error of HREM image matching

J Pizarro, E Guerrero, P Galindo, A Yañez, T Ben[1] and S I Molina[1]

Departamento de Lenguajes y Sistemas Informáticos. CASEM, Universidad de Cádiz, Facultad de Ciencias, Polígono Río San Pedro s/n 11510, Puerto Real, Spain
[1] Departamento de Ciencia de los Materiales e Ing. Metalúrgica y Q. Inorgánica Universidad de Cádiz, Facultad de Ciencias, Polígono Río San Pedro s/n 11510, Puerto Real, Spain

ABSTRACT: In this paper we describe a pattern recognition system implemented to determine thickness and defocus from HRTEM simulated images. A specific task has been designed to quantify the influence of certain operation parameters of a transmission electron microscope in the global recognition error rate. This influence allows us to estimate human recognition confidence when applying pattern matching to the determination of thickness and defocus from HRTEM maps. The images considered in this task correspond to InP with the sphalerite crystalline structure and were simulated using the EMS computer software package.

1. INTRODUCTION

Computer-based image analysis is becoming increasingly important in the derivation of quantitative data from atomic resolution images. Images directly related with the projected atomic configuration in crystals can be obtained using high resolution transmission electron microscopy (HRTEM). However, high-resolution operation and image interpretation are complicated by the rapid, and often, complex variations in image appearance with changes not only in defocus and thickness, but also in some other parameters, such as the beam energy, beam spread, beam tilt, illumination divergence, lens aberrations, etc. The image detail depends so strongly on sample thickness and image defocus, that in general the sample structure cannot be determined uniquely from a single image. To determine these parameters, experimental images can be compared with calculated HRTEM images.

Image simulation can provide several sources of additional information about the specimen. First, it can reveal which features of the image are due to artefacts produced by aberrations in the electron microscope and which image features are due to the specimen itself. Image simulation is an aid in interpreting the image recorded in the electron microscope. Second, it is relatively simple to change instrumental parameters in the simulation that would be difficult if not impossible to change in practice.

Hence, questions such as which values of absorption coefficient, beam convergence or defocus spread are the best for defocus and thickness estimation can only be answered properly if done using a method of experiment design (O'Keefe 1998). A specific task has been designed for the determination of thickness and defocus from HRTEM images and taking into account certain tunable operation parameters of the transmission electron microscope.

2. METHODOLOGY

A map of HRTEM images was generated for InP with the sphalerite crystalline structure and the electron beam along [110]. The proposed procedure consists of considering simulated images using various defocus and thickness values, and finding a consistent reasonable set which matches the details of the observed images over as wide a range as possible.

Different approaches to quantitative extraction of relevant information from HRTEM have been

used in the literature (Galindo et al 2003, Bonnett 2000, King et al 1993). In this work micrographs were simulated in order to get upper and lower limits of beam semi-convergence and defocus spread at three different values of the absorption coefficient (Ac). These limits point out the range of values in which focus and thickness estimation will be reliable enough. Confidence was measured as the difference between real and estimated values. When these differences were higher than 3 layers or 3 defocus values respectively, estimations were considered unreliable.

Matching was carried out by means of the normalized cross-correlation of both matrices, the base matrix that represents a simulated image and a simulated micrograph matrix. Each base image consisted of 180x256 grey values both in the interval [0,255] and each simulated micrograph consisted of 90x128 grey values so that we ensure that the experimental image is contained in the simulated images.

The simulated micrograph is scanned across the base image column by column and row by row. The program then produces an output matrix whose values represent the similarity between both images. It assumes values between –1 and 1. Thus, the more similar a *nxm* sub-array of pixels is to the simulated micrograph, the closer to unity will be its correlation coefficient. The estimated thickness and defocus will be the thickness and defocus of the image in the HRTEM map which better matches with the micrograph.

3. EXPERIMENTAL RESULTS

For three different values of Ac (0, 0.25 and 0.05), a set of 5000 base HRTEM images of InP with the electron beam along [110] were simulated using the EMS software package (Stadelmann 1987), corresponding to 50 different thickness values (from 1 to 100 layers steps 2, 1 layer=0.415 nm) and 100 different objective lens underdefocus values (from 0 to 99 nm step 1). The image calculations were carried out using the multislice approach and parameters were set to the following values: accelerating voltage 200 kV, objective lens aperture diameter 14 nm^{-1}, aperture shift and origin shift (0,0,0) and objective spherical aberration coefficient, Cs=0.5 mm. The typical defocus spread value used was 0 nm and the electron beam semi-convergence 0 mrad.

Experiments were carried out in two different stages. At the first stage, a wider range of defocus (0, 25, 50, 75 and 100 nm) and thickness (1, 20, 40, 60, 80 and 100 layers) were considered. At the second stage, experiments were centred around Scherzer defocus values (from 30 to 55) and thicknesses of 16, 22, 28, 34 layers.

Simulated micrographs were generated setting a certain Ac value and varying the beam convergence from 0 to 2 mrad (0.1 mrad step). The remaining parameters were fixed to typical values. When considering spread of focus, the procedure was similar, for a certain Ac, a range of spread of focus values was considered, whereas the remaining microscope parameters were fixed to typical values. At the second stage, these ranges were also limited.

3.1 First Stage

From all the experiments, it was observed that comparing results for different Ac values did not yield any significant conclusion. Analysis was independently made for spread of focus and beam semi-convergence. Maximum confidence was encountered for:

- defocus spread lower than 6 nm,
- beam semi-convergence lower than 0.6 mrad.

3.2 Second Stage

At this stage, ranges of spread of focus and beam semi-convergence were reduced and simulated micrographs were generated around Scherzer focus (43 nm). The parameters were: defocus from 30 to 55 nm, step 1, thickness 16, 22, 28, 34 layers, defocus spread from 0 to 5 nm, (step 1 nm) and beam semi-convergence from 0 to 0.5 mrad (step 0.1 mrad). From the experiments it was observed that thickness and defocus differences were between –3 and 3 nm.

Tables 1 and 3 show experimental results for different thickness and defocus values when Ac = 0.5 and spread of focus was 5 nm.

Thickness (Layers) \ Defocus (nm)	38	39	40	41	42	43	44	45	46	47	48	49	50
16	1	0	1	1	2	-1	0	0	0	0	1	1	1
20	1	1	1	2	-1	0	-1	0	0	0	0	0	-1
22	1	2	1	2	-1	-1	-1	0	0	0	0	0	-1
28	1	1	1	-2	-2	-1	-1	0	0	0	0	0	-1
34	0	1	0	0	-1	-1	0	0	0	0	0	0	0

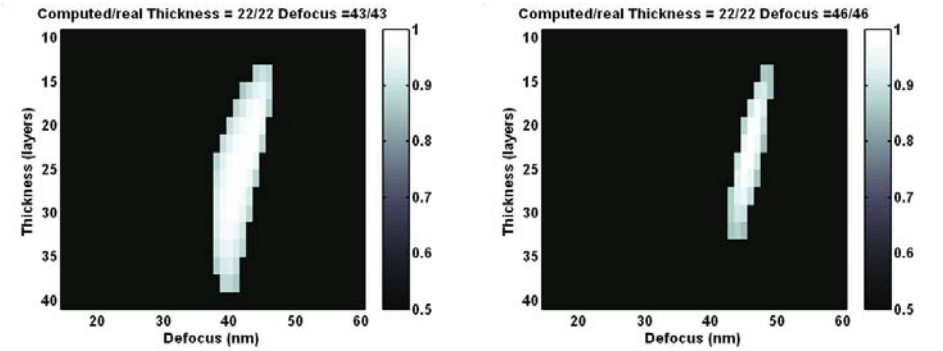
Table 1: Thickness differences between real and computed values when Ac= 0.5 and defocus spread = 5 nm.

Thickness (Layers) \ Defocus (nm)	38	39	40	41	42	43	44	45	46	47	48	49	50
16	-1	-1	-2	-2	-3	2	1	0	0	0	-1	-1	0
20	-1	-1	-2	-3	2	1	1	0	0	0	0	0	0
22	-1	-2	-2	-2	2	1	1	0	0	0	0	0	1
28	-1	-1	-1	2	2	1	1	0	0	0	0	0	1
34	-1	-1	0	0	1	1	0	0	0	0	0	0	0

Table 2: Defocus differences between real and computed values when Ac= 0.5 and defocus spread = 5 nm.

The experiment was repeated varying the defocus spread from 6 to 10 nm (step 2 nm) and the beam semi-convergence from 0.6 to 1.5 mrad (step 0.3 mrad). It was observed that although thickness and defocus differences between real and computed values increased, no significant differences were encountered for defocus values from 45 to 47 nm.

Figure 1 shows similarity maps between work image and template when Ac was 0.5 and the beam semi-convergence 0 mrad. Only values above 80% are shown. White colours maximise chance of being selected. The smaller the white area the smaller the thickness and defocus variance computed. These areas decrease approximately from 30 nm to 37 nm, then increase up to Scherzer defocus and get the lowest values between 45 and 47 nm to increase again. Defocus values between 45 and 47 provide the smallest areas of maximal chance of being selected in the similarity maps. We can observe from Fig. 1 that the white area is bigger at Scherzer focus that at 46 nm. Figure 2 shows the number of pixels whose values are above 80%. Note that for a defocus value of 46 nm the smallest area is obtained.



(a) (b)

Fig. 1: Maps of similarity between work image and template when the Ac=0.5 and the beam semi-convergence was 0 mrad. (a) Scherzer defocus = 43 nm (b) Defocus = 46 nm.

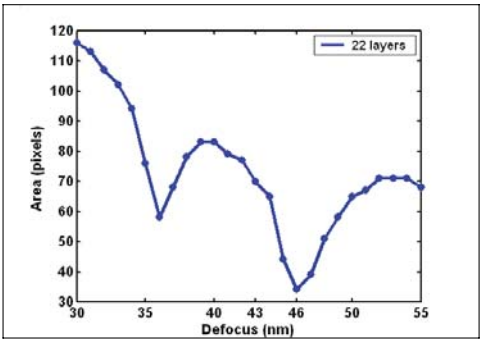


Fig. 2: Area of similarity greater than 0.8 at different defocus values.

In order to get high confidence in thickness and defocus estimation with low variance values, defocus spread values should be fixed between 0 and 5 nm, beam semi-convergence should be fixed between 0 and 0.5 mrad and defocus values between 2 and 4 nm greater than Scherzer defocus.

4. CONCLUSIONS

A specific task has been designed for the determination of thickness and defocus from HRTEM images. In this work this task has been successfully applied to InP. The present paper has just shown some preliminary results, considering simulated images as experimental ones. The intent of this paper is to provide related results and experiences that may aid in the pursuit of similar work when real experimental micrographs are considered. In this case, since contrast and intensity discrepancies from experimental and simulated images are higher, reliable results in defocus and thickness estimation are more difficult to obtain.

ACKNOWLEDGEMENTS

This work was financed by Spanish MCyT under NANOSELF project (TIC2002-04096), by the network of excellence SANDiE (Contract NMP4–CT– 004-500101 of the VI European Framework Programme) and the Junta de Andalucía (PAI research groups TIC-145 and TEP -0120).

REFERENCES

Bonnett N 2000 Advances in Imaging and Electron Physics **114**, 1
Galindo P L, Ponce A and Molina 2003 S I Inst. Phys. Conf. Ser. **180**, 23
King W and Campbell G 1993 Ultramicroscopy **51**, 128
O'Keefe M A 1998 Proceeding of XIVth International Congress for Electron Microscopy **1**, 573
Stadelmann P A 1987 Ultramicroscopy **21**, 131

ConceptEM: a new method to quantify solute segregation to interfaces or planar defect structures by analytical TEM and applications to inversion domain boundaries in doped zinc oxide

T Walther, A Rečnik[1] and N Daneu[1]

Center of Advanced European Studies and Research (caesar), Ludwig-Erhard-Allee 2, D-53175 Bonn, Germany
[1] Dept. Nanostructured Materials, Jožef-Stefan-Institute, Jamova 39, SI-1000 Ljubljana, Slovenia

ABSTRACT: Multiple scattering of electrons within the specimen degrades the spatial resolution in scanning or nano-probe transmission electron microscopy (TEM). It also reduces significantly the chemical signal from a local defect. Hence, the accuracy of analytical TEM is much lower than its sensitivity. A new technique has been developed for determining small amounts of solute atoms incorporated into well-defined planar defects in solids. The method is based on recording series of analytical spectra taken with different electron beam diameters centered above a defect which is oriented nearly edge-on. A linear least-squares fit is performed and the segregation level determined from the slope of the fitting curve. This concept of nearly concentric electron probes in analytical TEM (conceptEM) can be applied to both energy-dispersive X-ray (EDX) or electron energy-loss spectroscopy (EELS). For the study a nano-probe mode is used but no scan unit is needed. Reliability and accuracy have been modeled and applications to doped ZnO are presented.

1. INTRODUCTION

Analytical transmission electron microscopy (TEM) is based on the acquisition of chemical signals from either characteristic energy losses (electron energy-loss spectroscopy, EELS) or s (energy-dispersive X-ray spectroscopy, EDXS). Because of the ability to form very small electron probes the spatial resolution can be high. However, multiple scattering of the electrons even within a moderately thick foil leads to beam broadening of typically a few nanometres. While this degrades the spatial resolution in imaging only slightly, a high, unspecific background signal reduces significantly the chemical signal obtained from a local defect. The accuracy in determining any chemical composition locally is directly related to the uncertainty in the knowledge of the interaction volume which can often not be determined with sufficient accuracy because of the influences of thickness (beam broadening) and orientation (channeling). Both effects are particularly pronounced, relative to the electron beam size, for well focused electron probes. This makes chemical studies by high-resolution scanning TEM (STEM) inherently less quantitative than expected unless large scan windows are used. The accuracy of analytical TEM/STEM in terms of both precision and reproducibility is thus often several orders of magnitude worse than the corresponding detection limit.

2. METHOD AND NUMERICAL MODELLING

2.1 Description of the Method of ConceptEM

We have developed a new technique for determining accurately small amounts of solute or dopant atoms incorporated into well-defined planar defects in solids, such as twin boundaries, stacking faults, inversion domain boundaries, anti-phase domain boundaries or other types of special grain boundaries. The new method is based on recording series of analytical spectra taken with different electron beam diameters centered above the defect which is oriented almost edge-on. Without any broadening or channeling and for a defect plane much thinner than the electron beam

width, the chemical signal from the matrix atoms is expected to be directly related to the cylindrical volume of analysis as given by the product of $\pi r^2 t$ where r denotes the beam radius and t the specimen thickness. The chemical signal from solute atoms incorporated into the planar defect, on the other hand, increases linearly with the section of the defect sampled by the electron beam, which can be expressed by the product $2rdt$ where d represents the effective chemical width of the defect, i.e. its structural width multiplied by the fractional occupancy of solute atoms. Hence, the ratio of matrix/solute counts, corrected by the corresponding EDXS k-factors or EELS ionization cross-sections, should simply be given by $0.5\pi r/d$. Therefore, a linear least-squares fit can be performed and the segregation level determined from the slope of the fit line. More details on the theory and approximations can be found elsewhere (Walther 2004). This concept of nearly concentric electron probes in analytical TEM (conceptEM) can be applied to EELS or to EDXS. It necessitates a nano-probe mode but no scan unit. We have modeled the effects of beam broadening, a finite chemical defect width compared to the initial electron beam size (Walther et al 2004), finite solid solubilitiy of solute atoms in the matrix (Walther 2004) and stochastic displacements/drift of the electron beam from the boundary position (Walther et al 2002) which cause deviations from this simple linear behaviour.

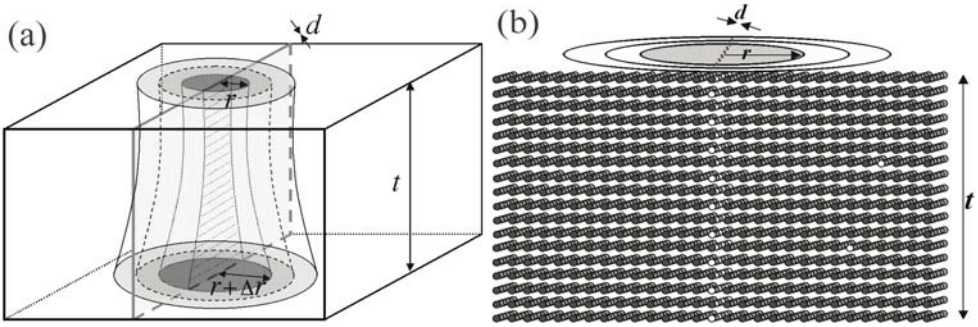


Fig. 1: Sketch of the principle of beam broadening (a); computer model for the numerical test (b).

2.2 Numerical Test of the Method

Reliability and accuracy of the conceptEM method have been tested numerically under conditions using simulations for a specific interface geometry drawn schematically in Fig. 1b, as a function of specimen thickness and other parameters (Walther 2004). The default parameters were Z=14 (silicon), U=100kV, t=100nm, x=0 (no solid solubility) and $\beta=\pi$ (collection of all electrons scattered forward). Calculations suggest an accuracy in the determination of the Gibbsian solute excess at a special grain boundary down to ±1% of a monolayer or ±0.1 atoms/nm^2. This is more than one order of magnitude better than that of current standard techniques based on single or multiple independent measurements. Modeling also indicates a monotonic relationship between the accuracy (rel. difference between output and input chemistry) and the linear correlation coefficient after least-squares fitting, i.e., the precision obtainable experimentally is the better the straighter the curve is the data points form.

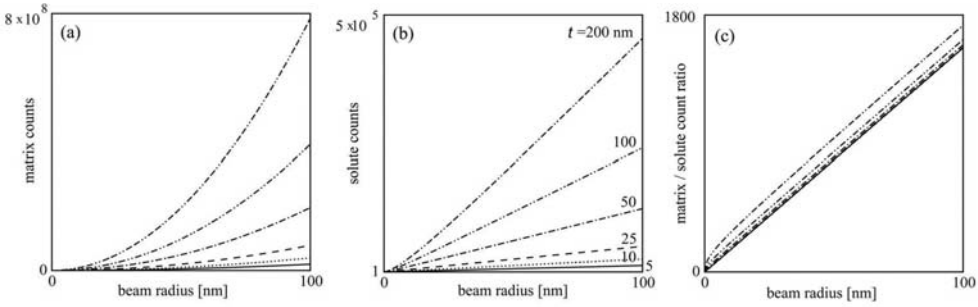


Fig. 2: Plots of the number of matrix atoms (a), solute atoms (b) and their ratio (c) sampled by a beam of U=100kV electrons passing through a silicon specimen (Z=14) of thickness t.

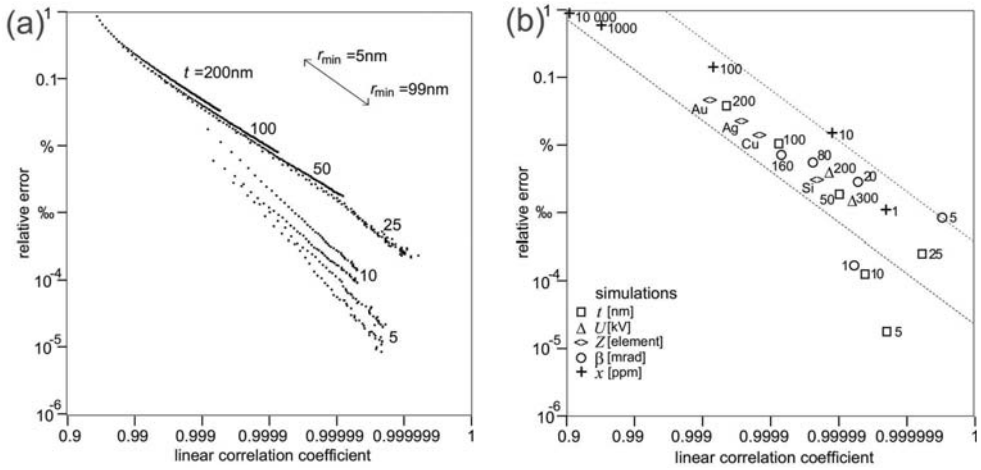


Fig. 3: Scatter plots of relative error (i.e. relative difference between output and input effective chemical widths) vs. linearity of the curves obtained (a) for beam radii r≥r_{min} by varying the minimum radius for the fit and (b) for different model parameters using data from r_{min}=5nm to r_{max}=100nm (b).

3. EXPERIMENTAL APPLICATIONS

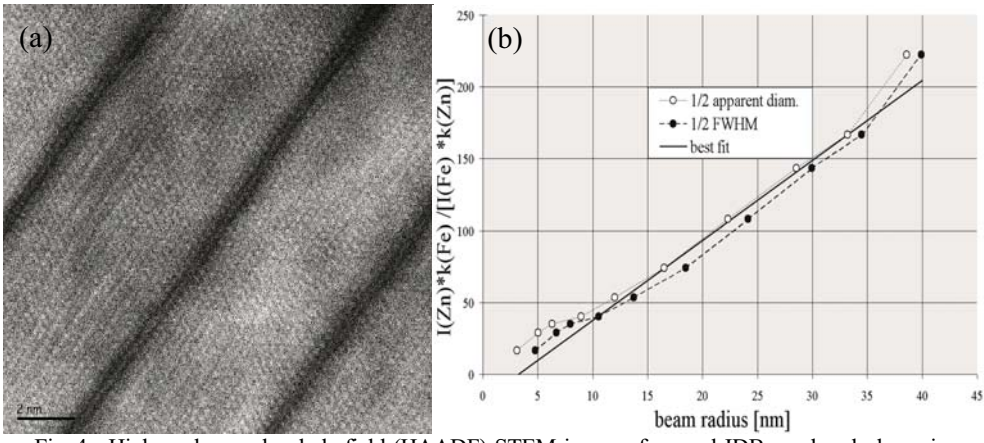


Fig. 4: High-angle annular dark–field (HAADF) STEM image of several IDBs on basal planes in Fe_2O_3-doped ZnO sintered at 1350°C (a). ConceptEM analysis of ten EDX spectra from an isolated IDB (b). From defect-free regions we calculated a constant background signal of 1.02±0.06 at% Fe, which was subtracted from the Fe signal. This can be explained by a combination of solid solubility, pole-piece stray X-rays or additional faults on pyramidal planes inclined at 60° to the electron beam. The slope of the best fit to the solid data points yields an effective chemical width of the IDB of d=0.2653±0.0197nm. This amounts to 102±8%, i.e. full, occupancy of the basal plane by iron atoms.

If zinc oxide (ZnO) is mixed with other oxides and then sintered at high temperatures, the resulting microstructure often contains planar defects many of which are inversion domain boundaries (IDBs). We have studied these IDBs both structurally and chemically in the systems of ZnO doped with Fe_2O_3, SnO_2 (Daneu et al 2002) and Sb_2O_3 (Recnik et al 2001 and 2002) where they occur on (0001) basal planes of the wurtzite structure. Along the c-axis of ZnO the spacing of the atomic planes occupied by cations is given by c/2=0.26nm. We investigated the chemistry of these IDBs by EDXS using a JEOL 2010F FEG-TEM equipped with an atmospheric thin window Si(Li) detector controlled by Oxford Instruments Link ISIS 300 software using the standard Cliff-Lorimer k-factor correction. Structurally the IDBs

consist of single planes of octahedral interstices filled by cations. The results from conceptEM analyses are shown in Figs. 4 and 5 and demonstrate that the octahedral positions are either completely filled by iron, half occupied by tin or occupied to a third by antimony atoms. Considering that an octahedral site is surrounded by six O^{2-} anions that share their electrons with four neighbours each, a trivalent cation would be required for charge neutrality (Pauling's principle). This is the case for a filling of the octahedral sites by either pure Fe^{3+}, or for a mixture of ½ Sn^{4+} + ½ Zn^{2+} or a mixture of 1/3 Sb^{5+} + 2/3 Zn^{2+}. High-resolution lattice images and HAADF STEM images have confirmed a symmetric in-plane honeycomb structure of the IDB for the Sb_2O_3-doping that agrees with this fractional filling (Recnik et al 2001). We suggest the fractional filling of a basal plane by cations with an average charge of 3+ is a general rule for IDBs in ZnO as long as vacancies remain negligible.

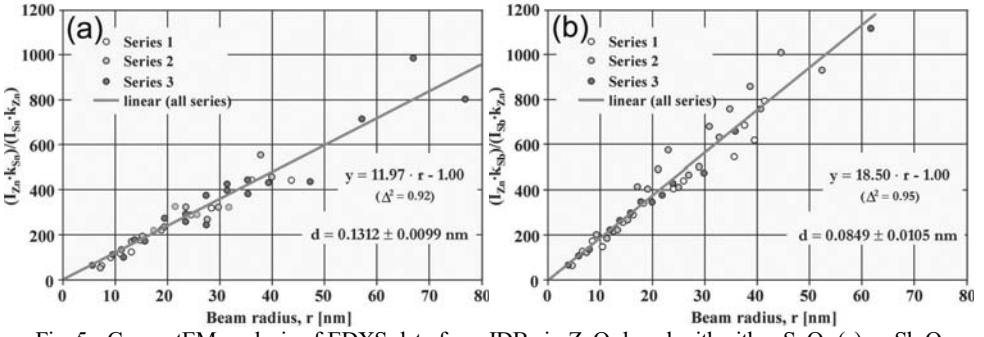


Fig. 5: ConceptEM analysis of EDXS data from IDBs in ZnO doped with either SnO_2 (a) or Sb_2O_3 (b). The effective chemical fault widths obtained here correspond to fractional occupancies of the basal planes of 50±4% by tin and 33±4% by antimony atoms, respectively.

4. CONCLUSIONS

A new analytical TEM method has been presented. ConceptEM allows to determine highly accurately the amount of solute or dopant atoms incorporated into a crystallographically well-defined planar defect. The experimental precision down to ±0.4 atoms/nm^2 has still not reached the theoretical limit of ±0.1atom/nm^2, but it improved previous measurements by an order of magnitude in accuracy and helped to solve the atomic structure of IDBs in differently doped zinc oxide. From these a general structural concept for IDBs on basal planes in ZnO has been proposed. The method of conceptEM is also expected to be beneficial more generally for the quantitative study of interfaces in semiconductors because it should allow to measure doping or segregation levels locally quite precisely: the above error bars of areal atomic densities convert to a few at% precision in the determination of the chemical composition of an individual (001)Si monolayer or interface within a hetero-structure.

ACKNOWLEDGEMENTS

Part of this work was performed while TW worked at the University of Bonn where Dr F Wolf prepared the specimen material and Prof W Mader supported the study. Financial support by the German Ministry for Education and Research and the Slovenian Ministry of Education and Science (bilateral Slovenian-German BMBF project no. SVN 99/021) is also gratefully acknowledged.

REFERENCES

Daneu N, Walther T and Rečnik A 2002 Proc. 15th Int. Conf. Electron Microsc., eds R Cross, J Engelbrecht and M Witcomb (Durban, Microsc. Soc. South Africa) **3**, 63

Rečnik A Daneu N, Walther T, Mader W 2001 J. Am. Ceram. Soc. **84**, 2657

Rečnik A, Daneu N, Walther T, Kawasaki M and Mader W 2002 Proc. 15th Int. Conf. Electron Microsc. **1**, 531

Walther T, Rečnik A, Daneu N 2002 Proc. 15th Int. Conf. Electron Microsc. **1**, 535

Walther T 2004 J. Microsc. **215**, 191

Walther T, Daneu N, Rečnik A 2004 Interface Science **12**, 267

Electron holography of doped semiconductors: when does it work and is it quantitative?

R E Dunin-Borkowski[1,3], A C Twitchett[1], P A Midgley[1], M R McCartney[2], T Kasama[3,1], D Cooper[1] and P K Somodi[1]

[1] Department of Materials Science and Metallurgy, University of Cambridge, Pembroke Street, Cambridge CB2 3QZ, UK
[2] Department of Physics and Astronomy, Arizona State University, Tempe, Arizona 85287-1504, USA
[3] Frontier Research System, The Institute of Physical and Chemical Research, Hatoyama, Saitama 350-0395, Japan

ABSTRACT: The application of off-axis electron holography to the measurement and interpretation of variations in electrostatic potential in doped semiconductors is described and reviewed. Both experimental measurements and computer simulations of electrostatic potentials in thin specimens are presented, and the degree to which parameters such as the built-in voltage and the depletion width across a *p-n* junction can be measured reliably is discussed.

1. INTRODUCTION

There is a pressing need for the development of a reliable, high spatial resolution technique that can be used to obtain quantitative information about dopant distributions in semiconductors, both for the evaluation of process parameters and to provide input to simulations of dopant diffusion. Off-axis electron holography in the transmission electron microscope (TEM) offers the potential to provide such information. The technique, which is illustrated schematically in Fig. 1 and described in detail elsewhere (e.g. Dunin-Borkowski et al 2004), is used to record the phase shift of a high-energy electron wave that has passed through a thin (<1 μm) TEM specimen. In the absence of dynamical diffraction, the phase shift $\phi(x,y)$ can be related to the electrostatic potential $V(x,y,z)$ by the relation

$$\phi(x,y) = C_E \int V(x,y,z)\,dz \qquad (1)$$

where z is a direction parallel to the incident electron beam and C_E is a specimen-independent constant that takes a value of 7.3×10^6 rad V^{-1} m^{-1} at a microscope accelerating voltage of 200 kV. If V does not vary with z in a specimen of thickness t, and if there are no electrostatic fringing fields outside the specimen, then Eq. 1 can be rewritten in the form

$$\phi(x,y) = C_E V(x,y) t(x,y). \qquad (2)$$

According to Eqs. 1 and 2, a phase image recorded using electron holography can be used to measure the potential in a semiconductor specimen, projected in the electron beam direction. The potential can then be interpreted to provide information about the distribution of electrically active dopant atoms. However, in practice phase images acquired from doped semiconductors are affected by the physical and electrical nature of the specimen surface. Furthermore, examination in the TEM can result in charging of the specimen. These effects can change the electrostatic potential in the thin specimen from that expected from its bulk properties, and must be understood if electron holography is to be applied to the characterisation of dopant distributions reliably and quantitatively.

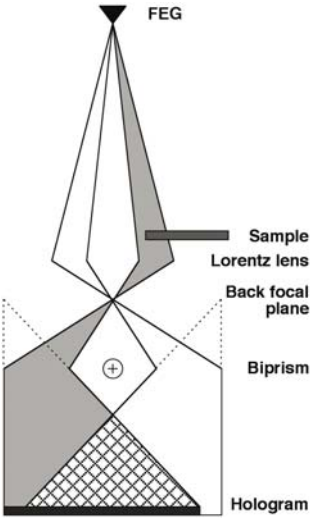


Fig. 1. Illustration of the setup used to generate off-axis electron holograms. The sample occupies approximately half the field of view. The field emission gun (FEG) electron source provides coherent illumination. The biprism causes overlap of the object and (vacuum) reference waves. The Lorentz lens provides an optimal field of view and interference fringe spacing.

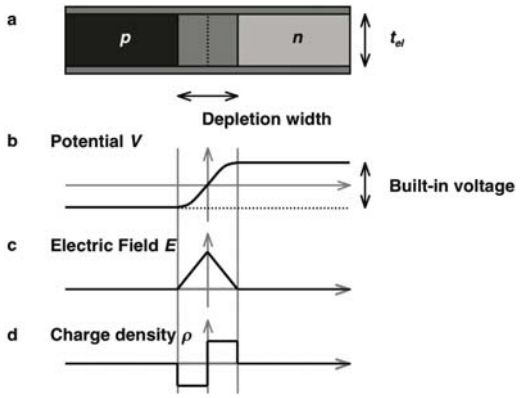


Fig. 2. a) Schematic diagram showing the cross-sectional geometry of a TEM specimen that contains a *p-n* junction. t_{el} is the 'electrically active' specimen thickness. The shaded areas at the top and bottom surfaces of the specimen represent electrically passivated (or depleted) layers, whose physical and electrical nature is affected by TEM specimen preparation. b)-d) are schematic diagrams of the electrostatic potential, electric field and charge density profiles, respectively, across an abrupt, symmetrical *p-n* junction. The sign convention for the potential is consistent with the mean inner potential of the specimen being positive relative to vacuum.

2. OFF-AXIS ELECTRON HOLOGRAPHY OF DOPED SEMICONDUCTORS

The electrostatic potential in a TEM specimen of a doped semiconductor comprises the mean inner potential V_0 (which is related to the composition and density of the specimen and takes a value of ~ 12 V in Si), the depletion region potential V_d , and any electrostatic fringing fields that may be present outside the specimen surfaces. (According to this definition, the step in potential across a *p-n* junction is associated with a variation in V_d rather than V_0 ; this distinction is subjective, and it would also be possible to define the step in potential in terms of a variation in V_0). The dopant atoms are typically assumed to be electrically 'active' within specimen thickness t_{el} , which is smaller than the total specimen thickness t as a result of the effects of surface depletion and specimen preparation. If this description, which is necessarily simplistic and phenomenological, is used, if fringing fields are neglected (this is not always a valid assumption), and if V_0 does not change in the specimen in the electron beam direction, then Eq. 2 can be rewritten in the form

$$\phi(x,y) = C_E \left[V_0(x,y) t(x,y) + V_d(x,y) t_{el}(x,y) \right]. \quad (3)$$

The definition of t_{el} , and the expected forms of the potential, electric field and charge density across a *p-n* junction (Sze 2002), are illustrated schematically in Fig. 2. The three graphs are drawn on the assumption that the 'transition region' on each side of the depletion region is negligibly small - an assumption that can be assessed experimentally (see below). According to Eqs. 1-3 and Fig. 2, *n*- and *p*-type regions in a doped semiconductor should be revealed in a phase image as regions of bright and dark contrast, respectively.

3. RESULTS FROM UNBIASED SILICON DEVICES

3.1 Two-Dimensional Dopant Profiling

The first unequivocal demonstration of two-dimensional mapping of the electrostatic potential in an unbiased doped semiconductor using off-axis electron holography was achieved for metal-oxide-semiconductor (MOS) Si transistors by Rau et al (1999). More recently, electron holography results from similar transistors were compared with process simulations by Gribelyuk et al (2002). Figure 3a shows a contoured image of the electrostatic potential in a 0.35 µm Si device from this study. The contours correspond to potential steps of 0.1 V, and the B-doped regions are delineated clearly. The sample was prepared using tripod wedge-polishing and finished with low-angle Ar ion milling. Figures 3c and d show a comparison between simulations and line profiles obtained from Fig. 3a, both laterally across the junction and with depth. 'Scaled loss' and 'empirical loss' models, which account for B segregation into the oxide and nitride layers, are shown. The scaled loss model, which leads to stronger B diffusion, assumes uniform B loss across the structure, while the empirical loss model assumes segregation of B at the surfaces of the doped regions and provides a better match to the experimental results. Figure 3b shows a simulated potential map of the same device, based on the empirical loss model, which matches the experimental image in Fig. 3a closely.

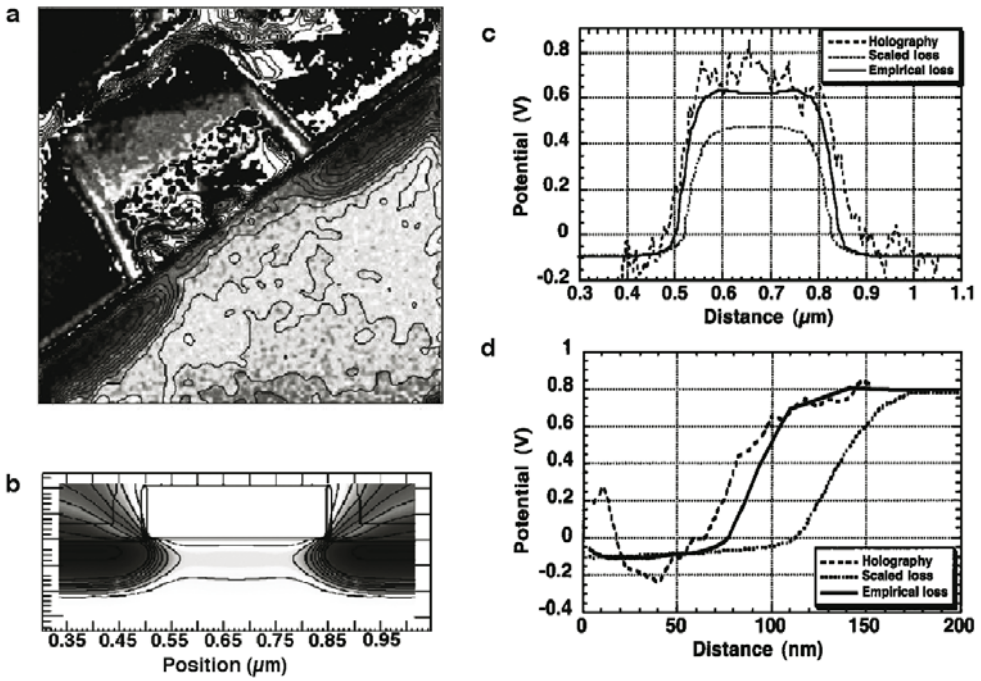


Fig. 3. a) Electrostatic potential distribution in a 0.35 µm silicon MOS transistor, with a contour step of 0.1 V, recorded at 200 kV using a Philips CM200 FEG-TEM. b) Two-dimensional map of the potential determined from a process simulation based on the 'empirical loss' model, with a contour step of 0.1 V. c) Lateral and d) depth profiles obtained from the image shown in a). Predictions from process simulations for 'scaled loss' and 'empirical loss' models are also shown.

3.2 Specimen Preparation, Specimen Geometry and Phase Image Interpretation

Despite the success of studies such as that shown in Fig. 3, it is important to recognise that it is highly challenging to obtain such results reliably. The effects of specimen preparation, and in particular the electrical state of the specimen surface, may account for many of the anomalous results seen in early experiments. It is also difficult to interpret phase images quantitatively. For example, a phase image can only be used to determine an unknown value for the built-in voltage across a *p-n* junction if the electrically active specimen thickness can be measured independently. In addition, a measured phase profile is remarkably insensitive to small changes in the charge density across a *p-n* junction. Quantitative criteria that can be used to determine these parameters from measurements are rarely used to assess the electrical properties of devices within TEM samples. All of these issues must be balanced with three more general limitations on the geometry and quality of a TEM specimen that are essential for electron holography. First, the region of interest must lie within 1-2 μm of a region of vacuum to provide a reference wave that can be overlapped onto the specimen. Second, the specimen should be as uniform in thickness as possible, and it should be oriented to a weakly diffracting orientation to avoid the effects of diffraction contrast on the measured phase shift. Finally, charging due to secondary electron emission in the TEM, which can result in band-bending, junction biasing and fringing fields that can perturb the vacuum reference wave, should be minimised.

3.3 Charging and Thickness Corrugations in Focused Ion Beam Milled Specimens

We begin by illustrating some of the issues that are encountered when electron holograms are acquired from TEM specimens that have been prepared using focused ion beam (FIB) milling. Although this technique is known to result in substantial gallium implantation and significant physical damage to the specimen surface, it has the advantage over polishing and cleaving of site-specificity, and it allows a region of vacuum for a reference wave to be machined close to the area of interest. In addition, an optimal, uniform specimen thickness for holography of 200-500 nm can be achieved with ease. As a result, it is used widely to prepare specimens for electron holography.

Figure 4 illustrates two key issues that may be encountered when using off-axis electron holography to characterise a Si device, in which a series of transistors was located at a depth of several μm below the surface of the wafer and separated from it by metallisation layers (Dunin-Borkowski et al 2005). Such transistors present a representative challenge for TEM specimen preparation for holography, both because the metallisation layers result in thickness corrugations in the doped regions of interest and because they must, at least in part, be removed to provide a vacuum reference wave. An additional difficulty arises from the possibility that the overlayers, which contain oxides, may charge during examination in the TEM. Conventional 'trench' FIB milling was used to prepare a specimen of nominal thickness 400 nm. A bright-field image of one of the transistors is shown in Fig. 4a.

Figure 4b shows electron holographic phase contours recorded from region '1'. Instead of the expected phase distribution, which should be proportional to the mean inner potential multiplied by the specimen thickness, elliptical contours are visible in each oxide region, and a fringing field is present outside the specimen edge. These effects result from charging of the oxide due to secondary electron emission during electron irradiation. Figure 4c shows a similar image acquired after coating the specimen on one side with ~20 nm of carbon. Charging is now absent, there is no fringing field, and the contours follow the change in specimen thickness. Line profiles, generated along line '2' from the phase images that were used to form Figs. 4b and c, are shown in Fig. 4d. The dashed and solid lines correspond to results obtained before and after carbon-coating the specimen, respectively. The dotted line shows the difference between these lines. If the charge is assumed to be distributed throughout the thickness of the specimen, then the electric field in the oxide is 2×10^7 V/m. The effect of charging on the dopant potential is highly significant because the phase gradient in Fig. 4d continues into the Si substrate. As a result, the dopant potential is always undetectable before carbon coating, whether or not a phase ramp is subtracted from the recorded images.

Thickness corrugations in the specimen result when regions that have a lower sputtering yield block a material that has a faster sputtering yield. A simple approach for removing the effect of these thickness variations is illustrated in Fig. 4e. In a phase image of the carbon-coated specimen, the thickness corrugations are prominent, and the doped region is barely visible as a region of faint dark

contrast. As the thickness corrugations are approximately straight, they can be inferred from the substrate and back-projected across the image. This image can then be subtracted from the original phase image to show the doped region more clearly. Alternatively, 'back-side' FIB milling from the substrate side of the wafer can be used. A further advantage of back-side milling is that charging effects are absent and carbon-coating is not required because of sputtering and redeposition onto the oxide during milling.

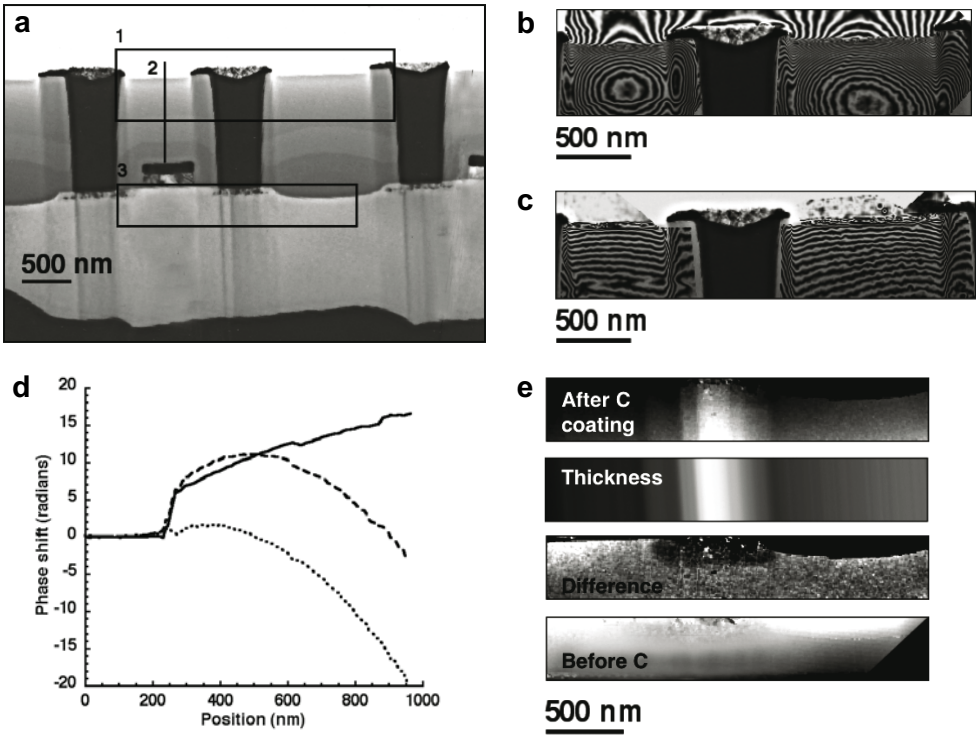


Fig. 4. a) Bright-field image of a focused ion beam milled (0.5µm gate) Si transistor of nominal thickness 400 nm. Thickness corrugations are visible in the substrate. The gates are tungsten silicide, while the amorphous layers above the gates are silicon oxides that have different densities. b) Eight times amplified phase contours obtained from the region marked '1'. Charging results in electrostatic fields outside the specimen and elliptical contours in the oxide layers. c) is the equivalent phase image obtained after coating the specimen on one side with 20 nm of carbon. d) shows one-dimensional profiles obtained from the phase images along the line marked '2'. The dashed and solid lines were obtained before and after coating the specimen with carbon, respectively. The dotted line shows the difference between the solid and dashed lines. e) Phase images acquired from region '3'. The uppermost image shows thickness corrugations after coating the specimen with carbon [Black=0, White=9 rad]. The next image shows the thickness corrugations alone, inferred from the Si substrate below the doped region [Black=0, White=9 rad]. Below is the difference between these images, illustrating one approach for removing the effects of 'curtaining' from phase images. The doped region is now visible [Black=0, White=2.5 rad]. The lowest images shows the result of applying the same approach before coating the specimen with carbon. There is now a gradient in phase from the top to the bottom of the image, and the doped region is not visible [Black=0, White=20 rad].

3.4 Charging in Wedge-Polished Specimens

Different TEM specimen preparation techniques influence specimen charging in different ways. Figure 5 shows results obtained by McCartney et al (2002) from a 'wedge-polished' one-dimensional *p-n* junction in Si. The specimen was prepared from a *p*-type wafer that had been subjected to a shallow B implant and a deeper P implant, resulting in the formation of an *n*-type well and a *p*-doped surface region. Phase images were obtained both before and after coating one side of the specimen with 40 nm of carbon. Phase profiles that had been obtained from the uncoated sample showed an initial increase in the measured phase shift on going from vacuum into the specimen (Fig. 5c). However, they then decreased steeply and became negative at large thicknesses. This behaviour was not observed after carbon coating (Fig. 5d), suggesting that it results from charging from the electron-beam-induced emission of secondary electrons, as in Fig. 4b.

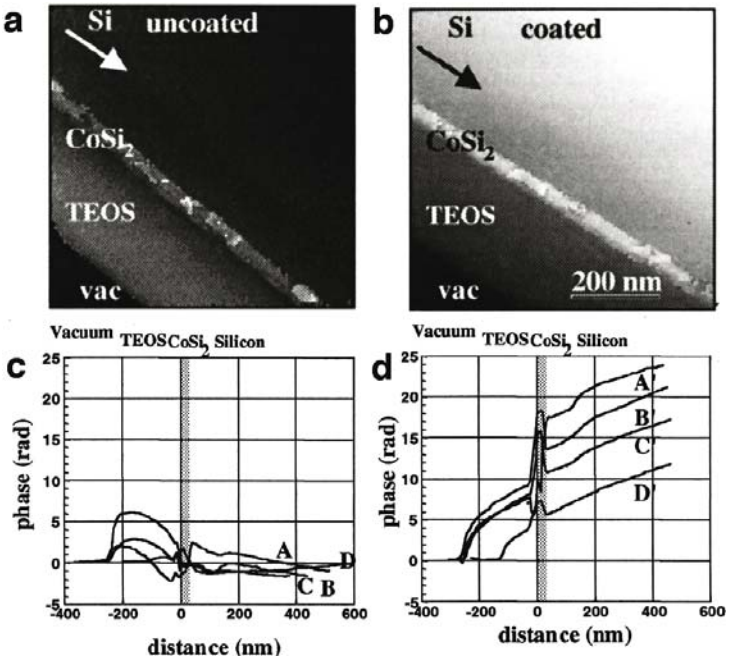


Fig. 5. a) Phase image of a one-dimensional *p-n* junction prior to carbon coating. b) Phase image from a similar region after carbon coating. c) Phase profiles determined from uncoated specimens. At a distance of 180 nm from the top of the $CoSi_2$ (grey region), the specimen thicknesses are A=250 nm, B=170 nm, C=120 nm and D=50 nm, measured from holographic amplitude images. d) Phase profiles after coating. At 180 nm, the thicknesses are A'=280 nm, B'=220 nm, C'=160 nm and D'=85 nm.

3.5 Electrically Altered Surface Layers in Focused Ion Beam Milled Specimens

The importance of assessing damage, implantation and specimen thickness variations in FIB-milled TEM specimens that contain *p-n* junctions has been discussed by Wang et al (2002a-c). One of these studies involved milling a 45° specimen thickness profile, from which phase images were used to determine that the built-in voltage across a junction with a dopant concentration of 10^{15} cm^{-3} was 0.71±0.05 V, the specimen potentials on the *p*- and *n*-sides were 11.50±0.27 and 12.1±0.40 V, respectively, and the electrically inactive layer thickness was 25 nm on each specimen surface.

Similar issues are illustrated in Fig. 6 for a Si *p-n* junction comprising a B-doped layer on an Sb-doped substrate, with nominal dopant concentrations in excess of 10^{18} cm^{-3} (Twitchett et al 2002). Figure 6a shows a phase image of the junction, in which the *p*- and *n*-sides exhibit dark and bright contrast, respectively. A grey band along the specimen edge results from the presence of a depleted, passivated or damaged surface layer, which is seen in cross-section here but is thought to run around the entire sample surface. The specimen was prepared using FIB milling in 'trench' geometry, with the region of interest protected from gallium implantation and damage by depositing a Pt strap onto the wafer surface. As a result of the relatively large distance of 2.5 μm between the wafer surface and the junction, FIB cuts were made to provide a vacuum reference near the junction for holography, as shown in Fig. 6b. The microscope was operated at 200 kV to minimise the effects of knock-on damage, and the specimen was tilted by 1-2 ˚ from <100>, while keeping the junction edge-on to better than 0.2˚, to ensure that contributions to the contrast from dynamical diffraction were minimised. Figure 6c shows line profiles across the junction measured from phase images for three unbiased specimens. The profiles agree qualitatively with the expected variation in potential shown in Fig. 2. In contrast to Fig. 4b, no electrostatic fringing field is visible in Fig. 6a outside the specimen, which had not been carbon-coated, indicating that its surface is an equipotential. By comparing the contrast with predictions, and by measuring the specimen thickness using both convergent beam electron diffraction and holographic amplitude images, the recorded phase images were used to infer the presence of a layered structure in the TEM membrane, with amorphous outer surface layers surrounding inner, crystalline electrically inactive surface layers, themselves surrounding crystalline electrically active material, as shown schematically in Fig. 6d. An increase in the depletion width across the junction was also inferred to occur close to the specimen surface (Twitchett et al 2004).

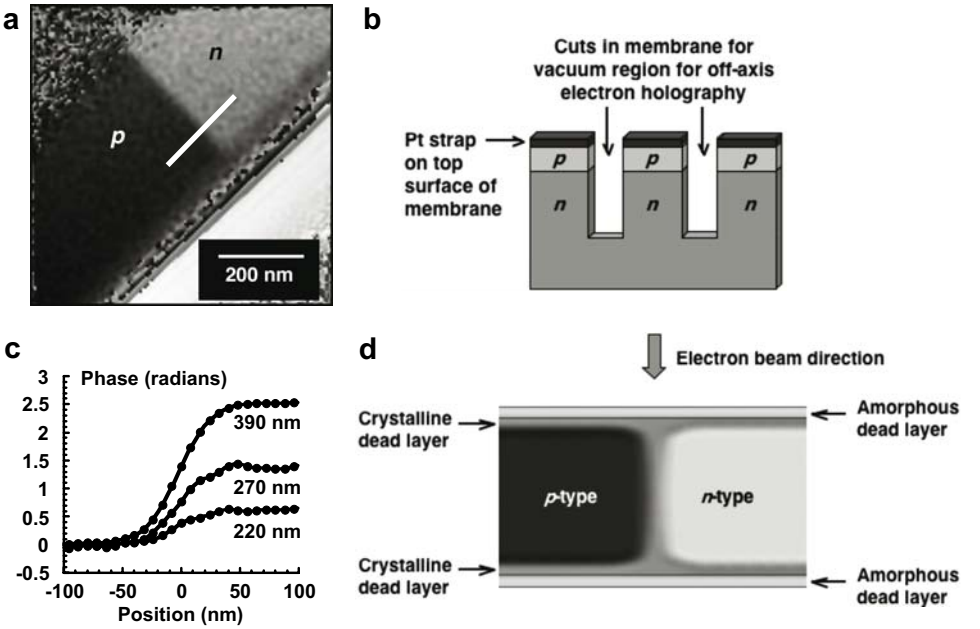


Fig. 6. a) Phase image reconstructed from an off-axis electron hologram of a Si *p-n* junction sample. The sample edge is at the lower right of the image. No attempt has been made to remove phase 'wraps' lying along this edge. The white line shows the region from which phase profiles were obtained. b) Schematic diagram showing the FIB cuts to the membrane, which are required to provide a vacuum reference wave close to the region of interest for electron holography. c) Phase profiles measured from three unbiased FIB-milled specimens of crystalline thickness 220, 270 and 390 nm. d) Schematic diagram showing, in cross-section, the physical and electrical structure of a TEM specimen inferred from this study.

4. RESULTS FROM BIASED SILICON DEVICES

The development of an approach that can be used to apply a bias to a semiconductor *in situ* in the TEM is of interest both for the characterisation of devices under operating conditions and to assess the validity of examining 'unbiased' specimens, parts of which may be floating. Unwanted contributions to the contrast from thickness variations and strain can also be removed by taking the difference between phase images recorded with different voltages applied to the specimen. Figure 7a shows a TEM specimen holder, designed and built by E A Fischione Instruments, Inc., that allows a semiconductor to be examined under an applied bias, as well as allowing the sample to be transferred to a scanning electron microscope, a FIB workstation or an Ar ion miller in a universal cartridge. The cartridge is used to make contacts to the front and back surfaces of the specimen via a conducting block and a spring. Figure 7b shows the specimen geometry for biasing. A parallel-sided membrane is FIB-milled at the corner of a 1 mm 90° cleaved square of wafer. Figure 7c shows line profiles across the Si *p-n* junction described in Fig. 6, now obtained from phase images acquired with different reverse bias voltages applied to the specimen. The height of the potential step across the junction increases linearly with reverse bias. The measurements were used to infer the presence of 25±5 nm of electrically inactive crystalline material on each sample surface. Figure 7d shows a phase image obtained from a 90° cleaved wedge that had *not* been FIB-milled. An electrostatic fringing field is visible. Such fields are never observed outside *unbiased* cleaved wedges or any FIB-milled samples. The results in Fig. 7c are consistent between unbiased specimens and those to which contacts (but no voltage) were applied.

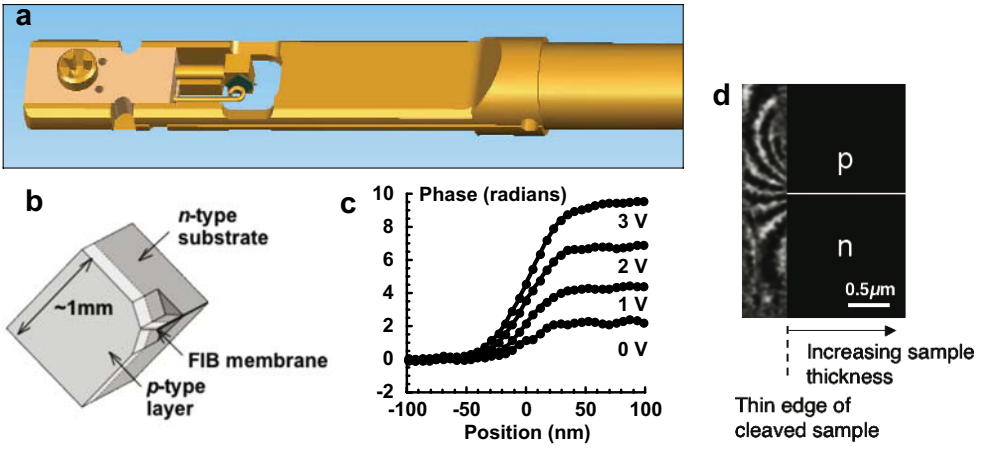


Fig. 7. a) Design drawing of the end of an ultra-high-tilt two-contact cartridge-based biasing holder with a sample in the cartridge. b) Specimen geometry for biasing. The specimen is prepared by cleaving a 1-2 mm square of wafer, one corner of which is FIB-milled parallel to the wafer growth direction. c) Line profiles of the phase shift across the Si *p-n* junction, measured as a function of reverse bias for a sample whose crystalline thickness is 390 nm. d) Four-times-amplified cosine of the measured phase, showing the electrostatic fringing field in vacuum outside the position of the *p-n* junction in a 90° cleaved wedge that had not been FIB-milled, at a reverse bias voltage of 2 V.

5. SIMULATIONS OF ELECTROSTATIC POTENTIALS IN THIN SPECIMENS

The charge density across a *p-n* junction can in principle be derived from a measured potential distribution using Poisson's equation. It is also a sensitive measure of the effect of TEM specimen preparation on the properties of a semiconductor device. Unfortunately, as a result of the presence of noise, it is difficult to do this directly. A solution to this problem is to fit a simulation empirically to a phase profile, and then to

differentiate the fitted rather than the experimental profile to infer the charge density across the junction. The application of this approach to the phase profiles shown in Figs. 6c and 7c indicates that the transition regions on each side of the depletion region are 10-20 nm in extent, and more significantly that the fitted charge densities are a factor of ten lower than expected. The same approach shows that the charge density, which is expected to remain unchanged, increases with applied bias from the value measured for an unbiased specimen to a value much closer to that expected for this device. This observation suggests that some of the dopant that was passivated by specimen preparation may be reactivated by *in situ* biasing, which may be used to remove some of the damage to the electrical properties of a device caused by TEM specimen preparation.

Commercial process simulation software has been used to simulate phase contrast from *p-n* junctions, and to suggest that electron-beam-induced positive charging of the surface of a TEM specimen, at a level of 10^{13} to 10^{14} cm^{-2}, may create an inversion layer on the *p*-side of the junction and explain the absence of fringing fields outside the specimen surfaces (Beleggia et al 2001). Figure 8 shows alternative simulations, in which semi-classical equations that describe the charge and potential in a parallel-sided Si sample that contains a *p-n* junction are solved with the Fermi level on the specimen surface set to ensure that it is an equipotential (Somodi et al 2005). The simulations show that, as either the dopant concentration or the specimen thickness decreases, a correspondingly smaller fraction of the specimen retains electrical properties that are close to those of the bulk device. The average step in potential across the junction through the specimen thickness, which is found to be insensitive to the surface state energy, is reduced from that in the bulk device. This reduction is greatest for low sample thicknesses and dopant concentrations. As a result of additional complications from oxidation, physical damage and implantation, these simulations are likely to underestimate the true modification of the potential in a TEM specimen from that in the original device.

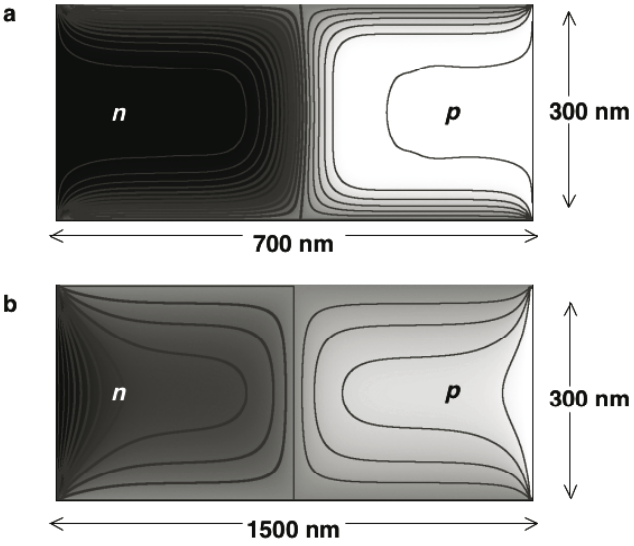


Fig. 8. Computer simulations of electrostatic potential distributions in parallel-sided Si specimens of thickness 300 nm containing abrupt, symmetrical *p-n* junctions formed from a) 10^{17} and (b) 10^{16} cm^{-3} of Sb (*n*-type) and B (*p*-type) dopants. The potential at the specimen surfaces is set to 0.7 eV above the Fermi level. Contours of spacing 0.05 V are shown. The horizontal scale is different in each image in order to show the variation in potential close to the position of the junction. The simulations were generated using a 2-dimensional rectangular grid.

6. PROSPECTS FOR THE FUTURE

The examples described above show that further work is required to obtain a full understanding of the effect of TEM specimen preparation on results obtained from semiconductor devices using electron holography. Electrical biasing experiments for the *in* situ examination of working devices using electron holography are possible. For unbiased specimens prepared using FIB milling, results obtained with and without electrical contacts to the active regions of the device are identical to within experimental error. The effect of specimen preparation is likely to be different for different doped semiconductors. For example, Fig. 9 shows that FIB milling affects GaAs *p-n* junction specimens

much more strongly than similar Si specimens. One of the most exciting developments in electrical holography, which may be used to understand these issues and to provide quantitative information about three-dimensional nanoscale doped regions in semiconductors, is the application of the technique together with electron tomography to provide three-dimensional information about electrostatic fields in materials. Figure 10 shows a preliminary result illustrating the measured three-dimensional potential inside an FIB-milled TEM specimen containing a *p-n* junction directly. The results illustrated in Figs. 9 and 10 are described in more detail elsewhere in these proceedings.

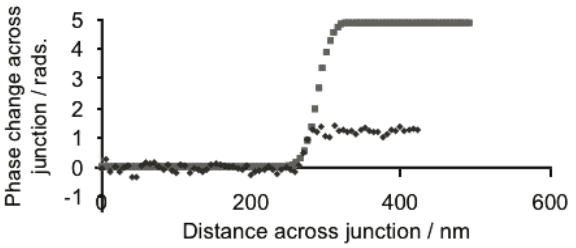


Fig. 9. Phase profiles measured from an FIB-milled GaAs specimen of crystalline thickness 470 nm (black), and predicted on the basis of the expected built-in voltage across the junction (grey). The inferred total crystalline dead layer thickness is 350 nm.

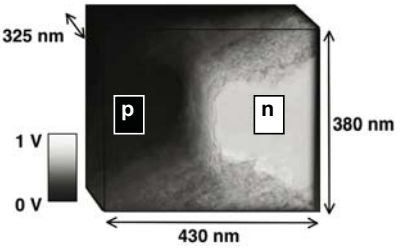


Fig. 10. 3-D electrostatic potential in a specimen prepared using FIB milling in a geometry similar to that in Fig. 7b measured from electron holograms acquired every 2° over ±70°.

ACKNOWLEDGMENTS

We thank J Li, R F Broom and S B Newcomb for contributons to this work, and the Royal Society, the EPSRC and Newnham College, Cambridge for support. We thank the Center for High-Resolution Electron Microscopy at Arizona State University for the use of facilities. We are grateful to E A Fischione Instruments, Inc., for specimen holder development.

REFERENCES

Beleggia M, Fazzini P F, Merli P G and Pozzi G 2003 Phys. Rev. B **67**, 045328

Dunin-Borkowski R E, McCartney M R and Smith D J 2004 Encyclopaedia of Nanoscience and Nanotechnology, ed H S Nalwa (American Scientific Publishers) **3**, p 41

Dunin-Borkowski R E, Newcomb S B, Kasama T, McCartney M R, Weyland M and Midgley P A 2005 Ultramicroscopy **103**, 67

Gribelyuk M A, McCartney M R, Li J, Murthy C S, Ronsheim P, Doris B, McMurray J S, Hegde S and Smith D J 2002 Phys. Rev. Lett. **89**, 5502

McCartney M R, Gribelyuk M A, Li J, Ronsheim P, McMurray J S and Smith D J 2002 Appl. Phys. Lett. **80**, 3213

Rau W D, Schwander P, Baumann F H, Hoppner W and Ourmazd A 1999 Phys. Rev. Lett. **82**, 2614

Somodi P K, Dunin-Borkowski R E, Twitchett A C, Barnes C H W and Midgley P A 2003 Inst. Phys. Conf. Ser. **180**, 501

Sze S M 2002 Semiconductor Devices (New York Wiley)

Twitchett A C, Dunin-Borkowski R E and Midgley P A 2002 Phys. Rev. Lett. **88**, 238302

Twitchett A C, Dunin-Borkowski R E, Hallifax R J, Broom R F and Midgley P A 2004 J. Microsc. **214**, 287

Wang Z, Hirayama T, Sasaki K, Saka H and Kato N 2002a Appl. Phys. Lett. **80**, 246

Wang Z, Kato T, Shibata N, Hirayama T, Kato N, Sasaki K and Saka H 2002b Appl. Phys. Lett. **81**, 478

Wang Z, Sasaki K, Kato N, Urata K, Hirayama T and Saka H 2002c J. Electron Microsc. **50**, 479

Why does a p-doped area show a higher contrast in electron holography than a n-doped area of the same dopant concentration?

A Lenk, U Muehle[1] and H Lichte

Institute of Structure Physics, Triebenberglabor, Dresden University, 01062 Dresden, Germany
[1] Infineon Technologies Dresden GmbH & Co OHG, Germany

ABSTRACT: Holographic measurement of semiconductor dopant profiles combined with focused ion beam (FIB) preparation has become increasingly important. Electron holography in a transmission electron microscope (TEM) delivers 2D-projected potential images of a 3D-object. However, for an exact quantitative evaluation it is necessary to understand the potential distribution in a FIB-specimen along the electron beam. Because the distribution is averaged in the 2D-projection, the structure along z is lost. It is shown that the averaging process has an unexpectedly different impact on the 2D-projections for complementarily doped structures. The result is a remarkably stronger signal and better contrast for p-doped structures in the phase image, compared to that of n-doped structures.

1. INTRODUCTION

The steady development of semiconductor technology towards continuously shrinking device dimensions has raised the need for a reproducible and reliable analysis method for measurement of dopant concentrations. Rau et al (1999) has shown that off-axis electron holography is capable of providing the required information. The electrostatic potential of a specimen produces a phase shift of an electron wave. The phase shift $\Delta\phi$ increases linearly with the electrostatic potential V of the object:

$$\Delta\phi(x,y) = C_E \cdot V_{proj}(x,y) = C_E \cdot \int_{object} V(x,y,z)dz \qquad (1)$$

C_E is the interaction constant depending on the accelerating voltage of the microscope, the z-direction is given by the electron beam in the microscope. The potential V can be described as the sum of the material's mean inner potential V_{mean} (about 12V for Si) and the potential difference ΔV_{pn} at the p-n junction (depending on dopant concentration, up to 1.2V). For specimens with z-independent potential structure, which can be delivered by a FIB (Lenk 2001), the integral above simplifies to proportionality in thickness t. Then, the phase shift $\Delta\phi$ can be written as:

$$\Delta\varphi(x,y) = C_E \cdot \left(V_{mean} + \Delta V_{pn}(x,y)\right) \cdot t \qquad (2)$$

However, it was found that the measured potential difference ΔV_{pn} did not match the theoretically expected values. Therefore, Rau et al (1999) presumed the existence of an electrically inactive surface layer t_0, the so-called 'deadlayer'. Whereas V_{mean} is supposed to be unchanged in the layer, ΔV_{pn} does not contribute there. This leads to a further specification of the expected phase shift:

$$\Delta\varphi(x,y) = C_E \cdot \left(V_{mean} \cdot t + \Delta V_{pn}(x,y) \cdot (t - 2t_0)\right) \qquad (3)$$

To obtain t_0, samples of the same p-n junction have been prepared at several thicknesses. Two plots of phase signal ΔV_{pn} at the p-n junction versus foil thickness t have been linearly fitted by Lenk (2004), resulting in the thickness $2t_0$. For the first plot, the thickness values were estimated from the holograms, following McCartney et al (1994), for the second plot they were measured in a scanning electron microscope (SEM). The deadlayer thickness $2t_0$ was found as 80nm and 95nm, respectively.

A FIB prepared lamella has surface layers amorphized by the cutting ion beam. Thickness measurement of those layers by Langer et al (2000) has revealed a thickness of 16.4nm at each side, which is remarkably smaller than the measured deadlayer thickness t_0. This suggests that the deadlayer

reaches into the crystalline part of a FIB-lamella. Twitchett et al. (2002) found different thicknesses of a crystalline part of the deadlayer, depending on sample thickness.

However, it seems to be unlikely that there is a sharp border between the electrically inactive deadlayer and the electrically fully-active core. Therefore, we suppose a transition zone between both areas. In order to measure the potential structure of a FIB-lamella in z-direction, i.e. the thicknesses of amorphous layer, deadlayer and of the supposed transition zone, specially prepared cross-sections of FIB-lamellae have been prepared for investigation with electron holography.

2. PREPARATION OF NEEDLES

Preparations of cross-sectioned FIB-lamellae have already been successfully realized by Langer et al (2000). The lamellae were stabilized with epoxy or sputtered silicon, then a second cut perpendicular to the lamella was performed, resulting in an embedded cross-section. The technique was used for structural investigations, e.g. thickness measurement of the amorphous layer. However, the potential structure of such a specimen does not represent the conditions in a freestanding lamella, since the stabilizing material has an electric potential that is different from vacuum.

Since our FIB-lamellae for electron holography have thicknesses of between 200nm and 400nm, it is possible to manufacture freestanding needles without any stabilization of the lamella. Figure 1 shows a needle, which was cut from a normal FIB-lamella. The high-resolution bright field image gives details of the edge of the needle in Fig. 2. The corresponding profile scan reveals an amorphous layer of 19nm thickness. Furthermore, there is a darker layer, where the crystalline structure has been obviously altered by the FIB treatment. Both layers added together result in a 33nm thick surface layer of former crystalline silicon substrate that has been physically altered by the ion beam.

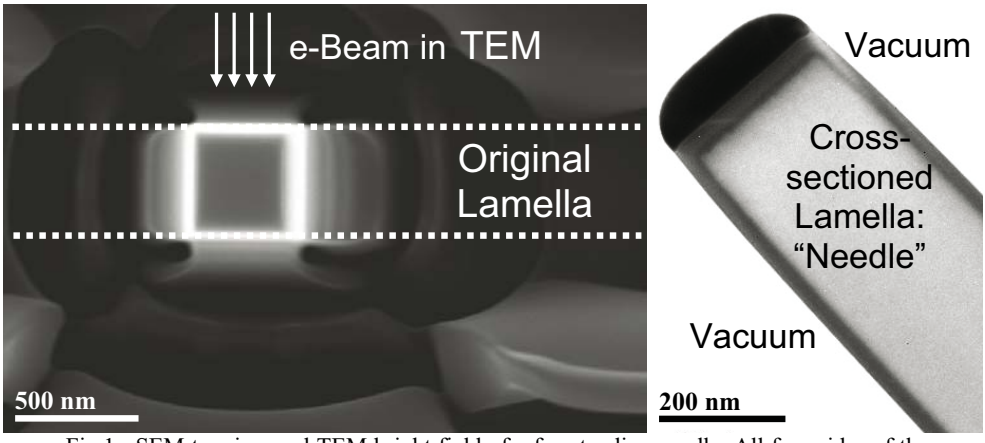


Fig.1. SEM topview and TEM bright field of a freestanding needle. All four sides of the needle have been equally treated in the FIB. Therefore, the orientation of the needle does not have to be changed relative to the electron beam to see the surface layers.

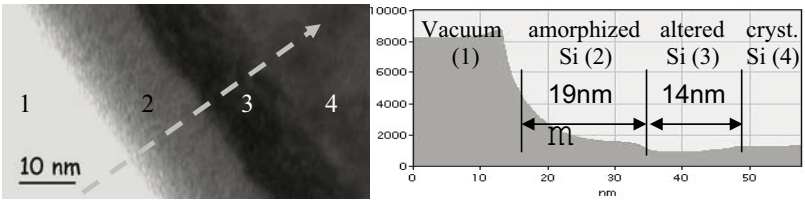


Fig.2 A high-resolution TEM image shows the layers at the lateral edge of a needle in detail, the arrow marks the profile scan.

3. EXPERIMENTAL RESULTS OF DIFFERENTLY DOPED NEEDLES

3.1 p-Doped Needle and n-Doped Needle in Comparison

Different wafers with a homogeneously doped surface layer have been used to prepare needles. The layers contained As (n-doped needle) and B (p-doped needle). Phase images reveal the measured potential structure in Fig. 3. The doped areas and the physically altered surface layers are clearly visible. Although the dopant layers have a constant depth, the p-n junctions of both needles are bent near the physically altered layers. The area where the junctions start bending can be understood as the presumed transition zone. This transition zone is obviously wider at the n-doped needle.

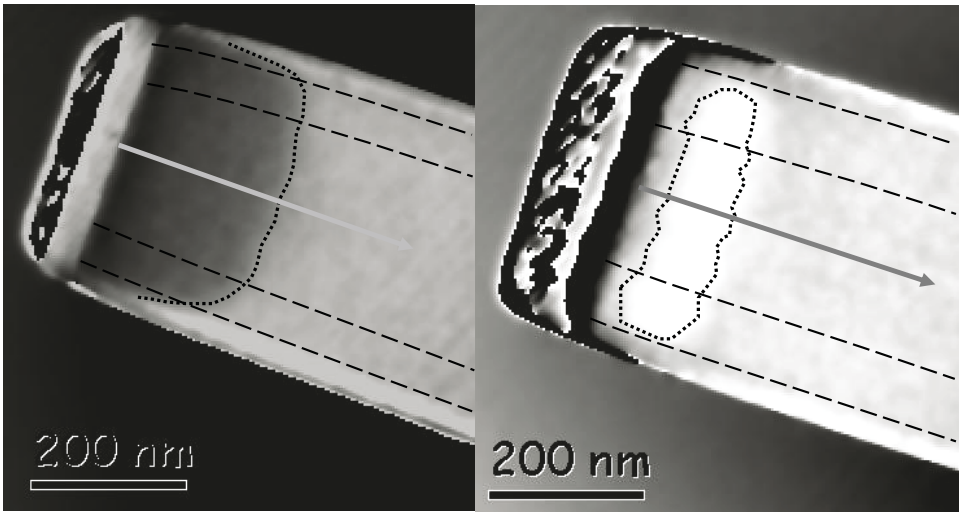
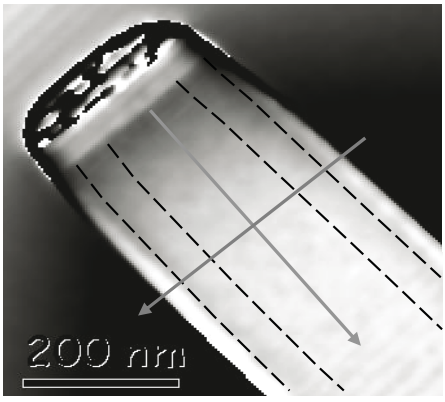


Fig.3. Needles from a homogeneously p-doped wafer (left) and from a homogeneously n-doped wafer (right). The dotted line marks the measured p-n junction, whereas the dashed lines characterize the transition zones. The area between the transition zone and vacuum is physically altered by FIB-preparation (see layers shown in Fig 2). The arrows mark the profile scans of Fig. 5.

3.2 Needle from Deeper Wafer Substrate

A needle from the deeper substrate of a wafer has no doped layer, still its potential descends at the edge of its crystalline core, shown in the phase image in Fig.4. Again a transition zone is found.



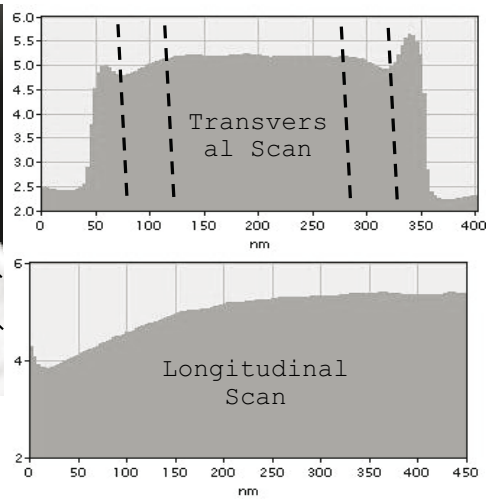


Fig.4. Phase image of a needle without p-n junction. The dashed lines cover the transition zones at both sides; arrows mark profile scans.

4. DIFFERENCE OF THE PROJECTED POTENTIALS IN P- AND N-DOPED NEEDLE

As cross-sections of a FIB-lamella, the needles can be used to show the difference between the projected potential distribution measured with electron holography and the potential distribution in the electrically fully-active core. Therefore, two profile scans have been extracted from the images of the doped needles. The scans have the same length and coordinates (see arrows in Fig. 3), but average over different widths. One averages over about 65nm so that only the inner core area contributes, whereas the wider scan, corresponding to the projecting electron beam, averages over the whole needle width. Comparison of both scans (Fig. 5) should reveal differences of the ΔV_{pn} that really exist in the core and the ΔV_{pn} that is finally measured in the projected phase image. Surprisingly, for the n-doped needle the difference is remarkable, whereas for the p-doped needle it is only a minor effect.

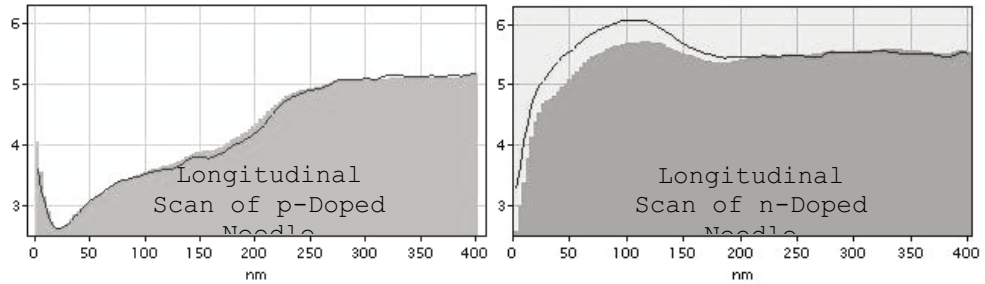


Fig.5: Profile scans corresponding to the arrows in Fig.3. The dark line represents the scan from the inner core area; the grey area represents the scan that is averaged over the whole needle width.

5. SUMMARY

The proposed transition zone between the electrically inactive deadlayer on the surface of a FIB-lamella and the electrically fully-active core has been found for all kind of investigated silicon needles. It was demonstrated that the projection of the potential distribution along the electron beam in the TEM, in combination with the shown difference in potential distribution for complementary doped areas, leads to a difference in signal strength between both types of dopants.

ACKNOWLEDGEMENTS

Thanks to all members of Triebenberg Lab in Dresden, the "Physical Failure Analysis (PFA)" division of Infineon Technologies Dresden, especially the TEM-group, and the State of Saxony for supporting this work.

REFERENCES

Langer E, Engelmann H J, Volkmann B and Zschech E 2000 FIB induced damages of SEM/TEM samples of semiconductor devices, 4th European FIB Users Group Meeting (EFUG2000)

Lenk A 2001 Optimierung der Focussed Ion Beam (FIB)-Lamellenpräparation für die elektronenholographische Abbildung der Dotiergebiete von MOSFET-Transistoren, Diploma-Thesis, Dresden University

Lenk A 2004 Proc. 13th European. Microscopy Congress, eds G Van Tendeloo (Belgian Society for Microscopy), Volume II p 373

McCartney M R and Gajdardziska-Josifovska M 1994 Ultramicroscopy **53**, 283

Rau W D, Schwander P, Baumann F H, Hoppner W and Ourmazd A 1999 Phys Rev Lett **82**, 2614

Twitchett A C, Dunin-Borkowski R E and Midgley P A 2002 Phys Rev Lett **88**, 238302

Interference electron microscopy of reverse-biased p-n junctions

P F Fazzini, P G Merli[1], G Pozzi and F Ubaldi

Dept of Physics, INFM and CNISM, University of Bologna, Bologna, 40127, Italy
[1] IMM-CNR Sezione di Bologna, CNR, Bologna, 40129, Italy

ABSTRACT: Electron interferometry experiments on straight reverse-biased p-n junctions have been carried out in a transmission electron microscope. The trends of the interference fringes as well as the shape of the interference region are able to give direct information about the phase variation across the junction. Agreement between theory and experiments is obtained by introducing a suitable surface density charge produced by the beam at the interface between the silicon and the native oxide. The results confirm in a more reliable way the main achievements formerly obtained through out-of-focus observations.

1. INTRODUCTION

Dopant profile investigation is an important issue for the semiconductor industry, as the spatial distribution and the concentration of the dopant atoms are key factors in understanding device operation and validating device simulation. Electron microscopy phase-contrast techniques, like holography or the more standard Lorentz microscopy methods, can be very helpful or even essential in the determination of two-dimensional dopant distributions on the nanometer scale. For electron holography, a resolution of 5-10 nm with a sensitivity of 0.1 V has been documented (Rau et al 1999, McCartney et al 2002, Twitchett et al 2002, Gribelyuk et al 2002). Important limitations are the yet not clearly defined effects of the electron beam-device interaction and of specimen preparation that calls for the presence of a "dead layer". This is a purely phenomenological quantity having the effect of deleting the external fringing field expected from the law of electrostatics and of introducing modifications to the phase shift capable of reconciling theory and experiment.

In order to unravel the physical mechanism beyond this "dead layer" starting from first principles, we guessed a charging of the native oxide under the action of the electron beam (Beleggia et al 2001, 2003). Recent observations of reverse-biased p-n junctions in a transmission electron microscope (TEM) by means of the out-of-focus method have shown that an agreement between experiment and theoretical interpretation can be reached under the aforementioned assumption. The simulation of the device in these conditions has shown that not only the external field topography is strongly influenced by the presence of this surface charge (in particular no external field is present in the unbiased case, in spite of the fact that a built-in potential is present between the n and p regions) but also the internal one, where the standard one-sided step topography (Grove 1962) is no longer valid.

In this paper the problem is faced using electron interferometry observations (Missiroli et al 1981). This kind of experiment provides results that are more directly and easily interpreted than the former out-of-focus observations (Beleggia et al 2003) and support more convincingly our achievements about the existence and the role of the charged layer (Beleggia at al 2001, 2003).

2. EXPERIMENTAL METHODS AND RESULTS

The electron interference experiments have been carried out by inserting an electron biprism at the level of the intermediate aperture in a Tecnai F20 TEM equipped with a Schottky source. The observed object is a p-n junction in a silicon specimen - ion beam thinned to a final thickness of about 150 nm - separating two regions resulting in having a constant doping of $5x10^{15}$ cm^{-3} (n-region) and

$1x10^{19}$ cm^{-3} (p-region).

The interference fringe system produced by the electron biprism, is made up of parallel lines modulated by the diffraction effects due to the biprism edge (Missiroli et al 1997). When the specimen is overlapped by the interference fringes, the shape of the interference field and the trend of the enclosed fringes are affected by the presence of the junction.

It is worth noting that the specimen was defocused so that a faint contrast line L is visible corresponding with the region of highest electric field, allowing the junction to be located. The defocus distance amounts to -2.7 mm (Fazzini et al 2004).

The experimental results obtained operating in the free-lens mode with the objective lens switched off and the biprism negatively biased at –5 V (divergent condition) are reported in Fig. 1. It shows interferograms with a reverse bias of the p-n junction of 0 V (a), 1.6 V (b) and 3.1 V (c) respectively. They point out that the effect of the electric field associated with the junction is that of displacing (compare the relative position of the bend contour B in the three images) and deforming the interference fringe system both as regards the shape of the interference field as well as the trend of the fringes.

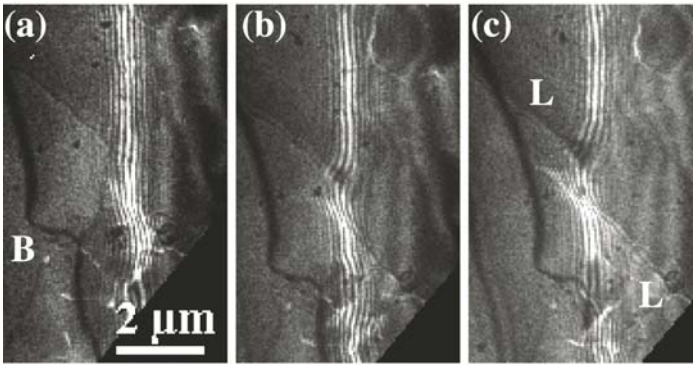


Fig. 1. Electron interference images of the p-n junction. The biprism voltage amounts to -5 V while the junction reverse bias is 0 V in (a), 1.6 V in (b) and 3.1 V in (c).

In particular it is important to note that at 0 V reverse bias, Fig. 1a, there is a bending of the fringes mainly when they cross the region where the junction is present while they run rather straight far from it, apart from the influence of other specimen features e.g. thickness variations or contamination. When a reverse bias of 1.6 V is applied, Fig. 1b, the bending of the fringes increases, and in the region where their spacing is larger (in correspondence with the upper contrast line associated to the defocused junction) their intensity decreases, whereas in correspondence with the lower contrast line the interference field is deformed into a cusp-like shape. These image features are emphasized at 3.1 V reverse bias, Fig. 1c. It can be also ascertained by looking at the fringe system at grazing incidence, that the fringes are bent also in regions far away from the junction.

By comparing these experimental findings with the results of the theoretical simulation of the device we will show that they give a support stronger than out-of-focus images to the existence and influence of surface charged layers.

3. INTERPRETATION OF THE INTERFERENCE IMAGES

As in former work (Beleggia et al 2003) we have taken into account the effects of the surface charge on the internal and external field distribution across a p-n junction arising between two regions having the doping previously reported and a thickness of 150 nm. From the data given by the device simulation software (ISE TCAD), we have calculated the phase shift due to the internal and external field, and deduced the object wave-function. Then the effect of the biprism on the object wave-function has been simulated carrying out a complete wave-optical analysis of the image formation.

The propagation of the object wave-function to the biprism plane has been calculated by using the Fast Fourier Transform (FFT) algorithm. The resulting image has then been multiplied by the transmission function of the biprism (Missiroli et al 1981,1997) and back-propagated to the plane conjugate to the final recording screen. Since this plane is not conjugate to the specimen plane, the image of the junction is slightly defocused (-2.7 mm as in the experiments) showing the contrast line locating the junction (see Fig. 1). Disregarding partial coherence effects it has been possible to obtain the results shown in the following figures.

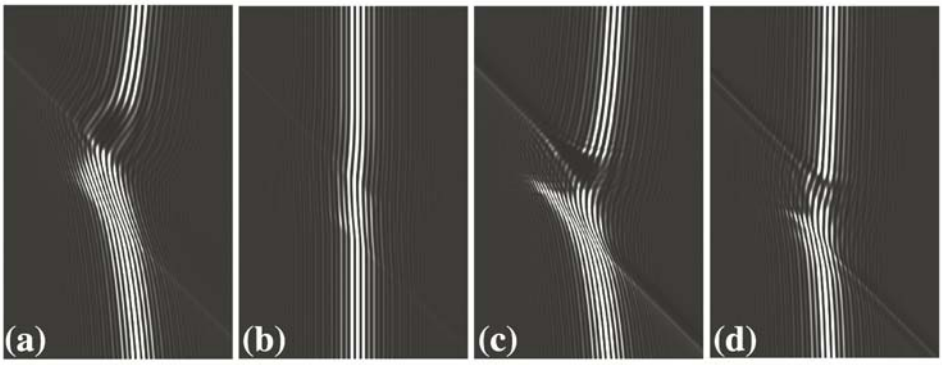


Fig. 2. Simulated interference images for an applied bias of 3 V, –5 V of biprism voltage and an out of focus distance of –2.7 mm. (a) no surface charge, (b) no surface charge and no external field, (c) surface density charge of $1x10^{13}$ e.c./cm^2, (d) surface density charge of $2x10^{13}$ e.c./cm^2.

Let us first consider the case of the junction biased at 3V, Fig. 1c, where the effects in the image are more impressive. We have taken a defocus distance of –2.7 mm, as in the experiment. Fig. 2a reports the interference image calculated for no surface charge, so that in this case both internal and external field contribute to the phase shift. It can be seen that the overall trend of the fringes and of the shape of the interference field is in rough agreement with the corresponding experimental result in Fig. 1c. By assuming that the effect of the "dead layer" is that of deleting the external field, leaving the internal one unchanged, we have simulated this behavior in Fig. 2b, which shows that the overall effect on the interference fringe system is strongly diminished confirming the predominant role of the external field. Figures 2c and d report the interference images calculated for surface density charges having the values of $1x10^{13}$ e.c./cm^2 and $2x10^{13}$ e.c./cm^2 respectively. It can be ascertained that the overall agreement with the experimental image is rather satisfying for the lower density charge, Fig. 2c, whereas for the highest value, Fig. 2d, the external field is almost completely deleted, thus resulting in disagreement with the experiments. This value can be assumed as the upper limit for the charge surface density.

In order to refine the range we have considered a lower surface charge density of $7.5x10^{12}$ e.c./cm^2 and simulated (see Fig. 3) the whole series of experimental data. The external field due to the built-in potential alone (no reverse bias is applied) is partially cancelled but becomes again influential by increasing the reverse bias. Therefore, the interference fringes are bent only across the junction for a 0 V bias, Fig. 3a, but display a long range bending at higher voltages, due to the restored influence of the external field, Fig. 3b and c. Also the shape of the interference field displayed by the contrast of the fringes within the region where the contrast is reduced, and the nearby spike-like shape of the interference fields are more clearly visible with respect to the experimental results (Fig.1) as perfect coherence is assumed in the simulations.

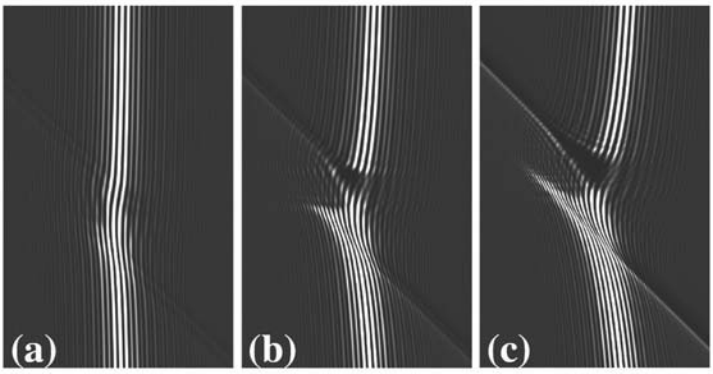


Fig 3. Simulated interference patterns for an out of focus distance of –2.7 mm, a biprism voltage of –5 V and a surface density charge of 7.5×10^{12} e.c./cm^2: (a) 0 V reverse bias, (b) 1.6 V reverse bias, (c) 3.1 V reverse bias.

Both these effects, which, according to the geometric optical approximation (Missiroli et al 1997), are related to the gradient of the phase through the deformation of the biprism edges, are in agreement with the reduction of the depletion layer width associated to the charged layers. Therefore they are less detectable in the unperturbed case, Fig. 2a, where the depletion layer is much larger.

It is worth noting, comparing Fig. 2c with Fig. 3c, that the small change in the charge densities used in simulations does not significantly affect the interference patterns.

4. CONCLUSIONS

In conclusion, these interferometric observations support more convincingly than the former out-of-focus ones the presence of the external field in our specimen, linked in a rather complex way to the charging up of the oxide layers. Although some experimental data are not yet accurately known, nonetheless the qualitative agreement between theory and experiment is rather impressive.

ACKNOWLEDGMENTS

Useful discussions with Drs A. Roncaglia, A. Migliori and the technical assistance of S. Patuelli are gratefully acknowledged. This research has been supported by FIRB funding, contract RBAU01M97L.

REFERENCES

Beleggia M, Cardinali G C, Fazzini P F, Merli P G and Pozzi G 2001 Inst.Phys.Conf.Ser. **169**, 427
Beleggia M, Fazzini P F, Merli P G and Pozzi G 2003 Phys.Rev.B **67**, 045328
Fazzini P F, Merli P G and Pozzi G 2004 Ultramicroscopy **99**, 201
Gribelyuk M A, McCartney M R, Li J, Murthy C S, Ronsheim P, Doris B, McMurray J S, Hedge S and Smith D J 2002 Phys. Rev. Lett. **89**, 025502
Grove A S 1962 Physics and Technology of Semiconductor Devices (New York, J. Wiley and Sons)
McCartney M R, Gribelyuk M A, Li J, Ronsheim P, Doris B, McMurray J S and Smith D J 2002 Appl. Phys. Lett. **80**, 3213
Missiroli G F, Pozzi G and Valdrè U 1981 J. Phys. E **14**, 649
Missiroli G F, Matteucci G and Pozzi G 1997 Advan. Imag. Electron. Phys. **99**, 171
Twitchett AC, Dunin-Borkowski R and Midgley PA 2002 Phys. Rev. Lett. **88**, 238302
Rau W D, Schwander P, Baumann F H, Hoppner W and Ourmazd A 1999 Phys.Rev.Lett. **82**, 2614

Off-axis electron holography of focused ion beam milled GaAs and Si p-n junctions

D Cooper, A C Twitchett, I Farrer[1], D A Ritchie[1], R E Dunin-Borkowski and P A Midgley

Department of Materials Science and Metallurgy, University of Cambridge, Pembroke Street, Cambridge CB2 3QZ, U.K.
[1] Semiconductor Physics Group, Cavendish Laboratory, Madingley Road, Cambridge CB3 0HE, U.K.

ABSTRACT: Si and GaAs p-n junctions have been characterised in the transmission electron microscope using off-axis electron holography. Focused ion beam milling was used to prepare parallel-sided membranes with thicknesses of 200-500 nm. Off-axis electron holograms were acquired at 200kV in order to assess the effect of specimen preparation on the electrostatic potentials measured across the junctions.

1. INTRODUCTION

Off-axis electron holography is a powerful transmission electron microscopy (TEM) technique that can be used to provide high spatial resolution two-dimensional maps of the phase shift of a high-energy electron wave that has passed through a specimen. The phase shift is proportional to the electrostatic potential integrated in the electron beam direction, suggesting that variations in potential arising from the presence of dopant atoms in a semiconductor can be measured. The technique promises to fulfil the requirement of the semiconductor industry for a dopant profiling technique that has sub-10nm spatial resolution.

Off-axis electron holography is also sensitive to variations in specimen thickness. A thickness variation of 10nm results in a phase change of just under one radian in Si, which can be as much as 50% of the phase change across a p-n junction in a 400-nm-thick specimen.

The study of semiconductor samples in the electron microscope requires a highly site-specific specimen preparation technique. Currently, only focused ion beam (FIB) milling can satisfy this requirement. FIB milling involves the use of a 30kV Ga^+ ion beam to sputter material from a bulk device to prepare an electron-transparent membrane containing the area of interest. Unfortunately, the Ga^+ ions damage the crystalline sample, resulting in the presence of amorphous layers on the membrane surfaces, and additional electrically-altered crystalline near-surface layers (Twitchett et al 2002). These damaged surfaces influence the phase shift across the a p-n junction measured using electron holography.

It is important to understand the effect of the artefacts introduced by different TEM sample preparation techniques on the measured phase shift in a doped semiconductor specimen. The results of electron holography experiments on FIB-prepared Si and GaAs p-n junctions are presented here.

2. EXPERIMENTAL DETAILS

TEM samples of Si and GaAs p-n junctions were prepared using an FEI 200 FIB Workstation operated at 30 kV. The Si p-n junction was grown using molecular beam epitaxy (MBE) and comprised a 2.5-μm-thick 4×10^{18} cm^{-3} B-doped (p-type) layer on a 4×10^{18} cm^{-3} Sb-doped (n-type) substrate. GaAs p-n and n-p junctions were also grown using MBE. Each sample contained a

1.0-μm-thick 1×10^{18}cm^{-3} Be-doped (n-type) layer and a 1.0-μm-thick 1×10^{18} cm^{-3} Si-doped (p-type) layer on an undoped GaAs substrate. Parallel-sided membranes were FIB-milled with total thicknesses ranging between 200 and 500 nm. Care was taken to minimise Ga^+ implantation into the samples by exposing the region of interest at only a glancing angle to the beam. Final thinning was performed at a low beam current (150 pA) and care was taken to avoid re-deposition of sputtered material onto each sample.

Off-axis electron holograms were acquired using a Philips CM300-ST field-emission gun transmission electron microscope (FEGTEM) operated at a voltage of 200 kV. The holograms were formed using a Lorentz mini lens with the objective lens turned off and a rotatable Möllenstedt-Duker biprism located in the selected area aperture plane of the microscope, and were recorded on a 2048 pixel charge coupled device (CCD) camera. A schematic diagram of the experimental set up is shown in Fig. 1. A biprism voltage of 100V was used to obtain a holographic overlap width of approximately 750 nm with a fringe spacing of 5 nm. The samples were tilted a few degrees from <100> to minimise diffraction contrast across the specimen, whilst taking care to ensure that each junction was edge-on with respect to the electron beam.

Reference holograms were acquired after each hologram of a region of interest to remove any geometrical distortions associated with the imaging a recording system. Figure 1b shows a schematic diagram of the process used to reconstruct phase and amplitude images.

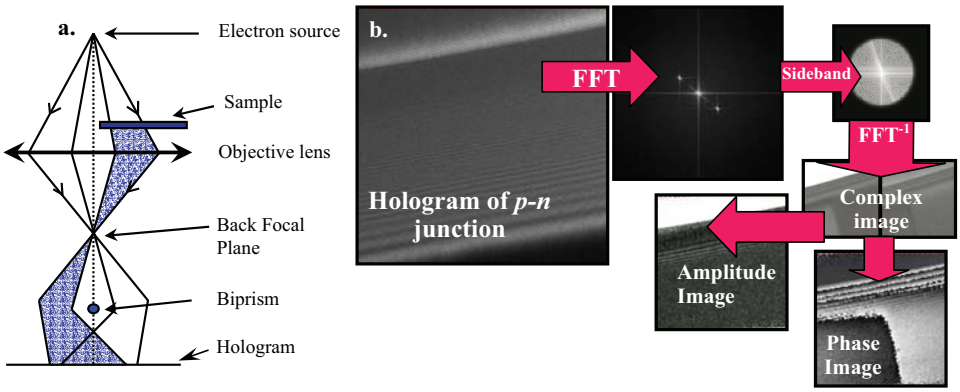


Fig. 1. (a) Schematic diagram illustrating the formation of an off-axis electron hologram. (b) Diagram illustrating the reconstruction of phase and amplitude images.

3. RESULTS AND DISCUSSION

Phase and amplitude images were reconstructed from off-axis electron holograms of all of the GaAs and Si FIB-prepared membranes. The total membrane thickness, t, of each sample was calculated in units of inelastic mean free path, λ from the measured normalised holographic amplitude, A (Gajdardziska-Josifovska and McCartney, 1994) by using the equation

$$t/\lambda = -2 \ln A.$$

Crystalline membrane thicknesses were also measured using convergent beam electron diffraction (CBED).

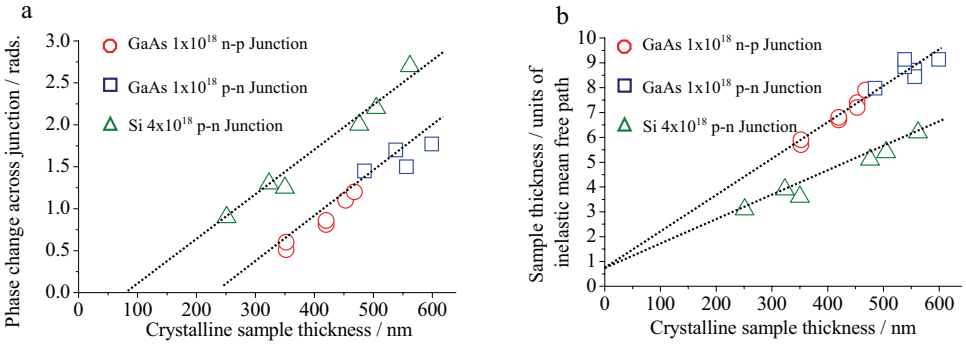


Fig. 2. (a) Phase change across junction, plotted against crystalline sample thickness determined by CBED. (b) Sample thickness measured in units of inelastic mean free path, plotted against crystalline sample thickness determined by CBED.

Figure 2a shows the measured phase changes, φ, across the junctions for all of the samples, plotted as a function of the crystalline thickness of each sample (measured using CBED). The built-in potential, V_{bi}, across the p-n junction is related to the measured phase change Δφ by the relation

$$\Delta\varphi = C_E V_{bi} t_{el}$$

where C_E is a microscope-dependent constant and t_{el} is the electrically active thickness of the sample. The built-in voltage,V_{bi}, was calculated from the gradient of the plot in Fig. 2a to be 0.77 +/- 0.1 V for GaAs and 0.78 +/- 0.06V for silicon. The non-zero x-intercept indicates that the electrically active thickness of the membrane is smaller than the crystalline thickness, and that part of each membrane is electrically inactive. FIB milling is known to create not only amorphous surface layers, but also point defects from knock-on damage to a significant depth in the membrane. These point defects can affect the electrical properties of the semiconductor, altering the electrically active dopant concentration in the near-surface region. The results in Fig. 2a indicate that the effects of such electrical damage extend further into GaAs than Si membranes, with crystalline, electrically inactive regions of 125 and 45 nm on each surface respectively. Their presence increases the membrane thickness required to detect a given phase change across a p-n junction in GaAs to a thickness at which inelastic scattering becomes significant, reducing the signal to noise ratio.

Figure 2b shows a plot of t/λ as a function of crystalline sample thickness for the Si and GaAs FIB-prepared membranes. The x-intercept reveals the thickness of the amorphous surface layers introduced by FIB-preparation. These are found to be 21 nm and 27 nm at each surface for GaAs and Si respectively, in agreement with other recent results (Yabuuchi et al 2005, Twitchett et al 2003). The gradient can be used to calculate the mean free path for inelastic scattering, λ, which is 66 +/- 2nm for GaAs and 99 +/- 4nm for Si. The empirically calculated mean free paths are 133 nm for GaAs and 125 nm for Si (Malis 1988). Previous experiments using electron holography have found λ_{Si} to be 88 nm (Chou and Libera 1998). The experimentally determined value of λ for GaAs may be significantly smaller than predicted due to the presence of relatively thick electrically altered layers near each membrane surface. These layers are expected to contain many point defects, which would act as additional scattering centres, thereby lowering the overall inelastic mean free path.

Figures 3a and b show the experimentally measured phase change across a p-n junction for both Si and GaAs. As indicated in the earlier results, the phase change is much smaller across the p-n junction in GaAs owing to the presence of much thicker electrically-altered surface layers. The signal to noise ratio observed in the GaAs experimental profile is also significantly lower than observed for Si, highlighting the problems associated with examining dopant potentials in GaAs devices. The membrane thicknesses required to measure any detectable phase change are significantly higher than in Si, and inelastic scattering generates significant background noise that reduces the quality of the phase signal measured.

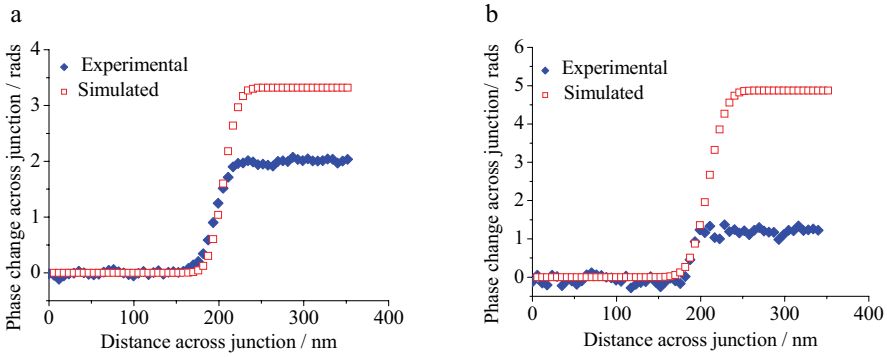


Fig. 3. Calculated and experimental phase variation across 470-nm–thick membranes containing p-n junctions in (a) Si and (b) GaAs.

This study indicates that alternative sample preparation methods must be investigated to reduce the depth of damaged surface layers in order to obtain better quality holograms of GaAs membranes, including additional methods that may reduce surface damage on FIB-prepared membranes such as low-energy Ar-ion milling, chemical etching and low temperature annealing.

4. CONCLUSIONS

Off-axis electron holograms have been acquired from Si and GaAs p-n and n-p junctions. This work has shown that for both GaAs and Si there are significant electrically altered surface layers. These layers may be associated with Ga^+ implantation and further cascade effects at the surfaces during FIB milling. The measured phase changes across the junctions are lower than anticipated, especially for the GaAs specimens. The mean free paths for inelastic scattering and the thicknesses of the amorphous surface layers have also been measured.

In order to successfully characterise the electrical properties of semiconducting devices using electron holography, a greater knowledge of the effects of sample preparation is required, as well as the development of more advanced sample preparation techniques.

ACKNOWLEDGEMENTS

We thank the EPSRC, Newnham College, Cambridge and the Royal Society for financial support.

REFERENCES

Chou T M and Libera M 2003 Ultramicroscopy **94**, 31
Gajdardziska-Josifovska M and McCartney M R 1994 Ultramicroscopy **53**, 283
Malis T et al 1988 J. Electron Microsc. Technol. **8**, 193
Twitchett A, Dunin-Borkowski R E and Midgley P A 2002 Phys. Rev. Lett. **88**, 238302
Twitchett A, Dunin-Borkowski R E, Hallifax R J, Broom R F and Midgley P A 2003 J. Microsc. **214**, 287
Yabuuchi Y, Tametou S, Okano T, Inazato S, Sadayama S, Yamamoto Y, Iwasaki K and Sugiyama Y 2004 J. Electron Microsc. **53**, 471

Towards quantitative electron holography of electrostatic potentials in doped semiconductors

P K Somodi, R E Dunin-Borkowski, A C Twitchett, C H W Barnes[1] and P A Midgley

Department of Materials Science and Metallurgy, University of Cambridge, Pembroke Street, Cambridge CB2 3QZ, UK
[1]Department of Physics, University of Cambridge, Madingley Road, Cambridge CB3 0HE, UK

ABSTRACT: Simulations of the electrostatic potential within thin Si samples containing an abrupt *p*-*n* junction have been compared with experimental measurements obtained using off-axis electron holography from samples prepared using focused ion beam milling. In order to obtain agreement between the simulated and experimental potential profiles, a layer of altered dopant concentration is introduced at the specimen surface.

1. INTRODUCTION

The quantitative characterisation of electrostatic potential distributions associated with the presence of dopant atoms is of fundamental importance for the development of future generations of nanoscale semiconductor structures and devices. Off-axis electron-holography (Völkl et al 1998) is increasingly used to determine the potential within doped semiconductors. However the step in potential across a *p*-*n* junction is usually found to be less than expected (Twitchett et al 2002, Rau et al 1999). This discrepancy has been partially accounted for by the introduction of equipotential surfaces on the specimen (Somodi et al 2004). Here we compare experimental electron holography results with two-dimensional simulations of the electrostatic potential across a *p*-*n* junction. In the simulations we introduce layers with altered dopant concentrations at the specimen surfaces to model the effect of sample preparation for electron microscopy on the electrostatic potential in a thin specimen.

2. COMPARISON OF EXPERIMENTAL AND SIMULATED RESULTS

Three Si *p*-*n* junction samples containing Sb atoms in the *n*-type regions and B atoms in the *p*-type regions were prepared for electron holography using focused ion beam (FIB) milling. Convergent beam electron diffraction was used to determine that the crystalline sample thicknesses were 220, 270 and 410 nm. The dopant concentrations were measured using secondary ion mass spectrometry (SIMS) and were found to be 3×10^{18} cm^{-3} in the *n*-type region and 4×10^{18} cm^{-3} in the *p*-type region. The potential distributions in the specimens were measured using electron holography as described elsewhere (Twitchett et al. 2004a). Figure 1 shows raw and smoothed potential profiles across the *p*-*n* junction measured from each specimen.

Simulations of the potential within the Si specimens were performed in one- and two- dimensions by solving the standard semiconductor equations (Sze 2002) and using a finite element solver (Langtangen 2003). The one-dimensional simulations give the expected bulk-like potential across the junction to be 1.04 V. In the two-dimensional simulations values for the electrostatic potential on the top and bottom surfaces are required. Experimentally, electrostatic fringing fields are almost never observed outside the specimen close to the position of a *p*-*n* junction (Twitchett 2004b) indicating that these surfaces can be treated as equipotentials for the purpose of the simulations. The simulated potential distributions were averaged in the direction of the electron beam in order to generate results that are comparable to those obtained using electron holography. It has been shown that the averaged step in potential across the junction is independent of the value of the potential at the surface for the dopant

concentrations considered here (Somodi et al 2004). Therefore the potential at the surface is taken to be 0.7eV above the Fermi level in bulk-like *n*-type silicon as suggested by Lűth (2001).

Figure 1 shows simulated potential profiles for all three specimen thicknesses. The step in potential across the junction that would be inferred from a knowledge of the sample thickness is found to be 0.4 V experimentally and 0.97 V for the simulations, for a sample thickness of 220 nm. For a sample thickness of 270 nm these values were 0.7 V experimentally and 0.98 V from the simulations while for the 410 nm thick sample the corresponding values are 0.75 V and 1.00 V. Although the inclusion of equipotentials on the specimen surface in the simulations act to reduce the apparent step in potential across the junction, as compared with the expected bulk-like value, it does not fully account for the observed decrease in the step in potential measured using electron holography.

A further discrepancy is associated with the fact that the depletion width across the junction is significantly larger in the experimental data than in the simulations. In the smoothed experimental data the depletion width is defined to be the region over which the gradient of the potential (i.e. the electric field) is non-zero. The depletion width is measured experimentally to be 65 ± 10, 90 ± 10 and 65 ± 10 nm for sample thicknesses of 220, 270 and 410 nm respectively. In the case of the simulations long tails present in the electric field distribution require the use of an alternative method to find the depletion width. In this case the depletion width is defined to be the distance over which the charge density is non-zero, assuming that the charge density takes values of either zero or the average dopant concentration within the specimen. The depletion width, calculated by integrating the charge density and from a knowledge of the maximum value of the electric field, is found to be 25 ± 5 nm for all three sample thicknesses. A one-dimensional simulation gives the expected depletion width across the junction to be 23 ± 1 nm. The introduction of equipotentials on the specimen surfaces clearly does not account for the increase in the depletion width observed in the microscope.

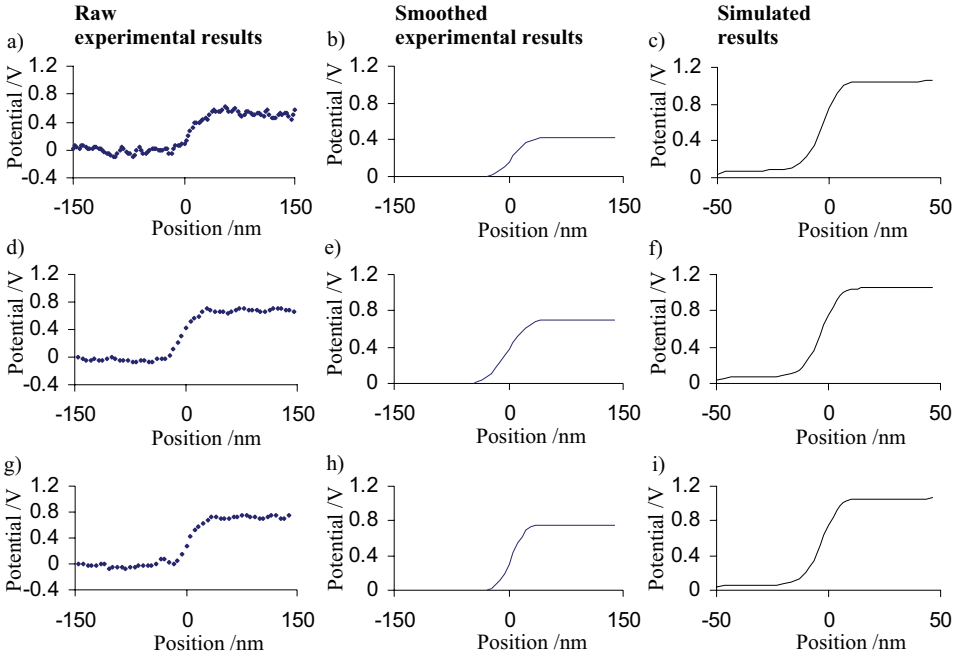


Fig. 1. The potential across a Si *p*-*n* junction doped with 3 x 10^{18} cm^{-3} of B in the *n*-type region and 4 x 10^{18} cm^{-3} of Sb in the *p*-type region. a), d) and g) show the raw experimental data from off-axis electron holography. b), e) and h) show the smoothed experimental data from which noise has been removed. c), f) and i) show simulated profiles. a), b) and c) are for samples of thickness 220 nm. d), e) and f) are for samples of thickness 270 nm. g), h) and i) are for samples of thickness 410 nm.

3. AN IMPROVED MODEL TO SHOW THE IMPACT OF FIB MILLING ON THE SILICON SURFACE

The experimentally observed decrease in the step in potential across the junction and increase in the depletion width are suggestive of a reduction in the electrically active dopant concentration in the sample. The dopant concentration measured using SIMS may not be the same as the electrically active concentration due to the effects of FIB milling on the sample. Here we model the effect of FIB milling on the potential within the sample by introducing a layer of lower dopant concentration on each surface of the sample as shown schematically in Fig. 2. The thickness of each layer *d* is varied, as is the dopant concentration in the layer.

The resulting simulated step in potential across the junction is shown as a function of *d* in Fig. 3, for the three sample thicknesses examined experimentally. It can be seen that the step in potential across the junction is further reduced by the introduction of surface layers of lower dopant concentration. Significantly, the reduction in the apparent step in potential is approximately independent of the dopant concentration in the surface layers, especially for smaller values of *d*. The corresponding variation in the simulated depletion width with surface layer thickness is shown in Fig. 4. The depletion width increases significantly with the introduction of surface layers and its value is approximately independent of the dopant concentration in the layers.

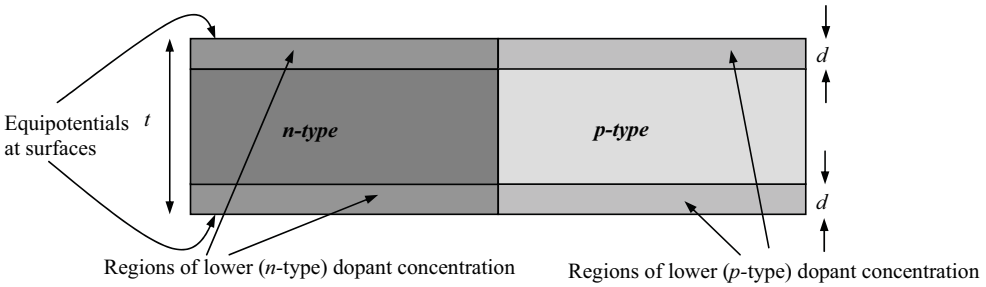


Fig. 2. Schematic diagram showing the geometry of the sample assumed in the simulations, with modified surface layers to model the effect of FIB milling.

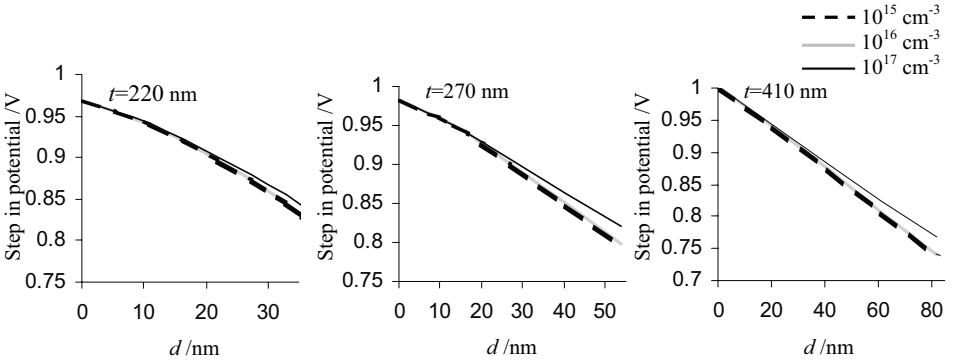


Fig. 3. Graphs showing the simulated variation in potential across the junction with surface layer thickness, for the indicated sample thicknesses. The dopant concentrations on the surface were taken to be 10^{15}, 10^{16} and 10^{17} cm^{-3}.

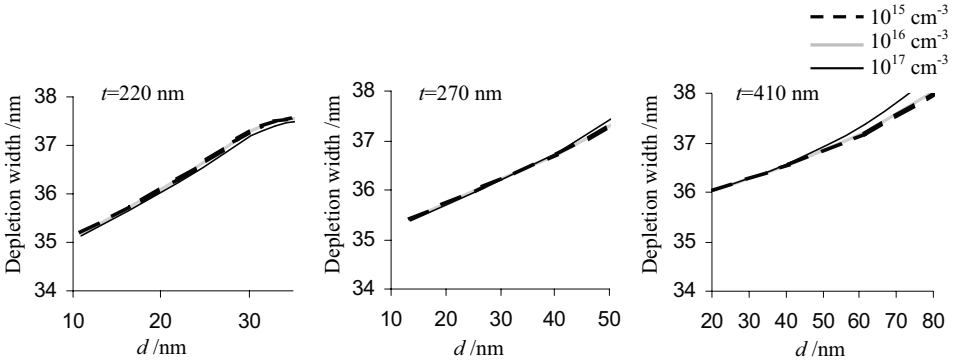


Fig. 4. Graphs showing the simulated variation in depletion width with surface layer thickness for the indicated sample thicknesses. The dopant concentrations in the surfaces layers are 10^{15}, 10^{16} and 10^{17} cm^{-3}.

The reduction in the step in potential across the junction seen in the experimental results, as compared with the value expected in bulk-like material, can be reproduced by these simulations. For larger sample thicknesses the surface layers of lower dopant concentration would need to account for almost half of the total sample thickness. For the smaller sample thicknesses the surface layers would have to dominate the sample. The larger depletion widths measured in the experimental data cannot be replicated in the present model. The discrepancy may be partially accounted for by the difficulty in measuring the depletion width. However it is more likely that the electrically active dopant concentrations in the centre of the sample are decreased from the nominal values measured using SIMS, in addition to the presence of altered surface layers.

4. CONCLUSIONS

It has been shown that the introduction of surface layers of lower dopant concentration in simulations decreases the potential across a *p-n* junction to values that are within agreement with values measured using electron holography. The large depletion widths measured using electron holography may be accounted for by a decrease in the electrically active dopant concentration throughout the thickness of the sample. These effects must be understood fully before electron holography can become a truly quantitative method to determine dopant profiles.

We are grateful to Philips Research Laboratories (Eindhoven) for provision of their p-n junction sample and to the EPSRC, Newnham College, Cambridge and the Royal Society for financial support.

REFERENCES

Langtangen H P 2003 Computational Partial Differential Equations (London, Springer) ch 3
Lűth H 2001 Solid Surface, Interfaces and thin films, (Heidelberg, Springer) p 349
Rau W D, Schwander P, Baumann F H, Hoppner W and Ourmazd A 1999 Phys. Rev. Lett. **82,** 2614
Somodi P K, Dunin-Borkowski R E, Twitchett A C, Barnes C H W and Midgley P A 2004 Proc. XIII Eur. Congr. Microsc. II, p 387
Sze S M 2002 Semiconductor Devices (Singapore, Wiley) ch 4
Twitchett A C, Dunin-Borkowski R E and Midgley P A 2002 Phys. Rev. Lett. **88,** 238302
Twitchett A C, Dunin-Borkowski R E, Halifax R J, Broom R F and Midgley P A 2004a J. Microsc. **214**, p 287
Twitchett A C, Dunin-Borkowski R E, Halifax R J and Midgley P A 2004b J. Phys. Condens. Mat. **16**, S181
Völkl E, Allard L F and Joy D C 1998 Introduction to Electron Holography (New York, Kluwer Academic/ Plenum Publishers)

Three-dimensional analysis of the dopant potential of a silicon *p-n* junction by holographic tomography

A C Twitchett, T J V Yates, P K Somodi, S B Newcomb[1], R E Dunin-Borkowski and P A Midgley

Department of Materials Science and Metallurgy, University of Cambridge, Pembroke Street, Cambridge, CB2 3QZ, UK
[1] Sonsam Ltd., Glebe Laboratories, Newport, Co. Tipperary, Ireland

ABSTRACT: Off-axis electron holography and tomography have been combined to examine the 3-D electrostatic potential associated with a Si *p-n* junction. The device was prepared in a novel specimen geometry using focused ion beam milling and a series of holograms was acquired over a tilt range of -70º to +70º. Simultaneous iterative reconstruction was used to reconstruct the 3-D electrostatic potential in the specimen. The experimental results were compared to simulations of the potential variation. Quantitative results from the central, 'bulk' semiconducting regions and from the surface layers were extracted from the 3-D reconstruction.

1. INTRODUCTION

Dopant profiling of semiconductor devices using off-axis electron holography has become more widely used in recent years, with many examples of the successful visualisation of dopant-related electrostatic potentials (e.g. McCartney et al 2002; Twitchett et al 2005). Although electron holography promises to provide fully quantitative results, the measured potential is a 2-D projection along the electron beam direction through the semiconductor membrane thickness, including all surface potential effects. These surface contributions are particularly significant when using electron holography to examine semiconductor device structures prepared from site-specific regions of device structures using focused ion beam (FIB) milling. This preparation technique is known to generate amorphous and electrically altered near-surface layers. In order to obtain a quantitative characterisation of the bulk and surface properties of a semiconductor membrane, a 3-D map of the electrostatic potential variation is required.

Electron tomography has been applied successfully to a number of different problems in materials science, in particular to the examination of catalysts and other small inorganic particles (Midgley and Weyland 2003). This technique involves the use of a series of images acquired over a large range of tilt angles to reconstruct 3-D properties of a specimen. However, its application in the fields of semiconductors and electron holography has been limited to date. The phase signal reconstructed from off-axis electron holograms satisfies the tomographic requirement that the signal is a monotonic function of the sample thickness, and it should therefore be possible to reconstruct the 3-D phase (and, therefore, the related electrostatic potential) associated with a doped semiconductor device. This measurement is particularly important for the quantitative determination of the electrostatic potential at an FIB-modified semiconductor surface, but also has significant relevance to the examination of many nanoscale semiconductor structures.

2. EXPERIMENTAL DETAILS

2.1 Sample Geometry and Specimen Holder

Samples for examination using off-axis electron holography must satisfy stringent geometrical requirements. There must be a vacuum region close to the area of interest and the sample thickness

must be close to the optimised membrane thickness for the material under examination (Rau et al 2002), which is usually ~ 200-300 nm for silicon. These requirements can be satisfied by FIB-prepared samples. However, a standard trench prepared FIB membrane is restricted in tilt to only ~ ± 10º due to shadowing by the trench walls, therefore making it unsuitable for tomography. A modified sample geometry has been prepared, illustrated in Fig. 1a, where a thin membrane is milled along the edge of a cleaved square of silicon that can be tilted through 360º without shadowing by the bulk specimen. This specimen was mounted in a Fischione two-contact electrical biasing tomography holder, illustrated in Fig. 1b, which is capable of tilts of ± 80º in the electron microscope. A silicon *p-n* junction device with nominal dopant concentrations of in excess of 10^{18}cm^{-3} in both *p* and *n* regions was prepared in this sample geometry for combined holography and tomography experiments.

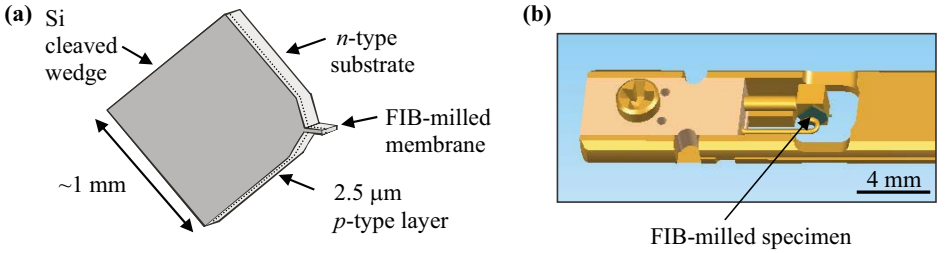


Fig. 1: (a) Schematic diagram of the sample geometry used for combined electron holography and tomography of a silicon *p-n* junction. (b) Diagram of the end of the Fischione TEM holder used for electrically biased electron tomography and holography.

2.2 Experimental Procedure

Off-axis electron holograms were acquired on a Philips CM300 field-emission TEM, which was operated in Lorentz mode and equipped with a Gatan imaging filter (GIF) 2000, using a biprism voltage of 100 V. Holograms were acquired over a tilt range of -70° to +70° at 2° intervals. Reference holograms were acquired every 10° in tilt in order to remove distortions associated with the imaging and recording system. Holograms were reconstructed immediately after acquisition using scripts written using Digital Micrograph software to ensure that the *p-n* junction was positioned within the field of view, as no alignment features on the sample are visible in an unprocessed hologram. Figure 2a shows an off-axis electron hologram acquired at zero degrees tilt (defined as the tilt that results in the junction being edge-on) and Fig. 2b shows the corresponding reconstructed phase image. Convergent beam electron diffraction was used to determine the crystalline thickness of the FIB-prepared membrane. This thickness was determined to be 330 nm, giving a total membrane thickness of 380 nm including the thickness of amorphous surface layers generated by FIB milling.

2.3 Data Analysis

Off-axis image and reference holograms were reconstructed to obtain phase and amplitude images using library programs written in the Semper image processing language (Saxton et al. 1979). The amplitude images were used to calculate normalised thickness (t/λ) maps of the specimen for each tilt angle. Figure 2c shows the t/λ map corresponding to the hologram in Fig. 2a, and Fig. 2d plots the variation in t/λ over the entire tilt range showing that a number of points lie away from the line of expected thickness variation. This variation may indicate that the specimen is in a strongly diffracting condition, which affects the measured phase and amplitude images, complicating the interpretation of the observed phase image. Such images were therefore excluded from the tomographic dataset used for 3-D reconstruction. At the specimen edge, a number of 2π phase 'wraps' are often present due to the abrupt thickness change present at the edge of the FIB-prepared specimen. These 'wraps' can lie directly on top of one another, preventing accurate phase unwrapping. In order to overcome this issue, the expected phase change was calculated (from the mean inner potential and thickness measurements) and used to determine the number of 2π wraps

present at the edge region. The phase in the specimen region in each reconstructed image was then adjusted to the corrected value.

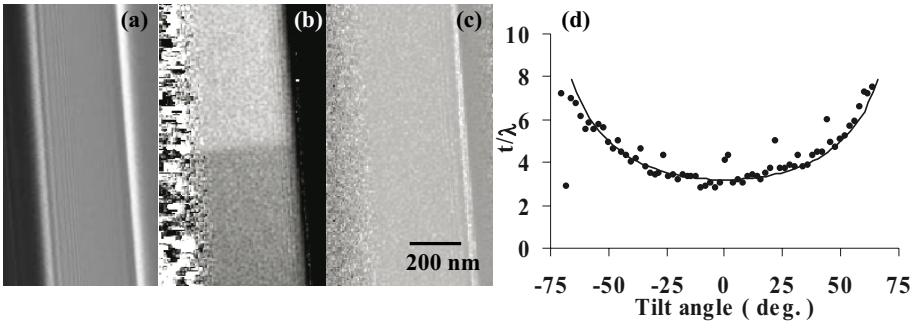


Fig. 2: (a) Off-axis electron hologram, (b) corresponding reconstructed phase image and (c) thickness (t/λ) map acquired at 0° tilt of the FIB-prepared silicon *p-n* junction. (d) Plot of the variation in thickness (t/λ) as a function of tilt angle. The solid line indicates the expected variation in thickness with tilt angle. The points lying away from the line indicate that the image is significantly affected by diffraction contrast. The corresponding images are excluded from the tomographic reconstruction.

From Fig. 2a, it can be seen that the original holograms do not contain any distinguishable features other than the interface between the specimen and the vacuum. The images were aligned using the interface to obtain a rotational and horizontal alignment, and using the junction position to align the images in the vertical direction. The simultaneous iterative reconstruction technique (SIRT) was used to reconstruct the 3-D electrostatic potential in the specimen. The thickness was constrained in the reconstruction to 380 nm (from the t/λ and CBED measurements) because the featureless membrane surfaces cannot be reconstructed accurately with the restricted tilt range due to the 'missing wedge' of information.

3. RESULTS AND DISCUSSION

A schematic diagram showing the expected electrostatic potential variation is shown in Fig. 3a, illustrating the amorphous and crystalline electrically inactive surface layers deduced previously (Twitchett et al 2004). The experimentally determined 3-D reconstructed electrostatic potential of the *p-n* junction, which is shown in Fig. 3b, can be observed qualitatively to show a comparable potential distribution to the expected variation. The voxel size in the reconstruction is 5.8 nm and the spatial resolution is 10 nm based on the Crowther equation (Crowther et al 1970). The phase resolution is 0.1 rad. (Lichte 1991). This 3-D data set can be used to extract information about the specimen, including line profiles across the *p-n* junction close to the centre and at the surfaces of the specimen. The tomographic reconstruction software re-scales the phase data automatically, and therefore the extracted experimental profiles have been adjusted such that the central profile (extracted from the 3-D dataset with a width of one voxel) matches the expected phase variation for bulk silicon. The potential variation indicated in Fig. 3b is only the dopant-related electrostatic potential, although the absolute value of the potential (relative to vacuum) can be used to determine the value of the mean inner potential (V_0). Theoretical line profiles, taken from simulations described elsewhere (Somodi et al 2003) are shown in Fig. 2c. Corresponding experimental line profiles are shown in Fig. 2d. These line profiles show good correlation between simulations and experimental results, indicating a significant increase in depletion width and a reduction in potential variation across the junction close to the membrane surfaces, due in part to the damage caused by FIB milling. Further simulations are required to model the point defects and amorphous layers present to provide a fully quantitative understanding of the potential at FIB-prepared sample surfaces. However, this preliminary result indicates that the near-surface layers of thin FIB-prepared membranes can make up a significant fraction of a TEM specimen, and must be considered carefully to provide a quantitative understanding of dopant potentials in semiconductor devices.

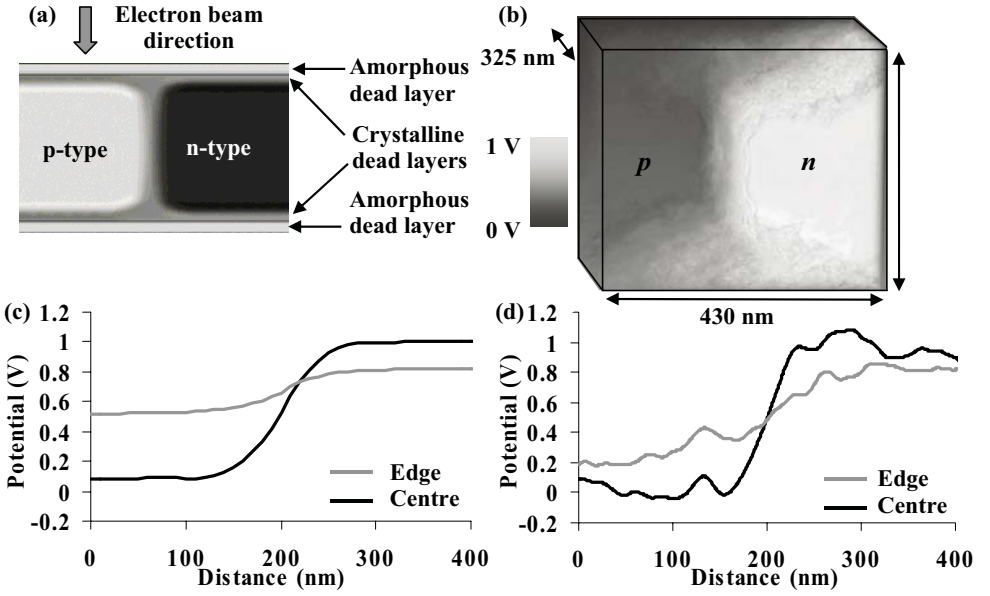


Fig. 3: (a) Schematic diagram showing the expected electrostatic potential variation in an FIB-prepared membrane containing a *p-n* junction. (b) Corresponding experimental 3-D electrostatic potential obtained using electron tomography. (c) Line profiles from the simulation of the expected electrostatic potential. (d) Experimental line profiles extracted from the centre and the edge of the tomographic reconstruction, showing the variation in electrostatic potential across the *p-n* junction.

4. CONCLUSIONS

Off-axis electron holography and tomography have been combined successfully to reconstruct the 3-D potential in a silicon FIB-prepared *p-n* junction device. The 3-D reconstruction provides information about the mean inner potential and dopant-related potential at any position in a thin specimen. Further work is required to optimise the tomographic reconstruction procedure to ensure a fully quantitative 3-D potential. This information could also be combined with an iterative reconstruction approach to use *ab initio* simulations to deduce the structures of the surface layers. Holographic tomography is a very promising technique for the quantitative examination of the 3-D electrostatic potential in semiconductor devices.

ACKNOWLEDGEMENTS

The authors would like to thank Dr R F Broom for his assistance and advice, Philips Research Laboratories (Eindhoven) for providing the silicon device and Newnham College, the Royal Society and the EPSRC for financial support.

REFERENCES

Crowther T A, DeRosier D J and Klug A 1970 Proc Roy Soc Lond **A317**, 319

Lichte H 1991 Ultramicroscopy **38**, 13

McCartney M R, Gribelyuk M A, Li J, Ronsheim P, McMurray J S and Smith D J 2002 Appl Phys Lett **80**, 3213

Midgley P A and Weyland M 2003 Ultramicroscopy **96**, 413

Rau W D, Schwander P, Baumann F H, Hoppner W and Ourmazd A 1999 Phys Rev Lett **82**, 2614

Somodi P K, Dunin-Borkowski R E, Twitchett A C, Barnes C H W and Midgley P A 2003 Inst Phys Conf Ser **180**, 501

Twitchett A C, Dunin-Borkowski R E, Hallifax R J, Broom R F and Midgley P A 2005 Microsc. Microanal. **11**, 66

Ab initio computation of the mean inner Coulomb potential for technologically important semiconductors

M Schowalter, A Rosenauer, D Lamoen[1], P Kruse[2] and D Gerthsen[2]

Institut für Festkörperphysik, Universität Bremen, 28359 Bremen, Germany
[1] Departement Fysica, Universiteit Antwerpen, 2020 Antwerpen, Belgium
[2] Laboratorium für Elektronenmikroskopie, Universität Karlsruhe, Germany

ABSTRACT: We computed the mean inner Coulomb potential for a variety of technologically important cubic and hexagonal type II-VI, III-V and group IV semiconductors with (1-10) surfaces and (11-20) surfaces, respectively. To take into account the redistribution of electrons due to the bonds of the atoms in a crystal, we carried out *ab initio* computations within the density functional theory (DFT) formalism. From the DFT computation, the Coulomb potential of crystal slabs with adjacent vacuum regions was derived and averaged within the crystal region yielding the mean inner Coulomb potential.

1. INTRODUCTION

The mean inner Coulomb potential (MIP) plays an important role in off-axis electron holography. For example, internal electrical fields, such as piezoelectric fields in strained InGaN/GaN quantum wells, can be measured accurately, if values of the mean inner Coulomb potentials of the involved materials are known (Cherns et al 1999). Cherns et al (1999) stated that the accuracy of the measurement strongly depends on the accuracy of the MIP. Another application is the measurement of the specimen thickness by measuring the phase shift $\Delta\Phi$ between electrons passing the specimen in vacuum and electrons traversing the specimen using electron holography (Rosenauer et al 2001). To derive the specimen thickness the relation $\Delta\Phi = C_E V_0 t$ is exploited, where t is the specimen thickness, V_0 is the MIP and C_E is a constant that only weakly depends on the acceleration voltage. The accuracy of the thickness measurement depends mainly on the accuracy of the MIP.

However, there are not many experimental values of the MIP for II-VI and III-V semiconductors and results are sometimes inconsistent. For example, for ZnS values of 10.2±0.5 and of 12.2 V were found by Buhl (1959) and Kikuchi and Nakagawa (1936), respectively. The MIP of GaAs was measured by Gajdardziska-Josifovska et al (1993) and Kruse et al (2003). They found values of 14.53±0.17 V and 14.18±0.20 V. Otherwise, in electron microscopy MIPs are typically calculated in the isolated atom approximation. In this approximation, the MIP is derived from atomic scattering factors f_j in the forward direction computed for isolated atoms. Such values were tabulated for many atoms by Doyle and Turner (1968), for instance. The MIP in the isolated atom approximation then is given by

$$V_0 = \frac{h^2}{2\pi meV} \sum_j n_j f_j(0) \qquad (1)$$

where h is Plank's constant, V is the volume of the unit cell, m and e are the mass and the charge of an electron and n_j is the number of atoms of type j. Using formula (1) and the atomic scattering factors from Doyle and Turner (1968) yield a MIP of GaAs of 15.27 V. This strongly deviates from the latest values of Kruse et al (2003).

The discrepancy between experimental values and values derived in the isolated atom approximation using equation (1) occurs because, in the isolated atom approximation, the redistribution of electrons due to the bonds of the atoms is neglected (Kim et al 1998). Kim et al

(1998) also showed that the redistribution of charge can be taken into account by *ab initio* computations within the density functional theory (DFT) formalism. In this work we compute the MIP of technologically important cubic and hexagonal type II-VI, III-V and group IV semiconductors using the DFT formalism.

2. THEORY

The MIP V_0 is defined as the zero Fourier component of the Coulomb potential $V_c(\mathbf{r})$ and can be written as

$$V_0 = \frac{1}{V_{\text{cryst}}} \int d^3 r V_c(\vec{r}) \tag{2}$$

where V_{cryst} is the volume of the crystal; the integration runs over the finite crystal and the zero point of the Coulomb potential is chosen in the vacuum at infinite distance from the crystal. High energy electrons typically used in transmission electron microscopy are scattered by the Coulomb potential only. Exchange and correlation effects between electrons of the electron beam and electrons of the specimen can be neglected for electron energies larger than 10keV (Saldin et al 1994). The definition above avoids ambiguities due to the freedom of choice of the zero point of the Coulomb potential and reflects the experimental situation, where an electron starts from far away from the specimen and traverses the specimen. Because of the long range nature of the Coulomb interaction, the MIP may depend on the type of surface of the crystal slab (Kim et al 1998).

The Coulomb potential of a crystal slab can be computed very accurately by *ab initio* computations within the DFT formalism. For that purpose, the Kohn-Sham equations (Kohn and Sham 1965) and the Poisson equation have to be solved self-consistently yielding the charge distribution and the Coulomb potential inside the crystal slab. In order to apply equation (2) to the computed Coulomb potential, the zero point of the Coulomb potential has to be set unambiguously and therefore DFT computations have to be carried out on cells where the crystalline slabs are surrounded by vacuum regions in one direction.

3. COMPUTATIONAL DETAILS

A typical cell of sphalerite type ZnS is shown in Fig. 1a. The cell consists of 6 monolayer (ML) ZnS and a vacuum region of about 0.5 nm. Coulomb potentials of such cells were computed using the full-potential-(linearized)-augmented-plane-wave+local orbitals ((L)APW+lo) code WIEN2k (Blaha et al 2001), which uses periodic boundary conditions. In this code the potential as well as the wave functions are described inside a sphere with radius R_{MT} (muffin-tin radius) around the atom positions by a series of spherical harmonics and outside the spheres by plane waves. For the computations the muffin-tin radii were set to nearly touching spheres and the plane wave vector cut-off K_{max} outside the muffin-tin spheres was set in such a way that $R_{MT}K_{max}=7.0$. The generalized gradient approximation (GGA) of Perdew et al (1996) was used as the exchange and correlation part of the potential within the Kohn-Sham equations.

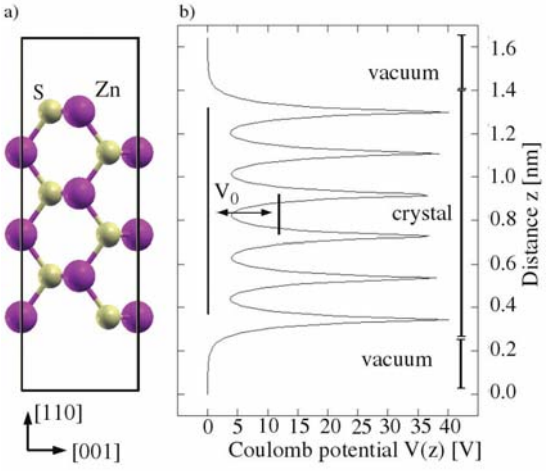


Fig. 1: a) ZnS slab used for the computation of the MIP. b) The computed Coulomb potential averaged in (110) planes plotted versus the distance in [110] direction.

The Coulomb potential computed using the WIEN2k code is averaged in planes parallel to the surfaces of the crystal slab yielding a profile of the Coulomb

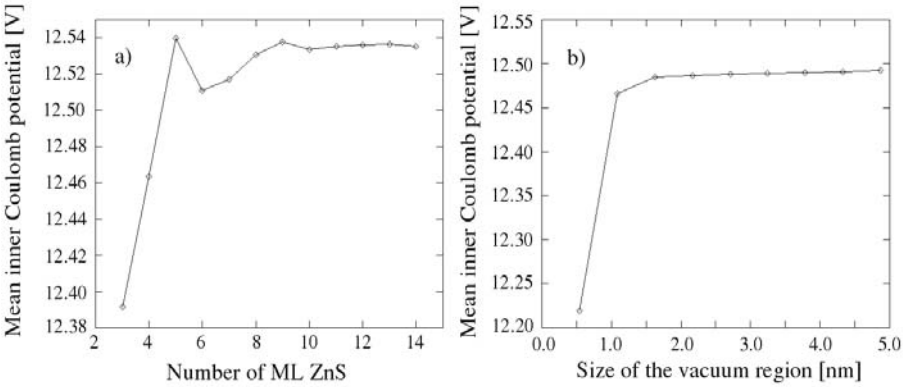


Fig. 2: a) The MIP of ZnS as a function of ML computed for cells with 0.496 nm vacuum. b) The MIP of ZnS as a function of the size of the vacuum region computed for cells with 3 ML ZnS.

potential. The profile corresponding to the cell in Fig. 1a is depicted in Fig. 1b. The maxima of the profile correspond to the positions of the atoms. The MIP is derived by averaging the Coulomb potential within the innermost ML of the slab for the interstitial region between the muffin-tin spheres and taking the Y_{00} components of the spherical harmonics series inside the muffin-tin spheres.

In order to ensure that the we deal with a "bulk" sample, the convergence of the MIP with respect to the number of ML material has to be checked. Fig. 2a depicts the MIP as a function of the number of MLs ZnS. It shows that 11 ML ZnS is enough to converge the MIP. In Fig. 2b the MIP is shown as a function of the size of the vacuum region. In order to ensure that the zero point of the Coulomb potential is set correctly, the size of the vacuum region has to be larger than 1.5 nm. Further computations in this paper are carried out for unpolar slabs with (110) surfaces for cubic materials and (11-20) surfaces for hexagonal materials consisting of 11 ML material and 1.5 nm vacuum.

4. RESULTS AND DISCUSSION

Material	MIP [V]
AlN	15.88
GaN	16.89
InN	18.9
ZnO	15.75
CdO(LDA)	17.26
CdO(GGA)	15.73

Tab. 1: MIP of hexagonal II-VI and III-V semiconductors. For CdO MIPs were computed using LDA or GGA lattice parameters.

Ab initio computations of structures described in the previous section were carried out using the generalized gradient approximation (GGA) (Perdew et al 1996). It was shown before that the choice of the exchange and correlation potential in the Kohn-Sham equations only slightly influences the value of the MIP (Schowalter et al 2004). With the exception of CdO, the crystalline slabs were generated taking the experimental lattice parameter of the semiconductor materials instead of lattice parameters computed from *ab initio* methods (for CdO: a_{GGA}=0.3645 nm, c_{GGA}=0.5909 nm; a_{LDA}=0.3542 nm,c_{LDA}=0.57321 nm). *Ab initio* lattice parameter exhibit the tendency to be approximately 1-2% too small or too large depending on the approximation used for the exchange and correlation potential. According to Eq. (1), the computation of the MIP using lattice parameters, which are slightly off, yields MIPs, which are too large or too small (Schowalter et al 2004), respectively. Tab. 1 lists the MIP of hexagonal type semiconductors. The MIPs of CdO were computed from lattice parameters calculated by DFT using the local density approximation (LDA) and the GGA. The MIP computed from LDA lattice parameter is larger than the MIP computed from GGA lattice parameter, because the LDA lattice parameter is smaller than the GGA lattice parameter. A difference of about 3% in lattice parameter yields the difference of about 27% in the MIPs according to Eq. (1).The influence of the redistribution of charge due to the bonds of the atoms in the crystal can be seen from the values in Tab. 2. One column shows MIPs computed by our DFT approach using the GGA for the exchange

Material	MIP(DFT)	MIP(EXP)
AlN	14.23	
GaN	16.82	
InN	17.35	
AlP	11.39	
GaP	13.63	14.38±0.12
InP	13.90	14.53±0.07
AlAs	12.34	
GaAs	14.19	14.24±0.08
InAs	14.34	14.50±0.08
AlSb	12.89	
GaSb	14.45	14.08±0.05
InSb	14.28	
Si	12.57	12.52±0.71
Ge	14.67	

Tab 3: Theoretical ("MIP(DFT)") and experimental ("MIP(EXP)") values of the MIP of cubic III-V and group IV semiconductors in Volts. Experimental values measured by a state-of-the-art measurement technique were taken from Kruse et al (2003).

Material	MIP(DFT) [V]	MIP(IAA) [V]
ZnS	12.64	13.56
CdS	13.08	13.96
ZnSe	13.19	13.96
CdSe	13.26	13.99
ZnTe	13.82	13.50
CdTe	13.67	13.50

Tab. 2: MIP of cubic II-VI semiconductors computed from DFT computations (DFT) and in the isolated atom approximation (IAA).

and correlation part of the Kohn-Sham potential, whereas the other column ("MIP(IAA)") shows MIPs computed using Eq. (1) and atomic scattering factors from Doyle and Turner (1968). In most cases the isolated atom approximation overestimates the MIP, especially for semiconductors containing lighter elements.

To check the accuracy of the computed values, the MIP of III-V and group IV semiconductors are compared with experimental values of Kruse et al. (2003) in table 3. The experimental values were measured using an accurate state-of-the-art measurement technique. The theoretical values only slightly deviate from experimental values, but show a better agreement than values computed in the isolated atom approximation.

5. CONCLUSIONS

We computed the MIP for a variety of technologically important cubic and hexagonal III-V, II-VI and group IV semiconductors. The values are in better agreement with experimental values measured by Kruse et al (2003) than values computed in the isolated atom approximation.

REFERENCES

Blaha P, Schwarz K, Madsen G K H, Kvasnicka D and Luitz J 2001 ISBN 3-9501031-1-2
Buhl R1959 Zeitschrift für Physik **155**, 395
Cherns D, Barnard J and Ponce FA 1999 Solid State Commun. **111**, 281
Doyle P and Turner P 1968 Acta Cryst. A **24**, 390
Gajdardziska-Josifovska M, McCartney M R, de Ruijter W J, Smith D J, Weiss J K and Zuo J M 1993 Ultramicroscopy **50**, 285
Kikuchi S and Nakagawa S 1936 Zeitschrift für Physik **88**, 757
Kim M Y, Zuo J M and Spence J C H 1998 phys. stat. sol. a **166**, 445
Kohn W and Sham L J 1965 Phys. Rev. **140**, A1133
Kruse P, Rosenauer A and Gerthsen D 2003 Ultramicroscopy **96**, 11
Perdew J P, Burke K and Ernzerhof M 1996 Phys. Rev. Lett. **77**,3865
Rosenauer A, Gerthsen D, Van Dyck D, Arzberger M, Böhm M and Abstreiter G 2001 Ultramicroscopy **51**, 11
Saldin D K and Spence J C H 1994 Ultramicroscopy **55**, 397
Schowalter M, Lamoen D, Rosenauer A, Kruse P and Gerthsen D 2004 Appl. Phys. Lett. **85**, 4938

Part V

Self-Organised and Quantum Domain Structures

Electron beam induced deposition of position and size controlled structures on the nanometre scale

K Furuya, K Mitsuishi, M Shimojo, M Song, M Tanaka and M Takeguchi

National Institute for Materials Science, 3-13 Sakura, Tsukuba, Ibaraki 305-0003, Japan

ABSTRACT: Electron beam induced deposition (EBID) was carried out with gas introduction systems attached to field emission scanning and transmission electron microscopes (FE-SEM and FE-TEM). Using tungsten and iron carbonyl, arrays of dots and three dimensional structures were fabricated in the range of 1 to 20 nm in diameter. Post-deposition annealing of iron nanostructures resulted in the formation of crystalline alpha-iron and iron carbide phases.

1. INTRODUCTION

As compared with the photolithographic process, focused beam induced fabrication is one of the promising techniques, because of the size and position controllability, and of the high resolution resulting from its short wavelength. The maskless patterning by both deposition and lithography becomes possible when organic or metal-organic gases are introduced in the beam irradiated area.

One problem is the minimum size of patterns. A focused ion beam (FIB) was first used, but the deposits were in a range of several 100 nm due to the probe size. Electron beam induced deposition (EBID) has mainly been performed with scanning and transmission electron microscopes (SEMs and TEMs) (Koops 1988, Matsui 1988). The smallest structures fabricated have a typical width of 15-20 nm, no matter how small the primary electron beam is. This is believed to be due to the spread of secondary electrons more than 15 nm in diameter, rather than primary electrons. However, we have tried to minimize the size by reducing this effect with ultra high vacuum field emission (UHV-FE) SEM and TEM (Mitsuishi 2003, Tanaka 2004, Shimojo 2004, Takeguchi 2004), which can produce more focused beams under very low gas pressure.

Another problem is the structure of the deposits. At room temperature, an amorphous phase and/or a mixture of nanocrystals were usually formed with a considerable amount of carbon when metal carbonyl gases such as $W(CO)_6$ and $Fe(CO)_5$ were used. They cannot be low electric-resistivity materials. Steady electric and magnetic properties can appear in well-defined phases, which are likely to be crystalline structures with specific stoichiometry. Hence, composition and crystallinity of the nanometre-sized deposits are important issues.

In the present study, we report the importance of not only the probe size but also the partial pressure of the precursor gas for the resolution limit of EBID, and of the post-deposition heat treatment to obtain a crystalline phase.

2. EXPERIMENTAL

Two types of gas introduction systems were newly developed. Both consist of an external variable leak valve, a gas nozzle which is about 1mm in diameter, and a heating system. Schematic drawings attached to the 200 keV UHV-FE-TEM and 30 keV UHV-FE-SEM are illustrated in Fig. 1a and 1b, respectively (Tanaka 2004, Shimojo 2004). The microscopes were evacuated by sputter ion pumps to $1x10^{-7}$ Pa. The end of the nozzle is located at the position about 3 mm off the vertical and 5 mm off the horizontal from the sample center. Each source has a stop valve, and can be evacuated separately by a turbo molecular pump for rough pumping. This system makes it simple and easy to

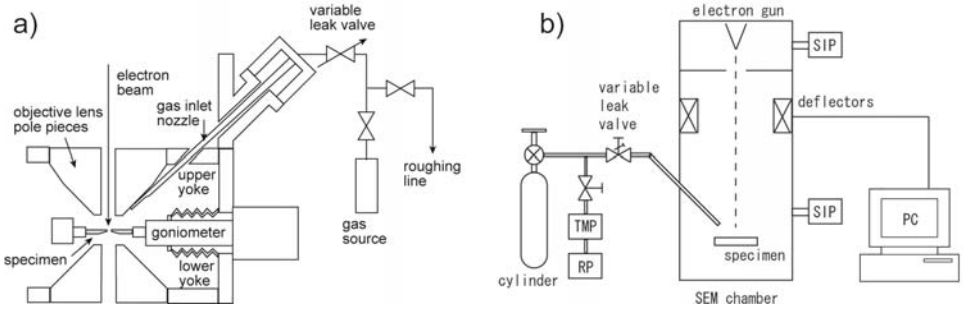


Fig. 1. Schematic illustrations of the microscope and the gas inlet system. a) for ultra high vacuum field emission transmission electron microscope (UHV-FE-TEM) and b) for ultra high vacuum scanning electron microscope (UHV-FE-SEM)

change precursors for each experiment. Various precursors, solids, liquids and gases can be attached to the system.

The substrates used in this study were carbon grids and Si (111) thin films. The EBID was done at room temperature with the precursor gases of $W(CO)_6$ and $Fe(CO)_5$ under a pressure of about $1x10^{-6}$-$1x10^{-4}$ Pa. The electron beam intensity used was about $5x10^3$-$5x10^4$ A/cm^2 and the probe size was about 1-2 nm with TEM and 2-5 nm with SEM.

3. RESULTS AND DISCUSSION

The effect of partial pressure (namely, the flow rate) of precursor gas was precisely examined with UHV-FE-TEM with the precursor gas $W(CO)_6$. Figure 2 shows typical TEM photographs of lines and an array of the nano-dots by changing pressure of the precursor using a 2 nm-sized probe. The size of the dots becomes smaller as the partial pressure decreases from about $1x10^{-5}$, $5x10^{-6}$ to $2x10^{-6}$ Pa for a deposition time of about 10 s. In Fig. 2a, the average dot size is about 5 nm, while in Fig. 2b and 2c, they are about 4 nm and 3 nm, respectively. The enlarged image of the dots in Fig. 2d shows the lattice fringes of the Si substrate to calibrate the actual size of the dot at about 2.4 nm. Interestingly, we could seldom observe dot-formation with a partial pressure of less than $1x10^{-6}$ Pa, regardless of the beam intensity. We infer that there is a critical partial pressure for dot fabrication although there is a possibility that the nano-dots were too small to distinguish.

Figure 3 shows an array of dots formed with a 1nm probe and a deposition period of 5s. The

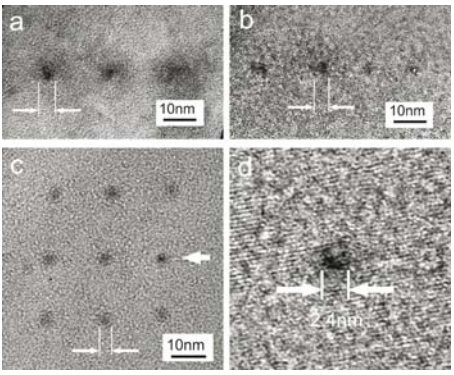


Fig. 2. The partial pressure dependence of the nano-dot size by EBID. a) Dots formed with $1x10^{-5}$ Pa, b) $5x10^{-6}$ Pa, c) $2x10^{-6}$ Pa, and d) one of the dots in c) with a size of 2.4nm.

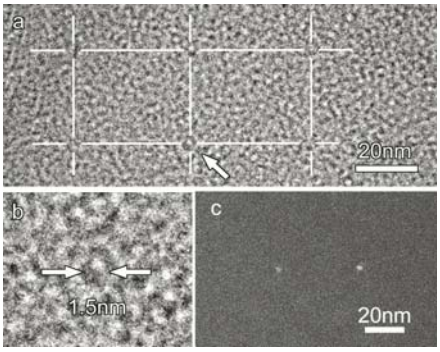


Fig. 3. An array of the smallest W nano-dots by EBID. a) TEM image of the array, b) a magnified image of a dot by an arrow in a), and c) corresponding HAADF-STEM image.

dots are located in the intersecting points of the white lines, but it is hard to distinguish them from the amorphous substrate. One of the dots is enlarged in Fig. 3b. The size of the dot should be about 1.5 nm, which, we believe, is a record size ever made by the EBID. To prove their existence, high angle annular dark field (HAADF) STEM images were taken and shown in Fig. 3c. Since HAADF-STEM produces Z-contrast images, i.e., a heavy atom makes a brighter contrast, W atoms can be easily distinguished from Si atoms. The distance between the dots and the size of the dots almost match our estimation. Hence it is pointed out that they are the nano-dots.

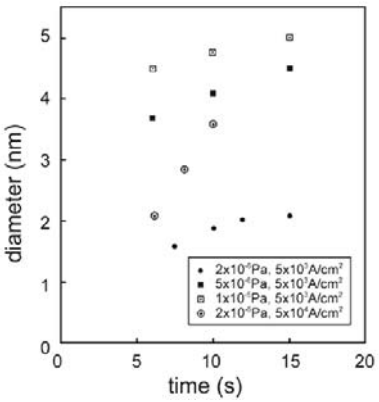


Fig. 4. The relation between the dot-size and the irradiation time as a function of the partial pressure.

The dependence of the dot-size upon partial pressure and deposition time is summarized in Fig. 4. The tendency is obvious: the better the vacuum, or the shorter the time, the smaller the dot. For a current density of $5x10^3$ A/cm^2, the partial pressure dependence is more apparent. For a gas pressure of $2x10^{-6}$ Pa, the current density dependence is also shown. The smallest dot size is about 1.5 nm with 5 s deposition at $1.5x10^{-6}$ Pa with a 1 nm probe. To our knowledge, this is the smallest record ever made by EBID.

Nanodots, nanorods and free-standing square-shaped frames were fabricated by EBID in the UHV-FE-SEM with the precursor gas $Fe(CO)_5$, and the structures were examined with UHV-FE-TEM. Figure 5a shows a TEM image of nanostructures formed on a carbon grid film at room temperature. The nanorods were fabricated by moving the beam from the edge to vacuum at a speed of 2 nm/s. Subsequently, square-shaped frames were also fabricated on the top of a nanorod in a

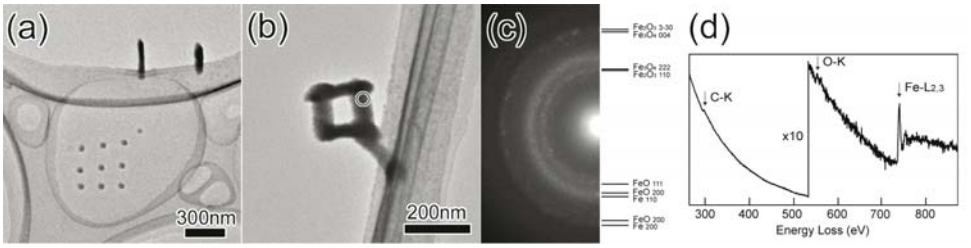


Fig. 5. TEM images of a) nanodots and nanorods, b) a free-standing square-shaped frame produced from $Fe(CO)_5$ gas, c) electron diffraction pattern taken at a circle in b) and d) EELS spectrum from the same area as c).

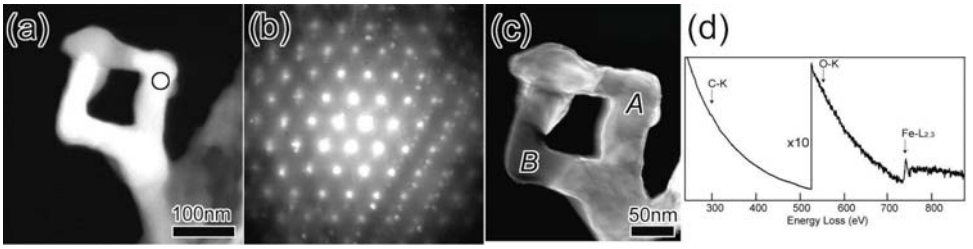


Fig. 6. a) A HAADF-STEM image of the free-standing square frame from $Fe(CO)_5$ gas after a heat treatment at about 873 K for 1 h, b) electron diffraction pattern taken at the circle in a), showing the formation of an alpha-iron phase, c) dark field TEM image of the square frame, showing grain structures and d) EELS spectrum from the same area as b).

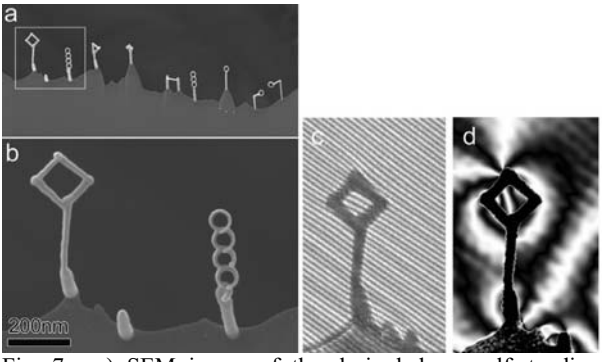


Fig. 7. a) SEM image of the desired-shape self-standing nanostructures on a thin silicon substrate by EBID with $Fe(CO)_5$ at room temperature, b) an enlarged image in a flame in a), c) electron hologram and d) reconstructed phase (interference) image in b). Phase was amplified by 4 times.

similar manner. Figure 5b shows a TEM image of a typical square frame structure. The line widths of the rods and the frames are 30-50 nm. The diffraction pattern (Fig. 5c) and the electron energy loss spectrum (EELS) (Fig. 5d) from the region in the circle in Fig. 5b indicate that the free-standing rods and frames were composed of iron, carbon and oxygen, and that the diffraction indices and corresponding ring positions are in agreement with that of alpha-iron and possible iron oxides. Iron carbides were excluded for the present as-deposited structures as reported elsewhere (Sethuraman 1994). Hence, it is deduced that some faint polycrystalline-like rings were from the iron oxide nanocrystals existing near the surface and broad rings were from the amorphous phases on the inside.

After a heat treatment at about 873 K for 1 h, the surface oxide layers disappeared and the free-standing nanorods and frames transformed into single crystal or polycrystalline phases. Figure 6a shows a HAADF-STEM image of the square frame after heating. The diffraction pattern is shown in Fig. 6b. This is identical to that of alpha-iron, taken near the <111> zone axis. A dark field TEM image indicated in Fig. 6c clearly exhibits the grain structure in the square-shaped frame. The grains labeled *A* and *B* in the figure were of an alpha-iron phase with different crystallographic orientation, but others were of iron carbide phases. Oxygen and carbon were hardly detected in EELS taken from the grains *A* and *B*, as is shown in Fig. 6d. Alpha-iron grains were formed only in the free-standing nanorods and frames. Some nanorods and frames were transformed into crystalline iron carbides such as Fe_3C, Fe_5C_2, Fe_7C_3, and Fe_2C (Takeguchi 2004).

Figures 7a and 7b show an SEM image and its enlargement of variously shaped free-standing iron nanostructures formed on a Si edge at room temperature. Their line width was 30-50 nm. After transferring the specimen to the TEM, electron holography was employed to characterize their magnetic properties. The magnetization of the structures was made by introducing the specimen into the magnetic field of the objective lens of the TEM with a flux density of about 2 T and tilted about 30^o. The component of the magnetic field parallel to the rod growth direction is calculated to be about 1 T. After that, the objective lens was turned off, and then the residual magnetic field is estimated to be less than 100mT. This magnetic field produced an electron hologram for the nanostructures in Fig. 7c. Reconstructing it digitally by a computer, a phase image was obtained and shown in Fig. 7d as a COS intensity (so-called "interference micrograph"), where the phase was amplified 4 times. The spacing of the dark lines corresponds to a phase shift of 1.57 rad, which corresponds to a magnetic flux of 1.03×10^{-15} Wb. It is found that magnetic fields were leaking from the nanostructure body and the whole was likely to be one 'nano-magnet' because of the square and ring shapes.

REFERENCES

Koops H W P, Weiel R, Kern D P and Baum T H 1988 J. Vac. Sci. Technol. B **6**, 477

Matsui S and Ichihashi T 1988 Appl. Phy. Lett. **53**, 842

Mitsuishi K, Shimojo M, Han M and Furuya K 2003 Appl. Phys. Lett. **83**, 2064

Sethuraman A R, Stencel J M, Rubel A M, Cavin B and Hubbard C R 1994 J. Vac. Sci. Technol. A **12**, 443

Shimojo M, Takeguchi M, Tanaka M, Mitsuishi K and Furuya K 2004 Appl. Phys. A **79**, 1869

Takeguchi M, Shimojo M, Mitsuishi K, Tanaka M and Furuya K 2004 Superlattices and Microstructures **36**, 255

Tanaka M, Shimojo M, Mitsuishi K and Furuya K 2004 Appl. Phys. A **78**, 543

The structure of coherent and incoherent InAs/GaAs quantum dots

D Zhi, M J Hÿtch[1], R E Dunin-Borkowski, P A Midgley, D W Pashley[2], B A Joyce[3] and T S Jones[4]

Department of Materials Science and Metallurgy, University of Cambridge, Pembroke Street, Cambridge CB2 3QZ, UK
[1] Centre d'Etudes de Chimie Metallurgique, CNRS, 15 rue G. Urbain, 94407 Vitry-sur-Seine, France
[2] Department of Materials, Imperial College, London SW7 2AZ, UK
[3] Department of Physics, Imperial College, London SW7 2AZ, UK
[4] Department of Chemistry, Imperial College, London SW7 2AZ, UK

ABSTRACT: During the heteroepitaxial growth of semiconductors, misfit-induced strain causes various growth and relaxation phenomena. These include the formation of islands or dots (elastic relaxation of pseudomorphic misfit strain) and the formation of dislocations preferentially at sites of high strain. We have studied strain relaxation in InAs/GaAs quantum dots (QDs). Due to strain-induced renormalization of the surface energies of their facets, an array of QD islands with uniform size and shape can be formed. With increased InAs coverage, incoherent QDs start to form, and the samples with both coherent and incoherent QDs can exhibit bimodal size distributions, with coherent strained QDs that are smaller than incoherent plastically-relaxed QDs. The transition point was determined by both plan-view and cross-sectional transmission electron microscopy (TEM). In the region where two types of QDs coexist, coalescence may occur between adjacent dots and the larger QDs grow at the expense of smaller QDs. By means of both high-resolution transmission electron microscopy (HRTEM) and the measurement of the displacement field of a QD, we have established that misfit dislocations start to form at the QD edge at the beginning of the coherent/incoherent QD transition. Misfit relaxation in large QDs is then accommodated by the generation of misfit dislocation arrays (plastic relaxation), and also by the distortion of lattice planes (elastic strain relaxation).

1. INTRODUCTION

The formation of semiconducting quantum dots in lattice-mismatched heterostructures has been extensively studied in recent years. One of the major problems in the heteroepitaxial structures is that the lattice mismatch between the epitaxial layer and its substrate may introduce misfit dislocations at the interfaces in order to relieve the misfit strain. The phenomenon of strain relaxation in hetroepitaxial InGaAs/GaAs films has been extensively studied earlier (Zou et al 1994). The formation of 3D nano-sized epitaxial islands via the Stranski- Krastanow (S-K) growth mode as the result of strain energy accumulation as well as other complex physical reasons like surface reconstruction and elemental surface segregation has now been employed as the way for self-assembly of the quantum dot structures.

In the self-assembly of InAs/GaAs quantum dots, the 2D-3D transition was observed to happen at the deposition of 1.7-1.8 monolayers (MLs) of InAs, as evidenced by atomic force microscopy (AFM) and scanning tunnelling microscopy (STM) (Joyce et al 1998). When the InAs deposition amount increases, the strain in the QD layer is accumulated. To accommodate or minimise the strain energy in the system, certain strain relief mechanisms should function in general, such as reorganisation of the shape of QDs and the introduction of misfit dislocations. If all the other growth

parameters were kept constant, then a growth series with increased InAs coverage from the critical amount will represent complete QD formation and structural evolution process. In this paper, we systematically investigate the structure of coherent and incoherent InAs QDs formed on GaAs(001) at different InAs coverage. The morphology and structure of these QDs are characterised using both plan-view and cross-sectional transmission electron microscopy (TEM).

2. EXPERIMENTAL

The QD samples were grown in a combined MBE-STM growth system that is also equipped with reflection high energy electron diffraction (RHEED) for in *situ* monitoring of growth mode change. The indium, gallium and arsenic cells were calibrated using RHEED oscillation on InAs (001) and GaAs (001) respectively. After initial thermal cleaning at 300 ºC, the native oxide layer was removed under As_2 flux at 620ºC. A 0.6 μm thick GaAs buffer layer was grown at 580 ºC and the substrate temperature reduced to 510 ºC for the deposition of 300Å of GaAs. InAs was then deposited at a growth rate of 0.016 MLs^{-1} and the InAs coverage ranged from 1.75 to 3.8 monolayers.

In similar fashion to our previous TEM study (Zhi et al 2001, 2004), the plan-view and cross-sectional specimens for TEM were produced using conventional sample preparation techniques, involving mechanical thinning followed by ion-milling using Ar^+ at 3-5 keV. Thinned specimens were examined using a JEOL 2010 TEM operating at 200 kV. A geometric phase technique is also applied to analyse the HRTEM images of the QDs in order to measure their displacement fields (Hÿtch et al 2003).

3. RESULTS AND DISCUSSIONS

The formation of QDs was observed by TEM in the QD samples with the InAs coverage larger than 1.7ML. Figure 1a shows a plan-view bright-field TEM image of the QD sample with 1.75 ML InAs coverage. The image was taken under Laue diffraction conditions and along the [001] direction. The detailed structure of the above QDs formed at 1.75 ML indium coverage was then observed by the cross-sectional HRTEM lattice image, as illustrated in Fig. 1b. The defect-free coherent QD was found to form at a surface step with a height difference of about two MLs. Although from TEM observation it is not clear when and how the observed step is formed, the surface steps produced by the 2D growth mode earlier at lower InAs coverage facilitate QD formation by creating more nucleation sites.

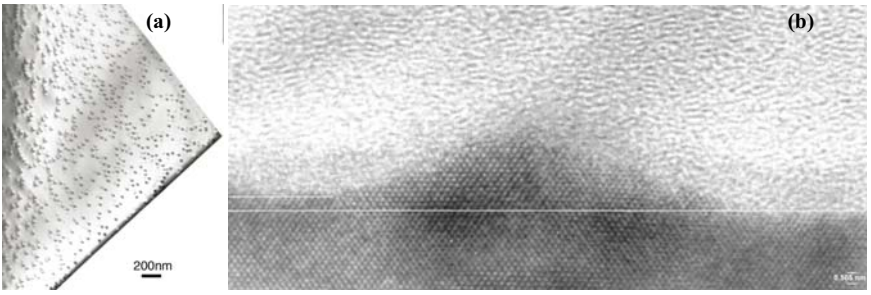


Fig. 1. (a) [001] zone axis bright-field plan-view TEM image of uncapped QDs grown with 1.75 ML InAs deposited at a growth rate of 0.016 MLs^{-1}. (b) [110] zone axis HRTEM image of an uncapped QD grown with 1.75ML InAs deposited at a growth rate of 0.016 MLs^{-1}.

Figure 2a shows a typical on-zone plan view TEM image taken from the QD sample with 2.2ML of InAs coverage, which shows the uniform, dense, coherent QDs present on the surface. These QDs are uniformly distributed and isolated from each other. The QD density was found to increase with the InAs coverage and reaches a maximum with an InAs coverage of 2.2ML. Both plan

view and cross-sectional TEM images from these samples also show the increase of QD diameter with the InAs coverage increasing from 1.75ML to 2.2ML. From the above TEM images, only one type of QD, i.e. coherent strained QDs, was observed from the sample with InAs coverage ranging from 1.75 to 2.2ML. It was also observed that these coherent InAs QDs have a uniform size distribution. For InAs coverages over 2.4 ML, however, it was found that the QDs adopt a bimodal distribution of size and the QD number density begins to decrease. This bimodal QD distribution can be observed by plan-view TEM, as shown in Fig. 2b. Two types of QD can then be distinguished for the QD samples with InAs coverages over 2.4 ML, i.e. small coherent strained QDs and large plastically relaxed QDs. The relaxed QDs can be easily identified by the presence of moiré fringes inside them on plan-view TEM images.

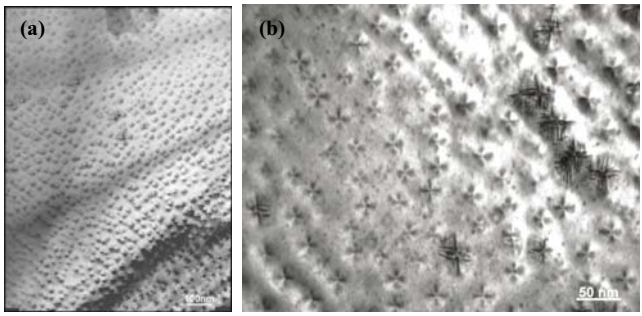


Fig. 2. (a) [001]-zone bright-field TEM image of uncapped QDs grown with 2.2ML InAs deposited at a growth rate of 0.016 MLs^{-1}. (b) [001] plan-view bright field TEM image of uncapped QDs with 2.7ML of InAs deposition.

Using the cross-sectional HRTEM images, we have observed that misfit dislocations are actually generated from the edge of the QDs (Figs. 3a and 3b). This observation can be further confirmed by the measurements of the displacement field around a QD, as shown in Figure 3c.

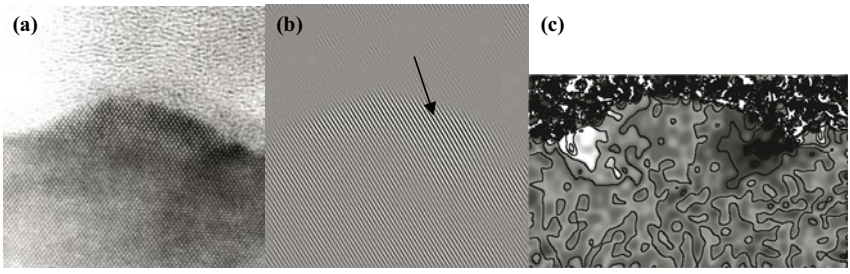


Fig. 3. (a) [110] cross-sectional HRTEM image of a smaller InAs QD with 2.7 ML InAs deposition. (b) reconstructed image by inverse Fourier transformation using the sideband $\bar{1}1\bar{1}$, a misfit dislocation is indicated by arrow, (c) a lattice rotation contour map measured for the QD shows two dislocations formed at the QD edges.

For the samples with InAs coverages in the range of 2.7 to 3.8ML, the fraction of relaxed QDs increases with increasing InAs coverage. The dimensions of the relaxed QDs are 30-50nm. The distances between contiguous moiré fringes are found to be smaller for larger incoherent QDs. For relaxed QDs with base sizes over 30 nm, the lattice distortion in the top region of the QD and the generation of misfit dislocations close to the InAs/GaAs interface could be observed directly in cross-sectional HRTEM images. Figure 4 is a [110] cross-sectional HRTEM image taken near the edge of a large QD in a 2.7ML InAs coverage sample, showing a misfit dislocation. In this case, the misfit

dislocation can be identified as a 60º dislocation with $\mathbf{b} = \mathbf{a}_{QDlayer}/2$ <101>, as shown in the Burgers vector analysis on the lattice image of Fig. 4.

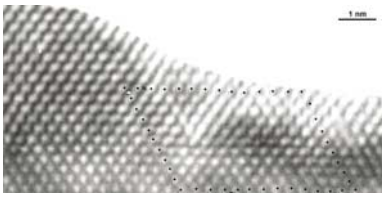


Fig. 4. [110] cross-sectional HRTEM image of an unburied QD. The black dotted line shows the determination of Burgers vector.

For higher InAs coverage, such as 3.8ML (not shown here), cross-sectional lattice images of large relaxed QDs show the introduction of an array of misfit dislocations close to the interface with the GaAs substrate. These misfit defects can be identified as 90º edge dislocations, using a similar Burgers vector analysis. In this high-lattice-mismatch system, the morphological transition takes place at the critical thickness from two-dimensional layer-by-layer growth to three-dimensional island nucleation, believed to be induced by strain with consideration of the surface condition of the materials in the system. Here, with increasing InAs coverage during MBE growth, the accumulated strain is first relieved by coherent island formation and then by dislocation generation at the island edges (e.g. 60º dislocation generation at the QD side edges). As more InAs is deposited, adjacent QDs may coalesce and a variety of defect types may be created.

4. CONCLUSIONS

This study shows that InAs/GaAs QDs grown at low InAs coverage are coherent. They are small in size (~13-20 nm) and have a uniform size and shape distribution, in a dense arrangement (10^{10}-10^{11}cm^{-2}). With increasing InAs coverage, incoherent QDs start to form, and samples with both coherent and incoherent QDs usually exhibit bimodal size distributions, where coherently strained QDs are smaller than incoherent plastically-relaxed QDs. Where the two types of QD coexist, Ostwald ripening may occur, where large QDs grow at the expense of small QDs. Misfit relaxation in large QDs is accommodated by the generation of misfit dislocations, and also by the distortion of lattice planes (elastic strain relaxation).

REFERENCES

Hÿtch M J, Putaux J-L and Pénisson J-M 2003 Nature **423**, 270

Joyce B A, Jones T S and Belk J G 1998 J. Vac. Sci. Tech. B **16**, 2373

Zhi D, Davock H, Murray R, Roberts C, Jones T S, Pashley D W, Goodhew P J and Joyce B A 2001 J. Appl. Phys. **89**, 2079

Zhi D, Wei M, Dunin-Borkowski R E, Midgley P A, Pashley D W, Jones T S, Joyce B A, Fewster P F and Goodhew P J 2004 Microelectron. Eng. **73-74**, 604

Zou J, Cockayne D J H and Jiang S S 1994 J. Appl. Phys. **75**, 7317

Electron microscopy and optical spectroscopy of single InAs/InP quantum dots

D Chithrani[1,2], D D Perovic[1], R L Williams[2], J Lefebvre[2], P J Poole[2] and G C Aers[2]

[1] Department of Materials Science and Engineering, University of Toronto, Canada
[2] Institute for Microstructural Sciences, National Research Council, Canada

ABSTRACT: A technique is described which allows one to position a single InAs quantum dot or quantum dot arrays on the top of square based, pyramidal shaped InP nano-templated mesas. A simple geometrical calculation shows 80% of the InP material is incorporated during the template formation. Positioning of either a single quantum dot or quantum dot arrays is achieved depending on the size of the mesa top surface and the amount of dot material deposited as shown using both scanning electron microcopy and optical microscopy. Photoluminescence spectra from a single InAs quantum dot exhibits a clear s- and p-shell structure for the first time in this material system.

1. INTRODUCTION

Single InAs/InP quantum dots, which emit at a wavelength of around 1.55 μm, can be positioned with nanometer-scale precision on predetermined substrate sites using substrate patterning techniques (Chithrani et al 2004). This technique allows one to produce high optical quality quantum dots as result of positioning the quantum dots *in situ* on these templates. This technique also allows one to study the spectroscopy and microscopy of single quantum dots and dot molecules without recourse to post growth patterning processes. It is important to understand the growth of these nano-templates and also how one can position a single quantum dot or dot arrays on mesa tops of these nano-templates.

2. NANO-TEMPLATE FABRICATION

Square-based trenches, with edges running along [100] and [010] directions, are opened in the oxide using electron-beam lithography and reactive ion etching (Lefebvre et al 2002). CBE growth of InP on such patterned substrates is highly selective and proceeds only in the areas of exposed substrate. For square-shaped windows with edges running along the [100] and [010] directions, the {101} type crystal facets persist during growth, to produce a square-based pyramidal template as shown in Fig. 1a. Material deposited directly onto the existing {101} facets migrates up and onto the (001) top surface, where it is incorporated into the growing template. The diffusion of source material away from the low growth facets is again used to reduce the lateral dimensions of the mesa top, and to produce nano-scale templates for the growth of single quantum dots and quantum dot arrays. The large differences in growth rate between different crystallographic planes results in the appearance of different crystallographic facets (Sugiura et al 1992). In addition to the expected {110} type sidewalls, inequivalent (111)A and (111)B edges are also observed. For the growth conditions employed here, the fastest growing plane is (001), followed in decreasing order by (111)A, (011), and (111)B (Finnie et al 1997).

Depending upon the geometry of the initial trench opening and the amount of deposited material ‘h’, the templates can be tailored to produce any desired dimensions of (001) mesa top facets (see Fig. 1b). The ultimate goal is to control the top width of the templates in the regime where the

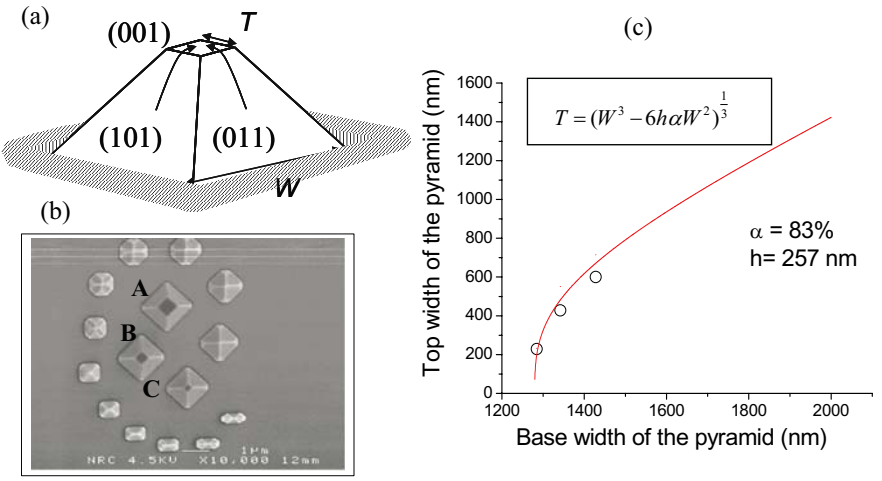


Fig. 1. (a) Schematic illustration showing the type of square-based InP nano-template used to selectively position single InAs quantum dots, (b) SEM images of series of InP pyramidal nano-templates with different orientation and dimensions, (c) Theoretical curve (solid line) corresponding to the top width of the template as a function of starting width of the template; open circles represent the experimental data points obtained from pyramids A to C in Fig. 1b.

width is of the order of the lateral dimensions of the quantum dot. In this manner one can accurately locate either a single quantum dot or an array of quantum dots in a predetermined geometry. Figure 1c illustrates the reduction of top facet width "T" as a function of starting width "W" for a constant amount of material (InP) deposited "h", as calculated using the equation depicted in Fig. 1c (h=257nm in this case). According to the SEM images shown in Fig.1b, the value of α is approximately 0.83, meaning that 83% of the deposited material is incorporated into the InP nano-template. Data corresponding to pyramidal templates A, B and C (see Fig.1a) are marked as open circles in the graph (c) in Fig.1. Agreement of the experimental data with the theoretical curve shows the controllability of the nano-template fabrication and hence the reproducibility.

It should be noted that an analogous relationship as shown in Fig. 1c was obtained for [010] elongated trapezoidal mesas where $T= (W^2 - 4\alpha hW)^{1/2}$ with $\alpha \sim 0.45$. This relationship allows for controlled templating of linear arrays of quantum dots (Chithrani et al 2004)

3. InAs QUANTUM DOTS ON InP NANO-TEMPLATES

Upon producing a template of an appropriate size, InAs quantum dot material is deposited during which time most of the material on the {101} side facets migrates onto the (001) mesa top facet. In this way, the amount of InAs can be controlled, which can produce either a single quantum dot or dot arrays on the mesa top facets. Figure 2a shows photoluminescence data from a series of capped pyramids with base width varying from 462 to 814 nm. The inset of Fig. 2a shows SEM images of uncapped samples grown in a series of parallel experiments. The quantity of InAs reaching the (001) mesa surface, through both surface migration and direct deposition, increases as function of decreasing pyramid dimensions. Accordingly, whilst the number of dots in each pyramid decreases as a function of decreasing mesa dimension, the dot height increases simultaneously. This increase in dot height produces a red shift of the emission spectrum, whilst the reduction of the number of dots gives rise to a considerable simplification of the emission spectrum. If one can choose the conditions appropriately, then for small enough pyramid dimension, a single InAs dot can be positioned at the

pyramid apex. In the case shown in Fig. 2a, the choice of template dimension and quantity of InAs deposited results in excitonic emission close to λ=1.6μm for the smallest template studied.

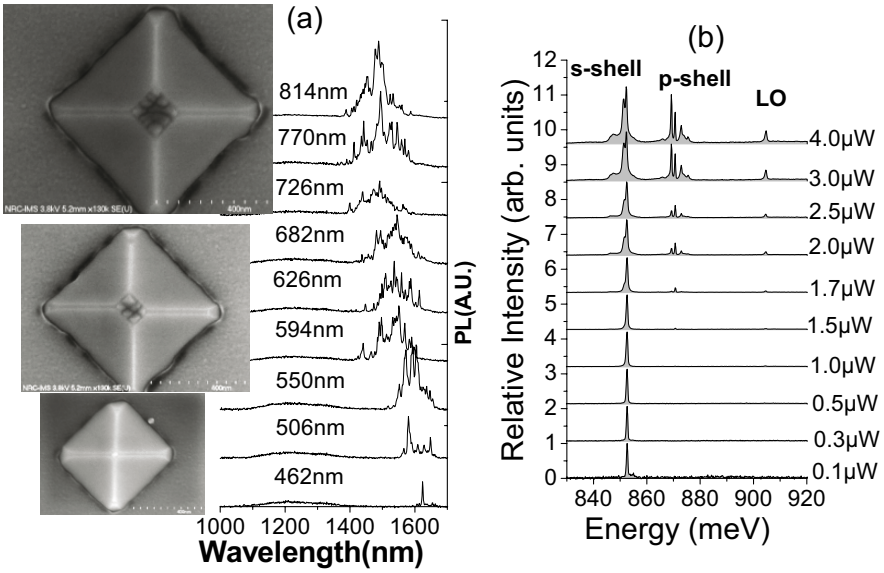


Fig. 2. (a) Photoluminescence from InAs/InP quantum dots on a series of single nano-templates. Numbers on each of the spectrum give the starting width of the base (W). Reduction in number of quantum dots as a function of decreasing width of the template is illustrated in the SEM images, (b) Photoluminescence from a single quantum dot located on top a pyramidal nano-template. Clear s- and p-shell structure is observed as a function of

Figure 2b shows photoluminescence data, as a function of excitation power, collected from the s- and p-shells of a single InAs/InP quantum dot grown at the apex of a second pyramidal nano-template. This second template was designed to produce a dot with an emission energy that is closer to the optimum wavelength for the InGaAs detector used in the PL experiments. At low excitation power, the spectrum consists of a single sharp line, which we attribute to the recombination of a single electron-hole pair in the s-shell. The width of this line is 0.8meV, close to the resolution limit of our spectrometer, whilst the emission energy is 852meV (1.48μm). For clarity of presentation, the individual spectra are offset along the y-axis and scaled to the peak intensity at 852meV. At higher excitation intensity, biexciton emission appears approximately 1meV below the single exciton line. This biexciton emission results from the annihilation of a single exciton in the presence of a second exciton of opposite spin. Due to the Coulomb induced re-normalization, an energy shift of 1meV is observed between the exciton and biexciton emission lines.

Occupation of the p-shell is observed at almost the same excitation intensity for which the biexciton emission appears. The first p-shell line appears at an emission energy of 871meV, corresponding to a separation between the ground and first excited states of only 19meV. This small splitting between s- and p-shells suggests a large lateral dimension for the InAs/InP quantum dot.

The p-shell can accommodate a maximum of four optically active excitons. At low excitation intensity, the first p-shell transition, 3X, is observed as the result of the annihilation of a single exciton in the p-shell in the presence of a biexciton in the s-shell. Further increases in the pump power result in transitions associated with 4X-6X occupation and the emission spectra show complexity associated with the many body renormalization effects discussed by Bayer and co-workers (2000).

4. SUMMARY

In conclusion, the spectroscopy and microscopy of single quantum dot and quantum dot molecules on pyramidal nano-templates has been studied. Optical spectroscopy of a single quantum dot located at the apex of a nano-template shows clear s- and p-shell structure for the first time in this material system.

REFERENCES

Bayer M, Stern O, Hawrylak P, Fafard S and Forchel A 2000 Nature **405**, 923
Chithrani D, Williams R L, Lefebvre J, Poole P J and Aers G C 2004 Physica E **21**, 290
Finnie P, Charbonneau S, Buchanan, Lacelle C, Fraser, J and Roth A P 1997 J. Appl. Phys. **82**, 4883
Lefebvre J, Poole P J, Fraser J, Aers G C, Chithrani D and Williams R L 2002 J. Crystal Growth **234**, 391
Sugiura H, Hishida T, Iga R, Yamada T and Tamamura T 1992 J. Crystal Growth **121**, 579

Vertical correlation-anticorrelation transition in InAs/GaAs quantum dot structures grown by molecular beam epitaxy

M Gutiérrez, M Hopkinson, M Herrera[1], D González[1] and R García[1]

Department of Electronic and Electrical Engineering, University of Sheffield. Mappin Street, Sheffield S1 3JD, United Kingdom
[1] Departamento de Ciencia de los Materiales e I.M. y Q.I., Universidad de Cádiz. Apartado 40, 11510 Puerto Real, Cádiz, Spain

ABSTRACT: This paper shows the first experimental evidence of anticorrelated InAs/GaAs quantum dot structures grown by molecular beam epitaxy. As previous authors have predicted theoretically, a transition occurs between correlated and anticorrelated vertical arrangements depending on the ratio between the layer separation and the average spacing between quantum dots in a single plane. These vertically anticorrelated quantum dot systems are observed to be an efficient way to keep the size and density of the islands constant, which is of crucial importance for the optoelectronic applications of these heterostructures.

1. INTRODUCTION

There is great interest in vertically stacked (or correlated) InAs/GaAs quantum dot (QD) strained-layer superlattices for studies of the electronic coupling of quantum dot wave functions. The vertical elastic interaction of strained islands during the epitaxial growth of these QD superlattices can lead to a lateral ordering and size homogenization of the dots (Tersoff et al 1996). The elastic distortion associated with QDs extends into the surrounding material and creates preferential regions for the onset of three dimensional growth occurring in the subsequent strained layer (Yao et al 1991, Xie et al 1995, Shchukin et al 1995). But, whilst lateral ordering of islands has not been observed to affect the island size, vertical interactions between evolving strain fields has been observed to modify the size and shape of such islands and this fact makes it very difficult to fabricate electronically coupled QDs based on closely vertically separated QDs.

Vertical anticorrelation, in which subsequent quantum dots stack in the space between the underlying QDs and not along vertical alignment with the islands below, has been recently observed in certain structures. In particular, this has been reported for the growth of highly anisotropic II-VI, for example CdSe QDs in a ZnSe matrix (Straßburg et al 1998). Here, the anisotropy comes from the intrinsic surface stress tensor and the anisotropy of the bulk elastic modulus tensor which in the FCC lattice favour the orientation of spontaneously ordered structures in the elastically soft directions [100] and [010] (Wang et al 1994, Guryanov et al 1996, Bressler-Hill et al 1994). Despite this, in the case of In(Ga)As islands on GaAs(001) substrates there have been no reports of the formation of anticorrelated structures.

Shchukin et al (1998) have shown theoretically that both correlated and anticorrelated dot structures can occur due to the interference of strain fields from underlying QD lattices in any elastically anisotropic cubic crystal. Their results give a valuable insight into this phenomenon showing that the transition between correlation and anticorrelation depends on the ratio between the layer separation z and the average spacing between quantum dots in a single plane d, as z/d. We note the comments that small changes in this factor can lead to dramatic changes in the kind of correlation

and also that the preferred direction for modulation in stacked structures occurs theoretically along the soft [100] directions.

The present work has been done in order to improve our understanding of the stacking process of InAs/GaAs (001) QD systems. Firstly, we will analyze structural aspects of the vertical correlation such as the effect of vertical In segregation upon the size increase of vertical correlated InAs islands. Secondly, taking into account the elastic anisotropy of the crystal, we will explain the possibility of a transition from correlated to anticorrelated structures.

2. EXPERIMENTAL

To examine the vertical interactions on the morphology of stacked quantum dots two InAs QD samples were grown by standard molecular beam epitaxy methods on nominally on-axis (± 0.05°) GaAs substrates. The first sample, labeled A, consisted of 5 layers of 3 monolayers (MLs) of InAs separated by 25 nm of GaAs barriers. After the growth of the first 15 nm of each GaAs barrier layer the temperature was increased and held for a long time to produce the total evaporation of In from the growth surface. Later the temperature was decreased to grow the rest of the barrier layer under conventional GaAs growth conditions. The second sample, labeled B, consisted of 5 layers of 2.2 ML of InAs and 35 nm GaAs barriers, all of them grown using standard growth temperature conditions for InAs/GaAs systems.

Plan view and [110] cross-sectional transmission electron microscopy (TEM) specimens were prepared by mechanical polishing followed by ion milling in a Gatan PIPS instrument at low incidence angle. Diffraction contrast TEM images were taken using a Philips 430 microscope operating at 300 kV.

3. RESULTS AND DISCUSSION

Recently the need to attempt to fabricate electronically coupled QDs based on closely vertically separated QDs has driven the need to produce correlated structures where the island size remains constant during the stacking process. Vertical correlation of QDs has been proposed for many authors to get in-plane size homogenization of these islands, however it has been observed that stacking increases the size and reduces the density of dots grown in the layer above. These observations have been explained in the bibliography from two different approximations: first, vertical segregation of In from a QD layer to the layer above or second, the strain field profile induced for the buried islands. So, our first objective in this work was to determine which mechanism is the main one in the QD size increase of our structures: In segregation or strain field.

Figure 1 shows a 200 DF TEM micrograph of sample A in which the temperature was increased after the growth of the first 15 nm of GaAs barriers to guarantee the total evaporation of In atoms from the surface, i.e. avoiding In vertical segregation. As can be observed, due to the stacking effect, the density was reduced 50% from the bottom layer to the top one. Specifically, the bottom layer density is $\boldsymbol{\rho} = 13.1\times10^4$ cm^{-1} and the top layer density is $\boldsymbol{\rho} = 7.1\times10^4$ cm^{-1}. However, although there is a clear QD size increase from the bottom to the top layer (height increase $\boldsymbol{\Delta h}$ = + 68% and width increase $\boldsymbol{\Delta w}$ = + 51%), the aspect ratio $\boldsymbol{h/w}$ for all the layers was the same and equal to 0.2. Assuming a cone island shape this would mean that the volume of the islands has increased + 300%. From these data one can estimate that the average In concentration of the dots on the top layer is ~25% of the concentration of the bottom ones. So, it seems clear that during the stacking process of correlated QD structures, the increase of size islands is not due to the In segregation effect, but that the elastic energy profile of the buried layers is fundamental to vertical QD alignment.

Although vertical correlation decreases the size distribution of InAs QDs, it decreases the QD density, and increases the QD size layer on layer by dilution of the concentration. It also deteriorates the GaAs spacer quality. From these conclusions, it would seem impossible to vertically stack QDs to get high quality optically coupled QDs structures or, at least, another growth approach is necessary.

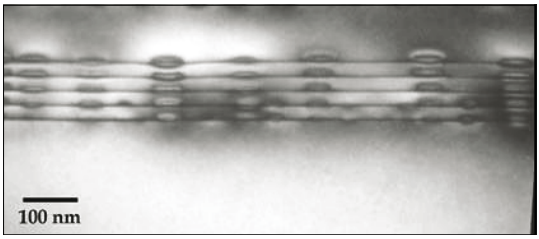


Fig. 1. Low magnification cross section 200 DF TEM image of sample A where vertical correlation of QDs is clearly observed.

Traditionally, the true isotropic strain profile has been applied to models of the vertical correlation effect. However, this approximation is not strictly correct since any zinc-blende structure, such as GaAs, is anisotropic. Holy et al (1999) have applied the anisotropic energy profile to theoretically determine the position of the energy minimum above buried QD layers. In the case of (001) GaAs, the authors predicted that a QD generates a two minimum energy profile in the <110> direction. So, assuming the Holy calculations, the width broadness of the islands in sample A is possibly explained in terms of the anisotropic energy profile on the surface above a strained quantum dot. The two strain minima above the islands in sample A would be placed at 10.5 nm from the vertical. Since the width of the bottom islands in this sample is $\boldsymbol{w}$ ~39 nm, to get two individual islands in the second layer with centres separated by 21 nm is not possible. The distance between the two minima generated by a single island is shorter than the dimensions of this island and so the islands above would coalesce to form a single large island perhaps exhibiting a hump-back shape as is commonly seen.

But from the Holy theory, it would be possible to get vertically shifted islands due to the strain generated by the islands below using the appropriate geometrical parameters. Sample B was designed to have an island width and density and a barrier thickness consistent with this anisotropy theoretical model. Figure 2 shows a 220 BF TEM micrograph of the sample B, where in accordance with these authors it is observed that the islands are shifted respect to the vertical position of the buried ones by an angle of 23º. In this anticorrelated structure, as in the case of sample A, the QD aspect ratio is 0.2. So, when vertical correlated structures are not obtained, the distribution of QD is not arbitrary and there is a preferential shift angle. In this anticorrelated structure, the density and size do not change with the number of layers and so the In concentration can be estimated to be the same in all layers. Moreover, comparing Figs. 1 and 2, it can be observed that in the case of sample A, InAs QDs are grown on an undulating GaAs surface whilst in sample B the QDs grow on a flat surface, i.e. GaAs spacer layers are grown with better quality which would allow one to get structures with thinner barriers. Thus, the change from vertical correlated to anticorrelated stacking improves significantly the quality parameters of QD multilayers in terms of QD size and density of the upper layers and even regarding the flatness of the barrier layers.

4. CONCLUSIONS

In common with many other reports, vertical correlation of QD stacks is observed to show a reduction (~50%) of the QD density from the bottom to the top layer and a significant QD size increase due to In dilution. We have shown that these effects are not due to vertical In segregation, but instead can be easily explained by the anisotropic elastic interaction energy between a buried QD layer and subsequent QDs. However by making use of the intrinsic anisotropy of the crystal and choosing carefully the QD and barrier layer dimensions, it is possible to get anticorrelated InAs QD structures as is the case of sample B (using 2.2 ML of InAs and 35mm barrier thickness).

Vertically anticorrelated structures offer a much improved size and density distribution compared to the correlated case and, therefore, these structures are presented as an alternative tool to get optically coupled QDs. In general, elastic anisotropy cannot be considered as insignificant in the

InAs-GaAs system and may indeed explain a number of other unresolved effects related to the growth of InAs QD structures.

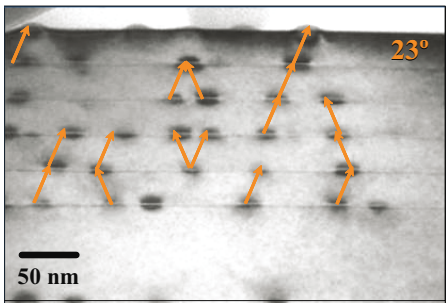


Fig. 2. Cross section 220 BF TEM image of sample B. The arrows show the 23ºpreferential shift angle in the vertical stacking of InAs QDs structures.

ACKNOWLEDGEMENTS

This work is supported by EPSRC (UK), the Ministerio de Educación, Cultura y Deporte of the Government of Spain and by the network of excellence SANDIE (Contract NMP4-CT-2004-500101 of the VI European Framework Program) and the Junta de Andalucía (PAI research group TEP-0120).

REFERENCES

Bressler-Hill V, Lorke Al, Yarma S, Pond K, Petroff P M and Weinberg W H 1994 Phys. Rev. B **50**, 8479

Guryanov G M, Cirlin G E, Golubok A O, Tipisev S Ya, LedentsovN N, Shchukin V A, Gundmann M, Bimberg D and Alferov Zh I 1996 Surf. Sci. **352**, 646

Holy V, Springholz G, Pinczolits M and Bauer G 1999 Phys. Rev. Lett. **83**, 356

Shchukin V A, Bimberg D, Mayshkin V G and Ledentsov N N 1998 Phys. Rev. B **57**, 12 262

Shchukin V A, Ledentstov N N , Kopev P S and Bimberg D 1995 Phys. Rev. Lett. **75**, 2698

Straßburg M, Kutzer V, Pohl U W, Hoffmann A, Broser I, Ledentsov N N, Bimberg D, Rosenauer A, Fischer U, Gerthsen D, Krestnikov I L, Maximov M V, Kop'ev P S and Alferov Z I 1998 Appl. Phys. Lett. **72**, 942

Tersoff J, Teichert C and Lagally M G 1996 Phys. Rev. Lett. **76**

Wang P D, Ledentsov N N, Sotomayor Torres C M, Kop'ev P S and Ustinov V M, Appl. Phys. Lett. **64**, 1526

Xie Q, Madhukar A, Chen P and Kobayashi N 1995 Phys. Rev.Lett. **75**, 2542

Yao J Y, Andersson T G and Dunlop G L 1991 J. Appl. Phys. **69**, 2224

Effect of annealing on anticorrelated InGaAs/GaAs quantum dots

M Gutiérrez, M Hopkinson, A I Tartakovskii[1], M S Skolnick[1], M Herrera[2], D González[2] and R García[2]

Department of Electronic and Electrical Engineering, University of Sheffield. Mappin Street, Sheffield S1 3JD, UK
[1] Department of Physics and Astronomy, University of Sheffield, Sheffield S3 7RH, UK
[2] Departamento de Ciencia de los Materiales e I.M. y Q.I., Universidad de Cádiz. Apartado 40, 11510 Puerto Real, Cádiz, Spain

ABSTRACT: The effect of rapid thermal annealing on a vertically anticorrelated array of InGaAs/GaAs (001) quantum dot structures is presented. Analysis of the structure shows that after this treatment there is a spontaneous change in the island distribution, resulting in an increase in the QD density without changing the QD size. The results confirm theoretical studies in which anticorrelated dot structures occur due to the interference of strain fields from underlying islands in elastically anisotropic cubic crystals.

1. INTRODUCTION

One of the remarkable properties of strain induced nanometer-sized islands, known as quantum dots (QDs) is the presence of a number of selection processes which control aspects as island size and inter-island spacing, such that at close to equilibrium the islands can be 'self organized'. Over the last decade, much attention has been focused on multilayers of QDs ordered both in the lateral and vertical directions (Kuan and Iyer 1991, Yao et al 1991, Xie et al 1994, Solomon et al 1996, Tersoff et al 1996, Ledentsov et al 1996 and Heinrichsdorff et al 1997). Theoretical treatments have been successfully applied to explain that the vertical correlation occurs when the separation between multilayers is sufficiently small such that the subsequent QDs grow under the influence of the strain field of the buried ones. These treatments are based on accounting for the strain-induced migration of atoms of the growing layer to positions above underlying islands (Xie et al 1995). However, the detailed mechanism is still the subject of considerable debate, depending on the relative importance of nucleation and post nucleation effects. For example, it has been suggested that preferential sites for nucleation will occur above buried islands, although this argument may be unimportant, since we believe, as others (eg: Ledentsov et al 1996) that correlation process take place after the initial nucleation of a very high density of initial nucleation sites. However, vertical anticorrelation, in which subsequent quantum dots stack in the space between the underlying QDs, has been only observed in certain materials systems, eg: II-VI systems (Straßburg et al 1998). The large elastic anisotropy of these materials was the explanation given by Holy et al (1999) for this behavior. Shchukin et al (1998) have demonstrated theoretically that both correlated and anticorrelated dot structures can occur due to the interference of strain fields from underlying QD lattices in any elastically anisotropic cubic crystal. So, the transition between correlation and anticorrelation can be understood only under the consideration of elastically anisotropic crystals. Despite these theoretical studies which suggest that the same effects may be observable in III-V systems, there have been no previous reports of vertically anticorrelated III-V quantum dots.

Recently we have found by careful choice of the structural parameters, such as dot size and lateral and vertical separation that high quality anticorrelated structures can be obtained in InGaAs/GaAs (001) QDs systems with a relatively high density. In this paper we discuss the results

of annealing of these structures, which is shown to bring about domains of correlated and anticorrelated QDs which could be generated by changes in the local strain anisotropy following indium migration at the elevated temperature.

2. EXPERIMENTAL

Two 16 repeat 5.5 ML $In_{0.5}Ga_{0.5}As$ quantum dot samples were grown by standard molecular beam epitaxy methods on nominally on-axis (± 0.05°) GaAs substrates. For these multilayer samples a nominal interdot layer spacing z consisting of 25 nm of GaAs was used. After the growth, one of these samples was subjected to rapid thermal annealing (RTA) (30s at 850 ºC) to improve the optical properties of the QDs without major changes in the dot structure.

Plan view (PV-) and [110] cross-sectional (CS-) transmission electron microscopy (TEM) specimens were prepared by mechanical polishing followed by ion milling in a Gatan PIPS instrument at low incidence angle. Diffraction contrast TEM images were taken using a Philips 430 microscope operating at 300 KV.

3. RESULTS AND DISCUSSION

We have examined the compositionally sensitive (002) reflection in the <110> cross section of both 16 layer samples. Our InGaAs QDs multilayer array without RTA treatment showed the surprising observation that the dots of upper layers are positioned in the spaces between the islands below, instead of vertically above such islands (Fig. 1). Numerous authors have observed that the stacking of InGaAs/GaAs QDs layers produce vertical correlation which increases the size of the islands and decreases the dot in-plane density. However, in the observed vertical anticorrelation arrangement the dot density and size remain constant after the stacking of numerous QD layers as can be clearly observed in Fig. 1.

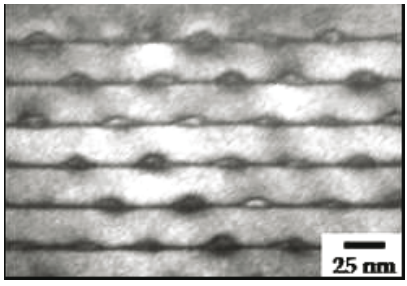


Fig. 1. Cross section 200 DF TEM image of an InGaAs/GaAs QD structures without annealing treatment

Since the elastic energy distribution for any zinc-blende material is characterized by the anisotropy ratio $A = 2c_{44}^c / \left(c_{11}^c - c_{12}^c\right)$, this vertical anticorrelation in InGaAs self-assembled quantum dot superlattices can be explained from the vertical anisotropic elastic strain field interaction of the islands. This surface anisotropy favors surface diffusion in the $[\bar{1}10]$ direction (Cotta et al 1993, Kasu and Kobayashi 1997 and Sudijono et al 1992) and, most importantly, changes both the depth and the position of the energy minima (Holy et al 1999) with respect to elastically isotropic spacer layers where the energy minimum is always above the tops of the buried QDs. According to these authors, for (001) GaAs systems (A> 1.5) the strain minima exhibits a four fold symmetry which helps to define a preferred square arrangement of the dots within the growth plane above.

An examination of the low magnification TEM images of the annealed sample showed the presence of different domains, which from their initial appearance we describe as anticorrelated (A) and

correlated (C) domains. Figure 2 is a picture of this sample, the enlarged inserts show near perfect A and C domains. Note that the island size was observed to be the same in both regions and also equal to the dimensions of the islands in the sample without annealing treatment ($\boldsymbol{h}$ ~5.7 nm and $\boldsymbol{w}$ ~29.1 nm). However, the QD density changes significantly from A domains (2.2×10^5 cm^{-1}) to C domains (3.1×10^5 cm^{-1}). A more detailed observation of the C domains shows that these are not "conventional" vertically correlated quantum dots, but rather that there are additional dots in between the anticorrelated alignment. In the right hand insert of Fig. 2, the island marked with the white arrow is not in the same vertical plane as the islands marked with black arrows. We believe the C domains appear as a consequence of the formation of additional islands between the four dots within the same plane after the RTA process as is sketched in Fig. 3.

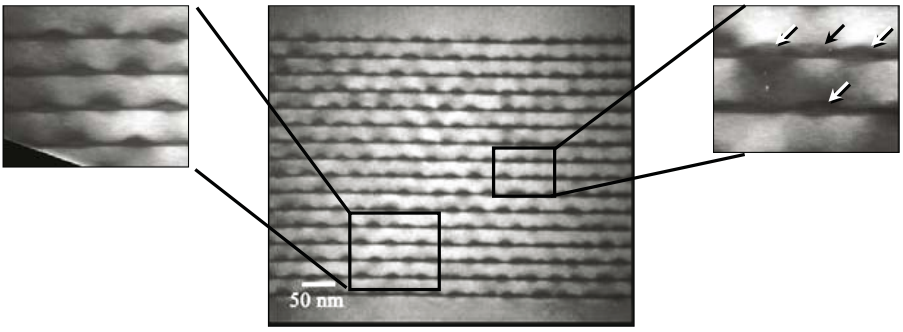


Fig. 2. Cross section 200 DF TEM image of an InGaAs/GaAs QD structures after rapid thermal annealing treatment. The enlarged inserts show perfect anticorrelation domains, at the left and, at the right and marked with a white arrow, the presence of an island formed after the annealing process.

There are a few theoretical models to explain the behavior and formation of the anticorrelated domains for III-V systems. Shchukin et al (1998) explain the anticorrelated alignment of QDs by considering that the buried islands produce a uniaxially anisotropic elastic force density in the zinc-blende crystal matrix. They demonstrate mathematically that under certain geometrical conditions, the interaction between the strain fields of two islands is close enough to produce a minimum of the energy which is not vertically above the islands below, and so produces different arrangements of QDs depending on the system geometry. Amongst the different possibilities, perfectly anticorrelated structures, i.e. structures where the islands are placed just in the middle of the islands of the layer bellow in the same (110) plane, show an energetic preference.

Rapid thermal annealing (RTA) has been used to modify or improve the optoelectronic properties of QD systems and although intermixing is known to exist, giving a dissolution of indium from the QDs and a reduction in size on increasing the anneal temperature, the quantum dots are not generally assumed to appear or disappear or to change their alignment. This thermal treatment applied to the anticorrelated structure, however, has shown a surprising effect. This thermal process has activated new QD nucleation sites, being the first time this behavior is observed in InAs/GaAs QD systems. It is known that the annealing treatment reduces the QD size, so indium diffusion from the islands to the wetting layer could be expected at the annealing temperature. This phenomenon changes the dot-wetting layer system to a new thermodynamic equilibrium at the annealing temperature.

However, on cooling it is possible that the indium does not simply return to the original dot sites but, instead, forms new islands at the next most energetically favorable position, which is at the centre of four islands placed in the same (001) plane as predicted by the Shchukin et al (1998) theory. This explanation does suggest that transfer of indium to and from the wetting layer is quite fluid at the annealing temperature (~850^{o}C). Further studies of the influence of anisotropic strain profiles and annealing treatments in the structure of the InGaAs wetting layer are needed to clarify these experimental observations.

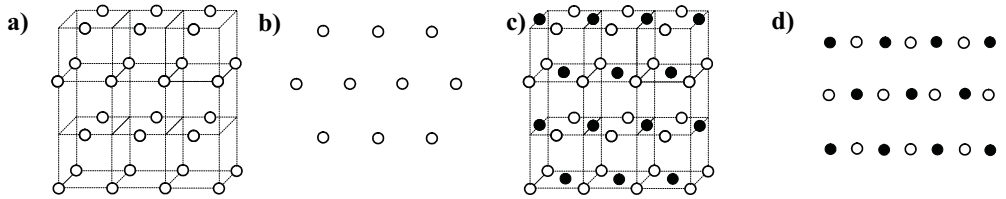


Fig. 3. Three dimensional schema of a) anticorrelated QD structure and c) anticorrelation structure where extra islands (black circles) have been created after RTA process. The schemas in b) and d) are bidimensional projections in the {001} plane of a) and c) schemas respectively.

4. CONCLUSIONS

In summary, we have studied the effect of annealing multilayer stacks of InGaAs quantum dot structures separated by nominal 25 nm spacer layers. In the as-grown condition, these multilayers are observed to show almost perfect vertical anticorrelation, where dots above stack within the space between the underlying dots such that individual layers represent a shift in the [110] direction of the whole 2D array. The presence of the anticorrelated alignment can be explained from the interference of anisotropic strain fields of the buried QDs. Rapid thermal annealing at 850 ^{o}C of this structure has been observed to substantially change its morphology. After the heating process, the spontaneous formation of additional islands occurs, increasing the QD density without changing the QD size. The change is from a perfect anticorrelated structure to a structure in which extra islands are formed in between the original dot array.

ACKNOWLEDGEMENTS

This work is supported by EPSRC (UK), the Ministerio de Educación, Cultura y Deporte of the Government of Spain and by the network of excellence SANDIE (Contract NMP4-CT-2004-500101 of the VI European Framework Program) and the Junta de Andalucía (PAI research group TEP-0120).

REFERENCES

Cotta M A, Hamm R A, Staley T W, Chu S N, Harriott L R, Panish M B and Tempkin H 1993 Phys. Rev. Lett. **70**, 4106

Heinrichsdorff F, Krost A, Kirstaedter N, Mao M H, Grundmann M, Bimberg D, Kosogov A O and Werner P 1997 Jpn. J. Appl. Phys. Part 1 **36**, 1129

Holy V, Springholz G, Pinczolits M and Bauer G 1999 Phys. Rev. Lett. **83**, 356.

Kasu M and Kobayahi N 1997 J. Cryst. Growth **170**, 246

Kuan T S and Iyer S S 1991 Appl. Phys. Lett. **59**, 2242

Ledentsov N N, Shchukin V A, Grundmann M, Kirstaedter N, Böhrer J, Schmidt O, Bimberg D, Ustinov V M, Egorov A Y, Zhukov A E, Kop'ev P S, Zaitsev S V, Gordeev N Y, Alferov Z I, Borovkov A I, Kosogov A O, Ruvimov S S, Werner P, Gosele U and Heydenreich J 1996 Phys. Rev. B **54**, 8743

Shchukin V A, Bimberg D, Mayshkin V G and Ledentsov N N 1998 Phys. Rev. B **57**, 12 262

Solomon G S, Trezza J A, Marshall A F and Harris J S Jr. 1996 Phys. Rev. Lett. **76**, 952

Straßburg M, Kutzer V, Pohl U W, Hoffmann A, Broser I, Ledentsov N N, Bimberg D, Rosenauer A, Fischer U, Gerthsen D, Krestnikov I L, Maximov M V, Kop'ev P S and Alferov Z I 1998 Appl. Phys. Lett. **72**, 942

Sudijono J, Johnson M D, Snuder C W, Elowitz M B and Orr B G 1992 Phys. Rev. Lett. **69**, 2811

Tersoff J, Teichert C and Lagally M G 1996 Phys. Rev. Lett. **76**

Xie Q, Chen P and Madhukar A 1994 Appl. Phys. Lett. **65**, 2051

Xie Q, Madhukar A, Chen P and Kobayashi N 1995 Phys. Rev.Lett. **75**, 2542

Yao J Y, Andersson T G and Dunlop G L 1991 J. Appl. Phys. **69**, 2224

Nanoanalysis of InAs/GaAs quantum dots using low-loss EELS spectra

A M Sánchez[(a)], M H Gass, A J Papworth, R Beanland[1], V Drouot[1] and P J Goodhew

Department of Engineering, Materials Science & Engineering, University of Liverpool, Liverpool L69 3GH, UK
[1] Bookham Technology, Caswell, Towcester, Northants NN12 8EQ, UK

ABSTRACT: The elemental distribution in InAs/GaAs quantum dots has been analysed using the *d* transition edges in the imaginary part of the dielectric function, $\varepsilon_2(E)$, obtained from the electron energy loss spectrum from a Kramers-Kronig analysis. Changes in the plasmon peak parameters have also been observed in areas of the InAs quantum dot with respect to the GaAs.

1. INTRODUCTION

Laser heterostructures based on InAs quantum dots (QDs) grown on GaAs substrates have received great attention due to the possibility they offer for future generations of optoelectronic devices (e.g. Lee et al 1999), including applications within the 1300-1550 nm fibre optical communication waveband. The understanding and improvement of these devices requires the characterization of such structures. Low-loss electron energy loss spectroscopy (EELS) is a technique which yields a lot of information. It can provide compositional information through elemental maps using the transitions in the absorption spectrum (Gass et al 2004 and Sanchez et al 2004). However, it can also provide an insight into the electronic structure, i.e. band gap.

In this paper, the imaginary part of the dielectric function has been used to determine the elemental distribution in an InAs QD heterostructure. We also investigate the properties of the bulk plasmon for an InAs/GaAs QD system. The elemental maps were obtained using interband transitions from 3d states. These maps are derived from the imaginary part ($\varepsilon_2(E)$) of the dielectric function of the InAs/GaAs system, using the transitions in the absorption spectrum (<40eV).

2. EXPERIMENTAL

The investigated sample was grown by metal-organic vapour phase epitaxy (MOVPE) in an Aixtron 2400 reactor on 3" (001) GaAs substrates misoriented 2° towards <011>. The structures consist of one layer of QDs, made of a layer of InAs and a layer of InGaAs, in GaAs barriers. The growth conditions are the same as described for the sample F of reference Drouot et al (2003). The investigations were carried out using a VG HB601 UX FEG-STEM operating at 100kV on a cross-section specimen. The STEM was equipped with the Gatan ENFINA^{TM} parallel electron energy loss spectrometer (PEELS) system. Electron energy-loss spectroscopy has previously been used to investigate the electronic structure in III-V heterostructures (Lakner et al 1998, Keast et al 2002, Gass et al 2004, Sanchez et al 2004). Analysis using the low-loss region of the EEL spectrum (<50eV) allows the energy resolution to be optimized through the use of much smaller apertures. The EEL data was acquired using a small

[(a)]Present address: Departamento de Ciencia de los Materiales e I. M. y Q. I. Universidad de Cadiz. Apdo. 40 E-11510 Puerto Real (Cadiz), Spain
Author to whom correspondence should be addressed; electronic mail: ana.fuentes@uca.es

collection aperture (β=1.34 mrad) and an energy resolution of 0.35 eV was measured from the full width half maximum (FWHM) of the zero loss peak (ZLP).

3. RESULTS AND DISCUSSION

3.1 Compositional Analysis Using the Absorption Spectrum (<40 eV)

A spectrum image (SI) of the low-loss region was recorded in an area containing InAs quantum dots. Compositional analysis of the quantum dots has been carried out using the semi-core transitions in the imaginary part [ε_2(E)] of the dielectric function. The d transitions sit on the back of the plasmon peak, making it very difficult to fit the background for all the spectra. In ε_2(E), the removal of the plasmon peak gives rise to a better background fit. The ε_2(E) spectrum was calculated via the Kramers-Kroning transformation (Johnson et al 1975, Isaacson et al 1989) from the single scattering distribution spectrum for the heterostructure. The background level was calculated for each spectrum in the map individually. An energy window was placed over the edge between 20 and 24 eV defining the integral, and the edge intensity was calculated. The Ga 3d edge starts at 20 eV in GaAs (Mkoyan et al 2003). By setting the average composition of Ga to a nominal value of 100% of the Group III elements in the GaAs region, the concentration of the quantum dots can be determined. The map shown in Fig. 1a thus corresponds to the distribution of Ga, using the Ga 3d transition in the absorption spectrum ε_2(E). The distribution of Ga is not completely homogeneous in the heterostructure; however, there exists a clear decrease in the Ga distribution in areas corresponding to the InAs quantum dots. In these areas the Ga concentration is less than 80%. We have also used the In 4d transition in this heterostructure with an energy window placed over the edge between 18.3 and 19.5 eV (The In 4d edge starts at 18.3 eV in InAs (Aspnes et al 1979)). The background subtracted spectrum image using the In 4d transition is shown in Fig. 1b. Taking into account that the thickness of the specimen in the analysed area is >60 nm and the small size of the quantum dots <15nm, the InGaAs quantum well gives rise to a higher Ga value than would occur if the InAs quantum dot could be isolated from the matrix. The quantitative information we can obtain from the In 4d transition (Fig. 1b) is less accurate than using the Ga 3d, as the area integrated is very small, and the noise in the data is large. Nevertheless, it can be observed that where there is a depletion of Ga, an increase of In is present.

3.2 Mapping of the Plasmon Peak Parameters in the Heterostructure

By fitting a Gaussian function to the plasmon peak it is possible to determine peak energy with a resolution better than the 0.1 eV between data points in Fig. 1c. The variation in plasmon peak energy has been calculated using a map of a relatively large area of GaAs from which 800 EELS spectra were recorded. In this data set the standard deviation of the fitted plasmon peak energy was 7meV.

Figure 1c shows a map of the plasmon peak energy *Ep'* in the same region as the Ga and In maps. The map of *Ep'* has been calculated from the experimental plasmon peak position map (E_{max}) and removing the effect of the damping, Γ, using

$$E_p'^2 = \overline{E}_g^2 + E_p^2/\varepsilon_c = E_{\max}\sqrt{4E_{\max}^2 + \Gamma^2} - E_{\max}^2 . \qquad (1)$$

The InAs quantum dots are clearly visible as a darker region; *Ep'* shifts to a lower energy in the area corresponding to the InAs quantum dot and in the quantum well region. The observed peak shifts are related to changes in the mean energy gap ($\overline{E}_g$), the energy of a plasmon excited in a free electron gas (E_p) and the dielectric function of the core electrons and positive ions (ε_c) rather than details of plasmon decay. It is not possible to directly solve equation (1) for its component parameters from knowledge of only the plasmon peak energy E_{max} – however, it seems likely that a more

complete analysis of plasmon peak energy and shape will enable these different components to be extracted and mapped independently.

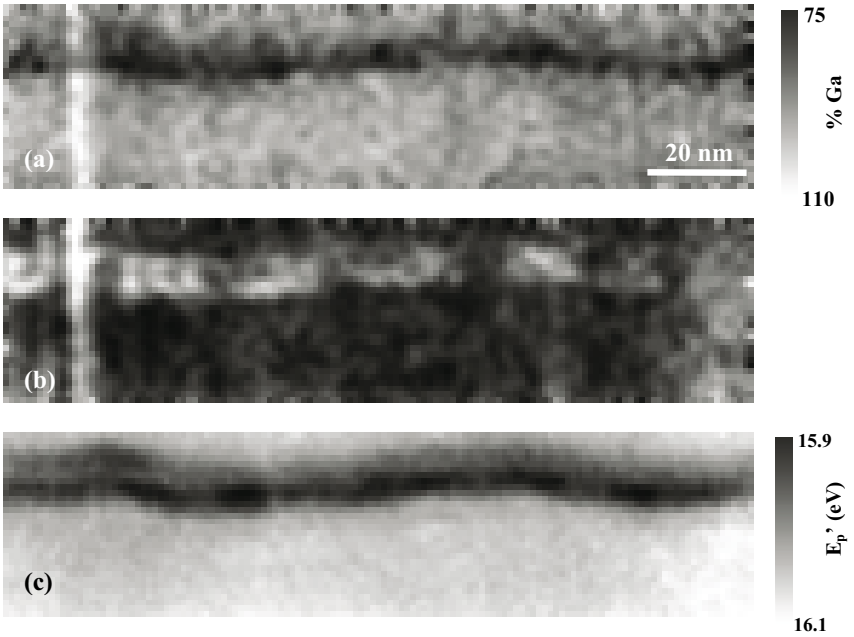


Fig. 1. Background subtracted spectrum images using **(**a) Ga 3d **(**b**)** In 4d in ε_2(E) absorption spectra. **(**c**)** Map of E_p' parameter in the same area.

4. CONCLUSIONS

We have measured Ga and In distributions in InAs QDs using EELS. Kramers-Kronig transformations have been applied to calculate the imaginary part of the dielectric function of the material, ε_2(E). The major peak situated at 20-24 eV corresponds to the Ga 3*d* transition, and it has been used to map the Ga elemental distribution. An inhomogeneous Ga distribution has been observed in the heterostructures, however there exists a clear decrease in the Ga distribution in areas corresponding to the InAs quantum dots. The plasmon peak mapping can be applied on a nm scale, with significant changes in E_p' as the composition of the material varies. *Ep'* shifts to a lower energy in the area corresponding to the InAs quantum dot. This shift is related to changes in the electronic properties of the material, $\overline{E}_g$, E_p and ε_c.

ACKNOWLEDGEMENTS

AMS would like to acknowledge support from EPSRC for many aspects of this work.

REFERENCES

Aspnes D E, Cardona M, Saile V, Skibowski M and Sprüssel G 1979 Sol. Stat. Com. **31**, 99

Drouot V, Beanland R, Button C C, Wang X Y, David J P R, Ouali F F and Holden A J 2003 Inst. Phys. Conf. Ser. **180**, pp. 107-110

Gass M H, Papworth A J, Bullough T J and Chalker P R 2004 Ultramicroscopy **101**, 257

Isaacson M J 1989 J. Chem. Phys. **56**, 1803
Johnson D W 1975 J. Phys. A **8**, 490
Keast V J, Scott A J, Kappers M J, Foxon C T and Humphreys C J 2002 Phys. Rev. B **66**, 125319
Lakner H, Rafferty B and Brockt B 1998 J. Microsc. **194**, Pt 1, 79
Lee U, Lee D, Lee H, Noh S, Leem J and Lee H 1999 Appl. Phys. Lett. **74**, 1597
Mkhoyan K A, Silcox J, Alldredge E S, Ashcroft N W, Lu H, Schaff J and Eastman L F 2003 Appl. Phys. Lett. **82**, 1407
Sanchez A M, Gass M, Papworth A J, Goodhew P J and Ruterana P 2004 Phys. Rev. B **70,** 035325

Structural analysis of the effects of a combined InAlAs-InGaAs capping layer in 1.3-μm InAs quantum dots

C M Tey, A G Cullis, H Y Liu[1], I M Ross and M Hopkinson[1]

Department of Electronic & Electrical Engineering, EPSRC FEGTEM Facility, University of Sheffield, Sheffield S1 3JD, UK
[1] Department of Electronic & Electrical Engineering, EPSRC National Centre for III-V Technologies, University of Sheffield, Sheffield S1 3JD, UK

ABSTRACT: A structural and compositional study of the effects of different thicknesses of InAlAs in the combined two-level InAlAs-InGaAs capping layer on InAs/GaAs quantum dots has been performed. Scanning transmission electron microscopy has been employed to determine the dot size and shape. Energy-loss filtered transmission electron microscopy imaging has been has been used to qualitatively determine the elemental distribution in the vicinity of quantum dots. An increase in the height of the quantum dots has been observed when the thickness of InAlAs capping layer is increased. In addition, there is evidence to suggest that the concentration of aluminium near the apex of the quantum dots is significantly reduced. Based on surface chemical potential thermodynamics, the increased height of InAs/GaAs quantum dots with increasing InAlAs capping layer thickness may be explained as a consequence of the higher indium adatom density above the capping layer and the subsequent suppression of the indium atom detachment rate from the InAs quantum dots.

1. INTRODUCTION

The growth of In(Ga)As quantum dots (QDs), formed via the Stranski-Krastanow growth mode, is subject to extensive fundamental research due to the possibility of improving the performance of lasers (Bimberg 1999). In particular, research on GaAs-based QD lasers emitting at the important telecommunication wavelength of 1.3-μm has progressed rapidly. The growth of an InGaAs strain-reducing capping layer (SRL) above the InAs/GaAs QDs has been widely employed in order to extend the emission wavelength to 1.3-μm or longer. However, this growth technique will result in a decrease in the confinement potential barrier, which leads to a degradation of the laser performance (Mukai et al 2000). Instead, an InAlAs-InGaAs combined two-level capping layer has been developed to increase the confinement of the InAs QDs for advanced laser applications (Liu et al 2003a), with excellent photoluminescence (PL) results obtained. The room-temperature QD ground-state PL intensity has increased by a factor of ~450. In addition, an energy separation between the ground and the first-excited state of 93meV has been obtained by this growth technique.

However, the origin of these optical improvements due to the Al-containing capping layer overgrowth process remains unclear. Therefore, the growth mechanism based on the structural characterisation of such an Al-containing capping layer is crucial. Despite the resolution capabilities of the electron microscope, imaging or analytical, there remain difficulties in determining the geometries and compositions of capped QDs, as described elsewhere (Tey et al 2005). Hence, in this work we have systematically investigated the structural properties of InAs QDs with different InAlAs-InGaAs capping layer thicknesses by applying two complementary transmission electron microscopy (TEM) techniques, ie scanning TEM (STEM) and energy-filtered TEM (EFTEM). Based on the results obtained, the most likely growth mechanism for the InAlAs overgrowth layer is presented.

2. EXPERIMENTAL

The samples under investigation were grown in a VG V80H molecular bean epitaxy (MBE) system on semi-insulation Si-doped GaAs(100) substrates. 2-nm of $In_{0.2}Al_{0.8}As$ and 4-monolayers (MLs) of GaAs were employed as a strained buffer layer (SBL) before 3.0-MLs of InAs were deposited with the associated QD formation. The InAlAs-GaAs SBL was used, instead of a more conventional GaAs SBL or InGaAs SBL, to increase both the matrix and confinement potential of the buffer layer (Liu et al 2003b). The capping layers deposited comprised y-nm of $In_{0.2}Al_{0.8}As$ and (6 - y)-nm of $In_{0.2}Ga_{0.8}As$, where y = 1.5, 3.0 and 6.0-nm. The growth temperature for InAs QDs and InAlAs-InGaAs capping layer was 510°C. These layers were embedded between 150-nm GaAs and 100-nm $Al_{0.37}Ga_{0.63}As$ layers.

TEM cross-sectional samples were prepared using conventional sample preparation techniques, including mechanical thinning and polishing, and Ar^+ ion-milling at 5kV followed by low energy ion-milling at 400V to remove any milling artefacts. The specimens were examined using a JEOL 2010F field emission gun TEM/STEM operating at 200kV accelerating voltage. The instrument is fitted with a Gatan imaging filter and a dedication STEM attachment with associated high angle annular dark field (HAADF) detector.

3. RESULTS AND DISCUSSION

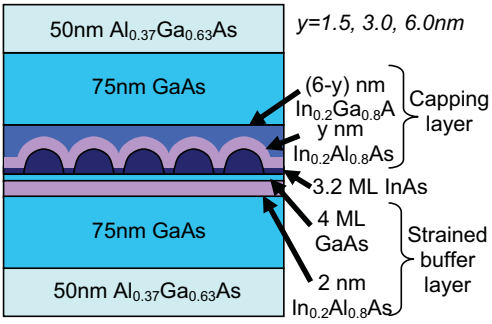


Fig. 1. Schematic diagram illustrating the composition of the epitaxial layer of the QD structure.

Figure 1 shows the schematic diagram of the grown epitaxial layer of the QD structure, where the thickness of the $In_{0.2}Al_{0.8}As$ capping layer, y = 1.5, 3.0 and 6.0-nm for sample A, B and C, respectively. Figures 2a-c show a series of high magnification HAADF-STEM images of InAs QDs from samples A, B and C respectively. The images were obtained using the <011> zone axis alignment. The InAs QDs are shown as the regions of brightest contrast. The $In_{0.2}Al_{0.8}As$ layers from the SBL and capping layer are shown as lines of darkest contrast sandwiching the InAs wetting layer (WL). A brightness profile labelled x-y shown in Fig. 2(d) was obtained across the region adjacent to the embedded QD with a 6.0-nm InAlAs capping layer. The region of darker contrast above the wetting layer, which is attributed to the Al-rich region, was measured to be less than 5-nm, as opposed to 6-nm of $In_{0.2}Al_{0.8}As$ deposited. This result suggests that the aluminium adatoms have separated from the indium adatoms in the surface-strained InAlAs capping layer at the growth temperature of 510°C. The regions of higher average atomic number, implied by the distinctly brighter contrast, above the region of darker contrast would indicate that profound indium segregation has occurred.

The InAs QDs appear to exhibit lens cross-sectional shape, with an average base diameter of approximately (22.6, 33.2, 31.9)-nm and an average height of approximately (7.3, 8.3, 9.3)-nm, respectively, as shown in Fig. 3. Nonetheless, the contrast is not very distinct around the apex region of the QDs. This is probably due to some elemental intermixing between In, Ga (and possibly Al) atoms at the periphery of the QDs, or segregation has occurred (Cullis et al 2002). The base diameter of the QDs has increased substantially with increasing thickness of the $In_{0.2}Al_{0.8}As$ capping layer from 1.5-nm to 6.0-nm. Furthermore, a subsequent increase of $In_{0.2}Al_{0.8}As$ capping layer thickness results in a corresponding significant increase in the height of QDs, in agreement with previous work on similar materials using atomic force microscopy (AFM) (Wei et al 2002).

Wei et al (2002) attributed the increased QD height to aluminium accumulation on top of the InAs QD, which prevents the indium atoms incorporated in the QDs from diffusing to the WL. However, the contrast modulation observed in the HAADF STEM images shown in Figs. 2a-c

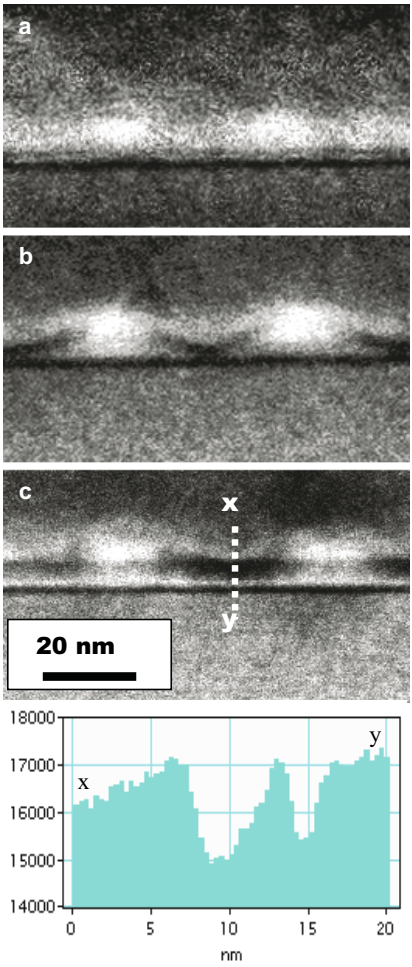


Fig. 2(a), (b) and (c) show high magnification HAADF STEM images of InAs QDs for samples A, B and C respectively. Fig 2(d) shows the brightness intensity profile of region x-y as shown in Fig 2(c).

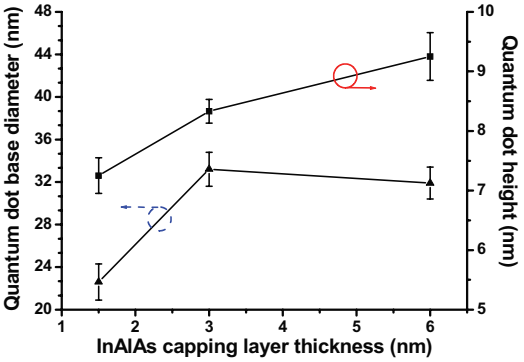


Fig. 3. Graph shows the average QD base diameter and height for different InAlAs capping layers, i.e. y = 1.5, 3.0 and 6.0-nm

suggests a significant reduction or absence of aluminium on top of the QDs. Nonetheless, HAADF STEM only shows the mean Z value of the layer. Due to the complex quaternary structural composition, consisting of Al, In, Ga and As, it is difficult to give a definitive measure of aluminium distribution. Thus, EFTEM elemental imaging was applied to map the aluminium distribution in the vicinity of the QDs.

The EFTEM aluminium maps shown in Figs. 4a and b were obtained using the aluminium $L_{2,3}$ edge, with the specimen tilted 3 (±1) degrees off the <110> zone axis to avoid electron channelling and to minimize diffraction contrast contributions. The three-window background subtraction method was employed to obtain an aluminium map around the QDs (Egerton 1996). Specimen thickness was kept well below t/λ=1.0 where λ is the inelastic mean free path. In Figs. 4a and b, the locations of InAs QDs are indicated with rectangles, and the bright contrast in the EFTEM images indicates the presence of aluminium. From Figs. 4a and b, what is apparent is a significant reduction in the aluminium signal on top of the InAs QDs , in particular in the case of the 6.0-nm InAlAs capping layer, with most of the aluminium apparently segregated laterally to the periphery of the QDs. Contrary to Wei et al (2002), which reported that aluminium adatoms are deemed immobile at the growth temperature of 510°C, our results corroborate the findings of Xie et al (1994) which suggests that mobile surface aluminium adatoms migrate away from the apex of the InAs QDs during the initial InAlAs overgrowth. This can be understood through the presence of energetically unfavourable nucleation sites for aluminium adatoms at the apex of the elastically relaxed InAs islands as a result of large differences in lattice constant between InAs and AlAs.

It is well known that strain driven migration is the dominant thermodynamically favoured mechanism which results in the morphological evolution of the QD during the overgrowth process (Songmuang et al 2003, Ledentsov et al 1996). However, for an InAlAs capping layer there are more indium atoms on the surface of the layer between InAs islands during the capping process compared with the surface of an InGaAs capping layer due to the enhanced indium segregation within the InAlAs overgrowth layer (Tey et al 2005). This is probably attributed to the poor In-Al intermixing due to large difference between the InAs and AlAs bond energies that could cause alloy clustering and

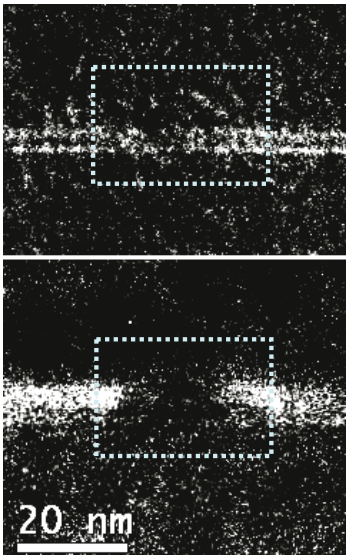


Fig. 4(a) and (b) show aluminium EFTEM maps for samples B and C. The rectangle frame indicates the position of a QD.

compositional modulation (Tournie et al 1991). The higher concentration of indium adatoms on the overgrowth surface, contributed by the InAlAs capping layer, will decrease the surface chemical potential gradient between the QDs and the capping layer. Moreover, the surface elastic energy is reduced due to the lower lattice mismatch between the QDs and the capping layer surface layer (Liu et al 2005). As a consequence, the detachment rate of indium atoms from InAs QDs and subsequent migration to the capping layer surface is suppressed and thus the height of the QDs is preserved more efficiently during the InAlAs capping layer overgrowth.

4. CONCLUSIONS

In conclusion, a structural study on the effects of InAlAs-InGaAs capping layer on InAs QDs has been carried out. Based on HAADF STEM imaging and EFTEM elemental mapping, we provide a new structural and compositional analysis which shows a profound reduction in the aluminium concentration on top of the QDs. Our results also show that subsequent increase of $In_{0.2}Al_{0.8}As$ capping layer thickness results in a corresponding increase in the height of QDs. Indium segregation and reduced aluminium adatom surface mobility within the InAlAs overgrowth has been suggested to increase the indium atom density on the surface of the InAlAs capping layer. Thus, a reduction of the indium detachment rate from InAs QDs during InAlAs overgrowth is proposed as a possible mechanism for the increased InAs QD height.

REFERENCES

Bimberg D, Grundmann M and Ledentsov N N, Quantum Dot Heterostructures 1999 (John Wiley, Chichester) *and references therein*

Cullis A G, Norris D J, Walther T, Migliorato M A and Hopkinson M 2002 Phys. Rev. B **66,** 081305(R)

Egerton R F 1996 Electron Energy Loss Spectroscopy in the Electron Microscope (Plenum, New York)

Ledentsov N N, Shchukin V A, Grundmann M, Kirstaedter N, Böhrer J, Schmidt O, Bimberg D, Ustinov V M, Egorov A Yu, Zhukov A E, Kop'ev P S, Zaitsev S V, Gordeev N Yu, Alferov Zh I, Borovkov A I, Kosogov A O, Ruvimov S S, Werner P, Gösele U and Heydenreich J 1996 Phys. Rev. B **54,** 8743

Liu H Y, Sellers I R, Hopkinson M, Mowbray D J and Skolnick M S 2003a Appl. Phys. Lett. **83,** 3716

Liu H Y and Hopkinson M 2003b Appl. Phys. Lett. **82,** 3644

Liu H Y, Tey C M, Sellers I R, Beanland R, Mowbray D J, Skolnick M S, Hopkinson M and Cullis A G 2005 J. Appl. Phys. *in press*

Mukai K, Nakata Y, Otsubo K, Sugawara M, Yokohama N and Ishikawa H 2000 Appl. Phys. Lett. **76,** 3349

Songmuang R, Kiravittaya S and Schmidt O G 2003 J. Cryst. Growth **249,** 416

Tey C M, Liu H Y, Cullis A G, Ross I M and Hopkinson M 2005 J. Cryst. Growth **258,** 17

Tournie E, Zhang Y H, Pulsford N J and Ploog K 1991 J. Appl. Phys. **70,** 7362

Wei Y Q, Wang S M, Ferdos F, Vukusic J, Larsson A, Zhao Q X and Sadeghi M 2002 Appl. Phys. Lett. **81,** 1621

Xie Q H, Chen P and Madhukar A 1994 Appl. Phys. Lett. **65,** 2051

Microstructural studies of InAs/GaAs self-assembled quantum dots grown by selective area molecular beam epitaxy

J C C Lin, I M Ross[1], P W Fry[2], A I Tartakoskii[2], R S Kolodka[2], R Hogg, M Hopkinson, A G Cullis[1] and M S Skolnick[2]

EPSRC National Centre for III-V Technology, University of Sheffield, Sheffield, S1 3JD, UK
[1] Department of Electronics and Electrical Engineering, University of Sheffield, Sheffield, S1 3JD, UK
[2] Department of Physics and Astronomy, University of Sheffield, Sheffield, S3 7RH, UK

ABSTRACT: In this paper, we report the positional and size modulation of self assembled InAs/GaAs quantum dots grown by selective area solid source molecular beam epitaxy. Scanning electron microscopy and atomic force microscopy indicate a reduction in the size and dot density within ~50μm of a polycrystalline covered dielectric mask in the uncapped deposits. These findings were confirmed by low temperature micro-photoluminescence in the corresponding capped material. In addition, capped samples were examined using scanning transmission electron microscopy. The observed reduction in the dot size and density was attributed to the migration of indium from the patterned mesa towards the polycrystalline covered mask.

1. INTRODUCTION

Selective area epitaxy (SAE) is a powerful tool, allowing the realization of sophisticated devices that benefit from a local thickness modulation of the deposited material (Gibbon et al 1993). SAE has more recently been extended to the precise positional control of semiconductor nanostructures for integrated optoelectronic and quantum information processing. To date these studies have been limited to growth techniques using metal-organic sources such as metal organic vapour phase epitaxy (Tachibana et al 2000, Kim et al 2002) and chemical beam epitaxy (CBE) (Tsui et al 1997, Poole et al 2002). Nevertheless solid source molecular beam epitaxy (MBE) remains one of the most widely used techniques for the growth of self-assembled quantum dots (QDs). This is in the main due to the high level of accuracy in determining the thickness of the deposited material and the sensitivity of the QD properties to these parameters. However, there have been very few reports of the application of SAE, for example using a dielectric mask, by solid source MBE as a consequence of the low growth selectivity between the mask and epitaxial area, which results in the formation of a polycrystalline deposit on the masked area. To overcome this problem, periodic supply epitaxy (PSE) has been developed to reduce such deposition in MBE (Nishinaga and Bacchin 2000). By manipulating the group III adatom pause-to-supply ratio, a polycrystalline-free mask area around the bulk epitaxial area can be obtained. However, in practice SAE generally leads to an undesirable increase in the growth time. In this paper, we report the positioning of optically active self-assembled quantum dots by selective area solid source MBE. PSE has been applied in a reduced schedule to reduce but not eliminate the formation of a polycrystalline deposit on the dielectric mask but still maintain acceptable reactor processing times.

2. EXPERIMENTAL

Patterned wafers were prepared by the deposition of 100nm thick SiO_2 mask pattern onto a GaAs (001) substrate by plasma enhanced chemical vapor deposition, electron beam lithography and reactive ion etching. Groups of six identical SiO_2 masks of length 1.3mm parallel to the GaAs [110] direction were organized in matrices consisting of various mask and spacing dimensions. The width of the masks and the

spacing between the masks were 1, 2, 3 and 4μm and 0.5, 0.75, 1.0, 1.25, 1.5, 2.0, 2.5, 3.0, 4.0μm respectively. Prior to the MBE growth, oxygen plasma cleaning was applied to remove any residual PMMA, the wafer degreased and oxygen desorption performed at 400°C for 2 hours. A solid-source VG Semicon V90H MBE system was used to deposit a 200nm GaAs buffer layer in 40 pulse cycles. Each pulse cycle consisted of a 5nm GaAs growth at 590°C at rate 0.2 nm/sec and an interrupt of 2 minutes at 620°C whilst maintaining a constant As pressure. Four, 1 nm AlAs marker layers were inserted within this 200nm GaAs layer growth before the 1st, 11th, 21st and 31st pulse cycles, at the same 590°C with a rate of 0.072nm/sec. The QDs were formed by depositing 2.5ML of InAs at 500°C with a deposition rate 0.05ML/sec. The substrate was then crash cooled to room temperature. For optical characterization, a second sample was prepared identical to the first one, with the addition of a capping layer consisting of 10nm of GaAs grown at 590°C and 200nm of GaAs/AlAs identical to the previously described buffer layer. Microstructural characterisation of the uncapped dots was performed using a combination of atomic force microscopy (AFM) (Dimension 3100) and scanning electron microscopy (SEM) (JEOL 6500F). Cross-sectional thin sections were prepared from the capped samples for examination in the scanning transmission electron microscope (STEM) by focused ion beam (FIB) milling (JEOL Fabrika). STEM analysis was performed in a JEOL 2010F TEM operating at 200kV. Micro-photoluminescence spectroscopy (μPL) was conducted at 7K using a 0.2nW He-Ne laser exciting an area ~2μm in diameter. The PL response was spectrally resolved and detected by a cooled Ge detector.

3. RESULTS and DISCUSSION

In this report we will focus our attention on the interesting modulation in the QD size and density around the periphery of the masked area and as a function of distance along the mesa ridges. Figure 1 shows a low magnification SEM image of one end of a typical mesa and mask arrangement in this instance the capped 4μm mesa and 2μm mask geometry.

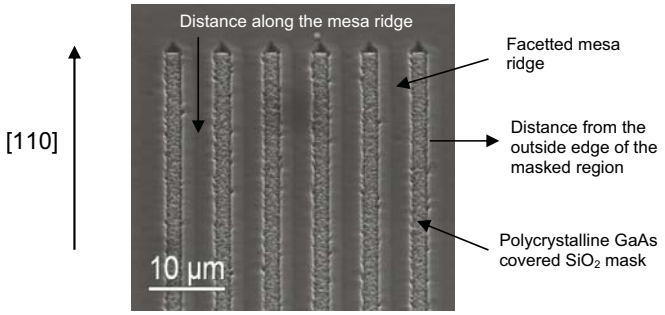


Fig. 1: SEM image illustrating the 4μm mesa and 2μm mask geometry.

Figure 2a shows one end of a mesa between two parallel mask regions in the corresponding uncapped sample to that shown in Fig. 1. The polycrystalline deposit over the underlying SiO_2 mask and the formation of QDs is clearly observed. Detailed examination of the QDs on the epitaxial material between the parallel mask regions reveals a bimodal structure consisting of randomly orientated QDs forming extensively around the periphery of the mask regions and lines of self-aligned QDs forming along the intersection of the top and sidewall facets. In this instance these facets correspond to the GaAs (001) and (111)B facets respectively. These observations were in agreement with the findings of previous workers investigating CBE grown InAs QDs on GaAs (Zhang et al 1998) and similar experiments concerning Ge QDs on Si (001) mesas (Kamins and Williams 1997). The formation of lines of self-aligned QDs is attributed to both strain relief at the edge of the mesa and the high availability of atomic steps for QD nucleation. SEM observations and AFM measurements were used to quantify the QDs. The self-aligned QDs on the edges of the mesa ridges were found to be well defined and more uniformly distributed compared to the other QDs. However, on the whole a general decrease in the average QD height was recorded as a function of distance from each end of the mesa ridges from ~7.9nm in the bulk GaAs to ~5.8nm 20μm from the end of the mesa ridge. On the other hand, the average dot diameter

remained roughly constant (~25nm) at all positions. Interestingly, the dot density was also observed to reduce significantly in the epitaxial material with distance away from the mesa edge. For the 4μm mesa and 2μm mask geometry a dot density of $1.6x10^{10}/cm^2$ was measured adjacent the polycrystalline covered mask reducing to $2.8x10^{9}/cm^2$ ~1.4μm distant from the edge. Moreover, there was a further modulation in the non self-aligned dot density as a function of distance along the mesa, from $1.24x10^{10}/cm^2$ a few microns from the open-end (Fig. 2b) to $7.6x10^{9}/cm^2$ 27μm further along the ridge (Fig. 2c). At a distance along the mesa of ~50μm the only dots observed were those formed at the edge of the ridge (which remained almost uninterrupted along the entire length of the mesa). A gradual reduction in dot density was also observed from a distance of ~100μm outside the mask defined area, from $\sim1.96x10^{10}/cm^2$ in the bulk non-paterned GaAs to $\sim3.5x10^{9}/cm^2$ 2-3μm from the outer mask strip.

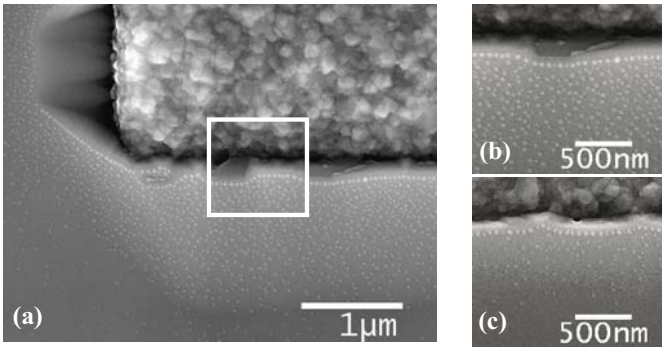


Fig. 2: (a) SEM image of the uncapped sample showing one end of a 4μm wide mesa adjacent a 2μm wide masked region. (b) Image of the region defined by the box in Fig2a, a line of QDs is seen clearly at the edge of the ridge. (c) A 27μm offset along the mesa shows a reduction of QD density at the centre of the ridge while the line of QDs is still observed along the mesa edge.

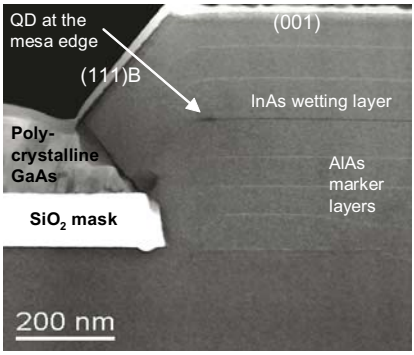


Fig. 3: [110] BF-STEM image through the edge a single capped mesa ridge ~50μm from one end showing the facetted growth of the epitaxial material and the presence of a single QD.

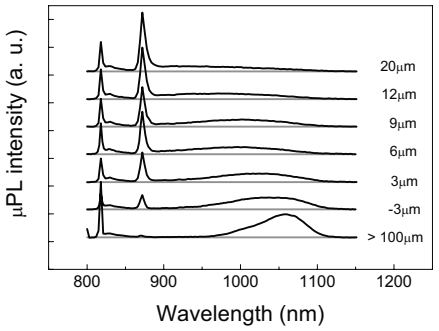


Fig. 4: μPL spectrum series at various distances from the end of the mesa ridge for the pattern group with a 4μm wide mesa between two 2μm wide masked regions.

A BF-STEM image of a FIB prepared cross-section through a single capped mesa ridge from the structure shown in Fig. 1, sampled ~50μm from the end of the mesa ridge is shown in Fig.3. The cross-section highlights the presence of the polycrystalline deposit over the SiO_2 masks and the facetted mesa growth. The facetted structure derives from the different growth rates of the GaAs (001) and (111)B, the latter being the slower growing plane. An enhancement in the thickness of the deposited epitaxial material adjacent to the masked regions is observed, attributed to the lateral diffusion of material on the masks prior to complete coverage by the polycrystalline deposit. Hence,

preferential growth along the GaAs (001) (top facet) and (111)B (sidewall facet) results in a non-planar surface of the epitaxial material which in turn impacts upon the the QD self-assembly.

Figure 4 shows a series of μPL scans obtained from the capped 4μm mesa, 2μm wide mask pattern group. The μPL spectrum from a distance ~100μm from the patterned region is dominated by ground state QD emission at 1060nm, with a higher energy shoulder at 1000nm attributed to an excited state of the QDs. The 2D wetting layer shows a weak signal at 870nm and the bulk GaAs signal is observed at 820nm. As the laser is translated along the centre of the mesa ridge between the masks, a strong reduction in the μPL intensity is recorded along with a strong increase in the wetting layer emission (870nm). This is consistent with the reduction in the QD density observed in our structural studies. In addition, a strong blue-shift of the QD ground state emission is observed, again consistent with our observations of a reduction in the QD height along this direction. The observed reduction in dot density close (<50μm) to the SiO_2 masks can be explained in terms of the transport of indium during growth. The μPL response from the wetting layer at the centre of the mesa structure gave a slightly shorter wavelength to that derived from the mask regions. The longer wavelength wetting layer μPL response from the mesa ridge suggests that the indium concentration may be higher within this region, implying the migration of In from the area surrounding the mask region during growth. It has been reported that at low growth rates and/or high growth temperatures group III adatoms may migrate from the top (001) facet down the (111)B sidewall and away from the mesa under certain conditions (Zhang et al 1998). No evidence for the formation of QDs or a continuous wetting layer was observed on the (111)B sidewall facets. This supports the proposition that In migrates towards the polycrystalline covered mask which in turn reduces the InAs coverage on the top (001) facet below the critical thickness for dot formation at the central regions of the mesa ridges. The increase in the QD density around the ends of the mesa ridges can be explained in terms of the increased number of atomic steps available for QD nucleation adjacent to the mask region. Therefore, in this case, the formation of a polycrystalline deposit, normally seen as a disadvantage of selective area MBE may be in fact be a useful tool in the control of selective QD growth. The potential to utilize this phenomenon to achieve active and passive layers by modulating the In coverage thus controlling the QD size, and hence the operating wavelength, is currently being assessed.

4. SUMMARY

We have reported the microstructural characterization of optically active, self-assembled InAs/GaAs QDs grown by selective area solid source MBE. Examination of the uncapped QDs revealed a bimodal distribution of QDs consisting of isolated lines of self-aligned QDs forming along the edges of the mesa structures and randomly orientated QDs forming around the periphery of the mask defined region. Overall, a positional and size modulation was seen; a reduction in the size and dot density within ~50μm of a polycrystalline covered dielectric mask was observed, which was confirmed by low temperature μPL. This is attributed to the migration of In adatoms towards the GaAs polycrystalline covered mask. The presence of a polycrystalline deposit on the dielectric mask therefore provides a potentially useful means to modify the properties of QD-based materials.

ACKNOWLEDGEMENT

The authors acknowledge the Engineering and Physical Sciences Research Council (EPSRC) for supporting this work (GR/R65626/01 and GR/S02150/01).

REFERENCES

Gibbon M, Stagg J P, Cureton C G, Thrush E J, Jones C J, Mallard R E, Pritchard R E, Collis N and Chew A 1993 Semicond. Sci. and Technol. **8**, 998
Kin H J, Motohisa J and Fukui T 2002 Appl. Phys. Lett. **81**, 5147
Tachibana K, Someya T, Ishida S and Arakawa Y 2000 J. Crystal Growth **221**, 576
Tsui R, Zhang R, Shiralagi K and Goronkin H 1997 Appl. Phys. Lett. **71**, 3254
Poole P J, Lefebvre J and Fraser J 2003 Appl. Phys. Lett. **83**, 2055
Nishinaga T and Bacchin G 2000 Thin Solid Films **367**, 6
Zhang R, Tsui R, Shiralagi K, Convey D and Goronkin H 1998 Appl. Phys. Lett. **73**, 505

Chemical composition and strain distribution of InAs/GaAs(001) stacked quantum rings

T Ben, A M Sánchez, S I Molina, D Granados[1], J M García[1] and S Kret[2]

Dpto. de Ciencia de los Materiales e Ingeniería Metalúrgica y Q. I. Facultad de Ciencias. Campus Río San Pedro, Pto. Real. (Cádiz), Spain
[1] Instituto de Microelectrónica. de Madrid, CNM (CSIC).C/ Isaac Newton 8, PTM 28760- Tres Cantos. (Madrid). Spain
[2] Institute of Physics PAS, Al. Lotników 32/46, 02-688. Warsaw, Poland

ABSTRACT: The strain and composition distributions of InAs/GaAs(001) stacked self-assembled quantum rings (QRs) grown by MBE have been analyzed. Transmission electron microscopy (TEM) images revealed a high degree of vertical arrangement of quantum rings for samples spaced by a GaAs spacer layer thickness $t_s \leq 6$ nm. The peak finding method was applied to high resolution transmission electron micrographs in order to plot strain maps, revealing that the higher strained areas were in the ring core and close to it. The existence of another layer with similar strain to the wetting layer was also clear from the peak finding strain analysis. The transverse compositional profiles taken from 002 DF TEM images show the existence of In-rich regions within the nano-rings and an In(Ga)As well defined layer surrounding them, which is formed during the growth process.

1. INTRODUCTION

Low-dimensional semiconductor structures have attracted much attention because they are promising for opto-electronic devices. For instance, semiconductor quantum dots confine electrons and holes in three dimensions and have therefore atomic-like properties. Furthermore, the electronic properties of low-dimensional nano-objects with annular geometries are important since these systems can exhibit a number of interesting properties: The ground state possesses a nonzero angular momentum with increasing normal magnetic field (Govorov et al 2002, Lorke et al 2000), the existence of a trapping magnetic flux and persistent current which is not affected by the presence of random scatterers (Petersson et al 2000) and the permanent dipole moment of excitons in quantum rings can be higher (Warburton et al 2000) than for quantum dots. Likewise, Granados et al (2003) showed the possibility of tailoring PL emission by controlling the size and shape of quantum rings (QRs).

A narrow-size distribution and dislocation-free growth is crucial to yield macroscopic and tuned effects in opto-electronic devices. For thin enough spacer layers, stacking of self-assembled nanostructures produces vertical correlation and improved size homogeneity due to the strain field of the buried nanostructures at the surface of the spacer layer, where the new nanostructure layer will be formed (Xie et al 1995, Sprinholz et al 2000, Brault et al 2000).

Although conventional analyses by TEM are extremely useful and versatile tools for the characterization of material, nowadays quantitative methods applied directly to HRTEM images represent an important advance to determining the strain and composition of the epitaxial nanomaterials (Hÿtch et al 1998, Rosenauer et al 1996).

In this work we have studied the vertical arrangement of stacked InAs QRs grown at 500ºC on GaAs (001) substrates, as a function of the GaAs spacer layer thickness. Compositional distribution profiles have been defined from TEM micrographs recorded with 002 reflections under dark field conditions. With the aim of extracting the strain field distribution, particularly interesting regions of the ring have been examined in depth by the peak finding method (Kret et al 2003).

2. EXPERIMENTAL

The studied samples were grown by molecular beam epitaxy (MBE). As has been explained before in detail (Granados et al 2003), the growth consisted of the deposition of InAs quantum dots (QD) on a GaAs substrate (001); after that, about 2nm of GaAs cap layer was deposited at 500ºC. The competition between the change of surface energy and the Ga-In alloying led to structures which are known as quantum rings. Following the same steps, three stacks of buried InAs QRs, separated by a GaAs spacer layer were grown. We have investigated three samples with spacer layer thicknesses of 3, 4.5 and 6nm, respectively.

For TEM examination, the samples were mechanically pre-thinned down to a thickness of about 90µm. Subsequently, they were dimpled to the final thickness of approximately 20µm. Finally, ion milling (Ar+) was carried out applying a gradually decreasing acceleration voltage under cooling with liquid nitrogen to minimize damage. TEM images have been obtained with a JEOL 1200EX, while HRTEM images were taken with JEOL 2010F and JEOL 3000F microscopes operating at 120, 200 and 300kV, respectively.

3. RESULTS

Figure 1 displays a couple of 002 DF cross sectional TEM (XTEM) images that correspond to samples with t_s= 3nm (a) and 6nm (b). While the sample spaced by 3nm of GaAs layers exhibits an obvious vertical ordering, a certain degree of arrangement loss is observed for the sample spaced by 6nm of GaAs layers, given that stacked rings groups, but also some non-stacked elements, can be observed. Some stacked and non-stacked QRs are pointed out by single and double arrows respectively in Fig. 1b. An intermediate case is presented for a spacer layer thickness of 4.5nm, which leads sometimes to a loss of the QR circular shape.

As reported in previous work (Granados et al 2004), if we look at the centre of each nano-object in the images of Fig. 1, several contrasts are observed. Firstly two darker contrasts are observed, one of them corresponding to the horizontal InAs wetting layer, and the another one to the InAs of the QR core with a spherical shape or a volcano-like morphology, left after the de-wetting process, whose contrast depends on the section analyzed. Moreover, two grey contrasts are shown, that are associated (i) to the compressing GaAs layer used in the generation of the QRs and, over it, (ii) an In(Ga)As layer that comes out from the original dot. This layer and the semi-empty core are the main parts which compose the annular morphology. The spacer and capped layers between the stacked rings appear with brighter contrast. These results give us a consolidation of the models proposed in previous work (Anders et al 2002, Erner et al 2000).

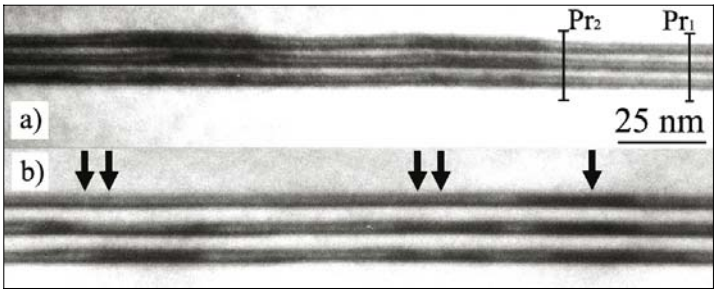


Fig. 1: 002 DF TEM images of stacked InAs QRs with 3 (a) and 6 (b) nm spacer layer.

Figure 2 depicts the different ring areas mentioned before using several grey levels. In this case the ring is shown without the cap layer growth as spacer. Figure 3 exemplifies a qualitative composition distribution profile for the region in between two rings extracted from the 002 DF TEM micrographs (see Pr_1 in Fig. 1a). Three peaks, P_1, P_2 and P_3, linked (from left to right side in the figure) to the 1st, 2nd and 3rd stacked rings layers respectively, are mainly illustrated in this profile. Each peak is deconvoluted to two gaussian curves (labelled with G_{i1} and G_{i2} on the original profile,

where i= 1, 2 or 3). The intensity profile due to GaAs has been subtracted from the original profile before the application of the deconvolution process. From the two deconvoluted gaussian curves, the highest intensity curve is ascribed to the InAs wetting layer and the lowest intensity curve to the above mentioned In(Ga)As layer. The In(Ga)As peak maximum is 30, 40, and 16% respectively below the InAs peak for the 1st, 2nd and 3rd stacked rings layers, respectively. This result helps to understand the Ga/In alloying process occurring during the ring generation.

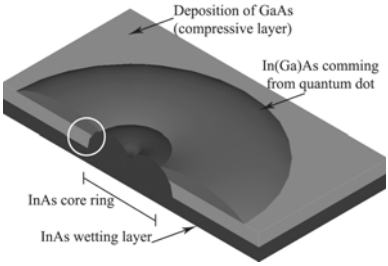


Fig. 2: Schematic drawing detailing the different areas of an uncapped ring. The encircled area corresponds to profile Pr_2 of Fig. 1(a).

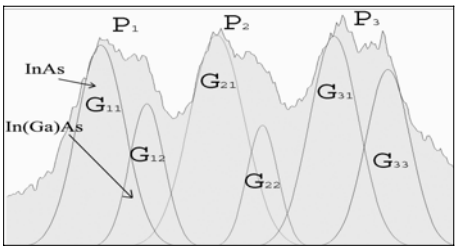


Fig. 3: In composition distribution profile along [001] for region in between two rings whose peaks have been adjusted to Gaussians.

We have also acquired composition distribution profiles (see Pr_2 in Fig. 1a) through regions around the edge of the ring core (corresponding to the encircled area of Fig. 2). It is worth mentioning that the In(Ga)As layer usually presents an In composition lower than that of the wetting layer, though for a few of these analysed areas that layer presents a composition similar to the wetting layer. Due to the TEM specimen preparation process, very different ring sections can be found in the electron-transparent slice. Due to this fact, we have concentrated our attention on a few noteworthy and less confusing ring areas, such as the core edge and the region in between two of rings.

Figure 4a shows one of the HRTEM images analysed by the peak finding method corresponding to a region where just the In(Ga)As upper layer is joined to the ring core. The displacement vectors between maximum intensity positions on the image and reference lattice determined in the substrate (or in another reference region of the material) are identified, and the strain field is plotted by the derivation of these vectors with respect to the spatial coordinates (Kret et al 2003). The determined strain map (measured with respect to the GaAs lattice parameter) along [001] (ε_{zz}) is shown in Fig. 4b.

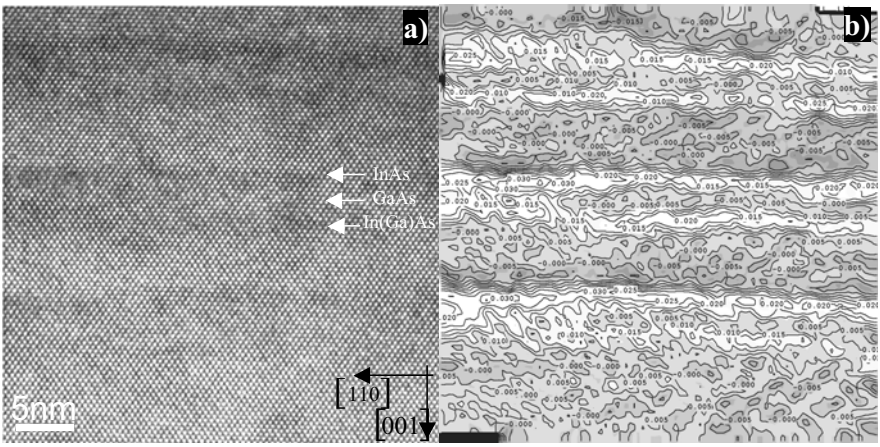


Fig. 4: a) HRTEM image of the sample consisting of three InAs stacked rings layers with 6 nm spacer layer thickness. b) Contour plot of the experimental strain map ε_{zz} determined from the HRTEM image.

The strain field map of Fig. 4b reveals a more highly strained region near of the ring core for the second and third layers. That is, an increase of the strain field occurs for the upper layers (see the right side of Fig. 4b). Nevertheless, the same number of InAs monolayers has been deposited for the QD formation for the three stacked quantum ring layers, and so we can ensure that the In incorporated amount is higher than that introduced into the MBE chamber for the second and third layers. The GaAs compressing layers have a strain close to the GaAs spacer layers. Next to and on top of each ring core, a layer with a strain smaller than the wetting layer is appreciated. In a few cases this layer can have a strain similar to (or even slightly larger than) the strain of the wetting layer. From this result and the compositional profiles we conclude that the In(Ga)As layer formed during the de-wetting process has, in some few cases, similar to (or slightly larger than) the In composition of the wetting layer, decreasing as we move away from the ring core.

4. CONCLUSION

A vertical correlation of QRs is reached for spacer layer thickness ts ≤ 6nm. 002 dark field TEM image profiles reveal clearly an In-rich core in the ring left after occurrence of the dot de-wetting process, and an In(Ga)As layer which begins next to this core and spreads along on the GaAs compressing layer up to the adjacent ring.

The ε_{zz} strain maps determined by the peak finding method confirm the existence of an In-rich core in the ring and an In(Ga)As layer highly strained. This method together with transversal profiles for 002 DF TEM images allow us to conclude, in some few cases, that the In(Ga)As layer composition is similar to (or slightly larger than) the wetting layer composition in the region close to ring core.

ACKNOWLEDGEMENTS

This research was supported by Spanish MCyT under project NANOSELF (TIC-2002-04096-C03-02), Junta de Andalucía (PAI research group TEP-0120) and network of excellence SANDiE (Contract NMP4-CT-2004-500101 of the VI European Framework Programme).TEM measurements were carried out in the DME-SCCYT, University of Cádiz and UCM.

REFERENCES

Anders S, Kim C S, Klein B, Keller Mark W and Mirin R P 2002 Phys. Rev. B **66**, 125309

Brault J, Gendry M, Marty O, Pitaval M, Olivares J, Grenet G and Hollinger G 2000 Appl. Surf. Sci. **162–163,** 584

Erner P W, Cheerschmidt K S, Akharov N D Z, Illebrand R H, Rundmann M G and Chneider R S 2000 Cryst. Res. Technol. **35**, 6-7

Granados D and García J M 2003 Appl. Phys. Lett. **85** (15), 2401

Granados D, García J M, Ben T and Molina S I 2004 Appl. Phys. Lett. **86** (7), 071918

Hÿtch M J, Snoeck E and Kilaas R 1998 Ultramicroscopy **74**, 131

Kret S, Ruterana P, Delamar C, Benabras T and Dluzewski P 2003 Nitride Semiconductors, Handbook on Materials and Devices (Wiley-Vch HmBh & Co. KgaA Heppwnheim, Germany). p. 439-485

Lorke A, Luyken R J, Govorov A O, Kotthaus J P, Garcia J M and Petroff P M 2000 Phys. Rev. Lett. **84**, 2223

Pettersson H, Warburton R J, Lorke A, Karrai K, Kotthaus J P, Garcia J M and Petroff P M 2000 Physica E **6**, 510

Rosenauer A, Kaiser S, Reisinger T, Zweck J and Gebhardt W 1996 Optik **102**, 63

Springholz G, Pinczolits M, Mayer P, Holy V, Bauer G, Kang H H and Salamanca-Riba L 2000 Phys. Rev. Lett. **84**, 20

Tersoff J, Teichert C and Lagally M G 1996 Phys. Rev. Lett. **76**, 1675

Warburton R J, Schäflein C, Haft D, Bickel F, Lorke A, Karrai K, Garcia J M, Schoenfeld W and Petroff P M 2000 Nature **405**, 926

Xie Q, Madhukar A, Chen P and Kobayashi N P 1995 Phys. Rev. Lett. **75**, 2542

In distribution in InGaAs quantum wells and quantum islands

D Litvinov, D Gerthsen, A Rosenauer[1], T Passow[2], M Grün[2], C Klingshirn[2] and M Hetterich[2]

Laboratorium für Elektronenmikroskopie and Center for Functional Nanostructures (CFN), Universität Karlsruhe, D-76128 Karlsruhe, Germany
[1] Institut für Festkörperphysik, Universität Bremen, D-28359 Bremen, Germany
[2] Institut für Angewandte Physik and CFN, Universität Karlsruhe, D-76128 Karlsruhe, Germany

ABSTRACT: The In distribution in epitaxial InGaAs layers grown by molecular-beam epitaxy on GaAs (001) was investigated using transmission electron microscopy (TEM). InGaAs layers with In concentrations between 16 % and 28 % were deposited at temperatures between 500 °C and 548 °C. In concentration profiles were obtained from high-resolution TEM images by composition evaluation by lattice fringe analysis. The quantum wells and quantum islands are characterized by an asymmetric In distribution demonstrating the strong influence of In segregation. A significant increase of the In segregation efficiency is observed with increasing growth temperature.

1. INTRODUCTION

Heterostructures based on InGaAs have attracted considerable interest owing to their applications in optoelectronics. More recently, InAs quantum-dot systems are also considered as devices for spin storage in quantum information processing (see e.g. Imamoglu et al 1999). In particular for the latter application, small InAs quantum dots with the highest possible In concentration are required to obtain a strong confinement potential and large separation between quantized states.

In the present work we have analysed In segregation during molecular-beam epitaxy (MBE) growth, which is the main origin of intermixture between the group-III elements leading to a reduction of the average In concentration in InGaAs nanostructures. Quantitative measurements of the In distribution in the InGaAs quantum wells (QWs) and quantum islands were performed on an atomic scale by high-resolution (HR) transmission electron microscopy (TEM) combined with the composition evaluation by lattice fringe analysis (CELFA) technique. This allows the evaluation of In segregation efficiencies as a function of the In concentration and substrate temperature during the growth.

2. EXPERIMENTAL PROCEDURES

The samples were grown by MBE on a GaAs(001) substrate. After the growth of a GaAs buffer layer at 570 °C, the substrate temperature was reduced to the growth temperature of the InGaAs layer. The structures were capped by ~ 30 nm GaAs. Sample 1 contains three InGaAs layers grown at 535 °C, which are separated by GaAs layers with a thickness of 28 nm. The nominal parameters of the three $In_xGa_{1-x}As$ layers in sample 1 are: 23 monolayers (ML) and $x=0.28\pm0.02$, 20 ML and $x=0.16\pm0.02$, 22 ML and $x=0.25\pm0.02$. These values were determined by *in-situ* reflection high-energy electron diffraction (RHEED) oscillations. Only during the deposition of the first InGaAs layer, a transition between two-dimensional (2D) and three-dimensional (3D) growth is observed by

RHEED. The growth was interrupted before the deposition of the InGaAs layers to change the In-cell temperature. The As:Ga beam equivalent pressure ratio was 15:1 for the whole structure. Five other samples were analysed containing only one $In_xGa_{1-x}As$ QW with a nominal thickness of 22 ML and x=0.25 ± 0.02 which were deposited at different growth temperatures between 500 °C and 548 °C.

The structural properties were studied by TEM of cross-section samples viewed along the [010]-zone axis prepared according to Strecker et al (1999). A Philips CM 200 FEG/ST electron microscope with an electron energy of 200 keV was used for the TEM investigations. The In concentration in the InGaAs layers was obtained on an atomic scale by CELFA evaluation of HRTEM lattice-fringe images taken under (002) two-beam conditions with the (002) reflection oriented on the optical axis. Briefly, the local In concentration was determined by measuring of the amplitude of the chemically sensitive (002) reflection for ternary InGaAs with respect to simulated amplitudes using GaAs as a reference. The details are outlined by Rosenauer and Gerthsen (1999).

3. RESULTS AND DISCUSSION

Figure 1 presents a cross-section dark-field image of sample 1 taken with the (002) reflection, which is composition-sensitive in the sphalerite structure. Three InGaAs layers can be identified by their lower brightness. The first InGaAs layer (bottom) with x=0.28 ± 0.02 contains defect-free 3D islands with lateral sizes up to 40 nm and cores with a bright contrast which intensifies towards the top of the island (Fig. 1). The calculation of the (002) dark-field intensity for InGaAs with the Bloch-wave method using the EMS program package (Stadelmann 1987) shows that bright contrast of InGaAs with respect to GaAs is observed for In concentrations higher than ~ 18 % if structure factors computed with the density functional theory formalism are used. A bright contrast can be also identified in the middle of the top InGaAs QW in Fig. 1. This indicates that the true In concentration in the middle of this layer is higher than 18 %, corresponding to the nominal In concentration x=0.25 ± 0.02 for this layer. The intensity profile of the (002) dark-field images can be used to determine the local composition. However, the error of this method is relatively large.

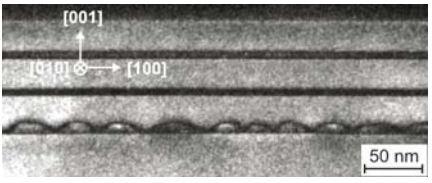


Fig. 1. Dark-field TEM image of a [010] cross-section sample 1 taken with **g** = (002).

The accuracy of the composition analysis is improved by the CELFA technique, which allows the quantitative determination of the In distribution on an atomic scale. Averaged In concentration profiles are presented in Fig. 2a as a function of the distance along the [001]-growth direction for the QWs 2 and 3 of sample 1 (top layers in Fig. 1). The In segregation efficiency R was evaluated on the basis of the concentration profiles using an empirical segregation model. According to Muraki et al (1992), the In distribution can be described by

$$x(n) = \begin{cases} 0 & : \quad n < 1 \\ x_0(1-R^n) & : \quad 1 \le n \le N \\ x_0(1-R^N)R^{n-N} & : \quad n > N \end{cases}, \qquad (1)$$

where n is the number of MLs in growth direction, x_0 the nominal In concentration, and N the total amount of deposited In expressed in MLs of InAs. Using R, x_0 and N as fit parameters, Eq. (1) was fitted to the experimental profile shown in Fig. 2 (solid curves). The shape of the In concentration profiles in layers 2 and 3 is non-symmetrical, the descending part of the curve resulting from In segregation during GaAs deposition on the InGaAs QW. In segregation efficiencies of 0.80±0.01 for layer 2 and 0.79±0.01 for layer 3 are derived from the profiles in Fig. 2a. Averaged values for R yield R=0.805±0.015 for layer

2 and R=0.795±0.015 for layer 3. Note, that both layers were grown at the same temperature of 535 °C and their R is not affected by the differing values for x_0 within the error limit.

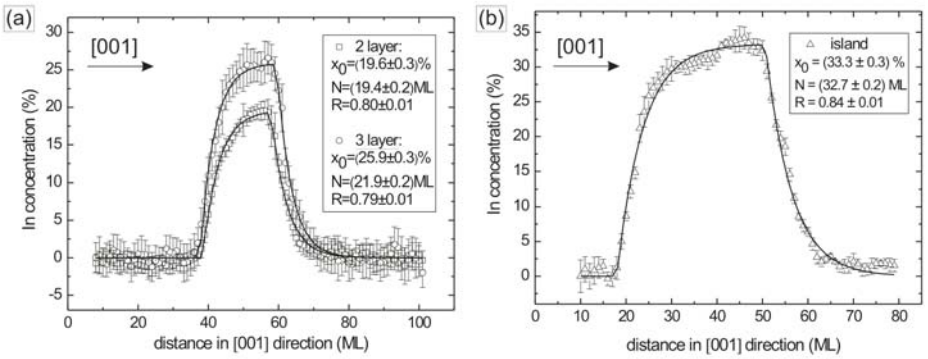


Fig. 2. In concentration profiles averaged along the [100] direction as a function of the [001] distance in units of ML (a) for the centred (squares) and top (circles) InGaAs QWs of sample 1, (b) for an island of the bottom InGaAs layer of sample 1. The solid curves correspond fits according to the model of Muraki et al (1992). The error bars give the standard deviation obtained by the averaging along the respective ML.

Figure 2b shows a concentration profile, which was obtained from an island of the bottom layer of sample 1 (Fig. 1). We observe pronounced In segregation as well, with a segregation efficiency of 0.84 ±0.01. The determination of R for several islands gives an average value R=0.86±0.04, which is slightly higher compared to the QWs (~ 0.8). The possible causes for the relatively large standard deviation in the case of the islands are discussed below.

One possible error concerns the deviation from the required two-beam condition due to bending of lattice planes in strained islands and thin TEM samples. However, it was shown by Rosenauer et al (2001), that the effect of lattice-parameter variation and lattice bending on the amplitude of the (002) beam is rather small. Measurements of local lattice parameters in the islands (not shown here) by strain state analysis (Rosenauer and Gerthsen 1999) reveal a strong increase of the local lattice parameters, not only at the top but also at the bottom of each island. This could imply a high In concentration at the top and bottom. However, we observe an increasing amplitude of the (002) reflection, i.e. an increasing In concentration, only in the upper part of the islands which is reasonable due to In segregation.

We also have to consider the effect of an InGaAs island embedded in a GaAs matrix, which is contained in a thin HRTEM sample, on the measured In distribution. The island size is relatively large in our case (~ 40 nm in diameter). If the island is situated symmetrically in the TEM specimen with a thickness ≤ 15 nm, we do not observe an influence of the embedding matrix almost up to the top of the island. Thus, its real In concentration profile will be measured. If the island is positioned asymmetrically in the TEM specimen or if the thickness of the TEM specimen is larger than 15 nm, a reduced In concentration will be measured in the upper part of the island. The measured In concentration profile will then differ from the true profile which is the most likely origin for the variation of the R values in islands.

The temperature dependence of the In segregation efficiency was investigated by analysing InGaAs QWs with identical In concentration (~ 25 %), thickness (22 ML) and deposition conditions apart from the substrate temperature. The results for R in the temperature range between 500 °C and 548 °C are shown in Fig. 3. The In segregation efficiency increases significantly from 0.65 to 0.85, which clearly shows that In segregation is strongly dependent on the growth temperature. Our values for R at different growth temperatures differ from literature data (e.g. Rosenauer et al 2001, Martini et al 2003) indicating that In segregation depends also on other growth parameters, e.g. the beam equivalent pressures of the elements.

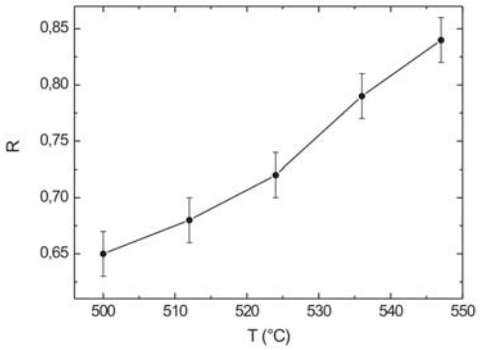


Fig. 3. In segregation efficiency *R* averaged in different regions of the quantum wells as a function of the growth temperature *T*. The error bars give the standard deviation obtained by the averaging of the measured values *R* from the different regions of the QWs.

4. SUMMARY

We have studied In segregation during MBE growth of InGaAs quantum-well and quantum-island structures. Our results show that the In segregation efficiency in the quantum wells does not depend significantly on the In concentration in the investigated range between 16 and 25 %. A Stranski-Krastanow transition takes place if the In concentration exceeds 25 % at a substrate temperature of 535 °C. Due to the large size of the islands, reliable measurements of the In concentration in islands could be carried out which yield an In segregation efficiency of 0.86±0.04. The analysis of the In distribution in quantum wells with an In concentration of ~ 25 % shows that the segregation efficiency increases with growth temperature from 0.65 at 500 °C to 0.83 at 548 °C.

ACKNOWLEDGEMENTS

The authors gratefully acknowledge the financial support by the Deutsche Forschungsgemeinschaft (DFG) within project A2 of the Center for Functional Nanostructures (CFN) at the University of Karlsruhe (Germany).

REFERENCES

Imamoglu A, Awschalom D D, Burkard G, DiVincenzo D P, Loss D, Sherwin M and Small A 1999 Phys. Rev. Lett. **83**, 4204

Martini S, Quivy A A, da Silva M J, Lamas T E, da Silva E C F, Leite J R and Abramof E 2003 J. Appl. Phys. **94**, 7050

Muraki K, Fukatsu S, Shiraki Y and Ito R 1992 Appl. Phys. Lett. **61**, 557

Rosenauer A and Gerthsen D 1999 Advances in Imaging and Electron Physics **107**, 121

Rosenauer A, Gerthsen D, Van Dyck D, Arzberger M, Böhm G and Abstreiter G 2001 Phys. Rev. B **64**, 245334

Stadelmann P A 1987 Ultramicroscopy **51**, 131

Strecker A, Mayer J, Baretzky B, Eigenthaler U, Gemming T H, Schweinfest R and Rühle M 1999 J. Electron Microscopy **48**, 235

Activation energy for surface diffusion in GaInNAs quantum wells

M Herrera[1], D González[1], J G Lozano[1], M Hopkinson[2], M Gutierrez[2], P Navaretti[2], H Y Liu[2] and R García[1]

[1] Departamento de Ciencia de los Materiales e I. M. y Q. I., Universidad de Cádiz, Apartado 40, 11510 Puerto Real, Cádiz, Spain
[2] Department of Electronic and Electrical Engineering, University of Sheffield, Mappin Street, Sheffield S1 3JD, UK

ABSTRACT: The analysis by transmission electron microscopy of GaInNAs/GaAs(001) quantum wells grown at different temperatures in the range 375-420 ºC is reported. Our results with the 220BF reflection have shown the existence of periodic strain contrasts in all the wells, associated with composition fluctuations in the alloy. These contrasts are more pronounced with increasing growth temperature, revealing a kinetic limitation for the formation of the phase separation. With the theoretical equation proposed by Cahn and the amplitude of the intensity profiles taken from 220BF micrographs, the activation energy for surface diffusion in GaInNAs is calculated.

1. INTRODUCTION

Nowadays, the GaInAsP/InP alloy is one of the most widely used systems for the active layer of 1.3 μm semiconductor lasers with telecommunication applications. However, this system has as a major disadvantage the poor carrier confinement, which produces temperature-dependent threshold currents and makes thermoelectric cooling indispensable. To overcome this problem, III-V-N alloys with low bandgap energies such as GaAsN and GaInNAs have recently been investigated, on the basis that they are expected to have much larger conduction-band offsets (Kondow et al 1996). In combination with the presently available GaAs/AlAs distributed Bragg reflector technology, the GaInNAs alloy could give optimized vertical-cavity lasers for the long wavelength region. Up to now, GaInNAs quantum wells have shown a vertiginous pace of progress in laser characteristics (Ustinov and Zhukov 2000).

Nevertheless, the structural properties of the GaInNAs alloy and its heterostructures remain poorly understood. The optical quality of this system strongly degrades with increasing N concentration (Li et al 2001) possibly due to the large miscibility gap and phase separation. The phase separation problem has been partially overcome by growing GaInNAs at low temperature (Bi and Tu 1997), but the efficiency of light emission is degraded (Xin and Tu 1998), being partially recovered by annealing. Thus, the growth temperature seems to be one of the key parameters to obtain good quality GaInNAs heterostructures. In this work, the effect of the growth temperature on the composition fluctuations in GaInNAs quantum wells is investigated.

2. EXPERIMENTAL

The GaInNAs samples studied in this work have been grown by molecular beam epitaxy (MBE) on (001) GaAs substrates in a VG V80H MBE system equipped with an Oxford Applied Research HD25 radio-frequency plasma source for N. The N flux was controlled by monitoring the intensity of the atomic N plasma emission with a photodiode. The nitrogen content in the epilayers was calibrated from the x-ray diffraction analysis of bulk samples and GaNAs quantum wells grown using similar plasma emission intensities. Three GaInNAs quantum wells 8 nm thick with 38% In and 2.3% N have been sandwiched between $GaN_{0.007}As$ barriers. Strain relief layers of $Ga_{0.88}In_{0.12}N_{0.019}As$ have been grown before and after each well in all the samples. Five structures have been considered,

grown at different temperatures: 375º, 385º, 400º, 410º and 420ºC.

Specimens were prepared by mechanical thinning followed by Ar^+ ion milling for cross-sectional transmission electron microscopy (TEM) analysis. TEM studies were performed with JEOL EX1200 and JEOL 2011 microscopes.

3. RESULTS

The analyses of the GaInNAs samples by TEM with the 220 reflection in bright field conditions (hereafter 220BF) have shown the existence of a variation of the contrast along the quantum wells, exhibiting alternate dark and light regions with a periodicity of about 20 nm, as shown in Fig. 1a for the structure grown at 420 ºC. A detailed analysis at higher magnification has revealed that structural defects such as dislocations or planar defects are absent in these systems. Moreover, the study with 002DF has shown that the wells have flat morphology, without 3D features that could be responsible for the modulation of the contrast observed with 220BF. The appearance of the observed variations in the contrasts of the quantum wells is related to the elastic strain of the atomic planes in the material because of the existence of composition fluctuations in the alloy (Herrera et al 2004). The study of samples grown at temperatures in the range 375-420 ºC has shown that the intensity of the strain contrast is higher on increasing this growth parameter. In order to quantify the differences found between the studied samples, the intensity profile from 220BF micrographs taken in the upper well of each system and normalized with respect to the GaAs substrate has been considered. This analysis corroborated the amplification of the strain contrast with temperature and, consequently, of the magnitude of the composition fluctuations in the alloy.

Following these results, the quantum wells considered have been carefully studied with the composition sensitive 002DF reflection, and the intensity profiles have also been taken from the upper well in each structure. Strikingly, no variations of the contrast have been found with this reflection. This result is related to the fact that we are considering a quaternary alloy, and the composition of the system can fluctuate in the group III sublattice and also in the group V one. The intensity of the 002DF reflection in the $Ga_{1-x}In_xN_yAs_{1-y}$ alloy can be expressed as (Grillo et al 2001)

$$I_{002} = C|F|^2 = 4C(f_{III} - f_V)^2 = 4C[x f_{In} + (1-x)f_{Ga} - y f_N - (1-y)f_{As}]^2 \qquad (1)$$

where C is a factor that depends on thickness and imaging conditions, F is the structure factor and f are the atomic scattering factors. In an alloy with modulated composition, the increase in In and N content in a particular area (Δx and Δy, respectively) produces a decrease in the composition of these constituents in the same proportion in other region, given that we are considering a closed system. Consequently, to obtain the same dark field intensity in two chemically different regions of the material A and B, it should be satisfied the condition

$$I^A_{002}(x + \Delta x, y + \Delta y) = I^B_{002}(x - \Delta x, y - \Delta y). \qquad (2)$$

Solving, we obtain

$$\Delta x = -\frac{f_{As} - f_N}{f_{In} - f_{Ga}} \Delta y = -2.2\Delta y. \qquad (3)$$

Therefore, to observe a uniform contrast in the image of a GaInNAs quantum well with 002DF it is necessary that each increase in the N composition, Δy, comes accompanied by a simultaneous decrease in the In content, Δx, in an approximate proportion $\Delta x \approx -2.2\Delta y$. According to this, our results by TEM show that the composition fluctuations in the studied quantum wells should consist of alternate areas of the material rich in In and poor in N, and vice versa (Herrera et al, in press). This composition profile explains the high intensity of the strain contrasts found with 220BF in these structures, in comparison to GaInAs quantum wells (Herrera et al 2004).

4. DISCUSSION

The analysis of GaInNAs structures by TEM has revealed the existence of strain contrasts with the 220BF reflection in all the studied quantum wells. According to Vegard´s law, the lattice parameter of an alloy is a direct function of its composition in each region of the material. For this reason, composition inhomogeneities in alloy constituents with different atomic radii (r_{In}:1.66Å *vs.*

r_{Ga}:1.41Å, and r_{As}:1.39Å *vs.* r_N:0.92Å) introduce a modulation of the lattice parameter of the alloy and, as a result, elastic strain in the planes located between the areas with different composition. In relation to this, the 002DF reflection has shown the absence of a variation of the contrasts in the quantum wells, indicating that the composition profile in the GaInNAs alloy should be formed by regions rich in In and in N, alternatively. Therefore, the intensity of the strain contrasts observed with 220BF should be sensitive to the fluctuations in both In and N. At this point, it should be mentioned that although an evolution with temperature of the contrasts found with 220BF reflection has been observed, 002DF micrographs have not shown a variation of the contrast in the quantum wells with the growth temperature. This result suggests that the composition fluctuations in the GaInNAs quantum wells are increased with the growth temperature, but keeping the relation $\Delta x \approx -2.2\Delta y$ approximately constant. Following this, the measurement of the variations in the intensity of the strain contrasts with temperature could constitute a proper estimate of the evolution in the amplitude of the phase separation.

The relation between the amplitude of the phase separation produced by diffusion in a crystal and the temperature of the process has been proposed by Cahn (1968). Cahn has developed an equation for the evolution with time t of the composition c of an alloy with periodic phase separation as

$$\frac{\partial c}{\partial t} = M\left\{\left(\frac{\partial^2 F}{\partial c^2}\right)\nabla^2 c\right\} + \text{non linear terms} \qquad (4)$$

where M is the diffusion mobility and F is the free energy of the system. This equation has a simple sine wave solution (Cahn 1961) of the form $c - c_0 = e^{R(\overline{\beta})t}\cos\overline{\beta}\overline{r}$, where $R(\overline{\beta})$ is obtained by substituting this solution back into the diffusion equation, as

$$R(\overline{\beta}) = -M\beta^2\left(\frac{\partial^2 f}{\partial c^2}\right). \qquad (5)$$

The mobility M can be expressed as a function of the growth temperature as $M = M_0 e^{-Q/RT}$ (Cahn 1968), where Q is the activation energy of the diffusion process and M_0 is the pre-exponential factor. From these equations, the amplitude in the composition profile could be related to the growth temperature by

$$c - c_0 \propto e^{e^{-Q/RT}}. \qquad (6)$$

We have used the amplitude of the intensity profiles taken from 220BF micrographs as an estimate of the magnitude of the phase separation in the alloy GaInNAs. Figure 1b shows a plot of the double logarithm of the amplitude in the intensity profiles from 220BF micrographs *vs.* the inverse of the growth temperature of each sample. In accordance with Cahn´s theory, the slope of this graph is related to the activation energy for surface diffusion (E_{ac}) in the alloy. From this plot, we have obtained a value of E_{ac}=0.26±0.04 eV for the adatom diffusion in GaInNAs. As explained above, the strain contrasts observed in our study are sensitive to fluctuations in both In and N. However, the fact that no major differences in the contrasts of the wells have been observed with 002DF when increasing the growth temperature suggests that either the kinetics of the diffusion process for both alloy constituents is quite similar or that the process is mainly governed by one of them and the second one is adapted to it. In this sense, it should be mentioned that the studied quantum wells contains 38% of In but just 2.3% of N, therefore the behaviour of In is expected to have major effects on the microstructure of the GaInNAs quantum wells. In the literature, it has been reported a value of 0.35 eV for the activation energy of In diffusion on GaAs with the surface reconstruction 001(2x4), 0.25 eV for (111)A and 0.29 eV for (111)B (Matthai and Moran 1998); there have also been published values 0.22 eV for the diffusion of In in InAs quantum dots (Shiramine et al 2002) and 0.13 eV and 0.29 eV for the diffusion of In on $In_{0.66}Ga_{0.33}As$(001)-2x3 for the directions $[1\,\bar{1}\,0]$ and $[110]$ (Kratzer et al 2003), respectively. The energy of activation for GaInNAs structures calculated in this work is of the same order of magnitude as the values found in the literature for In in Ga(In)As alloys. We have not found in the literature diffusion data for N in GaIn(N)As comparable to our experimental results, but the obtained values suggest that it could be the surface diffusion of In atoms that controls the phase separation in the GaInNAs alloy.

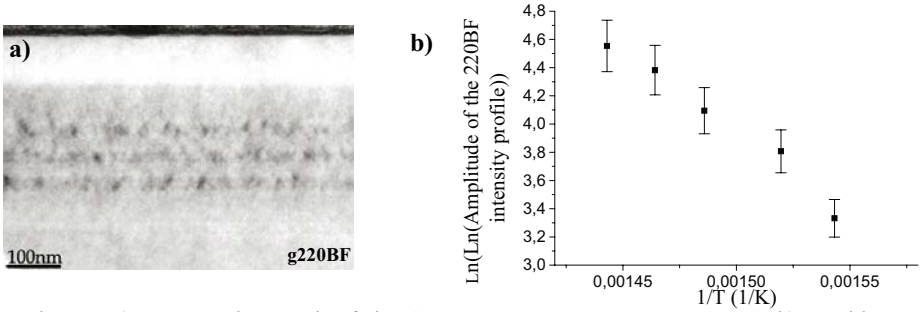


Fig. 1: a) 220BF micrograph of the GaInNAs structure grown at 400ºC; b) Double logarithm of the amplitude in the intensity profiles taken from the upper well of the studied samples in 220BF micrographs *vs*. the inverse of the growth temperature.

5. CONCLUSIONS

We have studied the influence of the growth temperature on the microstructure of GaInNAs/GaAs(001) quantum wells. The analysis with the 220BF reflection has shown the appearance of strain contrast in all the wells, increasing with the growth temperature in the range 375-420 ºC. This strain contrast has been associated with a phase separation in the alloy, therefore the formation of these composition fluctuations is kinetically limited by the growth temperature. With the theoretical equation proposed by Cahn and the amplitude of the intensity profiles taken from the upper well in 220BF micrographs, we have calculated the activation energy for surface diffusion in GaInNAs, obtaining 0.26±0.04 eV. This value is quite similar to that corresponding to In in Ga(In)As, suggesting that it is the diffusion of In atoms which governs the phase separation process in the GaInNAs alloy.

ACKNOWLEDGEMENTS

Financial support from the Spanish ministry of Education, EPSRC (UK) and CICYT project MAT2001-3362 (Spain) is gratefully acknowledged.

REFERENCES

Bi W G and Tu C W 1997 Appl. Phys. Lett. **70,** 1608
Cahn J W 1961 Acta Met. **9,** 795
Cahn J W 1968 Trans. Metall.Soc.of AIME **242,** 166
Grillo V, Albrecht M, Remmele T, Strunk H P, Egorov A Yu and Riechert H 2001 J. Appl. Phys. **90,** 3792
Herrera M, González D, Hopkinson M, Gutierrez M, Navaretti P, Liu H Y and García R J. Appl. Phys. in press.
Herrera M, González D, Hopkinson M, Navaretti P, Gutierrez M, Liu H Y and García R 2004 Semicond. Sci. Technol. **19,** 813
Kondow M, Uomi K, Niwa A, Kitatani T, Watahiki S and Yazawa Y 1996 Jpn. J. Appl. Phys. **35,** 1273
Kratzer P, Penev E and Scheffler M 2003 Appl. Surf. Sci. **216,** 436
Li W, Turpeinen J, Melanen P, Savolainen P, Uusimaa P and Pessa M 2001 Appl. Phys. Lett. **78,** 91
Matthai C C and Moran G A 1998 Appl. Surf. Sci. **123-124**, 653
Shiramine K, Itoh T, Muto S, Kozaki T and Sato S 2002 J. Crystal Growth **242**, 332
Ustinov V M and Zhukov A E 2000 Semicond. Sci. Technol. **15,** R41
Xin H P and Tu C W 1998 Appl. Phys. Lett. **72,** 2442

Growth and surface structure of silicon nanowires observed in real time in the electron microscope

F M Ross, J Tersoff, S Kodambaka and M C Reuter

IBM T. J. Watson Research Center, Yorktown Heights, New York 10598, USA

ABSTRACT: We describe the surface structure and growth kinetics of silicon nanowires formed by the vapour-liquid-solid process. Observations were made *in situ* in a transmission electron microscope during growth, and show that at high growth temperatures the wire sidewalls are faceted and the Au-Si eutectic droplet at the wire tip decreases in volume during growth. We account for these observations with a model based on Au diffusion, which involves migration of Au down the wire surface and consequent Au-induced surface faceting.

1. INTRODUCTION

Silicon nanowires grown by the vapor-liquid-solid (VLS) process (Wagner and Ellis 1964) have been suggested for applications such as interconnects or frameworks for three dimensional devices (McAlpine et al 2003, Cui et al 2003, Chung et al 2000, Law et al 2004). As with other nanostructures formed using self-assembly processes, understanding the growth mode in detail would be helpful in optimising the structures which can be formed using this technique. In this paper we, therefore, describe observations of the growth of VLS nanowires in real time, and we obtain measurements of the structure and growth kinetics of individual wires. In our experiments Si wires were grown using an Au-Si eutectic droplet as the catalyst. We will show that during growth, especially at higher temperatures, shrinkage of the droplets on the wire tips occurs, leading to tapering of the wires. The shrinkage rate is consistent with Au diffusion down the wires or along their surfaces. Furthermore, the wire sidewalls appear faceted, also suggesting the presence of Au on the surface. Faceting creates a sawtooth appearance which can be modeled as an oscillatory growth process dependent on surface energetics. We will discuss the relevance of the faceting and Au diffusion phenomena to potential electronic applications of Si nanowires.

2. *IN SITU* OBSERVATIONS OF Si NANOWIRE GROWTH

Observations of wire growth were made in a UHV-TEM having gas handling capabilities which enable chemical vapour deposition to be carried out *in situ*. Si deposition was carried out by exposing a heated specimen to disilane gas while it remained under observation in the polepiece (Hammar et al 1995). A “reflection mode” geometry proved convenient for examining nanowires during growth. A Si(111) wafer was patterned with Au dots ~30nm in diameter, and was then cut into 4x0.5mm strips. After cleaning, each strip was mounted in the heating holder with the Au-covered surface vertical, and was heated to well above the Au-Si eutectic temperature (370^{o}C). The Au dots formed Au-Si eutectic droplets which were larger than the initial Au dot size due to uncontrolled coalescence. On exposure to disilane, Si then dissolved into the droplets, diffused through them and was deposited at the droplet/substrate interface, forming an epitaxial wire in accordance with the VLS mechanism (Wagner and Ellis 1964). Since the wires grew in the 111 direction laterally away from the substrate, they could easily be seen in cross section in the 110 direction, with the specimen being tilted if necessary to avoid overlap of wires in the beam direction. Weak beam (g, 3g) imaging conditions were used with g=220 to resolve the wire surface structure and thickness as well as any internal defects such as twins.

Since the growth pressure is limited by the pumping capabilities of the microscope to a maximum value of 10^{-5} Torr, to achieve a reasonably fast growth rate (several nm per minute) a growth temperature of 550-650^{o}C was used. This is higher than is conventionally used in chemical vapour deposition of VLS wires and resulted in unusual wire growth kinetics which will be described below. The substrate temperature was calibrated after growth using an infrared pyrometer.

3. Si NANOWIRE SURFACE STRUCTURE AND DROPLET DYNAMICS

In Fig. 1 we show an image acquired during the growth of a Si nanowire. This large wire had a diameter of about 220nm, although diameters of 30-200nm are more typical. Tilting experiments showed that the wire is a prism whose axis is the 111 direction and whose sidewalls are made up of {211} facets. Its cross section is a distorted hexagon with alternating longer and shorter sides.

Close examination of this and other images shows that the six {211} sidewalls are faceted rather than smooth, giving a "sawtooth" appearance. This periodic sawtooth faceting was seen in all our experiments. It is especially visible on the upper sidewall of the wire in Fig. 1, although it does occur on the opposite sidewall too; we find that the sawtooth structure is always most visible on the three narrower sidewalls. The facets are not symmetrical with respect to the (211) direction, and they do not appear to have low index surface normals. As the wire grows, time resolved imaging shows that the facets form in a zigzag fashion, with the wire growing alternately slightly wider and then narrower. We suppose that these facets are related to the presence of Au on the {211} sidewalls, since Au is known to induce faceting on other low-index Si surfaces (Seehofer et al 1995, Minoda et al 1999, Meyer zu Heringdorf et al 1998, Zdyb et al 2001).

This oscillatory growth mode can be explained qualitatively by considering the role of surface energetics (Ross et al 2005). If sidewalls parallel to the growth direction were the most stable, the wire could grow with these parallel sidewalls and sawtooth facets would not be seen. However, suppose that inclined facets have a lower energy, so that the wire must either widen or narrow as it grows. Since the volume of the eutectic droplet is constant, a widening wire would result in a reduced contact angle for the droplet, generating an inward force which effectively raises the energy required to create additional amounts of the widening facet and thereby favours introduction of the narrowing facet. By considering the energies of the three interfaces present (the wire surface, the droplet surface and the droplet-wire interface), and a presumed energy barrier (edge energy) to switching between facets, we find that the facet repeat length is expected to be proportional to the wire diameter. This is indeed observed experimentally (Ross et al 2005).

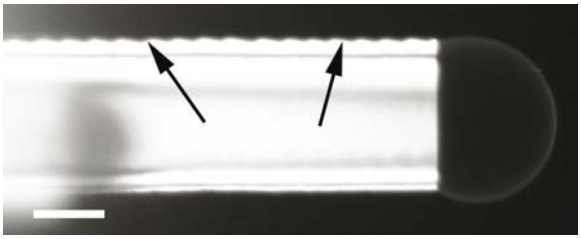


Fig. 1. Weak beam image of a large (220nm diameter) wire with a uniform series of facets. The eutectic droplet and sawtooth surface are visible, as is the planar eutectic/wire interface. The wire was grown at 600^{o}C and 1x10^{-6} Torr disilane and the two types of sawtooth facets seen are 11.2^{o} and 23.3^{o} from the 211 sidewall normal (arrows). The scale bar is 100nm.

The sidewall faceting suggests that the eutectic droplet is quite mobile at the growth temperature, changing its three dimensional structure to accommodate changes in the wire cross sectional area. Real time observations show that droplets can in fact be quite unstable, especially at higher temperatures, occasionally even moving off the top of the wire and overhanging one side (Fig. 2). We believe that larger scale movements like this are responsible for the kinking often seen during wire growth.



Fig. 2. Droplet dynamics on the end of a wire during growth at 640 ^{o}C and 1.1x10^{-6} Torr. These images, recorded during the space of 12 seconds, show the droplet in different configurations, either on the top wire surface (right hand image), partially hanging over the side (left hand image) or the front or back (middle image). The scale bar is 50nm.

The sawtooth faceting we have described is a general growth phenomenon which is expected to be present in any growth system in which the orientations parallel to the growth direction are not the most stable. It is interesting in the context of electronic mobility and scattering in devices made of VLS nanowires. For example, in the case of Si wires used as channels in wraparound gate transistors, the non-planar interfaces may lead to enhanced carrier scattering. If the interface roughness were fixed, smaller diameter wires would be expected to show worse mobility, but in this case, narrower wires may be just as usable as thicker wires since their surface roughness would be reduced proportionally. The sawtooth faceting may also be important in attempts to fabricate core-shell structures, where a second material is deposited on the surface of a previously grown nanowire; again narrower wires may be advantageous for the smoothest interface.

4. Si NANOWIRE GROWTH KINETICS

As well as showing nanowire surface structure without environmental effects such as oxidation, *in situ* growth experiments allow us to measure the growth kinetics of individual wires. In Fig. 3 we show a series of images acquired during the growth of a single wire. The sawtooth faceting is visible on individual images. However, by considering the entire growth sequence, a striking change in the volume of the eutectic droplet also becomes visible. As the droplet shrinks, the wire tapers (by forming different amounts of each facet) and its growth eventually terminates.

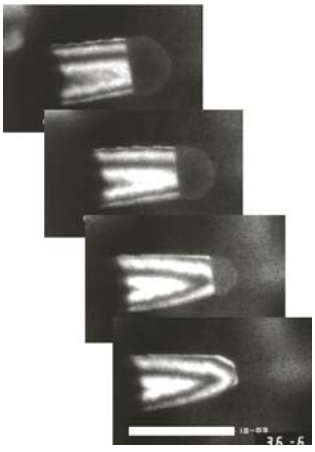


Fig. 3. Several images in a weak beam sequence recorded during wire growth at 600^{o}C and 3.6x10^{-6} Torr disilane. The images are offset so that the growth of the wire is apparent, and the interval between successive images is 310, 290 and 70 seconds. The wire had an initial diameter of 60nm but clearly tapers during growth, with growth eventually terminating as the droplet disappears. For this wire the growth rate was 0.16nm/sec, >10 times faster than disilane growth under the same conditions. The scale bar is 100nm.

In this and other cases, an analysis of the rate at which the droplet shrinks suggests that evaporation of the Au can not account for the droplet kinetics (Kodambaka et al 2005), since the vapour pressure of Au at the growth temperature is too low. Furthermore, deposition of a layer of Au on the surface of the wire, or deposition of Au in the bulk of the wire, are also not possible explanations. For example, for the wire shown in Fig. 3, a layer of Au of 1-3nm in thickness would have to be deposited on the wire surface to account for all the material lost from the droplet, and this is not seen in the images. Instead, we believe that the droplet shrinks because Au diffuses down the surface of the wire and ends up either in the bulk of the substrate (for example at defects) or on the substrate surface. Annealing experiments, in which wires are held at the growth temperature under UHV without supply of disilane, show that the droplet

shrinks in an approximately linear fashion (Kodambaka et al 2005) which is consistent with surface diffusion. Of course, the sawtooth faceting we described above also suggests the presence of Au on the wire surface.

As with the surface faceting described in section 3, the droplet shrinkage may be important when using Si nanowires in electronic applications. The solubility of Au in Si is so low at the growth temperatures used (Plummer et al 2000) that very little Au is expected to be present in each wire. However, if Au diffuses down the wire into adjacent regions of the substrate, it may create deep level states which could affect the performance of nearby circuit components. Growth at a lower temperature but higher growth rate, as is commonly achieved by using a higher disilane pressure, should minimise Au diffusion effects. But it may also be worth considering the use of other catalysts to minimise any impact on electronic properties.

5. CONCLUSIONS

In situ TEM experiments have enabled us to visualise the VLS growth of Si nanowires from Au-Si eutectic droplets in real time. At the relatively high temperatures used in this study, we find that Au diffusion is an important process which controls the tapering of the wires as well as, we believe, the sawtooth faceting on their surfaces. The migration of Au through VLS Si wires is expected to alter their electronic properties as well as those of the substrate, and should be considered when using the wires in electronic applications. However, at lower temperatures, where both the diffusivity and solubility of Au are lower, these effects are likely to be reduced; it is also possible that the presence of a greater H coverage on the surface during lower temperature growth may also be significant in suppressing Au surface diffusion.

An important challenge is to extend this type of *in situ* analysis to lower temperatures and higher pressures which are more similar to conventional wire growth conditions. We are presently designing a differentially pumped sample geometry which will allow a higher gas pressure to be maintained around the growing wires without compromising the microscope performance, so that the dynamics of Au motion can be measured under a wider range of growth conditions.

ACKNOWLEDGEMENTS

We gratefully acknowledge C T Black and R Sandstrom of IBM, Yorktown Heights, NY for lithographic processing and Au deposition on the Si(111) wafers, and P W Voorhees of Northwestern University, Evanston, IL, and R M Tromp of IBM, Yorktown Heights, NY, for stimulating discussions.

REFERENCES

Chung S-W, Yu J-Y and Heath J R 2000 Appl. Phys. Lett. 76, 2068
Cui Y, Zhong Z, Wang D, Wang W U and Lieber C M 2003 Nano Letters **3**, 149
Hammar M, LeGoues F K, Tersoff J, Reuter M C and Tromp R M 1995 Surf. Sci. **349**, 129
Kodambaka S, Tersoff J, Reuter M C and Ross F M 2005 *in preparation*
Law M, Goldberger J and Yang P 2004 Ann. Rev. of Mater. Res. **34**, 83
McAlpine M C, Friedman R S, Jin S, Lin K-H, Wang W U and Lieber C M 2003 Nano Letters **3**, 1531
Meyer zu Heringdorf F-J, Kaehler D, Horn-von Hoegen M, Schmidt Th, Bauer E, Copel M and Minoda H 1998 Surf. Rev. and Lett. **5**, 1167
Minoda H, Yagi K, Meyer zu Heringdorf F-J, Meier A, Kaehler D and Horn-von Hoegen M 1999 Phys. Rev. B **59**, 2363
Plummer J D, Deal M D and Griffin P B 2000 Silicon VLSI Technology: Fundamentals, Practice and Modeling (Prentice Hall)
Ross F M, Tersoff J and Reuter M C 2005 Phys. Rev. Lett. *submitted*
Seehofer L, Huths S, Falkenberg G and Johnson R L 1995 Surf. Sci. **329**, 157
Wagner R S and Ellis W C 1964 Appl. Phys. Lett. **4**, 89
Zdyb R, Strozak M and Jalochowski M 2001 Vacuum **63**, 107

Self-catalytic growth of gallium nitride nanoneedles under Ga-rich conditions

Andrew S W Wong, Ghim W Ho[1], Pedro M F J Costa, Rachel A Oliver and Colin J Humphreys

Department of Materials Science and Metallurgy, University of Cambridge, Pembroke Street, Cambridge, CB2 3QZ, UK
[1] Department of Electrical Engineering, Nanoscience Centre, 11 JJ Thompson Ave, Cambridge, CB3 0FF, UK

ABSTRACT: We describe the growth of gallium nitride nanoneedles synthesized via a self-catalytic process . Transmission electron microscopy studies confirmed the gallium nitride nanoneedles to be single-crystalline with a predominant (10-10) growth direction. The nanoneedles are facetted and no catalyst particles are observed at their tips. We propose that the nanowires formed from nanosized gallium droplets supersaturated with nitrogen, but under Ga-rich conditions, the nanowires tapered to form nanoneedles. Excess Ga in the metallic droplets then reacted to form gallium nitride microcrystals.

1. INTRODUCTION

Semiconductor nanostructures have received a lot of attention as building blocks for future nanotechnologies (Wu et al 2002). Gallium nitride is of particular interest because of its applications in short wavelength optoelectronic devices, high-power/temperature electronics, high mobility field effect transistors and nanolasers (Huang et al 2002, Johnson et al 2002). Nanowires are usually synthesized by the vapour-solid-liquid (VLS) route (Wu et al 2002, Duan and Lieber 2000). However, the VLS growth mechanism involves the supersaturation of catalyst particles of transition metals such as Fe, Ni and Co with precursor species, leading to the formation of solid nanowires at the solid-liquid interface. The drawback of this synthesis route is that it uses metal catalyst particles which remain attached and contaminate the monocrystalline nanowires. Earlier studies (Stach et al 2003) using *in-situ* transmission electron microscopy (TEM) have shown that the self-catalytic growth of gallium nitride nanowires is possible. Here we describe the synthesis of gallium nitride nanoneedles grown by chemical vapour deposition (CVD) using a self-catalytic route under Ga-rich conditions. The interrupted growth of gallium nitride nanoneedles via a self-catalytic process and the co-existence of Ga droplets, facetted GaN microcrystals and GaN nanoneedles have been observed.

2. EXPERIMENTAL

Our approach to gallium nitride nanoneedle growth makes use of a tube furnace heated to 950^{o}C for 20 min. Typical chamber pressures and ammonia flow rates are 100 Torr and 30 sccm respectively. SiO_2/Si substrates without any transition metal catalyst were used in this study. The Ga metal source material and the silicon dioxide/silicon substrate were placed prior to heating in a quartz boat with the substrate positioned 5 mm downstream from the source. The chamber was filled with argon prior to and after growth to ensure growth only occurred when the desired temperature had been reached.

The nanostructures were studied using a LEO field emission gun scanning electron microscope (FEG-SEM) and Phillips CM300 FEGTEM operated at 300 kV. For TEM studies, the nanostructures were dispersed onto a holey carbon copper grid. The microcrystals were studied using electron beam back scattered diffraction (EBSD).

3. RESULTS AND DISCUSSION

Figure 1a is an SEM image of a specimen grown under Ga-rich conditions. Structures of varying shapes and sizes can be seen. Higher magnification views of the sample surface reveal both micro- and nano-sized structures. In Fig. 1b we see two approximately spherical particles, a facetted microcrystal and an elongated nanostructure. SEM-EDX studies performed on the almost spherical particle (indicated by the box in Fig. 1b) reveal that it contains only Ga whereas the faceted microcrystal sandwiched between the two spherical particles contains both Ga and N (see Fig. 2). Figures 1c and d show that the nanostructures taper to a needle-like tip. It is interesting to note the co-existence of nanostructures, microcrystals and excess Ga metal. Figure 1e shows the facetted surface of the microcrystals. Figures 1f and 1g show that more than one nanowire can be associated with a single GaN crystal. Figure 1h shows a tapered nanostructure growing out of a Ga droplet.

Figure 3a shows a low resolution TEM image of a GaN nanoneedle with the corresponding diffraction pattern down the [0001] zone axis. Extensive TEM studies on several tens of nanowires show the predominant growth direction to be (10-10). Lattice-resolved, high-resolution TEM images of the nanoneedles confirm the needles to be single-crystalline with the wire axis along the (10-10) direction (see FFT of HRTEM image). No catalytic particles are observed at the tip of the GaN nanoneedle. The dark bands in the HRTEM image (Fig. 2b) are associated with the changes in thickness in the facetted nanoneedle. Detailed SEM studies also suggest that the nanoneedles may be facetted.

TEM cannot be used to study the crystal structure of the observed microcrystals as they are not electron transparent. An alternative method to determine the local crystal structure from a thick specimen is to use EBSD analysis.

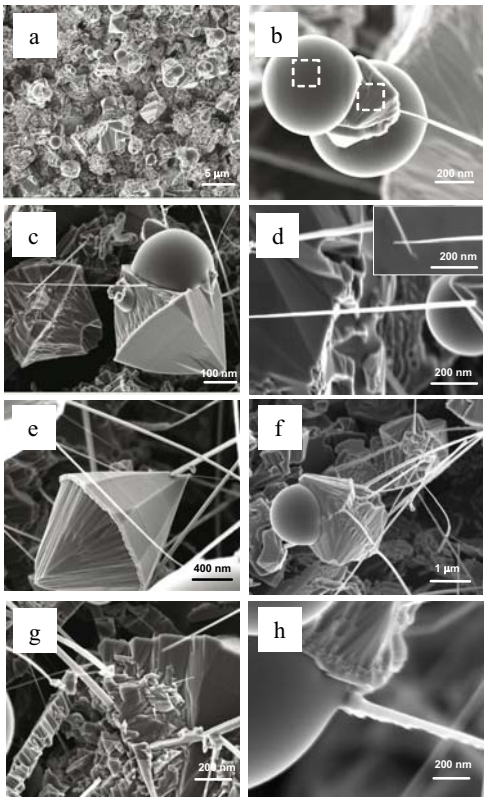


Fig. 1: SEM images of sample grown under Ga-rich condition (a) low magnification view of sample surface, (b) higher magnification SEM image show co-existence of GaN nanostructures, GaN crystal and Ga droplets (EDX analysis was performed on this nanostructure to determine its chemical composition. Boxes indicate region analysed, see Fig.2, (c-d) show nanostructures to be GaN nanoneedles, (e-g) GaN crystals are facetted and more than one nanoneedle can be associated with a GaN crystal and (h) nanoneedle growing out of a Ga droplet.

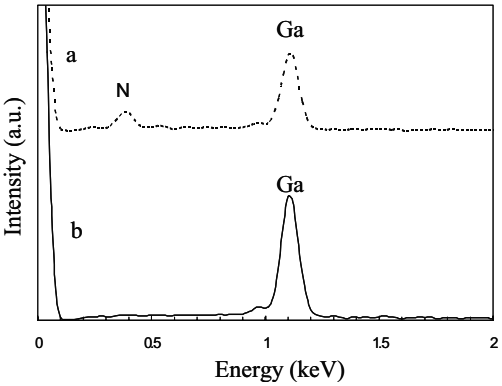


Fig. 2: EDX spectra obtained from nanostructure in Fig.1b, (a) crystal and (b) droplet. EDX confirmed the crystal to be GaN and droplet to be Ga. Subsequent structural studies show that the GaN has wurtzite structure.

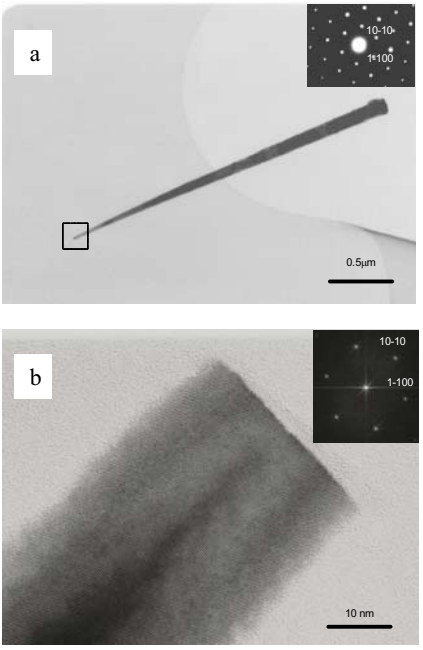


Fig. 3: shows the (a) low resolution TEM image of a GaN nanoneedles with corresponding diffraction pattern down the [0001] zone axis, (b) lattice-resolved, high-resolution TEM image obtained at the tip of the nanoneedle (indicate by box in Fig. 3a).

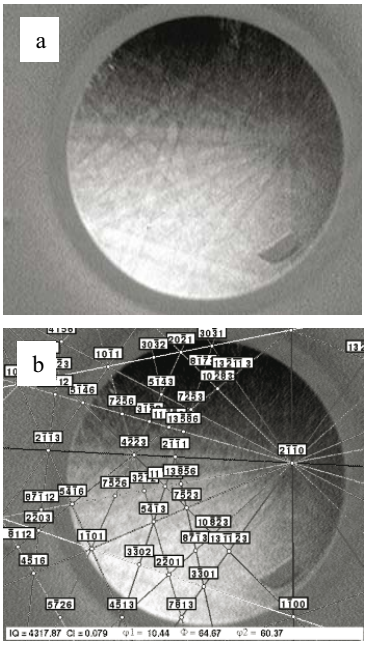


Fig. 4: shows the (a) experimental Kikuchi pattern collected from one of a facet of the crystal, (b) indexed pattern superimposed on the experimental pattern. The pattern is clearly that of wurtzite GaN.

Figure 4a shows the experimental Kikuchi pattern collected from one facet of the crystal. Figure 4b shows the indexed pattern superimposed on the experimental pattern. The pattern is clearly that of wurtzite GaN. Attempts to get a Kikuchi pattern from the Ga droplet were unsuccessful as specimen heating resulted in the melting of the material because Ga has a melting point of 29.5^{o}C.

The growth mechanism of the nanoneedles is proposed as follows: Nano-sized Ga metal droplets form and are supersaturated with active nitrogen from the ammonia source. This results in nanowire formation self catalysed by the Ga droplet. As the Ga supply increases, the diameter of the droplet and thus the nanowire increases, resulting in tapering of the nanowires forming needle-like nanostructures. Figure 1h clearly shows the nanostructure coming out from the Ga droplet, which is expected since Ga is acting as a self-catalyst. Eventually the droplet reaches such a large size that it can no longer support nanoneedle formation. Subsequently, the reaction of the Ga droplet with the nitrogen results in the formation of the

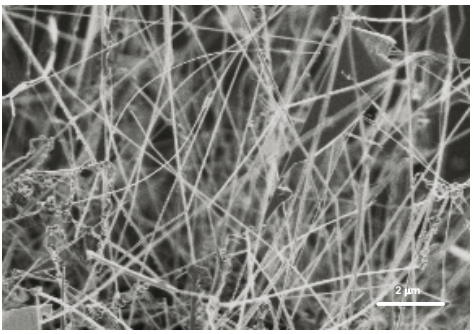


Fig. 5: SEM image of a specimen grown with 50% less Ga then before. GaN nanowires are observed.

facetted GaN microcrystals instead of nanowires. This suggested mechanism may be supported by other data. The observed nanoneedles, microcrystals and Ga doplets are absent when the Ga flux is lower, whilst all other growth conditions are kept the same. Figure 5 shows the SEM image of nanostructures prepared with 50% less Ga. Only GaN nanowires are observed in this sample. This suggests that the nanowires are formed due to self catalysis by small Ga droplets which do not grow due to the limited Ga flux. Subsequently, no microcrystals are observed.

4. SUMMARY

In summary, GaN nanoneedles have been successfully grown using CVD via a self-catalytic route. Large Ga droplets and GaN microcrystals are observed at the same time. The crystal structure of the nanoneedles has been confirmed to be wurtzite by TEM and that of the microcrystals has been confirmed by EBSD. A mechanism for nanoneedle growth has been postulated.

REFERENCES

Duan X and Lieber C M 2000 J. Am. Chem. Soc. **122**, 188
Huang Y, Duan X, Cui Y and Lieber C M 2002 Nano Lett. **2**, 101
Johnson J, Choi H, Yang P and Saykally R 2002 Nature Mater. **1**, 101
Stach E A, Pauzauskie P J, Kuykendall T, Goldberger J, He R and Yang P 2003 Nano Lett. **3**, 867
Wu Y, Fan R and Yang P D 2002 Int. J. Nanosci. **1**, 1

Nanocontacts fabricated by focused ion beam: characterisation and application to nanometre-sized materials

F Hernández, O Casals, A Vilà, J R Morante, A Romano-Rodríguez, M Abid[1], J-P Abid[2], S Valizadeh[3], K Hjort[3], J-P Collin[4] and A Jouati[4]

Enginyeria i Materials Electrònics, Departament d'Electrònica, Universitat de Barcelona, C/. Martí i Franqués, 1, E-08028 Barcelona, Spain.
[1] Laboratoire de Physique des Matériaux Nanostructurés, École Polytechnique Fédérale de Lausanne, EPFL, CH-1015 Lausanne, Switzerland
[2] Laboratoire d'Electrochimie Physique et Analytique, École Polytechnique Fédérale de Lausanne, EPFL, CH-1015 Lausanne, Switzerland
[3] Ångströmlaboratoriet, Universitet Uppsala, Lägerhyddsvägen 1, SE-751 21 Uppsala, Sweden
[4] Laboratoire de Chimie Inorganique, Université Louis Pasteur, 4, rue Blaise Pascal, F-67000 Strasbourg, France

ABSTRACT: A dual-beam focused ion beam unit has been used to deposit platinum contacts on nanomaterials using both electron- and ion-assisted deposition. Characterization of deposited platinum has been performed and the feasibility of using these nanocontacts to extract electrical parameters of materials demonstrated. The advantage of combining electron- and ion-assisted deposition is discussed.

1. INTRODUCTION

Electrical characterisation of nanometre-sized materials has been a challenging issue because of the difficulties in fabricating electrical contacts with submicrometre precision to access these materials (Jortner and Rao 2002). Although electron-beam lithography (EBL) is the most used technique to fabricate these contacts, focused ion beam (FIB) lithography has been also used as an alternative to EBL thanks to not requiring masks and being a single-step process. Nevertheless, damage introduced by ion bombardment, which is used to perform an ion-assisted chemical vapour deposition (IACVD) process, has restrained the use of this technique (Wei et al 1999, Ziroff et al 2003). Some groups have attempted to fabricate electrical contacts by using low ion currents in the proximity of the nanomaterials in order to reduce the damage. However, ion exposure is not eliminated and the contacted nanomaterials are modified (Ziroff et al 2003, de Marzi et al 2004). The recent appearance of the dual-beam systems (conventional FIB microscopes combined with scanning electron microscopes (SEMs)) could help to solve the problems produced by ions. Due to the fact that interaction between electrons and the sample is less destructive, performing an electron-assisted deposition on the nanostructure to be contacted and finishing the rest of the contact with the help of ions can avoid undesired surface damage and nanostructure modification.

Nanowires (NWs) and nanoparticles (NPs) of different materials have been electrically contacted in 2- and 4-probe configurations with the help of both electron- and ion-assisted deposition and the possibility of extracting their electrical parameters demonstrated. The quality of deposited platinum has been evaluated as a function of time, applied current, dimensions and chemical composition, and the behavior of electrical contacts between platinum and different materials has been as well studied.

2. EXPERIMENTAL

NWs of different materials (NiO, SnO_2conductive polymer and Au) and WO_3-NPs (Rossinyol 2004) have been dispersed over the surface of SiO_2/Si substrates with photo lithographically pre-patterned Ti/Ni/Au microelectrodes and an FEI dual beam 235 FIB used to localize the desired NPs or NWs and fabricate the platinum contacts using $C_9H_{16}Pt$ as metalorganic precursor and Ga^+ ions or electrons accelerated to 30kV or 5kV, respectively. Ion beam currents between 10pA and 100pA have been selected in all experiments and ion images of the contacted nanomaterials intentionally avoided. Electrical measurements have been performed with the help of microprobes and a Keithley Source Measure Unit (SMU) 2400. Resistances of both ion- and electron-assisted platinum have been evaluated by depositing stripes, whose dimensions range between (height x width x length) 0.13x0.17x10µm and 5x5x15µm, among 4 gold microelectrodes. Chemical characterization of the deposited platinum has been obtained by auger electron spectrometry (AES) using a PHI 670 spectrometer.

3. RESULTS

3.1 Electrical Properties of Deposited Platinum

Ion-assisted deposited platinum has a resistivity much higher than bulk platinum, ranging from 1.5mΩ·cm for stripes with cross sections of 5x5µm^2 to 5.25mΩ·cm with cross sections of 0.13x0.17µm^2 (Fig. 1), and AES observations have shown that this platinum (27%) is highly contaminated with carbon (65%) originated during the metalorganic precursor decomposition and gallium (8%) coming from the ion beam.

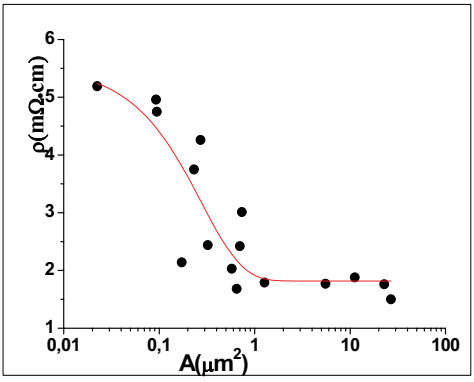


Fig.1. Resistivity of ion-assisted deposited platinum stripes in function of their cross-section area.

Contact electrical resistance between ion-assisted deposited platinum stripes and microelectrodes increases with decreasing contact area ($R_c = \rho_c / A$), where R_c is the contact electrical resistance, ρ_c is known as the electrical contact resistivity and A the contact area. The value found for ρ_c is 210±20Ω·µm.

Resistance versus current (R(I)) plots of the ion-assisted deposited platinum stripes present a parabolic behaviour with decreasing resistance for high intensities (Fig. 2), demonstrating that due to the high carbon contamination, its electrical behavior is typical of a negative temperature coefficient (NTC) material, when heated. No change in the resistance has been observed up to current densities of 10^{10}A/m^2, and no degradation has been detected after two weeks. Electron-assisted deposited platinum has a resistivity between 100 and 1000 times higher than ion-assisted deposited. This difference could be produced by the fact that Ga contamination, which is introduced in ion-assisted deposited platinum during the deposition process, could help to reduce the resistivity, acting as a doping element. R(I) plots of electron-assisted stripes present the same parabolic behavior, demonstrating that the thermal response is also controlled by carbon contamination.

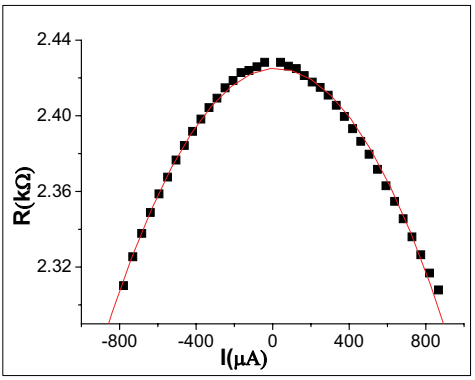


Fig. 2. R(I) curve of an ion-assisted deposited platinum stripe.

3.2 Contacting Nanometer-Sized Materials Using a Dual Beam FIB

NWs of different materials (NiO, SnO_2, conductive polymer and Au) and WO_3-NPs have been contacted in 2- and 4-probe configuration (Fig. 3) by combining the electron- and ion-assisted platinum deposition, avoiding imaging the selected particle with ions, which could irreversibly modify it. 2- and 4-probe measurements of contacted nanostructures have been performed and an

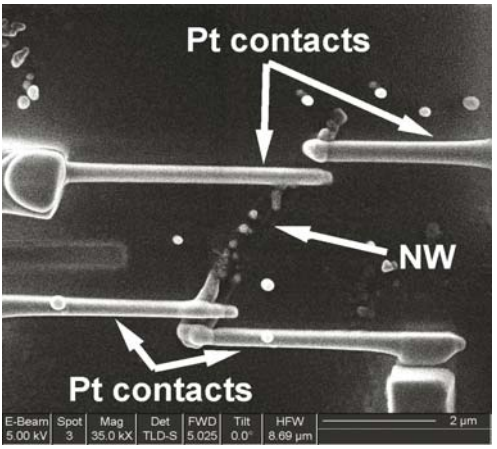


Fig. 3. Conductive polymer NW contacted in 4-probe configuration.

ohmic behaviour has always been found (Fig. 4). Because of the high resistivity of the deposited platinum and the contact resistance between platinum and the nanostructure, 4-probe measurements are required to extract the electrical parameters of the contacted nanostructures.

Stability of the contacts has been measured as a function of time and applied current. Good stability of contacts formed on a NiO nanowire has been observed after 22 days and no degradation after applying a current of 700nA for 20 minutes. All measured nanostructures are destroyed at current densities above $10^{10}A/m^2$. Therefore, we can conclude that electrical contacts fabricated using this procedure are good and reliable enough to fabricate nanodevices, which are required to operate for a long time.

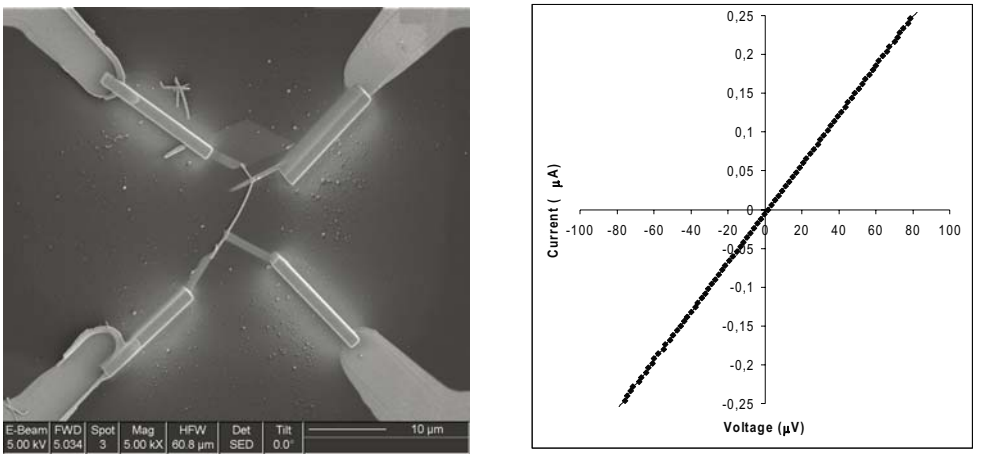


Fig. 4. Au NW contacted in 4-probe configuration (left image) and I-V curve (right image).A ρ=2.75·10-4 Ωcm has been found, slightly higher than that for bulk Au, due to the crystallinity of the NW.

4. CONCLUSIONS

Pt contacts between nanomaterials and microelectrodes have been fabricated with the help of a dual-beam FIB unit. Electron-assisted deposition has been performed in the proximity of the nanomaterials, finishing the contacts with an ion-assisted deposition process. Following this fabrication method, damage introduced on nanomaterials by ion bombardment is reduced. Deposited platinum has a high resistivity because of carbon contamination originating during the fabrication process, so 4-probe electrical measurements are required to avoid a contact resistance contribution. Characterization of fabricated contacts has revealed an ohmic behavior and good stability as a function of time and applied current.

REFERENCES

Wei B, Spolenak R, Kohler-Redlich P, Rühle M and Arzt E 1999 Appl. Phys.Lett.**74,** 21
Jortner J and Rao C N R 2002 Pure Appl. Chem. **74**, 1489
de Marzi G, Iacopino D, Quinn A. J and Redmond G 2004 J. Appl. Phys. **96**, 6
Rossinyol E, Hernández F, Romano A, Peiró F, Cornet A and Morante J R 2004 Eurosensors XVIII
Ziroff J, Agnello G, Rullan J and Dovidenko K 2003 Mat. Res. Soc. Symp. Proc. **772**

Cross-sectional studies of epitaxial growth of InP and GaP nanowires on Si and Ge

M A Verheijen, E P A M Bakkers, A R Balkenende, A L Roest, M M H Wagemans, M Kaiser, H J Wondergem, and P C J Graat

Philips Research, Prof. Holstlaan 4, WY42, 5656 AA, Eindhoven, The Netherlands

ABSTRACT: Heteroepitaxial growth of III-V wires on Si and Ge was performed using either MOVPE or laser ablation. The epitaxial relation between wire and substrate was studied using cross-sectional TEM and X-ray diffraction. For both GaP wires on Si and InP wires on Ge perfect epitaxy was observed. In the initial stage of the growth process, the gold particles partly sink into the Si substrate. During subsequent wire growth, the Si that had been dissolved in the gold particle is excreted above the Si surface. Due to the interaction of the gold particle with the substrate, the final substrate/wire interface displays a roughness on the nanometer scale.

1. INTRODUCTION

Semiconducting nanowires are potential building blocks for bottom-up nanoelectronics (Huang et al 2001). In order to integrate these nanowires into silicon technology, heteroepitaxial growth of the wires on silicon or related substrates is a prerequisite. In addition, the quality of the epitaxy and the interface are of importance. In this paper studies on heteroepitaxial growth of GaP and InP wires on silicon and germanium substrates are presented (Bakkers et al 2004, Mårtensson et al 2004). Attention was addressed to three issues: i) the possible presence of defects at the interface, ii) interface roughness and iii) sharpness of the chemical composition profile across the interface. This was performed by high resolution transmission electron microscopy (HRTEM) studies in combination with high angle annular dark field (HAADF), and energy dispersive X-ray (EDX) analysis. Both initial stages of gold-mediated VLS growth as well as wire/substrate interfaces of micron-sized wires were studied.

2. EXPERIMENTAL

The wires were grown via the VLS (vapour-liquid-solid) method by either using laser ablation (Bakkers and Verheijen 2003) or metal-organic vapour phase epitaxy (MOVPE) (Haraguchi et al 1992). The substrates were etched in a buffered oxide etch (BOE:12.5 % HF). Gold was deposited either by evaporating an equivalent of a 2 Å gold film or spin coating colloidal Au particles.

In order to obtain cross-sectional samples of nanowires on a substrate, two different preparation techniques were used: focused ion beam (FIB) preparation and mechanical polishing down to electron transparency. Both preparation routes started with the deposition of a 500 nm thick SiO_2 layer by means of plasma enhanced chemical vapour deposition (PECVD). The purpose of this oxide layer was twofold: 1) to provide mechanical stability to the wires during the preparation, and 2) to prevent vertical impact of Ga ions during the FIB preparation process. FIB preparation was used to make cross-sections through individually selected nanowires. Mechanical polishing was applied in order to obtain an overview of the variations in morphology of a large series of wires within one single sample. Typically, several tens of wires were present in a mechanically polished sample. Both preparation techniques allowed for high resolution imaging of the substrate /wire interface. TEM studies were performed using a TECNAI F30ST operated at 300 kV.

3. THE INTERACTION OF GOLD WITH THE SUBSTRATE

The first stages of VLS growth of a III-V nanowire on a silicon substrate were studied. Prior to the VLS growth itself, gold is deposited. The as-deposited sample shows small pyramid-shaped gold islands on top of the silicon substrate (see Fig.1a).

After introduction of the precursors in the gas phase the group III and group V elements are dissolved in the gold particles. In the subsequent wire growth stage only a fraction of the gold particles present on the surface exhibit wire growth. This can be explained by the high density of gold particles present on the surface in combination with a limited supply of growth units from the gas phase.

Figure 1b shows an overview image of a Si(111) substrate covered by AuGa particles. The composition of these particles was determined by EDX to be $Au_{70}Ga_{20}P_{10}$. (Regarding the phase diagram this composition is not likely to be present in a single particle. More likely, the EDX analysis has averaged over a small GaP domain and an AuGa particle.) The resulting surface of the Si(111) substrate is considerably roughened. The eutectic particles have 'sunk' into the substrate, thereby creating a surface with faceted pits. The faceted sidewalls of these pits form crystallographic planes which have different orientations than the original {111} surface, enabling deviating growth directions for the wires. This phenomenon was already predicted by Krishnamachari et al (2004) in order to explain the preferential $<111>_B$ growth of InP wires on InP <100> substrates in case the Au was annealed prior to wire growth. If this annealing was avoided, $<111>_B$ growth did not occur implying that pit formation was avoided.

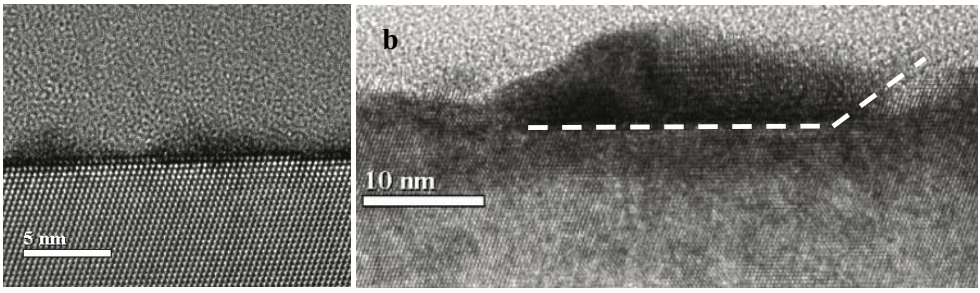


Fig. 1: a) HRTEM image of gold nanoparticles on Si(111) prior to any heat treatment. b) HRTEM image of a AuGa particle that has formed a faceted pit in the silicon substrate. The dashed lines indicate the orientations of the facets.

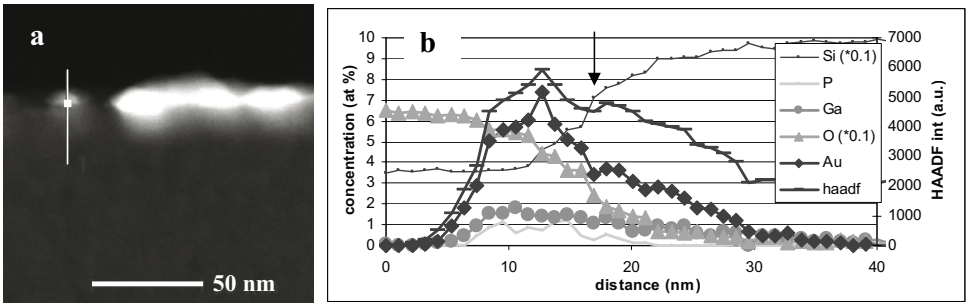


Fig. 2: a) HAADF image of AuGa particles on Si(111). The vertical line indicates the line that was scanned downwards during EDX spectrum acquisition. b) Composition profile calculated from the EDX line scan. The block on the line in the HAADF image corresponds to the position of the Si surface, indicated by an arrow in the EDX profile. The left part of the profile is dominated by the SiO_2 that was used for embedding the nanowires prior to sample preparation.

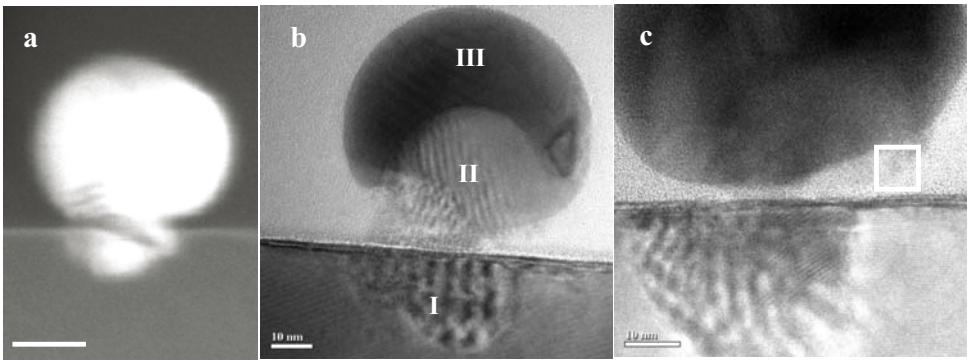


Fig. 3: a) HAADF image of a AuIn particle with diffusion of Au into the Si. b and c) TEM images of a Si(111) substrate with AuIn particles that yielded only limited growth (starting from colloidal gold particles). The white square in c) indicates the position of a silicon nanoparticle.

Figure 2 shows a HAADF image of the final stage of GaP growth on Si(111). AuGa islands appear bright in this image. Adjacent to this region also GaP nanowires were present, as will be presented in section 4. The results of an EDX line scan performed parallel to the surface normal are also shown in Fig. 2. The analysis clearly shows that the bright contrast in the substrate below the AuGa particles is due to the presence of significant amounts of Au, Ga, and P in the substrate. Importantly, these profiles were similar for FIB prepared and mechanically polished samples. Thus, the Ga-profile is not a FIB induced artifact. Similar results were obtained for wire growth of GaAs, InAs, and InP on Si starting from an evaporated gold film.

The use of colloidal Au-particles instead of a thin gold film yielded comparable phenomena. Again, only part of the gold particles resulted in extended wire growth. Figure 3a shows a Si(111) surface with an AuIn particle that exhibited only limited growth. The substrate appeared to be covered by a discontinuous layer of SiO_2. At one distinct position the gold has diffused into the substrate, as can be judged from the HAADF contrast. HRTEM studies at this position showed the epitaxial relation between nanowire and substrate. The presence of Au in the substrate was confirmed by using EDX. The bright field TEM image in Fig. 3b shows three distinct regions of interest: I) an area with Moiré fringes in the substrate, indicating the presence of a crystal lattice with lattice constants deviating from silicon, which can be explained by the in-diffusion of gold. II) an InP-only part. III) a cap with composition $Au_{68}In_{32}$. The flat substrate surface indicates that the in-diffusion of gold in the silicon must have resulted in the removal of some silicon atoms from the substrate. Careful HRTEM studies confirmed this: the excess of silicon was excreted from the eutectic particle just above the substrate surface. Figure 3c indicates a region with lattice constants that can only be assigned to the Si lattice. Excreted silicon particles were unambiguously identified at the foot of three nanowires.

4. THE INTERFACE BETWEEN WIRE AND SUBSTRATE

Figure 4 displays cross-sectional TEM images of GaP on Si(111) (a,b) and InP on Ge(111) (c). InP on Ge displays an atomically flat interface and perfect epitaxy. In some wires Shockley partial dislocations were observed at the interface, leading to a rotation of the InP lattice over 1.4±0.3º around the [011] axis with respect to the Ge lattice, as was determined by a fast Fourier transformation (FFT) of the HRTEM image. However, high resolution XRD pole figure measurements showed that the crystal lattice orientations of wire and substrate were identical within 0.09º. Thus, the dislocations and the resulting tilt of the wire must be due to relaxation in the thin TEM sample (Bakkers et al 2004). The GaP-Si interface as shown in Fig.4b is more rough. The dark line most likely indicates the compositional boundary. Note the presence of a twin boundary several atomic layers above the interface (see arrow). No dislocations were observed at this interface. The FFT image of Fig. 4b showed perfect epitaxy: the GaP and Si spots showed complete overlap. An EDX compositional profile of the GaP/Si interface is displayed in Fig. 5. The peak in the Ga- and P-

profiles is due to the slightly broadened foot of the GaP wire. Contrary to the profile of the adjacent AuGaP particle that was shown in Fig. 2, at the position of the wire no gold was detected in the substrate (at a detection limit of 0.2 %). This implies that the in-diffusion of gold in the substrate does not occur prior to but during the wire growth process. Thus, the formation of a wire lifts the gold containing particle from the surface and thereby inhibits gold diffusion into the substrate. The surface roughening appears to be a phenomenon that occurs during the formation of the eutectic particle, i.e. prior to wire growth.

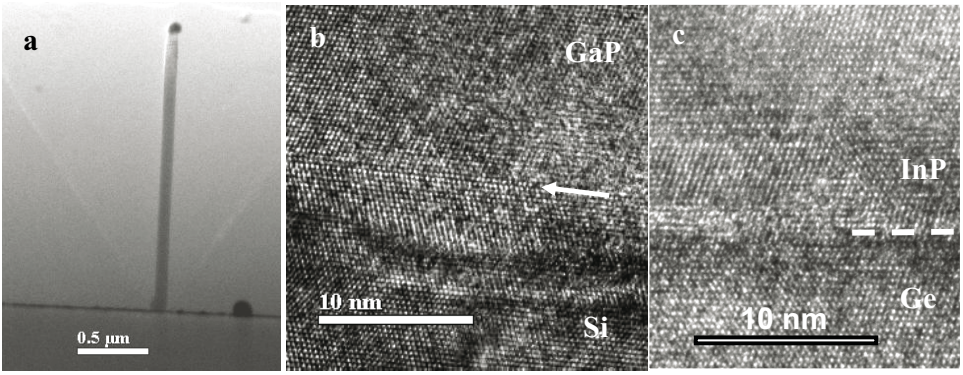


Fig. 4: a) TEM overview image of an epitaxially grown GaP wire on Si. b and c) HRTEM images of the interfaces of, respectively, a GaP wire on Si(111) and an InP wire on Ge(111).

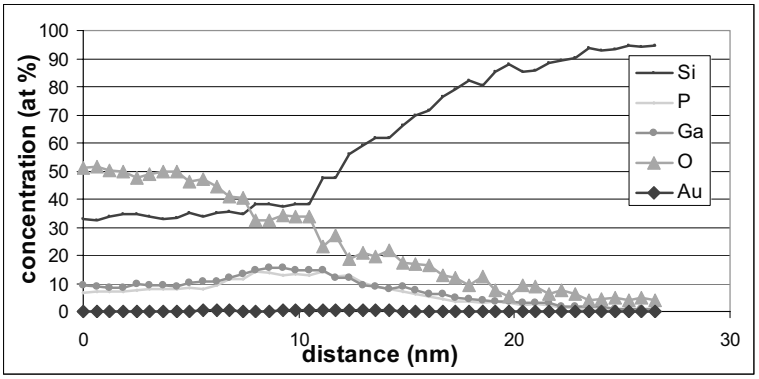


Fig. 5: Composition profile over the GaP-Si interface of Fig. 4b. The left part of the profile is dominated by the SiO_2 that was used for embedding the nanowires prior to sample preparation.

REFERENCES

Bakkers E P A M, van Dam J A, De Franceschi S, Kouwenhoven L P, Kaiser M, Verheijen M A, Wondergem H and van der Sluis P 2004 Nature Materials **3,** 769

Bakkers E P A M and Verheijen M A 2003 J. Am. Chem. Soc. **125**, 3440

Haraguchi K, Katsuyama K, Hiruma K and Ogawa K 1992 Appl. Phys. Lett. **60**, 745

Huang Y, Duan X, Cui Y, Lauhon L J, Kim K-H and Lieber C M 2001 Science **294,** 1313

Krishnamachari U, Borgstrom M, Ohlsson B J, Panev N, Samuelson L and Seifert W 2004 Appl. Phys. Lett. **85**, 2078

Mårtensson, T, Svensson C P T, Wacaser B A, Larsson M W, Seifert W, Deppert K, Gustafsson A, Wallenberg L R and Samuelson L 2004 Nano. Lett. **4**, 1987

Quantitative measurements of the inhomogeneous strain field of stacked self-assembled InAs/InP(001) quantum wires by the Peak Finding Method

T Ben, S I Molina, R García, D Fuster[1], M U González[1], L González[1], Y González[1] and S Kret[2]

Departamento de Ciencia de los Materiales e I. M. y Q. I., Universidad de Cádiz, Apdo. 40, 11510 Puerto Real, Cádiz, Spain
[1] Instituto de Microelectrónica de Madrid (IMM-CNM-CSIC), Isaac Newton 8, 28760 Tres Cantos, Madrid, Spain
[2] Institute of Physics PAS, Al. Lotników 32/46, 02-688. Warsaw, Poland

ABSTRACT: Stacks of InAs self-assembled quantum wires (QWr) grown by solid source molecular beam epitaxy on InP (001) substrates have been studied by both transmission electron microscopy (TEM) and high resolution transmission electron microscopy (HRTEM). Samples with an InP spacer layer thickness ≤ 10 nm are shown to exhibit stacked quantum wires well arranged along directions close to [001]. The analysis of some HRTEM images by the Peak Finding Method demonstrates the existence of an inhomogeneous strain field distribution throughout the InP spacer layers. The growth front of the InP spacer layers shows the lowest stress for the growth of further InAs wires on the areas located on top of each buried wire. The InAs wires are preferentially formed on these lowest stress surface areas.

1. INTRODUCTION

During the last few decades many studies have been completed on opto-electronic semiconductor materials and devices based on low dimensional structures. In this field Fafard et al (1996) and González et al (2000) have demonstrated the specific interest of self-assembled quantum wires (QWr) to generate active layers for lasers with emitting wavelengths between 1.3 and 1.55 μm. However it is well known that the size distribution broadening of self–assembled nanostructures is a disadvantage for their use in advanced optoelectronic devices.

Several authors have used conventional transmission electron microscopy (CTEM) and high resolution transmission electron microscopy (HRTEM) (Salem et al 2003, Springholz et al 2000, Wang et al 1998) to shed light on the mechanisms influencing the formation of both arrangements and size distributions of stacked nano-objects. Quantitative methods to extract the strain field directly from HRTEM images as well as the advance of computational methods are the last steps forward to determine the strain and composition of the epitaxial nanomaterial formed (Hÿtch et al 1998, Rosenauer et al 1996).

Stacking of nanostructures has been proposed as an efficient method for improving nanostructure size distributions (Tersoff et al 1996). Our work has focused to the study of the structural properties of stacks of InAs QWr separated by InP spacer layers with different thicknesses. A detailed analysis of the strain field in the wires, their surrounding regions and through the spacer layers has been carried out by the Peak Finding Method (Kret et al 2003).

2. EXPERIMENT

Samples investigated consist of six stacked InAs / InP(001) QWr grown by solid source molecular beam epitaxy (MBE). Each stacked QWr layer is separated from the next one by an InP

spacer layer with a thickness (t_s) of 5, 10 or 20 nm. The InAs thickness deposited for QWr formation in each layer, θ_i, is the critical thickness, θ_{ci}, as determined from *in situ* observation of 2D -3D transition of reflection high energy electron diffraction (RHEED) patterns ($\theta_i = \theta_{ci}$, for I = 1,...6). We will also present results obtained on a new set of two samples consisting of four stacked QWr layers and a spacer layer thickness of 5 nm. The two samples of this set differ on the InAs deposited to form the QWr. The first sample of this set was grown under similar conditions to the set above presented. In the second one, the InAs thickness deposited for the QWr formation is the same for all QWr layers and is equal to the critical thickness for the first QWr layer grown ($\theta_i = \theta_{c1} = 1.9$ monolayers, for i = 1,...4).

For TEM examination the samples were mechanically thinned up to approximately 20 μm and subsequently electron transparency was obtained using the precision ion polishing system at up to 4 kV and 4º of beam tilt. This investigation was performed with the JEOL transmission electron microscopes JEM 1200EX and JEM 2010F operating at 120 and 200 kV, respectively.

For the application of the Peak Finding Method (Kret et al 2003) to measure the strain field, special care has been taken during HRTEM imaging and micrograph digitisation to easily relate the positions of the HRTEM image maximum-minimum intensity positions and the projected positions of the atomic columns in the studied materials.

3. RESULTS

Figure 1 shows a couple of 002 DF TEM images that correspond to samples with spacer layer thickness of 20 (left image) and 5 nm (right image). The QWr are randomly distributed in the sample with a spacer layer thickness of 20 nm. Almost perfect vertical alignment of the wires is achieved for $t_s = 5$ nm (right image of Fig. 1). On the contrary, a high degree of vertical ordering appears in the QWr locations when $t_s = 10$ nm (image not shown). In this case the wires are stacked along a direction tilted approximately 7º with respect to [001].

In agreement with earlier work (Gutierrez et al 2003, Fuster et al 2004) and in the light of this result it is concluded that the spacer layer thickness influences the strain propagation through the spacing layer.

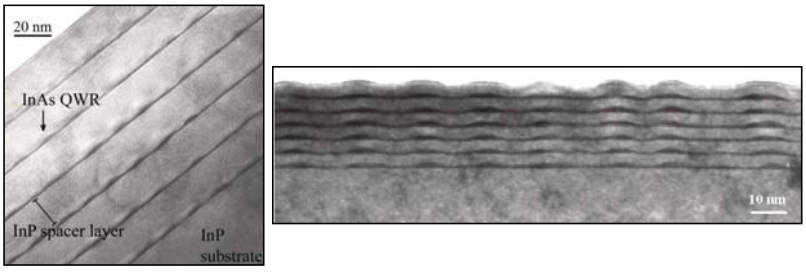


Fig. 1: 002 DF TEM images of six QWr layers stacks. The left and the right images are related to the sample with InP spacer layer thickness of 20 and 5 nm

Figure 2 presents one of the analysed HRTEM images by the Peak Finding Method. From this micrograph, the displacement vectors between maximum intensity positions related to the projected potential columns are identified, and the strain field is plotted by the derivation of these vectors with respect to the spatial coordinates. The strain map along [001] (ε_{zz} with respect to the equilibrium InP lattice parameter) resulting from this analysis is shown in Fig. 3. This map reveals an inhomogeneous strain field inside and in the region around the wires.

The lowest strain areas of InP for subsequent InAs growth are above the wires and are marked on the map with symbols m_1 and m_2. The highest strain areas (located in the InAs wires) are marked with M_1, M_2 and M_3. The maximum strain point for the first wire (M_1) is not located in its centre and the corresponding lowest InP strain area for subsequent InAs growth is therefore shifted. This fact leads to the generation of the new wire in a preferential region slightly tilted with respect to the growth direction. This tilt can easily be quantified by measuring the angle that the growth direction forms with the straight line joining points M_1 and M_2. It also worth to mention that the areas with

maximum strain for subsequent InAs growth (e.g. region B in Fig. 3) are located just in between each couple of wires. This justifies the difficulty to grow InAs on these areas, as experimentally observed.

From the analysis of the strain map shown in Fig. 3, we can conclude that the wires generate a strain field around them and this field increases the lattice parameter of the InP material of the spacing layer located just on the wires. This creates reduced stress in preferential sites for the nucleation of subsequent InAs QWr.

Due to the electron-transparent specimen thickness changes, the real values of the strain will be

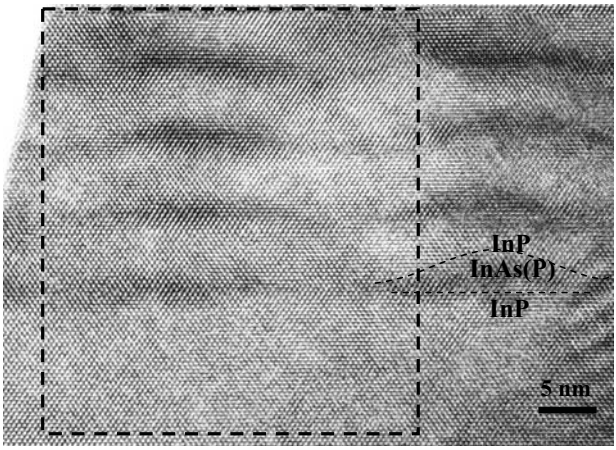


Fig. 2: HRTEM image of the sample consisting of four stacked layers of wires with a spacer layer thickness of 5 nm grown by the deposition of the InAs quantity to achieve, as measured by RHEED, the 3D critical thickness to form the wires in each QWr layer. The area of interest is labelled by a dotted rectangle.

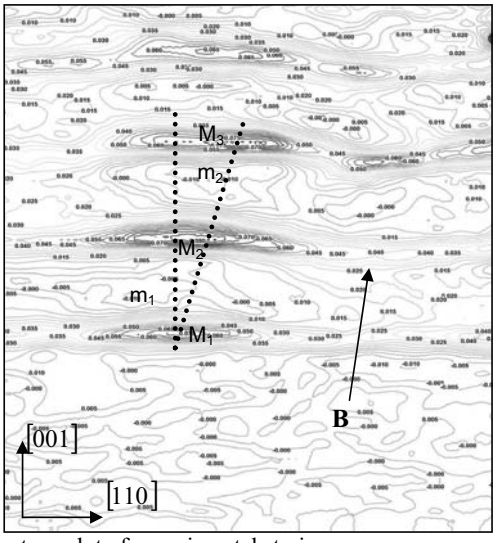


Fig. 3: Contour plot of experimental strain map ε_{zz} corresponding to the region of HRTEM image of Fig. 2 labelled by a dotted square.

larger than the strain values determined in this work for the thinner areas. In the analysis of the HRTEM image corresponding to Figs. 2 and 3, the specimen thickness decreases along the growth

direction, that is, when we move upwards in the image. Therefore, the real strain values will be larger than the values shown in Fig. 3. The difference between the determined strain and the real strain will be more important for the thinner areas of electron-transparent specimen, that is, for the grown wires of the upper stacks. Taking into account this consideration and the obtained strain values for the stacked wires, it can be stated that the strain in the wires increases or is roughly constant along the growth direction.

Similar analyses to the previous one have been carried out on a sample consisting of stacks of four QWr layers with a spacer layer thickness of 5 nm where the InAs thickness deposited for the QWr formation is the critical thickness for the first QWr layer grown ($\theta_i = \theta_{c1} = 1.9$ monolayers, for i = 1,...4). The tendency to increase the ε_{zz} strain for the second and following stacked wires is again observed in this sample. The main difference is that the shapes of the wires in this sample are strongly changed for the second and the next layers. This means that the growth of wires obtained by depositing just the 3D InAs critical thickness represents an improved approach to obtain a more homogeneous distribution of shapes and sizes of the formed wires, useful for the fabrication of improved devices.

4. CONCLUSION

The ε_{zz} strain maps determined by the Peak Finding Method confirm that the existence of an inhomogeneous strain field in stacked InAs quantum wires grown by MBE on InP (001) substrates explains the influence of the InP spacer layer thickness on the degree of vertical aligment of the wires. Likewise, the selection of an adequate InP spacer layer thickness and the deposition of InAs critical thicknesses for the 3D onset in each stacked QWr layer improves the shape homogeneity of the wires.

ACKNOWLEDGEMENTS

This research was supported by Spanish MCyT under project NANOSELF (TIC-2002-04096-C03-02), Junta de Andalucía (PAI research group TEP-0120) and network of excellence SANDiE (Contract NMP4-CT-2004-500101 of the VI European Framework Programme).TEM measurements were carried out in the DME-SCCYT, University of Cádiz and UCM.

REFERENCES

Fafard S, Wasilewski Z, McCaffrey J, Raymond S and Charbonneau S 1996 Appl. Phys. Lett. **68,** 991

González L, García J M, García R, Briones F, Martínez-Pastor J and Ballesteros C 2000 Appl. Phys. Lett. **76**, 1104

Fuster D, González M U, González L, González Y, Ben T, Ponce A and Molina S I 2004 Mat. Res. Soc. Symp. Proc. **794**, T5.3.1

Fuster D, González M U, González L, González Y, Ben T, Ponce A and Molina S I 2004 Appl. Phys. Lett. **84** (23), 4723

Gutiérrez H R, Cotta M A and de Carvalho M M G 2003 J. Cryst Growth **254**, 1

Hÿtch M J, Snoeck E and Kilaas R 1998 Ultramicroscopy **74**, 131

Kret S, Ruterana P, Delamar C, Benabras T and Dluzewski P 2003 Nitride Semiconductors, Handbook on Materials and Devices (Wiley-Vch HmBh & Co. KgaA Heppwnheim, Germany). p. 439-485

Rosenauer A, Kaiser S, Reisinger T, Zweck J and Gebhardt W 1996 Optik **102**, 63

Tersoff J, Teichert C, and Lagally M. G. 1996 Phys. Rev. Lett. **76**, 1675

Salem B, Brémond G, Hjiri M, Hassen F, Maaref H, Marty O, Brault J and Gendrey M 2003 Mat. Sci. Eng. B **101**, 259

Springholz G, Pinczolits M, Mayer P, Holy V, Bauer G, Kang H H and Salamanca-Riba L 2000 Phys. Rev. Lett **84**, 20

Wang B, Zhao F, Peng Y, Jin Z, Li Y and Liu S 1998 Appl. Phys. Lett. **72**, 2433

Measurement of the mean inner potential of ZnO nanorods by transmission electron holography

E Müller, P Kruse, D Gerthsen, A Rosenauer[1], M Schowalter[1], D Lamoen[2], R Kling[3] and A Waag[4]

Laboratorium für Elektronenmikroskopie, Universität Karlsruhe, D-76128 Karlsruhe, Germany
[1] Institut für Festkörperphysik, Universität Bremen, Otto-Hahn-Allee 1, D-28359 Bremen, Germany
[2] Departement Fysica, Universiteit Antwerpen, B-2020 Antwerpen, Belgium
[3] Abteilung Halbleiterphysik, Universität Ulm, D-89069 Ulm, Germany
[4] Institut für Halbleitertechnologie, Universität Braunschweig, D-38106 Braunschweig, Germany

ABSTRACT: The mean inner potential of ZnO was measured by means of electron holography in a transmission electron microscope. To overcome the problem of imprecise knowledge of the sample thickness, ZnO nanorods with well-defined geometry and diameter were used in this study. The phase of the transmitted beam of the image wave yields a mean inner potential of 15.9 ± 1.4 V for ZnO. This value is in good agreement with the calculated value of 15.8 V using *ab initio* density functional theory computations.

1. INTRODUCTION

The mean inner potential (MIP) is known as the volume average of the Coulomb potential of a solid (O´Keefe et al 1994) and corresponds to the zero-order Fourier coefficient of the crystal potential. It depends on the chemical composition and the structure of the solid. Besides the fundamental importance of the MIP, precise values are also required for quantitative image analysis and image simulations in transmission electron microscopy (TEM). This study focuses on the determination of the MIP of ZnO since this material has been considered as a promising material for optoelectronic devices in the past few years. Due to its band gap energy of 3.3 eV and the large exciton binding energy of 60 meV, ZnO could be suited for the fabrication of laser diodes in the ultraviolet spectral range.

However, only one experimental value for the mean inner potential of ZnO has been published so far by Elfwing and Olson (2002) who found V_0 = 21 V applying electron holography in a transmission electron microscope. But this value differs significantly from the theoretical value V_0 = 16.1 V which was calculated using the EMS program package (Stadelmann 1987). It has to be noted that values calculated using EMS are derived from electron scattering factors computed for isolated atoms, neglecting the redistribution of the electrons due to the bonding of atoms in a crystal. The redistribution of the electrons can be taken into account by an *ab initio* computation of the MIP within the density functional theory formalism (Kim et al 1998). The computation of the MIP using the *ab initio* approach described by Kruse (2004) and Schowalter et al (2004) yielded a slightly reduced value of the MIP for ZnO of 15.8 V.

Due to the discrepancy between the experimental and theoretical values of the MIP and the technological importance of ZnO we have performed measurements of the MIP using off-axis transmission electron holography. The key point of our study is that we are able to obtain precise thickness values of the analysed specimens, which typically limit the accuracy of MIP measurements, by using ZnO nanorods with a well-defined shape and diameter.

The MIP can be determined by transmission electron holography by measuring the phase shift of the electron wave transmitted through the sample (image wave) with respect to a reference wave, which only propagates through the vacuum. In the absence of internal magnetic and electrical fields and under conditions where strong dynamical diffraction can be neglected, the phase shift between reference and image wave $\Delta\varphi$ is determined by the MIP $V_0(x,y,z)$ and the sample thickness $t(x,y)$ (Reimer 1984):

$$\Delta\varphi(x,y) = C_E V_0 t(x,y) \tag{1}$$

The interaction constant $C_E = (2\pi e/\lambda)\cdot(E+E_0)/E(E+2E_0)$ is given by the kinetic energy of the electrons E, the elementary charge e, the wavelength λ and the rest energy of the electron E_0. C_E was determined to be $7.29\text{x}10^6$ rad V^{-1} m^{-1} for the microscope used in this study (Kruse et al 2003).

Potential sources of error using Eq.(1) are (i) deviations from kinematical diffraction conditions, (ii) fluctuation of the electron energy affecting C_E, (iii) the presence of electrostatic fields due to charging in the vicinity of the sample (iv) inaccurately known TEM specimen thickness, the latter being the most serious factor. In our study, we have minimized this error by analysing nanorods with well-defined shape and diameter. Under those circumstances, electron holography becomes a rather accurate method for the determination of the MIP.

2. EXPERIMENTAL TECHNIQUES

The investigated ZnO nanorods were grown by metalorganic vapor-phase epitaxy (MOVPE) using a modified Aixtron 200 RF horizontal flow reactor. N_2O was used as oxygen source, the group II precursor was diethylzinc (DEZn), and nitrogen was used as carrier gas. A-plane oriented Al_2O_3 has been used as a substrate material. More details about the growth process can be found elsewhere (Kling et al 2004).

TEM samples were prepared by mechanically scraping the nanorods – cylinders with a length of about 1 μm and a diameter of 20 to 40 nm - from the substrate and depositing them on a circular copper grid covered by a thin holey carbon film. Thus, artefacts due to typical TEM specimen preparation procedures like dimpling and ion milling can be avoided. The electron holographic investigations were performed with a Philips CM200 FEG/ST microscope equipped with a Möllenstedt-Düker biprism. The holograms were recorded with a slow-scan CCD camera with 2048x2048 pixels. The principle of the technique and the numerical reconstruction procedure are outlined in detail by Lehmann and Lichte (2003) and Kruse et al (2003).

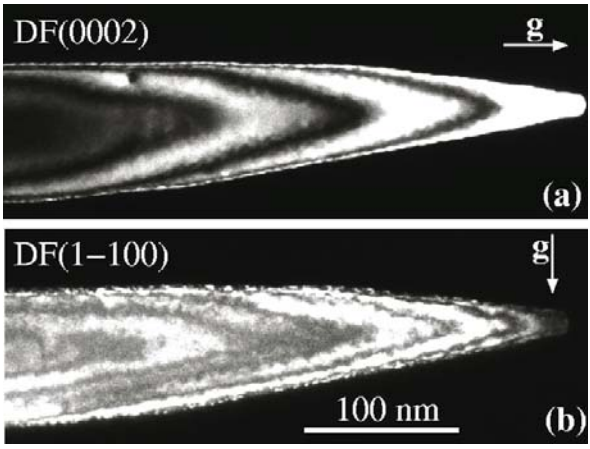


Fig. 1. Dark field images taken with (a) $\vec{g}$ =(0002) and (b) $\vec{g}$ =($1\bar{1}00$)

3. EXPERIMENTAL RESULTS

Dark-field images (Fig. 1) taken under two-beam conditions with two different imaging vectors $\vec{g}$ reveal the high structural quality of the ZnO nanopillars.

The electron holography was carried out at the tip of the ZnO nanorod, which was placed in the interference field generated by applying a voltage of 150 V to the biprism which yields a distance of

the interference fringes of 0.13 nm. To provide a good mapping of the interference fringes the magnification was set to a value of 770000. To avoid strong dynamical diffraction conditions the nanorod was tilted about 11° away from the $[1\bar{1}20]$-zone axis to minimize the intensity of the Bragg reflections. A hologram was recorded (Fig. 2) and after removing carefully the specimen from the field of view a reference hologram was taken using the same microscope settings and unchanged optical parameters.

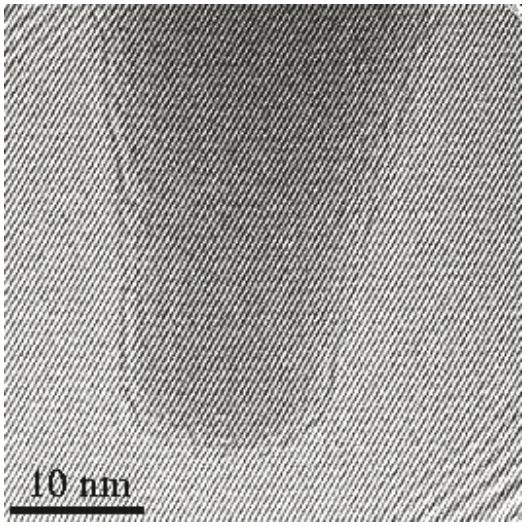


Fig. 2. Off-axis electron hologram

After taking the holograms, the nanorod was tilted back to the $[1\bar{1}20]$-zone axis and the biprism was removed. Subsequent recording of a high-resolution TEM (HRTEM) image allowed precise magnification determination by using the known lattice plane distances of ZnO for calibration.

The phase and amplitude of the image wave were extracted numerically from the sideband of the digitised hologram according to the procedure outlined by Lehmann and Lichte (2003). The reconstructed phase of the image wave is depicted in Fig. 3. A line scan perpendicular to the longitudinal axis (indicated in Fig. 3) was performed. The phase value of the vacuum region was subtracted and the remaining phase shift due to the presence of the sample is shown in Fig. 4. The phase scan perpendicular to the axis of the nanorod is averaged over a narrow band in the y-direction. Consequently the obtained curve depends only on x and can be compared with the relative phase shift:

$$\Delta\varphi(x) = C_E V_0 t(x) \tag{2}$$

The profile of the curve Fig.4 suggests a thickness dependence that corresponds to an object with circular axial symmetry. Thus we can assume for the thickness t(x):

$$t(x) = 2\sqrt{r^2 - x^2} / \cos(\alpha) \tag{3}$$

where r is the radius of the circular nanorod. The angle α represents the tilt of the longitudinal axis of the nanorod with respect to the direction perpendicular to the electron beam. The determination of the angle α was estimated from the goniometer tilt. Due to the uncertainty in the measurement of the tilt angle and the determination of the magnification an error of 4.2 % was evaluated for Eq. (3).

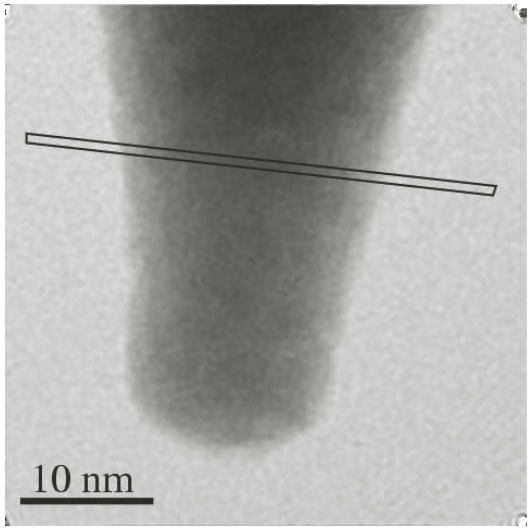


Fig. 3. Phase of the image wave

4. DISCUSSION

Using Eq. (3) we can fit a curve $\Delta\varphi(x) = C_E V_0 t(x)$ to the measured profile. The main fit parameter is the MIP V_0. The fitted curve shown in Fig.3(b) provides a value for $|V_0|$= 15.5 V with a standard deviation of ± 0.032 V. As a result of the tilting towards kinematical diffraction

conditions and the small thickness of the sample below typical extinction distances of the Bragg reflections the deviations due to dynamical contributions are very small. Bloch-wave calculations performed with the EMS program package show that the dynamical contributions are below 1% for the tilted sample. Taking into account all relative errors of the contributing factors the resulting MIP can be determined to $|V_0|$ = (15.5± 1.1) V. Averaging over values from four different nanorods we obtained a value of $|V_0|$ = 15.9 ± 1.4) V.

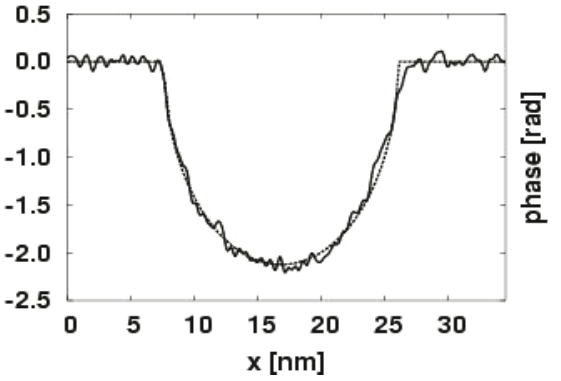


Fig. 4. Phase line scan (continuous) and the fitted curve (dashed line)

5. SUMMARY

The experimental value for the mean inner potential of ZnO nanorods was determined to be $|V_0|$ = (15.9 ± 1.4) V which is in good agreement with the calculated value of 15.8 V using *ab initio* computations. Analysing nanoparticles with known shape and size provides an inherent advantage over using conventional TEM samples where the sample thickness cannot be measured accurately enough to determine the MIP. Therefore, this approach can be extended to all other materials where nanoparticles are available.

ACKNOWLEDGEMENTS

The authors are very much indebted to M Lehmann and H Lichte (Technical University Dresden) for their valuable help in solving experimental problems and fruitful discussions. The work was financially supported by the network of competence “Functional Nanostructures” of the state of Baden-Württemberg (Germany) and the Deutsche Forschungsgemeinschaft (DFG).

REFERENCES

Elfwing M and Olson E 2002 J. Appl. Phys. **92**, 5272
Kim M Y, Zuo J M and Spence J C H 1998 Phys. Status Solidi A, **166**, 445
Kling R, Kirchner C, Gruber Th, Reuss F and Waag A 2004 Nanotechnology **15**, 1043
Kruse P, Rosenauer A and Gerthsen D 2003 Ultramicroscopy **96**, 11
Kruse P 2004 Bestimmung des mittleren inneren Potentials von III-V Halbleitern (Berlin, Mensch und Buch), PhD thesis
Lehmann M and Lichte H 2002 Microsc. Microanal. **8**, 447
O´Keefe M and Spence J C H 1994 Acta Cryst. A **50**, 33
Reimer L 1984 Transmission Electron Microscopy (Berlin-Heidelberg, Springer) p. 56
Schowalter M, Lamoen D, Rosenauer A, Kruse P and Gerthsen D 2004 Appl. Phys. Lett., **85**, 4938
Stadelmann P 1987 Ultramicroscopy **21**, 131

Quantum effects in band gap-modulated amorphous carbon superlattices

V Stolojan, P Moreau[1], M J Goringe[2] and S Ravi P Silva

Advanced Technology Institute, University of Surrey, Guildford, GU2 7XH, UK
[1] Institut des Matériaux Jean Rouxel, Université de Nantes-CNRS, Laboratoire de Chimie des Solides, 44322 Nantes, France
[2] School of Engineering, University of Surrey, Guildford, GU2 7XH, UK

ABSTRACT: Diamond-like carbon (DLC) films, with their controllable optical band gaps from 1-4eV, have promised much as electronic semiconducting materials for many years. In particular, hydrogenated amorphous carbon films (a-C:H) have attracted interest in their possible use in light emitting diodes, flat panel displays and solar cells. Photoemission in these films can be explained by the electron-hole recombination at sp^2-bonded carbon clusters, enhanced by the quantum-confinement of the rigid sp^3-matrix. The speed of such devices can be improved by constructing homogenous carbon superlattices from alternate high and low band-gap a-C:H layers. Here, we measure directly the electronic properties across superlattices, using energy loss spectroscopic profiling (ELSP) in a transmission electron microscope (TEM). By analysing the valence losses across the layers, we characterise the electronic structure of the films. By modelling the influence of the interface collective modes of oscillation (interface plasmons), we show that the measured changes in the bulk plasmon energies of the wells are due to quantum confinement and are predicted using the 'particle-in-a-box' model. These a-C superlattice structures have the potential of introducing a highly versatile novel large area amorphous semiconductor that is carbon based and deposited at room temperature.

1. INTRODUCTION

Band-gap modulated artificial structures tailor the energy levels by quantizing the electron wavefunction's momentum and energy. They have been introduced as a practical solution to the demand for increasing speeds of operation, beyond the fundamental limits available with atomic energy levels. The resulting quantized energy levels in these artificial superlattices are controlled by the well's width and depth. These energy levels can also degenerate into bands, when tunnelling is controlled through the heights and widths of the barriers separating the wells. This can lead to the tailoring of devices for specific applications, such as high-frequency generators for the mobile phone industry.

2. EXPERIMENTAL METHOD

2.1 Energy Loss Spectroscopic Profiling (ELSP)

A Gatan imaging filter (GIF) attached to a TEM provides a three-dimensional data set (3D) which can be recorded using a two-dimensional detector (the charge-coupled-device CCD). The three dimensions available are the two dimensions of the magnified projected image of the sample and the one energy loss dimension. An energy filtered image is essentially a slice, at constant energy, through this 3D data set (Fig. 1a). An energy loss spectrum requires the integration of the two spatial dimensions, and this is done by the quadrupole lenses of the GIF in one of the spatial dimensions and by binning in the CCD over the other dimension. However, we can see that, before binning, the CCD actually records a 2D image with one spatial axis and one energy loss axis orthogonal to the spatial

axis (Fig. 1b). ELSP is applicable to linear features, such as planar interfaces, when they can be rotated so that they lie parallel to the spatial axis integrated by the quadrupoles (Walther 2003). The image recorded at the CCD is then a set of spectra where each one corresponds to a linear section of the sample, parallel to the interface, taken at positions across the interface. The number of positions (and hence the sampling of the spatial dimension) is controlled by the dispersion provided by the quadrupoles, the chromatic aberration, sample drift and, if several images are averaged for improving the signal-to-noise ratio, by the ability to align accurately ELSP images with respect to each other.

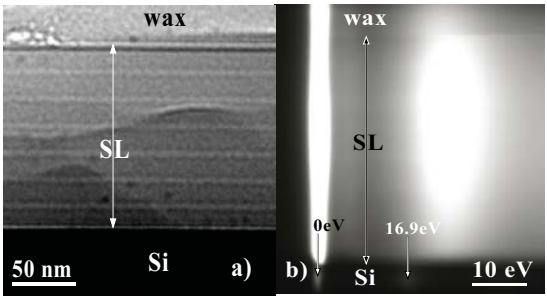


Figure 1 a) Energy filtered image of a superlattice at ~-5µm defocus, showing the wells with bright contrast. **b)** The corresponding low loss ELSP image; the vertical axis is identical, to within a scaling factor, to Fig. 1a.

2.2 Sample Preparation and Characteristics

The homogenous superlattices were deposited on Si(100) substrates using plasma-enhanced chemical vapour deposition, by alternating the biasing voltage between -190V (for wells) and -265V (for barriers), under computer control (Silva et al 1994a). Cross-sectional TEM samples were prepared by mechanical grinding and polishing, followed by ion-beam polishing. Test barrier and well films were deposited under identical conditions, and were etched away from the Si substrates using a HF:HNO_3 acid mix. Samples were analysed in a Philips CM200 (200kV, LaB_6) TEM fitted with a GIF2000 spectrometer. The average energy dispersion and spatial dispersion used for ELSP were 0.1 eV/pixel and 0.45 nm/pixel (calibrations were performed for each individual experiment). Table 1 summarises some of the properties of the barriers and wells (Davis et al 1995).

Sample	Well	Barrier
Optical bandgap	**1.5eV**	**2.8eV**
Refractive index	**2.2**	**2.1**
H concentration	**36%**	**33%**
Sp^2	**87%**	**74%**

Table 1 Properties of test films deposited under identical conditions as the barriers and wells of the superlattices (Silva et al 1994a, Davis et al 1995).

2.3 Data Processing

For each superlattice, we collected 40 ELSP images containing the valence loss across the superlattices, 40 ELSPs with the beam going through the vacuum and another 40 with the beam through the vacuum and a preset voltage wobble on the drift tube, for energy calibration purposes. Each ELSP set was aligned in energy to within a pixel and the valence loss set was also aligned in the spatial dimension on either the superlattice/Si interface or the superlattice/mounting wax interface (or both) to within a pixel. The spatial alignment parameters thus gathered are good measure of the sample drift within one acquisition period (0.5 s for all ELSP images). The final images contained were ~600x600 pixels, i.e. 600 spectra sampling the dimension perpendicular to the interface with ~0.45 nm/pixel. For each spectrum, the origin of the energy loss scale was determined to within 20 meV using a Lorentzian fit to the zero-loss peak and similarly the energy dispersion was determined from the calibration ELSP. The plasmon energy was determined using a Lorentzian curve to within 10 meV.

3. SPATIAL RESOLUTION

The issue of spatial resolution can be resolved into two distinct items: one relates to the experimental set-up (chromatic aberration, sample drift, data processing) and the other relates to the spatial extent of the energy loss event studied.

The experimental spatial resolution in this case is mostly affected by the ability to align the ELSP images to within a pixel; for a normal distribution of positions about the centre, this leads to a broadening of ~0.95 nm. The short exposure times used lead to a 0.1 pixel broadening. The influence of chromatic aberration is negligible due to the small range of the energy loss of interest.

The event delocalisation for collective excitations (plasmons) is quite broad, up to several nanometres (Rivacoba et al 2000). However, at the interfaces between two dielectrics, interface plasmons can be established. These surface states, much more confined normal to the interface than bulk plasmons, act to screen out the contribution of the bulk plasmons to the scattering cross-section. This is known as the 'begrezungs' effect and manifests mathematically as a subtraction of the bulk contribution from the total scattering cross section, as one approaches the interface (Howie 1983). This means that the final result is not a superposition of the surface excitation to the bulk excitation but a replacement. We modelled the energy loss of the relativistic electron using the classical dielectric approach (Garcia-Molina et al 1985) for a sandwich interface (Turowski et al 1994, Moreau et al 1997), using dedicated software (Walsh 1992). This was done using the dielectric functions extracted from the energy loss spectra of barrier and well test layers grown under identical conditions as the superlattices. Figure 2a shows the change in the plasmon energy of the well as a function of well width, indicating that the plasmon energy of the well is defined down to well widths of ~ 1nm, beyond which the surface plasmons couple and the plasmon energy measured, is no longer representative of the well. Figure 2b models the variation of the plasmon energy across a 3nm wide well, corrected for the experimental broadening of 1nm. The ~1÷1.5 nm region over which the plasmon energy changes from its barrier to its well value is an overall measure of the spatial resolution of this method when using valence losses, applied to sandwich structures.

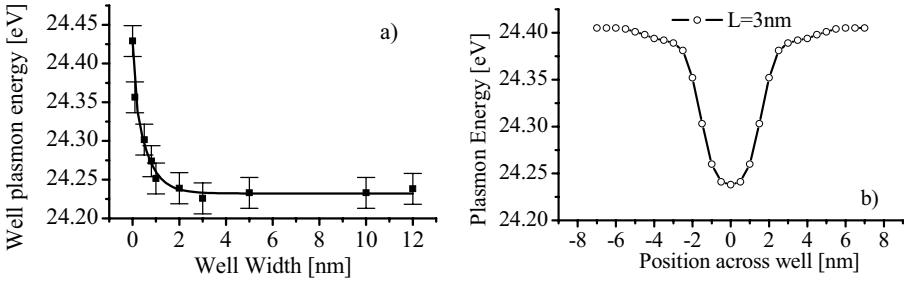


Fig. 2 a) variation of the plasmon energy in the middle of the well, as a function of well width. The line fit is a guide to the eye. b) variation of the plasmon energy across a 3nm wide well, corrected for the 1nm experimental broadening.

4. RESULTS

The plasmon energy E_P for electrons bound by a bandgap E_G can be expressed as:

$$E_p^2 = E_0^2 + E_G^2 \qquad (1)$$

where $E_0^2 = \hbar^2 ne^2 / m\varepsilon_0$ is the free electron plasmon energy (Egerton 1996). Figure 3a shows a typical profile of the plasmon energy across a superlattice. The gap energy here is the Penn gap, a parameter modified from the optical band gap to account for scattering of electrons at Brillouin zone boundaries and non-dipole transitions. The Penn gaps are calculated (Penn 1962) as $E_{gbarrier}$=13.210eV and E_{gwell}=12.36eV. Assuming that the free electron values do not change with well widths, Fig. 3b shows the experimental change in the Penn gap of the wells, as a function of well widths. This can be modelled using the 'particle-in-a-box', where the well depth is 0.425eV (half of the Penn bandgap difference). By matching the wavefunction at the boundary, we calculate the expected change in the Penn bandgap due to quantum confinement within a well of changing width, using the effective mass as a parameter (Silva et al 1994a).

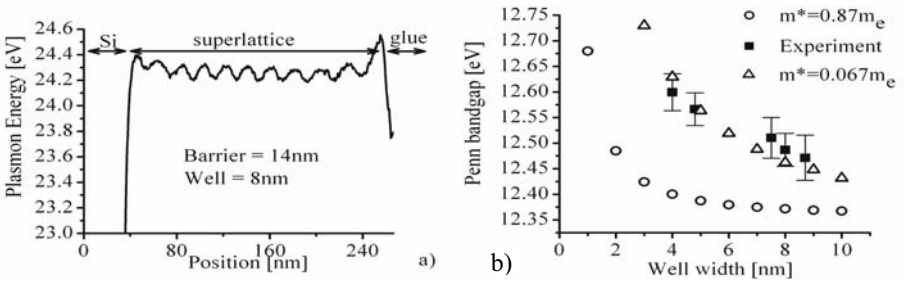


Fig. 3 a) The variation of the plasmon energy across a typical superlattice. b) The measured Penn bandgap energies compared with the predicted changes in bandgap energy, for $m^*=0.067m_e$ (open triangles) and for $m^*=0.87m_e$ (open circles).

There are two values of the effective mass available in literature, which are applicable here. The first, $m^*=0.87m_e$ has been used to describe the relationship between the density of valence electrons and the plasmon energy for a range of amorphous carbons (Ferrari et al 2000), whilst the second, $m^*=0.067m_e$ has been used to describe the measured change in the optical bandgaps of the superlattices studied here, as a function of well width (Silva et al 1994b). Figure 3b shows the theoretical predictions for each of the two effective masses, and we can see that $m^*=0.067m_e$ is a good fit of the experimental data. This value of the effective mass is a consequence of the 'particle-in-a-box' model used and can be related to the large length of the barriers and consequently the very small amount of tunnelling in this case.

5. CONCLUSION

We have confirmed that effects associated to quantum confinement are possible in amorphous carbon semiconductor architectures and that these can be investigated using valence losses to a spatial resolution approaching 1nm. This is because of the screening provided by the surface plasmons established at the interfaces between the barriers and wells of the superlattices.

ACKNOWLEDGEMENTS

We are very grateful to the EPSRC for funding through the Portfolio Partnership Grant.

REFERENCES

Davis C A, Silva S R P, Dunin-Borkowski R E, Amaratunga G A J, Knowles K M and Stobbs W M 1995 Phys. Rev. Lett. **75**, 4258

Egerton R F 1996 EELS in the Electron Microscope 2nd Ed. (New York, London - Plenum Press) ch. 3

Ferrari A C et al 2000 Phys. Rev. **B62**, 11089

Garcia Molina R, Gras Marti A, Howie A and Ritchie R H 1985 J. Phys. **C18**, 5335

Howie A 1983 Ultramicroscopy **11**, 141

Moreau P, Brun N, Walsh C A, Colliex C and Howie A 1997 Phys. Rev. **B56**, 6774

Penn D R 1962 Phys. Rev. **128**, 2093

Rivacoba A, Zabala N and Aizpurua J 2000 Prog. Surf. Sci. **65**, 1

Silva S R P, Ravi P et al 1994a Thin Solid Films **253**, 20

Silva S R P, Ravi P et al 1994b Jpn. J. Appl. Phys. **33**, 6458

Turowski M A, Kelly T F and Batson P E 1994 J. Appl. Phys **76**, 3776

Walsh C A 1992 Computer Programmes for the Calculation of Electron Energy-Loss Spectra from Interfaces Between Dielectric Media (Cavendish Laboratory, Cambridge)

Walther T 2003 Ultramicroscopy **96**, 401

Structure of rolled-up semiconductor nanotubes

N Y Jin-Phillipp, Ch Deneke[1], J Thomas, M Kelsch, R Songmuang[1], M Stoffel[1] and O G Schmidt[1]

Max-Planck-Institut für Metallforschung, Heisenbergstr.3, D-70569 Stuttgart, Germany
[1] Max-Planck-Institut für Festkörperforschung, Heisenbergstr.1, D-70569 Stuttgart, Germany

ABSTRACT: In this paper, structures of InAs/GaAs and SiGe/Si rolled-up nanotubes (RUNTs) are characterized by using high-resolution transmission electron microscopy (HRTEM) and spatially-resolved electron energy loss spectroscopy. Free-standing RUNTs as well as their cross-sections are investigated. It is found that the walls of the nanotubes are mainly crystalline, and are composed of alternating crystalline and oxide containing noncrystalline layers. Defects form in some nanotubes, where the rolling involves a misorientation.

1. INTRODUCTION

Nanotechnology requires new structures in the nanometre-range with rigorously controllable size, shape, and positions. One of the recent developments is three-dimensional semiconductor nanostructures, which are realized using two-dimensional epitaxial layers by releasing the thin layers from their substrates (Prinz et al 2000, Schmidt and Eberl 2001). RUNTs have been fabricated using bilayers such as InGaAs/GaAs, SiGe/Si, and $Ga_xIn_{1-x}P/Ga_yIn_{1-y}P$. Their diameters and positions may be well controlled by the design of the bilayer and the releasing process. For their potential electronic, optoelectronic, and nanofluid applications, a sound knowledge of their structures is a prerequisite. This paper reports structural and compositional characterization of InGaAs/GaAs and SiGe/Si RUNTs.

2. EXPERIMENTAL

Bilayers of 1.4 monolayer (ML) InAs/14 ML GaAs as well as 6nm $Si_{0.67}Ge_{0.33}$/ 12nm Si were grown by molecular beam epitaxy (MBE) on GaAs and Si (001) substrates, respectively. In order to release the bilayer from the substrate, an etchant-sensitive sacrificial layer was deposited before the strained bilayer. In the case of the InAs/GaAs system, an AlAs underlayer was chosen, whereas in SiGe/Si system, the bilayer was heavily B-doped, and an undoped Si layer was sacrificial. The etchant for the AlAs layer was 25 vol % HF solution with a surfactant of benzalkonium chloride (Deneke et al 2004), whereas for the Si layer an aqueous NH_4OH solution (Golod et al 2001). Due to the high inherent elastic misfit strain in the bilayers, the released layers rolled up to form RUNTs.

Free-standing RUNTs were obtained by cleavage. Cross-sectional TEM specimens were prepared by the standard method, as well as by focused ion beam (FIB) milling. A thin layer of Ti was deposited on the surface of the etched wafer, in order to protect the tubes. TEM and HRTEM were performed on a Philips CM200 operated at 200kV and a JEOL 1250 atomic resolution microscope (ARM) with an acceleration voltage of 1250kV, respectively. Spatially-resolved electron energy loss spectroscopy (EELS) was performed on a dedicated scanning transmission electron microscope VG HB501 operated at 100kV. The probe diameter was ~1nm, and an energy dispersion of 0.7eV/channel was used.

3. RESULTS AND DISCUSSION

3.1 InAs/GaAs Nanotubes

Most InAs/GaAs RUNTs have tightly packed shells, even with a rotation as high as ten (Deneke et al 2004). Figure 1a shows a bright-field (BF) image of a NT with an inner diameter of

~250nm. The tube has performed two and a half rotations during the roll-up process. A selected area electron diffraction (SAED) pattern from the region across the entire tube diameter is shown in Fig. 1b. By indexing the diffraction pattern, it is clear, that the nanotube axis is close to <010>. For most reflections five separate diffraction spots are observed. This is because the rotation axis was slightly away from <010>, so that the top- and bottom- half of the NT are different in orientation, an analogue to a chiral carbon nanotube. The "helicity angle" is ~ 0.5°. Additionally, there exists a small misorientation between the different shells of the bilayers, which may be compared with a multi-walled carbon nanotube of multi-helicity.

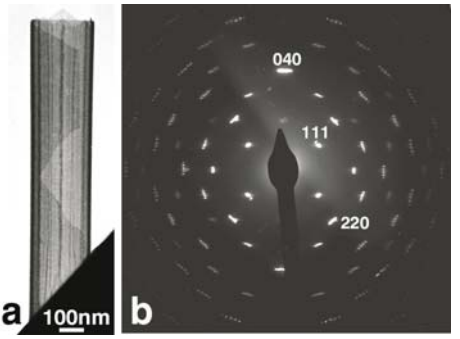


Fig. 1. (a) BF image of an InAs/GaAs RUNT, (b) SAED pattern from region across the entire diameter of the tube.

Figure 2a shows a HRTEM image of half of another tube with an inner diameter of ~200nm. The RUNT has performed three rotations. In the sidewall region on the right side of the image, the three shells of InAs/GaAs bilayer are almost perpendicular to the image plane, i.e. at a {100}-pole position. Three crystalline regions in the NT sidewall may be clearly identified by their ordered lattice image patterns. A region of the outermost shell marked with **b** is enlarged in Fig. 2b, revealing the atomic resolved lattice image of GaAs and InAs. The unit cell of the lattice is outlined with the white square in Fig. 2b. These regions with lattice image pattern, marked with I in Fig. 2a, are separated by regions, which do not show any ordered image pattern and are denoted as regions II. The irregular image pattern in the regions II may be due to the distortion of the lattice, as well as due to the existence of a non-crystalline layer between the native crystalline shells, and will be further studied by spatially resolved EELS. The lattice image from the outermost shell close to a {110}-pole position from the rectangular region **c** is seen in Fig. 2c, showing a face-centred cubic Bravais lattice. A somewhat mosaic-like structure with fringes along both {111} planes may be recognized. The formation of the RUNT is accompanied by the formation of stacking-faults (SFs). This may arise from the twist of the bilayer due to the slight change of the rotation axis during rolling.

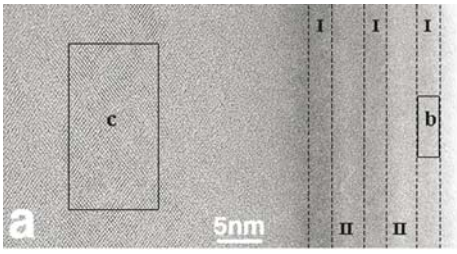
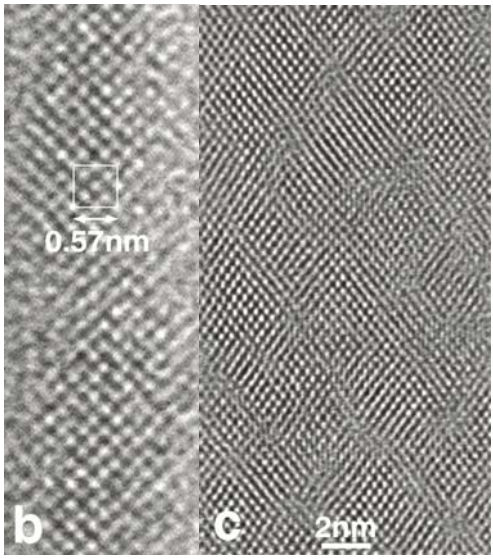
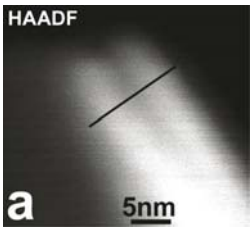


Fig. 2. (a) Many-beam BF image of a InAs/GaAs NT with three rotations, (b) enlarged HRTEM image from region **b** in (a) close to a {100} pole position, showing lattice image of the outmost shell, (c) Wiener-filtered HRTEM of region **c** in (a) close to a {110} pole position, revealing mosaic structure of stacking faults along both sets of {111} planes.





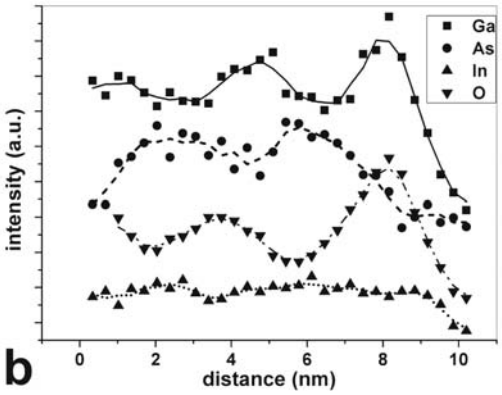
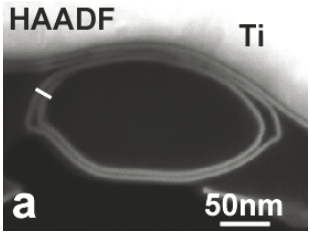


Fig. 3. EELS line-scan at a NT wall with double shells: (a) HAADF image with the position of the scans indicated by a black line, (b) Intensities of EELS edges of various elements. Line is drawn as an eye guide.

In order to clarify the chemistry of the layer between the crystalline shells, as well as to investigate the element distribution of the shells, EELS line-scans across NT sidewalls were performed. Figure 3a shows a high-angle annual dark-field (HAADF) image of a sidewall of a RUNT with two rotations. In addition to the expected EELS edges, Ga(L), In(M), and As(L), the O(K) edge is also observed. Since the energy range of EELS edges Ga(L) and As(L) are far away from those of elements O(K) and In(M), two sequential scans along a same line, indicated by a black line in Fig. 3a, with different energy ranges were performed. Figure 3b illustrates the background subtracted intensity profiles for different elements. Due to the bending of the double shells at the sidewall, the layers as well as the thickness of the layers, which the electron beam penetrates, varies at different positions along the scan-line. The intensity of In shows less change because of its weak signal. It is clear, that As exhibits two peaks of intensity, which are associated with the two shells of the tube wall, whereas Ga and O exhibit three peaks. The change of the intensity of Ga across the sidewall of the NT synchronizes with the change of O, and anticorrelates, however, with the change of As. This indicates that although the bilayer remains mainly crystalline, as proved by HRTEM, an oxide layer forms during the wet etching and the rolling process. Considering the bending effect, the thickness of the noncrystalline layer must be smaller than the regions of irregular image pattern observed in Fig. 2c. Further EELS investigation on a cross-sectional specimen (Fig. 4) confirms that the peak position of Ga intensity coincides with the peak position of O intensity and the trough in As intensity. The amorphous layer between the crystalline shells is mainly, therefore, Ga-oxide. (The two shells of the bilayer are obviously separated with a small distance, so that there are two intensity sub-peaks of Ga and O corresponding to the two surface layers between the two As peaks of the shells.) It is, therefore, clear that the walls of the InAs/GaAs nanotubes are composed of alternating native crystalline and oxide noncrystalline layers. Although many InAs/GaAs NTs have tightly packed shells, we notice that the shells of the NT in Fig. 4a are rather loose after two rotations.



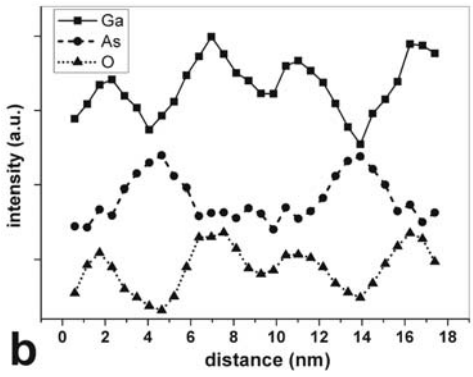
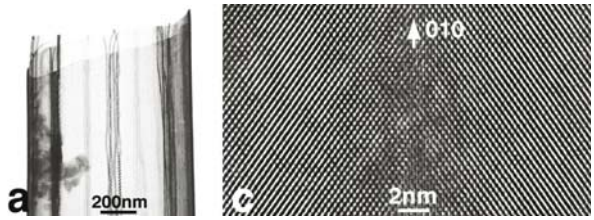


Fig. 4. EELS line-scan on a cross-sectional sample. (a) HAADF image, the scan position is indicted with a white line, (b) EELS intensities of elements.

3.2 SiGe/Si Nanotubes

Figure 5a shows a SiGe/Si RUNT with slightly more than one rotation. Using the atomic lattice image of the NT sidewall (Fig. 5b), the thickness of the crystalline region for each shell is measured as ~12 nm, whereas the non-crystalline region between the shells is ~ 6nm, and the non-crystalline region on the surface of the RUNT is ~3nm in thickness. No defect has been found in the NT. The HRTEM image of the shell close to a {110}-pole position shown in Fig. 5c indicates a perfect symmetrical bending of the bilayer along <010>.



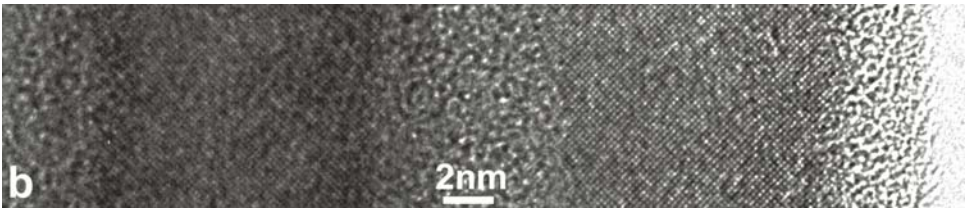


Fig. 5. (a) BF image of a SiGe/Si RUNT. (b) HRTEM image of the sidewall of the NT. (c) HRTEM image of the shell close to a {110}-pole position, showing perfect crystal structure.

4. CONCLUSION

Structures of rolled-up InAs/GaAs and SiGe/Si nanotubes are characterized by TEM, HRTEM, and spatially-resolved EELS. It is found that the walls of the nanotubes remain mainly crystalline, and are composed of alternating crystalline and oxide-containing noncrystalline layers. In the case of InAs/GaAs RUNTs, the noncrystalline layer is Ga-oxide rich. Defects, especially SFs, form in some nanotubes, where the rolling of the bilayer involves a misorientation.

REFERENCES

Deneke C, Jin-Phillipp N Y, Loa I and Schmidt O G 2004 Appl. Phys. Lett. **84**, 4475

Golod S V, Prinz V Ya, Mashanov V I and Gutakovski A K 2001 Semicond. Sci. Technol. **16**, 181

Prinz V Ya, Seleznev V A, Gutakovsky A K, Chekhovskiy A V, Preobrazhenskii V V, Putyato M A and Gavrilova T A 2000 Physica E **6**, 829

Schmidt O G and Eberl K 2001 Nature **410**, 168

Defects and interfaces in nanoparticles

C R Perrey, J Deneen and C B Carter

Department of Chemical Engineering and Materials Science, University of Minnesota, Minneapolis, MN 55455, USA

ABSTRACT: As the dimensions of semiconductors are reduced into the nanoscale, the defects and interfaces that may be present have taken on new importance. In many cases, these nanoscale materials may have properties that are unique to their size and morphology. Using the transmission electron microscope, observations of these interfaces can shed light on the possible formation processes undergone by the nanoparticles and lead to further advances in nanoscale semiconductor manufacturing.

1. INTRODUCTION

Nanoparticles and nanoparticle-based structures have been found to exhibit unique properties. Even for materials as commonplace as silicon (Si), nanoscale materials can show surprising deviations from bulk behavior. This can yield advantages in terms of chemical, mechanical (Perrey et al 2002a, Gerberich and Mook 2003, Gerberich et al 2003), magnetic, optical, and electronic properties (Gleiter 1989). However, the extent of these deviations is a function of the nanoparticle size, structure, and morphology.

One of the major challenges to harnessing the potential of nanotechnology is the manufacturing of these nanoscale materials. An acceptable production process will require the flexibility to produce materials of varying chemistry and size in a reproducible manner. Plasma-based processes show great promise for the manufacturing of these nanoscale materials (Fauchais et al 1983, Bapat et al 2003). They allow large quantities of chemically diverse materials to be deposited on a wide range of substrates. However, plasma processes are very complex and difficult to model. Additionally, different types of plasmas can yield seemingly disparate results even for a single material, as in the case of Si (Perrey et al 2003). A fundamental understanding of the nanoparticle formation processes in such systems is necessary if plasmas are to be considered as a viable production method of nanoscale materials.

When considered in tandem, the inherently small size of the nanoparticles and the energetic environment in the plasma system prevents the direct observation of the dynamic processes involved in particle formation. Because of this, these processes are best understood by the study of the particles after they have been formed and deposited. However, this implies backing out information post formation, which is a nontrivial task. This study applies techniques of transmission electron microscopy (TEM) for the observation of the defects that have been observed in such plasma-produced nanoparticles. It also considers what such defects imply for nanoparticle formation.

2. EXPERIMENTAL

Si nanoparticles were produced using two different plasma processes. The first, hypersonic particle plasma deposition (HPPD) incorporates a thermal plasma and a rapid expansion to nucleate nanoparticles (Rao et al 1998, Neuman et al 1999, Di Fonzo et al 2000, Perrey et al 2002b). By passing the resulting particles through an aerodynamic lens assembly, a relatively monodisperse deposition can be obtained on a TEM grid. The other nanoparticle generation method uses a constricted mode silane-argon plasma with a unique filamentary discharge. This process uses a low

gas flow rate and deposits Si nanoparticles directly onto TEM grids (Bapat et al 2003, Bapat et al 2004). The nanoparticles produced were studied using a Philips CM30 TEM operating at 300 kV.

3. RESULTS

As seen in previous studies, the HPPD process produces Si nanoparticles that are predominantly spherical in appearance (Rao et al 1998, Neuman et al 1999, Di Fonzo et al 2000, Perrey et al 2002b, Perrey et al 2003). The most common defect seen in these 'nanospheres' are atomically flat twin boundaries. Figure 1 is a bright-field (BF) TEM image of such a nanoparticle; the {111} twin boundary in this particle horizontally bisects the Si nanosphere. HRTEM imaging of such boundaries showed that these twin boundaries are indeed atomically flat throughout the bulk of the particle (Perrey and Carter 2005).

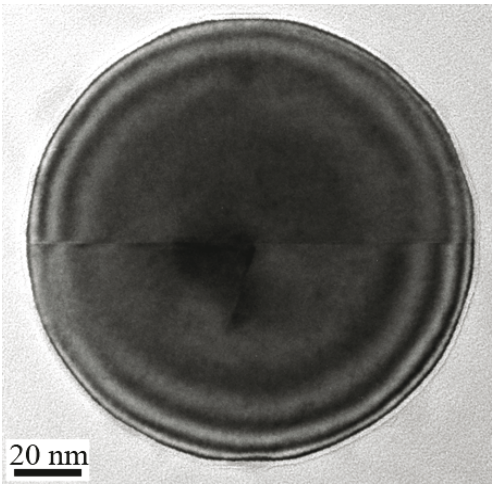


Fig. 1: Bright-field TEM image of a Si nanoparticle with a twin boundary that bisects the particle.

Other Si particles contained interfaces dramatically different than crystallographic defects. Figure 2 is a BF TEM image of a Si nanoparticle that is only partially crystalline. The left half of the nanoparticle is crystalline while the right half is amorphous. The interface between these regions is decidedly not flat, and if tilted and imaged in the TEM along different crystallographic directions, the shape of this interface was found to be convex, with the crystalline region impinging into the amorphous region (Perrey and Carter 2005). This is a crucial result as it helps determine the solidification process.

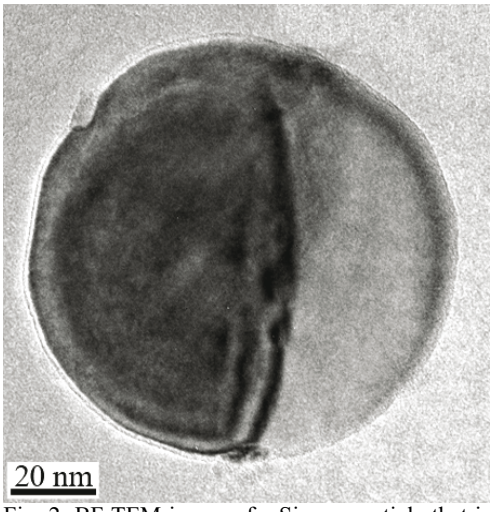


Fig. 2: BF TEM image of a Si nanoparticle that is not completely crystalline.

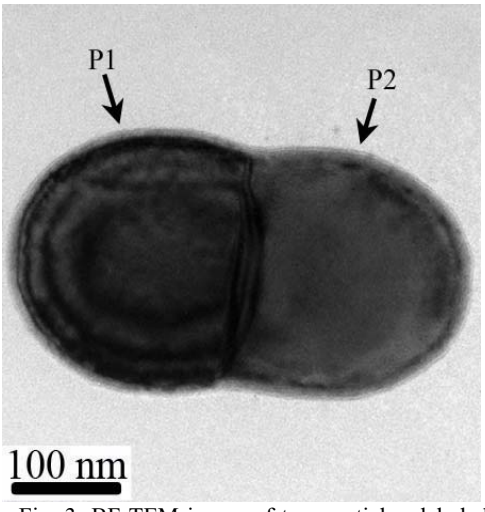


Fig. 3: BF TEM image of two particles, labeled 'P1' and 'P2' that have partially coalesced.

In some plasma processes, the interfaces observed were not only those in an individual particle. Figure 3 shows two Ti nanoparticles that have partially coalesced (sintered). In Fig. 3, these particles

are labeled as 'P1' and 'P2.' Using selected-area diffraction, the crystallographic orientation between these particles was found to be $[1\bar{2}10]_{P1}/[22\bar{4}0]_{P2}$ and $[10\bar{1}0]_{P1}/[0001]_{P2}$. The appearance of these spherical sintered particles is dramatically different from particles produced by the inductively-coupled filamentary discharge. Figure 4 shows two particles produced by this method; these particles are not spherical but instead exhibit clear crystallographically oriented faces. In this image, the particle at the top of the image is viewed along [001] and appears cubic in shape while the other particle is oriented along [111] and is triangular in shape. These particles do not appear to have sintered as the Ti particles in Fig. 3, but instead are aligned with the {001} and {111} facets facing each other.

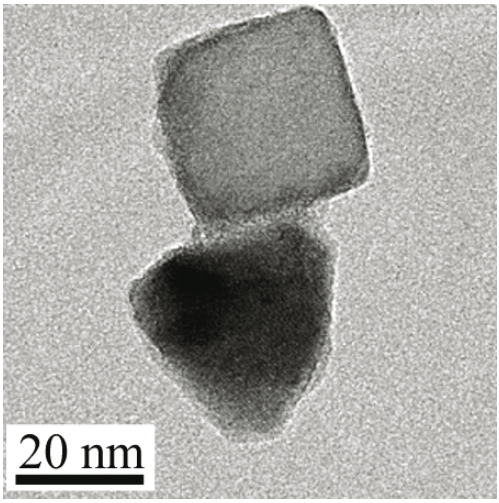


Fig. 4: BF TEM image of highly oriented Si nanoparticles that are agglomerated.

The shapes, defects, and interfaces produced by these different plasma processes provide important insight into the formation of the nanoparticles. For the HPPD process, spherical particles form that may sinter or incompletely crystallize; particles that have crystallized often contain atomically flat twin defects. Such behavior is consistent with a rapid solidification from the liquid phase from a single point on the surface of the nanoparticle (Perrey and Carter 2005). If these particles interact during this process, coalescence and sintering may occur. In contrast, the highly oriented Si particles as shown in Fig. 4 contain many facets and aligned interfaces with only evidence of agglomeration. This infers that the particles were formed in a less dynamic process and did not have the time or energy to activate sintering processes. However, the shape of these particles is indicative of a formation mechanism based on atomic condensation and annealing (Bapat et al 2004).

4. CONCLUSIONS

The defects and interfaces that are present in plasma-produced nanoparticle depositions provide unique insights into the formation and sintering process of small volumes. In this work, the HPPD process has been shown to produce spherical particles with interfaces consistent with a rapid solidification from the liquid phase. In comparison, a constricted mode argon-silane plasma yielded particles that exhibited faceting and did not sinter. The absence of sintering implies that the highly oriented crystalline particles are formed and then agglomerate in a less-energetic region of the plasma system.

ACKNOWLEDGEMENTS

This work was funded by the NSF-NIRT program through grant NSF/DMI-0103169, NSF grant CTS-9876224, and NSF NIRT grant DMI-0304211. We would also like to acknowledge our collaborators on the HPPD project (W W Gerberich, S L Girshick, J Hafiz, J V R Heberlein, P H McMurry, W M Mook, R Mukherjee, X Wang) and the constricted mode plasma project (A Bapat and U Kortshagen).

REFERENCES

Bapat A, Anderson C, Perrey C R, Carter C B, Campbell SA and Kortshagen U 2004 Plasma. Phys. Contr. Fus. **46**, 1

Bapat A, Perrey C R, Campbell S A, Carter C B and Kortshagen U 2003 J. Appl. Phys. **94**, 1969

Di Fonzo F, Gidwani A, Fan M H, Neumann D, Iordanoglou D I, Heberlein J V R, McMurry P H, Girshick S L, Tymiak N, Gerberich W W and Rao N P 2000 Appl. Phys. Lett. **77**, 910

Fauchais P, Bourdin E, Coudert J F and McPherson R (1983) Topics in current chemistry (plasma chemistry IV), ed Boschke F L (Springer, Berlin) p. 59

Gerberich W W and Mook W M 2003 Pour la Science **41**, 19

Gerberich W W, Mook W M, Perrey C R, Carter C B, Baskes M I, Mukherjee R, Gidwani A, Heberlein J V R, McMurry P H and Girshick S L 2003 J. Mech. Phys. Solids, **51**, 979

Gleiter H 1989 Prog. Mater. Sci., **33**, 223

Neuman A, Blum J, Tymiak N, Wong Z, Rao N P, Gerberich W, McMurry P H, Heberlein J V R and Girshick S L 1999 IEEE T Plasma Sci. **27**, 46

Perrey C R and Carter C B 2005 J. Mater. Sci., *submitted*

Perrey C R, Lentzen M and Carter C B 2003 Microsc. Microanal. **9**, 394

Perrey C R, Mook W M, Carter C B and Gerberich W W 2002a Mat. Res. Soc. Symp. Proc. **740** I3.13.1

Perrey C R, Thompson R, Carter C B, Gidwani A, Mukherjee R, Renault T, McMurry P H, Heberlein J V R and Girshick S L 2002b Mat. Res. Soc. Symp. Proc. **740**, I4.6.1

Rao N P, Tymiak N, Blum J, Nauman A, Lee H J, Girshick S L, McMurry P H and Heberlein J 1998 J. Aerosol Sci. **29**, 707

TEM characterization of magnetic Sm- and Co-nanocrystals in SiC

J Biskupek, U Kaiser, H Lichte[1], A Lenk[1], G Pasold[2] and W Witthuhn[2]

Electron Microscopy Group of Materials Science, University Ulm, Germany
[1] Institute of Structure Physics, Dresden University, Germany
[2] Institute of Solid State Physics, Friedrich-Schiller-University Jena, Germany

ABSTRACT: This paper presents analytical TEM characterization of magnetic Sm- and Co-nanocrystals buried in SiC. High resolution TEM has been applied to analyse the lattice structure and crystallography of the nanocrystals: Lorentz microscopy has been applied to study their magnetic properties on the nanometre scale, revealing single-domain ferromagnetic structures.

1. INTRODUCTION

The growth of magnetic nanocrystals inside a semi-conducting matrix is aimed at the development of new devices for data information storage and high sensitive magnetic sensors (Pokrant et al 1998). As properties of nanostructured materials may differ from their bulk counterparts in terms of magnetic anisotropy, magneto-resistance, Curie-temperatures and susceptibility (Shi et al 1996, Leslie-Pelecky and Rieke 1996), careful characterization on the nanometre scale is required. Theoretical studies propose ferromagnetism for transitional metal-doped SiC (Miao and Lambrecht 2003, Shapnikov and Sobolev 2004) with impurity concentrations above 3%. The integral magnetic properties of Fe-, Ni-, and Mn-implanted SiC were experimentally investigated (Theodoropoulou et al 2003) showing ferromagnetism after a maximum impurity concentration of 5% (dose 5×10^{16}cm^{-2}). However, corresponding transmission electron microscope (TEM) studies did not reveal precipitates. Nanocrystals formed after germanium and erbium ion implantation into SiC and annealing were found in earlier studies (Kaiser 2001, Schubert et al 2002, Kaiser et al 2004).

Magnetic and electrical properties of individual nanostructures can be studied by electron holography on Lorentz-microscopes after subsequent reconstruction of the phase images, which contain information about the electrical and magnetic fields (Lehmann and Lichte 2002).

Here, nanocrystals are studied that were formed after ion implantation of the rare earth element Sm and the transition metal Co into 4H-SiC that may lead to Sm-, Co- and SmCo-nanocrystals (if both elements are implanted into the same substrate).

2. EXPERIMENTAL

Nanocrystals within 4H-SiC were created by high-dose ion implantation. TRIM calculations (Biersack and Ziegler 1996) were used to determine the ion energy necessary for maximum content location of foreign atoms in a depth of around 100 nm. The 4H-SiC crystal was tilted by 6° to 8° away from the zone-axis orientation to avoid channelling. 10^{17}cm^{-2} 200 keV Co^+ ions, 10^{16}cm^{-2} 400 keV Sm^+ ions respectively, 2×10^{15} cm^{-2} 400 keV Sm ions and 8×10^{15} cm^{-2} 200 keV Co ions have been implanted into 4H-SiC. All ion implantation experiments were carried out at high temperatures (700°C) followed by rapid thermal annealing for 120 seconds at 1600°C under a protective gas atmosphere at 200 mbar. (For more details on the implantation procedures see (Schubert et al 2003)).

Thin cross-sectional TEM sample were prepared using standard techniques including mechanical polishing, dimpling and argon ion etching.

Conventional-, z-contrast- (high angle annular darkfield (HAADF)) and high-resolution

transmission electron microscopy (HRTEM) was performed using a JEOL JEM 3010 TEM operating at 300kV. Electron holography used a Philips CM200 FEG microscope operating at 200 kV equipped with a field emission gun, a Möllenstedt biprism and a Lorentz-lens operating in Lorentz-mode (objective lens switched off, Lorentz-lens active). Phase reconstruction of holograms has been realized with the HoloWorks Package for Gatan Digital Micrograph (Voekl et al 1995). HRTEM image calculation has been carried out using the program Musli (Chuvilin and Kaiser 2005).

3. RESULTS

Figure 1 shows nanocrystals after Sm- (Fig. 1a), SmCo- (Fig 1b) and Co- (Fig 1c) ion implantation within 4H-SiC revealed by their z-contrast. The higher implantation dose ($10^{17}cm^{-2}$) for the case of Co leads to larger average sizes of the nanocrystals (Fig. 1c), compared to the lower dose experiments ($10^{16}cm^{-2}$) used for the Sm and SmCo implantations (Fig. 1a,b).

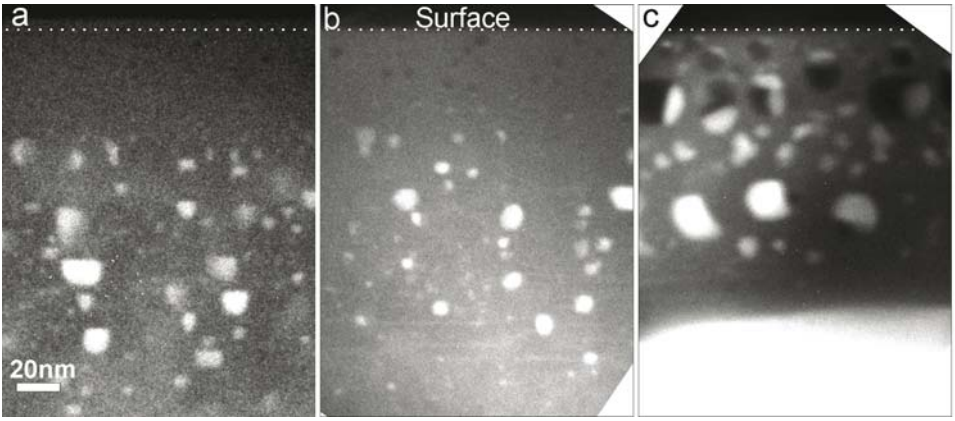


Fig. 1. Nanocrystals within 4H-SiC. (a) Sm-implantation, (b) Sm and Co co-implantation, (c) Co-implantation.

HRTEM image- and FFT-pattern analysis (Biskupek and Kaiser 2004) revealed that the nanocrystals appear in separate phases as $SmSi_2$-, Co_2Si- and $SmSi_2$- and Co-nanocrystals. An example of experimental and calculated HRTEM images for the case of facetted Co_2Si-nanocrystals is shown in Fig. 2.

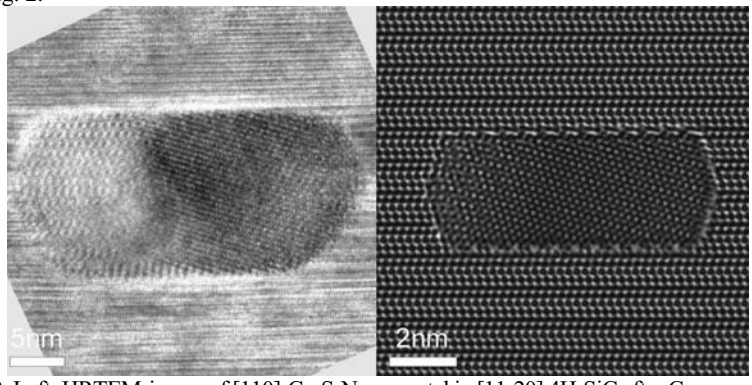


Fig. 2. Left: HRTEM-image of [110]-Co_2S-Nanocrystal in [11-20] 4H-SiC after Co-implantation and annealing. Right: Calculated model of the embedded Co_2Si-Nanocrystal in (a).

Magnetic parameters of individual nanocrystals seen in Fig. 3a were obtained by using electron holograms and subsequent phase reconstruction of the electron wave. To investigate the magnetization in a

TEM, the environment of the object has to be free from strong magnetic lens fields, consequently, the objective lens has to be switched off and instead, the so-called Lorentz-lens has to be used. Holograms of the Co-particles were taken in "Lorentz-mode". The reconstructed phase images reveal magnetic dipoles in nanocrystals created in a sample depth of about 80 nm to 100 nm (Fig. 3b). The fields of the magnetic dipoles are randomly oriented (Fig. 3c). The comparison between the brightfield image (Fig. 3a) and the phase image (Fig 3c) shows that the magnetic dipoles stem from nanocrystals. It also shows that the near-surface defects, as voids, (Gorelik et al. 2002, Biskupek et al. 2005) are electrically active (see Fig 3b area marked 5 and 3c (5)).

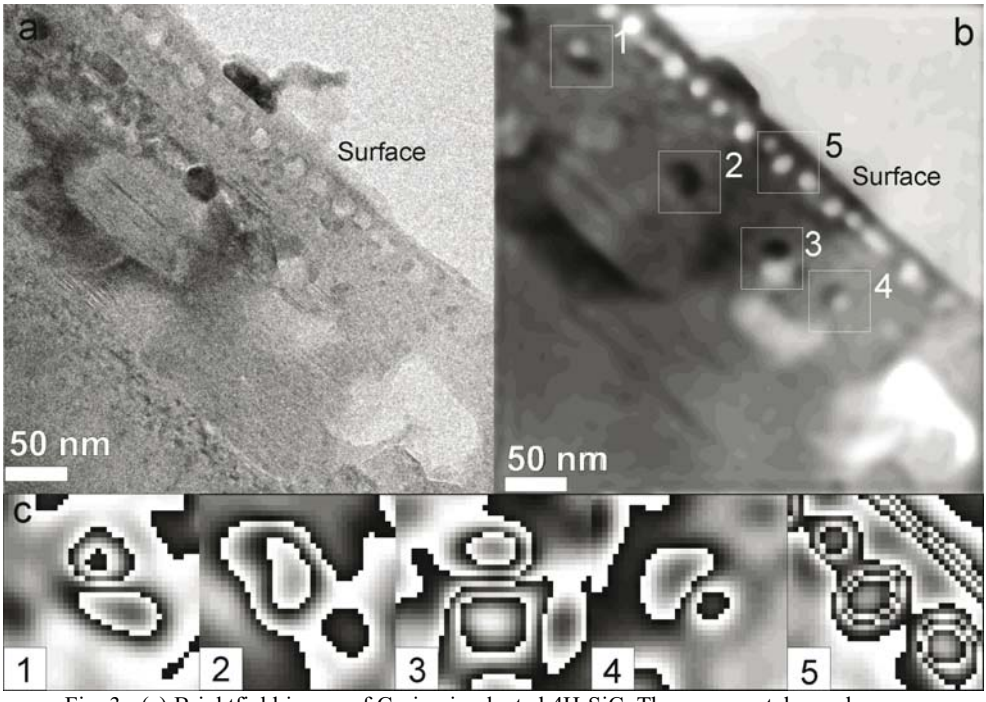


Fig. 3. (a) Brightfield image of Co-ion implanted 4H-SiC. The nanocrystals can be seen by their dark absorption contrast. (b) Phase image of the electron wave from the same sample region as shown in (a). Magnetic dipoles (c) are marked with boxes 1-4, electrically active regions caused by matrix defects near the surface are shown in 5.

The calculated electron phase, based on the interaction of electrons and a magnetic particle within the matrix, is shown in Fig. 4a. It can be clearly seen that the calculated phase fits reasonably well to the experimental measurements shown in Fig 4b. The phase shifts show the asymmetric behaviour expected from magnetic dipoles. The magnetization M and the magnetic flux Φ can be calculated using equation 1 when measuring the absolute phase shift φ_{mag} and the area A around the magnetic flux (Voekl et al 1995). The absolute phase shift reaches more than $\pi/2$, which corresponds to magnetization values of 2 Tesla.

$$\varphi_{mag} = 2\pi \frac{e}{h}\Phi \;; \Phi = \mathrm{MA} \qquad \text{Equation 1}$$

4. CONCLUSION

HRTEM investigations and image calculations verified the existence of Co-rich (Co_2Si) and Sm-rich ($SmSi_2$) nanocrystals within the SiC matrix even after lower dose ion implantation ($10^{16}cm^{-2}$). Magnetic dipoles in nanocrystals formed within SiC after $10^{17}cm^{-2}$ Co implantation and subsequent annealing could be revealed in a sample depth of 80nm-100nm using electron holography and subsequent phase reconstruction.

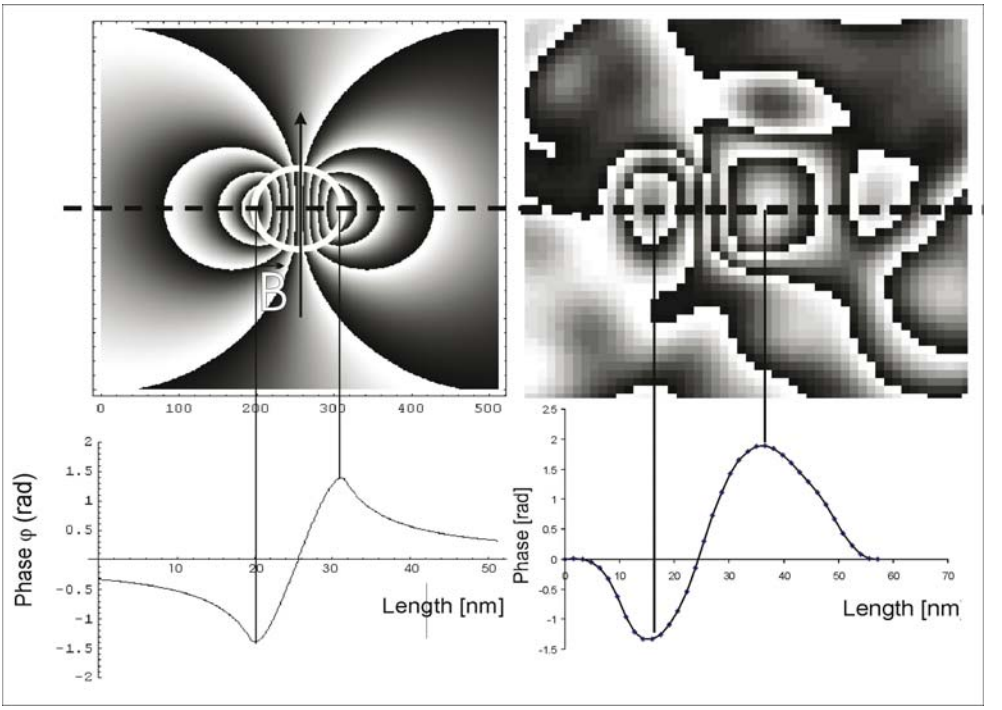


Fig. 4. (a) Calculated phase shifts of the electron wave caused by magnetic field within a crystalline matrix. (b) Experimentally measured phase shift of dipole 3 shown in Fig 3.

ACKNOWLEDGEMENT

We are grateful to G Lenk for ion implantation.

REFERENCES

Biersack J P and Ziegler J F 1996 The stopping and ranges of ions in matter. Vol. 1 (Berlin, Pergamon Press)

Biskupek J and Kaiser U 2004 J. Electron Microscopy **53**, 601

Biskupek J, Kaiser U, Lichte H, Lenk A, Gemming T, Pasold G and Witthuhn W 2005, J. Magnetism Magnetic Materials, *in print*

Chuvilin A and Kaiser U 2005 Ultramicroscopy *accepted*

Gorelik T, Kaiser U, Schubert Ch, Wesch W and Glatzel U 2002 J. Mater. Res. **17**, 479-486

Kaiser U 2001, J. Electron Microscopy **50**, 251

Kaiser U, Muller D A, Chuvilin A, Pasold G and Witthuhn W 2004 Microsc. Microanalysis **10**, 1

Lehmann M and Lichte H 2002 Microsc. Microanalysis **8**, 447

Leslie-Pelecky D L and Rieke R D 1996 Chem. Materials **8,** 177

Miao M S and Lambrecht W R L 2003 Phys Rev B **68**, 125204

Pokrant S, Herwig C, Hihara T, and Becker J A 1996 Eur. Phys. J. **D 9**, 509

Schubert C, Kaiser U, Gorelik T, Hedler A, Kräußlich J, Wunderlich B, Heß G, Goetz K, Glatzel U and Wesch W 2002 J. Appl. Phys. **91**, 1520

Shaposhnikov V L and Sobolev N A 2004 J. Phys.: Condens. Matter **16**, 1

Shi J, Gider S, Babcock K and Awschalom D D 1996 Metal and Semiconductor Science **271**, 937

Theodoropoulou N, Hebard A F, Chu S N G, Overberg M E, Abernathy C R, Pearton S J, Wilson R G, Zavada J M and Park Y D 2002 J. Vac. Sci. Technol. **A 20**, 579

Voelkl E, Allard L F and Frost B 1995 J. Microsc. **180,** 39

Microscopy of nanoparticles for semiconductor devices

J Deneen, C R Perrey, Y Ding[1], A Bapat[2], S A Campbell[1], U Kortshagen[2] and C B Carter

Department of Chemical Engineering and Materials Science; University of Minnesota, Minneapolis, MN 55455, USA
[1] Department of Electrical and Computer Engineering; University of Minnesota, Minneapolis, MN 55455, USA
[2] Department of Mechanical Engineering; University of Minnesota, Minneapolis, MN 55455, USA

ABSTRACT: The miniaturization of semiconductor devices brings the impending need for nanoscale components for which nanoparticles of semiconductor materials are uniquely suited. However, their small length scales are known to produce properties unique from those of their bulk form. Full characterization of the nanoparticles suggested for use in devices becomes imperative. This study investigates silicon nanocubes prepared by a constricted-mode capacitive silane-argon plasma. These cubes have been proposed as key components in nanoscale transistors. Various techniques are used to examine these particles and their implementation in a potential device is explored.

1. INTRODUCTION

The impending end of conventional, top-down integrated circuits has incited a great interest in nanoparticle devices. While many groups, such as Gleiter (1989), Takagi et al (1990) and Esaki (1999), have investigated the optical and electrical properties of nanoparticles and other groups, including Butté et al (1999 and 2000), have studied the use of nanoparticles in thin films, relatively few have explored integrating nanoparticles into electronic devices. The fabrication of nanoparticle devices involves several fundamental challenges. The reliable production of nanoparticles of known size and chemistry with low defect density is imperative. The transmission electron microscope (TEM) is an invaluable characterization tool for investigating the structure and chemistry of the nanoparticles and the interfaces involved in their implementation in a device. The current study explores silicon nanocubes and their incorporation into nanoscale transistors.

2. EXPERIMENTAL

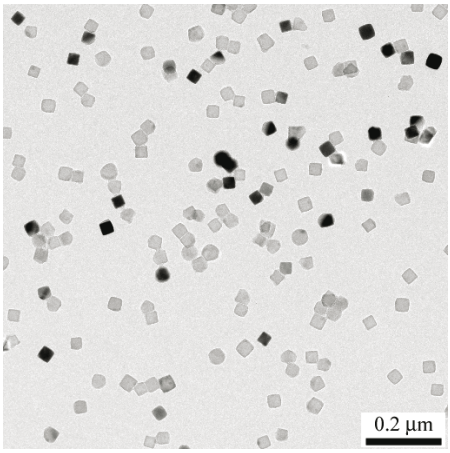
Nanoparticles of silicon are created using a constricted-mode capacitive silane-argon plasma as described in a paper by Bapat et al (2004). This process uses a low gas flow rate and deposits particles on the desired substrate. This study looks at cubes deposited on amorphous TEM support films and those in a device structure, described in more detail is section 3.2. The TEM investigation utilized the Philips CM30, an FEI F30 FEG-TEM, and a Philips CM20.

3. RESULTS

3.1 Silicon Nanocubes

The silicon nanocubes are highly faceted with (100) faces and a low defect density. An overview of the cubes is shown in Fig. 1. Not every cube is in perfect alignment with the beam, and as a consequence only some of the cubes are strongly diffracting. The cube shape can be seen

more clearly in Fig. 2, which shows a single nanocube. The particles are highly monodisperse with an edge length of about 40 nm. During deposition the cubes typically land on the (100) faces and there is no significant particle agglomeration. While some small clusters can be found, they are typically on the order of 3-5 particles. However, the devices proposed in this paper rely on single particles and clustered particles are undesirable. This naturally leads to the question of when this clustering occurs.



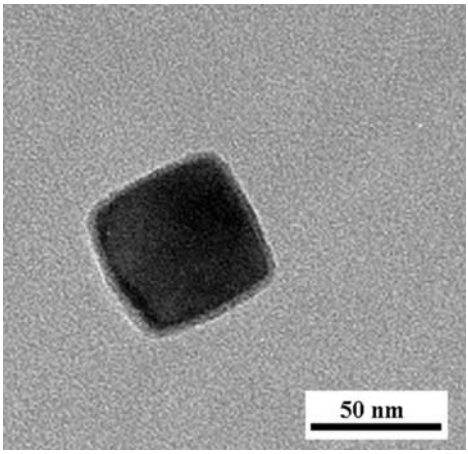
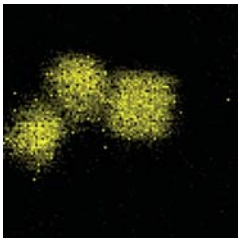
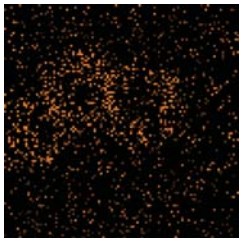


Fig. 1 (left): Bright field image of the silicon nanocubes illustrating the monodisperse deposition.

Fig. 2 (right): Bright field image of a single nanocube.

Previously described by Perry et al (2003), C_S-corrected imaging was used to investigate the surface of the nanocubes. A thin amorphous layer on the order of a few nanometers was found on the surface of the cubes. As shown in Fig. 3, further analytical TEM determined this to be an oxide which was present both on the particle surfaces and between particles in small clusters. This verifies that the amorphous layer was formed after exposure to air and suggests that the clustering also occurs after removal from the plasma system. This is highly desirable for device production. For the depositions shown, the particles were caught using an amorphous carbon support film. When integrated in a device the particles would land on a metal or metal-silicide surface and should bond rather than be free to migrate after removal from the plasma system.





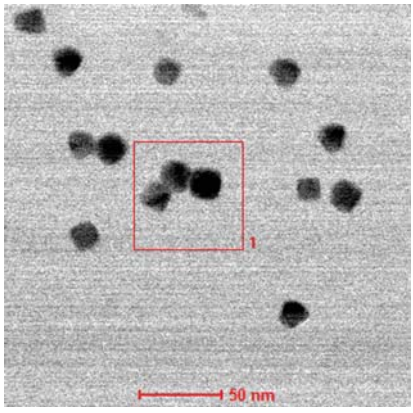


Fig. 3: STEM image (right) of nanocubes with the box denoting the area mapped in the images above. The silicon map is shown above, left; the oxygen map is shown above, right.

3.2 Nanocube Devices

The silicon nanocubes are proposed as an integral component in a nanoscale transistor. The fabrication process involves a series of depositions, planarizations and etchings. First a silicon wafer is prepared using a tradition RCA cleaning. A layer of platinum is sputter deposited on the surface and the nanocubes are then deposited on the Pt source layer. This is followed by the deposition of the gate oxide to a thickness greater than that of the particle, followed by a planarization step and subsequent etching to a thickness about one third of that of the particle. The gate and second oxide are deposited similarly, followed by the drain metal. A schematic of the fabrication process is shown in Fig. 4. Finally, this is made into a cross-section TEM sample using traditional dimpling and ion-milling techniques.

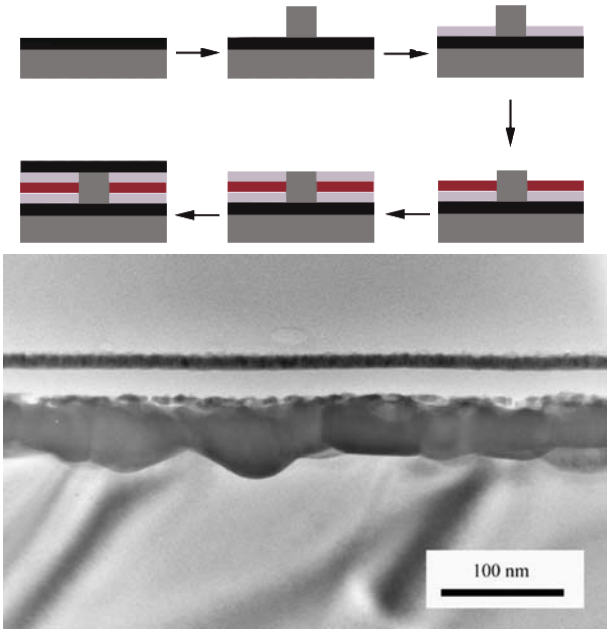


Fig. 4 (top): Schematic of the device fabrication method. The layers surrounding the particle are made by an over-deposition followed by planarization and etching.

Fig. 5 (bottom): Bright field image of a cross section of the the transistor sample. No nanocubes are in this area.

An initial effort at making a transistor sample revealed some preliminary processing problems. In order to work through the processing steps systematically, the first "device" attempted did not include all of the steps described above. Rather, it was only fabricated up to and including the gate metal as shown in Fig. 5 and 6.

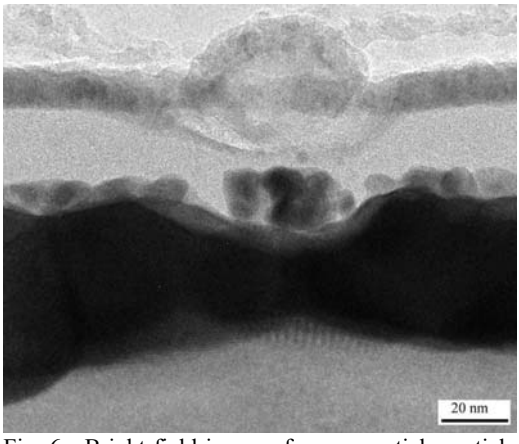


Fig. 6: Bright field image of a nanoparticle particle cross section. The amorphous layer above the gate is the glue line.

It should be noted that the Pt/Si interface is typically relatively rough since this reaction is driven as far to completion as possible to prevent the nanocubes from being consumed by a silicide upon deposition. However, the Pt/SiO_2 interface is quite rough although AFM imaging prior to particle deposition confirmed that the as-deposited Pt layer was quite smooth. In this sample the gate oxide was SiO_2, which requires a 500 °C processing step. It is likely that the high processing temperature caused grain growth in the Pt layer resulting in a layer of large grains covered by a layer of small, rather uneven grains.

Figure 6 shows a cross-section of a nanoparticle which fully illustrates the detrimental grain growth of the Pt layer. The nanoparticle, instead of being in contact with the Pt layer, is "floating" in the oxide. Both high resolution imaging and EDS have

proven that this is a silicon particle. The rough surface produced by the grain growth is detrimental to the device production because the cubes cannot maintain contact with the Pt surface. Also, the oxide layer can easily penetrate the small grains of the source. Furthermore, the processing may have caused the distorted shape of the silicon particle.

An effort to eliminate the layer of small grains was made by changing the gate oxide to HfO_2, which requires a much lower processing temperature. Figure 7 illustrates the success of this method. The Pt layer is composed only of large, flat grains.

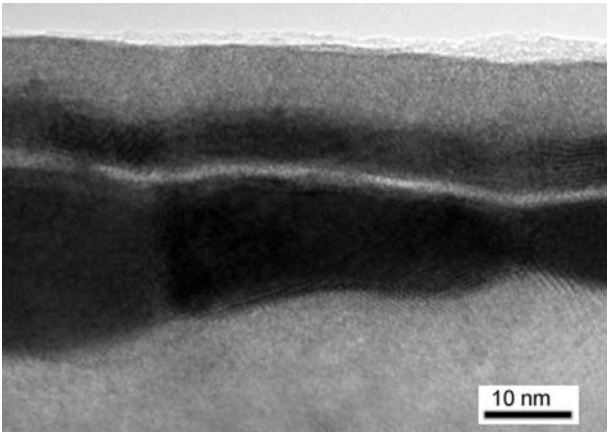


Fig. 7: Bright field image showing the layer cross section. Note that the gate oxide is thinner than in the previous sample (only a few nanometers). In this case a layer of SiO_2 has been deposited on top of the gate metal.

4. CONCLUSIONS

The nanocube particles presented show great promise for use in nanoscale transistors. Their highly faceted cube-shaped structure and low defect density make them idea candidates. While some particle clustering is observed it has been shown that this most likely occurs after removal from vacuum. The particles seem to maintain their deposition chemistry after interaction with the source metal. Initial attempts at incorporating these particles into a device have had some problems which have been quickly solved: future studies are promising.

ACKNOWLEDGEMENTS

This work was funded by the NSF under grant number NSF-DMI-0304211. JD and CBC gratefully acknowledge support from the 3M Heltzer Endowed Chair. The authors would also like to thank Dr. Martina Luysberg, Research Center Jülich, for many helpful discussions. In addition, we are ever indebted to Nicole Munoz for her help with sample preparation.

REFERENCES

Bapat A, Anderson C, Perrey C R, Carter C B, Campbell S A and Kortshagen U 2004 Plasma Phys. Control. Fusion **46**, B97

Butté R, Meaudre R, Meaudre M, Vignoli S, Longeaud C, Kleider J P and Roca i Cabarrocas P 1999 Phil. Mag. B **79**, 1079

Butté R, Vignoli S, Meaudre M, Meaudre R, Marty O, Saviot L and Roca i Cabarrocas P 2000 J. Non-Cryst. Sol. **266-269**, 263

Esaki L 1999 NanoStructured Materials **12**, 1

Gleiter H 1989 Prog. Mater. Sci. **33**, 223

Murphy C J and Coffer J L 2002 Applied Spectroscopy **56**, 16A

Perrey C R, Carter C B, Bentley J and Lentzen M 2003 Micros. Microanal. **9**(Suppl. 2), 412

Takagi H, Ogawa H, Yamazaki Y, Ishizaki A and Nakagiri T 1990 Appl. Phys. Lett. **56**(24), 2379

Structural and electrophysical properties of a nanocomposite based upon the Si-SiO_2 system

L M Sorokin, V I Sokolov, A E Kalmykov and L V Grigoryev[1]

Ioffe Physico-technical Institute, St.- Petersburg, Russia
[1] Physical Research Institute, St.- Petersburg University, St.- Petersburg, Russia

ABSTRACT: By conventional TEM it was shown that the nanocomposite fabricated on the basis of an oxidized porous silicon layer consisted of silicon oxide with crystalline silicon inclusions of two kinds connected with each other: rounded particles with sizes in a range 5-30 nm and continuous 3D network of nanowires with thicknesses of about several nanometers. The current-voltage characteristics (CVC) of the nanocomposite were measured for different modes of charge carrier excitation. The densities of thermally- and photo-activated traps and the effective mobility of charge carriers were estimated.

1. INTRODUCTION

Recently silicon nanocomposites have been intensively investigated. It was shown that there is a noticeable photoluminescence in the visible region at the room temperature because of quantum confinement (Das and McGinnis 1999, Schmidt at al 1992, Bisi at al 2000, Wu at al 2000, Ballucani at al 1999, Stewart at al 2000, Dimova-Malinovska 1999). The porous silicon being a nanostructured material is already used for manufacturing of optoelectronic elements (Das and McGinnis 1999, Balagurov at al 2000, Cullis at al 1997). Current oscillation observed in thermooxidized porous silicon (Ablova et al 2003) indicates the presence of nanocrystals. However there are not enough full structure data in the above papers to provide evidence of nanocrystal formation. That is why the aim of the present work is to obtain structural data of the Si:SiO_2 nanocomposite by transmission electron microscopy (TEM) and to investigate the current transport mechanism.

2. EXPERIMENTAL

Porous samples used for experiments were prepared from (100) silicon (B-doped, ρ~10Ωcm) wafers of 350μm thickness. The anodic etching was performed at a constant current density of 300 mA/cm^2 for 5 minutes in the horizontal cell (Fig.1), the HF concentration being 30%. After etching the samples were washed in a stream of distilled water and then they were oxidized at 1223K in steam. The time of oxidation was varied so that, in the grown SiO_2 film, inclusions of silicon nanoparticles were formed. The oxide thickness was about 0.15 μm. To measure the voltage-current characteristics of nanocomposite samples a standard technique was utilized.

The nanocomposite structure has been investigated using an EM-200 electron microscope operated at 100kV. Thinning down to a thickness transparent for electrons with E=100 keV energy was carried out using a chemical-dynamic technique, in a CP-8 solution, from the opposite side to the porous layer up to formation of a window in the centre of the silicon part of sample, with preservation of a SiO_2 layer. If the oxide layer turned out to be too thick, the sample was subjected to Ar+ ion milling (I = 4-6 μA, U = 5 kV) from the upper side of the oxide layer.

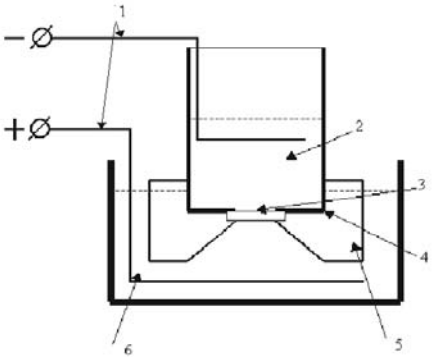


Fig. 1. Anodic etching cell.
1 – electrodes
2 – 30% HF solution
3 – sample
4 – Teflon bowl
5 – Teflon screw
6 – bath with electrolyte

3. RESULTS

3.1 The Nanocomposite Structure.

The structure of the sample after oxidation is presented in Fig.2. For this sample, ion milling was deliberately not performed so as to save the integrity of the composite upper layer which is responsible for the electrophysical properties of the nanocomposite. The corresponding electron microdiffraction pattern shows a diffuse halo and very weak spot reflections caused by residual silicon layer. So the sample region under study consists mainly of oxide. In corresponding images individual dark rounded particles can be seen. Their size is in the range of 5-30nm. Some of them are surrounded with a light contrast aureole. The inclination of a sample in the microscope down to 30° has not revealed the elongated form of these particles that should be expected, if the porous layer represented a columnar structure. The dark particles are situated in an unclear cellular structure. Their estimated density is found to be more than ~10^9 cm^{-2}. After ion milling with the oxide side of the sample, the electron microdiffraction pattern shows a weakened halo and strong silicon reflections belonging to the (100) initial orientation of the silicon sample (Fig.3). On the basis of this result it is possible to conclude that after electrochemical etching the near surface layer of the sample retains the structure of the single crystal silicon. Some arc-like reflections (marked with arrows) indicate the small

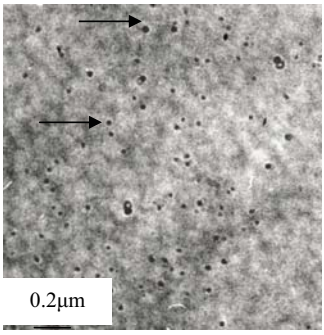


Fig.2. Structure of near-surface area sample. Arrows mark nanoparticles.

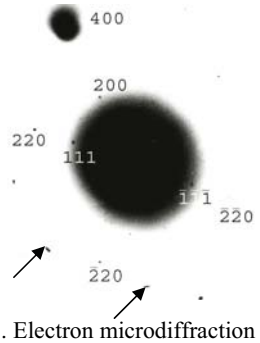


Fig.3. Electron microdiffraction pattern of sample area.

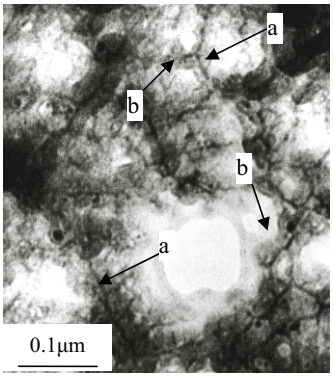


Fig.4. Si- nanowires (a-arrows) coated with silicon oxide (b-arrows).

disorientation of the adjacent silicon particles. Comparison of the dark field image taken for a (111) silicon reflection (Fig. 3), with the bright field image allows us to conclude that all dark contrast particles seen in Fig. 2 represent nanoparticles of the near surface layer of the sample. As to the light contrast aureole around the dark contrast particles in the bright field image, it can be caused by their oxidation because the amorphous oxide gives rise to weaker contrast in bright field image as compared with contrast of the crystalline particle at the reflection position.

At a large magnification, the cellular structure looks like a network formed by dark contrast thin (~5 nm) strings (Fig. 4). The strings, in turn, are surrounded with a "coat". Taking into account that the microphotograph is produced using the diffraction contrast mode, it is possible to conclude that the dark strings represent silicon nanowires coated with silicon oxide. The wires are non-uniform in thickness. In some places they represent a sequence of closely located fine particles separated from each other.

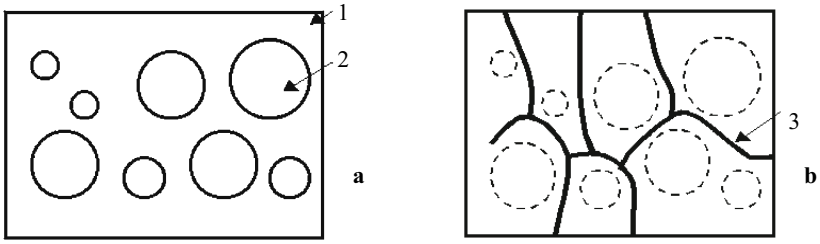


Fig. 5. Model of process of formation nanocomposite, a – silicon wafer after etching, b – silicon wafer after oxidation; 1 – porous silicon wafer, 2 – pores, 3 – silicon wire.

In Fig. 5 the model of the process of formation of a nanocomposite is schematically drawn. As a result of etching pores are formed, whose walls are thinned during oxidation until the formation of a silicon network structure. After electrochemical etching, walls between pores have various thicknesses. This has resulted in various thicknesses of silicon wires (Fig.2) being formed after oxidation of a porous layer. Evidently, separately located large particles (~30 nm) are the thickest sites of regions between pores, which are not oxidized completely.

3.2 Current Transport Properties.

For investigation of the transport characteristics of the nanocomposite, the CVC measurements were carried out at various excitation modes of charge carriers, with the following estimations of carrier mobility value and density of traps. Electrons injected from electrodes and photo stimulated from traps are the source of non-equilibrium charged carriers in a thermo oxidized porous silicon layer. As shown in this work, the average size of silicon nanoparticles is about ten nanometers. Then, the value of the maximum strength of an electrical field E_m on the surface of a silicon nanoparticles, for the case of a non-uniform dielectric containing conductive spherical nanoinclusions, can be estimated by the following relation (Skanavi 1958):

$$E_m=<E>/0.63 \quad (1)$$

Hence, the value of the electrical field E_m on the surface of a silicon nanoparticle located inside the dielectric matrix does not exceed 320kV/cm. The height of a Si-SiO_2 barrier for electrons due to photoemission measurements and of CVC for injection (Deal at al 1966, Goodman 1966) is more than 2.7eV. That allows us to exclude tunneling emission through a triangular barrier (because of the low value of E_m) and charge transfer over a potential barrier (because of the presence of a high barrier on the Si-SiO_2 interface and the absence of an irradiation impact by short-wave irradiation) out of consideration for the current transport mechanisms in the dielectric of the nanocomposite. The transport of charge carriers in weak electrical fields can occur by means of a system of located states distributed in the forbidden gap of the dielectric (Hill 1971). Then, it is possible to admit that the charge carrier transport in the nanocomposite layer occurs by means of the hopping mechanism (Baraban at al 1985, Korzo 1977).

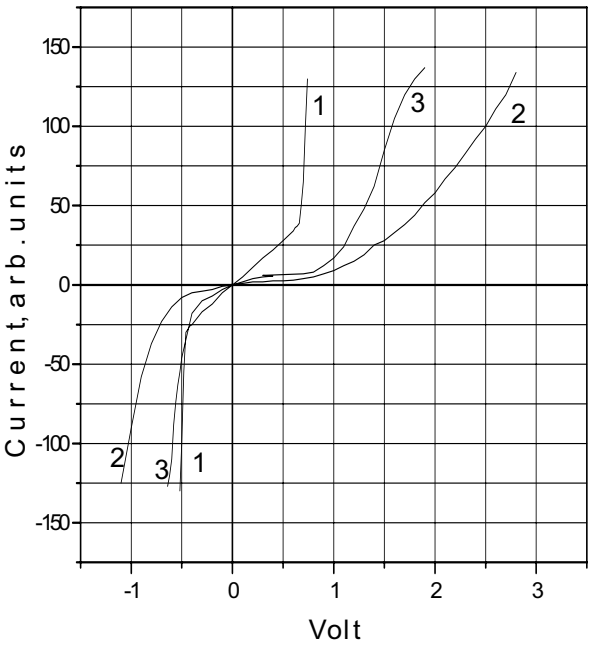


Fig. 6. Current-voltage characteristics of the nanocomposite curve 1 - the sample understudy is at room temperature and is irradiated by light of the maximal energy of quantum not exceeding 1.8eV; curve 2 – the sample is at room temperature without impact by light irradiation; curve 3 – the sample is in darkness and at 100K, then irradiated by light of the same quantum energy as for curve 1.

In Fig. 6, a CVC series, measured for various modes of nanocomposite excitation, is presented: 1 - the sample is at room temperature and irradiated by light of the quantum maximum energy not exceeding 1.8eV; 2 – the sample is at room temperature without irradiation by light; 3 – the sample is in darkness and at 100K, then irradiated by light of the same quantum energy as for curve 1. For the estimation of density of shallow thermo activated and photo stimulated traps, let us to consider CVC (1). In general there are thermo activated charge carriers with concentration n_0 and non-equilibrium carriers with concentration n_t in the nanocomposite. A possible source of charge carriers with concentration n_0 can be groups of shallow traps thermo activated at room temperatures, which are located in the near surface area of the silicon nanoparticles. At room temperature, the deep traps are filled and do not participate in transport of charge carriers. At the voltage U_0 over +0.68V, a drastic increase of current is observed. This can be explained by considering that the injected charge prevails over the charge caught on traps. Using the following relation (Korzo 1977, Lampert 1970), the density n_t of shallow thermo activated traps can be estimated:

$$n_t = n_0 = 2.21 \times 10^{20} \cdot U_0 \qquad (2)$$

where U_0 is the voltage of transition in the CVC from Ohm's law to a sharp increase of current. According to (2), the calculated density of traps is equal $1.5 \times 10^{20} cm^{-3}$. The value of effective mobility of charge carriers in the nanocomposite at the voltage U_0 can be estimated using the following formula (Korzo 1977, Lampert 1970):

$$\mu_{eff} = (8 \cdot I \cdot L^3)/(9 \cdot \varepsilon \cdot \varepsilon_0 \cdot U) \qquad (3)$$

where - ε - a relative dielectric permeability of SiO_2, $U=U_0$, L - thickness of a dielectric layer, I - value of the current at the voltage $U=U_0$. In this case, the effective mobility is 0.45×10^{-15} $cm^2/V \cdot s$. Similar analysis of the CVC(1) branch for a negative potential applied to the sample gives rise to almost the same values for n_t and n_t. It allows us to suppose the identical mechanism of carrier transport in both cases. As to the density of traps in the thermal silicon dioxide layer, it is in a range of 10^{19}-10^{21} cm^{-3}. In the absence of light, (CVC(2)) the processes of photo activation of traps can be neglected. Non-equilibrium charge carriers n_t are injected only from an electrode. As is seen, the other current dependence in comparison with CVC(1) proves the presence of a distribution of activated traps. That means another approach to an estimation of the density of traps is necessary in this case. Namely, the model should be used of a normal distribution (Gauss) of electrically active defects of an activation energy near to the middle of the forbidden gap of the dielectric (Baraban 1985, Korzo 1977). In this case for estimation of n_t the following formula should be used (Lampert 1970):

$$n_t=1.84x10^{20}\cdot U_1 \qquad (4)$$

where - U_1- the voltage of the CVC transition from the linear dependence to the power law case. The calculation of the n_t value gives $0.94x10^{20}$ cm^{-3}. The μ_{eff} value calculated from (3) is equal to $0.45x10^{-16}$ $cm^2/V\cdot s$. One can note that the μ_{eff} value for CVC(2) is almost an order less than for CVC(1). This can be explained on the basis of the model of hopping conductivity (Hill 1971, Korzo 1977) when the localized states are situated at various distances from each other and have various energies of activation.

In the case of CVC (3) all the shallow thermally activated traps "are frozen" and do not introduce a contribution to processes of carrier transport. As is seen, the positive CVC(3) branch is complicated. In this respect, for estimation of trap density and effective mobility of charge carriers the CVC(3) negative branch should be considered. It consists of two parts: linear region and power dependence $I \approx U^{3.4}$. The voltage U_1 is equal 0.32V. The concentration n_t, in this case, calculated from (4) is equal $0.58x10^{20}$ cm^{-3}. The effective mobility of the charge carriers μ_{eff} calculated from (3) is equal $1.6x10^{-16}$ $cm^2/V\cdot s$. Thus, the carrier transport mechanisms are similar to those considered earlier for negative branches of CVC (curves 1 and 2 in Fig. 6).

For control of reliability, for an estimation of effective mobility of charge carriers, measurements of current relaxation were carried out for the nanocomposite after a voltage jump of 1V

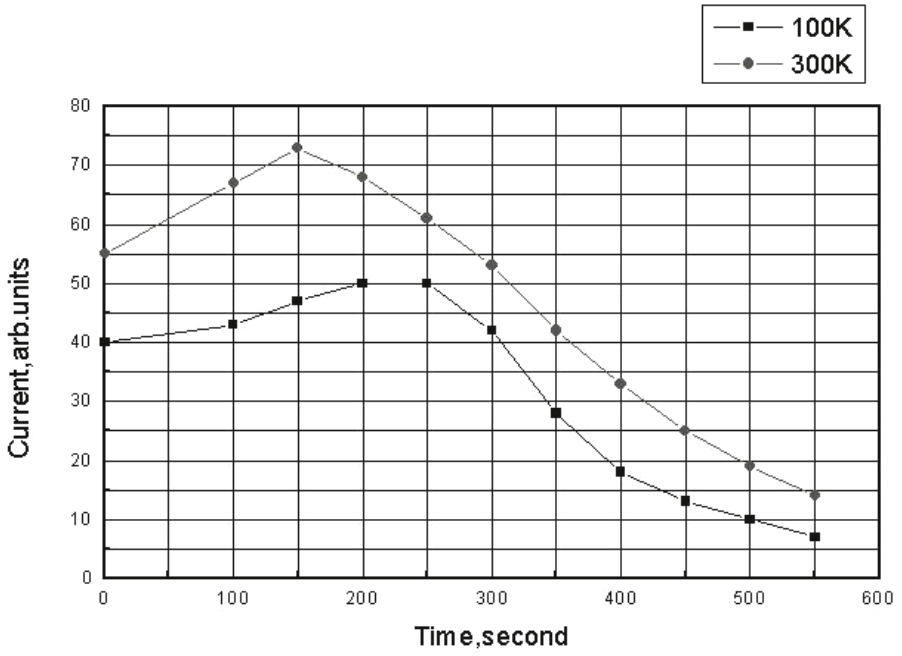


Fig. 7. Transitive currents in thermally oxidized porous silicon.

was applied to the sample at 100 and 300K. The typical dependence of the current relaxation on time is shown in a Fig. 7. The relaxation time is connected to the establishment of dynamic balance between free traps and those filled by charge carriers. This time depends on the mobility of carriers, the thickness of the nanocomposite layer, the value of the impulse of the applied voltage and the number of defects in this layer. The presence of maxima on the relaxation current curves testifies to the slow response of the process of deliverance of carriers from traps. According to Lampert (1974), it is possible to estimate the size of the effective mobility of charge carriers using the following formula:

$$\mu=0.786\cdot L2/(U\cdot t) \qquad (5)$$

For a thickness of the nanocomposite layer L=0.15μ, U=1V and t, according to maximum in a Fig. 7, we obtain $\mu= 1.2\cdot10^{-16}$ $cm^2/V\cdot s$ and $0.75\cdot10^{-16}$ $cm^2/V\cdot s$, accordingly, for temperatures of 300K and

100K. The comparison of these values of effective mobility of a charge with values of μ, calculated on stationary CVC, shows that they coincide in order of magnitude. That is why it is possible to conclude that, in both experiments, the same mechanism of current conduction is realized.

4. CONCLUSION

As is shown, a Si-SiO_2 nanocomposite can be fabricated by oxidation of porous silicon. The nanocomposite consists of silicon oxide with silicon inclusions constituting nanoparticles and continuous 3D networks of nanowires. The density of the thermally activated traps in the volume of the nanocomposite is found to be ~ 0.94×10^{20} cm^{-3}. The value of μ_{eff} is equal 0.45×10^{-16} $cm^2/V \cdot s$. In comparison with the known data for μ_{eff} this value calculated from the present experiment is essentially smaller. This discrepancy could be caused by the strong capture of the charge carriers on the traps and the long residence time on the capture defects located in the large area Si:SiO_2 interface. The density of the traps activated by light illumination amounts to not less than 0.58×10^{20} cm^{-3}. The value of μ_{eff} in this case is equal 1.6×10^{-16} $cm^2/V \cdot s$. Thus, varying modes of charge carrier excitation allow us to separate the contributions of both types of trap (thermally and photo activated) to current transport. Revealing the presence of strong capture on traps and the effect of photosensitivity in the visible spectral range, allows us to consider the nanocomposite as a prospective material for applications in functional devices for microelectronics.

ACKNOWLEDGEMENTS

The work was partly supported by the Grant on the fundamental investigations program of the RAS.

REFERENCES

Ablova M S, Zamoryanskaya M V, Khasanov R I and Sokolov V I 2003 Techn. Phys. Lett. **29**, 459
Balagurov L A, Bauliss S C, Orlov A F, Unal B and Yarkin D G 2000 Abstr. Int. Conf. On Porous Semiconductors – Science and Technology, (Madrid, Spain) p 53
Ballucani M, Bondarenro V, Lamedica G, Yakovleva V A and Ferrari A 1999 Appl. Phys. Lett. **74** 1960
Baraban A P, Konorov P P, and Kruchinin A A 1985 Optoelectronics and Semiconductor Technique **N7** 54 (in Russian)
Bisi O, Ossicicni S and Paveci L 2000 Surf. Sci. Rep. **38** 1
Cullis A G, Canham L T and Calcott P D J 1997 J. Appl. Phys. **82** 909
Das B and McGinnis S P 1999 Semicond. Sci. Technol. **14** 998
Deal B E, Snow E N and Mead C A 1966 J. Phys. Chem. Sol. **27** 1873
Dimova-Malinovska D 1999 J. Luminesc. **80** 207
Goodman A M 1966 Phys. Rev. **144** 558
Gusev A I and Rempel A A 2001 Nanocrystalline Materials, (Moscow, Physmathlit) p 224 (in Russian)
Hill R M 1971 Phil. Mag. **24** 1307
Korzo V F and Chernyaev V N 1977 Dielectric films in Microelectronics, (Moscow, Energy) p 157 (in Russian)
Lampert M A and Mark P 1970 Current Injections in Solids, (New York and London, Academic Press) p 413
Schmidt T, Lischka K and Zulehner W 1992 Phys. Rev. B **45** 8989
Skanavi G I 1958 Physics of Dielectrics **2,** (Moscow, Physmathlit) p 907 (in Russian)
Stewart M, Robins E G, Geders T W, Allen M J, Choi H Ch and Buriak J M 2000 Abstr. Int. Conf. On Porous Semicond. – Science and Technology, (Madrid, Spain) p 51
Wu X L, Xiong S J, Fan D L, Gu Y, Bao X M, Sui B B and Stokes M J 2000 Phys. Rev. B **62** R7759

HRTEM and XRD analysis of P6mm and Ia3d double gyroidal WO_3 structures

E Rossinyol, J Arbiol, F Peiró, A Cornet, J R Morante, L A Solovyov[1] B Tian[2] and D Zhao[2]

Enginyeria i Materials Electrònics, Departament d'Electrònica, Universitat de Barcelona, C/. Martí i Franqués, 1, Barcelona, E-08028 (Spain). Contact e-mail: erusinol@el.ub.es
[1] Institute of Chemistry and Chemical Technology. K. Marx av., 42 660049, Krasnoyarsk. Russia
[2] Molecular Catalysis and Innovative Materials Laboratory, Department of Chemistry, Fudan University. Shanghai 200433, China.

ABSTRACT: In this work, we have used mesoporous silica SBA-15 and KIT-6 as templates for the synthesis of different WO_3 mesostructures. These materials show a small particle size, about 5-15nm, and a large surface area. We report the synthesis pathways of these mesoporous oxides and their structural characterization. In the case of the KIT-6 replica sample, a single crystal composes the hexagonal ring that forms the uncoupled subframework with Ia-3d double gyroidal symmetry. In distinction to this monocrystalline structure, the particles observed in SBA-15 replica are randomly oriented in the mesostructured framework. The 3D reconstruction of the gyroidal structure after imaging the sample between –60 and 60º is also presented.

1. INTRODUCTION

Some metal oxides, deposited either as nanoparticles or as a thin film, change their resistance in the presence of reducing or oxidising atmospheres. As the adsorption is a surface effect, one of the most important parameters to tailor the sensitivity of the sensor material is the surface area. Li and Kawi (1998a) have shown that a direct relationship was found between the surface areas of SnO_2 sensors and their sensitivities to 500ppm of H_2. According to these results, increasing of the surface area involved an increases of the sensitivity of the sensor. For this purpose, mesoporous tungsten oxide has been synthesized.

Nanostructured mesoporous materials have been widely studied in the development of catalytic systems (Arbiol et al 2002) due to their large, controllable pore size and high surface area. The pore structure, such as pore size and channel conductivity can be designed for practical application and a variety of synthetic pathways have been proposed for the development on these nanostructures (Yu et al 2003). Since the successful synthesis of MCM-41 (Li and Kawi 1998b, Beck et al 1992, Yu et al 2003 and Liu et al 2002) great efforts were made to synthesize mesoporous oxide materials other than silica. Mesoporous materials of many oxides, such as TiO2, SnO2, ZrO2, WO3… synthesized by self-assembly pathway using block-copolymers as a surfactant (soft template route), present an amorphous pore wall and low thermal stability. Recently, novel methodologies for preparing nanomaterials have been developed by using mesoporous materials with pore diameter of 2-50nm as host to accommodate different oxides (Ryoo et al 1996, Han et al 2000, Zhu et al 2003, Zhao et al 1998, Yang et al 2003 and Tian et al 2004). In this synthesis pathway, known as the hard template route, the voids of a preformed mesoporous solid are utilized and impregnated with desired precursors. The subsequent mineralization of these precursors and removal of the former solid templates may lead to mesostructures with other compositions and crystalline frameworks.

In this work, we have used SBA-15 and KIT-6 as templates for the síntesis of WO_3. Tungsten oxide is a material widely used for the detection of NO_2, important for monitoring environmental pollution resulting from combustion or automotive emissions (Shimizu and Egashira 1999, Teoh et al 2003). We have reported here the synthesis pathways of this mesoporous oxide and its structural and electrical characterization.

2. EXPERIMENTAL

2.1 Synthesis

Two different mesoporous silica templates were synthesized: a two-dimensional p6mm hexagonal structure, SBA-15, and a three-dimensional Ia-3d cubic mesostructure, KIT-6. SBA-15 was synthesized in acidic conditions using the Pluronic P123 triblock copolymer ($EO_{20}PO_{70}EO_{20}$) as template and tetraethyl orthosilicate (TEOS, 98%, Aldrich) as a silicon source (Zhao et al 1998). KIT-6 was prepared also in acidic conditions using a mixture of Pluronic P123 and butanol (Kleitz et al 2003).

For the synthesis of mesoporous oxide, 0.15 and 0.2g of SBA-15 (and the same amounts of KIT-6) were dissolved in ethanol with 0.4g of phosphotungstic acid. After 30min stirring, both solutions were dried at room temperature in air atmosphere and calcined at 350ºC for 4h. The silica/oxide mixture was dissolved again in ethanol with 0.2g of precursor, dried at room temperature in air atmosphere and calcined at 550ºC. Finally the silica template was removed with HF.

2.2 Characterization.

XRD analysis have been performed in a Siemens D5000 diffractometer, working with the K_α of the Cu and a Bruker D4 X-ray powder diffractometer. TEM characterization has been carried out using a Philips CM30 SuperTwin electron microscope operating at 300 keV and HRTEM was performed using a JEOL JEM 2010F electron microscope operating at 200kV with field emission gun. The Raman spectra were recorded at room temperature using a Jobin Yvon T64000 spectrograph equipped with a bidimensional CCD detector. The excitation source was a Ar+ Coherent INNOVA 300 laser. Computer image simulations have been obtained using the EMS software package.

3. RESULTS AND DISCUSSION

Wide-angle XRD patterns for both WO_3 samples present a mixture of monoclinic and triclinic phases (Fig. 1). The peaks are quite broad and low in intensity, revealing that the mesoporous walls of this oxide are composed of nanocrystalline frameworks. Low angle XRD patterns of tungsten oxide products obtained from the cubic Ia-3d mesoporous silica template exhibit characteristic peaks of the same space groups as the silica template. Three typical domains, undisplaced frameworks (UD), displaced frameworks (DP), and uncoupled subframework (UC) can be present in the KIT-6 replica sample. The low angle pattern clearly shows the 110 reflection, whose intensity indicates that the material contains a large amount of displaced and/or uncoupled frameworks (space group $I4_132$ or lower (Tian et al 2004)). According to the Solovyov et al (2002) model and assuming ~70 % of uncoupled framework, the calculated XRD pattern shows good agreement with the observed peak intensities (Fig. 2). The resolution is limited by the mesostructure lattice imperfection, as these gyroidal materials prepared by this method have normally a partially distorted lattice (not perfectly cubic). There are different options to explain the majority formation of the uncoupled framework: i) if we use less precursor (specially one step impregnation), then most framework should be uncoupled, and ii) as the crystallization of WO_3 is very easy, the crystallized nanoparticles may block the microchannels within the mesopore walls, hindering the mass transport between different channels. Both effects can promote the presence of the uncoupled framework. As a detailed modeling is impossible due to the material distortion and the presence of displaced frameworks, we performed a TEM analysis to verify the conclusions about the material anatomy.

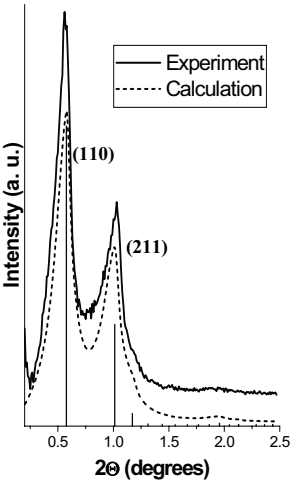


Fig. 1. Experimental (background corrected) and calculated XRD patterns of WO_3 gyroidal replica assuming ~ 70 % of uncoupled framework model.

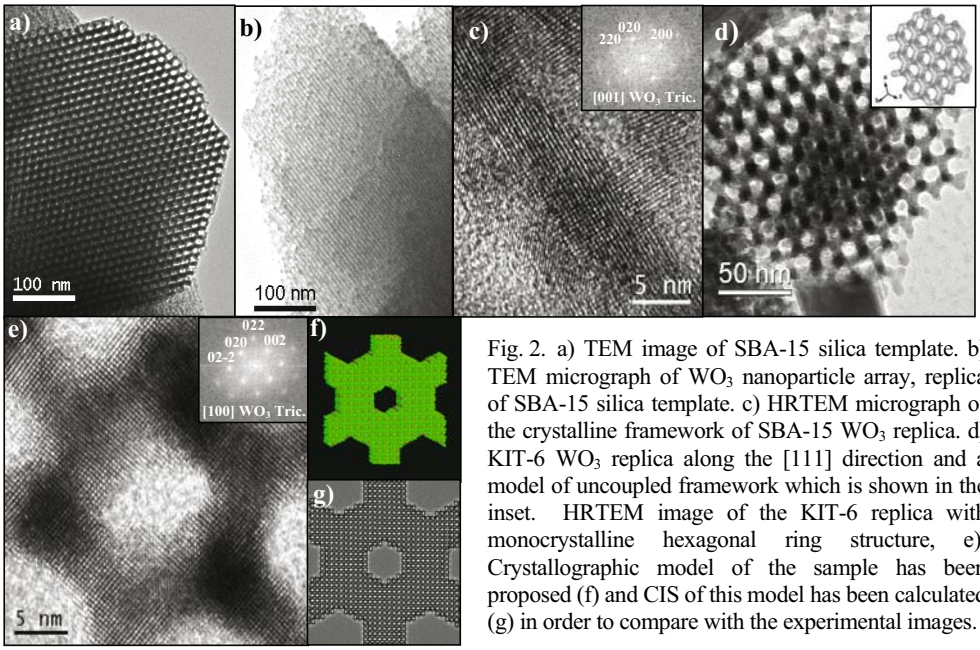


Fig. 2. a) TEM image of SBA-15 silica template. b) TEM micrograph of WO_3 nanoparticle array, replica of SBA-15 silica template. c) HRTEM micrograph of the crystalline framework of SBA-15 WO_3 replica. d) KIT-6 WO_3 replica along the [111] direction and a model of uncoupled framework which is shown in the inset. HRTEM image of the KIT-6 replica with monocrystalline hexagonal ring structure, e). Crystallographic model of the sample has been proposed (f) and CIS of this model has been calculated (g) in order to compare with the experimental images.

A detailed study of the mesoporous structure has been performed by TEM. WO_3 replica of SBA-15 was constructed by hexagonally packing a nanoparticle array (Figure 2a, b and c). These nanoparticles are uniform in diameter **(**~5 nm**)** due to the confined growth in the channels of the mesoporous silica template. Nevertheless, the cubic WO_3 sample shows a highly ordered mesostructure in the three-dimensional Ia-3d space group as a replica of the KIT-6. The uncoupled subframework, can be observed in Fig. 2d, and a model of the structure is presented in its inset. Detailed HRTEM studies have been performed in order to determine the atomic structure of both systems (images are presented in Figs. 2c and e). The power spectra obtained in both cases are presented as an inset in their corresponding image. We have found that WO_3 crystallized mainly in its triclinic phase. In the images of the examples, they correspond to [100] and [001] zone axes, for the KIT-6 and SBA-15 samples, respectively. In the case of KIT-6 replica sample (Fig. 2e), a single crystal composes the hexagonal ring that forms the uncoupled subframework. From power spectra and HRTEM images, we observed that although the morphology of the sample is complex, the structure is monocrystalline, without defects. A crystallographic model of the sample has been proposed (2f) and computer image simulation of this model has been calculated (2g) in order to compare with the experimental images. These models have been obtained using the software package Rhodius (Bernal et al 1998). We are currently working on the simulation of the connections between layers, which correspond to the most dense zones of the ring (ring's darkest junctions).In contrast to the monocrystalline structure observed in KIT-6 sample, the particles observed in the SBA-15 replica are randomly oriented in the mesostructured framework. We have also obtained a 3-D reconstruction of a WO_3 gyroidal aggregate by acquiring TEM BF micrographs for a large tilt angle range, from 60º to -60º. This series of images was obtained in a JEOL 1010 electron microscope operated at 100 KeV. Every 2-D TEM micrograph will act as a projection slice of the final 3-D reconstruction. This technique shows a high potential to solve technological problems or uncertainties on complex 3-D structures. The gyroidal pattern is difficult to observe when visualizing a single 2-D projection. However, once the 3-D reconstruction has been completed, the gyroidal morphology can be more easily evaluated. A complete animated 3-D TEM reconstruction of the WO_3 gyroidal aggregate is shown in the following URL:

http://nun97.el.ub.es/~arbiol/discdos/nanopart/web/Tomo/Model_2.html

The Raman spectra of WO_3 are presented in Fig. 3. The spectra yield information concerning the existence of different phases and the grain size of the nanocrystals. They indicate that WO_3 powders present a monoclinic (V) and triclinic (VI) phase mixture at room temperature, in agreement with the results reported earlier (Boulova and Lucazeau 2002 and Souza-Filho et al 2000) and confirmed by XRD. Low frequency

spectra (Fig. 3) show important differences between the two structures. SBA-15 replica does not present relevant variations in the spectra for different positions of the sample but, on the other hand, in the KIT-6 replica sample the spectra exhibit important changes. The differences in the spectra recorded are due to an inhomogeneity of the cubic sample, related to the ratio between the displaced, undisplaced and uncoupled subframeworks.

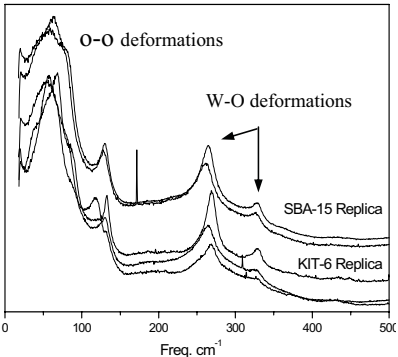


Fig. 3. Low frequency Raman spectrum of WO_3 replica synthesized with both templates. The inhomogeneity of KIT-6 replica is due to the presence of the three domains, undisplaced, displaced and uncoupled subframeworks.

4. CONCLUSIONS

We have reported the synthesis of tungsten oxide in two-dimensional hexagonal p6mm and three-dimensional cubic Ia3d mesostructures. Structural characterization shows that both structures are highly crystalline ordered and thermally stable. XRD modeling with ~70 % of uncoupled framework model shows good agreement with the observed peak intensities. This model has been confirmed by TEM. Single crystal hexagonal rings with a triclinic structure set up the atomic morphology of the KIT-6 replica that forms the uncoupled subframework. On the contrary, the particles observed in SBA-15 replica, are randomly oriented in the mesostructured framework. We have also shown that 3D-TEM reconstruction is a powerful tool when trying to visualize complex 3-D structures and obtain a fast and reliable idea of their morphology. Due to their high surface area and highly crystalline framework, these materials are expected to be very important for catalytic applications, mainly in the field of semiconductor gas sensors.

ACKNOWLEDGEMENTS

This work was partially supported by E.U. Nanos4 project. EME is with CeRMAE, Center on Advanced Materials for Energy of the Generalitat de Catalunya.

REFERENCES

Arbiol J, Rossinyol E, Cabot A, Peiró F, Cornet A, Morante J R, Chen F and Liu M 2004 Electrochem. Sol. Stat. Lett. **7**, J17
Beck J S Vartuli J C, Roth W J et al 1992 J. Am. Chem. Soc. **114**, 10834
Bernal S, Botana F J, Calvino J J, López-Cartes C, Pérez-Omil J A and Rodríguez-Izquierdo J M 1998 Ultramicroscopy **72**, 135
Boulova M and Lucazeau G 2002 J. Solid State Chem **167**, 425
Han Y J, Kim J M and Stucky G D 2000 Chem. Mater. **12**, 2068
Kleitz F, Choi S H and Ryoo R 2003 Chem Comm, 2136
Li G J and Kawi S 1998a Mater. Lett. **34**, 99
Li G J and Kawi S 1998b Talanta **45**, 759
Liu X, Tian B, Yu C, Gao F, Xie S, Tu B, Che R, Peng L M and Zhao D 2002 Angew. Chem. **41**, No 20
Ryoo R, Kim J M, Ko C H and Shin C H 1996 J Phys. Chem **100,** 17718
Shimizu Y and Egashira M 1999 MRS Bull. **24**,18
Solovyov L, Zaikovskii V I, Shmakov A N, Belousov O V and Ryoo R 2002 J. Phys. Chem B. **106**, 12198
Souza-Filho A G, Freire V N, Sasaki J M, Mendes Filho J, Julião J F and Gomes U U 2000 J. Raman Spectrosc. **31**, 451
Teoh LG, Hon Y M, Shieh J, Lai W H and Hon M H 2003 Sens and Act. B **96**, 219
Tian B, Liu X, Solovyov L A, Liu Z, Yang H, Zhang Z, Xie S, Zhang F, Tu B, Yu C, Terasaki O and Zhao D 2004 J. Am. Chem. Soc. **126**, 865
Yang H, Shi Q, Tian B, Lu Q, Gao F, Xie S, Fan J, Yu C, Tu B and Zhao D 2003 J. Am. Chem. Soc. **125**, 4724
Yu C, Tian B and Zhao D 2003 Cur. Op. Solid State and Mat. Sci. **7** 191
Zhao D, Feng J, Huo Q, Melosh N, Fredrickson G, Chmelka B F and Stucky G D 1998 Science **279**, 548
Zhu K, He H, Xie S, Zhang X, Zhou W, Jin S and Yue B 2003 Chem. Phys. Lett. **377**, 317

Part VI

Processed Silicon and Other Device Materials

Research highlights and impacts upon industry for nanoelectronics in the university system of Taiwan

You-Lin Wu, Huey-Liang Hwang[1] and Chuen-Horng Tsai[2]

Department of Electrical Engineering, National Chi-Nan University, Puli, Nantou, Taiwan 545
[1] Institute of Electronic Engineering, National Tsing-Hua University, Hsinchu, Taiwan 300
[2] Department of Engineering Science and System, National Tsing-Hua University, Hsinchu, Taiwan 300

ABSTRACT: Four outstanding research-oriented universities in Taiwan, National Central University, National Chiao-Tung University, National Tsing-Hua University, and National Yang-Ming University, were integrated to form The University System of Taiwan (UST) on Oct. 30, 2002 to achieve academic excellence through integrating research impetus and sharing research and education resources. Selective research subjects on nanoelectronics being carried out in the UST will be highlighted and their impact on the electronic industries of Taiwan will be described.

1. INTRODUCTION

The electronic products amount to almost 30% of shipments from Taiwan each year and retain a high yearly growth rate, which leads among several industries. Based on the demands on more advanced electronic key components, many R&D activities are therefore being carried out in several leading IC manufacturers, as well as many research-oriented universities in Taiwan. The UST integrates the research efforts and resources of the four most outstanding research-oriented universities in Taiwan, National Central University, National Chiao-Tung University, National Tsing-Hua University, and National Yang-Ming University. Due to their close locations to the Taiwan Hsinchu Science Park, two members of the UST, National Chiao-Tung University and National Tsing-Hua University, contribute to many projects with government support and collaborate with the IC manufacturers in the Science Park, in particular for nanoelectronics-related projects. In this paper we will describe the main research projects for nanoelectronics in the UST, which are divided into three parts, advanced process and device structure for Si nano-CMOS technology, carbon nanotube-based electronics and Si nanodots and their applications.

2. ADVANCED PROCESS AND DEVICE STRUCTURE FOR Si NANO-CMOS TECHNOLOGY

According to the SIA roadmap the feature sizes in the fabrication of integrated circuits will approach 70 nm in 2010. However, new materials and novel device structures are necessary and a lot of technology challenges have to be overcome before the 70 nm technology node can be actually achieved. One of the nano-electronic projects in the UST directed by Professor H.L. Hwang of National Tsing-Hua University focuses on the development of new technologies for next generation nano-CMOS. This project is financed by the Ministry of Economic Affairs of Taiwan, the National Science Council and the TSMC, which involves 1. high-k dielectrics and low-k ILD layers in nano-MOSFETs, 2. nano-scaled interconnects, and 3. the integration of metal-gate/high-k/SiGe MOSFETs. Some of the research results of this project will be presented. For high-k dielectrics, both HfO_2 and ZrO_2 have been investigated. Figure 1 shows the I_{DS}-V_{DS} and I_{DS}-V_{GS} characteristics of an n-channel MOSFET fabricated with amorphous HfO_2 gate dielectrics (Chiu et al 2005a). The equivalent oxide thickness (*EOT*) 2.75 nm is extracted from the measured saturation capacitance in the accumulation mode. The effective dielectric constant of HfO_2 thin films following annealing was evaluated as 19.3 in accumulation mode. Electron trapping in HfO_2 film was observed when a MOS capacitor was biased

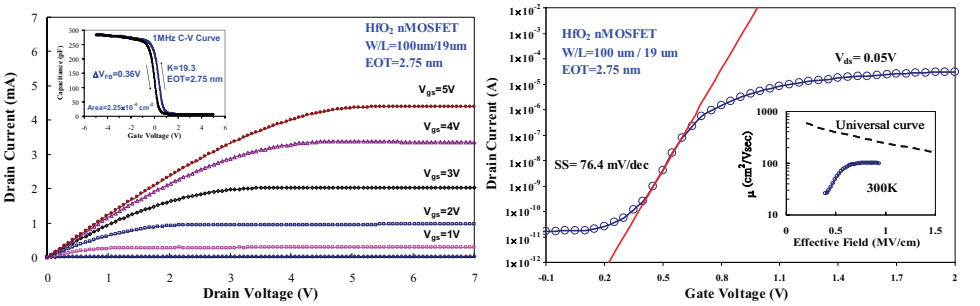


Fig. 1 (a) I_{DS}-V_{DS} and (b) I_{DS}-V_{GS} characteristics of n- channel MOSFET fabricated with HfO_2 gate dielectrics.

at inversion. The effect of interface charge trapping is negligible. Good current switching capability and a maximum channel electron mobility of 102 cm^2/V-s at V_G = 1.1V in the MOSFETs with amorphous HfO_2 gate oxide were achieved. In particular, we investigated the surface recombination velocity and the minority carrier lifetime by using the gated diode method. For ZrO_2, the current transport mechanism in the Al/ZrO_2/Si structure was studied, and the results indicated that the dominant conduction mechanisms at high temperatures were Schottky emission, modified Schottky emission and Poole-Frenkel emission in a high electric field, medium electric field and low electric field, respectively (Chiu et al 2005b). Other high-k dielectrics we have investigated are Gd_2O_3 (k = 14), and Y_2O_3 (k = 18). By using the ultra-high vacuum vapor deposition method, an abrupt interface between the high-k dielectric Gd_2O_3 and Si can be produced (Kwo et al 2002). This stable interface is rather difficult to achieve by using other high-k dielectrics. The emphasis of our future trend of research for high-k dielectrics will be placed on the growth of high-k dielectrics by atomic-layer deposition (ALD) for application in nano-MOSFETs. Low-k ILD layers including a-C:N and a-C:N:F materials by ECR-CVD have been extensively studied as well in this project (Liu et al 2001). A photo-assisted MOCVD system was constructed for nano-scaled interconnects, and pure copper film can be obtained with excellent step coverage at temperatures as low as 100 ~ 125℃ (Wu et al 2005). On the other hand, the use of high-k dielectric degrades the carrier mobility in a MOSFET and a possible solution is to replace the poly-silicon gate with a metal gate. The integration of a metal-gate, a high-k dielectric and the SiGe MOSFET is also an investigation topic in the project (Huang 2003, Chin 2003).

3. CARBON NANOTUBE-BASED ELECTRONICS

Carbon nanotubes (CNT) are large macromolecules that are unique for their size, shape, and remarkable physical properties, which were discovered by Iijima (1991). Currently, the physical properties of CNT are still being discovered and disputed. What makes it so difficult is that nanotubes have a very broad range of electronic, thermal and structural properties that change depending on the different kinds of nanotube (defined by diameter, length, and chirality, or twist). A team led by Prof. C.H. Tsai of National Tsing-Hua University in the UST has been engaged in research on CNT-based electronics. Through an industrial-cooperative project with a domestic company, Nano Architect Research Co., in Hsinchu Science Park, the team developed a technique called "*in-situ* catalytic chemical vapor deposition" (Lee et al 2003 and Tsai 2004) which can be applied to a variety of applications, such as field emission displays, field effect transistors, fuel cells, scanning probe tips, sensors and so on. Figure 2 shows the SEM picture of micro-triode array with self-aligned carbon nanotubes grown by ICP-CVD for field emission device applications. Normally the microelectrode array is fabricated by conventional photo-lithography processes. In these processes, catalyst metal was deposited inside the gate hole to grow vertically aligned CNTs as the cold electron emitter controlled by the gate voltage. The CNTs can be bundles or a single individual carbon nanotube depending on the application. To avoid the so called field screening effect, which limits the field emission current, a

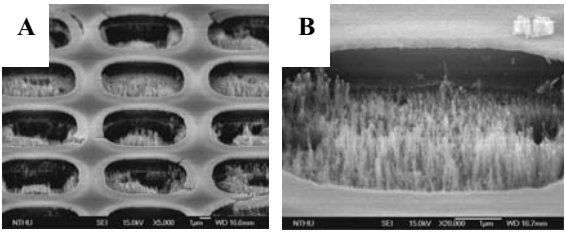


Fig. 2 SEM picture of micro-triode array with self-aligned carbon nanotubes grown by ICP-CVD

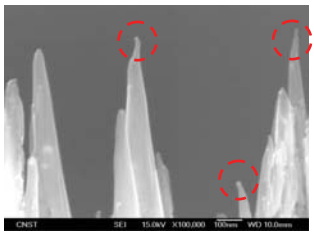


Fig. 3 Tip of CNTs can be reshaped by using ion sputtering treatment after CNT growth

novel process of controlling the CNT density by using ion sputtering treatment of the catalyst before CNT growth has been developed (Lin et al 2004). The field emission current can thus be successfully increased more than two orders of magnitude. The ion sputtering treatment can also be applied to the process after CNT growth. It turned out that the CNT tip can be reshaped to a cone shape of much smaller radius of curvature, and the catalyst metal on top of the carbon tubes was removed (see Fig. 3) (Weng et al 2004). Investigation of CNT-FET is also underway.

4 Si NANODOTS AND THEIR APPLICATIONS

Light emission from silicon has become the subject of intense scientific and technical interest to make a silicon-based light source for opto-electronic applications giving compatibility with standard ULSI silicon processing technology. Self-assembled silicon nanodots embedded in silicon oxide and silicon nitride are of great interest in recent years not only for their unique optical properties that yield very efficient light emission (Pei et al 2002, Tong et al 1999) but also for the possibility of producing Si-based nanoelectronic devices such as resonant tunneling diodes RTD (Mazumder 1998). The RTD has been recognized as the key device for future high-speed circuit applications. A team led by Prof. H.L. Hwang at National Tsing-Hua University has successfully grown Si nanodots in hydrogenated amorphous Si-rich silicon nitride (a-SiN_x:H) (Pei and Hwang 2003). Both the photoluminescence and electroluminescence of a-SiN_x:H films were investigated. The photoluminescence (PL) from Si nanodots embedded in a-SiN_x:H film prepared by plasma-enhanced CVD has been observed and the strong visible PL (blue– white–orange) could be adjusted by changing the process gas flow rate ratio. Figure 4 shows the current–voltage characteristic of Si nanodots embedded in an a-SiN_x:H film. An obvious current jump is observed in both the as-deposited and the annealed samples. Interestingly, the current jump was not found in the sample without Si nanodots. Therefore, the current jump is associated with the Si nanodots. Both electron and hole tunneling transport through Si nanodots in a-SiN_x:H film were observed at room temperature. Negative differential resistance in the current–voltage characteristics (Pei et al 2005) was observed for hole tunneling. These results indicate the potential applications of Si nanodots in RTD devices. Figure 5 depicts the electroluminescence (EL) of Si nanodots embedded in an a-SiN_x:H film. The EL device structure is ITO/*a*-$SiN_{0.56}$:H/Al, with light emitting from the ITO layer. The emitted light can be recognizable by the naked eye in the dark, under a 14 V forward bias. White EL spectra from ~ 400 to 750 nm, with a central peak at 560 nm, were observed. Results of our investigation demonstrate that Si nanodots in a-SiN_x:H films can have potential applications in nano-flash-memory, single-electron devices, Si light emitting devices, and resonant tunneling devices.

5. SUMMARY

In this paper, we present several ongoing nanoelectronic research projects in the UST including advanced processing and device structure for Si nano-CMOS technology, carbon nanotube-based electronics and Si nanodots and their applications. As demonstrated in the previous sections,

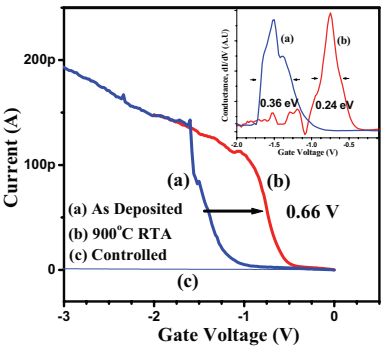


Fig. 4 I-V characteristic of Si nanodots embedded in a-SiN_x:H films for (a) as-deposited, (b) annealed, and (c) controlled samples.

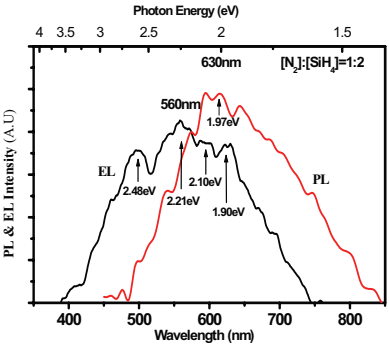


Fig. 5 Electroluminescence of Si nanodots embedded in a-SiN_x:H films

some important results on high-k dielectrics, low-k ILD layers, CNT materials, CNT-FETs and Si nanodots have been achieved. These results will contribute to the electronic industries in Taiwan and the research for nanoelectronics is kept on going under the coordination of CNST of the UST through financial support from the government, the UST and the electronic industry of Taiwan.

REFERENCES

Chin A 2003 Samsung, Korea, More Si RF on Intl. Microwave Symp.

Chiu F C, Juan T P, Lai B C, Lin S A., Lee J Y M and Hwang H L 2005a IEEE Electron Device Lett, *accepted*

Chiu F C, Lin Z H, Chang C W, Wang C C, Chuang K F, Huang C Y, Lee J Y M and Hwang H L 2005b J. Appl. Phys. *accepted*

Huang C H 2003 Technical Digest of IEDM pp. 319-322

Iijima S 1991 Nature **354**, 56

Kwo J, Hong M, Korton A R, Queeney K L, Chabal Y J, Opila R L Jr., Muller D A, Chu S N G, Sapjeta B J, Lay T S, Mannaerts J P, Boone T, Krautter H W, Krajewski J J, Sergnt A M and Rosamilia J M 2001 J. Appl. Phys **89**, 3920

Lee W Y, Liao T X, Juang Z Y and Tsai C H 2003 14th European Conference on Diamond, Diamond-Like Materials, Carbon Nanotubes, Nitrides & Silicon Carbide, Sept. 7-12

Lin C T, Wei H W, Leou K C, Lai H J and Tsai C H 2004 The 9th International Conference on New Diamond Science and Technology

Liu X W, Lin J H, Jong W J and Shih H C 2002 Thin Solid Films **409**, 178

Mazumder P, Kulkarni S, Bhattacharya M, Sun J P and Haddad G I 1998 Proc. IEEE **86**, 664

Pei Z, Chang Y R and Hwang H L 2002 Appl. Phys. Lett. **80**, 2839

Pei Z and Hwang H L 2003 Appl. Surf. Science, 212, 760

Pei Z, Su A Y K, Hwang H L and Hsiao H L 2005 Appl. Phys. Lett. **86**, 63530

Tong J F, Hsiao H L and Hwang H L 1999 Appl. Phys. Lett. **74**, 2316

Tsai C H 2003 Workshop on carbon nanotubes and their applications, University System of Taiwan, Hsinchu.

Weng C H , Leou K C, Wei H W, Juang Z Y, Wei M T, Tung C H and Tsai C H 2004 Applied Physics Letters **85** 4732

Wu Y L, Hsieh M H, Huang K C and Hwang H L 2005 Thin Solid Films, *accepted*

TEM investigations of epitaxial high-κ dielectrics on silicon

E Bugiel, H J Osten, A Fissel[1], O Kirfel[1] and M Czernohorsky

University of Hannover,
Institute for Semiconductor Devices and Electronic Materials, Appelstr. 11A
[1] Information Technology Laboratory, Schneiderberg 32, D-30167 Hannover, Germany

ABSTRACT: We present results for epitaxial growth of crystalline rare-earth oxides as potential high-κ dielectrics. From TEM (including HREM and electron diffraction) we find that on Si(001) oriented surfaces, crystalline Pr_2O_3, Gd_2O_3, and Nd_2O_3 grow in the Mn_2O_3 structure as (110)-domains, with two orthogonal in-plane orientations. On Si(111), we obtain epitaxial growth of Pr_2O_3 having the hexagonal La_2O_3 structure, but Nd_2O_3 grows in the cubic Mn_2O_3 structure in the twinned A/B orientation. We also investigated other substrate orientations and the formation of amorphous interfacial layers and silicide inclusions between the substrate and rare-earth oxide layers. A model is proposed for silicide inclusions based on the Moiré pattern. Without a silicon capping layer, diffusion-driven accumulation of oxygen seems to control the Nd_2O_3/Si(001) interface properties at elevated temperatures.

1. INTRODUCTION

Crystalline oxides on Si are of increasing importance. In ultra-scaled devices, SiO_2 has to be substituted by alternative high-κ materials (Osten et al 2000) if the SiO_2 reaches a thickness below 1.5 nm. Crystalline insulators (oxides) have the advantage over amorphous ones, such as no recrystallisation during high temperature treatment and defined interface properties. On the other hand, crystalline insulators on Si are also under discussion for application in new epitaxial heterojunction devices, such as resonant tunnelling diodes (Wang et al 2002).

However, the preparation of epitaxial oxides involves more effort, but it has the additional advantage of enabling defined interfaces engineering. The Si/dielectric interface properties influence the device performance significantly. The interface structure will determine the density of defects that are known to impact carrier mobilities. Often, the interface is not stable and changes during and after growth (Fissel et al 2002).

In order to gain a better understanding of the interface and layer formation processes, we have performed TEM investigations of different crystalline rare-earth oxides grown on Si(001) and on other Si orientations grown by molecular beam epitaxy (MBE). Such crystalline rare-earth oxides are candidates with a high potential for high-κ dielectrics with very promising electrical properties (Osten et al 2003, Osten 2003). All investigated oxides form layers of cubic structure consisting of two domains in {110}-orientation on Si(001), whereas Pr_2O_3 appears in the hexagonal form on Si(111).

2. EXPERIMENTAL

The rare-earth oxides were grown on hydrogen-terminated 4" Si substrates in an 8" multi-chamber Si MBE-system. Source material of granular rare earth oxide was evaporated using an electron beam evaporator. We characterised the layers by transmission electron microscopy (cross-section and plan-view images combined with selected area diffraction (SAD)). The TEM samples were prepared by a fast high-energy ion beam thinning technique (Bugiel 1997).

3. RESULTS AND DISCUSSION

3.1 Rare-Earth Oxides on Si(001) Substrate

The chemical nature of the films was determined using a high-resolution XPS system connected *in vacuum* to our growth chamber. The results indicate a rare-earth to oxygen ratio of 1.5. Selected area diffraction on plan-view samples show the same characteristic patterns for all three investigated rare-earth oxides as described for Pr_2O_3 (Bugiel et al 2001). On Si(001) oriented surfaces, crystalline Pr_2O_3 grows in (110) domains, with two orthogonal in-plane orientations, due to the (2x1)-Si(001) dimer orientation on stepped surfaces (Fissel el al 2003). Figures 1a and 1b show high resolution plan-view and cross-sectional micrographs of Pr_2O_3 on Si(001), respectively. The domain boundary is marked by dotted line.

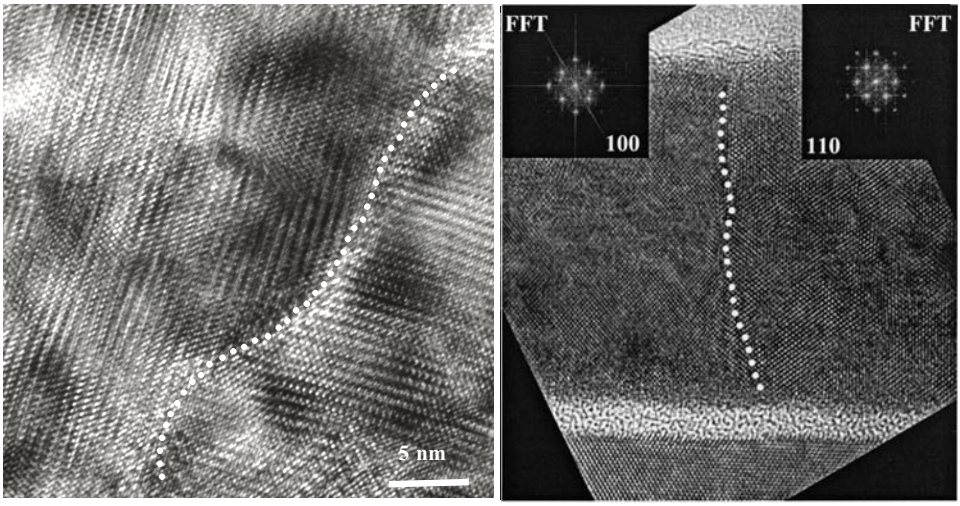


Fig. 1: a) HREM plan-view micrograph of Pr_2O_3 on Si(001). b) HREM cross-sectional micrograph with FFT patterns. A domain boundary is marked in both micrographs.

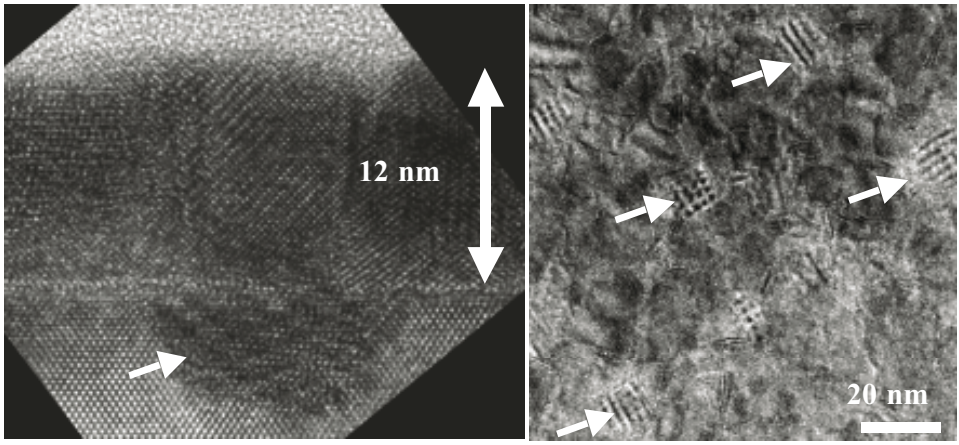


Fig. 2: (a) HREM cross-sectional micrograph and (b) plan view micrograph of Nd_2O_3 on Si(001). The silicide inclusion leading to Moiré contrasts in the plan view image are marked by arrows.

An amorphous double layer at the interface between the Pr_2O_3 and the Si substrate can be seen in Fig. 1b. EFTEM investigations of the lower interface layer (bright contrast) show enrichment with oxygen, in agreement with Nigro et al (2003). Such oxygen-rich layer, like SiO_2, at the interface has a strong effect on the electrical properties and can be a showstopper for substitution of SiO_2. Capping the oxide surface with silicon before air contact can prevent the formation of such amorphous interface layer. For Nd_2O_3, we did not find such strong tendency for amorphous interface layer formation. Instead, such amorphous interfacial layer occurs only after medium temperature annealing in oxygen-containing environment. Figs. 2a and 2b show the appropriate XTEM micrographs in high resolution and plan-view, respectively for Nd_2O_3.

There is no amorphous interface layer visible in Fig. 2a, but we find coherent inclusions beneath the Nd_2O_3 layer in the Si substrate surface. Fig. 2b exhibits regions of moiré contrast relating to the inclusions.

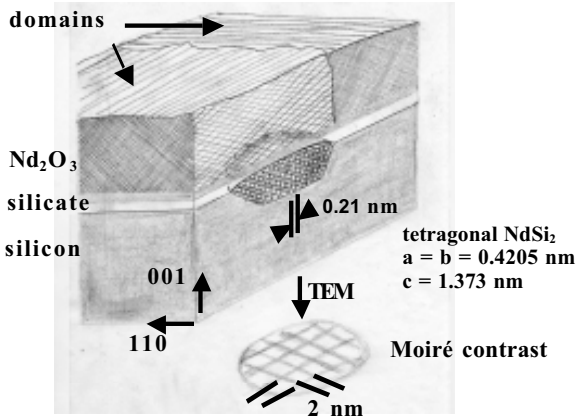


Fig. 3: Scheme (sketch) illustrating coherent silicide formation beneath the Nd_2O_3 layer in the Si substrate surface.

Based on the lattice parameters derived from the Moiré pattern, we conclude that the inclusions consist of tetragonal $NdSi_2$ in epitaxial relationship to Si(001), as illustrated in Fig. 3. Sometimes silicide inclusions were also found in case of Pr_2O_3. After heat treatment the typical amorphous double layer (as shown in Fig. 1b) can be found up to the depth of the silicide formation. That means that the double layer structure is formed by diffusion of oxygen from the residual gas through the oxide layer to the interface.

Such a process can cause a disappearance of the silicide inclusions. Analogous to Pr_2O_3, the Si top layer does also suppress the oxygen diffusion

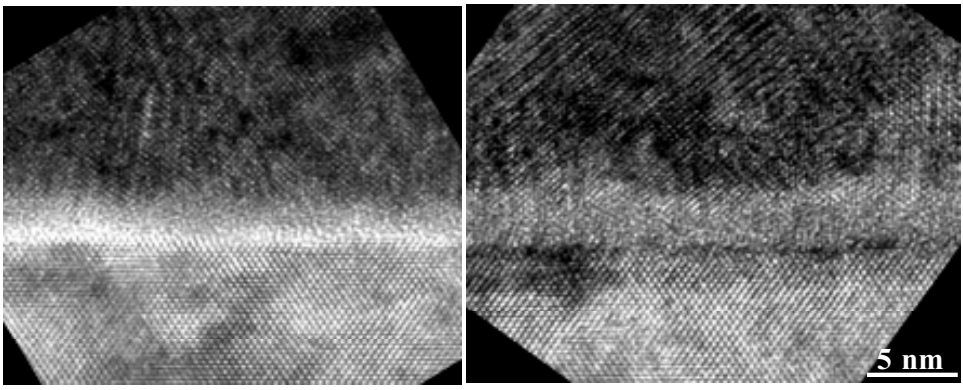


Fig. 4: (a) HREM cross-section micrographs of Gd_2O_3 on Si(001) before and (b) after heat treatment.

Gd_2O_3 is even more stable against silicide formation and, moreover to a certain extent, against oxygen diffusion than Nd_2O_3. Figure 4 shows XTEM micrographs of Gd_2O_3 in high resolution before and after heat treatment, respectively. For the as-grown layer, we found a thin (about 1 nm) amorphous interface layer, but we did not see any silicide inclusions (Fig. 4a). After heat treatment, no remarkable increase of the thickness of this amorphous interface layer occurs (Fig. 4b). That makes this material favourable for high-κ applications.

3.2 Rare-Earth Oxides on other Substrates

Figure 5 shows the cross-sectional micrographs of Nd_2O_3 layers on Si(111) overgrown with Si. In contrast to Pr_2O_3, which grows in the hexagonal phase (Bugiel et al 2001), Nd_2O_3 grows in the cubic phase. Here we see the A/B-type (111) twinning nature of the c-Nd_2O_3 to Si(111) substrate. The presence of A/B-type (111) twinning has been found in many binary metal oxide growth experiments on Si(111), such as PrO_2 (Fork et al 1990), Y_2O_3 (Hunter et al 2000), and CeO_2 (Tye et al 1994). Also CaF_2 growth on Si(111) shows this effect (Wang et al 2004). We also investigated the influence of other substrates on the phase formation of Pr_2O_3. For the growth on Si(113), we found the simultaneous formation of the oxide in both phases. On amorphous SiO_2, we observed the formation of crystalline Pr_2O_3 in the cubic phase.

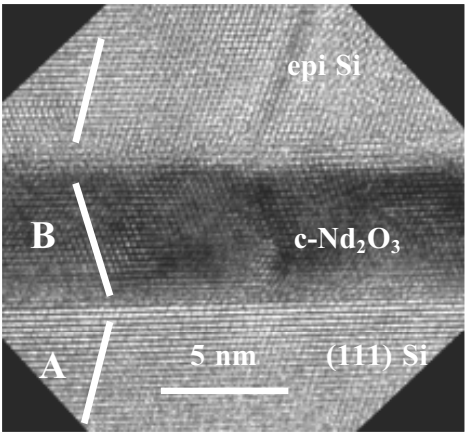


Fig. 5: HREM cross-sectional micrographs of Nd_2O_3 on Si(111).

4. SUMMARY

We showed TEM results for the growth of three crystalline rare-earth oxides on Si substrates with different crystallographic orientations. On Si(001) oriented surfaces, crystalline Pr_2O_3, Nd_2O_3, and Gd_2O_3 grow as (110) domains, with two orthogonal in-plane orientations. Pr_2O_3 shows the strongest tendency to form an amorphous interface layer to the Si substrate due to air contact. A Si capping layer can suppress this effect. Coherent silicide inclusions were found beneath the Pr_2O_3 and Nd_2O_3 layers in the Si substrate surface. Gd_2O_3 does not show this behaviour. Hexagonal Pr_2O_3 grows epitaxially on Si(111) but Nd_2O_3 grows in the cubic phase in the twinned B-orientation to the Si(111) substrate. Pr_2O_3 grows on other substrates partly simultaneously in both phases.

ACKNOWLEDGEMENTS

This work was partly founded by the German Federal Ministry of Education and Research (BMBF) under the KrisMOS project (01M3142D). We would also like to thank Dr. Feldhoff from the University of Hannover for using the TEM equipment.

REFERENCES

Bugiel E 1997 Proc. MRS Meetings, eds R M Anderson and S D Walck **480**, 89
Bugiel E, Liu J P and Osten H J 2001 Inst. Phys. Conf. Ser.**169**, 411
Fissel A, Dabrowski J and Osten H J 2002 J. Appl. Phys. **91**, 8986
Fissel A, Osten H J and Bugiel E 2003 J. Vac. Sci. Technol. B **21**, 1765
Fork D K, Fenner D B and Geballe T H 1990 J. Appl. Phys. **68**, 4316
Hunter M E, Reed M J, El-Masry N A, Roberts J C and Bedair S M 2000 Appl. Phys. Lett. **76**, 1935
Nigro R L, Raineri V, Bongiorno C, Toro R, Malandrino D and Fragala I L 2003 Appl. Phys. Lett. **83**, 129
Osten H J 2003 Compound Semiconductors **9**, 29
Osten H J, Bugiel E and Fissel A 2003 Proc. MRS Meetings, eds. B D Weaver, M O Manasreh, C Jagadish and C Zollner **744**, 15
Osten H J, Liu J P, Gaworzewski P, Bugiel E and Zaumseil P 2000 IEDM Technical Digest, 653
Tye L, Chikyow T, El-Masry N A and Bedair S M 1994 Mater. Res. Soc. Symp. Proc. **341**
Wang C, Müller B H and Hofmann K R 2002 IEEE Si Nanoelectronics Workshop Abstracts, 111
Wang C R, Müller B H, Bugiel E and Hofmann K R 2004 J. Vac. Sci. Technol. A **22**/5, 2181-2187

Damage layer in silica-based low-k material induced by the patterning plasma process studied by energy-filtered TEM

O Richard, F Iacopi, Zs Tőkei and H Bender

IMEC, Kapeldreef 75, B-3001 Leuven, Belgium

ABSTRACT: The damage layer induced by the patterning plasma process in silica-based low-k material is studied by energy-filtered TEM. It is found that the damage layer, ~10 nm thick, has a lower carbon content and a higher oxygen content than the bulk of the low-k material.

1. INTRODUCTION

Due to the continuous miniaturization, the silicon oxide used as intermetal dielectric for interconnect wires has to be replaced by a material with a lower dielectric constant. The capacitance increases with shrinking distance between the interconnecting lines, resulting in an increase of the signal transmission delay and of the dynamic power consumption. The ideal intermetal dielectric material should have, among others, the following properties: low dielectric constant ($k < 3.9$ standard value of SiO_2), isotropic dielectric function, thermal and mechanical stability, and it should be manufacturable.

Different low-k materials and different deposition processes are currently under study. This work is focused on a silica-based (SiCO:H) porous material.

During the plasma process applied for the patterning, a damage layer is formed on the sidewalls of the trenches. This layer, typically 5-20 nm thick, increases the interline dielectric capacitance and has therefore to be as thin as possible. The aim of this work is to study by energy-filtered TEM the thickness and composition of the damage layer and to explore the analytical limitations.

2. EXPERIMENTAL

The following analyses are performed with Cu meander forks (nominal width and spacing: 80 / 80 nm) embedded in SiCO:H low-k material using the damascene technology. In our case this technology can be described schematically as followed: The dielectric layer, 150 nm thick SiCO:H, is deposited on 30 nm SiC / 500 nm SiO_2 / Si substrate and patterned by lithography. The interconnect trenches are formed by dry etching of the dielectric stack. The photoresist used during the lithography process is then removed by dry ashing. A Ta(N) / Ta metallic copper diffusion barrier, about 8 nm thick, is next deposited. The trenches are filled by electroplated copper and the excess copper is removed by chemical-mechanical polishing. A passivation layer stack consisting of 50 nm SiC(N), 330 nm SiO_2 and 500 nm Si_3N_4 is finally deposited.

The TEM cross-section specimens are prepared by a focus ion beam wedge milling technique. The energy-filtered TEM investigations are performed with a Philips CM30 FEG microscope, operating at 300 kV, equipped with a post-column Gatan Imaging Filter (GIF). The Digital Micrograph^{TM} software is used in order to acquire and process the energy-filtered elemental maps. The concentration profiles are calculated from the obtained elemental maps taking into account the appropriate theoretical ionisation cross section (Hofer et al 1997) and normalized with the three considered elements (C, O and Si). Medium electron doses are required in order to avoid sample modifications that render the correlation between the different element maps impossible.

3. RESULTS AND DISCUSSION

3.1 Standard Process

Cross-section TEM image and energy-filtered TEM carbon and oxygen elemental maps of copper lines embedded in a SiCO:H layer are presented in Fig. 1a, 1b and 1c, respectively.

The concentration profiling direction is perpendicular to the metallic barrier - low-k material interface. In order to decrease the statistical noise, the counts of the elemental maps are integrated over a 45 nm wide area perpendicular to the profiling direction (windows on Fig. 1c). The carbon, oxygen and silicon concentration profiles (Fig. 1d) calculated from the corresponding elemental maps are presented from the Ta(N) / Ta metallic barrier - low-k material interface.

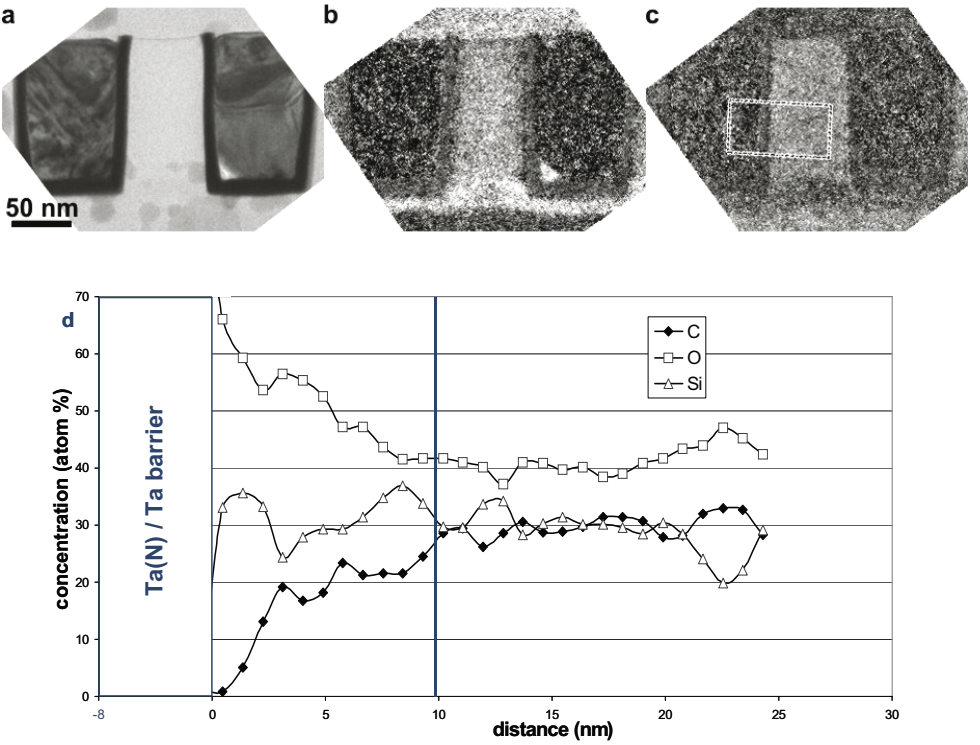


Fig. 1: Cross-section TEM image (a), carbon (b) and oxygen (c) elemental maps, and concentration profiles for the carbon (full diamonds) oxygen (open squares) and silicon (open triangles) (d). The silicon elemental map is not presented here. The position of the barrier is marked by the box.

The dark contrast features observed outside the copper lines and the hole in the bottom of the right copper line (Fig. 1a) are due to a copper corrosion effect related to the focused ion beam TEM specimen preparation (Bender et al 2004). This effect is still not fully understood.

Whereas no contrast differences indicating the presence of a damage layer are observed on the TEM cross-section image (Fig. 1a), a slightly darker contrast layer compared to the bulk is observed for the carbon elemental map (Fig. 1b) near the interface with the metallic barrier and a slightly brighter contrast layer is observed at the same location for the oxygen elemental map (Fig. 1c).

The carbon and oxygen concentration profiles show clearly the presence of an about 10 nm thick layer (vertical line) (Fig. 1d) with a lower carbon and a higher oxygen contents than the bulk. This damage layer, silicon oxide like, is induced by the processing.

For this processed SiCO:H material, a k value of 3.5 is obtained from the capacitance measurements (Tőkei et al 2005) whereas the k value of the pristine material should be 3.0. This difference is due to the dielectric damage occurring during the process. The detection of a damage layer resulting in an increase of the final k value has also been observed for other SiCO:H materials (Iacopi et al 2004).

3.2 HF-Dip Sample Before the Metallic Barrier Deposition

A second sample has been processed in a similar way. In order to remove the silicon oxide like damage layer an 1% HF-dip treatment is performed for 3 minutes before the deposition of the Ta(N) / Ta metallic barrier. It is worth noting that the SiCO:H pristine low-k material is not etched during the 1% HF-dip treatment. The corresponding TEM cross-section image, energy-filtered TEM carbon and oxygen elemental maps are presented in Fig. 2a, b and c, respectively. The carbon, oxygen and silicon concentration profiles are presented in Fig. 2d.

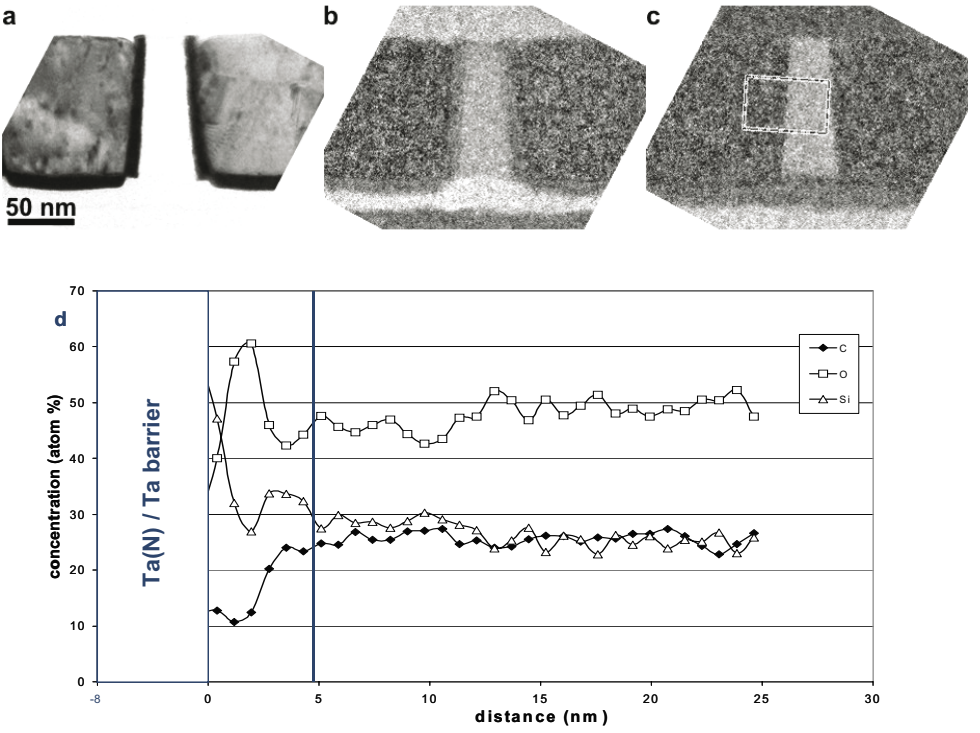


Fig. 2: Cross-section TEM image (a), carbon (b) and oxygen (c) elemental maps and concentration profiles for the carbon (full diamonds), oxygen (open squares) and silicon (open triangles) (d). The silicon elemental map is not presented here. The position of the barrier is marked by the box.

The horizontal layer, under the metallic barrier and under the low-k material, exhibiting a bright contrast in the carbon elemental map (Fig. 2b) and a dark contrast in the oxygen elemental map (Fig. 2c) is the SiC layer. The surface of the Ta(N)/Ta metallic barrier deposited in the bottom of the trenches is more or less aligned with the surface of the SiC layer under the SiCO:H layer. On the cross-section TEM image (Fig. 2a), a shift of the barrier deposited on the "vertical" walls is observed at both sides at the bottom of the trenches. These shifts, about 9 nm wide, correspond to the low-k

material which has been etched during the HF-dip treatment. The thickness of the damage layer determined from the concentration profile (Fig. 1d) is about 10 nm what is in good agreement with the observed shift (Fig. 2a). It indicates that after the HF-dip treatment the damage layer has been removed almost entirely. However, on the carbon, oxygen and silicon concentrations profiles (Fig. 2d) calculated from the corresponding elemental maps, still an about 5 nm thick layer with a lower carbon content, a higher oxygen and silicon content than the bulk is observed.

The best lateral resolution possible at an interface on the concentration profiles under the used experimental conditions has been measured with a silicon substrate covered with the same kind of low-k material. In this case, no damage layer is expected, moreover the roughness of the low-k material layer / silicon substrate interface is low. For this test sample the thickness of the interface measured from the concentration profiles is about 5 nm.

It means that it will not be possible with the methodology used above to detect a damage layer thinner than 5 nm. Therefore the effect observed on the concentration profiles in Fig. 2d is probably due to the lateral resolution at the interface, in other words no damage layer is present. It is worth noting that the roughness of the low-k / metallic barrier interface plays also a role in the observed effect. Moreover it cannot be excluded that the Ta(N) / Ta barrier deposition induced some carbon depletion; the resulting damage layer due to this effect should be in any case thinner than 5 nm.

Comparing the structures presented in Fig 1a with the structures presented in Fig. 2a, it is observed that the slope of the interface is not identical for both samples; the low-k / metallic barrier interfaces of the first sample (Fig. 1a) have a more steep slope than the same interface for the second sample (Fig. 2a). It indicates that the thickness of the damage layer is not constant over the whole height of the structure; the damage layer being slightly thinner at the bottom of the trenches.

4. CONCLUSIONS

The composition and thickness of a damage layer introduced in the SiCO:H layer by a standard process has been studied by energy-filtered TEM. The damage layer is silicon-oxide-like and about 10 nm thick. A similar structure with an HF-dip treatment performed before the Ta(N) / Ta metal barrier deposition is also analysed. An interfacial layer, about 5 nm thick, with a composition different than the bulk is obtained. This thickness corresponds with the lateral resolution that can be expected under these conditions so that the observation of this layer is probably a limitation of the measurement procedure due to the effect of the interface.

ACKNOWLEDGEMENTS

P Van Marcke (IMEC) is aknowledged for the preparation of the TEM specimens. The TEM and EFTEM analysis is performed in the EMAT laboratory from the University of Antwerp. The IMEC low-k/Cu group is acknowledged for providing samples.

REFERENCES

Bender H, Richard O, Benedetti A, Van Marcke P and Drijbooms C 2004 Proceedings 8th European focused ion beam users group meeting, http://www.imec.be/efug/EFUG2004_Bender.pdf

Hofer F, Grogger W, Kothleiter G and Warbichler P 1997 Ultramicroscopy **67**, 83-103

Iacopi F, Travaly Y, Stucchi M, Struyf H, Peeter S, Jonckheere R, Lennissen L H A, Tökei Zs, Sutcliffe V, Richard O, Van Hove M and Maex K 2004 MRS **812**, F.1.5.1-F.1.5.6

Tőkei Zs, Van Aelst J, Waldfried C, Escorcia O, Roussel P, Richard O, Travaly Y, Beyer G P and Maex K 2005 Proc. IRPS, in press

Measurement of field-emission properties of a single crystal silicon emitter using scanning electron microscopy

T C Cheng, H T Hsueh, W J Huang, M N Chang, J S Wu[1] and S C Kung[2]

National Nano Devices Laboratories,1001-1 Ta-Hsueh Road, Hsinchu, Taiwan, 30050, ROC
[1] National Chaio Tung University, Hsinchu, Taiwan 30010, ROC
[2] Industrial Technology Research Institute[3], Chung Hsing Rd., Chutung, Hsinchu, Taiwan, ROC

ABSTRACT: Comparison of field emission properties between a single crystal silicon emitter and a silicon emitter array are investigated in this letter by utilizing scanning electron microscopy (SEM) and a small tungsten probe having an apex radius of approximately 90nm. The interelectrode distance is controlled to within tens of nanometers. The measured I-V data, fitted using the Fowler-Nordheim model, revealed that the turn-on field of an individual emitter is much higher than that of an emitter array consisting of 288 nearly identical emitters. This observation is further supported by a simplified electric-field calculation. Experimental results also indicate that the anode area may be an important factor of in determining field emission.

1. INTRODUCTION

The field-emission properties have been studied intensively for various materials in the past decade, in which performance was found to strongly depend on the inherent morphology (Ng et al 2002) and the density of materials (Nillson et al 2000), to name only a few. Materials used for electron emission, such as diamond, diamond like carbon (DLC) and carbon nanotubes (CNTs) on a silicon wafer, have been demonstrated for possible commercial applications (Brodie and Spindt 1992). Therefore, electron emission based on silicon materials is also of great importance due to the advantage in integrating silicon-based vacuum microelectronics and silicon integrated circuit technology.

Several commercial applications have been proposed using the field emission phenomenon such as field emission displays, microwave power devices and the electron gun in various visualization equipments (Spindt et al 1976). Past studies found that the emission characteristics of field emitters depend on tip sharpness, emitter material, aspect ratio of tip and surface conditions (Temple 1999). Many field-emission measurement techniques have been developed to deal with different applications. For example, Gangloff et al (2004) used a metal-ball anode (250μm in diameter) to measure the self-aligned, gate arrays of individual nanotube and nanowire emitters. Bonard et al (2002) measured the field emission of an individual carbon nanotube using SEM, and found that both the geometry of the carbon nanotube and electrode distance between the carbon nanotube and anode are the important factors for field emission. In addition, results from these studies also showed that the density of emitters determines the performance of emission devices. However, the measured field-emission properties often result from a specific area of CNTs or a bundle of carbon nanofibers (CNFs), mainly because the uniformity of carbon nanotubes is difficult to control in practice and the anode area is much larger than the actual emitting areas of CNT tubes. To understand the mechanism for emission with a particular anode, it is interesting to measure the field-emission relationship between total emission area and a single emitter. In this letter, a silicon nanotip array that is much easier to control in terms of its uniformity and geometry is used as the emitter for the measurement of field-emission properties using scanning electron microscopy.

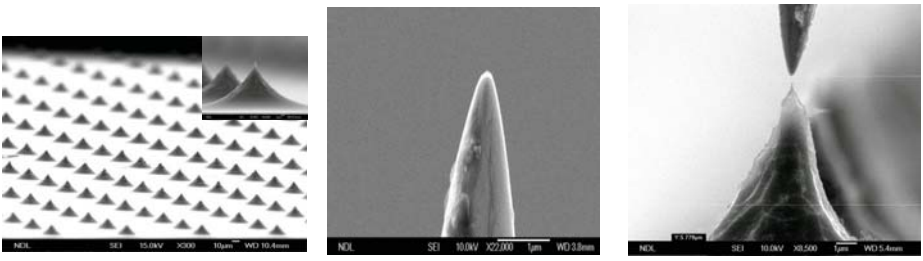
2. EXPERIMENTS

The emitter array is fabricated by ICP dry plasma etching with a three-step procedure. First, after an RCA clean, a 10μm circular AZ4620 photoresist mask is patterned by anisotropic etching to produce high aspect ratio circular rods (25μm height). Etching was carried out in a commercial vertical reactor (Oxford plasma Lab 100) using a mixture of SF_6 and O_2 with higher RF power because of higher ion bombardment. Second, isotropic etching, as shown in Fig. 1a, is used to produce sharp emitters by an undercutting effect under the mask with proper plasma control. In this procedure, a higher SF_6 concentration is necessary to make the isotropic etching by the chemical reaction between SF_6 and the silicon rods. Finally, the silicon tips are placed in a furnace for oxidation and then are removed by BOE wet etching to make the nanotip array. In addition, wet etching by BOE also ensures that there is no negative oxide layer on the surface of the nanotip. A negative oxide layer will degrade the field-emission performance and the reliability of the emitter (Chen and El-Gomati 1999), thus making the Fowler-Nordleim plot nonlinear (Huang 1996). Each emitter, as shown in Fig. 1b and purposely arranged in a periodic manner, has the same field enhancement factor, β, depending on the emitter geometry, which has the same contribution for emission current according to the Edgcombe relation,

$$\beta = 1.2(2.5 + \frac{h}{r})^{0.9} \quad (1)$$

where h and r represent the height of the emitter and radius at the apex, respectively.

To measure the field-emission properties of a single emitter, a tungsten probe is facbricated by electrolysis with KOH solution. First we cut the tungsten filament about 1cm in length and clip it on the anode of the electrobath. Second, we turn on the power supply with a certain power such that electrolysis occurs in the KOH electrobath. During this process, light emission occurs due to the reaction of the tungsten filament with the KOH solution. A nanotungsten probe can be formed once the light emission disappears. As shown in Fig. 1b, the diameter and apex radius of the tungsten anode was 1μm and 90nm, respectively. The concentration of the KOH solution is a key factor in forming a sharp tip.



(a) (b) (c)

Fig. 1. SEM images of (a) Si nanotip array after dry plasma etching with height of 20μm and (b) the image of tungsten anode in SEM instrument. (c) Field emission is measured by aligning the emitter apex and the anode apex for a small separation by SEM. The top tip is the tungsten anode and the lower tip is the Si emitter.

The single emitter was measured by a vacuum field emission apparatus, where the distance between the emitter and anode could be controlled within the accuracy of the order of a nanometre in the in-situ SEM image. The nanotungsten probe installed on a nanomotor is used as the anode for silicon tip. To align the emitter with the anode apex, we could first focus on the emitter apex and then drive the piezoelectric nanomotor to move the anode into the required position. Alignment is not considered to be correct until the apex of anode is clearly shown by real imaging of SEM. In this single emitter measurement, the electrode distance between these two apices is maintained as 46nm

throughout the study, unless otherwise specified. The applied voltage on the anode, with the substrate grounded, ranges from 0 to 250 volts, while the chamber pressure is maintained lower than 9.6×10^{-7} torr. In contrast, a corresponding experiment with large flat anode is done without SEM control. For this experiment, the distance between the anode and the sample is maintained at 50μm with a maximum applied voltage of 1000 volts.

3. RESULTS and CONCLUSION

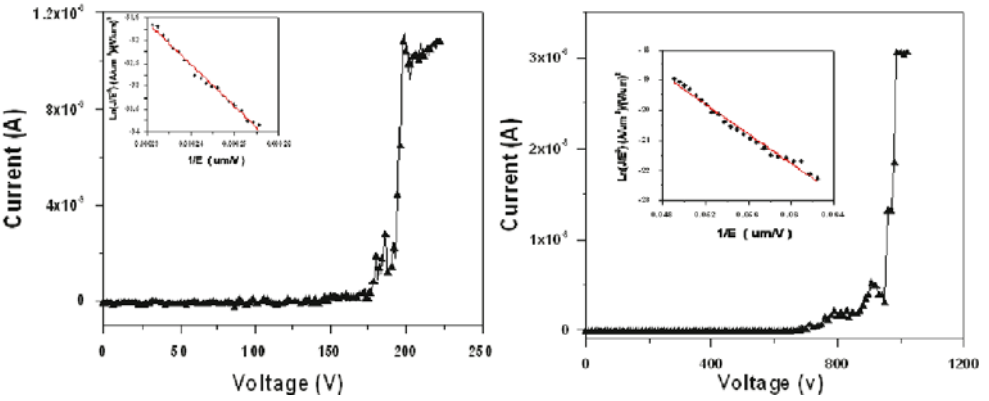
Typical results of electron field-emission properties of the single tungsten nanotip to single silicon emitter and flat plate to silicon emitter array (288 emitters) are illustrated, respectively, in Figs. 2a and 2b. Figure 2(a) shows the I-V characteristics of a single silicon emitter with the corresponding Fowler-Nordheim plot (FN plot) as the inset. The maximum voltage applied at the anode is constrained to be less than 250 volts because the high anode resistance results in the meltdown of the tungsten nanotip when higher voltage is applied. Emission current density is calculated using the cross section of the tungsten anode as the emission area and achieves Je as $10 nA/\mu m^2$, under 3913V/μm applied field which is close to the result analyzed using the Fowler-Nordheim model (FN model) as 4039 V/μm. Furthermore, in the current case, the FN plot can be written as

$$FN \quad plot = \frac{-6.44 \times 10^9 \phi^{1.5}}{\beta} \tag{2}$$

where ϕ is 4.52eV as the work function of the silicon emitter and β is the field enhancement factor. As shown in equation (2), using a typical value encountered for a silicon emitter, one obtains a field enhancement factor of 1.3. In addition, the emission properties of corresponding experiment using a large flat anode are shown in Fig. 2b with the associated FN plot as the inset. The turn-on field for emission of the silicon emitters is about 16 V/μm from the direct calculation and is very close to the 15 V/μm from the FN model. The resulting fitted value of field enhancement factor from the FN plot is β=386. By comparing these two experiments, the turn-on field of a single emitter using a tungsten nanotip is extraordinarily higher than that of the emitter array using large plate anode.

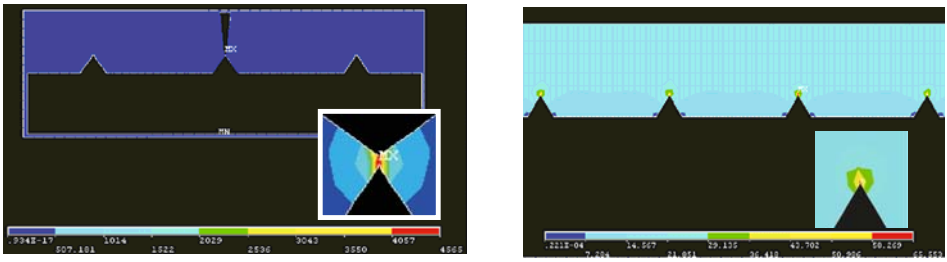
To further understand the experimental findings, simplified two-dimensional electrostatic fields are simulated, respectively, for the two configurations we are interested in. Resulting distributions of electrostatic field are shown in Fig. 3. In Fig. 3a, calculations show that the extraordinarily high field between the emitter and the tungsten anode is about 4057-4565V/μm. The distribution of the turn-on electric field (4039.1V/μm) is restricted and confined at a very small distance between the apexes of the emitter and anode. It is implied that the electrons are emitted from the silicon nanotip to the tungsten anode in a confined small region, which depends on the size of the vacuum gap between tip and anode. On the other hand, as shown in Fig. 3b, there exists a different distribution of electric field for the case of the silicon tip using large flat anode. As expected, the highest electric field occurs at the top of the each silicon emitter with a value of 58V/μm. It is clearly shown that most of the average field between emitters and flat anode is in the range of 14~16V/μm. According to the experimental result as shown in Fig. 2b, the electrons can be emitted from the silicon emitters if the local electrostatic field is greater than the turn-on field (15 V/μm). The simulation results indicate that the emission current measured from the flat anode results from the contribution of all silicon emitters. It is interesting to note that the emission phenomenon not only depends on the density and geometry of the emitters (Nillson et al 2000) but also depends on the geometry of the anode because it can change the distribution of the electrostatic field.

In summary, the turn-on field emission behavior of a single emitter is revealed by utilizing scanning electron microscopy with a tungsten nanotip anode. Comparing the experimental and calculated results, the turn-on field analyzed by the Fowler-Nordheim model is similar to the calculated results with a large flat anode and a nano-tungsten anode. By following the FN law, the extracted field enhancement factor for a single silicon emitter measurement is low when compared with that obtained using a large plate anode. In addition, it is important to point out that the field emission performance is also affected by the geometry of the anode.



(a) (b)

Fig. 2. Field emission behavior of (a)a single emitter for distance 46nm between the emitter and the sharp anode. Analysis using Fowler-Nordheim model shown in the inset indicates the emitter can be turned on at [that the turned-on field is estimated as E_0= 4065 V/μm. (3913.043) (b)the result of average measurement with distance 50μm between the emitters and the flat anode. The turned-on field analyzing from the inset graph is estimated as 11.7 V/μm.



(a) (b)

Fig. 3. Simulated results of the electrostatic field between the silicon emitter and (a) tungsten nano anode, (b) large flat anode.

REFERENCES

Bonard J M, Dean K A, Coll B F and Klinke C 2002 Phys. Rev. Lett. **89**, 197602
Brodie I and Spindt C A 1992 Adv. Electron. Electron Phys. **83**, 1
Chen L and El-Gomati M M 1999 Ultramicroscopy **79**, 135
Gangloff L, Minoux E and Teo K 2004 Nano Lett**. 4**, 1575
Huang Q A 1996 Appl. Surf. Sci. **93**, 77
Ng K L, Yuan J, Cheung J T and Cheah K W 2002 Solid State Commun. **123**, 205
Nillson L, Groening O, Emmenegger C and Schlapbach L 2000 Appl. Phys. Lett. **76**, 2071
Spindt C A, et al 1976 J. Appl. Phys. **47**, 5248
Temple D 1999 Mater. Sci. Eng. Rept. **24**, 185

Efficient, room-temperature, near-band gap luminescence by gettering in ion implanted silicon

D J Stowe, K J Fraser, S A Galloway[1], S Senkader, R J Falster[2] and P R Wilshaw

Department of Materials, University of Oxford, Parks Road, Oxford, OX1 3PH, UK
[1] Gatan UK, Ferrymills 3, Osney Mead, Oxford, OX2 0ES, UK
[2] MEMC Electronic Materials SpA, viale Gherzi 31, 28100 Novara, Italy

ABSTRACT: The production of dislocations by boron or silicon ion implantation followed by a short, high temperature anneal is found to greatly enhance near-band edge cathodoluminescence at room temperature. A strong luminescence peak at ~1154nm is observed. This luminescence is independent of the presence of a p-n junction and persists if the dislocations are removed by chemical etching at room temperature. We propose that the enhanced luminescence is due to the dislocations acting as gettering centres during the anneal step resulting in material with a lower concentration of non-radiative recombination centres than the as-grown wafers.

1. INTRODUCTION

Silicon is the material of choice for most microelectronics applications. This technology is currently approaching a bottleneck where the speed and complexity of inter-device communication will become the limiting factor in overall performance and ease of manufacture. To enable continued performance improvement, optical interconnects between devices have been proposed to replace electronic ones (Pavesi 2003, Forchel and Malinverni 1998). However, the indirect band gap nature of silicon makes it a poor optical emitter. A number of approaches to improving the luminescence efficiency of silicon are under investigation, including quantum confinement (Canham 1990), suppression of non-radiative recombination paths (Green et al 2001), inclusion of radiative centres (Zheng et al 1994) and Raman scattering (Rong et al 2005).

Recent work by Ng et al (2001) has shown that the introduction of dislocation loops and a p-n junction into n-doped silicon via boron ion implantation and high-temperature annealing can significantly improve luminescence efficiency at room temperature. The mechanism proposed was spatial confinement of carriers between the dislocations and the p-n junction, resulting in reduced opportunity for non-radiative recombination and thus enhanced radiative recombination and light emission. However, other, later work (Stowe et al 2003) indicated that enhancement of luminescence efficiency still occurred when the ion implantation did not introduce a p-n junction and it was suggested that the cause for the enhanced luminescence was radiative recombination at the dislocations themselves. The present work investigates further the relationship between dislocations in silicon and the enhanced room temperature luminescence efficiency.

2. EXPERIMENTAL

The wafers used in this work were made by the Czochralski process, both n- and p-type (doped with phosphorus and boron respectively) with resistivity of 5-10Ωcm. Boron or silicon ions were implanted into the polished surface of the samples which were subsequently annealed at 900^{o}C for 10 minutes (Si samples) or 15 minutes (B samples). Boron implantation was carried out at 30keV, silicon at 80keV. Four distinct sample sets were created: “nB” - boron implanted into n-type material (producing dislocations in a highly doped region with a p-n junction), “pB” - boron implanted into p-

type material (dislocations present in a highly-doped region but with no p-n junction) and “nSi” and “pSi” - silicon implanted into both n- and p-type material (dislocations present in a moderately-doped region without a p-n junction).

To investigate the effect on luminescence of thermally removing the dislocations, some pieces of samples from categories pB, nB, pSi and a control sample were further annealed at 1150^{o}C for 5 minutes. This was carried out in sealed and evacuated silica tubes to minimize contamination. After initial cathodoluminescence (CL) examination other samples were given a planar etch in an HF/HNO_3 mixture to remove the dislocations chemically, then re-examined.

CL examination was carried out at room temperature using a Gatan MonoCL3 system and a liquid-nitrogen-cooled germanium Northcoast E0-817L detector attached to a JEOL 6500F scanning electron microscope. Samples prepared by ion milling with an Ar+ high energy beam were also examined using a Philips CM20 transmission electron microscope. A more detailed account of this work will be published elsewhere.

3. RESULTS AND DISCUSSION

Defects caused by ion implantation coalesce on annealing to form dislocation loops. These can be seen in TEM images. Fig. 1a shows a cross-sectional view of the layer of dislocation loops ~200nm below the implantation surface of a sample and Fig. 1b is a plan view of the dislocation loops in a different sample.

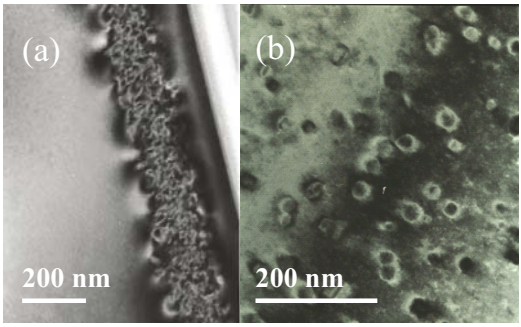


Fig. 1: Bright field TEM images of dislocation loops introduced by ion implantation; a) cross-sectional view of B+ implanted sample, dose $1x10^{16}$ cm^{-2}, b) plan view of Si+ implanted sample, dose $1x10^{15}$ cm^{-2}.

Cathodoluminescence spectra taken at a probe current of 200nA and an accelerating voltage of 30kV are shown in Fig. 2. In all cases, a large peak is observed at a wavelength of ~1154nm. No significant luminescence was observed at other wavelengths within the sensitivity of the detector (wavelengths shorter than 1600nm). Un-implanted, as-grown, control specimens show a negligible signal under the same conditions. Fig. 2a shows the effect on the luminescence intensity of increasing the ion implantation dose, and hence the dislocation density produced, while keeping other variables the same. There is a clear increase in intensity with dose, though the dependence is not linear. Fig. 2b shows two boron-implanted specimens with different substrates (so that one contains a p-n junction and the other does not) displaying comparable peak luminescence intensities. This indicates that the presence of a p-n junction is not required for the enhanced luminescence effect to occur. Using the detector sensitivity and collection efficiency of the CL system as specified by the manufacturer, the external quantum efficiency of nB and pB samples examined is found to be of the order of 5 $x10^{-6}$. This is lower than reported by Ng et al (2001), but is much higher than that observed in as-grown material. Our lower obtained efficiency is attributed to the greater degree of surface recombination taking place in cathodoluminescence compared to electroluminescence.

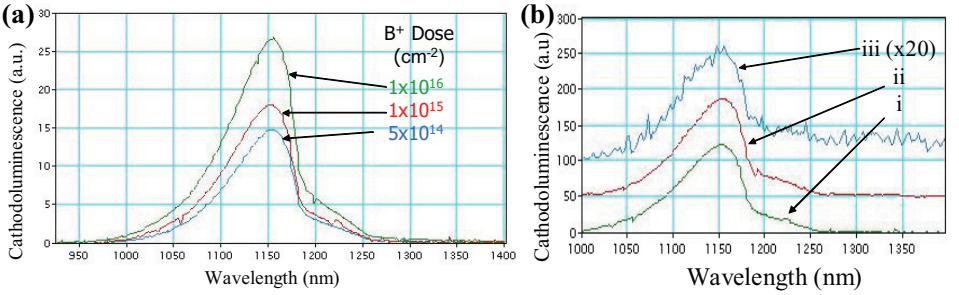


Fig. 2: Room temperature cathodoluminescence spectra; accelerating voltage = 30kV, probe current = 200nA; a) B^+ implanted specimens of dose $5x10^{14}$ cm^{-2}, $1x10^{15}$ cm^{-2} and $1x10^{16}$ cm^{-2}, b) i) B^+ implanted specimen dose $1x10^{16}$ cm^{-2} with a *p-n* junction, ii) B^+ implanted specimen dose $1x10^{16}$ cm^{-2}, no *p-n* junction, iii) Si^+ dose $1x10^{15}$ cm^{-2} specimen, *p*-type wafer. For clarity, curves ii) and iii) are displaced along the y-axis by 50 and 100 units respectively.

When the dislocations are removed by high temperature annealing, the room temperature luminescence intensity becomes negligible again, comparable to as-grown wafers. However, when the dislocations, which are in a band approximately 0.3μm below the specimen surface, are removed by chemical etching at room temperature, the effect on the luminescence is different. Fig. 3 shows the panchromatic luminescence intensity obtained from boron- and silicon-implanted samples as a function of the thickness of material removed by etching. Note that due to etch pitting it was not possible to obtain data from boron-implanted samples with less than 20μm removed. The enhanced luminescence effect does not disappear when the material containing the dislocations is removed in this way – indeed, the obtained intensity increases when the top surface layer is removed and then gradually decreases as more material is etched away. This disproves the suggestion that the enhanced luminescence is produced directly by the dislocations themselves and shows that the increased luminescence efficiency extends a considerable depth into the wafers.

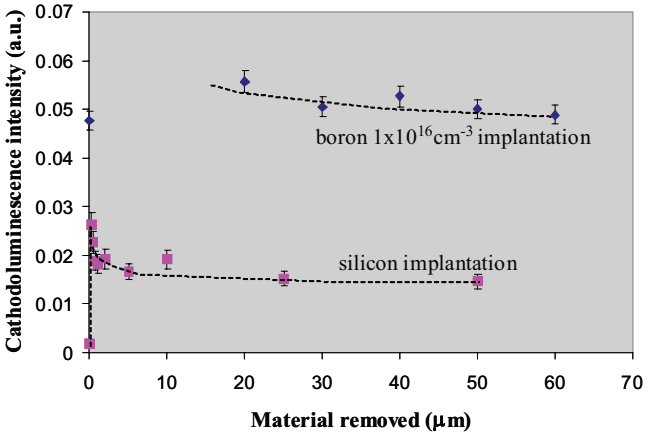


Fig. 3: Panchromatic cathodoluminescence efficiency as a function of the carrier generation concentration for a boron and silicon implanted specimen. Accelerating voltage used is 30kV.

These results show that the dislocations themselves are not directly responsible for the enhanced room temperature luminescence which we observe and the results are consistent with the proposal of Sobolev et al (2004), who studied similar material, that the dislocation loops formed during the post-implantation anneal act as gettering centres for transition metal impurities in the

silicon. These impurities, when present in the bulk, produce deep electronic levels which act as strong non-radiative recombination centres (with behaviour described by the Shockley-Read-Hall equation). By removing them, the non-radiative lifetime is increased. Consequently the efficiency of band-to-band radiative recombination increases.

The present results can be explained as follows: When the surface region of the material is removed by chemical etching, the dislocations and their decorating impurities are removed and because the process is carried out at room temperature there is no possibility for new impurities to be introduced. Thus the concentration of deep levels in the bulk material remains low, even in the absence of dislocations, and the luminescence enhancement is retained. However, when the dislocations are removed by annealing at 1150°C their gettering action is lost whilst the impurity atoms remain in the material. Thus, on cooling, a substantial metal impurity concentration is again present in the bulk and the radiative recombination enhancement, originally produced by the dislocations, is removed.

The weak dependence on ion implantation dose (i.e. dislocation density) of the luminescence intensity is also explained: a greater number of gettering sites allow for the removal of more impurity atoms, and hence a further reduction in the non-radiative recombination rate.

4. CONCLUSIONS

We have shown that the production of dislocations in silicon by ion implantation with either B or Si followed by an anneal at 900°C gives rise to an enhanced room temperature luminescence efficiency that does not depend on the presence of a p-n junction. Further we have shown that this effect is not directly due to the dislocations since the enhanced luminescence efficiency persists even when the dislocations have been entirely removed by chemical etching. These results, together with those obtained by removing the dislocations by a further anneal at 1150°C, support the proposal by Sobolev et al (2004) that the effect is due to the dislocations acting as gettering centres for transition metal impurities. The removal of these metal impurities leads to a reduction in non-radiative recombination and a corresponding increase in radiative recombination. This process enables relatively efficient luminescence to be obtained from silicon even at room temperature.

ACKNOWLEDGEMENTS

The authors would like to thank Oliver Krause and Peter Pichler for performing the ion implantation and anneals used in this study. This work was supported by an EPSRC grant.

REFERENCES

Canham L T 1990 Appl. Phys. Lett. **57**, 1046

Forchel A and Malinverni P (Editors) 1998 European Commission Technology Roadmap - Optoelectronic Interconnects for Integrated Circuits (Office for Official Publications of the European Communities, Luxembourg)

Green M A, Zhao J, Wang A, Reece P J and Gal M 2001 Nature **412**, 805

Ng W L, Lourenço M A, Gwilliam R M, Ledain S, Shao G and Homewood K P 2001 Nature **410**, 192

Pavesi L 2003 J. Phys.: Condens. Matter **15**, R1169

Rong H, Liu A, Jones R, Cohen O, Hak D, Nicolaescu R, Fang A and Pannica M 2005 Nature **433**, 292

Sobolev N A, Emel'yanov A M, Shek E I and Vdovin V I 2004 Solid State Phenomena **95-96**, 283

Stowe D J, Galloway S A, Senkader S, Mallik K, Falster R J and Wilshaw P R 2003 Physica B **340**, 710

Zheng B, Michel J, Ren F Y G, Kimerling L C, Jacobson D C and Poate J M 1994 Appl. Phys. Lett. **64**, 2842

On the mechanism of {113}-defect formation in Si

L I Fedina, S A Song[1], A L Chuvilin[2], A K Gutakovskii and A V Latyshev

Institute of Semiconductor Physics, 630090, pr. Lavrentjeva 13, Novosibirsk, Russia
[1] Samsung Advanced Institute of Technology, POB 111 Suwon, 440-600, Korea
[2] University Ulm, Albert-Einstein Allee 11, D-89081 Ulm, Germany

ABSTRACT: The initial stage of {113} defect formation includes self-ordering of <110>-split interstitial-vacancy (IV) pairs in the <332> directions within doubled nearest neighbour atomic chains in {113} planes accompanied by split axis alignment along those chains. The next stage includes 90° reorientation of split-interstitials followed by planar four-fold coordinated defects (FFCDs) formed on parallel {110} planes perpendicular to the chains accumulating IV pairs. The overlap of closely-adjacent FFCDs further creates large channels along <110> axes for the building of interstitial chains on {113}.

1. INTRODUCTION

The equilibrium structure of {113} defects introduced by electron irradiation at T=450°C has already been established by Takeda et al (1994); however, the mechanism for interstitial chain formation on {113} planes is still unclear. *Ab initio* calculations propose only compact configurations of interstitial clusters (Kim et al 2000). Recently, a new four-fold coordinated point defect (FFCD) corresponding to a close-bonded IV pair was proposed as a building block for more extended defects (Goedecker et al 2002). According to tight-binding molecular dynamics (TBMD) the IV pair is stable at room temperature due to an energy barrier for its recombination of 1.2eV (Tang et al 1997). In fact, we have already shown by using *in situ* HVEM (JEOL-1250, 1MeV) and HREM (JEOL-4000EX, 400keV) irradiations that at T=20-350°C self-interstitials and vacancies in Si aggregate together on {113} planes (Fedina et al 1997, 1998, 1999). However, the combined clustering of point defects in thick irradiated specimens leads to an amorphous phase on {113} planes partly transforming into an equilibrium structure, so that the clear mechanism eludes observation. Here we present the *in situ* HREM study of {113} defect evolution in a very thin Si sample at room temperature.

2. EXPERIMENTAL

The investigations were carried out with a JEOL-4000EX operated at 400keV. TEM specimens were prepared by chemical etching of (110) Fz-Si wafers implanted with boron ions of a high dose followed by thermal annealing at T=1150°C. The high boron concentration was necessary to increase the nucleation of clusters in a very thin TEM sample (Aseev et al 1994). Simulations of HREM images were performed with the multislice program MUSLI (Chuvilin and Kaizer 2005). Various defect structures were constructed within a 43Å x 42Å x 42Å supercell of Si and optimized by Mm^+ force field (HyperChem program). The differences between bond lengths of single defect configurations in our optimized models and ones obtained by *ab initio* calculations (Al-Mushadani and Needs 2003) were within 0.1Å for the case of the <110>-split interstitial and FFCD. For the case of the vacancy, optimization results in a strong inward relaxation (0.5Å), which is, in fact, no more than 0.2-0.4Å according to first-principle calculations (Ogut and Chelikovsky 2001, Al-Mushadani and Needs 2003). We will show later that the best fit between experimental and simulated images is obtained by modeling not including the relaxation of vacancies.

3. RESULTS AND DISCUSSION

Figures 1 a, b, c, d present experimental [110] HREM images of one and the same {113} defect with corresponding models superimposed with images taken after 5 (a, b) and 15 (c, d) minutes of irradiation. In Figs.1a, b the defect is represented only by local variations of the length of columns. In Figs.2c, d the defect becomes broader and obtains the features of equilibrium structure. The left part of the final {113} defect is disturbed by a gliding 60° dislocation, therefore we will further consider only the right part having a clear atomic structure. Images are obtained from very thin crystal (<50 Å) close to Sherzer focus and thus allow straightforward interpretation (Spence 1981): white spots correspond to channels in the Si lattice viewed in the [110] direction and dark ones correspond to the projection of [110] atomic chains on (110) plane. At the initial stage {113} defect appears to form a sequence of doubled

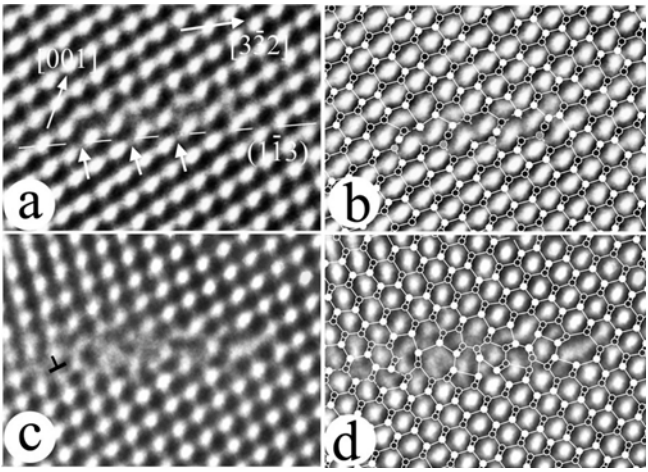


Fig. 1. Evolution of {113} defect structure during *in situ* HREM irradiation: 5 (a, b) and 15 (c, d) minutes. c, d) experimental models super-imposed with HREM images. Flux of electrons is about 10^{20} electrons/cm^2 s^1.

nearest neighbour columns located in the (113) plane, one of which is elongated and the second one is shortened in the [001] direction (see Fig.1). The column length deviation in both cases reaches to about 40% in comparison to the columns of the perfect crystal. Such localized variations strongly suggest an accumulation of opposite type point defects within the nearest neighbour [110] atomic chains in the form of close-spaced IV pairs. According to first principle calculations, the most stable structure of neutral self-interstitial atom is the split-<110 > configuration (Gharaibeh et al 2001). The centre of the split is shifted by 0.7Å in <100> direction, thus extending to about 50% the {110}-projection of atomic chain along which the split axis is oriented. Note, that chain's atoms in {110} projection are distanced by 1.34Å. This agrees well with 40% column extension in the [001] direction detected by HREM. Therefore, we conclude that experimental column extension is introduced by axial orientation of split-interstitial along [110] atomic chain accumulating interstitials. On the contrary, a vacancy leads to shortening of the atomic chain projection on (110). However, single point defects cannot be detected by HREM within a reasonable specimen thickness. So, we should associate column length deviations with multiple point defects aligned along neighbouring [110] atomic chains.

We have constructed several models with a different distance between IV pairs placed along [110] neighbouring chains in second neighbour positions. We have found that it is not possible to create split-configurations at the distance 3.84Å with [110] split axis orientation. After Mm$^+$ force field optimization the length of the split reaches 2.43Å similar to the value of 2.432Å found by first principles calculations (Al-Mushadani and Needs 2003) leaving only 1.4Å between split-configurations. This model seems to be not realistic from physical point of view (model not shown). The model of defect chains with the distance of 7.68Å between IV pairs viewed along chains and end-on is shown in Fig.2 a, b. Simulated HREM images of this model including various relaxation modes of vacancies are presented in Fig.2 c-e in comparison with experimental image of {113} defect in initial stage. The best fit of experimental and simulated images is obtained by using the model with non-relaxed vacancies. One can conclude that HREM image is not sensitive to small real relaxation around vacancies. If the distance between IV pairs reaches 15.36Å, they are practically not seen by HREM (few% of column length deviations, image not shown). It may mean that to visualize 40% column length deviations by HREM, the distance between IV pairs should be no more than 7.68Å.

There seems to be only one reason for ordered aggregation of point defects on {113} plane, which is based on self-ordering of point defects driven by their non-isotropic strain fields. But calculation of strain fields even for a single IV pair needs both a large supercell and *ab initio* methods. These data do not exist in the literature. Electron-paramagnetic-resonance studies have shown that the vacancy has D_{2d}

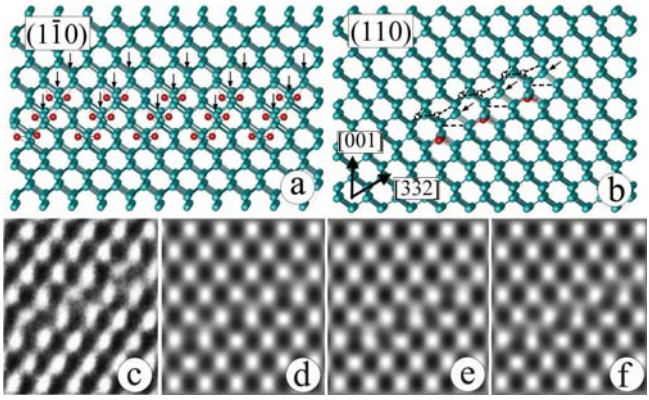


Fig. 2. {113} defect at the initial stage viewed along defect chains (a) and end-on (b). Dark balls are [110]-split-interstitials. Arrows show vacancies. Broken lines in b) present the way of IV pair transformation to FFCDs (see the text). c-f) experimental HREM image (c) in comparison with simulated ones (defocus -360Å) obtained by this model including various modes of vacancy relaxation: d) non-relaxed; e) no bonding; f) fully bonded.

symmetry, which is consistent with Jahn-Teller distortion (Watkins 1976). Low symmetry of both point defect configurations suggests the possibility of strain field compensation by close location of point defects. As a result close-spaced IV pairs become very stable and can be visualized by HREM.

At the next stage, a clear broadening of {113} defect develops on the (110) plane perpendicular to the direction of chains accumulating IV pairs (Figs. 1c, d). The position of five- and seven-fold rings at the right edge of {113} defect corresponds to the model of single FFCD proposed by TBMD simulation (Tang et al 1997). According to this simulation, the reason for FFCD formation instead of IV annihilation is the local distortion around the split-interstitial induced by the close approach to the vacancy. Spontaneous recombination occurs only for V-I pairs separated by first and second nearest-neighbour point defect distances along the split axis. In all other directions corresponding to non axial locations of vacancy, FFCD should form upon their close contact. These TBMD results are in excellent agreement with the HREM observation of IV pair transformation to FFCDs.

The schematic way of FFCD formation is shown by broken lines in Fig. 2b and the optimized model is presented in Figs. 3a, b. Transformation of an IV pair includes one jump of an interstitial to the nearest atomic chain followed by 90° reorientation of its split's axis. This is necessary to create planar FFCD on (110). After such reorientation one of two (upper) five-fold rings of FFCD corresponding to a single IV pair should form. Second (bottom) a five-fold ring of an FFCD is created due to atomic bonding around a vacancy. Between these five-fold rings two seven-fold rings belonging to a single FFCD should appear in the [3-32] direction to form the (1-13) defect plane. However, closely-adjacent IV pairs create the number of overlapped seven-fold rings in the [3-32] direction on {110} plane. Note, that initially IV pairs are distanced by 7.68Å in the [110] direction. Reorientation of distanced split-interstitials under FFCD formation allows an additional IV pair to be inserted between FFCDs as is also shown in the model in Figs. 3a, b. From comparison of the simulated model HREM image with the experimental one, we conclude that FFCDs distanced at 7.68Å are not visualized by HREM, only the distanced IV pairs are well detected (see Fig. 3g, h). Transformation of additional IV pairs produces FFCDs distanced by 3.84Å, thus leading to an appearance of eight-fold rings for building of interstitial chains (see Figs. 3 c, d). In this case the simulated HREM image in Fig. 3i corresponds well to the experimental one in the final stage (Fig. 3g). Note that, in this model, left and right interstitial chains inserted into eight-fold rings are different. The left one consists of six atoms and the right one of eight atoms providing different contrast of interstitial chains. The final model of equilibrium structure of {113} defect shown in Figs. 3 e, f is created by FFCDs location exactly at each (110) plane. The HREM image simulated using this model agrees well with the one observed by Takeda (1994) for small {113} defect (in his PEIIEP notation) introduced by 2MeV irradiation at T=450°C (see Fig. 3j). Such an image of {113} defect is not realized during 15 minutes of HREM irradiation at room temperature.

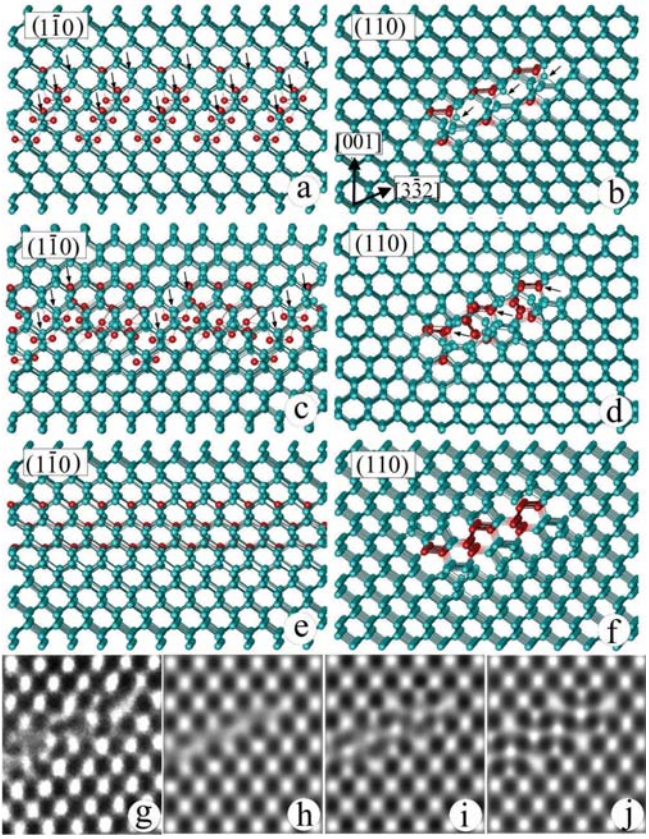


Fig. 3. a, b) The {113} defect as a mix of FFCDs and IV pairs viewed along defect chains (a) and end-on (b); c, d) model with increased number of FFCDs and interstitial chains inside eight-fold rings; e, f) equilibrium structure. Dark balls are interstitials. Arrows show vacancies; g, h, i, j) the experimental (g) and simulated HREM images (defocus -360Å) of the {113} defect obtained by models b, d, f, respectively.

4. CONCLUSIONS

Finally, we conclude that the mechanism of {113} defect formation is based on self-ordering of IV pairs in <332> directions within doubled nearest neighbour atomic chains on {113} accompanied with split alignment along chains. Axial orientation of <110>-split-interstitials does not allow them to be placed with a distance less than 7.68Å. The next step of {113} defect evolution includes 90° reorientation of split-interstitials followed by planar FFCD formation on {110} planes perpendicular to chains accumulating IV pairs. This allows an additional IV pair to be inserted to form parallel FFCDs at each (110) plane. Closely set IV pairs on {113} transform to overlapped FFCDs providing an appearance of eight-fold rings on the defect plane. Large channels become the sites for an additional insertion of supersaturated interstitials. As a result perfect interstitial chains are built on {113} plane to create the equilibrium structure.

REFERENCES

Al-Mushadani O K and Needs R J 2003 Phys. Rev. B **68,** 235205
Aseev A, Fedina L, Hoehl D and Barsch H 1994 Clusters of Interstitial atoms in Silicon and Germanium (Berlin, Academy Verlag) p.59
Chuvilin A and Kaizer U 2005 Ultramicroscopy **104**, 73
Fedina L, Gutakovskii A, Aseev A, Van Landuyt J and Vanhellemont J 1997 In situ Microscopy in Material Research (Dordrecht, Kluwer) ch 4
Fedina L, Gutakovskii A, Aseev A, Van Landuyt J and Vanhellemont J 1998 Phil. Mag. A **77**, 423
Fedina L, Gutakovskii A, Aseev A, Van Landuyt J and Vanhellemont J 1999 Phys. Stat. Sol. (a) **171**, 147
Gharaibeh M, Esreicher S K, Fedders P A and Ordejon P 2001 Phys. Rev. B **64**, 235211
Goedecker S, Deutsch T and Billard 2002 Phys. Rev. Lett. **88**, 235501
Kim J, Kirchhoff F, Wilkins J and Khan FS 2000 Phys. Rev. Lett. **84**, 503
Ogut S and Chelikovsky J 2001 Phys. Rev. B **64**, 245206
Spence J C H 1981 Experimental high-resolution electron microscopy (Clarendon, Oxford), p.23
Tang M L, Colombo L J, Zhu J and de la Rubia T D 1997 Phys. Rev. B **55**, 14279
Takeda S, Kahyama M and Ibe K 1994 Phil. Mag. A **70**, 287
Watkins G D 1976 Defects and their structure in non metallic solids (Plenum, New-York) p.203

The evolution of low defect density structures in silicon-on-sapphire thin films during post-ion implantation heat treatments

W R McKenzie[1], H Domyo[2], T Ho[2] and P R Munroe[1]

[1]School of Materials Science and Engineering, University of New South Wales, Sydney, NSW 2052, Australia
[2]Peregrine Semiconductor Australia Pty Ltd, Homebush, NSW 2140 Australia

ABSTRACT: (100) silicon thin films grown on $(1\bar{1}02)$ sapphire substrates represent the most significant of the silicon-on-insulator technologies and have been used for many years in the production of integrated circuits. This paper presents a TEM study of the evolution of crystalline defects during the heat treatments designed to improve the quality of the films. Planar defects were found to be isolated to the outer surface of the films, whilst dislocations were abundant throughout. Defect density was considerably reduced by annealing at higher temperatures.

1. INTRODUCTION

Silicon-on-insulator technologies offer many advantages over conventional bulk silicon in the performance of integrated circuits (IC's). Silicon-on-sapphire (SOS) is the most mature and significant of these technologies and is currently being used in the production of high density IC's.

The crystalline defects in (100) silicon films on $(1\bar{1}02)$ sapphire substrates, grown by chemical vapour deposition (CVD), include planar defects lying parallel to {111} silicon planes, domain mis-orientation and misfit dislocations running approximately perpendicular to the sapphire interface.

Planar defects are believed to form as a result of stress in the film from a lattice mismatch between the silicon and sapphire (Ponce 1982). Domain mis-orientation dislocations, formed at the boundaries of (100) silicon domains, have been identified to form in the early stages of CVD processing (Abrahams et al 1976). Misfit dislocations are thought to form at the sapphire interface as a result of a lattice mismatch between the silicon and substrate (Ponce 1982). The lack of misfit dislocations has been speculated in many studies to be a result of an incoherent interface formed due to the high degree of freedom of Si-O bonds at the sapphire interface (Ponce 1982).

In the quest to make transistors smaller, faster and use less power, many advances have been made to the manufacture of SOS films in order to reduce the number of crystalline defects. The most important improvement made to as-grown SOS films was initially described by Lau et al (1979). This "improvement" process involves firing energetic silicon ions at the CVD silicon film to produce an amorphous layer to all but the outer surface of the silicon. The film is annealed to allow solid phase epitaxial regrowth from this remaining crystalline seed back towards the sapphire interface at ~550^{o}C. Once the recrystallisation is complete a higher temperature treatment is used to anneal out most remaining unstable defects (above 900^{o}C) leaving a film with a very low defect density.

It has been reported that the density of dislocations is not noticeably affected by the ion implantation and regrowth anneal (Carey et al 1983). The most important improvement to film quality is in the reduction in the number of planar defects. This has been predicted to be from overgrowth since the (100) silicon grows ~10 times faster than the {221} material in the planar defects, during regrowth at 550^{o}C (Amano and Carey 1981).

This paper takes a closer look at the improvement process by analysing samples at various stages of the ~550^{o}C regrowth anneal to investigate their defect structure using transmission electron microscopy (TEM). The aim of this work is to identify the source of the defects and methods of termination of the remaining defects in order to further improve the quality of the films.

2 EXPERIMENTAL PROCEDURE

Silicon on sapphire films were prepared by Peregrine Semiconductor Australia Pty Ltd. The process to fabricate the films, described by Amano and Carey (1981), was followed up until the first annealing stage. The specimens were heated in a nitrogen atmosphere to 550°C at a rate of approximatly 30°C/min. Samples were produced corresponding to annealing times of 0, 30 and 60 minutes at this temperature before being air-cooled. Other SOS specimens were examined including a CVD only film, a post ion implantation, and a fully processed (~550°C and >900°C anneals) film.

For each sample a cross-sectional TEM specimen was prepared using an FEI Nova 200 Nanolab focussed ion beam (FIB) instrument. This was done by way of the "lift-out" technique, details of which are given by Giannuzzi and Stevie (1997). This process involves milling and detaching a TEM foil from the bulk with the FIB then transferring the foil to a carbon coated copper TEM grid using a micromanipulator. TEM specimens were analysed with a 200kV Philips CM-200 TEM using a double tilt holder. For the sample annealed at 550°C, specimens were imaged using diffraction conditions to generate contrast from either the twins or the dislocations.

3. RESULTS AND DISCUSSION

Figure 1A shows the as-grown CVD silicon film with planar defects, parallel to {111} planes, it can be seen that they have a higher density closer to the sapphire-silicon interface. Figure 1B shows the structure following ion implantation; the region adjacent to the sapphire has become amorphous (a-Si), but the region furthest from that interface remains crystalline (c-Si), although heavily damaged. Figure 1C shows the remaining crystalline region that acts as a seed during re-growth, at an orientation that highlights the presence of residual planar defects in this area.

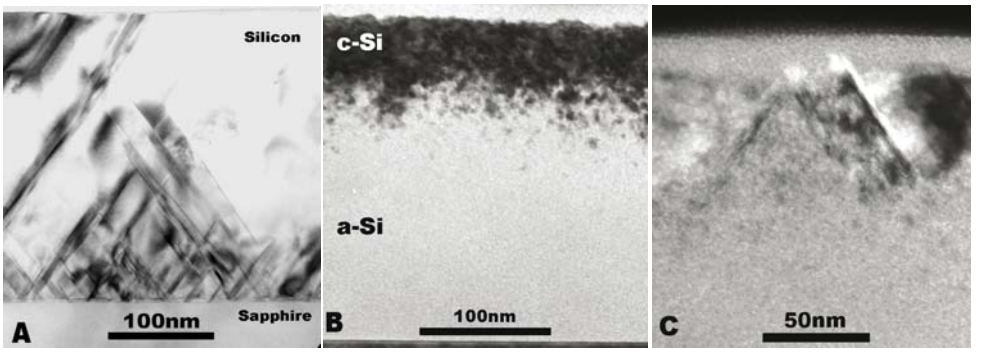


Fig. 1: Bright field TEM images of A) As-deposited CVD silicon showing the twin structure. B) the silicon film after the ion implant showing the crystalline (c-Si) and amorphous (a-Si) regions. C) The c-Si region shown in B tilted to diffraction conditions to highlight the presence of planar defects.

The regrowth of the crystalline silicon during post-implantation annealing can be seen in Fig. 2. The time each specimen was held at 550°C is indicated. For the 0 minute anneal (i.e. air-cooled immediately once 550°C is reached), approximately 2/3 of the silicon film is seen to have recrystallised with the boundary between the a-Si and c-Si moving as an interface towards the sapphire in a non-uniform manner. Presumably, this regowth occurred during the heating cycle to 550°C. At this point the planar defects appear to have almost completely regrown with the (100) Si, but have been terminated very close to this interface. After 30 minutes most of the crystalline silicon has regrown except for an isolated patch of a-Si remaining at the sapphire interface. It is only after 60 minutes that all the a-Si has recrystallised. It can be seen that the faults have not extended whilst the specimen is held at 550°C. These results suggest that the recrystallisation grows both (100) and {221} silicon at equal rates during heating to 550°C, where most re-crystallisation takes place. It is only at a

temperature of 550°C where the (100) silicon finally overgrows the {221} material, so that the planar faults are terminated.

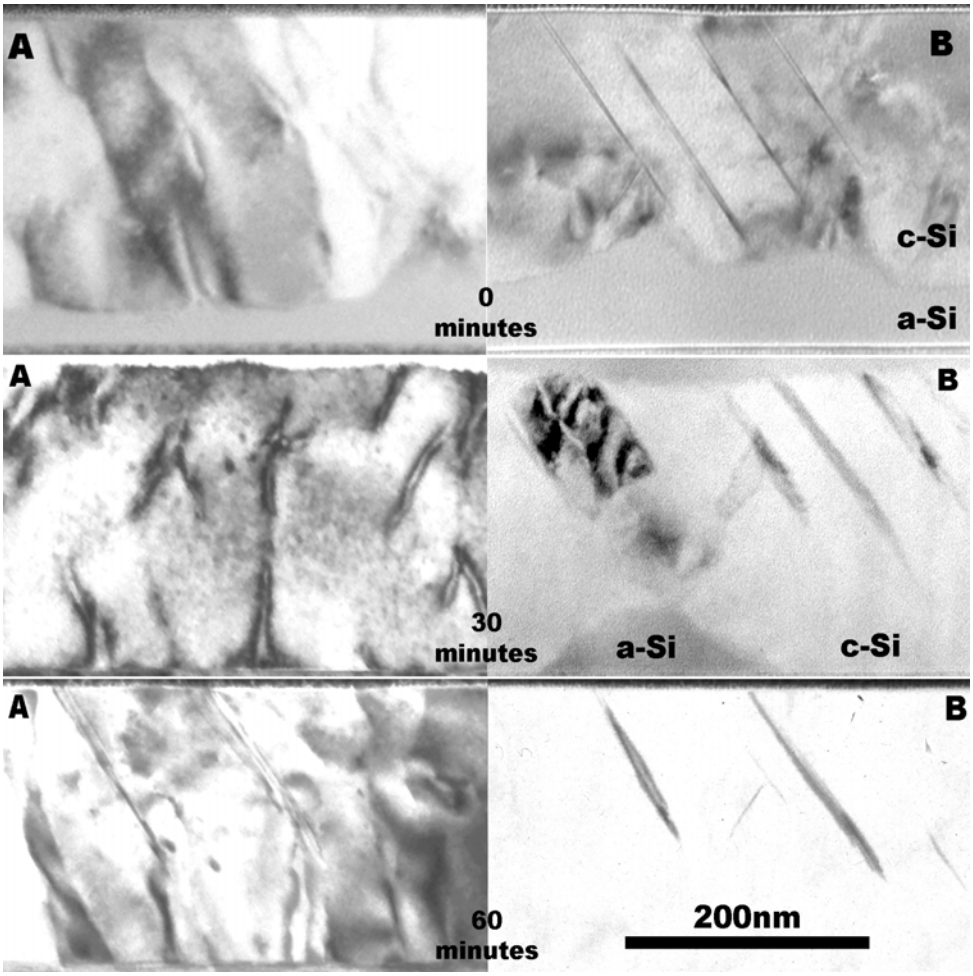


Fig. 2: Bright field TEM images taken with a beam orientation parallel to: A {200} plane to highlight dislocations, labeled "A", and a {111} plane to highlight planar faults, labeled "B". Annealing times for each sample at 550°C are indicated. All samples are of the same magnification.

Images in Fig. 2 labelled A were taken at orientations to emphasise dislocation contrast. They show the evolution of dislocations as a function of the re-growth of the crystalline silicon at this temperature. For the 0 minute sample dislocations appear as boundaries to areas of differing contrast indicating regions of slightly different crystallographic orientation. This suggests that these defects are domain mis-orientation dislocations. For the 30 and 60 minute anneal samples, dislocations, typically spaced 50-100nm apart, extend in an approximately perpendicular direction from the silicon-sapphire interface up towards the free surface. It is likely such defects are associated with the lattice misfit between the silicon and sapphire. These form to accommodate the lattice strains generated as the crystalline silicon approaches the sapphire.

After the final anneal above 900°C, seen in Fig. 3, all dislocations appear to have been removed

giving evidence supporting the theory that the flexibility of oxygen bonds at the interface accounts for some of the lattice mismatch previously forming the dislocations (Ponce 1982).

Prior to device processing, this outer silicon layer, containing most of the planar faults, is etched leaving a thinner film free of planar defects. Figure 3 shows this remaining layer in a film that has been subject to an additional heat treatment above 900°C. The remaining planar defect in this image is believed to be one of few extending through the entire film. The residual dislocation density is very low.

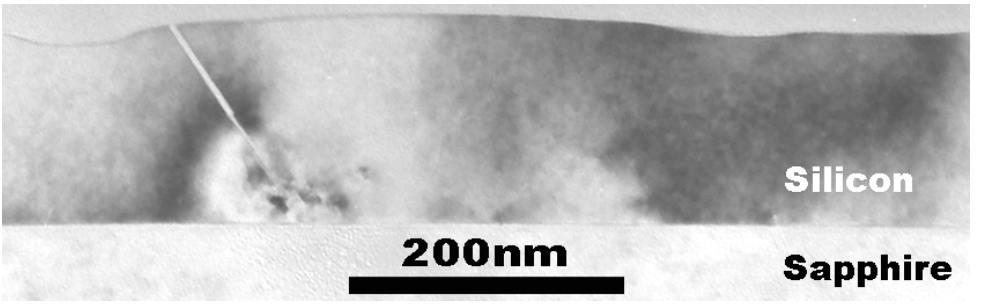


Fig. 3: Bright field TEM image showing the silicon film structure after completion of the improvement process showing a single planar defect.

4. CONCLUSIONS

The recrystallisation process and defect growth have been characterised as a function of annealing time for heat treatments carried out at 550°C as part of the improvement process used to reduce the defect density of silicon on sapphire thin films. The recrystallisation proceeds, nonuniformly, as an interfacial movement from the seed crystal towards the silicon-sapphire interface. Most regrowth occurred during the heating cycle to 550°C. However, the film was only seen to become fully crystalline after holding for 60 minutes at this temperature.

Planar defects in the regrown material originate from those remaining in the crystalline seed after the ion implant. These are seen to grow with the amorphous-crystalline interface towards the sapphire during heat-up, but their growth is limited by overgrowth of the (100) silicon once 550°C is reached.

Domain mis-orientation and lattice mismatch dislocations were present in the films processed at 550°C only. These appear to be removed during subsequent annealing above 900°C.

ACKNOWLEDGEMENTS

The authors wish to thank the Australian Research Council for the provision of funding and Associate Professor Michael Ferry for useful discussions.

REFERENCES

Abrahams M S, Buiocchi C J, Smith R T, Corboy J F Jr., Blanc J and Cullen G W 1976 J. Appl. Phys. **47**, 5139

Amano J and Carey K 1981 Appl. Phys. Lett. **39**, 163

Carey K W, Ponce F A, Amano J and Aranovich J 1983 J. Appl. Phys. **54**, 4414

Giannuzzi L A and Stevie F A 1999 Micron **30,** 197

Lau S S, Matteson S, Mayer J W, Revesz P, Gyulai J, Roth J, Sigmon T W and Cass T 1979 Appl. Phys. Lett. **34**, 76

Ponce F A 1982 Appl. Phys. Lett. **41**, 371

HREM study of an epitaxial growth defect

A Renard and B Domengès

LAMIP, Laboratoire de microélectronique ENSICAEN-PHILIPS, 2 rue de la Girafe, BP 5120, F-14079 Caen Cedex 5, France

ABSTRACT: A nanometre-scale epitaxial growth defect is characterized by HREM, thanks to the ability of focused ion beam technology to prepare electron transparent foils of site-specific structures. A nanometre-scale seed-like crystallite was localized at the interface between a substrate and its epitaxial layer. Microstructural characterization and chemical assessment led to the conclusion that it might be produced by the presence of residual chlorine at the surface of the silicon substrate during the epitaxial process, which would then induce polycrystalline growth.

1. INTRODUCTION

Though CVD epitaxial growth on silicon substrates is a well-known process, it can still give rise to problems. A typical epitaxial growth defect will be polycrystalline grains surrounded by stacking faults (Chew et al 1985) which must be differentiated from particles of crystal origin related to octahedral voids in silicon substrates (Vanhellemont et al 1997). The TEM technique, assisted by the FIB TEM sample preparation technique is a very helpful tool to analyse such localized defects. In the following case study, we present an HREM TEM study of such a growth defect formed during the silicon epitaxial process with boron doping.

2. EXPERIMENTAL

2.1 Epitaxy

The epitaxial growth is achieved in a chemical vapor deposition vertical cylinder reactor (radiantly heated « barrel » type) at high temperature, the reaction chamber being heated with a quartz IR lamp system. After an HCl surface etching step (about 100 nm etched) source gases, silicon tetrachloride with diborane for doping, are mixed and carried by a high flow of H_2 (200 L/min) during deposition, which is performed at atmospheric pressure at 1150 °C. The layer is grown on a P type substrate, <100> oriented, till a thickness of 12 µm is reached and exhibits a resistivity of 12 Ohm.cm.

2.2 Physical Failure Analysis Techniques

First optical inspection of the 5 inch wafers was made by a surface scanning laser defect counter (Surfscan) and showed a rough density of 0.24 defects per cm² (about thirty defects per wafer). Second, defective wafers were inspected by visible light microscopy.

Scanning Electron Microscopy was performed in an FEI XL40 S FEG equipped with the UHR through-the-lens detector and EDAX PHOENIX energy dispersive X-ray microanalysis system. Top views of the surface of epitaxial layer as well as localized cross-section views were obtained. In order to distinguish substrate from epitaxial layer, which are characterized by a strong difference in doping, Wright solution had to be used prior to SEM observation of cross-sections as a contrast enhancer.

Transmission electron microscopy was performed in a JEOL 2011 FEG electron microscope equipped with a high-resolution objective lens (C_s = 1 mm) and EDAX PHOENIX system. A thin sample lamella has been prepared in an FEI XP200 focussed ion beam miller, using the in-situ lift-off technique (Roberts 2001).

3. RESULTS

3.1 Optical Microscopy and SEM

Optical microscopy as well as SEM study emphasized the relationships of the defects and substrate main crystallographic axes. Indeed, square defects were observed, as large as 30µm x 30µm, and oriented parallel to the <110> substrate crystallographic direction (Fig. 1a). The top view SEM observation of the defect surface shows a square based pyramid-like morphology (Fig. 1b).

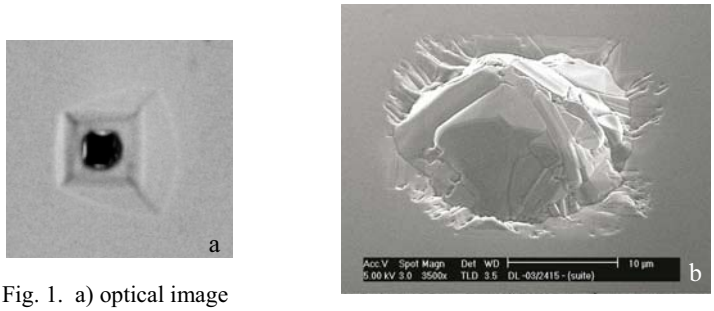


Fig. 1. a) optical image
b) top-view SEM image of the defect (tilted)

The rather large size of the defect allowed cross-section specimen preparation by the grinding-polishing technique. Nevertheless, their observation in the SEM without any chemical contrast enhancement did not allow any microstructural characterization. Once the latter had been carried out, SEM images clearly showed the interface between the epitaxial layer and the silicon substrate, also the polycrystalline structure of the defect was observed and it seemed to originate from almost the beginning of the epitaxial layer (Fig. 2). Furthermore, in higher magnification SEM images, small grains could sometimes be distinguished that might be related to the origin of the defect. Its nanometre size required further investigation by TEM, which was then undertaken on a FIB-prepared lamella.

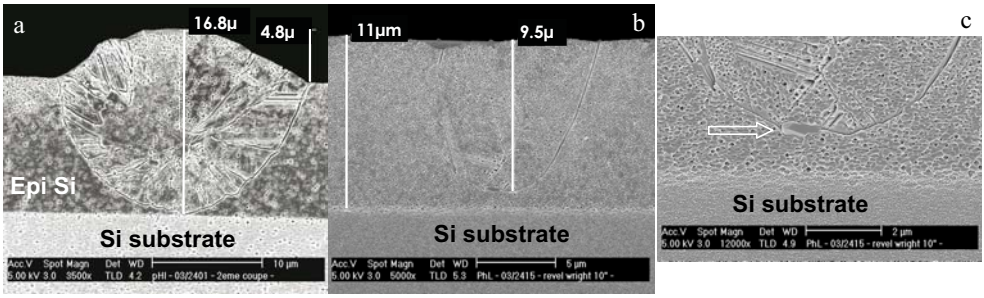


Fig. 2. SEM images of revealed cross-sections of two different defects a) protruding large defect (22µm wide) and b) 18 µm wide defect, c) detail of b) showing a grain of different size and contrast. Grain boundaries are observed in the defect indicative of polycrystalline growth.

3.2 TEM Study

The defect being very deep, subsequent thinning had to be performed in the FIB between different series of observations. The defective area shows a contrast characteristic of polycrystalline silicon microstructure, which was confirmed by electron microdiffraction patterns. Figure 3 shows the low and medium magnification TEM images at different step of thinning, the area of interest being arrowed. A small crystallite can be distinguished, in agreement with SEM observations, which might be at the origin of the defective growth. The thinning of the lamella clear appears on the boarder of

the polycrystalline area, which shows fewer and fewer thickness fringes, also the size of the crystallite is slightly smaller, but still observable, so that HREM study could then be undertaken.

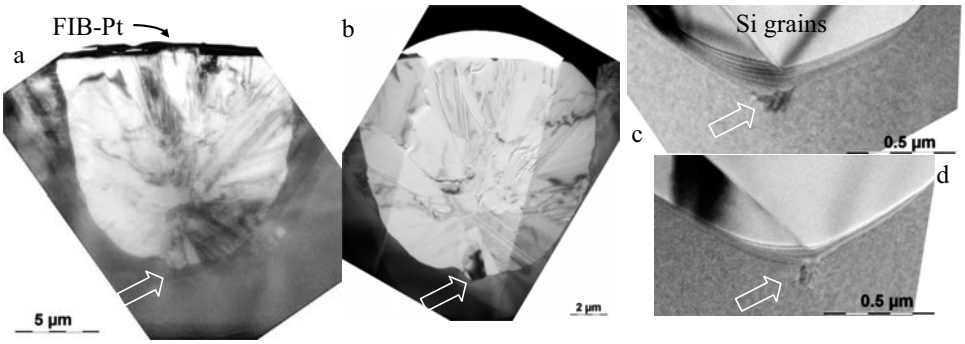


Fig. 3. Low and medium magnification TEM images. a) and c) first preparation, b) and d) after subsequent FIB thinning. The crystallite, possibly at the origin of the defect, is arrowed.

In a similar way to non-revealed SEM images and as expected from a good quality epitaxial growth, it is impossible to distinguish between the silicon substrate and epitaxial silicon on high resolution images, excepted for the defective area. The only information is the depth of the defect, 12µm, that is at the exact beginning of the silicon epitaxial deposition.

As observed in high resolution images (Fig. 4), the crystallite microstructure is closely related to the silicon framework. The FFT of the fringe area is characterized by extra spots along the $<111>_{Si}$ reciprocal direction and spaced at 1/3 of d_{111}*, as compared to regular Si area FFTs. The corresponding microdiffraction also allows the observation of weak extra dots. Thus, the fringes correspond to a localized superstructure of silicon framework characterized by a spacing of 3 x $d_{111\ Si}$ = 9.4 Å. This superstructure is established on a zone as large as 50nm x 100nm. The high resolution image of Fig. 5 shows that the contrast related to this superstructure is quite different from those of {111}-defect. The periodicity along <111> direction is unchanged and, perpendicularly, two rows of bright dots out of every three are darkened. This relates to the change in the Si-Si bond structure.

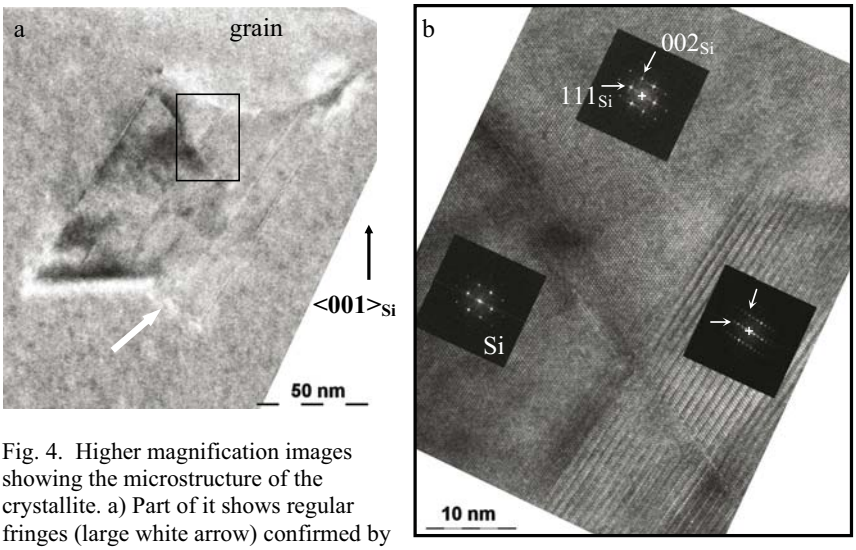


Fig. 4. Higher magnification images showing the microstructure of the crystallite. a) Part of it shows regular fringes (large white arrow) confirmed by the FFT insets on the high-resolution image b) corresponding to the rectangular area in a).

EDX analyses have also been performed in an attempt to identify some other element. Though no clear evidence of any other species could be established, a low signal of Cl was notified, boron being hardly detectable.

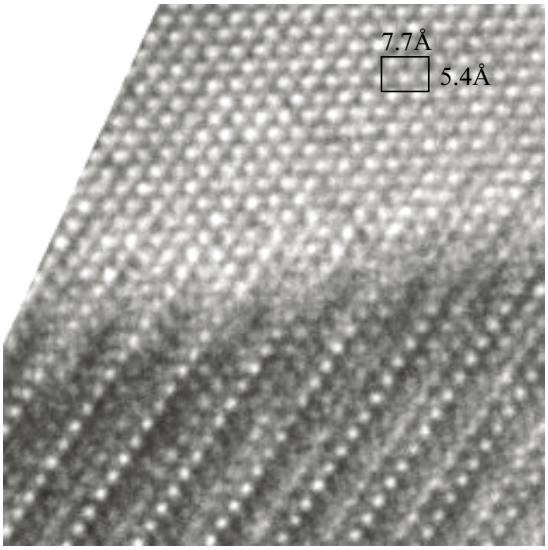


Fig. 5. High-resolution detail of the interface between Si framework and crystallite. Perpendicular to <111>, one row of bright dots of three remains almost unchanged. The Si (110) cell is inserted.

4. DISCUSSION

Such a wide superstructure area can hardly be due to self-interstitial/vacancy agglomerates (Fedina et al 1997, Vanhellemont et al 1997). Considering similar macroscopic TEM observations of silicon layers grown by molecular beam epitaxy on silicon substrates (Chew 1985), ours cannot be explained only by the formation of a polycrystalline silicon particle. Also, it seems to us improbable that observed contrast on such a wide regular area could be due to simple Moiré patterns related to overlapping twins. Thus, the reactive gases used for the synthesis of our epitaxial layer must be considered, especially silicon tetrachloride, as examples of residual chlorine in atomic layer deposition and chemical vapour deposition can be found in the literature (Kim et al 2003, Moriwaki and Yamada 2001). We will retain the idea that residual chlorine locally creates bonds with the surface silicon atoms in a similar way to the $Si_5Cl_{12}SiCl_4$ structure (Fleming 1972). In order to validate this interpretation, calculation of simulated images is in progress.

5. CONCLUSIONS

A growth defect in epitaxial silicon on a silicon substrate during IC processing has been studied by SEM and HREM TEM techniques. Considering the results of the detailed observations, it appeared probable that residual chlorine is responsible for the stabilization of a crystallite which will lead to polycrystalline silicon growth.

REFERENCES

Chew N G, Cullis A G, Warwick C A, Robbins D J, Hardeman R W and Gasson D B 1985 Microsc. Semicond. Mater. Proc. **76**, 129
Fedina L, Gutakovskii A, Aseev A, Van Landuyt J and Vanhellemont J 1997 J Microsc. Semicond. Mater. Proc. **157**, 43
Fleming D K 1972 Acta. Crystallogr. **B28**, 1233
Kim J, Hong H, Ghosh S, Oh K Y and Lee C 2003 Jpn. J. Appl. Phys. **42**, 1375
Moriwaki M and Yamada T 2001 Jpn. J. Appl. Phys. **40**, 2679
Roberts H and Otterloo B 2001 EFUG (Arcachon)
Vanhellemont J, Bender H and Van Landuyt J 1997 Microsc. Semicond. Mater. Proc. **157**, 393

Resonant Raman microscopy of stress in silicon-based microelectronics

E Bonera and M Fanciulli

Laboratorio MDM-INFM, via C. Olivetti 2, 20041, Agrate Brianza (MI), Italy

ABSTRACT: The use of Raman microscopy for the characterisation of strain in microelectronics could not follow the unceasing downscaling of devices without the use of resonance techniques. An excitation source matching the silicon direct bandgap dramatically reduces the penetration of light without significant loss of signal-to-noise-ratio. The investigated volume is limited to strained regions only, and the result is a far better sensitivity. We present a study of the enhancements and drawbacks brought by this technique when applied to the characterisation of some processes in microelectronics.

1. INTRODUCTION

Raman spectroscopy is a tool for local stress determination (Brunner et al 1989, DeWolf 1996). By measuring the phonon spectrum of silicon on the spatial scale of 1 μm, it is possible to correlate the stress-induced variations in the energy of the main band with the variations in atomic displacement and hence the strain and stress. The main Raman band located at 520.5 cm^{-1} is shifted by a value $\Delta\omega$ usually within the range of 1 cm^{-1}. After some assumptions, one can estimate the stress σ using the linear relationship $\sigma = k \cdot \Delta\omega$, where $k = k_u = 500$ MPa/cm^{-1} or $k = k_h = 200$ MPa/cm^{-1} mostly uniaxial or hydrostatic stress, respectively.

If one considers the possibility of extending the use of Raman spectroscopy for the future technological nodes of microelectronics, the main limitation is the diffraction-governed spatial resolution. As a matter of fact, the true problem is not the resolution itself, as it is not always necessary to resolve small structures to get information about the stress state of a device. The true issue is rather the fact that when the structures are smaller than the investigated volume, averaging between the Raman spectra generated by the strained regions and the unstrained bulk underneath results in a significant reduction of sensitivity. The solution is to transform the technique from a bulk technique to a surface technique. This is achieved using excitation with an energy higher than the direct bandgap of silicon (Holtz et al 1999). The ultra-violet (uv) excitation allows restriction of the penetration depth d_p and thus the sampled volume to a few nanometers below the silicon surface, reducing the volume averaging into a surface averaging, and therefore increasing the sensitivity. On the other hand, as the intensity of the Raman signal depends on the sampled volume, in order to avoid a significant loss of signal-to-noise (s/n) ratio, it is necessary to take advantage of the enhancement of the Raman effect resulting from an excitation energy that matches the direct bandgap of silicon at 3.4 eV (Dietrich and Dombrowski 1999, Dombrowski et al 1999).

In this contribution we will show that the use of a resonant excitation brings an enhancement in sensitivity that allows the characterisation of structures and manufacturing processes otherwise invisible to below-resonance excitations. In addition, we will show that it is possible to get relevant information not only for structures that can be spatially resolved, but also from structures smaller than the $\lambda/2$ limit.

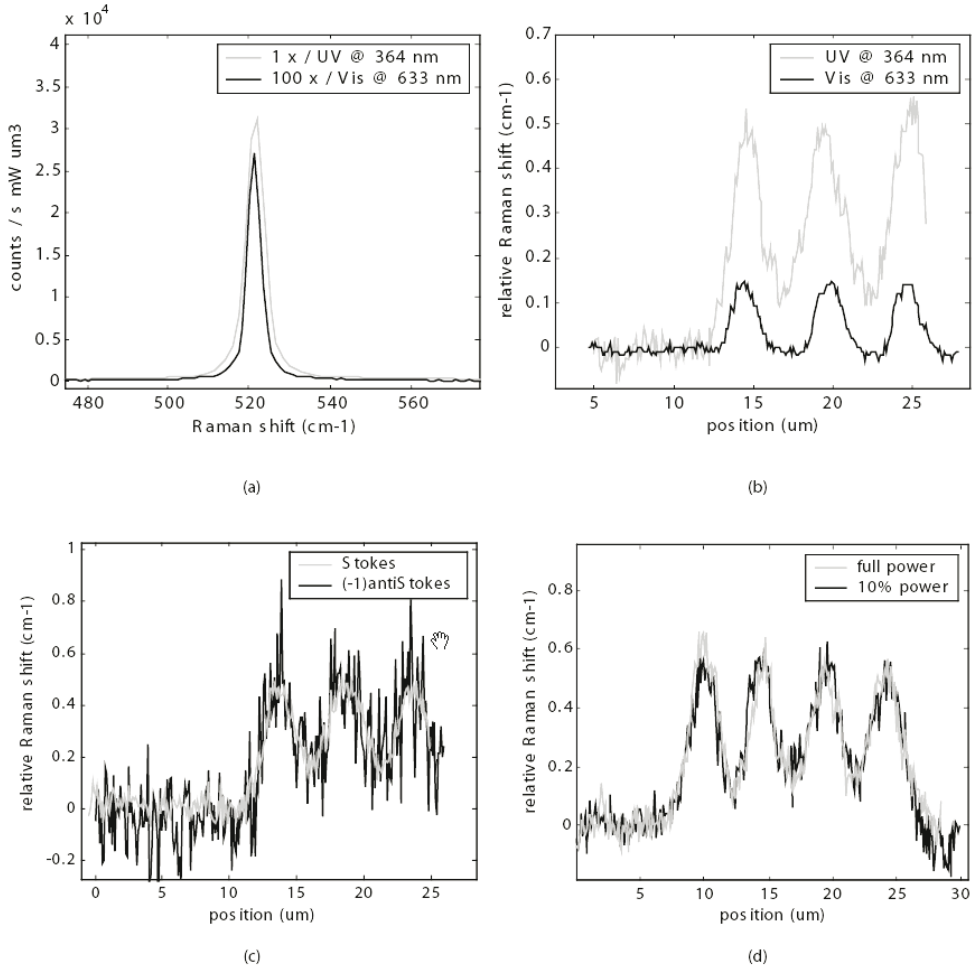


Fig. 1. (a) A single Raman spectrum from excitation of 633 nm (red) and 364 nm (uv). The spectrum from red is magnified 100 times. (b) Comparison between two scans on the same patterned sample using red and uv excitations. (c) Reliability check of the uv scan obtained comparing the shift from the Stokes and anti-Stokes channels. (c) The same scan performed with the uv excitation with full and 10% power.

2. EXPERIMENTAL

2.1 Samples

In this work we investigate the stress in arrays of shallow trench isolations (STI) from a real industrial manufacturing process (Chang and Sze 1996). Each STI is an empty trench dug in a z ≡ (001) silicon wafer for a depth t = 250 nm, infinitely extending along y ≡ (110). The process step we present here follows the filling of the trench with silicon dioxide. Two adjacent STI define inside the active area (AA) of the device that will be grown over.

As compared to the excitation wavelength λ, we measured both large structures (consisting of alternations of 2 μm wide AA and 3 μm wide STI) and small structures (consisting of alternations of 100 nm wide AA and 100 nm STI).

2.2 Experimental Setup

The experimental setup is based on a Renishaw Invia spectrometer. The instrument optics are adapted to use a Spectra Physics Ar+ laser as an excitation source, optimised for the emission line at 3.4 eV / 364 nm, matching the direct bandgap of silicon. This excitation wavelength reduces d_P to 10 nm. Using the crystalline silicon wafer crystallographic directions as a reference system, all the experiments are preformed in a z = (001) backscattering geometry. Figure 1a shows the comparison of the spectrum obtained in a flat wafer using this configuration and a non-resonant configuration based on a HeNe red laser with λ = 633 nm and d_P = 1.5 μm, operating with the same power at the sample and the same integration times. The intensity of each spectrum is normalised with respect to the investigated volume, and the red configuration is magnified by a factor of 100 to compare it directly. The overall intensity of the signal is of the same order of magnitude as the resonant configuration probes one hundredth of the volume, but has a hundred-fold enhancement due to the electronic resonance.(Renucci et al 1975) This is fundamental to get a sufficiently high s/n ratio to perform a fast analysis (5 minutes for a 30 μm scan with a 0.1μm stepsize) that allows also bidimensional mapping. The infinity-corrected 0.5NA UV refractive objective yielded a lateral resolution of 1 μm.

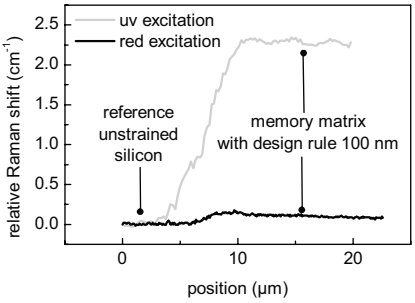


Fig. 2. Raman map of the stress in an array of 100 nm active areas spaced by 100 nm shallow trench isolations. On the left the wafer is not structured and the Raman shift is used as a reference.

3. DISCUSSION

In Figure 1b the comparison of the results obtained by off-resonance (red) and resonant (uv) excitations on large structures is presented. There is a factor of five between the observed maximum shifts, and this is due to the fact that the off-resonance measurement is limited by bulk averaging. This is of fundamental importance if one considers that the instrumental error on the determination of the stress-induced shift is 0.05 cm^{-1}, and the maximum shift observed with the red configuration is only 0.1 cm^{-1}. One could point out that the resonant excitation can not yield any kind of information about the stress state of any region below 10 nm. This is true, and actually represents the major limitation of the technique, but there are also two other considerations. First, one could think that the shape and distribution of the stress tensor across the volume of the active area would be anyway too complicated to be reconstructed quantitatively, and the surface stress can be taken anyway as an indication of the overall stress in the structure. Second, and more important, the first superficial 10 nm are the most interesting because the electrons will travel only in this region.

Optical artefacts can affect the measurement significantly, and the most reliable method to exclude the presence of optical artefacts is to perform the same scan observing both the Stokes and the

anti-Stokes parts of the Raman spectrum. Figure 1c shows that the two phonon energy spectra overlap ensuring that the measurement is reliable. (Bonera et al 2002) The anti-Stokes map is noisier because of its lower intensity. Generally, we observed that in resonance conditions, there are less optical artefact, probably due to the fact that the focussing process is less important because of the extremely low penetration depth.

The power at the sample is 10 mW, and this could raise questions about the influence of the heating of the sample to the final result. To investigate this issue, we performed the same experiment with a power at the sample reduced to 10% of the initial value. The two maps presented in Fig. 1d overlap and this means that all the heat absorbed by the sample is indeed dissipated by the bulk silicon. The analysis of the ratio of Stokes and anti-Stokes intensities at full-power confirms that the temperature is close to room temperature.

Finally, we want to show that the technique can be applied also to structures much smaller than the wavelength. In Fig. 2 we show the map obtained of alternations of 100 nm AA and STI. On the left-hand side, the silicon wafer is not patterned and therefore is taken as a reference. Moving towards the right-hand side, the scan reaches the structures and, although of course it is not possible to resolve each of them, the surface-averaged Raman shift yields important information about the stress state in the structures. Notice that, in this case, the difference between red and uv configurations is even higher than in the case of large structures.

4. CONCLUSIONS

We have presented a study of the application of Raman spectroscopy for the qualitative determination of stress in microelectronic devices. We showed that the reduction of averaging due to the strongly reduced penetration depth is fundamental to increase the sensitivity of the technique for the microelectronics of today. In addition, we showed that it is still possible to obtain useful information also with structures much smaller than the wavelength, suggesting that the employment of Raman spectroscopy to characterise stress in microelectronics could be extended for the future technological advances specified by the International Technology Roadmap for Semiconductors.

REFERENCES

Bonera E, Fanciulli M and Batchelder D N 2002 Appl. Spec. **56**, 560
Brunner K, Abstreiter G, Kolbesen B O and Meul H W 1989 Appl. Surf. Sci. **39**, 116
Chang C Y and Sze S M 1996 ULSI Technology (McGraw-Hill, New York)
DeWolf I 1996 Semicon. Sci. Technol. **11**, 139
Dietrich B and Dombrowski K F 1999 J. Raman Spec. **30**, 893
Dombrowski K F, DeWolf I and Dietrich B 1999 Appl. Phys. Lett. **75**, 2450
Holtz M, Carty J C and Duncan W M 1999 Appl. Phys. Lett. **74**, 2008
Renucci J B, Tyte R N and Cardona M 1975 Phys. Rev. B **11**, 3885

TEM study of silicon implanted with fluorine and boron applied to piezoresistor manufacturing

M Wzorek, J Kątcki, J Ratajczak, B Jaroszewicz, K Domański and P Grabiec

Institute of Electron Technology, Al. Lotników 32/46, 02-668 Warsaw, Poland

ABSTRACT: The technological processes of subsequent implantation of fluorine and boron ions are investigated by means of transmission electron microscopy. The quality of amorphous layers, formed by fluorine implants of different energies is determined. The nature and depth occurrence of residual defects after furnace annealing are investigated and the crystal quality of piezoresistors, obtained by boron implantation, with and without fluorine pre-amorphization, is compared.

1. INTRODUCTION

Silicon exhibits a large piezoresistive effect (Smith 1954). A suitable configuration of piezoresistive elements (*e.g.* Wheatstone bridge) can be used for transducing changes in the mechanical stress to easily measurable voltage changes (Pfann and Thurston 1961). Wheatstone bridge gauges are commonly used in silicon *MEMS* technology (Cibuzar 2001).

The piezoresistive elements should implement several requirements such as a low temperature coefficient of resistance (TCR) and a low leakage current. In order to obtain a *p*-type silicon piezoresistor, an *n*-type silicon wafer can be implanted with B^+ ions and subsequently annealed. After implantation the silicon wafer is highly damaged. During successive annealings the crystalline lattice is restored and the boron profile is broadened, but residual defects always occur (Mader 1988). The extended defects can cross the depletion region, giving rise to leakage current.

However, the amount of residual defects can be distinctly reduced when an amorphization is applied just before the boron implantation. Fluorine implantation can be applied for this purpose. BF_2^+ molecular ions implantation, with a dose above $1 \cdot 10^{15}$ cm^{-2}, results in the formation of an amorphous layer. Using this doping technique, activation of boron can be achieved at low temperatures (Tsai and Streetman 1979) and channelling effects can be suppressed (Wilson 1983). These advantages over the conventional B^+ implantation technique are used for shallow *p*-*n* junction formation (Biasse et al 1985). Alternatively, fluorine and boron ions can be implanted separately (Biasse et al 1987). The technique of subsequent implantation of fluorine and boron applied to piezoresistor fabrication is investigated in the present study.

When the appropriate implantation energy, dose and substrate temperature are used, fluorine implantation results in the formation of an amorphous layer (Biasse et al 1987). It was found that an amorphous layer reorders during annealing by solid-phase epitaxial growth (Csepregi et al 1977, Prasad et al 1976). The regrowth rate is highly influenced by the substrate orientation (Csepregi et al 1978), the type of the dopants and their concentrations (Csepregi et al 1977). Appropriate annealing of the amorphized silicon leads to its complete recrystallization. In order to obtain a low leakage current, the depletion region should be located below the original amorphous-crystalline interface (Biasse et al 1987).

2. EXPERIMENTAL

The technological processes of preamorphization and boron implantation were investigated by means of transmission electron microscopy (TEM). All specimens were studied in the JEM-200CX electron microscope operating at 200 kV; the specimen preparation procedure was described by Kątcki et al (1995).

In order to obtain a low defect-density, the *n*-type (100) oriented Czochralski-grown silicon wafers were first implanted with $^{19}F^{+}$ ions. For all implantation processes the target was cooled to about room temperature, the tilt angle was set to 7º. The silicon wafers were implanted with different energies, all with the dose of $3 \cdot 10^{15}$ cm^{-2}. The annealing was performed at 600ºC and cross-sectional TEM (XTEM) images were obtained.

The specimens, first amorphized by fluorine implantation, were then implanted with B^{+} ions and subjected to the multi-step furnace annealing in order to obtain a *p-n* junction. First two annealing steps were performed in a N_2 atmosphere – at 600ºC for 3h and at 800ºC for 1h. The last annealing step was performed at 1100ºC for 2h in N_2 and O_2 ambient. The crystal quality of the piezoresistors, obtained with and without fluorine pre-amorphization, was compared using TEM. Cross-sectional and plan view specimens were investigated.

3. RESULTS

The recrystallization of the silicon lattice is a thermally activated process. The activation energy is constant for different orientations of the crystal and it is attributed to the reorientation events of a small group of atoms in the amorphous material, near the amorphous-crystalline interface (Drosd and Washburn 1982).

After annealing of a silicon substrate with an amorphous surface layer, the crystalline lattice is restored except the area of the original amorphous-crystalline interface. Extrinsic defects can be found in this area by TEM (Mader 1988). These are dislocation loops, which evolve during annealing and are the result of the presence of excess Si interstitial atoms below the crystalline-amorphous interface. It is found that during annealing these defects coarsen via the Ostwald ripening mechanism (Bonafos et al 1998).

The recrystallization of the buried amorphous layers was investigated by Sadana et al (1982). If the amorphous region is well defined, annealing at 600ºC results in the complete recrystallization and in the formation of two, secondary damaged layers.

The samples implanted with fluorine ions of energy 35, 50, 70 and 90 keV (all with the dose: $3 \cdot 10^{15}$ cm^{-2}) were annealed at 600ºC for 1 h. Cross-sectional TEM micrographs of these samples are presented in Fig. 1. Regarding these results, some qualitative information about the amorphous layers can be obtained.

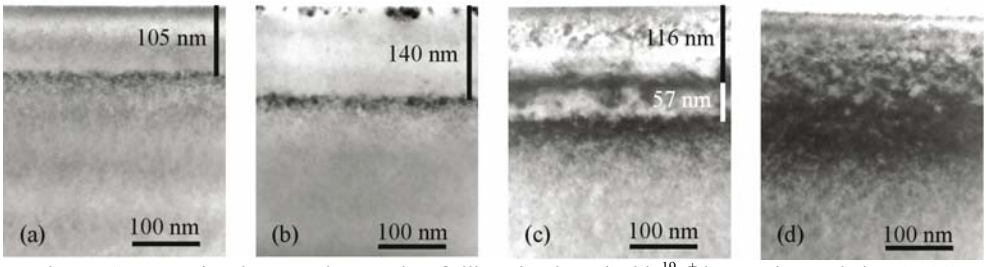


Fig. 1: Cross-sectional TEM micrographs of silicon implanted with $^{19}F^{+}$ ions and annealed at 600°C for 1h in N_2 atmosphere: (a) 35 keV, $3 \cdot 10^{15}$ cm^{-2}, (b) 50 keV, $3 \cdot 10^{15}$ cm^{-2}, (c) 70 keV, $3 \cdot 10^{15}$ cm^{-2}, (d) 90 keV, $3 \cdot 10^{15}$ cm^{-2}.

Annealing of the sample implanted with the energy of 35 keV has resulted in the complete recrystallization. One defective layer has formed 105 nm below the surface (Fig. 1a). The lack of the second, upper defective area evidences the lack of the upper amorphous-crystalline interface in the as-implanted sample. Fluorine implantation has resulted in the formation of an amorphous, continuous, surface layer, which was also confirmed by the selected area diffraction study of the as-implanted sample.

In the case of the samples implanted with the energy of 50 keV, the defective layer is located at the depth of about 140 nm (Fig. 1b). There is a visible disturbance of the upper defective layer just below the surface. This may indicate that there was an amorphous layer in the as-implanted sample and the upper amorphous-crystalline interface was located just below the surface.

During annealing of the sample implanted with F^+ ions of the energy 70 keV, two secondary damaged layers have formed (Fig. 1c). Only the lower one's position indicates the depth of the amorphous-crystalline interface in the as-implanted sample (Sadana et al 1982). These results evidence the presence of a buried, amorphous layer in the as-implanted sample.

A cross-sectional TEM micrograph of the sample implanted with 90 keV F^+ ions is presented in Fig. 1d. Annealing at 600ºC has not resulted in the formation of the well-defined secondary damaged layers. This indicates that implantation had resulted in the formation of a buried, highly damaged area, but not in a well defined amorphous layer.

The as-implanted samples containing surface and buried amorphous layers (F^+ implantation – 50 keV and 70 keV respectively) were afterwards implanted with boron ions (40 keV, $3 \cdot 10^{14}$ cm^{-2}) and subjected to the multi-step furnace annealing: 600ºC(3h)/800ºC(1h)/1100ºC(2h). For comparison, boron was implanted also into the not-amorphized silicon wafer and the same annealing sequence was applied. The junction has formed at the depth of 2.8 μm in all investigated samples. Cross-sectional and plan view TEM images, obtained from the investigated specimens, are presented in Fig. 2.

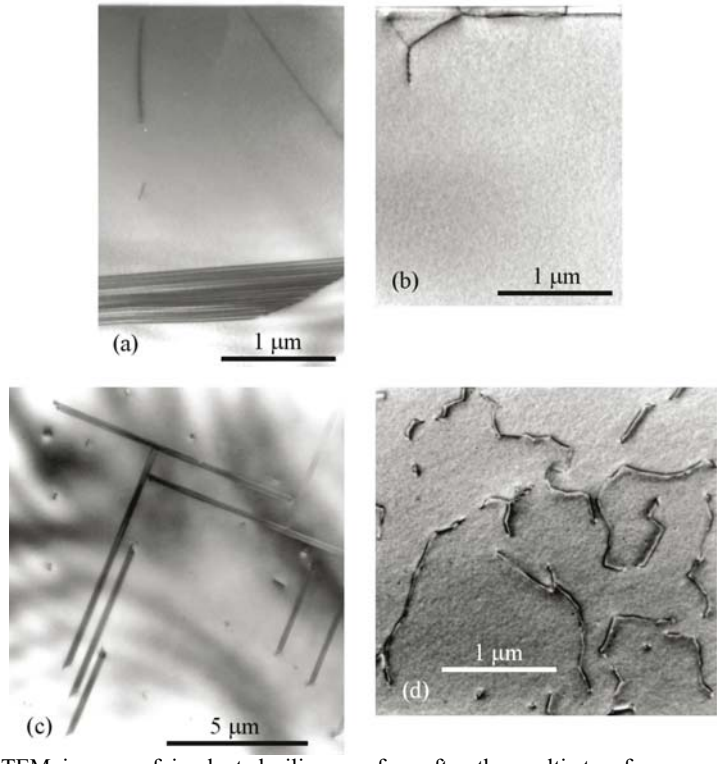


Fig. 2: TEM images of implanted silicon wafers after the multi-step furnace annealing - 600ºC(3h, N_2)/800ºC(1h, N_2)/1100ºC(2h, N_2 + O_2): (a) cross-sectional view of the boron implanted sample (B^+, 40 keV, $3 \cdot 10^{14}$ cm^{-2}), (b) cross-sectional view of the pre-amorphized (F^+, 70 keV, $3 \cdot 10^{15}$ cm^{-2}) and afterwards boron implanted (B^+, 40 keV, $3 \cdot 10^{14}$ cm^{-2}) sample, (c) plan view image of the same wafer as in Fig. a, (d) plan view image of the same wafer as in Fig. b.

After annealing of the boron implanted silicon wafer (without pre-amorphization), extrinsic stacking faults appear to be the dominant defects (Fig. 2a, 2c). During thermal oxidation at the SiO_2-Si interface the stacking fault embryos are formed as it was suggested by Hu (1974). During annealing these defects grow by absorbing more interstitials. The parts of extrinsic stacking faults, which are left after specimen thinning (they lie in the (111) planes and are inclined to the wafer surface), are visible in Fig. 2a and Fig. 2c. The average length of the stacking faults at the surface was estimated to be 9 ± 3 μm – the value was obtained by the measurements of etch pits after Secco

etching (Wzorek et al, to be published). Cross-sectional TEM investigations have shown that some of the mentioned defects are extending to even more than 3 μm below the surface (see Fig. 2a).

When a pre-amorphization is applied before boron implantation, no stacking faults are present in the annealed wafers. Intrinsic defects, which are left at the amorphous-crystalline interface, coarsen during annealing and undergo numerous reactions (Mader 1988). As a result, the formation of dislocation half loops is observed in the sample pre-amorphized by 50 keV fluorine implants. Cross-sectional TEM has shown these defects extending to the maximum depths of about 0.8 μm below the surface.

A cross-sectional and a plan view TEM micrograph of the boron implanted sample, pre-amorphized by fluorine implants of 70 keV, are presented in Fig. 2b and 2d respectively. After multi-step annealing, an irregular structure of dislocation segments has formed – Fig. 2d. This is probably the result of the numerous reactions between misfit dislocations (Ning 1997). The maximum distance from the surface, where the dislocations were found by XTEM, is 0.7 μm.

4. CONCLUSIONS

The samples implanted only with boron, without amorphizing fluorine implantation, show the defects extending to even more than 3 μm below the surface. The presence of dislocations in the depletion region causes leakage currents and degrades the quality of the *p-n* junction. XTEM images of the samples pre-amorphized by fluorine implantation show no extended defects with the exception of the area that spreads 800 nm and 700 nm below the surface for 50 keV and 70 keV fluorine implants respectively. When the pre-amorphization is applied, stacking faults are eliminated from the annealed samples.

XTEM investigations have shown that the extended defects are not present in the active area of the *p-n* junction if pre-amorphization is applied. Application of the fluorine implantation with proper energy and dose improves the junction quality.

ACKNOWLEDGEMENTS

The authors are very much indebted to Ms D Szczepańska and Mr J Gazda for assistance in specimen preparation and Ms J Wiącek for careful preparation of micrographs.

REFERENCES

Biasse B, Cartier A M, Spinelli P and Bruel M 1987 Nucl. Instr. And Meth. B **21**, 493
Biasse B, Cartier A M and Bruel M 1985 Nucl. Instr. and Meth. B **10/11**, 526
Bonafos C, Mathiot D and Claverie A 1998 J. Appl. Phys. **83**, 3008
Cibuzar G 2001 The Science and Engineering of Microelectronic Fabrication, Second Edition, ed Cambell S A (Oxford University Press) p 514
Csepregi L, Kennedy E F, Gallagher T J, Mayer J W and Sigmon T W 1977 J. Appl. Phys. **48**, 4234
Csepregi L, Kennedy E F, Mayer J W and Sigmon T W 1978 J. Appl. Phys. **49**, 3906
Drosd R and Washburn J 1982 J. Appl. Phys. **53**, 397
Hu S M 1974 J. Appl. Phys. **45**, 1567
Kątcki J, Ratajczak J, Maląg A and Piskorski M 1995 Microscopy of Semiconducting Materials 1995, eds A G Cullis and A E Statton-Bevan (Bristol:IOPP) p 273
Mader S 1988 Ion implantation: Science and Technology, ed Ziegler J F (Academic Press, Inc.) p 63
Ning X J 1997 Phil. Mag. A **75**, 115
Pfann W G and Thurston R N 1961 J. Appl. Phys. **32**, 2008
Prasad A, Baserman R, Germain P and Bourgoin J C 1976 Phys. Stat. Sol. A **35**, 109
Sadana D K, Washburn J and Booker G R 1982 Phil. Mag. B **46**, 611
Smith C S 1954 Phys. Rev. **94**, 42
Tsai M Y and Streetman B G 1979 J. Appl. Phys. **50**, 183
Wilson R G 1983 J. Appl. Phys. **54**, 6879
Wzorek M, Kątcki J, Płuska M, Ratajczak J, Jaroszewicz B, Domański K and Grabiec P, *to be published*

Silicides for advanced CMOS devices

A Lauwers, J A Kittl[1], M J H van Dal[2], O Chamirian, M A Pawlak, C Torregiani, J. Liu, A Benedetti, O Richard, H Bender, J G M van Berkum[3], M Kaiser[3], A Veloso, K G Anil, M de Potter and K Maex

IMEC, Kapeldreef 75, 3001 Leuven, Belgium
[1] Assignee at IMEC from Texas Instruments
[2] Philips Research Leuven, Kapeldreef 75, 3001 Leuven, Belgium
[3] Philips Research Laboratories, Prof. Holstlaan 4, 5656 AA Eindhoven, The Netherlands

ABSTRACT: The narrow line behaviour observed for Co-silicide and Ni-silicide is investigated. The thermal degradation of Ni-silicide, morphological degradation as well as phase instability, is discussed. It is demonstrated that the thermal stability of Ni-silicide can be improved by alloying with Pt or Ta. The formation of Ni-silicide contacts on SiGe substrates is investigated. The stress induced by the silicide itself is studied by finite element simulations and verified with convergent beam electron diffraction analysis. Finally, the use of Ni-silicide as a metal gate is discussed.

1. INTRODUCTION

Silicides have been used in self-aligned (SALICIDE) processes for several generations of complementary metal-oxide semiconductor (CMOS) devices, to reduce the sheet resistance and provide stable Ohmic contacts with low contact resistivity on gate and source/drain areas. One of the key considerations for SALICIDE processes is the ability to silicide small structures achieving low sheet resistance. The difficulty in obtaining the low resistivity C54 Ti-silicide phase on sub 0.25 μm poly-Si lines has driven the migration from Ti-silicide to Co-silicide. Co-silicide is facing similar problems as gate lengths are scaled below 40 nm. The Co-silicide narrow line effect is the main reason behind the migration from Co-silicide to Ni-silicide. In addition, Ni-silicide can be obtained at low temperatures, which is beneficial to obtain low contact resistance and is compatible with the presence of advanced ultra-shallow junctions. Si consumption is 35% lower for Ni-silicide compared to Co-silicide, which helps to reduce junction leakage and is an advantage for SOI devices. The major concern for Ni-silicide is its poor thermal stability.

For the 45 nm CMOS technology node, modifications of the conventional scaling schemes may be necessary. Alternative substrates, such as SiGe, are being considered to engineer the channel strain. Also the silicide formation itself has a big influence on the strain in the transistor channel. Metal gates are expected to replace partially silicided poly gates in order to eliminate poly depletion issues. A possible way to implement a metal gate, which has received a lot of interest lately, is by complete silicidation of a conventional poly gate.

This paper will cover the narrow line behaviour observed for Co-silicide and Ni-silicide. The thermal degradation of Ni-silicide, morphological degradation as well as phase instability, will be discussed. It will be demonstrated that the thermal stability of Ni-silicide can be improved by alloying with Pt or Ta. Furthermore, the formation of Ni-silicide contacts on SiGe substrates is studied. The stress induced by the silicide itself is studied by finite element simulations and verified with convergent beam electron diffraction (CBED) analysis. Finally, the use of Ni-silicide as a metal gate will be discussed.

2. NARROW LINE EFFECTS

2.1 Co-Silicide

It is found that an abrupt increase in sheet resistance occurs for Co-silicided poly gates when the gate length is reduced below 40 nm. (Kittl et al 2003) To elucidate the degradation mechanism of

Co-silicide on nanoscale poly-Si lines, the formation of Co-silicide in narrow lines was studied using electrical and morphological analysis (van Dal et al 2004a). Co-silicidation is typically done in a 2 step rapid thermal processing (RTP) sequence, in which the high resistivity Co-monosilicide is formed during the first step at a moderate temperature after which the unreacted metal is removed and the Co-monosilicide is transformed into the low resistivity Co-disilicide at higher temperature. Sheet resistance measurements were done after the first RTP step (540ºC) and after the second RTP step (700ºC). (Fig. 1a) After the first RTP step, a sheet resistance of 140 Ω/sq was obtained down to 30 nm gate length, which indicates the formation of CoSi. Apparently, the lateral scaling of the poly gates does not hinder the formation of CoSi. After the second RTP step, the sheet resistance was observed to drop to 6 Ω/sq for the lines with gate length higher than 40 nm, indicating transformation to the low resistivity $CoSi_2$. For gate lengths below 40 nm, the sheet resistance was found to increase to values as high as 3000 Ω/sq. Top view scanning electron microscope (SEM) inspections on the 30 nm gates indicated separation of the Co-silicide grains (van Dal et al 2004a).

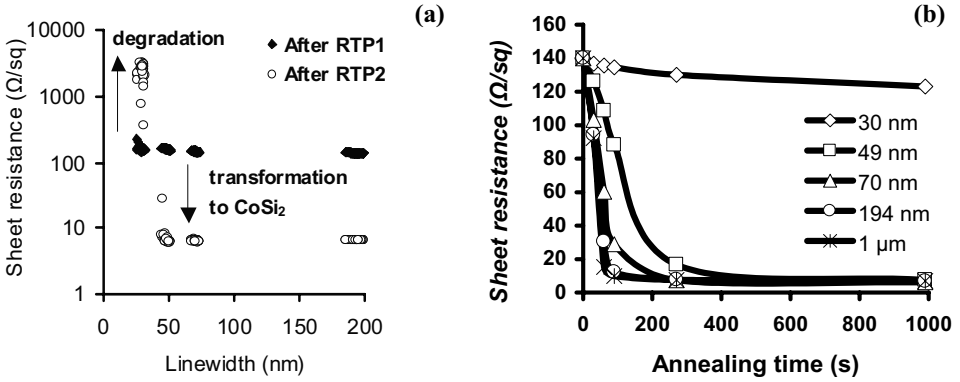


Fig. 1: (a) Co-silicide sheet resistance as a function of poly gate line width: after RTP1 at 540ºC (filled symbols) and after RTP2 at 700ºC (open symbols), (b) Co-silicide sheet resistance as a function of annealing time (at 650ºC) for different poly gate line widths.

To obtain a better insight in the morphological degradation of the $CoSi_2$ in the narrow lines, focused ion beam (FIB) cross sections were prepared along the length of a 30 nm wide and an 85 nm wide line and analysed with the transmission electron microscope (TEM). For the 85 nm wide line it is observed that the Co-silicide film is continuous and the silicide/Si interface is relatively smooth and well defined. (Fig. 2a) For the 30 nm wide line a completely different picture is obtained : the silicide/Si interface is irregular and locally inversion of the silicide and the poly-Si is observed: (see high angle annular dark field (HAADF) scan in Fig. 2b). From this analysis the mechanism of sheet resistance degradation in the sub 40 nm gates is identified as agglomeration of the Co-silicide.

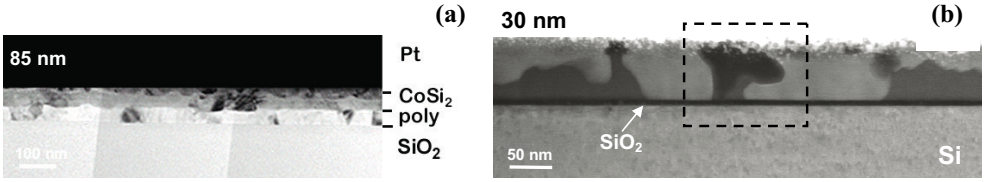


Fig. 2: TEM images of Co-silicided poly-Si lines cross-sectioned along the length of the line (a) bright field image of an 85 nm wide line, (b) HAADF image of a 30 nm line.

The rate with which CoSi transforms into $CoSi_2$ on narrow poly lines at a temperature of 650ºC was studied as a function of line width making use of sheet resistance measurements. (Fig. 1b) It was found that the transformation rate is reduced for lines with a gate length of ~ 49 nm and that the transformation rate is virtually zero for the 30 nm lines. It is thought that the reduction of the transformation rate for the narrow lines is due to a decrease in the availability of nucleation sites, similar to that seen for $TiSi_2$ formation on narrow features (Kittl et al 1995). The reduction of the transition rate of CoSi into $CoSi_2$ for the 30 nm wide lines can lead to the situation that agglomeration of CoSi precedes $CoSi_2$ formation.

2.2 Ni-Silicide

Whereas the sheet resistance of Co-silicided poly gates is found to increase drastically when the gate length is reduced below 40 nm, a reverse line width effect is observed for Ni-silicide as can be seen in Fig. 3a. The low sheet resistance observed on sub 100 nm Ni-silicided poly gates (typically two to three times lower than the sheet resistance of wide poly gates) is to be attributed to the excessive silicidation of the narrow poly gates. (Fig. 3b) Locally complete silicidation of the narrow poly gates is observed (Fig. 3c). The latter is undesirable, because fully silicided gates have a different work function compared to doped poly gates.

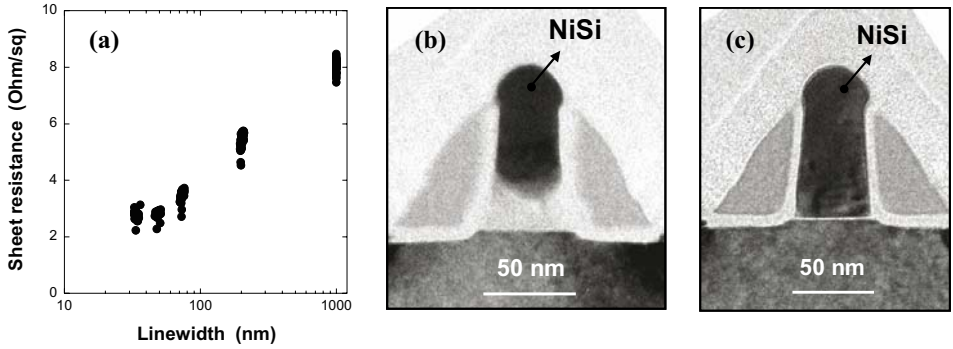


Fig. 3: (a) Sheet resistance of Ni-silicided narrow poly gates as a function of gate length, (b) X-TEM image showing excessive silicidation of sub 50 nm poly gate, (c) X-TEM image showing complete silicidation of sub 50 nm poly gate.

In typical salicide processes, the deposited metal film is fully reacted and the thickness of the resulting silicide is controlled only by the deposited metal thickness. In case of the Ni/Si reaction, with Ni being the main moving species throughout the reaction, Ni deposited on top of spacers surrounding narrow gates can diffuse and react to form a much thicker silicide film on the small features. Excessive silicidation is also observed at the edges of source/drain areas because Ni deposited on top of isolation or spacers can diffuse and react to form a much thicker silicide at the isolation or spacer edge. To prevent excessive silicidation of small features it is necessary to control the thermal budget before the selective etch of the unreacted Ni, thus controlling the silicide thickness on small features by limiting thermally the reaction. To reduce Ni diffusion, Ni-silicide can be formed in two steps. In the first step at low temperature Ni is fully reacted to Ni_2Si, the unreacted Ni op top of spacers and isolation is removed and in the second RTP step at higher temperature Ni_2Si is converted to NiSi. Ni_2Si has been reported to grow by diffusion-controlled kinetics (Gambino and Colgan 1998). This allows tuning the thermal budget of the first RTP step (by reducing the temperature or the time) such that it is barely sufficient to react the deposited Ni thickness to form Ni_2Si (Lauwers et al 2004).

3. THERMAL STABILITY

A key issue for implementation of NiSi is its low thermal stability. The effect on NiSi films of thermal treatments in the 550-900ºC range for times ranging from 30 sec to 60 min was studied by four-point sheet resistance measurements, SEM, TEM and GIXRD (grazing incidence X-ray diffraction). The study included NiSi films of various thicknesses on As and B doped single crystal (100) Si and polycrystalline Si. Two distinct behaviors were observed. The first behavior is characterized by a continuous increase in sheet resistance with anneal time, with the ratio of the sheet resistance after anneal to the initial sheet resistance increasing to values higher than 2. (Fig. 4a)

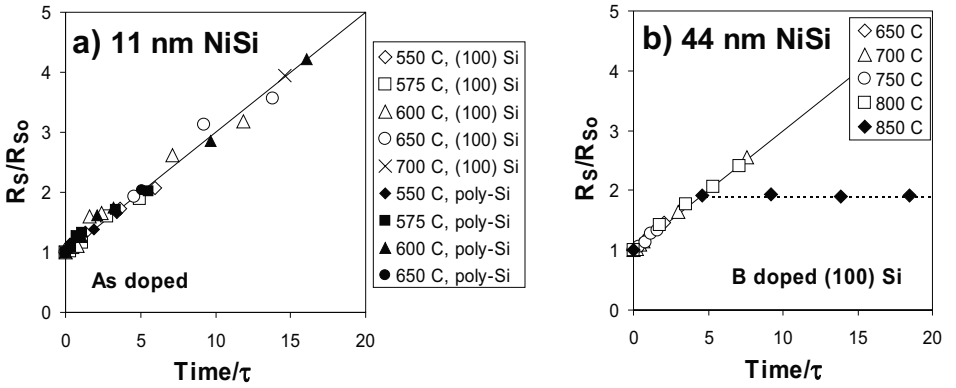


Fig. 4: Evolution of sheet resistance with anneal time at various temperatures for : (a) 11 nm NiSi films on As doped (100) and poly-Si, (b) 44 nm NiSi films on B doped (100) Si. Sheet resistance values R_s after anneals were normalized to the initial sheet resistance R_{so} of the NiSi films. Anneal times were normalized to a degradation time τ corresponding to a 20% increase in sheet resistance.

From SEM, TEM and GIXRD analysis it can be concluded that these films agglomerated while still in the NiSi phase. Cross sectional TEM analysis showed that, after agglomeration, the surface of the samples remained quite flat, with NiSi grains alternating with exposed Si that had regrown to the surface. In contrast, the NiSi-Si interface was very rough. This suggests that the silicide surface energy is significantly higher than the interface energy. The degradation of NiSi films on (100) Si starts with grain boundary grooving predominantly at the NiSi/Si interface. This stage of the agglomeration process is driven by the reduction of the grain boundary energy in the NiSi films. As grooves reach the film surface, Si becomes exposed. The exposed Si areas grow subsequently driven mainly by reduction of the high surface energy of the silicide. (Fig. 5a,b)

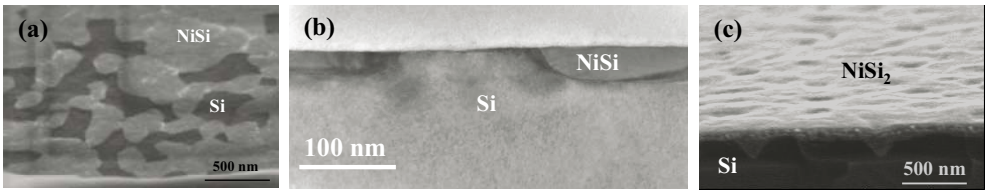


Fig. 5: (a) Top view SEM image of 22 nm NiSi film on (100) Si after annealing at 700ºC for 30 sec, (b) Cross sectional TEM image of 22 nm NiSi film on (100) Si after annealing at 700ºC for 30 sec, (c) Cross sectional SEM image of 66 nm NiSi film on (100) Si after annealing at 850ºC for 30 sec.

The second type of behavior observed in the isothermal anneals was an initial increase in sheet resistance after which the sheet resistance remained stable upon further annealing, with the ratio of

sheet resistance after anneal to initial sheet resistance remaining roughly constant at a value below 2. (Fig. 4b) This behavior is associated with the transformation of the NiSi films to $NiSi_2$ and was verified both by GIXRD and SEM. (Fig. 5c) From this study it is concluded that the initial mechanism of degradation was agglomeration for thinner NiSi films (22 nm and thinner) as well as for thicker films annealed for long times at low temperature. For thicker films annealed at higher temperature the degradation mechanism is transformation to the $NiSi_2$ phase. Arrhenius plots of degradation times τ (anneal time corresponding to a 20% sheet resistance increase) for NiSi films of different thickness are shown in Fig. 6a. The mechanism of degradation was agglomeration except for data points labeled as transformation to $NiSi_2$. Degradation times were longer for thicker films, indicating thermal stability improved with increasing film thickness. Activation energies for agglomeration were found to be ~2.4 eV on n+ or p+ (100) Si and ~3 eV on n+ poly-Si.

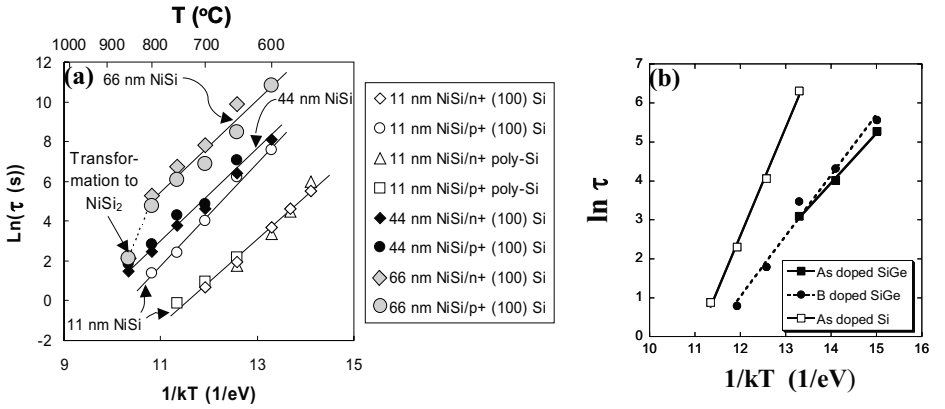


Fig. 6: Arrhenius plots of degradation times τ (corresponding to a 20% increase in sheet resistance) : (a) NiSi films of various thicknesses, (b) Ni(SiGe) films formed on As and B doped (100) $Si_{0.8}Ge_{0.2}$.

4. Ni-ALLOY SILICIDES

The effect of alloying Ni with 10% Pt or Ta on silicide properties was studied. From the transformation curves it follows that the Ni-alloy silicides are more stable than the pure Ni-silicide, as expected (Mangelinck et al 1999, Sun et al 2003, Wang and Feng 2003), where Ni(Pt) seems to improve the thermal stability of NiSi more efficiently (100ºC improvement) compared to Ni(Ta) (50ºC improvement). (Fig. 7a) GIXRD spectra of the samples annealed at 500ºC confirmed the formation of NiSi. (van Dal et al 2004b) An estimate of the amount of alloying element dissolved in NiSi can be made by determining the shift in the spectra compared to the pure NiSi reference and assuming Vegard's law. From the shift observed for Ni(Pt) it could be determined that about 9% Pt was dissolved in the NiSi film. For Ni(Ta) no shift is observed, indicating that Ta is not in solution in the NiSi film. (Fig. 7b) According to RBS analysis Ta has segregated towards the surface. A similar result was obtained by Sun et al. (2003), who stated that the Ta top layer reduces Ni and Si surface diffusion and thereby improves NiSi thermal stability.

Cross sectional TEM and GIXRD characterization indicate that the Ni-silicide films alloyed with Pt as well as those without Pt degrade morphologically while still in the monosilicide phase. TEM analysis of Ni(Pt)-silicide films on (100) Si after morphological degradation showed similar characteristics to those of NiSi films that agglomerated at lower temperatures. Relatively flat surfaces were observed with alternating silicide and exposed Si areas, as well as very rough interfaces. From the shift in the diffraction peaks (comparing samples with and without Pt) and assuming Vegard's law, it can be estimated that the amount of Pt in solution remained roughly constant as the films degraded morphologically. (Fig. 8)

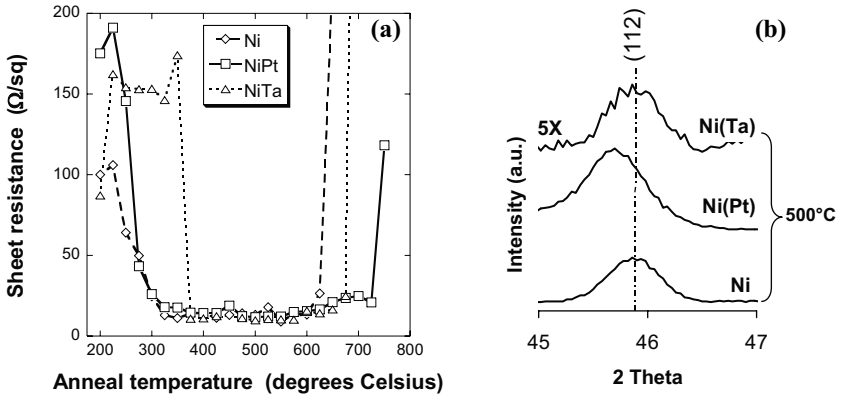


Fig. 7: (a) Transformation curves for the reaction of 10 nm Ni, 10 nm Ni(10% Pt) and 10 nm Ni(10% Ta) on undoped (100) Si, (b) Shift of (112) peak of Ni(Pt)Si and Ni(Ta)Si compared to the (112) peak of NiSi (GIXRD).

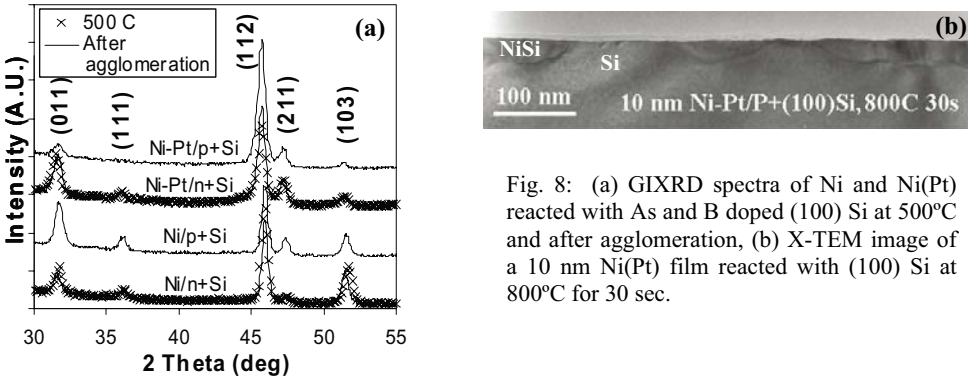


Fig. 8: (a) GIXRD spectra of Ni and Ni(Pt) reacted with As and B doped (100) Si at 500ºC and after agglomeration, (b) X-TEM image of a 10 nm Ni(Pt) film reacted with (100) Si at 800ºC for 30 sec.

5. SiGe SUBSTRATES

Ni-silicide formation on single-crystalline SiGe substrates with a 20% Ge content was investigated. Phase formation was studied for a one-step silicidation process in the temperature range of 200-850ºC. Transformation curves (silicide sheet resistance versus anneal temperature) for the reaction of 10 nm Ni with As – and B-doped SiGe are shown in Fig. 9a. Corresponding curves for the reaction of 10 nm Ni with pure Si are shown for comparison. The characteristics of the transformation curves are similar for Si and SiGe substrates. At low temperatures Ni-rich phases are formed (predominantly Ni_2Si or $Ni_2(SiGe)$). The plateau of low sheet resistance values indicates the formation of Ni-monosilicide or Ni-monogermanosilicide. The presence of Ni_2SiGe and NiSiGe was verified by XRD (Chamirian et al 2004). It is observed that the formation of the low resistive Ni-monogermanide is delayed to higher temperatures by the presence of Ge (around 350ºC versus 300ºC for pure NiSi). At elevated temperatures a sharp increase of the sheet resistance is observed. The thermal degradation of germanosilicide films is found to occur at lower temperatures than for pure NiSi films. As such the process window is narrowed from both sides by the addition of Ge.

SEM analysis of the degraded Ni-germanosilicide films indicates that morphological degradation is the degradation mechanism (Chamirian et al 2004). The kinetics of agglomeration of

Ni(SiGe) films were studied, following the degradation of sheet resistance with anneal times at various temperatures, and compared to those of NiSi. A lower activation energy (~ 1.6 eV) was found for the agglomeration of Ni(SiGe) films in comparison to NiSi films (~ 2.4 eV). (Fig. 6b) XRD studies indicate that at lower reaction temperatures (e.g. 450ºC) the Ge content in the Ni mono-germanosilicide films is similar to that in the substrate (20%, assuming Vegard's law). However, at higher temperatures (700ºC), a significant amount of Ge is expelled from the Ni(SiGe) grains. (Fig. 9b) It is likely that the Ge segregation plays a key role in the earlier onset and lower activation energy of agglomeration of Ni(SiGe) films.

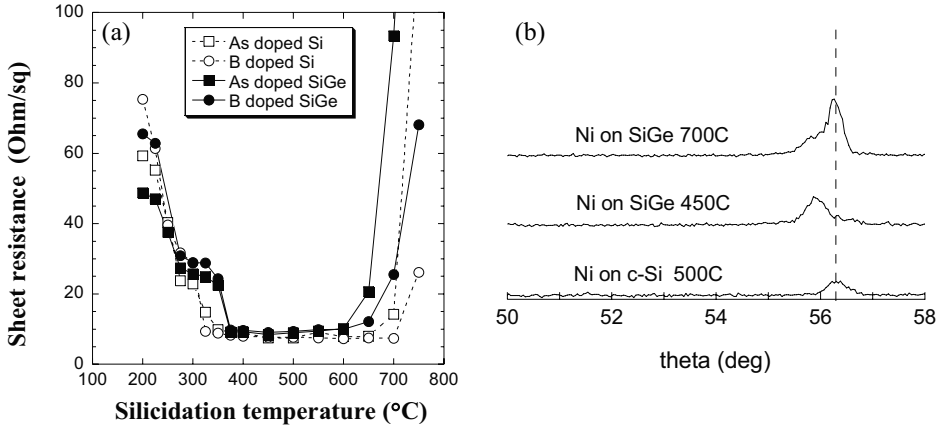


Fig. 9: (a) Transformation curves for (germano)silicidation of 10 nm Ni on As and B doped (100) SiGe with 20% Ge, (b) Shift of the Ni(SiGe) peak as compared to the NiSi peak (GIXRD).

6. SILICIDE INDUCED STRESS

The formation of a silicide on a Si substrate generates a high residual stress in the silicide film due to the large difference in thermal expansion coefficient between the silicide and the Si. Due to the existence of edge forces, discontinuities in the film introduced through the patterning give rise to localized stress fields in the substrate as well. Finite element simulations were done to understand how the presence of patterned silicides affects the stress in the transistor channel and how this stress depends on the variation of line dimensions (Torregiani et al 2004). To simplify the interpretation and the verification, the interaction between the silicide and the silicon was studied in a simple structure consisting of an array of silicide lines embedded in the silicon matrix. (Fig. 10)

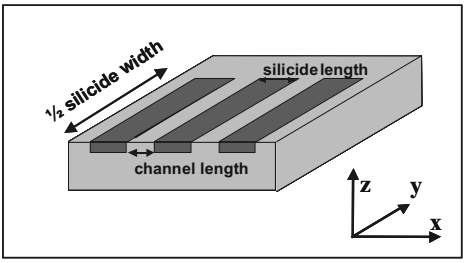


Fig. 10: Simplified structure with silicide lines embedded in the Si structure that is used for finite element modeling.

The simulations were completed for an array of 40 nm thick Co-silicide lines of varying length, width and spacing. The silicide width is varied between 200 nm and 10 μm, the silicide length between 20 and 200 nm and the spacing between the lines, here representing the channel length, between 20 and 200 nm. The formation of embedded silicide lines was found to induce tensile stress in the channel and compressive stress under the silicide. The effect of variation in silicide length and

channel length (spacing) is illustrated in Fig. 11 (only half channel is shown, silicide width is 2 μm). The stress that is present at the surface in the x-direction is plotted as a function of the position in the x-direction. In all cases, the highest stress in the channel is observed close to the edge. It is found that for increasing silicide length and constant channel length, the slope and the peak of the stress are intensified. On the other hand, it is found that the stress in the channel is increased for constant silicide length and decreasing channel length. This trend occurs because there is a superposition of the stress fields due to neighboring silicide lines as the channel length decreases. It is found that the maximum stress in the channel can be as high as 1 GPa.

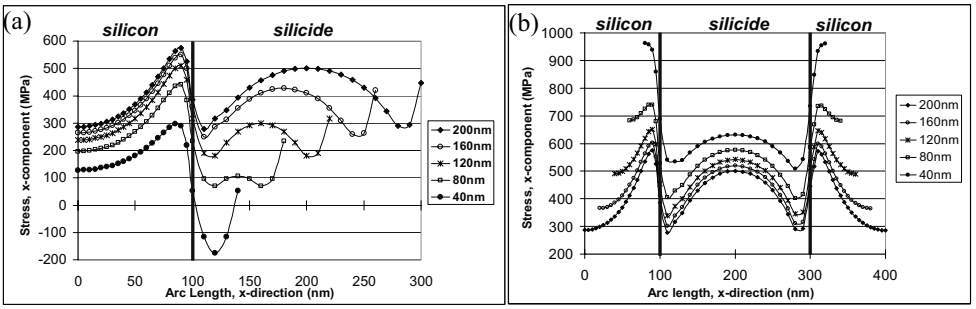


Fig. 11: Stress in the x direction at the surface as a function of x-position (a) for different silicide lengths (channel length = 200 nm), (b) for different channel lengths (silicide length = 200 nm).

The stress values found by finite element simulations were verified by CBED. The CBED technique for strain measurement is based on the strain induced shift of High Order Laue Zone (HOLZ) lines, which occur in the central disk of a CBED pattern. The position of these lines is very sensitive to small variations in lattice parameters, and therefore to strain (Armigliato et al 2001). Co-silicide lines with a thickness of 40 nm embedded in the Si substrate were fabricated making use of a silicide blocking mask, consisting of 20 nm Si-nitride on top on 20 nm Si-oxide. The silicide blocking mask can be considered as a dummy gate. TEM cross-sections were prepared by a modified in situ lift-out technique. Figure 12a shows a TEM image of a structure with 120 nm long Co-silicide lines separated by 480 nm long dummy gates. Strong strain contours around the silicided regions are clearly visible. The stress trend close to the silicide lines could not be determined by CBED due to the presence of high strain gradients and splitting of the HOLZ lines (Benedetti et al 2004). Stress values measured at the points indicated on the TEM image are listed in Table 1. The results from FEM simulations performed on a structure with the same dimensions as the one measured are shown in Fig. 12b. The presence of the dummy gate was taken into account in the FEM simulations. The points measured by CBED are marked with the same characters in Fig. 12a and the stress values obtained from FEM simulations are also listed in Table 1. The comparison of the values obtained from CBED and from FEM shows a good agreement in the stress sign and the order of magnitude.

7. FULLY Ni-SILICIDED POLY GATES

Several silicide phases can be formed in the Ni-Si system. For the reaction of a thin Ni film with a Si substrate, Ni-rich phases form first at low temperatures. Ni_2Si is generally the predominant phase at low temperatures and early stages of the reaction, forming a layer that grows by diffusion limited kinetics. At higher temperatures and as Ni is consumed, NiSi nucleates and grows also by diffusion limited kinetics. The presence of $Ni_{31}Si_{12}$ and Ni_3Si_2 at early stages of the reaction has also been reported (Lavoie et al 2003). As the reaction proceeds, NiSi grows fully consuming the Ni-rich silicides. $NiSi_2$ nucleates and grows at higher temperatures.

For Ni FUSI (fully silicided) gate applications, deposited Ni films are reacted with poly-crystalline films of limited thickness, deposited on top of a dielectric. The deposited Ni thickness (t_{Ni}) to Si thickness (t_{Si}) ratio controls (in combination with the thermal history) the reacted Ni/Si ratio and the phases obtained. It is essential for gate electrode applications that the silicide phase at the dielectric

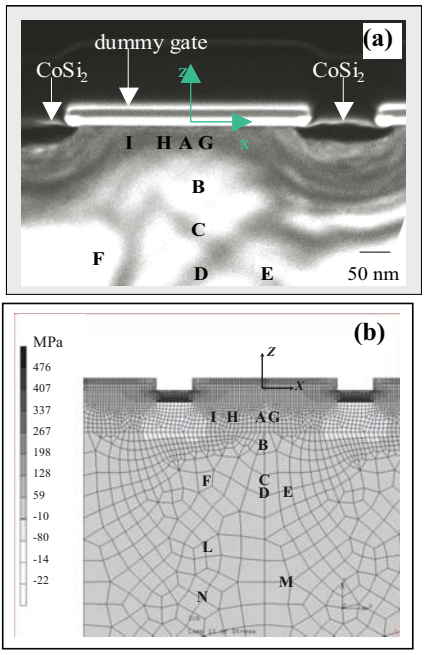
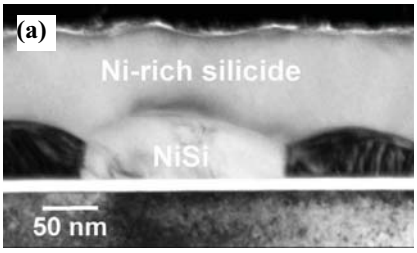


Fig. 12: (a) X-TEM image of a structure measured by CBED (silicide length = 120 nm, dummy gate length = 480 nm), (b) FEM simulation of the same structure (stress in x-direction).

POINT	X (NM)	Z (NM)	σ_{XX} (MPA) CBED	σ_{XX} (MPA) FEM
A	-10	-65	+100	+30
B	0	-150	0	+4
C	0	-240	0	+4
D	0	-270	-80	-6
E	+175	-270	-80	-4
F	-175	-250	-50	-4
G	+35	-65	+20	+29
H	-50	-65	+80	+30
I	-90	-65	+20	+29
L	-175	-400	0	-4
M	+175	-450	-70	-4
N	-175	-490	-20	-3

Table 1: Stress values obtained from CBED analysis and FEM modeling at the points indicated in Fig. 12.



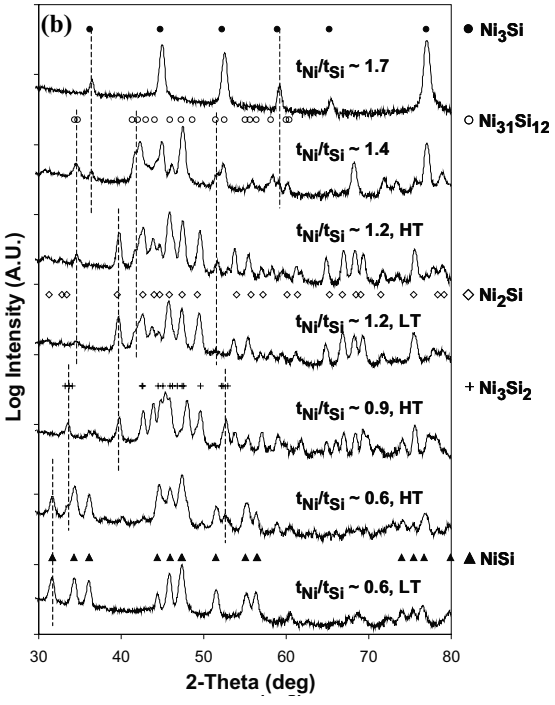


Fig. 13: (a) X-TEM of Ni FUSI gate stack showing bi-layer structure (NiSi was identified in the lower layer by Fourier transform of high resolution images), (b) XRD patterns of Ni-silicide on SiO_2 films for deposited Ni to poly-Si thickness ratios (t_{Ni}/t_{Si}) between 0.6 and 1.7 (LT and HT indicate lower and higher temperature processes respectively).

interface be well controlled, in order to ensure good control of the V_t of the devices. The phases and morphology after full silicidation for varying t_{Ni}/t_{Si} ratios and thermal processes were investigated, in order to assess and identify conditions for formation of gates with a controlled silicide phase at the dielectric interface. If processing temperatures are kept below the nucleation temperature of $NiSi_2$, a minimum t_{Ni}/t_{Si} ratio of ~ 0.55 is required to allow full silicidation of the gate with NiSi. A larger t_{Ni}/t_{Si} ratio (e.g. 0.6) is desirable, however, to ensure full silicidation and prevent the presence of Si pockets at the dielectric interface. As a result, when targeting NiSi as a gate electrode material, bi-layer silicide films are typically obtained with NiSi at the bottom and Ni-rich silicide on top. A TEM cross-section of such a gate stack is shown in Fig. 13a. The thickness of each layer depends on the Ni/Si ratio, with a larger proportion of Ni-rich silicide as the ratio is increased. The phases present in the upper Ni-rich layer can depend on the Ni/Si ration chosen and on the thermal history. Ni_2Si and Ni_3Si_2 were identified by XRD depending on the process conditions used.

Samples with t_{Ni}/t_{Si} ratios ranging between 0.6 and 1.7 were analysed by XRD and RBS. XRD indicates the presence of NiSi, Ni_3Si_2, Ni_2Si, $Ni_{31}Si_{12}$ and Ni_3Si as predominant phases for t_{Ni}/t_{Si} ratios of 0.6, 0.9, 1.2, 1.4 and 1.7 respectively. (Fig. 13b) RBS (not shown) suggests a layered structure with the more Ni-rich phase on top. No secondary phase is observed for a t_{Ni}/t_{Si} ratio of 1.7.

8. SUMMARY

In this paper, key considerations for SALICIDE processes were discussed: narrow line effects, thermal stability, compatibility with SiGe substrates, silicide induced stress and introduction of metal gates. The mechanism of sheet resistance degradation observed on sub 40 nm Co-silicided poly gates is identified as agglomeration of the Co-silicide. A reverse line width effect is observed on Ni-silicided poly gates due to excessive silicidation. Thermal degradation of thin Ni-silicide films was studied and the degradation mechanisms were identified. The use of alloying elements to improve the thermal stability of Ni-silicide was investigated. The formation of Ni-silicide on SiGe substrates was studied. It was found that the process window for the low resistance monosilicide phase is narrowed from both sides by the presence of Ge in the Si substrate. The stress induced in the transistor channel by the nearby source/drain silicide was studied by finite element modelling and verified by CBED analysis. The use of Ni-silicide as a metal gate electrode was investigated.

REFERENCES

Armigliato A, Balboni R, Frabboni S, Benedetti A, Cullis A G and Pavia G 2001 Inst. Phys. Conf. Ser. **169**, 467

Benedetti A, Bender H, Torregiani C, Van Dal M and Maex K 2004 Mater. Sci. Eng. B **114-115** *accepted for publication*

Chamirian O, Lauwers A, Kittl J A, Van Dal M, de Potter M, Lindsay R and Maex K 2004 Microelectron. Eng. **76** *accepted for publication*

Gambino J P and Colgan E G 1998 Mater. Chem. Phys. **52**, 99

Kittl J A, Prinslow D A, Apte P P and Pas M F 1995 Appl. Phys. Lett. 67, 2308

Kittl J A et al 2003 Mater. Res. Soc. Symp. Proc. **765**, 267

Lauwers A, Kittl J A, Van Dal M, Chamirian O, Lindsay R, de Potter M, Demeurisse C, Vrancken C, Maex K, Pagès X, Van der Jeugd K, Kuznetsov V and Granneman E 2004 Microelectron. Eng. **76**, 303

Lavoie C, d'Heurle F M, Detavernier C, and Cabral C 2003 Microelectron. Eng. **70**, 144

Mangelinck D, Dai J Y, Pan J S and Lahiri S K 1999 Appl. Phys. Lett. **75**, 1736

Sun M C et al. 2003 Symp. VLSI Tech 81

Torregiani C, Liu J, Vandevelde B, Degryse D, van Dal M J H, Benedetti A, Lauwers A and Maex K, 2004 Proc. Eurosime 2004 May 10-12, Brussels, p. 61

Van Dal M J H, Jawarani D, van Berkum J G M, Kaiser M, Kittl J A, Vrancken C, de Potter M, Lauwers A and Maex K 2004a J. Appl. Phys. **96**, 7568

Van Dal M J H, Akheyar A., Kittl J A, Chamirian O, de Potter M, Demeurisse C, Lauwers A and Maex K 2004b Mater. Res. Soc. Symp. 2004 Spring Meeting

Wang R N and J Y Feng 2003 J. Phys.: Condens. Matter **15**

Transmission electron microscopy characterisation of Ti and Al/Ti contacts on GaN and AlGaN/GaN

B Van Daele, G Van Tendeloo, W Ruythooren[1], J Derluyn[1], M R Leys[1] and M Germain[1]

EMAT, University of Antwerp, Groenenborgerlaan 171, 2020 Antwerpen, Belgium
[1] IMEC, Kapeldreef 75, 3001 Leuven, Belgium

ABSTRACT: Transmission electron microscopy has been applied to study Ti and Al/Ti contacts on GaN and AlGaN/GaN as a function of annealing temperature. This has lead to a profound understanding of the role of Al, both in the contact formation on n-GaN and on AlGaN/GaN. Al in the AlGaN decreases the N-extraction by Ti out of the nitride, because of the strong Al-N bond. Al in the metal bilayer also reduces the N-extraction by Ti due to a preferential alloy mixing.

1. INTRODUCTION

GaN-based devices are attracting a lot of attention, both for use in light-emitting diodes and in transistors. Device performance however is still limited by a lack of low-resistance Ohmic contacts. Only for n-GaN a standard metallization scheme exists. It typically has an Au/blocking layer/Al/Ti multilayer structure, with the blocking layer one of the metals Pt, Ti, Ni or Mo (Wang et al 2001, Lee et al 2000, Ruvimov et al 1996). The physics behind the contact formation on n-GaN is based on the creation of a tunnel junction due to the extraction of N by Ti out of the GaN upon thermal annealing (Kim et al 2002). As N vacancies are donors (Neugebauer et al 1994, Look et al 2003), a suitably high vacancy density near the GaN/metal interface is able to pin the Fermi level. Au on top of the metal stack is used to prevent oxidation of the contact. The blocking layer is meant to form a diffusion barrier in between the Au and the Al/Ti bilayer. The function of the Al in the metallization scheme has, within our knowledge, not been reported yet. It is however known that an optimum Al/Ti thickness ratio exists, which proves that the Al layer is necessary to obtain a good Ohmic contact (Motayed et al 2003).

In AlGaN/GaN transistor structures, the metal stack is supposed to make contact with a 2-dimensional electron gas (2DEG) located at the AlGaN/GaN interface. Usually the same metallization scheme as on n-GaN, with re-optimised parameters, is adopted to form a contact on AlGaN/GaN (Fay et al 2002, Jacobs et al 2002). It is however not clear yet which process does produce the better electrical coupling.

In this study, Ti and Ti/Al contacts, both on GaN and AlGaN/GaN, have been systematically studied as a function of the annealing temperature. The samples have been grown without blocking layer/Au cap to reduce the number of alloys possibly formed. This approach allowed us to determine the role of Al, both in the metallization scheme and in the AlGaN, on the mechanism responsible for Ohmic contact formation on GaN and AlGaN/GaN.

2. EXPERIMENTAL

An AlGaN/GaN structure, with 30% Al and 21nm thick, has been grown on (0001) sapphire in a 3 x 2'' close-coupled showerhead MOVPE reactor. Ammonia (NH_3), trimethylgallium (TMGa) and trimethylaluminium (TMAl) were used as precursors, N_2 was used as carrier gas. To exclude possible microstructural differences, all contacts have been deposited

on the same AlGaN/GaN wafer. The GaN samples (nominally undoped) have been prepared by selectively removing the AlGaN cap layer. Ti contacts were made by sputtering 20nm and evaporating 180nm. Ti/Al contacts are formed by sputtering 10nm Ti and evaporating 190nm Al. The policy was adopted to deposit the contacts without Au cap layer, in order to reduce possible metal-metal interactions. In this way, it was possible to circumvent unwanted reactions (between Au and Al, …) induced e.g. by a non-optimized metal thickness. All samples have been thermally annealed for 90s in an N_2 ambient in a rapid thermal anneal furnace, operating at constant power dissipation. End temperatures have been calibrated to be 805 and 991°C for a low temperature anneal and a high temperature anneal, respectively. These annealing conditions, applied to a standard Ti/Al/Ti/Au metal scheme on AlGaN/GaN, produce respectively Schottky and Ohmic contact behaviour. All samples have been investigated structurally and chemically using conventional, high-resolution and analytical transmission electron microscopy (TEM). The chemical analysis was performed combining electron-energy-loss spectroscopy (EELS), energy-dispersive X-ray spectroscopy (EDX) and high-angle annular dark-field imaging (HAADF). EELS data have been treated quantitatively using the EELSMODEL package (Verbeeck and Van Aert 2004), which is based on model fitting. The three analytical techniques have been verified for consistency (qualitatively) and determination of the phases is based on selected area electron diffraction.

3. RESULTS

In Ti contacts on GaN, the well-known N-extraction out of GaN by Ti has been observed. This results in the formation of a thick (>20nm) TiN layer. However, the reaction is much stronger than expected. At the same time, large voids are created in the GaN (Fig. 1). The size of the voids increases with increasing annealing temperature. These voids are created by the decomposition of GaN, as evidenced by the formation of a Ti-Ga alloy on top of the TiN.

Ti contacts on AlGaN/GaN show a decreased Ti-nitride interaction. In the sample annealed at low temperature, only the top part of the AlGaN is affected, while in the sample annealed at high temperatures, the entire AlGaN layer has transformed. The phase formed out of the former AlGaN is a highly defective Al+Ti+N containing layer, in which locally some cubic stacking, typical for the fcc TiN lattice, can be observed. Directly on top of the Al+Ti+N layer, a thin Ti-Ga alloy can be retrieved. The observed reaction can be interpreted as the substitution of Ga in the AlGaN by Ti.

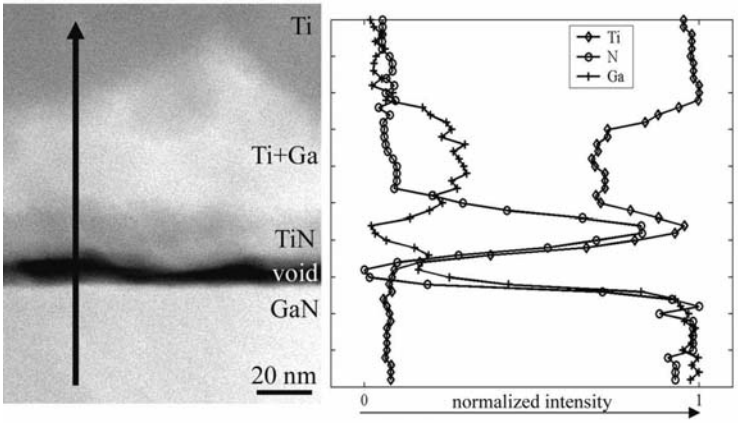


Fig. 1. HAADF image of a Ti contact on GaN, annealed at low temperature. On the right hand side, the normalized intensity of core-loss peaks in EEL-spectra is plotted for the elements Ti, Ga and N. The EELS scan is indicated by the black arrow in the HAADF image.

The N-extraction by Ti, that is possible when deposited on GaN due to a higher enthalpy of formation of TiN with respect to that of GaN, is therefore no longer possible on AlGaN. The fact that the enthalpy of formation of AlN is higher than that of TiN results in the fixation of the N in the AlGaN by Al. The only possible interaction is a substitutional replacement of Ga by Ti. The interaction between Ti on one side and GaN or AlGaN on the other side is thus different.

In Al/Ti contacts on GaN and AlGaN/GaN, annealed at low temperatures, the Ti-nitride interaction is very limited. The dominant process is the mixing of the Al/Ti bilayer, resulting in the formation of $TiAl_3$ precipitates and Al (Fig. 2). This time no voids have been formed in the GaN or AlGaN/GaN. Only a tiny interface reaction has occurred. Both on GaN and AlGaN/GaN, a thin (1nm) TiN layer has been formed. Determination of the phase is based on high-resolution images and on the detection of Ti near the interface in regions where Al (and not a $TiAl_3$ grain) is located next to the nitride.

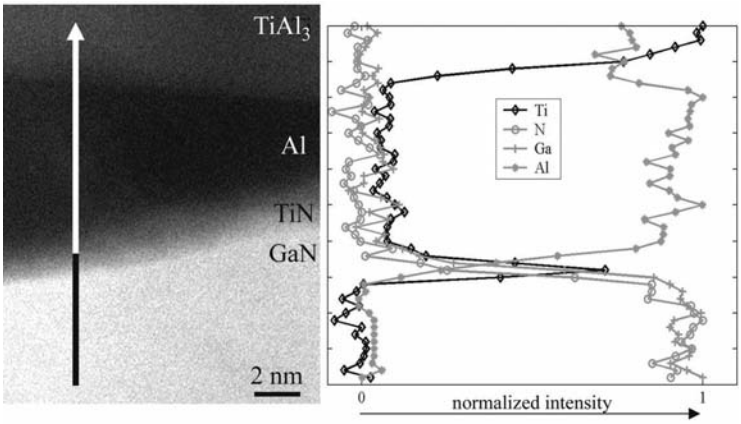


Fig. 2. HAADF image of an Al/Ti contact on GaN, annealed at low temperature. On the right hand side, the normalized intensity of core-loss peaks in EEL-spectra is plotted for the elements Ti, Ga, N and Al. The EELS scan is indicated by the black/white arrow in the HAADF image.

In Al/Ti contacts on GaN and AlGaN/GaN, annealed at high temperature, no Ti-nitride interaction and no Ti-Al mixing has been observed. The Al/Ti bilayer can be retrieved, but it is completely oxidised. Evidently this does not produce good contacts.

Despite this failure, we do not learn a lot about the annealing process. Besides knowing which processes are possible, it is necessary to know which process is dominant. At low temperature annealing Al-Ti mixing is dominant above the interaction between Ti and (Al)GaN, while at high temperature annealing oxidation is dominant above Ti-Al mixing and above the interaction between Ti and (Al)GaN.

4. CONCLUSIONS

Interpretation of the experimental results has lead to the understanding of the role of Al on the Ohmic contact formation on n-GaN and AlGaN/GaN. Two criteria are important: which processes can take place and which process is dominant? Al in the AlGaN keeps the N-bond. Because the enthalpy of formation of AlN is higher than that of TiN, Ti is not able to extract N out of the AlGaN like it does with GaN. Instead a substitutional replacement of Ga in the AlGaN by Ti has been observed. Al in the metal layer results in a preferential mixing of Ti and Al. The process is dominant with respect to N-extraction by Ti out of GaN. Oxidation of contacts annealed at high temperatures

has been observed, which is a result of investigating non-standard contact structures without a Au protection layer.

The mechanism revealed explains why Al/Ti contacts on n-GaN give better characteristics than pure Ti contacts. The Al slows down the interaction between the Ti and the GaN, resulting in a much more controlled N-extraction. The formation mechanism of Ohmic contacts on AlGaN/GaN can not be retrieved from these experiments. However, insight about the possible interactions and the consequences of Al in the AlGaN has been obtained.

ACKNOWLEDGEMENTS

This work has been performed within the framework of IAP V-1 and was supported by the European Space Agency (ATHENA project, ESTEC contract no. 14205/00/NL/PA). B. Van Daele is grateful to the Fund for Scientific Research – Flanders (F.W.O. – Vlaanderen).

REFERENCES

Fay M W, Moldovan G, Brown P D, Harrison I, Birbeck J C, Hughes B T, Uren M J and Martin T 2002 J. Appl. Phys. **92**, 94

Jacobs B, Kramer M C J C M, Geluk E J and Karouta F 2002 J. Cryst. Growth **241**, 15

Kim J K, Jang H W and Lee J L 2002 J. Appl. Phys. **91**, 9214

Lee C T and Kao H W 2000 Appl. Phys. Lett. **76**, 2364

Look D C, Farlow G C, Drevinsky P J, Bliss D F and Sizelove J R 2003 Appl. Phys. Lett. **83**, 3525

Neugebauer J and Van de Walle C G 1994 Phys. Rev. B **50**, 8067

Ruvimov S, Lilienthal-Weber Z, Washburn J, Duxstad K J, Haller E E , Fan Z F , Mohammad S N, Kim W, Botchkarev A E and Morkoç H 1996 Appl. Phys. Lett. **69**, 1556

Verbeeck J and Van Aert S 2004 Ultramicroscopy **101**, 207

Wang D F, Shiwei F, Lu C, Motayed A, Jah M, Mohammad S N, Jones K A and Salamanca-Riba L 2001 J. Appl. Phys. **89**, 6214

Dynamics of Au Adatoms on Electron-Irradiated Rough Si Surfaces

K Torigoe, Y Ohno, T Ichihashi[1] and S Takeda

Department of Physics, Graduate School of Science, Osaka University, 1-1, Machikaneyama, Toyonaka, Osaka 560-0043, Japan
[1] NEC Corp Ltd, Fundamental and Environmental Research Laboratories, 34 Miyukigaoka, Tsukuba, Ibaraki 3058501 Japan

ABSTRACT: We have examined the dynamics of Au adatoms on Si surfaces with surface roughness introduced by electron irradiation. Observing the areal distribution of Au nanoparticles on inhomogeneous rough surfaces by transmission electron microscopy, we have found that Au adatoms were preferentially assembled not on flat regions but on rough regions. We have proposed that the peculiar distribution of Au adatoms is formed since a rough surface acts as a sink for adatoms and the diffusion constant of adatoms on the rough surface is smaller than that on the unirradiated one.

1. INTRODUCTION

Atomic diffusion is one of the important factors in crystal growth. When crystals are grown on a surface, the surface diffusion of adatoms determines the shapes, the size and areal distributions of the crystals. The diffusion process has been well investigated on atomically controlled clean surfaces by means of STM (Mo et al 1991), ab initio calculations (Brocks et al 1991), and by other techniques (e.g. Shiraishi et al 1996). Examining the diffusion process of adatoms on a modified rough Si surface, we have recently found that adatoms preferentially assemble on a rough surface, presumably due to the strong binding energy of an adatom to the surface, and so the diffusion constant of adatoms on the surface is smaller than that on the flat one (Torigoe et al 2005). The self-assembling process, similar to other self-assembling processes (e.g., Homma et al 1997, Shibata et al 1999), has potential application in nanotechnology, since roughness of a nanometer scale can be formed at any position on any surface by scanning a focused electron beam. In this paper, we briefly summarize the dynamics of adatoms on rough surfaces and show that clusters of adatoms at any position can be formed using inhomogeneous rough surfaces.

2. EXPERIMENTAL

A thin Si(001) wafer with clean surfaces was prepared by heating at about 1200^{o}C in a pretreatment chamber of an ultrahigh vacuum transmission electron microscope (UHV-TEM) (JEOL JEM2000FX, with base pressure of 10^{-8}Pa). The sample was irradiated by high-energy electrons (160keV) at room temperature (RT), to introduce surface roughness on the electron exit surface. The morphology of electron exit surfaces has been studied with scanning tunneling microscopy, and the surfaces are rough (Ozaki et al 2001). The electron beam was converged to a circular area of a few micrometres on the surface, and the intensity along the radial direction, $I(r)$ can be described by a Gaussian function, $I(r) = I_0 \exp(-r^2/2\sigma^2)$, where r is the distance from the center of the irradiated area and σ (~60nm) is the half width of the electron beam. I_0 ranged from $0.6\text{x}10^{27}$e/m^2 to $9.0\text{x}10^{27}$e/m^2. Au was deposited on the electron exit surface in the pretreatment chamber at RT, and the surface was observed at RT. The sample was then annealed up to T=523K.

3. RESULTS AND DISCUSSION

3.1 Diffusion and Condensation of Au Adatoms on Rough Si Surfaces (Torigoe et al 2005)

Figure 1a shows a TEM image observed at RT. The black dots of a few nanometres in diameter represent Au nanoparticles. Au nanoparticles were formed uniformly far from the irradiated area,

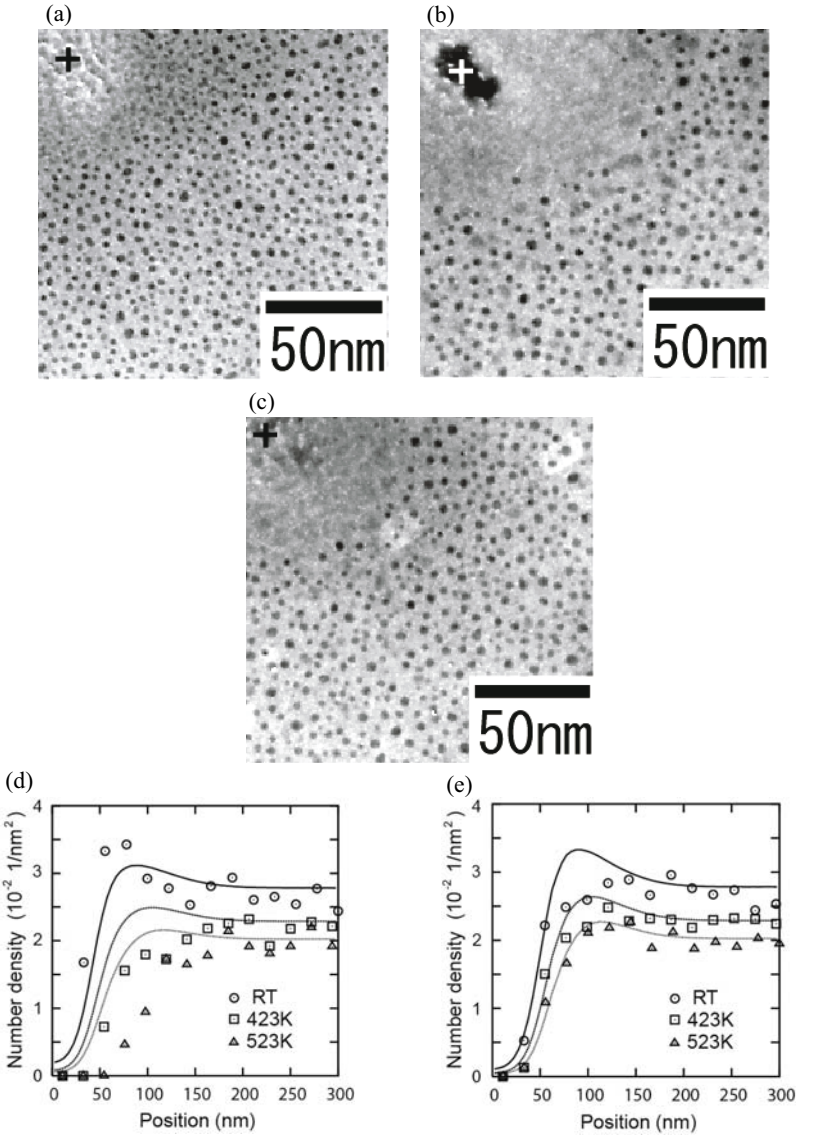


Fig. 1: (a)-(c) TEM images of Au deposited surfaces; (a) and (b) $I_0 = 1.8\text{x}10^{27}$ e/m^2, and (c) $I_0 = 3.0\text{x}10^{27}$ e/m^2. (a) As deposited. (b) and (c) Annealed at 523K. The crosses indicate the center of the irradiated area. The number density of Au nanoparticles as a function of r; (d) $I_0 = 1.8\text{x}10^{27}$e/m^2 and (e) $I_0 = 3.0\text{x}10^{27}$e/m^2. The circles, triangles and squares show the experimental results at RT, 423K and 523K, respectively. The curves correspond to the calculated results.

while no Au particle was observed in the irradiated area (r < ~50nm) (the circles in Fig. 1d). The depleted zone, in which the number density of Au nanoparticles is zero, expanded with increasing I_0 (e.g., Fig. 1d and 1e). With increasing T, the number density of nanoparticles far from the irradiated area decreased, and the depleted zone expanded. When the electron dose was small (I_0<3.0x10^{27}e/m^2), a large Au cluster, of a few tens of nm in diameter, was formed on the center of the irradiated area (Fig. 1b). On the surfaces irradiated with higher doses, such a large cluster was not formed (e.g. Fig 1c).

The growth process of clusters of adatoms is mainly controlled by the nucleation and Ostwald ripening mechanism. The nucleation process, controlled by migration and coalescence of adatoms, dominates the initial stage of the growth, and the ripening process determines the number density of clusters at later stages. The number density of clusters and the concentration of free adatoms on a flat surface have been examined with a thermodynamic theory (Zinke-Allmang et al 1992). In the theory, they are determined by the various parameters, such as diffusion constant of adatoms described with an activation energy, E. We have expanded the theory for adatoms on inhomogeneous rough surfaces in order to explain the peculiar distribution of Au nanoparticles on electron irradiated surfaces. In the expanded theory, it was assumed that $\mathrm{E}(r) = \mathrm{E}_0 + \Gamma I(r)$, where Γ is a constant and E_0 is the activation energy for surface diffusion on a flat surface, and the concentration of surface sinks for adatoms is in proportion to $I(r)^{\mathrm{n}}$ where n is a constant. The areal distribution of Au nanoparticles calculated with the theory well reproduced the experimental one, except at heavily irradiated areas: the number density of Au nanoparticles far from irradiated areas decreased with increasing T, and the depleted zone expands with increasing T and I_0, (e.g., Fig. 1d and 1e). According to the expanded theory, a number of free adatoms exist on a heavily irradiated area after annealing (e.g., Fig. 2). They would condense into a large cluster and the cluster may act as strong sink for adatoms, even though the effect is not considered at the present moment.

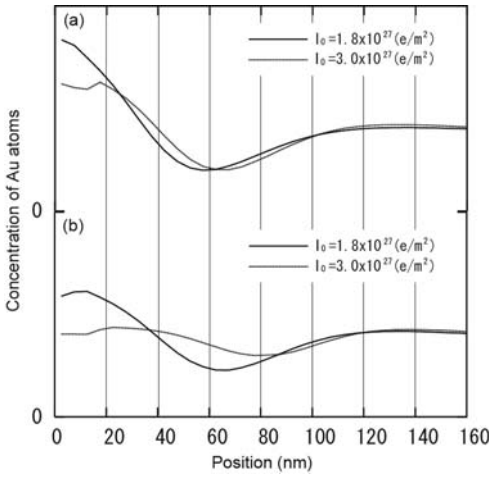


Fig. 2: The total amount of Au atoms at 523K. The solid and dotted lines correspond to the results on the surfaces irradiated with I_0=1.8x10^{27}e/m^2 and I_0=3.0x10^{27}e/m^2, respectively. (a) Γ = 1.4x10^{-29} eVm^2/e and (b)2.1x10^{-29} eVm^2/e. The concentration of atoms far from the irradiated area corresponds to the number of atoms accumulated into the nanoparticles. On the other hand, that in the irradiated area represents the free adatoms attracted into the area due to the effect of sinks on rough surfaces.

3.2 Control of the Distribution of Nanoparticles

Our model suggests that Au atoms diffuse into the irradiated areas from the surrounding area. When I_0 is low, the concentration of adatoms at the center of the irradiated area is the highest (Fig. 2). The concentration decreases with increasing I_0, because of a decrease of the diffusion constant of adatoms on the irradiated area. Therefore, an Au cluster of any size would grow selectively on an area irradiated with a moderate dose of electrons (e.g., Fig. 1b). The results demonstrate possible control of the distribution of nanoparticles with inhomogeneous rough surfaces. Various distributions are expected, because Γ depends on the species of the irradiated substrate and the deposited adatoms, as well as the electron flux.

4. CONCLUSIONS

We have investigated the dynamics of Au adatoms on electron-irradiated surfaces and found that Au adatoms assemble selectively on an electron irradiated surface.

ACKNOWLEDGEMENTS

This work was supported in part by the AIST-KAMSAI. We would like to express our sincere appreciation to Dr. T. Akita. This work was partly supported by the Grants-in-Aid for Scientific Research (A) 15201026 (2003-2006) and Grant-in-Aid for Young Scientist (A) (2) 15681006 (2003-2005), from the Ministry of Education, Science, Culture and Sports.

REFERENCES

Brocks G, Kelly P J and Car R 1991 Phys. Rev. Lett. **66**, 1729
Homma Y, Finnie P, Ogino T, Noda H and Urisu T 1999 J. Appl. Phys. **86**, 3083
Mo Y W, Kleiner J, Webb M B and Lagally M G 1991 Phys. Rev. Lett. **66**, 1998
Ozaki N, Ohno Y, Tanbara M, Hamada D, Yamasaki J and Takeda S 2001 Surf. Sci. **493**, 547
Shibata M, Stoyanov S S and Ichikawa M 1999 Phys. Rev. B **59**, 10289
Shiraishi K 1996 Thin solid films **272**, 345
Torigoe K, Ohno Y, Ichihashi T and Takeda S 2005 *in preparation for submission*
Zinke-Allmang M, Feldman L C and Grabow M H 1992 Surf. Sci. Rep. **16**, 377

Corrosion of FIB-milled Cu during air exposure

H Bender, O Richard, P Van Marcke and C Drijbooms

IMEC, Kapeldreef 75, BE-3001 Leuven, Belgium

ABSTRACT: Focused ion beam milling for cross-section imaging and specimen preparation for analysis by transmission electron microscopy leaves copper surfaces in a non-passivated state which is highly susceptible to different kinds of corrosion effects. This work discusses the corrosion effects on specimens stored in air for longer time. It is shown that investigation by TEM accelerates the subsequent corrosion, while treatment in an O_2/Ar plasma strongly suppresses the corrosion.

1. INTRODUCTION

Milling in a focused ion beam (FIB) unit through Cu metallisation structures results in a non-passivated Cu surface that is potentially susceptible to corrosion effects (Bender et al 2004). In-situ corrosion has been reported previously in the presence of low concentrations of I_2 in the FIB system (Bender et al 1999). The present work deals with corrosion effects observed on TEM specimens prepared under I_2-free conditions and which are related to the air exposure between the FIB preparation and the TEM analysis. The corrosion is investigated with TEM imaging and EFTEM compositional analysis. It typically results in fine speckled material spread over the thin foil and formation of voids in the Cu. The possibility to suppress the corrosion by passivating the Cu surface after the FIB preparation with an O_2/Ar plasma is explored. The nature of the surface layer on Ga ion beam scanned Cu layers exposed to clean room ambient with or without the plasma treatment is further investigated with Auger electron spectroscopy.

Although correlation with air exposure time exists, other parameters can sometimes also lead to corrosion in a variety of morphologies on the foils, i.e. irregularly and needle shaped crystals or flower-like appearances (Bender et al 2004). The conditions leading to these additional corrosion effects are not fully understood yet. In certain cases a relationship to poor barrier quality is found.

2. SPECIMEN PREPARATION AND EXPERIMENTS

The structures used for the analysis consist of dual layer dense Cu lines (nominal width and spacing 0.25 μm) with Ta/TaN barrier in SiO_2 dielectric. The lines in the lowest metal (M1) run parallel with the TEM foil, the ones of the upper metal (M2) are orthogonal to the TEM specimen. No passivation layer is present. The samples are diced for TEM preparation in 2mm × 70μm slices with an automated diamond bladed system with water cooling. All specimens discussed in this work are thinned by focused ion beam in a single beam FIB system using the trench milling technique and finalising the thinned foil in a wedge shape (Bender 1999). In order to protect the surface for the Ga ion beam damage during the initial scanning and Pt deposition, a SiO_2 protective layer is deposited ex-situ. Generally this is done by a low temperature CVD process (150ºC) before the sawing. Also samples without protective layer and with a sputtered glass layer deposited before or after the sawing are considered.

Several specimens are prepared identically. They are investigated and later re-investigated by TEM in a CM30 electron microscope at 300 keV at different ages after their preparation as indicated in Table 1. Some experiments are repeated to evaluate the reproducibility. EFTEM analysis is applied to characterize the corrosion. Some specimens are treated in an O_2/Ar plasma for 5 or 10 minutes in a

Fishione instrument under standard conditions as applied for cleaning of TEM specimens and specimen holders. The plasma cleaning is done shortly after the FIB preparation (# 6-8) or after the first and second TEM investigation (# 9 and 10). The thinned TEM specimens are stored before or between the observations in gelatine capsules.

The impact of the plasma cleaning on the Cu surface is also investigated by Auger electron spectroscopy on unpatterned Cu layers which are milled in the FIB system until the native surface oxide is removed and clear channelling contrast can be observed in the secondary electron image.

Table 1 : Summary of the timeline of the investigations and of the grade of corrosion as function of the age since the TEM specimen preparation, the treatment in the O_2/Ar plasma and the sequence of the TEM observations.

age (days) :		*0*				*14-17*	*24-31*	*55 & 117*
#	glass	TEM	O_2/Ar plasma	TEM	O_2/Ar plasma	TEM	TEM	TEM
1	CVD					weak (M2)	very severe	
2	CVD	no corrosion				severe		
3	before dicing	no corrosion					severe	
4	before FIB	no corrosion					severe	very severe
5	no glass	no corrosion					severe (voids top M2)	
6	CVD		5 min			minor (M2,M1,glass)		
7	CVD		5 min			minor (below M1)		
8	CVD		10 min			no corrosion		weak (M2)
9	CVD	no corrosion	5 min	no corrosion	5 min	minor (M2)	unchanged	
10	CVD	no corrosion	5 min	no corrosion	5 min	minor (M2,M1)		

3. RESULTS

3.1 Time Dependent Cu Corrosion

The corrosion effect is illustrated on Fig. 1 for a specimen that is stored after the thinning for 14 days before the first TEM investigation. Next to the Cu lines few speckles are present on the dielectric (Fig. 1a) while the Cu still looks normal. The same Cu line is 15 days later (age 29d) severely degraded (Fig. 1b). A high density of speckles is present concentric around the Cu lines on the dielectric and also on the Cu which seems partially converted to the speckled material over the full thickness of the specimen. Specimens which are observed as soon as possible after the thinning show no corrosion (Fig. 2a illustrates sample 2, similar observations for samples 3-5 and 9-10), while 14 days later severe corrosion is present (Fig. 2b). Comparison with sample 1 after 14 days indicates that the initial TEM observation at day 0 of specimen 2 accelerated the corrosion during the next two weeks. This impact of TEM investigation on the corrosion rate is generally observed, i.e. also on specimens 3-5 and other samples not discussed here. Although some effect of electron beam irradiation damage cannot be excluded, the more likely cause for this enhanced corrosion seems to be the carbon absorbed from the TEM residual vacuum during the investigation.

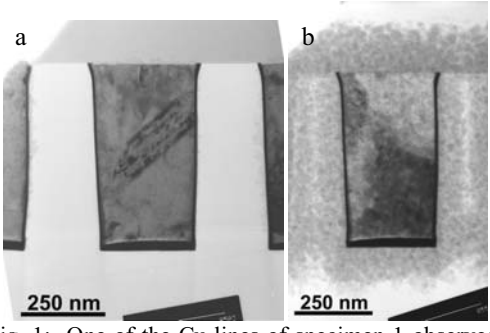


Fig. 1: One of the Cu lines of specimen 1 observed in the TEM for the first time after 14 days (a) and re-investigated 29 days after the specimen thinning (b).

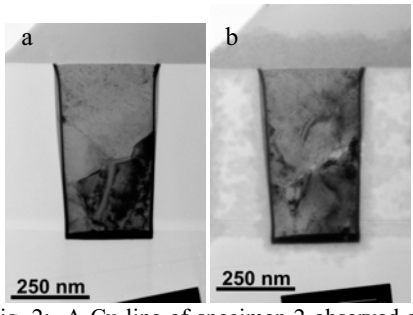


Fig. 2: A Cu line of specimen 2 observed as soon as possible after the thinning (a) and re-investigated 14 days later (b).

The absence of a protective layer on top of the Cu implies that during the scanning with the Ga ion beam before and during the initial Pt deposition, damage will be introduced and Ga implanted near the top surface of the Cu. This damage is not obvious on the TEM images taken shortly after the specimen thinning. During further storage of the specimen, severe corrosion occurs and holes are preferentially formed in the top of the Cu lines (Fig. 3). It could be an indication that the damage or the implanted Ga stimulates the corrosion. Also on the surfaces of the thinned foil such effects could act. The implanted dose is there however much lower and less deep in the foil than on the top surface.

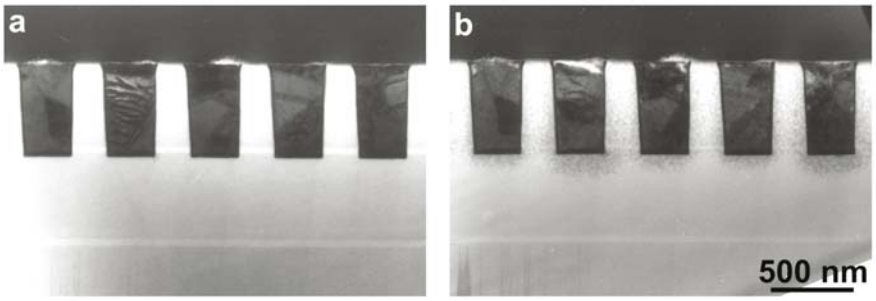


Fig. 3: TEM images obtained after 1 day (a) and reexamined after 24 days (b) for a specimen thinned without protective cap layer on top of the Cu lines.

3.2 Suppression of Cu Corrosion

Treatment of the thinned specimens in an O_2/Ar plasma allows the suppression of the time dependent corrosion. This is illustrated on Fig. 4 for a specimen that was stored for 17 days after the thinning which was followed by a 5 min O_2/Ar plasma treatment. Only some weak corrosion effects are present near the M2 lines. In other cases (#7) the corrosion was limited to the M1 Cu lines (not shown). A longer plasma treatment (10 min) results in a full suppression of the corrosion after 14 days and results only in a weak effect as observed during the re-examination at an age of 55 days (Fig. 5, #8).

The plasma treatment has no visible effect on the TEM specimens, as was checked with samples #9 and 10 that were investigated immediately after the thinning, subsequently plasma cleaned and checked again in the TEM. Before further storage they were cleaned again for 5 minutes. A few weeks later the corrosion was still minor whereas under similar conditions without plasma treatment severe corrosion is observed (compare with #2). Moreover 2 weeks later, at an age of 31 days, the corrosion has not increased further. Hence it can be concluded that the plasma treatment suppresses the rate of corrosion and that it furthermore results in a long time protection.

The effect of the plasma treatment on the FIB milled Cu surfaces is investigated by Auger depth profiling. A reference sample which is only scanned with the Ga ion beam shows some C and O on the surface which is due to absorption or slight oxidation during the transfer of the samples through the air between the FIB and Auger system. A low Ga signal is uniformly distributed in the top ~20-25 nm of the Cu. The samples that are treated in the O_2/Ar plasma after the FIB scanning, show a much thicker surface oxide (roughly estimated 5-7 nm) and a pile-up of the Ga at the Cu-oxide/Cu interface while all surface C is removed. The upper part of the oxide also contains F, which seems to originate from a contamination with vacuum grease in our plasma system. Whether this F plays a role in the suppression of the corrosion is under investigation. Increasing the plasma time from 5 to 10 minutes does not result in an increase of the Cu-oxide thickness, i.e. the plasma induced oxide growth is a self-limiting effect contrary to surface corrosion of Cu in air (Jian et al 1991, Apen et al 1998). The improved corrosion resistance for longer treatments as observed on the TEM specimens shows that the 5 minutes treatment is likely just below a critical duration. For the Auger experiment, test samples scanned under normal incidence are used. This condition leads to a much higher Ga content in the samples than under normal TEM specimen preparation conditions in which case the Ga ion beam scans almost parallel with the thinned foil. On Cu test samples which are scanned with the Ga ion beam on their sidewall, the Ga content at the Cu surface remains below the detection limit for Auger analysis.

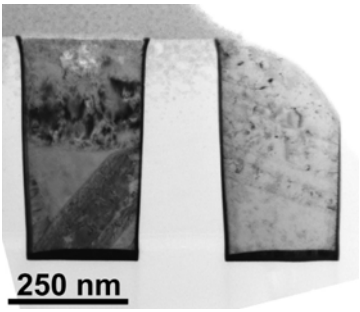


Fig. 4: TEM image of specimen 6 observed 17 days after the preparation which was followed by a 5 min O_2/Ar plasma treatment.

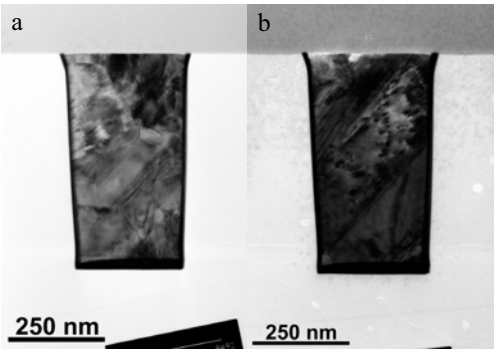


Fig. 5: Images of the same line investigated 14 days after the thinning which was followed by a 10 min O_2/Ar plasma treatment (a) and after subsequent further storage till an age of 55 days (b).

3.3 Composition of the Corrosion

The composition of the corroded material is studied by EFTEM. In all cases it shows that the speckled material contains Cu. The presence of oxygen is less trivial from the measurements as the corroded material is on top of Si-oxides or O containing SiC layers. In severe cases where the Cu lines are themselves transformed to the speckled material (e.g. Fig. 1b), the presence of C and O in the original Cu-lines is obvious, i.e. it is likely that a Cu-carbonate has formed in those cases.

4. CONCLUSIONS

FIB thinned Cu samples slowly corrode during storage in air resulting in a speckled contrast on the thinned foil and finally full degradation of the Cu. TEM observation stimulates the corrosion during subsequent storage of the samples. It is likely that the C contamination deposited on the surfaces of the thin foil in the TEM causes this enhancement. O_2/Ar plasma treatments efficiently remove the C contamination and result in a stable surface oxide that passivates the sample. Other corrosion effects resulting in crystals and needles on the thinned foil must be caused by other effects that are under further investigation.

ACKNOWLEDGEMENTS

For stimulating discussion and providing valuable information we greatly acknowledge Elvin Beach and Steve Rozeveld (Dow Chemical, Midland), Marie-Ange Iannello (Texas Instruments France), Marcel Verheijen (Philips Research, Eindhoven) and Rocco R. Cerchiara (Fischione Instruments). It is the authors' pleasure also to acknowledge the IMEC Cu-processing group for providing samples and extended discussions.

REFERENCES

Apen E, Rogers B R and Sellers J A 1998 J. Vac. Sci. Technol. A **26**, 1227

Bender H 1999 Inst. Phys. Conf. Ser. **164**, 593

Bender H, Jin S, Vervoort I and Lantasov Y 1999 Proceedings 25th International Symposium for Testing and Failure Analysis, (ASM International, Materials Park, Ohio) p 135

Bender H, Richard O, Benedetti A, Van Marcke P and Drijbooms C 2004 Proceedings 8th European Focused Ion Beam Users Group Meeting, http://www.imec.be/efug/EFUG2004_Bender.pdf

Jian Li, Mayer J W and Colgan E G 1991 J. Appl. Phys. **70**, 2820

Part VII

Device Studies

FIB applications for semiconductor device failure analysis

D M Donnet and H Roberts

Philips Semiconductors, 6534 AE Nijmegen, The Netherlands

ABSTRACT: As well the universal usage for SEM and TEM cross-sectional sample preparation, modern FIBs have other applications which make them extremely suitable for semiconductor device analysis. Foremost amongst these is the ability to modify existing IC circuitry. Particular attention will be paid to circuit modification of the latest generation of devices where the use of copper interconnects requires the use of different gas chemistries in the FIB and where the complexity of the device itself often only permits modifications to be performed through the backside of the chip.

1. INTRODUCTION

Failure analysis (FA) in the semiconductor industry is concerned with locating and finding the root cause of defects in IC devices (Boit 1999, Tracy 2002). Such defects can, in principle, occur during any stage of processing through too narrow process margins or through one-off incidents in the fab which result in yield loss. In addition, reliability failures are not apparent until the packaged device is actually performing its designated function; often out in the customer field. Thus failure analysts are confronted with problems at both the wafer level and finished (i.e. packaged) device level.

Whichever is the case, with transistor widths now under 100 nm and up to nine layers of metallisation, a set of advanced tools is required to locate the failing part of the device. In order to make good use of such a tool set, a failure analyst must be multidisciplinary with a wide range of competencies extending from design and test expertise, to materials science understanding and packaging expertise. One of the most important of these tools is the focused ion beam (FIB) because it is in itself a multi-functional tool which is central to virtually all FA activities (Verkleij 1999). This is illustrated in Fig. 1 which depicts a typical FA loop, demonstrating that the FIB can be used a various stages of this loop. In the following sections, examples are given that further illustrate the critical role that FIB plays in a modern semiconductor FA laboratory.

2. VOLTAGE CONTRAST

Passive voltage contrast in the FIB is the key that makes it such a powerful tool for semiconductor FA. The yield of the secondary electrons and ions generated when the positively charged primary beam impinges upon the sample surface depends greatly on the local surface potential. Insulators charge up, generating a large electric field thus inhibiting the emission of secondary electrons and the feature appears as dark contrast in the FIB image. Conductors do not charge up and a large secondary electron yield is generated and the feature appears bright in the FIB image. In this way, voltage contrast is used as an estimation as to whether a feature is electrically floating or grounded.

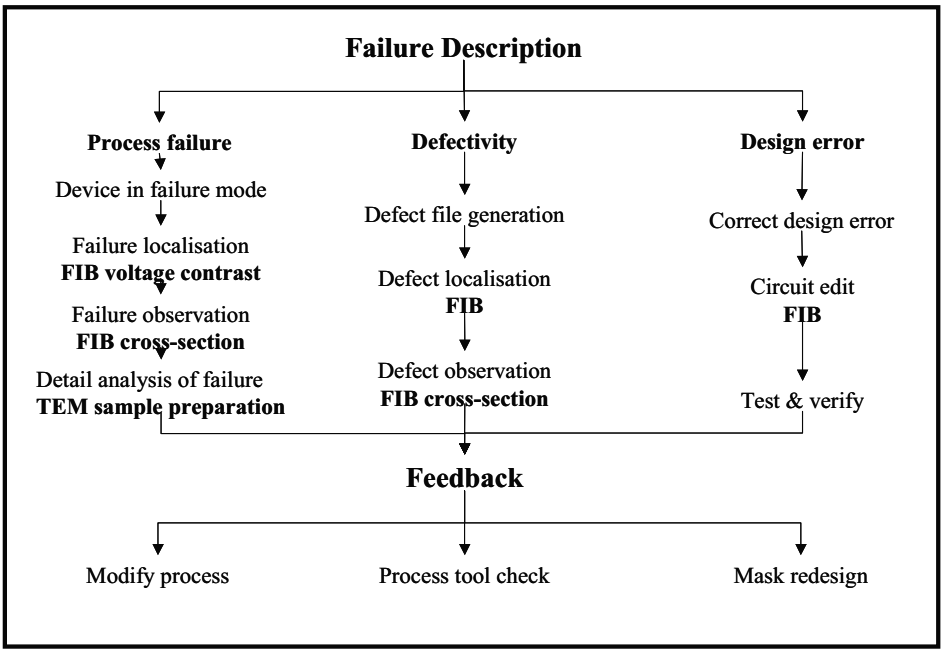


Fig. 1. Example of a typical failure analysis loop, demonstrating where FIB can be used.

Two uses of voltage contrast used to find a failure are provided in Fig. 2. Following testing a failure showing the fingerprint of a metal stringer (i.e. short circuit) was detected. Careful analysis of the design file narrowed down the possible regions where such a stringer can occur. Generally this is where there is a large amount of topography in the device and a sufficient overetch of the metal line is required to remove all metal residues. In Fig. 2a, a typical area of crossing metal lines is observed (position 1). At position 2, two cuts are made and show that the line is floating, however when cuts are made on either side of position 2, the line still appears electrically grounded, thus it is likely shorted to the adjacent line. To confirm this, a FIB cross-section is made exactly between the two top metal lines as indicated. The bright spot in the resulting FIB image (Fig. 2b) is the metal residue or stringer causing the short.

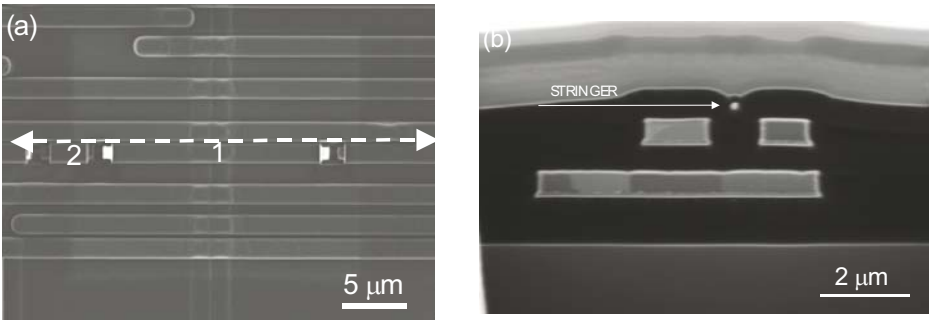


Fig. 2. Illustration of how voltage contrast is used to find location of metal stringers.

A second example of the use of voltage contrast is now presented. A lifetime fail in a memory cell was detected by a bitmap analysis. This provides the exact row and column coordinates of the failing bit. The sample is mechanically polished until contact level and then imaged in the FIB. Such contacts in N+ regions on substrate act as reverse diodes and do not conduct well, thus should appear dark in the FIB image. Fig. 3a shows the resulting FIB image from the failing bit which is clearly

bright. A FIB cross-section (Fig. 3b) shows that a short is the cause of the failure and subsequent TEM analysis revealed that Ti residues from silicidation were the cause of the short.

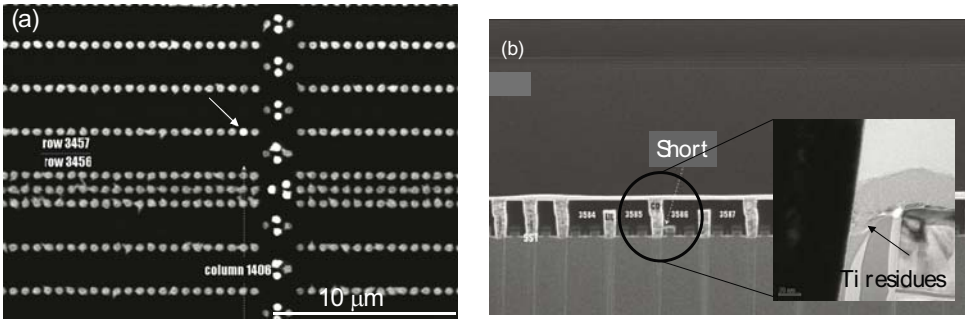


Fig. 3. a) Voltage contrast from a polished memory cell revealing the failing bit. b) Subsequent FIB and TEM cross section showing that a short caused by Ti residues was the explanation for the failure.

3. CROSS-SECTIONING

Cross-sectioning is the overwhelmingly most popular usage of the FIB for both semiconductor and non-semiconductor applications. With transistor dimensions shrinking to the sub 100 nm scale, the practical reasons behind this are not hard to understand. Whilst mechanical polishing is still an important skill for the failure analyst, the unparalleled precision and speed make the FIB uniquely suited for a number of important FA applications which are detailed below.

During wafer processing, defectivity maps are made of the devices after a number of important process steps. The cause of the defects is often nanoparticles which are unintentionally introduced in the deposition chambers. The defectivity file maps each individual defect position on the wafer. This file in combination with an accurate FIB stage allows each defect to be located and if necessary cross-sectioned to reach a conclusion to the root cause. In many cases, FIB voltage contrast, as outlined above, will prove sufficient, but often it is necessary to image in a scanning electron microscope (SEM) to reach the correct conclusion. This can be for reasons of resolution or the need to image insulator layers which do not image well in the FIB.

The development of dualbeam tools, in which both FIB and SEM columns are present, has helped greatly in this type of analysis since it is possible to observe the cross-section in SEM mode whilst the FIB is actually making the cross section. This allows for greater control when cross-sectioning through ever smaller defects or devices. It is important to note however that such dualbeams are generally only suitable for wafer level analysis. The height difference between a package and the device itself mean that at the eucentric position of the device it is likely that the package will made contact with the pole-piece of the SEM. Thus in an FA laboratory where packaged samples are still analysed a combination of single and dual-beam tools is still a requirement.

When more detailed analysis of the failure is require, the FIB can be used as a tool to prepare samples for transmission electron microscopy (TEM). There are a variety of different methods depending on sample geometry and available FIB apparatus. Here we concentrate on the in-situ lift-out technique (Donnet et al 2003). A lamella (whose thickness can vary as required) is lifted out from the IC device using a needle in the FIB and transported to and subsequently attached to a TEM sample grid for further thinning. The advantages of this method are clear; in principle a lamella from any sample geometry can be lifted out and it allows for further re-thinning following initial TEM observation.

An interesting example of this lift-out technique is shown in Fig. 4 which clearly illustrates how the combination of FIB-SEM-TEM can be used to solve an FA problem. In this case, a soldering problem arose between the Cu heatsink and the printed circuit board (a). As an initial stage, the

complete sample was embedded in epoxy and mechanically polished (b). This polished sample was then observed in the SEM where with the help of backscattered contrast it was possible to observe small regions in the Ni layer with enhanced P (b). To determine the phase of these regions, it was necessary to perform micro-diffraction in the TEM and the FIB was then used to lift-out a lamella from the area indicated and to attach it to the TEM grid (b).

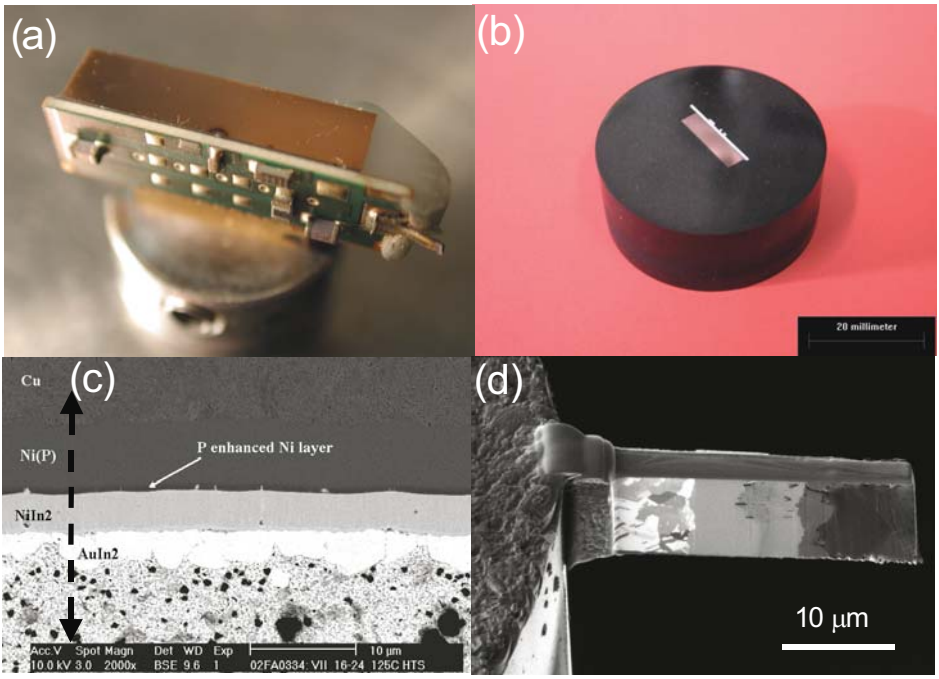


Fig. 4. TEM sample preparation from a mechanically polished device on a printed circuit board.

4. CIRCUIT EDIT

The local modification of circuits was in fact the first application of the FIB in the semiconductor industry. The unique ability of the FIB to both remove and deposit material allows for changes in circuit functionality, evaluation of design modifications and the correction of design errors to be realized. This can provide IC designers with prototype samples in a matter of hours without incurring the steep costs of mask redesign.

In the early days when circuitry dimensions could be measured in microns with a maximum of two layers of metallisation, FIB circuit edit was a rather simple task since direct navigation to the region of interest was easy given the large topography in such devices. Holes in the passivation and dielectric layers and cuts in the Al metallisation were made with enhanced gas etching. Pt (or W) deposition was used to make new interconnections with opened metal lines With the introduction of planarised processes however, no topographic contrast is available in the FIB thus navigation became more critical, but with the aid of design files and accurate measurements circuit edit proved possible down the 180 nm technology node.

For technology nodes below 120 nm, Cu metallisation with up to 9 metal layers are used, together with low-k dielectrics. In order to perform edits on such advanced processes a new approach is required with dedicated circuit edit FIBs (Casey et al 2002). These tools have a wide range of gas chemistries available to be able to mill cleanly through all present layers (Al and Cu metal lines, oxides, low-k dielectrics). In addition, the ability to deposit low ohmic metal and insulator (for repair)

are also required. When used in conjunction with an extremely accurate stage combined with software that allows overlay of the design file over the FIB image it is possible to mill small holes with aspect-ratios up to 10:1 which allows complex edits to be performed where it is impossible with more conventional equipment. An example of this is given in Fig. 4. Here it was necessary to change the voltage shifter by making two joins and three cuts on metal 1 and metal 2. This was a 90 nm technology device, the whole edit had to be performed in an area of 5 x 5 μm at a depth of more than 7 μm. In this device both Al and Cu metallisation are present as are both oxide and low-k dielectrics further complicating the process of editing. Thus it is critical to make use of all available gas chemistries in this edit. In Fig. 5(a)-(f), FIB images taken sequentially during the edit are presented. The final image (f) shows two joins and a single cut all within 2 μm of each other. It should be noted that no overspray of the metal deposition occurs, thus no subsequent cleaning of the region is required.

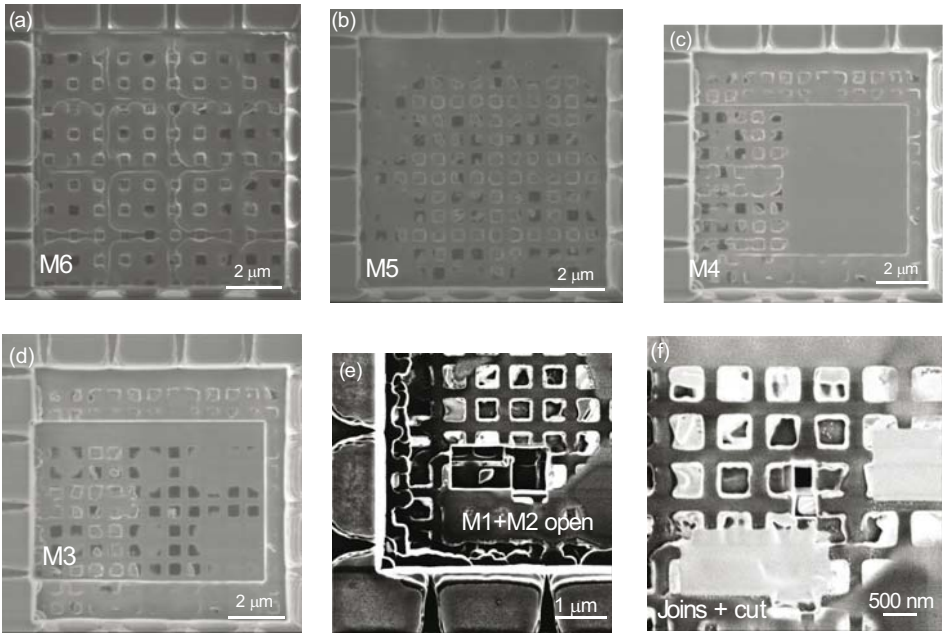


Fig. 5. FIB images taken sequentially during an edit. Note should be taken of the uniformity of the milling at all stages and that there is no overspray of the metal deposition.

A further complication arises if the required edit cannot be reached by milling from the top surface of the device. In these circumstances it is necessary to perform the edit through the backside of the chip (i.e. FIB mill locally through the Si substrate) and dedicated circuit edit FIBs are suitably equipped to do this. To enable this type of edit some sample preparation is required. Part of the package is removed and the Si substrate mechanically polished until a thickness of around 150 μm. FIB navigation is then performed using an internal IR optical microscope. Initially, a large (100 x 100 μm) hole is milled in the substrate until once again voltage contrast is utilised when the deep implanted wells can be observed. This observation is indicative that the milled hole is now close to the Si surface and more accurate navigation (using a sacrificial hole) and final milling are now required to reach the edit location as shown in Fig. 6a. Before any metal deposition is performed it is now necessary to insulate the walls of the Si hole otherwise the whole substrate will be connected. To illustrate this, a TEM cross-section from the edit in Fig. 6a was made (Fig. 6b), revealing the insulating layer and the subsequent metal deposition to make the edit. Thus with the correct preparation, it should be possible to perform most edits that an IC designer may request in such advanced processes.

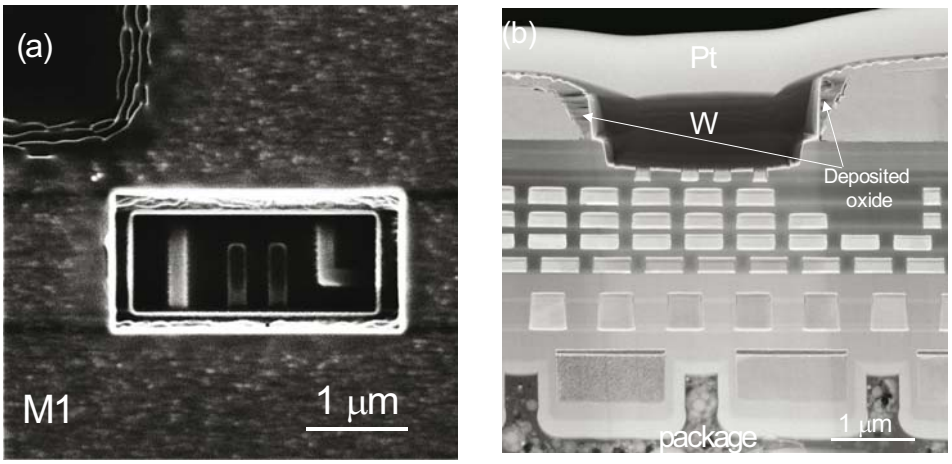


Fig. 6. a) FIB image of metal 1 lines reached through the substrate. b) TEM cross-section made through the region in (a) showing the insulating layer and W deposition.

5. CONCLUSION

A modern FA laboratory contains a number of FIB tools that can meet the different demands placed on them at different stages of the FA loop. Single beam tools are excellent for preparing both SEM and TEM cross-sections from samples of any geometry, whilst dualbeam tools are required for advanced cross sectioning. Finally, dedicated circuit edit tools are necessary to perform edits on advanced devices below the 120 nm technology node.

ACKNOWLEDGEMENTS

The authors would like to thank a number of colleagues from the FA department of Philips Semiconductors in Nijmegen in particular Ann De Veirman and Bert Otterloo for the example of the in-situ lift out sample and for their continued collaborations.

REFERENCES

Boit C 1999 Proc. ISPA **7**, 9
Casey J D et al 2002 Proc. ISTFA **28**, 553
Donnet D M, De Veirman A E M, Otterloo B and Roberts H 2003 Inst. Phys. Conf. **180**, 617
Tracy B 2002 Proc. ISFTA **28**, 69
Verkleij D 1999 Microelectron. Reliab. **38**, 869

A method for 3D failure analysis using a dedicated FIB-STEM system

T Kamino[1], T Yaguchi[1], M Konno[1], T Hashimoto[2], T Ohnishi[2] and K Umemura[2]

[1] Hitachi Science Systems, Ltd., 11-1 Ishikawa-cho, Hitachinaka, Ibaraki, 312-0057 Japan
[2] Hitachi High-Technologies Corp., 882 Ichige, Hitachinaka, Ibaraki, 312-8504 Japan

ABSTRACT: A method is proposed for the three dimensional physical failure analysis of electronic devices. A micro-sampling technique was employed for extraction of a piece of sample from a defective cell. The extracted sample was shaped into a pillar and mounted on the tip of a needled specimen stub. Physical failure analysis of the sample was then performed using a dedicated focused ion beam (FIB) – scanning transmission electron microscope (STEM) system. This technique was applied to the physical failure analysis of an inadequately insulated gate oxide layer in an electronic device.

1. INTRODUCTION

As the cell size of semiconductor devices continuously decreases, demands for physical failure analysis using the transmission electron microscope (TEM) or STEM are rapidly increasing. The first and most important thing in failure analysis using the TEM or STEM is sample preparation. It should be site specific and no damage or structural change should be given to the sample during the preparation. We have developed the micro-sampling technique to extract a piece of sample directly from a bulk sample (Ohnishi 1999). In this method, a micrometer sized sample is extracted by FIB fabrication and mounted on a FIB-STEM compatible specimen holder so that the sample can be additionally milled after STEM observation whenever required (Yaguchi 2003). Positional accuracy of this method in thin sample preparation is nearly 100nm and the method is now widely used for structural and elemental evaluation of specific sites in semiconductor devices (Kamino 2002). Recently, we have developed a new type of FIB-STEM compatible specimen holder with a sample rotation mechanism and needled specimen stub.

2. METHODS

2.1 Instrumentation

The FIB system (FB-2100) used in the method has an operating voltage ranging from 10kV to 40kV. The 40kV Ga ion beam is used for extraction of a micro-sample and also for rough milling of the extracted sample, and 10kV for final milling of the sample. The micro-sampling unit consists of a tungsten probe and the tungsten deposition gun was employed for extraction of a micro-sample and its mounting on a specimen stub. A STEM (HD-2300) with bright field (BF)-STEM, high angle annular dark field (HAADF)-STEM and secondary electron (SE) detectors was employed for physical failure analysis. The STEM was also equipped with an EDAX genesis EDX system and a real time jump-ratio imaging system that consisted of a two-window energy filter mounted beneath the STEM.

2.2 Sample Preparation from a Specific Site

The procedure for micro-sampling from a specific site is shown in Fig. 1. First, a protective layer of tungsten is deposited on the area to be observed (a). Next, trench milling is carried out

surrounding the area (b) and the sample is tilted to cut off the bottom of the area (c). After that, the sample is tilted back and a mechanical probe is adhered firmly to the corner of the area (d). Finally, the mechanical probe is lifted up to extract the sample (e). Time required for the whole procedure is about 20 min when the 40kV Ga ion beam is employed in the fabrication. A typical size of micro-sample for this method is 10-20μm^2

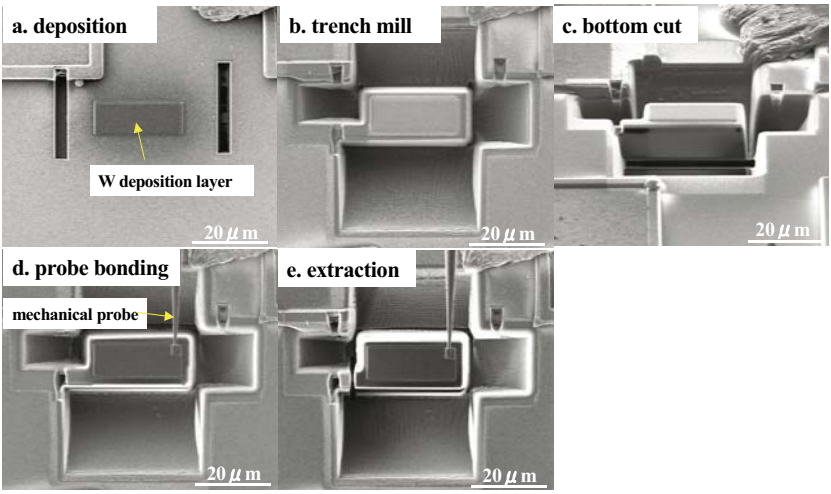


Fig. 1. Scanning ion microscopic images showing the procedure for extraction of a micro-sample from a site to be characterized.

2.3 Searching and Determination of the Position of a Failure in a Device

The extracted sample is transferred to STEM to determine the position of the site to be characterized. After the determination the sample is transferred back to the FIB system for further milling. Fig. 2 shows STEM images of a pillar shaped DRAM sample. The size of the sample is 2μm thick and 8μm wide. Fig. 2a, observed along the lower Al lines, shows the cross sectional structure of lines, plugs and gate. In this method, this kind of image is utilized for searching for a failure and also for

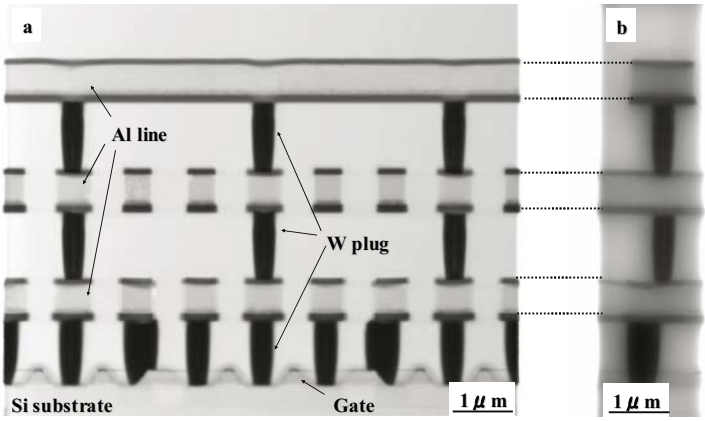


Fig. 2. Two directional STEM observation of a pillar shaped DRAM sample of 2μm thick and 8μm wide.

determination of the position of the failure. Figure 2b, observed along the upper Al line, demonstrates the thickness of the sample as well as the position of each W-plug. In determination of the position and the amount to be further FIB milled to obtain a thin sample for physical analysis, an image like Fig. 2b is essential because otherwise a small failure may be lost during thin sample preparation.

Figure 3 shows a STEM image of the same sample as shown in Fig. 2 but the thickness of the sample is 0.6μm and the bottom W-plug is located in the centre of the thinned sample. In this way, a failure can be found and the position of the failure can be determined precisely.

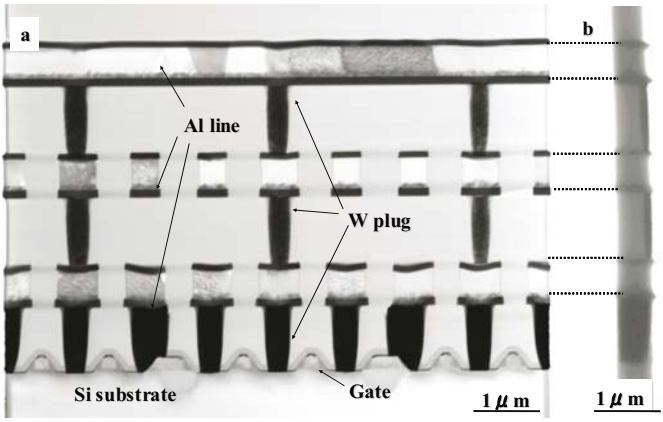


Fig. 3. Two directional STEM observation of a DRAM of 0.6μm thick and 8μm wide.

3. APPLICATION

The method was applied to the failure analysis of a Si device. STEM images of a defective site observed from various directions are shown in Fig. 4. In this site, abnormal crystal growth of Si was found in the substrate (Fig. 4a,c) and a gate (Fig. 4d). More important is contamination in the gate oxide which was clearly observed and suspected to be the site of device leakage current.

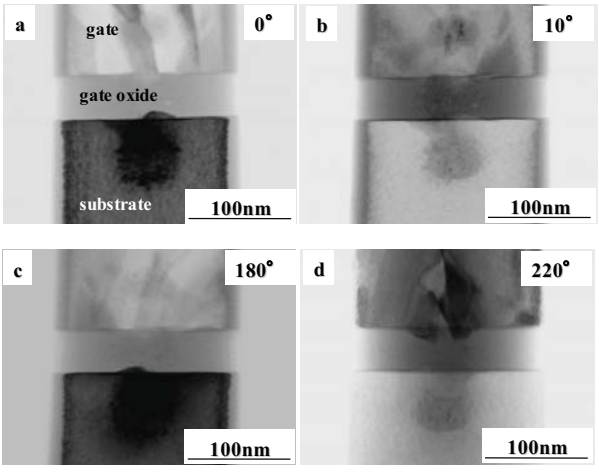


Fig. 4. STEM images of an inadequately insulating gate oxide in Si device observed from various directions (sample rotation angles : 0°, 1 0°,18 0°and 220°).

4. CONCLUSION

A method for sample preparation for physical failure analysis of Si devices and its application are discussed. Since the method employs STEM for determination of a site to be prepared, and additional FIB milling can be carried out repeatedly at any time, the positional accuracy in sample preparation is far better than for the conventional FIB milling technique. The method can be applied in a wide range of circumstances and an example is given.

REFERENCES

Kamino T, Yaguchi T, Kuroda Y, Hashimoto T, Ohnishi T, Ishitani T, Umemura K and Asayama K 2002 Proc. Microsc. Microanal.**8**, 48

Ohnishi T, Koike H, Ishitani T, Tomimatsu S, Umemura K and Kamino T 1999 Proc. 25th Int. Symp. For Testing and Failure Analysis, 449

Yaguchi T, Kamino T Ohnishi T, Hashimoto T, Umemura K and Asayama K 2003 Proc. 29th Int. Symp. For Testing and Failure Analysis, 282

Failure analysis studies in pseudomorphic SiGe channel *p*-MOSFET devices

A C K Chang, I M Ross, D J Norris, A G Cullis, Y T Tang[1], C Cerrina[1] and A G R Evans[1]

Department of Electronics and Electrical Engineering, University of Sheffield, Sheffield, S1 3JD, UK
[1] Department of Electronics and Computer Science, University of Southampton, Southampton, SO17 1BJ, UK

ABSTRACT: Two nominally identical series of pseudomorphic Si/$Si_{0.64}Ge_{0.36}$/Si *p*-channel MOSFET devices from adjacent locations of the same wafer were found to have radically different gate threshold voltages. Focused ion beam milling and transmission electron microscopy was employed to determine the structural differences between the devices from these two regions. Significant structural anomalies were found in the poorer performing devices consisting of fluctuations in the quality and thickness of the strained SiGe layer. These anomalies are believed to be the result of strain relaxation relating to the thickness of the strained layer relative to the critical thickness combined with temperature non-uniformities across the wafer during layer growth.

1. INTRODUCTION

The development of Si/SiGe heterostructure metal oxide semiconductor field effect transistors (MOSFETs) has been encouraged by their potentially higher carrier mobility, low cost and ease of integration into the current established Si processing technology. Compressively strained SiGe grown epitaxially on Si substrates can be used to create a two-dimensional hole-channel, which has a lower effective mass thereby contributing to an enhanced mobility. By selective band-gap engineering, pseudomorphic SiGe channel *p*-MOSFETs can be produced which provide a superior alternative to the lower hole mobility of conventional Si *p*-MOSFETs (Xie et al 1999). In order to optimize the development of such devices it is necessary to investigate thoroughly any process deviations and reliability related failures. Central to this task is the correlation of the device performance and its microstructure thereby, providing a sound understanding of the processing constraints that ultimately ensure high device yields. The application of focused ion beam (FIB) specimen preparation for subsequent analysis by transmission electron microscopy (TEM) is pivotal to this goal. Hence, in this study we report the direct correlation between device performance and microstructure for a series of pseudomorphic Si/$Si_{0.64}Ge_{0.36}$/Si *p*-channel MOSFET devices, prepared from two distinct regions of a single wafer found to exhibit very different electrical characteristics.

2. EXPERIMENTAL

The pseudomorphic SiGe *p*-channel devices examined in this study were grown by molecular beam epitaxy (MBE) the full details of which are presented elsewhere (Chang et al 2005). Due to the close proximity and narrow gate length of these devices, site-specific TEM specimens were prepared using a dedicated dual column FIB miller. This instrument consists of a JEOL 6500F field emission gun scanning electron microscope equipped with an Orsay Physics 10-30 keV Ga^+ ion column and a RAITH ELPHY *Quantum* Universal Nanolithography System. Subsequent TEM observation and microanalysis was performed in a JEOL 2010F field emission gun transmission electron microscope (FEGTEM) equipped with a Gatan imaging energy filter, an Oxford LINK/ISIS X-ray energy-dispersive spectrometer (EDS) and a scanning attachment allowing scanning transmission electron

microscopy (STEM) bright field (BF) imaging. TEM/STEM analysis was used in this instance primarily to investigate the dimensional variation and structural uniformity within the device gate oxide layer and to quantify the germanium concentration within the compressively strained SiGe channel and its corresponding thickness.

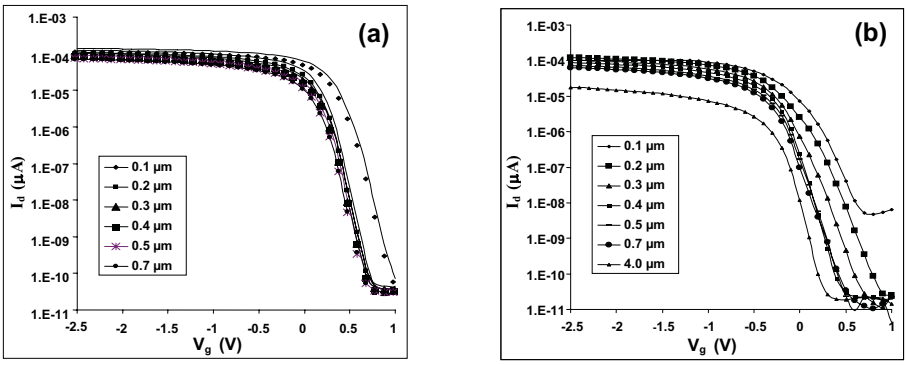


Fig. 1: I_d vs. V_g measurements of the SiGe strained channel *p*-MOSFET devices with various gate lengths from: (a) Area A, exhibiting a narrow spread in the sub-threshold currents and threshold voltages. (b) Area B, showing a broad spread in the sub-threshold currents and threshold voltages.

3. RESULTS AND DISCUSSION

On visual inspection, the processed wafer was observed to contain two distinct regions. The first region exhibited a uniform appearance (area A) while the second showed significant non-uniformity of the surface colouration (area B). Plots of the drain current (I_d) versus gate voltage (V_g) for a range of devices from these two regions are shown in Fig. 1a and 1b. Devices corresponding to Fig. 1a were derived from area A and show a series of consistent gate threshold voltages for the different device gate lengths studied with a spread of ~0.05V. The only exception to this was the data derived from the 0.1 μm gate length device, thought to be due to short channel effects (Tarr et al 1995). On the other hand, devices from the second region (area B), shown in Fig. 1b, produced a significant spread in the sub-threshold current as a function of all gate lengths with the spread in the threshold voltage of ~0.45V. Such non-uniform threshold characteristics are extremely undesirable and it was clear from both the electrical data and the visual inspection of the wafer surface that there were significant differences between the devices in areas A and B.

A STEM BF image of a nominally 200 nm gate length *p*-MOSFET device from area A is shown in Fig. 2a. Structural uniformity and symmetry in the SiGe pseudomorphically strained layer, poly-Si gate electrode, Si_3N_4 side wall spacers (SWS) and silicides above the designated gate and source/drain regions is clearly evident here. It was noted that small amounts of silicide were also present on the top edge of the SWS although this should not impact on the quality of the device unless a complete short of the gate to source/drain silicided regions occurs. In addition, typical end of range defects (caused by the high-energy shallow B^+ ion implantation during device processing) were also observed as patches of dark contrast below the source/drain regions. Fig. 2b shows a high resolution transmission electron microscopy (HREM) image of the active channel region (highlighted in Fig. 2a). The thicknesses of the gate oxide and strained $Si_{0.64}Ge_{0.36}$ *p*-channel were found to be 2.8 nm and 11.5 nm, respectively, which are consistent with the intended growth values of 3 nm and 10 nm. However, the 2 nm Si cap layer sandwiched between these two layers was unresolved, with the diffusion of Ge possibly accounting for the apparently thicker SiGe layer. EDS compositional analysis shows the Ge concentration in the SiGe layer to be 30±0.65 atomic %, which is lower than the intended growth concentration of 36 atomic % strengthening the argument that the Si cap may have undergone some level of diffusional intermixing with the *p*-channel.

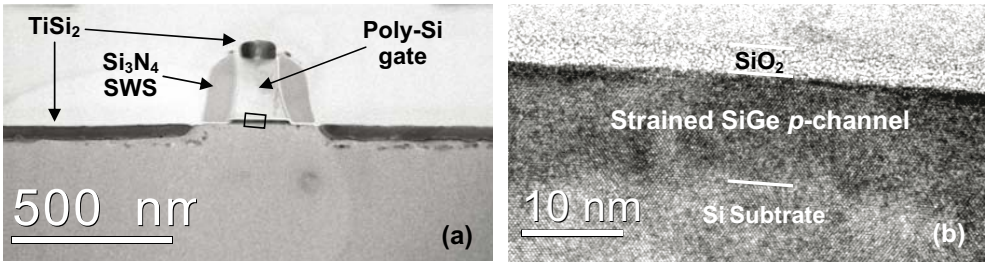


Fig. 2: Micrographs of the *p*-channel SiGe MOSFET devices from area A: (a) STEM BF image of an intended 200 nm gate length device, displaying structure uniformity and layer planarity. (b) HREM image of device under the gate electrode detailing evidence of $Si_{0.64}Ge_{0.36}$ and SiO_2 layers.

Figure 3a shows a STEM BF micrograph of a 300 nm gate length MOSFET device from the region of the wafer exhibiting poor electrical uniformity (area B). The image clearly reveals the $Si_{0.64}Ge_{0.36}$ strained layer below the gate electrode to be grossly non-uniform and undulating. An HREM lattice image of the region highlighted by the box in Fig. 3a is given in Fig. 3b, and despite the excellent crystallinity of the semiconductor channel, the SiGe layer is virtually undetectable in a number of areas. Moreover, the undoped Si buffer layer on either side of the device exhibits significant corrugations in the surface topography. These pronounced surface corrugations are thought to be a processing artefact, occurring during the subsequent etching of the non-device areas exasperated on further device processing. The observed irregularities in the microstructure, almost certainly account for the anomalous optical appearance of the visually inspected wafer, and appear to correlate well with the degraded electrical data previously presented in Fig 1b.

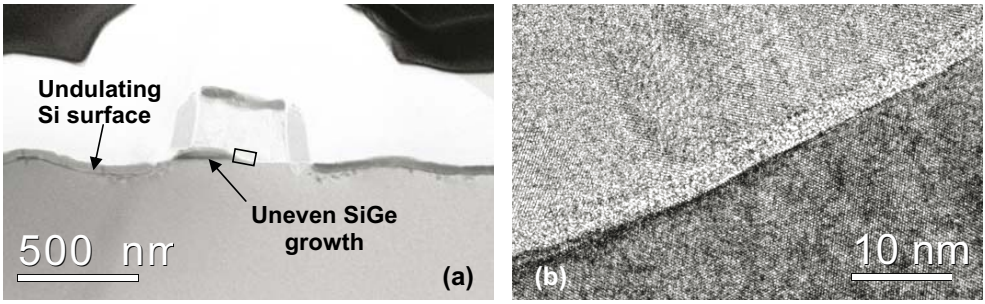


Fig. 3: Micrographs of the *p*-channel SiGe MOSFET devices from area B: (a) STEM BF image of an intended 300 nm gate length device, illustrating the non-uniform undulating morphology of the *p*-channel $Si_{0.64}Ge_{0.36}$ layer under the device gate. (b) HREM image of device under the gate electrode highlighting regions of the device where the SiGe layer is virtually undetectable.

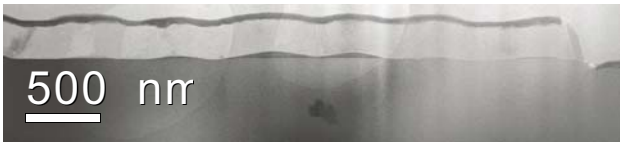


Fig. 4: STEM BF image of a 4 μm *p*-MOSFET device from area B, displaying the same device structure abnormality and ripple-like undulations similar to those seen in the 300 nm device.

To confirm the extent of the channel layer irregularities a series of larger gate length devices were FIB cross-sectioned to ensure this abnormality was consistent for all devices in area B. Figure 4 shows part of a 4 μm device revealing the same undulating ripple-like growth in the SiGe strained layer surface and resulting MOSFET device structure deformities and poly-Si gate electrode non-uniformity.

It is well known that growth instabilities during the deposition of SiGe alloys on Si can result in a roughened surface, which ultimately can lead to degradation in device performance. A critical layer thickness of 6.3 nm was proposed by Matthews and Blakeslee (1974) for a Ge concentration $x = 0.36$, above which relaxation would occur. As the intended thicknesses of the SiGe alloy layer in this study is 10 nm, one may expect such strained layer relaxation to occur. On the other hand, a metastable limit inferred from the work of People and Bean (1994) places the maximum thickness of such MBE grown alloy layers at ~32 nm before the onset of interfacial misfit dislocation nucleation. This suggests that the strained channel layers in this study exist within such a metastable range and some kinetic and/or thermodynamic relaxation mechanism such as those proposed by Schelling et al (2000) and Cullis et al (1992) is therefore highly likely to locally minimise the strain as demonstrated by the 'islanding' in Fig. 3a and 4. Moreover, Grasby et al (1999) have shown that by growing similar pseudomorphic $Si_{0.64}Ge_{0.36}$ layers at 705ºC, dramatic macro-roughening similar to the 'islands' observed in this work also occurs. The strained layers in this current study were grown at 670°C, hence it is possible that wafer temperature non-uniformity above the nominal growth temperature may have induced similar strain-induced relaxation, leading to morphological instabilities in some areas of the wafer that may correlate directly with the bad devices. Furthermore, temperature variations could also lead to local changes in surface step bunching (Cullis et al 1994) even on the underlying Si buffer layer, which would then exacerbate the undulations in the overlying SiGe.

4. CONCLUSIONS

In this study, we have highlighted the effect of non-uniform channel layer growth by the direct correlation of the microstructure and electrical characteristics in state-of-the-art pseudomorphic Si/SiGe *p*-channel MOSFET devices fabricated on Si. Two nominally identical sets of devices from adjacent locations of the same wafer were found to have radically different distributions in gate threshold voltages. Focused ion beam milling was used to prepare a number of site-specific cross-sections from each of the two regions for subsequent analysis using transmission electron microscopy. It was found that devices from the region giving a narrow range of gate threshold voltages (~0.05V) exhibited a uniform microstructure in general agreement with the intended growth parameters. However, in the adjacent region, which showed a large spread in the gate threshold voltages (~0.45V), profound anomalies in the microstructure were observed. These anomalies consisted of fluctuations in the quality and thickness of the SiGe strained layers that clearly accounted for the variation in the threshold voltages of these devices. The observed morphological defects are a likely consequence of strain relaxation relating to the thickness of the strained layer, relative to the critical layer thickness, combined with localised temperature fluctuations during growth. The results emphasize the importance of good layer growth uniformity to ensure optimum device yield.

ACKNOWLEDGEMENTS

The authors kindly acknowledge the Engineering and Physical Sciences Research Council (EPSRC) for supporting this work (GR/R65626/01 and GR/S02150/01)

REFERENCES

Chang A C K, Ross I M, Norris D J, Cullis A G, Tang Y T, Cerrina C and Evans A G R 2005 Thin Solid Films *in press*

Cullis A G, Robbins D J, Pidduck A J and Smith P W 1992 J. Cryst. Growth **123**, 333

Cullis A G, Robbins D J, Barnett S J and Pidduck A J 1994 J. Vac. Sci. Technol. A **12**, 1924

Grasby T J, Parry C P, Phillips P J, McGregor B M, Morris R J H, Braithwaite G, Whall T E, Parker E H C, Hammond R, Knights A P and Coleman P G 1999 Appl. Phys. Lett. **74**, 1848

Matthews J W and Blakeslee A E 1974 J. Cryst. Growth **27**, 118

People R and Bean J C 1985 Appl. Phys. Lett. **47**, 322

Schelling C, Springholz G and Schäffler F 2000 Thin Solid Films **369**, 1

Tarr N G, Walkey D J, Rowlandson M B, Hewitt S B and MacElwee T W 1995 Solid-State Electron. **38**, 697

Xie Y H 1999 Mat. Sci. & Eng. **R25**, 89

TEM specimen preparation technique for III-V semiconductor devices by using a novel FIB-Ar ion milling method

K Tanabe, T Matsuda, H Sasaki and F Iwase

Yokohama R&D Laboratories, The Furukawa Electric Co., Ltd., 2-4-3 Okano, Nishi-ku, Yokohama 220-0073, Japan

ABSTRACT: A special FIB-Ar ion milling method is applied, which utilizes a newly designed Cu grid with a thin metal foil for FIB micro-sampling, in order to remove FIB-damaged layers of site-specific regions in III-V semiconductor materials, including GaN, GaAs, AlGaAs, InP and InGaAs. It allows drastic reduction of the FIB-damaged layers to enable observation of clear HRTEM images. Based on cross-sectional TEM observations, EDS and AES analyses, it is found that structural and compositional properties of each damaged layer show very different features.

1. INTRODUCTION

For the past ten years, focused ion beam (FIB) milling has become popular as a specimen preparation technique for transmission electron microscopy (TEM) observation of submicron-scale semiconductor devices such as field-effect transistors and laser diodes. Particularly, the FIB system combined with a so-called "micro-sampling" unit (Ohnishi et al 1999) allows us to extract TEM specimens from specific regions of interest using a micro-probe to observe failure sites of a device with a high positioning accuracy of about 100 nm. However, the fact that high-energy (typically ~30 keV) Ga ions are used in FIB-processing and leads to the formation of damaged layers on both sides of the extracted specimen is well known. Since these damaged layers become obstacles with regard to clear high resolution transmission electron microscope (HRTEM) observation, it is difficult to evaluate the original specimen structure.

One effective way to remove these obstacles is milling the surfaces of specimens after FIB fabrication using a low-energy ion beam, such as a broad Ar ion beam (Kato et al 1999), 10 keV Ga ions (Walker and Broom 1997) and floating-type low energy Ar ions (Matsutani et al 2000).

A novel specimen preparation method using both conventional FIB and Ar ion milling instruments has been developed by the authors' group (Matsuda et al 2001) to remove damaged layers without equipping an FIB instrument with a special low-energy ion gun for the final specimen preparation process. This method is based on the use of a newly designed Cu grid with a thin metal foil for FIB micro-sampling. It enables us to achieve low energy Ar ion beam (2-3 keV) irradiation of both surfaces of the specimen fabricated by FIB, from all directions (360°) and at low angle (10-15°) with respect to the surface. The fact reveals that not only the damaged layers formed by FIB fabrication are efficiently removed, but also damage layers newly formed by Ar ion milling are suppressed. Therefore, high-quality HRTEM images at site-specific regions of interest can be observed easily and quickly using this developed technique for TEM specimen preparation. The developed technique was applied to the InP/InGaAsP multiple quantum well (MQW) structures in the edge emitting laser diode (Yabusaki and Sasaki 2002) and $CeO_2/Gd_2Zr_2O_7$ multilayers formed on a Ni-based alloy (Hastelloy) (Sasaki et al 2004), indicating that high-quality HRTEM images can be observed without remodeling both conventional FIB and Ar ion milling instruments.

In this paper, our unique specimen preparation method is applied to III-V semiconductor materials, including GaN, GaAs, AlGaAs, InP and InGaAs, to observe their high quality HRTEM images. Moreover, properties of damaged layers formed by FIB and Ar ion milling are systematically studied by cross-sectional TEM, energy dispersive X-ray spectroscopy (EDS), high angle annular dark field scanning transmission electron microscopy (HAADF-STEM) and Auger electron spectroscopy (AES) analyses.

2. EXPERIMENTAL

Structures of samples used in this study are as follows: (i) A GaN single layer on a (0001) sapphire substrate, (ii) an $Al_{0.34}Ga_{0.66}As$/GaAs epitaxial layer on a (001) GaAs substrate and (iii) an $In_{0.53}Ga_{0.47}As$/InP epitaxial layer on a (001) InP substrate. All the samples are grown by metal organic chemical vapor deposition (MOCVD). The Al and In composition in the AlGaAs and InGaAs layers are determined by an X-ray diffraction (XRD) measurement, respectively.

The outline of our method, to observe clear cross-sectional TEM and HRTEM images, is shown in Fig. 1. After tungsten is deposited on areas of interest, a few specimens are picked up by the FIB micro-sampling method (Fig. 1a). We use a half-cut Cu grid (3 mmϕ) with a single hole. And a thin foil is joined to the grid by epoxy glue, and the specimens are attached to a cross section of the thin foil using W deposition (Fig. 1b). Next, the specimens are thinned together with the thin foil (Fig. 1c). A FIB system combined with a micro-sampling unit (HITACHI FB2000A) was used for TEM specimen preparation. Ga ions are accelerated with an ion energy of 30 keV. Finally, the specimens are transferred to the Ar ion milling equipment (Gatan dual ion milling). For the final specimen preparation, dual broad Ar beams of low accelerating voltage of 2-3 keV are used to irradiate both sides of these specimens' surfaces at an angle of 15 degrees during specimen rotation (Fig. 1d). For GaN, GaAs and AlGaAs, the specimen was milled by Ar ions at room temperature (RT). On the other hand, the specimen was milled by Ar ions at liquid nitrogen temperature (77 K) for InP and InGaAs.

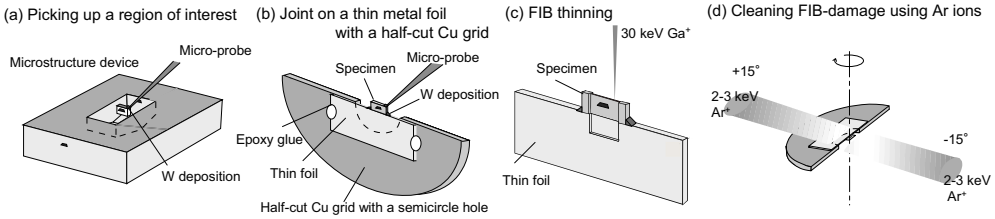


Fig. 1. The novel FIB-damage cleaning method using Ar milling

The procedure to evaluate a damaged layer using cross-sectional TEM, HAADF imaging, EDS and AES analyses is shown in Fig. 2. First, a damaged layer was intentionally formed on a surface of a bulk specimen by FIB (Fig. 2a). Next, in order to compare specimen surfaces milled by the 30 keV Ga ion beam and the low energy Ar ion beam, two types of specimens were prepared. One is a specimen without Ar ion milling, which has a damaged layer generated by FIB on the specimen surface (hereafter referred to as FIB milled specimen). The other is a specimen which had Ar ion milling applied (Fig. 2b) (hereafter referred to as FIB-Ar milled specimen). After that, an Au protective layer was immediately deposited on the surfaces of two types of specimen. This protective layer prevents deterioration of original properties of the damaged layers formed by FIB or Ar ion milling. So subsequent TEM specimen fabrication process would not affect analysis results significantly. The specimen was picked up by FIB micro-sampling method (Fig. 2c), thinned by FIB

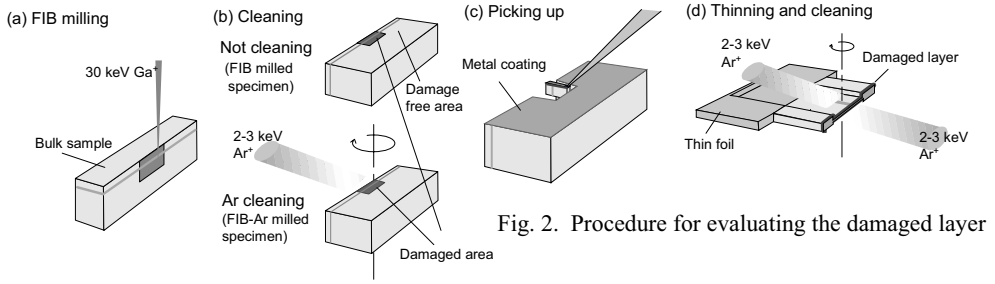


Fig. 2. Procedure for evaluating the damaged layer

and milled by dual Ar ion beams (Fig. 2d). Being a final Ar ion milling process (Fig. 2d), to remove both sides of damaged layers newly formed by FIB process (Fig. 2c and 2d), it is a very important

step for observation of a clear cross sectional HRTEM image of the original damaged layer.

Cross-sectional TEM and HRTEM images were observed using a HITACHI H9000UHR. The operating voltage of the microscope was 300 keV. HAADF imaging and EDS analysis were performed using a JEOL 2010F with an acceleration voltage of 200 keV. AES depth profiling was performed with a PHI 670 instrument. The electron voltage and current were 10 kV and 10 nA, respectively.

3. RESULTS AND DISCUSSION

3.1 Effect of Ar Ion Milling on TEM Specimen Preparation Process

Figure 3 compares images of the bright-field TEM and the HRTEM obtained from the GaN specimen without and with the final Ar ion cleaning process. In the case of carrying out the specimen preparation process without Ar ion cleaning, many black contrast features are observed in a bright field TEM image, as seen in Fig. 3a. Additionally, the HRTEM image exhibits anomalous lattice fringes, as shown in Fig. 3c. For the preparation process with Ar ion cleaning, on the other hand, such black contrasts are not seen on the bright field TEM image (Fig. 3b). And, crystal lattice fringes of the (0002) plane are clearly observed in the HRTEM image, as seen in Fig. 3d, indicating that a successful specimen preparation process for GaN is achieved with Ar ion cleaning.

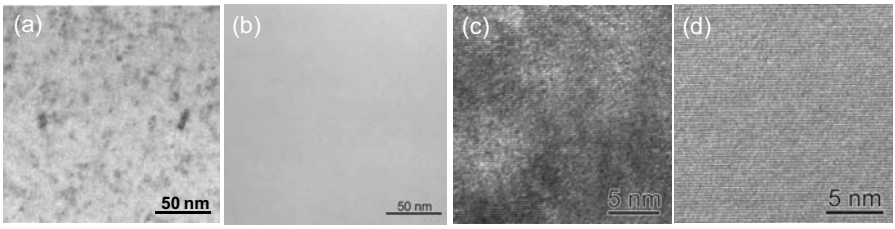


Fig. 3. Bright-field TEM images (a,b) and HRTEM images (c,d) of GaN, in (a) and (c) with 30 keV FIB, in (b) and (d) with 30 keV FIB + 3 keV Ar milling

Figure 4 shows images of the dark-field TEM (Fig. 4a and 4b) and the HRTEM (Fig. 4c and 4d) obtained from the GaAs specimen without and with the final Ar ion cleaning process. The clear dark-field TEM image of the specimen with Ar ion cleaning process can be seen (Fig. 4b). As seen in the HRTEM image (Fig. 4c), anomalous lattice fringes of the (002) planes are also included. For the GaAs specimen prepared with Ar ion cleaning, such anomalous fringes have disappeared in the HRTEM image (Fig. 4d).

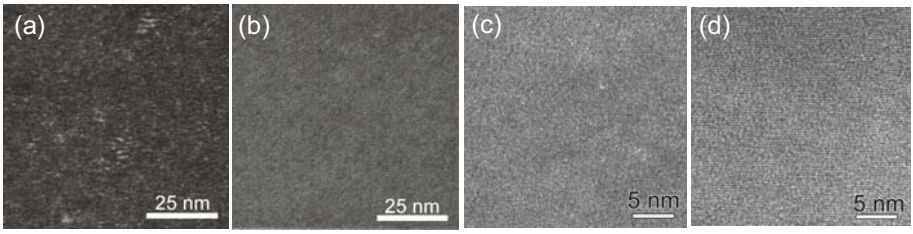


Fig. 4. Dark-field TEM images (a,b) and HRTEM images (c,d) of GaAs, in (a) and (c) with 30 keV FIB, in (b) and (d) with 30 keV FIB + 3 keV Ar milling.

Thus, it is confirmed that Ar ion cleaning during the final specimen preparation process is very effective in the subsequent observation of TEM and HRTEM. Additionally, our new technique makes it possible to investigate properties of the damaged layer formed on the surface of TEM specimens in detail.

3.2 Characterization of Damaged Layers Formed by FIB and Ar Ion Milling

Figure 5a and 5b exhibit cross-sectional bright-field TEM and HRTEM images taken with the incident electron beam along the (11-20) axis of GaN. Black contrasts are observed in the cross-sectional bright field TEM image, as seen in Fig. 3a. As seen in Fig. 5b, furthermore, it was found that the damaged layer of the FIB milled specimen consisted of two layers. The topmost layer, which corresponds to the white contrast region on the HRTEM image (Fig. 5b), is an amorphous phase and 3-4 nm in thickness. The subsurface layer contains several planar defects, which are circled in Fig. 5b. Total thickness of two layers was estimated to be 23-30 nm from the HRTEM image. Note that the interface beneath the damaged layer is very rough.

For the FIB-Ar milled specimen, on the other hand, the black contrast region observed in Fig. 5a has vanished on the bright-field TEM image (not shown here). It seems that the FIB-induced damaged layer is etched away by Ar ion milling. Figure 5c shows the cross-sectional HRTEM image taken from the FIB-Ar milled specimen. The topmost surface after Ar ion cleaning is covered with a 3-nm-thick amorphous layer formed by 3 keV Ar ions. The thickness of the damaged layer is drastically decreased due to the application of low-energy and low-angle Ar ion milling. In addition, the interface of damaged layer/GaN crystal becomes considerably flatter at the final step of TEM specimen preparation.

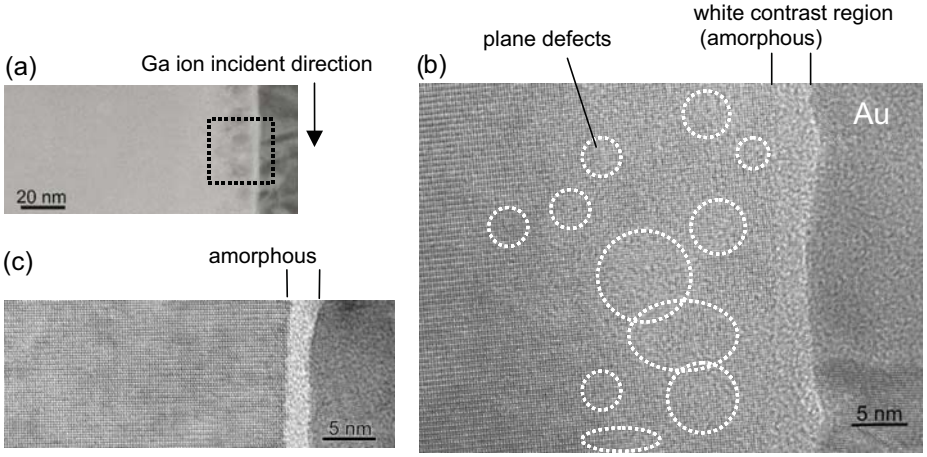


Fig. 5. Cross-sectional bright-field TEM image (a), cross-sectional HRTEM image (b) in GaN FIB milled area, and cross-sectional HRTEM image (c) in GaN FIB-Ar milled area.

The compositional properties of the surface of the FIB milled specimen are investigated by bright-field STEM, HAADF-STEM and EDS. EDS spectra, shown in Fig, 6a, and were measured at three spots, including the damage-free region (point 1), planar defects region (point 2) and the amorphous region (point 3) in the vicinity of the surface of the FIB milled specimen, shown in the bright-field image (Fig. 6b). Both spectra obtained from the damage-free and planar defects regions are almost the same peak shape. This means that there is no change of chemical composition before and after introducing the planar defects at the point 2 region. On the other hand, a high intensity of C and O peaks is detected in the EDS spectrum in the point 3 region. After the FIB processing, the specimen surface seems to be covered with surface contamination and native oxide layers.

A Z-contrast HAADF image, which is proportional to atomic number squared, indicates that heavy and light elements exist in the bright and dark contrast regions, respectively. As shown in Fig. 6c, the brightest region in the HAADF-STEM image corresponds to the Au protective layer with heavy mass. On the contrary, a dark contrast region is at the Au/specimen interface, meaning that light elements exist on the surface of the FIB milled specimen. Such existence of light elements is consistent with the high C and O intensity in the EDS spectrum shown at the bottom of Fig. 6b.

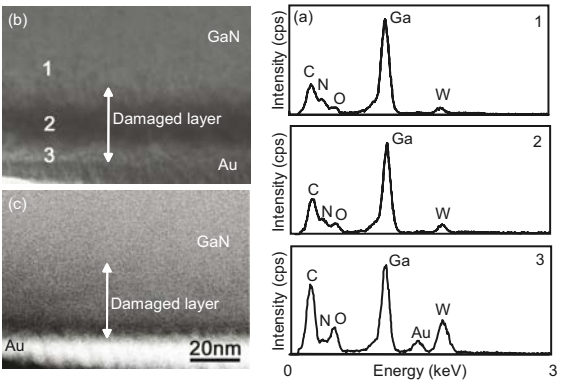


Fig. 6. EDS spectra (a) (point 1: damaged free region, point 2: defects region, point 3: amorphous region), BF STEM image (b) and HAADF image (c) of damaged layer of GaN

Figure 7 shows Auger depth profiles of C, O, N and Ga as a function of sputtering time. Analysis areas are both an FIB damaged area and a damage-free reference area in GaN, shown in Fig. 2b. Just after sputtering, C intensities rapidly decrease in depth profiles of both areas. Thus, C intensity in the EDS spectrum seems to be due to a surface contamination layer. On the other hand, in the initial stage of sputtering, a high oxygen intensity was detected in the depth profile obtained from the FIB damaged area, as seen in Fig. 7a. Such high-intensity oxygen peak was not observed in the depth profile of the damage-free reference area (Fig. 7b). These results indicate that the amorphous layer on the topmost surface of FIB milled specimen is an oxidized layer of GaN.

From the sputtering time of 2 min onwards, the ratio of Ga signal with respect to N signal taken from the FIB damaged area becomes constant. This value is very close to that obtained from the reference area (Ga/N=2.31), as shown in Fig. 2b, in spite of the fact that many Ga ions are implanted into GaN bulk.

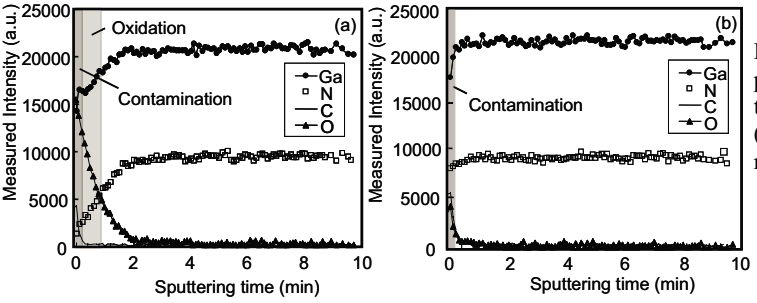


Fig.7. Auger depth profiles for GaN in the FIB-milled area (a) in the damage free reference area (b)

3.3 Comparison of Other III-V Materials (GaAs, AlGaAs, InP, InGaAs)

The features of the damaged layers formed on the other III-V semiconductor surfaces are briefly compared. The test samples of GaAs, AlGaAs, InP and InGaAs are examined. For their bulk materials, the FIB milled and FIB-Ar milled specimens are prepared through the same specimen preparation process. Results obtained from the cross-sectional HRTEM observation are summarized in Table 1.

	FIB (30 keV, Ga^+)		FIB + ion milling (3 keV, Ar^+, RT)	
Materials	Thickness(nm)	Features	Thickness(nm)	Feature
GaN	23 - 30	amorphous, plane defects oxidization layer	3.0 – 4.0	amorphous
GaAs	14 - 16	amorphous, microcrystal Ga rich and/or As poor	2.0 - 3.0	amorphous
$Al_{0.34}Ga_{0.66}As$	9 - 11	amorphous microcrystal	2.0 - 3.0	amorphous
InP	20 - 23	amorphous microcrystal	0.7 -1.5 (2 keV,LN_2)	amorphous
$In_{0.53}Ga_{0.47}As$	12 - 14	amorphous microcrystal	- 0.7 (2 keV,LN_2)	amorphous

Table. 1
The features of the damaged layers for III-V semiconductor materials

Among them, the thickness of the damaged layer on the FIB milled specimen of GaN is the thickest, being consistent with the cross-sectional TEM image, as shown in Fig. 5a and 5b. Furthermore, there are different features in terms of each damaged layer in these materials. The damaged layer contains a little amorphous in many microcrystals for GaAs and AlGaAs and a few microcrystals in amorphous material for InP and InGaAs. In the case of InP, InGaAs, GaAs and AlGaAs, it is presumed that recrystallization has occurred due to the Ga ion bombardment. As a result, the damaged layer contains microcrystals.

Figure 8 shows the Auger depth profiles of C, O, N and Ga as a function of sputtering time. Analysed areas are both an FIB damaged area and a damage-free reference area in GaAs. Immediately after sputtering, C and O intensities rapidly decrease in depth profiles of both areas. Thus, in the case of a GaAs FIB milled specimen, the detection of these C and O signals seems to be due to a surface contamination layer. It is found that Ga-rich and/or As poor layers exist beneath the surface contamination layer. These results show very different features between GaN and GaAs.

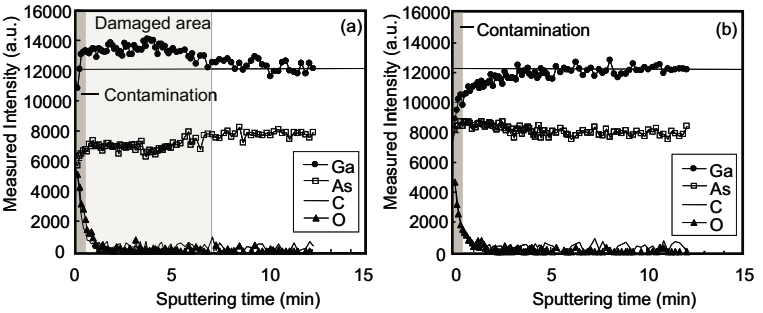


Fig. 8. Auger depth profiles for GaAs in the FIB-milled area (a), in the damage free area (b)

4. CONCLUSION

In the present work, a novel FIB-Ar milling method has been applied to site-specific specimens of III-V compound semiconductor materials, including GaN, GaAs, AlGaAs, InP and InGaAs. It has been shown that the reduction of the damaged layer formed with 30 keV Ga ions results in an effective improvement of HRTEM observation by a combination of FIB and Ar milling. Furthermore the features of these damaged layers have been evaluated experimentally based on cross-sectional HRTEM images, EDS analysis and AES analysis. It is found that the structural and compositional properties of each damaged layer shows very different features. These results indicate that the present specimen preparation technique is very effective for the observation of clear HRTEM images of III-V semiconductor materials. If this method is applied for other TEM analyses, such as EDS, electron energy loss spectroscopy (EELS) and electron holography, precise data without the influence of Ga implantation will be obtain.

REFERENCES

Kato N I, Kohno Y and Saka H 1999 J. Vac. Sci. Technol. A **17,** 1201

Matsuda T, Murayama Y, Yabusaki K 2001 Focused Ion Beam 2001

Matsutani T, Iwamoto K, Nagatomi T, Kimura Y, Takai Y, Shimizu R, Aihara R and Sakuma Y 2000 J. Surf. Anal. **7**, 314

Ohnishi T, Koike H, Ishitani T, Tomimatsu S, Umemura K, and Kamino T 1999 Proc. 25th Int. Symp. for Testing and Failure Analysis, 449

Sasaki H, Matsuda T, Kato T, Muroga T, Iijima Y, Saitoh T, Iwase F, Yamada Y, Izumi T, Shiohara Y and Hirayama T 2004 J. Electron Microsc. **53,** 497

Walker J F and Broom R F 1997 Inst. Phys. Conf. Ser. **157,** 473

Yabusaki K and Sasaki H 2002 Furukawa review 22: URL: http://furukawa.co.jp/review/index.htm

Focused ion beam micromilling of GaN photonic devices with gas enhanced etching techniques

W C Hung, T Wang, Hung-Cheng Lin [1], Guan-Ting Chen [1], Jen-Inn Chyi [1] and A G Cullis

Department of Electronic and Electrical Engineering, University of Sheffield, Mappin Street, Sheffield, S1 3JD, UK
[1]Department of Electrical Engineering, 2 National Central University ,Chung-Li 320, Taiwan, ROC

ABSTRACT: In this study, we shall present focused ion beam micromachining methods applied to facet modification and improvement in GaN-based laser devices. A 30 keV Ga+ ion beam was rastered over the GaN mirror facets. However, some redeposition occurred during processing. Therefore, we also improved the fabrication step by introducing gas-enhanced etching methods during ion beam milling.

1. INTRODUCTION

GaN-based materials are creating great interest for visible and UV light emitting devices since there are applications in displays, scanners, printers, etc. Much of the research to date still concentrates on the GaN growth technique. However, important fabrication issues remain regarding sample preparation and processing, especially for laser devices. In practice, a suitable laser cavity with high reflective mirror facets is hard to obtain due to current sample processing methods, which involve conventional cleaving M. (Khan et al 1991) or dry plasma etching (Binet et al 1998). Both techniques leave rough side-wall mirror facets and therefore degraded optical confinement. Focused ion beam (FIB) techniques of micro-machining (Orloff et al 2003) have been reported (Ito et al 1997, Katoh et al 1998) to produce flat and smooth mirror facets for GaN laser diodes. However, no quantitative analysis of GaN micromachining has been reported to date. In this paper, we present the results of improving FIB fabrication processes by applying gas enhanced etching methods to the GaN laser with a short-period cavity and semiconductor/air distributed Bragg reflector (DBR) mirrors.

2. EXPERIMENTAL

The 'Fabrika' dual column FIB system employs a liquid metal Ga^+ ion source, with associated ion optics, and a JEOL 6500F field emission scanning electron microscope (SEM). The presence of both the SEM and the FIB in a single system allows observation of the fabrication procedure during the milling. Figure 1 shows an illustration of the FIB and the SEM final pole-pieces inside the specimen chamber.

A 30kev Ga+ ion energy with 7.2μA emission current was preset: 250pA probe current was set to etch mirror facets and 125pA for laser gratings. The GaN laser was mounted on a sample block which was tilted 55 degrees normal to the ion beam.

The fluorine gas injector was placed approximately 180μm above the sample surface and 100μm from the milling area. Ten cycles of injector out-gassing were employed before injection of the gas.

The grating pattern was designed using a Raith software package, 12μm X 0.3μm (length X width) and 0.25μm line spacing was set to etch the laser grating. The SEM was used to observe the structures of the laser cavity, mirror facets and DBR gratings on the GaN samples.

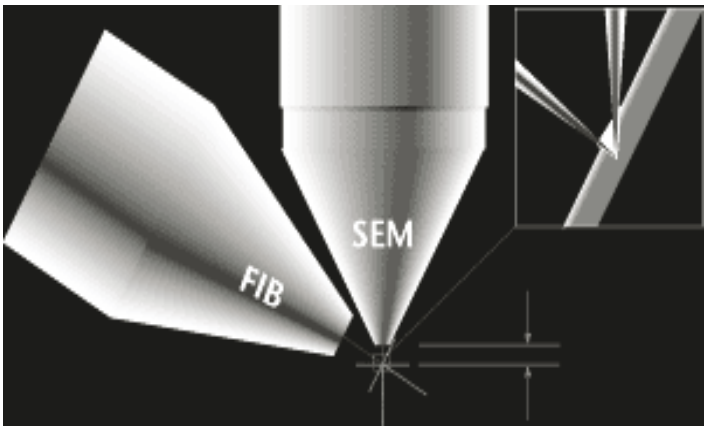


Fig. 1. Schematic diagram of FIB and SEM arrangement.

3. RESULTS

The first sample was provided by the University of Sheffield, where the laser facets were smooth after ion beam milling. Figures 2b and c show the difference due to ion beam milling.

To improve reflectivity further, a DBR grating was continuously etched with low probe current; however, nonuniform gaps were formed due to redeposition of material, as shown in Fig. 2d. This is likely to have occurred because the gaps were too small to allow the etched material to escape from the trench; as a result, the DBR grating was nonuniform. An improved processing step was then introduced by delivering fluorine gas into the milling area during ion beam etching. As shown in Fig. 2e, most of etched material was carried away by the fluorine gas and hence the grating became straight and clear. The optical properties of this sample will be reported elsewhere.

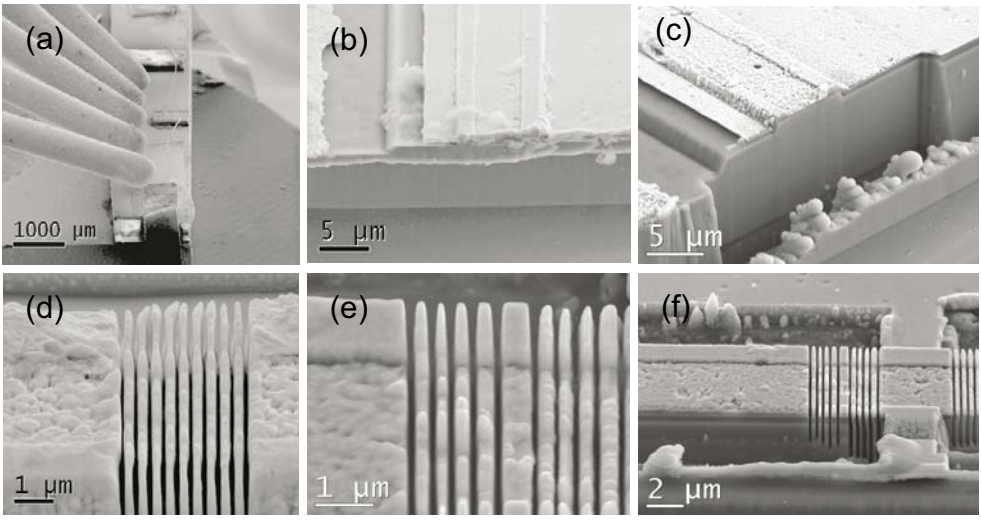


Fig. 2. (a) Positioning of gas injectors above GaN device region, (b) GaN laser front facet before ion beam milling, (c) GaN laser front facet after ion beam milling, (d) GaN laser grating milled by ion beam without supplying fluorine gas, (e) GaN laser grating milled by ion beam with fluorine gas assisted etching, and (f) illustration of GaN DBR grating at lower magnification.

Another GaN sample was supplied by the National Central University in Taiwan. Here, the same milling procedure was used as before to improve the mirror facets. However, the final mirror facets, although improved, were somewhat more rough than in the previous case. Figure 3 shows an SEM image of the surface roughness of the mirror facets after ion beam milling. As a result, some small lumps occurred as redeposited material on the mirror facets, which implied that an adjustment of the ion beam milling was required.

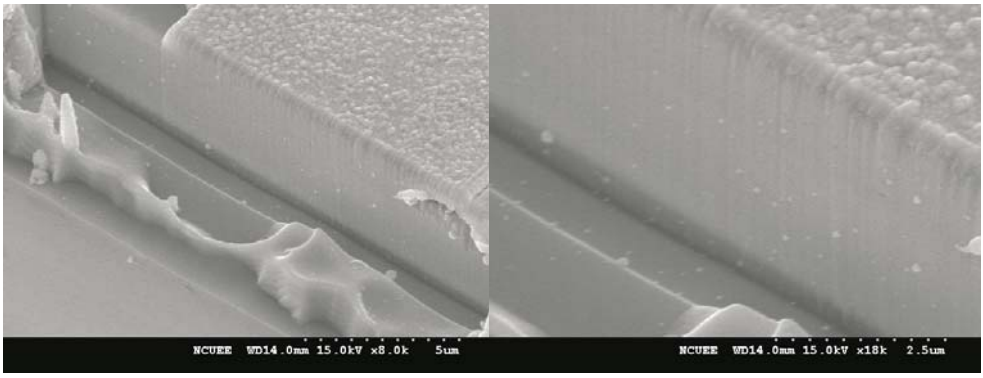


Fig. 3. GaN laser facets after ion beam milling.

However, the latter samples (from the Taiwan laboratory) showed distinct improvement in optical properties when measured. In fact, electroluminescence (EL) measurements as shown in Fig.4 indicate that light emission intensity for a given current density increased after the ion beam milling. Nevertheless, the device did not exhibit lasing for drive currents up to 300mA.

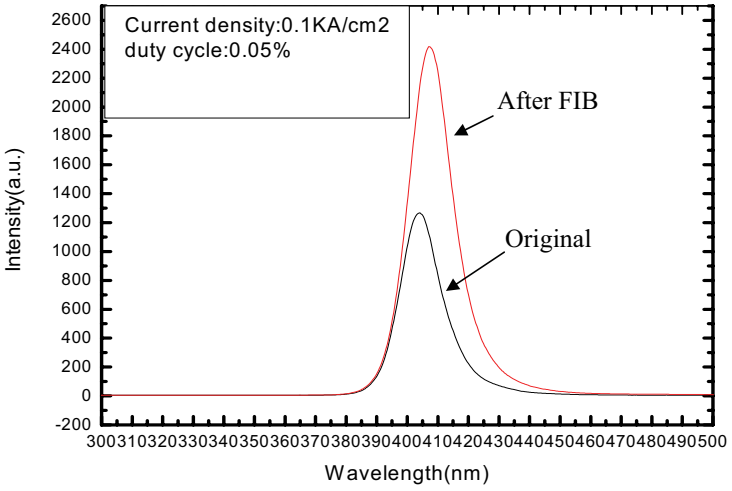


Fig. 4. EL measured light intensity increased after FIB milling.

4. CONCLUSION

We demonstrate focused ion beam micro machining techniques applied to the processing of mirror facets and DBR gratings on GaN laser devices. Redeposition effects can degrade the DBR grating structure but the grating can be improved after introducing a gas-enhanced etching step during the fabrication. Further test results in collaboration with the National Central University, Taiwan, show spontaneous emission was improved by focused ion beam milling of mirror facets. Further work is necessary to optimise stimulated emission. Therefore, in order to achieve this, we need to further optimise ion beam characteristics to get even smoother mirror facets, perhaps by introduction of gas-enhanced etching during the facet machining.

REFERENCES

Khan M A, Olson D T, Van Hove J M and Kuznia J N 1991 Appl. Phys. Lett. **58**, 1515

Binet F, Duboz J Y, Laurent N, Bonnat C, Collot P, Hanauer F, Briot O and Aulombard R L 1998 Appl. Phys. Lett. **72**, 960

Orloff J, Utlaut M and Swanson L 2003 High Resolution Focused Ion Beams, Kluwer Academic/ Plenum Publishers

Ito T, Ishikawa H, Egawa T, Jimbo T and Umeno M 1997 Jpn. J. Appl. Phys. Part 1 **36**, 7710

Katoh H, Takeuchi T, Anbe C, Mizumoto R, Yamaguchi S, Weitzel C, Amano H, Aksaki I, Kaneko Y and Yamada N 1998 Jpn. J. Appl. Phys. **36**, Part 2, L444

An organic two dimensional photonic crystal microcavity processed by focused ion beam milling

Wen-Chang Hung, A M Adawi[1], R Dean[1], A Cadby[1], L G Connolly[1], A Tahraoui, D G Lidzey[1] and A G Cullis

Electronic & Electrical Engineering, University of Sheffield, Mappin Street, Sheffield, S1 3JD, UK
[1] Department of Physics and Astronomy, University of Sheffield, Hicks Building, Hounsfield Road, Sheffield S3 7RH, UK

ABSTRACT: We demonstrate a two dimensional photonic crystal microcavity structure fabricated via focused ion beam (FIB) micro-machining techniques. The FIB, with the Ga ion beam directly rastered over a planar organic material, drilled small holes in a lattice configuration. The microcavity was created within the photonic crystal by a series of point defects giving an hexagonal feature in order to confine light into a small volume. This demonstration shows that use of the ion beam leaves undamaged organic material, which implies that the FIB can be applied to the design of a range of photonic crystal structures.

1. INTRODUCTION

Over the last decade there has been considerable worldwide effort to develop new physical structures to confine photons in one or more directions, what are called photonic crystals (Yablonovitch 1987, John 1987, Joannopoulos et al 1997). Essentially a photonic crystal alters the density of the available states for photons within a certain range of frequencies. Within the bands photons behave like free particles. However, within the gaps there are no available states for photons to exist. The drastic change in the density of states between bands and gaps opens the door to confine photons within a volume of the order of a cubic wavelength (Joannopoulos et al 1997). Creating a point defect (or a series of point defects) in the periodic structure of the photonic crystal may be used to trap light at a certain location (Smith et al 2001). Also light can be guided from one location to another by creating a line defect in the periodic structure of the crystal (Smith et al 2001). This makes photonic crystals of great interest, both for the physical understanding of fundamental phenomena such as the interaction of light with matter, and for the development of novel optoelectronic devices such as low threshold lasers (Park et al 2004) or single mode light emitting diodes (Yablonovitch 1993). Until now, most work has been done on inserting active material within microcavity in two dimensional photonic crystals based on inorganic materials such as InGaAsP quantum wells (Painter et al 1999), InAs quantum dots (Smith et al 2001) or Si/Ge quantum dots (David et al 2003). In this paper we report on fabricating a two dimensional photonic crystal microcavity embedded with molecular dye using the FIB. Organic materials have several advantages over inorganic materials, such as large oscillator strength which can result in large light matter interaction even at room temperature, in contrast to quantum dot sources, which are currently restricted to operation at cryogenic temperatures.

The conventional way of making a two dimensional photonic crystal microcavity is using lateral lithographic patterning (Gerard et al 1996, Rethmaier et al 1997) techniques. However, these techniques require a series of steps which can easily damage the organic active region. In this letter, we propose an alternative approach based on the FIB micro-machining technique (Orloff et al 2003). Such an approach is simpler than lithographic patterning, where the writing and the etching happen simultaneously, while in the lithographic patterning approach the writing and the etching are two separate steps, fully dry and nondestructive. In this method, a 30 keV Ga^+ ion beam directly writes a

patterned structure, where the ion beam interacts with solid materials and, therefore, sputters materials away, as illustrated schematically in Fig. 1.

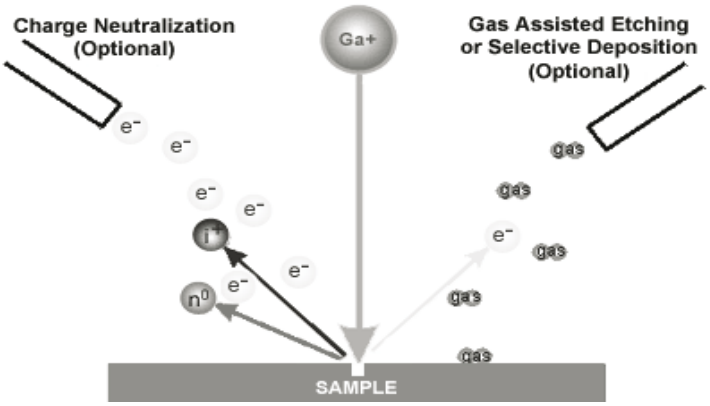


Fig. 1: Illustration of the ion beam interaction with a solid material.

2. EXPERIMENTAL

The structure we studied is a two dimensional waveguide photonic crystal is shown schematically in Fig. 2. The structure consists of a glass substrate coated with a 100 nm of indium tin oxide (ITO) of refractive index n_{ITO}=1.9, then an active organic layer was spin-cast on top of the ITO layer, and consisted of the molecular dye Lumogen Red (www.basf.com) doped into the matrix polymer polystyrene (n~1.58) at a concentration (by mass) of 5%. Lumogen Red was selected for this study as it has a particularly high photo-stability, being designed for various applications involving extended exposure to sunlight, with a PL quantum efficiency as high as 0.98 (www.basf.com). The thickness of the active layer is 100 nm. The structure was then finished by thermally evaporating 400 nm of the high refractive index material TeO_2 (n~2.05). To protect the organic film from damage from secondary electrons liberated during ion-beam writing, the sample surface was first coated with a 30 nm thick film of aluminium, which was then removed after writing the photonic structure using dry etching in $SiCl_4$ plasma. In this structure, the light is confined in the vertical direction by air from the top and by glass from the bottom. In order to improve the confinement from the back side we aimed to etch through to the glass substrate.

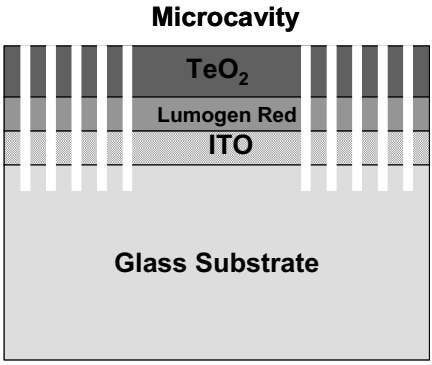


Fig. 2: Cross-sectional schematic of the photonic crystal microcavity section.

A liquid metal ion source (LMIS) of Ga^+ was supported with the JEOL 6500F scanning electron microscope (SEM) in the dual column FIB Fabrika system. This allows direct observation of the fabrication procedure during the ion milling. Figure 3a shows the outline structure of the Fabrika system and Fig. 3b shows an illustration of the FIB and SEM beams inside the specimen chamber.

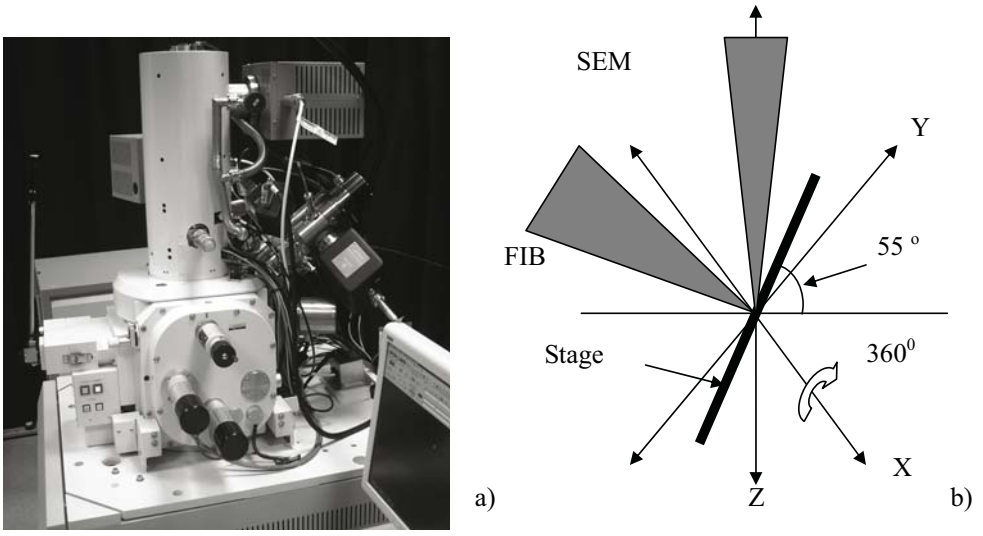


Fig. 3: (a) Outline structure of JEOL 6500 dual column system; (b) schematic diagram of FIB+SEM construction.

A 30keV Ga^+ ion energy with 7.2μA emission current was pre-set and probe current was measured at 72pA for direct etching. The planar organic sample was mounted on a sample block and fixed in the sample holder with 55 degree tilted normal to the ion beam. A thin Al layer was coated on the organic sample which helps the dissipation of excess charge buildup, and therefore avoids beam shifting during the fabrication.

A hole lattice pattern was designed using the Raith software package, which was applied to control the ion beam scan direction during the milling. Here, the lattice pattern was designed with periodic holes in an hexagonal form along X and Y directions, giving a 25μm by 25μm square area: each hole was designed to be about 75nm in diameter and the spacing was about 240nm between holes.

The milling parameter was preset on the Raith system; a 23ms drilling time with 0.03 μm beam step size was set for each hole and total milling time was estimated to be about one and a half hours. Finally, the energy of the SEM electron beam was reduced to 5keV during the ion beam milling.

3. RESULTS

Figure 4 shows the SEM images of the 25μm x 25μm photonic crystal structure milled with the 30 keV Ga^+ ion beam in approximately one and a half hours. As a result, the lattice constant of the photonic structure followed the design implemented by the Raith unit, but the etched holes were larger than expected, each hole being estimated as around 40nm larger than the original design.

In the middle of the structure, an unetched hexagonal area remained, which was used to confine the path of photon emission. The hexagonal structures could be made in different sizes; in this case, 8 missing holes along the side of the structure were provided as shown in Fig. 4.

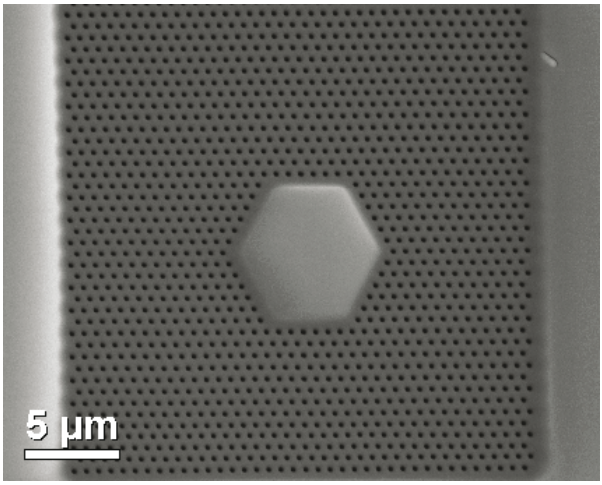


Fig. 4: Scanning electron micrograph of an organic two dimensional photonic crystal microcavity fabricated using FIB milling.

In order to confirm that the FIB milling does not damage the active material inside the structure, we performed PL measurements upon the sample using a micro-PL system. For excitation, the 442nm line of a HeCd laser was used, and then the PL was collected through a 0.5 NA lens and directed into a 0.25m spectrometer with a nitrogen-cooled CCD detector. Figure 5 shows the PL spectra from the microcavity and from an area unexposed to the FIB. It is clear that the microcavity was still emitting indicating that the FIB does not damage the organic layer through the writing process. More interestingly, the PL spectrum from the microcavity shows sharp peaks (see the inset of Fig. 5) unseen in the PL spectrum taken from an area outside the photonic structure, indicating that the photonic structure is able to confine light in the lateral directions. The Q-factor ($Q=\lambda/\Delta\lambda$) of the narrowest line at λ=611nm is 510. However, more work still needs to be done to optimize the structure and to give it a higher Q-factor.

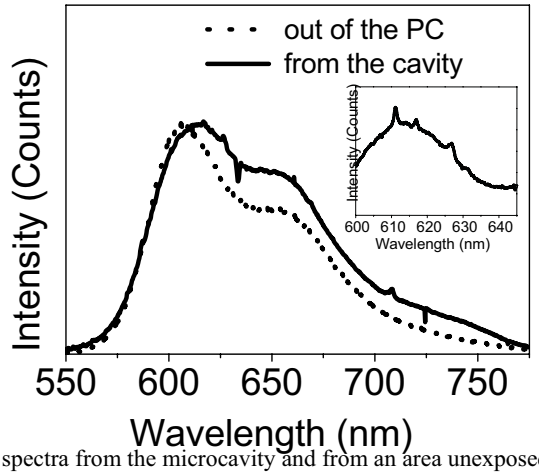


Fig. 5: PL spectra from the microcavity and from an area unexposed to the FIB.
Note: **.....**indicates a planar sample area and ____indicates the FIB drilled area (the insert shows an enlarged view of the peak from the latter area).

4. CONCLUSIONS

We have demonstrated that FIB milling is a nondestructive method which can be successfully used to fabricate organic two dimensional photonic crystal microcavities. Since the initial cavities we fabricated showed a relatively modest Q-factor, our cavities still need more optimization in order to achieve high Q-factor performance.

ACKNOWLEDGEMENTS

The authors would like to thank A Walker (University of Sheffield) and W Scott (JEOL Europe) for their experimental assistance.

REFERENCES

David S, El kurdi M, Boucaud P, Chelnokov A, Le ThanhV, Bouchier D and Lourtioz J-M 2003 Appl. Phys. Lett. **83**, 2509

Gerard J M, Barrier D, Marzin J Y, Kuszelewicz R, Manin L, Costard E, Thierry-Mieg Y and Rivera T 1996 Appl. Phys. Lett. **69**, 449

Joannopoulos J, Villeneuve P and Fan S 1997 Nature **386**,143

John S 1987 Phys.Rev.Lett. **58**, 2486

Orloff J, Utlaut M and Swanson L 2003 High Resolution Focused Ion Beams, Kluwer Academic/ Plenum Publishers

Painter O, Lee R K, Scherer A, Yariv A, O'Brien J D, Dapkus P D and Kim I 1999 Science **284**, 1819

Park H G, Kim S H, Kwon S H, Ju Y G, Yang J K, Baek J H, Kim S B and Lee Y H 2004 Science **305**, 1444

Rethmaier J P, Rohner M, Zull H, Schafer F, Forchel A, Reinecke T L and Knipp P A 1997 Phys. Rev. Lett. **78**, 378

Smith C J M, De La Rue R M, Rattier M, Olivier S, Benisty H, Weisbuch C, Krauss T F, Houdre R and Oesterle U 2001 Appl. Phys. Lett. **78**, 1487

Yablonovitch E 1987 Phys. Rev. Lett. **58**, 2059

Yablonovitch E 1993 J. Phys-Condens. Mater. **5**, 2443

Failure analysis of degraded (In,Ga)P/GaAs heterojunction bipolar transistors by TEM

H Kirmse, W Neumann, U Zeimer[1], R Pazirandeh[1] and W Oesterle[2]
Humboldt-Universität zu Berlin, Institut für Physik, Newtonstraße 15, 12489 Berlin, Germany
[1] Ferdinand-Braun-Institut für Höchstfrequenztechnik, Gustav-Kirchhoff-Straße 4, 12489 Berlin, Germany
[2] Bundesanstalt für Materialforschung und –prüfung, Unter den Eichen 87, 12203 Berlin, Germany

ABSTRACT: Degraded heterojunction bipolar transistors were characterized regarding their structural and chemical properties by transmission electron microscopy. Electron transparent cross-sections of the HBTs were prepared applying the focused ion beam technique. Diffraction contrast dark-field imaging revealed the coupling between drastic degradation and formation and propagation of dislocations originating from the (In,Ga)P emitter layer. Indium diffusion processes out of the emitter layer are enhanced for dislocation-free regions compared to dislocation-containing areas as shown by energy-dispersive X-ray spectroscopy line scans.

1. INTRODUCTION

(In,Ga)P/GaAs heterojunction bipolar transistors (HBTs) are widely used for high power applications in the microwave frequency band. Reliability and lifetime of these devices are important parameters for quality and market capability. The lifetime of HBTs is limited by the formation and propagation of dislocations as well as by diffusion processes.

HBTs under investigation were grown by metal organic vapour phase epitaxy and consecutively structured by lithographic processing. The 100 nm thick base region of the npn-type transistor consists of highly C-doped GaAs grown at 530°C whereas the 40 nm thick (In,Ga)P emitter layer was grown at 600°C (cf. schematic drawing of Fig. 1). These layers basically influence the performance of the HBTs. Degradation experiments revealed a catastrophic decrease of the performance of the HBTs after a period of about 150 h (Pazirandeh et al 2004).

In order to get a thorough understanding of the origin of degradation of the device, cross-sectional TEM lamellae were prepared by the focused ion beam (FIB) technique. In general, two orientations of cross-sections were prepared. Longitudinal cross-sections were cut parallel to the [110] direction along the elongated structure of the HBTs. These samples permit the analysis of dislocations generated during the degradation process by TEM diffraction contrast imaging over a wide field of view. For the investigations a TEM/STEM Hitachi H-8110 operated at 200 kV equipped with a LaB_6 cathode was utilized. The homogeneity of the chemical composition along the (In,Ga)P layer was inspected by energy-dispersive X-ray spectroscopy (EDXS) with a nominal probe size of 2 nm. The diffusion process perpendicular to the layer was analyzed for both areas with and without dislocations. Transverse cross-sections give an overview of the HBTs perpendicular to the elongated structure. In one and the same sample the base and emitter regions as well as the metallic contacts of emitter, base, and collector can be examined with respect to the stability of the contacts. Moreover, structural peculiarities of the (In,Ga)P layer were visualized by TEM dark-field imaging of these samples.

2. RESULTS AND DISCUSSION

TEM diffraction contrast imaging reveals the formation of dislocation loops at the interface between the (In,Ga)P emitter and the underlying GaAs base layer. The characterization of the dislocations is done by comparing several dark-field images of one and the same region as given in

Fig. 2. The images Figs. 2a-d exhibit strain sensitive contrast. In the images a) and c) dislocation lines are visible. The higher number of lines originating from the lower interface of the (In,Ga)P emitter layer compared to the upper one (cf., e.g., Fig. 2a) indicates that the thermal and mechanical stress is higher for the lower interface during the test of the HBT device. The dislocation lines are visible for diffraction vectors g = 004 and $g_c = \bar{1}\,11$ whereas for g = 220 and g = $1\,\bar{1}\,1$ the dislocations are invisible. Applying the g x b criterion a Burgers vector of 1/6 [$\bar{1}\,12$] is determined.

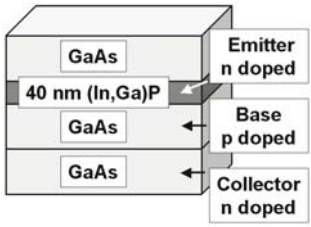


Fig. 1: Configuration of the hetero bipolar transistor

In order to correlate the presence of dislocations with chemical peculiarities of the (In,Ga)P emitter layer the predominately chemically sensitive 002 reflection was used for imaging (see Fig. 2e). The noisy contrast present within the emitter layer is almost the same as that of the strain sensitive images (cf. Figs. 2a–d). Hence, no clear indication for a fluctuation of composition can be found analyzing the 002 dark-field image.

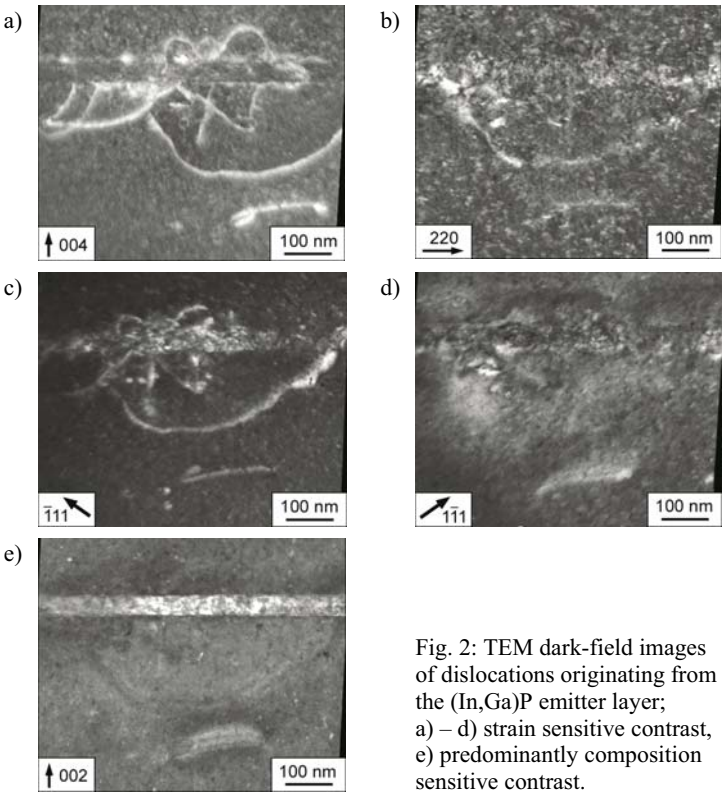


Fig. 2: TEM dark-field images of dislocations originating from the (In,Ga)P emitter layer; a) – d) strain sensitive contrast, e) predominantly composition sensitive contrast.

For detailed inspection of possible composition fluctuations of the (In,Ga)P emitter layer caused by the degradation process series of EDX spectra were recorded along the emitter layer (see Fig. 3). The examined region was free of dislocations. Numerical analysis of the individual point spectra yields the composition of each element. The composition profiles show no fluctuations exceeding the statistical error of ± 5 % at the length scale of 300 nm. The nominal value x for $In_xGa_{1-x}P$ is 0.48. The mean In content evaluated for the line scan of Fig. 3 (cf. black line marked by diamonds) amounts to about 14 at% equal to $x_{In} = 0.28$. The lower value compared to the nominal one can be explained both by diffusion of In perpendicular to the emitter layer into the adjacent material and by shift of ratio between In and Ga in favour of Ga due to implantation during FIB preparation using Ga ions. For

GaAs an enrichment of Ga by 1 at% was detected in comparison to Ar^+ ion milled GaAs. The presence of As in the (In,Ga)P layer is most likely due to redeposition during FIB preparation.

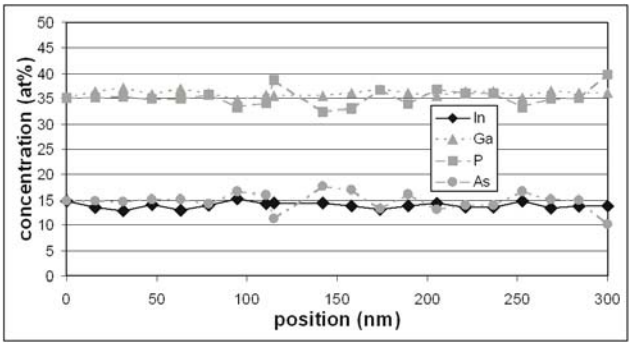


Fig. 3: Composition profile along the (In,Ga)P emitter layer by EDX line scan.

In addition to the line scans along the (In,Ga)P emitter layer, composition profiles of indium were taken across the (In,Ga)P emitter layer. The line scans were positioned at areas where dislocations were found as well as at dislocation free regions. In the scanning TEM (STEM) dark-field image of Fig. 4 the traces of EDX line scans are visible as dark lines due to modification of the amorphous surface layers by electron irradiation. For direct correlation of line scan position and presence of dislocations a TEM bright-field image was recorded prior to the EDX measurements.

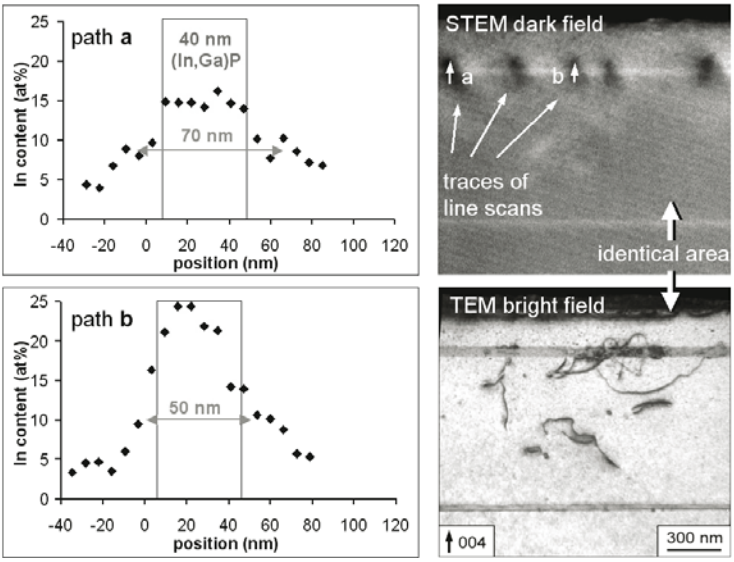


Fig. 4: Composition profile across (In,Ga)P emitter layer by EDX line scans and corresponding STEM dark-field image and TEM diffraction contrast image.

The full-width at half maximum (FWHM) of the In profile at the area free of dislocations (path a of Fig. 4) amounts to about 70 nm where the nominal thickness of the (In,Ga)P layer is 40 nm. Consequently, the large diffusion length causes low In content (ca. 15 at%) compared to the nominal value of 24 at%. Weaker diffusion is detected for dislocated areas (cf. path b). The FWHM is about 50 nm while the maximum In content is about 24 at%. Obviously, the formation of dislocations at the emitter layer, i.e., plastic relaxation of stress strongly affects the indium diffusion. Moreover, the dislocations may attract In atoms causing a diffusion along the (In,Ga)P emitter layer.

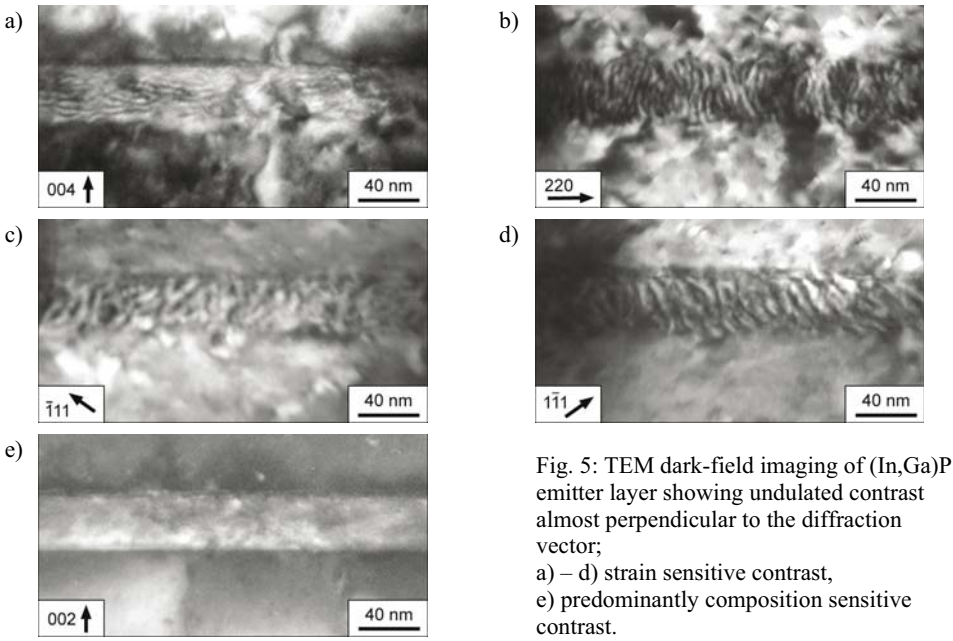


Fig. 5: TEM dark-field imaging of (In,Ga)P emitter layer showing undulated contrast almost perpendicular to the diffraction vector;
a) – d) strain sensitive contrast,
e) predominantly composition sensitive contrast.

Contrary to the longitudinal cross-sections of the HBTs, the inspection by strain sensitive TEM diffraction contrast imaging of the transverse ones yields undulating contrast almost perpendicular to the individual diffraction vector (see Fig. 5a–d). Estimation of the distance between the dark lines gives a value of 5 to 10 nm depending on the diffraction vector. As shown by other groups (In,Ga)P undergoes phase separation as well as super structure formation (Bellon et al 1989, Zolotoyabko et al 1999). For the samples under investigation no additional reflections are detected in selected area diffraction patterns due to the weak contribution of the only 40 nm thick (In,Ga)P emitter layer to the diffraction process. Detailed inspection applying high-resolution TEM fails due to the large thickness of about 100 nm of the FIB lamella. Nevertheless, 002 dark-field images can be utilized to gain information on fluctuation of the chemical composition. Fig. 5e was obtained from the same area as in Figs. 5a–d. Fluctuations of the image intensity are visible but no unambiguous correlation to the strain sensitive contrast can be found.

3. SUMMARY

FIB prepared cross-sections of HBTs were investigated with respect to their structural and chemical properties by TEM. The Burgers vector of the dislocations originating from the lower interface of the (In,Ga)P emitter layer was determined to be $1/6\,[\bar{1}\,12]$ utilizing extinction of the contrast from dislocation lines for two different diffraction contrast dark-field images. The diffusion of indium out of the emitter depends on its strain state. Plastic relaxation of the crystal lattice hinders the indium diffusion as revealed by EDXS line scans. The origin of the undulating contrast features present for the transverse cross-sections is possibly due to the strain state of the emitter layer.

REFERENCES

Bellon P, Chevaller J P, Martin GP, Dupont-Nivet E, Thiebaut C and Andre J P 1989 J. Appl. Phys. **66**, 2388
Pazirandeh R, Zeimer U, Kirmse H, Würfl J, Tränkle G and Österle W 2004 IEEE CSIC Digest, 71
Zolotoyabko E, Goldner A and Komen Y 1999 Phys. Rev. B **60**, 11014

Strain measurements of ULSI devices using LACBED with TSUPREM modeled displacements

A Kenda, H Cerva, P Pongratz[1], M Hierlemann[2] and R Liebmann[2]

Siemens Corporate Technology, Siemens AG, CT MM 7, Otto Hahn Ring 6, D-81739 Munich, Germany, now at Carinthian Tech Research AG, Europastr 4, A-9524 Villach, Austria
[1] Institute of Applied and Technical Physics, TU Vienna, Wiedner Hauptstr 8-10, A-1040 Vienna, Austria
[2] Infineon Technologies, Corporate Logic, Otto Hahn Ring 6, D-81739 Munich, Germany

ABSTRACT: Large angle convergent beam electron diffraction (LACBED) patterns recorded of trenches in silicon devices were compared with simulated LACBED patterns to determine the strain in the structure. Displacement fields stemming from stress simulations of a 2D device simulator (TSUPREM IV) were used as an input for the LACBED simulations. The LACBED far-fields are very well reproduced by the simulations whereas the near-fields close to the interfaces show that the device simulator overestimates the strain.

1. INTRODUCTION

Highly localized measurements of strain in semiconductor devices have been carried out for several years (e.g. Armigliato et al 1995, Armigliato et al 2004). Thereby a finely focused but convergent electron beam, preferably in a field emission gun microscope, generates convergent-beam electron diffraction (CBED) patterns from which the local strain state can be calculated. (Balboni et al 1998). This technique makes use of kinematical diffraction theory to speed up linescan and mapping measurements. However, a prerequisite is the careful selection of the crystallographic direction of the incident electron beam that allows for making use of the kinematical approach (Armigliato and Balboni 2005). In application practice one faces three situations: current device structure features are smaller or equal to sub-quarter micron, sharp HOLZ (higher order Laue zone) line detection needs a TEM specimen thickness of about 150nm and tilting the TEM cross section out of the commonly used high order <110> projection. This has the consequence that the finely focused electron beam running through the specimen is not parallel to the usual <110> device edges. Hence, one loses spatial resolution and moreover areas with rapidly changing strain gradients are intersected obliquely. Nevertheless the CBED approach has been applied successfully in a few cases (e.g. Senez et al 2003). Recently Kim et al (2004) applied a full dynamical diffraction approach by simulating only selected areas of the experimental CBED patterns.

Motivated by the constraints of the CBED technique we focused on the large angle (LA)CBED technique which by moving the focus of the convergent beam out of the specimen (Fig. 1a) superimposes image and diffraction information in the pattern from a larger volume of space (typically a cylinder with 800 nm diameter and the height being the specimen thickness). In order to interpret these patterns from an imperfect crystal (i.e. the device structure) simulations for the displacement field of the illuminated volume are needed which are then input into electron microscopical LACBED simulations. The authors reported the development of dynamical multibeam simulation software for CBED and LACBED methods which includes all HOLZ and absorption effects and is capable of inputting various displacement field models (Kenda et al 2001). Whereas the program was then tested for strain fields of dislocations only, we show here for the first time the results for shallow trench isolation (STI) structures. The displacement fields for the device structures were generated from 2D TSUPREM IV device simulations. When experimental and simulated patterns match, the strain state is obtained.

2. LACBED SIMULATION

For LACBED simulation a full treatment of dynamical electron diffraction including all HOLZ effects and absorption effects is essential. The algorithms used for intensity calculation are based on the scattering matrix formalism of Bloch Wave Theory. In the simulation the incident electron cone is considered to consist of several beams each having a different $\boldsymbol{K}$ and for LACBED each $\boldsymbol{K}$ has a different localization within the TEM specimen. To account for these geometrical facts column approximation is used. With the column consisting of s crystal slabs, each having a different thickness t, the total electron wave field $\boldsymbol{\Psi}$ after each slab can be written in matrix notation (Peng and Whelan 1990)

$$\boldsymbol{\Psi}(z) = \prod_{l=1}^{s} [\boldsymbol{Q}_l \underbrace{\boldsymbol{P}_l(Z_l)\boldsymbol{C}_l\boldsymbol{Y}_l(t_l)\boldsymbol{C}_l^{-1}\boldsymbol{P}_l(-Z_{l-1})}_{\boldsymbol{M}_l(z)} \boldsymbol{Q}_l^{-1}] \cdot \boldsymbol{\Psi}(0) \tag{1}$$

The TEM specimen is represented by a displacement field model where $Z_s = \Sigma\, t_l$. Considering N beams, $(Y)_{ij} = \exp(i\gamma^{(j)}z)\delta_{ij}$ is a $N \times N$ diagonal matrix, and $(C)_{hi} = C_h^{(i)}$ is a $N \times N$ matrix. $(P)_{gh} = \exp(ipz)\delta_{gh}$ is a $N \times N$ diagonal matrix, which contains HOLZ effects. If a slab is displaced by a vector $\boldsymbol{R}$, the scattering matrix becomes $\boldsymbol{M}' = \boldsymbol{Q}\boldsymbol{M}\boldsymbol{Q}^{-1}$, where $(\mathrm{Q})_{\mathrm{mm}} = \exp(-i\boldsymbol{m}\cdot\boldsymbol{R})$ is a $N \times N$ diagonal matrix (as already inserted in (1)). The necessary algorithms and geometrical considerations have been implemented in a versatile software package which has been presented before (Kenda et al 2001). A modular structure has been used in order to be able to process arbitrary strain fields, all crystal systems, and various specimen geometries. A displacement module selects the crystal slabs for the incident beams passing through the specimen and stores a displacement vector $\boldsymbol{R}$ for each slab in a formatted file. The LACBED simulation module reads the stored values of $\boldsymbol{R}$ to calculate the intensities of the exit beams using equation (1).

3. T-SUPREM IV SIMULATIONS

A state of the art 2D-device process modeling program is TSUPREM IV. The entire process history is modeled and the stress fields in a plane strain approximation can be displayed. After each process step the initial and boundary conditions change for the next step and new knots for the next finite element mesh are defined. Thus an accumulated displacement field $\boldsymbol{R}$ cannot be obtained by integration. To overcome this problem the authors derived the integral displacement field $\boldsymbol{R}$ by the following procedure. The silicon lattice is relaxed after a process step by fulfilling the surface condition that the normal component of the stress vanishes. The negative displacements that occur during this procedure are used as displacement field that describe the originally intrinsic stress.

A TEM specimen with finite thickness is modelled out of a 2D displacement field (in this case a plane strain TSUPREM IV finite element simulation (FEM)) by stacking identical planes with respect to the specimen orientation (see Fig. 1b). Field gradients $\mathrm{d}\boldsymbol{g}\cdot\boldsymbol{R}/\mathrm{d}\boldsymbol{r}$ occur in the specimen coordinate system along the projection of the correspondent $\boldsymbol{K}$. Because of the plane strain approximation there are no z-components.

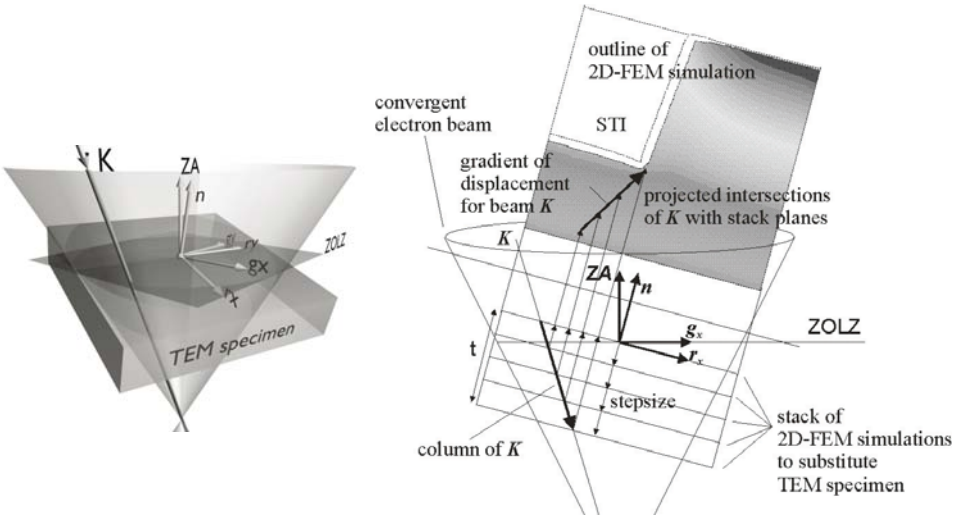
A 3D device simulation program that would produce reliable displacement fields was not yet available.

4. COMPARISON OF EXPERIMENT AND SIMULATION

LACBED patterns were acquired with a Philips CM200 FEG TEM equipped with a Gatan imaging filter. Due to the energy filter operation the effective accelerating voltage of 198.5 kV was found by minimising the difference of a reference pattern from unstrained silicon with perfect crystal simulations. A room temperature specimen holder is sufficient to carry out the LACBED experiments with a minimum of contamination.

The specimens were (100) Si wafers with arrays of shallow trench isolations nominally 250 nm deep and with a pitch of 250 nm. The trench was filled with a high density plasma oxide (HDP) and finally annealed.

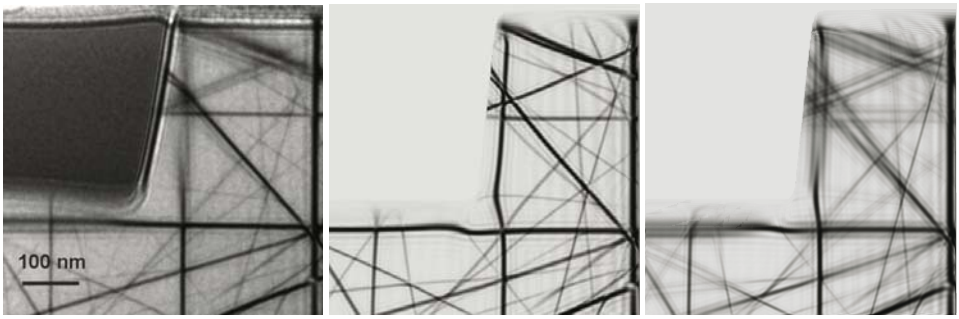
Figure 2 shows an STI sidewall and bottom in a specimen with 240 nm thickness. Close to the



(a) (b)

Fig. 1. (a) 3D schematic showing the arbitrary relation between electron beam ($\boldsymbol{g}_x$, $\boldsymbol{g}_y$, $\boldsymbol{ZA}$) and specimen coordinate system ($\boldsymbol{r}_x$, $\boldsymbol{r}_y$, $\boldsymbol{n}$), (b) Formation of the displacement field gradient $d\boldsymbol{g}\cdot\boldsymbol{R}/d\boldsymbol{r}$ for an incident beam $\boldsymbol{K}$ in a specimen made up of displacement sheets of 2D-FEM simulations.

Si/SiO_2 interfaces a splitting and blurring of the HOLZ line contrast is observed. In the simulated pattern (Fig. 2b) the splitting is partially reproduced (next to the STI top corner) but not the extensive blurring. A simple matching of the blurring could be achieved when a surface relaxation of the TEM specimen was permitted. A best match was obtained for a relaxation of about 50% at the specimen surfaces and 20% in the centre (Fig. 2c).



(a) (b) (c)

Fig. 2. (a) Experimental LACBED pattern of STI structure with the beam incident in [20 19-5] direction (i.e 10° off <110> along the (220) Kikuchi band), specimen thickness 240 nm. LACBED simulations without absorption and displacement inputs from TSUPREM IV calculations: (b) without, (c) with a Gaussian surface relaxation of the u_x, u_y- displacements in z-direction.

Choosing a large specimen thickness of over 300 nm minimises strongly the surface relaxation effects. Fig. 3a,b show an STI structure with a thickness of about 360nm. The LACBED contrast can be described very well by the 2d displacement field obtained by TSUPREM IV. Experiment and simulation show a very good agreement up to a distance of about 20 nm from the vertical Si/SiO_2 interface. Close to the vertical interface the simulations show stronger changes in the HOLZ line contrast which suggests stronger gradients in the displacement field. A comparison of strain measurements by the CBED point measurement technique with the presented LACBED technique clarified that the strains close to the vertical interface are overestimated. Studying the variation of

d$\boldsymbol{g}\cdot\boldsymbol{R}$/d$\boldsymbol{r}$ through a column next to split HOLZ lines revealed that it is not only the maximum value of the variation which is responsible for strong splitting but the existence of local extrema. The calculation time for the pattern in Fig. 3b excluding absorption effects was approximately 4 hours.

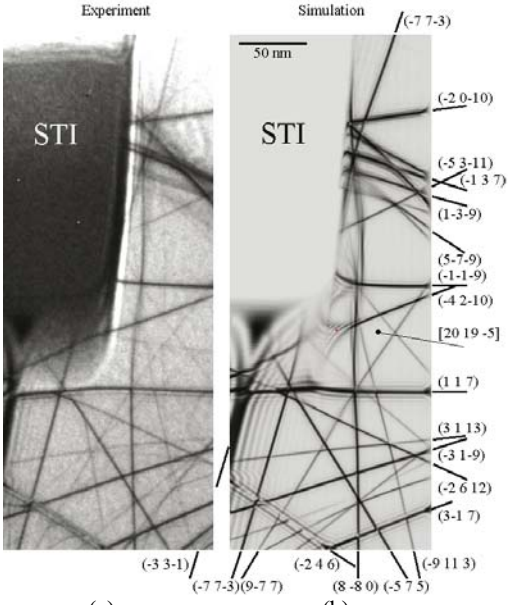


Fig. 3. (a) Experimental LACBED pattern of an STI structure with the beam incident in [20 19-5] direction (i.e 10° off <110> along the (220) Kikuchi band). (b) LACBED simulation specimen thickness 360 nm.

5. CONCLUSION

It has been shown that LACBED patterns of device structures can be simulated with success even when the displacement fields are derived from stress device simulations (TSUPREM IV) which make use of the plane strain approximation. It was found that currently the simulations overestimate the strains at the interfaces in a range of about 20 nm into the Si crystal. However, the method of matching experimental LACBED patterns with LACBED pattern simulations are the only means to enable strain investigations close to the interfaces. First an improvement of the physical strain models in device simulators is needed and second displacement fields from 3D device simulators.

REFERENCES

Armigliato A, Balboni R, Corticelli F, Frabboni S, Malvezzi F and Vanhellemont 1995 J Mat. Sci. Techn. **11**, 400

Armigliato A, Balboni R, Benedetti A and Frabboni S 2004 in High Pressure Crystallography, eds. Katrusiak A and McMillan P.F. (Kluwer Academic Publishers, Dordrecht) p 277

Armigliato A, Balboni R and Frabboni S 2005 Appl. Phys.Lett. **86**, 063508

Balboni R, Frabboni F and Armigliato A 1998 Phil. Mag. **A77**, 67

Kenda A, Cerva H and Pongratz P 2001 Inst. Phys. Conf. Ser. **169**, 477

Kim M, Zuo J.M. and Park G-S 2004 Appl. Phys. Lett. **84**, 2181

Peng L M, Whelan M J 1990 Proc. Royal Soc. **A431**, 111

Senez V, Armigliato A, De Wolf I, Carnevale G, Balboni R, Frabboni F and Benedetti A 2003 Microelectronic Engin. **70**, 425

T-SUPREM IV Users Manual Rel. 2001.2 Avant! Corp., TCAD Business Unit Freemont CA, USA

Electron holography for visualisation of different doped areas in silicon-germanium heterojunction bipolar transistors

U Muehle, A Lenk[1], A T Tilke[2], C Wagner, C Dahl and H Lichte[1]

Infineon Technologies Dresden GmbH & Co OHG; Koenigsbruecker Str. 180; 01099 Dresden; Germany
[1] Dresden University; Institute of Structural Physics; Triebenberg Laboratory
[2] Infineon Technologies North America , 2070 Route 52, Hopewell Junction, NY 12533

ABSTRACT: A bipolar transistor with a silicon-germanium base (HBT) was prepared by the focused ion beam technique for TEM-cross-sectioning, taking into account the special requirements of electron holography. A line plot from the phase image through the functional region includes the influences of different dopant content as well as different germanium concentrations on the mean inner potential. Interpretation of the superimposed contributions to the phase shift succeeds by using additional information from SIMS data.

1. INTRODUCTION

In many highly integrated circuits for modern wireless applications heterojunction bipolar transistors (HBTs) with a silicon germanium base are used (Tilke et al 2004). The investigated structure is a vertical device, consisting of a phosphorus doped collector region in the silicon substrate, followed by an epitaxially grown silicon-15%germanium-base, doped by boron. The emitter is built up by arsenic doped polycrystalline silicon, outdiffused into the top layer of the base epitaxy (Fig. 1).

For device optimisation, analytical investigations of dopant distributions on a nanometre scale are desired. Electron holography, indicating a different phase shift on the basis of local deviations in mean inner potential, is able to obtain information about the profile of the dopant (Rau et al 1999).

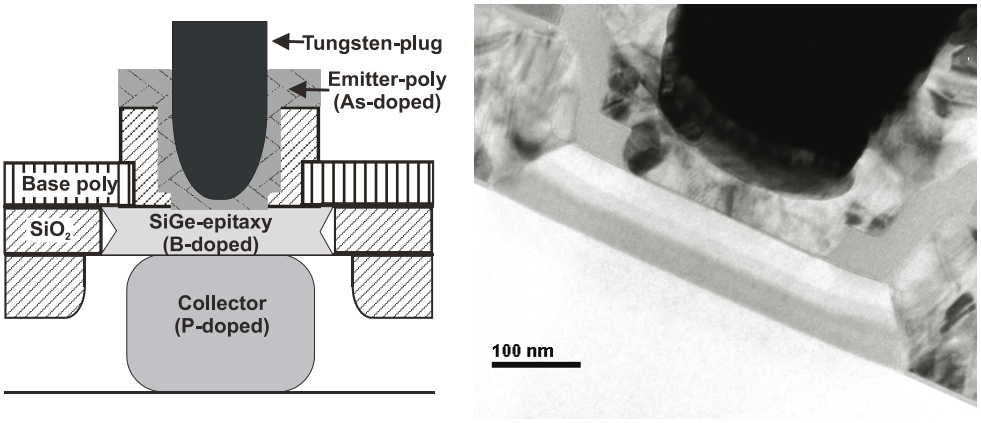


Fig. 1. Schematic demonstration of the device to be investigated (left hand side) and TEM-brightfield image (right hand side). Note that the specimen has been slightly tilted out of zone axis orientation to avoid dynamical effects and to emphasis the Ge-containing region with the enhanced z-contrast.

2. PREPARATION AND VISUALISATION

TEM-holography includes some special requirements on the TEM-sample. The differences in internal potential between differently-doped regions are in the range of about 1 V, whereas the mean inner potential of silicon is 11.9 V (Wang et al 1999). To achieve a sufficient amount of difference in phase shift a much larger samples thickness than in usual TEM-investigations is required. Long parallel devices in test structures give the ability to prepare samples of arbitrary thickness.

A second pre-condition for a sample suited to holography is the absence of thickness variations, because a variation in foils thickness of 1 % effects the phase shift in the same manner like potential differences of about 10 % (Lenk et al 2002). Preparation by focused ion beam (FIB) includes the so called "Curtaining" effect, caused by the different behaviour of materials under the ion beam. Therefore the material above the object of holographic investigation has to be as homogeneous as possible. A combination of mechanical grinding and polishing and chemical etching is able to remove most of the top layers before the final target preparation by FIB can be performed (Lenk 2001). This is also important for the vacuum wave nearby the details to be observed (Fig. 2).

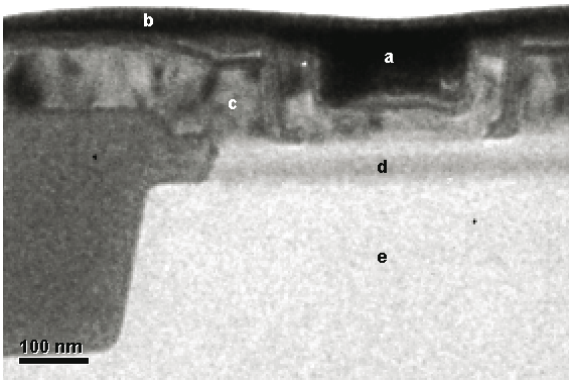


Fig. 2. Brightfield image of the sample, prepared for holographic investigation. Only a small residual of the tungsten plug remained after delayering of the sample (a). The surface is covered by platinum (b). In lower regions the polysilicon connection (c) of the germanium containing (d) base and the silicon single crystal, acting as collector (e) are to be recognised.

The holographic investigations were provided at the Institute of Structural Physics at Dresden University, using a CM 200 FEG, equipped with Lorentz-lens and biprism after Moellenstedt.

The result of this investigation, including Fourier transformation and filtering, is an image of the phase distribution (Fig. 3). For a better understanding of the phase shift behaviour a lineplot with a detailed consideration of the different regions is applied.

3. RESULTS AND INTERPRETATION

The line plot, displaying the phase shift versus location averages over a width of about 100nm in order to reduce the pixel dependent noise of the image. This is shown in Fig. 4, combined with a coordinated plot of the dopants and germanium concentration (Tilke et al 2005). A definition of common starting points succeeds using the borderline between polycrystalline silicon and single crystal.

A rough estimation of the differences in mean inner potential due to dopant concentration can be made using

$$\Delta V_{pn} = \frac{kT}{e} \ln\left(\frac{N_A N_D}{n_i^2}\right) \tag{1}$$

(Mueller et al 1995). This would lead to $\Delta V_{pn} = 1.14$ V for the transition between emitter and base and $\Delta V_{pn} = 0.95$ V for the transition between base and collector. For the evaluation of the real potential we have to take into account:

a) Due to the short dimension of the base it is not guaranteed, that the lowest level of potential is really achieved before the influence of next range is starting.
b) The mean inner potential of the base deviates from that of pure silicon caused by the germanium content following

$$V_{0,SiGe} = cV_{0\,Si} + (1-c)V_{0,Ge} \tag{2}$$

where $V_{0,Si}$ and $V_{0,Ge}$ are the mean inner potentials of pure Si and Ge and c is the Si-content in atomic fraction. This leads to a mean inner potential of 12V for SiGe4% and 12,3V for SiGe15%.

Now we are able to interpret the origin of the phase shift, depending on mean inner potential by

$$\phi = C_E\left(t - 2t_0\right)\cdot\left(V_{0,SiGe} + \Delta V_{pn}\right) \tag{3}$$

(Orchowski et al 2002) with t as foil thickness, t_0 is the thickness of an electrically inactive lateral layer (the so called "Dead layer") and C_E as an interaction constant, depending on accelerating voltage of the microscope.

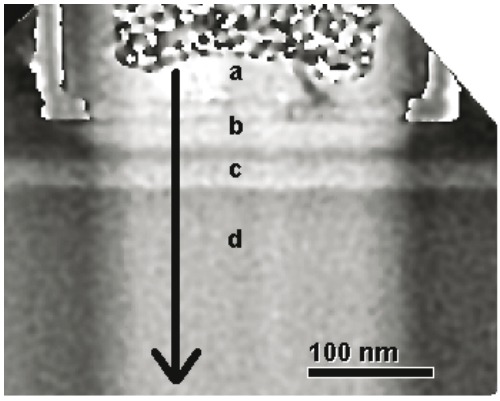
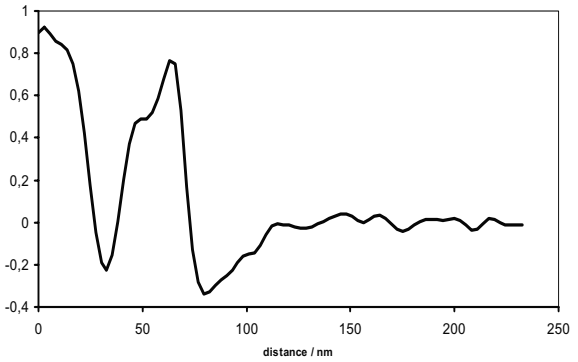


Fig. 3. Phase image of vertical HBT: Below the polysilicon connection (a) the As-doped Emitter (b), the B-doped and Ge containing base (c) and the lower P-doped collector (d) is situated. The arrow indicates the direction of the lineplot (see Fig. 4).

In the emitter range the phase shift strongly decreases under the impact of a steep decrease of arsenic content. The lowest value in the upper part of the base is partially compensated by the effect of germanium. Rising germanium content leads to a higher phase shift, nearly reaching the maximum value of the emitter. Here the influence of boron doping is more than compensated. Below the germanium rich region the phase shift strongly decreases and meets the normal transition between base and collector. The horizontal course of the phase shift into the deeper collector region was used for normalisation.

SUMMARY

It was shown that a target preparation of a complex device by FIB for electron holography can succeed. Using additional information of elemental distribution, the phase image can be explained in a semiquantitative manner. A complete understanding of the influence of the dead layer and of the different contributions of n-doped and p-doped regions seems to enable the possibility of complete analytical description of the phase shift distribution.



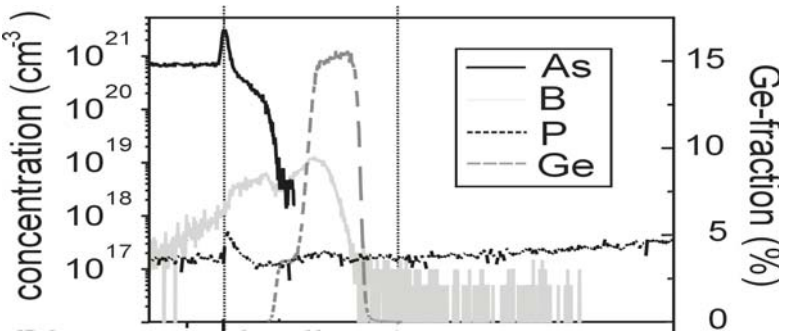


Fig. 4. Lineplot of phase shift, taken from Fig. 3 (right) in comparison to depth profile of element distribution (below), acquired by Secondary Ion Mass Spectroscopy (SIMS).

ACKNOWLEDGEMENTS

The work for this paper was partly supported by the EFRE fund of the European Community and by funding of the State Saxony of the Federal Republic of Germany (project number 7741).

REFERENCES

Lenk A 2001 Diploma thesis, Dresden University

Lenk A, Brand K, Lehmann M, Lichte H, Engelmann H J and Muehle U 2002 Int. Conf. Electron Microscopy Durban

Mueller R (Edt.) 1995 Grundlagen der Halbleiter-Elektronik, ISBN 3-540-58912-0

Orchowski A, Rau W D, Ruecker H, Heinemann B, Schwander P, Tillack B and Ourmazd A 2002 Appl. Phys. Lett. **80**, 2556

Rau W D, Schwander P, Baumann F H, Hoeppner W and Ourmazd A 1999 Phys. Rev. Lett. **82**, 2614

Tilke A T, Lenk A, Muehle U, Wagner C, Dahl C and Lichte H 2005 IEEE Trans. Electron. Dev. *accepted*

Tilke A T, Rochel M, Rothenhäußer S, Stahrenberg K, Wiedemann J, Berkner J, Wagner C and Dahl C 2004 IEEE Trans. Electron. Dev. **51**, 1101

Wang Y C, Chou T M and Libera M 1999 Appl. Phys. Lett. **70**, 1296

Ar sputter shadow method (ASSM) - a novel way to overcome the charging effect during AES bond pad analysis

Hui-Min Lo, Jian-Shing Luo and Jeremy D Russell

Physical Failure Analysis Department, Inotera Memories, Inc. Taoyuan, Taiwan, Republic of China

ABSTRACT: This paper discusses a novel technique using locally restricted Ar sputter for sample preparation, called ASSM, to overcome charging during AES analysis of polyimide surrounded bond pads. Subsequently, using Ar ion flooding, charging can be effortlessly reduced. Comparison of four anti-charging methods shows that ASSM has the advantage of obtaining reliable data easier than the others. It is suggested that ASSM generates conductive paths in the vicinity of the analysis area. XPS investigations indicate a reduced density of imide groups in the adjacent sputtered regions.

1. INTRODUCTION

Integrated circuit bond pads built by Al-Cu alloy are strongly affected by the aluminum surface, due to oxidation and residual contaminants. Thick oxide causes weak bonding and low conductivity, resulting in failure or reliability concerns. Fluorine residues react with moisture resulting in subsequent corrosion depending on the package type and environmental conditions. Auger electron spectroscopy (AES) signals come from within 5-6 nm of the surface, making AES a powerful tool for pad surface quality characterization, process troubleshooting and failure analysis. However, modern integrated circuits are covered by several μm thick polyimide around the pads causing unfavorable charging during AES investigations. Different methods to overcome this charging include sputter-coating, reducing the electron beam energy, increasing the sample tilt angle and using finely pierced Al foil covering the sample, with the disadvantage of increased analysis complexity in all cases (Seah and Spencer 2000).

In this paper, we report upon ASSM which can quickly and simply reduce charging, leaving a non-bombarded shadow area with un-affected pad properties at the edge. The advantage of ASSM will be indicated by comparison with other charge reduction methods. Furthermore, results from a real case related to F pad contamination using ASSM will be reported.

2. EXPERIMENTAL

Samples used in this study were 0.11 μm technology DRAM chips, manufactured by Inotera Memories Inc. in Taiwan, with 70×70 μm^2 square pads surrounded by about 6μm thick polyimide. AES spectra, mapping data and secondary electron micrographs were obtained using a PHI700 Auger Electron Spectrometer with cylindrical mirror analyser (CMA) manufactured by ULVAC-PHI, Inc. The electron and ion beam geometry is shown in Fig. 1a. The analysis chamber vacuum reaches 5×10^{-10} Torr. The incident angle of the Ar ion beam is fixed at 15 degrees to the sample surface, from which we obtain a shadow area of about 1/3 pad size which was untouched by Ar sputter and used for AES analysis, as shown in Fig. 1c. The sidewall step of polyimide shields the pad surface from damage during Ar sputter, as shown in Fig. 1b.The AES surface survey data were taken from an area of 8×6 μm^2 from the shadow area. The Ar ion sputtering for polyimide surface modification was performed at 3kV energy with 1×1 mm^2 raster size (current density=115 nA/mm^2) for one minute. The other charge reduction methods are

described in detail elsewhere (Briggs and Grant, 2003). Surface chemical changes of polyimide transformed from insulating to conducting were characterised by X-ray photoelectron spectroscopy (XPS), using a Kratos Ultra system with a monochromatic Al K_α X-ray source. The analysis area was approximately 0.3 × 0.7 mm^2.

3. RESULTS AND DISCUSSION

To eliminate charging and seek the optimal analysis parameters, electron beam energy, current, stage tilt angle and very low energy Ar ion flooding were evaluated. The Ar ion flooding carries some tens of eV positive ions, which are used to compensate charge without any sample surface damage. In ASSM, an optimum condition for AES analyses of these bond pad surfaces was found to be 5 kV energy and 10 nA current electron beam with/without stage tilt. Table 1 is a comparison summary of four workable anti-charge methods for bond pad analysis. It shows the ASSM has the advantage of being capable of applying higher electron beam energy and current which bring good signal/noise and more repeatable results regarding (quasi-) semi-quantitative analysis by AES. ASSM is not strongly dependent on the corresponding Ar ion flooding condition, whereas the other methods require careful and difficult optimisations. A set of comparison data done by ASSM and Al-foil method shows that ASSM has a more stable concentration distribution for each element than the Al-foil mask method, as shown in Table 2. Fig. 2 shows three SEM images with (a) stage tilt, (b) stage tilt and Ar ion flooding and (c) ASSM preparation, respectively. From the AES spectra, shown in Fig. 3, it is obvious that artefacts related to charging were dramatically reduced by applying ASSM. However, the as-sputtered sample doesn't instantly reach the charge equilibrium on the surface and the earliest acquired spectra show a charging bulge appearance between 100-200 eV, as shown in spectrum Fig. 4a, for example. By exposing to sufficient Ar ions (Ar ion flooding), charging can be substantially reduced, as shown in spectrum (b) of Fig. 4.

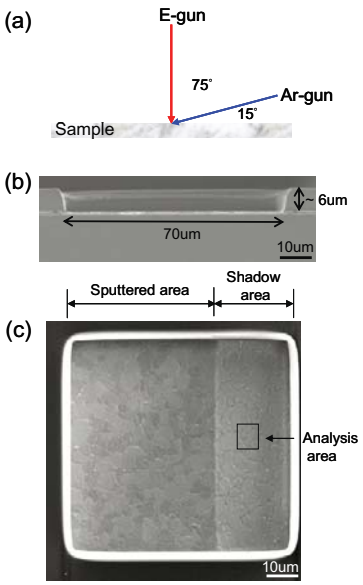


Fig. 1. (a) Schematic showing Ar ion beam sample geometry of AES system, (b) SEM image showing bonding pad X-sectional view and (c) Pad appearance after Ar sputter

Table 1 Electron and ion beams results of four sample preparation methods of charge reduction. It shows the summary of the experimental results of AES analysis on pads by using different methods.

Method	3kV 5nA	3kV 10nA	5kV 5nA	5kV 10nA	10kV 10nA	Ar ion Flooding	Ease of Use	Available Analysis Area	**Data Reliability**
ASSM		√	√	√*	√	Yes	Yes	Small	**Yes**
Al-foil Mask	√*	√	X	X	X	Yes	No	Small	**No**
Pt Coating			√	√*	√	No	Yes	Whole Pad	**No**
Grazing Angle	*	**X**	**X**	**X**	**X**	**Yes**	**No**	**Small**	**No**

Remark: √ means workable, √* means the best condition and X means unworkable.

Table 2 shows semi-quantitative results of the same condition samples by applying ASSM and Al-foil Mask Method

<ASSM Result>						<Al-foil Result>					
at%	O	Al	C	F	N	at%	O	Al	C	F	N
Pad-1	43.7	25.3	17.7	8.5	4.8	Pad-1	42.8	18.7	22.6	10.4	5.5
Pad-2	43.9	24.3	17.6	8.3	5.9	Pad-2	37.8	22.6	30	6.4	3.2
Pad-3	43.3	23.9	18.9	8.4	5.5	Pad-3	39.3	24.2	26.2	5.9	4.4
Pad-4	44.3	22.9	17.3	9.3	6.2	Pad-4	38.9	22.1	23.9	10.5	4.6



Fig. 2. Three SEM images acquired by AES spectrometer, (a) stage tilt 30°, (b) Ar ion flooding on and (c) ASSM, show different surface charging situations. (c) SEM image has no image distortion from charging.

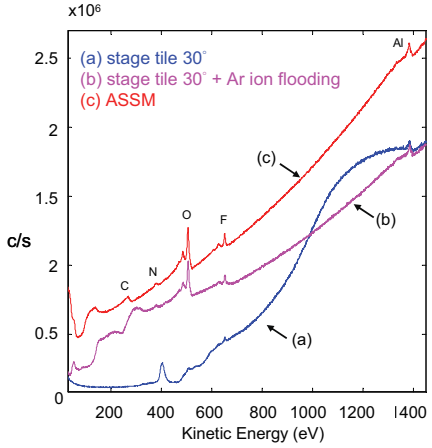


Fig. 3. Three AES spectra, corresponding to Fig. 2, show different surface charging situations.

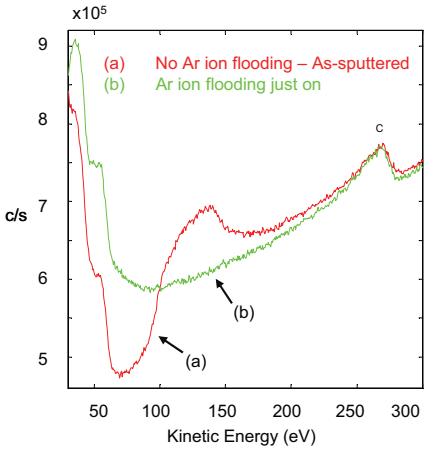


Fig. 4. AES spectra (a) without and (b) with Ar ion flooding

It is well known that polyimide mainly consists of C, H, O and N , e.g. Polymer ester. In order to elucidate why using the ASSM can reduce the sample charging, XPS was used to check the chemical bonding transformations of polyimide resulting from Ar sputter. The C1s signal envelope and the relative intensities of distinct contributing peaks were changed after Ar sputter, as shown in Fig. 5 and Table 3. For the polyimide sample, the peaks at higher binding energies are interpreted as the signals for -C-OH / -C-O-C- (286.5eV) , -C=O (287.8eV) and –CO-NR'-CO- (288.9eV) (Beamson et al, 1992) (Flitsch and Shih, 1990). The signal contribution of the 285eV C1s peak, C-H and C-C, increases after ASSM. It appears that the increase in C-H and C-C contributes to the better conductivity of the transformed polymer surface layer. Our results indicate that the 285eV peak plays a very important role on the conductivity of the polyimide surface. We suggest that it might be related to the formation of conducting or mobile fragments due to imide group cracking in the Ar-sputtered region. This may help to build up a conductive superficial path from the unaffected shadowed polyimide surface to edge and then down to the pad. Consistently, from AES analysis, a strong C peak and weak N and O peaks were detected on the Ar sputter treated polyimide surface.

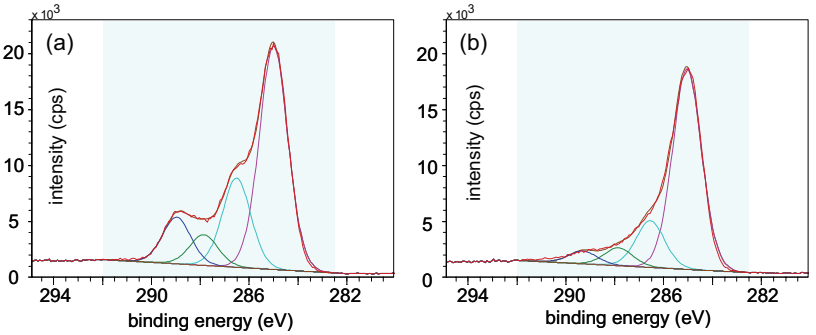


Fig. 5. XPS spectra shows C1s peak shape of polyimide surface (a) before and (b) after ASSM

To make sure no contamination by re-deposition of sputtered material occurs in the desirable shadow area during the ASSM, a thin Pt layer, about 80 nm, was firstly deposited on two sides of the pads by masking before applying ASSM. From AES analysis, no Pt element signal was detected on the whole pad area after Ar sputter.

Table 3 XPS data: intensity % of polyimide surface before and after Ar sputter treatment

Binding Energy (eV)	285.0	286.5	287.8	288.9
Relative Intensity (%) - before ASSM	57.5	22.9	7.7	11.9
Relative Intensity (%) - after ASSM	72.4	16.8	6.3	4.5

During a real-case analysis, a high density of flakes was observed on abnormal bonding pads. By ASSM, the surface was quickly identified to have abnormally high F and O content. The F and O element distribution by AES mapping is shown in Fig. 6.

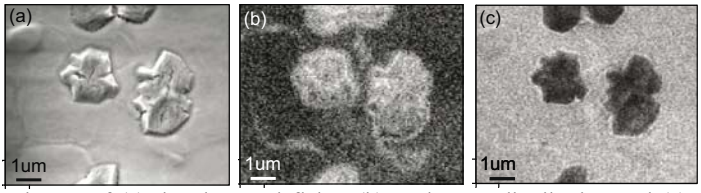


Fig. 6. SEM image of (a) the abnormal flakes (b) F element distribution and (c) O element distribution

It is well known that high residual F concentration on pads is very crucial for bonding. Higher F concentration easily results in corrosion, which causes bonding wire failures. Consequently, F residual control plays an important role in chip packaging. For pads with higher F surface concentration, after 4-6 weeks exposure in air, a corrosion phenomenon occurred. It is believed that F reacted with H_2O from the air and generated HF acid in the thin atmospheric surface electrolyte, causing corrosion. In addition, the corrosion phenomenon became more severe after exposure for a few more weeks from surface observation under OM. From a known mechanism for Cl assisted corrosion (Chang and Sze 1996), a possible explanation for the F corrosion is as follows,

$F^- + H_20 \rightarrow HF + OH^-$ ----------(1) $6HF + 2Al \rightarrow 2AlF_3 + 3H_2$ ----------(2)

The details of the mechanism and microstructure of corrosion will be the subject of a future report.

4. CONCLUSIONS

The results obtained in this work show ASSM is an easy, quick and reliable solution for bond pad analysis compared to other traditional methods. ASSM has the advantage of being capable of using higher electron current, which brings good AES signal/noise ratio and more repeatable results for semi-quantitative analysis. XPS helps to explain the improvement of the sample conductivity. For the next DRAM technology generations, pad size shrinks to $60 \times 60 \mu m^2$ and below, so the ASSM can aid efficient bond pad analysis.

ACKNOWLEDGEMENT

The authors are indebted to Michael Noeske (Fraunhofer IFAM, Bremen) for the XPS analysis data and valuable comments on the corrosion mechanism.

REFERENCES

Chang C Y and Sze S M 1996 “ULSI Technology”, (McGraw-Hill International Editions, Singapore) Ch.7 and 8

Beamson G and Briggs D 1992 “High Resolution XPS of Organic Polymers” (Wiley, Singapore)

Briggs David and Grant John T 2003 “Surface Analysis by Auger and X-ray Photoelectron Spectroscopy” (Cromwell Press, UK) p. 204-205

Flitsch R and Shih C Y 1990 J. Vac. Sci. Technol. **A 8**, 2376

Seah M P and Spencer S J 2000 J. Electron Spectroscopy and Related Phenomena **109,** 291

Part VIII

Scanning Electron and Scanning Probe Advances

Challenges and opportunities of Ångstrom-level analysis

P E Batson

IBM Thomas J. Watson Research Center, Yorktown Heights, New York, 10598

ABSTRACT: The IBM aberration corrected STEM is intended to obtain electronic structure by EELS from defects and interfaces in semiconductor device structures. It consists of three elements: a Nion aberration corrector to obtain a 0.08 nm probe size at 120 kV, an EELS spectrometer having about 60 meV resolution, optimized for electronic structure measurements, and a gun monochromator designed for high brightness transmission to allow EELS analysis using the small probe. Initial experience with the corrector shows that the probe is now easily reproduced if the corrector optics are carefully managed.

1. INTRODUCTION

With device structures today becoming ever smaller, it has become necessary to consider using atomic resolution for measurement of electronic structure of interfaces and defects. In addition, in the not very distant future, novel molecular-scale devices may be introduced. These will also require atomic-level analysis. In addition, it is likely that they will consist of atomic species that may be more susceptible to electron beam damage than the materials that make up today's devices. Therefore, aberration correction, as the most likely way forward to sub-Angstrom probe sizes using relatively low energy electron beams, has been fitted to the IBM spatially resolved EELS instrument.

As is the case anytime new capability is explored, results do not always follow our preconceptions. Therefore, great care needs to be taken to apply this new technique to avoid pitfalls. However, new analytical opportunities will almost certainly result. As semiconductor device sizes rapidly approach the atomic level, many quantities -- such as conductivity, mobility, breakdown, leakage, dielectric constant, dopant concentration, and even thickness -- lose their well known practical definitions. For instance, Si spheres lose their crystalline bandstructure when they become smaller than about 2-3 nm in size, potentially affecting conductivity and mobility. (Batson and Heath, 1993) At the outset, I have found that even a simple characterization of spatial resolution is sometimes elusive, requiring very careful control of the corrector, the specimen and data acquisition. Atomic motion in the presence of the sub-Angstrom electron beam is ubiquitous, requiring short exposure times to follow atomic-level movement. These challenges can sometimes be turned to advantage. For instance, atomic level motion, while being driven by beam interactions, clearly depends on the local atomic environment, allowing qualitative judgments to be made about local structural stability.

2. DESCRIPTION OF THE INSTRUMENT

2.1 The IBM HB501 Basic Machine

The VG Microscopes, Ltd STEM was delivered in 1983 operating at 100 kV with a probe size of about 0.5 nm. This instrument had one of the first virtual objective apertures and a two condenser illumination system, but did not have a gun lens. It was installed within a welded steel shielded room to reduce 180 Hz electrical interference. This room also helped to lower direct acoustic interference, but contributed some mechanical vibration in the floor via acoustic coupling of the walls and floor to nearby air conditioning equipment. During the 1980's, a Cs = 1.3 mm polepiece was added, and the EHT was increased to 120 kV in an effort to improve the prove size. At the same time, the objective

lens polepiece was raised about 150 μm to produce a 4x post-specimen compression for better EELS collection. With this arrangement, it was possible to resolve the Si [022] lattice spacing of 0.192 nm with a probe that carried 0.5-1 nAmp current -- suitable for EELS work.

2.2 The Wien Filter Spectrometer

The electron spectrometer is a Wien filter design mounted within a high voltage electrode above the specimen chamber (Batson 1986). On entering this electrode, beam electrons are decelerated to 30-100 eV before entering the Wien Filter. This device therefore provides mm/eV dispersion appropriate to sub-eV analysis. Although no second order optical correction was used, the spectrometer has demonstrated 70 meV resolution using 5 mR half angle collection at the specimen. An important feature of the deceleration process is the elimination of the effect of high voltage fluctuations on the EELS spectra. It is possible to obtain spectral position accuracy to ±20 meV in many cases, allowing the measurement of conduction band offsets in SiGe structures. This instrument was used to obtained bandstructure information from a single misfit defect structure near a strained Si quantum well (Batson 2000).

2.3 The Gun Monochromator

In spite of having a field emission limited system resolution of 0.3 eV, the system is still not capable of routine inspection of direct interband scattering in semiconductors. This is a result of the long low energy tail of intensity from the field emission source due to tunnelling from below the Fermi level which is 100x bigger than the inelastic scattering due to direct interband transitions. (Batson, et al. 1986) Therefore a monochromator system that cuts off this tail, producing a no loss beam that is more symmetric in shape, may allow direct measurement of the band gap. The monochromator was designed in collaboration with H W Mook and P Kruit of Delft University (Mook et al 1999). Briefly, it consists of a short Wien filter positioned at high voltage after the extraction electrode of the field emission source, but before acceleration to the final beam energy. The Wien filter does not provide focussing in this case, but only energy dispersion. Focussing is done by simple electrostatic optics, corrected by six stigmation electrodes which are part of the Wien filter. The dispersed beam is apertured by 150 nm nanoslits machined into a Pt coated silicon nitride film. At IBM the gun electrode was modified to provide additional electrical feedthroughs and a new EHT tank was built to accept the Wien filter electronics which must float at the microscope acceleration potential. This device demonstrated a system resolution of 60 meV in conjunction with the EELS spectrometer when operated at 20 kV. Measurements of brightness suggest that this was achieved without loss of brightness beyond that required by the narrow energy range passed by the slits. When the Nion aberration corrector was installed, the monochromator was removed, returning the system to simplify the installation procedure.

2.4 The Nion Aberration Corrector

In 2001, the first commercial version of the Nion, Co. quadrupole-octupole corrector was installed (Dellby et al 2001). This device brought the STEM electron optics to a theoretical limit of about 0.07 nm at 120 kV. However, since the original system was designed to operate in the 0.2-0.5 nm range, none of the instrumental stabilities were capable of this level of performance. Therefore, as has been the case with each corrector installation, a period of time has been required to bring the microscope and its environment to the required level. In the present case, this process was been made more complex by the presence of the modifications required by the non-standard spectrometer and monochromator. For instance, the need for a CCD camera system, to record electron shadow map (Ronchigram) images between the specimen and the spectrometer, required a redesign of the spectrometer coupling optics. Uncertainty about electron trajectories between the gun and the corrector also required the removal of the monochromator prior to the corrector installation.

2.5 System Control, Data Acquisition and Analysis

Prior to the addition of the corrector, the Wien Filter spectrometer and STEM panel were controlled using the IBM high level APL2 language. This is an interpretor based language having

native support for complex matrix and vector arithmetic. It also has many C-based routines to manipulate non-APL software and hardware. This has been retained and extended to include the Nion corrector. Therefore it has facilitated some independent development of corrector tuning capability, allowing contributions to confidence in this new field. Also, with the availability of new display technology, a 200dpi flat screen replaces the original STEM displays. Most operational and imaging interaction is therefore retained at the STEM console, within one programming environment. Post experiment data analysis is also done within this environment.

STEM beam scanning control is retained by the VG Microscope electronics, while 1024x1024 10 bit image data is collected by a National Instruments frame grabber. This arrangement retains the excellent VG system for mains synching to reduce AC interference.

2.6 Summary of Mechanical Changes

Figure 1 summarizes the changes required for this project. To make room for the mono-chromator, the gun flange can be dropped 4 cm by insertion of a ring spacer at the flange. The monchromator and tip are mounted on a new EHT feedthrough which can be connected to the microscope eht either using a 12-core cable or by a modified VG cable. Thus the gun can be returned to the original operational configuration by removing the ring spacer, remounting the original tip assembly, and replacing the new cable with the old cable.

The Nion corrector replaces the VG scan coils, immediately below the objective lens. Scanning is accomplished using new coils designed by Nion situated within the bore of the objective lens field coils. The ADF detector was modified to allow automatic retraction. The Nion CCD camera for Ronchigram acquisition was positioned between the specimen chamber and the Wien filter spectrometer, requiring extensive redesign of the spectrometer coupling optics. This design utilizes a wide bore, long focal length cylindrical lens situated below the CCD to provide large collection and a set of multipole optics to optimally shape the beam for the Wien filter spectrometer. Finally a new CCD camera having smaller pixels, together with a tapered fibre optic bundle, is intended to produce spectra having 10 meV channels. Not shown in this figure is a small scintillator mounted in one position of the VOA aperture to provide a video signal for monochromator setup. This will allow alignment of the monochromator without requiring beam passage through the corrector.

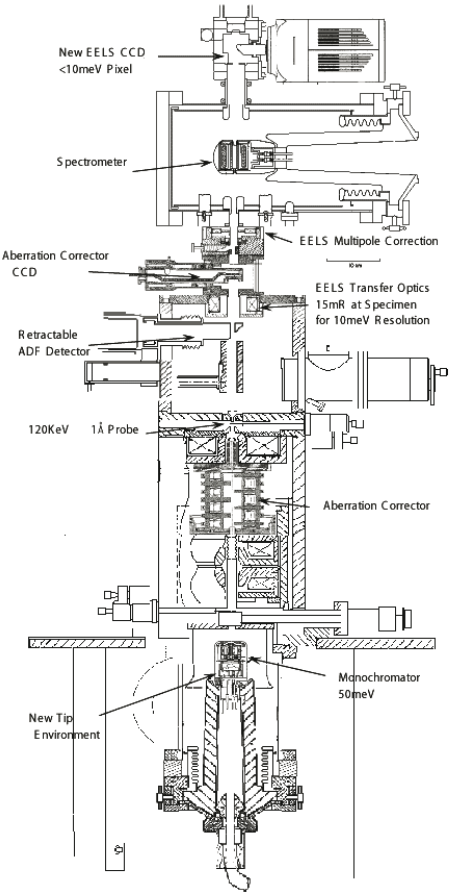


Fig. 1. Summary of final mechanical arrangement. Presently, the monochromator has been removed to allow a better understanding of the aberration corrector operation.

3. PRESENT IMAGING PERFORMANCE

3.1 Reproducibility of Corrector Tuning

The complexity of this system is very high, with each of the required three tasks (imaging, spectroscopy and monochromation) being quite demanding and uncertain of outcome. Therefore it is imperative that each task be refined to a very reliable level if the whole system performance is to be approached. Tuning of the corrector is performed using Ronchigram patterns, (Ronchi 1964) described for this particular installation by Batson (2003). In order to reproduce probe conditions, this process uses target third order coefficients, chosen to optimally balance fourth and fifth order coefficients that are not controlled. This is analogous to using defocus to oppose spherical aberration at Scherzer defocus in the uncorrected instrument. Table 1 summarizes the coefficients which are routinely obtained. Once this third order tuning is accomplished, these aberration coefficients are used to calculate a predicted probe wavefront shape.

Coeff	Value	Target (nm)
C1 =	-1992.62	-2000.00
C12a =	-4.72	.37
C12b =	14.50	.05
C21a =	821.38	30.85
C21b =	-454.78	-373.62
C23a =	-64.95	-48.28
C23b =	-70.17	-97.32
C3 =	-21683.08	-19944.78
C32a =	-7047.13	-6627.15
C32b =	-1065.43	-871.01
C34a =	-7171.30	-6561.26
C34b =	7558.98	6953.26
C45a =	23257.60	.00
C45b =	14581.77	.00
C43a =	157647.03	.00
C43b =	317776.32	.00
C41a =	-100744.96	.00
C41b =	1219987.99	.00
C5 =	44036570.36	.00
C56a =	-574852.38	.00
C56b =	4764472.21	.00
C54a =	18663131.98	.00
C54b =	-19778172.65	.00
C52a =	14083539.56	.00
C52b =	1851017.20	.00

Table 1. Typical aberration coefficients in nanometers, derived from the tuning process.

The coefficients are identified using the following system suggested by Krivanek: the first subscript describes the radial exponent; the second describes axial symmetry, and the letter denotes the orientation of the axial variation. Therefore the phase of the probe electrons can be written (Batson 2003):

$$\chi(k,\phi) = K_0 \sum_n \frac{(k/K_0)^{(n+1)}}{(n+1)} \sum_m \left[C_{nma} \cos(m\phi) + C_{nmb} \sin(m\phi) \right] \quad (1)$$

with *(m + n)* odd and $m < n + 1$. In this formulation, K_0 is the incident electron wavevector, and k is perpendicular component of this wavevector. The incident angle $\theta = k/K_0$. and φ is the axial angle. The phase can then be used to construct the wave front, *Sin* χ, and the probe shape. *Sin* χ closely resembles the Ronchigram pattern at focus, allowing a comparison with experiment. (Lupini 2001) The probe wavefunction is obtained:

$$\Psi_p(\vec{r}) \propto \int_{aperture} e^{-i\chi(\vec{k}) - i\vec{k}\cdot\vec{r}} \, d\vec{k} \quad (2)$$

Figure 2 summarizes results using the values from Table 1. In Fig. 2a I show the calculated *Sin* χ which may be compared with the Ronchigram in 2b. The circle in 2a illustrates the area covered by a 50mR wide probe forming aperture. Fig 2c shows the resulting probe, calculated using optimum values for focus, astigmatism and coma (C_1, C_{12}, and C_{21}), and measured values for 3-fold coma (C_{23}) and higher coefficients up to and including fifth order. This method captures the limiting behaviour of the high order coefficients, but recognizes that the low order coefficients are adjusted by hand during imaging. Figure 2d predicts an experimental shape for a gold atom derived from a scattering calculation using the predicted probe shape and the Au projected potential. These results may then be compared with experimental Au atom images, as in Fig. 2e, and with line scans across those atoms as

compared with experimental Au atom images, as in Fig. 2e, and with line scans across those atoms as in Fig. 2f. In this result, it can be seen that the Ronchigram angular scale and axial symmetry agrees nicely with the predicted *Sin* χ. Also the measured atom width agrees with the predicted value. On the other hand, the probe tails are somewhat larger than predicted. This process is repeated each time the corrector is tuned for optimum performance to ensure repeatable operation.

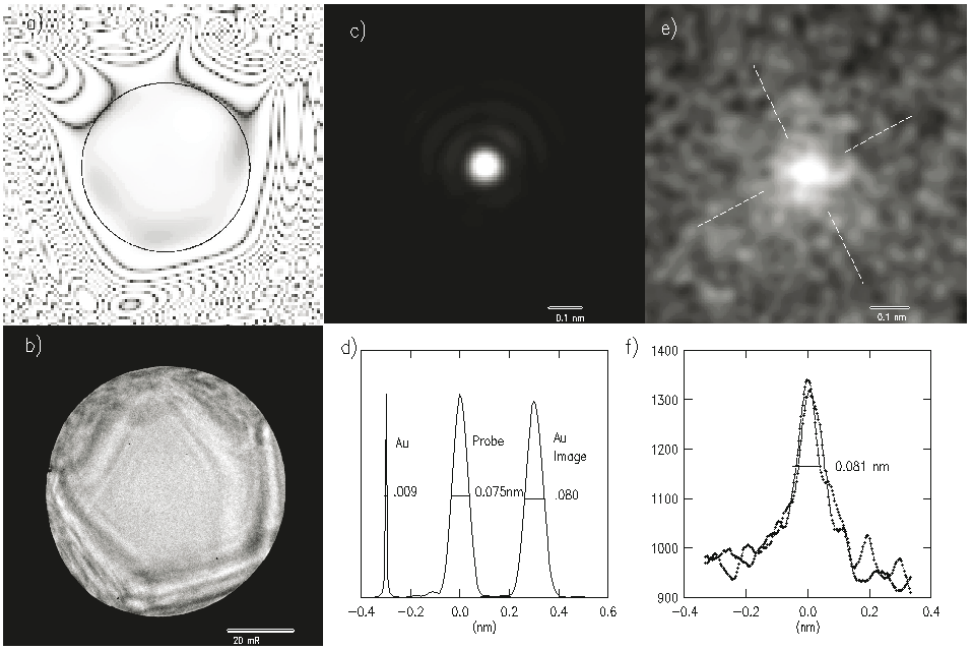


Fig. 2. a) Calculation of wave front *Sin* χ with a 50 mR aperture indicated, using the aberrations summarized in Table 1. b) Measured Ronchigram. c) Calculated probe, corresponding to a). d) Au atom potential, probe shape and convolution of probe with the Au potential. e) Single atom image with indicated line scans for the single atom measurement shown in f).

This performance is obtainable with beam currents of order 70-150 pAmp using the room temperature field emission source. Thus, we have given up about a factor of 5x in current from the uncorrected instrument. This will require an increase in efficiency in the Wien filter spectrometer order to combine the sub-angstrom imaging and EELS at sub-100meV resolution.

3.2 Single Atom Dynamics

Perhaps the most striking difference between corrected and uncorrected operation is the contrast available from single atoms. It is not unusual for gold atoms on a carbon substrate to present 50% contrast as shown in Fig. 2f. Therefore it is easy to follow movement of atoms using 0.1-0.2 sec exposure times. Figure 3 shows the formation of a five atom cluster by the joining of a single atom with an existing cluster. This cluster cannot be planar, because the indicated distances in projection are of order 0.15 nm, much smaller than the Au dimer bonding distance of about 0.25 nm on the carbon surface. This propensity to form structures which extend up away from the surface is present even in single Au dimmers (Batson et al 2002). In passing, this example also shows some of the ambiguities that arise. One of the atoms in the original cluster is brighter than average, while one of its neighbours is less so. This may signify rapid motion which happens during the imaging process. It would be interesting to increase the imaging speed to several tens of frames per second to investigate this possibility.

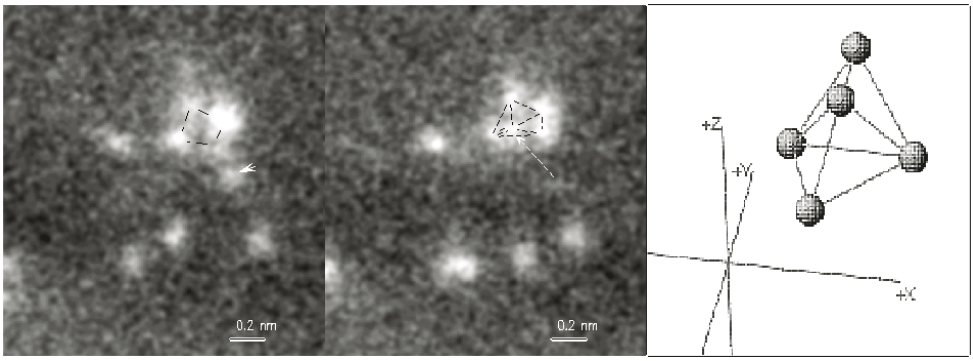


Fig. 3. The left two frames show two successive 0.2sec exposures of Au atoms on carbon. During the interval between the two frames, the indicated atom moved into the cluster of atoms to create the five atom cluster illustrated by the model in the right panel.

3.3 Silicon [110] Projection

Even the simplest semiconductor structure has presented challenges because the "dumbbell" spacing is only 0.135nm. In addition, the atomic layers that make this structure are not at the same height, and so channelling of the probe electrons can produce difficulty in interpretation. For instance, a simple convolution of the probe with the projected structure suggests that imaging using a 0.08nm probe will produce about 70% contrast. The experiment produces a puzzling 30-40%. Multislice calculations for annular dark field STEM imaging show that, for areas of order 20nm thick, 40% contrast is about right. Detailed investigation of the probe channelling shows that a probe centred between the two atom columns physically shifts over onto the column within about 10 nm. Thus, scattering to large angles is stronger than it would be if the probe remained concentrated between the columns.

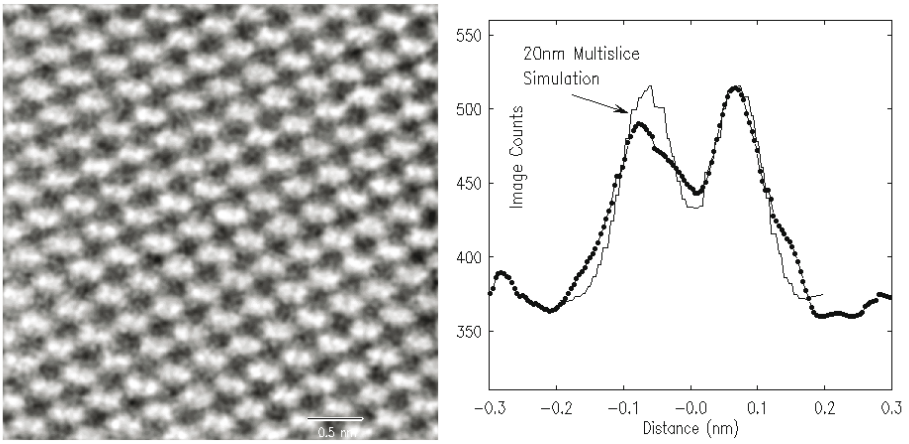


Fig. 4. On the left is an image of the [110] projection of silicon showing the 0.135nm "dumbbell" spacing. On the right is a comparison between a line scan of one of the dumbbells and a multislice calculation for 20nm thick silicon using a 0.08nm probe size.

Close examination of Fig. 4 will also reveal that the apparent structure is distorted, that the dumbbell spacing is irregular and that there is quite a lot of noise. These effects are instrument related. Future instruments must be designed with stabilities and linearities which are at least 10x better than the system spatial resolution. This suggests that positional stabilities of 0.005nm must be attained. Finally, it can also be remarked that the measured profile appears to exhibit longer tails than are predicted by the calculation, a result which is similar to that observed above with the single Au atoms. This behaviour is probably a result of instabilities which contribute to electron optical drift. But some contribution is probably also from the difficult task of setting focus, astigmatism and coma by hand, when the apparent focus criteria are sub-Angstrom features at the edges of the probe.

3.4 A Technological Example: Hi-K Dielectric

Figure 5 shows an example from a recent examination of an HfO_2 high dielectric structure investigated for a future field effect transistor gate insulation. This structure consists of polycrystalline Si, HfO_2, SiO_x and underlying single crystal Si. On the left, I show the STEM bright field image and on the right the annular dark field result. For those familiar with STEM imaging, the image on the left is a surprise. We are not used to getting such strong contrast in bright field, having argued in the past that the standard transmission electron microscope beats the STEM for this imaging due to the parallel nature of its collection. This is probably still true, but the improvement in contrast shown above for atomic level imaging apparently also produces a marked improvement in this imaging.

The dark field image, of course shows strong contrast for the heavy Hf. In the oxide, it is clear that the very small probe is an advantage if the specimen is kept thin. Then, it is possible to image the lattice in spite of the very large contrast. It is possible, for instance, to image the interface between the Hf oxide and the overlying poly-crystalline Si. In the SiO_x, which appears featureless in bright field, there is a strong signal from Hf atoms. Under the probe, these atoms migrate several nanometres, usually towards the Si substrate in this example.

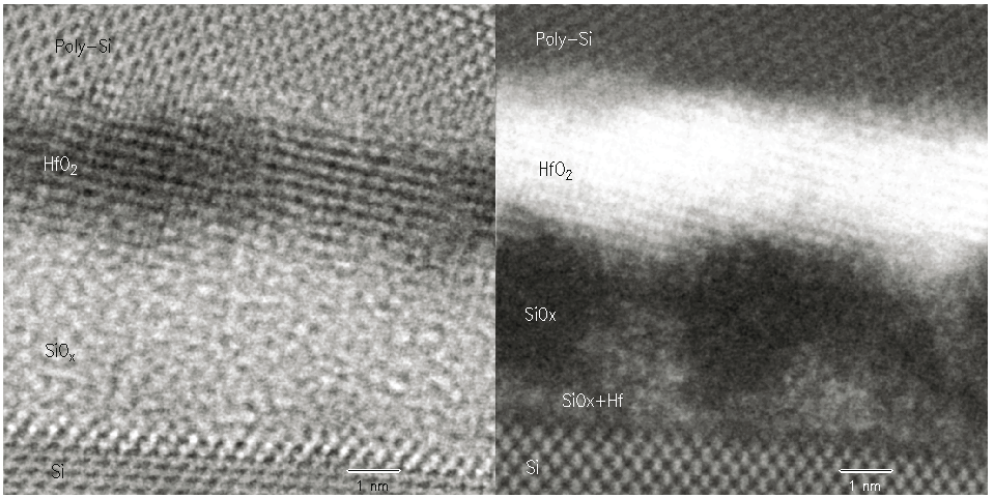


Fig. 5. An example of a “Hi-K” gate dielectric structure. On the left is a bright field STEM image at Gaussian focus using a 40mR wide collector aperture. On the right is the same area and focus viewed using the annular dark field detector. Hf can be observed within the oxide in this image.

4. MONOCHROMATOR

Figure 6 summarizes results from the monochromator project (Mook et al 1999). This device produces a magnified, energy dispersed image of the probe inside the gun. There a 150nm wide aperture can be used to select a narrow range of electron energies. The middle panel shows the results as the magnified probe is scanned across the aperture. The right panel shows the performance of the system including the spectrometer for small angles at 20kV.

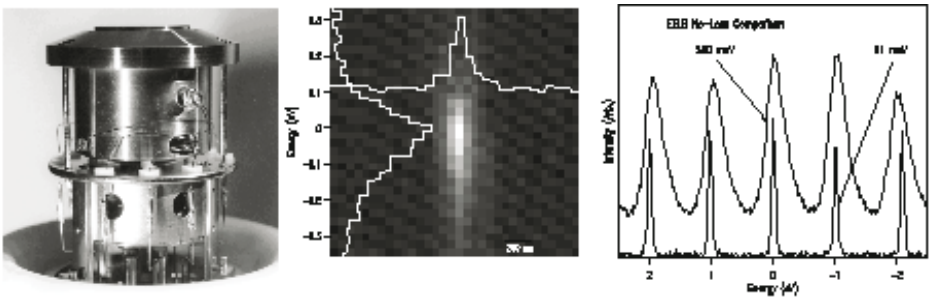


Fig. 6. Current progress on the monochromator system. The left panel shows the mechanical setup. The middle shows an image of the transmission as a function of position and energy. The right panel compares the energy loss resolution with and without the monochromator.

5. CONCLUSIONS

This is a very exciting time for microscopy of semiconductors. Clearly, instruments are now at a threshold of capability that will allow detailed atomic structure evaluation using quite substantial probe currents, necessary for analytical use. Finally, this operation can be accomplished at a relatively low probe voltage, at least below the damage threshold of silicon for direct impact displacement damage. This report is intended to demonstrate that the imaging capability appears to be well in hand. The task now is to combine this imaging with high resolution EELS to obtain information about electronic structure. It is hoped that this instrument will also be capable of obtaining scattering in the sub-100meV region to begin exploration of near edge structure of the conduction band.

ACKNOWLEDGEMENTS

I am deeply indebted to O L Krivanek and N Dellby for provision of the corrector and for their willingness to collaborate using a system that is unusual even by dedicated STEM standards. I acknowledge as well the collaboration and continued patience of H W Mook and P Kruit with the monochromator project. I want to thank also J Silcox, and K A Mhkoyan for extensive discussion about multislice technique.

REFERENCES

Batson P E 1986 Rev. Sci. Inst. **57,** 43
Batson P E, Kavanagh K L, Woodall J M and Mayer J W 1986 Phys. Rev. Lett. **57**, 2729
Batson P E 2003 Ultramicrosopy **96**, 239
Batson P E 2000 Phys. Rev. B **61**, 16633
Batson P E, Dellby N and Krivanek O L 2002 Nature **418**, 617
Batson P E and Heath J R 1993 Phys. Rev. Lett. **71**, 911
Dellby N, Krivanek O L, Nellist P D, Batson P E and Lupini A R 2001 J. Electron Micros. **50**, 177
Lupini A R 2001 Dissertation (University of Cambridge)
Mook H W, Batson P E and Kruit P 1999 EMAG **161**, 223
Ronchi V 1964 Applied Optics **3**, 437

Sub-Ångstrom and 3-dimensional STEM for semiconductor research

A R Lupini, M F Chisholm, M Varela, K Van Benthem, A Y Borisevich, Y Peng, W H Sides, J T Luck and S J Pennycook

Mailstop 6031, Condensed Matter Sciences Division, Oak Ridge National Laboratory, Oak Ridge, TN 37831, USA

ABSTRACT: Electron microscopy has been one of the foremost tools for analysis of semiconducting materials and, in turn, benefits from the processing power provided by faster computers. As semiconductor devices become ever smaller and faster, the shrinking of components means that even single dopant or impurity atoms can significantly affect device performance. Thus the enhanced resolution, sensitivity and new techniques enabled by aberration correction should ensure that this relationship continues.

1. INTRODUCTION

There are many links between the semiconductor industry and electron microscopy. Transmission electron microscopy (TEM) has traditionally been used for analysis of semiconductors and is able to provide atomic lattice resolution images of many materials. In turn, the improvements in processing speed enabled by advanced semiconductor devices also enhance the capabilities of electron microscopes. A high speed computer is essential for the operation of an aberration corrected microscope and allows advanced image processing techniques, such as tomography, reconstruction or deconvolution, to be applied.

2. ABERRATION CORRECTED STEM

The scanning transmission electron microscope (STEM) is uniquely suited to some problems because of the ease of interpretation of the Z-contrast images (Jesson and Pennycook 1995) combined with the possibility of *simultaneous acquisition* of the electron energy loss spectrum (EELS). A simplified schematic of a STEM is shown in Fig. 1. The STEM works by forming a focused electron probe, with a diameter that can be less than 1 Ångstrom (Nellist et al 2004), which is scanned over the sample. The electrons scattered to various detectors are collected and used to form an image as a function of position. One disadvantage of this arrangement is that the image points are acquired in series, while the principal advantage is that many different signals can be collected at the same time.

The resolution-limiting factors for most electron microscopes (TEM and STEM) are the imperfections of the lenses. In 1936 Sherzer proved that round electron lenses will always suffer from spherical aberration, resulting in a degraded image. Aberration correction consists of exploiting one of several loop-holes in this proof to eliminate the aberrations (Scherzer 1947). Breaking rotational symmetry is the method that has shown most success, through using either octupoles and quadrupoles (Dellby et al 2001) or hexapoles and projector lenses (Haider et al 1998). As well as improved resolution (Nellist et al 2004), aberration correction in STEM has demonstrated enhanced sensitivity to single atoms (Wang et al 2004; Varela et al 2004) and lighter elements (Chisholm et al 2004).

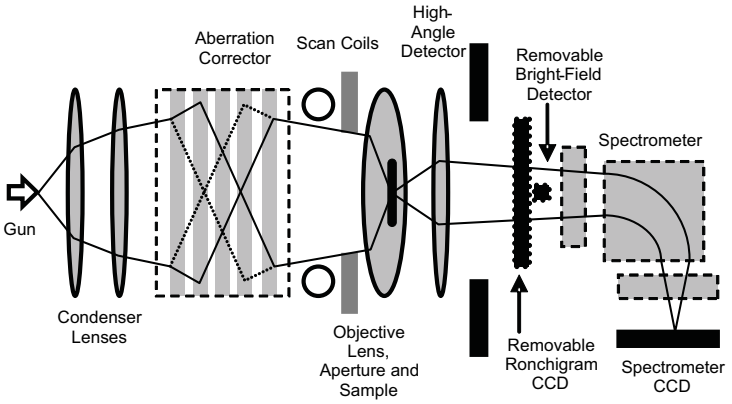


Fig. 1. Simplified schematic showing the important components of an aberration corrected STEM, fitted with a variety of detectors and an EEL spectrometer.

3. RESOLUTION

One of the main reasons for the development of aberration correctors was the desire for increased resolution. It is therefore essential to have a way of measuring resolution. One problem is that there are at least three common definitions of "resolution" in electron microscopy: (i) Point resolution, (ii) information limit and (iii) delocalization. Exactly which of these is most important depends on what information is being sought from the electron micrograph.

Delocalization is particularly interesting because it has several distinct meanings: Firstly the underlying interaction can be delocalized and is not just a function of a single coordinate (Allen et al 2003). Secondly delocalization already has a specific meaning in bright-field TEM (Coene and Jansen, 1992), where different spatial frequencies from a single defect can transfer to different places in the image. Finally the beam can spread out as it propagates through a finite thickness and is also channelled to the attractive potential of aligned columns. This means that any electron microscope image, and even the exit wavefunction, cannot always be simply related to a projection of the crystal potential.

It is also important to consider contrast-based resolution measurements. The weakness is that these do not necessarily differentiate between the three definitions given above. However, these are perhaps the most important because they determine what can be experimentally measured. Figure 2(a) shows silicon viewed down the [112] axis with the "dumbbells," which are less than 0.8 Å apart, resolved.

One technique for showing that a spatial frequency is present in an image is by examining the diffractogram. Figure 2(b) verifies the resolution of the 0.8 Å separation and also shows apparent information transfer to 0.6 Å. It is important to realize that features in the diffractogram can arise for several reasons and care needs to be taken to ensure that features are not due to nonlinearities in the imaging system, such as clipping (summarized by several authors, including Nellist et al 2004). For coherent bright-field images spots also arise from the sum and difference of frequencies in the image. Therefore this method only applies to incoherent images, such as Z-contrast images, where this does not occur (Peng et al 2005). For Z-contrast imaging the spots in the diffractogram relate to the probe size, at least for moderate thicknesses, as shown in Fig. 2(c) and in more detail by Peng et al (2005). In the limit of a single layer, the image would be a convolution between the probe and an object function. As the sample becomes thicker, the magnitude of the high-spatial-frequency Fourier components in the images generally decreases until they are lost in the noise.

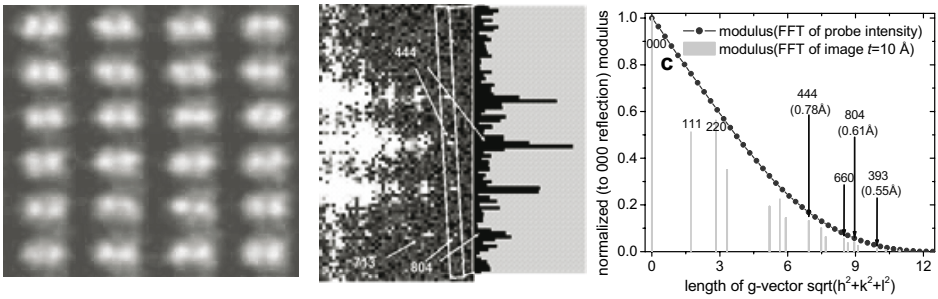


Fig. 2. (a) Aberration corrected Z-contrast image showing Si viewed down the [112] axis. Bright spots are the atomic column locations. The 0.8 Å [444] (dumbbell) spacing is resolved. (b) The Fourier transform demonstrates information transfer to 0.6 Å. **(c)** Intensity of Fourier transform of a simulated image and simulated probe.

4. THREE DIMENSIONAL STEM

One of the enduring problems of electron microscopy is that it offers only a two-dimensional view of the three-dimensional world. Several three-dimensional techniques already exist, such as atom probe microscopy and tomography. Each of these techniques offers its own advantages and disadvantages. However, there still remains a need for high-resolution three-dimensional techniques that can quickly survey a large area, are compatible with EELS acquisition, apply to a wide variety of samples (such as insulators) and offer single atom sensitivity.

In order to provide new methods that address some of these needs, we have implemented a three-dimensional STEM technique. This relies on a consequence of aberration correction; the increased size of the objective aperture. Anyone familiar with photography will know that as the aperture size (f-number) is increased, the depth of focus is decreased. In a diffraction limited system, the optical depth of focus ΔZ and the horizontal Rayleigh resolution criterion ΔR for an aperture size θ and wavelength λ can be given as:

$$\Delta Z = \varepsilon \frac{\lambda}{\theta^2}, \quad \Delta R = 0.61 \frac{\lambda}{\theta}$$

where ε is a constant that varies with the resolution criterion used. It is common to use $\varepsilon = 1$ for the 80% criteria, while $\varepsilon = 1.77$ would correspond to the FWHM and $\varepsilon = 2$ corresponds to the vertical distance from the maximum to the first zero on axis.

This shows that the depth of focus actually improves faster than the transverse resolution following aberration correction. It is thus possible to obtain a three-dimensional dataset in a STEM by scanning a series of two-dimensional images and changing the focus between frames. This technique is analogous to confocal optical microscopy. However, we do not use a pinhole to restrict the collected signal in the same way, so the point response function is not the same. Using typical values for an aberration-corrected STEM at 300 kV this predicts a horizontal resolution of about half an Ångstrom and a vertical resolution of several nm. While the resolution is worse in the vertical direction, this is not necessarily a severe problem. Firstly there are still many situations where nm-scale vertical resolution will provide indispensable information (van Benthem et al in preparation; Wang et al 2004; Pennycook et al 2004). More importantly, future generations of aberration corrected STEM will offer larger aperture angles and are likely to bring the depth resolution into the sub-nm regime.

Furthermore, it has been shown in optical confocal microscopy, that the depth *sensitivity* can be rather better than the resolution and even better than the wavelength (Lee and Wang, 1997). We can also use a similar principle: If the object (in this case a single atom) is smaller than the resolution, it can be possible to obtain the depth within the sample more precisely than the depth resolution (van Benthem et al in preparation). Simply put; it can be possible to find the maximum of a smooth curve with a precision that is better than the FWHM of that curve.

An obvious next step is the deconvolution of the three-dimensional point response function.

One of the problems with most forms of deconvolution, for example Richardson-Lucy or Maximum Entropy, is that as well as sharpening the image features they also amplify the noise (Puetter et al 2005). Thus if a feature is resolved in a deconvolved image, how does one know if it is really significant, or just an artefact of the deconvolution process and noise? Also, most algorithms typically assume simple models for the noise, which are not always accurate. Therefore most deconvolution techniques produce pretty images, but greatly increase the chances of artefacts or incorrect interpretations. In order to resolve this issue, we are implementing deconvolution techniques in both two and three dimensions based on a Pixon method (Puetter et al 2005) that includes more accurate models for the noise. It is possible that the primary benefit of deconvolution may not be just improved resolution, but the ability to quantify, locate and identify objects with a greater degree of certainty.

One difficulty is that in a periodic crystal, electrons are attracted to the potential of the aligned columns. Therefore three-dimensional interpretation of data from a crystal is rather more complicated than for the simple case of a free-space probe (Peng et al 2004). Thus, in aligned crystals, quantitative use of this technique will require extensive image simulations. However, Varela et al (2004) used the variation with depth of the EELS signal to good advantage by combining it with Z-contrast imaging. Through comparing the EELS intensity on the column containing a single dopant atom and those on adjacent columns to dynamical calculations, it was possible both to detect a single La atom and to estimate the depth of that atom within the crystal.

A drawback of comparing experimental STEM images to simulations is that a full calculation can be computationally expensive. It is significantly quicker to calculate the electron intensity inside the crystal and this is frequently performed to save computation time. However, as previously shown (Lupini et al 2003), when interpreting the *image* intensity it is a little naïve to consider only the *electron* intensity in the crystal, because not all of the electron intensity distribution contributes equally to the image (also see Allen et al 2003). A relevant example of this is the simultaneous acquisition of phase-contrast bright field and Z-contrast images. In both cases the electron intensity distribution in the sample is the same, but the bright field image is coherent, while the Z-contrast image is incoherent.

In summary, aberration correction not only allows improved resolution and sensitivity in conventional imaging, but may allow the development of some exciting new techniques.

REFERENCES

Allen L J, Findlay S D, Oxley M P and Rossouw C J 2003 Ultramicroscopy **96**, 47

Chisholm M F, Lupini A R, Pennycook S J, Ohkubo I, Christen H M, Findlay S D, Oxley M P and Allen L J 2004 Microsc. Microanal. **10**, (Suppl 2), 256

Coene W and Jansen A J E M 1992 Scanning Microsc Suppl **6**, 379

Dellby N, Krivanek O L, Nellist P D, Batson P E and Lupini A R 2001 J. Electron. Microsc. **50**, 177

Haider M, Uhlemann S, Schwan E, Rose H, Kabius B and Urban K 1998 Nature **392**, 1998

Jesson D E and Pennycook S J 1995 Proc. Royal Soc. London A **449**, 273

Lee C-H and Wang J 1997 Optics Communications **135**, 233

Lupini A R and Pennycook S J 2003 Ultramicroscopy **96**, 313

Nellist P D, Chisholm M F, Dellby N, Krivanek O L, Murfitt M F, Szilagyi Z S, Lupini A R, Borisevich A, Sides W H and Pennycook S J 2004 Science **305**, 1741

Peng Y, Lupini A R, Borisevich A Y, Travaglini S M and Pennycook S J 2004 Microsc. Microanal. **10**, (Suppl 2), 1200

Peng Y, Borisevich A, Lupini A R and Pennycook S J 2005 Proc. Microsc. Microanal. Conf., *to be published*

Pennycook S J, Lupini A R, Borisevich A, Peng Y and Shibata N 2004 Microsc. Microanal. **10**, (Suppl 2), 1172

Puetter R C, Gosnell T R and Yahil A 2005 Ann. Rev. Astron. Astrophys. **43**, *in press*

Scherzer O 1947 Optik **2**, 114

Varela M, Findlay S D, Lupini A R, Christen H M, Borisevich A Y, Dellby N, Krivanek O L, Nellist P D, Oxley M P, Allen L J and Pennycook S J 2004 Phys. Rev. Lett. **92**, 095502

Wang S W, Borisevich A Y, Rashkeev S N, Glazoff M V, Sohlberg K, Pennycook S J and Pantelides S T 2004 Nature Materials **3**, 274

Cathodoluminescence studies of AlGaAs/GaAs core-shell nanowires

Anders Gustafsson, Niklas Sköld, Werner Seifert and Lars Samuelson

Department of Solid State Physics and the Nanometer Structure Consortium, Lund University, Box 118, S-221 00 Lund, Sweden

ABSTRACT: We have studied nanowires with a GaAs core, covered by an AlGaAs shell, using low temperature cathodoluminescence. The main emission from the core is due to carbon acceptors, though we observe a weak emission from excitons. A general observation is that the emission is much stronger, and more well-defined, from the top half of the nanowire. The AlGaAs shell emission varies in emission energy and spatial origin in an irregular fashion.

1. INTRODUCTION AND GROWTH

Over the past few decades, there has been a quest for the perfect system for fabricating high-quality quantum wires, or nanowires. Many approaches have been tried with varying successes, for examples see e.g. Gustafsson et al (1998). In this study we present cathodoluminescence (CL) data from nanowires grown by a technique introduced by Wagner (1970) that has seen a revival over the past few years, due to improvements in the fabrication steps of the techniques (Ohlsson et al 2001).

The nanowires in this study were grown with gold as the seed particles. The growth takes place at the interface between the metal particle and the semiconductor, where the growth takes its epitaxial information from the substrate. The growth conditions were chosen so that virtually no growth takes place on the bare semiconductor surface, only beneath the metal particle. The important feature is that the size of the particle determines the area of growth of the semiconductor underneath. This results in the growth of pillars with a very high aspect ratio. With a random size of the particles, the diameter of the pillars is also random. However, with a well-controlled size of the particle, the resulting pillars have an identical diameter and identical height. With a size of particles in the range 10 - 50 nm, the pillars are in fact nanowires.

The gold particles used as seeds in this study were produced by the aerosol technique and size-selected. This technique has been described in detail elsewhere (Magnusson et al 1999). In this study, we concentrate on nanowires grown from gold particles with a diameter of 40 nm. Under the present growth conditions in our metal-organic chemical vapour deposition (MOCVD) chamber, the preferred growth direction is <111> (Seifert et al 2004). To produce an array of parallel nanowires, the most suitable substrates are (111)-oriented. Therefore, we used (111)-oriented GaAs substrates to produce the GaAs nanowires. The 40-nm diameter nanowires were grown (450°C) to a length of 3.5 - 4 μm. To avoid leaving the GaAs side surfaces exposed, the nanowires were covered by a layer of AlGaAs, grown at higher temperatures (650°C), where growth takes place without the aid of metal particles, however there is still some particle-mediated growth, giving an AlGaAs core at the top of the nanowire. This type of core-shell structure improves the light emission from the nanowires by 2-3 orders of magnitude in resonant (excitation below the band gap of the shell) photoluminescence studies. The thickness of the AlGaAs shell is either 20 nm or 55 nm, giving a total diameter of either 80 or 150 nm. The term “diameter” is used loosely as the cross-section is hexagonal rather than cylindrical. The 80 nm sample will be referred to as sample #1 and the 150 nm sample as sample #2.

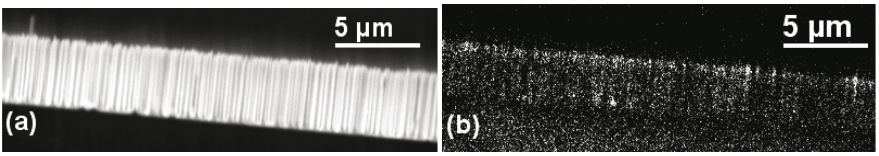


Fig 1. a) a low-magnification SEM image of a typical sample and b) a CL image of the same area recorded at 1.459 eV. The substrate is at the bottom of the image and the growth direction towards the top of the images. (Sample #2)

2. CATHODOLUMINESCENCE STUDIES AND RESULTS

The CL studies were performed in a dedicated scanning electron microscope (SEM) with a lHe cold stage. The nanowires were studied as grown, still attached to the substrates, in side view, and at a temperature of 6-8 K. The studies were performed at an acceleration voltage of 2.5-10 keV and a probe current of about 100 pA. The choice of the acceleration voltage was based on two criteria, (1) The acceleration voltage must be high enough to penetrate the AlGaAs shell to the core and (2) The acceleration voltage must be low enough to keep most of the primary excitation in the nanowire. Otherwise, the scattering of the electrons after a nanowire will reduce the contrast in the SEM images, making it difficult to observe the structures. All the images presented here have the substrate at the bottom of the images, with the growth direction towards the top of the images.

Figure 1 shows two low-magnification images of the same area, (a) shows the normal SEM image, where the substrate appears dark and the nanowires appear bright. There is a dense array of nanowires that have a length of about 4 µm. In the CL image, using the 1.495 eV emission, the substrate appears bright and the upper part of the nanowires is brighter than the lower part. Fig. 2a shows two spectra, one recorded with the electron beam scanning over the nanowires and one reference spectrum recorded from the substrate. They both show similar features, though the emission from the substrate is much stronger, mainly due to a larger volume. The spectra are dominated by the emission related to the carbon acceptor in GaAs at 1.495 eV, but we can also observe the excitonic emission from GaAs at 1.52 eV. In addition, we observe a broad emission above 1.52 eV in the nanowire spectrum, related to the AlGaAs shell. Fig. 2b shows a spectrum recorded from the top half of the nanowires, including the emission from the AlGaAs. There is an additional broad emission around 1.85 eV (=$Al_{0.33}Ga_{0.67}As$), and several peaks around 1.6 eV (=$Al_{0.15}Ga_{0.85}As$). These peaks vary slightly in position and intensity from nanowire to nanowire. A series of average spectra were recorded with an increasing probe current. Over a range of 300, the main features of the spectra remain the same and the peak intensity of the main feature increases by a factor of 150, showing no saturation. The 50% drop in intensity can be attributed to a larger spot size of the electron beam at higher probe currents.

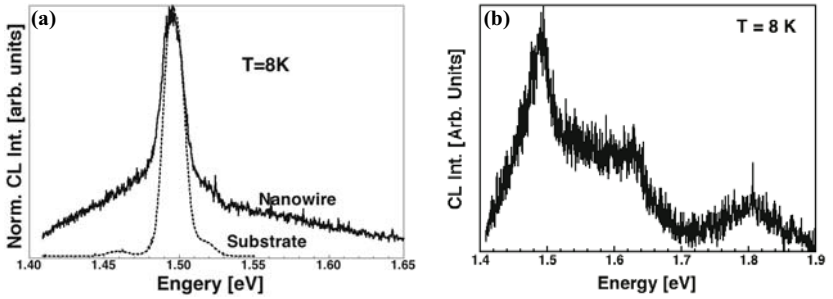


Fig. 2. a) two normalized spectra from the sample. The dashed line corresponds to the beam scanning over the substrate and the solid line to the beam scanning over a number of nanowires. b) a spectrum of the top half of the nanowires including all the emission from the AlGaAs. (Sample #2)

Figure 3 shows a series of images recorded from the same area. (a) shows the SEM image, where it is possible to observe the shape of the nanowires. The major part is straight and fairly identical in diameter. The bottom, where it is attached to the substrate is wider, showing a triangular,

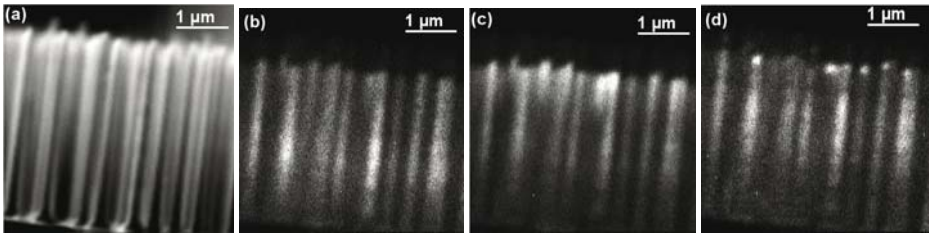


Fig. 3. A series of images of the same area of the sample. a) is an SEM image, b) and c) are CL images related to the GaAs core and d) is related to the AlGaAs. (Sample #2)

probably determined by {11X} planes. The top is tapered where the tip is determined by the original gold particle. In the 1.45 eV CL image (b), the middle part is the brightest and in the 1.495 eV CL image (c), the upper part of the nanowires is much brighter that the lower part. It is also evident that the top 0.5 µm is completely dark in this image. In the 1.55 eV CL image, the emission is concentrated to a very small region just above the 1.495 eV emission, well below the tip of the nanowire. The peak position of this emission varies from nanowire to nanowire, and not all of them exhibit this type emission. The intensity of (b) is multiplied by a factor of 5.

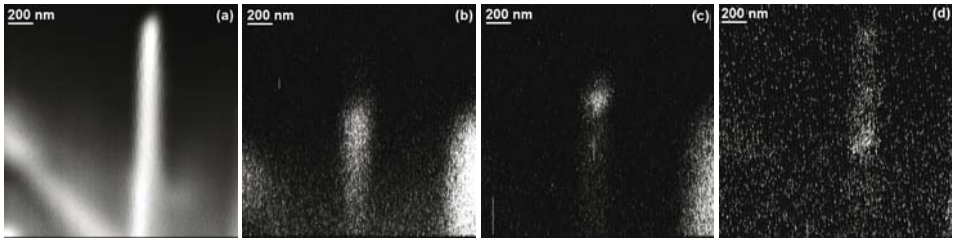


Fig. 4. A series of images of the upper part of a single nanowire. a) is an SEM image, b) is the emission related to the carbon acceptor, c) and d) are related to the AlGaAs. The images of b) and c) have the same intensity, whereas the intensity of the image of d) has been multiplied by 50 times. (Sample #2)

Figure 4 concentrates on the top region of a single nanowire. (a) shows the SEM image of the nanowire. The spatial resolution is limited by a combination of factors, e.g. the probe size of the SEM, the vibrations of the cold stage running at 8 K and a slight vibration of the nanowire due to charging. Using GaAs substrates, this effect is not so important, but using a higher band gap, e.g. GaP, substrates, this effect can be very severe, as the substrate is insulating at low temperatures. As in previous images, the 1.495 eV emission (b) is concentrated to an 0.5 µm region near the top, and the 1.55 eV emission (c) is concentrated to an even smaller region above the 1.495 eV emission. For comparison, we also show an additional emission from the AlGaAs, at 1.65 eV (=$Al_{0.2}Ga_{0.8}As$). Part of this emission comes from the top part of the nanowire.

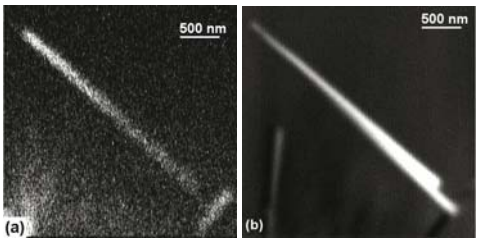


Fig. 5. Images of a pair of nanowires, broken off from the substrate. a) CL image at 1.495 eV and b) SEM image. The emission exhibits the same pattern as the attached nanowires. (Sample #1)

The data presented so far has been from sample #2, with the thicker shell. For comparison, Fig. 5 shows a pair of nanowires from sample #1. The CL image at 1.495 eV (a) shows the familiar bright upper part and darker lower part. These nanowires were accidentally broken off from the substrate. This also illustrates that the bright top is not an effect of waveguiding that could occur in a nanowire, which could lead to loss of emission into the substrate, or even carrier diffusion into the substrate. It is also noticeable that the dark part of the top is much smaller in this nanowire.

In addition to the images presented here, we have recorded images in the whole range from 1.0 to 2.0 eV. There is emission below 1.45 eV, but it is too weak for images to be recorded. In the range, 1.6 - 2.0 eV, the images appear patchy, without any clear patterns. The emission is mainly centred around 1.85 eV. The emission from the AlGaAs shell is only observed for sample #2, with its thicker shell.

3. DISCUSSION AND CONCLUSIONS

The CL from the GaAs core is dominated by emission related to carbon acceptors. The incorporation of carbon is quite probable at the low growth temperature, so it is not surprising that this is the main emission peak. This can also explain the high spatial resolution we observed in the images, especially for the 1.55 eV-emission, where the capture of carriers at acceptors will prevent further diffusion of carriers and electron-hole pairs. Spot-mode spectra from various parts of the nanowire supports the results from the 1.495 eV-images. As the excitation is moved from the top of the nanowire, the 1.495 eV-emission gets weaker. At the same time it gets broader and shifts down a further 25 meV in energy.

The AlGaAs emission can be divided into several parts: (i) the AlGaAs that grows on the side of the GaAs core, (ii) the AlGaAs that grows via the metal particle on top of the core; the AlGaAs core, and (iii) the AlGaAs that grows on the side of the AlGaAs core. The only part of the emission where the spatial origin can be pinpointed is the 1.56 eV emission, which comes from just on top of the GaAs core, but not from the entire top. The rest of the emission in the range 1.6-1.9 eV has no specific point of origin. The interpretation of the CL images is that the GaAs core grows to its full length, then as the temperature is increased and the Al source is turned on, the Al content in the particle mediated core growth gradually changes from GaAs to the intended AlGaAs composition. Therefore, the volume nearest the GaAs has an intermediate Al content. Finally, the AlGaAs shell and the AlGaAs core have almost the same composition, leaving three different emission energies, originating in areas of different band gap.

The fact that the emission from the first part of the nanowire is weaker is not yet fully understood. One reason can be related to the structural quality of the growth. The growth of nanowires in the <111>-direction can be quite difficult as the stacking sequence is not as well defined as for normal planar growth. As the area of the structure is quite small, it is easy for the nanowire to change its stacking sequence. The normal A-B-C-A-B-C… sequence can easily change into A-B-C-B-A-C… This leads to what can be viewed as a stacking fault, but as the whole plane is terminated by the sides of the nanowire, leaving the nanowire dislocation free. This means that we can view the stacking faults as a series of twins. The only time the change in the stacking sequence is of real importance is when the sequence becomes A-B-A-B-A-B…, which is the signature of a hexagonal structure rather than the cubic structure, which can influence the band gap of the material. The twins can also hamper the transport of carriers along the growth direction of the nanowire. The twinning appears to be higher in the first part of the nanowire and this might hamper the emission. A second possibility is that some growth actually takes place on the sides of the cores during the core growth. As the growth conditions are far from ideal, this might actually give rise to non-radiative recombination centers and the longer the sides have been exposed, the more centres are produced, leaving the top part most unaffected.

Future studies will include transmission electron microscopy to determine the crystalline quality of the present samples, and different nanowire lengths will test the second theory. Nanowires grown in different crystallographic directions [e.g. (001)] have lower densities of twins, so they will make good comparisons.

REFERENCES

Gustafsson A, Pistol M-E, Samuelson L and Montelius L 1998 J. Appl. Phys. **84**, 1715

Magnusson M H, Deppert K, Malm J O, Bovin J O and Samuelson L 1999 J. Nanopart. Res. **243**

Ohlsson B J, Bjork M T, Magnusson M H, Deppert K and Samuelson L and Wallenberg L R 2001 Appl. Phys. Lett. **79**, 3335

Seifert W, Borgström M, Deppert K, Dick K A, Johansson J, Larsson M W, Mårtensson T, Sköld N, Svensson C P T, Wacaser B A, Wallenberg L R and Samuelson L 2004 J. Crystal Growth **211**

Wagner R S 1970 Whisker Technology (New York, Wiley) p 47

Carrier diffusion lengths of (In,Ga)As, GaAs and (In,Ga)(As,N) quantum wells studied by spatially resolved cathodoluminescence

U Jahn, T Flissikowski, H T Grahn, R Hey, E Wiebicke, A K Bluhm, J Miguel-Sánchez[1] and A Guzmán[1]

Paul-Drude-Institut für Festkörperelektronik, Hausvogteiplatz 5-7, 10117 Berlin, Germany
[1] ISOM, Universidad Politécnica de Madrid, ETSI Telecomunicación, Ciudad Universitaria s/n, 28040 Madrid, Spain

ABSTRACT: The diffusion length of excess carriers (L_d) of an (In,Ga)As and GaAs single quantum well (QW) determined by cathodoluminescence exhibits a thermally activated increase up to 100 K and is independent of the detection energy (E). L_d of an (In,Ga)(As,N) QW, however, decreases both with increasing temperature (T) and at low T with increasing E. The qualitative difference of $L_d(T,E)$ between the quaternary and binary QW is explained in terms of different transport mechanisms (hopping versus tunnelling) in connection with the presence of localized states.

1. INTRODUCTION

Nitrogen doping of (In,Ga)As introduces various highly localized bound states in the host lattice. The interaction of these localized states with the conduction band states leads to the observed band gap shrinkage. Moreover, for low temperatures (< 100 K), the luminescence spectra are mainly due to the recombination of localized states (Polimeni et al 2001). For quantum wells (QWs), localization effects due to interface fluctuations lead to a significant reduction of the mobility of excess carriers and, therefore, to very short diffusion lengths (L_d) at low temperatures (T) (Hillmer et al 1989). There are only a few reports on diffusion length measurements in (In,Ga)(As,N) layers or QWs in the literature. Kurtz et al (2002) have estimated L_d indirectly from simulations of the measured internal quantum efficiency of solar cells consisting of (In,Ga)(As,N) layers fabricated by molecular-beam epitaxy (MBE). They found L_d=0.5 and 0.03 µm for electrons and holes, respectively, which significantly limits the performance of such devices. In order to investigate the impact of localization on the carrier transport in (In,Ga)(As,N) layers, we have measured L_d as a function of T and energy (E) in (In,Ga)As/GaAs, GaAs/(Al,Ga)As and (In,Ga)(As,N)/GaAs single QWs fabricated by MBE.

2. EXPERIMENTAL DETAILS

The samples under investigation have been selected in terms of a large variation of the impact of carrier localization on the recombination properties of excess carriers. Sorting the samples from weak to strong localization effects, we consider the following single QWs. A 10-nm-thick (In,Ga)As/GaAs QW with an InAs mole fraction of 0.2, a 4.8-nm-thick GaAs/(Al,Ga)As QW with barriers consisting of short period GaAs/AlAs superlattices corresponding to an AlAs mole fraction of 0.3 and a 7-nm-thick (In,Ga)(As,N)/GaAs QW with In and N contents of 30 and 2%, respectively.

L_d has been determined by the cathodoluminescence (CL) scanning method proposed by Zarem et al (1989). Excess carriers are excited by the electron beam through a metal mask, which is opaque for the respective recombination-related CL. With increasing distance with respect to the edge of the mask, the CL intensity detected outside the mask decreases as follows:

$$I_{CL}(x) = I_0 \exp(-\frac{x}{L_d})$$

Thus, the slope of the exponential decay of $I_{CL}(x)$ provides the value of L_d. By varying the photon energy, for which the CL scan is acquired, this method allows for a measurement of L_d as a function of E. The sample temperature has been varied between 5 and 200 K using a He-cooling stage. The spatial resolution of this method is limited by the abruptness of the mask edges and by the scattering of the incident electrons. For the chosen beam energy of 10 keV, the resolution has been estimated to be about 0.15 to 0.2 µm. The recombination dynamics of the QWs has been characterized by time-resolved photoluminescence (PL).

3. RESULTS AND DISCUSSION

Figure 1 shows L_d for the different materials as a function of temperature. The respective CL scans have been acquired at a photon energy corresponding to the maximum of the CL spectra (open symbols). We additionally show $L_d(T)$ for the (In,Ga)(As,N) QW measured at the low-energy tail of the CL spectrum (full triangles). For the (In,Ga)As and GaAs QWs, $L_d = \sqrt{D\tau}$ increases with increasing T (up to 100 K), which reflects the expected increase of both the diffusivity (D) and the carrier lifetime (τ) as has already been shown by Hillmer et al (1989). At low temperatures, L_d of the GaAs QW decreases down to a value close to the resolution limit of the measurement. Thus, the actual diffusion length is probably much smaller. L_d of the (In,Ga)As QW, however, can be reliably measured even for the lowest values of T and amounts to 1 µm at 6 K. This difference between L_d of the (In,Ga)As and GaAs QW reflects the different impact of carrier localization on the transport in the considered QWs.

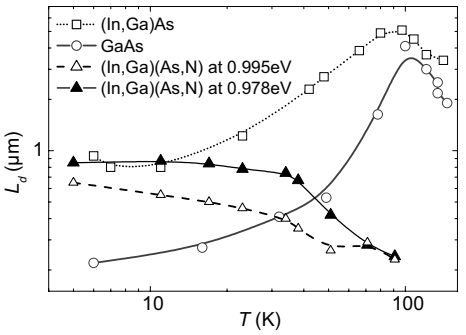


Fig. 1. Carrier diffusion length of three single QWs as a function of T. The photon energy, at which L_d has been measured, corresponds to the maximum of the respective CL spectrum (open symbols). The data represented by full triangles were obtained on the low-E tail of the spectra.

A generally accepted criterion for carrier localization is the energy dependence of the decay time of the luminescence intensity (τ_d), which is shown in Figs. 2a and 2b for the (In,Ga)As and GaAs QW, respectively. While τ_d of the (In,Ga)As QW does not significantly vary with E, the strong reduction of τ_d with increasing E of the GaAs QW indicates the capture of high-E carriers by low-E (localized) states within their lifetime. Thus, τ_d on the high-E side of the spectrum is reduced by transfer and capture processes of the excited carriers, while τ_d on the low-E side of the spectrum is dominated by the lifetime of localized carriers. Therefore, $\tau_d(E)$ of the GaAs QW clearly exhibits the signature of carrier localization at low T, which is not the case for the (In,Ga)As QW indicating a negligible contribution of carrier localization in this structure. The result of Fig. 2b confirms that the very small diffusion length of the GaAs QW is mainly caused by effective carrier localization at low T.

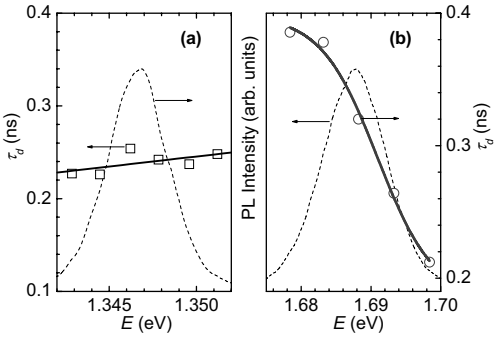


Fig. 2. Decay time of the PL intensity of (a) the (In,Ga)As and (b) the GaAs QW as a function of energy at 5 K. The dashed lines represent the corresponding PL spectra, the bold lines serve as a guide to the eye.

A completely different behaviour is observed for the (In,Ga)(As,N) QW. We found a blue shift of the CL spectrum with increasing excitation density and an S-shaped temperature dependence of the peak energy of the spectra (not shown) as clear indications for carrier localization. Moreover, several authors (Mair et al 2000, Kaschner et al 2001, Vinattieri et al 2003) report on an even more pronounced decrease of $\tau_d(E)$ with increasing E in (In,Ga)(As,N) QWs – resembling the one of this work – as has been observed for the GaAs QW in Fig. 2b. Despite these clear indications of strong carrier localization, we observe a rather large diffusion length at low T in this structure (triangles in Fig. 1) as well as a thermally activated decrease instead of an increase of L_d with increasing temperature. Consequently, carrier localization observed in the recombination properties of the GaAs and (In,Ga)(As,N) QW has a different effect on the transport properties of the binary QW as compared with the quaternary one. An additional peculiar feature of the (In,Ga)(As,N) QW is observed, when we vary the photon energy, at which L_d is measured. The open and full triangles of Fig. 1 represent $L_d(T)$ of this structure measured at different photon energies. For low temperatures, we clearly obtain larger L_d values for the lower photon energy as compared with the higher one.

In Fig. 3, we compare the energy dependence of L_d of the quaternary QW with the ones of the GaAs and (In,Ga)As QWs at 5 K. While the measured L_d value is nearly independent on the photon energy in the (In,Ga)As [Fig. 3a] and GaAs [Fig. 3b] QWs, it shows a significant energy dependence in the (In,Ga)(As,N) QW [Fig. 3c]. For the latter, L_d decreases from 1.1 µm down to a value comparable with the resolution limit of the measurement, when E is varied from the low-E to the high-E tail of the CL spectrum. Clearly, the presence of localized states leads only in the GaAs QW to a low value of L_d over the whole energy range as would be expected for strong localization. In the (In,Ga)(As,N) QW, we exclusively observe the expected small values of L_d at the high-E tail of the spectrum. Obviously, the energy dependence of L_d reflects features of the localization centres regarding the carrier transport, which cannot be distinguished by the recombination dynamics of the QWs alone. In the following, we qualitatively discuss the impact of hopping and tunnelling as dominating transport mechanisms in conjunction with localized states on the energy dependence of L_d in order to explain the experimental data shown in Fig. 3.

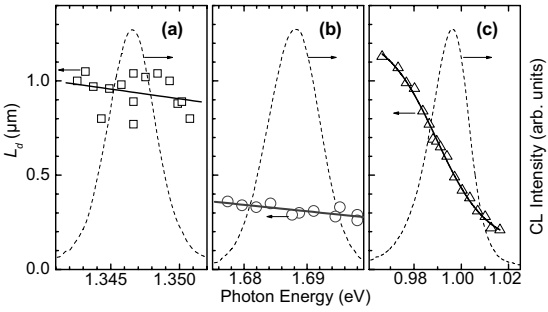


Fig. 3. Energy dependence of L_d of (a) the (In,Ga)As, (b) the GaAs and (c) the (In,Ga)(As,N) QW at 5 K. The dashed lines represent the corresponding CL spectra.

The density and nature of the present localization centres have a significant effect on the carrier transport from the excitation position towards the edge of the metal mask [cf. Fig. 4a]. In Figs. 4b and 4c, the situation for low and high densities of localization centres is sketched, respectively. In the case of low densities, the spatial distance of localized states is sufficiently large to prevent carrier tunnelling between the localization centres (traps). Depending on the energetic depth of the traps, carriers or excitons, which have been captured by the trap centres, can move by hopping from trap to trap (weak localization) or are strongly localized so that they are unable to move within their lifetime. For the latter, transport is possible only before the capture of free excitons, i. e., exclusively via extended states. The available time for the transport is restricted by the capture time, i. e., by the trapping into the localization centres. Once the free excitons have reached the edge of the mask, I_{CL} can be detected. Since the relaxation takes place after the transport, the value of L_d derived from $I_{CL}(x)$ does not depend on the photon energy, at which the CL is detected. The same argument holds for the case of hopping transport (weak localization), since the transport occurs over and not through the barriers between the traps. Consequently, when the carriers reach the mask edge by hopping there is no memory left about the relaxation during the transport. Hence, the energy distribution of the CL is again a result of relaxation *after* transport, and L_d does not depend on E. The actual value of $L_d(E)$ of the (In,Ga)As and GaAs QW of Figs. 3a and 3b represent examples for low or even negligible and strong localization effects, respectively. Since in both cases L_d is nearly independent on E, the transport occurs via extended states or via localized states by hopping.

The situation is different for large trap densities, where tunnelling between the localization centres takes place as sketched in Fig. 4c. Here, relaxation and transport exhibit a preferential energetic direction namely from high- towards low-E states. Excitons captured by traps with small localization energy (high-E side of the energy distribution of the localized states) can move by tunnelling between these traps and can also be captured by energetically deeper centres. Consequently, the carriers relax downwards during transport. If the CL detection energy is chosen to be on the high-E side of the spectrum, exclusively those excitons contribute to $I_{CL}(x)$ which move via extended or high-E localized states with small lifetimes due to the high trapping probability. Thus, we expect small diffusion lengths. If the detection energy is set to the low-E side, principally the whole spectrum of excitons can contribute to $I_{CL}(x)$ due to the possibility of successive downwards relaxation during the transport. Therefore, successive sequences of transport and relaxation can result in the observation of large values of L_d for $I_{CL}(x)$ detection at low energies. According to the model sketched in Fig. 4, we attribute the observed energy dependence of L_d, which is shown in Fig. 3c for the (In,Ga)(As,N) QW, to a tunnelling-assisted transport between trap centres in conjunction with a sequential relaxation down to the lowest localized state of the QW. The reduction of L_d with increasing T (Fig. 1) is probably due to thermally activated nonradiative defects. As reported, e.g., by Fischer et al (2004), nitrogen doping is connected with the formation of point defects and correlated with a strong thermally activated PL quenching.

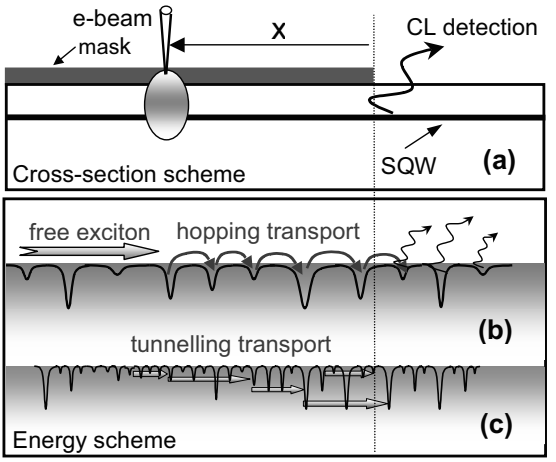


Fig. 4. (a) Schematic diagram of the L_d measurement by the CL scanning method and energy scheme of the QW states consisting of extended and localized ones for (b) low and (c) high densities of localized states.

In summary, we propose to consider the CL scanning measurement of $L_d(E)$ as a method to distinguish between hopping-assisted and tunnelling transport for hetero-structures containing a certain distribution of localized states.

ACKNOWLEDGEMENTS

The authors acknowledge fruitful discussions with S Dhar and O Brandt.

REFERENCES

Fischer C H and Bhattacharya 2004 J. Appl. Phys. **96**, 4176

Hillmer H, Forchel A, Hansmann S, Morohashi M, Lopez E, Meier H P and Ploog K 1989 Phys. Rev. B **39**, 10901

Kaschner A, Lütgert T, Born H, Hoffmann A, Egorov A Y and Riechert H 2001 Appl. Phys. Lett. **78**, 1391

Kurtz S R, Klem J F, Allerman A A, Sieg R M, Seager C H and Jones E D 2002 Appl. Phys. Lett. **80**, 1379

Mair R A, Lin J Y, Jiang H X, Jones E D, Allerman A A and Kurtz S R 2000 Appl. Phys. Lett. **76**, 188

Polimeni A, Capizzi M, Geddo M, Fischer M, Reinhardt M and Forchel A 2001 Phys. Rev. B **63**, 195320

Vinattieri A, Alderighi D, Zamfirescu M and Colocci M 2003 Appl. Phys. Lett. **82**, 2805

Zarem H A, Sercel P C, Lebens J A, Eng L E, Yariv A and Vahala K J 1989 Appl. Phys. Lett. **55**, 1647

An analysis of the alpha parameter used for extracting surface recombination velocity in EBIC measurements

Vincent K S Ong and Oka Kurniawan

School of Electrical and Electronics Engineering, Nanyang Technological University, Block S2, Nanyang Avenue, Singapore 639798, Singapore

ABSTRACT: This paper gives an in-depth analysis of the parameters affecting the alpha parameter which is used for extracting the surface recombination velocity in EBIC line scan measurements. The analysis shows that the alpha versus normalized surface recombination velocity curve is a function of both the normalized beam depth as well as the normalized scanning range. However, it was found that the impact of the variations in these two parameters on the accuracy in extracting the surface recombination velocity is not significant. The analysis was further verified with the use of computer simulation.

1. INTRODUCTION

It was shown in Ong et al (1994) that a simultaneous extraction of both the minority carrier diffusion length and the surface recombination velocity can be done by using the equation:

$$I = kx^{\alpha} \exp(-x/L) \qquad \text{Eqn. 1}$$

where I is the EBIC current, k is a constant, x is the beam distance from the junction as shown in Fig. 1, L is the minority carrier diffusion length, and α is a fitting parameter. Since alpha is a function of the value of the surface recombination velocity, it can be used to extract the surface recombination velocity of the material.

It was later shown that the relationship between alpha and the normalized surface recombination velocity can be modeled with a normal distribution function (Ong 1998). The surface recombination velocity can be readily obtained once the alpha value is known if the alpha versus normalized surface recombination velocity curve does not depend on any other parameters.

However, Zhu et al (2003) found that the alpha parameter is also a function of the beam depth. Hence, the accuracy of extracting the surface recombination velocity by using the normal distribution curve would be in question.

In order to extract the surface recombination velocity accurately by using the method described in Ong (1998), it is important to analyze the parameters that alpha depends on and how these parameters affect the alpha versus normalized surface recombination velocity curve. This paper gives a complete analysis of the alpha parameter with the use of the analytical equation. The impact of the various parameters on the accuracy is also given. The analysis is then verified by using computer simulation.

2. ANALYTICAL EQUATION FOR ALPHA

The analytical equation for alpha can be derived from Eqn. 1. In experiments, the alpha value is obtained by a fitting process within a scanning range. Within this scanning range the alpha value is assumed to be constant and the current I can be approximated as in Eqn. 1.

Taking the natural logarithm of Eqn. 1 and differentiating with respect to x gives:

$$\frac{d\ln(I)}{dx} = \frac{\alpha}{x} - \frac{1}{L} \quad \text{Eqn. 2}$$

Using the relationship $d\ln(I)/dx = 1/I(dI/dx)$, Eqn. 2 can be rearranged to give:

$$\alpha = \left(\frac{1}{I}\frac{dI}{dx} + \frac{1}{L}\right)x \quad \text{Eqn. 3}$$

The exact expression for the analytical equation of the alpha parameter can be obtained by substituting the analytical expressions for *I* and *dI/dx* into Eqn. 3. The expressions for the current and its derivative depend on the configuration of the collector. In the case of the normal-collector configuration, the expressions for a point source are given as (Luke 1996):

$$I(x,z) = GI_b\left\{\exp(-x/L) - \frac{2S}{\pi}\int_0^\infty \frac{u\exp(-\sqrt{u^2+1}\,\frac{z}{L})\sin(ux/L)}{(u^2+1)(S+\sqrt{u^2+1})}\,du\right\} \quad \text{Eqn. 4}$$

$$\frac{dI}{dx}(x,z) = GI_b\left\{-\frac{1}{L}\exp(-x/L) - \frac{2S}{\pi L}\int_0^\infty \frac{u^2\exp(-\sqrt{u^2+1}\,\frac{z}{L})\cos(ux/L)}{(u^2+1)(S+\sqrt{u^2+1})}\,du\right\} \quad \text{Eqn. 5}$$

where *G* is the generation factor, I_b is the beam current (Holt 1989), and *S* is the normalized surface recombination velocity.

Substituting Eqns. 4 and 5 into Eqn. 3 gives the analytical expression for alpha. Solving Eqn. 3 numerically for several values of *S* gives the curve of alpha versus the normalized surface recombination velocity as shown in Fig. 2. This plot has the same shape as the one in Ong (1998).

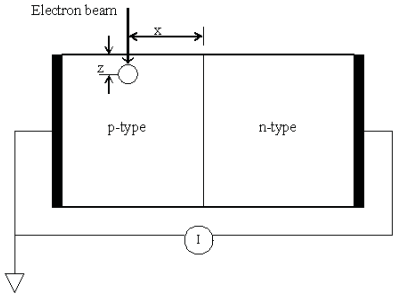


Fig. 1 Normal-collector configuration

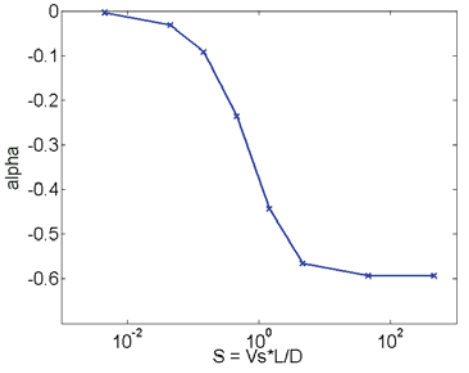


Fig. 2 Alpha curve versus normalized surface recombination velocity from the analytical Eqn. 3.

3. ANALYSIS USING ANALYTICAL EQUATION

Eqns. 3 to 5 show that the alpha curve depends on two parameters. They are the normalized scanning location from the junction and the normalized depth of the generation volume, *z/L*. It is important to note that the term *x/L* refers to the location of the scanning range from the junction where the data for the fitting process is taken. This is because Eqn. 3 was derived by assuming that alpha does not vary with distance. This is true within the scanning range only. Therefore, varying the term *x/L* means varying the location where alpha is constant, which is the scanning range. It can be seen that the alpha parameter does not depend directly on *L*. Rather its dependency on *L* is through *x/L* and *z/L*. The analytical equation of alpha also shows that the curve does not depend on the beam current, I_b. This is because the term GI_b cancels out in Eqn. 3.

The plots of Eqn. 3 for different values of z/L are shown in Fig. 3. The alpha curve is affected by the normalized depth only at higher values of surface recombination velocities. Larger values of z/L cause the lower portion to move upward as shown in Fig. 3. However, alpha curve changes imperceptibly for $z/L \leq 0.1$.

The plot for different values of the scanning location is shown in Fig. 4. Increasing the scanning location will shift the middle portion of the curve to the left and the lower portion of the curve upward. The rate of change in the alpha curve as the scanning location varies is larger at smaller values of scanning locations. Therefore, the effect of the normalized beam distance from the junction on the alpha curve is significant only at small values of scanning locations.

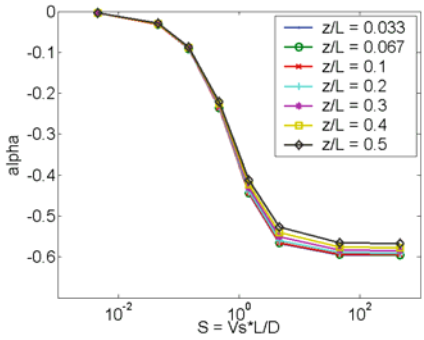


Fig. 3 Alpha curves for different z/L, from Eqn. 3 with $x/L = 3$ and $L = 3\mu m$.

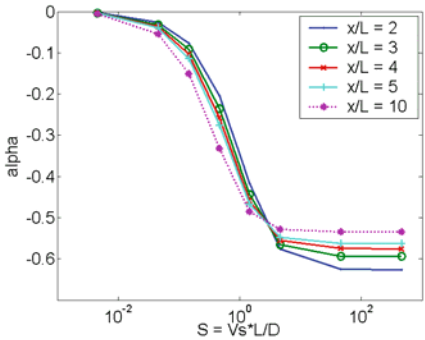


Fig. 4 Alpha curves for different scanning location (x/L), from Eqn. 3 with $z/L = 0.1$ and $L = 3\mu m$.

The analysis of the alpha parameter with the use of Eqn. 3 reveals that the alpha parameter is a function of the beam distance from the junction. This means that different EBIC scanning ranges could result in different values of alpha.

4. VERIFICATION

The analysis using the analytical equation was verified with the 2-D device simulation software MEDICI. In this case, the current values obtained from the simulations were fitted into Eqn. 1 to extract both the minority carrier diffusion length and the alpha parameter. The curves for alpha at different normalized depths and scanning ranges are shown in Figs. 5 and 6, respectively.

Figure 5 shows somewhat the same trend as Fig. 3 but less profound. The effect of z/L is only significant at the higher values of surface recombination velocities. The curves in Fig. 5 also change imperceptibly for $z/L \leq 0.1$. On the other hand, Fig. 6 shows that increasing the starting location of the scan by L while reducing the scanning width by the same amount has the same effect as increasing the scanning location in the analytical equation for alpha. This indicates that the effect of varying the starting location on the alpha curve is more dominant.

The alpha values in Figs. 5 and 6 were obtained by fitting the EBIC current values for a range of beam locations into Eqn. 1. This fitting process seems to average out the actual effect of x/L on the alpha curve. This is the reason that Fig. 6 shows smaller variation compared to Fig. 4.

5. IMPACT ON ACCURACY

The impact that x/L and z/L have on the accuracy of extracting surface recombination velocity can be seen in Table 1. The alpha values from MEDICI simulations in Figs. 5 and 6 were used to extract the surface recombination velocity by using the method in Ong (1998).

The results indicate that the accuracy is not affected much as the z/L ratio changes from 0.067 to 0.3. For the surface recombination velocity of 1×10^5 cm/s, the errors increase as z/L increases. This agrees with the previous analysis. The impact of changing the scanning range is also not very

significant. The impact on the middle portion of the alpha curve will be more significant as the starting location is increased further. This is because the middle portion will be shifted further from the normal distribution function which is used for the extraction.

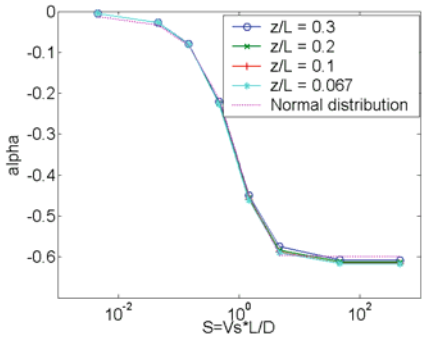


Fig. 5 Alpha curves from MEDICI simulations for different z/L. The scanning range used is from $x/L = 3$ to $x/L = 14$ and $L = 3\mu m$.

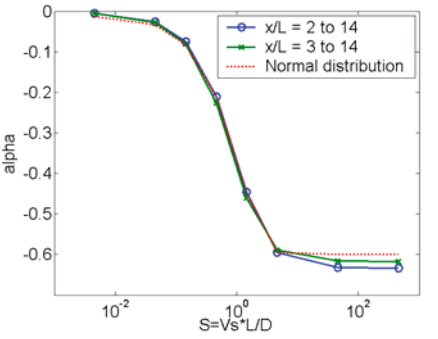


Fig. 6 Alpha curves from MEDICI simulations for different scanning range. The simulations used $z/L = 0.067$ and $L = 3\mu m$.

Table 1 Error in extracting surface recombination velocity

	Error for different z/L					Error for different scanning range	
v_s (cm/s)	Error (%) $z/L = 0.3$	Error (%) $z/L = 0.2$	Error (%) $z/L = 0.1$	Error (%) $z/L = 0.067$	v_s (cm/s)	Error (%) $x/L = 2$ to $x/L = 14$	Error (%) $x/L = 3$ to $x/L = 14$
0	∞	∞	∞	∞	0	∞	∞
1×10^2	-295.34	-291.30	-291.30	-295.34	1×10^2	-283.22	-295.34
1×10^3	-27.38	-25.70	-25.28	-24.45	1×10^3	-32.82	-24.45
3.16×10^3	-4.50	-2.61	-1.88	-1.59	3.16×10^3	-11.00	-1.59
1×10^4	5.65	7.71	9.02	9.15	1×10^4	-0.90	9.15
3.16×10^4	-0.07	3.24	5.48	5.93	3.16×10^4	-1.55	5.93
1×10^5	-29.95	-22.50	-15.08	-13.18	1×10^5	3.76	-13.18
1×10^6	-	-	-	-	1×10^6	-	-
1×10^7	-	-	-	-	1×10^7	-	-

6. CONCLUSION

It has been shown that the analytical expression for alpha can be used to analyze the alpha parameter. The alpha versus the normalized surface recombination velocity curve depends on two parameters. They are the normalized depth of the generation volume and the normalized scanning range. The accuracy in extracting the surface recombination velocity by using the method in Ong (1998) is not affected much when the normalized depth changes. The accuracy is affected only in extracting high surface recombination velocities. Similarly, changing the starting location of the scanning range affects the accuracy only slightly, and the most affected region is in the middle range values.

REFERENCES

Holt D B 1989 The Conductive Mode. SEM Microcharacterization of Semiconductors. D B Holt and D C Joy. (New York, Academic Press), 241-338

Luke K L 1996 J. Appl. Phys. **79**, 3058

Ong V K S 1998 Rev. Sci. Instrum. **69**, 1814

Ong V K S, Phang J C H, et al. 1994 Solid-State Electron. **37**, 1

Zhu S-Q, Yang F-H, et al 2003 Semicond. Sci. Technol. **18**, 361

The effects of boundary conditions on dopant region imaging in scanning electron microscopy

M Ferroni, P G Merli[1] and V Morandi[1]

INFM Sensor Laboratory – Dipartimento di Chimica Fisica per l'Ingengeria dei Materiali, Universita' di Brescia, via Valotti 9, 25133 Brescia, Italy
[1] CNR-IMM, Sezione di Bologna, via Gobetti 101, 40129 Bologna, Italy

ABSTRACT: A specimen structure with a gradual variation in composition, an Sb doped region in Si, has been investigated by scanning electron microscopy, operating with backscattered electrons and secondary electrons. Numerical simulations and experimental observations have been carried out in order to highlight the influence of the boundary conditions on the capability to detect the implanted region. Moreover, it will be shown that a proper choice of the microscope operating conditions may achieve either enhanced compositional contrast or an analytical condition for dopant profiling.

1. INTRODUCTION

Within the description of an incoherent sequential imaging process, a specimen compositional feature may be revealed if it generates a number of electrons sufficiently different from that of the neighbouring regions. More precisely, the visibility of the feature, having a location defined by the probe, depends on the difference in the number of electrons collected by the detector when the beam is positioned on it (N_A) or on the neighboring region (N_B). Indeed, such a difference defines the contrast ($C = (N_A - N_B) / \max (N_A,N_B)$) and consequently the threshold current: i.e. the minimum beam current which must be employed to detect that specific level of contrast between the two points (Goldstein et al 1981). From the threshold current and the main features of the instrument, such as gun brightness and aberrations of the objective lens, it is possible to deduce the probe size that defines the resolution.

This approach was successfully used to explain experimental results concerning the compositional imaging with backscattered electrons (BSE) as well as with secondary electrons (SE) in scanning electron microscopy (Merli et al 1996 and references therein) and highlights the significant role of the neighbouring regions, referred to hereinafter as the boundary conditions, on the visibility of compositional specimen detail.

In this paper, experimental results concerning the visibility of an Sb-doped region in specimen, observed with BSE as well as with SE, will be reported. The BSE imaging has been performed using a solid state annular detector located below the pole piece of the objective lens whereas the SE images have been acquired using the usual Everheart-Thornley detector (ETD). Numerical simulation of the effects of different boundaries will highlight the physical mechanism responsible for hindering or enhancing the doped-region's visibility and the operating conditions suitable to describe the dopant profile.

2. MATERIALS AND METHODS

The investigation concerns Sb-implanted silicon. The implantation energy was 23 keV and the dose was 2×10^{15} atoms/cm^2. The simulated (Lulli et al 1997) as-implanted dopant profile (see Fig. 1) indicates a spatial extension of the doped region of about 40 nm and a maximum concentration of about 2.7 % located at a depth between 15 and 20 nm. The specimen has been subsequently annealed at a temperature of 1000°C for 2 min; a thermal treatment that does not modify the peak position and

the spatial extension of the doped region. The annealed specimens have been observed on cross-sections after a deposition of a poly-crystalline layer of 300 nm above the doped region. In order to have a flat surface without roughness or steps, the cross sections have been prepared using the techniques normally employed in transmission electron microscopy but avoiding the final thinning. The experimental observations were carried out with a SEM LEO 1525 equipped with a Schottky emitter. The simulations have been performed using a Monte Carlo code already described (Merli et al 2001).

3. EXPERIMENTAL RESULTS

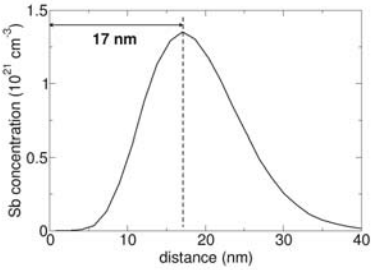


Fig. 1: Simulated as-implanted profile of the Sb-doped Si specimen.

Figure 2a shows a BSE image of the bulk cross-sectioned specimen observed at a beam energy, E, of 20 keV, using a probe size of about 2 nm, and operating at a working distance, WD, of 5 mm. The BSE signal is collected with the solid state detector. The high atomic number of Sb produces an increase in the BSE signal so that the doped region is visible as a brighter region over the uniform background produced by undoped Si. The corresponding scan profile, reported in Fig 2b), shows a width of the doped region and a position of the peak in good agreement with the simulated profile of Fig. 1. Figure 2c shows a SE image of the same region of the specimen, obtained with the ETD and operating in the same electron-optical conditions,. The doped region is again visible with the same features as Fig. 2a). As already pointed out (Merli et al 2005) the source of compositional contrast in the SE images is the production of SE by BSE at the exit surface of the specimen (SE2) or on the environment (SE3).

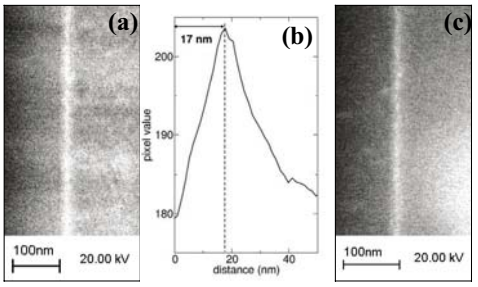


Fig. 2: (a) BSE image at 20 keV of the doped layer; (b) corresponding scanning profile; (c) SE image at 20 keV with ETD. WD = 5 mm.



Fig. 3: SE image at 5 keV obtained with ETD and WD = 10 mm.

Figure 3 reports a SE image obtained at 5 keV, operating with the ETD and at a WD of 10 mm. The quality of the image is clearly improved, as pointed out in Merli et al (2005): the doped region is visible with the same characteristics of the previous images, but with a higher contrast. It is worth noting that, without the presence of the poly-silicon layer, the observation of the same specimen under the same electron optical conditions does not allow us to detect the doped region.

4. DISCUSSION OF THE RESULTS

Figures 4a and 4b report the simulated BSE yield, η, versus position for different beam energies (E = 1, 5, 10 and 20 keV) and the two different boundary conditions reported on the bottom: with or without the poly-Si layer. The probe size has been assumed of 2 nm. It is possible to observe that in the conditions shown in Fig. 4a, the BSE yield provides information on the doped layer, even if

with a very faint signal, only operating at very low energy, (e.g. at 1 keV in the figure). A qualitative explanation is the following: a fraction of the electrons incident on the doped region are scattered toward the boundary of the specimen where there is the vacuum and no BSE can be generated. This fraction increases with the energy so that, above a few keV, any signal related to the presence of the doped layer vanishes. When the poly-Si layer is present the doped region is visible at any energy; however it should be noted that the contrast increases in the energy range 1 – 5 keV, then decreases with increasing E. Again the diffusion of the electrons toward the boundary of the 300 nm thick poly-Si layer reduces the production of BSE.

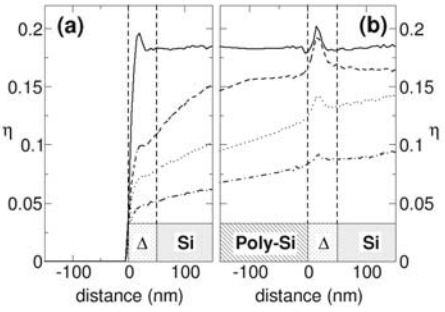


Fig. 4: BSE simulated profile for different boundary conditions and beam energies. (a) nothing on the top of the doped region (indicated with Δ); (b) 300 nm of Poly-Si. Continuous line: E = 1 keV; dashed line: E = 5 keV; dotted line: E = 10 keV; dashed-dotted line: E = 20 keV.

In order to have a better understanding of the phenomenon in Figs. 5a and 5b the simulation of the BSE yield is shown when the doped region is bounded by layers having a higher atomic number: Cu and Pt. Figure 5a refers to the presence of a Cu layer having a thickness of 300 nm. It shows that at 1 keV the presence of dips and bumps is clearly evident, which is a typical feature of the BSE yield at an interface between materials having different atomic numbers (Konkol et al 1994, Konkol et al 1995). It has the following qualitative explanation. When the beam is in a region of high atomic number, Z, and moves towards the interface with a region of lower Z, at a distance depending on the energy, the interaction volume, V_{int}, will cross the interface and the electrons will emerge from the surface of the lighter material. Because of the longer mean free path a higher fraction of these electrons would exit than if their path had been entirely within the material with higher Z. Therefore a bump occurs in the profile on the side having a higher atomic number. Similarly, the reverse effect gives rise to a dip on the side with lower Z. As quantitatively shown in Fig. 5a, the enlargement of V_{int} with E increases the width of the dips and bumps. Due to the presence of Sb, the result is a progressive reduction of the peak, on the Si side, that vanishes at about 5 keV. For a material having a higher Z such as Pt (Fig. 5b), the same phenomenon causes a disappearance of the peak at about 3 keV.

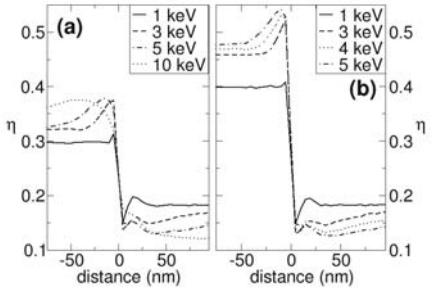


Fig. 5: BSE simulated profile for different boundaries at different energies. (a) 300 nm of Cu; (b) 300 nm of Pt.

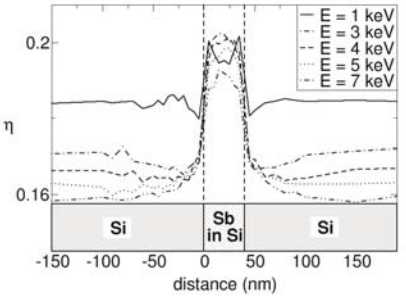


Fig. 6: BSE simulated profile for a 40 nm layer of Sb doped Si (with a constant concentration of 2.7 %, embedded in a Si matrix) for different energies.

In summary, a boundary represented by a material having a Z higher than for Si allows us to detect the presence of the doped region only at very low energy. A reverse but similar phenomenon occurs for material having a lower Z. Then it is possible to deduce that the best boundary is represented by a material having an atomic number very similar or equal to that of Si, as poly-Si.

However the variation in the average value of Z due to the presence of Sb will produce dips and bumps also in this case, and again the beam energy will play an important role in the observation conditions. In order to illustrate this phenomenon Fig. 6 shows the dependence on E of the BSE profile of a 40 nm doped layer having a constant Sb concentration of 2.7 %. It is possible to see that the dips and bumps disappear going from 1 keV to 5 keV, and that there is a maximum contrast between 3 and 4 keV, then the contrast progressively decreases. Thus, as already reported (Merli et al 2002, 2003), for V_{int} much smaller than the size of the investigated layer, an analytical observation condition is achieved, where the intensity of the signal is equal to that of a homogenous material. For V_{int} of the order of the detail size there is an energy tuning condition. The contrast is enhanced and higher than that provided by two homogeneous bulk materials. A further increase of V_{int} causes a progressive contrast decrease.

Figure 7 shows the BSE yield versus position for the doped layer in the low-energy range. Again the dips are visible at very low energy (at 1 keV in the figure), but they are asymmetrical as a consequence of the shape of the doped profile that causes a more evident dip on the poly-Si side. The dips disappear for a rising energy and the contrast increases for an energy of about 3 - 4 keV. Then it decreases slowly. Following the same arguments used for the interpretation of contrast with a homogeneous layer of different composition we can infer that there is a condition of maximum contrast suitable to detect the doped layers and to provide information on the peak position and the width of the doped region. However the possibility to describe the profile, under analytical conditions, is achieved only operating at very low energy (1 keV and below).

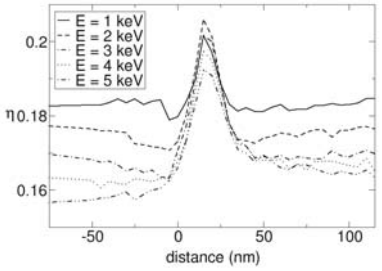


Fig. 7: BSE simulated profiles of the doped region bounded by 300 nm of Poly-Si at different energies.

5. CONCLUSIONS

The visibility of an Sb-doped region in silicon was proven to depend on its boundaries as well as on the microscope operating conditions. Numerical simulation and BSE imaging indicated that an average atomic number for the surrounding regions nearly equal to that of Si may improve the visibility for the doped region. Moreover a proper choice of the beam energy may give rise to different observation conditions: an analytical one at low energy, suitable to describe the profile of the dopant, and a condition of maximum contrast suitable to detect the doped layers and to provide information on the peak position and on the width of the doped region

ACKNOWLEDGEMENTS

This research project is partially supported by MIUR, Project Code RBAU01M97L.

REFERENCES

Goldstein J I, Newbury D E, Echlin P, Joy D C, Fiori C and Lifshin E 1981 Scanning Electron Microscopy and X-Ray Microanalysis, (Plenum Press. New York and London)
Konkol A, Wilshaw P R and Booker G R 1994 Ultramicroscopy **55**, 183
Konkol A, Booker G R and Wilshaw P R 1995 Ultramicroscopy **58**, 233
Lulli G, Bianconi M, Nipoti R, Albertazzi E, Cervera M, Carnera A, and Cellini C 1997 J. Appl. Phys. **82**, 5958
Merli P G, Migliori A, Nacucchi M and Vittori Antisari M 1996 Ultramicroscopy **65**, 23
Merli P G, Migliori A, Morandi V and Rosa R 2001 Ultramicroscopy **88**, 139
Merli P G and Morandi V 2002 Adv. Img. Elec. Phys. **123**, 375
Merli P G, Morandi V and Corticelli F 2003 Ultramicroscopy **94**, 89
Merli P G, Morandi V, Savini G, Ferroni M and Sberveglieri G 2005 Appl. Phys. Lett. **86**, 101916

A cross-sectional scanning tunneling microscopy study of GaSb/GaAs nanostructures

R Timm, A Lenz, J Grabowski, H Eisele and M Dähne

Institut für Festkörperphysik, Technische Universität Berlin, Hardenbergstr. 36, D-10623 Berlin, Germany

ABSTRACT: We present cross-sectional scanning tunneling microscopy results of GaSb quantum wells and dots in GaAs. A fascinating potential of this technique for the investigation of overgrown nanostructures is demonstrated by revealing structural details of GaSb dots and wells with atomic resolution, by introducing a method to obtain the local stoichiometry, and by discussing different contributions to the image contrast in combination with the type-II band alignment.

1. INTRODUCTION

Semiconductor quantum dots (QDs) and wells (QWs) are currently at the center of widespread interest due to their unique electronic properties and potential applications in optoelectronics. Both for understanding the fundamental physics and to improve the epitaxial growth of nanostructures, a detailed knowledge about the structural, compositional and electronic properties of overgrown QDs and QWs, as well as knowledge about the mechanism of dot formation is essential.

Cross-sectional scanning tunneling microscopy (XSTM) is a very powerful tool and a suitable method to investigate semiconductor nanostructures, since it has the ability to reveal shape, size and stoichiometry of quantum dots with atomic resolution (Liu et al 2000, Lenz et al 2002, Bruls et al 2002). Additionally, even the strain (Flebbe et al 1999) and electronic properties of nanostructures (Grandidier et al 2000) can be analyzed. In contrast to the more common top view STM (Jacobi 2003), XSTM allows to study QDs after the capping process, which is necessary for nearly all applications and was found to significantly change the QD structure (Eisele et al 2003, Lenz et al 2004) and thus the electronic properties.

GaSb QDs in GaAs, though less intensively studied than the InAs/GaAs material system, are very promising for applications like charge storage devices due to their staggered type-II band alignment with confined holes but no electron confinement within the dots (Hatami et al 1995), resulting in a large hole confinement energy and long recombination lifetimes (Geller et al 2003). Because of this special band alignment, GaSb/GaAs nanostructures are also a challenging system for the investigation by XSTM, being sensitive to local electronic properties.

Recently, we have shown first XSTM results on GaSb quantum dots in GaAs (Timm et al 2004) and on the dot formation process (Timm et al 2005). In this contribution, we present a systematic XSTM study of GaSb/GaAs nanostructures, demonstrating the ability of XSTM to yield information on the structure of QWs, QDs and possible QD precursors, on the local stoichiometry of these structures, and on electronic effects related to the type-II band alignment.

2. EXPERIMENT

A home-built STM is used under ultrahigh vacuum (UHV) conditions with a base pressure lower than 5×10^{-9} Pa. By cleaving the samples within UHV, a clean (110) surface is obtained and examined with XSTM at room temperature in the constant-current mode, using electrochemically etched tungsten tips that were further cleaned *in situ* by electron bombardment. All STM images shown here were taken at a tunneling current of 80 pA.

Three samples with a different amount of GaSb and different growth interruption (GrI) times were investigated. All samples have been grown by metalorganic chemical vapor deposition with growth conditions similar to those described by Müller-Kirsch et al (2001). In the first sample, GaSb

was deposited for 21 s and immediately overgrown with GaAs. The GaSb deposition time in sample 2 was 22 s, which was expected to produce a quantum well near the critical thickness of dot formation. Here, the GaSb growth was followed by a GrI of 2 s. For the third sample, finally, a GaSb deposition time of 25 s was chosen, followed again by a GrI of 2 s for dot evolution.

3. RESULTS AND DISCUSSION

3.1 Structure of Quantum Wells and Dots

Overview images of the three different GaSb layers are shown in Fig. 1a-c. The lines perpendicular to the [001] growth direction represent the atomic zigzag chains at the (110) cleavage surface (Feenstra 1987), showing each second atomic monolayer. Parallel to these chains the GaSb layers can clearly be seen with a bright image contrast.

In Fig. 1a the GaSb quantum well of sample 1 is shown, which extends over only one atomic chain and has a discontinuous appearance, consisting of GaSb parts and antimony-free gaps. These gaps are smaller at higher amounts of deposited GaSb (Fig. 1b,c), but can be found in all three samples, agreeing well with top-view STM results (Thibado et al 1996) on GaSb layers grown on GaAs which consist of GaSb islands separated by small trenches filled with GaAs.

The GaSb quantum well in sample 2 near the critical thickness of dot formation (Fig. 1b) extends over nearly two atomic chains and shows a higher image contrast than that of sample 1 (Fig. 1a). The contrast in STM images general consists of a structural and an electronic part. Here, the latter is dominated by the different band gaps of GaSb and GaAs, respectively, leading to a higher tunneling probability on GaSb than on GaAs. In XSTM images of cleaved nanostructures, a relaxation of the strained material out of the cleavage plain leads to an additional structural contrast. Thus, the higher image contrast of the QW in sample 2 compared with sample 1 stands for larger strain and a higher tunneling probability, both indicating a larger amount of GaSb within the QW.

In sample 3, shown in Fig. 1c, distinctive QDs were found. The image contrast of these dots is much higher than that of the QWs, due to the considerably larger strain within the dots, a larger GaSb content and additional confined states. The dots are rather small compared with the InAs/GaAs system, with base lengths varying between 5 and 8 nm and heights ranging from 1.5 to 2 nm (Timm 2004). The shape of the dots resembles that of a rather flat, truncated pyramid, though no exact structure can be identified due to the small size and a slightly inhomogeneous contrast. From the XSTM images a dot density of ~3 x 10^{10} cm^{-2} can be derived. The QDs are embedded within an inhomogeneous wetting layer, extending over about two atomic chains or ~1 nm.

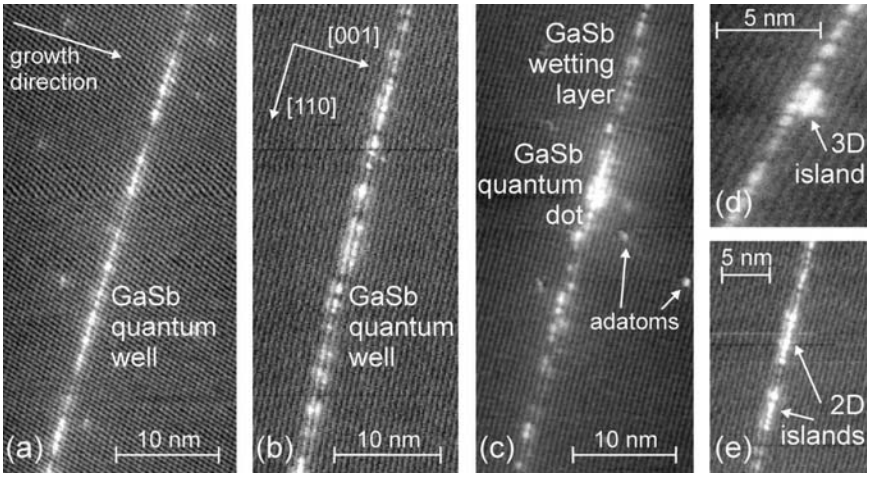


Fig. 1. Filled-state XSTM images of (a-c) the GaSb layers in the three different samples, (d) a small 3D GaSb island in sample 3, and (e) flat 2D GaSb islands in sample 2. The images are taken at sample voltages of V_S = -3.0 V (a,b), -2.3 V (c), -3.3 V (d), and –1.8 V (e).

3.2 Onset of Dot Formation

Within the wetting layer of sample 3, also small but distinctive 3D islands like that shown in Fig. 1d with a base length of only 2.5 nm and a height of about 1.5 nm were found. These islands with a density of about 5 x 10^{10} cm^{-2} are assigned to an early stage of QD formation.

Also in sample 2, containing the QW near the critical thickness, small island-like structures could be found with a high density of about 6 x 10^{11} cm^{-2}. However, these 2D islands are rather flat, but show a much brighter image contrast than the surrounding QW, as shown in Fig. 1e. In this sample no three-dimensional structures were found, and we assume the observed 2D islands to possibly act as QD precursors (Timm et al 2005).

3.3 Local Stoichiometry

A closer view of a representative QD is given in Fig. 2a. The inhomogeneous contrast of the dot indicates an intermixed material instead of pure GaSb. We have developed a method to quantitatively analyze the local stoichiometry from XSTM data (Flebbe et al 1999, Timm et al 2004): At strained semiconductor heterostructures, the local lattice constant, which can be associated with the distance between neighboring atomic chains, is a measure of the chemical composition, as it depends directly on the stoichiometry and additionally on the strain, which is also a function of the composition.

Figure 2b shows the variation of this chain distance across the QD in Fig. 2a, evaluated for the dot center (straight line), the outer parts of the dot (dashed line) and for the wetting layer far away from any dot (dotted line). The range of the increased chain distance extends over four atomic chains at the dot center and over three chains at the dot edge with the highest GaSb content in the central chain, which nicely agrees with an optical inspection of the image contrast. The obtained chain distances are compared with calculated results for the relaxation of a strained GaSbAs layer, based on continuum mechanics on an atomic scale (Eisele 2002). Considering some additional effects discussed in detail elsewhere (Timm et al 2004), we

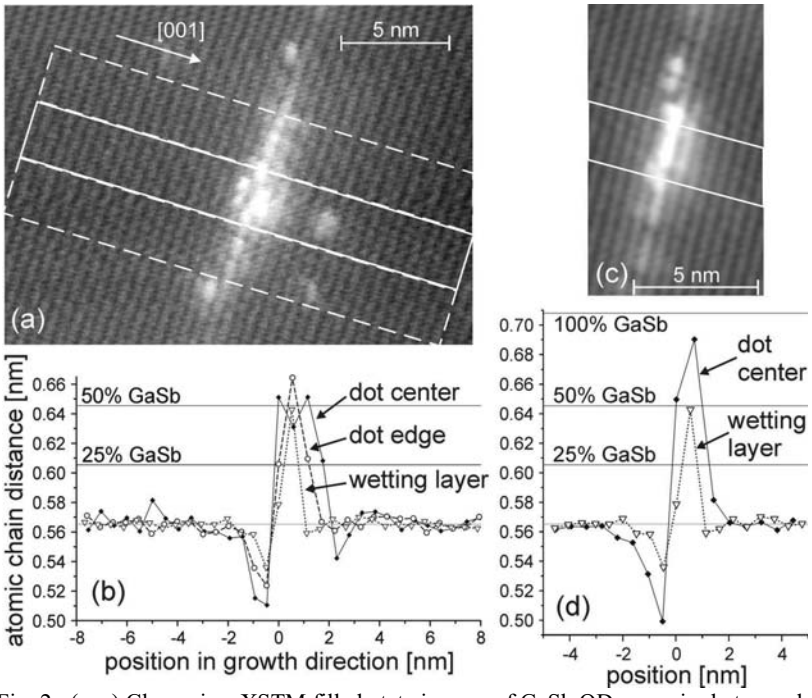


Fig. 2. (a, c) Close-view XSTM filled-state images of GaSb QDs, acquired at sample voltages of V_S = -1.6 V. (b, d) Variation of the distance between neighboring atomic chains across the QD in (a, c), averaged in [110] direction within narrow stripes, as indicated in (a, c). The indicated stoichiometries correspond to calculated chain distances of a 2D $GaSb_xAs_{1-x}$ layer.

obtain a GaSb content within the center of this QD of 60–70% and within the wetting layer of 40-50%, with an error of 10%. The local stoichiometry of the QDs found in sample 3 can vary up to nearly pure GaSb, as can be seen in Fig. 2d for the small dot with a homogeneous, bright contrast shown in Fig. 2c.

3.4 Electronic Properties

All STM images in Fig. 1 and 2 are taken at negative sample voltages and show thin, sharply defined GaSb layers. At this bias polarity, the filled valence band states are imaged, which can be assigned to the group-V atoms like As and Sb. At positive sample voltages the empty conduction band states are imaged, being sensitive to the group-III atoms like Ga. Indeed, at positive sample voltages no such sharp contrast change can be seen at the GaAs/GaSb interface, but instead a wide bright contrast of the GaSb layers, which is smoothly broadened over several nm (not shown here). This novel contrast mechanism is related to the specific band alignment of the GaSb/GaAs material system and can only be explained if the effect of tip-induced band bending is taken into account, which will be published in detail soon.

4. CONCLUSION

In conclusion, we presented XSTM results on buried GaSb QDs and QWs in GaAs. Distinctive dots with base lengths of 5 to 8 nm and a flat shape were studied. Small 3D- and 2D-islands were found in two different samples, possibly representing an early stage of dot formation or QD precursors, respectively. The ability of XSTM to analyze the local stoichiometry of QDs and QWs was demonstrated. Finally, different contributions to the specific image contrast were discussed.

The authors want to thank L Müller-Kirsch, K Pötschke, U W Pohl and D Bimberg for providing samples and R M Feenstra for helpful discussions. This work was supported by projects Sfb 296, Da 408/4, and Da 408/8 of the Deutsche Forschungsgemeinschaft as well as by the European Commission in the SANDiE Network of Excellence.

REFERENCES

Bruls D M, Vugs J W A M, Koenraad P M, Salemink H W M, Wolter J H, Hopkinson M, Skolnick M S, Long F and Gill S P A 2002 Appl. Phys Lett. **81**, 1708

Eisele H 2002 Cross-Sectional Scanning Tunneling Microscopy of InAs/GaAs Quantum Dots (Berlin, Wissenschaft und Technik)

Eisele H, Lenz A, Hennig Ch, Timm R, Ternes M and Dähne M 2003 J. Crystal Growth **248**, 322

Feenstra R M, Stroscio J A, Tersoff J and Fein A P (1987) Phys. Rev. Lett. **58**, 1192

Flebbe O, Eisele H, Kalka T, Heinrichsdorff F, Krost A, Bimberg D and Dähne-Prietsch M 1999 J. Vac. Sci. Technol. B **17**, 1639

Geller M, Kapteyn C, Müller-Kirsch L, Heitz R and Bimberg D 2003 Appl. Phys. Lett. **82**, 2706

Grandidier B, Niquet Y M, Legrand B, Nys J P, Priester C, Stiévenard D, Gérard J M and Thierry-Mieg V 2000 Phys. Rev. Lett. **85**, 1068

Hatami F, Ledentsov N N, Grundmann M, Böhrer J, Heinrichsdorff F, Beer M, Bimberg D, Ruvimov S S, Werner P, Gösele U, Heydenreich J, Richter U, Ivanov S V, Meltser B Ya, Kop'ev P S and Alferov Zh I 1995 Appl. Phys. Lett. **67**, 656

Jacobi K 2003 Prog. Surf. Sci. **71**, 185

Lenz A, Timm R, Eisele H, Hennig Ch, Becker S K, Sellin R L, Pohl U W, Bimberg D and Dähne M 2002 Appl. Phys. Lett. **81**, 5150

Lenz A, Eisele H, Timm R, Becker S K, Sellin R L, Pohl U W, Bimberg D and Dähne M 2004 Appl. Phys. Lett. **85**, 3848

Liu N, Tersoff J, Baklenov O, Holmes J A L and Shih C K 2000 Phys. Rev. Lett. **84**, 334

Müller-Kirsch L, Heitz R, Pohl U W, Bimberg D, Häusler I, Kirmse H and Neumann W 2001 Appl. Phys. Lett. **79**, 1027

Thibado P M, Bennett B R, Twigg M E, Shanabrook B V and Whitman L J 1996 J. Vac. Sci. Technol. A **14**, 885

Timm R, Eisele H, Lenz A, Becker S K, Grabowski J, Kim T-Y, Müller-Kirsch L, Pötschke K, Pohl U W, Bimberg D and Dähne M 2004 Appl. Phys. Lett. **85**, 5890

Timm R, Grabowski J, Eisele H, Lenz A, Becker S K, Müller-Kirsch L, Pötschke K, Pohl U W, Bimberg D and Dähne M 2005 Physica E **26**, 231

Atomistic structure of spontaneously-ordered GaInP alloy revealed by cross-sectional scanning tunneling microscopy and polarized cathodoluminescence spectroscopy

Yutaka Ohno

Department of Physics, Graduate School of Science, Osaka University, 1-1 Machikane-yama, Toyonaka, Osaka 560-0043, Japan

ABSTRACT: Cross-sectional scanning tunnelling microscopy on a CuPt-ordered GaInP alloy revealed that atomic layers of InP on $(\bar{1}11)$ and $(\bar{1}\bar{1}0)$, sandwiched between the ordered domains, are formed. Polarized cathodoluminescence spectroscopy in a transmission electron microscope revealed that the InP layers act as quantum wells (QWs) oriented on a slant with respect to the substrate and they emit photons linearly polarized parallel to the layers. The polarization of the photons was controlled through changes of QW structures depending on growth conditions.

1. INTRODUCTION

The CuPt-ordered structure, formed spontaneously in a GaInP alloy (Gomyo et al 1987), consisting of a monolayer superlattice (SL) of Ga-rich and In-rich planes, has been applied to various optical devices. One issue that has remained outstanding is the origin of the characteristic low-energy emission. Antiphase boundaries (APBs), at which the sequence of Ga-rich and In-rich layers is 180^{o} out of phase (Su et al 1994), are inevitably introduced during the spontaneous growth of SLs, and the SLs including APBs emit photons with energies lower than the band gap energy (Eg). Some structural models have been proposed (Smith et al 2003, Kops et al 2000, Mattila et al 2003). However, the origin is still unclear since the atomistic structure of APBs could not been obtained experimentally. I have recently found, by means of cross-sectional scanning tunnelling microscopy (XSTM), that atomic layers of InP sandwiched between SLs are formed on APBs (Ohno 2005). Polarized cathodoluminescence (p-CL) spectroscopy in a transmission electron microscope has revealed that the InP layers on APBs emit low-energy photons linearly polarized parallel to the layers (Ohno 2005). In this paper, I briefly summarize the results and show that the polarization of the photons can be controlled through changes of the structure of APBs, depending on growth conditions (e.g., Su et al 1994, Takeda et al 1999).

2. EXPERIMENTAL METHODS

Samples were undoped $Ga_{0.5}In_{0.5}P$ layers (1 μm thick) grown on a GaAs substrate by MOVPE (the growth temperature 650 ^{o}C, growth rate 0.4 nm/s, III/V ratio 370). The substrate was 2^{o} or 10^{o} off from (001) towards $[\bar{1}10]$, so the ordering mainly occurred on $(\bar{1}11)$ (e.g., Takeda et al 1999). A small chip of a sample was installed into an ultra-high vacuum (UHV) scanning tunnelling microscope (JEOL, JST-4500T), and then cleaved at a UHV of 10^{-8} Pa so as to make a clean (110) surface. A W tip etched electrochemically was approached on a GaInP SL with a UHV scanning electron microscope (Ozaki et al 2001). XSTM images were obtained at room temperature by the constant-current mode (a set current of about 100 pA). A sample voltage of about +3 V was used so as to image the empty-state density associated with In and Ga atoms. Polarized-CL spectra and TEM images were obtained simultaneously (Ohno and Takeda 1995) from a (110) cross section (about a few hundred nm thick) of a sample, at the temperature of about 20 K. A beam of 80 keV electrons was used for fear of varying the atomistic structure of GaInP SLs (Ohno et al 1999).

3. RESULTS AND DISCUSSION

3.1 Low-Energy Emission from InP QWs Formed on APBs (Ohno 2005)

Figure 1a shows a XSTM image of a GaInP alloy grown on a 2° miscut substrate. The diamonds in Fig. 1b denote primitive mesh units of a c(2x2) structure. It is considered that the heights on XSTM images of GaInP SLs are determined by two factors, i.e., the difference of the bond length for In-P to that for Ga-P and the band offset at the InP/GaP interface (Liu et al 1998), and so the height of the *n*-th In layer, nearby the surface, would be higher than that of the *n*-th Ga layer on empty-state images. Figure 1c shows the corresponding model of a SL. The bright dots on the net points in Fig. 1b represent In atoms on the 1st layer. Similar c(2x2) structures were observed on filled-state images (Liu et al 1998, Heinrich et al 1998), and a bright dot on the net points was explained as a topmost P atom bonded to two In atoms (Liu et al 1998).

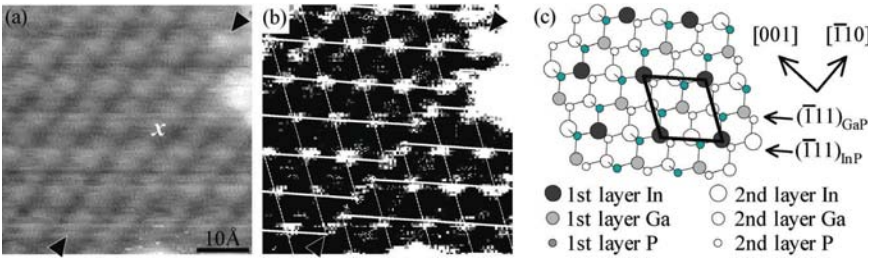


Fig.1. (a) An empty-state image of GaInP SLs. The image is not filtered or artificially enhanced in any way. APBs are extended along the atomic rows indicated by the arrows. (b) The areas where the image heights are in the range from (x-0.01) nm to (x+0.01) nm in (a), in which x is the image height at *x*. The areas arrange on diperiodic nets. (c) The corresponding model for GaInP SL.

XSTM revealed that the alloy consists of small domains (a size of 5-10 nm) of SLs bounded by APBs. APBs were distinctly observed on XSTM images. In Fig. 1b, for example, the sequence of In rows along [1$\bar{1}$2] was 180° out of phase at the row along [$\bar{1}$10] indicated by the arrows. The [$\bar{1}$10] row was not the sequence In-Ga-In-Ga... but In-In... in the 1st layer. About half of APBs consist of similar single In rows, i.e., the sequence In-In... in the 1st layer, along [1$\bar{1}$2], [001], [$\bar{1}$10], or [$\bar{1}$12]. The other APBs consist of single Ga rows of the sequence Ga-Ga... in the 1st layer. The total length of the single In rows along [*hkl*] (*hkl* = 1$\bar{1}$2, 001, $\bar{1}$10, or $\bar{1}$12), $I_{[hkl]}$, was almost the same as that of the single Ga rows along [*hkl*], and $I_{[1\bar{1}2]} : I_{[001]} : I_{[\bar{1}10]} : I_{[\bar{1}12]} \sim 8:11:4:3$.

APBs in the alloy were observed as dark bands in a TEM image (Fig. 2a). Since many parts of the bands were narrow, many planar segments of the APBs were nearly perpendicular to (110), in the thin TEM specimen. A single In (or Ga) row along [1$\bar{1}$2], [001], [$\bar{1}$10], or [$\bar{1}$12] in XSTM images would be interpreted as the cross section of an atomic layer of InP (or GaP) lying on ($\bar{1}$11), ($\bar{1}$10), (001), or (1$\bar{1}$1), respectively. The TEM specimen emitted low-energy CL photons with energies of *E*g-20 meV and *E*g-33 meV (Fig.2b). Analyses (Ohno and Takeda 2002) of the p-CL data revealed that the low-energy CL photons with *E*g-20 meV, with the maximum intensity (about 7 in an arbitrary unit) at about $\phi = 50°$, was linearly polarized along [1$\bar{1}$2], while that with *E*g-33 meV, with the maximum intensity (about 12) at about $\phi = 90°$, was linearly polarized along [001]. As a result, the low-energy CL photons with *E*g-20 meV or *E*g-33 meV were, respectively, polarized parallel to the planar segments on ($\bar{1}$11) or ($\bar{1}$10) of APBs. Since APBs expand two-dimensionally, the total area of the planar segments of APBs observed as single rows along [*hkl*] on XSTM images is, as an approximation, proportional to $I^2_{[hkl]}$. The ratio between the total areas of the planar segments on ($\bar{1}$11) and on($\bar{1}$10), $I^2_{[1\bar{1}2]} : I^2_{[001]} \sim 64:121$, was comparable to the ratio between the maximum intensities of the low-energy CL photons with *E*g-20 meV and *E*g-33 meV; 7:12. These results support the proposition that the low-energy CL photons with

*E*g-20 meV or *E*g-33 meV, respectively, correlate with the planar segments on ($\bar{1}11$) or ($\bar{1}10$) of APBs. The CL photons that would be emitted from the planar segments on (001) and ($1\bar{1}1$) of APBs were scarcely observed, since the total areas of these segments were rather small.

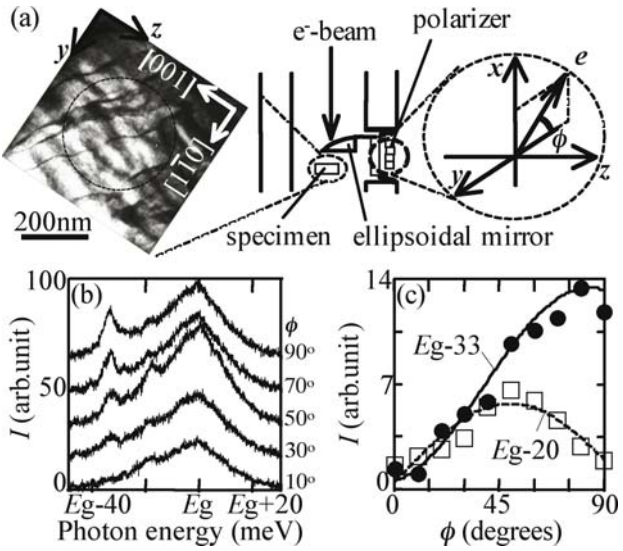


Fig. 2. (a) The experimental setup for p-CL spectroscopy. The left figure shows a dark-field TEM image of GaInP SLs on a 2° miscut substrate obtained from a SL reflection. The encircled area is characterized. A CL photon emitted from the specimen is reflected on an ellipsoidal mirror and the reflected photon is transmitted through a linear polarizer. Then, the transmitted photon is collected into a CCD detector through a monochromator. It is defined that **x** // an electron beam, and **z** // the rotation axis of the polarizer. The transmission direction ***e*** of the polarizer is determined by the rotation angle ϕ, and $\phi = 0°$ when ***e*** // **y**. The specimen was set in order that **z** // [001]. (b) p-CL spectra for various ϕ. (c) CL intensities vs. ϕ. The solid or broken curve is a calculated CL intensity for the QW on ($\bar{1}10$) or ($\bar{1}11$), respectively.

It has been proposed experimentally that the low-energy emission arises from disk-like InP layers on APBs acting as QWs (Kops et al 2000), and a theoretical study of the layers has revealed that the model explains various properties of the low-energy emission (Mattila et al 1999). Based on the InP QW model, the ϕ-dependent intensity of the photons emitted from a QW and then transmitted through my apparatus for p-CL spectroscopy was calculated (Ohno and Takeda 2002). The result for the QW on ($\bar{1}11$) or ($\bar{1}10$), respectively, explained well the ϕ-dependent intensity of the CL photon with *E*g-20 meV or *E*g-33 meV (Fig. 2c). The energy of the photons emitted from a QW should decrease with increasing the QW thick. The thickness of the InP layers on ($\bar{1}11$) or ($\bar{1}10$), respectively, was estimated to be 0.33 nm or 0.40 nm with XSTM data, and the former value was smaller than the latter one. Moreover, an InP layer thinner (0.28 nm) or thicker (0.57 nm) than the ($\bar{1}11$) and ($\bar{1}10$) InP layers, grown artificially in a GaInP alloy, emits photons with higher (*E*g-14 meV) or lower (*E*g-47 meV) energy, respectively (Carlsson et al 1994). Thus the polarization, intensity, and photon energy of the low-energy CL photons, emitted from my sample, were explained with the InP QW model.

3.2 Control of the Polarization of Low-Energy Emission

It is known that the extension directions of APBs depend on growth conditions (Takeda et al 1999). For example, Fig. 3a shows a TEM image of a GaInP alloy grown on a 10° miscut substrate, in which many planar segments of APBs extend, on average, along [001]. Polarized CL spectroscopy

revealed that the specimen emits low-energy CL photons, with about *E*g-30 meV, linearly polarized along [001] (Fig. 3b), as expected in the InP QW model. This result clearly shows that we can control the polarization of low-energy CL photons by varying growth conditions.

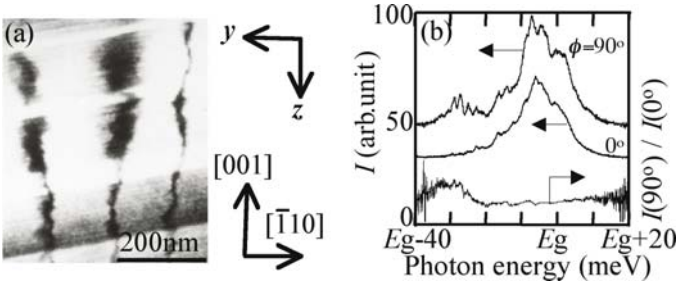


Fig. 3. (a) A dark-field TEM image of GaInP SLs on a 10° miscut substrate obtained from a SL reflection. The specimen was set in order that **z** // [001]. (b) p-CL spectra for $\phi = 0°$ and 90°.

4. CONCLUSION

Observing the arrangements of atoms by XSTM and obtaining p-CL spectra at a high spatial resolution, I have revealed the novel atomistic structure of CuPt-ordered GaInP; slanting QWs are formed spontaneously in the ordered structure. Ordered structures are commonly formed in group III-V (e.g., Chakrabarti and Kunc 2003) and II-IV (e.g., Lee et al 2002) ternary semiconductors, and similar QWs could be found in such structures. I expect that the use of my experimental method will become of increasing importance for the detection and quantitative understanding of novel optical properties in nanostructures.

ACKNOWLEDGEMENTS

This work was partially supported by the Ministry of Education, Science, Sports and Culture, Grant-in-Aid for Young Scientist (A)(2) No.15681006, 2003-2005. GaInP SLs were provided by Mitsubishi Chemical Co. I am indebted to Prof. S. Takeda for fruitful discussions.

REFERENCES

Carlsson N, Seifert W, Petersson A, Castrillo P, Pistol M E and Samuelson L 1994 Appl. Phys. Lett. **65**, 3093
Chakrabarti A and Kunc K 2003 Phys. Rev. B **68**, 045304
Gomyo A, Suzuki T, Kobayashi K, Kawata S, Hino I and Yuasa T 1987 Appl. Phys. Lett. **50**, 673
Heinrich A J, Wenderoth M, Rosentreter M A, Engel K, Schneider M A, Ulbrich R G, Weber E R and Uchida K 1998 Appl. Phys. A **66**, S959
Kops U, Blome P G, Wenderoth M, Ulbrich R G, Geng C and Scholz F 2000 Phys. Rev. B **61**, 1992
Lee H S, Lee J Y, Kim T W, Lee D U, Choo D C and Kim M D 2002 J. Appl. Phys. **91**, 5657
Liu N, Shih C K, Geisz J, Mascarenhas A and Olson J M 1998 Appl. Phys. Lett. **73**, 1979
Mattila T, Wei S H and Zunger A 1999 Phys. Rev. Lett. **83**, 2010
Ohno Y 2004 *submitted*
Ohno Y and Takeda S 2002 J. Electron Microsc. **51**, 281
Ohno Y, Kawai Y and Takeda S 1999 Phys. Rev. B **59**, 2694
Ohno Y and Takeda S 1995 Rev. Sci. Instr. **66**, 4866
Ozaki N, Ohno Y, Tanbara M, Hamada D, Yamasaki J and Takeda S 2001 Surf. Sci. **493**, 547
Smith S, Mascarenhas A, Ahrenkiel S P, Hanna M C and Olson J M 2003 Phys. Rev. B **68**, 035310
Su L C, Ho I H and Stringfellow G B 1994 J. Appl. Phys. **75**, 5135
Takeda S, Kuno Y, Hosoi N and Shimoyama K 1999 J. Crystal Growth **205**, 11

Carrier distribution in quantum nanostructures studied by scanning capacitance microscopy

F Giannazzo, V Raineri, S Mirabella[1], G Impellizzeri[1], F Priolo[1], M Fedele[2] and R Mucciato[2]

CNR-IMM, sezione di Catania, Stradale Primosole 50, I-95121, Catania, Italy
[1] MATIS-INFM and Dipartimento di Fisica e Astronomia, Università di Catania, Via S. Sofia 64, I-95123 Catania, Italy
[2] 2M Strumenti, Via G. Pontano 9, I-00141 Roma, Italy

ABSTRACT: We addressed issues related to quantitative carrier profiling by scanning capacitance microscopy (SCM) on doped layers with different dimensions, starting from thick (~5 μm) uniformly doped Si layers down to $Si/Si_{1-x}Ge_x/Si$ quantum wells with nanometre width. We preliminarily discuss the influence of the SCM hardware on the quantification, by comparing the analyses performed on Si calibration standards with two different atomic force microscopes, i.e. DI3100 by Veeco and XE-100 by PSIA, equipped with different SCM sensors. Furthermore, concentration sensitivity and spatial resolution are deeply discussed considering measurements on special designed samples containing quantum wells of $Si_{0.75}Ge_{0.25}$ layers strained between Si films. Measurements were taken on sample cross-sections and on bevelled samples. A nanometre SCM spatial resolution was demonstrated not only in terms of signal sensitivity, but also in terms of quantitative majority carrier profiling.

1. INTRODUCTION

Scanning capacitance microscopy (SCM) represents one of the main two-dimensional carrier profiling methods in semiconductors, due to its wide dynamic range (from 10^{15} to 10^{20} cm^{-3}) and high spatial resolution (Bussmann et al 2004). SCM has the advantage to be unaffected by the mobility changes inside the semiconductor, and, therefore, it is in principle particularly useful for an independent measurement of the carrier concentration profiles in $Si/Si_{1-x}Ge_x/Si$ heterostructures, which usually exhibit a depth modulation both in carrier concentration and carrier mobility. A disadvantage of SCM is its concentration dependent spatial resolution. In fact, SCM spatial resolution is limited by the SCM probe diameter for doping concentrations $\geq 10^{18}$ cm^{-3}, while it is limited by the Debye length in the semiconductor for lower doping concentrations. Concentration resolution and spatial resolution, therefore, are not independent in SCM. This property makes difficult the quantitative measurement of nanometre doping profiles in the cross-section configuration. In this paper, we demonstrate that, by opportunely choosing the geometry in sample preparation (i.e. cross section or angle bevelling) quantitative SCM measurements can be performed on doped layers with different dimensions, starting from thick (~5 μm) uniformly doped Si layers down to $Si/Si_{1-x}Ge_x/Si$ quantum wells with nanometre width.

2. EXPERIMENTAL DETAILS

Experiments were carried out on the Si and SiGe test samples described in the following. Samples (A) and (B) are, respectively, unipolar p-type and n-type staircase Si samples, consisting of a set of 5 μm thick uniformly doped layers, with concentration ranging from 5×10^{15} cm^{-3} to 8×10^{19} cm^{-3} for p-type and from 5×10^{14} cm^{-3} to 2×10^{19} cm^{-3} for n-type Si. These samples have been extensively discussed in other work (Giannazzo et al 2004). Sample (C) is a molecular beam epitaxy (MBE)

grown Si sample consisting of a 0.15 μm thick buffer layer with a 3×10^{19} cm^{-3} uniform B concentration and of a 0.70 μm thick multispike structure. This structure contains a set of five well-separated B spikes with the same width (FWHM=3 nm) and with different peak concentrations increasing towards the surface (from 1×10^{17} to 1×10^{19} cm^{-3}). Samples (D) is an MBE grown p type doped Si sample containing five $Si_{0.75}Ge_{0.25}$ wells with identical width of 5 nm, which are compressively strained between thicker Si layers. These heterostructures represent very efficient quantum wells (QWs) for holes. The five different QWs contain five different B spikes (FWHM of 2 nm) with peak concentrations ranging from 7×10^{18} cm^{-3} to 2×10^{16} cm^{-3}.

Samples (A) and (B) were prepared in the cross-section (XS) configuration, while samples (C) and (D) were prepared both in the XS and angle bevelling (AB) configurations. The thin oxide layer which is necessary for SCM measurements has been obtained by UV light exposure in an ozone ambient [5]. Conductive diamond coated Si tips, which demonstrated the best performances in terms of mechanical robustness and reproducibility of SCM measurements (Yabuhara et 2002), have been used as the SCM probes.

SCM analyses were performed in the constant ΔV mode by two different atomic force microscopes, i.e. DI3100 by Veeco and XE-100 by PSIA, equipped with different SCM sensors. The comparison between the two equipments will be used to undertake the hardware aspects.

3. RESULTS AND DISCUSSIONS

Samples (A) and (B) have been already extensively used as reference calibration standards to study how the main elements involved in the MIS nanodevice formation (tip, dielectric and dielectric/semiconductor interface) affect the SCM measurements and which is their respective influence on quantification of SCM data (Giannazzo et al 2004). Here, we use them to address a different aspect, i.e. how different hardware implementations of the SCM system can affect the measurement on samples prepared under identical conditions and carried out with the same tips. To this aim, we compared the SCM measurements on the samples (A) and (B) prepared in identical conditions by two different state of the art systems (i.e. DI3100 by Veeco and XE-100 by PSIA), both equipped with SCM sensors based on the RCA capacitive pick-up principle (Palmer et al 1982).

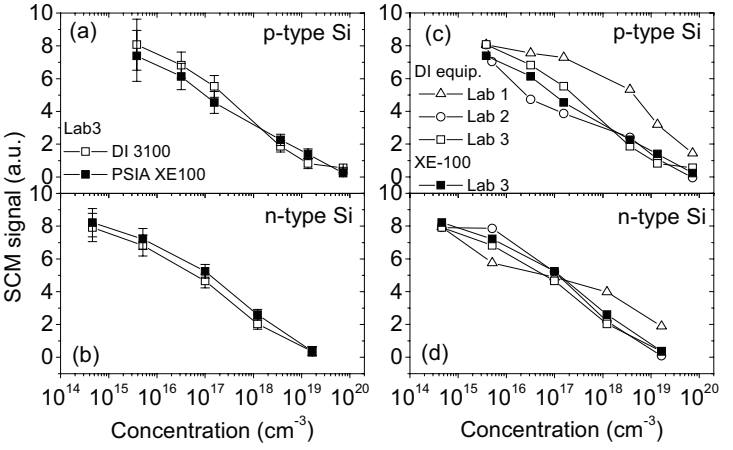


Fig. 1. SCM signal vs. concentration calibration curves measured on sample (A) (a) and (B) (b) by the DI3100 (open symbols) and XE-100 (full symbols) equipments. The error bars correspond to the range of variability of the SCM signal over a set of five different measurements performed on the same sample region during five different days. Calibration curves obtained on sample (A) (c) and (d) by different laboratories (Lab 1, 2, 3) by using the DI equipments (open symbols) and by Lab 3 using XE-100 equipment (full symbols).

In Figs.1a and 1b we report the comparison between the SCM signal vs. concentration calibration curves measured on sample (A) and (B), respectively, by the DI3100 (open symbols) and XE-100 (full symbols) equipments. We applied identical AC bias amplitudes, while the DC biases have been chosen in order to maximize the SCM signal excursion between the lowest and highest doping levels. The error bars correspond to the range of variability of the SCM signal over a set of five different measurements performed on the same sample region during five different days (Giannazzo et al 2004). This variability can be attributed to changes in the MIS nanodevice, due to the degradation of the conductive diamond tip coating, or to charge trapping in the thin oxide. The agreement is good, in the compared concentration range. In Figs.1c and 1d we show with open symbols the comparison between the calibration curves obtained by different laboratories in the context of a recent round robin (Duhayon et al 2004). All of these labs used DI equipments, but performed slightly different samples preparations procedures (Duhayon et al 2004). The full symbols in Figs. 1c and 1d represent the SCM data measured with the XE-100 equipment. All of these results show that different state-of-the-art equipments exhibit comparable concentration resolutions evaluated on staircase calibration standards like sample (A) and (B). Therefore, the SCM signal mainly depends on the physics of the MIS nanodevice on which the SCM analysis is based.

In the following we will discuss what happens when passing from the characterization in the XS configuration of a set of very thick (5 μm) uniformly doped Si layers with different concentrations to the characterization of a set of ultranarrow (3 nm) B spikes with different concentrations. In Fig. 2a, we report the 2D SCM measurement on the XS of sample (A) together with the SCM vs depth profile obtained from this measurement, while in Fig. 2b the results on the sample bevelled to obtain 100 times magnification in the depth direction are reported (note that the depth scale is rescaled by the magnification factor). It is evident that the spatial resolution and sensitivity for the XS configuration are too poor to clearly separate the contributions of the different spikes. In particular, the deepest spike (the lowest concentration one) is not visible at all, due to the averaging effect in the probed sample region, which is concentration dependent. Moreover, the 0.15 μm uniformly doped buffer layer is measured only as a bell shaped profile. On the contrary, the profiles measured on the 100 magnification sample presents well separated contributions due to the different spikes and, in particular the deepest spike with the lowest peak concentration is well characterized. Therefore, by AB, we have been able to improve both the spatial and concentration resolution on these ultranarrow B spikes. However, the carrier profile still exhibits a broadening, with a characteristic asymmetric tail extending towards the surface.

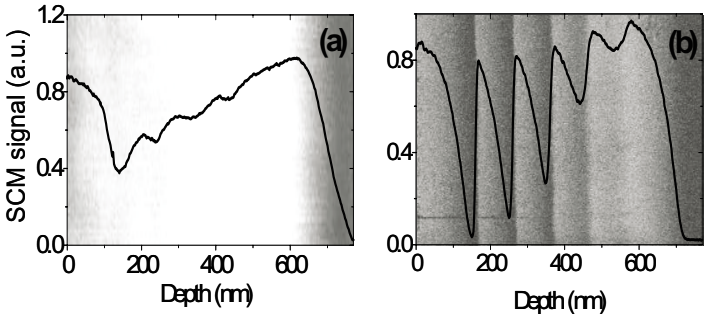


Fig. 2. 2D SCM measurement together with the SCM vs. depth profile obtained from this measurement on the cross section (a) and on the beveled surface (100 times magnification) (b) of sample (A) . Note that the depth scale is rescaled by the magnification factor.

In the following we will show the SCM profiles when the B spikes are embedded in Si/SiGe/Si QWs, which do not allow the free redistribution of majority carriers (holes) out of the QW width. In Fig. 3 we report the SCM measurement on the sample (B) bevelled to obtain a 50 times magnification, together with the carrier concentration vs depth profile obtained from the quantification of the measured SCM vs. depth profile, according to the procedure illustrated in (F Giannazzo et al 2004). The profile was measured by applying a proper negative DC bias (-0.9 Volts) to the tip (Giannazzo et al 2005).

The FWHMs measured on the hole concentration vs. depth profiles for all the five spikes are included inside the nominal well widths of 5 nm. Moreover, the hole peak concentrations are in good agreement with those measured by secondary ions mass spectrometry (SIMS) for all the B spikes, except for the highest one, whose peak concentration is more than a factor of two lower than the SIMS one. Furthermore, it should be noted that the same SCM spike exhibits very long tails starting from a concentration of 8×10^{17} cm^{-3}, much longer than the tails exhibited by all the other spikes, which can be attributed to the quantum hole distribution beyond the potential well. This behaviour for the highest concentration spike suggests that a hole concentration of 2×10^{18} cm^{-3} could completely fill all the energy states available in the quantum well, with the consequent falling out of the holes in excess to this concentration.

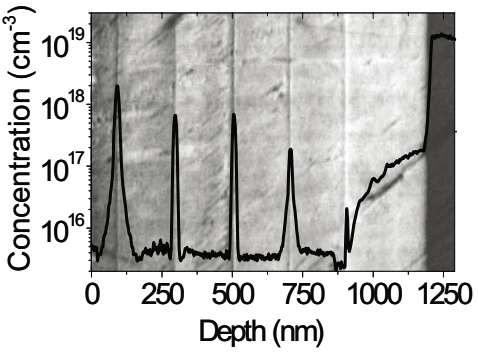


Fig. 3. SCM measurement on sample (B), together with the carrier concentration vs depth profile obtained from the quantification of the measured SCM vs. depth profile.

4. CONCLUSION

In conclusion, we demonstrated that, by opportunely choosing the geometry in sample preparation (i.e. cross section or angle bevelling) quantitative SCM measurements can be performed on doped layers with different dimensions, starting from thick (~5 μm) uniformly doped Si layers down to $Si/Si_{1-x}Ge_x/Si$ QWs with nanometre width.

ACKNOWLEDGEMENTS

The authors thank S di Franco, from CNR-IMM, sezione di Catania, for the expertise technical assistance and E Napolitani, from MATIS-INFM and Dipartimento di Fisica, Università di Padova, for SIMS analyses.

REFERENCES

Bussmann E and Williams C C 2004 Rev. Sci. Instrum. **75**, 422

Duhayon N et al 2004 J. Vac. Sci. Technol. B **22**, 385

Giannazzo F, Raineri V, La Magna A, Mirabella S, Impellizzeri G, Piro A M, Priolo F, Napolitani E and Liotta S F 2005 J. Appl. Phys. **97**, 014302

Giannazzo F, Goghero D and Raineri V 2004 J. Vac. Sci. Technol. B **22**, 2391

Giannazzo F, Goghero D, Raineri V, Mirabella S and Priolo F 2003 Appl. Phys. Lett. **83**, 2659

Yabuhara H, Ciappa M and Fichtner W 2002 J. Vac. Sci. Technol. B **20**, 783

Palmer R C, Denlinger E J and Kawamoto H 1982 Capacitive-pickup circuitry for VideoDiscs, RCA-Review, **43**, 194

Mapping of the effective electron mass in III-V semiconductors

M H Gass, A M Sanchez[1], A J Papworth[2], T J Bullough[2], R Beanland[3] and P R Chalker[2]

Department of Materials Science and Metallurgy, Pembroke St, University of Cambridge, CB2 3QZ, UK
[1] Departamento de Ciencia de los Materiales e IM y QI, Universidad de Cádiz, Apdo 40 E-11510 Puerto Real (Cadiz), Spain
[2] Department of Engineering, University of Liverpool, L69 3GH, UK
[3] Bookham Inc, Caswell, Towcester, Northants, NN12 8EQ, UK

ABSTRACT: The effective mass in semiconductors is related to the mobility of charge carriers as well as the density of states. As electron mobility inherently influences semiconductor device performance, knowledge of the effective electron mass (m_e*) is important, and significant effort is applied to obtain accurate values. In this work, low-loss electron energy loss spectroscopy is exploited to produce maps showing the variation of m_e* with nanometer scale resolution for a range of semiconductors. The calculated values of all systems have proven to be in agreement with the literature.

1. INTRODUCTION

Central to understanding the performance of semiconductor devices is the measurement of the electron or hole effective masses. The effective mass allows electrons and holes to be treated as classically charged particles, and in semiconductors is related to the mobility of charge carriers as well as the density of states. The mobility μ can be calculated using,

$$\mu = \frac{ek_BT}{m^*} \quad (1)$$

where e is the electronic charge, k_B is the Boltzmann constant and T is temperature. Following equation 1, the smaller the effective mass, the higher the mobility. This paper will concentrate on the effective electron mass (m_e*), which is related to the electron mobility. As electron mobility inherently influences semiconductor device performance, knowledge of m_e* is important and significant effort is applied to obtain accurate values.

Many groups have experimentally measured the variation of m_e* with composition for different semiconductor alloys using direct methods such as cyclotron resonance (Hai et al 2000) and indirect methods such as the analysis of the carrier confinement energies (e.g. Pan et al 2001). Several groups have calculated the electron effective mass from the plasmon frequency (ω_p) using the formula,

$$m_e^* = \frac{n\ e^2}{\omega_p^2 \varepsilon_0 \varepsilon_\infty} \quad (2)$$

where n is the number of electrons associated with the plasmon, ε_0 the permittivity of free space and ε_∞ the high frequency dielectric constant. Various values for ω_p and n have been used in equation 2. For example, m_e* can be determined using techniques such as infrared spectroscopic ellipsometry and micro-Raman scattering from the plasma-LO phonon modes of doped zinc-blende semiconductors (Metzger et al 2002), hexagonal InN (Kasic et al 2002) and GaN (Perlin et al 1995) with n taken to be the Hall concentration. The m_e* has also been determined using synchrotron-excited ultraviolet photoemission spectroscopy from the surface plasmon of TiN (Walker et al 1998), in which case n was presumed to be dependant on the number of Ti3d states involved in bonding.

All previously published results for m_e* have been single value averages from point or bulk analyses of samples. It has not been possible to investigate local changes in m_e* on a nanometer scale. The properties of semiconductor devices and therefore m_e* change with elemental composition, and although the average m_e* of a quantum well laser can be determined using conventional carrier measurements, quantum wells (and dots) often contain non-uniform elemental compositions. In a previous publication (Gass et al 2004), we reported the mapping of the plasmon frequency (ω_p) with nanometer resolution in a scanning transmission electron microscope (STEM), over a cross-sectional GaInNAs quantum well surrounded by GaAs. From the plasmon frequency map, the average difference between m_e* for the quantum well and m_e* for the GaAs substrate was obtained.

It will be shown that by applying the *Kramers-Kronig* transformation to the electron energy loss spectra at each pixel acquired within a spectrum image, using a field emission gun STEM, m_e* can be mapped at nanometer resolution. Nanoscale maps of m_e* for a GaInNAs/GaAs quantum well, and InAs quantum dots in GaAs will be presented. Finally, the procedure will be applied to the point analysis from a wurtzitic GaN epilayer.

2. EXPERIMENTAL

Ion beam thinned cross-sections of the samples were analysed in a VG HB601UX STEM, equipped with a Gatan Enfina electron energy loss spectrometer achieving a 0.30eV full width half maximum zero loss peak. Spectrum images were acquired with pixel sizes in the region of 1nm, an EELS spectrum is acquired at each pixel and E is the energy range of the spectrum. In this work, a 'map' is defined as a 2D representation of information, where each pixel contains only a value. For analysis of the low-loss EELS spectrum, both the zero loss peak and plural scattering were removed using a Fourier log deconvolution routine to obtain the single scattering distribution (SSD).

The low-loss region (energy loss <100 eV) of the EELS spectrum contains the zero loss peak, information about energy-loss transitions from valence band to the conduction band, and plasmons. The valence plasmon can be defined as an oscillation of the valence electrons, which have been promoted to the conduction band minimum. The valence plasmon energy is related to the effective electron mass (m_e*):

$$m_e^* = \frac{n\,\hbar^2}{E_p^2 \varepsilon_0 \varepsilon_\infty} \tag{3}$$

where $\hbar$ is Plank's constant, E_p is the plasmon energy (in eV), ε_∞ is the high frequency dielectric constant and n is the density of electrons that have been promoted to the conduction band minimum at the plasmon energy. It is possible to calculate the effective electron mass at the conduction band minimum from E_p, as long as n and ε_∞ are known. The plasmon energy E_p was determined from the SSD by fitting a Gaussian to the plasmon peak and taking its centre to be E_p. E_p is calculated at every pixel within the spectrum image and the resulting map of E_p shows the variation in plasmon energy over the mapped region.

By applying the *Kramers-Kronig* transformation to the SSD, the imaginary parts of the dielectric function $\varepsilon_2(E)$ can be determined. From $\varepsilon_2(E)$ the spectrum of the effective number of electrons per unit volume, n_{eff}, which is a function of energy, can be calculated using:

$$n_{eff}(\varepsilon_2) = \frac{2\varepsilon_0 m_0}{\pi \hbar^2 e^2} \int_0^\infty E' \varepsilon_2(E') dE' \tag{4}$$

the density of electrons associated with the valence plasmon, n, is then taken to be the effective electron density $n_{eff}(E)$ at the plasmon energy E_p. Using the accepted value of 44.2 atoms per nm^3 for the atomic density of GaAs, an average electron density of 3.4 electrons per atom is obtained from the experimental data (E_p=16eV), slightly under the 4 valence electrons per atom average for GaAs. This procedure is applied to every pixel and a map is produced of n.

Ideally the variation of ε_∞ across the mapped area should be included in the calculation of m_e*. ε_∞ can be extracted from the effective dielectric constant $\varepsilon_{0,eff}(E)$ related to ε_2:

$$\varepsilon_{0,eff}(E) = 1 + \frac{2}{\pi} \int_0^{E_0} \frac{\varepsilon_2(E)}{E} dE \tag{5}$$

ε_∞ is taken to be the intensity of $\varepsilon_{0,eff}(E)$ when it reaches a plateau (generally <20eV) and a map is produced. The maps of E_p, n and ε_∞ are then put back into equation 3 to produce a map of m_e*.

3. RESULTS

The three figures show the bright field images of the III-V structures as well as E_p and m_e* as false colour maps. It can be seen from E_p in Fig. 1 that the GaInNAs QW is non-uniform, but shows a general decrease in plasmon energy with respect to the GaAs (E_p = 16.0eV), this is expected as although the introduction of In to GaAs reduces E_p and the introduction of N to GaAs increases E_p at similar rates, the concentration of In is much greater than N. Figure 2 shows a similar decrease in plasmon energy over the GaInNAs QW and the increasing Al concentration in the graded layer can clearly be seen with a resulting decrease in E_p. In both Fig.s 1 and 2, the maps show an increase of m_e* through the QW, with m_e* for GaAs measured at ~0.075 m_0, this is expected as even small additions of N to GaInAs have been seen to increase m_e*. It is also observed in Fig. 2 that m_e* increases gradually with the increase in Al concentration.

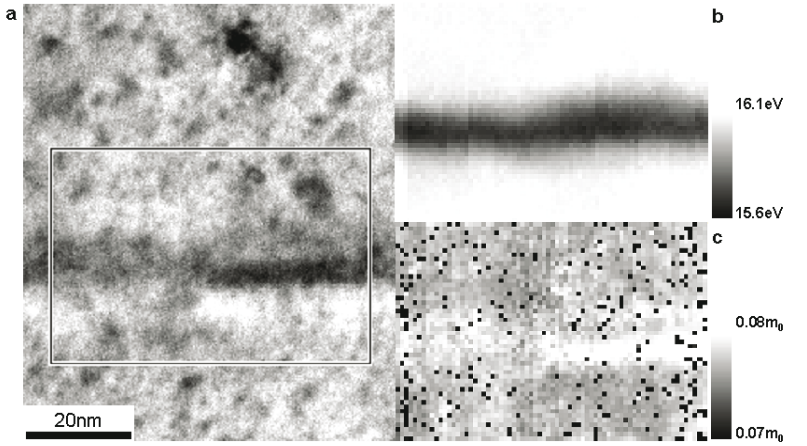


Fig. 1. a) A bright field image of a $Ga_{0.65}In_{0.35}N_{0.01}As_{0.99}$ QW flanked by GaAs, the EELS data was acquired from the boxed region, b) the map of E_p calculated from the SSD, and c) the map of m_e*. The black pixels in c) are due to poor removal of the ZLP.

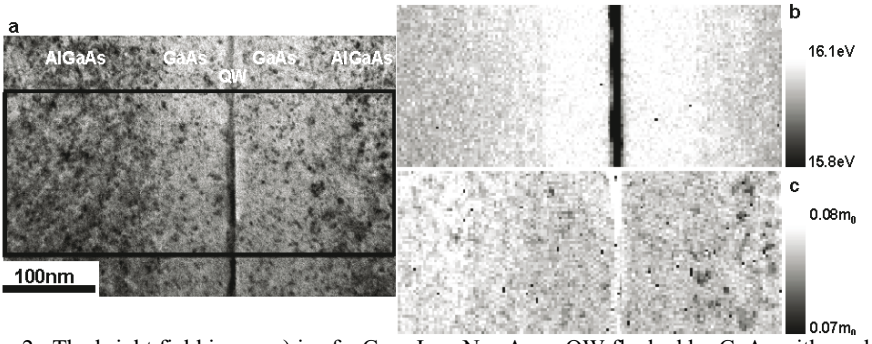


Fig. 2. The bright field image a) is of a $Ga_{0.65}In_{0.35}N_{0.01}As_{0.99}$ QW flanked by GaAs with graded AlGaAs layers either side, the EELS data was acquired from the boxed region. b) shows the map of E_p, and c) the map of m_e*, where an increase can be seen over the QW and in the AlGaAs layers. Note that a constant value of 10.89 was used for ε_∞ rather than a map as the map of ε_∞ was found to add an unacceptable level of noise to the resulting map of m_e*.

The InAs QDs in Fig. 3 show a decrease in plasmon energy with respect to GaAs, as well as a decrease in m_e*. The observed decrease in E_p and m_e* is not as great as expected for InAs, as the QDs have a diameter of ~20nm and are in a specimen ~70nm thick. The QDs analysed are therefore $Ga_xIn_{1-x}As$.

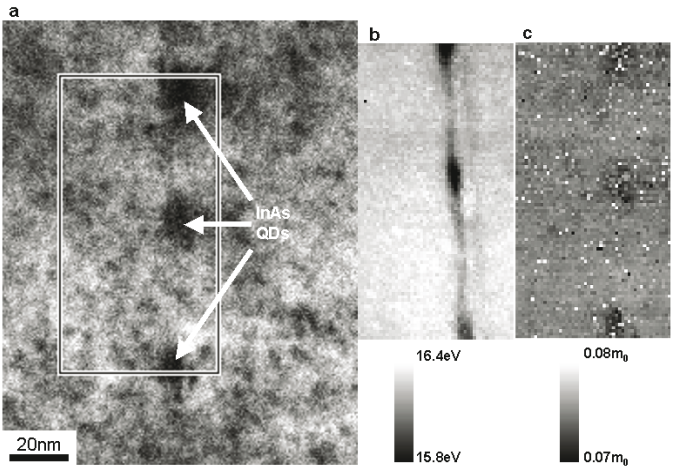


Fig. 3. a) The bright field image shows InAs QDs in a GaAs matrix, the EELS data was acquired from the boxed region. b) shows the map of E_p, and c) the map of m_e*, where a decrease can be seen over the QDs. Note that a constant value of 10.89 was used for ε_∞ rather than a map as the map of ε_∞ was found to add an unacceptable level of noise to the resulting map of m_e*.

As a final test of the proposed methodology, m_e* for bulk wurzitic GaN has also been determined using the same procedure. Using the accepted value of ε_∞ = 5.35 for GaN, and experimental values from EELS data of E_p = 19.42eV and n = 26.8 electrons per m^3, the value of m_e* has been calculated as $0.183m_0$, in agreement with the accepted values, where m_e* (GaN) = 0.20 m_0 from cyclotron resonance measurements (Drechsler et al 1995).

4. SUMMARY

By applying the *Kramers-Kronig* transformation to EELS spectra, m_e* has been determined for a range of direct-gap semiconductors and for the first time, the fluctuation of m_e* on a nanometre scale can be shown. The results obtained for the different materials are in good agreement with experimental and theoretical values for both GaAs and GaN. Other research groups have used the same calculation (equation 3) for determining point or bulk values for m_e* where the data has been obtained from several different experimental techniques.

REFERENCES

Drechsler M, Hoffman D M, Meyer B K, Detchprohm T, Amano H and Akasaki I 1995 Jpn. J. Appl. Phys. Part 2, **34**, L1178

Gass M H, Papworth A J, Joyce T B, Bullough T J and Chalker P R 2004 Appl. Phys. Lett. **84,** 1453

Hai P N, Chen W M, Buyanova I A, Xin H P and Tu C W 2000 Appl. Phys. Lett. **77**, 1843

Kasic A, Schubert M, Saito Y, Nanishi Y and Wagner G 2002 Phys. Rev. B **65**, 115206

Metzger W K, Wanlass M W, Gedvilas L M, Verley J C, Carapella J J and Ahrenkiel R K 2002 J. Appl. Phys. **92**, 3524

Pan Z, Li L H, Lin Y W, Sun B Q, Jiang D S and Ge W K 2001 Appl. Phys. Lett. **78**, 2217

Perlin P, Litwin-Staszewska E, Suchanek B, Knap W, Camassel J, Suski T, Piotrzkowski R, Grzegory I, Porowski S, Kaminska E and Chervin J C 1995 App. Phys. Lett. **68**, 1114

Walker C G H, Matthew J A D, Anderson C A and Brown N M B 1998 Surf. Sci. **412**, 405

Reconstruction of images of surface height in scanning electron microscopy

C G H Walker, M M El Gomati[1] and V Romanovsky[1]

YSBL, Department of Chemistry, University of York, Heslington, York, YO10 5DD, UK
[1] Department of Electronics, University of York, Heslington, York, YO10 5DD, UK

ABSTRACT: Existing scanning electron microscopes provide poor estimation of the height of surface features. Although topographic information can be provided by the use of several detectors, they provide an estimation of local surface angle, not the height of surface features. A new low energy scanning electron microscope equipped with a six fold detector was used to acquire images of the local surface angle of a sample. In addition, a technique which has not been previously applied to SEM data was used to integrate the images of the differential of the surface height. The algorithm is fast and resistant to noise which should allow almost real time reconstruction of images of surface height.

1. INTRODUCTION

The scanning electron microscope (SEM) is widely used within the semiconductor manufacturing industry and is frequently used in critical dimension (CD) work. However, although the SEM provides accurate information for the horizontal dimensions x and y, it does not provide good vertical scale (z) data. However, using detectors placed at different angles it is possible to determine the local surface angle (dz/dx, dz/dy) at each point in the image. In order to determine the surface height, such images should be integrated. Unfortunately, noise and distortion within the images of local surface angle makes this a difficult task.

Castle and Zlidan (1997) reviewed surface topography measurements using SEM and reported that a major problem for surface topography measurements in the SEM is the diffusion and scattering of high energy electrons within the substrate. A method of reducing the energy of the primary beam electrons has been introduced by Frank et al (2000). However, until now, this technique allowed electrons to be acquired at just one take off angle. A new low energy SEM is introduced in a paper at this conference (Romanovsky et al 2005) which is equipped with a six fold detector which allows the acquisition of dz/dx and dz/dy images.

"Shape from Shading" (SFS) is a name given to a technique which is used to derive a surface height image from just a single image of an object illuminated by light. An intermediate stage within SFS is to derive an image of the local surface angle (i.e. dz/dx and dz/dy) images. Hence, there are similarities between SFS and attempts to derive SEM height images. This has been noted before (Horn and Brookes 1985, Carlsen 1985, Beill and Carlsen 1990, Beill and Carlsen 1991, Reimer et al 1987, Bony et al 2004, Ahammad and Mukherjee 2002, Scherer et al 1999, Danzl and Scherer 2003, Paluszynski and Slowka).

However, these previous attempts have been unsatisfactory in that they can be computationally expensive to implement and suffer from noise (e.g. Carlsen 1985). Frankot and Chellappa (1988) introduced an approach to integrating noisy dz/dx and dz/dy images to produce a best fit height image. To the authors' knowledge, this approach has never been used on SEM images. It should be emphasised that the SFS methods assume that the reconstructed surface does not have any sudden discontinuities in height, i.e. the method is ideally suited to samples which have a surface topography similar to "rolling hills" and not to the Grand Canyon!

2. SURFACE INTEGRATION

The method of Frankot and Chellappa (1988) involves the use of Fourier Transforms to integrate the dz/dx and dz/dy images. If $C_x(\omega)$ is the Fourier Transform of the dz/dx image and $C_y(\omega)$ is the Fourier Transform of the dz/dy image, then Frankot and Challapa (1988) showed that the Fourier Transform of the height image, $C(\omega)$, is given by

$$C(\omega) = \frac{-j\omega_x C_x(\omega) - j\omega_y C_y(\omega)}{|\omega_x|^2 + |\omega_y|^2} \qquad (1)$$

where ω is the spatial frequency vector and ω_x and ω_y are the spatial frequencies in x and y directions respectively.

Inspection of equation (1) reveals that at $\omega_x = 0$, there is no contribution from $C_x(\omega)$ and similarly for ω_y. This implies that if the dz/dz and dz/dy images have a non-zero average value, then the reconstructed height image will ignore these values (i.e. $C_x(\omega=0)$ and $C_y(\omega=0)$). Hence, the input dz/dx and dz/dy images should be processed to have a zero average value prior to applying equation (1). In addition, the reconstructed surface image will be distorted by the need for periodic boundary conditions. These difficulties can be overcome by forming mirror images of the dz/dx and dz/dy images such that the height image has zero average slope in both x and y directions and has the same height on opposite sides of the height image. The resulting input image is shown in Fig. 1 assuming that the initial dz/dx and dz/dy images form an L shape. The resulting image has four times the area of the original image. After inverse Fourier Transforming the $C(\omega)$ image, the original quarter of the image is used as the final height image.

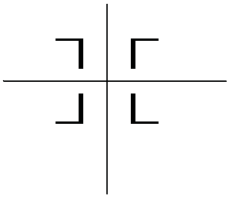


Fig. 1. Schematic image showing how the input images are reflected to create new images consisting of 4 mirrored versions of the original images. The original image is shown at bottom right and has an L form. The dz/dx image is multiplied by -1 for the two mirrored images on the left hand side and the dz/dy image is multiplied by -1 for the two mirrored top images. In this way, the final image, z(x,y), should have a zero average slope in the x and y directions and have periodic boundary conditions.

3. SCANNING LOW ENERGY ELECTRON MICROSCOPY

The low energy SEM instrumentation used in this work is described by Romanovsky et al (2005) in this conference. The method by which the dz/dx and dz/dy images were formed is shown in Fig. 2.

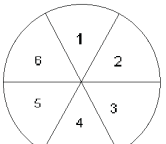


Fig. 2. The detector used to acquire the images. If I1 and I4 are the signals on detectors 1 and 4 respectively, then the dz/dy image was formed using (I1-I4)/(I1+I4)

Similarly, the dz/dy image was formed using:
((I5+I6)-(I2+I3))/(I2+I3+I5+I6)

4. EXPERIMENT AND RESULTS

The sample was an anisotropically etched Si(100) substrate creating polyhedra with eight (133) facets, four (111) facets and one (001) facet on the top. The etched sample was kindly provided by

Dr. K. Bean, Central Research Laboratories, Texas Instruments, Dallas. The samples were imaged at 70eV primary beam energy. Figure 3 shows the dz/dx image and Fig. 4 shows the dz/dy image. Figure 5 shows Fig. 4 expanded according to the method described in Fig. 1. Although there are facets on each side of the polyhedra, these are difficult to discern in Figs. 3 and 4. The images were processed with the help of Matlab files written by Kovesi (2004). The reconstructed surface topography is shown in Fig. 6. Although the facets within the polyhedra are not visible, they are also difficult to discern in the original dz/dx and dz/dy images. In addition, the dz/dy images show bright features above and to the right of the features and the dz/dx images tend to be brighter on the left and above. This will cause difficulties for the reconstruction algorithm and needs further future work. The dz/dx image shows the flat area on the right to be darker than the flat areas on the left. This causes the final reconstructed image to have different slopes in these regions. Since the low energy SEM technique is particularly surface sensitive, then these regions could have slightly different surface composition or surface electronic behaviour.



Fig. 3. The image of the differential with respect to x, dz/dx. Note that the image is bright on the left and dark on the right of each feature. The image appears to be darker on the flat region at the far right as compared to the flat regions at the left hand side of the image. This will lead to some inaccuracies in the reconstructed image.



Fig. 4. The image of the differential with respect to y, dz/dy. The image is brighter above a feature and darker below it. The features also appear to be somewhat brighter on the right of the features. It is not clear why this should be, but it could lead to distortions in the reconstructed image.

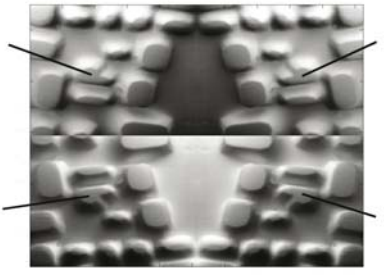


Fig. 5. The image of the differential with respect to y, dz/dy expanded according to the approach outlined in Figure 1. Note that in the upper half of the image the features are bright above and dark below each feature. In the reflection below, the opposite is the case. The lines point to the same feature in each of the four reflections.

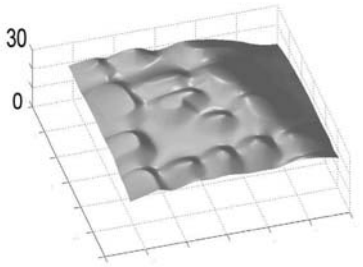


Fig. 6. Image of the reconstructed surface. The height image can be used to find the actual dimension or volumes of the features within the image. The sudden bend downwards at the right is caused by the dz/dx image is darker in this area (see Fig 3). The height is given in μm.

5. CONCLUSIONS

The low energy SEM equipped with a six detectors provides information which can be used to show local surface angle. The images of surface angle were integrated using a method involving Fourier Transforms which had not previously been applied to SEM data. The resulting height image can be used to provide useful new information on the dimension of features within semiconductor materials. The algorithm is fast and could be applied in almost real time and could equally be applied in ordinary SEMs using more widely used detectors such as Backscattered electron detectors.

ACKNOWLEDGEMENT

We thank Prof M Prutton for his assistance with the work presented in this paper.

REFERENCES

Ahammad P and Mukherjee A 2002 22nd Annual BACUS Symp. Photomask Technol. Proc. SPIE **4889**, 365

Beill W and Carlsen IC 1990 J. Microsc. **157**, 127

Beill W and Carsen IC 1991 Machine Vision and Appl. **4**, 271

Bony A, Heid A, Takakura Y, Satzke K and Meyrueis P 2004 Integrated Optics, Devices, Materials and Technologies VIII, Proc. SPIE **5355**

Carlsen IC 1985 Scanning **7**, 169

Castle JE and Zlidan PA 1997 J. Phys. D: Appl. Phys. **30**, 722

Danzl R and Scherer S 2003 vrvis Tech. Rep. TR VRVis 2003 03 (http://vrvis.at/TR/2003/TR_VRVis_2003_030_Full.pdf)

Frank L, Mullerova I and El Gomati MM 2000 Ultramicroscopy **81**, 99

Frankot RT and Chellappa R 1988 IEEE Trans. Pattern Anal. Machine Intell. **4**, 439

Horn B K P and Brooks M J 1989 Shape from Shading, (Cambridge MA, MIT Press)

Kovesi P (2004) (http://www.esse.uwa.edu.au/~pk/)

Paluszynski J and Slowka W Wroclaw Univ. Tech., Fac. Mic. Elec. Phot. (http://www.wemif.pwr.wroc.pl/zue/3drece/)

Reimer L, Böngeler R and Desai V 1987 Scanning Microscopy **1**, 963

Romanovsky V, El Gomati MM and Day J 2005 *this Proceedings volume*

Scherer S, Klaus A and Pinz A 1999 Proc. Workshop Austr. Assoc. Patt. Recog. **99**

Low energy scanning analytical microscopy (LeSAM) for Auger and low voltage SEM imaging of semiconductors

V Romanovsky, M El-Gomati, T Wells and J Day[1]

University of York, Dept. of Electronics, York, YO10 5DD, UK
[1] University of Bristol, Tyndall Avenue, Bristol BS8 1TH, UK

ABSTRACT: A new low energy scanning analytical microscope (LeSAM), combining scanning electron microscopy (SEM), scanning low energy electron microscopy (SLEEM), Auger electron spectroscopy (AES) and scanning Auger mapping (SAM), was realized using a new mini-electron column in conjunction with a cylindrical mirror analyser (CMA). The SLEEM mode of operation uses a cathode lens in which the specimen is negatively biased. In this arrangement, electrons pass through the microscope at high energy and are decelerated to a low incidental energy at the specimen. A novel 6 segment angular resolved in-lens detector is employed for signal detection. The new mini-electron column in SLEEM mode gives high resolution for primary incident beam energies of a few eV. For AES and SAM modes of operation a 6 segment angular resolved detector is also employed for signal detection.

1. INTRODUCTION

For true SEM surface studies very low energy electron probes, <10eV, are required to confine the interaction volume and subsequent signal electron generation to a specimen surface (Reimer 1998). At present commercially available microscopes operate with primary beam energies from 1-30keV in standard imaging modes. A number of microscopes can operate even below 200eV, however, the use of the such low beam energies causes reduced image resolution due to low beam current, increased aberrations and sensitivity to electrostatic or magnetic fields (i.e. defocusing the probe by SE collecting field) (Frank et al 2000).

Operation in the SLEEM cathode lens mode overcomes the above-mentioned problems of conventional LEEM. In the SLEEM mode, the sample is biased negatively forming a decelerating lens between the sample and the anode of the microscope. The primary electrons are accelerated through the electron column at high energy and are decelerated to the probe energy at the specimen surface by the decelerating field formed in the cathode lens, with probe energies <10eV. Also using very low energy electron probes can reduce or in some cases completely get rid of charging on non-conductive or poorly conductive samples.

2. MINI-ELECTRON COULMN AND SLEEM DETECTOR

The present LeSAM was developed for the investigation of semiconductor surfaces and dopant contrast in semiconductors due to surface ad-layers. The electrostatic electron column is 45mm in diameter and 85 mm long including the electron source and a 6 segment in-lens detector for SLEEM imaging. For high brightness, a Schottky Field Emitter (SFE) was used as the electron source. The vacuum constraints for operating a SFE were not a problem as the LeSAM is operated in ultra high vacuum (UHV) to maintain surface cleanliness. The cathode, suppressor and extractor are constructed as one pre-aligned mini-module (provided by YPS) with dimensions of 20mm diameter and 20mm length. This configuration ensures easy installation and high precision of mechanical alignment of the cathode to the rest of the column, which due to the small dimensions is very important for achieving small spot sizes <30nm (Mullerova et al 2003). For the final alignment of the beam onto the electron optical axis, a two-stage deflector system is used. Scanning and astigmatism correction was implemented using an 8-pole electrostatic, double stage deflection system,

giving a field of view around 1 mm for a working distance of 5 mm. A schematic configuration of the new column is shown in Fig .1. The column has been operated up to a beam energy of 10 kV.

In the middle of the column is the mirror electrode that has a small aperture of <100µm. The mirror electrode has two important functions:

1. As the primary beam-limiting aperture.
2. In the SLEEM mode deflecting the signal electrons back onto the 6 segment detector electrodes.

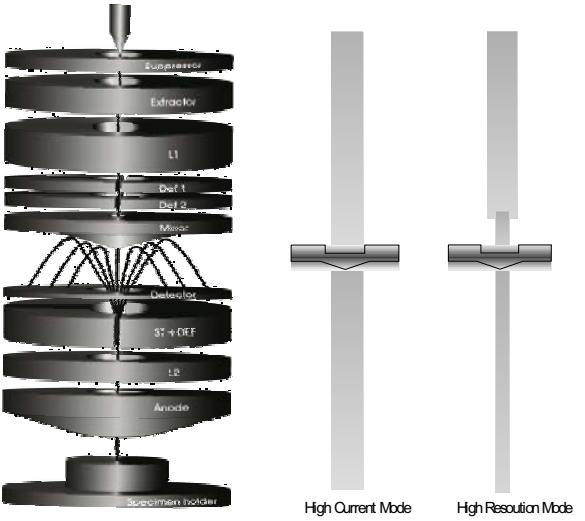


Fig. 1. The schematic configuration of he new LeSAM column operating in Hi-Current or Hi-Resolution mode

It is possible to operate the microscope in two different modes as shown in Fig. 1. In the high-resolution mode for SEM and SLEEM imaging, the crossover is created before the beam limiting aperture and only electrons close to the electron optical axis are used for imaging. In the high current mode for AES the crossover is created in the aperture and nearly all the electrons hit the sample. In this mode we can deliver sample currents of over 100nA for high speed SAM imaging.

The in-lens detector consists of a mirror lens, micro channel plate and detection electrodes. The detector is divided into six equal channels covering a 360° angle. All six channels of the new detector are connected with special preamplifiers by miniature gold plated relays. These relays are driven by a microprocessor and allow the detector channels to be joined together in any combination. The amplifiers float at a potential and are connected through opto-isolation amplifiers directly with a high-speed A/D computer card. The maximum scanning resolution is 4096x4096 points. All inputs have a resolution of 16 bits.

3. CMA 6-CHANNEL DETECTOR

The original Channeltron detector for the CMA was replaced with a new double channel plate detector. The detection electrode was divided into 6-channels covering 360°. In this configuration, it is possible collect CMA spectra from all 6 channels at the same time which allows for the elimination of topographic effects in the Auger spectra. New low-noise amplifiers have been developed to increase the SNR of the collected data. Fig. 2 shows an example of auger spectra collected by the CMA detector. The differences in the spectra seen are due to the topography of the sample.

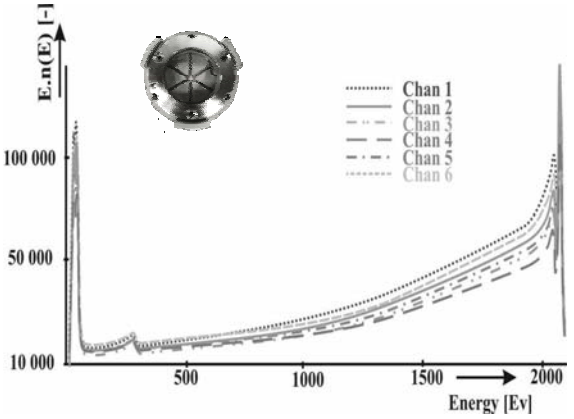


Fig. 2. 6-Channel CMA detector and 2keV primary beam Auger spectra collected by the detector.

4. COMBINATION OF SLEEM IMAGING AND AES

In many cases the observed contrast in SEM images changes as a function of the beam energy. Unforeseen surface and sub-surface artefacts cannot always be identified and the history of the sample combined with SEM imaging alone does not provide enough data for reliable image interpretation. For example, the explanation of the exploitation of low-energy electrons to observe contrast between differently doped semiconductor regions in SLEEM (Petrovic et al 1995). Also false artefacts, due to surface topography and subsurface atomic number variations, affect surface elemental mapping in SAM.

The combination of SEM and AES modes of operation in the LeSAM allows for better understanding of surface and subsurface atomic number variations for present image acquisition techniques. The corresponding 6 CMA and 6 in-lens detector channels have the same orientation for the signal electrons allowing correlation of the data collected by the two different detectors.

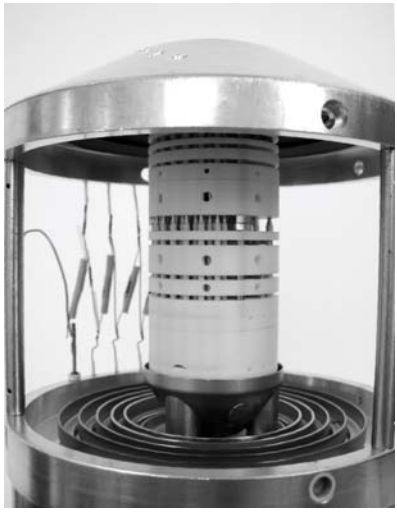
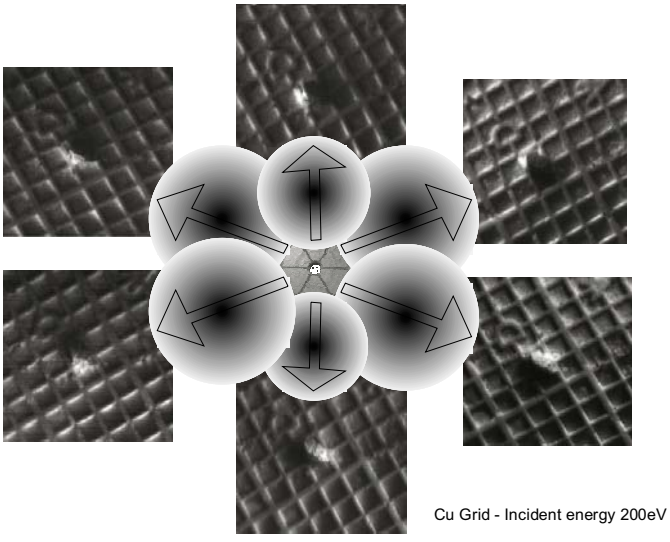


Fig. 3. New scanning low energy electron microscope accommodated in the CMA

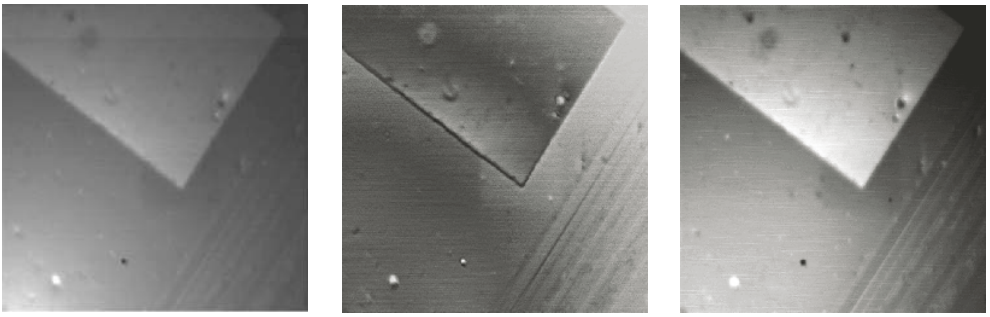
Figure 3 shows the new high resolution and fully electrostatic mini-column accommodated inside the cylindrical mirror analyser (CMA). The software developed allows parallel acquisition and display of all six SLEEM channels in real time. The software also has SAM mapping for the six independent CMA channels as well as standard Auger spectral acquisition. The latest version of this software created by J. Day is undergoing further development.

5. RESULTS



Use of the 6-channel in-lens SLEEM detector for imaging in the cathode lens mode shows large differences in the images from each channel. The topographical and material contrast obtained increases as the incident electron energy is decreased, as shown in the micrographs in Fig. 4. By software manipulation of the micrographs, it is possible to produce pseudo RGB micrographs and increase material and topographic contrasts.

Fig. 4. Micrographs of a copper grid acquired using the 6 channel in-lens SLEEM detector. Beam energy = 3.5kV; Incident electron energy = 200eV; field of view = 0.5mm



a) Micrograph from channel 1 *b) Topographic contrast* *c) Material contrast*

Fig. 5. Examples of Micrographs of Si showing the material and topographic contrast, by adding and subtracting signals collected from opposite channels of In-lens detector. (3kV Beam , 20eV landing energy), field of view = 0.1mm

Figure 5 (converted to greyscale) shows software manipulation of the images to produce an increase in the topographic contrast (Fig. 5b) and the material contrast (Fig. 5c) in comparison to Fig. 5a. 3D surface reconstruction from micrographs collected with the 6 channel SLEEM detector has been performed by software developed by Walker et al (2005).

6. CONCLUSION

With the new microscope working in the cathode lens mode it is possible to collect very low energy images in the range of a few eV. SLEEM images at low incident beam energy are highly surface sensitive and used in combination with the AES and SAM modes of operation make the LeSAM a powerful surface science analytical tool due to the ability to detect different surface generated signals and characterise them topographically and for materials studies. In addition to the LeSAM, the UHV system incorporates an ion gun for sample cleaning, two metal evaporators for in-situ thin film deposition and a sample heater for annealing samples up to 1000^{o}C.

The multiple modes of operation and subsequent data collected with the LeSAM will help to better understand observed surface phenomena. One area of research the LeSAM is currently being employed for is the SE contrast between differently doped semiconductor areas, as reported by Zaggout and El-Gomati (2005).

ACKNOWLEDGEMENT

This project was supported by the Royal Society (UK).

REFERENCES

Frank L, Mullerova I and El Gomati M M 2000 Ultramicroscopy **81**, 99
Mulerova L and Frank L 2003 Advances in Imaging and Electron Physics **407**, 128
Petrovic D D et al 1995 Ultramicroscopy **104**, 58
Reimer L 1998 Scanning Electron Microscopy p 230
Walker C, Gomati M M and Romanovsky V 2005 *this Proceedings volume*
Zaggout F and El Gomati M M 2005 *this Proceedings volume*

The electric field and dopant distribution in p-i-n structures observed by ionisation potential (dopant contrast) microscopy in the HRSEM

E Grunbaum[1], Z Barkay[2], Y Shapira[1,2], K Barnham[3], D B Bushnell[3], N J Ekins-Daukes[3], M Mazzer[3] and P R Wilshaw[4]

[1] Dept. of Physical Electronics, Faculty of Engineering, Tel-Aviv University, Israel
[2] Wolfson Applied Materials Research Centre, Tel-Aviv University, Israel
[3] Dept. of Physics, Imperial College of Science, Technology & Medicine, London, UK
[4] Dept. of Materials, University of Oxford, UK

ABSTRACT: The method of ionisation potential (dopant contrast) microscopy in the HRSEM is applied to the study of the electric field distribution in p-i-n structures used as quantum well solar cells. Our results show a secondary electron signal which varies between the different layers, being greatest in the p–type and smallest in the n-type regions respectively. The stacks of 8 nm wide quantum wells and their corresponding barriers are clearly distinguished in the intrinsic region of the devices. In-situ observation of reverse biased structures has been performed to determine the effect of bias on the potential distribution within the devices.

1. INTRODUCTION

The development of quantum well solar cells (QWSCs) has been pioneered by Keith Barnham and his collaborators at the quantum photovoltaic group, Imperial College, London since 1990 (Barnham et al 1996, 2002, Ekins-Daukes et al 2002). These cells consist of III-V compound layers (such as GaAs) doped to form a p-i-n structure and a number of thin layers (quantum wells, QWs) of another III-V compound (such as InGaAs) with a lower energy gap; these layers are inserted into the intrinsic (i) region, thus forming a stack of periodic barrier-quantum wells. The quantum wells absorb over a wider range of the solar spectrum, thus increasing the efficiency of the solar cell.

The knowledge of dopant concentration and distribution, as well as the resultant electric field distribution in electron devices such as QWSC, is of utmost importance. Particularly in QWSCs the background doping must be low to preserve the field across the i-region in order to keep the quantum and collection efficiencies high (Barnham et al 2002). The observation of secondary electron (SE) contrast by high resolution scanning electron microscopy (HRSEM) is promising (Barkay et al 2003, Castell et al 2003, Elliot et al 2002, Grunbaum et al 2004, Sealy et al 2000, Venables et al 1998).

The potential and field distributions are related to the SE contrast curves and their derivatives. In this work we have measured the SE contrast produced from these devices under zero applied bias and with various reverse bias potentials.

2. EXPERIMENTAL

The QWSC devices were grown by metal-organic vapour epitaxy at Sheffield University. The layouts of the layers for the samples QT1629 and Qt1410R with 10 and 20 QWSCs are given in Tables 1 and 2. Cross-sections are prepared by cleavage of the sample. A HRSEM with a cold field emission electron gun (JEOL 6700F) has been used, combined with a semi-in lens secondary

[1] Enrique Grunbaum's e-mail for correspondence: enrique@eng.tau.ac.il

electron (SE) detector, which provides efficient collection of SEs allowing observation of nanometre scale features. An accelerating voltage of 1 kV was used to reduce the effect of charging and to optimise the ionization potential contrast. A beam current of 30 pA was used. The SE signal profile is displayed after averaging over the selected area (the marked rectangle shown in the images below). Two values of reverse bias were supplied to the specimens at well determined time intervals via an electronic timing circuit and a flat lithium battery mounted on the specimen table next to and underneath the specimen, respectively. This method avoids the problem of connecting an external voltage source to the specimen which had to be introduced into the HRSEM through a load-lock.

Table 1: Layout of layers in sample QT1629

Layer	Thickness (nm)	Doping (cm^{-3})
GaAs	220	Zn p $3x10^{19}$
$Al_{0.8}GaAs$	43	C p $5x10^{18}$
GaAs	400	C p $2x10^{18}$
$GaAsP_{0.08}$	**9.3x10**	**i barriers**
$In_{0,1}GaAs$	**8 x10**	**i QWs**
$GaAsP_{0.08}$	**9.3x10**	**i barriers**
GaAs	2000	Si n $2x10^{17}$
GaAs	300	Si n $1.5x10^{18}$
GaAs	substrate	n^+

Table 2: Layout of layers in sample QT1410R

Layer	Thickness (nm)	Doping (cm^{-3})
GaAs	1000	Zn p $3x10^{19}$
$Al_{0.8}GaAs$	43	C p>$5x10^{18}$
GaAs	400	C p $2x10^{18}$
$GaAsP_{0.06}$	**22.7x20**	**i barriers**
$In_{0,17}GaAs$	**8x20**	**i QWs**
$GaAsP_{0.06}$	**22.7x20**	**i barriers**
GaAs	3000	Si n $2x10^{17}$
GaAs	300	Si n$1.5x10^{18}$
GaAs	substrate	n^+

3. THEORY OF THE IONISATION POTENTIAL (DOPANT) CONTRAST

The difference in SE emission, observed as contrast between n, i and p regions, is due to the difference in ionisation energy of the different regions (Sealy et al 2000). The ionization energy is defined as the energy required to move an electron from the top of the valence band to the vacuum level at the SE detector and for pn junctions the difference in this energy from one side of the junction to the other is of the order eE_{bi} where e is the electronic charge and E_{bi} the built-in voltage. The SEs are mainly emitted from the region near the surface of the specimen.

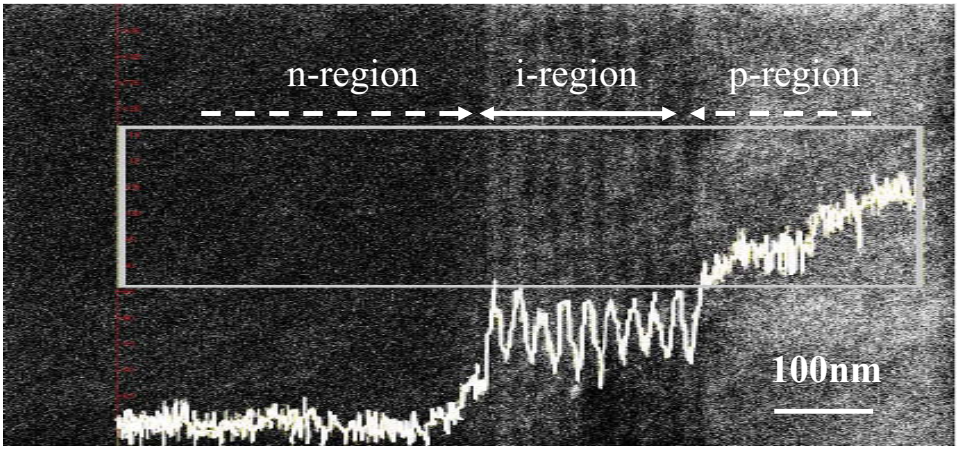


Fig. 1: HRSEM SE line-scan micrograph of sample QT1629: GaAs solar cell with 10 InGaAs QWs (layout of layers in Table 1).

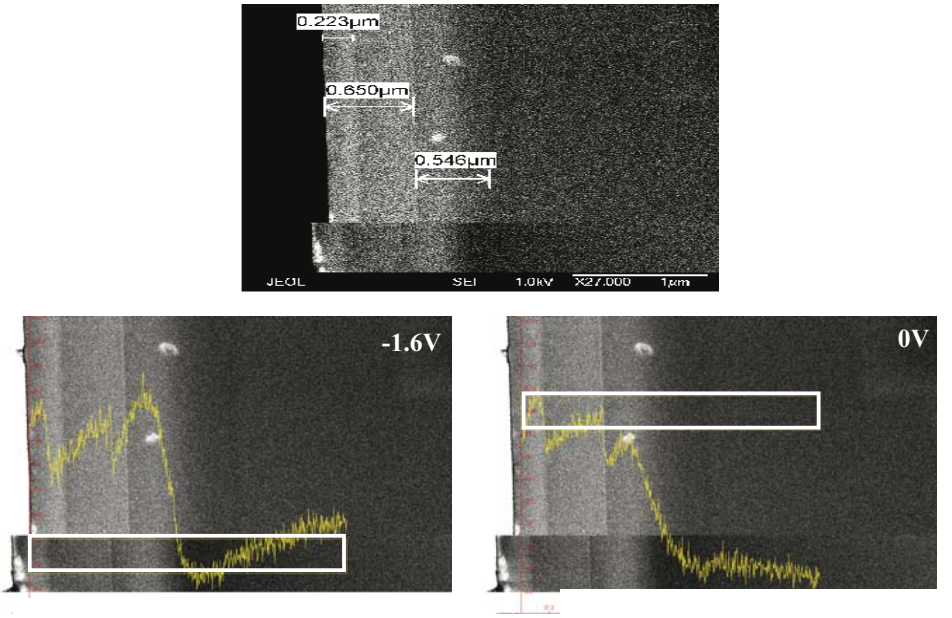


Fig. 2: QT1597 sample with the same layer layout as in sample QT1629 (table 1), but 20 QWs: the upper image shows the lateral dimensions of the two differently doped p-regions and the i-region, which are clearly visible due to the dopant contrast; these dimensions agree with those of the designer (table 1). The bias applied to the specimen was changed after approximately 80% of the scan was complete. The other two images are of the same micrograph and show, superimposed, line scans obtained from evaluating the digital data taken from the two areas outlined by a rectangle: lower (bias -1.6 V), upper (no bias).

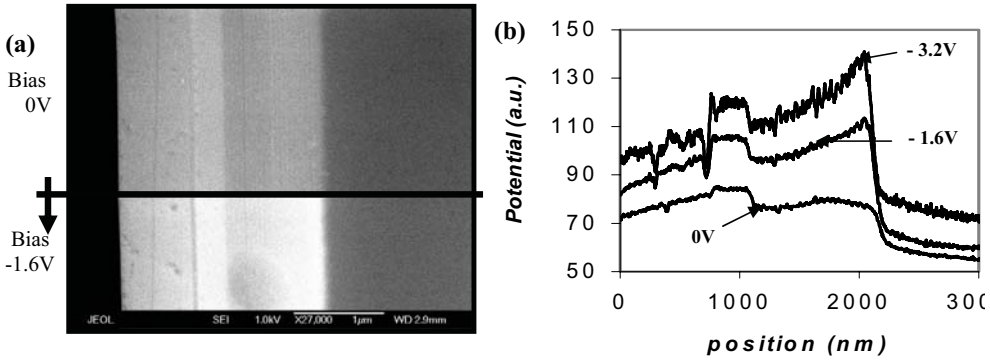


Fig. 3: HRSEM SE line-scan micrographs of sample QT1410R: GaAs solar cell with 20 InGaAs QWs (layout of layers in table 2); a) Bias change from 0 V to -1.6 V during image scan for recording; b) Graph showing three SE line scans obtained with applied biases of 0V, -1.6V, -3.2V.

4. RESULTS AND DISCUSSION

The micrographs of Figs. 1 and 3a clearly show the following features:
i) A periodic structure of 8 nm wide QWs (bright stripes and maxima in the SE signal profile) and their corresponding barriers. There is no difference in doping between the wells and the barrier layers. However, due to their compositions, the top of the valence band in the QW is at a higher energy than the top of the valence band in the adjacent barrier layer. This results in the QW having a lower ionisation energy than the barrier layer and it is this effect that leads to the secondary electron contrast observed. A similar result was obtained using a single QW laser specimen (Barkay et al 2003, Fig. 3).
ii) An increasing SE signal giving a dopant contrast between the n, i and p regions. It represents the potential distribution within these regions.
iii) A large difference in signal level between the beginning of the p-region and the end of the n-region. This is dependent on the built-in potential across the junction.
iv) On applying a reverse bias, the resultant SE contrast curves show the changes representing the new potential distribution in the device: the changes take place mainly in the transition from the n- to i-region. This differs from the potential distribution that was expected, namely that it would change uniformly across the intrinsic region. This behaviour needs further investigation and the results of a previous study by SEM voltage contrast in thin films may shed light on this problem (Barkay 1989).
v) Details of the potential curves vary for different specimens and for different areas of observation within a particular specimen cross-section. This is attributed to the variation in cleavage quality and the carbon contamination layer produced during SEM observation.

5. CONCLUSIONS

HRSEM provides easily obtainable information on:
i) The active dopant concentration making visible the various regions of the device thus allowing the measurement of their dimensions by the HRSEM and their comparison with the specifications given by the designer (see Fig. 2).
ii) The associated ionisation potential distribution and the associated electric fields due the built-in potential and applied bias on a nanometer scale.

ACKNOWLEDGEMENTS

The authors are very grateful the cooperation of Ezra Shaked of the Dept of Physics, Tel-Aviv University regarding the skilful design of the electronic circuit for the periodic in situ biasing of the specimen.

REFERENCES

Barkay Z, Dwir B and Deutscher G 1989 Thin Solid Films **182**, 97
Barkay Z, Grunbaum E, Shapira Y, Wilshaw P, Barnham K, Bushnell D B, Ekins-Daukes N J and Mazzer M 2003 Inst. Phys. Conf. Ser. **179**, 143
Barnham K, Ballard I, .Barnes J, Connolly JP, Griffin P, Grunbaum E, Kluftinger B G, Nelson J, Tsui E and Zachariou A 1996 Proc.7th Sede Boqer Symposium on Solar Electricity Production 13
Barnham K, Ballard I, Connolly J P, Ekins-Daukes N J, Kluftinger B G, Nelson J and Rohr C, 2002 Physica E**14,** 27
Castell M R, Muller D A and Voyles P M 2003 Nature Materials **2**, 129
Ekins-Daukes N J, Bushnell D B , Connolly J P, Barnham K,.Mazzer M, Roberts J S, Hill G and Airey R 2002 Physica E**14,** 132
Elliott S L, Broom R F and Humphreys C J, 2002 J. Appl. Phys., **91**, 9116
Grunbaum E, Barkay Z, Shapira Y, Wilshaw P, Barnham K, Bushnell D B, Ekins-Daukes N J and Mazzer M 2004 Proc.12th Sede Boqer Symposium on Solar Electrictiy Production p 167
Sealy C P, Castell M R and Wilshaw P R 2000 J. Electron Microsc. **49,** 311
Venables D, Jain H and Collins D C 1998 J. Vac. Sci. Tech., **B16**, 362

Localized energy levels associated with dislocations in ZnSe revealed by polarized CL spectroscopy under light illumination

Yutaka Ohno

Department of Physics, Graduate School of Science, Osaka University, 1-1, Machikane-yama, Toyonaka, Osaka 560-0043,Japan

ABSTRACT: Localized energy levels of 90°α partial dislocations in a ZnSe/GaAs epilayer were determined by means of polarized cathodoluminescence spectroscopy under light illumination in a transmission electron microscope. A dislocation glided under the illumination of a monochromatic light whose photon energy was above 2.07-2.40 eV. The glide would take place due to electronic recombination via a localized energy level associated with the dislocation.

1. INTRODUCTION

ZnSe has a revival of interest in its potential applications in light emitters, which may offer a number of advantages over the commercial GaN-base diodes. A key issue that has hampered the commercial application of the emitters is their degradation under operating conditions. One origin of the degradation is substitutional N atoms on Se site (N-acceptors). It is considered that Se vacancies are formed during operation via a transition of the substitutional N atoms to stable interstitial atoms (Gundel et al 1999), and they are preferentially accumulated into a compressed epilayer in a light emitter (Ebe et al 2002) since they help to decrease the elastic energy in the epilayer. The other origin is partial dislocations (PDs) bounding stacking faults (SFs), which are produced inevitably during the epitaxial growth. The lifetime of a light emitter is drastically lengthened by reducing the density of the PDs (Kato et al 1998), since dislocation dipoles are nucleated from the PDs during operation (Tomiya et al 1995, Hua et al 1994, Guha et al 1993a and 1993b) and the dipoles, as well as the PDs and SFs, act as non-radiative recombination centres (Guha et al 1993a). It is proposed that the dipoles are introduced via the migration of point defects (Chuang et al 1996), which are presumably Se vacancies formed by the preceding process, so as to reduce the compression stress around the PDs (Tomiya et al 1995, Hua et al 1994). The role of the PDs in degradation has not been fully understood. By means of polarized-cathodoluminescence (p-CL) spectroscopy under light illumination, as well as transmission electron microscopy (TEM), I have recently found out that a PD glides under illumination of a light, that is similar to the light emitted from usual ZnSe-base light emitters, and the dislocation glide introduces anisotropic stress around the PD, by which the migration and clustering of vacancies would be enhanced at room temperature (Ohno 2005). In this paper, I briefly summarize the result concerning the dislocation glide and discuss the glide mechanism.

2. EXPERIMENTS

Specimens were undoped ZnSe epilayers of 80 nm thickness [thinner than the critical thickness for misfit dislocation (about 100 nm, Horsburgh et al 1998)], in which SFs of Shockley type bounded by 90° PDs existed, grown on a GaAs(001) wafer. A disk of 3 mm in diameter was cut from a wafer and the GaAs surface was mechanically dimpled until the centre of the disk was sufficiently thin for TEM and p-CL spectroscopy. The thickness was estimated to be a few hundred nm, so ZnSe layer and GaAs substrate were simultaneously characterized. I actually observed CL arising through a band-to-band transition in GaAs. I used a beam of 160 keV electrons whose flux was about 50 Am^{-2}. The probe size on a specimen surface was about 1 μm in diameter. Both TEM images and p-CL spectra scarcely varied during the illumination of the beam. A visible light as well as an electron beam

illuminated simultaneously a specimen surface with an apparatus for *in-situ* photoluminescence spectroscopy in a transmission electron microscope (Ohno and Takeda 1995). I used a monochromatic light with a photon energy of 3.10 eV, 2.48 eV, 2.07 eV, or 1.77 eV (the power density ~10^3 W/m^2) or laser light at 2.41 eV from an Ar^+ ion laser (~10^4 W/m^2). The light was not polarized, or as is otherwise noted in the text. The specimen temperature under the illumination was estimated to be 35 K.

3. RESULTS AND DISCUSSION

3.1 Photo-Induced Stress via the Glide of 90°α PDs (Ohno 2005)

During the illumination with laser light, the SFs lying on (111) and $(11\bar{1})$ expanded (Fig. 1) while those on $(\bar{1}11)$ and $(1\bar{1}1)$ scarcely varied (not shown). In other words, only the 90°α PDs glided. The area of a SF scarcely varied without laser illumination.

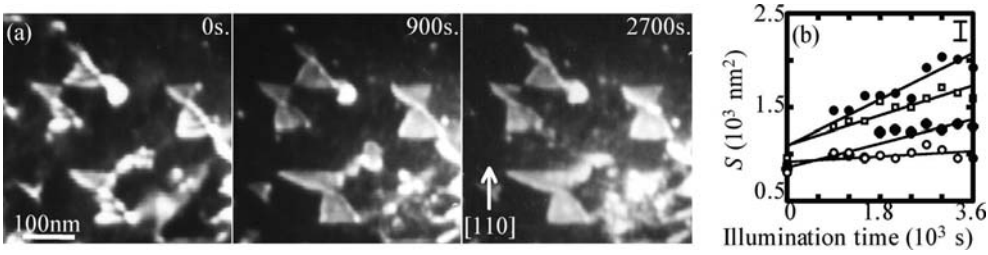


Fig. 1. (a) TEM images of SFs during laser illumination. (b) The area of a SF on (111) or $(11\bar{1})$, S increases at a constant rate during laser illumination.

The CL light emitted from a GaAs substrate was measured (Fig. 2a), and the energy was lower than that from bulk GaAs crystals due to the tensile stress arising from the misfit between ZnSe and GaAs (Fig. 2b). The stress along [110] was larger than that along $[1\bar{1}0]$, since the intensities of the light polarized along $[1\bar{1}0]$ and [110], $I_{[1\bar{1}0]}$ and $I_{[110]}$, were maximal and minimal, respectively* (Tang et al 1994). The degree of linear polarization, defined by $\mathrm{DLP} = (I_{[1\bar{1}0]} - I_{[110]})/(I_{[1\bar{1}0]} + I_{[110]})$, was estimated to be about 20 %. Since the substrate was thin, the absolute value of the tensile stress should be almost the same as that of the compression stress in the ZnSe epilayer on the substrate**. DLP decreased by laser illumination (Fig. 2). This means that the compression stress along [110] decreased. This result is consistent with the TEM data, since the compression stress along [110] would decrease with increase of the areas of the SFs lying on (111) and $(11\bar{1})$ (Ohno et al 2003).

---

* The peak intensities of the CL spectra in Fig. 2b were fitted with a function $I = A + B\cos[(\phi - C)/\pi]$ in which A, B, or C was a constant, and C was estimated to be 10~30°. Assume that a specimen set as in Fig. 2a emits a light linearly polarized along $[1\bar{1}0]$. It is simulated (Ohno and Takeda 2002) that the intensity of the light measured by my apparatus is maximum (minimum) at ϕ~15° (~105°). The simulation reproduces well the experimental data.

** The estimated value of DLP ~ 20 % is much higher than the value reported by Schreiber et al 2000 (~5% for an epilayer of 100 nm thick). The compression stress in a ZnSe/GaAs epilayer would be a function of the number density of the stacking faults bounded by 90°α PDs, n_α, and that by 90°β PDs, n_β (Ohno et al 2003). It is well known that the number densities depend on growth conditions. n_α and n_β were estimated to be ~10^9 cm^{-2} and ~10^8 cm^{-2}, respectively, in my epilayers. A non-isotropic stress in the epilayers might be introduced due to the difference between n_α and n_β..

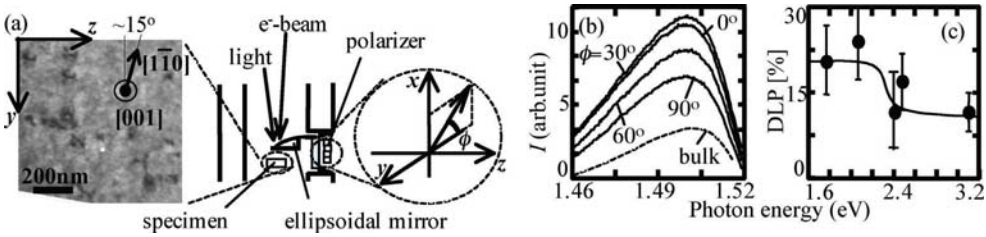


Fig. 2. (a) The experimental setup for p-CL spectroscopy. CL light emitted from a specimen is reflected on an ellipsoidal mirror and the reflected light is transmitted through a linear polarizer. Then, the transmitted light is collected with a CCD detector through a monochromator. It is defined that **x** // an electron beam, and **z** // the rotation axis of the polarizer. The transmission direction ***e*** of the polarizer is determined by the rotation angle ϕ, and $\phi = 0^{o}$ when ***e*** // **y**. A specimen was set in order that the [110] axis is nearly parallel to **z**. (b) p-CL spectra of a GaAs substrate without light illumination (solid lines), and a CL spectrum of a bulk GaAs crystal, which emits non-polarized CL light, obtained at the same condition (the broken line). (c) DLP of a specimen illuminated with a monochromatic light for 600 s.

3.2 The Glide Mechanism of 90°α PDs

I discuss the mechanism of the photo-induced glide of the 90°α PDs. The dislocation glide would be assisted with an extra amount of energy provided by light, as well as with the compression stress arising from the misfit. DLP decreased distinctly after the illumination of the monochromatic light with the photon energies of 2.41 eV, 2.48 eV and 3.10 eV, owing to the photo-induced expansion of SFs, while it scarcely varied after illumination using light with 2.07 eV and 1.77 eV (Fig.2d). Thus, the minimum energy needed for the dislocation glide was in the range 2.07-2.41 eV. The estimated energy is much larger than the activation energy for the thermal movement of dislocations in ZnSe (about 1 eV, Yonenaga 1998) and is smaller than the band gap energy for ZnSe (about 2.8 eV). It is very likely that the PDs glide due to electronic recombination (Maeda and Takeuchi 1996) via a localized energy level in the band gap. It is proposed that the PDs form one-dimensional localized energy levels along the dislocation cores, so called dislocation bands (Hilpert et al 2000). Suppose a dislocation band mediates the dislocation glide. The mobility of the PDs should depend on the linear polarization of illuminating light, since the absorption of light via a dislocation band is polarized preferentially along the Burgers vector (Razumova and Khotyaintsev 1998). However, under the illumination of a light linearly polarized along ***E*****,** the PD with the Burgers vector nearly parallel to ***E*** and that nearly perpendicular to ***E*** glided simultaneously with about the same mobility (Fig. 3). Moreover, the PD absorbs the light with the photon energy of 2.67 eV via a dislocation band (Shreter et al 1996), and this energy is somewhat larger than the estimated energy. The "soliton" defect (Heggie and Jones 1983) on the PDs may mediate the dislocation glide, as proposed in Si (Nunes et al 1996). A soliton defect forms localized energy levels in the band gap and the atomistic structure around the defect is reconstructed due to the recombination effect (Justo and Assali 2001). The PDs may glide even in a stress-free epilayer so as to reduce the electronic energy of the epilayer (Ha et al 2004, Miao et al 2001), similar to PDs in SiC (Galeckas et al 2002). Further study is needed to reveal the glide mechanism.

4. CONCLUSION

I have examined the localized energy levels associated with the 90°α PDs in ZnSe by means of p-CL spectroscopy under light illumination. The method will be also applied to explore the dynamic nature of defects involving the surrounding atoms in nonequilibrium states, such as photo-induced transformation, nucleation and growth of nanostructures under illumination with light or electron beams.

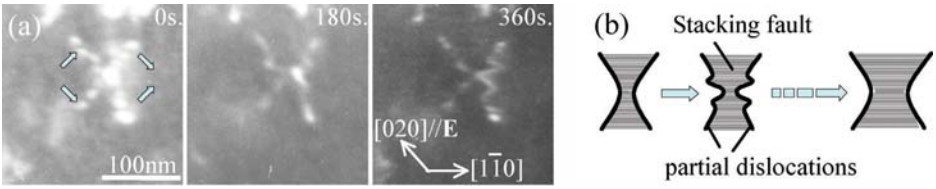


Fig. 3. (a) The initial stage of photo-induced expansion of SFs, observed with an electron beam nearly parallel to [001]. It is observed by the weak-beam TEM technique using the $2\bar{2}0$ diffraction spot, so the $90^{o}\alpha$ PDs bounding the SFs on (111) and $(11\bar{1})$ are observable but the SFs are invisible. The arrows in the left figure denote the Burgers vectors of the PDs projected on the figure. Laser light polarized linearly along [020] illuminates the specimen. (b) A schematic view of the glide process. Four PDs glide simultaneously. A segment near the ZnSe/GaAs interface on each PD primarily glides.

ACKNOWLEDGEMENTS

This work was partially supported by the Ministry of Education, Science, Sports and Culture, Grant-in-Aid for Young Scientist (A)(2) No.15681006, 2003-2005. The author is indebted to Prof S Takeda for his constructive comments and discussion.

REFERENCES

Chuang S, Ukita M, Kijima S, Taniguchi S and Ishibashi A 1996 Appl. Phys. Lett. **69**, 1588
Ebe H, Zhang B P, Sakurai F, Segawa Y, Suto K and Nishizawa J 2002 Phys. Stat. Sol. (b) **229**, 377
Galeckas A, Linnros J and Pirouz P 2002 Appl. Phys. Lett. **81**, 883
Guha S, DePuydt J M, Haase M A, Qiu J and Cheng H 1993a Appl. Phys. Lett. **63**, 3107
Guha S, DePuydt J M, Qiu J, Hofler G E, Haase M A, Wu B J and Cheng H 1993b Appl. Phys. Lett. **63**, 3023
Gundel S, Albert D, Nurnberger J and Faschinger W 1999 Phys. Rev. B **60**, R16271
Ha S, Skowronski M, Sumakeris J J, Paisley M J and Das M K 2004 Phys. Rev. Lett. **92**, 175504
Heggie M and Jones R 1983 Philos. Mag. B **48**, 365
Hilpert U, Schreiber J, Worschech L, Horing L, Ramsteiner M, Ossau W and Landwehr G 2000 J. Phys.: Condensed Matter. **12**, 10169
Horsburgh G, Prior K A, Meredish W, Galbraith I, Cavenett B C, Whitehouse C R, Lacey G, Cullis A G, Parbrook P J, Mock P and Mizuno K 1998 Appl. Phys. Lett. **72**, 3148
Hua G C, Otsuka N, Grillo D C, Fan Y, Han J, Ringle M D, Gunshor R L, Hovinen M and Nurmikko A V 1994 Appl. Phys. Lett. **65**, 1331
Justo J F and Assali L V C 2001 Appl. Phys. Lett. **79**, 3630
Kato E, Noguchi H, Nagai M, Okuyama H, Kijima S and Ishibashi A 1998 Electron. Lett. **34**, 282
Maeda K and Takeuchi S 1996 Dislocation in Solids, eds. Nabarro F R N and Duesbery M S (North-Holland, Amsterdam) p443
Miao M S, Limpijumnong S, and Lambrecht W R L 2001 Appl. Phys. Lett. **79**, 4360
Nunes R W, Bennetto J and Vanderbilt D 1996 Phys. Rev. Lett. **77**, 1516
Ohno Y 2005 *submitted*
Ohno Y, Adachi N and Takeda S 2003 Appl. Phys. Lett. **83**, 54
Ohno Y and Takeda S 2002 J. Electron. Microsc. **51**, 281
Ohno Y and Takeda S 1995 Rev. Sci. Instrum. **66**, 4866
Razumova M A and Khotyaintsev V M 1998, Phys. Stat. Sol. (b) **210**, 791
Schreiber J, Hilpert U, Horing L, Worschech L, Konig B, Ossau W, Waag A and Landwehr G 2000 Phys. Stat. Sol. (b) 222, 169
Shreter Y G, Rebane Y T, Klyavin O V, Aplin P S, Axon C J, Young W T and Steeds J W 1996 J. Cryst. Growth **159**, 883
Tang Y, Rich D H, Lingunis E H and Haegel N M 1994 J. Appl. Phys. **76**, 3032
Tomiya S, Morita E, Ukita M, Okuyama H, Itoh S, Nakano K and Ishibashi A 1995 Appl. Phys. Lett. **66**, 1208
Yonenaga I 1998 J. Appl. Phys. **84**, 4209

Electron microscopy characterisation of ZnS:Cu:Cl phosphors

A Łaszcz, J Kątcki, J Ratajczak, M Płuska and M Cie

Institute of Electron Technology, Al. Lotników 32/46, 02-668 Warsaw, Poland

ABSTRACT: Detailed study of the coexistence of zinc blende and wurtzite phases in the luminescent layer and quantitative relations between phases after ageing processes of ZnS:Cu:Cl phosphors has been performed by means of cross-sectional transmission electron microscopy (XTEM). The diffraction analysis of as-fabricated phosphors revealed that in the ZnS:Cu:Cl layer only the zinc blende phase exists. However, in aged phosphors both zinc blende and wurtzite phases with the zinc blende phase dominating can be observed. Additional cathodoluminescence (CL) analysis of ZnS:Cu:Cl grains carried out in a scanning electron microscope (SEM) confirmed that the Cu-dopant influenced the luminescence properties of ZnS:Cu:Cl phosphors.

1. INTRODUCTION

Zinc sulphide is a very interesting material for fabrication of optoelectronic devices. Its luminescence properties mean that it is widely applied in display technologies (Alexander 1988). Two structure types of zinc sulphide are known: cubic zinc blende ZnS (f.c.c.) and hexagonal wurtzite ZnS (c.p.h.). At room temperature the most stable phase is zinc blende, with an insignificant amount of stable wurzite (Ma et al 2003).

The ZnS-powder electroluminescent devices demonstrated insufficient brightness and serious degradation (Yu et al 1995). Monocrystalline ZnS grains activated with ions of various elements, mainly Cu and also Cl, Al or Mn, enhance the intensity of electroluminescence.

The display emission depends on the dopant concentration in ZnS. CL spectra of as-fabricated ZnS:Cu:Cl-powder phosphors with various Cu concentrations were analysed in the study of Chen et al (2001). They proved that ZnS:Cu:Cl powders with Cu content of 120, 200, 400 ppm exhibit green emission, ranging from 475 to 525 nm. However, the emission of powders with the concentration of Cu over 800 ppm tend to blue band emission which ranges from 425 to 475 nm, while the phosphors containing less than 80 ppm of the Cu dopant exhibit emission in the range of 450 to 550 nm.

As a result of the Cu-doping process the Cu_xS phase, especially the most stable Cu_2S phase, precipitated on the surface of ZnS grains (Yu et al 1995). The influence of humidity and high electric field can cause a transformation of Cu_2S into CuS or Cu. Also, the transformation of ZnS from the zinc blende to the wurzite phase in a luminescent layer can occur (Wierewkin 1983).

The aim of this paper was detailed study of the zinc blende to wurtzite phase transformation in the luminescent layer of the ZnS:Cu:Cl phosphors caused by ageing processes.

2. EXPERIMENTAL

The ZnS powder was produced by the reaction of zinc salts with H_2S. An activation process of the ZnS powder with Cu was carried out by annealing of a mixture of ZnS and Cu_2S powders at 1000-1020°C in the HCl and H_2S atmosphere. The concentration of Cu in ZnS grains ranges from 1000 to 10000 ppm.

Phosphor samples were fabricated as multilayer structures consisting of an electrode layer (Ag, C and the acrylic lacquer), a dielectric layer ($BaTiO_3$), a luminescent layer (ZnS:Cu:Cl grains covered with a very thin acrylic lacquer film) and an indium thin oxide (ITO) transparent electrode.

The following samples were studied: *i)* the ZnS:Cu:Cl powder; *ii)* as-fabricated phosphors; *iii)* phosphors aged at the temperature of 40°C in a humidity of 98 %, for 384 h; and *iv)* phosphors aged at a voltage of 180 V and a temperature of 20 ±3°C, for 1000 h.

TEM specimens were prepared by the method described by Kątcki et al (1995). The TEM diffraction analysis was carried out by means of the JEM-200CX transmission electron microscope operating at 200 kV. CL spectra were obtained in SEM XL30 using a MonoCL detector.

3. RESULTS AND DISCUSSION

A schematic diagram of the ZnS:Cu:Cl-powder phosphors and an SEM cross-sectional view of the phosphors are shown in Fig. 1a and b.

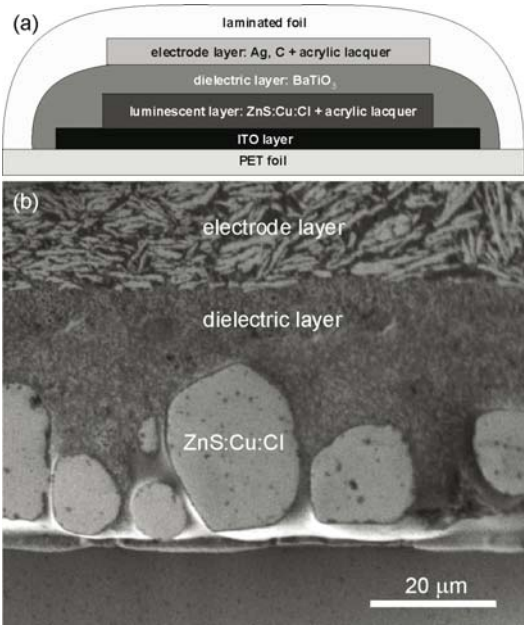


Fig. 1. ZnS:Cu:Cl phosphors: (a) a schematic diagram; (b) an SEM cross-sectional view.

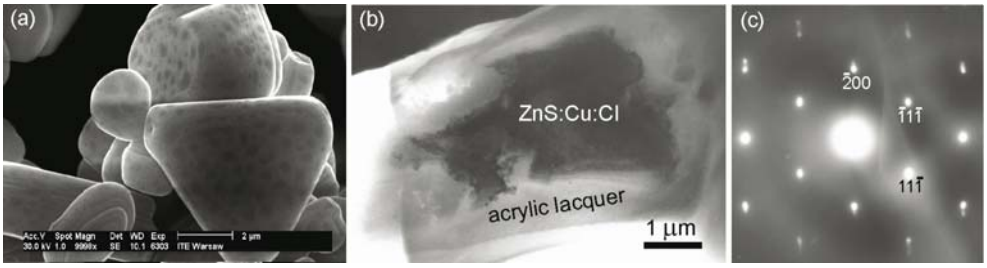


Fig. 2. (a) An SEM view of the ZnS:Cu:Cl powder; (b) a cross-sectional TEM view of a ZnS:Cu:Cl grain; (c) [011]-oriented diffraction pattern of the as-fabricated phosphor grain.

In Fig. 2a an SEM view of the ZnS:Cu:Cl powder is presented. The precipitates of Cu_xS phase located on the surface of ZnS:Cu:Cl grains are visible as dark spots. The size of ZnS:Cu:Cl grains ranges from 2 to 25 μm.

Figure 2b presents a TEM cross-section of a ZnS:Cu:Cl grain in the as-fabricated phosphors. The diffraction analysis revealed that in the luminescent layer only the zinc blende phase exists (Fig. 2c). In most grains microtwins are observed.

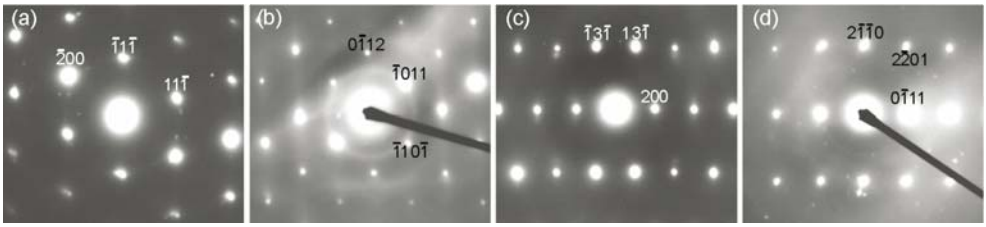


Fig. 3. TEM diffraction patterns of ZnS:Cu:Cl phosphors aged in high humidity: (a) [011]-oriented zinc blende grain; (b) [01$\bar{1}$1]-oriented wurzite grain; and aged at high electric field: (c) [013]-oriented zinc blende grain; (d) [01$\bar{1}$2]-oriented wurzite grain.

The analysis of diffraction patterns of phosphors aged both in high humidity and at high electric field proved the coexistence of zinc blende and wurtzite phases in the luminescent layer (Fig. 3). The study of ZnS:Cu:Cl grains in phosphors aged in high humidity proved that in about 30% of grains the transformation from the zinc blende to wurzite phase took place. This transformation was observed in almost 25% of grains of samples aged at high electric field. In both types of samples numerous microtwins can be observed.

The CL spectra of the ZnS:Cu:Cl powder and cross-sections of as-fabricated and aged ZnS:Cu:Cl phosphor samples were analysed.

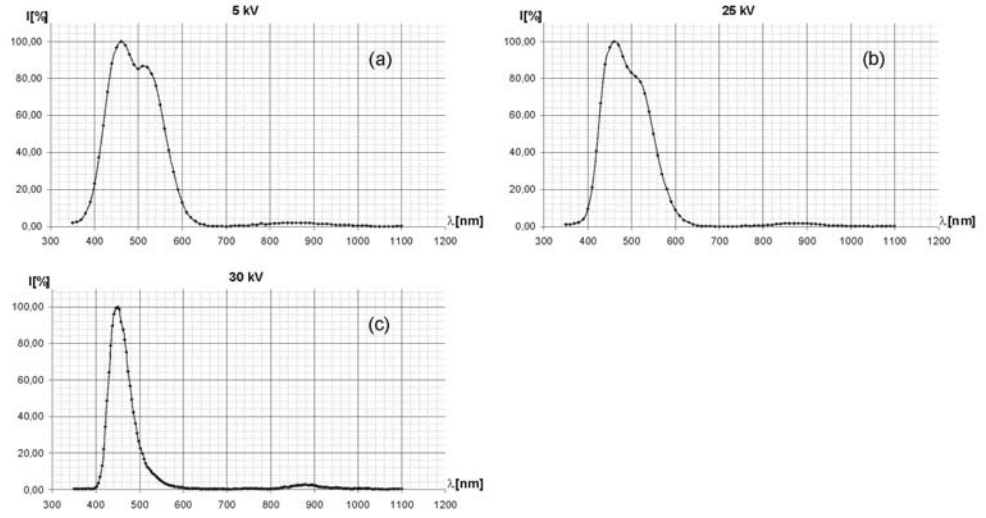


Fig. 4. Cathodoluminescence spectra of: (a) the ZnS:Cu:Cl powder at 5 and (b) at 25 kV; (c) a cross-section of a ZnS:Cu:Cl phosphor sample at 30 kV.

The CL investigation of the ZnS:Cu:Cl powder demonstrated emission spectra with two peaks, i.e. 460 nm in the blue and 510 nm in the green emission range (Fig. 4a and b). The CL study carried out at the low voltage (5 kV, Fig. 4a) showed that the shallow penetration of grains by the electron beam gives a strong peak in the green emission range (with the peak maximum at 510 nm). At the

higher voltage (25 kV, Fig. 4b), the deeper penetration of the electron beam caused reduction of the green emission.

Results obtained for as-fabricated and aged ZnS:Cu:Cl phosphor samples were identical. The CL spectrum taken from a cross-section of the ZnS:Cu:Cl phosphor (Fig. 4c) showed the emission in the range of 400 to 550 nm with the peak at 450 nm (the blue region).

The CL analysis showed a nonuniform concentration of Cu in ZnS:Cu:Cl grains. In the case of the CL analysis of a ZnS:Cu:Cl powder at the low electron beam voltage, the green emission comes from the surface of grains where the dopant concentration is high. At the higher electron beam voltage, the electron beam penetrates the areas located deeper in the sample, where the Cu concentration is lower. It causes the green emission to disappear. Inside ZnS:Cu:Cl grains where the concentration of Cu is close to zero, the CL spectra exhibit only pure blue emission from ZnS. The CL analysis proved that the Cu dopant concentrates mostly close to the surface of the ZnS:Cu:Cl grains.

4. CONCLUSIONS

As a result of the ageing process, a phase transition in the luminescent layer of ZnS:Cu:Cl phosphor samples occurred. The diffraction analysis of as-fabricated phosphors revealed that in the ZnS:Cu:Cl layer only the zinc blende phase existed. The same analysis proved that in aged samples of phosphor up to 30% of grains transformed from the zinc blende to wurzite phase. In ZnS:Cu:Cl grains of both type of phosphors microtwins were present.

The CL study demonstrated the influence of Cu-dopant on the luminescence properties of phosphors. It proved that most Cu atoms concentrate in the subsurface area of ZnS:Cu:Cl grains.

ACKNOWLEDGEMENTS

The authors are very much indebted to Ms D Szczepańska and Mr J Gazda for assistance in specimen preparation and Ms J Wiącek for careful preparation of micrographs.

REFERENCES

Alexander P W, Sherhod C and Stowell M J 1988 J. Phys. D: Appl. Phys. **21**, 1635

Chen Y Y, Duh J G, Chiou B S and Peng C G 2001 Thin Solid Films **392**, 50

Kątcki J, Ratajczak J, Maląg A and Piskorski M 1995 Microscopy of Semiconducting Materials 1995, eds A G Cullis and A E Statton-Bevan (Bristol: IOPP) p 273

Ma C, Moore D, Li J and Wang Z L 2003 Advanced Materials **15**, No. 3, 228

Wierewkin J N 1983 Degradation processes in a electroluminescence of solid states (Leningrad, Nauka, in Russian)

Yu I I, Senna M and Takahashi S 1995 Materials Research Bulletin **30**, No. 3, 299

Resistive contrast in R-EBIC from thin films

K Durose and H Tatsuoka[1]

Department of Physics, University of Durham, South Road, Durham, DH1 3LE, UK
[1] Faculty of Engineering, Shizuoka University, Hamamatsu, 432-8561, Japan

ABSTRACT: The ability of the remote electron beam induced current method in the SEM to extract resistivity profiles from thin films is explored by modelling and experiment. A simple model of resistors in parallel was used to describe resistance of the film/substrate combination that controls resistive image contrast. It was demonstrated that the resistivity of barriers in a film could be measured to within 2% accuracy if the substrate resistivity exceeded that of the barrier by ~15 times or more. Results from CdS/glass and β-$FeSi_2$/Si indicate that the method can be used in practice to extract useful resistivity profiles. However, where the conductive paths between the beam position and the contact are not linear, anomalous image contrast may result, which would be interpreted as unphysical resistivities using the simple one-dimensional model.

1. INTRODUCTION

In the remote electron beam induced current (R-EBIC) mode of the SEM, the current flowing through a semiconducting specimen having two contacts under the influence of an electron beam is measured. The term 'remote' alludes to the condition that the contacts are separated by many times the carrier diffusion length. A simplified circuit for the experiment is shown in Fig. 1. Both 'resistive' and 'peak and trough' contrast may be present in images, which are in effect maps of the conventional current flowing to earth via a differential amplifier. The R-EBIC experiment was first demonstrated by Russell et al (1980), while resistive contrast was analysed by Russell and Leach (1995) and the subject reviewed and further explained by Holt et al (1996).

Some properties of resistive contrast – which is the subject of this work – are now presented. Resistive contrast arises since the sample acts as a current divider to the electron beam. When the beam is at the LHS of the sample (Fig. 1), the conventional current is high, and for a uniform sample it decreases linearly until the contact at the RHS is met. The R-EBIC current for the beam being at a point x on a sample of resistance R_{tot} may be calculated from the beam current and the resistance of the part of the sample lying between the beam position and the LHS contact ie:

$$I_{REBIC} = I_{beam}\left\{\frac{R_{tot} - R_{left}}{R_{tot}}\right\}$$

For a uniform region of the sample, the resistance R_{left} is given by:

$$R_{left} = \sum \frac{\rho \Delta x}{A} = \frac{\rho x}{A}$$

It follows that the resistivity profile of a general sample may be extracted from the differential of the normalized R-EBIC signal, providing the total resistance of the sample and its cross sectional area are known. For the case of a thin film, it might be expected that this procedure will only give accurate results if the substrate is resistive compared to the layer and any resistive barriers within it. In this paper a simple discrete element circuit model is used to explore the limits over which thin film R-

EBIC may be used to measure resistivity profiles. Some examples of experimental studies of R-EBIC from CdS/glass and β-$FeSi_2$/Si are presented.

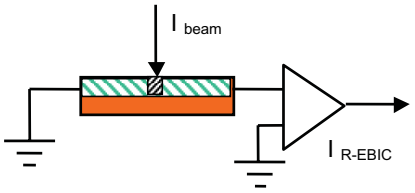


Fig. 1 Configuration for R-EBIC of a thin film on its substrate. The sample acts as a current divider with the signal recorded being the current flowing to earth via the amplifier.

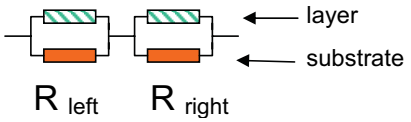


Fig. 2 Equivalent circuit model of R-EBIC for a thin film on a conducting substrate used in this work.

2. MODELLING METHOD AND EXPERIMENTS

R-EBIC currents were modelled for thin films (Fig. 1) by assuming that contributions to the resistance could be described by discrete resistors in parallel, as shown in Fig. 2. Hence $1/R_{left} = 1/R_{left(substrate)} + 1/R_{left(layer)}$. For the modelling it was assumed that the substrate and layer had identical thicknesses and widths, and a 100μm contact separation was employed. The layer resistivity was 20Ω-cm and it contained a barrier with a resistivity of 200Ω-cm at its centre. The substrate resistivity was a variable. Both the R-EBIC signals and the resistivity profiles (nominally for the films) that could be recovered from them were calculated using a spreadsheet. Contact and shape effects were neglected.

R-EBIC results for both thin film CdS and for β-$FeSi_2$/Si are reported. The CdS was grown by chemical bath deposition; that is by the thermal decomposition of thiourea in the presence of aqueous Cd^{2+}. The p-$FeSi_2$ was grown on 1000Ω-cm Si substrates by a variation of hot wall epitaxy. Both were contacted using evaporated In dots. R-EBIC signals were recorded using a Matelect ISM5 dedicated EBIC amplifier using beam currents of between $1.10^{-9} – 2.10^{-8}$A in a JSM 848 SEM.

3. MODELLING OF R-EBIC FROM THIN FILMS ON CONDUCTIVE SUBSTRATES

Figure 3 (a and c) shows the results of modelling the normalised R-EBIC response for thin films on susbstrates with resistivities of 3000 and 500Ω-cm respectively. Both of the responses are qualitatively similar. For each there are regions at either end with identical gradients, and these correspond to the film of resistivity 20Ω-cm. The central, steeper portion of the graphs marks the position of the resistive boundary (ρ = 200Ω-cm). By using the method outlined in section 1 it was possible to recover the resistivity profile of the sample i.e. the profile that would be ascribed to the film of interest in a real experiment. These profiles are shown in Fig. 3 (b and d). For the 3000Ω-cm substrate, the barrier resistance was estimated as 195Ω-cm (2.5% error), while for the 500Ω-cm substrate it was 175Ω-cm (12.5% error). Clearly, for measurement of the resistivity profiles of thin films, a resistive substrate (relative to the film features) will give more accurate profiles. Modelling was used to examine a wide range of layer, barrier and substrate resistivities, and the error in resistivity profile recovery, for both the barrier and layer, were thoroughly investigated. For barrier measurement, the error was reduced to ~2% when the ratio of substrate/barrier resistivity was > 15. Generally it was found that the error for the barrier resistivity was less than for the barrier for a given substrate resistivity, but that the error was influenced by whether the measurement was for the LHS or the RHS of the barrier itself. This became especially noticeable for the case of very conductive substrates.

A further property of R-EBIC profiles relevant to the experiments is as follow, and is described using the sense of the current convention and amplifier position in Fig. 1: Regardless of the substrate and layer resistivity profiles, for the case of the discrete circuit element model used here, the R-EBIC

current must always decrease as the beam is scanned from left to right. This is because the cumulative resistance on the left (right) of the beam will always increase (decrease).

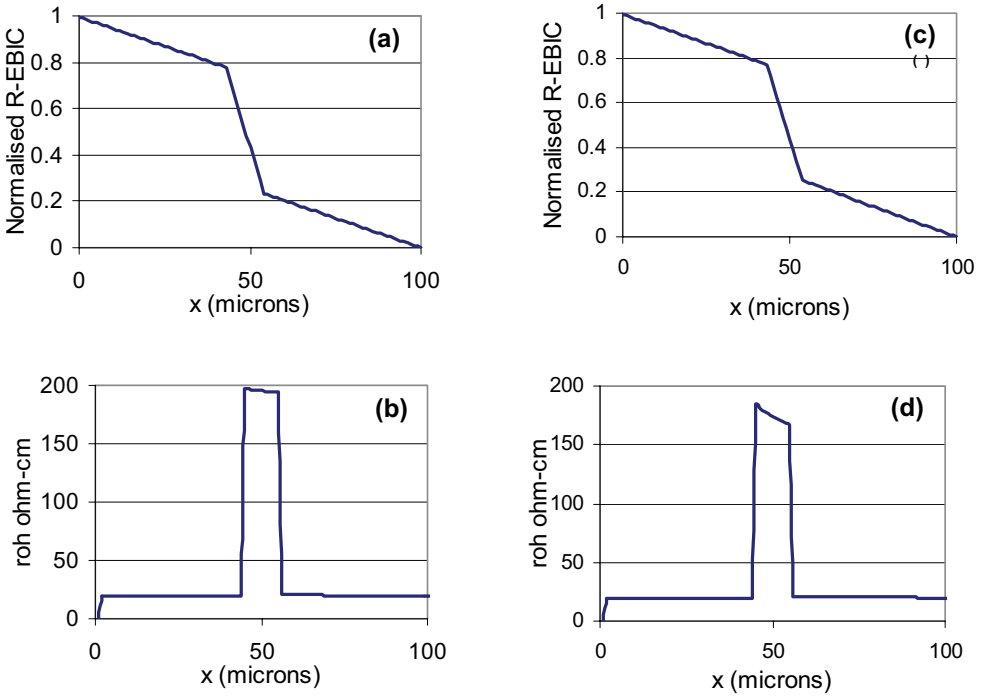


Fig. 3 Modelled R-EBIC line scans for a sample with a 20Ω-cm film and a 200Ω-cm barrier for the case of 3000 (a,b) and 500Ω-cm (c,d) substrates. The lines scans (a and c) are qualitatively similar, but use of a more conductive substrate leads to errors in the resistivity derived from them for the resistive barrier.

4. R-EBIC FROM CdS/glass and β-$FeSi_2$/Si

4.1 CdS/Glass Film

Fig. 4 shows the resistivity profile recovered from R-EBIC of a CdS/glass film. The low magnification R-EBIC image from which Fig. 4 was extracted showed a gradation from 'white' to 'black' contrast, but it was relatively noisy. The peak at the left is an artefact related to the 'bright' contact location. Generally the resistivity was about 0.01Ω-cm, but with considerable variation on the scale of 100μm. Just to the right of the centre of the line scan is peak rising to ~0.03Ω-cm. This feature was easily visible in the R-EBIC image and represents a resistive barrier in the film itself. Other smaller peaks represent resistivity variation that is itself undesirable for solar cell fabrication.

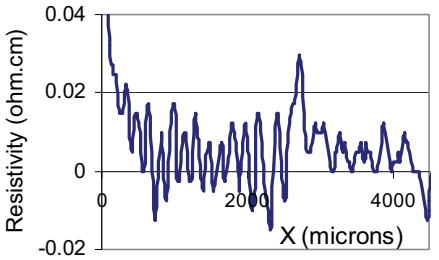


Fig. 4 Resistivity profile derived from R-EBIC for a CdS(100nm)/glass film.

4.2 β-$FeSi_2$/Si

Fig. 5a is an SE mode image of the surface of a layer indicating the discontinuous nature of the films. Cross section TEM revealed that the films had reacted with the substrate to form trough like inter-grain regions. The R-EBIC image shown in Fig 5b corresponds to the same area as Fig 5a, and is from the mid point between the In contacts which were 800μm apart. Analysis of the R-EBIC signal from these films was complicated by the fact that the near-contact regions showed a junction collection effect. However the central parts of the line scans taken between the two contacts was linear. By subtracting the linear (resistive) contribution from the near-junction EBIC signal, the latter was shown to be associated with a diffusion length of ~7.5μm. Hence the image in Fig. 5b is many diffusion lengths distant from the contacts and the contrast may be presumed to be due to resistive discontinuities. However, the line scan in Fig. 5c, taken from the same image, shows anomalous behaviour (see section 3): there are both negative and positive gradients. This is inconsistent with the discrete circuit element model used in this work. Nevertheless the contrast could still be resistive – the pathways for conduction on a non-uniform thin film sheet could be labyrinthine – i.e the most conductive paths to the contact from the beam position need not be the shortest and may not follow the beam scan line.

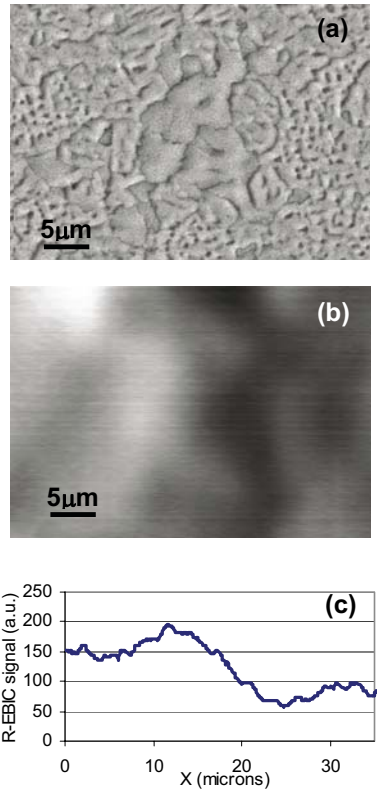


Fig. 5 $FeSi_2$(100nm)/Si. a) SE mode image, b) R-EBIC image of region 500μm distant from the contacts, c) line scan of (b) showing an anomalous signal having both positive and negative gradients.

5. CONCLUSIONS

The errors present in evaluating the resistivity profiles of thin films on substrates from R-EBIC have been evaluated using a simple model of resistors in parallel. Generally, the resistivities of barriers in the films could be expected to be measured accurately, providing the substrate has a resistivity > 50 times that of the barrier. Practical results from CdS/glass and $FeSi_2$/Si indicate that resistivity profiles can usefully be extracted from R-EBIC line scans. Nevertheless, for some samples the conductive paths operating may not be the shortest ones. Hence, 'anomalous' contrast can result which makes the simple extraction of resistivity profiles unphysical in such cases.

ACKNOWLEDGEMENTS

The authors are grateful to T Hyman and M Archbold for the preparation of the CdS/glass sample and to T Arakawa, Y Souno, S Makiuchi and H Kuwabara for work on growing the silicides.

REFERENCES

Russell G J, Vincent B, Robertson M J and Woods J 1980 J. Mater. Sci. **15**, 939
Russell J D and Leach C 1995 J. European Ceramic Society **15**, 617
Holt D B, Raza B and Wojcik A 1996 Mater. Sci. Eng. **B42**, 14

A diode model for SEM-REBIC contrast in ZnO varistors

A G Wojcik and L E Wojcik[1]

Faculty of Engineering, University College London, Torrington Place, London, WC1E 7JE, UK
[1]BAE SYSTEMS, Farnborough Aerospace Centre, Farnborough, GU14 6YU, UK

ABSTRACT: A previous resistor-based model of terrace contrast obtained under SEM-REBIC observation of sectioned ZnO varistors, shed light on the internal electrical behaviour of the ceramic but lacked the ability to closely predict the distinctive overall shape of linescan traces. The model has been extended here to include elements which exhibit diode behaviour with corresponding improved correspondence to measured data. It is postulated here that the diode elements are in fact representative of grain boundaries and that REBIC contrast in polycrystalline ZnO is more correctly modelled as a combination of "diodic" and resistive elements. Linescans obtained from deliberately damaged varistors lose their distinct non-linear shape, suggesting a destruction of the grain boundary diodes and their replacement by purely resistive elements. This has obvious implications for failure analysis studies.

1. INTRODUCTION

Remote contact electron beam induced current (REBIC), is a variation on the EBIC technique that simplifies specimen preparation and allows the observation of global charge carrier effects. First described by Matare and Laakso (1969), REBIC has been successfully used on electrical ceramics such as ZnO and, as shown here, can additionally provide some information on localized phenomena, even though global (i.e. integrated) behaviour is measured. Terrace line contrast is one such global/local effect and this has been well documented for ZnO varistor material (e.g. see Wojcik and Mason 2001). The terrace lines are significant in that they should be able to shed light upon the grain boundary electrical phenomenon within the oxide, and this in turn should lead to a better understanding of the use of the material for varistor devices. In a previous paper (Wojcik and Wojcik 2003), the authors presented a simple model, based on a one dimensional resistive element array, that provided a plausible explanation for the terrace lines and suggested that the visual contrast, and the attendant REBIC linescan traces, were a result of the interaction of resistive elements of distinctly different magnitude possibly corresponding to the bulk and grain boundary resistivity of the ZnO grains respectively.

Terrace lines are easily observed in REBIC images (see Fig. 1 below). Quantitative REBIC linescan measurements can be made using a suitably calibrated current amplifier, and these usually reveal a series of steps in the signal magnitude, superimposed upon a steady increase, as the electron beam injection point moves physically closer to the input of the amplifier – overall generating a staircase appearance. The near flat portion (tread) of the steps corresponded to the grain, and the near vertical portion of the steps (riser) to the grain boundary, response. Although the model predicted that the individual slopes within the linescan profiles were interdependent upon each other, (hence a change in the grain boundary resistance would impact both upon the gradient of the tread *and* the riser), it was suggested that by carefully measuring the gradients, and with a knowledge of the magnitude of the injected current, an estimation of the local resistance of the grains and their boundaries could be made from an overall global linescan response.

The model's main failing was its ability to only predict the linescan response of ZnO microstructures which showed "poor" varistor behaviour (as determined by other tests). Commercial quality material generated a distinct, non-linear staircase response under REBIC.



Fig. 1. REBIC micrograph of ZnO terrace line contrast (marker = 10μm).

In this paper, these observations and the model are discussed more fully and a significant modification is made to the purely resistive model developed previously by adding elements which exhibit diode behaviour. The work has shown that this so called "diodic-resistive" model can produce simulated terrace line contrast that more closely represents that observed under experimental conditions. Furthermore, attempts were made to damage varistor structures by applying repeated over-voltage conditions and this has generated a significant effect upon the observed diodic-resistive behaviour. Some thoughts on how this might impact upon failure analysis of varistors is given here.

2. BACKGROUND THEORY

Electrical ceramics such as ZnO can show localised EBIC effects under electron beam examination, but their overall contrast response is usually governed by the purely resistive nature of the material and its interaction with the injected beam current. If no, or minimal, charge amplification occurs in a homogeneous material, when an incident electron beam is absorbed, REBIC contrast is simple to model. Within the capabilities of modern current amplifiers (Wojcik 1999), and referring to Fig. 2 below, the specimen would be expected to generate a smooth image contrast that runs linearly between bright (large measured current) and dark (small measured current), corresponding to when the beam is close to the input of the current amplifier and when it is close to the earthed contact on the specimen (Fig.2 A and B, respectively). If the specimen contains discontinuities such as grain boundaries, charge trapping or charge separation could indeed alter the REBIC contrast and superimpose local variations upon the global linear REBIC response.

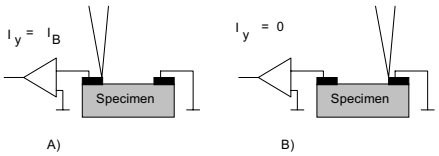


Fig 2. Conditions at extremes of beam travel. I_y = REBIC, & I_B = incident beam current.

Local variations in resistivity should also impact upon the contrast and it was this phenomenon that was thought to be responsible for the terraces discussed above. The algebraic model developed, consisted of parallel chains of high and low resistance elements. When a simulated constant current was injected into the model a staircase "linescan" response was generated. This was corroborated experimentally using a fabricated array of resistors and a constant current generator (below Fig. 3).

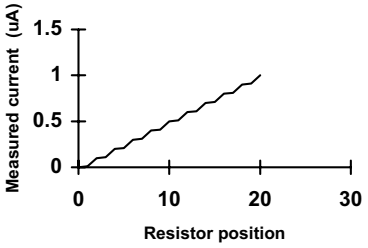


Fig. 3. Experimental trace obtained for case for resistor chain of 100 Ohms and 1 kOhm elements. Here $\mathbf{I_B}$ = 1.00μA (data from Wojcik and Wojcik 2003).

For both the algebraic and experimental models, the simulated "linescans" corresponded well to REBIC linescans obtained from laboratory ZnO samples but poorly to those from commercial grade ZnO devices (see later). The clue to the model's failing came when linescans were obtained from deliberately damaged commercial varistors. These results are presented below.

3. EXPERIMENTAL METHOD

For the experimental work, specimens were mounted for REBIC studies according to established procedures (Wojcik and Mason 2001). A Matelect ISM5A current amplifier was used for REBIC charge collection/measurement and imaging. Linescan acquisition was via the instrument's corresponding computer control interface and software. Linescans were obtained perpendicular to the REBIC contact pads, arranged as two linear strips on the ZnO surface, and taken approximately along the centre line of the specimen. To deliberately damage devices, voltages in excess of the varistor's specified breakdown were applied for a fixed period of time. A 20% overvoltage for 60 seconds was often found too aggressive, producing a material of too low a resistivity to image successfully. Lowering the voltage failed to generate any damage. Specimens were eventually selected at the 20% level that lay within the dynamic range of the apparatus.

To aid in revising the resistive model, a diode-resistor array was assembled from resistors and/or 1N148 diodes. A constant current source was used to inject the excitation current at various points along the chain. A picoammeter (Matelect PCI-3) was used to measure the current in the circuit in a manner described elsewhere (Wojcik and Wojcik 2003).

4. RESULTS AND DISCUSSION

Linescan data for commercial varistor devices has been reported earlier (ibid) but is included here for clarity (Fig. 4). The important observation here is the sharp non-linear decline in the REBIC signal as the beam traverses the specimen, which is in contrast to previously reported experimental results (Wojcik and Mason 2001) and to the linear staircase prediction generated by the purely resistive model cited above. Some subsidiary terraces can still be defined on the linescan (and were corroborated by qualitative images) but these appear to be superimposed upon the dramatic and non-linear change in the REBIC signal. This response strongly suggested the existence of non-linearly resistive, diode-like, behaviour within the material, most probably occurring within the grain boundary areas.

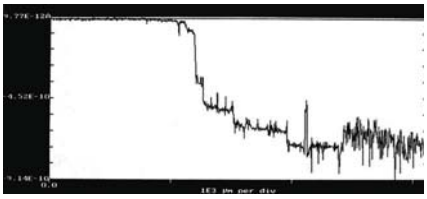
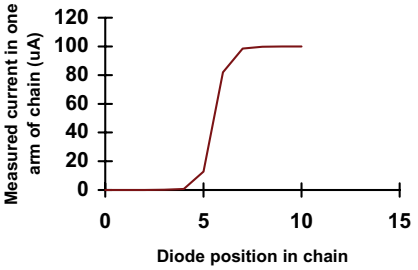


Fig. 4. REBIC Linescan trace obtained from section commercial ZnO varistor specimen showing terraces and dramatic drop.

It is accepted that correct varistor behaviour normally depends upon a marked non-linearity in the IV characteristics and hence the above observation and assertion comes as no great surprise, but it is interesting to see how the global (i.e. integrated) response impacts upon the REBIC response, which after all is capable of far more localised probing of the material's electrical behaviour. Further to this, the results of laboratory tests on the component arrays are worth discussing.

The response from a collection of diodes (i.e. no resistors) is shown in Fig. 5a below. Here, we see a strong correlation between the shape of the linescan and the experimental model's response. The forward voltage breakdown behaviour of the individual diodes is clearly highly influential in determining the linescan shape. Similar results were obtained for chains of diodes and resistors, with the "diodic" behaviour often swamping the resistive behaviour (although this may well be a function of the relative magnitudes of diodic and resistive elements chosen).



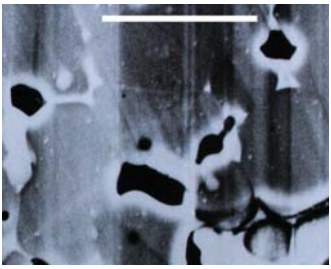


Fig. 5. a) Experimentally modelled REBIC response for a Si diode chain using 100 μA injected current, b) Diode contrast in ZnO under REBIC (bar = 1 μm).

Local diodic behaviour within ZnO could generate true EBIC contrast which would then be superimposed upon the overall linescan response and this was confirmed by experimentation. Fig 5b (above) is a micrograph taken under REBIC conditions that clearly shows enhanced current generation, indicative of diode sites, at probable grain boundary locations.

The complexity of algebraically modelling the integration of an array of non-linear IV resistive (i.e. diode) responses precluded inclusion of a revised mathematical model here, but some interesting preliminary results have been obtained for hypothetical arrays of diodes and resistors, which suggest that if non-linear resistive elements were present, the linescan responses obtained would be a function of the injected current (in other words, the beam current). As a consequence of this, the possibility emerges that the breakdown characteristics of diodic elements in polycrystalline electrical materials such as ZnO could be obtained through REBIC linescans undertaken at different beam currents. This work will be described in a future paper.

An interesting response was observed for the deliberately damaged varistor specimens. A representative linescan is shown in Fig. 6 below. This appears to have reverted to the old resistive-only model, in that the linescan reveals an almost linear response.

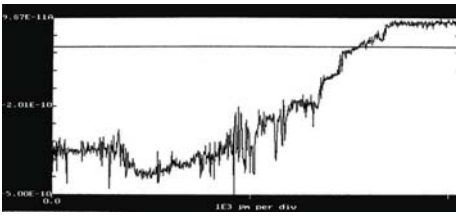


Fig. 6. REBIC linescan obtained from deliberately damaged ZnO varistor device showing absence of sharp transition in the response.

This response was repeated on several specimens and appears to indicate that the failure of the varistor to behave as a varistor is commensurate with the destruction of the diodic nature of the grain boundaries. Once destroyed, the varistor globally becomes a linear conductor exhibiting only minor localised terrace-line REBIC contrast, as generated by the remanent variation in the levels of grain boundary and grain resistivity. This appears to point to a possible REBIC based method for failure analysis of varistor devices and other electrically active ceramics.

REFERENCES

Matare H F and Laakso C W 1969 J. App. Phys. **40**, 476
Wojcik A G 1999 Inst. Phys. Conf. Ser. **164**, 693
Wojcik A G and Mason L E 2001 Inst. Phys. Conf. Ser. **169**, 579
Wojcik A G and Wojcik L E 2003 Inst. Phys. Conf. Ser. **180**, 589

The effect of barrier height variations in alloyed Al-Si Schottky barrier diodes on secondary electron contrast of doped semiconductors

F Zaggout and M El-Gomati

Department of Electronics, University of York, Heslington, York YO10 5DD, UK

ABSTRACT: The effect of heat treatment on the electrical behavior of aluminum on n-type silicon (Al/Si Schottky junctions) is used to study the effect of barrier height variation on secondary electron dopant contrast by annealing to 500°C. In this study, the variation of the Schottky barrier height has been detected as an increase of the contrast between Al on p^+ and Al on n-type Si doped regions. This increase is attributed to a decrease in the SE yield of the Al/n-type Si contact due to an increase in the Schottky barrier height after annealing.

1. INTRODUCTION

Secondary electron (SE) dopant contrast in the low voltage SEM has been explained by several models. However, while there is an acceptance of the electronic origin of this phenomenon, there is no agreement on its exact mechanism. Howie et al (1995) first attributed the SE contrast as due to band bending at the interface of the two differently doped semiconductors. Sealy et al (2000), on the other hand, explained the cause of the contrast to be due to the built in voltages of the n- and p-type semiconductors. This condition leads to patch fields forming at the surface of the sample and hence different ionization energies of the secondary electrons from the p- and n-type regions. These two models are plausible explanations for clean semiconductor surfaces, where the specimen environment is of ultra high vacuum quality. Samples that are transported in air, or those that have their surfaces treated outside the vacuum system, normally end up with several monolayers of foreign atoms residing on the surface; e.g. H, C and O. The effect of surface contamination on the resulting contrast was taken into account by El-Gomati and Wells (2001), who explained the obtained contrast as due to the formation of a metal-semiconductor (M-S) contact on the sample surface. These M-S junctions, depending on the material work functions, give rise to ohmic and Schottky contacts. The result is two different secondary electron yields showing contrast between the two regions.

The work presented here is aimed at further illustration of the secondary electron contrast in doped semiconductors. We investigate the relationship between the barrier height of Schottky contact and their secondary electron yield, as reflected in the contrast (brightness) level in low voltage SEM.

2. SAMPLE PREPARATION

The specimen used in this work is made in the form of boron-diffused patterns into a phosphorus-doped n-type silicon (111) substrate. The doping concentration of the n-type substrate is about $4\sim6\times10^{14}cm^{-3}$, while the p^+ areas had a carrier concentration of $1\times10^{19}cm^{-3}$ and the depth of the doping was about 5 μm. The sample was first ultrasonically cleaned in IPA and then dipped in HF to remove any native oxide on the surface. Aluminum metal was evaporated to a film thickness of about 7nm at a pressure of less than 4×10^{-6}mbar, through a metal mask to give several circular contacts (~0.42 mm diameter). The sample was then inspected in a Vega SEM, at different accelerating voltages. An Everhart-Thornly detector was used for SE image collection. The SEM, with a thermionic electron source, can obtain a base pressure of 6×10^{-5} mbar in the sample chamber

thermionic electron source, can obtain a base pressure of 6×10^{-5} mbar in the sample chamber routinely. After initial imaging the sample was then annealed in a 10% Hydrogen and 90% Nitrogen atmosphere to 500°C for 10 min. The sample was allowed to cool down to room temperature in the forming gas prior to loading into the SEM for SE imaging.

3. RESULTS

Figure 1 shows the contrast between p^+ and n-type Si regions that have a thin Al film of the order of 7 nm deposited. These images were collected with a beam of 1keV incident electrons. The images clearly show the contrast between the n- and p^+-type doped regions with an Al surface layer is increased after annealing. It is clear that the brightness of the n-type substrate with an Al surface layer is much higher than its value after annealing. This indicates that the SE yield from the n-type region is reduced as a result of the increased barrier height after heating the sample.

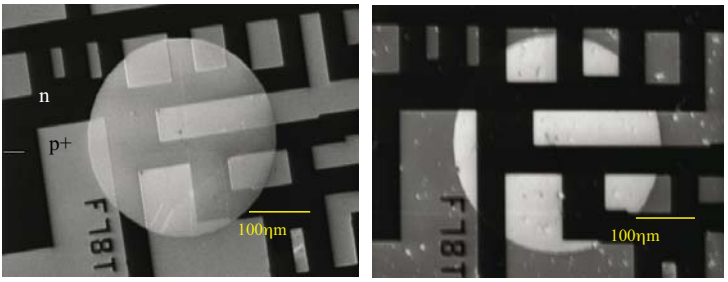


Fig. 1. (a) Room temperature. (b)After annealing to 500°C for 10 minutes.

The two samples were imaged in the SEM with different primary electron energies in the range 1 keV to 10 keV. The contrast obtained between the n- and p-type doped regions at each incident electron energy is used as a measure of the SE yield from these two regions. The contrast values are calculated from the digitally analysed images according to the following expression

$$C_{p^+/n} = (Cp^+ - C_n) / 256$$

where C_{p^+} and C_n are the average pixel intensities of the p^+ doped layer and n-doped substrate, respectively.

The reduction of the SE yields from the Al on n-type regions leads to enhanced contrast as shown in Fig. 2.

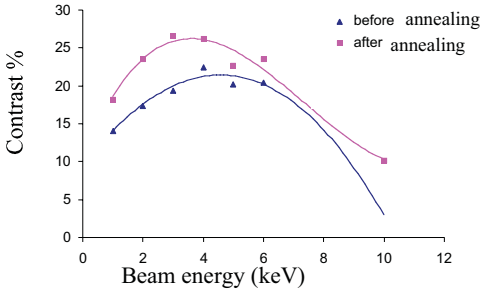


Fig. 2. The contrast as measured from images taken at different accelerating voltages before and after annealing. Note the enhanced contrast after annealing.

4. DISCUSSION

The observed contrast within the Al covered structures can be explained by the M-S contact model. For $\phi_{Al} < \phi_{si}$, Schottky barriers are formed between Al and n-type Si and between Al and p-type Si of low dopant concentrations. An ohmic contact is normally formed between Al and p^+ doped region (Rhoderick and Williams 1988). This causes Al on the n-type Si regions to appear darker than Al on p^+ doped Si regions in the SE mode as shown in Fig. 1a.

4.1 The Effect of Heat Treatment

Heat treatment is a practical application used in the manufacture of Schottky diodes, and in principle is used to control the barrier height in the case of Al-Si contacts. This phenomenon has been extensively studied because of its technological importance.

Chino (1973) first reported that Al/Si contacts, heated above 450°C showed a significant change in I/V characteristics, which, in the case of n-type Si, could be described in terms of an increase in the barrier height. Card (1975) reported that Al-p-type Si contacts show complementary behavior, with barrier height decreasing due to annealing over the same temperature range, as shown in Fig. 3

The enhanced contrast in the experiment carried out in this study can be explained as due to increasing the Schottky barrier between Al and n-type silicon. At temperatures around 500°C Si is taken up into solid solution by the Al to an amount determined by the solubility limit at the particular temperature. On cooling, an interfacial layer of Si is formed between the Si and Al that contains Al atoms. This layer of Si is doped p-type, because Al is an acceptor. So, the net space charge density is negative near the Al/Si-Al interface, and the bands become bent downwards as shown in Fig.4. In the case of p-type Si, the Al doped layer causes the depletion region to become narrower, so that the effective barrier height is reduced. Further no change in barrier height in the case of Al/ p^+ doped Si contacts was reported.

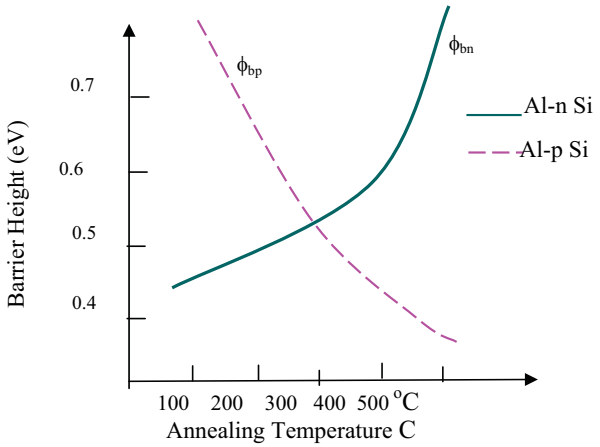


Fig. 3. Barrier height of Al contacts to n-type Si and p-type Si, as a function of annealing temperature: Card (1974).

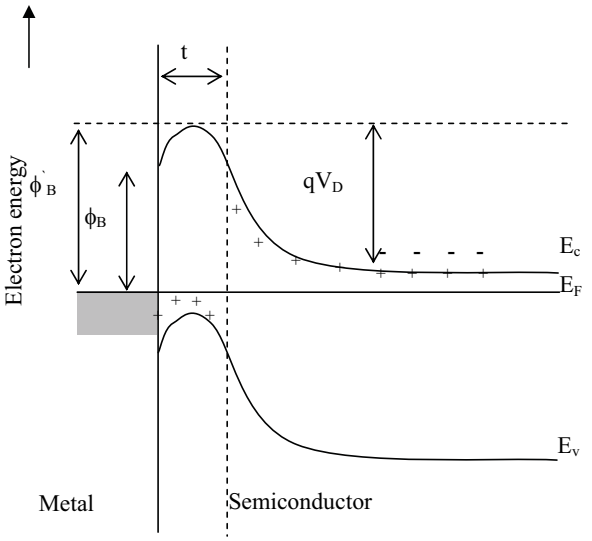


Fig. 4. Band diagram for Al –Si contact after heat treatment (Basterfield et al 1975).

5. CONCLUSIONS

The effect of heat treatment on the electrical behaviour of Al/Si contacts has been used to study the effect of barrier height variation on the secondary electron dopant contrast by annealing the sample to 500°C. Analysis of the collected SE images shows enhanced contrast by a factor of 8.95% after annealing. This increase is caused by an increase of the barrier height between the Al layer and the n-type Si by up to 0.35eV. The increased barrier is caused by extending the Al overlayer further into the Si sample, which changes the net charge near the interface, resulting in a higher barrier for the SE generated in the n-type Si. This is compared with an ohmic contact made between the Al film and the p^+ doped region.

The results presented here show a dependence of the SE contrast of doped semiconductors on surface layers due to the formation of M-S contacts, which provides further support for this model.

ACKNOWLEDGEMENTS

The authors would like to thank T R C Wells for critical reading of the manuscript. F. Zaggout would like to thank the University of Misurata, Libya for financial support.

REFERENCES

Basterfield J, Shannon J M and Gill A 1975 J. Solid-State Electron. **18,** 290
Card H C 1975 Solid State Commun. **16**, 87
Chino K 1973 Solid State Electron. **16**, 119
El-Gomati M M and Wells T R C 2001 J. Appl. Phys. Let. **79**, 2931
Rhoderick E H and Williams R H 1988 Metal–Semiconductor Contacts, second edition, Oxford, Clarendon Press, ch.5
Sealy C, Castell M and Wilshaw P 2000 J. Electron Microsc. **49**, 311

Author Index

Abid J.-P. 291
Abid M. 291
Abouzaid M. 171
Adawi A.M. 427
Aers G.C. 247
Ambacher O. 131, 135
Anil K.G. 379
Arbiol J. 333
Azize M. 51

Bakkers E.P.A.M. 295
Balkenende A.R. 295
Bapat A. 323
Barkay Z. 503
Barna Á. 159
Barnard J.S. 25, 59
Barnes C.H.W. 225
Barnham K. 503
Batson P.E. 451
Beanland R. 163, 259, 491
Bedell S. 89
Ben T. 191, 195, 271, 299
Benassayag G. 93
Bender H. 347, 379, 397
Benedetti A. 379
Bethoux J.M. 51
Biskupek J. 319
Bluhm A.K. 467
Bonera E. 371
Borisevich A.Y. 459
Bougrioua Z. 51
Brown P.D. 143, 155
Buca D. 97
Bugiel E. 343
Bullough T.J. 491
Bushnell D.B. 503

Cabié M. 93
Cadby A. 427
Campbell S.A. 323
Campion R.P. 143, 155
Carter C.B. 83, 315, 323
Casals O. 291
Caymax M. 97
Cerrina C. 413
Cerva H. 437
Chalker P.R. 491
Chamirian O. 379
Chang A.C.K. 111, 413
Chang M.N. 351
Chen G.-T. 423
Cheng T.C. 351
Cherns D. 45
Cherns P.D. 55
Chisholm M.F. 459
Chithrani D. 247
Cho M.H. 3
Cho S.-J. 171
Chung K.B. 3
Chuvilin A.L. 359
Chyi J.-I. 423
Cież M. 511
Cockayne D.J.H. 177
Collin J.-P. 291
Connolly L.G. 427
Cooper D. 203, 221
Coraux J. 3
Cornet A. 333
Costa P.M.F.J. 287
Cros A. 3
Cullis A.G. 111, 263, 267, 413, 423, 427
Czernohorsky M. 343

Dahl C. 441
Dähne M. 479
Daneu N. 199
Datta R. 59
Daudin B. 3
Dawson P. 25
Day J. 499
De Mierry P. 51
de Potter M. 379
Dean R. 427
Delimitis A. 71
Deneen J. 83, 315, 323
Deneke Ch. 311
Dennemarck J. 79
Derluyn J. 389
Dimakis E. 71
Ding Y. 323
Domański K. 375
Domengès B. 367
Domenicucci A. 89
Domyo H. 363
Donnet D.M. 403
Doole R.C. 177
Drijbooms C. 397
Drouot V. 259
Dunin-Borkowski R.E. 203, 221, 225, 229, 243
Durose K. 515

Edmonds K.W. 143, 155
Eisele H. 479
Ekins-Daukes N.J. 503
El-Gomati M. 499, 523
Elwenspoek M. 75
Evans A.G.R. 413

Falster R.J. 355
Fanciulli M. 371
Farrer I. 221
Favre-Nicolin V. 3
Fay M.W. 143, 155
Fazzini P.F. 217
Fedele M. 487
Fedina L.I. 359
Ferroni M. 475
Fichtner P.F.P. 97
Filatov D.O. 107
Fissel A. 343
Flissikowski T. 467
Förster Ch. 131
Fournel F. 93
Foxon C.T. 143, 155
Fraser K.J. 355
Fry P.W. 267
Furuya K. 239
Fuster D. 299

Galindo P. 191, 195
Gallagher B.L. 143, 155
Galloway S.A. 355
García J.M. 271
García R. 139, 251, 255, 279, 299
García-Cristóbal A. 3
Garro N. 3
Gass M.H. 163, 259, 491
Georgakilas A. 71
Germain M. 389
Gerth G. 103
Gerthsen D. 167, 233, 275, 303
Giannazzo F. 487
Glas F. 147, 151
Godfrey M. 25
Gomati M.M El 495
González D. 139, 251, 255, 279
González L. 299
González M.U. 299
González Y. 299
Goodhew P.J. 163, 259
Goringe M.J. 307
Gösele U. 103
Graat P.C.J. 295
Grabiec P. 375
Grabowski J. 479
Graham D.M. 25
Grahn H.T. 467
Granados D. 271
Grigoryev L.V. 327
Grün M. 275
Grunbaum E. 503
Guerrero E. 191, 195
Gustafsson A. 463
Gutakovskii A.K. 359
Gutiérrez M. 139, 279, 251, 255
Guzmán A. 467

Han Y. 143, 155
Hartmann J.M. 93
Hashimoto T. 409
Hawkridge M. 45
Heera V. 159
Hernández F. 291
Herrera M. 139, 251, 255, 279
Hetherington C.J.D. 177
Hetterich M. 275
Hey R. 467
Hierlemann M. 437
Hill G. 63
Hjort K. 291
Ho G.W. 287
Ho T. 363
Hogg R. 267
Hollaender B. 97
Hommel D. 17, 79
Hopkinson M. 139, 251, 255, 263, 267, 279
Houben L. 183
Hsueh H.T. 351
Huang W.J. 351
Hueging N. 97
Humphreys C.J. 13, 25, 29, 55, 59, 287
Hung W.C. 423, 427
Hutchison J.L. 177
Hwang H.-L. 339
Hÿtch M.J. 243

Iacopi F. 347
Ichihashi T. 393
Impellizzeri G. 487
Iwase F. 417

Jäger W. 117
Jahn U. 467
Jain A. 67
Jalabert D. 3
Jaroszewicz B. 375
Je J.H. 21
Jin-Phillipp N.Y. 311
Jones T.S. 243

Jouati A. 291
Joyce B.A. 243

Kaiser M. 295, 379
Kaiser U. 319
Kalmykov A.E. 327
Kamino T. 409
Kappers M.J. 13, 25, 29, 55, 59
Karakostas Th. 71
Kasama T. 203
Kątcki J. 375, 511
Kehagias Th. 71
Keim E.G. 75
Kelsch M. 311
Kenda A. 437
Kirfel O. 343
Kirkland A.I. 177
Kirmse H. 433
Kittl J.A. 379
Kling R. 167, 303
Klingshirn C. 275
Kodambaka S. 283
Kolodka R.S. 267
Komninou Ph. 71
Konno M. 409
Kortshagen U. 323
Kret S. 271, 299
Krijnen G.J.M. 75
Kröger R. 17, 79
Kruse C. 79
Kruse P. 167, 233, 303
Kübel C. 17
Kumar S. 83
Kung S.C. 351
Kurniawan O. 471
Kwon Y.B. 21

Lamoen D. 151, 233, 303
Łaszcz A. 511
Latyshev A.V. 359
Lauwers A. 379
Lefebvre J. 247
Lemaître A. 147
Lenk A. 213, 319, 441
Lentzen M. 183
Lenz A. 479
Leys M.R. 389
Lichte H. 213, 319, 441
Lidzey D.G. 427
Liebmann R. 437
Lin H.-C. 423
Lin J.C.C. 267
Litvinov D. 275
Liu C. 171
Liu H.Y. 139, 263, 279
Liu J. 379
Llorens J.M. 3
Lo H.-M. 445
Loo R. 97
Lozano J.G. 139, 279
Luck J.T. 459
Luo J.-S. 445
Lupini A.R. 459
Luysberg M. 97, 183

Maex K. 379
Mahajan S. 33
Mantl S. 97
Matsuda T. 417
Maximov G.A. 107
Mazzer M. 503
McAleese C. 13, 55
McCartney M.R. 203
McKenzie W.R. 363
Merli P.G. 217, 475
Midgley P.A. 203, 221, 225, 229, 243
Miguel-Sánchez J. 467
Mirabella S. 487
Mitsuishi K. 239
Mocuta A. 89
Molina S.I. 191, 195, 271, 299
Moon D.W. 3
Moon Y.-T. 171
Morales F.M. 131, 135
Morandi V. 475
Morante J.R. 291, 333
Moreau P. 307
Morkoç H. 171
Morschbacher M.J. 97
Mucciato R. 487
Muehle U. 213, 441
Müller E. 167, 303
Munroe P.R. 363
Murray R.T. 63

Navaretti P. 139, 279
Neumann W. 433
Newcomb S.B. 229
Nikolitchev D.E. 107
Norris D.J. 111, 413
Nouet G. 21, 67, 71, 171
Novikov S.V. 143, 155

O'Neill A.G. 111
Oesterle W. 433
Ohnishi T. 409
Ohno Y. 393, 483, 507
Oliver R.A. 13, 29, 287

Olsen S.H. 111
Ong V.K.S. 471
Osten H.J. 343

Papworth A.J. 163, 259, 491
Parbrook P.J. 63
Pashley D.W. 243
Pasold G. 319
Passow T. 275
Patriarche G. 147
Pawlak M.A. 379
Pazirandeh R. 433
Pécz B. 159
Peiró F. 333
Peng Y. 459
Pennycook S.J. 459
Perovic D.D. 247
Perrey C.R. 83, 315, 323
Pezoldt J. 131, 135
Pizarro J. 191, 195
Płuska M. 511
Ponchet A. 93
Pongratz P. 437
Poole P.J. 247
Pozzi G. 217
Pretorius A. 17
Priolo F. 487
Proietti M.G. 3

Raineri V. 487
Rajagopalan S. 117
Ratajczak J. 375, 511
Rečnik A. 199
Redwing J.M. 67
Renard A. 367
Renevier H. 3
Reuter M.C. 283
Richard O. 347, 379, 397
Ritchie D.A. 221
Roberts H. 403
Rocher A. 93
Roest A.L. 295
Romano-Rodríguez A. 291
Romanovsky V. 495, 499
Rosenauer A. 17, 79, 151, 233, 275, 303
Ross F.M. 283
Ross I.M. 63, 111, 263, 267, 413
Rossinyol E. 333
Rouvière J.-L. 3
Roy R. 89
Russell J.D. 445
Ruterana P. 21, 67, 171
Ruythooren W. 389

Sadana D.K. 89
Samuelson L. 463
Sánchez A.M. 163, 259, 271, 491
Saravanan S. 75
Sasaki H. 417
Schmidt O.G. 311
Schöne J. 117
Schowalter M. 17, 151, 233, 303
Schubert L. 103
Seifert W. 463
Senkader S. 355
Shapira Y. 503
Shimojo M. 239
Sides W.H. 459
Silva S.R.P. 307
Singh P. 67
Sköld N. 463
Skolnick M.S. 255, 267
Skorupa W. 159
Smeeton T.M. 25
Sokolov L. 103
Sokolov V.I. 327
Solovyov L.A. 333
Somodi P.K. 203, 225, 229
Song M. 239
Song S.A. 359
Songmuang R. 311
Sorokin L.M. 327
Spiecker E. 117
Stauden Th. 135
Stoffel M. 311
Stolojan V. 307
Stowe D.J. 355

Tahraoui A. 427
Takeda S. 393
Takeguchi M. 239
Tanabe K. 417
Tanaka M. 239
Tang Y.T. 413
Tartakovskii A.I. 255, 267
Tatsuoka H. 515
Tersoff J. 283
Tey C.M. 263
Thevenard L. 147
Thomas J. 311
Thust A. 183
Tian B. 333
Tilke A.T. 441
Tillmann K. 183
Timm R. 479
Titchmarsh J.M. 177
Tőkei Zs. 347

Torigoe K. 393
Torregiani C. 379
Tottereau O. 51
Tsai C.-H. 339
Twitchett A.C. 203, 221, 225, 229

Ubaldi F. 217
Umemura K. 409
Urban K. 97, 183

Valizadeh S. 291
Van Benthem K. 459
van Berkum J.G.M. 379
Van Daele B. 389
van Dal M.J.H. 379
van der Laak N.K. 13, 29
Van Marcke P. 397
Van Tendeloo G. 389
Varela M. 459
Veloso A. 379
Vennéguès P. 51
Verheijen M.A. 295
Vilà A. 291

Waag A. 167, 303
Wagemans M.M.H. 295
Wagner C. 441
Walker C.G.H. 495
Walther T. 199
Wang Ch. 135
Wang K. 143
Wang T. 423
Weih P. 135
Wells T. 499
Werner P. 103
Wiebicke E. 467
Williams R.L. 247
Wilshaw P.R. 355, 503
Witthuhn W. 319
Wojcik A.G. 519
Wojcik L.E. 519
Wojdak M. 67
Wondergem H.J. 295
Wong A.S.W. 287
Wu J.S. 351
Wu Y.-L. 339
Wzorek M. 375

Xiao B. 171

Yaguchi T. 409
Yamaguchi T. 17
Yáñez A. 191, 195
Yates T.J.V. 229
Yun F. 171

Zaggout F. 523
Zakharov N. 103
Zeimer U. 433
Zhao D. 333
Zhi D. 243

Subject Index

3D-imaging 333
Ab initio calculation 359
Ab initio computation 233
Aberration correction, lens 459
Aberration corrector, lens 451
Ageing processes 511
Aluminium gallium arsenide 463
Aluminium gallium nitride 51, 55, 63, 389
Aluminium nitride 3, 33, 51, 55, 75, 79
Aluminium-copper alloy 445
Amorphous carbon 307
Amorphous silicon 363, 375
Analysis, semiconductor device 409
Anneal, rapid thermal 379
Annealing 29, 255
  furnace 375
  rapid thermal 319, 389
Anodic etching 327
Anti phase boundary 83
Anticorrelation, quantum dot 255
Antimony implantation 475
Antiphase boundary 483
Antisite defect 147
ASSM argon sputter shadowing 445
Atomic force microscopy 13, 29, 33, 75, 267
Auger electron spectroscopy 417, 445, 499

Back scattered electron detector 495
Back scattered electron, imaging 475
Band alignment, type II 479
Bend contour 93
Bevel polishing 117
Bond pad analysis 445
Boron ion implantation 375
Bubble coalescence 97
Buffer layer 67

Cadmium sulphide 515
Calculation, *ab initio* 151
Cantilever epitaxy 33
Carbon acceptor 463
Carbon nanotube 339, 351
Carrier localisation 25
Carrier profiling 487
Carrier, diffusion length 471
Carrier, effective mass 307
Cathodoluminescence 355, 463, 467, 511
  polarized 507
Charge carriers mobility 327
Charging effect 217, 445
Charging, specimen 203
Chemical vapour deposition 283, 287, 367
  UHV 131
Circuit editing 403
Clustering, adatom 393
CMOS device 379
Cobalt ion implantation 319
Cobalt silicide 203, 319, 379
Columnar growth 171
Composition determination 151
Composition fluctuation 279
Computation, *ab initio* 233
Computation, first-principles 233
Concept EM 199
Convergent beam electron diffraction 143
  large angle 437
Correlation, quantum dot 251
Crack, epitaxial layer 51, 63
Cracking, layer 55
Cross-correlation, normalized 195
Cross-sectional electron microscopy 3, 33, 45, 63, 131, 139, 159, 167, 213, 243, 275, 295, 343, 375, 379, 397, 403, 413, 417, 441
Cross-sectional scanning tunnelling microscopy 483
Cu corrosion 397
CuPt-ordering 483
Current – voltage characteristic 327
Curvature, sample 93

Damage layer, plasma processing 347
Dark-field imaging 433
Dead layer, surface 213
Defect, {113} 359
Defect, antisite 147
Defect, epitaxial 367
Defect, interstitial 147
Defect, platelet 97
Defocus estimation 195
Density functional theory 151, 233
Deposition, electron beam induced 239
Device degradation 433
Device simulation 217
Diamond 159
Dielectric, hi-K 339, 343, 451
Diffraction, electron 131, 343
Diffraction, X-ray 3, 51, 67, 75, 89, 117, 379
Diffractogram, electron 459
Diffusion length 467
  carrier 471
Diffusion, adatom 393

Dislocation 433
core structure 183
density 59
edge 55, 59, 167
electrostatic potential 167
large area analysis 117
line charge 167
loop 51, 97
misfit 17, 21, 51, 55, 71, 97, 117, 159, 243
mixed 55, 59
nucleation 97
screw 59
threading 21, 33, 55, 63, 71, 167
Dislocation loop, Frank 139
Distributed Bragg reflector 79, 423
Dopant concentration 511
Dopant contrast 203, 503, 523
Dopant profile 217
Dopant profiling 213
Dopant-potential 229
Doping profile 475
DRAM device 445

EBSD diffraction, electron backscattered 287
Effective mass, carrier 307
Effective mass, electron 491
Electroluminescence 423
Electron backscattered diffraction 287
Electron beam induced current 471, 515, 519
Electron beam induced deposition 239
Electron diffraction 131, 343, 511
convergent beam 143
Electron diffractogram 459
Electron energy loss spectroscopy ..... 45, 55, 143, 163, ... 199, 239, 259, 307, 311, 389, 451, 459, 491
Electron holography ..... 167, 213, 217, 221, 225, ... 229, 233, 303, 319, 441
off-axis 203
Electron interference 217
Electron irradiation 393
Electron monochromator 451
Electron tomography 229
Electron, backscattered 475
Electron, effective mass 491
Electron, silicon field emission 351
Electronics, carbon nanotube 339
Electrostatic potential 203, 217
3-D 229
Energy filtered TEM 263, 307, 347
Energy level, localized 507
Epitaxial growth on sapphire 171
Epitaxy, cantilever 33
Epitaxy, layer overgrowth 33
Epitaxy, pendeo- 33
Exit-plane wave function reconstruction 183

Failure analysis 403
3D 409
Ferromagnetic semiconductor 143, 147
Field emission, silicon 351
Finite element analysis 93
First-principles computation 233
Fluorine ion implantation 375
Focused ion beam 295
milling ..... 63, 79, 93, 111, 213, 221, 225, 229, 267, ... 291, 367, 379, 397, 403, 409, 413, 417, ... 423, 427, 441
Fowler-Nordheim model 351

Gadolinium oxide 339, 343
Gallium aluminium arsenide 417
Gallium antimonide 479
Gallium arsenide 151, 183, 417
as substrate ..... 155, 159, 163, 243, 251, 255, 259, 263, ... 267, 271, 275, 311, 467, 479, 507
nanowire 463
Gallium indium arsenide nitride 139, 279
Gallium indium phosphide 483
Gallium manganese arsenide 143, 147
Gallium manganese nitride 143, 155
Gallium nitride ..... 3, 13, 21, 25, 29, 33, 45, 51, 55, 59, 63, ... 71, 79, 83, 159, 183, 287, 389, 417, 423
Gallium phosphide 295
Gas sensor 333
Gate oxide 343
Geometric phase 191
Germanium 117
Gettering, impurities 355
Gold adatom 393
Gold particle 463
Gold-silicon eutectic 283
Growth, self-catalytic 287
Gyroidal structure 333

Hafnium oxide 339
Hafnium dioxide 451
Height reconstruction 495
Helium bubble 97
Helium ion implantation 97
Heterojunction bipolar transistor 433
Heterophase interface 71
Hexapole lens 459
High angle annular dark field imaging ..... 25, 45, 55, 111, ... 239, 263, 311, 389
High angle scattering, electron 103

High resolution electron microscopy ..... 3, 17, 21, 33, 45, ... 71, 79, 131, 159, 191, 195, ... 271, 287, 299, 303, 311, 319, ... 333, 343, 359, 367, 417
lens corrected 177
High-K dielectric 339
High-resolution electron microscopy 13, 183
Holography, electron ..... 167, 221, 225, 229, ... 233, 303, 319, 441
HOLZ lines 437
Hopping conduction 467
Howie-Whelan equations 167
HREM 171
Hydride vapour phase epitaxy 45

IC analysis 403
Image delocalisation 183
Image matching, electron microscope 195
Image simulation 359
Imaging, 3D 333
Imaging, three-dimensional 459
In situ electron irradiation 359
In situ electron microscopy 283
InAs indium arsenide 251
Indium aluminium arsenide 263
Indium arsenide ..... 151, 243, 247, 263, ... 267, 271, 299, 311
Indium gallium arsenide ..... 117, 151, 163, 255, 259, ... 263, 275, 417, 467
Indium gallium arsenide nitride 467
Indium gallium nitride 13, 17, 25, 29, 79
Indium gallium phosphide 117, 433
Indium nitride 67, 71
Indium phosphide 247, 295, 299, 417
Indium tin oxide 427
Inner potential, mean 303
Interface, epitaxial 159
Interface, nanoparticle 315
Interlayer 55
Inversion boundary 83
Ion etching, gas-enhanced 423
Ion implantation, in silicon 97, 355, 375, 475
Ion implantation, in silicon carbide 319
Ion scattering, medium energy 3
Iron silicide 515

Junction, p-n 229

Kramers Kronig analysis 259
Kramers Kronig transformation 491

Laser facet 423
Laser, vertical cavity surface emitting 79
Lattice imaging ..... 3, 13, 17, 21, 33, 45, 71, 79, 131, 159, ... 177, 183, 191, 195, 271, 287, 299, 303, ... 311, 319, 333, 343, 359, 367, 417
Lens corrector 177
Lens, aberration correction 459
Lens-corrected electron microscope 83
Lens-corrected electron microscopy 451
Localization, state 467
Localized energy level 507
Low energy scanning analytical microscope 499
Low energy scanning electron microscopy 495
Low voltage SEM 499
Low-K dielectric 347
Luminescence, silicon 355
Lumogen Red 427

Magnetic dipole 319
Manganese arsenide precipitate 143, 155
Mean inner potential 233
Metal organic chemical vapour deposition ..... 13, 17, 21, ... 25, 29, 45, 51, 55, 59, 63, 79, ... 247, 259, 295, 479, 483
Metal organic precursor, cracking 239
Microanalysis, ConceptEM 199
Microanalysis, X-ray 111, 147, 199
Misfit calculation 159
Misfit dislocation 17, 21, 55, 71, 97, 117, 159, 243
Mn atom, interstitial 147
Mn atom, substitutional 147
Mn doping 171
Mn rich precipitates 171
$MnZnO_3$ 171
Mobility, charge carrier 327
Moire fringes 89
Molecular beam epitaxy ..... 17, 71, 103, 107, 139, 143, ... 147, 221, 243, 251, 263, 267, 271, ... 275, 279, 299, 311, 343, 413, 487, 507
plasma assisted 155
plasma enhanced 3
Monochromator, electron 451
Morphological instability 413
MOSFET 89, 111
characterisation 413
silicon germanium 339
Multiple quantum well structure 103

Nano-CMOS 339
Nanocomposite 327
Nanocontact 291
Nanocrystal, cobalt-rich 319
Nanocrystal, samarium-rich 319
Nanodot array 239
Nanoelectronics 339

Nanofabrication 239, 291
Nanoneedle 287
Nanoparticle 323, 393
  silicon 327
Nanopipe 63
Nanorod, zinc oxide 303
Nanosaw 83
Nanostructure, directly written 239
Nanostructure, free-standing 239
Nanostructure, self-assembled 107
Nanotube, carbon 339
Nanotube, semiconductor 311
Nanowire 287, 291, 295, 463
  3D network 327
  silicon 283
Neodymium oxide 343
Nickel silicide 379
Nucleation 21
  layer 33

Octupole lens 459
Ohmic contact 389
Oxidation, silicon 327
Oxygen impurity 45

Partial dislocation 507
Peak finding 191
  method 271, 299
Peak pairs algorithm 191
Pendeo-epitaxy 33
Phase image 319
Phase transformation 511
Phosphor 511
Photo-induced glide 507
Photo-induced stress 507
Photoluminescence 25, 29, 67, 247, 267
Photonic crystal 427
Photovoltage spectroscopy 107
Piezoelectric semiconductor 75
Piezoresistor 375
Plasma cleaning 397
Plasma deposition, hypersonic particle 315
Plasma deposition, silane-argon 323
Plasma etching 427
Plasmon delocalisation 307
Plasmon excitation 163, 259, 491
Platelet defect 97
P-n junction 217, 221, 225, 229
Polarity, buffer layer 67
Polarized cathodoluminescence spectroscopy 483
Polyimide 445
Polysilicon gate 379
Polytypes, silicon carbide 131
Poole-Frenkel emission 339
Porous silicon 327
Positive phase contrast imaging 183
Potential distribution 213
Promethium oxide 343
Quadrupole lens 459
Quantitative microscopy 191
Quantum confinement 307
Quantum dot 3, 13, 17, 29, 243, 247, 255, 259, 263, 267, 275, 479
  array 247
  correlation 251
Quantum ring 271
Quantum well 25, 139, 163, 275, 279, 467, 479, 483, 487, 503
Quantum wires 299

Raman microscopy, resonant 371
Rapid thermal anneal 379
Rear earth oxide 343
Recombination, nonradiative 463
Recombination, radiative 463
Reflection high energy electron diffraction 275
Remote EBIC 515, 519
Residual lens aberrations 183
Resistivity profiling 515
Resolution, sub Ångstrom 459
Ronchigram 177, 451
Rutherford backscattering spectroscopy 97

Salicide process 379
Samarium ion implantation 319
Samarium silicide 319
Sample preparation, TEM 403
Sapphire, as substrate 33, 59, 71
Scanning Auger mapping 499
Scanning Auger microscopy 107
Scanning capacitance microscopy 487
Scanning low energy electron microscopy 499
Scanning transmission electron microscopy ... 25, 55, 111, 163, 263, 409, 413, 451, 459
Scanning tunnelling microscopy, cross-sectional 479, 483
Schottky barrier 523
Secondary electron 523
Segregation, elemental 199, 275
Segregation, germanium 111
Selected area electron diffraction 155
Selective area epitaxy 267
Selective growth 393
Self-ordering IV pairs 359
Self-organisation, islands 29
Shallow trench isolation 371, 437
Shape from shading 495
Shottky emission 339
Silica, porous 347

Silicon carbide 131, 135, 159
ion implantation 319
Silicon defects 359
Silicon device 217, 437
Silicon dioxide 89, 343, 451
mask 267
Silicon nanodot 339
Silicon nanowire 283
Silicon, amorphous 363, 375
Silicon, as substrate 103, 131, 135, 311, 393, 413
Silicon, field emission tip 351
Silicon, ion implantation 355, 375
Silicon, luminescence 355
Silicon, nanocube 323
Silicon, nanoparticle 315, 327
Silicon, on insulator 363
Silicon, on sapphire 363
Silicon, oxidation 327
Silicon, p-n junction 229
Silicon, porous 327
Silicon-germanium alloy ..... 89, 93, 103, 107, 111, ... 311, 379, 413, 441, 487
Silicon-germanium on insulator 89
Silicon-germanium relaxation 89
Silicon-gold eutectic 283
SIMOX substrate 89
Simulation, computer 225
Simulation, device 217, 437
Simulation, image profile 475
Simulation, ion implantation 475
Site selectivity 247
Site specific sample preparation 409
Solar cell 503
Specimen preparation 203
Spherical-aberration correction 183
Spintronics 143
Sputter deposition 171
Sputtering, reactive 75
Stacking fault 83, 135, 139, 183, 507
Static atomic displacement 151
Stem measurement 93
Strain determination 191
Strain engineering 89
Strain mapping 191
Strain measurement 93, 163, 271, 437
Strain relaxation 97, 135, 243
Strain state analysis 17, 79
Strain, biaxial 3
Stranski-Krastanow growth 13
Stress measurement, electronic devices 371
Stress relief, by cracking 63
Stress, silicide induced 379
Structural modelling 359
Structure factor 147, 151
Substrate, virtual 111
Superlattice 79, 307
Surface angle measurement 495
Surface height, measurement 495
Surface integration 495
Surface morphology 75
Surface recombination velocity 471
Surface roughness 393
Surface, damage layers 417

Tellurium dioxide 427
Templating 247
Thermally mixed SGOI 89
Thickness estimation 195
Threading dislocation 21, 59, 71
Titanium nitride 389
Titanium silicide 379
Tomography, electron 229
Topography, surface 495
Transistor, nanoscale 323
Transition zone, specimen 213
Trap, activated 327
TSUPREM device simulator 437
Tungsten oxide, mesoporous 333
Tungsten silicide 203
Tunnelling conduction 467
Twin defect 135, 363

Valence loss 307
Vapour-liquid-solid growth 103, 283, 295
Varistor 519
Virtual substrate 111

Weak-beam imaging 33, 55, 59, 117, 283, 507
Whisker growth 103
Wien filter 451

X-ray diffraction 3, 51, 67, 75, 89, 117, 379
X-ray microanalysis 111, 143, 147, 199, 417, 433
X-ray photoelectron spectroscopy 445

Z-contrast 17, 459
Zemlin tableau 177
Zinc oxide 167, 199, 303, 519
Zinc selenide 507
Zinc sulphide 83, 511
Zirconium oxide 339
ZnO 171

SPRINGER PROCEEDINGS IN PHYSICS

60 **The Physics and Chemistry of Oxide Superconductors**
Editors: Y. Iye and H. Yasuoka

61 **Surface X-Ray and Neutron Scattering**
Editors: H. Zabel and I.K. Robinson

62 **Surface Science**
Lectures on Basic Concepts and Applications
Editors: F.A. Ponce and M. Cardona

63 **Coherent Raman Spectroscopy**
Recent Advances
Editors: G. Marowsky and V.V. Smirnov

64 **Superconducting Devices and Their Applications**
Editors: H. Koch and H. Lübbing

65 **Present and Future of High-Energy Physics**
Editors: K.-I. Aoki and M. Kobayashi

66 **The Structure and Conformation of Amphiphilic Membranes**
Editors: R. Lipowsky, D. Richter, and K. Kremer

67 **Nonlinearity with Disorder**
Editors: F. Abdullaev, A.R. Bishop, and S. Pnevmatikos

68 **Time-Resolved Vibrational Spectroscopy V**
Editor: H. Takahashi

69 **Evolution of Dynamical Structures in Complex Systems**
Editors: R. Friedrich and A. Wunderlin

70 **Computational Approaches in Condensed-Matter Physics**
Editors: S. Miyashita, M. Imada, and H. Takayama

71 **Amorphous and Crystalline Silicon Carbide IV**
Editors: C.Y. Yang, M.M. Rahman, and G.L. Harris

72 **Computer Simulation Studies in Condensed-Matter Physics IV**
Editors: D.P. Landau, K.K. Mon, and H.-B. Schüttler

73 **Surface Science**
Principles and Applications
Editors: R.F. Howe, R.N: Lamb, and K. Wandelt

74 **Time-Resolved Vibrational Spectroscopy VI**
Editors: A. Lau, F. Siebert, and W. Werncke

75 **Computer Simulation Studies in Condensed-Matter Physics V**
Editors: D.P. Landau, K.K. Mon, and H.-B. Schüttler

76 **Computer Simulation Studies in Condensed-Matter Physics VI**
Editors: D.P. Landau, K.K. Mon, and H.-B. Schüttler

77 **Quantum Optics VI**
Editors: D.F. Walls and J.D. Harvey

78 **Computer Simulation Studies in Condensed-Matter Physics VII**
Editors: D.P. Landau, K.K. Mon, and H.-B. Schüttler

79 **Nonlinear Dynamics and Pattern Formation in Semiconductors and Devices**
Editor: F.-J. Niedernostheide

80 **Computer Simulation Studies in Condensed-Matter Physics VIII**
Editors: D.P. Landau, K.K. Mon, and H.-B. Schüttler

81 **Materials and Measurements in Molecular Electronics**
Editors: K. Kajimura and S. Kuroda

82 **Computer Simulation Studies in Condensed-Matter Physics IX**
Editors: D.P. Landau, K.K. Mon, and H.-B. Schüttler

83 **Computer Simulation Studies in Condensed-Matter Physics X**
Editors: D.P. Landau, K.K. Mon, and H.-B. Schüttler

84 **Computer Simulation Studies in Condensed-Matter Physics XI**
Editors: D.P. Landau and H.-B. Schüttler

85 **Computer Simulation Studies in Condensed-Matter Physics XII**
Editors: D.P. Landau, S.P. Lewis, and H.-B. Schüttler

86 **Computer Simulation Studies in Condensed-Matter Physics XIII**
Editors: D.P. Landau, S.P. Lewis, and H.-B. Schüttler